Marina Yusoff · Nor Hayati Abdul Hamid
Mohd Fadzil Arshad · Ahmad Kamil Arshad
Ahmad Ruslan Mohd Ridzuan · Haryati Awang
Editors

InCIEC 2015

Proceedings of the International
Civil and Infrastructure Engineering
Conference

Springer

InCIEC 2015

Marina Yusoff · Nor Hayati Abdul Hamid
Mohd Fadzil Arshad · Ahmad Kamil Arshad
Ahmad Ruslan Mohd Ridzuan
Haryati Awang
Editors

InCIEC 2015

Proceedings of the International Civil
and Infrastructure Engineering Conference

Editors

Marina Yusoff
Faculty of Computer and Mathematical
  Sciences
Universiti Teknologi MARA
Shah Alam, Selangor
Malaysia

Nor Hayati Abdul Hamid
IIESM
Universiti Teknologi MARA
Shah Alam, Selangor
Malaysia

Mohd Fadzil Arshad
IIESM
Universiti Teknologi MARA
Shah Alam, Selangor
Malaysia

Ahmad Kamil Arshad
IIESM
Universiti Teknologi MARA
Shah Alam, Selangor
Malaysia

Ahmad Ruslan Mohd Ridzuan
IIESM
Universiti Teknologi MARA
Shah Alam, Selangor
Malaysia

Haryati Awang
IIESM
Universiti Teknologi MARA
Shah Alam, Selangor
Malaysia

Printed on acid-free paper

Contents

Part I
Bioremediation and Engineering

Removal of Hexavalent Chromium by Magnetite in Groundwater

Nurul Aqilah Abdul, Jalina Kassim and Amnorzahira Amir

Abstract Hexavalent chromium (Cr^{6+}) is a toxic contaminant that contaminates soil and groundwater and is listed as a priority contaminant. This study investigates removal of Cr^{6+} by magnetite (Fe_3O_4) in groundwater. The removal of Cr^{+6} is significantly dependent on the amount of reactive surface area on the surface of Fe_3O_4. Approximately 20 % of Cr^{+6} was removed by Fe_3O_4 in 20 min of reaction time. The removal of Cr^{+6} increases by 2 times as the concentration of Fe_3O_4 increases from 0.1 to 0.5 g. Results from this study provide a basic understanding of Cr^{6+} by Fe_3O_4 and can be suggested to be implemented at the real site contaminated with Cr^{+6}.

Keywords Cr^{6+} · Magnetite · Iron bearing soil mineral · Removal efficiency

1 Introduction

Chromium is listed by the USEPA as the top priority contaminant [1] which usually originates from anthropogenic sources. The wide spread of chromium is due to its intensive use in industries such as leather tanning, wood preservative, electroplating, and metal finishing [1–4]. Chromium is released from these industries through effluents [5] directly to the environment and thus contaminates the water sources, especially the groundwater environment.

In the environment, chromium exists in several oxidation states, e.g., Cr^{+0}, Cr^{+2}, Cr^{+3}, Cr^{+6} [6].

N.A. Abdul (✉) · J. Kassim · A. Amir
Faculty of Civil Engineering, Universiti Teknologi MARA,
40450 Shah Alam, Selangor, Malaysia
e-mail: aqilah_dikun@yahoo.com

J. Kassim
e-mail: jalina@salam.uitm.edu.my

A. Amir
e-mail: amnorzahira@salam.uitm.edu.my

However, it predominantly exists as trivalent chromium Cr^{+3} and hexavalent chromium Cr^{+6} [2]. Each of this speciation metal has its own characteristics such as bioavailability, toxicity, transport characteristic, and solubility in the natural environment [7]. Hexavalent chromium, (Cr^{+6}), is highly toxic and mobile in the environment [3, 5, 6, 8] and can cause skin irritation, liver damage, edema, and others [1]. Due to this characteristic, even a small amount of Cr^{+6} released into the environment can accumulate and become harmful for life.

Trivalent chromium (Cr^{+3}) is a trace element which is important in living organisms. Lack of chromium in the human body may have several impacts such as impaired glucose tolerance and glycosuria, while in animals it causes impaired growth and decrease in longevity.

Moreover, Cr^{+3} is less toxic and immobilized in the environment and can become a nutrient to the environment at a certain concentration [5, 6]. Both cannot be degraded once they are released to the environment. Hence, it is important to reduce Cr^{+6} to Cr^{+3} in the soil and the groundwater system [1].

In the natural environment, the toxic metal can be reduced to nontoxic encouraged by microorganisms [9] and also by abiotic natural reductants. The reductant serves as an electron donor which reduces Cr^{+6}. In the anoxic condition, Cr^{+6} attenuation can be obtained by dissolved Fe (II), FeS_2, FeS, and other reduction species [10]. From the previous research, it has been proved that Cr^{+6} in the groundwater system can be reduced to Cr^{+3} by natural organic matter such as fulvic acid and humic acid [8]. Besides, it has also been shown that toxic Cr^{+6} can be reduced by iron bearing soil mineral, magnetite, pyrite, mackinawite, and green rust [2, 7, 8]. Hence, in order to develop remedial technologies, the redox chemistry to reduce Cr^{+6} to Cr^{3+} needs to be applied to treat the contamination of soil and groundwater.

Previous research has shown that ferrous iron is important to reduce Cr^{+6} in the environment as the amount of ferrous iron is abundant in suboxic and anoxic. One of the sources of ferrous iron is magnetite, Fe_3O_4 [7], which has the ability to reduce Cr^{+6} to Cr^{+3}. Fe_3O_4 is one of the iron bearing minerals in the geosphere which has received much attention as a natural reductant for Cr^{+6} [7]. In soil, ferrous iron Fe (II) accumulates as iron oxide mineral, Fe_3O_4.

The reduction of the contaminant in the environment usually occurs through surface reaction [6, 11]. In soil and groundwater, the fate of Cr^{+6} is influenced by complexation and redox reaction. Reductive degradation occurs on the surface of Fe_3O_4 which is influenced by the density of reactive site. Cr^{+6} absorbed to the Fe_3O_4 surface will interact with each other by accepting the electron from ferrous iron which is available at the Fe_3O_4 surface.

Thus the redox reaction between ferrous iron and the Cr^{+6} was important to remediate the soil and groundwater system [6].

The aim of this study is to provide the fundamental knowledge to understand the reduction of Cr^{+6} by Fe_3O_4. We investigate the removal of Cr^{+6} by Fe_3O_4 and the effect of concentration of Fe_3O_4 on the removal of Cr^{+6} by Fe_3O_4.

2 Materials and Methods

2.1 Chemicals and Reagents

The chemicals utilized in this research were potassium dichromate ($K_2Cr_2O_7$) (Merck), Magnetite (Fe_3O_4) (99 %, Sigma Aldrich), Biological buffer Trizma, 2-Amino-2-(hydroxymethyl)-1, 3-propanediol (99 %, Sigma Aldrich) in order to maintain the pH solution and hydrochloric acid, HCl (98 %, ChemAR) to adjust the buffer to the desired pH. The following chemicals were used for colorimetric method: 1,5 diphenylcarbazide, H_2SO_4, acetone (99 %, Merck), anhydrous Na_2CO_3, and NaOH pallet (99 % Merck). Deaerated deionized water (DDW) was prepared using ultrapure water (18 Ω cm) purged by N_2. Anaerobic chamber was maintained purged with 95 % N_2 and 5 % H_2. All reagents and solutions used in the experiments were prepared using DDW.

2.2 Batch Experiment

Batch experiments were conducted to determine removal of Cr^{6+} by Fe_3O_4. To investigate the effectiveness of Cr^{6+} removal by Fe_3O_4, experiments were conducted in 40 mL amber glass vials. TRIS buffer solution (50 mM) was prepared using TRIS sodium salt and DDW. pH of buffer solution was adjusted to the desired pH using 0.1 M HCl acid. The exact amount of Fe_3O_4 0.10 g was weighted and transferred to each vial and TRIS buffer solution (50 mM) was poured into each vial without headspace to keep the pH suspension constant at pH 7.2. Cr^{6+} with a concentration of 1.0 mg/L was then introduced into each vial to initiate removal reaction between Fe_3O_4 and Cr^{6+}. Vials were then rapidly capped, mounted on a tumble mixer, and rotated at 7 rpm at room temperature (25 ± 0.5 °C) for 30 min.

The removal of Cr^{6+} was determined by measuring aqueous concentration of Cr^{6+} in the Fe_3O_4 suspension at each sampling time. At sampling time, samples were centrifuged for 5 min at 5000 rpm, and then aliquots of aqueous solution were collected to measure the Cr^{6+} concentration. Concentration of Cr^{6+} was determined by HACH Spectrophotometer DR5000, Method 8023. Samples and controls were prepared in duplicate. Samples were prepared by following the same procedures as the batch test described above.

To investigate the effect of the contact time by Fe_3O_4, various times (2, 5, 10, 15, 20, 30 and 45 min) were set up. 2.5 g/l of Fe_3O_4 concentration was used and the initial concentration of the Cr^{+6} was constant at 1 mg/l at pH 7.

To study the effects of the Fe_3O_4 concentrations on the removal of Cr^{+6} different concentrations of Fe_3O_4 (0.10, 0.20, 0.30 and 0.50 g) were weighted and transferred into vials. Initial concentration of Cr^{6+} was set at 1.0 mg/L at pH 7.2.

2.3   Analytical Procedure

Chromium, Cr^{6+} Concentration

Concentration of Cr^{6+} was determined using HACH Spectrometer DR5000, following Method 8023. Measurement wavelength of Cr^{6+} is 540 nm. The optimum detection range for this method was 0.010–0.7 mg/L. Aliquots of aqueous solution collected from samples and controls were transferred to 10 ml sample cell and ChromaVer® 3 Reagent Powder Pillow was added for Cr^{6+} determination.

3   Results and Discussion

3.1   Effect of Contact Time on Removal of Cr^{+6} by Fe_3O_4

Figure 1 shows the effect of contact time on the removal of Cr^{+6} by Fe_3O_4 at pH 7 by varying the contact times (2, 5, 10, 15, 20, 30 and 45 min) while the other parameters were constant. The result shows the removal of Cr^{+6} increase as the contact time was increased before reaching the equilibrium state and after reaching the equilibrium state the removal was constant [12]. Approximately 20 % of Cr^{+6} was removed by Fe_3O_4 in 20 min. This indicates that at the initial time, high density of reactive site was available on the surface of Fe_3O_4 for removal of Cr^{+6}.

However, no significant removal of Cr^{+6} by Fe_3O_4 was observed at the end of the contact time. These results show that the reactive site of Fe_3O_4 becomes saturated and is not able to remove Cr^{+6}. The reactive site was exhausted caused by the repulsive force among bulk phase and solute molecules of solid [12].

This finding suggests that reactive chemical species (e.g., Fe^{2+}) on the surface of Fe_3O_4 strongly controls the kinetic removal of Cr^{+6} in this system.

Fig. 1 The effect of contact time on the removal of Cr^{+6}. Magnetite concentration = 0.1 g, initial concentration of Cr^{+6} = 1 mg/L, pH = 7, agitation speed: 7 rpm
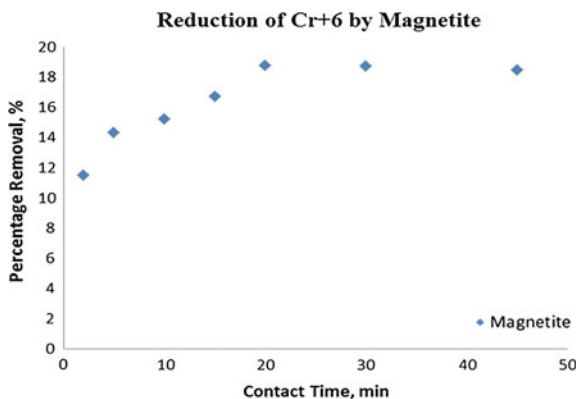
Fig. 2 The effect of
magnetite dosages on the
removal of Cr^{+6}. Initial
concentration of
$Cr^{+6} = 1$ mg/L, pH = 7,
agitation speed = 7 rpm
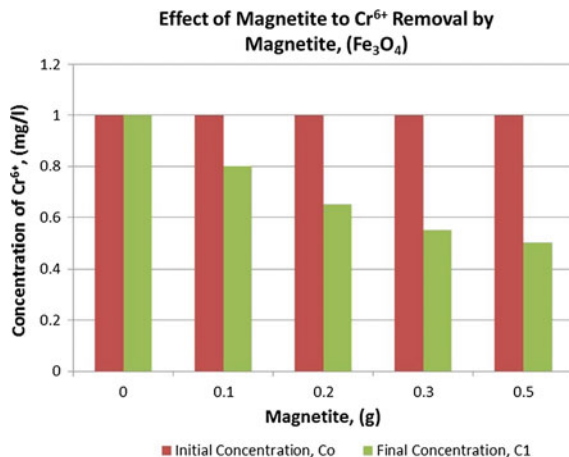
3.2 Effect of Magnetite Concentration on Removal of Cr^{+6} by Fe_3O_4

Figure 2 shows the effect of magnetite removal of concentration on Cr^{+6} by Fe_3O_4.

Experimental results show that the removal percentage of Cr^{+6} increases with increasing Fe_3O_4 concentration. High kinetic removal of Cr^{+6} by Fe_3O_4 was observed with the increasing concentration of Fe_3O_4 (0.1, 0.2, 0.3 and 0.5 g) at pH 7.

The removal of Cr^{+6} increases by 2 times as the concentration of Fe_3O_4 increases. This suggests that the active site available increases as the concentration of Fe_3O_4 increases from 0.1 to 0.5 g.

This result is consistent with previous studies of Cr^{6+} removal using nano zerovalent iron (nZVI). Yu et al., Liu et al. and Fu et al. report that efficiency of Cr^{6+} removal significantly increased with the increased in nZVI loading [13–15].

4 Conclusion

From this study the use of Fe_3O_4 as the absorbent for Cr^{+6} removal from soil and groundwater system was investigated. With respect to the biogeochemical condition, the removal of Cr^{+6} increased with the increase of contact time and magnetite concentration. Increasing the amount of magnetite concentration provides more reactive surface area and thus the removal of Cr^{+6} will continuously increase until it becomes saturated. It is proven that the reactive surface area on the surface of Fe_3O_4 plays a significant role to control kinetic removal of Cr^{+6}. Experimental results from this study can be used as a reference to identify potential reaction mechanisms that may involve during removal of Cr^{+6} by Fe_3O_4 in groundwater. This method can be suggested to be implemented at the real site contaminated with Cr^{+6}.

References

1. Hu, J., I.M.C. Lo, and G. Chen, *Comparative study of various magnetic nanoparticle for Cr (IV) removal.* Science Direct, 2007. **56**(249–256)
2. Ronald, R., Patterson, and S. Fendorf, *Reduction of Hexavalent Chromium by Amorphous Iron Sulfide.* Environmental Science & Technology, 1997. **31**: p. 2030–2044.
3. Ignaz, J.B. and J.H. Stephen, *Influence of Mineral Surfaces on Chromium(VI) reduction by Iron(II).* Environ. Sci. Technol, 1999. **33**: p. 4285–4291.
4. Boddu, V.M., et al., *Removal of Hexavalent Chromium from wastewater using a new composite chitosan biosorbent.* Environ. Sci. Technol, 2003. **2003**: p. 4449–4456.
5. He, Y.T. and S.J. Traina, *Cr(IV) Reduction and Immobilization by Magnetite under alkaline pH Condition: The role of Passivation.* Environ. Sci. Technol, 2005. **39**: p. 4499–4504.
6. Choi, J., Y. Jung, and W. Lee, *Fe(II)-initiated reduction of hexavalent chromium in heterogeneous iron oxide suspension.* Korean J. Chem. Eng, 2008. **25**(4): p. 764–769.
7. Crean, D.E., et al., *Engineering Biogenic Magnetite for Sustained Cr(IV) Remediation in Flow-through System.* Environ. Sci. Technol, 2012. **46**: p. 3352–3359.
8. Jiang, W., et al., *Cr(VI) Adsorption and Reduction by Humic Acid Coated on Magnetite.* Environmental Science & Technology, 2014. **48**(14): p. 8078–8085.
9. Cheng, Y., et al., *Bioremediation of Cr(VI) and immobilized as Cr(III) by Ochrobactrum anthropi.* Environ. Sci. Technol, 2010. **44**: p. 6357–6363.
10. Wadhawan, A.R., A.T. Stone, and E.J. Bouwer, *Biogeochemical Control on hexavalent chromium formation in estuarine sediment.* Environ. Sci. Technol, 2013. **47**: p. 8220–8228.
11. Jung, Y., J. Choi, and W. Lee, *Spectroscopic investigation of magnetite surface for the reduction of hexavalent chromium.* Science Direct, 2007. **68**: p. 1968–1975.
12. Werkneh, A.A., N.G. Habtu, and H.D. Beyene, *Removal of hexavalent chromium from tannery wastewater using activated carbon primed from sugarcane bagasse: Adsorption/desorption studies.* American Journal of Applied Chemistry, 2014. **2**(6): p. 128–135.
13. Fu, J., Ma, J, Xie, L., Tang, B., Han, W. & Lin, S., *Chromium removal using resin supported nanoscale zero-valent iron.* Journal of Environmental Management, 2013. **128**: p. 822–827.
14. Yu, R.-F., Chi, F-H., Chemg, W-P. & Chang, J-C, *Application of pH, ORP, and DO monitoring to evaluate chromium(VI) removal from wastewater by the nanoscale zero-valent iron (nZVI) process.* Chemical Engineering Journal, 2014. **255**: p. 568–576.
15. Qiu, X., Fang, Z., Yan, Z., Gu, F. & F. Jiang, F,, *Emergency remediation of simulated chromium(VI) – polluted river by nanoscale zero-valent iron: Laboratory study and numerical simulation.* Chemical Engineering Journal, 2012. **93–194**: p. 358–365.

Screening of Medium with Different Range of Waste Frying Oil (WFO), Sodium Nitrate (NaNO₃) and Sodium Chloride (NaCl) for Biosurfactant Production by Thermophilic *Anoxybacillus* sp. Using Fractional Factorial Design (FFD)

Nurul Fatihah Khairuddin, Tengku Elida Tengku Zainal Mulok, Khalilah Abdul Khalil, Wan Siti Atikah Wan Omar and Sabiha Hanim Saleh

Abstract In this study, culture medium was optimized for economic production of biosurfactant by *Anoxybacillus* sp. using different waste frying oil, sodium nitrate, and sodium chloride concentrations. Screening step was performed using the Design-Expert software (2 level full factorial design). The response variables are of value for surface tension reduction in the cell-free-culture medium as it indicates the biosurfactant production. The yield of biosurfactant was found to be the highest when surface tension was at the lowest value (42.30 mN/m) at a temperature of 55 °C, agitation 130 rpm, 9 % (v/v) waste frying oil (WFO), 0.5 % (w/v) sodium nitrate (NaNO₃), and 0.02 % (w/v) of sodium chloride (NaCl). The biosurfactant was observed to stable in the face of exposure to extreme temperature changes, pH conditions, and salinity. These physiochemical properties demonstrate the potential for using waste frying oil as an inexpensive material for biosurfactant production.

Keywords Biosurfactant · Surface tension · Waste frying oil · *Anoxybacillus* sp. · Full factorial design · MEOR

N.F. Khairuddin (✉) · T.E.T.Z. Mulok · K.A. Khalil
Faculty of Applied Sciences, School of Biology, Universiti Teknologi MARA,
40450 Shah Alam, Selangor, Malaysia
e-mail: nurulfatihah8826@gmail.com

W.S.A.W. Omar
Faculty of Applied Sciences, School of Biology, Universiti Teknologi MARA,
26000 Bandar Tun Razak Jengka, Pahang, Malaysia

S.H. Saleh
Faculty of Applied Sciences, School of Chemistry and Environment,
Universiti Teknologi MARA, 40450 Shah Alam, Selangor, Malaysia

1   Introduction

Due to economic concerns, environmental issues, and restrictive law, the demand for biologically produced chemicals is steadily increasing. Microbial surfactant or commercially known as biosurfactant are biomolecules that are synthesized by a variety of microorganisms. Biosurfactants are amphiphilic molecules that have two domains, hydrophobic and hydrophilic [1]. The accumulations of these molecules at the interface induce the formation of micelles which can lead to the reduction of surface and interfacial tensions. This enhances the solubility and mobility of the insoluble or hydrophobic compounds [3, 22]. Biosurfactants are usually synthesized under specific growth conditions either on water miscible or oily substrate [5, 22]. Biosurfactants have huge potential to replace synthetic (chemically-produced) surfactants that are currently used, which will cause bad side effects with long-term use. Unlike most synthetic surfactants, many biosurfactants function effectively at extremes of temperature, salinity, wide range of pH, low toxicity, better foaming (useful in mineral processing), and environmental friendly nature [20]. For these reasons, biosurfactants have gained importance in various commercial applications in biological industries, food processing, pharmaceuticals, biomedical, cosmetics, and agricultural industries. Moreover, they are also suited for petrochemical and environmental application such as bioremediation of polluted sites, oil spill management, and enhanced oil recovery [2].

Pakpitcharoena et al. [14] claim that thermophilic *Anoxybacillus* sp. is a biosurfactant producer, but studies of biosurfactant production using this genus are scarce. In addition, there are no reports on the production of biosurfactant by *Anoxybacillus* sp. using waste frying oil. The uses of thermophilic organisms for biotechnological processes are of great importance as their biochemical pathway can adapt easily to industrial conditions, especially at high temperatures. Most of them are nonpathogenic with high secretion capacity. The genus *Anoxybacillus* belongs to the order *Bacillales* under the *Firmicutes* phylum in the domain bacteria. The first strict anaerobic *Anoxybacillus* sp., *Anoxybacillus pushchinensis*, was isolated from manure [16]. In addition to *A. contaminans* [9], which was isolated from contaminated gelatine from a manufacturing plant, other newly described species originated from various geothermal sites around the globe. Examples of these species include *A. flavithermus*, *A. gonensis*, *A. ayderensis*, *A. kestanbolensis* and *A. amylolyticus* [18]. Recently, *Anoxybacillus salavatliensis* was isolated from a well pipeline [7].

Although the advantages of biosurfactant are well known, only a few biosurfactants are produced on a large scale for commercial application, mainly due to their considerable production and recovery costs. Therefore, aiming at the use of these *Anoxybacillus* sp. in producing large-scale biosurfactants, the yields must be improved which can be achieved through optimization of the culture media. In this work, biosurfactants produced by previously isolated *Anoxybacillus* sp. were optimized through proper manipulation of various ranges of carbon (waste frying oil, WFO), nitrogen (sodium nitrate, $NaNO_3$), and salinity (sodium chloride, NaCl)

using fractional factorial design (FFD) for screening more than 2 factors which varied over 2 levels and identified interaction among the factors toward the response.

2 Materials and Methods

2.1 Microorganisms

The biosurfactant-producing bacteria (*Anoxybacillus* sp.) previously isolated from a natural hot spring located in Sungai Klah, Tanjung Malim, Perak, Malaysia was used. The isolate was preserved at -80 °C in an NB medium supplemented with 20 % (v/v) glycerol solution. The composition of NB medium was (g/l): D(+) glucose, 1: Peptone, 15; NaCl, 6; yeast extract, 3. The pH was adjusted to 7.0.

2.2 Media Preparation and Culture Conditions

The cultivation was performed with a 250 mL Erlenmeyer flask containing 100 mL of minimal salt medium (MSM) supplemented with 1 % (v/v) trace element and 10 % (v/v) of inoculum (10^{-7} of cell density). The WFO, $NaNO_3$, and NaCl were added separately. The composition of the MSM (g/L): KH_2PO_4-0.2; K_2HPO_4-0.3; $MgSO_4.7H_2O$-0.5; $CaCl_2$-0.15; $NaCl_2$-0.5; $NaNO_3$-1. The composition of trace element was (mg/L): $ZnSO_4.7H_2O$-50; $MnCl_2.4H_2O$-400; $CoCl.6H_2O$-1; $CuSO_4.5H_2O$-0.4; H_3BO_2-2; $NaMoO_4.2H_2O$-500 [4]. The medium was cultured at temperature 55 °C and shaken at 130 rpm. Sampling was done after 4 days of cultivation period for analysis.

2.3 Determination of Surface Tension Activity

All the measurements were made on culture supernatant after cell removal by centrifugation at 7500 rpm for 15 min in a centrifuge (Heraeus Biofuge) at 4 °C. The surface tension was then analyzed at room temperature using Drop shape Analyzer, DSA 100 (KRUSS, Germany). The experiments were performed in duplicate.

2.4 Experimental Design: Fractional Factorial Design (FFD) and Data Analysis

A preliminary screening was carried out based on FFD with 3 factors which included waste frying oil (WFO), sodium nitrate ($NaNO_3$), and sodium chloride

Table 1 Experimental range levels of the independent variable using 2^3 fractional factorial design

Independent variables	Code levels		
	−1	0	+1
A: WFO % (v/v)	1	5	9
B: NaNO$_3$ % (w/v)	0.1	0.3	0.5
C: Salinity % (w/v)	0.02	0.07	0.13

(NaCl); the design matrix for the experiments are shown in Table 1. A 2^3 full FFD was conducted to determine the factors and their range of composition in the media that most influenced the response, which was surface tension. The experimental setting with 16 duplicated runs varied over 2 concentration levels (−1, +1) with 5 replicated runs at center points in order to estimate the pure error and thus give the prediction of the model [12]. The statistical experimental design and regression analysis were carried out using the Design-Expert software (Stat-Ease Inc., MN, USA, version 6.0.6).

An analysis of variance (ANOVA) was performed to further evaluate the model in order to determine the significant factors on surface tension.

2.5 Determination of Biosurfactant Stability

Cell-free broth obtained after harvesting the culture supernatant at 7500 rpm for 15 min was used for stability studies of the surface tension (mN/m) reduction. Five milliliters of cell-free culture supernatant at 4 days of incubation were exposed to various temperatures (55–25 °C, 25–4 °C, 25–70 °C, 25–100 °C, 25–121–25 °C, 25–121–4 °C) and at different ranges of pHs (2–12). The electrolyte effect was also tested at different range of salinity ((w/v): 2–10 %). The stability of the biosurfactant was measured based on the value of surface tension reduction (mN/m).

3 Results and Discussion

3.1 Fractional Factorial Design (FFD) and Data Analysis

The factorial design enables the identification of the medium components that play a significant role on cell growth as well as the ranges within the medium components vary. A 2^3 FFD was employed and for each of these factors, a wide range of concentrations was selected as shown in Table 1, whereas factor A (WFO) ranging from 1 to 9 % (v/v), B (NaNO$_3$) ranging from 0.1 to 0.5 % (w/v), and C (NaCl) ranging from 0.02 to 0.13 % (w/v).

Results of the experimental design performed to achieve the optimum medium condition response for surface tension reduction are shown in Table 2. For each run,

Table 2 Screening of variables using factorial design with surface tension reduction as the response

Run	WFO % (V/V) A	NaNO$_3$ % (w/v) B	NaCl % (w/v) C	Response surface tension (mN/m)
1	+1	+1	+1	47.47
2	+1	+1	+1	47.77
3	+1	+1	−1	43.09
4	+1	+1	−1	44.02
5	+1	−1	+1	54.48
6	+1	−1	+1	54.50
7	+1	−1	−1	49.15
8	+1	−1	−1	49.36
9	−1	−1	−1	58.35
10	−1	−1	−1	57.45
11	−1	−1	+1	58.32
12	−1	−1	+1	56.13
13	−1	+1	−1	53.12
14	−1	+1	−1	53.33
15	−1	+1	+1	55.20
16	−1	+1	+1	55.12
17	0	0	0	42.30
18	0	0	0	45.62
19	0	0	0	45.68
20	0	0	0	46.07
21	0	0	0	47.09

the surface tension reduction was measured as a response that is proportional to the production of biosurfactant [17, 21]. The experimental setting with 16 duplicated runs varied over 2 concentration levels (−1, +1) with 5 replicated runs at center points (0). Based on the results obtained, the value of surface tension reduction varied from 58.35 to 42.30 mN/m after 4 days of cultivation.

The effects of the medium composition on surface tension were examined in Table 2. Based on the result obtained, the lowest value of surface tension was achieved when *A, B,* and *C* were at the middle level (0). WFO and NaNO$_3$ were used by *Pseudomonas aeruginosa* zju.um1as raw materials for fermentation of rhamnolipids [23], whereas Liu et al. [13] reported that *Alcaligenes* sp. S-XJ-1 produced the highest yield of biodemulsifier achieved with increases of WFO. According to Bergey's manual, a common characteristic of all *Anoxybacillus* sp. is independence from NaCl and a comparatively low resistance to salt (5–6 % NaCl inhibit growth). The results prove that the growth of isolated *Anoxybacillus* sp. is influenced by the increased and decreased concentrations of WFO, NaNO$_3$, and salinity. The value of surface tension was varied from 42.30 to 58.35 mN/m after cultivation for 4 days.

Table 3 Anova results of the first-order model for 2^3 full factorial design

Source	DF	Sum of square	Mean of square	F or t value	Significant (prob > F)
Model	6	353.67	58.95	45.41	<0.0001
Curvature	1	184.10	184.10	141.81	<0.0001
Residual	13	16.88	1.30	–	–
Lack-of-fit	1	0.52	0.52	0.38	0.5490
Pure error	12	16.36	1.36	–	–
Correlation error	20	554.65	–	–	–
$R^2 = 0.9545$	Adjusted $R^2 = 0.9334$		–	–	–

Table 4 Regression analysis of the 2^3 full factorial design

Variable	DF	F value	p-value
A	1	157.41	<0.0001
B	1	71.81	<0.0001
C	1	21.47	0.0005
AB	1	6.55	0.0238
AC	1	12.45	0.0037
ABC	1	2.75	0.1211

The analysis of variance (ANOVA) of the first-order model is shown in Table 3, while regression analysis is shown in Table 4. The p-value was used to determine the significance of each coefficient and the degree of interaction between each independent variable [6]. The independent variables are more significant with greater F-value and smaller p-value (less than 0.005) [6, 12]. If p-value is greater than 0.1000, it indicates that they are insignificant [6, 12]. From the result, the model and several factors interaction (BC (data not shown) and ABC) were not significantly different ($p > 0.005$) and the R^2 value obtained was more than 90 % (data not shown). The quality of fit of the equation is expressed by the determination coefficient R^2. The coefficient of determination, R^2, is an indicator of fitting the model to the experimental data [10].

The insignificant factors were removed from the experimental design in order to improve the result. In this study, only factor CB was removed because of its influence on the response (surface tension) since the bacterial was unable to produce biosurfactant in the absence of carbon source in the medium to support the bacterial growth [3]. Although factor ABC is insignificant, it must be considered in the medium optimization since the value of the regression coefficient was attained with a very high coefficient of determination, $R^2 = 0.9545$ and adjusted $R^2 = 0.9334$. The value of 0.9545 obtained indicated that the model could be explained with ∼95 % of the variability in response by the first-order model. The adjusted model showed no significant lack-of-fit, meanwhile the p-value of the model was <0.0001, thus indicating that the model is highly significant and the

relationship between the surface tension and the factors is adequately represented [12].

As a result, final-order Eq. (1) was generated based on the first-order model to determine the surface tension response (y_1) to the medium composition consisting of WFO (A), NaNO$_3$ (B), and NaCl (C) factors which gave:

$$y = 42.30 - 3.57A - 2.41B + 1.32C - 0.73AB + 1.00AC - 0.47ABC \quad (1)$$

For every unit increased in C and AC, an increase of 1.32 and 1.00 units was observed, respectively, in y. In contrast, for every unit increase in A, B, AB, and ABC, y will decrease by 3.57, 2.41, 0.73, and 0.47 units respectively.

The response surface plot of interaction between A and B on surface tension is shown in Fig. 1a. The lowest value of surface tension was achieved when A and B were at the maximum level. The use of high concentrations of A and B were carbon and nitrogen source function as a growth supporter to the bacteria and later contribute to the synthesis of biosurfactant and thus reduce the surface tension [19]. The response surface plot of interaction between A and C shown in Fig. 1b indicates that the value of surface tension is reduced at the lowest concentration of C and at the highest concentration of waste frying oil (A). From this result, it is proved that the higher and the lower value of each variable affects the growth of *Anoxybacillus* sp.

3.2 Study of Biosurfactant Stability

The stability of the biosurfactant was checked by subjecting the fermentation broth at 4 days of incubation to conditions of high stress, which includes temperature, pH, and salinity. The surface tension showed little variation and remained nearly constant at around 42–43 mN/m when the temperature was varied from 4 to 121 °C. From the results obtained in Table 5, it is shown that the biosurfactant is stable when it is introduced to extreme temperature changes.

With respect to pH variation from 2 to 12 as shown in Table 6, the values of surface tension centered around 42 mN/m without large deviations. The lowest surface tension was recorded when the sample was at pH 7 and the highest surface tension value was recorded at acidic condition which was at pH 2, 42.97 mN/m respectively. The surface activity of the sample relatively remained stable between pH 10 and 12 indicating preference for alkaline conditions.

The salinity was varied over the range of 0–10 % (w/v). As shown in Table 7 the effect on surface tension was around 42 mN/m; the result was observed to be similar to the effect of pH with largely no changes but the lowest value of surface tension reduction was recorded when introducing the biosurfactant at concentration of salinity at 6 % (w/v) which was 42.09 mN/m. According to Bergey's manual, at 5–6 % (w/v) NaCl the growth of *Anoxybacillus* sp. is inhibited, but from the result, the surface tension activity was stable within that range of NaCl [15].
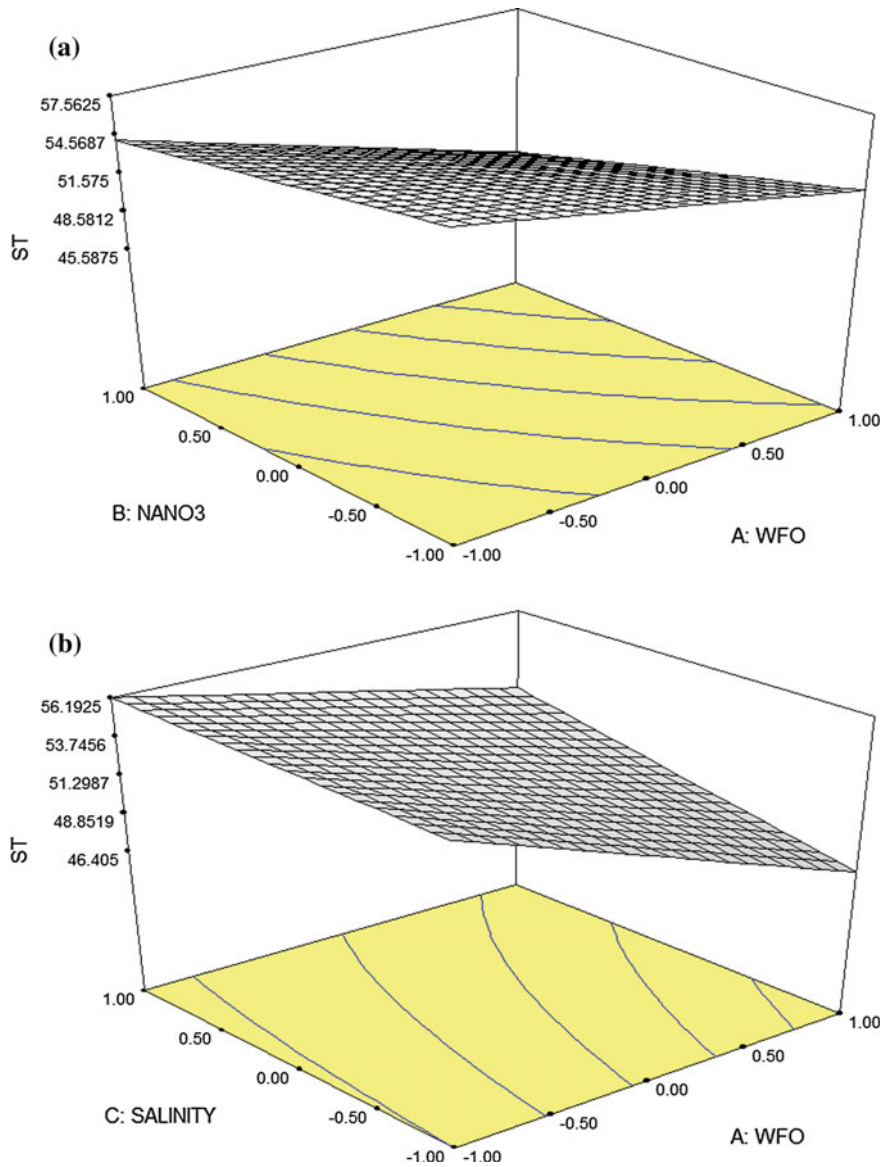
Fig. 1 Response surface plot of the interaction between **a** carbon source (WFO) and nitrogen source (NaNO$_3$) **b** carbon source (WFO) and salinity (NaCl) at 4 days cultivation period

The production of biosurfactant by microorganisms has been a subject of increasing interest in recent years, especially due to their increasing potential application. In the present study, results showed that *Anoxybacillus* sp. producing biosurfactant was stable at different temperature, pH, and salinity. It agrees with the

Table 5 Effect of surface tension on temperature changes

Temperature changes (°C)	Surface tension (mN/m)
From 55 to 25 °C	42.47
From 55 to 25 °C then to 4 °C	42.69
From 55 to 25 °C then to 70 °C	42.81
From 55 to 25 °C then to 100 °C	43.03
From 55 to 25 °C then to 121 to 25 °C	42.52
From 55 to 25 °C then to 121 to 4 °C	42.82

Table 6 Effect of surface tension on pH changes

pH	Surface tension (mN/m)
2	42.97
4	42.76
6	42.81
7	42.37
8	42.47
10	42.50
12	42.76

Table 7 Effect of salinity on surface tension

Salinity % (w/v)	Surface tension (mN/m)
0	42.20
2	42.35
4	42.47
6	42.09
8	42.45
10	42.46

stability results showed by *Bacillus sphaericus* EN3 and *Bacillus azotoformans* EN16 [11]. There are several reports on the stability of biosurfactants at extreme conditions [8, 9]. Taking into cognizance the optimum conditions for the biosurfactants' activity, one can suggest the potential applicability of these surfactants in microbial enhanced oil recovery (MEOR) since these conditions (high temperature, pH, and salinity) prevail in oil reservoirs.

4 Conclusion

In conclusion, through the 2^3 full factorial design, it was observed that the range of waste frying oil, sodium nitrate, and sodium chloride at concentrations of 1–9 % (v/v), 0.1–0.5 % (w/v), and 0.02–0.13 % (w/v), respectively, were the most significant range for biosurfactant production by *Anoxybacillus* sp. In addition, the

produced biosurfactant with high stability at different temperature changes, pH, and salinity makes these biosurfactants potential candidates to be used in bioremediation of contaminated sites and in the petroleum industry (MEOR) where drastic conditions are very common.

References

1. Adamu, A., Ijah, U.J.J., Riskuwa, M.L., Ismail., H.Y., and Ibrahim, U.B. (2015). Study on Biosurfactant Production by Two *Bacillus* Species. *International Journal of Scientific Research in Knowledge, 3*(1), 13–20. doi: http://dx.doi.org/10.12983/ijsrk-2015-p0013-0020
2. Al-Sulaimani, H., Joshi, S., Al-Wahaibi, Y., Al-Bahry, S.N., Elshafie, A., and Al-Bemani, A. (2011). Microbial biotechnology for enhancing oil recovery: Current developments and future prospects. *Biotechnol. Bioinf. Bioeng. J, 1*, 147–158.
3. Ariji, A. L., Rahman, A.R.Z.N.R., Basri, M., and Salleh, B.A. (2007). Microbial surfactant. *Asia Pacific Journal of Molecular Biology and Biotechnology, 15*(3), 99–105.
4. Balch, W. E., Fox, G.E., Magnum, L.J., Woese, C.R., and Wolfe, R.S. (1979). Methanogens: Reevalution of a unique biological group. *Microbiol. Rev, 43*, 260–296
5. Cameotra, S. S. a. M., R.S. (2004). Recent applications of biosurfactants as biological and immunological molecules. *ELSEVIER, 7*, 262–266.
6. Chaganti, S. R., Kim, D.H., Lalman, J.A., and Shewa, W.A. (2012). Statistical optimization of factors affecting biohydrogen production from xylose fermentation using inhibited mixed anaerobic cultures. *INTERNATIONAL JOURNAL OF HYDROGEN ENERGY, 37*, 11710–11718.
7. Cihan, A. C., Ozcan, B., and Cokmus, C. (2010). Anoxybacillus salavatliensis sp. nov., an ®-glucosidase producing, thermophilic bacterium isolated from Salavatli, Turkey. *J. Basic Microbiol, 50*, 1–11.
8. Davishi, P., Ayatollahi, S., Mowia, D., and Niazi, A. (2011). Biosurfactant production under extreme environmental conditions by an efficient microbial consortium, ERCPP1-2. *Colloids surfaces and Biointerfaces*. doi: http://dx.doi.org/10.1016/j.colsurfb.2011.01.011.
9. De Clerck, E., Rodriguez-Diaz, M., Vanhoutte, T., Heyrman, J., Logan, N.A., and DeVos, P. (2004). Anoxybacillus contaminans sp. nov. and Bacillus gelatini sp. nov., isolated from con taminated gelatin batches. *Int. J. Syst. Evol. Microbiol.*, 941–946.
10. Galonde, N., Brostaux, Y., Richard, G., Nott, K., Jerôme, C., and Fauconnier, M.L. (2013). Use of response surface methodology for the optimization of thelipase-catalyzed synthesis of mannosyl myristate in pure ionic liquidNadine. *Process Biochemistry, 48*, 1914–1920. doi: http://dx.doi.org/10.1016/j.procbio.2013.08.023
11. Ibrahim, M. L., Ijah, U.J.J., Manga, S.B., Bilbis, L.S., and Umar, S. (2013). Products and Partial characterization of biosurfactant produced by crude oil degrading bacteria. *Intentional Biodeterioration and Biodegradation, 81*, 28–34.
12. Khalilah, A. K., Shuhaimi, M., Rosfarizan, M., Arbakariya, A., Yamin, S., Yazid, A. M., Siti-Aqlima, A., and Farrah, A. D. (2014). Optimization of Milk-Based Medium for Efficient Cultivation of *Bifidobacterium pseudocatenulatum* G4 Using Face-Centered Central Composite-Response Surface Methodology. *Hindawi Publishing Corporation, BioMed Research International, 2014*, 1–11
13. Liu, J., Peng, K., Huang, X., Lu, L., Cheng, H., Yang, D., Zhou, Q., and Deng, H. (2011). Application of waste frying oils in the biosynthesis of biodemulsifier by a demulsifying strain *Alcaligenes* sp. S-XJ-1. *Journal of Environmental Sciences, 23*(6).

14. Pakpitcharoena, A., Potivejkulb, K., Kanjanavasa, P., Areekita, S., and Chansiria, k. (2008). Biodiversity of thermotolerant Bacillus sp. producing biosurfactants, biocatalysts, and antimicrobial agents. *ScienceAsia, 34*, 424–431. doi: 10.2306/scienceasia1513-1874.2008. 34.424

15. Paul De Vos., G., G.M., Jones, D., Krieg, N.R., Ludwig, W., Rainey, F.A., Schleifer, K.H., and Whitman, W.B. (2009). Bergey's Manual of Systematic Bacteriology. *Springer, 3*(2).

16. Pikuta, E., Lysenko, A., Chuvilskaya, N., Mendrock, U., Hippe, H., Suzina, N., Nikitin, D., Osipov, G., and Laurinavichius, K. (2000). Anoxybacillus pushchinensis gen. nov., sp. nov., a novel anaerobic, alkaliphilic, moderately thermophilic bacterium from manure, and description of Anoxybacillus flavithermus comb. *nov, Int. J. Syst. Evol. Microbiol, 50*, 2109–2117.

17. Płaza, G. A., Pacwa-Płociniczak, M., Piotrowska-Seget, Z., Jangid, K., and Wilk, K. A. (2011). Agroindustrial wastes as unconventional substrates for growing of *Bacillus* strains and production of biosurfactant. *Environment Protection Engineering, 37*(3), 63–71.

18. Poli, A., Esposito, E., Lama, L., Orlando, P., Nicolaus, G., de Appolonia, F., Gambacorta, A., and Nicolaus, B. (2006). Anoxybacillus amylolyticus sp. nov., a thermophilic amylase producing bacterium isolated from Mount Rittmann (Antarctica). *Syst. Appl. Microbiol, 29*, 300–307.

19. Pradnya, A. J., and Dhiraj, B.S. (2014). Effect of carbon and nitrogen source on biosurfactant production by biosurfactant producing bacteria isolated from petroleum contaminated site *Advances in Applied Science Research, 5*(6), 159–164

20. Santos, D. C. S., Fernandez, G.L., Alva, R.C.J., and Roque, A.D.R.M. (2010). Evaluation of substrates from renewable-resources in biosurfactants production by Pseudomonas strains. *African Journal of Biotechnology, 9*(35), 5704–5711.

21. Saravanan, V., and Vijayakumar, S. (2014). Production of biosurfactant by *Pseudomonas aeruginosa* PB3A using agroindustrial wastes as a carbon source. *Malaysian Journal of Microbiology, 10*(1), 57–62.

22. Singh, A., Hamme, V.D.J., and Ward, P.O. (2007). Surfactants in microbiology and biotechnology: Part 2. Application aspects. *Biotechnology Advances*(25), 99–121.

23. Zhang, H., Xiang, H., Zhang, G., Cao, X an Meng, Q. (2009). Enhanced treatment of waste frying oil in an activated sludge system by addition of crude rhamnolipid solution. *Journal of Hazard Material, 167*, 217–223.

Escherichia coli Wild Type Cells Disruption by Low Intensity Ultrasound for Bacterial Disinfection

N.M. Budari, M.F. Ali, K.H. Ku Hamid, K.A. Khalil, M. Musa and N.F. Khairuddin

Abstract Bacterial contamination issues are commanding the attention of water and wastewater treatments. There are many treatment methods to eliminate pathogenic bacteria. Therefore, finding efficient disinfection methods is essential to achieving safe water and protecting the human health. Therefore, this paper aims to isolate and identify *Escherichia coli* from municipal wastewater treatment plant and to investigate the performance of flow cell ultrasound as the bacterial disruption. In order to confirm the identification of *Escherichia coli* isolated, 16S rRNA sequence analysis was involved. In this particular study, the performance of flow cell ultrasound was measured by disruption of *Escherichia coli* cells concentration (10^4 cfu/ml), two types of flow rate (25 and 70 ml/min) with varies amplitude and power intensity. *Escherichia coli* isolated was determined and high homology was found that 16 s rRNA sequence of *Escherichia coli* with a level of identity 95 %. The flow rate at less power intensity and less oscillations amplitude at 35 % is statistically significant and higher of bacterial disruption than the greater power

N.M. Budari (✉) · M.F. Ali
Faculty of Civil Engineering, Universiti Teknologi MARA (UiTM),
40450 Shah Alam, Malaysia
e-mail: ainis_0311@yahoo.com

M.F. Ali
e-mail: mdfozi@salam.uitm.edu.my

K.H. Ku Hamid · M. Musa
Faculty of Chemical Engineering, Universiti Teknologi MARA (UiTM),
40450 Shah Alam, Malaysia
e-mail: kuhalim@salam.uitm.edu.my

M. Musa
e-mail: mohibah@salam.uitm.edu.my

K.A. Khalil · N.F. Khairuddin
Faculty of Applied Science, Universiti Teknologi MARA (UiTM),
40450 Shah Alam, Malaysia
e-mail: khali552@salam.uitm.edu.my

N.F. Khairuddin
e-mail: nurulfatihahkhairuddin@yahoo.com

intensity, $p = 001$. Meanwhile, higher flow rate was affected by increases of cycle treatment and consequences of the higher disruption of *Escherichia coli* cells. In addition, ultrasound technology, which includes as an advance technology as improvements to the sustainable technology associated with the increases of public health and environmental quality.

Keywords Flow cell ultrasound · *Escherichia coli* · Bacterial disruption · Low intensity ultrasound

1 Introduction

The rapid growth in urbanization and industrialization causes more water-related disease in the environment. Common water-related pathogenic microbes include bacteria, viruses, protozoa, and other organisms. Among them, pathogenic bacteria can occur on surface water in large numbers, either being excreted in feces or occurring naturally in the environment. Disease causing bacteria that can be transmitted by water include the genera of *Escherichia, Shigella, Salmonella, Legionella,* and *Campylobacter,* etc. [1]. These pathogenic bacteria can lead to severe or fatal diseases, such as tuberculosis, pneumonia, typhoid fever, diarrhea, cholera, etc. [2]. Increasingly, bacterial contamination issues are commanding the attention of water and wastewater treatments [3]. There are many treatment methods to eliminate pathogenic bacteria. Therefore, finding efficient disinfection methods is essential to achieving safe water and protecting the human health [4–6].

In this study, *Escherichia coli* isolated from municipal wastewater treatment plant was chosen as Gram-negative bacteria. *Escherichia coli* were non-spore forming and facultative anaerobic bacterium of the family *Enterobacteriaceae* and as a rod-shaped cellular morphology bacterium that is commonly found in the lower intestine of warm-blooded organism [7]. *Escherichia coli* such as 0157:H7, are pathogenic and they can cause serious food poisoning in human [4, 8]. The morphology of bacterial cells is a straight cylindrical rod with the diameter of 1.1–1.5 µm and the length of 2.0–6.0 µm. The growth pH condition of *Escherichia coli* species is from 5–9 and the optimal growth temperature occurs at 35–37 °C [4]. *Escherichia coli* are covered by pili. These help the organisms as possible mediators of attachment to urinary tract epithelial cells of the host and may cause urinary tract infections [9].

Ultrasound treatment with sonochemistry method revealed the destruction and disintegrates of physical and chemical contaminants and pathogenic microorganism [10, 11]. The efficiency of ultrasound treatment in disruption of microorganism in the water with the simultaneous effects of bubble collapse which comprises the generation of localized spots with high temperature and pressure, reactive free radicals, and turbulences induced by the oscillations of bubbles [10, 12]. Ultrasound technology includes as an advance technology in the disinfection process, as

Table 1 Operation condition of flow cell ultrasound

Amplitude on ultrasound generator (%)	Power intensity (W/cm^2) $Q = 25$ ml/min	Power Intensity (W/cm^2) $Q = 70$ ml/min
35	0.4184	1.0268
50	0.5468	1.0781
64	0.6135	1.1038
92	0.9190	1.2578

improvements to the sustainable technology associated with the increases of public health and environmental quality.

Numerous studies have found that *Escherichia coli* cells can be disrupted by ultrasound treatment in disinfection process. However, there are limited studies on the disruption of *Escherichia coli* wild type cells by lower energy consumptions to increase the ultrasonic application efficiency especially to increase technical and economic feasibility. Therefore, this paper aims to isolate and identify of *Escherichia coli* from municipal wastewater treatment plant and to investigate the performance of flow cell ultrasound as the bacterial disruption in the disinfection process. In order to confirm the identification of *Escherichia coli* isolated, 16S rRNA sequence analysis was involved. In this particular study, the performance of flow cell ultrasound with *Escherichia coli* cells (10^4 cfu/ml), was investigated with three independent variables, namely (i) flow rate (25 and 70 ml/min), (ii) varies of amplitude and power intensity (Table 1), (iii) sonication time (50 min) meanwhile one dependent variable involved disruptions of cells (% cfu/ml).

2 Methodology

2.1 Isolation and Identification of Escherichia Coli

One 500 ml water sample was collected as a grab sample for the cultivation and isolation of *Escherichia coli*. The samples were collected in sterilised 500 ml Polyethylene bottles in order to avoid any contamination [13]. The samples were stored at ±4 °C during the sampling event in the College Mawar Wastewater Treatment Plant UiTM Shah Alam and continuously stored at ±4 °C, including the transportation time <0.5 h, until processing in the lab, within 12 h [14, 15].

Activity for isolation and cultivation is conducted under biological hazard safety cabinet, as a purpose for eliminating contamination from the environment. Enrichment process was conducted to support the growth of *Escherichia coli* wild type cells, where samples were then enriched in 40 ml of Nutrient Broth (NB) (Oxoid, Hampshire, United Kingdom (CM0001)), vortex, and incubated at 35–37 °C for 24 h. Function of enriched process as purpose of adaptation in the new environment and supports the growth of bacteria. A loopful (10 μl) of each enrichment was then plated in duplicate on *Escherichia coli* selective agar, Eosin
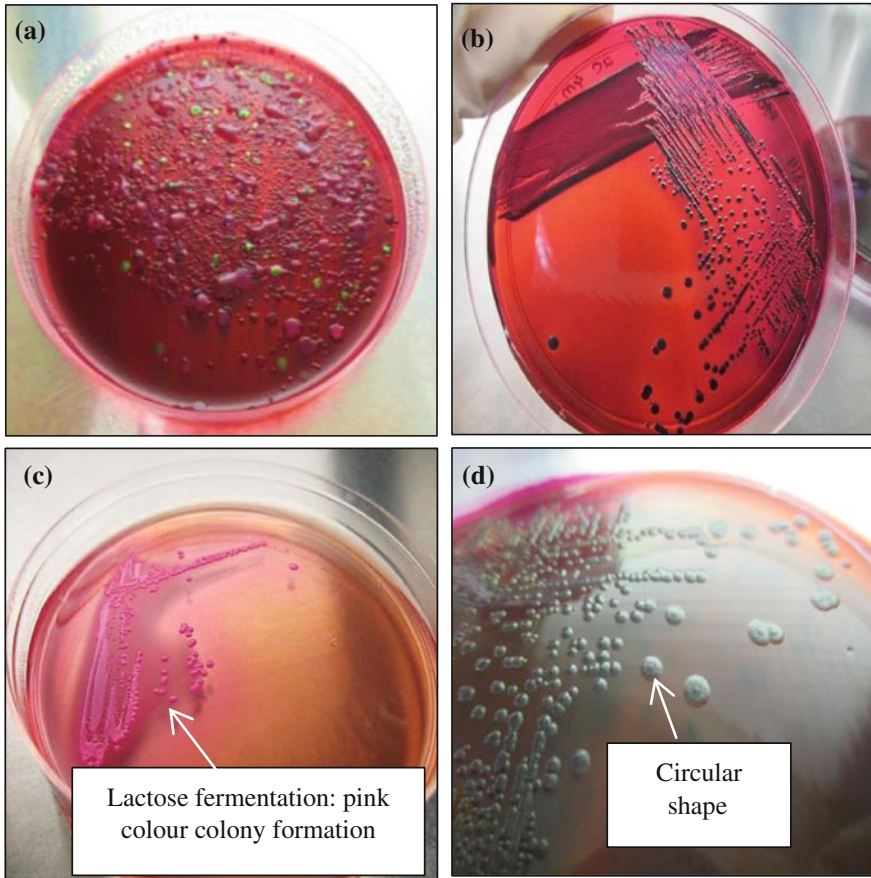
Fig. 1 **a** Mixed culture of wastewater bacteria effluent in EMB agar, **b** Pure culture of *Escherichia coli* in EMB agar, **c** Pure culture of *Escherichia coli* in SS agar, **d** Shape of colony for *Escherichia coli* in EMB agar

Methylene Blue agar (EMB) (Merck, Darmstadt, German) for the isolation process. Plates were incubated at 35–37 °C for 24 h and resulting green metallic sheen on Eosin Methylene Blue agar for *Escherichia coli* (Fig. 1a). Selections were considered presumptive *Escherichia coli* bacteria. For long-term storage of isolated bacteria, bacteria from the pure nutrient broth (Oxoid, Hampshire, United Kingdom (CM0001)), cultures were transferred to new nutrient broth (NB), and the NB were incubated at 35–37 °C for 18 h and after incubation were stored at 4 °C [15–17]. As further analysis, Gram staining method was observed by Olympus CX21FS1 educational microscope with magnification 100 times (Olympus, Melville, New York). More detailed analysis for identification of *Escherichia coli* by 16S rRNA sequence gene was sent to Tropical Infectious Diseases Research & Education Centre (TIDREC), Faculty of Medicine, Universiti Malaya.
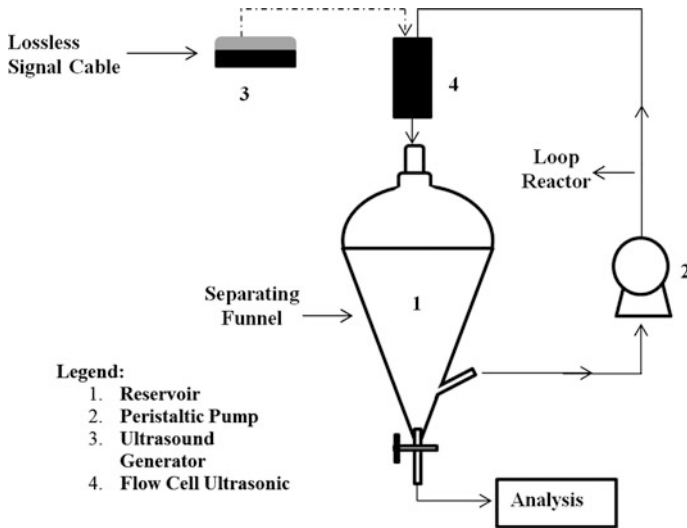
Fig. 2 Schematic diagram of experimental setup

2.2 Flow Cell Ultrasound

Flow cell ultrasound was fabricated as continuous flow process and to increase the 50 min residence time the reactor was adjusted to loops reactor as seen in schematic diagram of the experimental setup (Fig. 2). The specification of ultrasonic was operating at 30 kHz of a constant frequency with adjustment of amplitude 35, 50, 64, and 92 % to the system (Table 1) and 50 min sonication time. Amplitude from ultrasound generator produced varied power intensities and depended on the flow rate in the looping system (Table 1). One inlet (influent) for sample water and one outlet for sample effluent are designed at the flow cell ultrasonic. The volume of water sample was 50 ml, where phosphate buffered saline was used as sonication media for ultrasound treatment with 10^4 cfu/ml of *Escherichia coli* cells (Oxoid, Hampshire, United Kingdom (BR0014)). The nozzle was fabricated by piezo-ceramic technology as a drive for piezoelectricity and the function such as the production electronic frequency generation.

2.3 Statistical Analysis

Statistical analysis was conducted by using SPSS statistics 17 software. The analysis involved one sample t-test and the probability value involved is less than 0.05.

3   Results and Discussion

3.1   Colony and Cellular Morphological Characterization

As further analysis for confirmation of identification of *Escherichia coli* isolated, various methods were used such as morphological observation followed by 16S rRNA sequence gene method in order to know the specific identification of the *Escherichia coli* isolated. A morphological characteristic of the bacteria isolated was shown in Table 2. Colony and cellular morphological characterizations of isolation were carried out using fresh cultures on eosin methylene blue agar, respectively.

The colony *Escherichia coli* isolated appeared circular with diameter size ranging from 1.5–2.5 mm with incubation 24 h, 35–37 °C on eosin methylene blue agar (Fig. 1d). The *Escherichia coli* isolation was observed as dark blue black with a green metallic sheen in color. The colony surface was shiny and moist in the agar plate [18]. *Escherichia coli* was isolated by Gram-stains method and observed under microscopy with magnified 100 times. The observation revealed that *Escherichia coli* appeared as single and pair rods, stained pink after preserved with safranin stain, and the motility of the cell as motile bacteria movement (Fig. 3) [18].

3.2   Electrophoresis and 16S rRNA Sequence Analysis

Further analysis to the confirmation of *Escherichia coli* isolated, gel electrophoresis result interprets that ladder of *Escherichia coli* isolated DNA fragments match up to the recognized bands of the ladder *Escherichia* sp. (Figure 4), meanwhile, 16 s rRNA sequence analysis was analyzed using NCBI BLASTn program. The

Table 2 Morphological features of the *Escherichia coli* isolation

Morphological feature	Observation
Colony formation	
Color	Dark blue black with green metallic sheen
Size	1.5–2.5 mm (18 h incubation)
Surface	Shiny
Texture	Moist and less sticky
Edge	Entire
Elevation	Raised
Shape of colony	Circular
Cellular morphology	
Cell shape	Rod
Gram staining	Gram-negative (Fig. 3)
Cell motility	Motile
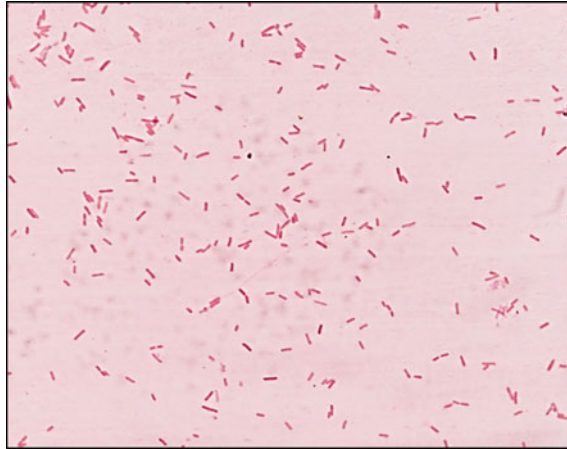
Fig. 3 Gram-negative *Escherichia coli* (taken with light microscopes and magnified 100 times)

Notes:
Fragment 1 – approximately 750 bp
Fragment 2 – approximately 580 bp
Fragment 3 – approximately 580 bp
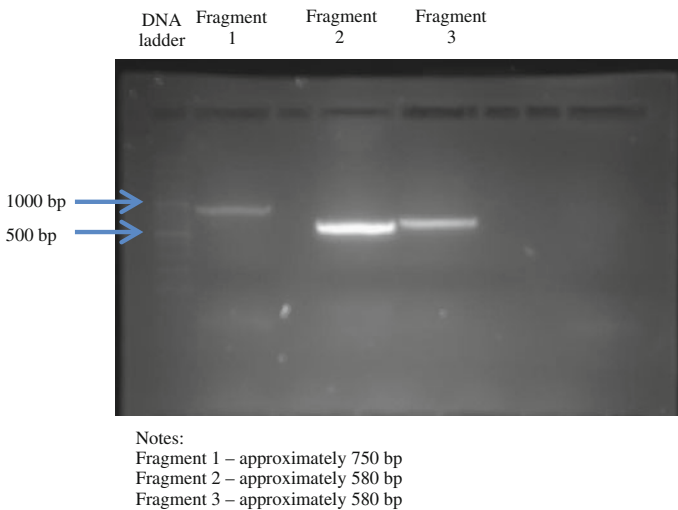
Fig. 4 Electrophoresis result of *Escherichia coli* isolated

nucleotide sequence of the 1089 bases for 16S rRNA gene of the *Escherichia coli* isolated was determined and high homology was found that 16 s rRNA sequence of *Escherichia* sp., with level of identity 95 % (Table 3). From (Table 3) result interpretation the identity of *Shigella* sp. on the same level (95 %), as further analysis and to confirm that bacteria isolated was *Escherichia* sp., pure culture from stock of bacteria isolated was spreaded in the Salmonella Shigella agar (SS agar). Hence after incubation, bacteria will ferment the lactose in the media, resulting in bacterial growth with a pink color, and this fermentation revealed that isolated bacteria involve *Escherichia coli* (Fig. 1c).

Table 3 Phenotypic identification of *Escherichia coli* isolated bacteria

Description	Query cover (%)	Identity (%)	E-value	Accession no.
Escherichia sp.	100	95	0.0	JN626182.1
Shigella sp.	100	95	0.0	JN626189.1

Table 4 Inoculum of *Escherichia coli* isolated bacterial in nutrient broth enrichment

Date	No. of colony	Size of colony (mm)	Plate count (cfu/ml)
04/11/2014	2	2.0	1.00×10^8
04/11/2014	2	2.0	3.10×10^8
10/11/2014	2	2.0	2.81×10^8
10/11/2014	2	2.0	3.00×10^8
13/11/2014	2	2.0	1.69×10^8
07/03/2015	2	2.0	1.91×10^8
Average			2.25×10^8

3.2.1 Inoculum Preparation of Bacterial

Escherichia coli isolated for specification two colonies of 2.0 mm diameter size from eosin methylene blue agar was grown in 10 ml nutrient broth for incubation of 18 h, from the result this fermentation produces 10^8 cfu/ml inoculum concentrations. Meanwhile, for 10^4 cfu/ml cells a diluted process was conducted in 10^{-5} (Table 4).

3.2.2 Flow Cell Ultrasound as Bacterial Disruption

This study investigated an effect ultrasound irradiation on bacteria disruption. From the Fig. 5 the results are in agreement with the generally accepted that *Escherichia coli* cells could disrupt with flow cell ultrasound treatment with strong correlation coefficient R^2 (>0.95). One sample t-test was conducted to analyze percentage removal of bacterial disruption with 95 % confidence interval. The flow rate (25 and 70 ml/min) for less power intensity is statistically significant and higher of bacterial disruption than the greater power intensity, $p = 001$. It was observed that lower power intensity and lower oscillation amplitude resulted in higher cells disruption. As an effect increases of surface area through the ultrasound treatment, the energy dissipation over sonication media would be extensive area in flow cell ultrasound, hence, higher of disruption cells at amplitude 35 %, (Q 25 ml/min = 0.4184 W/cm^2) and (Q 70 ml/min = 1.0268 W/cm^2) [19]. The increases of surface area increased the disruption performance and supported by fewer impedance difference between water and microorganism, approximately 5 %, therefore, the water and microorganism cells are coupled, the energy transfer by transmission of sound energy due to mechanical wave function through the cells and resulted cells disruption [5, 20].
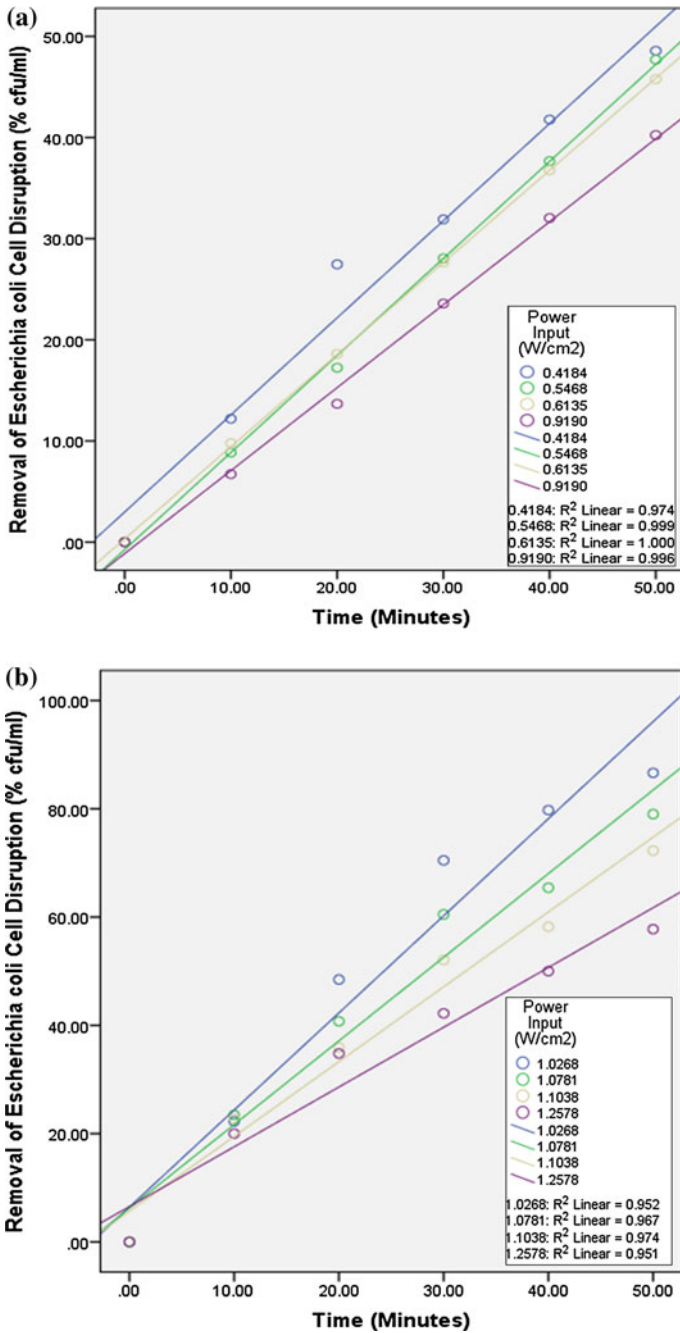
Fig. 5 Effect *Escherichia coli* cell disruption in concentration (10^4 cfu/ml), flow rate (**a** 25 and **b** 70 ml/min), at 50 min sonication time

Furthermore, Fig. 5 was interpret that the higher flow rate resulted higher disruption in the flow cell ultrasound (86.64 %) as compared to lower flow rate (48.57 %). Higher flow rate was affected by increases of cycle treatment (loop reactor) and consequences to the higher disruption of *Escherichia coli* cells. The mechanical effects of ultrasound as bacterial disruption are more noticeable at lower ultrasound frequencies, in addition, 18–30 kHz sonication devices were needed to be applied for large scale industrial application. Therefore, for this research low frequency 30 kHz was used as design parameter for bacterial disruption. The mechanical effects may include cell lysis and loss of cell viability [20, 21].

4   Conclusions

In conclusion, bacteria isolated from the municipal wastewater treatment plant were *Escherichia coli.* Morphological features of *Escherichia coli* isolated by eosin methylene blue agar were observed as dark blue black with green metallic sheen in color. Meanwhile, Gram stain method under microscopy resulted that *Escherichia coli* appeared as single and pair rods stain pink-red after preserved with safranin stain, as further, *Escherichia coli* isolated was high homology by 16 s rRNA sequence of *Escherichia* sp., with the level of identity 95 %.

The flow rate (25 and 70 ml/min) at less power intensity and less amplitude 35 % is statistically significant and higher of bacterial disruption than the greater power intensity, $p = 001$. Meanwhile, In the aspect of flow rate, higher flow rate was affected by increases of cycle treatment and consequences to the higher disruption of *Escherichia coli* cells.

In addition, flow cell ultrasound technology was nontoxic and low-cost method and gave positive value to the return on investment and is urgently needed in the water treatment and the requirement of new innovative technology is a highly essential since it will help to produce a green technology for microbial pathogen removal.

References

1. Centers for Disease Control and Prevention (CDC), "The Safe Water System." 2014.
2. World Health Organization (WHO), "Guidelines for drinking-water quality.," *WHO chronicle*, vol. 38, no. 3. Jan-2008.
3. World Health Organization (WHO), "Emerging Issues in Water and Infectious Disease," 2003.
4. C. Yanmin, "Visible-light-driven Photocatalytic Disinfection of Bacteria by the Natural Sphalerite," The Chinese University of Hong Kong, 2011.

5. N. M. Budari, M. F. Ali, K. H. K. Hamid, and M. Musa, "Ultrasonic Irradiation on Microorganism Disruption in Water Disinfection Process – A Mini Overview," *Appl. Mech. Mater.*, vol. 754–755, pp. 676–681, 2015.

6. N. M. Budari, M. F. Ali, and J. Kassim, "Physical Contaminants Removal from Continuous Process of Water Filtration by a New Low-Cost Palm Shell Charcoal," *Adv. Mater. Res.*, vol. 911, pp. 397–404, Mar. 2014.

7. M. H. Dehghani, "Effectiveness of Ultrasound on the Destruction of E. coli," *Am. J. Environ. Sci.*, vol. 1, no. 3, pp. 187–189, 2005.

8. N. M. Budari, M. F. Ali, J. Kassim, and S. M. Omar, "Burnt Oil Palm Shell Filter Media for Bacterial Removing by Single- and Dual-Media Filtration," in *2013 IEEE Business Engineering and Industrial Applications Colloquium (BEIAC)*, 2013, pp. 419–424.

9. C. Svanborg Eden and H. A. Hansson, "*Escherichia coli* Pili as Possible Mediators of Attachment to Human Urinary Tract Epithelial Cells," *Infect. Immun.*, vol. 21, no. 1, pp. 229–237, 1978.

10. R. A. Al-Juboori and T. F. Yusaf, "Improving the Performance of Ultrasonic Horn Reactor for Deactivating Microorganisms in Water," *IOP Conf. Ser. Mater. Sci. Eng.*, vol. 36, pp. 1–13, Sep. 2012.

11. A. H. Mahvi, "Application of Ultrasonic Technology for Water and Wastewater Treatment," *Iran. J. Public Health*, vol. 38, no. 2, pp. 1–17, 2009.

12. J. Rooze, E. V. Rebrov, J. C. Schouten, and J. T. F. Keurentjes, "Dissolved Gas and Ultrasonic Cavitation—A Review," *Ultrason. Sonochem.*, vol. 20, no. 1, pp. 1–11, Jan. 2013.

13. N. Gera and S. Doores, "Kinetics and Mechanism of Bacterial Inactivation by Ultrasound Waves and Sonoprotective Effect of Milk Components," *J. Food Sci.*, vol. 76, no. 2, pp. 111–119, 2011.

14. S. Börjesson, S. Melin, A. Matussek, and P. Lindgren, "A Seasonal Study of the MecA Gene and *Staphylococcus aureus* Including Methicillin-Resistant *S. aureus* in a Municipal Wastewater Treatment Plant," *Water Res.*, vol. 4, no. 43, pp. 925–932, 2009.

15. R. E. R. Goldstein, "Antibiotic-Resistant Bacteria in Wastewater and Potential Human Exposure Through Wastewater Reuse," University of Maryland, 2013.

16. R. E. Rosenberg Goldstein, S. a. Micallef, S. G. Gibbs, A. George, E. Claye, A. Sapkota, S. W. Joseph, and A. R. Sapkota, "Detection of Vancomycin-Resistant Enterococci (VRE) at Four U.S. Wastewater Treatment Plants that provide Effluent for Reuse," *Sci. Total Environ.*, vol. 466–467, pp. 404–411, 2014.

17. A. Naquin, J. Clement, M. Sauce, R. Grabert, M. Sherpa, and R. Boopathy, "Presence of Antibiotic Resistant Staphylococcus aureus in Sewage Treatment Plant," *J. Water Susainability*, vol. 4, no. 4, pp. 227–236, 2014.

18. M. A. Zinnah, M. R. Bari, M. T. Islam, M. T. Hossain, M. T. Rahman, M. H. Haque, S. A. M. Babu, R. P. Ruma, and M. A. Islam, "Characterization of *Escherichia Coli* Isolated from Samples of Different Biological and Environmental Sources," *Bangl. J. Vet. Med.*, vol. 5, no. 1&2, pp. 25–32, 2007.

19. G. Andaluri, E. V Rokhina, and R. P. S. Suri, "Evaluation of Relative Importance of Ultrasound Reactor Parameters for the Removal of Estrogen Hormones in Water," *Ultrason. Sonochem.*, vol. 19, pp. 953–958, 2012.

20. J. H. Gibson, D. Hai, N. Yong, R. R. Farnood, and P. Seto, "A Literature Review of Ultrasound Technology and Its Application in Wastewater Disinfection," *Water Qual. Res. J. Can.*, vol. 43, no. 1, pp. 23–35, 2008.

21. E. Günerken, E. D'Hondt, M. H. Eppink, L. Garcia-Gonzalez, K. Elst, and R. Wijffels, "Cell Disruption for Microalgae Biorefineries," *Biotechnol. Adv.*, vol. 33, no. 2, pp. 243–260, 2015.

Comparative Debark and Macronutrients Content from Retting Water Using 1:2 and 1:10 Kenaf Weight to Water Volume Ratio

G. Siti Aisyah, S. Zul Hilmi, A.H. Nabilah Huda, M.T. Ramlah, M.J. Janmaizatulriah and S.A. Sharifah Aminah

Abstract Experimental study on debark and macronutrients content from kenaf-retted water of 1:2 and 1:10 (kenaf weight to water volume ratio) is presented. The work involves the examination of the macronutrients parameter such as ammoniacal nitrogen (NH_3–N), nitrate (NO_3), total phosphorus (TP), and potassium (K). From the experiments it was found that the 1:2 ratio tank precedes debark process much faster and contains higher macronutrients than 1:10 ratio. However, both of the retted water notified may not be suitable and unable to support aquatic life without pretreatment. Actually this wastewater was rich with macronutrients and beneficial for crop fertilizer. Therefore, utilizing the existing macronutrient components from the retting process which is locally available offered an advantage and must be fully utilized.

Keywords Debark · Kenaf · Macronutrients · Retted water · Tank retting

G. Siti Aisyah (✉) · S. Zul Hilmi · A.H. Nabilah Huda · M.T. Ramlah · M.J. Janmaizatulriah
Faculty of Civil Engineering, Universiti Teknologi MARA (UiTM),
Shah Alam, Malaysia
e-mail: aisyah_ghazali86@yahoo.com

S. Zul Hilmi
e-mail: zhsaidin@gmail.com

A.H. Nabilah Huda
e-mail: huda_nabilah10@yahoo.co.uk

M.T. Ramlah
e-mail: ramlah_2007@gmail.com

M.J. Janmaizatulriah
e-mail: janmaizatulriah@salam.uitm.edu.my

S.A. Sharifah Aminah
Faculty of Applied Science, Universiti Teknologi MARA (UiTM),
Shah Alam, Malaysia
e-mail: sharifah459@salam.uitm.edu.my

1   Introduction

Kenaf term originated from Persian word which explain the character of warm season, short-day and herbaceous annually plant [1]. It is commercially cultivated in more than 20 countries in which more than 95 % of total productions resulted from China, India, and Thailand. The fiber from kenaf basically possesses several features which are able to produce high grade product of pulp, protective wrapping for fruits and vegetables, board, textiles and filters for paper, packaging, and composite industries, respectively [2, 3]. So, this is one of the reasons why so many countries were currently paying more attention on research and promotion of kenaf which includes Malaysia. According to Maziah [4] these initiatives will help to revitalize kenaf as the nation's third commodity crop and promoting greater use of green renewable resources. Therefore, to making sure this aim to be realistic the total plantation area was increased up to 2000 ha with 949 numbers of growers participating in kenaf plantation in Peninsular of Malaysia currently [5].

It shall bear in mind, before fiber from kenaf was extensively used, it must undergo retting process. Retting is actually the common technical term for 'rotting' used in natural fiber extraction process. This process has been used for thousands of years and it is a fact that retting is one of the most important determining factors for the quality of natural fibers. Retting also, a step of plant tissue removal and releasing cellulosic fiber through the microbial activity primarily bacteria [6]. Studies have shown that the plant which does not undergo retting process had several disadvantages. In example, Gopu Raveendran et al. [7] revealed the non-retted fibres containing higher impurities (38 %) compared to the retted ones (0.3–16.5 %). Moreover, Dhakal et al. [8] demonstrated that non-retted fibers resulted in a significant decrease in tensile and flexural strengths due to high water absorption rate. Therefore, it was clear that the non-retted fiber may affect the fiber integrity and esthetics include coarse, dirt, and low tensile strength. In some particular extend, this is the reasons why retting process was so crucial and important.

Traditional retting in river, canal, ponds, and any open water catchments namely, water retting brought serious attention among water researchers and scientist. It requires large ratio ranges in between 1:15 and 1:30 of stem weight to water volume [9]. The huge water consumption usage then lead too much wastewater generation. Despite, performing retting inside water moving and large retting area also causes this method to be time intensive, whereby in the range of 14–28 days to produce fibers [10]. These become constraints for the larger production where the manufacturer needs to bear on labor cost with the minimal production hence, makes the plant fiber production industry not competitive.

In addition, prolonging the fermentation period was liberating large quantities of organic matter and chemicals into the environment, leading to increases in nitrogen (N), phosphorus (P), and potassium (K) levels. According to Van Dam et al. [11], the high macronutrient contains will decrease in pH and dissolved oxygen

(DO) concentration, and cause extensive damage to the living aquatic life in the retted area. Besides, too long dealing with fermentation water causes skin irritation and breathing problems among the retting workers. Thus, it was the possibly reason why it had been closed in Western countries [12].

Nowadays, the conventional water retting technique has been replaced by tank retting in order to compensate the above-mentioned problems. Numerous studies have shown the benefits of tank retting and one of major benefits is that the weight of stem to volume water ratio can be controlled and minimized in stagnant. Das et al. [13] for example success to reduce the previous ratio to 1:10 using plastic tank to ret jute stem under Indian climate. However, none studies so far have been carried out for kenaf using that ratio and below than that have been presented.

Besides, there are not many papers reported on water quality obtained from kenaf retting tank. Among those papers, most of them are only monitoring pH, DO, biochemical oxygen demand (BOD), chemical oxygen demand (COD), and hardness of retted water obtained from retted area via river and pond. On top of that, retted liquor was able to be used as fertilizer but to the best of our knowledge there are no papers address on the concentration of the macronutrients. In reflection to the above problems and the gaps in the previous research, a study on retting water macronutrient contents was carried out using two different ratio weights of kenaf to water volume: 1:2 and 1:10. The objectives of the experiment are to determine the macronutrient concentrations and to assess the performance of kenaf retting in respect to fiber debarking process against low water requirements.

2 Experimental

Kenaf at the age of 120 days was obtained from National Kenaf and Tobacco Board (NKTB). The kenaf was randomly cut in equal length of 15 cm. They were divided into two groups of kenaf mass, 2.5 and 0.5 kg named as 1:2 and 1:10 in different tanks, respectively. 5 L of tap water was then placed in both tanks. The retting water was monitored for 0 (before kenaf was inserted), 1, 3, 5, and 7 days through visual examination and analyzed with respect to macronutrients concentration.

In order to determine retting efficacy, the fiber was assessed by 'Touch and Feel' method following Haque et al. as in Ref. [14]. This method was recommended by Bangladesh Jute Research Institute. The macronutrient contents such as NH_3-N, NO_3, TP, and K were determined by using a UV-Vis Spectrophotometer (HACH DR5000, USA) according to the Nessler method (8038) (single wavelength; 425 nm), cadmium reduction method (8192) (single wavelength; 507 nm), PhosVer 3 with acid persulfate digestion (8190) (single wavelength; 880 nm) and tetraphenylborate method (8049) (single wavelength; 650 nm), respectively [15]. This method of HACH was adapted from standard methods for the examination of water and wastewater. All the units of macronutrient concentrations were in mg/L.

3   Results and Discussion

3.1   Kenaf Debark

The progress of fiber kenaf debark is given in Table 1. Initially at Day 1, the green stalk was still hard and green in color for both tanks. The significant different on kenaf stalk was observed when the utmost color of layer changes. It can be seen that the green stalk turns to yellowish in color on Day 3 for the ratio of 1:2. This corresponds with the kenaf outer layer which can be peeled off easily. Meanwhile at the same day, the 1:10 ratio kenaf was still greenish in color and the outer layer cannot be extracted. Continuously, the 1:2 ratio precedes the debark of kenaf as most stalk turn in black and the fiber was colorless at Day 5 and soft fiber was easily obtained at Day 7, respectively. In contrast the 1:10 ratio fiber still intact and stiff, hence hard to extract. It shows that increases mass of kenaf hence reduce the ratio was accelerate retting process. This could be explained that macronutrients leached out from the plants and remains in the water thus help to promote microbial process. According to Ahmed and Akhter [16], this component will provide macronutrients for the microorganisms to grow and succeed in completing the retting process.

3.2   Ammoniacal Nitrogen (NH₃–N)

In general NH_3–N measures the health of water in respect to ammonia content. The experimental result for the level of NH_3–N is depicted in Fig. 1. In the present experiment, each of the 1:2 values was higher than 1:10 retting water tank. It is possibly due to introducing more kenaf weight in a 1:2 tank resulting much of decaying organic matter. Prolong the retting period up to 7 days causes NH_3–N values up to 15.5 and 3.8 mg/L for 1:2 and 1:10 retting water, respectively. Thus indicated, the 1:2 tank surpassed the recommended value (15 mg/L) by the

Table 1   The debarking progress for 1:2 and 1:10 ratios (kenaf weight to water volume ratio)

Fig. 1 Comparison of
NH$_3$–N in 1:2 and 1:10 retting
water tanks
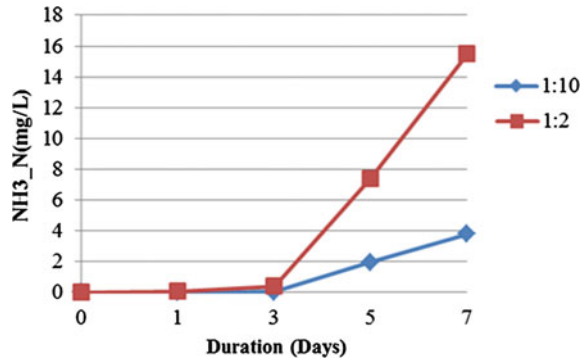
Malaysian wastewater effluent standard A [17] after a week of kenaf retting process. Although it was clearly observed the 1:10 tank is comparably low in NH$_3$–N level but the debarking process was much slower than 1:2 tank.

The higher values of NH$_3$–N basically prove the decayed plant gummy materials and microbial process that had taken in place. This corresponds with fiber which was soft and easily obtained as figured out for 1:2 tank. The result found here also correlated with the findings of Nabilah Huda et al. [18] but differs with the findings of Haque et al. [14]. It might be due to difference in geographical location, amount of water, time period, etc. However, it shall be noted the high level of NH$_3$–N is toxic to many fish and aquatic organisms in the receiving stream if the water was discharged directly without any treatment. It can block oxygen transfer in the gills of fish and reduce the photosynthetic activity. Based on Ref. [19], some of methods shall be adopted for NH$_3$–N removal such as air stripping, breakpoint chlorination, and ion exchange.

3.3 Nitrate (NO$_3$)

N is the most important element in fertilizer. The plants respond quickly when N was applied. This element encourages above ground vegetative growth and gives a deep green color to the leaves. Principally, plants roots will take up N in the form of NO$_3$. As shown in Fig. 2, the level of NO$_3$ released is in the range of 0–12 and 0–30 mg/L for the 1:10 and 1:2 tanks, respectively. Thus, it indicated that the NO$_3$ released almost two times in the 1:2 tank than in the 1:10 tank at day 7. This result is related to NH$_3$–N which describes nitrification–denitrification process. The trend of NO$_3$ released was increased along the experiment for both the water samples but it comparatively has low NO$_3$ values (45 mg/L) stipulated by USEPA. Basically, NO$_3$ presented in wastewaters was percolating from sources such as decaying plants, agricultural fertilizers, and domestic sewage [20]. In respect to retting process the NO$_3$ may come from fertilizer and retted process itself. The NO$_3$

Fig. 2 Comparison of NO_3^- in 1:2 and 1:10 retting water tanks
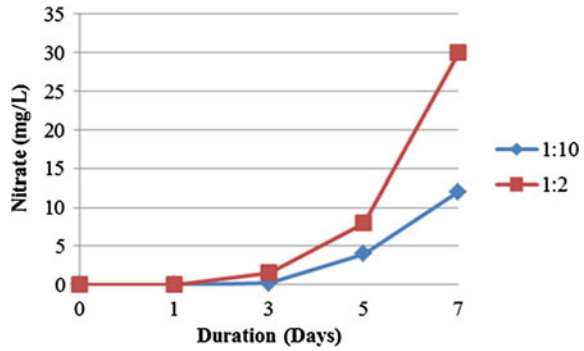
content of more than 100 mg/L will have significant impact on bitter taste of water and may cause physiological problem [21].

Although the present experiment result was lower value than all the above-mentioned level and effects but the rise in NO_3 level will promote the overgrowth of algae, other organism and fouls the water system if directly discharged to ponding waterways. Actually, plants may use NO_3 from the soil to satisfy its macronutrient requirement and accumulate in their leaves and stems. The NO_3 presenting in the retted water would be beneficial if utilized and returned back for kenaf cultivation.

3.4 Total Phosphorus (TP)

TP present in the waterways is in the form of PO_4^{3-}. As shown in Fig. 3, level of TP for the 1:2 tank in the range of 0–135.5 mg/L, whilst for the 1:10 tank was exhibited in lower range of 0–40.5 mg/L. In respect to the study, the higher level of TP is due to leaching of PO_4^{3-} from the stalk and rotting plant process converted by bacteria. The increased level of TP often indirectly may harm the environment by causing bacterial growth and promote surplus of algae blooms.

Fig. 3 Comparison of TP in 1:2 and 1:10 retting water tanks
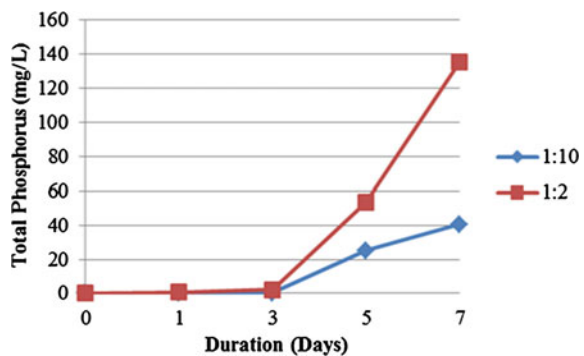
The USEPA recommends the water that contain TP concentration not exceeding 0.10 mg/L in streams not discharging directly into reservoirs and not exceeding 0.05 mg/L in streams discharging directly into reservoirs. TP commonly is associated with eutrophication—the enrichment of a body of water with nutrients resulting in accelerated algal or plant production. Eutrophication can result in fish kills, unpleasant odors, loss of recreational value, and other water quality-related problems. It was found the TP level of 1:2 was two times higher than coconut pond retting reported as in Ref. [22]. The P is a part of every living cell in plant. Each of plant activity such as growth respiration and reproduction depend upon phosphorous levels. So, P is a needed element in plant.

3.5 Potassium (K)

K is one of the important elements in plants for protein synthesis, opening and closing stomata for proton pumping purposes. From the observation, the trend of the K depicted were similar to the other previous three macronutrient parameters, whereby at early retting stages the level of K was very low which is almost zero (Fig. 4). However after 3 days, the level of K starts to rise up for both tanks. Reading of K was relatively three times higher (2190 mg/L) in the 1:2 tank than the 1:10 tank (833 mg/L) at day 7. It was the higher reading as compared to other macronutrients, since K is an essential component in kenaf stalk.

In addition, the higher concentration of K was dangerous to human, as it causes skin disease. It may be the reason why more than 50 % of female retting workers suffered including irritations, peeling, and cracks in hands and legs when they are exposed too long in fermentation water without use of personal protective equipment (PPE) [23]. It shall be noted that K is the third essential fertilizer element. It is essential for photosynthesis, protein synthesis starch formation, and translocation of sugars. All root crops generally give response to application of K. Thus, it was indicating that this retted water is beneficial to use as crop liquid fertilizer.

Fig. 4 Comparison of K in 1:2 and 1:10 retting water tanks
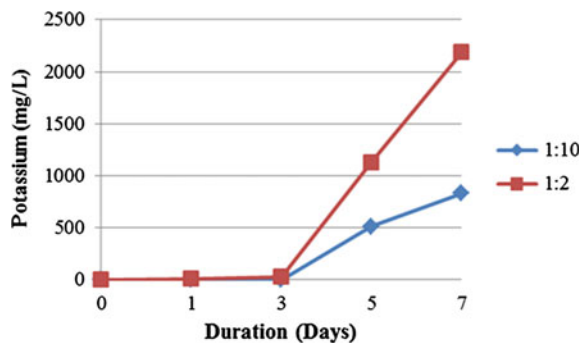
4 Conclusion

Keeping in view of all these results, it can be concluded that the 1:2 ratio helps to execute the kenaf debark process much faster than 1:10 ratio. It was corresponded with the higher macronutrients level in the 1:2 tank compared to the 1:10 tank. It can be observed clearly that the process of debarking started on day 3 and continuously rised up until day 7. Although in the 1:10 tank, the macronutrients level were comparatively lower than in the 1:2 tank but both of the effluents were not suitable to be discharged to downstream without a proper pretreatment. In regard to this problem, we recommend that the effluent could be utilized for kenaf cultivation stages, as liquid fertilizer.

References

1. A. Ashori, J. Harun, W. Raverty and N.M. Yusoff Mohd, "Chemical and morphological characteristics of Malaysian cultivated kenaf (*Hibiscus cannabinus*)," Fiber Polym. Plast. Technol. Eng, 2006, vol.45, pp. 4–131.
2. J.C. Villar, E. Revilla, N. Gomez, J.M. Corbajo and J.L. Sumon, "Improving the use of kenaf for kraft pulping by using mixtures of bast and core fibers," Ind. Crops Prod, 2009, vol.29, pp. 7–301.
3. M.T. Paridah, A.W.N. Hafizah, A. Zaidia, I. Azmi, M.Y.M. Nor and M.Y.N. Yuziah, "Bonding properties and performance of multi-layered kenaf board," J. Trop. Sci, 2009, vol.21, pp. 22–113.
4. M. Maziah, "Natural fibres for the 3rd milennium," JEC Composite Magazines, vol.55, pp. 24–28, February- March 2010.
5. National Kenaf and Tobacco Board (NKTB), " Laporan penanaman kenaf (Kenaf cultivation report)," 2014, http://www.lktn.gov.my, Accessed on 11th May 2015.
6. A. Thygesen, M. Liu, A.S. Meyer and G. Daniel, "Hemp fibres: enzymatic effect of microbial processing on fibre bundle structure," Proceedings of the 34th Risø International Symposium on Materials Science: Processing of fibre composites-challenges for maximum materials performance, 2013, pp. 373–380.
7. N. Gopu Raveendran, S. Ashutosh, Z. Malgorzata and R. Vijaya, "Comparative evaluation of physical and structural properties of water retted and non-retted Flax fibers," Fibers, 2013, vol. 1, pp. 59–69.
8. H.N. Dhakal, Z.Y. Zhang and M.O.W. Richardson, "Effect of water absorption on the mechanical properties of hemp fibre reinforced unsaturated polyester composites," Composites Science and Technology, 2006, Article in Press.
9. Food and Agriculture Organization of the United Nations, "Improved Retting and Extraction of Jute Project Findings and Recommendations," 1998, http://www.fao.org, Accessed on 12th April 2013.
10. R. Farida, R. Sudjindro and H. Budi, "Uji Effektivitas Isolat Indigenous Air Rendaman Kenaf Sebagai Inokulum dalam Proses Retting Kenaf," (Effectiveness of Indegenous Isolate Kenaf Retted Water as Inoculum during Kenaf Retting Process), Prosiding Seminar Nasional Inovasi Perkebunan, 2011, pp.162–174.

11. J.E.G. Van Dam, and H.L. Bos, "A Comprehensive review on the environmental impact on natural fibers in industrial applications," 2004, http://www.fuo/es/common/ecg/343/en/esc_4.pdf. Accessed on 11th May 2015.
12. D.E. Akin, J.A. Foulk, R.B. Dodd and D.D McAlister III, "Enzyme-retting of flax and characterization of processed fibers," J. Biotechnol. 2001,vol.89, pp.193–203.
13. D. Biswapriya, C. Kalyan, G. Sagarmoy, M. Bijan, T. Sudipta, and C. Ashis, "Effect of efficient pectinolytic bacterial isolates on retting and fibre quality of jute," Industrial Crops and Products, 2012, vol. 36, Issue 1, pp. 415–419.
14. M. Shamsul Haque, A. Zakaria, Md. Asaduzzaman, M.A. Quashem and A. Firoza, "Distribution and activity of microbial population for jute retting and their impact on water of jute growing areas of Bangladesh," Pakistan Journal of Biological Science, 2002, vol.5 issue 6, pp. 704–706.
15. Hach Company, Standard Manual Procedure. Hach Company World Headquarters: United State, 2014.
16. Z. Ahmed, and F. Akhter, "Jute retting: an overview," Journal of Biological Sciences, 2001, vol. 1, Issue 7, pp. 685–688.
17. DOE: Environmental Quality Act, Environmental Quality (Sewage and Industrial Effluents) Regulations, Department of Environment, Malaysia 1974.
18. A.H. Nabilah Huda, R. Mohd Tajuddin, Z. Ahmad and M.O. Nazrin, "Determination of optimum debark time in retting process of kenaf fiber production," International Sustainability and Civil Engineering Journal, 2012, vol.1, no.2, pp.14–18.
19. Indah Water Konsortium (IWK), "Sewerage fact: ammonia," http://www.iwk.com.my, Assessed on 13th May 2015.
20. F.O. Abulude, G.O. Obidiran and S. Orungbemi, "Determination of physico-chemical parameter and trace metal contents of drinking water samples in Akure Nigeria. Trends in Applied Sciences Research," 2006, vol.1: 534–537.
21. B.N. Uba and O. Aghogho, " Rainwater quality from different roof catchments in Port-Harcourt District," Institute Public Analyst of Nigeria News, Nigeria, 2001, pp: 11–14.
22. C.F. Simple Lotus, B. Xavier Innocent, G. Prabhakaran and V.A.J Huxley, " Physicochemical variations of different coconut husk ponds," Journal of Basic and Applied Biology, 2012, vol.6, no.3 & 4, pp. 114–117.
23. M. Najee and M.C., "Philipose Pollution of Ashtamudi Estuary due to retting of coconut husk and its environmental impacts," International Journal of Scientific and Engineering Research, 2013, vol.4. no.8.

Experimental Study on Local Scour Before and After the Channel Bend

Mohd Fais Mohd Noor, Junaidah Ariffin and Hamidon Ahmad

Abstract Experimental studies on local scour at bridge pier are explored widely both theoretically and experimentally. There are many factors involved in the magnitude of local scour depth at piers such as velocity of the approach flow, depth of flow, size and gradation of bed material, and bridge pier itself. This paper presents a comprehensive review and highlights thus far in study of the effects of sediment discharge on local scour before and after the channel bend. Lately, the addition of many types of structures has extremely altered the morphology of river regimes, and caused major influence on the transport and deposition of sediment. During the unforeseeable circumstances such as river floods, extreme erosion, denudation of forest, and mass wasting at the upstream zone the scour hole can happen and can affect failure to the bridge pier. The development in the theoretical and laboratory findings on the effects of sediment discharge on local scour before and after the channel bend will be of importance to the science of river morphology as this contributes to the shaping of the river landscape for future studies.

Keywords Local scour · Sediment discharge · Channel bend · Transport and deposition of sediment · River morphology

M.F.M. Noor (✉) · J. Ariffin · H. Ahmad
Faculty of Civil Engineering, Universiti Teknologi MARA,
40450 Shah Alam, Malaysia
e-mail: mr_fais87@yahoo.com

J. Ariffin
e-mail: junaidahariffin@yahoo.com

H. Ahmad
e-mail: Hamid8392@salam.uitm.edu.my

1   Introduction

Scour is a natural phenomenon initiated by the erosive action of flowing water, excavating and carrying away material on the bed and banks of alluvial channel [1]. Studied by [2], a national study for the Federal Highway Administration (FHWA) stated that 383 bridge failures caused by catastrophic floods showed that 25 % involved pier damage and 75 % involved abutment damage. Different materials scour at different rates. Then, a second and more extensive study explored by [3] indicated that local scour at bridge piers to be a problem about equal to abutment scour problems. Excessive local scouring around the bridge piers become one of the major reasons to bridge collapse especially during floods and extreme erosion at the upstream zone. During flood flows, scour induced bridge failures as a result of unsteady flow with complex geometric and dynamic features. Flow interacts with mixtures of sediments which may range from alluvial sands to clays and weathered rocks. However, the presence of clay banks, rock outcrops, sand and shingle bars may result in different geometrical features during a flood. The problem is often complicated by the large variety of shapes, alignments, and approaches used for piers and abutments. Further, large random changes in foundation geometry can be caused by floating debris, e.g., trees, being trapped upstream of bridge piers. Natural scouring affect changes in the plan, cross section, and even location of a river. Bends and narrows of a river channel tend to scour during floods and fill at low flows.

Arved and Robert [1] acknowledged that the types of scour which may occur at a bridge site could be grouped as follows:

(a) General scour of the stream which would occur irrespective of whether the bridge was there or not.
(b) Localized scour (or constriction scour) which may occur because of the constriction of the waterway and rechanneling of berm flow by the bridge.
(c) Local scour which is caused by the local flow field around the piers and abutments.

Local scour involves in removal of material from around piers, abutments, spurs, and embankments. It is caused by an acceleration of flow and resulting vortices induced by obstructions to the flow. Local and localized scour can occur in two ways by clear-water scour and live-bed scour. Results from a study by [4] defined as the abrupt decrease in bed elevation near a pier, due to erosion of bed material by the local flow structure induced by the pier.

The scour in different conditions of transport can be divided into the following categories;

(a) Clear-water scour occurs if the bed material in the natural flow upstream of the scour area is at rest.
(b) Live-bed scour, also referred to as scour with bed material sediment transport, occurs when flow induces a general movement of the bed material.

2 Experimental Study

2.1 Description of the Equipment

Experiments were conducted in the physical flume model which was located in Hydraulic Laboratory, Faculty of Civil Engineering, Universiti Teknologi MARA, Shah Alam, Malaysia. The physical flume model can be shown in Fig. 1. The physical river model has an area of 7 m × 6 m. Model built with specifications of 2.25 m radius or curvature (R), 0.9 m channel width (W), 2.5 ratio radius over width (R/W) and 180° of bend angle. The physical river model system was supported by five main elements that are (i) flow control, (ii) water storage, (iii) sedimentation output measurement, (iv) water level measurement, and (v) outlet for discharge.

The inlet and outlet of flow was controlled by the valves which control the water circulation of inflow and outflow in this physical flume model. Water discharged into the physical flume model system is supplied from a tank. Depth of water levels were measured using a measuring tape installed at both entrance and exit. Sediment trap and the sediment tank located at the outlet point of the channel were used to trap and avoid the deposit from entering the pump.

2.2 Description of the Experiments

The cylindrical pier was placed at the middle of the channel section of the channel bend. The shape of the cylindrical pier is similar to the circular bridge pier and the size of cylindrical used is 100 mm diameter was fixed to the bottom to simulate real

Fig. 1 The physical flume model
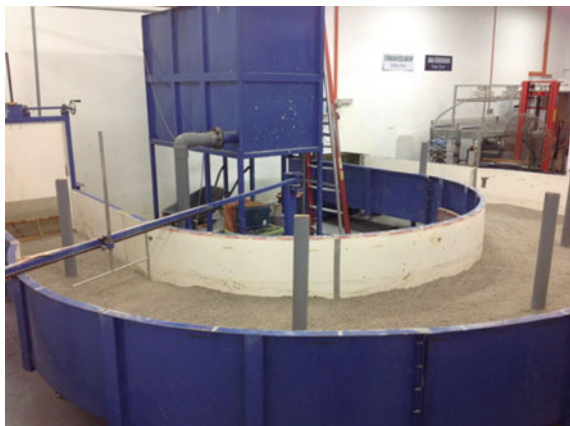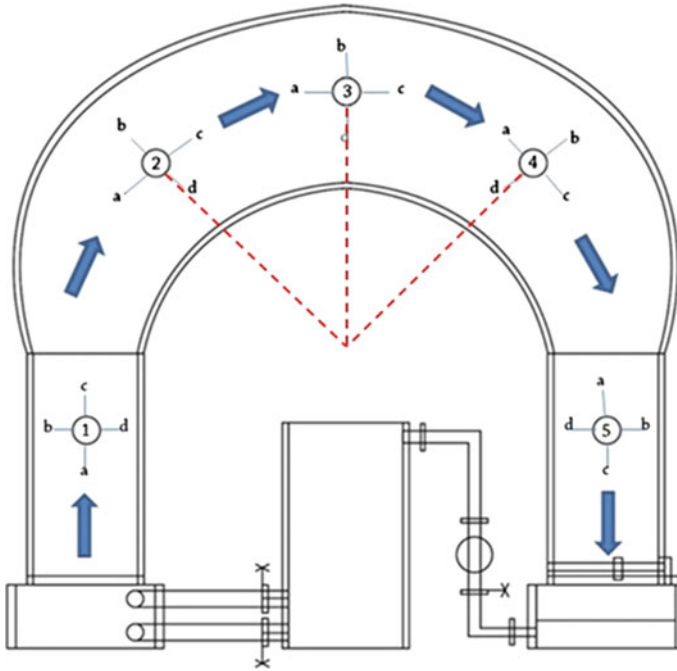
Fig. 2 Pier location

piers on the channel bend. Figure 2 shows the location of the pier. The Pier 1 located before enters the bend channel while Pier 5 located after exits the bend channel. The types of sand used in the experiment is poorly graded sand with sizes of D30 = 0.60 mm, D50 = 0.84 mm, and D60 = 0.96 mm. The curved obtained from the particle size distribution test for this experiment as shown in Fig. 3. The horizontal layer of sand 200 mm was leveled thoroughly using the sand scraper and when the sand was ready the channel bend was gradually filled with water up to a depth of 200 mm. The gradient of the flume was made gentle to specified slope.

The pump was turned on and the water flow started. The flow depth and the discharge for each experiment could be controlled by adjusting the pump pressure. The experiment began when the water level reached at the desired depth and it was stabilized. The experiment's duration is fixed to 6 h and the velocities and the sediment release for each experiment were recorded. After 6 h, the pump was turned off and the water was drained so that the local scour around the cylindrical piers could be measured. Table 1 is the summary of the experimental conditions on the flow rate and sediment release conducted.
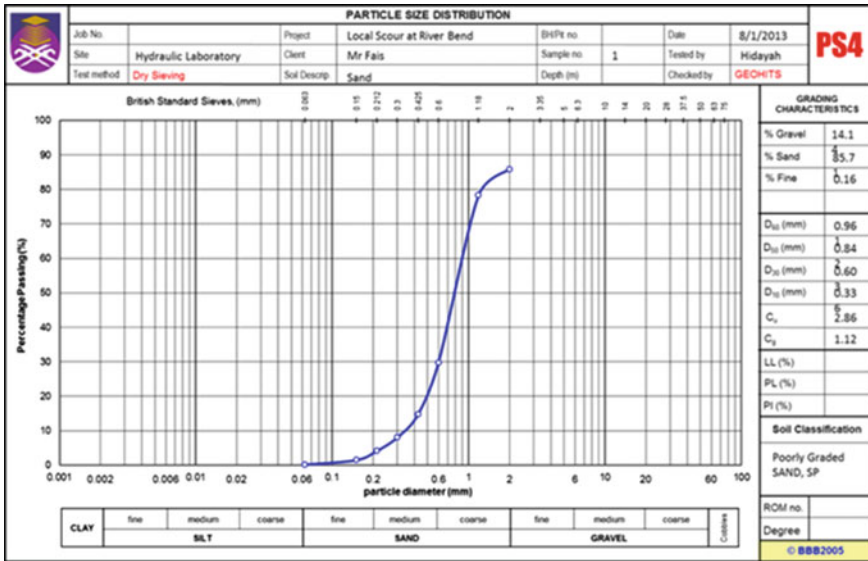
Fig. 3 The particle size distribution of the sand for this experiment

Table 1 The summary of the experimental conditions on the flow rate and sediment release conducted

Case No.	Discharge, Q (m³/s)	Sediment discharge, Q_s (m³/s)
1	0.11	Gradual sediment release 2.78×10^{-7}
2	0.17	Gradual sediment release 2.78×10^{-7}
3	0.22	Gradual sediment release 2.78×10^{-7}
4	0.11	Gradual sediment release 5.56×10^{-7}
5	0.17	Gradual sediment release 5.56×10^{-7}
6	0.22	Gradual sediment release 5.56×10^{-7}

3 Results and Discussions

The variation of local scour depth around the cylindrical pier can be directly observed in the channel bend through a relocatable profiler scale attached to the pier after the water was drained after a 6 h run of the experiment. This approves the findings [5, 6] on investigated the time development of the local scour around the oblong pier fitted with and without a collar plates and introduced a design method to predict the local scour depth with time. The local scour profile for before and after channel bend at pier 1 and 5 for different of discharge, Q and two type of sediment discharge, Qs of 2.78×10^{-7} and 5.56×10^{-7} m³/s are shown in Figs. 4 and 5.
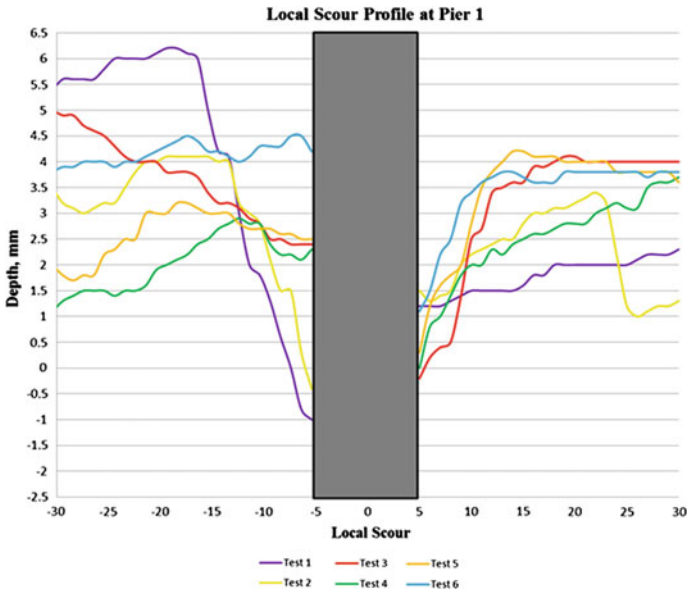
Fig. 4 The local scour profile at Pier 1
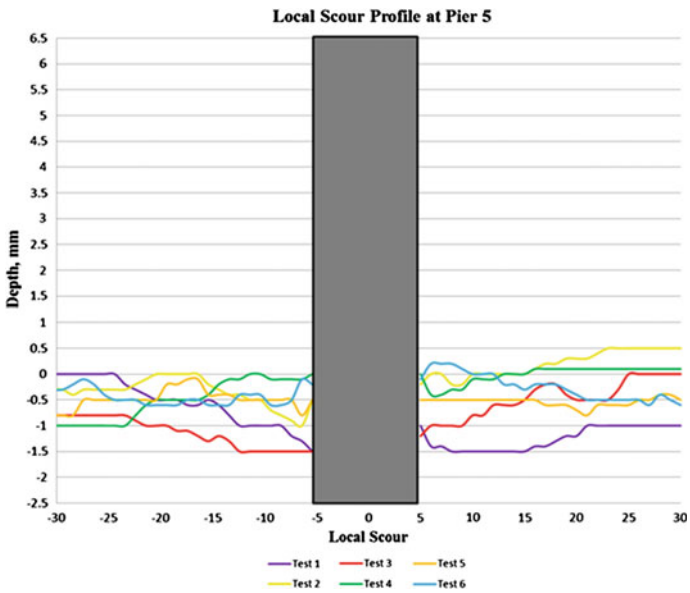
Fig. 5 The local scour profile at Pier 5

The results obtained from the plotted of the scour depth show the discrepancy on the local scour pattern around the cylindrical pier due to different flow rate and different sediment discharge. The observation from experiments showed that the depth of the local scour at the upstream is comparatively higher than the downstream side of the pier especially at Pier 1 before the channel bend. The cross section at Pier 1 shows an accumulation of the sand at upstream of the pier. Meanwhile, there are slightly changes of deposition activity at downstream of the pier. However, from the cross section at Pier 5 after the channel bend show there are little changes at upstream and downstream of the pier. This approves the finding [7] on the maximum local scour caused by piers with floating debris accumulation can be conservatively predicted by using an effective pier diameter.

This is directly proportional with the increase in the flow rate in longitudinal as well as in the transverse direction of which the maximum depth of the local scour show increasing trend. This confirms the finding by [8] on detailed of the changing flow patterns at a cylindrical pier with respect of local scour development. It is clear that the maximum depth of scour is dependent on the flow rate as well as time. The study by [9] determined the relationship of the effectiveness of a pier shape and different flow rate on the scour depth. The study on the bend channel had explored by [10] and through the finding, there is a change of flow pattern due to the presence of bend which result in the scour depth development. The results of flow pattern of the experiment are quite similar by the previous researcher [11] on the general development of the scour pattern at the upstream of the pier along plane of symmetry with respect to time.

4 Conclusion

This paper highlights in general, the results of experimental study on local scour at bridge pier. The studies were being developed in many ways to fulfill their research objectives. An experimental investigation on local scour around cylindrical pier before and after the bend channel has been presented. Performing the sequence of experiments and analyzing the results presented here in this study for scour depth at cylindrical piers at channel bend, following conclusions can be drawn

 (i) The depth of scour increase with rate of flow, scour depth was more with higher flow rate.
 (ii) It is observed that sediment release also influence the scour depth. The increasing in sediment release can caused the shallow of the river. The increase in the riverbed due to the shallow of water can endanger people living next to the river.
 (iii) Maximum scour depth tends to occur at the upstream of the pier. It was noticed that maximum of scour depth was increasing with increase of flow and time as well.

Review has found that the interaction between the flow and sediment discharge as primary factors responsible for the change in local scour. These two factors can be regarded as agent of change of the local scouring at bridge pier. This finding by [12] recognized the three cases of scour holes at piers in armored beds depending on the pier width, flow depth, armor gravel, and bed-sand sizes. The presented data can be used in monitoring, improving and testing results of numerical simulations. Thus, the above review provides considerable justifications to pursue this study.

References

1. Arved, J.R., & Robert, E. (1983). Clear-Water Scour at Cylindrical Piers. Journal of Hydraulic Engineering. Vol. 109, 338–350. ISSN: 0733-9429.
2. Chang, F. F. M., (1973). A Statistical Summary of the Cause and Cost of Bridge Failures. Federal Highway Administration, U.S. Department of Transportation, Washington, D.C.
3. Brice, J. C. and J. C. Blodgett, (1978). Countermeasures for Hydraulic Problems at Bridges. Vol. 1 and 2, FHWA/RD-78-162 & 163, Federal Highway Administration, U.S. Department of Transportation, Washington, D.C.
4. Shen, H. W., Schneider, V. R., and Karake, S. (1969). Local Scour around Bridge Piers. Journal Hydraulic Div., ASCE, 95(6), 1919–1939.
5. Alireza, M., Mahmood, S.B. Abdolkarim, E. (2010). Reduction of local scour at a bridge pier fitted with a collar in a 180 degree flume bend (Case study: oblong pier). Journal of Hydrodynamics. 22(5). Supplement: 669–673
6. Md. Faruque, M., & Hiroshi, N. (2003). Design Method of Time-Dependent Local Scour at Circular Bridge Pier. Journal of Hydraulic Engineering. Vol. 129, 420–427. ISSN: 0733-9429
7. Melville, B. W. and Dongol, D. M. (1992). Bridge Pier Scour with Debris Accumulation. Journal Hydraulic Engineering. 118: 1306–1310
8. Melville, B.W. and Raudkivi, A.J. (1977). Flow characteristics in Local Scour at Bridge Piers, J. Hydraulic. Research, ASCE, Vol. 15, pp. 373–380.
9. Elsabaie, I.H., (2013) An Experimental Study of Local Scour around Circular Bridge Pier in Sand Soil. International Journal of Civil & Environmental Engineering IJCEE-IJENS Vol. 13 No. 01.
10. Vaghefi, M., Ghodsian, M., and Neyshabouri, S. A. A. S., (2012). Experimental Study On Scour Around A T-Shaped Spur Dike In A Channel Bend. Journal of Hydraulic Engineering, 138 (5), pp.471–474.
11. Dargahi, B. (1990). Controlling Mechanism of Local Scouring. Journal Hydraulic Engineering, ASCE, Vol. 116, No.10, pp. 1197–1214.
12. Subhasish, D., Sumer, B.M. Jorgen, F. (2006). Control of Scour at Vertical Circular Piles under Waves and Current. Journal of Hydraulic Engineering. Vol. 132, 270–279. ISSN: 0733-9429

Fabrication of Polysulfone Membrane Incorporated with Crystalline Silica: The Effect of Casting Rate

Hamizah Mokhtar and Ramlah Mohd Tajuddin

Abstract Polysulfone (PSf) membrane incorporated with crystalline silica (SiO_2) was fabricated via phase inversion method. This study investigates the effect of SiO_2 and PVP as additive for different dope formulation of PSf membrane. SiO_2 is an abundant compound around the earth that is naturally occurring such as clay and graphite. They are widely used in industries to produce silica gel, colloidal silica, and fumed silica. In this study, experimental investigation was conducted focusing on different casting rate. Casting rate was varied from 7.3 to 10 ms^{-1}. Performances of PSf membrane were measured in term of pure water flux (PWF) by using distilled water and salt rejection (SR). The results indicate that the best dope formulation was at membranes containing 3 % of silica where successfully do rejection of 69.84 % and optimum flux rate of 39.45 Lm^{-2} h^{-1}. The result also shows that casting rate influences the final performance of membrane. The increase of casting rate would give good results in water flux and salt rejection. As a conclusion, 8.00 ms^{-1} was an ideal casting rate with the values of 77 % rejection and 39.24 Lm^{-2} h^{-1} permeation.

Keywords Casting rate · Crystalline · Polysulfone · Silica

1 Introduction

Polysulfone (PSf) membrane has been commonly used in membrane fabrication attributable to its low cost, good mechanical properties, anti-compaction, greater film ability, and strong thermal and chemical stabilities [1]. Membrane separation is

H. Mokhtar (✉)
Institute for Infrastructure Engineering and Sustainable Management (IIESM),
Universiti Teknologi MARA, 40450 Shah Alam, Selangor, Malaysia
e-mail: ami_872001@yahoo.com

R.M. Tajuddin
Faculty of Civil Engineering, Universiti Teknologi MARA,
40450 Shah Alam, Selangor, Malaysia
e-mail: ramlah160@salam.uitm.edu.my

one of the best water purification. Membrane can be used in water filtration system although it is widely use in medical sector and in food industry [2]. Membrane performances are determined based on fluxes, low fouling behavior, high selectivity, strong chemical, mechanical, and thermal stability in operating circumstances, good compatibility with the working environment, and relatively cost effective. In contrast with the traditional separation process such as distillation and evaporation, membrane technology is independent of thermodynamically imposed efficiency limitations on heat utilization. In the 1960s, with the development of high performance synthetic membrane, membranes emerged as a viable means of water purification [3]. Currently, there are various types of membranes such as reverse osmosis, nanofiltration, ultrafiltration, and microfiltration. Membranes are proven to have ability to treat wastewater effectively; however, there is weakness on membrane where its hydrophobic absorption may cause fouling [3]. Some modifications on membrane surface is the common method that has been used to minimize the fouling problem and hence increase hydrophobic properties of membrane. One of the modification methods is addition or substitution of additive into membrane formulation. Significant changes to the performance and characteristics of membrane occur with addition of small amount of additive into dope formulation [4, 5]. Furthermore, the addition of additive can change the phase separation kinetic, thermodynamic mechanism and solvent capacity and also enhance pore distribution, mechanical and physical properties of membrane [5, 6].

Commonly used additives in dope formulation are silica, zeolite, graphite, metal oxide nanoparticles, and carbon nanotube [5, 7]. Nanosilica has been widely used in polymer, concrete and as inorganic filter to improve the properties of polymeric and mechanical properties. Nanosilica also can be extracted from rice husk ash, sorghum vulgarae seed heads and bagasse ash by precipitation method, biodigestion and sol–gel process. Nanosilica which has a maximum dimension of about 30 nm, is an inorganic material that has promise of beneficial properties such as excellent stability, high chemical clarity, large surface area, strong adsorption, and good dispersal ability. Previous study by Harun et al. [5] reported that the addition of silica in membrane casting can act as anti-fouling mechanism and improve permeability and resistance ability. In Huang et al. [6], the membrane conductivity and mechanical properties were improved by adding fumed silica. Moreover, the effect of silica additive also improve molecular weight cut off (MWCO), pore density, pore size, and surface porosity in the membrane [5]. Therefore, in this study, SiO_2 was used as an additive to modify the dope formulation of polysulfone membrane. SiO_2 was added into dope solution at concentration of 1–6 %. The pure water flux test and salt rejection test were conducted by cross flow filtration method to evaluate the performance of membrane.

2   Research Method

Main materials used in this research were Polysulfone Resin (PSf), N, N-Dimethylacetamide (DMAc), poly vinylpyrrolidone (PVP), crystalline silica (SiO$_2$) and Sodium chloride (NaCl). Polymer chosen is PSf due to its thermal, mechanical and chemical stability. DMAc used as a solvent due to its ability to dissolve wide variety of polymers. PVP was added as additive since it has greater degree of hydrophilicity that can possibly modify the membrane structure to achieve better fluxes and reduce fouling. Figure 1 illustrates the crystalline silica (SiO$_2$). Experimental investigation was done in laboratories of UiTM Shah Alam. Table 1 shows the properties of SiO$_2$ used in dope solution.

Fig. 1 Crystalline silica (SiO$_2$)

Table 1 Properties of SiO$_2$ used in dope solution

Properties	Value
Appearance	Crystalline
SiO$_2$ (wt%)	30 ± 1 %
Na$_2$O (wt%)	0.5 %
pH	8.5–10.5
Temperature	20 °C
Density	1.19–1.22 gcm^{-3}
Particles size	10–15 nm

Table 2 Dope composition

Dope	PSf (%)	DMAc (%)	PVP (%)	SiO$_2$ (%)
M1	21	71	7	1
M2	21	71	6	2
M3	21	71	5	3
M4	21	71	4	4
M5	21	71	3	5
M6	21	71	2	6

2.1 Preparation of Dope Solution

This study includes six dope compositions with different percentages of SiO$_2$, N, N-Dimethylacetamide (DMAc), polysulfone (PSf), and Polyvinylpyrolidone (PVP). Table 2 shows the dope composition formulae for membrane formulation.

2.2 Preparation of Dope Solution and Membrane Fabrication

The PSf were dried by temperature 50 °C for 24 h before being used in casting formulation. Then, casting formulations were prepared by dissolving the ratio between PSf: PVP: DMAc: SiO$_2$. PSf was added into the vessel containing the solvent DMAc and stirred continuously by using a magnetic stirrer to make sure the polymer is well mixed. This procedure was repeated until all the required amount of polymer is added. This process was controlled at desired range 60 °C temperature and 400 rpm speed. The solution was stirred until it becomes homogeneous. Next, the additive, PVP was added in the solution and followed by additive SiO$_2$. Then, the mixing process was continued until a homogeneous solution is obtained. After that, the dope solution was poured and cooled in a clean 1 L storage glass bottle. This step is surface treatment of membrane fabrication process which involved evaporating the solvent on the membrane surface by allowing air being sucking out of the air hood. Later on, the dope solution undergo coagulation steps where the membrane sheets were immersed into appropriate liquid at appropriate temperature so that the membrane will harden and detach from the casting plate. The dope solution was cast using casting knife with range thickness 100–125 μm and immersed into coagulation bath containing distilled water under room temperature. The flat sheet membrane was air-dried for 24 h at room temperature (27 ºC). Finally, the membranes were cut into ring shape about 6 cm diameters before placed in the cell (Fig. 2).

Fig. 2 Flat sheet membrane casting machine

2.3 Pure Water Flux Test

The performance of Polysulfone membrane was evaluated based on pure water permeation fluxes (PWP) and solute rejection rates (SR). The flat sheet membrane was cut into a circle form before it was installed in filtration membrane cell. The pure water flux test was carried out by using distilled water. Pure water flux calculation is as below:

$$F = \frac{Q}{A \cdot \Delta t} \tag{1}$$

where F is permeation flux for distilled water and wastewater ($Lm^{-2}\ h^{-1}$), Q is volumetric flow rate of permeation solution, A is crossflow surface area (m^2), and Δt is time interval on which permeate volume is taken (h).

2.4 Salt Rejection Test

Salt (NaCl) rejection test is a method for selection of the best performance of membrane emphasis on the various casting rate by determining the flux and

rejection through the membrane using sodium chloride (NaCl) solution. The salt solution of concentration 500 mg/L was prepared.

The absorbance was measured by using the conductivity meter. The rejection can be defined as percentage of solute concentration reduction of permeate stream relative to feed stream and can be calculated as below:

$$SR = \left(1 - \left(\frac{C_P}{C_F}\right)\right) \times 100 \tag{2}$$

where C_p and C_f are solute concentration in the feed and permeate solution, respectively.

2.5 The Effect of Casting Rate on Membrane Performance

The casting rate is determined by controlling the air pressure and casting speed. Previous researches proved that the air pressure affected the casting speed. The air pressure can be fixed at constant values. The casting rate will affect the membrane fabrication in the wet/dry phase inversion process. The casting knife notch was set at 150 μm, assuming no contact between knife and glass plate, the casting method done under declared air pressures. Presently, flat sheet membranes are used herein for laboratory-scale experiments, which is the most appropriate form. Furthermore, flat sheet membranes are also widely utilized in plate-and-frame and spiral wound systems. Casting was carried out at ambient atmosphere (27 °C and 84 % relative humidity). The flat sheet casting shear rate can be calculated using the Eq. (3) as follows:

$$\gamma = \frac{v}{g} \tag{3}$$

where v is the velocity of casting knife and g is the gap setting of casting knife. After that, the nascent membrane was quenched immediately into an aqueous bath at room temperature (28 °C) and then air-dried.

3 Results and Discussion

Analysis of the suitable formulation of membrane were summarized and discussed in pure water permeation and salt rejection of membrane and effect of casting rate on membrane performance section.

3.1 Pure Water Permeation and Salt Rejection

The effect of SiO_2 as an additive on the pure water flux (PWF) and salt rejection performance is illustrated in Fig. 3. From the figure, the flux increases when the SiO_2 content increases up to 3 %. The PWF of 1 % SiO_2 is 25.68 % $Lm^{-2} h^{-1}$, 2 % silica is 27.60 $Lm^{-2} h^{-1}$ and 3 % silica is 39.45 $Lm^{-2} h^{-1}$, this increasing behavior might due to the SiO_2 3 % is more hydrophilicity compare to the other percentages of SiO_2. However, the PWF decreases to 38.28, 35.47, and 35.31 $Lm^{-2}h^{-1}$ when the SiO_2 increases to 4, 5 and 6 %, respectively. Similar trend reported by [8] shows the 2 % of silica was the optimum for water permeability. This is due to the interactions between contaminants and membrane surface were reduced by silica particles of the membrane surface. At 3 % of SiO_2, hydrophilicity of the membrane increases and consequently it attracts water molecules into the composite membrane. Moreover, hydrophilicity properties may also facilitates water penetration through the membrane thus enhances the flux. Nevertheless, higher concentration of SiO_2 will cause the pure water flux to decrease immediately. As a consequence, the hydrophilicity of membrane also decreases which shown in Fig. 3 where the pure water flux suddenly drops at the 4 % of SiO_2. At 5 % SiO_2, the flux rate keeps on dropping and remains constant at 6 % of SiO_2. Thus, based on this trend, the optimum flux rate can be considered at membrane which contains 3 % of SiO_2.

Figure 3 also describes the effect of addition of SiO_2 in terms of percentage of salt rejection. The results indicates that at 2 and 3 % of SiO_2, the salt rejection were quite similar approximately 73 % rejection. The salt rejection was gradually decreasing from 70 to 50 % after addition of 4 % SiO_2 until 6 % SiO_2. According to the results, the 3 % SiO_2 shows the highest NaCl rejection due to the optimal mixture SiO_2 that result in good hydrophilic properties. The high hydrophilicity membrane may reduce the interactions between hydrophobic contaminants and the membrane surface; hence, the rejection properties were improved effectively [8].

Fig. 3 Pure water permeation and salt rejection of different dope formulation
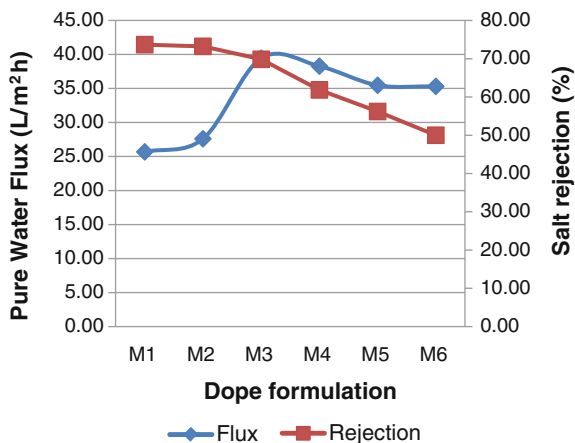
This clearly showed by the rejection properties of SiO_2 when it is added to PSf membrane. However, with more addition of SiO_2 will bring to the low value of rejection. This may be due to crystalline effect of the SiO_2 that has low compatibility when mixed with polymer. Therefore, the small particles can be a small defect and this surely will affect the rejection value.

3.2 Effect of Casting Rate on Membrane Performance

Five membranes under varied casting rate were fabricated for this experiment. The membrane is tested using pure water flux test and salt rejection.

Figure 4 illustrates the performance of membrane in pure water flux for different casting rate. The results show that the pure water flux decreases slightly at casting rate 8.0 ms^{-1} and after that it dropped sharply at casting rate 8.6 ms^{-1}. Similar trend were reported by [9–11] where the value of flux decreased when the casting rate is increases due to higher casting rate had better resistance for salt (NaCl) solution permeation. The pure water flux decreases from 39.32 to 38.64 $\text{Lm}^{-2} \text{ h}^{-1}$ as the casting rate increases from 7.3 to 10.0 ms^{-1}. The rheological behavior of the dope solution may cause the decreasing of permeability of the membrane since at the first stage of membrane fabrication, it is casted by the casting knife. Moreover, the molecular chains of the dope solution tend to align themselves appropriately at higher casting rate than those experienced in lower casting rate. This enhanced orientation initiating the polymer molecular to compact to each other. As a result, the apparent dense layer thickness increased with the increasing in the casting speed.

Figure 5 describes the salt rejection of the membrane at various casting rate. The result shows the efficiency of the membrane to reject sodium chloride (NaCl) solution. Based on experimental results, the percentage removal of NaCl solution were 67, 77, 79, 83, and 87 % for casting rate 7.3, 8.0, 8.6, 9.3 and 10.0 ms^{-1}, respectively. This result indicates that the increase in the casting rate results in the

Fig. 4 Pure water permeation of different casting rate
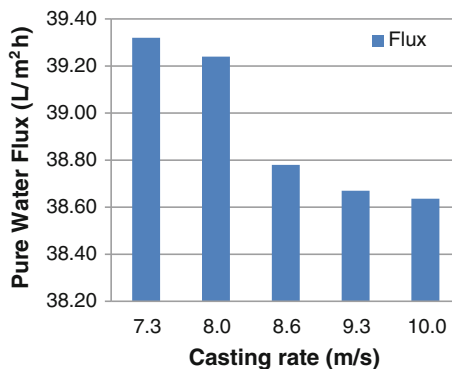
Fig. 5 Salt rejection of different casting rate
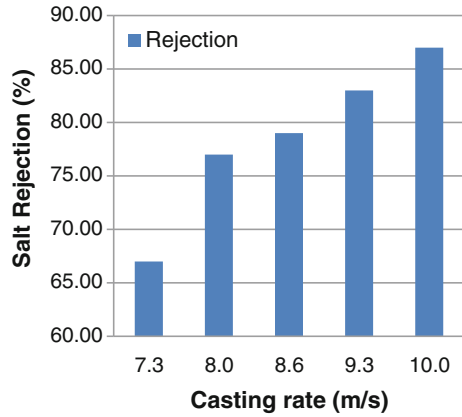
decreasing of the permeability of the entire salt rejection. The salt removal behavior depends on the lower free volume or a tighter dense oriented structure that formed during dry phase inversion at the outer surface of the membrane.

Figure 6 describes both characteristic and performance of membrane in term of pure water flux and salt rejection. Therefore, from both results of flux performance and salt (NaCl) rejection of polysulfone membrane, the ideal membrane was at the casting rate of 8.00 ms^{-1} with 77 % salt rejection and 39.28 $Lm^{-2} h^{-1}$ pure water fluxes. Thus, dope formulation of M3 (PSf = 21 %, DMAc = 71 %, PVP = 5 %, SiO_2 = 3 %) at casting rate 8.0 ms^{-1} were selected for wastewater treatment.

Fig. 6 Pure water flux and salt rejection of membrane
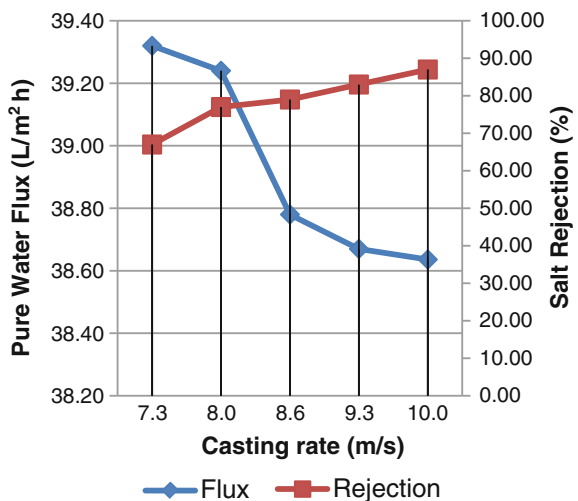
4   Conclusions

In this study, polysulfone membrane incorporated with crystalline SiO_2 were successfully prepared using casting technique containing additive 1–6 % SiO_2 with DMAc as a solvent. The addition of SiO_2 was affecting the performance of the membranes in terms of permeability and rejection. According to the results, permeability and rejection of the membranes increases by the increment of the percentage of silica. Furthermore, the increasing percentage of silica improves the hydrophilicity of the membrane. The membrane of dope M3 with 3 % of silica gives excellent water flux and the highest rejection. Casting rate has a significant effect on the performance of polysulfone membrane. The value of flux increases when the casting rate decreases and totally affects the percentage of salt (NaCl) rejection. The 8 ms^{-1} was the ideal casting rate since it tends to align the polymer molecular chains causing the polymer molecules packed close to each other.

References

1. H. Yua, Y. Caoa, G. Kanga, J. Liua, M. Li, Q. Yuana. "Enhancing antifouling property of polysulfone untrafiltration membrane by grafting zwitterionic copolymer via UV-initiated polymerization." Journal of Membrane Sciences. 342, 2009, pp 6–13.
2. D. Hellman. "A novel process of membrane fabrication: thermally assisted evaporative phase separation (TAEPS)." Journal of Membrane Science, 230 (1–2), 2004. pp 99-101.
3. A. N. I. Idris, C. M. Kee and I. A hmed. " Effect of Monosodium Glutamate Additive on Performance of Dialysis Membrane". Journal of Engineering Science and Technology, 3(2), 2008, pp172–179.
4. K. kogutid and K. Kuns "RO and NF membrnae fouling and cleaning and pore size distributuion variations". Desalination, 150, 2002, pp 13–120.
5. Z. Harun, M. R. Jamalludin, M. Z. Yunos, M. F. Shohur and A. F. Ismail. " The effect of Amorphous Rice Husk Silica to the Polysulfone Membrane Speration Process". Applied Mechanics and Materials, 701, 2013, pp 319–322.
6. J. Huang, J. Xue, K. Xiang, X. Zhang, C. Cheng, S. Sun, and C. Zhao. " Surface modification of polyethersulfone membrnaes by blending triblock copolymer of methoxyl poly(ethylene glycol)- polyurethane- methoxyl poly(ethylene glycol)." Colloids and Surfaces B: Biointerfaces, 88(1), 2011, pp 315–324.
7. H. T. Dang, R. M. Narbaitz, T. Matsuura and K. C. Khulbe. "A Compariosn of Commercial and Experimental Ultrafiltration Membranes via Surface Property analysis and fpuling test." Water Quality Research Journal, Canada, 41(1), 2006, pp 84–93.
8. E. Yuliwati, A.F. Ismail, W.J. Lau, B.C. Ng, A. Mataram, M.A. Kassim. "Effects of process conditions in submerged ultrafiltration for refinery wastewater treatment: Optimization of operating process by response surface methodology". Desalination 287, 2012, pp 350–361.
9. P. Aptel, N. Abidine, F. Ivaldi and J. P. Lafaille. "Polysulfone Hollow Fiber Effect of Spinning Conditions on Ultrafiltration Properties". Journal of Membrane Science, 22, 1985, pp 199–207.

10. A. F. Ismail, S. J.Shilton, I. R. Dunkin, and S. L. Gallivan. "Direct Measurement of Rheologically Induced Molecular Orientation in Gas Separation Hollow Fiber Membranes and Effect on Selectivity". Journal of Membrane Science, 126, 1997, pp 133–137.
11. I. D. Sharpe, A. F. Ismail, and S. J. Shilton. "A Study of Extrusion Shear and Forced Convection Residence Time in The Spinning of Polysulfone Hollow Fiber Membranes for Gas Separation". Separation and Purification Technology, 17, 1999, pp 101–109.

Removal of Lead by Nanoscale Zerovalent Iron in Surfacewater

Raja Hafizzuddin Raja Amir Iskandar, Jalina Kassim, Mohd Fozi Ali and Amnorzahira Amir

Abstract This study investigates removal of Lead (Pb^{2+}) by nanoscale zerovalent iron (nZVI) in surface water under various environmental conditions. Particles size of synthesized nZVI was in the range of 35.57–49.62 nm (<100 nm) and congregated to each other. Remarkable removal of Pb^{2+} ($k = 0.30$ min^{-1}) was observed in nZVI suspension (0.32 g/L) in 10 min, while no significant of Pb^{2+} removal was observed in suspension alone at neutral pH. The removal of Pb^{2+} was significantly dependent on the suspension pH and concentrations of Pb^{2+} and nZVI. Percent removal of Pb^{2+} significantly decreased as the concentrations of Pb^{2+} increased. Removal efficiency of Pb^{2+} decreased (49–25 %) as the pH increased from neutral to basic conditions (pH 7–9). As concentration of nZVI increased (0.06–0.10 g/L), the removal efficiency increased approximately 1.67 times (42–70 %). Experimental results from this study provide basic knowledge on the role of nZVI as a reductant to remove Pb^{2+} in surface water at different environment conditions.

Keywords Pb^{2+} · nZVI · Surface water · Removal efficiency

R.H.R.A. Iskandar · J. Kassim · M.F. Ali
Faculty of Civil Engineering, Universiti Teknologi MARA,
40450 Shah Alam, Selangor, Malaysia
e-mail: black_radja@yahoo.com

J. Kassim
e-mail: jalina@salam.uitm.edu.my

M.F. Ali
e-mail: mohdfozi@salam.uitm.edu.my

A. Amir (✉)
Institute for Infrastructure Engineering and Sustainability Management (IIESM),
Faculty of Civil Engineering, Universiti Teknologi MARA,
40450 Shah Alam, Selangor, Malaysia
e-mail: amnorzahira@salam.uitm.edu.my

1 Introduction

Lead (Pb) is one of the heavy metals that are known for its toxicity and could cause adverse impact on human health and environment. The toxicity of heavy metals can collapse the immune system of a human body leaving the human body defenseless and open a gateway to all kind of diseases [1, 2]. Due to their ability of bioaccumulation, metals can be assimilated into food chain and concentrated in aquatic organism to a level that affects their physiological states [3]. Health issues due to exposure of Pb may include poor muscle coordination, nerve damage, increased blood pressure, hearing and vision impairment, reproductive problems, and retarded fetal development [4]. Suratman and Sefie found that samples collected from groundwater and surface water within Selangor region were contaminated with heavy metals such as lead, copper, zinc, and chromium [5]. Therefore, remediation technology to remove heavy metals in surface water is urgently needed.

Presently, numerous remediation technologies such as chemical precipitation, flotation, and adsorption had been engineered to remove, separate, destroy, and contain these toxic heavy metals [6]. Remediation of surface water using the conventional method such as the ex situ treatment pump-and-treat, steam treatment, flushing with solvent and surfactants, and natural attenuation via bio and phytoremediation is expensive and time consuming [7, 8]. The earliest passive in situ treatment introduced is permeable reactive barriers (PRBs) using granular zerovalent iron, however this treatment significant fault is that it can only concentrate on contaminant plumes that flow through the barrier ergo they do not contribute to the active removal of the source [8]. Recent remediation technology which has proven its effectiveness in treating organic and inorganic contaminants is remediation using nanoscale zerovalent iron (nZVI) [8–10]. The aforementioned remediation technology is very effective in transforming halogenated organic compounds such as tetrachloroethene (PCE), trichloroethene (TCE), and carbon tetrachloride (CT) into chloride and capable of reducing heavy metals such as lead, uranium, and mercury [8, 11]. nZVI offers an advantage over conventional method because of its simplicity, unique physicochemical properties, and nontoxicity [9]. The high surface-to-volume ratio of nZVI stimulates mass transfer to and from the solid surface resulting in likelihood for contaminant degradation [9, 12]. The reaction kinetic rate of nZVI is strongly dependent on the total reactive surface area of nZVI [9, 11]. Muller et al. state that the usage of nZVI technology is extensive in the United States and that there is no regulation and current laws regarding its usage, whereby in Europe took a precautionary attitude on the aforementioned technology albeit field applications conducted in *Bornheim*, *Germany*, *Horice* and *Pisecna*, *Czech Republic* produced a promising result in term of contaminants remediation [8].

This study highlights the charcterization of nanoscale zerovalent iron (nZVI). Removal of Lead (Pb^{2+}) by nZVI was investigated under various environmental condition. Effects of different pH condition and different concentration of nZVI were also investigated.

2 Materials and Methods

2.1 Lists of Chemicals

For the preparation of nZVI, chemical utilized include, iron chloride ($FeCL_3$) (98 %, Aldrich), sodium borohydride ($NaBH_4$) (99 %, Aldrich), and acetone (99 %, Merck). Buffer solutions were prepared by using MOPs, $pK_a = 7.2$ for pH 6.5–9 and hydrochloric acid (HCL) (0.1 M, Merck). For the determination of Pb^{2+} chemicals utilized include, chloroform, dithiver metals reagent powder pillow, citrate buffer powder pillow, potassium cyanide, sodium hydroxide solution 5.0 N, acetone, and lead nitrate ($Pb(NO_3)_2$) stock solution were utilized for the determination of Pb^{2+}. For the experiments, all reagents and solutions used were prepared using ultra pure water (18 Ω cm).

2.2 Synthesize of nZVI

For this study, synthesis of nZVI was performed by using Sodium borohydride ($NaBH_4$) (0.9 mM, 1000 mL) and iron chloride ($FeCl_3$) (0.11 mM, 1000 mL), following proposed method by Wang and Zhang [13]. The $NaBH_4$ performs as a reducing agent to convert $FeCl_3$ to nZVI. Both $NaBH_4$ and $FeCl_3$ were mixed by dropping $NaBH_4$ solution into $FeCl_3$ solution continuously while stirring consistently at 1000 rpm. Fe^{3+} will be reduced to Fe^0 by hydrogen generated during the reaction. To collect the nZVI, the black iron particles that were formed were separated from the solution by centrifuging the solution at 3000 rpm for 10 min. The collected nZVI was then washed twice with DDW and once with ethanol before dried and stored in an aerobic chamber.

2.3 Batch Experiments

In order to determine the removal efficiency of Pb^{2+} by nZVI, batch experiments were performed. Experiments were conducted by using 250 mL beakers. MOPS buffer solution of 50 mM was prepared using MOPS sodium salt and DDW. 0.1 M HCL acid was utilized to adjust the pH of buffer solution to desired pH value. Exact amount 0.08 g of nZVI was weighted and transferred to each beakers and MOPS buffer solution (50 mM) was poured into each vials without headspace to maintain the pH suspension constant at 7. Pb^{2+} with concentration of 0.30 mg/L was then introduced into each beaker to initiate kinetic reaction between nZVI and Pb^{2+}. Vials were then rapidly capped, mounted on a tumble mixer, and rotated at 7 rpm at room temperature (25 ± 0.5 °C) for 30 min. Solution in the beakers was then mixed using the jar test mixer and was set at 7 rpm at room temperature (25 ± 0.5 °C) to

mimic the surface water flow for 10 min reaction time. After the solution is thoroughly mixed, the Dithizone Lead(II) detection method is used and then the sample is then analyzed using the HACH DR 2800 UV-Vis Spectrophotometer to measure the concentration of Pb^{2+}.

Batch kinetic experiments were conducted to investigate effect of nZVI concentrations, and pH on the removal of Pb^{2+} by nZVI. To investigate effect of nZVI on the removal of Pb^{2+} by nZVI at pH 7, three different concentrations of nZVI (0.06, 0.08, and 0.10 g) were weighted and transferred into beakers. Initial concentration of Pb^{2+} was set at 0.30 mg/L at pH 7. To study effect of pH on the removal Pb^{2+} by nZVI, 50 mM MOPS buffer and 0.1 M HCL were used to adjust and maintain the pH values constant at 7 and 9. Initial Pb^{2+} and nZVI concentrations were set at 0.30 mg/L and 0.32 g/L, respectively. Samples were prepared by following the same procedures as the batch test described above.

2.4   Analytical Procedures

- Characterization of nZVI-Environmental Scanning Electron Microscopy (ESEM) analysis was conducted to investigate surface morphology of the synthesized nZVI. ESEM was set up with LFD detection for wet samples (Quanta FEG 450) with 10 kV voltage and magnification of 100,000×, respectively. Sample of slurry nZVI was carefully packed under anaerobic condition to avoid its surface oxidation prior to analysis. The sample was vacuumed for 5 min to avoid interference between gas molecules and electron beam that used for imaging to enhance resulting images.
- Lead concentration-concentration of Pb^{2+} was determined using HACH DR 2800 UV-Vis Spectrophotometer, following Dithizone Lead(II) detection Method 8033. The optimum detection range for this method is 0.003–0.300 mg/L of Pb^{2+}. Aliquots of aqueous solution collected from samples and controls were transferred to 500 ml separatory funnel. A citrate buffer powder pillow was added and mixed well until dissolved. In a 100 ml graduated cylinder, 50 ml of chloroform and dithiver metals reagent powder pillows were prepared.

  30 ml of the chloroform mixtures was transferred into a 30 ml beaker and poured into the separatory funnel. The mixtures were shaken well and the funnel stopper was released every few seconds to release the gas. 5 ml of sodium hydroxide solution was then added into the separatory funnel and shaken well. Sodium hydroxide solution was dropped into the chloroform mixtures until the mixtures changes colors to orange and pink separated solutions. 2 g of potassium cyanide was then added. The pink colored solution was then transferred into 25 ml square sample cell for Pb^{2+} determination using DR 2800 UV-Vis Spectrophotometer to measure the concentration of Pb^{2+}.

3 Results and Discussion

3.1 *Characterization Study of nZVI*

Figure 1 presents the morphology and particle size of synthesized nZVI using ESEM at 100,000× magnification. The resulting image of nZVI shows that the size of nZVI was approximately 35.57–49.62 nm. It was uniformly aggregated to each other due the strong dipole–dipole magnetic of individual particles [9]. These results strongly confirmed that synthesized nZVI in this study was in nanoscales (<100 nm). This result indicates that the synthesized nZVI provides high reactive surface area which may contribute to high removal efficiency of Pb^{2+} which is expected in this study. Similar characterization study of nZVI was observed by other researchers [14–16].

3.2 *Removal of Pb^{2+} by nZVI*

Figure 2 shows the removal of 0.30 mg/L Pb^{2+} by 0.32 g/L nZVI at pH of 7. Result shows that there is no significant removal of Pb^{2+} in the absence of nZVI in the system. However, in a presence of nZVI acting as a reductant, the removal of Pb^{2+} can be observed as early as the first 5 min of reaction. The removal kinetic of Pb^{2+} removal by nZVI at pH 7 was 0.30 min^{-1}. This result indicates that nZVI play significant role to remove Pb^{2+} at pH 7.

Fig. 1 ESEM image of nZVI, magnified 100,000×
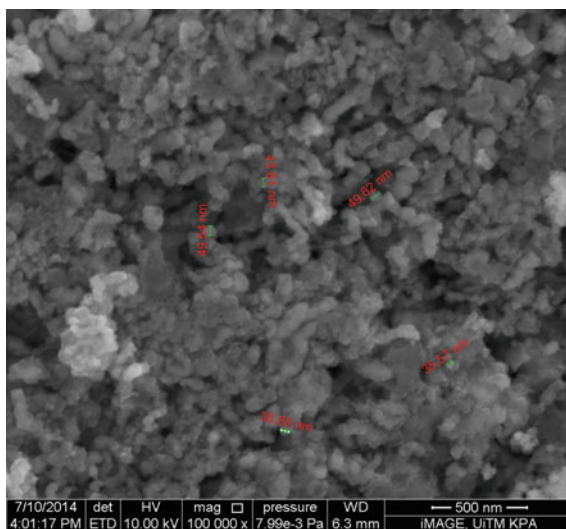
Fig. 2 Removal of Pb^{2+} by nZVI. (Initial condition nZVI = 0.08 g; Pb^{2+} = 0.30 mg/L; pH 7)
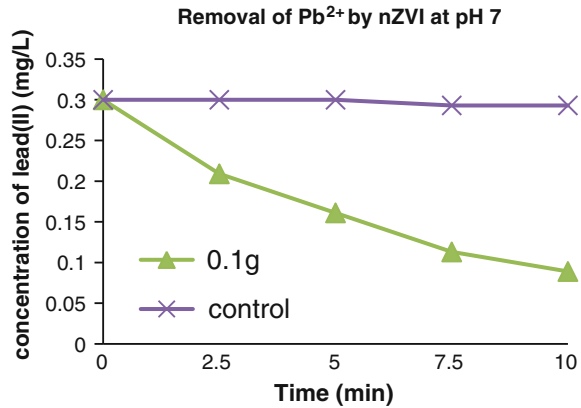
The reduction of Pb^{2+} by nZVI can be explained by the following redox equations below [17]:

$$Fe^0 + 2\bar{e} \rightarrow Fe^{2+} \quad E_0 = -0.44\,eV \tag{1}$$

$$Pb^{2+} + 2\bar{e} \rightarrow Pb^0 \quad E_0 = -0.13\,eV \tag{2}$$
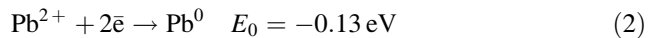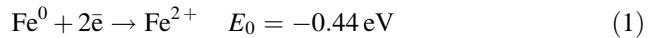
and

$$\Delta E = (\text{Oxidation species}) - (\text{Reduction species})$$
$$= (-0.44) - (-0.13) = -0.31\,eV$$

For negative value of ΔE, it is concluded that the spontaneous redox reaction occurs.

3.3 Effects of nZVI Concentration on Removal of Pb^{2+} by nZVI

Figure 3 illustrates the effect of nZVI concentration on the removal Pb^{2+} by nZVI. Similar trends were observed for all the three different concentrations of nZVI (0.06, 0.08, and 0.10 g) where concentration of Pb^{2+} gradually decreases throughout the reaction time. Result reveals that removal efficiency of Pb^{2+} increased from 42 to 70 % as the concentration of nZVI was increased from 0.06 to 0.1 g within 10 min of reaction time.

Higher removal efficiency was obtained at higher concentration of nZVI because the amount of reactive surface would likely to increase thus allowing more electrons to be transferred to the targeted contaminant [9]. Similar finding were obtained by Arshadi et al. where removal efficiency of Pb^{2+} increases from 15.6 to 89 % as nZVI concentration increases from 0.05 to 0.15 g [13]. However, Nik Redzauddin et al.

Fig. 3 Effect of nZVI concentration on the removal on the removal of Pb^{2+} by nZVI
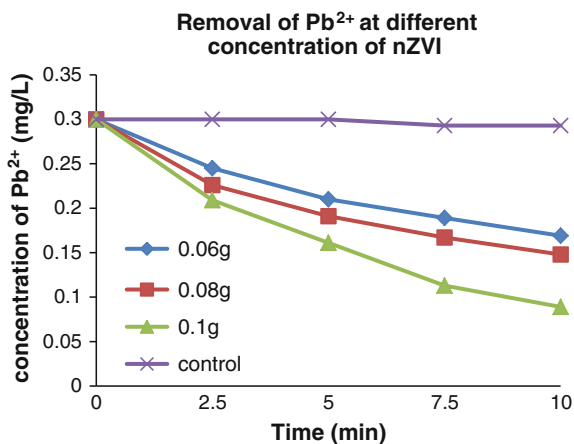
reports that removal of Zn by nZVI shows contrary findings to the result of this study. Removal kinetic rate, k of Zn significantly decreased (0.162–0.148 min^{-1}) as concentration of nZVI increased from 0.25, 1.25, and 2.50 mg/L [18]. This probably occurred due to the agglomeration of nZVI particles itself at high concentration of nZVI. The literatures have reported that agglomeration of nZVI may decrease the reactive surface area on the nZVI surface. Due to this reason, electron transfer from the reactive surface of nZVI to Zn was inhibited and Zn^{2+} could not be reduced to Zn [19, 20].

3.4 Effects of PH on Pb^{2+} Removal by nZVI

Figure 4 shows the effects of suspension pH on the removal efficiency of Pb^{2+} by nZVI. It was observed that the removal efficiency at pH 9 was 30 % which is 1.67 times lower than removal efficiency at pH 7 (50 %). This is probably due the

Fig. 4 Effect of pH on the removal of Pb^{2+} by nZVI
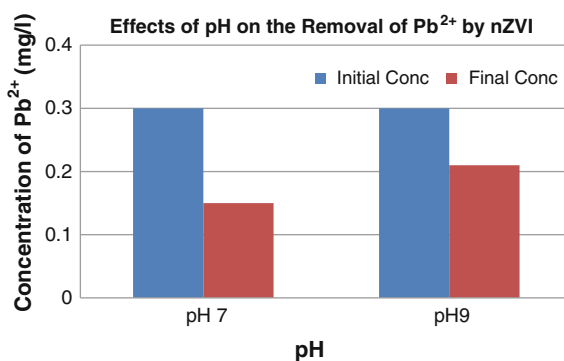
formation of passivation layer on the surface of nZVI. Literatures have reported that formation of passivation layer on the surface of nZVI at high pH condition probably decreases the removal efficiency of Pb^{2+} by nZVI [21, 22]. The formation of passivation layer decreases the density of reactive surface area (e.g., Fe^0 and Fe^{2+}) on the surface of nZVI [21].

4   Conclusion

This study provides significant finding on the removal of Pb^{2+} by nZVI in surface water. Optimum condition in removal of Pb^{2+} by nZVI in surface water was identified in this study [[nZVI]: 0.10 g, pH 7]. The removal efficiency of Pb^{2+} by nZVI is strongly influenced by the reactive surface area on the surface of nZVI at different environmental conditions. Higher concentration of nZVI would provide more reactive surface area thus contributing to high removal efficiency of Pb^{2+} in this system. Formation of passivation layer on the surface of nZVI at basic condition (pH 9) significantly decreased reactive surface area on the surface of nZVI thus contributes to lower removal efficiency of Pb^{2+}. Results from this study have significantly revealed that removal kinetic of Pb^{2+} by nZVI is strongly dependent on the reactive surface area on the nZVI surface. The experimental findings can provide basic knowledge to identify potential reaction mechanisms for the removal of Pb^{2+} by nZVI in surface water under various environmental conditions.

References

1. H. M. Salem, E. A. Eweida, and A. Farag, "Heavy metals in drinking water and their environmental impact on human health" ICEHM2000, Cairo University, Egypt, 2000, pp. 542–556.
2. S. Khan, Q. Cao, Y. M. Zheng, Y. Z. Huang and Y. Z. Zhu, "Health risk of heavy metals in contaminated soils and food crops irrigated with wastewater in Beijing, China", Environmental Pollution, 2008, vol 152, pp. 686–692.
3. S. M. Saeed and I. M. Shaker, "Assessment of heavy metal pollution in water and sediments and their effect on oreochromis niloticus in the Northen Delta Lakes, Egypt". International Symposium on Tilapia in Aquaculture 2008, pp. 475–489.
4. U.S. Environmental Protection Agency, "Lead and Environment" Retrieved from http://www.epa.gov/superfund/lead/health.htm
5. S. Suratman and A. Sefie, "Groundwater contamination at landfill sites in Selangor". XXXVIII IAH Congress, Krakow, Poland.
6. F. A. Caliman, B. M. Robu, C. Smaranda, V. L. Pavel, and M. Gavrilescu, "Soil and groundwater cleanup: benefits and limits of emerging technologies". Clean Technology Environmental Policy, vol 13, pp. 241–268.

7. L. B. Hoch, E. J. Mack, B. W. Hydutsky, J. M. Hershman, J. M. Skluzacek, and T. E. Mallouk, 2008 "Carbothermal Synthesis of Carbon Supported Nanoscale Zero- Valent Iron Particles for the Remediation of Hexavalent Chromium". Environmental Science & Technology, 2008, vol. 42, pp. 2600–2605.

8. N. C. Mueller, J. Braun, J. Bruns, M. Černík, D. Rickerby, and B. Nowack, "Application of nanoscale zero valent iron (NZVI) for groundwater remediation in Europe ". Springer-Verlag, 2011.

9. R. Singh, V. Misra and R.P. Singh, "Removal of hexavalent chromium from contaminated ground water using zero-valent iron nanoparticles". Environmental Monitoring and Assessment, 2011, vol 184, pp. 643–3651.

10. Z. E. Kashitarash, S. M. Taghi, N. Kazem, A. Abbass, and R. Alireza, "Application of iron nanoparticles in landfill leachate treatment – case study: Hamadan landfill leachate". Iranian Journal of Environmental Health Sciences & Engineering 2012, vol 9, pp. 36.

11. X. Li, J. Cao, and W. Zhang, "Stoichiometry of Cr(VI) immobilization using Nanoscale Zerovalent Iron (nZVI): A study with high-resolution X-ray Photoelectron Spectroscopy (HR-XPS)". Ind. Eng, Chem. Res, 2008, vol. 47, pp. 2131–2139.

12. S. Comba, A. D. Molfetta, and R. Sethi, 2010. "A Comparison between Field Applications of Nano-, Micro-, and Millimetric Zero-Valent Iron for The Remediation of Contaminated Aquifers". Water Air Soil Pollution, 2011, 215:595–607.

13. M. Arshadi, M. Soleymanzadeh, J. W. L. Salvacion and F. SalimiVahid, "Nanoscale Zero-Valent Iron (nZVI) supported on singuelas waste for Pb(II) removal from aqueous solution: Kinetics, thermodynamic and mechanism", Journal of Colloid and Interface Science. 2014, vol 426, pp. 241–251.

14. N. A. Miranda, S. E. Baltazar, A. Garcia, A.H. Romero, M. A Rubio and D. Altbir, "Lead removal by nano-scale zero valent iron: Surface analysis and pH effect", Materials Research Bulletin, 2014, vol 59, pp. 341–348.

15. N. Efecan. "Characterization of The Adsorption Behaviour of Aqueous Cd(Ii) and Ni(Ii) Ions on Nanoparticles of Zero-Valent Iron", Izmir Institute of Technology, 2008.

16. M. L. Alowitz & M. M. Scherer, "Kinetics of nitrate, nitrite and Cr(VI) reduction by iron metal", Environmental Science & Technology, 2002, vol 36, No. 3.

17. A. Saberi, 2012. "Comparison of Pb^{2+} removal efficiency by Zero Valent Iron Nanoparticles and Ni/Fe Bimetallic Nanoparticles". Iranica Journal of Energy & Environment, 2012, vol 3 (2), pp. 189–196.

18. N. N. I. Nik Redzauddin, J. Kassim and A. Amir, "Removal of Zinc by Nano-scale Zero Valent Iron in Groundwater" Applied Mechanics and Materials, 2015, vols 773–774, pp. 1231–1236.

19. N. Kržišnik, A. Mladenovič, A. A. Škapin, L. Škrlep, J. Ščančar & R. Milačič. "Nanoscale zero-valent iron for the removal of Zn^{2+}, Zn(II)-EDTA and Zn(II)-citrate from aqueous solutions", Journal of Science of the Total Environment,2014, vol 476–477, pp. 20–28.

20. U.S. Environmental Protection Agency, Nanotechnology White Paper, Science Policy Council, 2007.

21. M. L. Alowitz & M. M. Scherer, " Kinetics of nitrate, nitrite and Cr(VI) reduction by iron metal", Environmental Science & Technology, 2002, vol 36, no. 3.

22. F. Fu, J. Ma, L. Xie, B. Tang, W. Han & S. Lin. "Chromium removal using resin supported nanoscale zero-valent iron" Journal of Environmental Management, 2013, vol 128, pp. 822–827.

Evaluation of a Novel Sewage Treatment System by Combining a Primary Settled Basin with DHS Reactor

Akihiro Nagamachi, Tadashi Tagawa, Yuta Seto, Akinori Iguchi, Kengo Kubota and Hideki Harada

Abstract At present, 95 % of the total population of the Egypt country takes up residency in areas around of Nile, irrigation agriculture caused by using raw sewage exacerbate the issue of environmental health hazard risk in arid regions of Egypt. So, Egypt country goes ahead with effective utilization of treated sewage for irrigation, our international research consortium has proposed a novel concept of sewage treatment technology for risk reduction of health hazard and we focus on down-flow hanging sponge reactor (DHS) as sewage treatment technology. DHS behaved extremely well as sewage treatment technology in India and it is widely expected to dominate in a developing country. The method is a combination of the DHS for posttreatment and primary sedimentation tank for pretreatment. This method went live in Egypt in 2014. So, KNCT tried demonstrating experiment in Japan with the use of share of the same design as method. Preliminary experiment has confirmed the feasibility to satisfy a criterion for irrigation in EGYPT as an objective. Irrigation standard (TSS < 60 mg/L, BOD < 60 mg/L, COD_{total} < 80 mg/L, NO_3^- < 50 mg/L) set by Egypt government has achieved effective utilization of treated sewage for irrigation as objective. When hydraulic retention time (HRT) set 1 h as DHS's volume load of target, condition of operation of experiment is controlled by varying

A. Nagamachi (✉) · T. Tagawa
Department of Civil Engineering, National Institute of Technology,
Kagawa College, 355, Takamatsu 761-8058, Japan
e-mail: kankyoken.eco@gmail.com

Y. Seto
Department of Civil and Environmental Engineering, Nagaoka University
of Technology, 1603-1, Nagaoka 940-2137, Japan

A. Iguchi
Faculty of Applied Life Sciences, Nigata University of Phermacy
and Applied Life Sciences, 265-1, Nigata 956-0841, Japan

K. Kubota · H. Harada
Department of Civil and Environmental Engineering, Tohoku University,
6-6-06, Sendai 980-8579, Japan

treatment quantity of sewage. We started up the experiment provided that treatment quantity of sewage: 5 m³/day, HRT: 4 h. The experiment is performed in five stages. It has continued since March 2013 (Phase 1: HRT 4 h, Phase 2: HRT 2 h, Phase 3: HRT 1 h, Phase 4: HRT 2 h, and Phase 5: HRT 4 h). The preliminary experiment indicates the possibility of effective utilization of treated sewage for irrigation. The removal rate of biochemical oxygen demand (BOD) and suspended solids (SS) retains sufficient strength to meet irrigation standards. (Phase 1: 82 %(BOD) 97 %(SS), Phase 2: 92 %(BOD) 81 %(SS), Phase 3: 76 %(BOD) 65 %(SS) Phase 4: 81 %(BOD) 68 %(SS), Phase 5: 89 %(BOD) 88 %(SS)). The result of the profile analysis indicated that organics destruction occurred from the top of the reactor (1st stage) to the 3rd stage and the nitrification process proceed from the 4th stage to the 5th stage. On the other hand, the nitrification process of $NH_3^- – N$ was poor at Phase 3. We believe that this related to a blocked gap of media sponge. At Phase 4 and Phase 5, the removal rate of BOD and nitrification of the water was provided so as to lengthen the processing time. Improvement in the ability to remove $NH_3^- – N$ is vital to use the primary settled-DHS process for irrigation, because $NH_3^- – N$ is a toxic substance for agricultural irrigation.

Keywords Irrigation · Down-flow hanging sponge reactor (DHS)

1 Introduction

Japan accomplished economic development in the rapid economic growth period of the 1960s and established the position as the major economic power. However, it had a serious adverse effect for environment because harmful drainage was exhausted as non-processing in a shade of economic growth. Therefore, it is thought that reduction of the environmental load and maintenance of the water environment are important problems.

In Japan, activated sludge methods spread. However, the error of this method needs a large quantity of electricity and the maintenance is difficult. Therefore, it does not spread in the developing countries. In this way, the development of the cheap simple water processing technology is required. We develop a water processing technology on African land.

The most of African countries have drying zones,. where reservation of water resources is very difficult. In the developing countries, health environmental risks such as an alimentary system infection (typhoid, dysentery, and cholera) have occurred everywhere in Africa including an arid region. Nevertheless, domestic sewage is often used for irrigation without appropriate treatment. Irrigation reuse of treated domestic wastewater can be an option for securement of water resource in arid regions.

Fig. 1 The flow diagram of
the primary settled-DHS
system
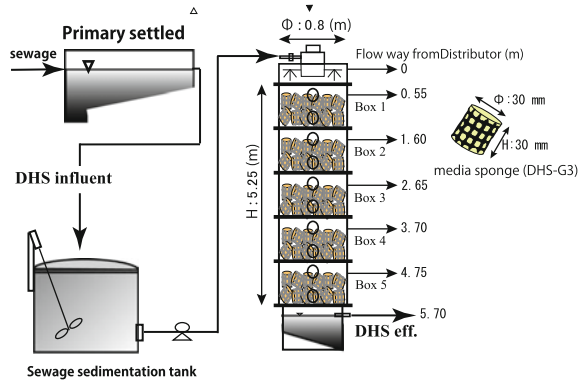
Therefore two problems are important in the developing countries

1. An improvement of the irrigation method and securing of safe water.
2. Promotion of the effective use to the farmland of sewage disposal water.

Here, we developed a novel domestic sewage treatment system, by combining a primary sedimentation tank and a down-flow hanging sponge (DHS) reactor (Fig. 1), for irrigation reuse.

Sewage is initially treated with a primary sedimentation tank to remove suspended solids, followed by subjecting to a DHS reactor.

2 Methodology

2.1 Mechanism of DHS Method

The process is an attached growth-type treatment process employing polyurethane sponges as support media for the growth of bacteria (Fig. 2). A concept of DHS is based on the conventional trickling filter. Therefore, air dissolves into the wastewater as it flows down the DHS reactor, and thus there is no need for external aeration. However, unlike trickling filters using rocks as a packing material, DHS employs polyurethane sponge as a support material (Fig. 3).

Polyurethane sponge is insoluble, not biodegradable, low cost, and highly mechanically stable. Furthermore, sponge material has a void ratio of more than 95 %, which provides an excellent site for growth and attachment of active biomass, resulting in a significant increase in SRT. Sludge is retained both inside and outside the sponge carrier. The enormous amount of biomass and very long SRT expedite the treatment process. Moreover, the DHS method provides adequate time for self-degradation of any attached biomass, reducing the production of excess sludge from the process [1].

Fig. 2 Mechanism of DHS treatment
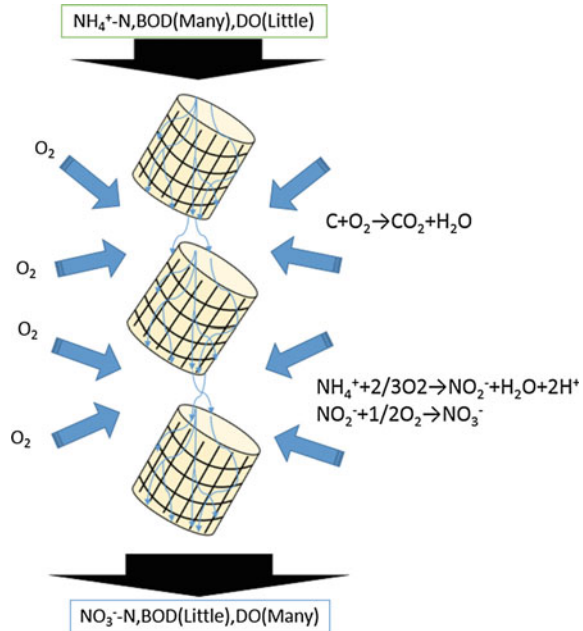
The structural advantages of DHS are as follows [1]:

1. Sponge—inexpensive and locally available
2. Compact—requires less land area
3. Operation—simple
4. No need of any external aeration
5. Negligible amount of excess sludge
6. Less mechanical parts—demands less maintenance

2.2 The Design of a Experiment System

The third-generation sponge was used as a structure form of DHS. The basic design concept of DHS was similar to that of the trickling filter. However, instead of the solid packing materials used in a trickling filter, small sponge pieces with an outer supporting material were used. Construction of the process was easier as it involved random packing of the sponge unit. Percentage occupancy of the sponge unit in the reactor was 36–38 % [1]. In the experiment, DHS reactor consists of a sponge carrier part of five layers, a sprinkler part, and a sedimentation tank (Fig. 1). DHS reactor was designed considering amount of processing sewages: 20 m^3/day, HRT: 1 h.

Fig. 3 DHS system

2.3　Experimental Method

In the experiment, start-up phase was carried out as amount of DHS processing sewage: 5 m³/day (we set gradually increasing the flow rate from 5 to 20 m³/day). The continuous feeding period for 56 days was set to Phase 1. We started an experiment at 20 m³/day from 133 days and carried out a water experiment of approximately 400 days. However, we reduced flow quantity and continued testing it because a good result was not provided by the organic matter removal and a nitrification reaction. We changed processing quantity of water and continued

operating to Phase 4. Currently, we got around to Phase 5 (HRT: 4 h, processing sewage: 5 m^3/day). In this study, we evaluate a treated water at the irrigation standard (BOD < 60 mg/L, TSS < 30 mg/L, NO$_3^-$–N < 50 mg/L).

3 Result and Discussion

3.1 The Result of Treatment Sewage

Figure 4 shows the results of a water temperature, BOD$_5$, NH$_4^+$–N, and NO$_3^-$–N. The operation of Phase 1 (flowrate: 5 m^3/day) was performed as sponge volumetric loading: 0.79 BOD kg/m^3/day. The removal ratio of BOD was gradually increasing from the start-up phase.

More, after 25 days operation, the removal rate of BOD was increased to 83 %. Finally, it became until BOD 96 % removal after 53 days of operation. The concentration of BOD in the effluent from the DHS reactor satisfied the irrigation standard of Egypt (BOD ≤ 60 mg/l) even the HRT of the DHS reactor was as short as 1 h at Phase 3. The HRT was changed each in Phase 4 and Phase 5 for 2 h for 4 h. The BOD removal rate was 75, 81 and 89 % each in from Phase 3 to Phase 5.

On the other hand, nitrification, which observed at the HRT of 2 h, was no longer detected at the HRT of 1 h. In Phase 4 and Phase 5, a nitrification reaction came to be seen again. As a result of quality of the water analysis, the NH$_4^+$–N density after the processing decreased dramatically in comparison with Phase 3 and, NO$_3^-$–N rosed drastically (NH$_4^+$–N; 22.0 mg/L: Phase 3, 16.8 mg/L: Phase 4, 9.4 mg/L: Phase 5, NO$_3^-$–N; 3.0 mg/L: Phase 3, 8.1 mg/L: Phase 4, 9.8 mg/L: Phase 5).

In Phase 3, if the water temperature is high (Water temperature >20 °C), the removal ability of organic matter decomposition is good. But, If the water temperature is low (Water temperature <20 °C), the removal ability of organic matter decomposition is gradually down. At the nitrification reaction, the same trend was obtained. In this way, our system has the possibility that we can use NH$_4^+$–N and NO$_3^-$–N acid-related nitrogen properly by managing the HRT while I let BOD density (BOD < 60 mg/L) be lucid.

3.2 Profile Analysis

The Profiling result on the operating condition of Phase 1–5 is shown in Fig. 5. The removal ratio of BOD (Phase 1: 74 %, Phase 2: 68 %, Phase 3: 53 %, Phase 4: 78 %, and Phase 5: 93 %) was obtained at the Box 3 eff. from the DHS.

Fig. 4 The result of BOD, NH_4^+–N, NO_3^-–N
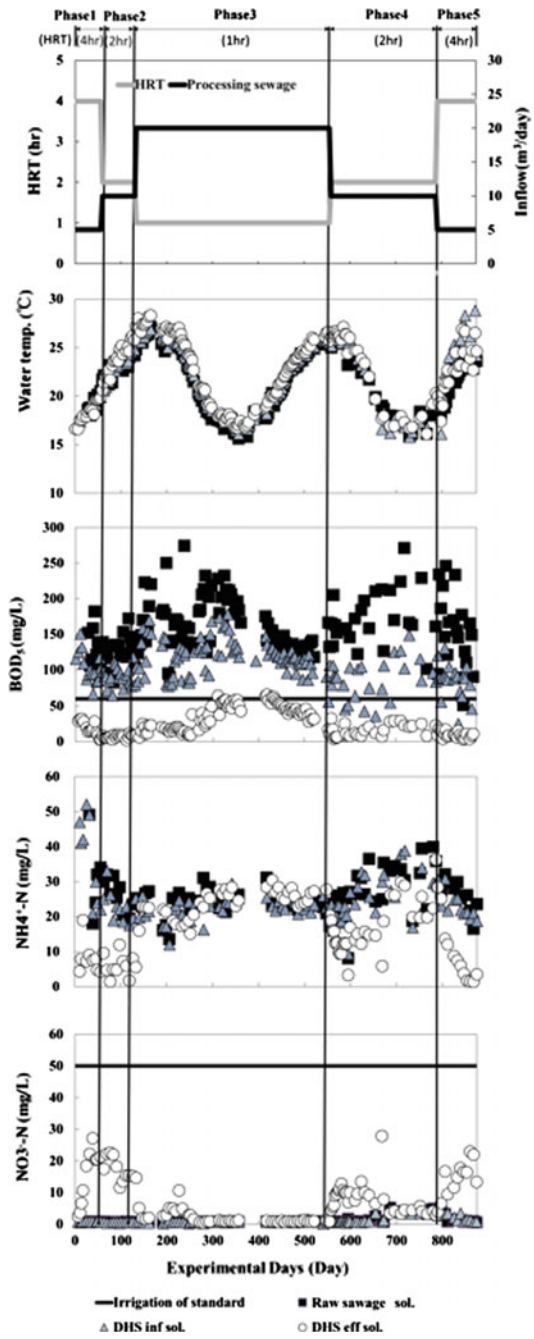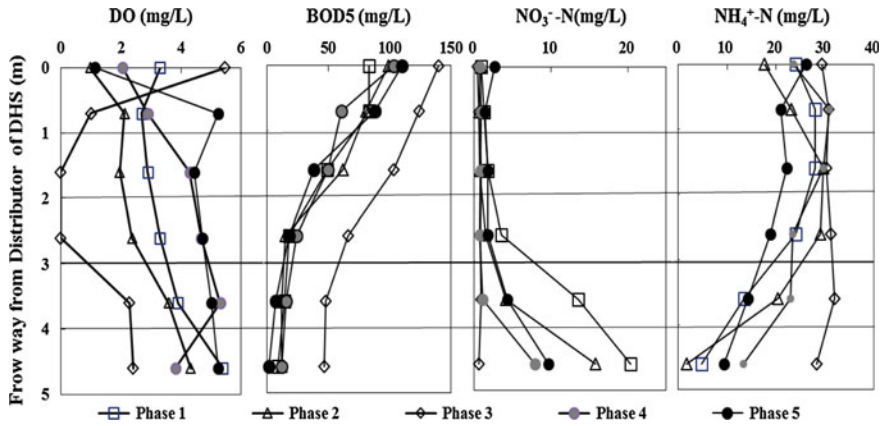
Fig. 5 The result of profile on the operating condition (Phase 1–5)

The nitrification reaction occurred in the lower part of DHS, and a decrease in NH_4^+ –N and increase in NO_3^- –N were seen mainly. Because organic matter volume load is high, the fast heterotrophic bacterium of the increase takes first priority and, in the upper reactor, dismantles organic matter, and it is thought that quality of the water environment suitable for nitrification was built in the reactor lower part that decreased of the organic matter load. Respectively, regarding to DO concentration, the oxygen supply was confirmed in the reactor (DO > 2 mg/L) at Phase 1–5. But, at Phase 3, rapidly consumption of DO was confirmed from top of the DHS to middle of the DHS. So, the removal ability for BOD is not good at Phase 3 [2, 3].

By a past study, as for the nitrification reaction, there is the report which became maximum at time with BOD density less than 8 mg/L. Thus, Do density existed enough, and a good nitrification reaction occurred when organic substance density was low.

4   Conclusion

From the obtained results, the following conclusions can be drawn:

(1) The concentration of BOD in effluent from the DHS reactor satisfied the irrigation standard of Egypt (BOD ≤ 60 mg/l) even the HRT of the DHS reactor was as short as 1 h.
(2) The nitrification reaction was found by managing the HRT more than 2 h.
(3) We had the possibility that I could make good use of NH_4^+ –N and NO_3^- –N by changing the HRT.

Due to the aforementioned reasons, this system has the possibility that I can manage the nitrification reaction while clearing BOD (≤60 mg/l) by managing the HRT. It is showed that there is a possibility to show enough results in the developing country.

References

1. Shigeki UEMURA, Hideki HARADA: Application of UASB Technology for Sewage Treatment with a Novel post treatment Process In: Environmental anaerobic technology applications and new developments, pp. 103–105.
2. Tsutomu OKUBO, Takashi YAMAGUCHI, Kengo KUBOTA, Hideki HARADA: Development of a novel sewage treatment system without external aeration - on-site evaluation of the performance of the 3rd generation dhs reactor in india (2008)
3. Tsutomu OKUBO, Hideki HARADA, Takashi ONODERA, Shigeki UEMURA, Takashi YAMAGUCHI, Akiyoshi OHASHI: Development of a novel sewage treatment technology minimum energy requirement – performance of organic matters removal by practical–scale DHS reactor (2010)
4. Yuta SETO, Tadashi TAGAWA, Tsutomu OKUBO, Shigeki UEMURA, Masanobu TAKAHASHI, Hideki HARADA: Experiment of Self-Sustainable Sewage Treatment System "Primary settled-DHS" with minimum Energy Requirement, INTERNATIONAL POST – GRADUATE SEMINAR 2013, Malaysia (2013)
5. Yuta SETO, Tadashi TAGAWA, Tsutomu OKUBO, Shigeki UEMURA, Masanobu TAKAHASHI, Hideki HARADA: Evaluation of Novel Domestic Sewage Treatment System for Reusing Irrigation, INTERNATIONAL POST – GRADUATE SEMINAR 2014, Malaysia (2014)
6. Yuta SETO, Tadashi TAGAWA, Yasuyuki TAKEMURA, Kengo KUBOTA, Akinori IGUCHI, Tsutomu OKUBO Shigeki UEMURA, Masanobu TAKAHASHI, Hideki HARADA: Development of Novel Domestic Sewage Treatment System by Combining Primary Sedimentation and Down-flow Hanging Sponge Reactor for Irrigation Reuse (2010)
7. Harremoes, P.: Criteria for nitrification in fixed film reactors, Wat, Sci. Tech., Vol. 52 No. 1–2, pp. 323–329, 2005

Investigation of the Potential Uses of a Low-Cost Water Purification Method in Indonesia

Shohei Ohno, Kagura Shima, Masato Kiji and Tadashi Tagawa

Abstract Presently, in many water bodies such as rivers and lakes of developing countries, household and industrial wastewater are drained directly. The above situation leads to environmental problems such as water pollution and offensive odor. The aim of this study is to investigate the use of a small-size, low cost, and energy-efficient wastewater treatment system to decrease water pollution in rivers. In this study, Slanted Soil Chamber Method (SSCM) was used, as the system can remove organic pollutants and nitrogen in wastewater with in situ purification. The comparison between Activated Sledge and SSCM shows the differences in cost, energy used, and purification level. From previous studies, SSCM showed effectivity in removing BOD, COD, T-N, T-P, and SS. This study indicated that SSCM can demonstrate 17 % electric consumption and 74 % footprint of Activated Sledge. In addition, a survey of the sanitation and situation of wastewater treatment system was conducted in Yogyakarata and Pekalongan, Indonesia, to investigate the potential installation of SSCM. The survey finding showed that probable causes of diarrhea, malnutrition, and malaria come from poor water environment and sanitation. Considering the cost, installing footprint, and average number of people per household, SSCM can be the best suited replacement for treating water in these local areas.

Keywords Biological purification · Kitchen wastewater · Gray water · In situ purification · Slanted soil chamber method (SSCM)

S. Ohno (✉) · T. Tagawa
Department of Civil Engineering, National Institute of Technology,
Kagawa College, Kagawa, Japan
e-mail: kankyoken.eco@gmail.com

K. Shima · M. Kiji
Yonden Consultants Co., Inc, Kagawa, Japan

1   Introduction

In the natural world, the best biological purification is the soil surface due to the wide bacterial diversity and amount of microorganisms. Based on this idea, SSCM was proposed by Kiji [1, 2]. The general purification ability of SSCM [1, 2] and design guides [3, 4] are known from previous studies. In this study, the adaptation of SSCM in Indonesia from the survey is suggested to decrease local water pollution. For example, in developing countries as in Indonesia, 50–75 % of the organic water pollution load is caused by household wastewater [5]. To mitigate problems associated with household wastewater, septic tanks have traditionally been used. However, effluent is still contaminated, as a septic tank is only capable of anaerobic purification.

In this study, the novel wastewater purification, Slanted Soil Chamber Method (SSCM) was used. The SSCM can treat not only organic pollutants but also nitrogen and phosphorus at low cost compared to the conventional treatment method. A survey of the sanitation and existing wastewater treatment system was conducted in Yogyakarata and Pekalongan, Indonesia, to investigate the potential applicants of SSCM. For these local areas such as Yogyakarata and Pekalongan where diarrhea, malnutrition, and malaria are common occurrences, the advantages that SSCM could bring to its water environment seem beneficial.

Previous studies and comparison between SSCM and Activated Sludge (AS) as follows:

(1) **The long-term purification experiment of kitchen wastewater [2]**

The kitchen wastewater of households is relatively small in quantity. However, it is one of the major polluters of rivers because BOD is highly concentrated and contaminated. Therefore, SSCM would be ideal as a countermeasure of various wastewaters including purifying the kitchen wastewater. SSCM provided highly effective purification level as a result of the experiment. As a result of the experiment, organic pollutant and nutrient removal was demonstrated at BOD 83 %, COD 80 %, T-N 73 %, T-P 81 % and SS 74 %.

Moreover, the subtopic of the experiment is to conduct it without any power supply, and to offer the most economical treatment system possible.

In this experiment, one set of three steps of piling up structure and soil media were used (Fig. 1).

(2) **The experiment of physical permeating capacity**

In this experiment, random packing sponge, Kanuma soil, and pumice stone were used as the filter medium. Three separate layers are filled with a single type of media, and water is passed through each layer sequentially. The water inflow limit indicates the water quantity which would fill the entire laminar chamber. Each water inflow limit is as shown in Table 1. In a previous study, it was suggested that SSCM demonstrated the greatest biological purification ability at 3–15 % of the water inflow limit. We call this the "actual water quantity."

Fig. 1 The experimental
setup of the kitchen
wastewater
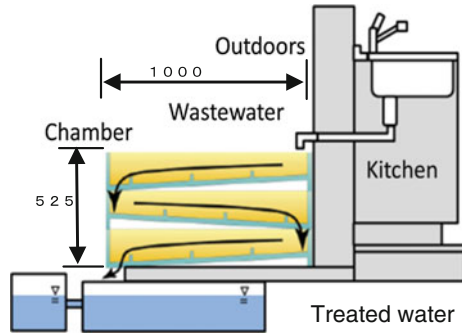
Table 1 Water inflow limit
and actual water quantity of
each media

Media	Water inflow limit (L/h)	Actual water quantity (L/h)		
		3 %	5 %	10 %
Kanuma soil	1638	49	82	164
Pumice	2016	60	101	202
Sponge	1638	49	82	164

Table 2 Comparison of the
footprint and electric power
consumption of the reactor

	Footprint (m^2)	Electric power consumption (kW/day)
SSCM	15.0	4.8
AS	20.8	50.0

(3) **Comparison between SSCM and AS**

Using the experiment of physical permeating capacity, SSCM can treat wastewater at a maximum of 39(t/d). From this result, we arranged a condition for SSCM to become more dominant than the conventional system.

(i) **Comparison of the necessary footprint**

Calculation conditions are shown below:

1. BOD concentration is fixed at 1,000(mg/L)
2. The height of the aeration tank of Activated Sludge is 4(m)
3. BOD volumetric loading of Activated Sludge is 0.6 (BOD/m^3 day)
4. SSCMs chamber size is 1(m) × 0.6(m)
5. The quantity of wastewater is fixed, 50 m^3/day

BOD is 1000 mg/L because SSCM showed ability for 83 % of purification for kitchen wastewater. To measure the necessary footprint sizes for treating the same amount of water using these two systems, the equation is shown below:

Fig. 2 Diagram of comparison between SSCM and AS in footprint and power
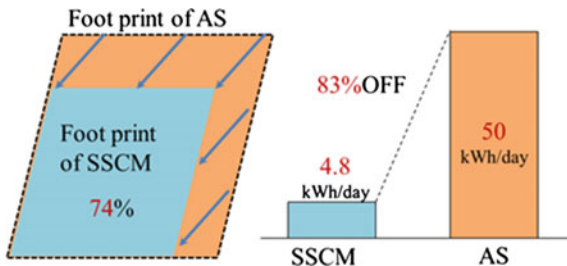
$$\text{Area}(m^2) = \frac{\text{The quantity of water}\left(\frac{t}{d}\right) \times \text{BOD}(\frac{mg}{L})}{\text{BOD volumetric loading}\left(\frac{kg}{m^3}\right) \times \text{Height(m)}} \times \frac{1000}{1000 \times 1000}$$

$$\text{Area of AS}(m^2) = 50\,(t/d) \times 1000\,(mg/L)/0.6(BOD/m^3)/$$
$$4\,(m)/1000 = 20.8\,(m^2)$$

According to the experiment of physical permeating capacity, SSCM can treat 82L wastewater per hour in 5 % actual water quantity. This means SSCM treatable 2 m^3/day and, treating 50 m^3 wastewater requires 25 unit of SSCM.

$$\text{Area of SSCM}(m^2) = 25\,\text{unit} \times 0.6\,(m^2) = 15\,(m^2)$$

As the result, if they treat wastewater of the same amount in 1,000 (mg/L) of BOD, SSCM shows a similar ability of purification at the setting area of approximately 74 % of Activated Sludge (Fig. 2).

The quantity of wastewater to be treated per day was taken as 200 t as most food factories in Shikoku, Japan, discharge a maximum of approximately 200 t of wastewater per day. As a result, if SCM is applied to the treatment of 200 t wastewater, then at a rate of 1.94 t/d, the total setting area of the treatment equipment would need to be 61.7 m^3. If an activated sludge method was installed in an area of equivalent size, it could be expected to remove the BOD in effluent by 740.4 mg/L. In the purification of kitchen wastewater, the SSCM reduced BOD by 83 % using three chambers. Consequently, the SCM could be applied to treat water with a BOD exceeding 740.4 mg/L if additional chambers were used.

(ii) Estimation of electric power consumptions

We estimated the electric power consumption required to treat 50 m^3/day of wastewater and compare the AS with the SSCM. Generally, AS requires water pumping facilities such as aeration tanks and pumps, which meant it requires approximately 0.6 kWh of power to treat 1 kg of BOD. Treating 50 m^3 of wastewater per day with BOD condition of 1000 mg/L and require treatment of 50 kg of BOD.

As a result, we estimate that 30 kWh/day of power consumption is required for AS. SSCM only needs electricity for pumping facilities. Power that requires for one pump to the amount of 50 m³ wastewater a day is as follows:

$$50 \, \text{m}^3/\text{day} \, \times \, 1.1 (\text{safety factor})/24 \, \text{h}/60 \, \text{min} = 0.04 \, \text{m}^3/\text{min}$$

The calculation shows that power consumption of the pump is 0.25 kW. As a result, total power consumption per day is as follows:

$$0.25 \, \text{kW} \, \times \, 0.8 (\text{efficiency factor}) \, \times \, 24 \, \text{h} = 4.8 \, \text{kW}/\text{day}$$

According to this estimate, it was extrapolated that the SSCM works equally as AS but it only uses 17 % of electricity of the latter (Fig. 2).

(iii) **Characteristic of purification ability of SSCM and AS**

This section shows the characteristic of purification ability of AS and SSCM to understand the aim of each purification.

In generally, sewage includes approximately 200 mg/L as BOD in Japan and AS can treats the sewage under 10 mg/L as BOD [6]. AS has great treatability with hydraulic reaction time (HRT) is 6–8 h and under the condition about aeration is constant. The BOD removal is approximately 95 %. Presently, AS roles sewage treating in advanced nation or a part of developing counties.

On the other hand, SSCM shows that can treat highly contaminated wastewater such as kitchen wastewater (Table 3) with no aeration and HRT at 20–50 min [1]. Kitchen wastewater shows 819 mg/L as BOD and SSCM effluent is 86 mg/L (Table 2). BOD removal is 86 %. Compare between AS and SSCM effluent's BOD shows SSCM was not easy to purify at low level BOD such as AS. In each

Table 3 The result of the purification experiment of the kitchen wastewater

		BOD		COD		T-N		T-P		SS	
Raw water (mg/L)	Total	819	±820	542	±671	30.6	±25.4	5.88	±4.7	153.0	±80
	Summer	921	±732	549	±446	33.2	±21.2	5.96	±4.3	196.0	±84
	Winter	867	±841	621	±811	28.4	±23.3	5.41	±5.0	141.0	±81
Treated water (mg/L)	Total	86	±69	51	±40	5.3	±2.8	0.70	±0.4	34.0	±21
	Summer	102	±103	65	±65	6.1	±3.1	0.81	±0.5	30.0	±21
	Winter	106	±39	51	±22	4.8	±2.2	0.67	±0.3	40.0	±28
Removals (%)	Total	83	±13	80	±16	73	±16	81	±14	74 %	±17 %
	Summer	79	±28	74	±33	71	±27	78	±18	82 %	±11 %
	Winter	79	±14	81	±12	76	±15	79	±18	68 %	±23 %

chamber, a nitrification reaction and denitrification reaction occurred. In T-P, the soil including phosphorus is generated biologically.

These reactions can remove T-N, retain T-P in the soil, and resorb nutrients to microbe.

2 Methodology

Mechanism of Slanted Soil Chamber Method (SSCM)

In the natural world, the best biological purification is a surface of the soil due to wide bacterial diversity and quantities of microorganism. Based on this idea, SSCM was proposed. Specifically, it comprises laminated chambers having an inclining base filled with soil. Wastewater is fed from the top, and purified as it passes through the soil, and finally appears from the bottom as treated water. A chamber size is $1000 \times 500 \times 175$ mm.

The structural advantages of SSCM are as follows:

1. Compactness with the laminated structure
2. Continuity of the purification effect with the impermeable wall and the inclining base
3. No (or less) energy cost with the inclined structure
4. Selectivity of media for SSCM (such as sponge, soil, and pumice stone)

SSCM has the impermeable wall and the inclining base. The impermeable wall can dam up water and save it and the inclining base can purify to get over the clogging media.

Moreover, the machinery part of SSCM is only a pumping installation. Therefore, it is promised to greatly reduce initial cost and running cost compared with conventional wastewater treatment (Fig. 3).
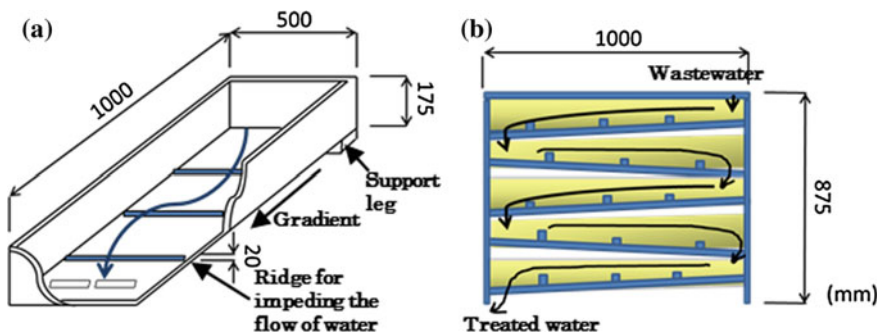
Fig. 3 Diagram of the slanted soil chamber; **a** cutaway diagram to show chamber interior, **b** stacked chambers during operation

3   Survey in Indonesia

The goal of the survey is to grasp the situation relating to lifestyle and the water environment in Yogyakarata, Semarang, and Pekalongan, Indonesia. The survey was conducted over 5 days in September, 2014. The aim of this survey is to understanding problems with installing SSCM in local houses and considering design factors.

The investigation included the following:

- Interviewing lifestyle and water environment to the locals.
- Observation of three established wastewater treatment plants
- Exchanging opinions with a local engineer

(1) **Interviews and survey**

The survey was conducted in Kolidetung Village, Flores Island, Indonesia by providing a questionnaire to 20 local residents (Fig. 4).

The questionnaire asked the kind of diseases which were thought to be caused by poor water environment. As listed in (Fig. 5) cough, fever, skin disease, diarrheal, and bloodshot were common answers.

In general, the diseases caused by unclean water supply and poor public sanitation can be listed as follows: diarrheal disease 39 %, malnutrition 21 %, and malaria 13 % [7]. In Kolidetung Village, the diseases such as diarrheal and malaria were frequent. The cause may be the lack of effective public sanitation system and also hygiene knowledge and practice.

Fig. 4 Taking questionnaire

Fig. 5 The kind of disease caused by water
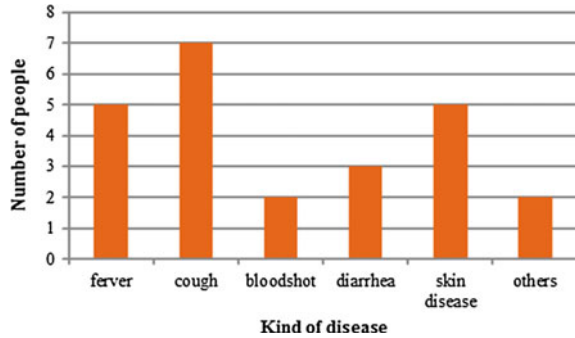
Table 4 Analysis result of river water, sewage, and its effluent

Sampling site	Semarang	Pekalongan	
Kind of water	River water	Sewage	Treated sewage
Kind of treatment	Untreated	Untreated	Treated
PH	7.1	7.2	7.6
BOD$_5$ (mg/L)	21	153	19
COD$_{cr}$ (mg/L)	91	214	52
T-N (mg/L)	4.8	30.0	17.0
T-P (mg/L)	6.6	14.6	13.0
SS (mg/L)	73	126	5

(2) Water quality survey

In the water quality survey, we analyzed river water, sewage, and wastewater effluent in Semarang, Pekalongan region, Java Island, Indonesia (Table 4).

They are split into four categories based on "Water quality control and the water pollution privation" in Indonesian government.

The lowest class, classIV usually used as irrigation water and the water of the same quality, is requiring BOD 12 mg/L, COD 100 mg/L, T-P 5 mg/L, and T-N 20 mg/L. When it is compared to the water of Semarang river, they exceeded the limitation set by Indonesian standards on BOD, T-P, and a high contamination COD was found. The same things could be said of wastewater treatment plant in Pekalongan. Those drained water contained highly concentrated nitrogen and phosphorus.

Semarang river smelled like sewage and water is black with high SS (Fig. 6). The situation draining household water was confirmed. And the high concentration of T-N and T-P curse eutrophication and grow more serious situation if more purify was not installed.

Fig. 6 Sampling site around Semarang region

4   Adaptation of SSCM in Indonesia

Gray water's organic pollutants account for 70 % of household wastewater's organic pollutants and kitchen wastewater account for 40 %. In this assuming, gray water was aimed since it has highly organic pollutants for river.

Installing SSCM to treat gray water is advisable because of below points:

The local conditions are as follows:

 (i) Available footprint is limited due to dense housing.
 (ii) Average occupancy in Indonesia is 4.0 people per house.
(iii) Funds available cost for treating wastewater are limited.

    (i) Our recommendations are to install water treatment equipment in the space between the houses. This is possible because treatment equipment using SSCM is highly adaptable. In case of installable underground, it is easy to collect wastewater from the kitchen, bathing area, and laundry using there difference of elevation.

    (ii) Assuming gray water quantity is 60 L/day per person and average residents per house is five people, the total quantity is about 300 L/day per house. This is well within the range of treatable water quantity for SSCM.

    (iii) In case of the densely housed area, Kricak district, the local administrator collects 500 Rupiah (approximately $0.04) sequentially from only one house per day as running cost of the plant.

Assuming the conditions of the gray water, BOD 400 mg/L, T-N 30 mg/L, T-P 6 mg/L, and SS 150 mg/L and installing one set of treatment chambers for each house. We expected 70–80 % removal for wastewater.

Fig. 7 Model of densely housed area
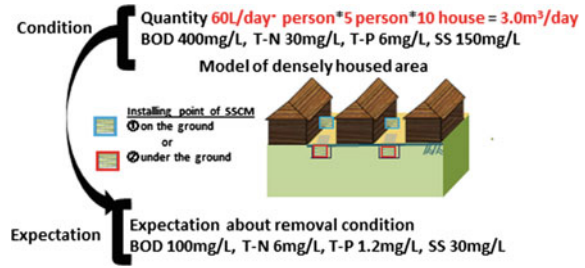
So we regard SSCM as potentially great system for decreasing water pollution and cleaner sanitation in Indonesia (Fig. 7).

- Kind of media

In Indonesia, soil, pumice, and sponge are available as media of SSCM. Sponge can demonstrate great purification ability, but it is difficult to reuse.

In case of using soil or pumice as media BOD, T-N, and T-P are also removable.

In addition, phosphorus and nutrient are obtained as organic manure after used the soil or pumice media. The method cannot use household wastewater but also effluent of sewage treatment and natural water such as polluted rivers.

5   Conclusion

As the result of this study, SSCM is best suited as small-sized gray water purification system to the developing countries.

From the obtained results, following conclusions can be drawn:

(1) From previous studies, SSCM has four structural advantages and it performs highly and effectively for removing BOD, COD, T-N, T-P, and SS. In addition, SSCM proves to be both ecologically and economically friendly.
(2) From the survey, the finding showed that the river pollution and generally unclean water were largely caused by lack of treating system.
(3) In the future work, actual demonstration of installment under the local condition is necessary.
    In addition, we are trying to optimize startup of the treatment system in view of seeding.
(4) SSCM not only adopts developing countries but also expects the good effect in advanced countries in the view of saving energy, resource circulation of phosphorous, and provision for eutrophication.

References

1. M. Kiji. "Consurrent Purification of Organic Pollutants and Nutrients by the Slanted-Soil-Chamber Method Using Carrier, Joural of Japan Society on Water Environment Vol. 37, No. 4 pp. 145–153, 2014, in Japan
2. M. Kiji.: "A study on purification of wastewater including BOD, nitrogen and phosphorus by SSCM" 2012, in Japanese
3. K. Shima., M. Kiji., T. TAGAWA.: "Development of ASall-scale food related wastewater treatment system by Slanted-Chamber Method", 2013.
4. K. Shima., M. Kiji., T. TAGAWA.: "Development of a low cost novel wastewater treatment system by Slanted-Chamber Method" Journal of Water and Environment Technology
5. Agenda 21, "For Environment And Development Needs Support of All Social Sectors", 1994
6. Kagawa prefecture, Koto river purification center, 'situation of operation and maintenance', http://www.kagawa-gesui.or.jp/center/koutou_jyokyo.htm (19.August.2015)
7. R. Clarke and J. King, "The Atlas of Water" Mapping The World's Most Critical Resource

Part II
Computational Methods and Applications

Particle Swarm Optimization Application for Timber Connection with Glass Fiber-Reinforced Polymer (GFRP) and Non-GFRP

Marina Yusoff, Dzul Fazwan Othman, Rohana Hassan and Anizahyati Alisibramulisi

Abstract Timber connection is one of the important aspects that need to be evaluated in construction and manufacturing. The end product produced from these sectors depends on the strength of the timber connection especially in building constructions. A lot of laboratory experiments to measure the strength of timber connection were done before proceeding with the transformation process of a product. However, these experiments require high cost and time-consuming. In addressing these issues, there is an alternative mean that can be applied to predict the strength of timber connection to overcome those problems. This paper addresses on the employment of particle swarm optimization (PSO) in a simulated timber connection for tensile test with and without glass fiber-reinforced polymer (GFRP). Data from laboratory experiment of tensile test of tropical timber were used. The PSO potentially can adapt the behavior of the timber and predict the maximum weight that can be supported by the timber connection. The findings are acceptable which obtained 99.39 % accuracy for GFRP joints and 95.34 % accuracy for non-GFRP joint. By using population size of 20, it has shown that PSO provides good results and has capability to predict the timber joint strength. Results show that by combining the glass fiber-reinforced polymer (GFRP) sheet, the timber joint gives better strength than timber joint without GFRP. Thus, the outcome of PSO application would encourage the engineer or related construction fields to predict the timber joint strength with various fiber-reinforced polymer or other composite material.

M. Yusoff (✉) · D.F. Othman
Faculty of Computer and Mathematical Sciences, Universiti Teknologi MARA,
40450 Shah Alam, Selangor, Malaysia
e-mail: marinay@tmsk.uitm.edu.my

M. Yusoff
Institute for Infrastructure Engineering and Sustainable Management (IIESM),
Universiti Teknologi MARA, 40450 Shah Alam, Selangor, Malaysia

R. Hassan · A. Alisibramulisi
Faculty of Civil Engineering, Universiti Teknologi MARA,
40450 Shah Alam, Selangor, Malaysia

1 Introduction

Timber has been used for many centuries for constructions and still popular as building materials. Timber is the wood of growing trees suitable for structural uses in building construction. Timber gives benefits in terms of cost, obtainability and strength, thus timber is widely used until now. Malaysia is not excluded from being one of the timber suppliers in this world. According to MIDA (2012), Malaysia has invested in wood-based industry [1]. The timber industry itself contributes about RM20 billion to the Malaysia exports a year and some RM13 billion each year to the domestic market [2]. There are two types of timber which are softwood and hardwood. The tropical in forest in Malaysia usually consists of hardwood such as Merpauh, Keruing, and Jelutong. Each hardwood timber has different specification in terms of strength, treatability, and physical properties.

A laboratory experiment needs to be conducted for determining the strength of timber joint [3]. The experiment requires a set of specialized tools and machine for instance by using universal testing machine. There are several ways to test the strength of the timber joint, such as tensile test, bending stress test, and compression test. However, the experiment requires a large number of timbers with a various types of species to determine the strength of timber joint. Besides the timber, the experiments require some composite material such as bolt, adhesive glue, and fiber-reinforced polymer in order to make a joint possible. Thus, the laboratory experiments require a lot of cost and it is time-consuming.

This paper addresses the use of computational method to help reducing cost and time of laboratory experiment. Previously, there are various computational techniques that have potential to give results a little bit same as laboratory experiment such as partcle swarm optimization (PSO) [4, 5] genetic algorithm, and Monte Carlo method [6]. A study by Yusoff et al. [5] simulates a laboratory experiment on timber joints which can assist the traditional experimental analysis with the finding of the possible end distance in a single shear timber joint using PSO. The authors further-mentioned fitness function of PSO in solving this problem is determined based on findings from datasets of laboratory experiment. Yusoff et al. [5] has suggested that a better computational result would be possible to obtain by the employment of the PSO technique on different types of timber, joints, and composites.

2 Related Work

Tensile test is one of common manual techniques that commonly use to predict strength of a timber connection. This technique requires special machine called universal testing machine in order to run the experiment. This machine is considered universal because it can be used for compression and bending test also. Figure 1 shows the universal testing machine.

Tensile test is based on tension capacity or pullout capacity. According to Favilla [7], tensile test is necessary to understand the properties of different materials and study the behavior of the material under certain load capacity. He also stated that the data from the test can be used to determine valuable material properties as such ultimate tensile strength, modulus of elasticity, and yield strength. The example of test procedure is from Shafenzi [8] as shown in Fig. 2.

Fig. 1 Universal testing machine
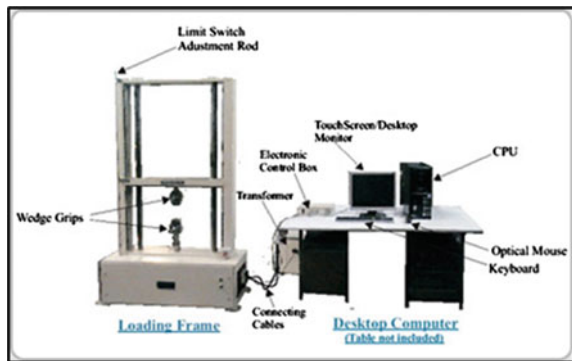
Fig. 2 Flowchart of procedure in tensile test
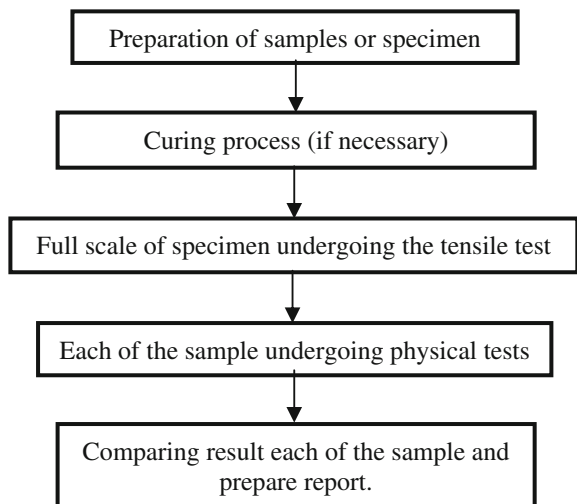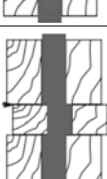
Table 1 Failure mode

Illustration	Failure mode	Description
	I_m	Dowel bearing strength of the main member (tenon) is exceeded. The tenon wood crushes
	I_s	Uniform bearing by the dowel (peg) exceeds the dowel bearing strength of the mortise sidewalls. The mortise sidewall wood crushes
	III_s	A hinge point occurs in the tenon near each shear plane and the peg ruptures or bends.
	IV	The peg bends with limited rotation, forming two hinges near each shear plane in the mortise sidewalls and one hinge in the center of the tenon
	V	The peg fails in cross-grain shear at each side of tenon (double shear failure)

Source Judd et al. [10]

Tensile test typically involves with the process of pulling out the specimen with certain load until the specimen reaches failure mode. Failure mode is a condition which happens when the specimen is no longer can sustain the load capacity. According to Hassan et al. [9], the failure mode is based on European Yield Model (EYM). The description of each mode in failure mode is shown in Table 1.

3 Particle Swarm Optimization

PSO was developed in 1995 by Kennedy and Eberhart based on birds flocking and fish schooling's social behavior [11, 12]. There are vast of particle swarm optimization design in solving a problem. This paper addresses the use of canonical PSO algorithm. Figure 3 shows the flowchart of the PSO algorithm from the first step until the optimal load capacity is attained. From the Fig. 4, the first step is initializing population with random particle position (x) and its velocity (v). The number of particles depends on the population size. The random particle position (x) is based on range of selected deformation or displacement data. The initial velocity range is between −1.0 and 1.0. After the initialization process, each particle will be evaluated based on its own fitness. If the particle I is the best among all existing particles then it was being declared as initial pBest and gBest. Then, the particle position and velocity will be updated. The new particle position and velocity, will be evaluated again based on its fitness and compete among them to get the pBest. The pbest will compete with the previous gBest. If the pBest win, it will become new gBest. This process will continue until reached maximum iteration. Finally, the current gBest is declared as optimal load capacity. Two types on inertia weight which is constant or fixed weight and ranged weight. The constant weight value is 0.9 that was taken from research by Bhattacharya and Samanta [13]. The ranged weight value is from −1.0 to 1.0 based on the suggestion of research in Yusoff et al. [5, 14].

4 Data Acquisition and Experimental Setup

4.1 Datasets Preparation

The timber and composite material connections were tested to make a comparison between the connection using GFRP material and without the GFRP material. The types of timber joints that have been tested are single shear and double shear. The strengthening material used for jointing the timber was the GFRP wrapper with 250 mm × 500 mm dimension. The timber has been fastened with 1.5 times diameter (1.5D) end distance where the diameter of the dowel is 20.6 mm. The single shear connection has been tested using Bintangor species while double shear connections were tested using Kapur species. Basically, the raw data from the actual experiment will be preprocessed to identify the equation of the fitness function. After that, the tabulated graph will be fitted with polynomial curve fitting tools. The polynomial curve fitting can fit the graph from 4th degree until 10th degree. A polynomial equation is produced to be used as fitness function in PSO algorithm. Some example of the preprocessed data is illustrated in Figs. 4 and 5.
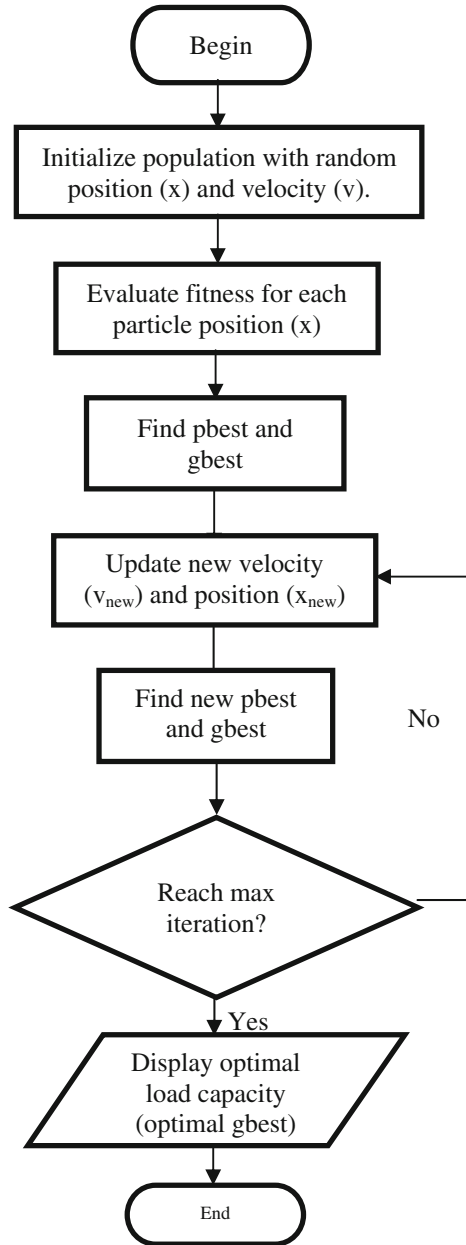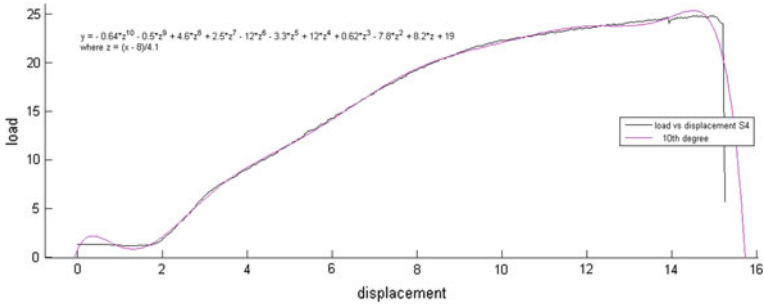
Fig. 4 Graph of half lap joint without GFRP
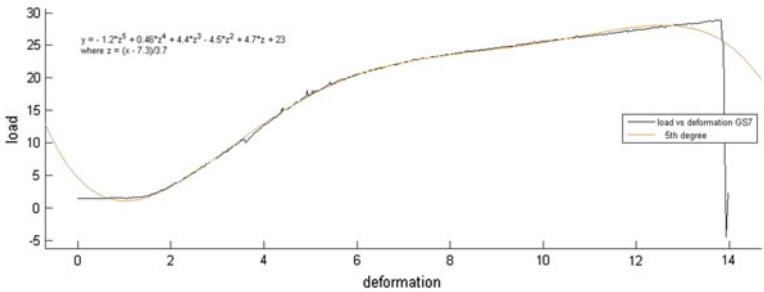
Fig. 5 Graph of half lap joint with GFRP

4.2 PSO Parameter Setting

PSO has several parameters to be initialized such as velocity, constant value of coefficient, inertia weight, and the number of random population. Table 2 shows parameter values used for predicting the timber joint.

Table 2 Parameter setting

Parameter	Values
Population size	10, 20, 30
Iteration size	5 and 10
Velocity, V	−1.0 to 1.0, −2.0 to 2.0, and −3.0 to 3.0
Inertia weight, W	0.9 and −1.0 to 1.0
Constant coefficient, C1 and C2	2.0

The system was tested using ten samples of displacement data from actual laboratory experiment. The data is tested one by one in order to get the most optimal load capacity. The best result from each data sample is selected based on certain criteria. The criteria should be followed sequentially in order to get only one best result from each data sample. The criteria are described below.

   i. Select the highest load capacity (kN).
  ii. If there is more than one load with higher value, choose the load that has highest displacement value (mm).
 iii. If there is more than one load with higher displacement value, choose the load that is gained from lowest population size value. This is for measuring the performance of the system

5   Findings and Discussion

The most optimal load capacity that has been achieved by the system is 28.1469 kN. The best result from each data sample is highlighted with bold font. From the result obtained, most data samples attained highest optimal load capacity at 20.2777 kN except for data sample 10 which only achieved 20.2776 kN. The best result from each data sample is highlighted with bold font. Table 3 shows compilation of best optimal load for each data sample.

Based on information displayed from Table 3, the maximum displacement a timber joint without GFRP can sustain until reaching optimal load of 20.2777 kN is 11.8477 mm. The result seems to get 95.34 % accuracy compared to the actual laboratory experiment result. The system is capable to get optimal load in population size of 30, iteration of 10, inertia weight from −1.0 to 1.0, and velocity from −1.0 to 1.0.

Table 3 Compilation of optimal load for timber joint without GFRP

Data sample	Population	Iteration	Weight	Velocity	Best displacement (mm)	Optimal load (kN)
1	20	10	0.9	−1.0 to 1.0	11.8463	20.2777
2	30	10	−1.0 to 1.0	−2.0 to 2.0	11.8470	20.2777
3	20	5	0.9	−1.0 to 1.0	11.8469	20.2777
4	30	5	0.9	−3.0 to 3.0	11.8470	20.2777
5	20	10	−1.0 to 1.0	−3.0 to 3.0	11.8432	20.2777
6	**30**	**10**	**−1.0 to 1.0**	**−1.0 to 1.0**	**11.8477**	**20.2777**
7	20	5	−1.0 to 1.0	−3.0 to 3.0	11.8458	20.2777
8	30	5	−1.0 to 1.0	−3.0 to 3.0	11.8428	20.2777
9	20	5	0.9	−3.0 to 3.0	11.8446	20.2777
10	30	10	0.9	−2.0 to 2.0	11.8422	20.2776

Table 4 Compilation of optimal load for timber joint with GFRP

Data sample	Population	Iteration	Weight	Velocity	Best deformation (mm)	Optimal load (kN)
1	20	10	−1.0 to 1.0	−2.0 to 2.0	12.4792	28.1469
2	20	5	0.9	−2.0 to 2.0	12.4796	28.1469
3	20	10	0.9	−2.0 to 2.0	12.4784	28.1469
4	30	10	−1.0 to 1.0	−1.0 to 1.0	12.4785	28.1469
5	20	10	0.9	−3.0 to 3.0	12.4775	28.1469
6	20	10	0.9	−3.0 to 3.0	12.4751	28.1469
7	20	10	−1.0 to 1.0	−1.0 to 1.0	12.4760	28.1469
8	30	10	−1.0 to 1.0	−1.0 to 1.0	12.4792	28.1469
9	**20**	**10**	**0.9**	**−3.0 to 3.0**	**12.4797**	**28.1469**
10	30	5	−1.0 to 1.0	−1.0 to 1.0	12.4788	28.1469

Fig. 6 Comparison between two timber joints based on load capacity

Comparison between Two Timber Joints
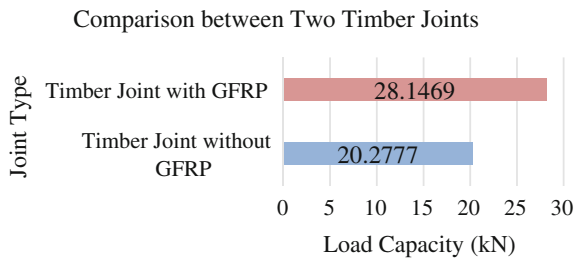
Based on information indicated from Table 4, the maximum deformation a timber joint with GFRP can sustain until reaching optimal load of 28.1469 kN is 12.4797 mm. The result seems to get 99.39 % accuracy compared to the actual laboratory experiment result. The system is capable to get optimal load in population size of 20, iteration of 10, inertia weight of 0.9, and velocity value from −3.0 to 3.0.

The result obtained from the system testing shows that by applying glass fiber-reinforced polymer (GFRP), the timber joints tend to increase the load capacity which can be sustained. Besides that, the timber joint with GFRP also tends to get optimal result quicker that non-GFRP timber joint since most GFRP timber joint samples get optimal load capacity in population size of 20 compared to non-GFRP timber joint. Figure 6 shows a comparison between two types of timber joints based on optimal load capacity that has been obtained by the system.

6 Conclusion

This project was successfully developed to primarily offer an alternative way of predicting the strength of timber joints with the use of artificial intelligence techniques, namely PSO. The outcome of this project is able to assist the people that

involved in various sectors, such as designer, engineer, architect, and contractor to find the optimal structural capacity of the strength of timber joint. The system is expected to help in minimizing time and cost of the conventional timber experiment.

References

1. Malaysian Investment Development Authority (MIDA).(n.d). *Industries in Malaysia,* from http://www.mida.gov.my
2. Teng, L. J. (2013). Timber industry needs restructuring: MTIB, *The Sun.*
3. Hassan, R., Ibrahim, A., Ahmad, Z., & Yusoff, M. (2014). Dowel-bearing strength properties of two tropical hardwoods. In *InCIEC 2013* (pp. 27–36). Springer Singapore.
4. Yusoff, M., Roslan, I. I., Alisibramulisi, A., & Hassan, R. (2015). Computational Approach for Timber and Composite Material Connection Using Particle Swarm Optimization. In *InCIEC 2014* (pp. 1141–1152). Springer Singapore.
5. Yusoff, M., Shalji, S. M., & Hassan, R. (2014). Particle swarm optimization for single shear timber joint simulation. In *InCIEC 2013* (pp. 117–126). Springer Singapore.
6. Asif, R., Siril, Y., & Mark, D. (2014). Simulation and Optimization Techniques for Sawmill Yard Operations—A Literature Review. *Journal of Intelligent Learning Systems and Applications, 06*, 21–21. doi: 10.4236/jilsa.2014.61003
7. Favilla, S. (2010). Tensile Testing Laboratory. https://stephanfavilla.files.wordpress.com/2011/03/tensile-testing-laboratory.pdf, retrieved 4 September 2015.
8. Shafenzi, S. (2013). *Tensile Behaviour of Bolted Timber Composite Connection for Merpauh (SG4).* (Bachelor of Engineering (Hons) Civil), Universiti Teknologi MARA.
9. Hassan, R., Ibrahim, A., & Ahmad, Z. (2012, 23–26 Sept. 2012). *Experimental performance of mortice and tenon joint strengthened with glass fibre reinforced polymer under tensile load.* Paper presented at the Business, Engineering and Industrial Applications (ISBEIA), 2012 IEEE Symposium.
10. Judd, J., Fonseca, F., Walker, C., & Thorley, P. (2012). Tensile Strength of Varied-Angle Mortise and Tenon Connections in Timber Frames. *Journal of Structural Engineering, 138*(5), 636–644. doi: doi:10.1061/(ASCE)ST.1943-541X.0000468
11. Kennedy, J., & Eberhart, R. (1995). Particle Swarm Optimization. In *In Proceeding of the IEEE International Conference on Neural Networks* (Vol. 4, pp. 1942–1948). Perth, WA, Australia.
12. Kennedy, J., & Eberhart, R. C. (1997). A Discrete Binary Version of the Particle Swarm Algorithm. In *Proceeding of the IEEE International Conference on Systems, Man, and Cybernetics* (Vol. 5, pp. 4104–4108). Orlando, FL, USA.
13. Bhattacharya, I., & Samanta, S. (2010). Parameter Selection and Performance Study in Particle Swarm Optimization. *AIP Conference Proceedings, 1298*(1), 564–570. doi: 10.1063/1.3516367
14. Yusoff, M., Ariffin, J., & Mohamed, A. (2015). DPSO based on a min-max approach and clamping strategy for the evacuation vehicle assignment problem. *Neurocomputing, 148*(0), 30–38. doi: http://dx.doi.org/10.1016/j.neucom.2012.12.083

Optimizing Network Architecture
of Artificial Neural Networks (ANNs)
in Rainfall-Runoff Modeling

K. Khalid, M.F. Ali, N.F.A. Rahman, M. Husaini and M.R. Mispan

Abstract Artificial neural networks (ANNs) are general-purpose techniques that can be used for nonlinear data-driven rainfall-runoff modeling. The fundamental issue to build a worthwhile model by means of ANNs is to recognize their structural features and the difficulties related to their construction. Without a doubt, the magnitude and quality of data, the type of noise, and the mathematical properties of the algorithm for estimating the usual large number of parameters are critical for the simplification performances of ANNs. There are many avoiding overfitting techniques in improving the generalization of ANNs. This paper was reported the optimization of the hidden neurons of nonlinear autoregressive with external inputs (NARX) neural network of the tropical river basin. For the Langat River Basin, eight or ten hidden neurons were found to be the most optimal for the ANN model. The next steps should be conducting the optimum numbers of inputs delay to be used for the model since the precise combination of the network architectures features will improve the accuracy level of ANN model.

Keywords Artificial neural networks · Hidden neurons · Nonlinear autoregressive with external inputs · Rainfall-runoff modeling

K. Khalid (✉)
Faculty of Civil Engineering, Universiti Teknologi MARA Pahang,
Jengka, Pahang, Malaysia
e-mail: khairikh@pahang.uitm.edu.my

M.F. Ali · N.F.A. Rahman
Faculty of Civil Engineering, Universiti Teknologi MARA,
Shah Alam, Selangor, Malaysia

M. Husaini
Center for Research and Innovation, UniKL Malaysian Spanish Institute,
Kulim, Kedah, Malaysia

M.R. Mispan
Soil & Water Management, MARDI, Serdang, Selangor, Malaysia

1 Introduction

Streamflow prediction for a river has been one of the most explored areas in the recent hydrologic study. It is a great concern for the prediction of streamflow with good probability and reliability since the watershed models may show high non-linearity. The models have been practised may vary from a physical, empirical, and numerical methods and other hybrid black box models for streamflow prediction. The main weaknesses observed in using physical model are the requirement of a more accurate and extensive data set that sometimes is tedious to acquire. The data-driven models may have an advantage within this framework as they require minimum data and may provide satisfactory results. Neural network (NN), genetic algorithm, and fuzzy and hybrid algorithms are some of the methods that have received lots of attention among all modeling techniques during recent decades. In recent years, artificial neural networks (ANNs) have proven to be an efficient alternative to traditional methods for modeling quantitative water resource variables [1, 2]. The ANN concepts and applications in hydrology have been discussed by the ASCE Task Committee on Application of ANN in hydrology, which concludes that ANNs may be perceived as alternative modeling tools earnest of further exploration [3, 4]. Many researchers demonstrated the application of ANNs with standard backpropagation algorithm for predicting streamflow [5–10]. ANNs consist of a large pool of processing units (generally referred to as neurons or nodes) which receive, process, and send information to each over a large number of weighted connections. Thus, ANNs gain experiential knowledge through a process of finding an optimal set of weights for the connections and threshold values (biases) for the neurons.

ANNs can be classified as single, bilayer and multilayers according to the number of layers, and as feedforward, recurrent and self-organizing according to the direction of information flow and processing [3]. The most popular ANNs are multilayer feed-forward neural networks, which are mainly multilayer perceptron (MLP) and radial basis function networks (RBF). The MLP is the most widely used in hydrological studies, thus the study was concentrated on the MLP network. Other network topologies that have found application in hydrology include RBF, Bayesian neural network (BNN), Kohenen self-organizing feature maps (SOFM), and Stacked neural network (SNN). A MLP network comprise of an input layer, one or more hidden layers and an output layer.

The critical constituent to build a good model by means of ANNs is to decide their structural features and the challenges allied to their construction in order to enhance the generalization performances of ANNs. It is prominent that two problems exist in relation to ANNs; (a) the curse of dimensionality; and (b) overfitting to training data [11]. The curse of dimensionality is the exponential expanding of the weight number with increasing dimension of the input space in order to produce function approximation while maintaining a stable level of accuracy. Overfitting is the competency of ANNs to fit training events precisely due to the large number of weights and them being very modifiable in mapping practising events. This

challenge produces negative effects on generalization if the noise is Gaussian and worse if the noise is non-Gaussian.

There are several methods to avoid overfitting, which are generally based on limiting fitting to training data by: (a) adding terms to the cost function, i.e., (a) regularization and cross-validation; (b) splitting the training set in order to control the fitting level; (c) acting on the number of weights, i.e., soft weight sharing, deleting weights and nodes such as optimal brain damage [11–13]. When ANNs begin to explain noise during training, weight estimation starts to be corrupted. One of the prominent way to avoid overfitting is through the selection of the best number of hidden neurons. By differing the number of hidden neurons, the validation subset allows one to regulate the accuracy level with respect to the noise level [11].

2　Methodology

Neural network (NN) models are parallel computing networks inspired by animal nervous system. A neural network typically consists of input layer (with "n" input neurons), one or many hidden layers (with "m" number of hidden layers and "o" number of hidden neurons), and an output layer (with "p" number of output neurons). Each layer will be interconnected with the weights. The information has to be feedforwarded from each input neuron to all hidden neurons through these weights. Then, information processes use transfer function (linear or sigmoid) at each hidden neuron. Then, all the processed values have to be summed up at each hidden neuron and information to be passed on to the output neuron through connecting weights. Then again, the information is to be processed through transfer function at output neuron to get final value. Bias is considered in order to eliminate or offset the dominant solutions at hidden layer and at output layer.

The whole process of feed-forward from the input layer to output layer is summarized as in Fig. 1. The inputs consist of a combination of rainfalls and available water capacity (AWC) of related soil series data sets, $x(t)$ and the
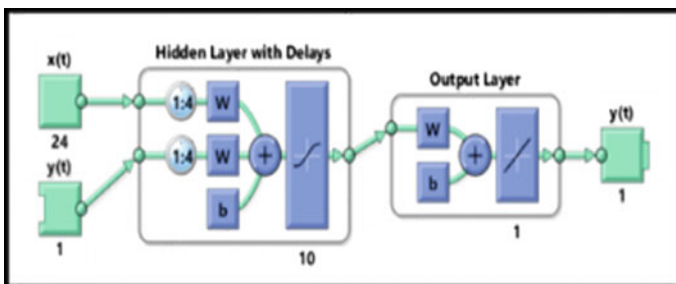
Fig. 1 The network architecture of ANN model

measured streamflow, $y(t)$. Where the next value of the stream flow $y(t)$ is regressed on previous values of the output streamflow and combination of rainfall is the historical values of an independent together with its AWC values. About 12 rainfall stations with its specific AWC along with the measured streamflow of Kajang station. A single hidden layer with 4 days delay is fixed while changing the hidden neurons numbers in gaining the optimum value of it. This combination is categorized as a nonlinear autoregressive with external (exogenous) input (NARX) neural network time-series modeling. The defining equation for the NARX model is shown in Eq. 1.

$$y(t) = f(x(t-1), x(t-2), \ldots, x(t-d), y(t-1), y(t-2), \ldots, y(t-d)) \quad (1)$$

The final observed value at the output layer is compared with the target value. The difference in error between the observed and predicted value is then evaluated. Then, a backpropagation process is used to backpropagate errors until the weights are optimized to obtain minimum error between the observed and predicted value. In backpropagation, partial derivatives with respect to the connected weights are calculated. The chain rule is used to get the updated weights. The updating continues until the stopping criteria are met (for thousand iterations or minimum difference in error is obtained). In this study, the Levenberg–Marquardt backpropagation is utilized as a learning technique of the training network. Learning rate accelerates the learning process, and momentum pushes the solution towards convergence. Minimization of mean squared error (MSE) is considered as the objective of the neural network.

3   Study Area

Langat River Basin, a tropical river watershed in Malaysia is chosen for the study in optimizing the hidden neuron number of ANN model. The basin occupies the south and south-eastern parts of Selangor, as well as a small portion of Negeri Sembilan and Wilayah Persekutuan, Malaysia (Fig. 2). Several studies have been conducted on the watershed in relation to water resources and hydrological behavior of the basin. Many studies were carried out on the hydrological processes of the basin including a historic water streamflow study by [14–16]. There are researchers explored the impact of land used change on streamflow and direct runoff [17, 18]. While there are a few papers reported in the literature on the neural network studies at Langat River Basin. Researcher [19] has demonstrated that the ANN give better performance compared to autoregressive integrated moving average (ARIMA) model in forecasting dissolved oxygen (DO). Another researcher is using ANN to predict a water quality index (WQI), [20]. Lastly, researcher [21] has proposed a hybrid wavelet-least square support vector machines (WLSSVM) model that combine both wavelet method and LSSVM model for monthly stream flow forecasting at the river basin.
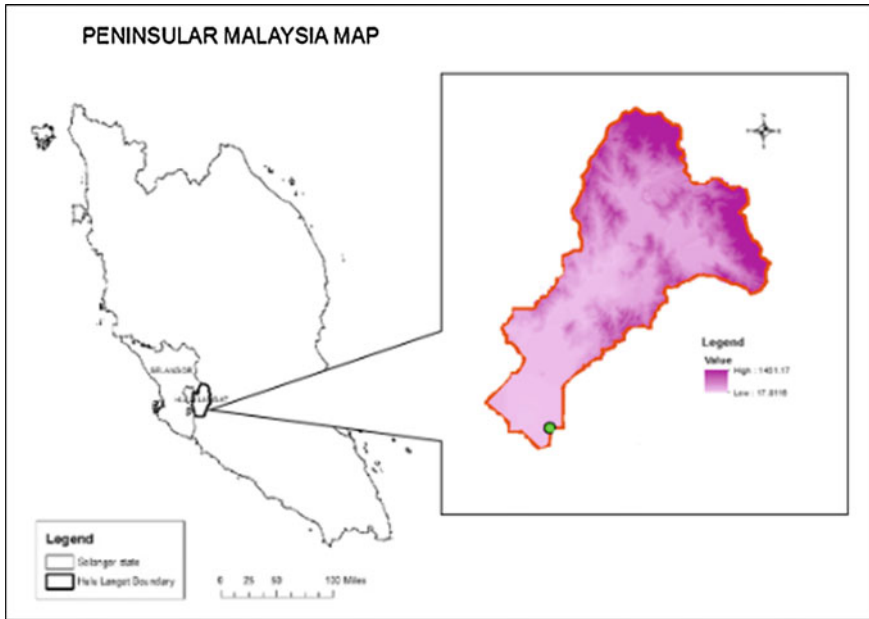
Fig. 2 The location of Langat River Basin

4 Results and Optimization Analysis

A The study was utilized artificial neural networks to predict a daily river streamflow at Langat River Basin. About 34 years daily rainfall and streamflow beginning from 1980 to 2013 were used in the model. The optimal value of network parameters was selected by trial and error. The best combination of the network parameters was used to optimize the network weights. There are two objective functions have been utilized of the neural network; the mean squared error (MSE) and the Pearson correlation (R).

MSE is the average squared difference between outputs and targets. The zero value of MSE is meant no error difference between outputs and targets. Minimization of MSE is considered as the objective of the neural network in selecting the optimal hidden neurons of the model. The study was only focussed on the optimizing of the numbers of hidden neuron of the ANN model. The model with eight hidden neuron was found to be the lowest MSE value in the ANN study with value of 34.7754 (Table 1). While the model error of the ten hidden neuron was observed very close to the eight hidden neuron with the MSE value of 34.9071. The MSE error was clearly increased when higher hidden neuron more was imposed in the model (Fig. 3).

The Pearson Correlation value was used to evaluate the model performance by measuring the correlation between outputs and targets. Model training is the initial

Table 1 Overall ANN model performance at different hidden neuron number

Hidden neuron	Total iteration	Epoch of best validation performance	MSE	Pearson correlation R-value
4	13	7	41.8085	0.7424
6	14	8	49.6208	0.7623
8	17	11	34.7754	0.7589
10	15	9	34.9071	0.7444
12	14	8	49.4532	0.7526
14	16	10	58.2851	0.7523
16	17	11	45.0106	0.7628

Fig. 3 MSE value at different number of hidden neurons
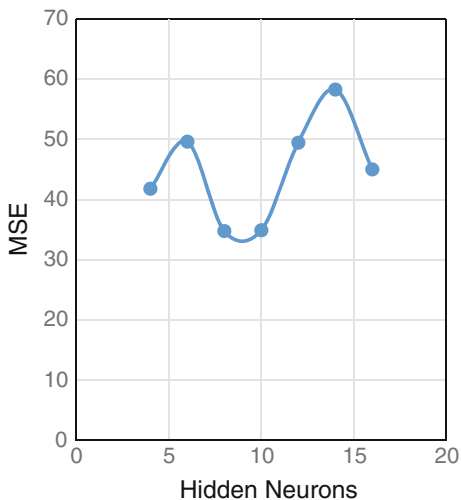
testing of the model train the dataset to get an input-output relationship. R-value ranges from 0 to 1, shows the correlation between the observed versus the simulated values. If the R-value is very close to zero, the model performance is considered unacceptable. In contrast, if the values are equal to one, then the model prediction is considered perfect. Table 2 shows the R-value of the four stages of ANN model development for a different number hidden neuron. It is observed that the Pearson Correlation value of the model was considered very well, and the R-value was scattered at more than 0.7000 for the all 34 years model simulation.

Validation and test values show almost comparable r values, ranging from 0.6881 to 0.7860. Validation is the process of determining the degree to which a model is an accurate representation of the real world from the perspective of the intended uses of the model. Validation and test can provide evidence that the model is sufficiently accurate for its intended use. It is also perceived that the Levenberg–Marquardt backpropagation is performed well as a learning technique of the

Table 2 The R-value at different hidden neuron number

Hidden neuron	R-value training	R-value validation	R-value test	R-value all data
4	0.7380	0.7618	0.7488	0.7424
6	0.7683	0.7671	0.7359	0.7623
8	0.7666	0.7601	0.7189	0.7589
10	0.8205	0.6881	0.6088	0.7444
12	0.8125	0.7845	0.4741	0.7526
14	0.7817	0.7185	0.6770	0.7523
16	0.7659	0.7860	0.7589	0.7628

training network in predicting the streamflow of the Langat River Basin. Figures 4 and 5 show the Pearson Correlation values of the four stages of ANN model development for 8 and 10 hidden neurons.
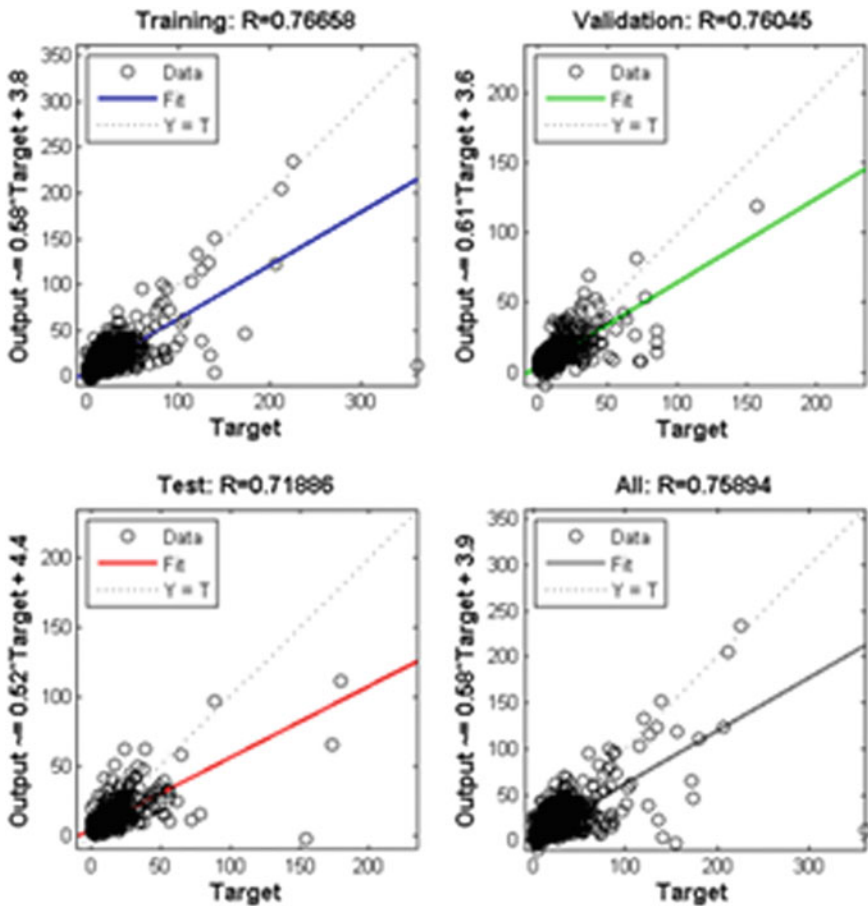
Fig. 4 The R-values of the four stages of ANN model development for 8 hidden neurons
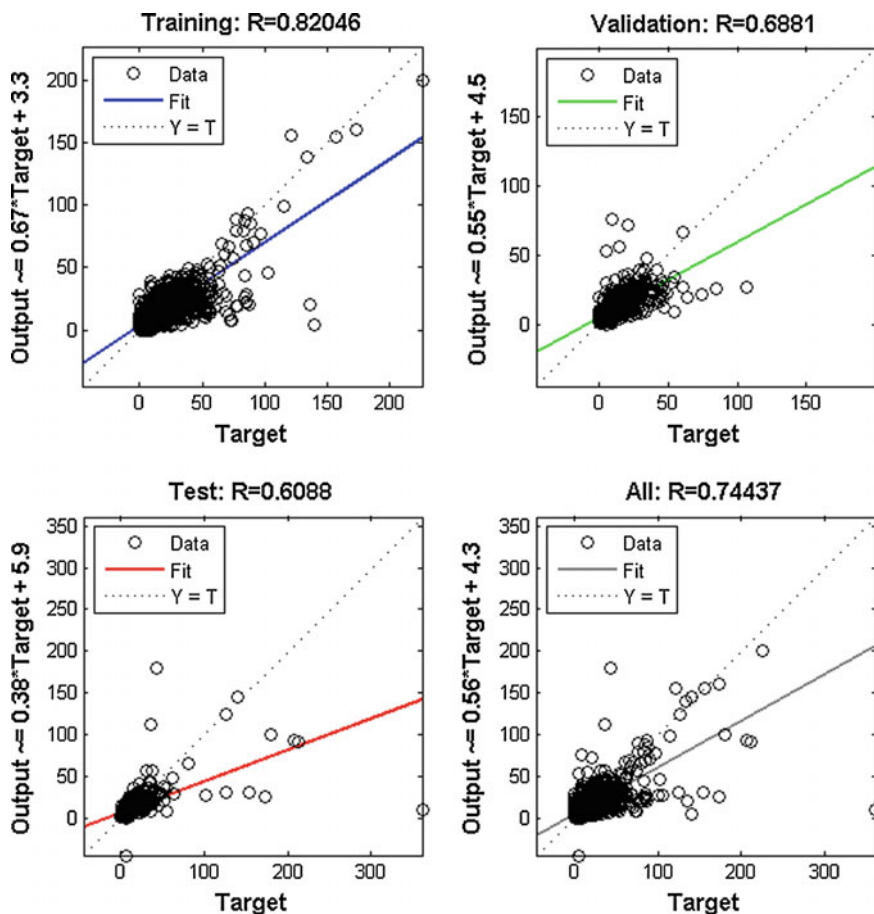
Fig. 5 The *R*-values of the four stages of ANN model development for 10 hidden neurons

5   Conclusion

A streamflow of the Langat River Basin was successfully modelled by artificial neural networks with a daily prediction for 34 years. The hidden neuron of eight or ten hidden neurons was found to be the most optimal for the ANN model in the study area. The optimization of the other techniques to avoid overfitting are recommended for improving the generalization performances of ANN. The advantages of ANN model include their capability of modeling complex, nonlinear hydrological processes without any assumption of the association patterns between input and output variables. ANN can self-adjust to a given set information and only requirement of little expertise of the problem under consideration to achieve prosperous applications. However, a major limitation to the use of ANN is in their

inability to produce transparent models, in that their internal processes are somewhat obscure and not interpretable. The next step should be integrating the ANN model application with the hydrologic physical model. The integration will improve the accuracy of simulation and prediction of the dynamic behavior of a streamflow over any time interval.

References

1. A.Y. Shamseldin, Application of neural network technique to rainfall-runoff modelling, J. Hydrol., 199 (3–4), 272–294, 1997.
2. J. Olsson, Neural networks for rainfall forecasting by atmospheric downscaling, J. Hydrol. Eng., 9(1), 1–12, 2004.
3. ASCE Task Committee on Application of Artificial Neural Networks in Hydrology, Artificial neural networks in hydrology. I: Preliminary concepts, J. Hydrol. Eng., 5(2), 115–123, 2000a.
4. ASCE Task Committee on Application of Artificial Neural Networks in Hydrology, Artificial neural networks in hydrology. II: Hydrologic applications, J. Hydrol. Eng., 5(2), 124–137, 2000b.
5. C.M. Zealand, D.H. Burn, and S.P. Simonovic, Short term streamflow forecasting using artificial neural networks. J. Hydrol., 214(1–4), 32–48, 1999.
6. P. Coulibaly, F. Anctil, and B. Bobe'e, Daily reservoir inflow forecasting using artificial neural networks with stopped training approach, J. Hydrol., 230(3–4), 244–257, 2000.
7. C.E. Imrie, S. Durucan, and A. Korre, River flow prediction using artificial neural networks: Generalization beyond the calibration range, J. Hydrol., 233(1–4), 138–153, 2000.
8. O. Kisi, River flow modeling using artificial neural networks, J. Hydrol. Eng., 9(1), 60–63, 2004.
9. W. Huang, B. Xu, and A. C. Hilton, Forecasting flows in Apalachicola River using neural networks, Hydrology Process., 18(13), 2545–2564, 2004.
10. M.A. Antar, I. Elassiouti, and M.N. Allam, Rainfall-runoff modeling using artificial neural networks technique: A Blue Nile catchment case study, Hydrology. Process, 20(5), 1201–1216, 2006.
11. S. Haykin, Neural Networks: A Comprehensive Foundation (second ed). Prentice-Hall Inc., Englewood Cliffs, New Jersey, USA, 1999.
12. S. J. Nowlan, & G.E. Hinton, Simplifying neural networks by soft weight sharing. In: Advances in Neural Information Processing Systems (ed. by J. Moody, S. Hanson & R. Lippmann), Vol. 4, 173–193. Morgan Kaufmann, San Mateo, California, USA, 1992.
13. O. Giustolisi, Sparse solution in training artificial neural networks. Neuro Computing 56C, 284–304, 2004.
14. H.Y. Hai, O. Jaafar, A. El-Shafie, S.A. Sharifah Mastura, Analysis of hydrological processes of Langat River sub-basins at Lui and Dengkil. International Journal of the Physical Sciences, 2011, Vol. 6(32), pp. 7390–7409.
15. M.F. Ali, N.F. Abd Rahman, K. Khalid and N.D. Liem, Langat river basin hydrologic model using integrated GIS and ArcSWAT interface. Applied Mechanics and Materials. Vol.567, 2014, pp 86–91.

16. K. Khalid, M.F. Ali and N.F. Abd Rahman, The development and application of Malaysian Soil Taxonomy in SWAT Watershed Model. ISFRAM 2014. Proceedings of International Symposium on Flood Research and Management. 2014, pp.79–88.
17. A. Amini, M.A. Thamer, G. Abdul Halim, K.H. Bujang, Adjustment of peak streamflows of a tropical river for urbanization. American Journal of Environmental Sciences, 2009, 5 (3): pp. 285–294.
18. M.F. Ali, N.F. Abd Rahman, K. Khalid, Discharge assessment by using integrated hydrologic model for environmental technology development". Journal of Advanced Materials Research, Vol. 911. 2014, pp 378–382.
19. J. Hafizan, M.Z. Sharifuddin, M. Zainol, and K. Azme, Dissolved oxygen forecasting due to land use activities using time series analysis at Sungai Hulu Langat, Selangor. Ecological Environmental Modelling, Proceeding of the National Workshop, Universiti Sains Malaysia, 3–4 September, 2001, p.157–164.
20. J. Hafizan., M.Z. Sharifuddin, T. Mohd Ekhwan, M. Mazlin, C.M. Hasfalina, C.M., Application of artificial neural networks for predicting water quality index. Jurnal Kejuruteraan Awam 16(2): 2004, 42–55.
21. A. Shabri, A hybrid model for streamflow forecasting using wavelet and least squares support vector machines. Jurnal Teknologi (Sciences & Engineering, 73:1, 2015, 89–96.

The Influenced of Localized Corrosion on the Natural Frequency in the Reinforced Concrete Beam

Noorli Ismail, Hanita Yusof and Mohd Faizal Md Jaafar

Abstract This study presents the use of natural frequency for the identification of damage location in detecting the location and severity of corrosion in reinforced concrete beam models. The simply supported beam was modeled with five different corrosion factors, f using DIANA Release 9.1 software. The simulation models was applied in uncorroded beam (Beam UC) and corroded beam with corrosion factor of 8 % (Beam LD8), 16 % (Beam LD16), 32 % (Beam LD32), and 64 % (Beam LD64). The total span of 2200 mm with 20 locations in the steel bar was analyzed for localized corrosion including the distance near to supports. The technique was necessitated with the performance of linear, nonlinear, and eigenvalue analysis. The ratio of frequency drop of $f_{corrode/uncorrode}$ was obtained to visualize all modes at the corroded location. The results of frequency drop illustrated that the poorest location of corrosion was detected at x/L between 0.4 and 0.7. It can be concluded, the ratio of $f_{corrode/uncorrode}$ can be used to damage indicator to detect the localized corrosion.

Keywords Finite element analysis · Natural frequency · DIANA software · Eigenvalue analysis

1 Introduction

Steel corrosion in reinforced concrete structures leads to severe deterioration processes. It is usually affect the ultimate and serviceability limit state performance of the structures. Generally, the visual inspection had been used to assess the damage

N. Ismail (✉) · H. Yusof
Faculty of Civil Engineering and Environmental, Universiti Tun Hussien Onn Malaysia, Batu Pahat, Johor, Malaysia
e-mail: noorli@uthm.edu.my; noorlii@yahoo.com

M.F.M. Jaafar
Faculty of Civil Engineering & Earth Resources, Universiti Malaysia Pahang, Gambang, Pahang, Malaysia
e-mail: faizaljaafar@ump.edu.mu

in structure. However, this type of inspection is failed to monitor the damage at early stage. Recently, the new techniques were developed using the changes in reduction of natural frequencies had been applied and often reliable to be the most convenient parameters to be used as damage detection in reinforced concrete [1–6]. Several approaches were presented for assessment of damage from natural frequencies measurement such as artificial neural network (ANN) [7], local stiffness indicator (LSI) [6, 8–10], and modal vector consistency [11, 12].

The information can play a vital role in the development of economical repair and periodic monitoring of damage such as cracking and corrosion. In present study, the changes in reduction of natural frequency of $f_{\text{corrode/uncorrode}}$ was obtained to visualize all modes at the corroded location. It is proposed the use of localized changes to locate damage by using the drop in natural frequencies by using finite element modeling. The calibration of FE models is based on the experimental works [13]. The determination of the damage location in reinforced concrete beam models due to load induced cracks and corrosion through three types of analysis namely linear, nonlinear and eigenvalue.

2 Finite Element Modeling

The width and height of the beams modeled were 150 and 250 mm, respectively. The length of the beam was 2400 mm with supports located 100 mm from each end of the beam. The beams were simply supported with concrete cover of 20 mm for each side as shown in Fig. 1. The anchorage was provided with length of 400 mm at each end of the beam. The high yield reinforcement was 16 mm diameter with two bars and no stirrups were provided.
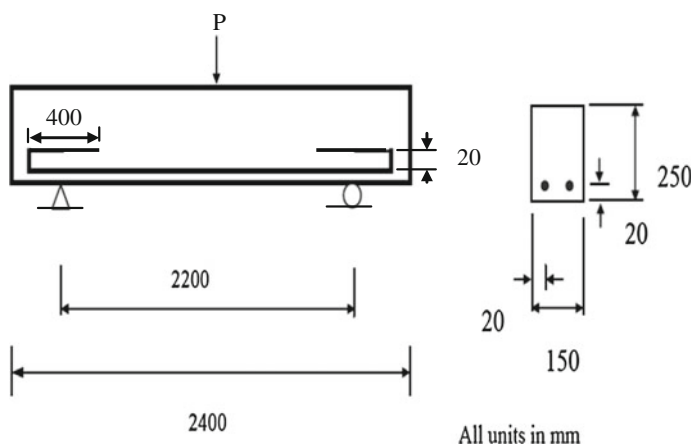
Fig. 1 Reinforced concrete beam plan

Fig. 2 Work plan in creating the models
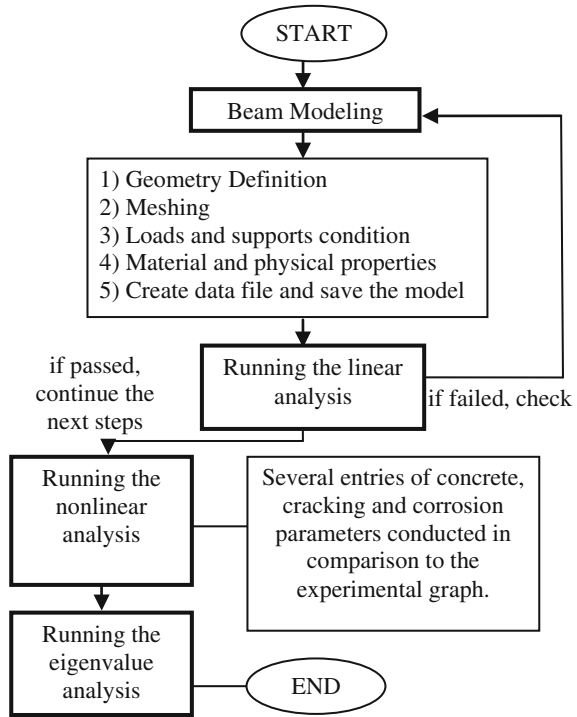
The calibration of the uncorroded beam model was categorized as the control beam. The second calibration model was a corroded beam. The concrete and modal parameters had to be ascertained using several entries of these parameters into the data file. The parameters involved were Young Modulus of concrete, E_c, constant tension cut-off, f_t and shear retention, β which were plotted in the load-displacement graph and compared to the graph provided in the experimental study. The purpose was to select the nearest parameters which were closely to the experimental graph. Figure 2 shows the work plan in creating the models.

2.1 Linear Analysis

The method of Sparse Cholesky was applied to the system of equilibrium equations as the direct solution method to solve the linear problem in the model. Once the equations were determined for each element, the stiffness was assembled in the each pair of nodal freedoms. The system matrix was generated by composing the stiffness matrix, k. The result indicated the small percentage difference of displacement between hand calculation and finite element analysis (FEA) was less than 13 %.

2.2 Non Linear Analysis

In nonlinear structural analysis, the additional input of material behavior is attached in the data file. The nonlinear phenomena involved are cracking and corrosion effects. The nonlinear analysis are performed when the result of linear analysis succeed. With the same data file, the nonlinear phenomenon studies the nonlinear behavior of the uncorroded and corroded model. First of all, the cracking parameters are implemented to the nonlinear material data in order to investigate the cracking behavior of the model. Second, the corrosion effect is studied using the CORROS option which had been introduced several entries of corrosion or reduction factor, *f*. Two (2) different command files are implemented in the analysis with the same nonlinear algorithm and convergence criteria was applied in the model. The iteration method used for the analysis is modified by Newton–Raphson.

The value of corrosion or reduction factor, *f*, 50 % was matched closely to the experimental graph of corroded beam [9]. The reduction factor is known as a percentage of material losses. The corroded beam in the experimental study was induced with an average amount of loss, 8 % of steel area. The value of *f*, 50 % which had been obtained from the finite element analysis was determined as 8 % of material losses.

2.3 Eigenvalue Analysis

In eigenvalue analysis, the subspace iteration method (SUBSPA) command was used to solve this type of eigenproblem. Parameter of convergence criterion (ECONVE) specified the tolerance of 10^{-9}. DIANA analyzed 50 number of iteration with 100 shift factor. In analyzing the data, zero or negative of eigenvalue can be obtained but if the analyze involves softening material behavior, the stiffness matrix cannot analyze the positive eigenvalues. The calculated frequencies are corrected according to the performed shift. The parameter of eigenpairs number (NMODES) was calculated 20 frequencies as the output.

The simulation models were created by using another value of corrosion factors, *f* in order to investigate the damage in localized corrosion. The corrosion factor of 8 % (Beam LD8), 16 % (Beam LD16), 32 % (Beam LD32), and 64 % (Beam LD64) were applied in these corroded beam models. The uncorroded beam was named as Beam UC. All corrosion factors were implemented at each locations of bar from the total 20 locations. To visualize all modes for all bars at the corroded location, the ratio of $f_{corrode/uncorrode}$ was obtained. The ratio was determined from the result of natural frequencies which had been obtained from eigenvalue analysis.

3   Results and Analysis

In determining the damage location in reinforced concrete beam models, three analysis was carried out using linear, nonlinear, and eigenvalue analysis. The effect of frequency drop to the cracking and corrosion was investigated by the ratio of $f_{corrode/uncorrode}$ in order to visualize all obtained modes. The corroded location, x/L which is L refers to the total span of the beam; 2200 mm and x value refers to the corroded location. The steel bar was divided to 20 with 110 mm per location. Figures 3, 4, 5 and 6 shows the comparison of frequency drop between uncorroded (UC) and corroded beam models for all four modes.

Figure 3 illustrates the lowest ratio located at $x/L = 0.475$ for all corroded beams which was located in the middle of the beam. The highest $f_{corrode/uncorrode}$ is observes at the location near the support at left or right support. Furthermore, the location of $x/L = 0.725$ stated the lowest ratio for all corroded beam as shown in Fig. 4. The highest $f_{corrode/uncorrode}$ located at $x/L = 0.13$, 0.175, and 0.475 which was near to the right support.

Figure 5 shows the lowest ratio located at $x/L = 0.525$ which was near to the center of beam. The three shapes of U was found at $x/L = 0.28$, 0.325, 0.675, and 0.725 which indicated the highest $f_{corrode/uncorrode}$. Figure 6 shows the lowest ratio located at $x/L = 0.625$ for all beam models. The highest ratio of $f_{corrode/uncorrode}$ indicated at the location near to the left and right support.
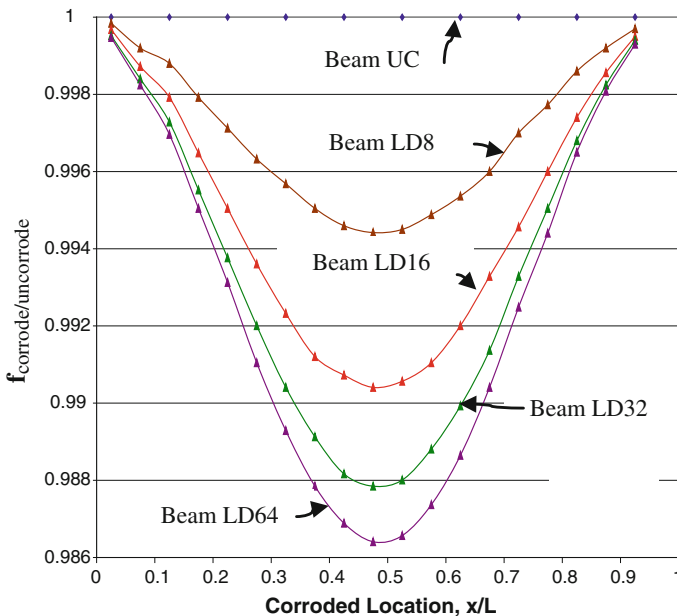
Fig. 3 Frequency drop for Mode 1
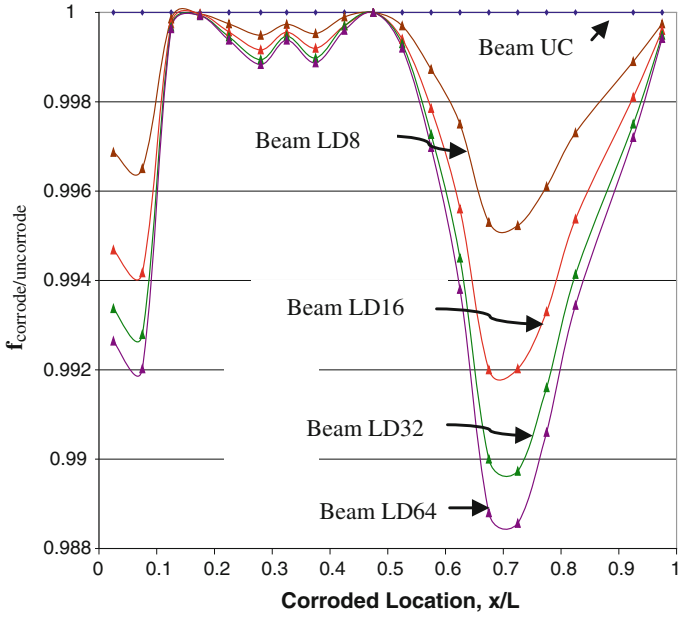
Fig. 4 Frequency drop for Mode 2
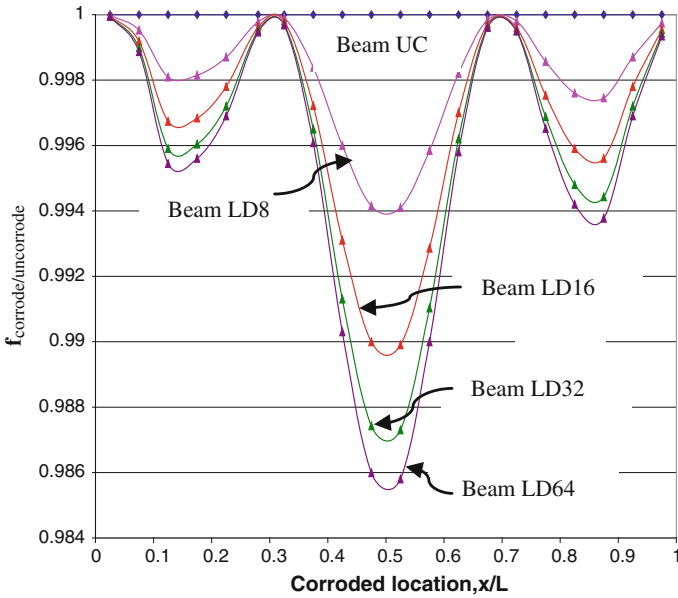
Fig. 5 Frequency drop for Mode 3
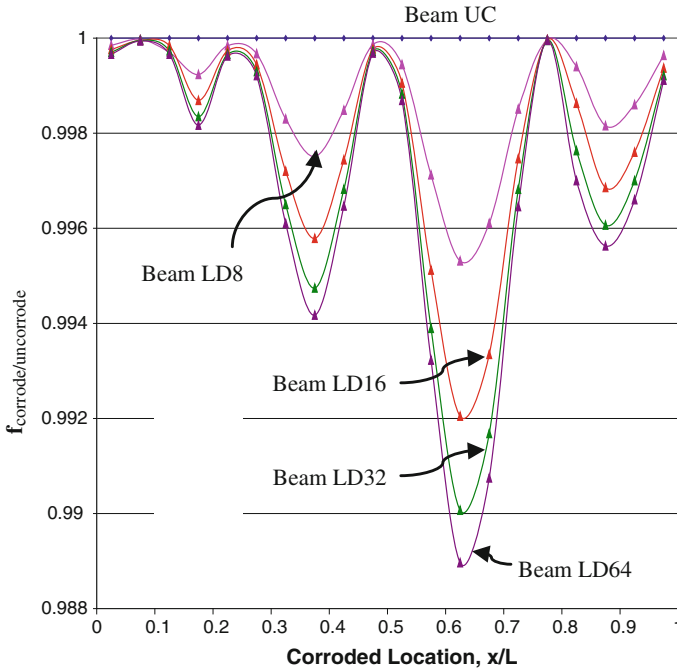
Fig. 6 Frequency drop for Mode 4

The frequency drop for all four modes which was plotted in Figs. 2, 3, 4 and 5 shows some trends. Overall, no frequency drop or highest ratio was indicated at the left and right of beams. In Mode 2, the ratio showed a gradual drop at the first location of the bar. Meanwhile, Mode 1 and Mode 4 indicated dramatically fall at the middle of the bar. The lowest ratio described that poor corrosion occurs at this point. A different trend is observed for Mode 2 and Mode 4. It illustrated the highest drop was located at the location between $x/L = 0.6$ and 0.7. It is confirmed the poorest condition of corrosion found in these locations. The graph shows several U shapes at Mode 3 and Mode 4. In Mode 4, the location of $x/L = 0.6$ was affected by moderate corrosion.

4   Conclusion and Discussion

Based on the result and findings from this research, it can be concluded that:

1. The frequency drop increased with the increasing of bar deterioration. Beam LD64 is the most affected due to the highest percentages of material losses applied in the model.

2. For further study, the combination of other modal parameters could be done in order to detect exactly location of damage. This is because the ratio of $f_{\text{corrode/uncorrode}}$ has restricted limitation as the damage indicator to detect the localized corrosion.

References

1. Emad E.D., Endah W., Tianjian Ji, Brian R.E., Improving FE models of a long span flat concrete floor using natural frequency measurements, J.Computers and Structures 80, pp 2145–2156, 2002.
2. Gawley F, Adams R.D, The locations of defects in structures from measurements of natural frequencies, J.Strain Analysis 14 (2), pp 49–57, 1979.
3. Salawu Q.S, Detection of structural damage through changes in frequency: a review, J.Engineering Structures Vol 19, No-9, pp 718–723, 1997.
4. Wang X., Hu N., Hisao Fukunaga, Yao Z.H., Structural damage identification using static test data and changes in frequencies, J.Engineering Structures 23, pp 610–621, 2001.
5. Patil D.P., Maiti S.K., Detection of multiple cracks using frequency measurements, J.Engineering Fracture Mechanics 70, pp 1553–1572, 2003.
6. Ismail Z., Abdul Razak H., Abdul Rahman A.G., Determination of damage location in RC beams using mode shape derivatives Original Research Article J.Engineering Structures, Volume 28, Issue 11, pp 1566–1573, 2006.
7. Antony Jeyasehar C., Sumangala K., Damage assessment of prestressed concrete beams using artificial neural network (ANN) approach, J.Computers and Structures 84, pp 1709–1718, 2006.
8. Ismail Z., Zhi C.O, Honeycomb damage detection in a reinforced concrete beam using frequency mode shape regression, J.Measurement 45, pp 950–959, 2012.
9. Noorli I., Local Stiffness Indicator (LSI) Evaluation In The Reinforced Concrete Beam Models, Proceeding of 4$^{\text{th}}$ Engineering Conference on Advanced And Innovation In Electrical, Electronics (ENCON 2011), Telecommunication Computing Engineering and Technologies, Riverside Majestic Hotel Kuching, 29 Nov – 2 Dis 2011.
10. Noorli.I, Abdul Razak.H, Ismail.Z, The effect of corrosion on the natural frequency and modeshapes in reinforced concrete beam models, Proceeding of International Conference on Science and Technology: Application on Industry and Education (ICSTIE'08), UiTM Penang, 12–14 Dec 2008.
11. Ricardo P., Consuelo H., Juan M.O., Identification of damage in RC beams using indexes based on local modal stiffness, J.Construction and Building Materials 22 pp 1656–1667, 2008.
12. Abdul Razak H., Choi F.C., Damage Assessment of Corroded Reinforced Concrete Beams Using Modal Testing, J.Structural Engineering, Mechanics and Computation, Volume 2, pp 1203–1215, 2001.
13. Choi F.C, Characterisation of Reinforced Concrete Beams subjected to Reinforcement, Corrosion Using Modal Parameters, Dissertation M.Eng.Sc, Fakulti Kejuruteraan, Universiti Malaya, 2001.
14. Choi F.C, Abdul Razak.H, The effect of Corrosion on the Natural Frequency and Modal Damping of Reinforced Concrete Beams, J.Engineering Structures 23, pp 1126–1133, 2001.

Idealized River Meander Using Improved Sine-Generated Curve Method

Irma Noorazurah Mohamad, Wei-Koon Lee and Raksmey May

Abstract The geometric features of meandering river are distinct. There are several factors which govern the meandering river path. Geometric variability of river meanders depends primarily on sinuosity, radius of curvature, meander wavelength, and river width. Idealized river meander planform is classically described using a sine-generated curve, which can be constructed from sinusoidal function of the meander angle in the down-valley direction. An improved method involves constructing the path as combinations of line and arc, with direct reference to practical dimensions instead of the turning angle. Owing to the diverse size and shape of tidal rivers, a realistic but idealized numerical model will greatly facilitate related research to better understand their physics and behaviors. This study improves the established methods on deriving and simplifying the river meander. Specifically, we examine the use of the improved sine-generated curve method to approximate the Lower Muda River and Lower Klang River. The suitability of the method in the construction of an idealized tidal river model for numerical study is evaluated.

Keywords Tidal river · Meander path · Idealized river model · Improved sine-generated curve

I.N. Mohamad (✉) · R. May
Faculty of Civil Engineering, Universiti Teknologi MARA, Shah Alam, Selangor, Malaysia
e-mail: irma1095@salam.uitm.edu.my

R. May
e-mail: may_raksmey@salam.uitm.edu.my

W.-K. Lee
Flood Control Research Centre (FCRC), Universiti Teknologi MARA, Shah Alam, Selangor, Malaysia
e-mail: leewei994@salam.uitm.edu.my

1   Introduction

Natural river experiences meandering process that produces inhomogeneous plan-form pattern in the form of a series of bends. The meandering process generally implies channel instability where slight perturbation causes erosion and deposition which leads to lateral migration of the river channel [1]. The process is a phe-nomenon attributed to the complex interactions between numerous physical pro-cesses as basin runoff travels from upstream catchment down-valley toward the sea.

Changes of river meander pattern have been investigated through empirical and statistical analyses, as well as field and experimental observations. Meander geometry is typically studied using series approach to account for its quasi-randomness [2, 3], or analyzing the underlying regularity [4–10]. The meander channel geometry analysis has been classified in three categories which are dependent variables, independent variables, and constraints [10–13]. Flowrate and sediment inflow were determined as independent variables. While, dependent variables such as velocity of flow, river width, depth of flow, channel slope, and radius of curvature were obtained through a series of physical condition [10].

Mathematical model is used to transform meander path to planimetric parameters view such as amplitude, wavelength, arc length, and arc angle [4–7, 14–18]. After that, meanders are typically idealized and approximated by generalized functions. This is typically true for most stable river form where the variability of erosion and deposition rate over time is minimized. In addition to generalized river meander pattern, a simpler method based on meander geometry dimensions such as arc and line pattern are developed by Mecklenberg and Jayakaran [19]. They defined completely geometrical dimensions of river meander by improving the sine-generated curve of [7].

This study describes the available empirical methods used on deriving and simplifying river meander pattern. The improved sine-generated curve method is then adapted and applied on selected tidal river in Malaysia, namely Lower Muda River (LMR) and Lower Klang River (LKR).

2   River Meander Planform

2.1   The Sine-Generated Curve

Sine-generated curve (SGC) is a theory-based analysis of river planform developed by Langbein and Leopold [7]. They discovered that the pattern of river meander can be described using a sinuous function, which defines the planimetric geometry of river meander using:

$$\phi = \omega \sin \frac{2\pi s}{M} \qquad (1)$$

Fig. 1 The sine curve function of SGC (adapted from [7])
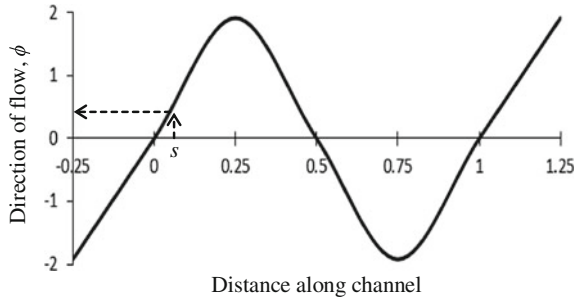
ϕ turning angle in the down-valley direction (in radians),
ω maximum turning angle (in radians),
s incremental distance along the meander path (unit length),
M total distance along the meander (unit length)

In natural cases, the applicability of the SGC theory is limited up to a maximum turning angle ω of 2.2 rad, beyond which a closed horse loop path resembling figure '8' is produced. The typical sine curve of the turning angle as a function of incremental distance along the path according to (1) is shown in Fig. 1. The corresponding river meander pattern in the *x-y* plane thus developed, i.e., the sine-generated, is as shown in Fig. 2.

Although the SGC method is an accurate representation of channel planform, the computation is complicated owing to the difficulty of applying the turning angle in the down-valley direction, which involves continual variation of the reference axis instead of a fixed Cartesian system.

Fig. 2 The river meander planform of SGC with maximum angle, $\omega = 1.92$ rad (adapted from [7])
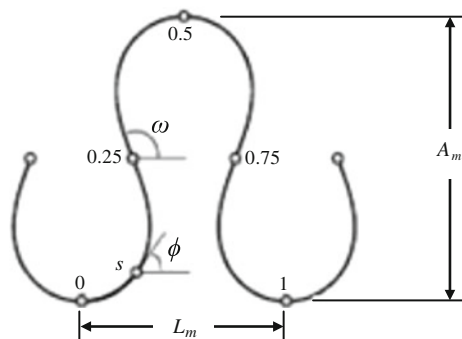
2.2 Improved Sine-Generated Curve

Reference [19] introduced the improved sine-generated curve (ISGC), where the geometrical dimensions of river meander such as meander wavelength L_m, stream length per meander M, sinuosity K, and amplitude A_m are used directly to approximate the meander pattern. Using the Bessel and Struve functions, they found higher precision in defining river meander pattern by promoting the combination of arc and line on the meander path as shown in Fig. 3.

Extension of the method to more generalized conditions based on the angle of direction β has been emphasized in this study. The respective equations for the meander geometry are as follows:
river sinuosity,

$$K = \frac{M}{L_m}, \tag{2}$$

radius of curvature,

$$R = \frac{L_m K^{1.27}}{16.34(K^{0.5} - 1)^{0.5}}, \tag{3}$$

angle of direction (in radians),

$$\beta = \cos^{-1}\left(\frac{16R^2 - 8A_m R + L_m\sqrt{4A_m^2 - 16RA_m + L_m^2}}{4A_m^2 - 16RA_m + L_m^2 + 16R^2}\right), \tag{4}$$

arc angle (in radians),

$$\theta = 2\beta, \tag{5}$$

Fig. 3 Illustration of arc and line pattern variables (adapted from [19])
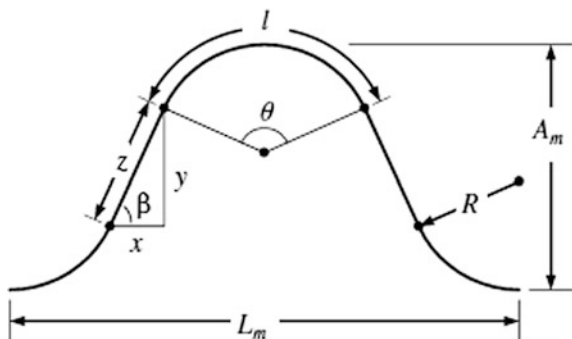
and arc length,

$$l = 2\beta R. \tag{6}$$

The component of x and y, as defined in Fig. 3, may be calculated using the following equations derived from geometrical considerations (note that determination of y precedes x in the case $\beta > \pi/2$):

$$y = \begin{cases} A_m - 2R + 2R\cos(\beta), & \beta < \frac{\pi}{2} \\ A_m - 2R - 2R\cos(\beta), & \beta > \frac{\pi}{2} \end{cases}, \tag{7}$$

$$x = \begin{cases} \frac{L_m}{2} - 2R\sin(\beta), & \beta < \frac{\pi}{2} \\ \frac{y}{\tan(\beta)}, & \beta > \frac{\pi}{2} \end{cases}. \tag{8}$$

Hence, the line path length,

$$z = \sqrt{x^2 + y^2}, \tag{9}$$

and the idealized river sinuosity,

$$K_i = \frac{4\beta R + 2z}{L_m}, \tag{10}$$

may be determined. In addition, the pattern connecting the arcs and lines can be simplified based on 24 segments on SGC.

3 Study Area

In this study, we consider the downstream part of Muda River in Kedah and Klang River in Selangor which are lowland river under tidal influence. The details related to both areas of study are provided as follows.

3.1 *Muda River, Kedah*

Muda River basin has a total catchment area of 4,210 km^2. The Muda River is the longest river in the State of Kedah measuring about 180 km, and is used primarily for irrigation scheme. The upper and middle reach of Muda River belong to the State of Kedah, whereas approximately 30 km from the river mouth forms the boundary between the states of Kedah and Pulau Pinang.

Fig. 4 Lower Muda River (*Source* Google Earth)

The Lower Muda River (LMR) (Fig. 4) is located on very mild bed slope of 1/2,300. The river channel width increases from 100 m at the Muda Dam (located 130 km upstream of the river mouth) to 300 m near the river mouth. Muda River is subjected to flood events during the transitional period between northeast monsoon and southwest monsoon season. Normally, flood happens due to joint occurrences of high rainfall intensities and high tide at the downstream of Muda Barrage. A disastrous flood was recorded on October 2003, affecting almost 45,000 people. The flood magnitude was recorded at 1,340 m^3/s, which is higher than the 50-year flood peaks [20, 21]. In addition, sand and gravel mining activities at LMR had been reported to cause salt intrusion up to 25 km from the river mouth [22].

3.2 Klang River, Selangor

Klang River basin is one of the biggest river basins in Selangor with a total catchment area of 1,288 km^2. Klang River has an estimated total length of 120 km. It originates from Ulu Gombak Forest Reserved area, and is fed by 13 major tributaries. The last major tributary is the Damansara River. Klang River exits on the west coast at Port Klang, where the tide is semi-diurnal and the estuary is well-mixed.

The Lower Klang River (LKR) (Fig. 5) is located in a flat and low lying plain. The river bed slope is mild at the Klang-Damansara confluence point ($\sim$1/2,300) and is near flat (1/7,000) when the river meets the sea. Meanwhile, the river width increases from 50 m at Klang-Damansara confluence point to 300 m at Port Klang estuary. The section of LKR selected in the present study starts from Taman Sri Muda down to Port Klang estuary where the effect of tide is most felt.

Fig. 5 Lower Klang River (*Source* Google Earth)

4 Result and Analysis

4.1 Idealized LMR and LKR

For the purpose of developing the idealized river meandering model, we focus on
the first meander sequence located at the river mouth of each river. The (x, y) co-
ordinates of LMR and LKR along its river centerline are discretized from satellite
images of Google Earth.

The arc-line patterns of river meander are constructed using the ISGC introduced
by Mecklenberg and Jayakaran [19]. The components of arcs and lines of the
idealized river meander pattern can be determined from known parameters, which
are stream length per meander M, and meander wavelength L_m such that the sin-
uosity K is M/L_m of the meander is also known a priori.

The arc-line pattern of the idealized river meander can be determined by entering
the sinuosity value in (3). The value of radius of curvature (R) together with the
known parameters $(L_m$ and $A_m)$ then been substituted in (4), which defines the angle
of direction β. Then, the arc angle θ, and arc length l can be determined from (5)
and (6), respectively. Now, the components of line pattern which are y, x, and z can
be specified through (7)–(9). For this study, the line pattern contributes only two
segment points instead of four points used by Mecklenberg and Anand [19] while
the arc points remain the same.

The ISGC method had been applied to two different tidal rivers as described in
the earlier section. For LMR, using input parameters $M = 2.400$ km, $L_m = 1.200$ km
and $A_m = 1.000$ km, the angle of direction β calculated is 1.467 rad. The arcs and
lines pattern produced is as shown in Fig. 6. Meanwhile, the arcs and lines pattern
of LKR is derived with input parameters $M = 8.500$ km, $L_m = 2.500$ km, and
$A_m = 2.800$ km, respectively, as shown in Fig. 7. Note that in the case of LKR, the
angle of direction β is 1.897 rad (larger than $\pi/2$). This proved that the ISGC
method can be used to describe the river meander pattern very well.

The radius of curvature R calculated from (3) describes an arc connecting to both
the curves and tangent lines. The radius of curvature R values for LMR and LKR

Fig. 6 Idealized meander pattern of Lower Muda River using arc-line combinations with the angle of direction, $\beta = 1.467$ rad and the radius of curvature, $R = 275$ m
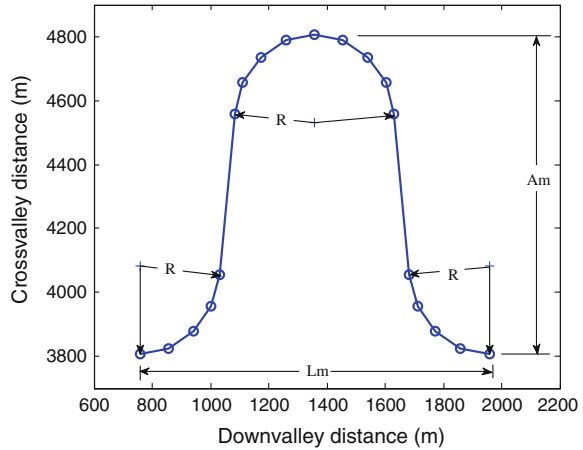
Fig. 7 Idealized meander pattern of Lower Klang River using arc-line combinations with the angle of direction, $\beta = 1.897$ rad and the radius of curvature, $R = 788$ m
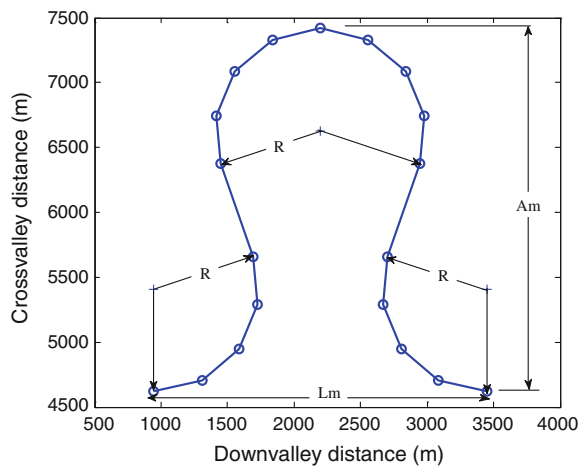
are 275 and 788 m, respectively. This describes linear relationships between R, K, and β. In addition, (3)–(10) illustrate the complete geometry of the arc-line pattern that allows practical dimensions for idealized river meander.

Following the approach used by Lee and Mohamad [23], the linear axis of the idealized river meander planform is rotated to a suitable polynomial function which acts as a reference axis to the actual river system. This allows the idealized river meandering pattern to be overlaid on the actual river and thus produces a more realistic representation of the original river. For both LMR and LKR, a degree-2 polynomial is found to fit the selected river reach. Figures 8 and 9 show the rotated idealized arc-line river meander for LMR and LKR, respectively. It can be observed that the idealized river meandering pattern for LMR and LKR realistically described their respective actual river meander pattern.

Fig. 8 Idealized LMR in polynomial references axis
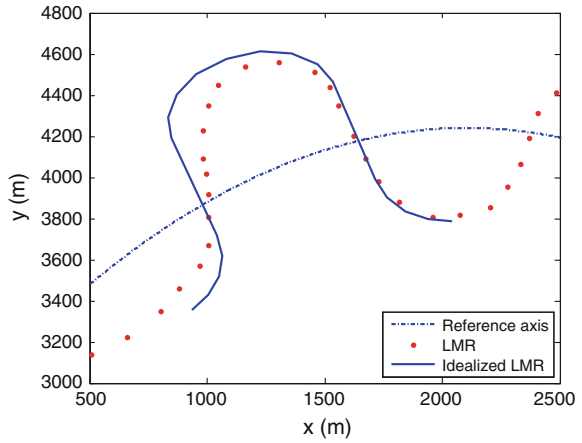
Fig. 9 Idealized LKR in polynomial references axis
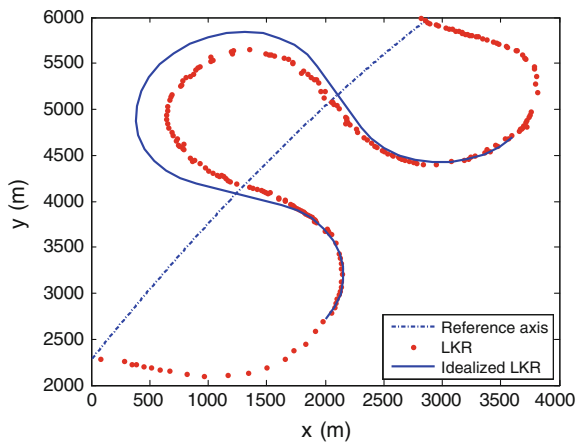
4.2 Sinuosity Index (SI)

Different sinuosity indices had been applied by various researchers to define the meandering form of river [24–26]. Each methods post their own advantages and disadvantages. A summary of sinuosity index, SI according to [25] is shown in Table 1.

Table 1 Sinuous index

SI	Class type
<1.05	Straight
1.05–1.3	Sinuous
1.3–1.5	Moderate meandering
>1.5	Meandering form

Based on the ISGC method, the river sinuosity K for LMR and LKR are 2.0 and 3.4, respectively whereas the idealized river sinuosity K_i for LMR and LKR are 2.2 and 3.0, respectively. Based on the sinuous classification in Table 1, it can be concluded that both LMR and LKR possess meandering form. The percent difference of SI between the idealized and the actual river are in the order of 10 % which suggest reasonably good approximation.

5   Conclusion

In this paper, we have described the formation of an idealized river meandering pattern using the improved SGC method that includes arc-line pattern rotated to a reference polynomial function. Equations adopted from [19] show this simplified method is very practical in defining the geometry of meandering river. Two test cases were conducted on Lower Muda River (LMR), Kedah and Lower Klang River (LKR), Selangor. The resulting arc-line patterns for both studies show the idealized pattern approximate the actual river planform satisfactory. This idealized river meandering pattern can potentially be used for the investigation of estuary-river system under various external forcing parameters.

References

1. A. Odgaard, and J. Abad, (2008). River meandering and channel stability. Sedimentation Engineering. pp. 439–459. doi: 10.1061/9780784408148.ch08. Accessed on 11th April 2015.
2. R. I. Ferguson, (1976). Disturbed periodic model for river meanders. Earth Surface Processes and Landforms, 1, pp. 337–347.
3. P.K. Swamee, B. Parkash, J.V. Thomas, and S. Singh, (2003). Changes in channel pattern of River Ganga between Mustafabad and Rajmahal, gangetic plains since 18th century. International Journal of Sediment Research, 18(3), pp. 219–231.
4. C. C. Inglis, (1947). Meanders and their bearing on river training. Institute of Civil Engineering London, Maritime and Waterways Engineering Division, 5(17), pp. 3–24.
5. L. B. Leopold, and M. G. Wolman, (1957). River channel patterns—braided, meandering and straight. U.S. Geological Survey Professional Paper 282B, U.S. Geological Survey, Washington, D.C.
6. L. B. Leopold, and M. G. Wolman, (1960). River meanders. Geological Society of America Bulletin, 71(6), pp. 769–793.
7. W.B. Langbein, and L.B. Leopold, (1966). River meanders-theory of minimum variance. Geological Survey Professional Paper 422-H. United States Government Printing Office, Washington D. C.

8. G. H. Dury, (1965). Theoretical implications of underfit streams. U.S. Geological Survey Professional Paper 452C, U.S. Geological Survey, Washington, D.C.

9. J. Zeller, (1967). Meandering channels in Switzerland. International Association of Scientific Hydrology, Symposium on River Morphology, Bern, Switzerland, 75, 174–186.

10. H. Chang, (1984a). Analysis of river meanders. Journal of Hydraulic Engineering, 110(1), pp. 37–50.

11. J. F. Kennedy, and N. H. Brooks, (1963). Laboratory study of alluvial streams at constant discharge. Proceedings of Federal Inter-Agency Sedimentation Conference, Miscellaneous Publication No. 970, Agricultural Research Service, pp. 320–330.

12. L. B. Leopold, M. G. Wolman, and J. P. Miller, (1964). Fluvial processes in geomorpliology, W. H. Freeman and Co., San Francisco, California, p. 522.

13. J. H. Mackin, (1948).Concept of the graded river. Bulletin of the Geological Society of America, 59, pp. 463–512.

14. S. V. Chitale, (1970). River channel patterns. Journal of Hydraulics Division, American Society of Civil Engineers, 96, pp. 201–221.

15. R. I. Ferguson, (1973). Regular meander path models. Water Resources Research, 9(5), pp. 1079–1086.

16. H. Chang, (1984b). Regular meander path model. Journal of Hydraulic Engineering, 110(10), pp. 1398–1411.

17. P. Y. Julien, (1985). Planform Geometry of meandering alluvial channels. Report CER84-85PYJ5, Department of Civil Engineering, Colorado State University, 49 p.

18. G. P. Williams, (1986). River meander and channel size. Journal of Hydrology, 88, pp. 147–164.

19. D.E. Mecklenberg, and A.D. Jayakaran, (2012). Dimensioning the sine-generated curve meander geometry. Journal of the American Water Resources Association, 48(3), pp. 635–642.

20. P.Y. Julien, A.A. Ghani, N.A. Zakaria, R. Abdullah, K.K. Kiat, J. Dinor, A. Manap, and F. Yusof, (2006). Design option of the flood mitigation plan of Sungai Muda, Kedah, Malaysia. Final Report prepared at REDAC, Universiti Sains Malaysia, Nibong Tebal, for DID Malaysia, 149p.

21. P.Y. Julien, A.A. Ghani, N.A. Zakaria, R. Abdullah, and C.K. Chang, (2010). Flood Mitigation Plan of the Muda River, Malaysia. Journal of Hydraulic Engineering, 136(4), pp. 251–261.

22. P.Y. Julien, J. Abdullah, and N.S. Muhammad, (2014). Keynote: Analysis extreme floods in Malaysia. Proceedings of International Symposium on Flood Research and Management. doi: 10.1007/978-981-287-365-1. Accessed on 20th April 2015.

23. W.K. Lee, and I.N. Mohamad, (2014). An idealized model of meandering tidal river. Proceedings of Regional Conference on Science, Technology and Social Sciences (RCSTSS), Pahang, 23–25 Nov 2014, UiTM Pahang.

24. J. E. Mueller, (1968). An introduction to the hydraulic and topographic sinuosity indexes. Annals of the Association of American Geographers, 58(2), pp. 371–385.

25. J. Horacio, (2014). River sinuosity index: geomorphological characterisation. Technical note 2. CIREF and Wetlands International, 6p.

26. B. A. Kumar, G. Gopinath, and M. S. S. Chandran, (2014). River sinuosity in a humid tropical river basin, south west coast of India, Arabian Journal of Geosciences, 7(5), pp. 1763–1772.

Part III
Concrete Waste and Earthquake Engineering

Vulnerability of High-Rise Buildings in Kuala Lumpur Subjected to Acheh Earthquake Event

Rozaina Ismail, Azmi Ibrahim and Azlan Adnan

Abstract The earthquake study is relevant even though Malaysia is outside the earthquake region but still had experienced and did suffer from major cases in the past like tsunami. Engineers should concern about and consider the loading for reinforced concrete building due to earthquake in Malaysia's building design procedure. The study addresses the earthquake study due to performance of critical frame reinforced concrete building which were subjected to low-intensity earthquakes effects. Building of Ampang Jaya Municipal Council (MPAJ), Employees' Provident Fund (KWSP), Block F (Public Work Department, JKR), and Department of Survey and Mapping Malaysia (JUPEM) were chosen as main models for this study. The building was analyzed using Finite Element Modeling (FEM) under different types of analyses using IDARC2D depend on variety of earthquake intensities from Time History Analysis (THA) considering low to medium earthquake intensities. The yield point at beam-column connections was analyzed to determine the damage index and the damage level of the building. The buildings analyzed, which were subjected to the Acheh earthquake ground motion, developed plastic hinge due to the earthquake intensity of 0.012 g for all buildings except building of Employees' Provident Fund (KWSP) which developed plastic hinge due to the earthquake intensity of 0.05 g and had damage indexes in the range 0.00 (no damage) to 1.0 (collapse). A greater damage index means that the members yield earlier and the plastic rotation is larger and vice versa. As for the result, the damage to columns is light, the damage level of most columns is "medium destruction," and the performance of the high-performance concrete is satisfactory.

R. Ismail (✉)
Institute for Infrastructure Engineering and Sustainable Management (IIESM),
Faculty of Civil Engineering, UiTM, Shah Alam, Selangor, Malaysia
e-mail: rozaina_fka_uitm@yahoo.com

A. Ibrahim
Department of Structures and Material, Faculty of Civil Engineering, UiTM,
Shah Alam, Selangor, Malaysia

A. Adnan
Department of Structures and Material, Faculty of Civil Engineering, UTM,
Johor Bahru, Johor, Malaysia

While the damage in the beams is much serious, the distribution of the damage index reflects the seismic design principle of "strong column, weak beam."

1 Introduction

Public building structures in Malaysia include offices, apartment, hospitals, and schools have been heavily developed for many states in the country. The performance of the structures against seismic hazard affects human safety, loss of properties, and maintenance cost. Despite the fact that Malaysia is free from any major earthquake event, pro-active steps to determine the effect of this disaster to our buildings should not be overlooked. Though Malaysia is located in a stable tectonic plate, being close to Sumatra and Philippines's subduction zones makes us subjected to earthquake risks at any time. As a step in understanding the seismic risk in our country, there is a need to determine the vulnerability of prevalent construction types in Malaysia, against earthquakes. Malaysia is surrounded by the low-intensity earthquake regions. There are major tectonic plates around Malaysia. Engineers should concern and consider about the earthquake impacts on buildings in Malaysian's building design procedure. According to Li et al. [1], the reinforced concrete frame has to meet the requirements of performance-based earthquake engineering, since the influence of damage should be considered when conducting a structural performance assessment.

In order to predict the likely impact of an earthquake on a built environment in any part of the country, it is essential to know the seismic vulnerability of the built environment in the affected areas. This information depends on the structural systems of the buildings to resist vertical and lateral loads, performance of similar buildings in past earthquakes, and engineering standards adopted during construction. The assessment of likely impact also depends on the location and distribution of vulnerable building stock in the affected areas. In many cases buildings and structures have proven to be inadequate to resist earthquake forces and the failure of these can be held responsible for most of the resulting human fatalities [2–5].

The performance normally involves a qualitative process of measurement. Due to the reflection and expectation of the damage state, the values and parameters should be measured quantitatively to assess the performance level. The ATC-13 damage level [6] in [7] is adopted in this study to define the damage state level.

Table 1 Description of selected public buildings in Kuala Lumpur

No.	Building name	Year built	Height (m)	No of story
1	Ampang Jaya Municipal Council (MPAJ)	1992	64.2	17
2	Employees' Provident Fund (KWSP)	1981	64.2	17
3	Block F (Public Work Department, JKR)	1977	64.2	17
4	Department of Survey and Mapping Malaysia (JUPEM)	1962	35.4	9

2 Description of Building

The paper presents an evaluation of public buildings as listed in Table 1. These government office buildings located in the city of Kuala Lumpur can accommodates up to 100 persons at one time.

3 Dynamic Nonlinear Analysis

The present work studies the intensities as reported by MMD [8]. The Sumatra–Andaman (Acheh earthquake) time history record is shown in Fig. 1 with 5000 number of outputs within 0.02 time steps with the maximum acceleration of 0.012 g. The Acheh earthquake occurred in December 26, at Indian Ocean near Acheh with magnitude 9.3 on Richter scale. The acceleration is simulated to four variations of earthquake intensities as follows: 0.05, 0.10, 0.15, and 0.2 g. This study used 5 % damped spectral acceleration as adopted in [7, 9–11].

4 Modeling Concept

Structural vulnerability refers to the susceptibility of those parts of a building that are required for physical support when subjected to an intense earthquake or other hazard. This includes foundations, columns, supporting walls, beams, and floor

Fig. 1 Time history record of Acheh Earthquake for peak ground acceleration 0.012 g (December 26, 2004) [8]
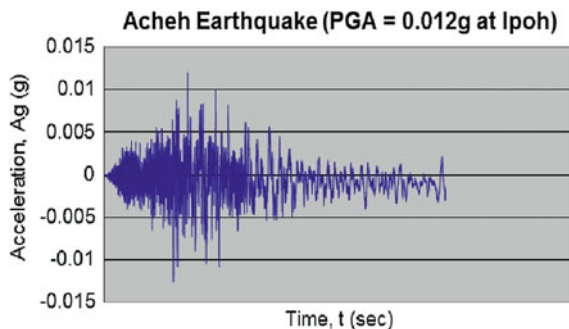
Table 2 Details structural elements for Ampang Jaya Municipal Council (MPAJ)

Elements	Floor level	Size (mm) $H \times B^a$	No of bars and bar diameter	Hoops
Beam	Ground	750 × 350	Top: 4 # 20	10 mm @ 125 mm
			Bot: 3 # 20	
Beam	1st–17th	450 × 300	Top: 5 # 25	5 mm @ 150 mm
			Bot: 3 # 20	
Column	Ground	500 × 1000	24 # 25	8 mm @ 150 mm
Column	1st–17th	550 × 300	10 # 25	10 mm @ 125 mm

[a]*Note B* width, *H* height

Table 3 Details structural elements for Employees' Provident Fund (KWSP)

Elements	Floor level	Size (mm) $H \times B^a$	No of bars and bar diameter	Hoops
Beam	Ground	900 × 350	Top: 2 # 32	10 mm @ 125 mm
			Bot: 2 # 25	
Beam	1st–17th	600 × 350	Top: 4 # 20	10 mm @ 125 mm
			Bot: 3 # 20	
Column	Ground–17th	600 × 900	20 # 25	10 mm @ 150 mm

[a]*Note B* width, *H* height

slabs. The properties of materials are 2500 N/mm^2 (E_c), 460 N/mm^2 (f_y), 27.6 N/mm^2 (f_c), and 25 mm for cover (c). A few assumptions have to be made in conducting this analysis. The floor diaphragm was assumed to be infinitely rigid so that the nodes within each floor level deformed the same amount laterally. The contribution of floor slab to the strength and stiffness was neglected. The columns were assumed to be fixed at the basement level. The value of damping coefficient for RC structure of 5 % was used. Tables 2, 3, 4, and 5 show the structural element.

Table 4 Details structural elements for Block F Public Work Department (JKR)

Elements	Floor level	Size (mm) $H \times B^a$	No of bars and bar diameter	Hoops
Beam	Ground	750 × 350	Top: 4 # 20	10 mm @ 125 mm
			Bot: 3 # 20	
Beam	1st–3rd	600 × 300	Top: 3 # 20	10 mm @ 200 mm
			Bot: 3 # 20	
Beam	3th–17th	550 × 250	Top: 2 # 25	10 mm @ 125 mm
			Bot: 2 # 25	
Column	Ground	600 × 450	16 # 32	8 mm @ 150 mm
Column	1st–17th	550 × 300	10 # 25	10 mm @ 125 mm

[a]*Note B* width, *H* height

Table 5 Details structural elements for Department of Survey and Mapping Malaysia (JUPEM)

Elements	Floor level	Size (mm) $H \times B^a$	No of bars and bar diameter	Hoops
Beam	Ground	450 × 300	Top: 5 # 25	5 mm @ 150 mm
			Bot: 3 # 20	
Beam	1st–9th	600 × 350	Top: 4 # 20	10 mm @ 125 mm
			Bot: 3 # 20	
Column	Ground–9th	600 × 450	16 # 32	8 mm @ 150 mm

[a]*Note B* width, *H* height

This includes the element size and reinforcement detailing for the beams and columns in each related building. Some of structural element data are referred from the structural drawings and some are estimated. The estimation of data for the structures which do not have complete drawings is done by referring from other available drawings which have similarity of structural design of the building.

British Standard [12] is referred to determine the loadings applied to the structure in the analysis steps to be applied as nodal loading in the modeling. The typical values of concrete compressive strength, f_c and reinforcing yield stress, f_y as 27.6 and 460 N/mm^2, respectively, were used in the analysis. The concrete modulus elasticity, E, as 25000 N/mm^2 and shear modulus, G, as 10000 N/mm^2 were taken in the design consideration. These values were applied for all of modal frames which were assumed designed for similar strength of materials and some data were referred from structural drawings.

There are two types of loads that are applied for each building in this study. Both of the loads are gravity and lateral loads. Gravity loads carried the dead load and life load for the structure itself. This loading represents dead and live loads. The earthquake load presents the lateral load. FORTRAN-based program developed by the University of Buffalo called IDARC2D was then used to carry out two-dimensional analyses on selected frames from each building. This program is able to compute what is known as "structural damage index" which can be defined as a way of quantifying numerically the seismic damage suffered by buildings. Details of structural members such as sizes of columns and beams, their steel reinforcements, and the cumulative column axial loads were taken from the results that were calculated by manual calculation and entered as input data in IDARC2D [13].

Nodal weights were calculated and were based on tributary areas to the node and frame in question. The models were analyzed using the modified design response spectra. The computed damage indices were tabulated for easy reference and comparison.

Once the damage index evaluation is desired, hysteretic behavior modeling of structural elements becomes important which is one of the most significant aspects of nonlinear structural analysis. Strength deterioration, strength degradation, non-symmetric response, slip-lock, and a tri-linear monotonic envelope are the parameters used in the hysteretic model. The hysteretic behavior of an element is traced by the model as it alters from one linear stage to another based on the history

Fig. 2 The hysteretic model: a Vertex Oriented hysteretic model has been used to model the elements [13]
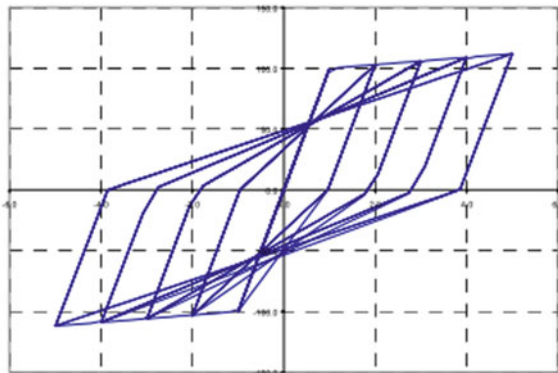
of deformations [13]. The effect of the hysteretic loops shape is shown in Fig. 2. A Vertex Oriented hysteretic model has been used to model the elements of the structures in this paper.

5 Result and Discussion

The performance level is a qualitative statement of damage. To be quantitatively defined, the performance level must be converted to the limiting values in the structural response parameter, which reflects the expected damage state. The plastic hinges due to structural local failures normally occur either at beam or column connections for moment resisting frame type of buildings.

5.1 Damage Pattern due to Plastic Hinge

The study focuses on damage level of the building and to know when the building starts yielding. Based on the result, for intensity 0.05 g, the damage index is equal to zero and based on Damage Levels as stipulated in ATC-13 [6] the damage level at minor represents free from damage. Tables 2, 3, and 4 show in detail the resultant of dynamic nonlinear analysis under various intensities as follows: 0.012, 0.05, 0.10, 0.15, and 0.2 g. These tables also show the damage index and time for each building. The building of Employees' Provident Fund (KWSP) had no damage when the 0.012 g intensity was applied to the building while the other buildings experienced damage. When the intensity 0.10 g was imposed to the buildings, all buildings were structurally collapsed.

In terms of damage pattern, the frame shows the locations of structural element where it started to yield, crack, or collapse. From the results, the modal frame experienced cracking and yielding at the beam elements at the early stage. The initial

Table 6 Summary of first yielding point and damage level for each building

Building name	Intensity (g)	Time (s)	Damage index (overall)	Damage level
Ampang Jaya Municipal Council (MPAJ)	0.012	11.66	0.023	Moderate
	0.05	2.375	0.072	Moderate
	0.10	2.225	1.000	Collapse
	0.15	2.125	1.000	Collapse
	0.20	0.105	1.000	Collapse
Employees' Provident Fund (KWSP)	0.012	0.000	0.000	None
	0.05	2.410	0.056	Moderate
	0.10	2.210	1.000	Collapse
	0.15	0.130	1.000	Collapse
	0.20	0.105	1.000	Collapse
Block F Public Work Department (JKR)	0.012	11.385	0.009	Minor
	0.05	2.400	0.054	Moderate
	0.10	2.250	1.000	Collapse
	0.15	0.130	1.000	Collapse
	0.20	0.105	1.000	Collapse
Department of Survey and Mapping Malaysia (JUPEM)	0.012	9.180	0.009	Minor
	0.05	2.940	0.380	Major
	0.10	2.300	1.000	Collapse
	0.15	0.140	1.000	Collapse
	0.20	0.115	1.000	Collapse

yield of the plastic hinge starts to develop at the beam in the first floor. Apart from the top floor, all beam ends act as plastic hinges, while only the columns show hinge behavior. The beams act as hinges earlier than columns, nearly forming an overall symmetrical beam hinge system. The structure performance measured by the quantitative damage index is more reliable than displacement-based design (Table 6).

5.2 Damage Analysis

The program developed by Kunnath et al. [5] is used in this study to provide a measure of the accumulated damage index sustained by the components of the building including the maximum-to-ultimate deformations ratio. Table 8 shows in detail the summary of overall damage index of the buildings. The overall damage index for the building which can be referred from the SEAOC damage level in Tables 1 and 7. The overall damage index for intensity 0.05 g categorized at minor level for which no damage occurred for Block K and Police Quarters. Block K experienced moderate (light) level that is no structural damage, some non-structural damage but at this intensity no structural element yielding for intensity 0.10, 0.15,

Table 7 The Structural Engineers Association of California (SEAOC) damage levels [6]

SEAOC EQ level	SEAOCdamage		ATC-13		
Minor	Without any damage	None		=	0
		Slight		<	0.01
Moderate	No structural damage, some non-structural damage	Light		≤	0.1
		Moderate		≤	0.3
Major	No collapse, some structural damage, non-structural damage considerable	Heavy		≤	0.6
		Major		<	1
Collapse	Collapse	Collapse		=	1

Table 8 Summary of first yielding point and damage level

No.	Building name	Overall structural damage index (g)				
		0.012	0.05	0.10	0.15	0.20
1.	Ampang Jaya Municipal Council (MPAJ)	0.023	0.072	1.000	1.000	1.000
2.	Employees' Provident Fund (KWSP)	0.000	0.056	1.000	1.000	1.000
3.	Block F (Public Work Department (JKR)	0.009	0.054	1.000	1.000	1.000
4.	Department of Survey and Mapping Malaysia (JUPEM)	0.009	0.380	1.000	1.000	1.000

and 0.20 g. The reinforced concrete frames completely collapsed in both Islamic Complex for 0.10 g intensity and Police Quarters for 0.15 g intensity applied.

6 Conclusion

It can be concluded that all buildings show different performance in terms of damage level when subjected to various earthquake intensities. The buildings analyzed, which were subjected to the Acheh earthquake ground motion, developed plastic hinge due to the earthquake intensity of 0.012 g for all buildings excluded building of Employees' Provident Fund (KWSP) which developed plastic hinge due to the earthquake intensity of 0.05 g and had damage indexes in the range 0.00 (no damage) to 1.0 (collapse). A greater damage index means that the members yield earlier and the plastic rotation is larger and vice versa. As for the result, the damage to columns is light, the damage level of most columns is "medium destruction," and the performance of the high-performance concrete is satisfactory. While the damage in the beams is much serious, the distribution of the damage index reflects the seismic design principle of "strong column, weak beam."

References

1. Li, G., Zhang, Y., and Li, H. *Seismic Damage Analysis of Reinforced Concrete Frame Using the Force Analogy Method*." J. Eng. Mech., 139(12), 1780–1789, 2013.
2. R. Moreno-Gonzalez & J. M. Bairan. *Seismic Damage Assessment for Waffled-Slabs Reinforced Concrete (RC) Buildings in Barcelona*, International Journal of Architectural Heritage: Conservation, Analysis, and Restoration, Volume 7, Issue 1, 2013
3. R. Ditommaso, M. Vona1, M. R. Gallipoli, and M. Mucciarelli. *Evaluation and considerations about fundamental periods of damaged reinforced concrete buildings*, Nat. Hazards Earth Syst. Sci., 13, 1903–1912, 2013.
4. Joel M. Barron and Mary Beth D. Hueste. *Diaphragm Effects in Rectangular Reinforced Concrete Buildings,* ACI Structural Journal: Technical Paper, September–October, Vol. 3, 89–98, 2004.
5. Kunnath, S. K., Reinhorn, A. M., and Lobo, R. F. *IDARC Version 3.0: A Program for the Inelastic Damage Analysis of Reinforced Concrete Structures*, Report No. NCEER-92-0022, National Center for Earthquake Engineering Research, State University of New York at Buffalo, 1992.
6. Surya Kumar V. Gunturi. *Building Specific Earthquake Damage Estimation*, Doctor of Philosophy Dissertation, Stanford University, San Francisco, 1992
7. R, Ismail, A, Adnan and A, Ibrahim. *Vulnerability of Public Buildings in Sabah Subjected to Earthquake by Finite Element Modeling*, The 2nd International Building Control Conference 2011, Procedia Engineering 20 (54–60), 2011.
8. Malaysia Meteorologi Department (MMD), Petaling Jaya, Selango.
9. R Ismail, NF Zamahidi. *An Evaluation of High-Rise Concrete Building Performance Under Low Intensity Earthquake Effects*, International Civil and Infrastructure Engineering Conference (InCIEC 2014), Springer Singapore, 79–86, 2015
10. R Ismail, H Mohd Saman, M Hassim. *Evaluation of Medium-Rise Reinforced Concrete Building Performance under Low Intensity Earthquake Effect*, Applied Mechanics and Materials, Vol 661, 106–110, 2014.
11. R Ismail, A Ibrahim, and A Adnan. *Effect of Input Variable for Neural Network Architecture in Prediction Building Damage Subjected to Earthquake*, International Civil and Infrastructure Engineering Conference (InCIEC 2013), Springer Singapore, 201–213, 2014
12. BS 6399:Part 1, Loading for Building, Part 1. Code of Practice for Dead and Imposed Loads. 1996.
13. Park, Y. J., Ang, A. H.-S., and Wen, Y. K. *Seismic Damage Analysis and Damage-Limiting design of R/C Buildings*, Civil Engineering Studies, Technical Report No. SRS 516, University of Illinois, Urbana, 1984.

Seismic Damage Analysis of Reinforced Concrete Frame of Public Buildings in Ipoh Subjected to Acheh Earthquake Event

Rozaina Ismail, Azmi Ibrahim and Azlan Adnan

Abstract This study addresses the vulnerability of public buildings in Malaysia subjected to earthquakes from Sumatra and Philippines. A case study that has been conducted on medium-rise reinforced concrete buildings which are mostly categorized as moment resisting frames. Block K (Federal Reserve Unit), Islamic Complex, and Police Quarters were chosen as main models for this study. The building was analyzed using Finite Element Modeling (FEM) under variety of earthquake intensities from Time History Analysis (THA) considering low to medium earthquake intensities. The yield point at beam-column connections was analyzed to determine the damage index and damage level of the building. The performance of critical frame reinforced concrete building when subjected to earthquake motion (Near source: Acheh) was addressed. The buildings evaluated were subjected to low-intensity earthquakes. There are different damage levels that affect the frames when different intensities are applied by looking at structural and non-structural damage. The level of the damage state (minor, moderate, major, collapse levels) has been defined as well. As a result, the high-rise building developed plastic hinge due to the earthquake intensity of 0.05 g and have damage indexes in the range 0.050 (light damage level) to 1.0 (collapse). A greater damage index means that the members yield earlier and the plastic rotation is larger and vice versa. As for the result, the damage to columns is light, the damage level of most columns is "medium destruction," and the performance of the high-performance concrete is satisfactory.

R. Ismail (✉)
Institute for Infrastructure Engineering and Sustainable Management (IIESM),
Faculty of Civil Engineering, UiTM, Shah Alam, Selangor, Malaysia
e-mail: rozaina_fka_uitm@yahoo.com

A. Ibrahim
Department of Structures and Material, Faculty of Civil Engineering,
UiTM, Shah Alam, Selangor, Malaysia

A. Adnan
Department of Structures and Material, Faculty of Civil Engineering,
UTM, Johor Bahru, Johor, Malaysia

1 Introduction

Tremors in Peninsular Malaysia and East Malaysia due to Sumatra and Philippine earthquakes have been reported several times. Engineers are concerned of the seismic vulnerability of public buildings due to lack of earthquake consideration in. Malaysia's building design procedure. Malaysia is located at the low-intensity earthquake region. There are major tectonic plates around Malaysia. Engineers should concern and consider about the earthquake impacts of buildings in Malaysian's building design procedure. According to Li et al. [1], the reinforced concrete frame has to meet the requirements of performance-based earthquake engineering, since the influence of damage should be considered when conducting a structural performance assessment.

Moreno-Gonzalez and Bairan [2] presents the performance of the building in low to moderate earthquake region. The results show that the buildings expected to have damages due to its poor expected performance and the seismic vulnerability study is very important to predict the damage of the buildings due to earthquake event. Ditommaso et al. [3] estimated the fundamental period of reinforced concrete buildings and damage of structural and non-structural elements.

Finite element modeling and analysis has been used extensively to solve the complicated structural problems involving nonlinear and dynamic problems. IDARC is used as the dynamic nonlinear analysis software to analyze the structures. Different intensities of earthquake load are applied to the structures to know the maximum allowable earthquake load intensities for the buildings. The overall vulnerability of the structures can be known from the damage indices [4, 5]. Due to the reflection and expectation of the damage state, the values and parameters should be measured quantitatively to assess the performance level. Table 1 shows the

Table 1 The Structural Engineers Association of California (SEAOC) damage levels [6]

SEAOC Earthquake level	SEAOC damage	ATC-13 damage factors (state)
Minor	Without any damage	D.F. = 0 (none)
		D.F. < 0.01 (slight)
Moderate	No structural damage, some non-structural damage	0.01 < D.F. ≤ 0.10 (light)
		0.01 < D.F. ≤ 0.30 (moderate)
Major	No collapse, some structural damage, non-structural damage considerable	0.30 < D.F. ≤ 0.60 (heavy)
		0.60 < D.F. < 1.0 (major)
Collapse	Collapse	D.F. = 1.0 (destroyed)

D.F. Damage factor = damage index

ATC-13 damage level [6] in [7] to define the damage state level which is adopted in this study.

2   Time History Analysis

The present work studies the intensities as reported by MMD [8]. The Sumatra–Andaman (Acheh Earthquake) time history record is shown in Fig. 1 with 5000 number of outputs within 0.02 time steps with the maximum acceleration of 0.012 g. The Acheh earthquake occurred in December 26, at Indian Ocean near Acheh with the magnitude 9.3 on Richter scale. The acceleration is simulated to four variations of earthquake intensities as follows: 0.05, 0.10, 0.15, and 0.2 g. This study used 5 % damped spectral acceleration as adopted in [7, 9–11].

3   Modeling Concept

Figure 2 shows the elevation view of the building for Block K (Federal Reserve Unit), Ipoh. The dimensions of three bay frames and four floor levels are 1@1.0 m and 5@3.2 m, respectively. The size of the beams and columns are 600 × 600 mm and 300 × 600 mm, respectively for all floor levels. The amount of the reinforcement in the frame element is 20Y32 for columns and 4Y25 at top as well as 3Y25 at bottom for beam element. The properties of materials are 2500 N/mm^2 (E_c), 460 N/mm^2 (f_y), 27.6 N/mm^2 (f_c), and 25 mm for cover (c).

British Standard [12] is referred to determine the loadings applied to the structure in the analysis steps to be applied as nodal loading in the modeling steps as shown in Fig. 4. FORTRAN-based program developed by the University of Buffalo called IDARC2D was then used to carry out two-dimensional analyses on selected frames from each building. This program is able to compute what is known as "structural damage index" which can be defined as a way of quantifying

Fig. 1 Time history record of Acheh Earthquake for peak ground acceleration 0.012 g (December 26, 2004) [8]
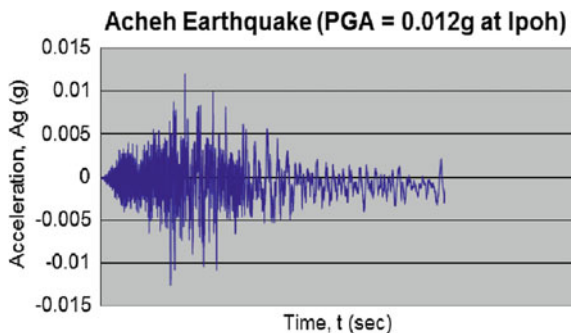
Fig. 2 The elevation view of
the building for Block K
(Federal Reserve Unit), Ipoh
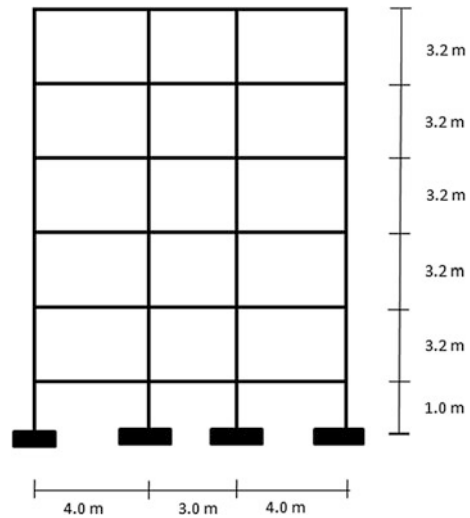
numerically the seismic damage suffered by buildings. Details of structural members such as sizes of columns and beams, their steel reinforcements and the cumulative column axial loads are taken from the results that are calculated manually and entered as input data in IDARC2D [13].

4 Result and Discussion

The plastic hinges due to structural local failures normally occur either at beam or column connections for moment resisting frame type of buildings. Figures 3, 4, and 5 show the development of plastic hinge for the building with earthquake intensities varying from 0.05 to 0.02 g. At 0.20 g, the plastic hinge initially formed on the beam at the first floor and above. These represent the sequences of damage state of frames under earthquake loading.

4.1 Damage Pattern due to Plastic Hinge

The performance level is a qualitative statement of damage. To be quantitatively defined, the performance level must be converted to the limiting values in the structural response parameter, which reflect the expected damage state. Based on the result, for intensity 0.05 g, the damage index is equal to zero and based on Damage Levels as stipulated in ATC-13 [6] the damage level at minor means free from damage. Tables 2, 3 and 4 show in detail the resultant of dynamic nonlinear
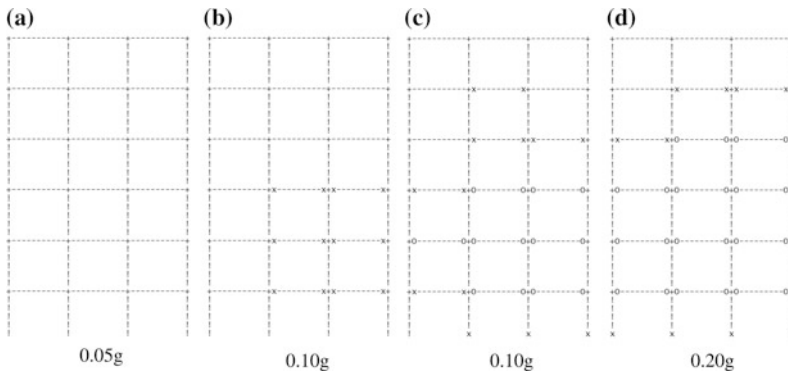
Fig. 3 Damage state frame under 0.05, 0.10, 0.15, and 0.20 g earthquake intensity for Block K (Federal Reserve Unit), Ipoh
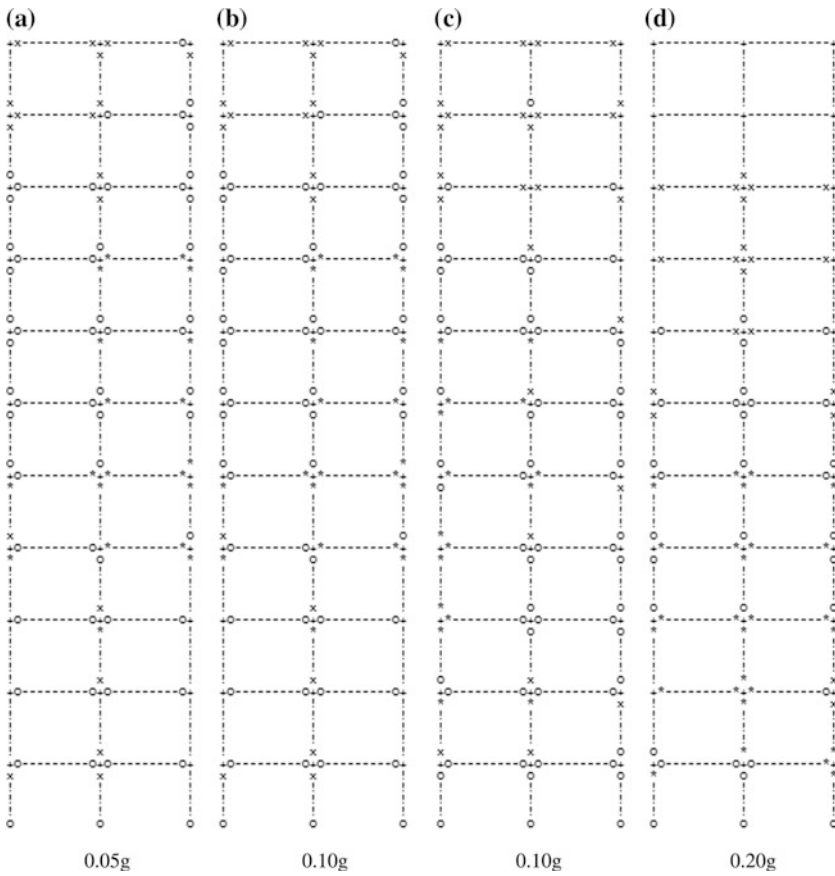
Fig. 4 Damage state frame under 0.05, 0.10, 0.15, and 0.20 g earthquake intensity for Islamic Complex, Ipoh
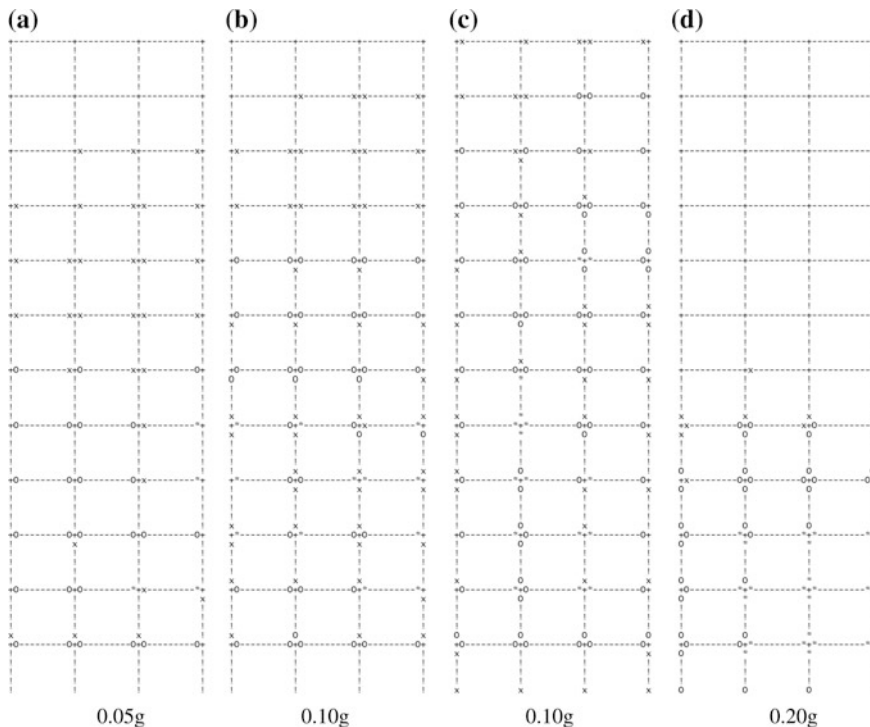
Fig. 5 Damage state frame under 0.05, 0.10, 0.15, and 0.20 g earthquake intensity for Police Quarters, Ipoh

Table 2 Summary of first yielding point and damage level for Block K (Federal Reserve Unit), Ipoh

Intensity (g)	Floor level	Location	Time (s)	Damage index (overall)	Damage level
0.05	–	–	–	0.000	None
0.10	–	–	–	0.019	Moderate
0.15	1	Beam	3.02	0.032	Moderate
0.20	1	Beam	0.12	0.017	Moderate

Table 3 Summary of first yielding point and damage level for Islamic Complex, Ipoh

Intensity (g)	Floor level	Location	Time (s)	Damage index (overall)	Damage level
0.05	1	Beam	2.59	0.050	Moderate
0.10	1	Beam	1.99	1.000	Collapse
0.15	1	Beam	0.15	1.000	Collapse
0.20	1	Beam	0.12	1.000	Collapse

Table 4 Summary of first yielding point and damage level for Police Quarters, Ipoh

Intensity (g)	Floor level	Location	Time (s)	Damage index (overall)	Damage level
0.05	2	Beam	5.45	0.137	Moderate
0.10	2	Beam	2.60	0.387	Major
0.15	2	Beam	0.21	1.000	Collapse
0.20	2	Beam	0.18	1.000	Collapse

analysis under various intensities as follows: 0.05, 0.10, 0.15, and 0.2 g. These tables also show the location and time for each yielding point. Blok K has no damage after 0.05 g intensity was imposed on it. This building started to experience 0.019 up to 0.017 damage index from 0.10 to 0.20 g applied. This value indicates that the structure is at the moderate damage criteria where there is light damage to the structure includes no structural damage but possibilities for some non-structural damage. However, Islamic Complex and Police Quarters experienced as moderate level as 0.05 g intensity applied. When the intensity 0.15 g was imposed on the buildings, both buildings were structurally collapsed.

In terms of damage pattern, the frame shows the locations of element structural where it started to yield, crack, or collapse. From the results, the modal frame experienced cracking and yielding at the beam elements at the early stage. The 'x' symbol shows the occurrence of crack for concrete frame, the 'o' symbol shows the yield of plastic hinge has developed and the '*' symbol shows the local failure which exceed criteria. Block K has experienced no damage at the early stage which 0.05 g intensity applied. For intensity 0.05 the damage pattern show the frame of Islamic Complex and Police Quarters has started experienced yielding and cracking. For example the initial yield of the plastic hinge starts to develop at the beam in the first floor. Apart from the top floor, all beam ends act as plastic hinges, while only the columns show hinge behavior. The beams act as hinges earlier than columns, nearly forming an overall symmetrical beam hinge system. The structure performance measured by the quantitative damage index is more reliable than displacement-based design.

4.2 Damage Analysis

The ATC-13 damage level [6] in [7, 9, 10] was adopted in defining the damage state level by referring to Table 6. The program developed by Park et al. [13] is used in this study to provide a measure of the accumulated damage index sustained by the components of the building including the maximum-to-ultimate deformations ratio. Table 5 shows in detail the summary of overall damage index of the buildings. The overall damage index for the building which can be referred from the SEAOC damage level in Tables 1 and 4. The overall damage index for the intensity 0.05 g categorized as minor level with no damage in Block K and Police Quarters.

Table 5 Summary of first yielding point and damage level

No.	Building name	Type of building	Overall Structural Damage Index (g)			
			0.05	*0.10*	*0.15*	*0.20*
1.	Block K	Medium-Rise	0.000	0.019	0.032	0.071
2.	Islamic Complex	High-Rise	0.050	1.000	1.000	1.000
3.	Police Quarters	High-Rise	0.137	0.387	1.000	1.000

Table 6 The Structural Engineers Association of California (SEAOC) Damage levels [6]

SEAOC EQ Level	SEAOC Damage	ATC-13		
Minor	Without any Damage	None	=	0
		Slight	<	0.01
Moderate	No Structural damage, some non-structural damage	Light	≤	0.1
		Moderate	≤	0.3
Major	No collapse, some structural damage, non-structural damage considerable	Heavy	≤	0.6
		Major	<	1
Collapse	Collapse	Collapse	=	1

Block K experienced moderate (light) level that means no structural damage, some non-structural damage but at this intensity no structural element yielding for intensity 0.10, 0.15, and 0.20 g. The reinforced concrete frames were completely collapsed in both Islamic Complex for 0.10 g intensity and Police Quarters for 0.15 g intensity applied.

5 Conclusion

It can be concluded that all buildings show different performance in terms of damage level when subjected to various earthquake intensities. The buildings analyzed, which were subjected to the Acheh earthquake ground motion, developed plastic hinge due to the earthquake intensity of 0.15 g for medium-rise building and had damage indexes of 0.032 (light damage level). Meanwhile the high-rise building developed plastic hinge due to the earthquake intensity of 0.05 g and had damage indexes in the range 0.050 (light damage level) to 1.0 (collapse). A greater damage index means that the members yield earlier and the plastic rotation is larger and vice versa. As for the result, the damage to columns is light, the damage level of most

columns is "medium destruction," and the performance of the high-performance concrete is satisfactory. While the damage in the beams is much serious, the distribution of the damage index reflects the seismic design principle of "strong column, weak beam."

References

1. Li, G., Zhang, Y., and Li, H. *Seismic Damage Analysis of Reinforced Concrete Frame Using the Force Analogy Method*." J. Eng. Mech., 139(12), 1780–1789, 2013.
2. R. Moreno-Gonzalez & J. M. Bairan., *Seismic Damage Assessment for Waffled-Slabs Reinforced Concrete (RC) Buildings in Barcelona*, International Journal of Architectural Heritage: Conservation, Analysis, and Restoration, Volume 7, Issue 1, 2013
3. R. Ditommaso, M. Vona1, M. R. Gallipoli, and M. Mucciarelli. *Evaluation and considerations about fundamental periods of damaged reinforced concrete buildings*, Nat. Hazards Earth Syst. Sci., 13, 1903–1912, 2013.
4. Joel M. Barron and Mary Beth D. Hueste. *Diaphragm Effects in Rectangular Reinforced Concrete Buildings,* ACI Structural Journal: Technical Paper, September–October, Vol. 3, 89–98, 2004.
5. Kunnath, S. K., Reinhorn, A. M., and Lobo, R. F. *IDARC Version 3.0: A Program for the Inelastic Damage Analysis of Reinforced Concrete Structures*, Report No. NCEER-92-0022, National Center for Earthquake Engineering Research, State University of New York at Buffalo, 1992.
6. Surya Kumar V. Gunturi. *Building Specific Earthquake Damage Estimation*, Doctor of Philosophy Dissertation, Stanford University, San Francisco, 1992
7. R, Ismail, A, Adnan and A, Ibrahim. *Vulnerability of Public Buildings in Sabah Subjected to Earthquake by Finite Element Modeling*, The 2nd International Building Control Conference 2011, Procedia Engineering 20 (54–60), 2011.
8. Malaysia Meteorologi Department (MMD), Petaling Jaya, Selango.
9. R Ismail, NF Zamahidi. *An Evaluation of High-Rise Concrete Building Performance Under Low Intensity Earthquake Effects*, International Civil and Infrastructure Engineering Conference (InCIEC 2014), Springer Singapore, 79–86, 2015
10. R Ismail, H Mohd Saman, M Hassim. *Evaluation of Medium-Rise Reinforced Concrete Building Performance under Low Intensity Earthquake Effect*, Applied Mechanics and Materials, Vol 661, 106–110, 2014.
11. R Ismail, A Ibrahim, and A Adnan. *Effect of Input Variable for Neural Network Architecture in Prediction Building Damage Subjected to Earthquake*, International Civil and Infrastructure Engineering Conference (InCIEC 2013), Springer Singapore, 201–213, 2014
12. BS 6399: Part 1, Loading for Building, Part 1. Code of Practice for Dead and Imposed Loads. 1996.
13. Park, Y. J., Ang, A. H.-S., and Wen, Y. K. *Seismic Damage Analysis and Damage-Limiting design of R/C Buildings*, Civil Engineering Studies, Technical Report No. SRS 516, University of Illinois, Urbana, 1984.

Seismic Site Classification of JKR Bridge at Sungai Sepang Using Multichannel Analysis of Surface Wave (MASW)

Rozaina Ismail, Azmi Ibrahim, Hanizah Ab Hamid, Taksiah A. Majid and Azlan Adnan

Abstract In seismic engineering, the dynamic property of the soil is one of the most important aspects in ground response analysis. Dynamic property is significantly affected by local soil deposits. Shear wave velocity (V_s) of soil is one of the main parameters in determining the amplification factor on ground surface. This study aims to determine the shear wave velocity profile of the bridge at Sungai Sepang by using multichannel analysis of surface wave (MASW) method. All the acquired raw data from the MASW field test were analyzed and it can be summarized to three major steps: First, filter the wiggle plot to the analyzable range of frequency of Rayleigh wave; second, develop the dispersion curves of Rayleigh wave phase velocity and; third, inversion of dispersion curve to obtain the V_s profiles. The filter and the development of dispersion curve processes were carried out by using Pickwin softwis (SeisImager/SW). Results show that the soil for bridge at Sungai Sepang is having a very low V_{s30}, which is 143.3 and 137.2 m/s, respectively. The soils are classified as Class E which can be considered soft soil according to Uniform Building Code (UBC). Based on the N-SPT value by using empirical formula, the value of V_{s30} ranges from 101.22 to 151.87 m/s by using different empirical formula. It can be concluded that the value of V_{s30} for bridge by using MASW is accepted since the value is near to the value of numerical equation from N-SPT value based on borehole data at Sungai Sepang site.

R. Ismail (✉)
Institute for Infrastructure Engineering and Sustainable Management (IIESM),
Faculty of Civil Engineering, UiTM, Shah Alam, Selangor, Malaysia
e-mail: rozaina_fka_uitm@yahoo.com

A. Ibrahim · H.A. Hamid
Department of Structures and Material, Faculty of Civil Engineering,
UiTM, Shah Alam, Selangor, Malaysia

T.A. Majid
Disaster Research Nexus, School of Civil Engineering,
USM, Gelugor, Penang, Malaysia

A. Adnan
Department of Structures and Material, Faculty of Civil Engineering,
UTM, Johor Bahru, Johor, Malaysia

1   Introduction

In seismic engineering, the most important aspect is to determine the dynamic properties of the subsurface geo-material structure.

The dynamic soil properties significantly influence the seismic response and performance of the structure above such as fundamental period and seismic demand and capacity. However, lacking of understanding of the geological information of the site often resorted to structure and environmental failures. Shear wave velocity (V_s) has become one of the most important properties in seismic site characterization from which in situ dynamic shear modulus of soil is determined due to its direct relationship with shear modulus via the soil mass density as well as its relative ease of measurement [1, 2]. The dynamic shear modulus (G_{max}) can be determined by the following expression:

$$G_{max} = \rho \cdot V_s^2 \tag{1}$$

According to Luna and Jadi [3], the measured V_s is generally considered as the most reliable parameter in obtaining the G_{max} for a soil deposit. The shear modulus is used to perform more advanced soil modelling and dynamic response of the soil–structure interactions. Shear modulus at low strain levels, γ ($<10^{-4\%}$) as measured by geophysical techniques will provide the elastic parameter for foundation analysis or earthquake engineering study. Besides, shallow V_s has long been recognized as the most important parameter in variable ground motion amplification and seismic site response for sedimentary formation [4]. Kuo et al. [5] claimed that determination of shear wave velocity is the key factor in theoretical simulation, strong ground motion prediction as well as amplification behaviour of site. Site characterization in calculating seismic hazards is usually based on the near-surface V_s. Since the amplitude of the shear wave is responsible in most damage in earthquake events, a lot of the researches have emphasized in estimating subsurface shear wave velocity rather than other geotechnical parameters.

The site amplification ratio and fundamental period as the function of V_s may give a significant impact on the structures above the soil. The softer soil beneath the structures generally may induce higher amplification to the seismic waves and resulted in severe damage to the structures during earthquakes. While the structure's fundamental period, T_1 must be kept away from the site period to avoid the resonance effect. In engineering practices, generally the structures are designed as fixed foundation with the assumption of fixity of the basement. However, in reality, the deformability of the soils beneath the structures may significantly magnify the intensity of the seismic demand of the structures.

Table 1 UBC site classification

Site classification	Soil description	V_{s30} (m/s)
A	Hard rock	>1500
B	Rock	760–1500
C	Very dense sand or soft rock	360–760
D	Stiff soil	180–360
E	Soft soil	<180

In most of the applications, average V_s from the surface to the depth of 30 m, V_{s30} is used for site classification. V_{s30} is commonly adopted by competent building codes to classify the sites for earthquake-resistant design of structures and as a predictor of earthquake ground motion amplification and potential hazard for soil [6]. The V_{s30} for soil can be determined by the following expression:

$$V_{s30} = \frac{30}{\sum_{i=1}^{n}\left(\frac{Z_i}{V_{si}}\right)} Z \tag{2}$$

where Z_i is the thickness of the ith layer and V_{si} is the V_s of the ith layer. Site classification plays an important role in the seismic design for the building structures. Difference in site classifications will give different elastic response spectrums. The higher elastic response spectrum for softer soil (Class D) induces higher seismic demand compare to stiffer soil (Class B) and hence larger seismic load in structure design. The site classification or soil categorization using V_{s30} is well documented in Uniform Building Code, UBC (1997) as shown in Table 1.

2   Field Test Set up

The field configuration of MASW is illustrated in Fig. 1. MASW test for site was carried out by employed GEOMETRICS Geode Ultra-Light Exploration Seismograph, a 24-channel seismograph with single geode operating software (SGOS) connected to the controller (a heavy-duty laptop). Total of 24 units of 4.5 Hz natural frequency of vertical geophones was used to detect the surface waves. Geophones were deployed linearly with the interval 0.5–2.5 m [7]. An active source was created by using an 8 kg sledgehammer vertical hit on a striker plate (Fig. 1). The nearest source to geophone offsets is in the range 5–20 m to meet the requirement of different types of soil hardness suggested by Xu et al. [8] also been adopted by Ismail et al. [9] as shown in Fig. 1. Table 2 shows the suggested offset corresponding to shallow shear wave velocity. The data acquisition parameters for MASW test is summarized in Table 3. The test was repeated with applying
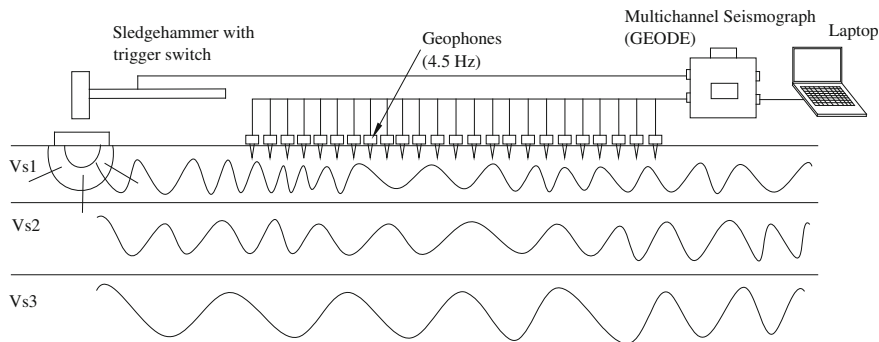
Fig. 1 MASW test field configuration

Table 2 Suggested offsets corresponding to shallow shear wave velocity

Material type	Shear wave velocity, V_s (m/s)	Offset (m)
Very soft	$V_s < 100$	1–5
Soft	$100 < V_s < 300$	5–10
Hard	$300 < Vs < 500$	10–20
Very hard	$V_s > 500$	20–40

Table 3 Data acquisition parameters

Parameter	Description
Geophone interval	0.5–2.5 m
Nearest offset	5, 10, 15 and 20 m
Sampling rate	0.125 m/s
Record length	1 s
Receiver/geophone	4.5 Hz vertical
Source	8 kg sledgehammer
Number of stacking	5

the active source at the front, back (nearest offsets) of the spread to obtain the consistency of the waves signal. Two set of data was collected for each nearest offset as the backup data for the test.

3 Data Acquisition and Procedures

All the acquired raw data from the MASW field test were analyzed and it can be summarized to three major steps: i. to filter the wiggle plot to the analyzable range of frequency of Rayleigh wave; ii. to develop the dispersion curves of Rayleigh wave phase velocity and; iii inversion of dispersion curve to obtain the V_s profiles.

(a)

(b)

(c)

(d)
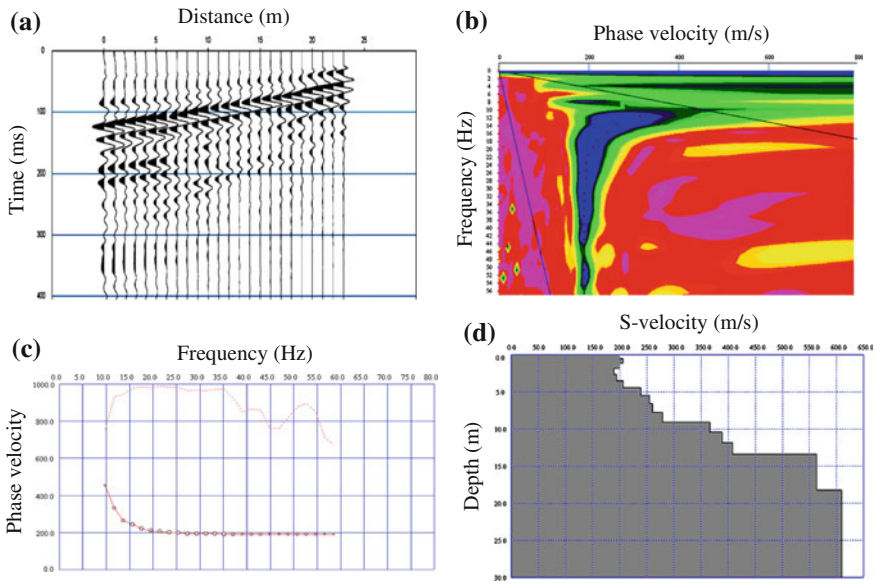
Fig. 2 Data acquisition and procession

The filter and the development of dispersion curve processes were carried out by using Pickwin software (SeisImager/SW). The raw wiggle plot obtained from the field test was filtered into the frequency range between 4 and 85 Hz to reduce the random noise effect and the interference of other seismic waves as in Fig. 2a to ensure that surface waves are used in the generating of dispersion curve. The amplitude of body wave and higher mode of Rayleigh wave may dominate over the fundamental mode at higher frequencies range if the noise recorded during field test is not well filtered. Only the fundamental mode of Rayleigh wave which between the analyzable frequencies range from 3 to 85 Hz were considered [10] as shown in Fig. 2b to generate dispersion curve with signal-to-noise ratio (S/N) (Fig. 2c). WaveEq software was employed to develop the one-dimensional V_s profile through inversion analysis of the dispersion curve as shown in Fig. 2d.

4 Shear Wave Velocity Distribution

The dispersion curves generated for L1 and L2 are possess certain degree of noise and higher mode of surface waves. By comparing the dispersion curves at various offsets (5, 10, and 15 m), the final picked dispersion curves and shear wave velocity profiles for L1 and L2 are shown in Figs. 3 and 4, respectively. Similar to Sungai
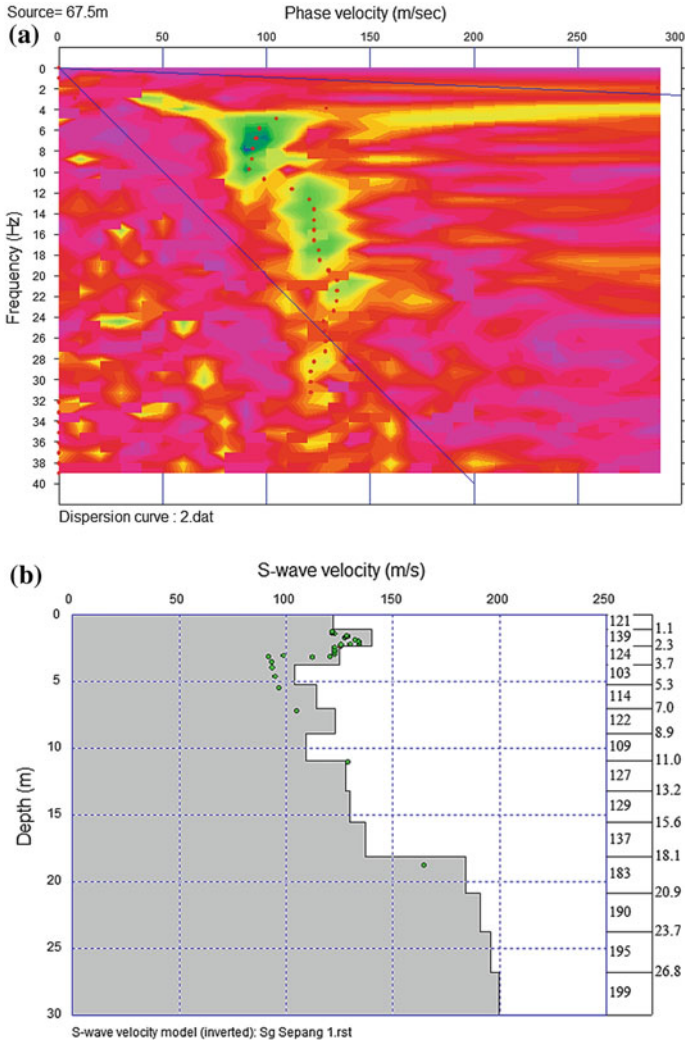
Fig. 3 Dispersion curve (**a**) and V_s profile (**b**) for L1

Sepang Kecil site, both sites possess very low shear wave velocity profiles ranging from 103 to 199 m/s various from the soil surface to 30 m depth. The low shear wave velocity may be associated to the thick layer of soft alluvial deposit near the river bank. The average shear wave velocity at 30 m depth, V_{s30} for L1 and L2 at Sungai Sepang are 143.3 and 137.2 m/s, respectively, and hence classified as Class E according to UBC soil classification (Table 2). The V_{s30} for both sites are summarized in Table 4. Basically, low V_{s30} (Class E) or soft unconsolidated sedimentary formation have higher amplification on the ground motion than stiffer soils (Class B or higher) [11]. This especially when earthquake wave travels from a
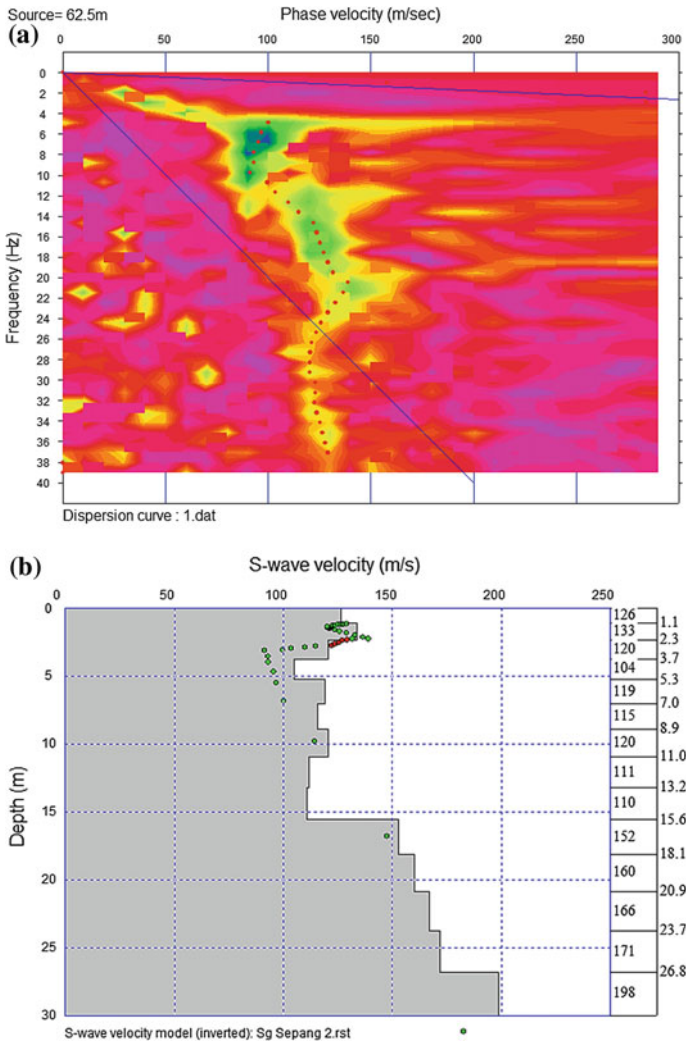
Fig. 4 Dispersion curve (**a**) and V_s profile (**b**) for L2

Table 4 Summary of V_{s30} and site classification for sites

Site	V_{s30} (m/s)	UBC site classification
L1	143.3	Class E
L2	137.2	Class E

high (consolidated soil) to low velocity medium (unconsolidated soil), a velocity decrease is observed. A part of the energy is transformed at the media boundary and leads to an amplification of the wave amplitudes due to energy conservation.

5   Summary

In conclusion, this MASW surveys were carried out on the both side piers of JKR's bridge (FT/005/344/50) crossing the Sungai Sepang. L1 and L2 sites shows that the site having a very low V_{s30}, which is 143.3 and 137.2 m/s, respectively. As a result for the site, the ground soils are classified as Class E which can be considered soft soil according to Uniform Building Code (UBC). Based on the N-SPT value by using empirical formula, the value of V_{s30} is ranging from 101.22 to 151.87 m/s by using a different empirical formula. It can be concluded that the value of V_{s30} for bridge by using MASW is accepted since the value is near to the value of numerical equation from N-SPT value based on borehole data at Sungai Sepang site.

References

1. Boore, D. M. 2006. Determining subsurface shear-wave velocities: a review. *Third International Symposium on the Effects of Surface Geology on Seismic Motion.* Grenoble, France.
2. Vera-Grunauer, X., Bray, J., Pestana, J., Kayen, R., Tandazo, E., Ramirez, J., Vera-Grunauer, J. & Mera-Ortiz, W. Site Characterization and Seismic Zonation of Guayaquil City, Ecuador. 8th U.S. National Conference on Earthquake Engineering, 2006 San Francisco, California, USA. Paper No. 1467.
3. Luna, R. and Jadi, H. Determination of dynamic soil properties using geophysical methods. First International Conference on the Application of Geophysical and NDT Methodologies to Transportation Facilities and Infrastructure, 2000 St. Louis, MO. pp. 1–15.
4. Luo, Y., Xia, J., Liu, J., Xu, Y. & Liu, Q. 2009. Research on the middle-of-receiver-spread assumption of the MASW method. *Soil Dynamics and Earthquake Engineering,* 29, 71–79.
5. Kuo, C. H., Cheng, D. S., Hsieh, H. H., Chang, T. M., Chiang, H. J., Lin, C. M. & Wen, K. L. 2009. Comparison of three different methods in investigating shallow shear-wave velocity structures in Ilan, Taiwan. *Soil Dynamics and Earthquake Engineering,* 29, 133–143.
6. Scott, J. B., Rasmussen, T., Luke, B., Taylor, W. J., Wagoner, J. L., Smith, S. B. & Louie, J. N. 2006. Shallow Shear Velocity and Seismic Microzonation of the Urban Las Vegas, Nevada, Basin. *Bulletin of the Seismological Society of America,* 96, 1068–1077.
7. Maheswari, R. U., Boominathan, A. & Dodagoudar, G. R. 2010b. Use of surface waves in statistical correlations of shear wave velocity and penetration resistance of Chennai soils. *Geotech. Geol. Eng.,* 28, 119–137.
8. Xu, Y., Xia, J. & Miller, R. D. 2006. Quantitative estimation of minimum offset for multichannel surface-wave survey with actively exciting source. *J. Appl. Geophys.,* 59, 117–125.
9. R Ismail, A Ibrahim, T. A Majid. 2015. Shear Wave Velocity Profile at the Kangkar Merlimau Bridge by Using Multi-Channel Analysis of Surface Wave (MASW), 24th Malaysian Science and Technology Congress 2015.

10. Anbazhagan, P., Kumar, A. & Sitharam, T. G. 2013. Seismic site classification and correlation between standard penetration test N value and shear wave velocity for Lucknow City in Indo-Gangetic Basin. *Pure Appl. Geophys.,* 170, 299–318.

11. Mahajan, A. K. 2009. NEHRP soil classification and estimation of 1-D site effect of Dehradun fan deposits using shear wave velocity. *Eng. Geol.,* 104, 232–240.

Analysis of Multi-column Pier of Bridge Using STAAD.Pro Under Static and Dynamic Loading

N.H. Hamid, M.S. Jaafar and N.S.U. Othman

Abstract Bridges in Malaysia are usually designed under static loading. Some major cities in Malaysia had experienced earthquake excitation or ground motion upon devastating tsunami and earthquake event held in Acheh back in 2004. Performing simple harmonic motion analysis for the single degree of freedom (SDOF) bridge structure under free vibration without damping using STAAD.Pro is a new adaptive study. The model of the bridge had modified specifications (from existing bridge in Jeli, Kelantan) suitable for dynamic analysis assignment. Commenced with the validation of the static loading for the modified prototype bridge pier structure using mathematical calculation, the comparison shown between analytical and theoretical was almost 0 %. Thus in dynamic analysis, two parameters are verified and validated using theories and calculation, which are maximum lateral displacement and Rayleigh frequency under six various percentages of drift. Numerical results indicate excellent accuracy when the percentage difference between analytical and numerical for maximum lateral displacement and Rayleigh frequency was only 4.705 and 2.18 %, respectively. It has a good accuracy and is acceptable to be used and compared in laboratory experiment of the same specimen for continuity of the study. Both static and dynamic analyses were successfully verified and validated. In supplementary, the free vibration without damping system analysis produces more information and relevant data that merely

N.H. Hamid (✉) · M.S. Jaafar (✉) · N.S.U. Othman (✉)
Faculty of Civil Engineering, Universiti Teknologi MARA,
40450 Shah Alam, Selangor, Malaysia
e-mail: norha454@salam.uitm.edu.my

M.S. Jaafar
e-mail: msjayie@yahoo.com

N.S.U. Othman
e-mail: amira_maiza@yahoo.com

could be used in researching the performance of the bridge structure under dynamic responses.

Keywords Bridge · Seismic · Rocking pier · Dynamic loading and analysis

1   Introduction

The huge earthquake excitation from neighboring, such as Banda Acheh, Sumatera could be felt in Malaysia is considered as long-distant earthquake excitations can cause damage to buildings and bridges. Second Penang Bridge which connects Batu Kawan in mainland and Batu Maung in the Island and spans about 24 km across the sea is the longest seismic design bridge in the world. Most of the mega project of bridges in Malaysia has induced the seismic loading into their design calculation, but what about the bridge that was constructed earlier in accordance to British Standard? Modeling of the prototype building is the best approach to be conducted using the existing bridge or even to every new design of bridges in a future. The main focus of this study is to look into the bridge bents and allowable displacements. How it moves and displaced during earthquake event should be investigated. The ability to design and use structural software to model the sub-assemblage of bridge pier under earthquake loading is important examine the seismic performance. Though seismic analyses can be done using modeling method for bridges are not much compared to buildings, the end results obtained showed that bridges behave in an interesting way that illustrates the mode of shape and damages of the bridge undergone some deformation.

This study is taking a wise step in conducting modeling analysis using STAAD. Pro [1] to a modified prototype of multi-column pier of unskewed bridge under static and dynamic load. The modification was made to the length, width, type of beam, and number of columns at pier from the original bridge. An analysis of undamped free vibration was applied to the model as the model was constructed and defined as single degree of freedom (SDOF). The intended objective needed to be achieved are (i) to model the modified bridge pier using STAAD.Pro, (ii) to perform static and dynamic analysis using STAAD.Pro and (iii) to validate each analysis between mathematical modeling and numerical calculation. The dimension of the modified prototype of bridge pier in cross-sectional view is as shown in Fig. 1 and the model properties are as shown in Table 1. It is to deliver a performance result of the pier, such as the lateral displacements of the bridge deck. The validation value of static and dynamic (seismic analysis) between analytical modeling and theoretically were obtained and discussed.
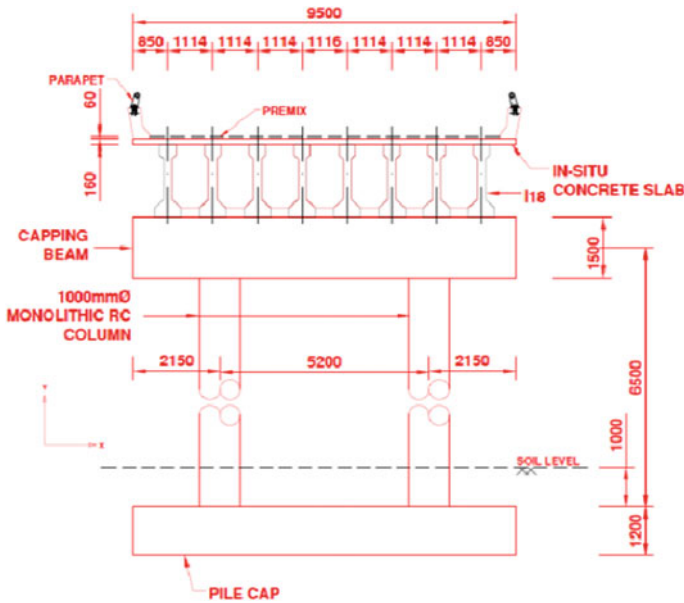
Fig. 1 Cross-sectional view of the bridge model

Table 1 Modified bridge prototype material properties

Item	Dimension			Unit weight (kN/m³)
	Thickness (mm)	Length (mm)	Cross-section area (m²)	
Pre mix	60	–	–	23.5
In situ slab	160	–	–	25
118 precast beam	–	18,800	0.598475	25
Parapet	–	18,800	0.185	25
Capping beam	1600	9500	2.4	25
Diaphragm	300	–	1.237	25
In situ column	1000	5750	0.785	25

2 Literature Review

It has been used widely to study the performance and the behavior of a structure under earthquake loading. In this study, the Time History Analysis was done by defining the acceleration with time function. Six predetermined bridge drift were calculated in order to obtain the amplitude (*A*) of the function. Different software might have different interface in data input, moreover the concept remains similar. In most of the THA done to structures, especially bridges, SAP2000 is frequently

used software, instead of STAAD.Pro. In this study, STAAD.Pro was used in conducting free vibration of undamped structure for multi-column pier of unskewed bridge. Though, previous researchers had done several works on bridge analysis under dynamic loading with various types of software and approach and also the purposes.

2.1 Dynamic Analysis on Skew Bridge

The direction of the bridge with the underneath traffic flow or river flow or even railway path is divided into two, whether it is skew (not perpendicular to the underneath flow) or unskewed (perpendicular or parallel to the underneath direction). Several studies had been performed for skew bridge under dynamic impact or loads. The bridge over the Yarriambiack Creek at Warracknabeal Victoria in Australia was tested under dynamic loading both in computer modeling and experimentally with 30° of skew angle [2]. The shaker (the actuator) for creating dynamic motion was positioned at two salient points on the bridge model (point A and point B) as shown in Fig. 2.

The model is tested using swept Sine Wave (SSW) displacement/forcing function with range of frequency between 0.5 to 50 Hz with maximum double amplitude of 80 kN excitation. The comparison between experimental and numerical was made for the natural frequencies of the model for both positions A and B. It came out acceptable between numerical and experimental results as close as 5 % in the percentage difference. Hence, results from experiment depicted that the optimal model fitting was done in the range of 10–30 Hz as it was already classified as outside of the range. It is rare to find a great condition of bridge construction in avoiding skew of the bridge. The skew angle could lead to the financial support of the whole bridge project. Most of the time, getting unskewed bridge is almost possible. But the skew angle can actually lessen the moment of the bridge pier and also the moments and displacement at the center span section [3]. The multi-span box girder bridge was analyzed under static loading with various skew angles being

Fig. 2 The plan view of Yarriambiack Creek Bridge test span depicting accelerometer grid
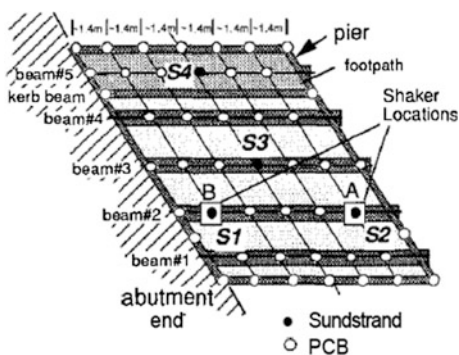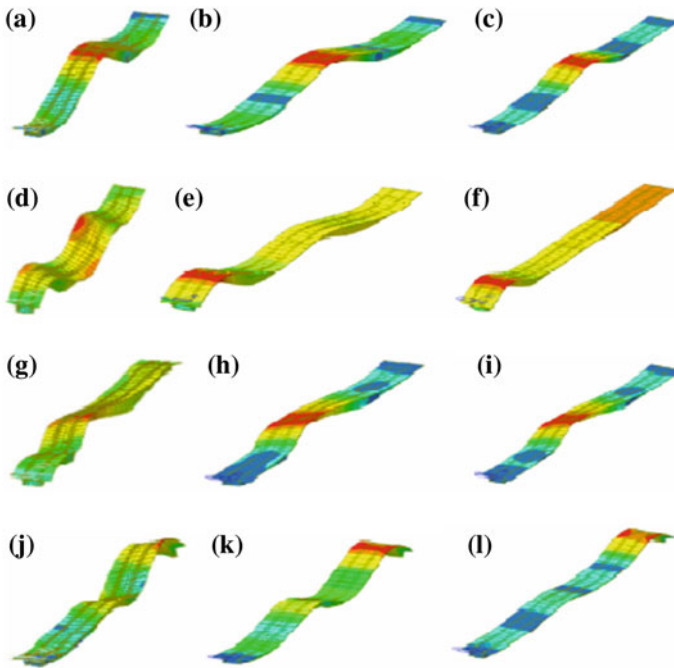
Fig. 3 Calculated mode shapes comparison of orthogonal double bearing, skewed bearing and orthogonal single bearing

assigned to the bridge model. The mode shapes for three type of bearing which are orthogonal double bearing (ODB), skewed bearing (SB), and orthogonal single bearing (OSB) as shown in Fig. 3. It shows that different skews and support conditions give minimal effect on the first mode shape of the model bridge. Increasing the skew apparently increases the first modal frequency, but no obvious trend for higher modes. It appears that with increasing the skew angle increases the apparent stiffness relative to mass.

2.2 Dynamic Analysis on Shape of the Bridge Deck

The shape of the bridge deck reacts differently when assigned to dynamic loading. Three different span of multi-span concrete bridge was tested using finite element method (FEM). The selected spans were 16-32-16 (64 m), 20-32-20 (72 m) and 20-40-20 (80 m) [4]. The cross sections of the studied bridge were T section, I section, and Box section with the option under skew angle of 0° and 30°. In order to obtain the frequencies at different node positions, considered speed is in the range of 30, 45, 60 kmph, 90–120 kph. A Laplace transform solution was performed for dynamic load factor (DLF). The observation is discussed and obviously, with the
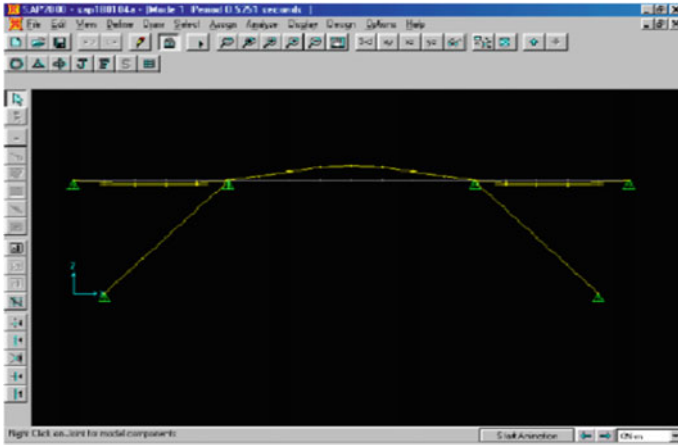
Fig. 4 Free vibration of the bridge in fundamental mode

increase of speed and span, the DLF also increases, while respond to the various section of the bridge, they were no appreciable changes. The DLF values also have no significant effect with the skew angle of the bridge (0° and 30°). From the free vibration of the bridge in fundamental mode, the largest DLF occurred at center of the mid span as shown in Fig. 4.

2.3 Free Vibration Without Damping

The earthquake excitation and bridge responses is subjected to earthquake ground motion in the form of ground acceleration or Peak Ground Acceleration, (PGA), denoted as Üg(t) is best explained as SDOF model of a bridge structure. Figure 5 shows a part of the longitudinal section of unskewed bridge. A simplified SDOF
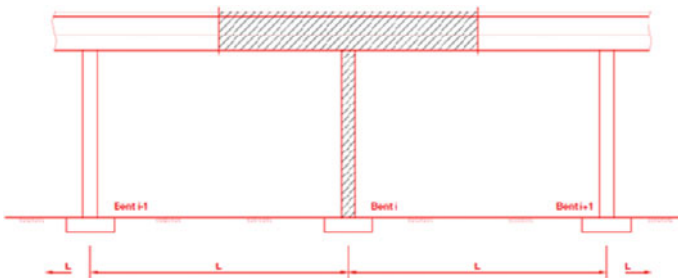
Fig. 5 Longitudinal section of unskewed bridge

model of a single column bent bridge under transverse earthquake ground acceleration input can provide similarity or approximation to the true seismic response of the bridge prototype as long as the bridge is unskewed and having constant span and equal heights of piers [5].

3 Methodology

3.1 Static Modeling and Analysis

In static modeling and analysis using STAAD.Pro, the material properties of the modified prototype bridge are as shown in Table 1. The concrete compressive strength is 40 N/mm^2 and Young Modulus of 35,000 N/mm^2. The dead loads for the analysis were from the self-weight of the beams, diaphragms, parapets, premixes, and concrete slab. The general dimension of the bridge model is 18 m (length) × 9.5 m (width) × 6.5 m (height to the center of the capping beam). In STAAD.Pro, the modified prototype bridge is modeled as skeletal statically determinate structure, comprises three member elements and four nodes. Node 2 and 3 were assigned as support and design loads were assigned along the member element with appropriate distance (according to the I18 beam position on capping beam) as shown in Fig. 6. The analytical result was then validated to mathematical calculation.

3.2 Dynamic Modeling and Analysis

Simple harmonic motion (SHM) of SDOF of the modified prototype bridge was also modeled using STAAD.Pro. The modeling construction was done as skeletal structure (framing structure) with six nodes and five member elements. Node 5 and node 6 were assigned as fixed support at the column, member 4 and member 5 were assigned as the pier column (1000 mm diameter, 6.5 m high) and member 1, 2, and 3 were assigned as the capping beam (1.5 m high × 1.6 m depth × 9.5 m length). The concentrated lumped mass was positioned on top of the model (automatically
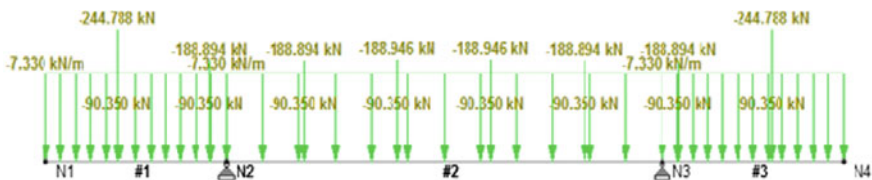
Fig. 6 Node numbers, member numbers, supports and loading distribution

centralized by STAAD.Pro system) and expressed as self-weight (in both direction, x and y-axis) of the bridge pier. In order to fulfill the SHM of equation, the stiffness (k) of the column was required. A predetermined drift value in percentage varies from 0.01, 0.1, 0.25, 0.5, and 0.75 to 1 % applied to the time-displacement and time-acceleration sine function.

An SHM is introduced to the model analysis which is intended to obtain the time-displacement function of the model. The maximum displacements of the top column of the model under the time history load case are also obtained. The second derivation of displacement versus time following the harmonic motion, $\ddot{u}(t) = -\varpi^2 A(\sin \varpi t)$ the acceleration amplitude is calculated according to the six conditions of drifts. The displacement amplitude (A) is pre-calculated according to the six conditions of drifts. The acceleration versus time function is plotted for each and every drift's value and tabulated for six conditions of period (T) and frequency (f). The angular frequency, (ϖ) is determined by the stiffness of the columns, (k) and the total mass of the skeletal structure (m).

3.2.1 Acceleration Versus Time Function in STAAD.Pro

Translational acceleration load are used to simulate the ground motion of the time history analysis acceleration record in STAAD.Pro. STAAD.Pro software assumes complete fixity to all supports (since the modified prototype bridge pier model are constructed as monolithic structure). Then STAAD.Pro automatically computes the acceleration loads at each nodes and structural model. During analysis, acceleration couples with mass and STAAD.Pro has distributed the mass of the model to all joints. For this model, node 1, 2, 3, and 4 are having similar distributed mass and there will be no mass distribution for joints or nodes that have been assigned as supports. In each and every set of the SDOF analysis, acceleration versus time function is plotted using the function of $\ddot{u}(t) = -\varpi^2 A(\sin \varpi t)$. The tabulated data of time (s) and acceleration amplitude (mm/s^2) is plotted using Microsoft Excel and a sine wave curve is drawn. The drawn curve from Microsoft Excel is considered as a theoretical result and the tabulated data is then used as input data for STAAD.Pro Time History-Acceleration Function command.

3.2.2 Displacement Versus Time Function in STAAD.Pro

Time-displacement function which resulted in the maximum displacement of the modified prototype bridge pier model is obtained upon the STAAD.Pro time history-acceleration loads analysis for SDOF system. The result retrieved from STAAD.Pro postprocessing mode was in graphic mode (the displacement vs. time curve).

3.2.3 Supplementary Results from Dynamic Analysis

Apart from the validation of the lateral displacement of the model, verification and validation of the Rayleigh frequency of the model were calculated as well. The equation for calculating Rayleigh frequency is dependent on the lateral displacement of the model, the magnitude of the horizontal force (by means the weight of the skeletal structure applied in horizontal direction, which is the self-weight in x-direction) and the mass of the skeletal model. Rayleigh frequency (whose units is in cycle per second, cps) produced from STAAD.Pro were then validated by the mathematical calculation of Rayleigh frequency Eq. (1) as below

$$= \frac{1}{2\pi} \left[\frac{W\Delta_x}{M\Delta_x^2} \right]^{\frac{1}{2}}, \tag{1}$$

where
W Weight of the skeletal structure (kN)
M Mass of the skeletal structure (kg)

4 Result and Discussion

Both static and dynamic analyses results were validated and verified using mathematical solution. The difference in percentages were calculated and the difference value has been limited to below 5 % and concluded as verified and acceptable.

4.1 Static Analysis Result and Discussion

For static analysis, the result of bending moment, BM (kN m), shear force, V (kN) and reaction at supports, R (kN) were summarized, compared between analytical (STAAD.Pro) and mathematical. The difference in percentage for bending moment, BM and shear force, V and support at reactions, R are as shown in Tables 2 and 3, respectively.

The comparison between analytical (STAAD.Pro) and theoretical verification was done for the static analysis. The validation was made for STAAD.Pro with the manual calculation. Theoretically, the value obtained for manual calculation did not show a huge different than the value STAAD.Pro had produced. Both tables containing summarized values for bending moment, shear force, and reaction at supports exhibit almost no differences between analytical and theoretical calculation. Therefore, the manual calculation procedure is correctly performed. Hereafter, the static analysis of the modified prototype of bridge pier is announced validated

Table 2 Percentage difference between analytical and theoretical results for bending moment and shear force

Beam	Analytical (STAAD. Pro)	Theoretical (manual calculation)	Bending moment percentage difference	Node	Analytical (STAAD. Pro)	Theoretical (manual calculation)	Shear Force percentage difference
	Moment (kN m)	Moment (kN m)	(%)		Shear force (kN)	Shear force (kN)	(%)
3	504.56	504.56	0	3	630.142	630.1415	0
2	504.56	504.56	0	2	577.598	577.598	0
2	−349.676	−349.677	0.003	–	–	–	–
3	0	0	0	4	0	0	0
1	0	0	0	1	0	0	0
1	−504.56	−504.56	0	2	630.142	630.1415	0
2	−504.56	−504.56	0	3	577.598	577.598	0

Table 3 Percentage difference between analytical and theoretical results for support reaction

Node	Analytical (STAAD.Pro)	Theoretical (manual calculation)	Percentage difference (%)
	Reaction (kN)	Reaction (kN)	
3	1207.74	1207.74	0
2	1207.74	1207.74	0
1	1207.74	1207.74	0
2	1207.74	1207.74	0

theoretically and the results are acceptable. Then, STAAD.Pro is satisfied to be used to prolong the study of the dynamic analysis.

4.2 Dynamic Analysis Result and Discussion

4.2.1 Time-Displacement and Rayleigh Frequencies

For SHM to be done in STAAD.Pro, acceleration amplitude was needed in time history fundamental command. The main parameters obtained are the maximum lateral displacement and the time-displacement curve of the modified prototype bridge pier model (a skeletal structure). Nonetheless, STAAD.Pro has produced other interesting results which can be discussed further in this chapter. The additional results are the mode shapes of the model, modal frequency, mass participation Rayleigh frequency, maximum base shear at times, and peak ground acceleration (PGA) extruded from time-acceleration relationships. In the modified prototype bridge pier model, validation and verification is made for the maximum lateral displacement and the Rayleigh frequency of the model. The best presentation

Table 4 Result comparison and percentage differences between analytical and theoretical analysis of the model

Drift (%)	Description	STAAD. Pro output	Manual calculation	Total time, T (s)	Percentage differences (%)
0.01	Maximum lateral displacement (mm)	0.6195	0.65	60	*4.69*
0.10		6.1953	6.5	90	*4.69*
0.25		15.4852	16.25	120	*4.71*
0.50		30.964	32.5	150	*4.73*
0.75		46.450	48.75	180	*4.72*
1.00		61.9531	65	210	*4.69*
0.01		19.98345	19.54939	60	*2.17*
0.10	Rayleigh frequency (cycle per second, cps)	6.31932	6.182061	90	*2.17*
0.25		3.99709	3.909878	120	*2.18*
0.50		2.82666	2.764702	150	*2.19*
0.75		2.30793	2.257369	180	*2.19*
1.00		1.99835	1.954939	210	*2.17*

of the validation comparison can be shown through Table 4 and is summarized into the percentage differences between the analytical and theoretical dynamic results. Both analyses show that with the increment of drift percentage value, the maximum lateral displacement of the model also increases. The increment of the lateral displacement is supported by the increment of the time (starting from 60 to 210 s) for the model to be analyzed. Initially at the drift of only 0.01 %, the maximum lateral displacement produced by STAAD.Pro is only 0.6195 mm and Microsoft Excel with 0.65 mm. When the drift percentage is at 1 %, the maximum lateral displacement from STAAD.Pro is 61.9531 mm lesser 3.0469 mm from Microsoft Excel output at 65.00 mm. The huge increment in lateral displacement occurred from 0.01 to 1 % of drift, which is 61.3336 mm for STAAD.Pro and 64.35 mm for Microsoft Excel. Hence, the average percentage differences between STAAD.Pro and Microsoft Excel shown in Table 4 are only 4.705 %. Therefore, time-displacement relationships produced by Microsoft Excel are considered acceptable since the average percentage difference is less than 5 %.

Additional validations output from STAAD.Pro, which was Rayleigh frequency for each and every maximum lateral displacement obtained. Rayleigh frequency is much dependent on the lateral displacement value as the weight (W) and mass (m) of the structure are constants. The result shows that at the lowest maximum lateral displacement of the model which is denoted by drift 0.01 %, the Rayleigh frequency is the highest among others, which are 19.98345 Hz from STAAD.Pro and 19.54939 Hz from theoretical calculation. The Rayleigh frequency values keep fluctuating between drift 0.1–0.75 % and ended up with the lowest Rayleigh frequency value at drift 1 % for 1.99835 Hz from STAAD.Pro and 1.954939 Hz from theoretical calculation. The drop of Rayleigh frequency from drift 0.01–1 % is almost 10 %. Percentage difference between analytical (STAAD.Pro) and theoretical results were also presented. The difference made was much lesser than the
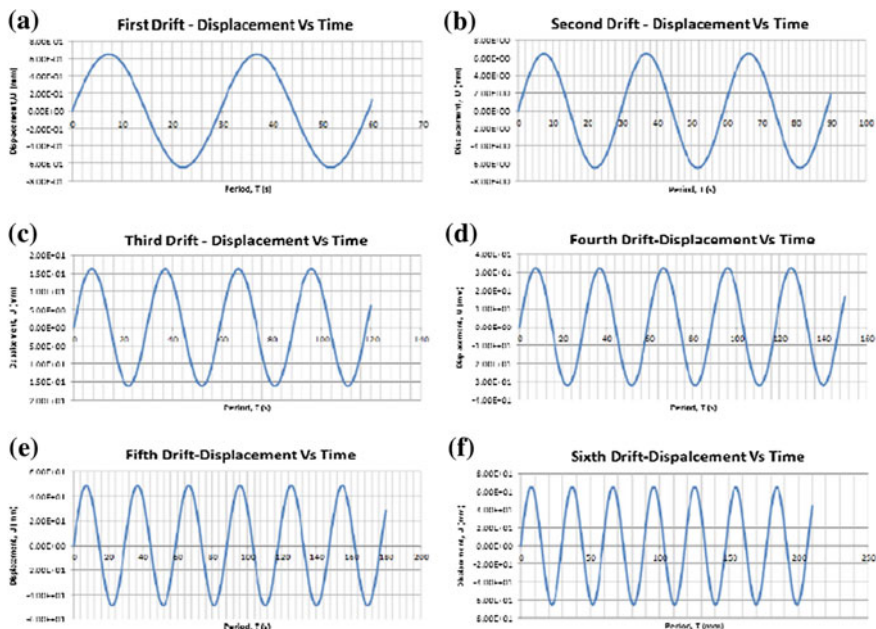
Fig. 7 Time-displacement curve for all 6 drifts of the modified prototype bridge pier model

comparison done to maximum lateral displacement of the model. For Rayleigh frequency average percentage difference is only 2.18 %, which is far lesser than the set limit of 5 % to make the results acceptable. The theoretical formula used can be said as verified and validated. The time-displacement relationships verified by Microsoft Excel as the requirement of this study for mathematical comparison are shown in Fig. 7.

4.3 Maximum Base Shear, Mode Shape and Modal Frequencies of the Model

With the increment in drift percentage and time, the maximum base shears also increase. Though, the time recorded for the maximum base shear [the maximum capacity of the model to withstand the dynamic motion in particular times based on peak ground acceleration (PGA)] [6] varies. The first two drifts percentage which are 0.01 and 0.1 %, the maximum base shear value are ten times higher but the time recorded are the same, which is 82.59 kN (at 7.033 s) and 825.92 kN (at 7.033 s), respectively as shown in Table 5. But starting from the third drift percentage of 0.25–1 %, the maximum base shear keeps increasing from 2064.399 kN (at 81.029 s) to 8259.241 kN (at 7.033 s).

Table 5 Maximum base shear, mode shape and modal frequencies for dynamic analysis produced by STAAD.Pro

Drift (%)	Maximum base shear (kN)	Maximum base shear time (s)	Mode 1 frequency (Hz)	Mode 2 frequency (Hz)	Mass participation at Node 1, Mode 1 (%)
0.01	82.59	7.033	6.891	149.444	100
0.10	825.92	7.033	6.891	149.444	100
0.25	2064.40	81.033	6.891	149.444	100
0.50	4127.94	81.029	6.891	149.444	100
0.75	6192.05	22.029	6.891	149.444	100
1.00	8259.24	7.033	6.891	149.444	100

STAAD.Pro mode shape results produce two types of mode shape, which are mode shape 1 (normal mode shape) and mode shape 2 (torsional mode shape). Figure 8 shows the normal mode shape which is the shape reflecting the usual lateral displacement of a model. Figure 9 shows the torsional mode shape in which the movement of the model of the bridge pier is like in twisting motion (torsion) due to the torsional ground motion effect.

Fig. 8 Mode shape 1, frequency 6.891 Hz (Normal Mode Shape)
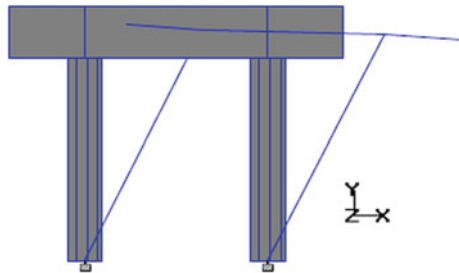
Fig. 9 Mode shape 2, frequency 149.444 Hz (Torsional Mode Shape)
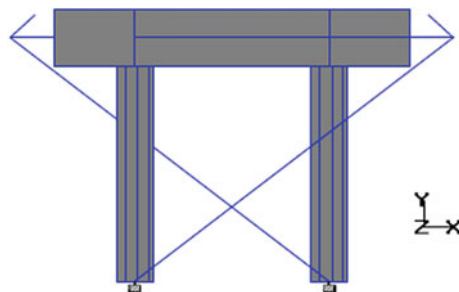
5   Conclusion

It has been demonstrated and performed that both static and dynamic analyses of the multi-column pier of unskewed bridge using STAAD.Pro were verified and satisfactory validated by concept of theories. Model analyzed under free vibration without damping system shows that with the increasing of drift percentage, the maximum lateral displacement also increases. On the other hand with the increment of drift percentage (corresponding to increasing of maximum lateral displacement), the Rayleigh frequency drops. The increasing of maximum lateral displacement and decreasing of Rayleigh frequency were due to the collective time assigned to the model. Overall, the results and comparisons obtained were acceptable and utilization of STAAD.Pro is appropriate. This study was only done in 2D analysis using STAAD.Pro (as STAAD.Pro is not a famous finite element analysis software (FEM) compared with ANSYS, CIS, RUAMOKO, SAP2000, etc.), yet has the great potential to prolong the study by performing 3D analysis using similar software and setting up laboratory experiment. Therefore, result from this study can be made as a comparison and input data to the laboratory works and search for the best performance of the bridge model under dynamic loading.

References

1. Clarke, R. (2003). STAAD Basics, Notes on the Effective Use of STAAD.Pro Rel. 3.1.
2. N. Haritos, H. a. (1995). Modal Testing of a Skew Reinforced Concrete Bridge. Department of Civil and Environmental Engineering, The University of Melbourne, Australia, 703–708.
3. X.H. He, X. A. (2012). Skewed Concrete Box Girder static and dynamic testing and analysis. *Elsevier.*
4. N. Munirudrappa, N. K. (2004). Response of Slant Legged Skew Bridge Under Dynamic Loading. *13th World Conference on Earthquake Engineering*, (p. Paper No:3151). Vancouver, B.C, Canada.
5. Priestley, M. (1996). *Seismic Design and Retrofit of Bridges.* California, San Diego, USA: John Wiley & Sons, Inc.
6. Wikipedia. (2013, December 16). Peak Ground Acceleration.

Repair and Retrofitting Bridge Pier Using CFRP and Tested Under In-plane Lateral Cyclic Loading

N.H. Hamid, M.E. Mohamad and M.A. Zainuddin

Abstract This paper investigates the seismic performance of the repair and retrofitting damage unskewed multi-column RC bridge pier under in- plane lateral cyclic loading. The main objective of this paper is to determine the seismic performance of repaired bridge pier in terms of lateral strength capacity, stiffness, ductility, damage state, and equivalent viscous damping. Three layers of Carbon Fiber Reinforced Polymer (CFRP) are wrapped along the damaged specimen. This technique is used to repair and strengthen the bridge pier column after damage due to earthquake. The experimental results show that the repaired bridge pier performed very well under in-plane lateral cyclic loading. It also increases the lateral strength capacity, ductility, and equivalent viscous damping as compared to the specimen before retrofitting. This technique can be recommended for repair of damages of bridges after the earthquake or any other natural disaster.

Keywords Seismic performance · Stiffness · Ductility · Damage state · Lateral strength capacity

1 Introduction

Retrofitting bridge technique using CFRP and steel plate is normally used in repairing the damages structures and infrastructures such as bridge piers, column, beam-column joint [1], wall-panel, tunnel-form building [2, 3], and wall-slab connections [4]. The material used to repair and strengthen the structures components includes steel jacketing, concrete jacketing, fiber reinforced polymer, and FRP bonding on the external surface of the member to be retrofitted. For strengthening of pre-stressed concrete structures, external post-tensioning or FRP retrofit may be appropriate to use. In the last decade, recent developments in the

N.H. Hamid · M.E. Mohamad (✉) · M.A. Zainuddin
Faculty of Civil Engineering, Universiti Teknologi MARA,
40450 Shah Alam, Selangor, Malaysia
e-mail: mohdelfie91@gmail.com

Fig. 1 30 m wide ramp of the bridge under construction collapsed (NST, 2013)

manufacturing of fiber reinforced polymer (FRP) composite materials have made these materials available in the market for a wide range of applications, including seismic retrofit of reinforced concrete columns. Malaysia often shocked by the news of the bridge collapse. For instance, the 30 m wide ramp at Batu Maung, Second Penang Bridge which is still under construction collapsed in the evening of June 6, 2013 [5] due to construction fault at the site. Figure 1 shows the collapse of 30 m wide at end of Second Penang Bridge. One person died due to the collapse of the bridge. Due to lack of supervision at site and negligence of putting a suitable support underneath the precast concrete deck caused end part of the bridge to collapse down.

Currently, there are no earthquake events which could cause these bridge collapses in Malaysia. Nevertheless, most bridges in Malaysia collapsed due to soil settlement, wear and tear, change in weather, poor workmanship, and design fault. On the other hand, East Malaysia is also affected by the tremor of the earthquakes from northern Sulawesi and southern Philippines. Mostly bridges in Malaysia are designing using non-seismic code of practice (BS8110) where did not considered the seismic loading. The First and Second Penang Bridge is exposed to vibration and seismic loading which comes from Sumatera. Therefore, seismic loading consideration in designing bridges is very important to cater for future earthquake which originates from long-distant earthquake and near-field earthquakes. Based on the problem arising due to earthquakes, most of the infrastructures and buildings in Malaysia are vulnerable to the earthquakes and the safety is still questionable. For sure, there will be a lot of structures damages to occur after the earthquake. Thus, this research is focused on the determination seismic performance after repair and retrofitting the unskewed multi-column RC bridge pier using Carbon Fiber Reinforced Polymer (CFRP) under in-plane lateral cyclic loading. The specimen were tested after retrofitting with CFRP wrapping and subjected to in-plane lateral cyclic loading.

2 Finding from Previous Research Work

Some research work had been conducted on improving the existing concrete bridge pier using CFRP and the peak lateral load capacity increased by 16 % [6]. Further experimental analysis was conducted on retrofitting existing circular column using CFRP and the lateral deformability improved by 5 % drift ratio [7]. More investigations were carried out on retrofitting existing rectangular column using oval-shaped jackets and CFRP had improved the stiffness and ductility [8]. Other applications of CFRP can also be applied for repaired and retrofitting single and double unit tunnel-form building [9, 10].The effectiveness of the FRP also can be used to improve the seismic shear strength of bridge pier column [11]. Therefore, it is important to repair the damage bridge pier and tested under in-plane lateral cyclic loading which represent the earthquake excitations. The limitation of this study is that one-third of two bridge piers were constructed and tested in laboratory with the grade concrete 40 Mpa for the foundation and 30 Mpa for the pier. Figure 2 shows the dimension of multi-column RC bridge pier system which consists of foundation beam, two circular bridge columns, and capping beam.

For the reinforcement details [8] proved that CFRP is extremely good in seismic performance with satisfaction stiffness and ductility. Hence, the proposed retrofitting scheme for unskewed two bridge piers by using CFRP wrapping.

The piers were wrapped using CFRP sheet from top to the bottom. Table 1 shows the mechanical properties of the CFRP.
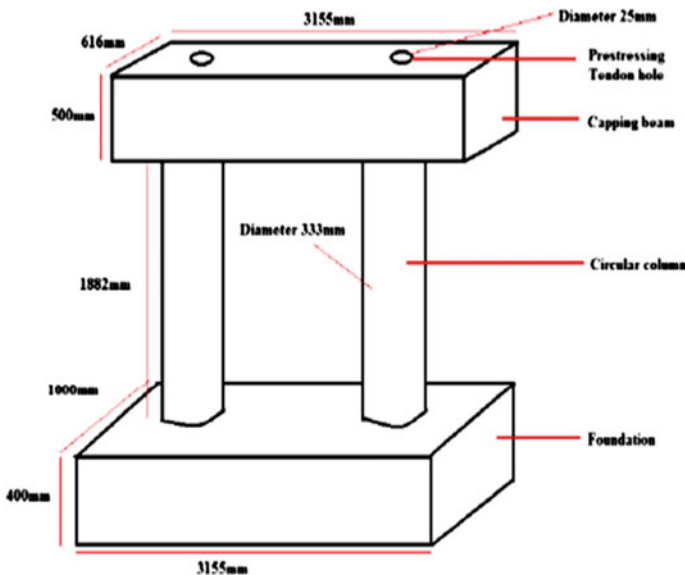
Fig. 2 One-third of unskewed multi-column bridge pier

Table 1 Mechanical properties of FRP (from manufacturer-LaMaCo Build Seal)

FRP material (sheet)	Tensile E-modulus (MPa)	Tensile strength (MPa)	Strain at break of fibre (%)
Carbon fibre (CFFS 230-Extra)	230	4900	1.80

Seismic retrofitting is the modification of existing structures to enhance the resistance to seismic activity due to earthquakes. The process of strengthening and retrofitting was applied to the damaged specimen to increase the lateral strength capacity, stiffness, and ductility of the piers bridge after suffering damage when subjected to in-plane cyclic loading.

3 Visual Observation of Damages Before Retrofitting

Figure 3 shows damages and several cracks on first column of the bridge piers. The first column suffered harsh damage once tested up to ±2.0 % drift. The damage part is recognized, which is a crack at the pier and spalling of concrete at the upper part of column. Figure 4 shows the damages and cracks on the second column where a lot of horizontal cracks were observed at top and bottom part of the column. These parts of the column experienced the plastic hinge zone (PHZ) and damages were also concentrated in this area. Therefore, these areas need to clean, grind, and

Fig. 3 Damages of the first column before retrofitting

Fig. 4 Damages of the second column before retrofitting
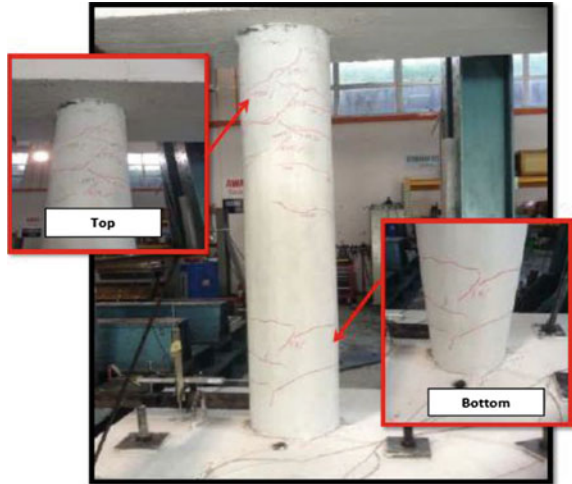
Fig. 5 Columns' surface was coated with Primer Epoxy Resin before wrapping with CFRP

remove the debris coming from cracks surface before repair and retrofitting took place. Seismic retrofitting is the modification of existing structures to enhance the resistant to seismic activity due to earthquakes.

Figures 3 and 4 show the two column of bridge piers before surface preparation and layering of the primer epoxy resin. Figure 5 shows the wrapping of the piers was using CFRP (Build Seal CFFS Extra 230) which has a tensile strength of 4900 MPa with 0.117 mm thickness and 1.8 % elongation. CFRP sheet was used to wrap the piers from top to the bottom.

Fig. 6 Location of LVDTs on the prototype bridge
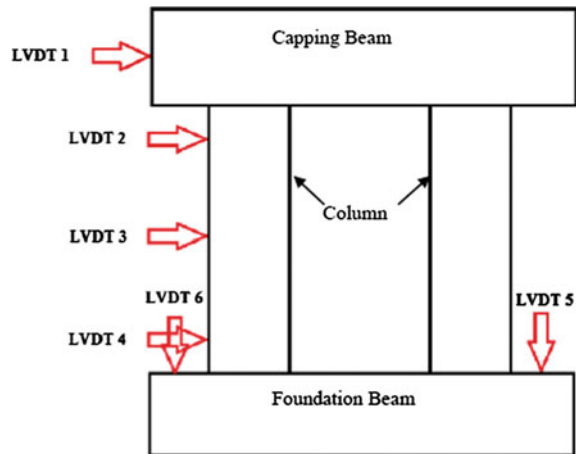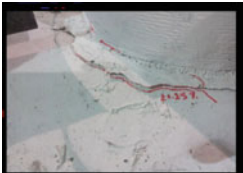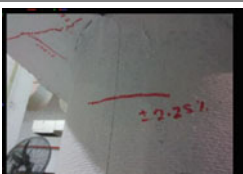
4 Calibration and Experimental Setup

Six numbers of Linear Variable Displacement Transducers (LVDT) were installed on the bridge sample as shown in Fig. 6. LVDT 1 was positioned horizontally at top of capping beam and has similar displacement as controlled by the double actuator while the LVDT 5 and LVDT 6 is set up vertically to measure uplift of the foundation beam during experimental work. The sample was tested with incremental drift of 0.25 % drift starting from ±0.01, ±0.25, ±0.5 %, and until the specimen failed.

5 Visual Observation on Damages After Retrofitting

The visual observation on the spalling of concrete cover, crack propagation, and splitting of CFRP were recorded and measured during testing. Table 2 shows the visual observation on columns and crack propagation at ±0.75, ±1.5, ±2.0, ±2.25, ±2.5, and ±2.75 % drift. All of the crack lines were marked using a red marker to indicate the movement of the cracks with increment of drift. Most of the cracks occurred at the column joint and the piers. It was observed that the largest part of the cracks occurred at the body and joints of the columns. Small numbers of cracks were observed at the capping beam and foundation through the testing.

Table 2 Visual observation during testing

Crack pattern	Drift percentage
	Cracks occurred at ±0.75 % drift
	Cracks occurred at ±1.5 % drift
	Cracks occurred at ±2.0 % drift
	Cracks occurred at ±2.25 % drift
	Cracks occurred at ±2.5 % drift
	Cracks occurred at ±2.75 % drift

6 Experimental of Results

6.1 Hysteresis Loop and Lateral Strength

From hysteresis loops, the parameters such as yield lateral strength, yield displacement, stiffness, ductility, and equivalent viscous damping can be calculated. Figure 6 shows the overall hysteresis loops of LVDT 1 for the repaired and retrofitting of damages bridge piers using CFRP. The maximum lateral strength capacity of 175.86 kN occurs at 2.25 % drift with maximum lateral displacement of 54.24 mm. The specimen lost its strength at 2.75 % drift and splitting of CFRP (Fig. 7).

Figure 8 shows hysteresis loops of before repair and retrofitting bridge piers. The ultimate load occurred at 1.5 % drift with 186.42 kN. Figure 9 shows the comparison of hysteresis loops before and after repair of the unskewed multi-column bridge piers tested under in-plane lateral cyclic loading. The repaired specimen has higher ductility while the unrepaired specimen has higher stiffness and lateral strength capacity.

6.2 Stiffness

The assumed stiffness of the structural members of a building influences the computed response of the building to ground shaking. Figure 10 shows the elastic
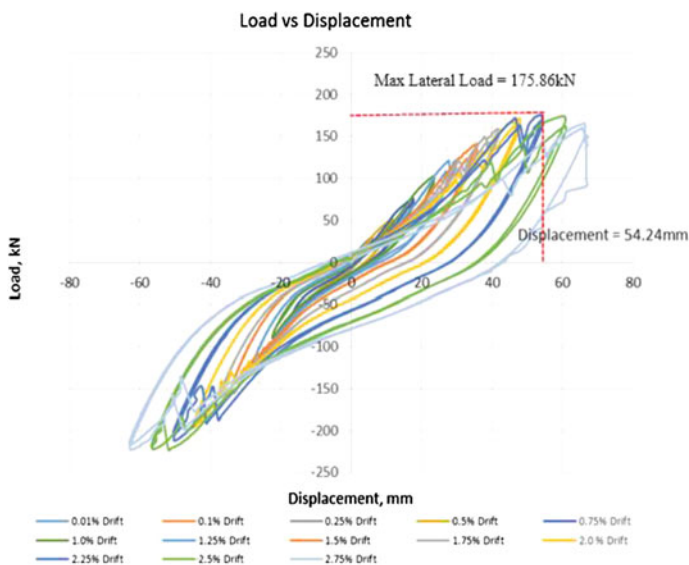
Fig. 7 Hysteresis loops for repaired specimen

Load vs Displacement
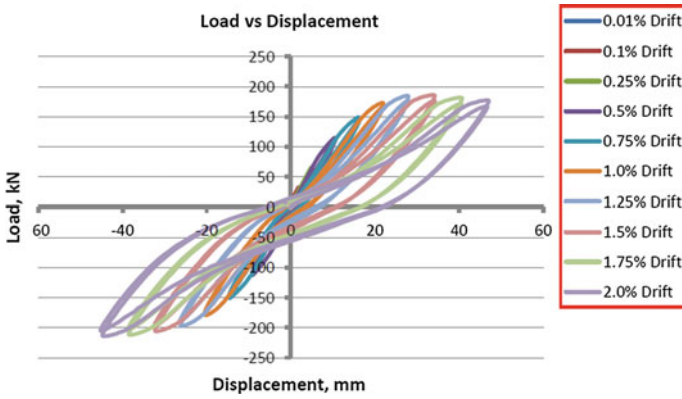
Fig. 8 Hysteresis loops for unrepaired specimen

Load vs Displacement
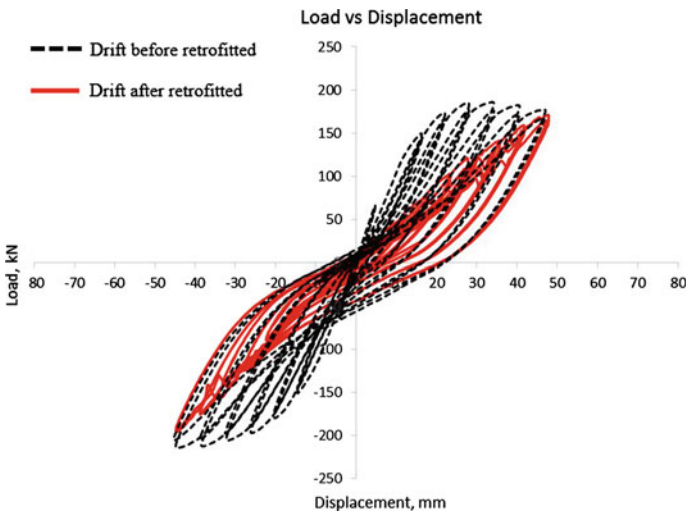
Fig. 9 Comparison of hysteresis loops

stiffness (K_e), secant stiffness (K_{sec}), and effective stiffness (K_{eff}) for pushing and pulling lateral load. The elastic stiffness is a linear ratio of yield lateral displacement (F_y) over yield lateral displacement (Δ_y). The yield lateral displacement (Δ_y) is determined by taking 75 % of maximum lateral load (F_{max}) and projected to the lateral displacement axis based on backbone curve envelope. The yield load (F_y) for the pushing direction is 131.8 kN and yield displacement (Δ_y) is 30 mm. The yield load for pulling direction is −167.25 kN and yield lateral load is 32 mm.

Table 3 displays the values of elastic stiffness, secant stiffness, and effective stiffness of repaired bridge pier for pushing and pulling directions based on data obtained from Fig. 10. It shows that the overall assessment of the elastic, secant,
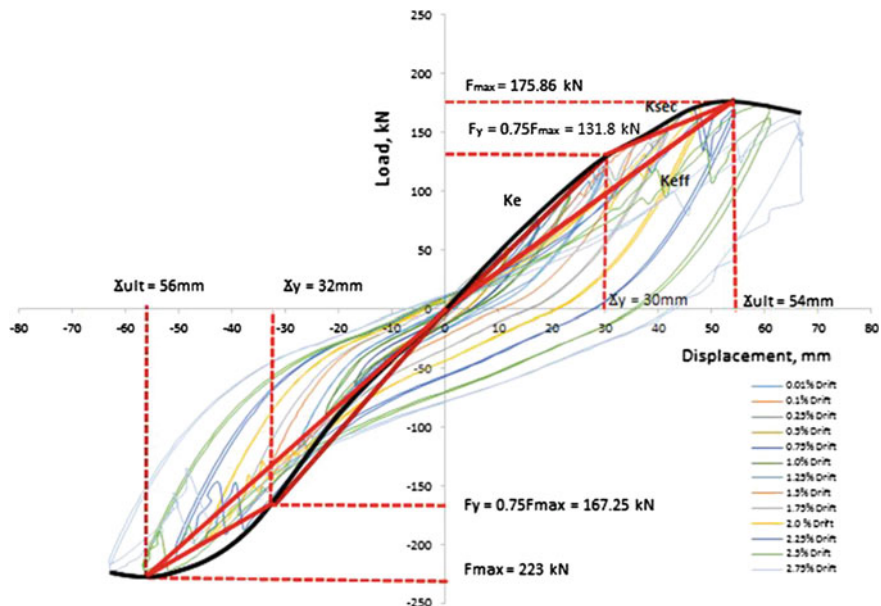
Fig. 10 Elastic stiffness, secant stiffness and effective stiffness for pushing and pulling Load

Table 3 Elastic stiffness, secant stiffness and effective stiffness for pushing and pulling directions

Stiffness (kN/mm)	Stiffness in pushing direction (kN/mm)	Stiffness in pulling direction (kN/mm)
K_e	4.4	5.22
K_{sec}	1.84	2.32
K_{eff}	3.26	3.98

and effective stiffness in the pulling direction exhibit higher values than pushing direction due to the fact that more loads are required to pull the specimen to zero displacement as compared in pushing direction. It can be concluded that the effective stiffness is higher than secant stiffness and secant stiffness has lower value as compared to the elastic stiffness for pushing and pulling directions.

Figures 11 and 12 show crack along the joint between pier and foundation with 200 and 150 mm opening gap. Some of the cracks formed are from the extension of the existing cracks. Therefore, this situation was categorized as under control condition of damages. This is because all of the cracks occurred were not very serious. Furthermore, there was no spalling of concrete and the tests do not cause the specimen to collapse.

Fig. 11 Failure of the joint at pulling direction after ±2.25 % drift
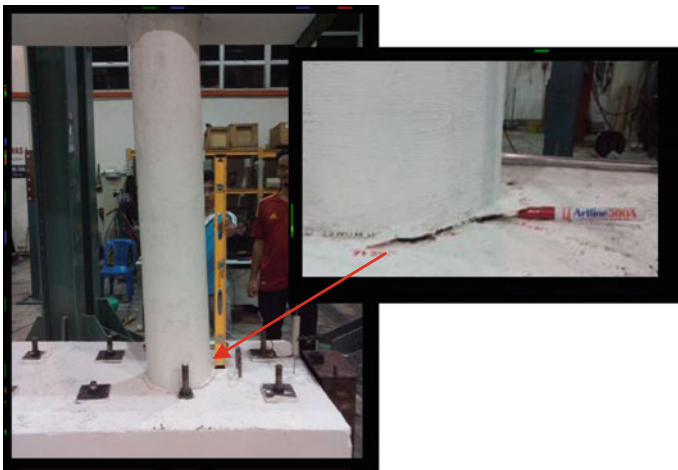
Fig. 12 Failure of the joint at pushing direction after ±2.25 % drift

6.3 Displacement Ductility

Ductility is the ability of the specimen to oppose the load that is applied to it without rupturing or breaking before failure. The specimen has experienced elastic phase, before reaching the ultimate load capacity as a final point of ductile behavior, which is when the load applied is directly proportional to displacement. Consideration of ductility for seismic practice is an important factor to evaluate the capacity of the structure and to resist seismic action. The calculation of

Table 4 Displacement ductility of the repaired specimen

Drift %	Max lateral load (kN)	Applied displacement (mm)	Yield displacement (mm)	Displacement ductility
0.01	2.88	0.16	30	0.01
0.1	12.72	2.2	30	0.07
0.25	29.87	5.92	30	0.20
0.5	51.46	11.82	30	0.39
0.75	76.17	17.58	30	0.59
1.0	102.45	23.24	30	0.77
1.25	121.4	29.74	30	1.00
1.5	141.19	35.6	30	1.19
1.75	158.95	41.68	30	1.39
2.0	171.18	47.6	30	1.59
2.25	175.86	53.82	30	1.79
2.5	174.3	60.34	30	2.01
2.75	166.02	66.02	30	2.20

displacement ductility (μ_Δ) is based on the ratio of the applied lateral displacement (Δ_{applied}) over the yield lateral displacement (Δ_y) as shown in Eq. 1.

$$\text{Displacement ductility, } \mu_\Delta = D_{\text{applied}}/D_y \tag{1}$$

Table 4 shows the displacement ductility for repaired specimen based on the data obtained during experimental work. The recorded ultimate lateral load for repaired bridge pier is 175.86 kN with ultimate lateral displacement of 53.82 mm. By using the values of yield lateral displacement, the displacement ductility for every drift percentage is calculated. The ductility at the ultimate is 1.79. The displacement ductility repaired and retrofitted for unskewed multi-column RC bridge pier is less than the required displacement ductility as specified by the Eurocode 8. According to current seismic code of practice as Eurocode 8, the appropriate displacement ductility value under Ductility Class Medium (DCM) should be between 3 and 6. Therefore, it can be concluded that the specimen was unable to deform under tensile stress without breaking and it is not safe if the structure was subjected to moderate and severe earthquake loading.

6.4 Equivalent Viscous Damping

Kinetic energy is stimulated in the model throughout the load which is applied to the specimen. Kinetic energy is conserved to potential energy. Therefore, the potential energy in the specimen gains from the hysteresis loop by calculating the

Fig. 13 Equivalent viscous damping for the first and second cycle of the repaired bridge pier
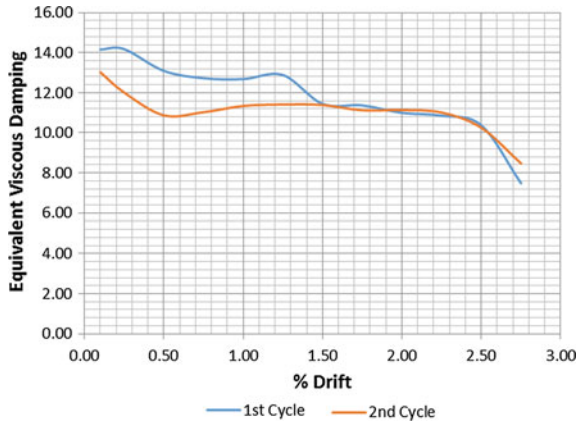
Equivalent Viscous Damping (ξ_{eq}) at LVDT1 for every drift applied to the repaired bridge pier. The main reason of determining equivalent viscous damping is to know how much energy dissipated in term of work done for every one complete cycle of each drift. Equation 1 is used to calculated the amount of ξ_{eq} for each cycle for every incremental of drift applied to the specimen.

$$\xi_{eq} = \frac{1}{4\pi}\frac{E_D}{E_{so}} \tag{2}$$

where E_D is the amount of work done under one complete cycle and E_{so} is the strain energy captured under the area of triangle at maximum lateral load and displacement.

Figure 13 shows the equivalent viscous damping of the first and second cycles for every incremental of drift. Generally, the first cycle of equivalent viscous damping is greater than the second cycle up to 1.5 % drift and becomes similar values from 1.5 % drift to 2.75 % drift. More energy is required to resist the lateral strength capacity of the specimen in first cycle as compared to second cycle.

Based on the EVD graph, the EVD starts with the highest value then decreases until the test is stopped. This is because the sample is in a rigid condition at the initial time and the 62 drift applied is the smallest drift. So, the sample is highly able to resist the drift applied. However, the EVD of the sample starts to get weak because the drift is continuously applied to the sample. Furthermore the EVD is slightly deceased due to sample tried to resist from oscillating. Based on that, it can be said that the sample has low capacity to restrain the dissipated energy under the cyclic loading test.

7   Conclusions and Recommendations

Based on the visual observation, analysis of results and discussion, the following conclusions and recommendations are as listed below:

(1) The seismic performance of repaired and retrofitted of unskewed multi-column RC bridge pier using CFRP under in-plane lateral cyclic loading enhanced in terms lateral strength and equivalent viscous damping.

(2) The maximum recorded lateral strength is 175.86 kN occurred at 53.82 mm and the yield lateral load is 131.8 kN along with yield lateral displacement of 30 mm.

(3) The maximum stiffness was recorded in pulling direction where the secant stiffness (K_{sec} = 2.32 kN/mm) is less than effective stiffness (K_{eff} = 3.98 kN/mm) and lesser than elastic stiffness (K_e = 5.22 kN/mm). Therefore, the result of the experiment was proven by the appearance of tilting of the specimen during the test as shown in Figs. 11 and 12.

(4) The ductility at the ultimate is 1.79 and it is beneath the range of the ductility factor for seismic practice which is within 3–6. From that, it can be said that the ductility of the sample is in a poor performance to resist the lateral load.

(5) It is recommended to use CFRP for the repairing the damage bridge piers either due to earthquake or any other natural disaster or man-made disaster.

(6) It suggested that to construct 3D bridge piers together with the deck and foundation beam for the future research work.

References

1. Hamid, N.H., Hadi, N.D. and Ghani, K.D., Retrofitting of Beam-Column Joint Using CFRP and Steel Plate, World Academy of Science, Engineering and Technology, International Science Index, 84, pp 783–788, (2013).

2. Anuar, S.H, Hamid, N.H., Hashim, M.H. (2014), Retrofitting of Single Unit Tunnel Form Building Using Steel Plate under Out-of-Plane Lateral Cyclic Loading, Applied Mechanics and Materials, 661, 95–99.

3. Hamid, N.H., Anuar, S.H., Azmi, N.L. (2014), "Retrofitting of a Double Unit Tunnel Form Building Using Additional RC Wall, Steel Angle and CFRP, Applied Mechanics and Materials, 661, 123–127.

4. Hamid, N.h Abdul and Masrom, M.A. (2012). seismic performance of wall-slab joint in industrialized building system (IBS) under out-of-plane reversible cyclic loading.

5. Fatt, L. K. (2013, June 6). Penang Second Bridge ramp collapses, one body found. Retrieved from New Straits Times: http://www.nst.com.my.
6. Pantelides, C. P., Gergely, J., Reaveley, L. D., & Volnyy, V. A. (1999). Retrofit of RC bridge pier with CFRP advanced composites. Journal of Structural Engineering, 125(10), 1094–1099.
7. Elnabelsy, G., & Saatcioglu, M. (2004). Design of FRP jackets for seismic retrofit of circular concrete columns. Emirates Journal for Engineering Research, 9(2), 65–69.
8. Endshaw, M. A., ElGawady, M., Sack, R. L., & McLean D. I. (2008). Retrofit of Rectangular Bridge Columns Using CFRP Wrapping, M.S. Thesis, Department of Civil and Environmental Engineering, Washington State University.
9. Anuar, S.A, Hamid, N.H.A. and Hashim, M.H. (2014), "Comparison of seismic behaviour for a single unit tunnel form RC building before and after repaired, Advanced Materials Research 905, 254–258.
10. Hamid, N.H., Saleh, S.M, Anuar, (2014) "Seismic performance of double-unit tunnel form building under in-plane lateral cyclic loading" Structures Under Shock and Impact XIII 141, 467.
11. Walkenhauer, B.J. (2010), Seismic Retrofit Of Cruciform-Shaped Columns In The Aurora Avenue Bridge Using Frp Wrapping, A Thesis Submitted In Partial Fulfillment Of The Requirements For The Degree Of Master Of Science In Civil Engineering, Department Of Civil And Environmental Engineering, Washington State University.

Compressive Strength and Water Absorption of Sewage Sludge Ash (SSA) Mortar

M.Y. Nurul Nazierah, K. Kartini, M.S. Hamidah and T. Nuraini

Abstract The mechanical and durability properties of mortar containing sewage sludge ash (SSA) are investigated in this study. The temperatures of 800 °C and 5 h duration were applied for the incineration process of the dried sewage sludge in order to obtain SSA. This SSA can be categorized as Class C pozzolan materials, as it meets the requirements specified by ASTM C618-12a. The compressive strength and water absorption tests were conducted for 7 and 28 days of curing. Interesting findings were observed at age 28 days, where all the SSA mortar (5–20 %) showed the higher strength value as compared to the control mortar. In addition, the SSA10% gave the highest compressive strength value among all, which is 55.94 MPa. The absorption rate at 28 days of all SSA mortar demonstrated a slightly lower value as compared with the control mortar. This explained that SSA has high resistance against durability. SSA5% had recorded the lowest rate of water absorption, which is 61.6 g/100 cm^2 at age 28 days. As conclusion, SSA has high prospective to be used as partial replacement for Portland cement with up to 20 % of replacement cement. Therefore, this had built a great contribution to waste minimization.

Keywords Sewage sludge ash · SSA · Sewage sludge · Mortar · Compressive strength · Water absorption

M.Y. Nurul Nazierah (✉) · K. Kartini · M.S. Hamidah
Faculty of Civil Engineering, University Teknologi MARA (UiTM),
Shah Alam, Selangor, Malaysia
e-mail: nazierahoon@gmail.com

K. Kartini
e-mail: ce_kartini2002@yahoo.com

T. Nuraini
Faculty of Civil Engineering, University Teknologi MARA (UiTM),
Permatang Pauh, Pulau Pinang, Malaysia

1 Introduction

The expansion of urbanization and industrialization over the time had prompted into dramatic increase of waste around the world and this is expected to keep boosting up in the future. Sewage sludge is the by-product generated from the wastewater treatment plant, which is considered as waste materials as well. Since past decade, these semisolid wastes are massively been dumped to the landfill and in some regions it is being discharged into the sea [1]. However, due to the space limitation, legislative barriers and the negative public perception on environmental impact, the landfill applications are no longer practical. Moreover, the sea disposal of sewage sludge is banned by EU Urban Wastewater Treatment Directive (1991) since 1999 due to the negative impact to the environment [2]. Therefore, looking for alternative in disposal of sewage sludge is becoming immediate concern.

Cement production contributed approximately 7 % of total global green house gas emissions [3] and its production is expected to increase 2.5 times between the year 2005 and 2050. Since the global warming, green house effect and the depletion of natural resources are becoming serious issues nowadays [4], this had forced the cement industry to review the usage of reusing by-product or waste as a resourceful approach. Various studies had been conducted in observing the potential of utilizing the sewage sludge to produce building and construction materials, including brick making [5–7], lightweight aggregates [8–10], paver block [3], tiles [11], as cement substitutions material for mortar and concrete [12–15], also as raw materials in cement blended production [16].

Few studies reported that sewage sludge ash (SSA) has low pozzolanic activity, which will reduce certain properties of the mortar and concrete [13, 17]. However, findings by other researchers discovered that the SSA could enhance the mechanical properties of mortar, where it mainly depends on the chemical composition of SSA [18]. Moreover, according to Tantawy et al. [19], the pozzolanic activity of sewage sludge may vary with the different incineration temperature. Nevertheless, the decency must be drawn into to the environmental impacts as sewage sludge are being reused. Hence, the aim of the present study is to investigate the effect of incineration temperature of 800 °C on the mechanical and durability of mortar containing SSA. This paper reported the initial outcome of the study based on the compressive strength and water absorption of SSA mortar.

2 Materials and Methods

2.1 Materials and Procedures

Dewatered sewage sludge was obtained from Indah Water (IWK) wastewater treatment plant at KLIA Sepang, Malaysia. The dewatered sewage sludge was dried under the hot sun during the day time for 3–5 days in order to remove 70–90 % of

the moisture content. This dried sewage sludge then undergoes incineration process to obtain the ashes form of sewage sludge and also to remove the organic matter content. The incineration process was conducted using gas kiln furnace with temperature of 800 °C and burned for 5 h. The Ball Mill (Two Tier Jar) was used to ground sewage sludge ash (SSA) with 30 rpm for 8 h to get the fine powder of SSA. The chemical composition analyses of SSA gathered were carried out using XRF PANalytical. Mining sand was used in this study, where the fineness modulus is 3.95. The grading of fine aggregate was conducted according to the ASTM C144-11 with sieve size between 0.063 to 5 mm. Locally made Type I Portland cement was used in this present study.

Mortar specimens were casted in cube mortar molds with the dimension of 50 × 50 × 50 mm. The mix proportion ratio used in this study is 1:3, with water cement ratio of 0.5. This ratio simplifies that one portion of cement was mixed with three portion of fine aggregates. Four batches of SSA mortar mixed were prepared with different percentages of SSA replacing cement, which are 5, 10, 15, and 20 %; and designated as SSA5%, SSA10%, SSA15%, and SSA20%, respectively. Another one batch of control mortar was also prepared for this study without adding SSA in the mixed proportion. After 24 h of casting, mortar specimens were demoulded and cured under the water curing condition. All the specimens are water cured and tested for compressive strength and water absorption at the age of 7 and 28 days.

2.2 Testing Specimen

(1) Compressive Strength Test: Compressive strength test of hardened mortar was conducted according to the ASTM C109-13 [20]. The data gathered from laboratory was recorded to the nearest 0.05 N/mm^2 and the average result obtained was rounded off to the nearest 0.1 N/mm^2. The compressive strength was calculated as given equation below;

$$f_m = P/A$$

where:
f_m compressive strength (MPa or N/mm^2)
P total maximum load (N)
A area of loaded surface (mm^2)

(2) Water Absorption Test: ASTM C1403 [21] is the standard that was used for determining the capabilities of mortar to be penetrated by water inside the specimens. At the age of testing, the samples were taken out from curing tank and been dried within ±1 h in room temperature. Then, the samples were oven dried for not less than 24 h with the temperature of 110 ± 5 °C. The samples were taken out from the oven and allowed to cool down for a minimum of 2 h

or until the specimens reach ambient temperature. The initial weights of the samples were measured as W_0. The weight of the samples after immersion was measured (in grams) for 15 min, 1, 4, and 24 h and recorded as W_T where T is time taken. Water absorption rate will be analyzed using the equation;

$$A_T = (W_T - W_0) \times 10{,}000/(L_1 \times L_2)$$

where:

W_T the weight of the specimen at time T in grams to the nearest 0.1 g,

W_0 the initial weight of the specimen in grams to the nearest 0.1 g,

L_1 the average length of the test surface of the mortar cube in mm to the nearest 0.5 mm, and

L_2 the average width of the test surface of the mortar specimen cube in mm to the nearest 0.5 mm

3 Results and Discussion

3.1 Chemical Composition

As suggested by the Monzó et al. [22], the chemical properties of sewage sludge varies, it depends on the sources of the wastewater and also the treatment process carry out within the plant. Table 1 illustrated the chemical composition analysis of the Portland cement and the SSA incinerated at 800 °C. There are four main compounds that were found in the SSA, which is SiO_2 (34.2 %), Al_2O_3 (18.4 %), Fe_2O_3 (7.36 %), and CaO (4.17 %). These four main compounds in the SSA were also spotted in the Portland cement, where the similar findings also claimed by Yen et al. [23]. Moreover, as referring to the ASTM C618-12a [24], this SSA can be categorized as Class C pozzolan materials, as it meets the chemical requirements

Table 1 Chemical composition of Portland cement and SSA (Mass in %)

Composition	OPC	SSA
SiO_2	14.2	34.2
Al_2O_3	3.16	18.4
Fe_2O_3	3.30	7.36
CaO	55.8	4.17
MgO	0.99	1.62
Na_2O	0.11	0.26
K_2O	0.53	2.08
P_2O_5	0.04	8.97
SO_3	4.03	3.64
TiO_2	0.16	0.83
Others	0.33	0.65

Fig. 1 Compressive strength of SSA mortar at 7 and 28 days
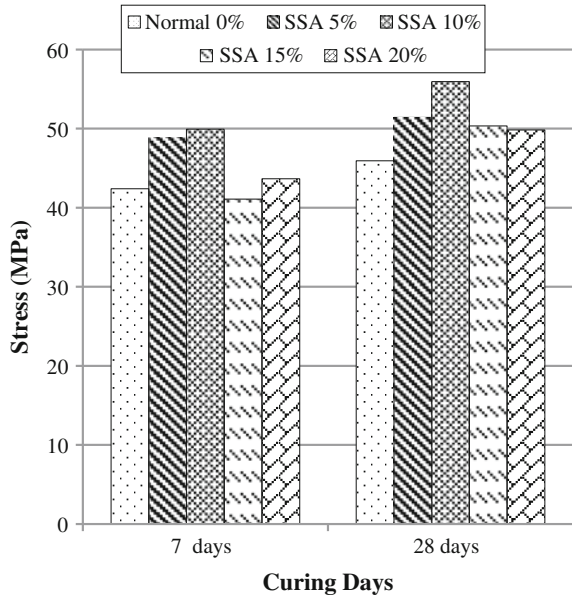
specified by the standard. The SiO_2 and CaO compounds found in the SSA are believed to affect the strength of samples [16]. Hence, theoretically, it implies that this SSA has the potential to be used as partial replacement for the Portland cement.

3.2 Compressive Strength

Figure 1 illustrated the analysis data for the compressive strength of SSA mortar and control mortar at the curing age of 7 and 28 days. From the figure, it can be suggested that all the samples demonstrated an increase in strength with respect to the increment of curing ages. As for the constraint for this study, the control mortar strength recorded at age of curing of 7 and 28 days is 42.38 and 45.93 MPa, respectively. By looking at the 7th days age of curing, most of compressive strength of the SSA mortar samples exceeded the control sample which is 48.85 MPa for SSA5%, 49.91 MPa for SSA10%, and 43.64 MPa for SSA20%; except for SSA15%, where the compressive strength recorded is 41.07 MPa. However, it is showed merely minor different with only 3.09 % differences from the control mortar.

The interesting finding of this data can be seen at the 28th days age of curing, where all the SSA mortar showed significant increase in compressive strength value as compared with control mortar. Respectively, the strength value for SSA mortars at 28 days of curing are 51.41 MPa for SSA5%, 55.94 MPa for SSA10%, 50.33 MPa for SSA15%, and 49.81 MPa for SSA20%. SSA10% had demonstrated

the best strength value as compared to all mortar samples for both age of curing 7 and 28 days. From this study, it is suggested that the SSA has the capability to partially replacing cement up to 20 % in order to enhance the strength of mortar. In addition, to get the best strength value of mortar, the optimum replacement of SSA can be considered as at 10 %.

This present findings produced totally reversed outcome as stated by other studies [13, 15], where their study suggested that SSA does not improve the strength of mortar. However, Tay et al. [16] in their study proved that SSA could enhance the cement properties and suggested that the temperature and duration of incineration process may play the role in producing good quality of SSA, other than chemical composition content. This finding somehow verified that the present SSA is a good pozzolanic material. Hence, this supported the theoretical suggestion earlier, where this SSA that burned at temperature of 800 °C, are potentially used as partial cement replacement in making mortar or cement.

3.3 Water Absorption

Figure 2 shows the result of water absorption rate for SSA sample taken at 24 h submersion at 7 and 28 days of curing. The results clearly demonstrated that the rate of water absorption for all SSA mortar and control mortar tended to decrease as the curing age increased from 7 to 28 days. This suggests that the hardening process of mortar had affected the binding between particle materials, where the pore volume

Fig. 2 Water absorption rate of SSA sample for 24 h submersion taken at 7 and 28 days
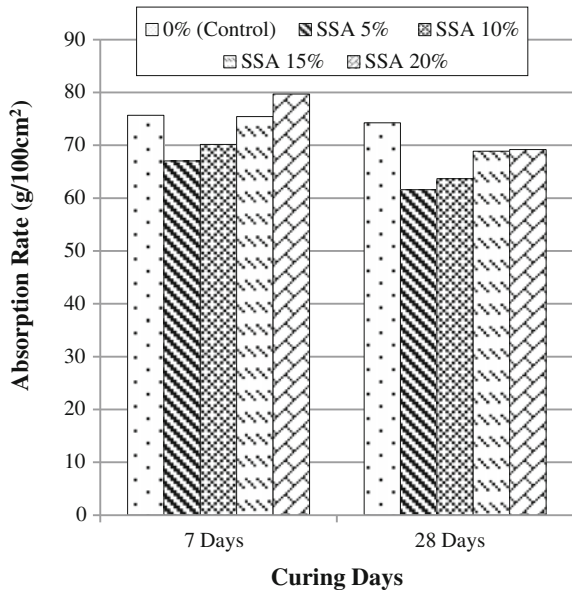
Fig. 3 Water absorption rate
of SSA mortar taken at
28 days
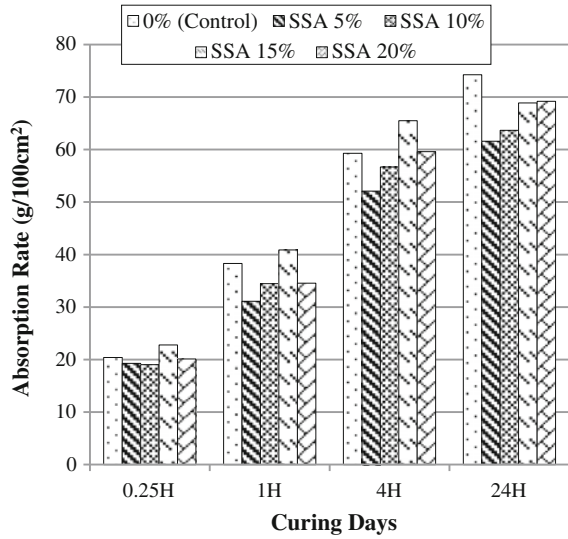
of mortar sample decreasing over the time. By looking at the result pattern among
SSA mortar, the absorption rate rises as the percentages of SSA increased. This
similar pattern was also found by Valls et al. [17] in his study on concrete sludge.
This can be explained, as more SSA been used in mortar mixed, the capacity to
absorb water will increase. This might be due to the certain increase of the voids
inside the mortar sample.

Referring to the findings at 28 days age of curing, the absorption rate of all SSA
mortar sample which had been immersed in water for 24 h are slightly lower as
compared with the control mortar. This explained that SSA has high resistance
against durability. Moreover, at 28 days curing, the SSA5% had recorded the lowest
rate of water absorption among all the SSA mortar including control mortar. The
rate of SSA5% mortar at age 28 days is 61.6 g/100 cm^2, as compared to the control
mortar which is 74.24 g/100 cm^2.

The water absorption rates of SSA mortar at 28 days are as shown in Fig. 3. This
data analyzes the absorption rate of mortar sample at T (time) taken on 15 min, 1, 4,
and 24 h of sample immersion in the water. The results had showed that the water
absorption rates for all mortar samples are increased relatively over time. These
results demonstrated that the water absorption rate for SSA5%, SSA10%, and
SSA20% mortar lie under the line of normal mortar sample, which implies that the
SSA mortar for 5, 10, and 20 % had the lower value of absorption rate. In contrary,
within the 4 h immersed in water, it is notice that absorption rate of the SS15%
mortar lies above the normal mortar line. However, after 24 h immersion, the data
recorded for this SSA15% mortar is slightly lower than the absorption rate value for
normal mortar. Hence, it simplifies that the SSA mortar has lower rate of water
absorption, thus higher resistance in term of its durability.

4 Conclusion

From this study, it is suggested that the sewage sludge ash (SSA) has the potential to be used as partial replacement for Portland cement. By conducting the major mechanical and durability properties test, the substitutions of SSA into the mixture of mortar will enhance the strength and absorption rate of the mortar. The results of this study are outlined as follows;

1. The compressive strength of SSA mortar increased as age of curing increased, from 7 to 28 days. Moreover, all the SSA (5–20 %) mortar executed higher strength value compared to the control mortar at 28 days of curing. The SSA10 % had demonstrated the highest value of compressive strength, 62.84 MPa at age 28 days. Even though the further increase of SSA in mortar reduces the compressive strength, the value at 20 % replacement is still above the control mortar strength.
2. The water absorption rate of SSA mortar decreased as the age of curing increased from 7 to 28 days. The lower rate of water absorption can be seen in all SSA (5–20 %) mortar as compared to the control mortar at curing age 28 days. From the study, 5–10 % replacement of SSA in mortar can be considered as having lower water absorption.

References

1. Tay, J.H., and Show, K.Y., (1992), Utilization of Municipal Wastewater Sludge As Building and Construction Materials, *Resources, Conservation and Recycling Journal*, Volume 6, 191–204.
2. Donatello, S., and Cheeseman, C. R., (2013), Recycling and Recovery Routes for Incinerated Sewage Sludge Ash (ISSA): A Review, *Waste Management Journal*, http://dx.doi.org/10.1016/j.wasman.2013.05.024.(in press).
3. Vijaya, K. K., (2012), Utilisation of Sludge Concrete in Paver Blocks, *International Journal of Emerging Trends in Engineering and Development*, Issue 2, Volume 4, 509–516.
4. Yen, C. L., Tseng, D. H., and Lin, T. T., (2011), Characterization of Eco-Cement Paste Produced from Waste Sludges, *Chemosphere Journal*, Volume 84, 220–226.
5. Chiang, K. Y., Chou, P. H., Hua, C. R., Chien, K. L., and Cheeseman, C., (2009), Lightweight Bricks Manufactured From Water Treatment Sludge and Rice Husks, *Journal of Hazardous Materials*, Volume 171, 76–82.
6. Tay, J.H., (1987), Bricks Manufactured From Sludge, *Journal of Environmental Engineering*, Volume 113, 278–284.
7. Weng, C. H., Lin, D. F., and Chiang, P. C., (2003), Utilization of Sludge as Brick Materials, *Advances in Environmental Research Journal*, Volume 7, 679–685.

8. Bhatty, J. I., and Reid, K. J., (1989), Moderate Strength Concrete from Lightweight Sludge Ash Aggregates, *The International Journal of Cement Composites and Lightweight Concrete*, Volume 11, No. 3, 179–187.

9. Chesseman, C. R., and Virdi, G. S., (2005), Properties and Microstructure of Lightweight Aggregate Produced from Sintered Sewage Sludge Ash, *Resources, Conservation and Recycling Journal*, Volume 45, 18–30.

10. Tay, J. H., Yip, W. K., and Show, K. Y., (1991), Clay-Blended Sludge as Lightweight Aggregate Concrete Material, *Journal of Environmental Engineering*, Volume 117, No. 6, 834–844.

11. Lin, D. F., Luo, H. L., and Zhang, S. W., (2007), Effect of Nano-SiO$_2$ on Tiles Manufactured with Clay and Incinerated Sewage Sludge Ash, *Journal of Materials in Civil Engineering*, Volume 19(10), 801–808.

12. Garcés, P., Carrión, M. P., García-Alcocel, E., Payá, J., Monzó, J., and Borrachero, M. V., (2008), Mechanical and Physical Properties of Cement Blended with Sewage Sludge Ash, *Waste Management Journal*, Volume 28, 2495–2502.

13. Lin, K. L., Chang, W. C., Lin, D. F., Luo, H. L., and Tsai, M. C., (2008), Effect of nano-SiO$_2$ and Different Ash Particle Sizes on Sludge Ash-Cement Mortar, *Environmental Management Journal*, Volume 88, 708–714.

14. Monzó, J., Payá, J., Borrachero, M. V., and Córcoles, A., (1996), Use of Sewage Sludge Ash (SSA)– Cement Admixtures in Mortars, *Cement and Concrete Research Journal*, Volume 26 (9), 1389–1398.

15. Pan, S. C., Tseng, D. H., Lee, C. C., and Lee, C., (2003), Influence of Fineness of Sewage Sludge Ash on the Mortar Properties, *Cement and Concrete Research Journal*, Volume 33, 1749–1754.

16. Tay, J.H., and Show, K.Y., (1994), Municipal Wastewater Sludge as Cementitious and Blended Cement Materials, *Cement & Concrete Composite Journal*, Volume 16, 39–48.

17. Valls, S., Yagüe, A., Vázquez, E., and Mariscal, C., (2004), Physical and mechanical properties of concrete with added dry sludge from a sewage treatment plant, *Cement and Concrete Research*, Volume 34, 2203–2208.

18. Lin, K. L., and Lin, C. Y., (2005), Hydration Characteristics of Waste Sludge Ash Utilized as Raw Cement Material, *Cement and Concrete Research Journal*, Volume 35, 1999–2007.

19. Tantawy, M. A., El-Roudi, A. M., Abdalla, E. M., and Abdelzaher, M. A., (2012), Evaluation of the Pozzolanic Activity of Sewage Sludge Ash, *ISRN Chemical Engineering*, Volume 2012, 1–8.

20. American Society for Testing and Material, ASTM C109-13. Compressive Strength of Hydraulic Cement Mortars. *ASTM International*, West Conshohocken, Pa.

21. American Society for Testing and Material, ASTM C1403 (2013). Standard Test Method for Rate of Water Absorption of Masonry Mortars. *ASTM International*, West Conshohocken, Pa.

22. Monzó, J., Payá, J., Borrachero, M. V., and Girbés, I., (2003), Reuse of Sewage Sludge Ashes (SSA) in Cement Mixtures: the Effect of SSA on the Workability of Cement Mortar, *Waste Management Journal*, Volume 23, 373–381.

23. Yen, C. L., Tseng, D. H., and Lin, T. T., (2011), Characterization of Eco-Cement Paste Produced from Waste Sludges, *Chemosphere Journal*, Volume 84, 220–226.

24. American Society for Testing and Material, ASTM C618-12a. Standard Specification for Coal Fly Ash and Raw or Calcined Natural Pozzolan for Use in Concrete. *ASTM International*, West Conshohocken, Pa.

Comparison of Seismic Performance Between Interior Beam-Column Joint Designed Using BS8110 and Eurocode 8

N.D. Hadi, A.G. Kay Dora and N.H. Hamid

Abstract This paper investigates the seismic performance differences between interior beam-column joint which designed with BS8110 and Eurocode 8 of a two-storey precast school building. Both specimens were designed, constructed and tested under in-plane lateral cyclic loading. Subsequent to testing, the interior beam-column joint designed using BS8110 experienced diagonal shear cracks at top of column while the joint designed using EC8 only suffered hairline cracks at beam-column interface. Overall seismic performance comparison shows that beam-column joint designed with EC8 has higher in-plane lateral strength, lateral displacement, stiffness, ductility and equivalent viscous damping than joint beam-column joint designed with BS8110. The maximum drift achieved by seismic joint is 2.25 % and non-seismic joint has maximum drift of 1.15 %. It can be concluded that the seismic joint has perform better than non-seismic joint due to the fact that more percentage of longitudinal and transverse reinforcement were used in seismic joint.

N.D. Hadi (✉) · N.H. Hamid
Faculty of Civil Engineering, Universiti Teknologi MARA Shah Alam,
40450 Shah Alam, Selangor, Malaysia
e-mail: farhanadiyana88@gmail.com

N.H. Hamid
e-mail: norha454@salam.uitm.edu.my

A.G. Kay Dora
Faculty of Civil Engineering, Universiti Teknologi MARA Pulau Pinang,
13500 Permatang Pauh, Pulau Pinang, Malaysia
e-mail: kaydora@ppinang.uitm.edu.my

1 Introduction

Up to date, most of the precast and conventional RC buildings in Malaysia were designed using BS8110 where there is no provision for seismic loading at all. There are many reinforced concrete code of practice that has been developed in countries experiencing major earthquake event. Some examples of current seismic code of practices available such as Eurocode 8, NZS3101 and ACI318-08 have included the partial safety factor for earthquake loading together with dead load and imposed load. Malaysia, Singapore and Thailand are susceptible to earthquakes from Sumatera and Philippines which located within the region of "Pacific Ring of Fire".

These earthquakes can also induce seismicity to the sleeping fault lines which located in Peninsular and East Malaysia. Bukit Tinggi Fault, Kuala Lumpur Fault and Lebir Fault are among of the many sleeping fault lines that contributed to earthquakes in Peninsular Malaysia. Some examples for the most recent near field earthquake that took place in Malaysia are the 2015 Ranau Earthquake, 2012 Mersing Earthquake and the 2008 Bukit Tinggi Earthquake with magnitude between 2.5 to 6.0 scale Richter.

Reinforced concrete buildings which are designed using British Standard (BS8110) are vulnerable to earthquake excitations where the failures of beam-column joint were observed in recent 2015 Ranau Earthquake. Some studies on exterior beam-column joint [1], interior beam-column joint [2], double unit tunnel form building [3], wall-slab joint of tunnel form building [4] and precast shear key wall panel [5] which were designed using BS 8110 had suffered severe damages, cracks, spalling of concrete cover and buckling of reinforcement bars. Visual observation on structural damages during experimental work, results of testing and analysis show that the non-seismic structures indicates vulnerability to lateral cyclic loading. This vulnerability includes the soft story mechanism. Soft story mechanism occurs as a result of inadequate transverse reinforcement in the joint and weak-column/strong-beam design [6].

In Eurocode 8: Part 1 BS EN1998-1:2004 (EC8), beam-column joint is the main point where the vertical load from the column and lateral load from beam meet before these loads transfer to the foundation beam. Ductile column is required to resist lateral load which comes from earthquake and apply the strong column-weak beam capacity design. In New Zealand, the advantage of using the concepts of weak-beam/strong-column design is acknowledged since the seventies [7]. Therefore, the intention of this study is to investigate the seismic behavior of interior beam-column seismic joint with fuse bars designed using EC8 and tested under in-plane lateral cyclic loading. The seismic performance of seismic joint will be compared with the non-seismic joint which designed to BS8110 [2]. By conducting the experimental work in the laboratory, it is expected that seismic joint will survive and perform better under earthquake excitations and remain functional post-earthquake excitations. Previous study on precast hollow core wall [8, 9] and reinforced concrete frame [10, 11] using EC8 showed excellent performance under

earthquake loading. Therefore, seismic performance of the interior beam-column joint designed using BS8110 will be compared to seismic performance of interior beam-column joint designed using EC8 in terms of lateral strength, stiffness, ductility and equivalent viscous damping.

2 Construction of Specimens

The seismic beam column joint was designed according to EC8 while the non-seismic beam column joint was designed according to BS8110 [2]. Both specimens consist of two in-plane beams and one out-of-plane beam anchored to the column. For EC8, the reinforcement bars near the joint were replaced with fuse bars and connected using bar-break coupler. The bar-break couplers replace the conventional lap splicing near the joint while fuse bars will act as energy dissipator and lessen the damage on beam-column joint. Some of the main advantages on the usage of fuse bars include good performance in dissipating energy, replaceable as well as providing high lateral resistance in the structure [9]. Figure 1 shows the reinforcement detailing for interior beam-column joint designed to EC8.

3 Specimens for Testing

Both specimens were constructed in Heavy Structural Laboratory, Faculty of Civil Engineering, UiTM Shah Alam. Nine numbers of LVDTs were used to measure the in-plane lateral cyclic loading. The first set of drift started at ±0.01 % and followed by ±05, ±0.1, ±0.25, ±0.5, ±0.75, ±1.0 and ±1.15 %. Two cycles of loading were imposed for each drift.

Figure 2 shows the experimental setup for interior beam-column joint which designed using EC8. The specimen consists of two beams (3500 × 40 × 40 mm) and the column (3500 × 40 × 40 mm) was constructed vertically on top of foundation beam. The drift started with ±0.01, ±0.05, ±0.1, ±0.22, ±0.5, ±0.75, ±1.0, ±1.25, ±1.50, ±1.75, ±2.0, ±2.25 and ±2.5 %. A total number of nine LVDTs were placed on seismic beam-column joint specimen to measure the lateral displacement and uplift of the foundation beam.

4 Visual Observation of Damages

Figure 3a, b illustrate the diagonal shear crack experienced by non-seismic joint at top of the column. During testing, the crack propagation patterns were observed for every increment of ±0.25 % drift. The in-plane lateral load was applied to the top of
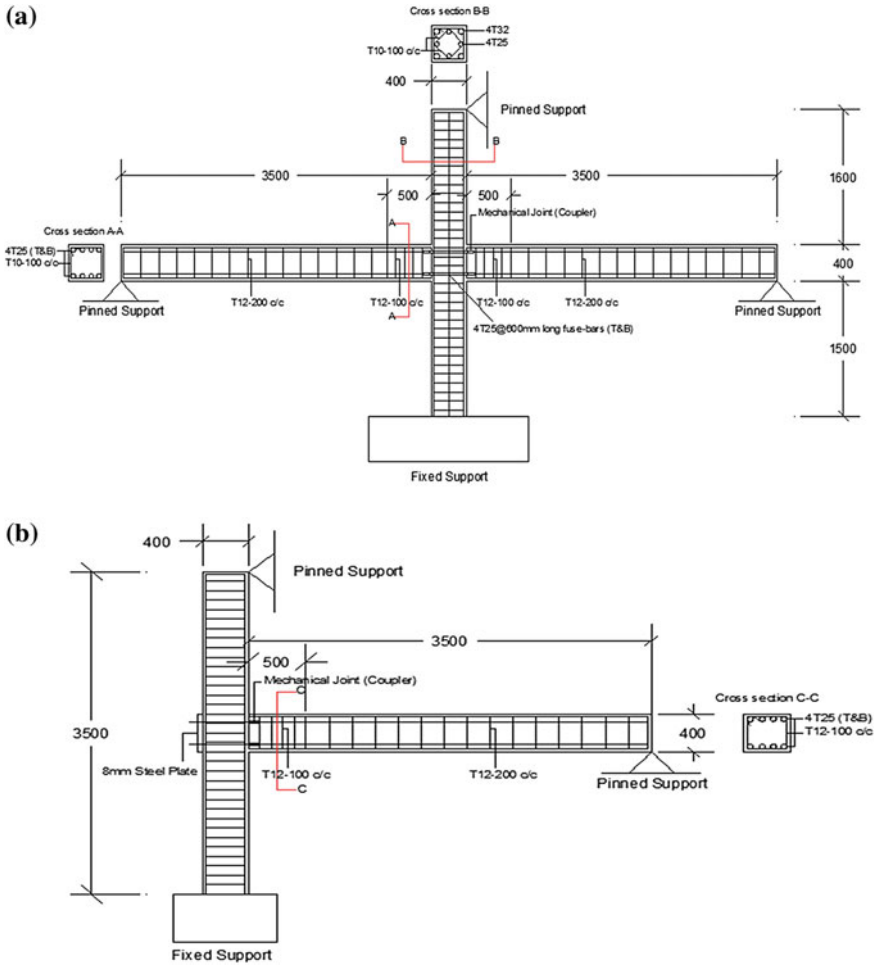
Fig. 1 Reinforcement detailing for interior beam-column joints **a** front view; **b** side view

Fig. 2 Experimental setup
and location of LVDTs on
interior beam-column joint
designed to EC8
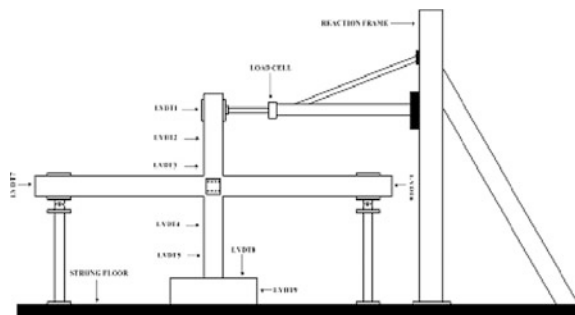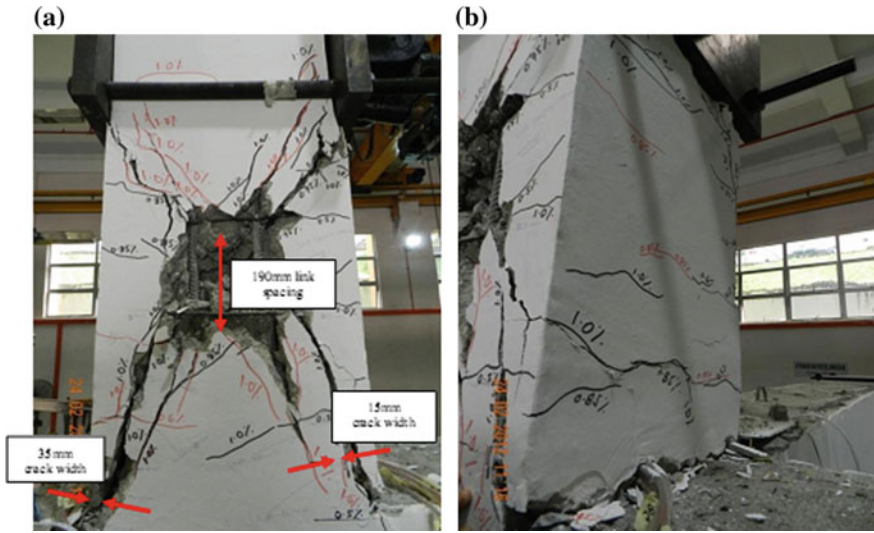
Fig. 3 *Diagonal* shear cracks occurred at *top* of the column for non-seismic joint **a** front view; **b** side view

column using double actuator. The non-seismic joint was tested up to ±1.15 % drift before the specimen experienced strength degradation. Cracks were observed at lower drift such as 0.25 % drift and more cracks were observed as the percentage increases. Shear cracks formed at the upper column and at the bottom column particularly below the corbels. Loading and unloading results in larger gap opening in between surface of corbel and beam and leads to spalling of concrete cover at top of corbel. Finally, the longitudinal bars were buckled and soft-story mechanism occurred for non-seismic joint.

Figure 4a, b exhibit the visual damage observation of beam-column joint during experimental work which designed using EC8 and labeled as seismic joint. Detailed visual observation was carried out after testing and severe diagonal cracks were observed at the upper part of column near the joint and no structural cracks such as diagonal and flexural crack occurred on the beams. The specimen behaves elastic from ±0.01 % until ±0.5 % for every successive cycle. At ±0.5 % drift, the specimen entered the inelastic region and become less stiff. The seismic joint experienced maximum drift at ±2.5 % drifts which is higher than non-seismic joint. Some of horizontal cracks were also observed at beam-column interface as the percentage of drift increases.
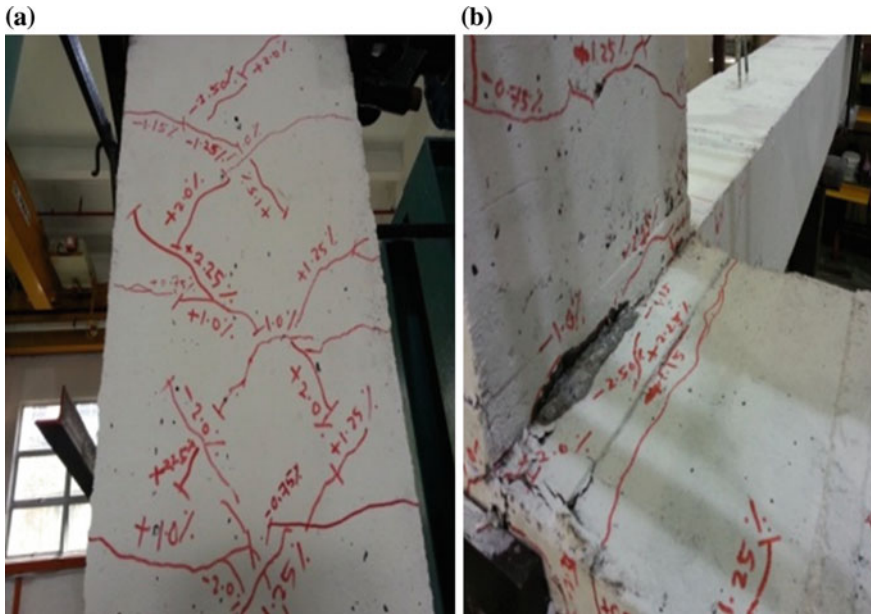
Fig. 4 Visual observation of damages for the seismic interior joint **a** *diagonal* cracks on the surface of *top* column; **b** *horizontal* cracks at column-beam interface

5 Experimental Results and Discussions

5.1 *Hysteresis* Loops and Lateral Strength

Hysteresis loop is used to measure the behavior of structure starting from elastic range until inelastic range. It can be obtained by plotting the graph of load vs displacement from loading and unloading branch to complete one cycle of movement which data gathered from the data logger. From the hysteresis loop, the parameters such as lateral strength capacity, stiffness, ductility and equivalent viscous damping can be determined. In this paper, only the experimental results from LVDT1 were analyzed.

Figure 5 shows the hysteresis loops of non-seismic joint measured using LVDT1 located at top of the column when tested under in-plane lateral cyclic loading. The drift was started from ±0.01 % drift up to ±1.15 % drift where the specimen lost its lateral strength. The maximum lateral load was recorded at 130 kN when ±1.0 % drift applied to the specimen. The backbone of the lateral strength curve shows that non-seismic joint was brittle and easily to collapse once it reached the maximum lateral load. The non-seismic joint can only resist minor earthquake and cannot resist moderate or severe earthquake.
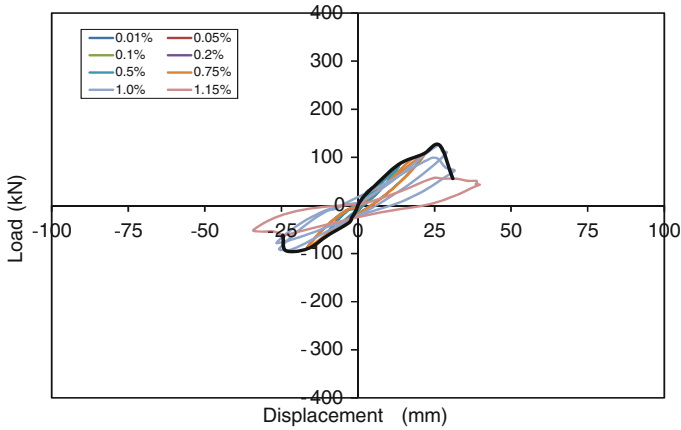
Fig. 5 Hysteresis loops for non-seismic joint

Figure 6 shows the hysteresis loops of the seismic joint which designed according to Ductility Class Medium (DCM) in EC8 by considering the Peak Ground Acceleration of 0.3 g. The specimen was tested under in-plane lateral cyclic loading staring from ±0.01 % drift until ±2.25 % drift with incremental of ±0.25 % drift. The specimen can sustain the lateral load up to ±2.25 % drift with a significant increase in stiffness and ductility before undergo strength degradation from ±2.25 to ±2.5 % drift. The inelastic behavior of the specimen was analyzed. The specimens undergo linear behavior starting from 0.01 to 0.75 % drift and inelastic range from 0.75 % until 2.5 % drift. The seismic joint reached the ultimate lateral load at 301.58 kN at 2.25 % drift and strength degradation starts at 2.25 % drift until 2.5 %
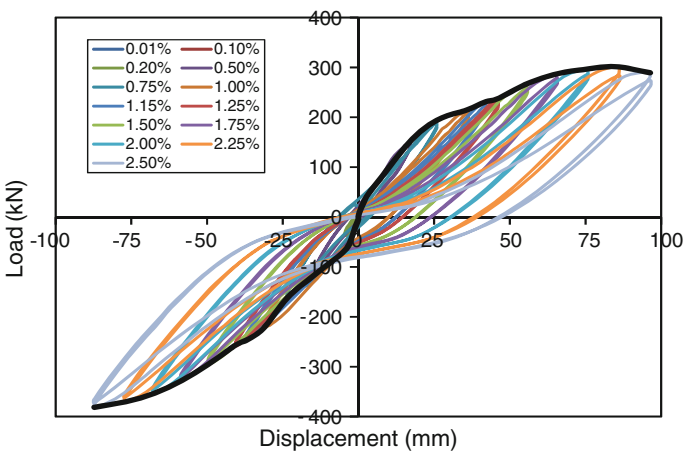
Fig. 6 Hysteresis loops for seismic joint designed using EC8

drift which is two times higher than non-seismic joint at 1.0–1.15 % drift with ultimate load of 130 kN. The values of yield load, yield displacement, ultimate load and ultimate displacement are used to calculate the stiffness and displacement ductility.

5.2 Stiffness

Stiffness is ratio of the force required to the specified deflection. Stiffness values in the positive and negative direction were determined by dividing the maximum load reached within a cycle by the corresponding displacement. Generally, the stiffness value decreases as the target drift increases. Figure 7 shows the stiffness degradation of non-seismic joint designed using BS8110 labeled as blue line and seismic joint designed using EC8 labeled as red line. Generally, the trend of stiffness decreases for both specimens. The stiffness for non-seismic joint starts at 19.56 kN/mm and decreased to 3.15 kN/m m where specimen demonstrates a nonlinear performance starting from ±0.75 % drift. Whereas the seismic joint in pushing direction has lower values at first cycle as compared to second cycle. The stiffness begins at 37.8 kN/mm and further decreased to 0.53 kN/mm. This is due to the high percentage of longitudinal reinforcement bars and cross ties provided in the column which contribute to higher stiffness in seismic joint as compared to non-seismic joint.
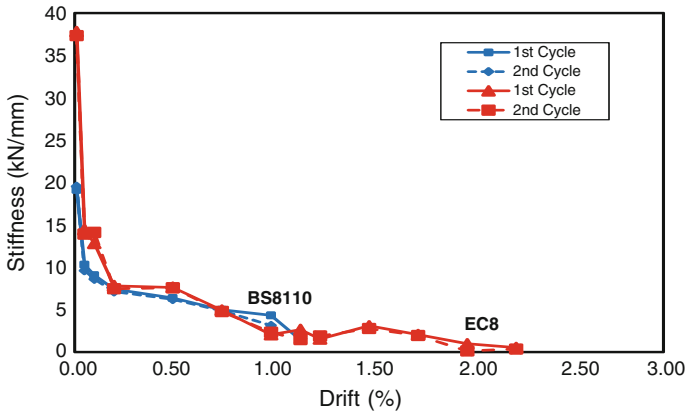
Fig. 7 Comparison of stiffness between seismic and non-seismic joint

5.3 Displacement Ductility

Displacement ductility can be calculated by taking the ratio of target displacement divide by the yield displacement. The displacement ductility of non-seismic joint at 1.15 % drift in the pushing direction is 1.99 while for seismic joint at 2.5 % drift is 3.76 as shown in Fig. 8. The experimental results proved that the seismic joint which designed using Eurocode 8 has higher displacement ductility and achieved DCM as compared to non-seismic joint as designed according to BS8110. It seems that the second cycle is more ductile than the first cycle. At ±1.15 % drift, the ductility value for pulling direction is higher than in pushing direction.

5.4 Equivalent Viscous Damping

The hysteresis energy dissipation is measured by equivalent viscous damping for a system under hysteretic behavior. Equivalent Viscous Damping (ξ_{eq}) is the ratio derived based on equating the total energy dissipated in the system to the sum of the energy dissipated by its individual members [12]. Equation 1 is used to calculate the equivalent viscous damping (ξ_{eq}) for each cycle based on the derivation obtained from Chopra [13]:

$$\xi_{eq} = \frac{1}{4\pi}\frac{E_D}{E_{so}} \tag{1}$$
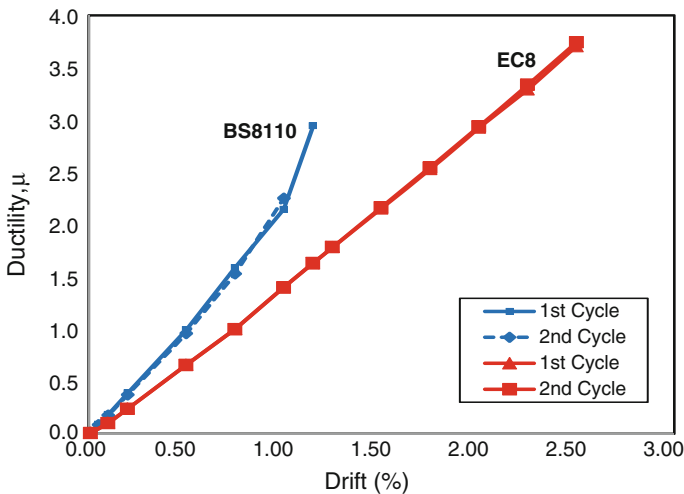
Fig. 8 Comparison of displacement ductility between seismic and non-seismic joint

where E_D, is the area enclosed by the hysteresis loops and E_{SO} is the area under the equivalent linear hysteresis curve.

Figure 9 shows the comparison of equivalent viscous damping between the non-seismic joint and seismic joint. The equivalent viscous damping is higher in the first cycle as compared to the second cycle because more energy is dissipated during first cycle to resist the elastic stiffness as compared to the second cycle. Furthermore, the energy absorption occurred in the first cycle leads to the smaller enclosed area of the hysteresis loop in the second cycle. However, the second cycle at ±1.0 % drift has higher value of equivalent viscous damping for non-seismic joint as compared with seismic joint. At this point, the non-seismic joint is experiencing a major crack upper part of the column. Therefore, there is a sudden increases of energy stored in joint is fully dissipated. Similar pattern occurred in seismic joint where the graph generally decreases for both cycles during the first part of the test to a minimum value corresponding to the lateral resistance provided. For the first cycle, the equivalent viscous damping for specimen starts to increase at 1.0 % drift up to failure at 2.50 % drift while for the second cycle it is start to increase at 0.75 % drift until failure at the same drift at 2.50 %. It also shows better energy dissipation capacity of specimen as well as better seismic behavior.
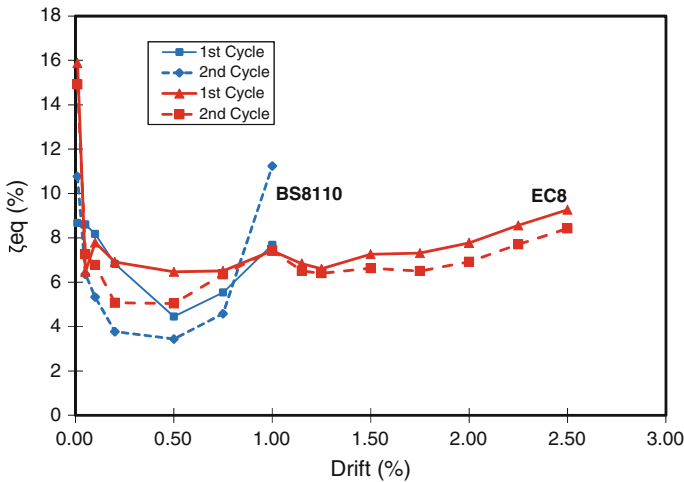
Fig. 9 Comparison of equivalent viscous damping between non-seismic and seismic joint

6   Conclusions and Recommendations

Based on the visual observation, results and data interpretation, the following conclusion can be drawn:

1. Interior beam-column joint designed using EC8 was able to sustain load up to 301.58 kN at 2.25 % drift before failing while interior beam-column joint designed using BS8110 was only able to sustain load up to 130 kN at 1.15 % drift.
2. Large crack opening experienced by column which designed using BS8110 as compared to EC8 due to the large spacings in between transverse reinforcement.
3. The overall seismic performance of the interior beam-column joint designed using EC8 has high lateral strength, stiffness, ductility, equivalent viscous damping as compared to interior beam-column joint designed using BS8110 at 2.5 % drift compared to BS8110 at 1.15 % drift.
4. It is recommended that the reinforced concrete buildings to be developed in medium seismic regions to adopt EC8 code of practise under Ductility Class Medium for reinforced concrete design since it has been proven to have displacement ductility of four through experimental work in Heavy Structural Laboratory.

References

1. A.G. Kay Dora and A. H. Nor Hayati, "Experimental Investigation on a non-seismic precast RC beam-column exterior joint under quasi-static lateral cyclic loading", Safety and Seismic Engineering V, Vol. 134, WIT Press, pp 827–837, 2013.
2. A.G. Kay Dora and A.H. Nor Hayati, "Experimental Investigation on Non-Seismic Precast Beam-Column Interior Joint Subjected to Lateral Cyclic Loading", ISBN No: 978–602-8605-08-3, pp. 1–8, 2013[Proceeding the 6th Civil Engineering Conference in Asia Region: Embracing the Future through Sustainability.
3. A.H. Nor Hayati, M.S. Saleha and A. Shamilah. "Seismic Performance Of Double-Unit Form Building Under In-Plane Lateral Cyclic Loading", Structures Under Shock and Impact XIII, Vol. 141, ISSN No: 1743–3509, pp 467–472, 2014.
4. A.H. Nor Hayati and M.M. Ashaari "Seismic Performance Of Wall-Slab Joints In Industrialized Building System (IBS) Under Out-Of-Plane Reversible Cyclic Loading", IACSIT International Journal of Engineering and Technology, Vol. 4, No.1, pp 26–33, 2012.
5. T.L.Y. Patrick. A. Azlan and A.H. Nor Hayati "Behaviour Factor And Displacement Estimation Of Low-Ductility Precast Wall System Under Seismic Actions", Earthquakes and Structures, Vol. 5, Issue 6, Techo-press, pp 625–655, 2013.

6. G. Ahmed and A. Said "Shear-Strengthening Of Beam-Column Joint" Journal of Engineering Structures, 24 (1), p.881–888, 2002.
7. P. Robert and P. Thomas, "Reinforced Concrete Structures", ISBN No-10: 0471659177, Publisher John Wiley and Sons, New York. 1975.
8. A.H Nor Hayati, " Seismic Damage Avoidance Design of Warehouse Buildings Constructed Using Precast Hollow Core Walls ", PhD Thesis, Department of Civil Engineering, University of Canterbury, Christchurch, New Zealand, 2006.
9. A.H. Nor Hayati and M. John. "Lateral Seismic Performance of Multipanel Precast Hollowcore Walls." Journal of Structural Engineering, *ASCE,* Vol.136, Issue 7, pp. 795–804. 2010.
10. E.C. Carvalho, C Ema and M.N. Fardis "Assessment of EC8 Provisions for Reinforced Concrete Frames", Paper No. 2049, 1996 [Eleventh World Conference on Earthquake Engineering].
11. A.B. Carlos and M.J.N. Priestley, "Equivalent Viscous Damping Equation For Direct Displacement Based Design", Journal of Earthquake Engineering, Vol. 9(2), pp257–278, 2005.
12. B.P. Telemachos and N.F. Michael "Seismic Performance Of RC Frames Designed To Eurocode 8 Or To The Greek Codes 2000". Bulletin of Earthquake Engineering, 2 (1), p.221–259, 2004.
13. K.C. Anil. "Dynamics of Structures: Theory and Applications to Earthquake Engineering", 4th Edition, Prentice Hall, Englewood Cliffs, New Jersey, 2012.

Rubberized-PET and Rubberized-Coconut Shell as Fine Aggregate in Concrete

A.R. Norhana, K. Kartini and M.S. Hamidah

Abstract Worldwide wastes of plastic bottles which are also known as poly-ethylene terephthalate (PET), rubber tyres and coconut shells increase due to its large scale production, high demand in scale revolution and also disposal problems encountered. This is an environmental issue as waste plastic bottles, tyre rubber and coconut shell are difficult to biodegrade and involve processes either to recycle or reuse. The choice of these waste materials to be used as aggregates replacement is very essential as their characteristics give benefits to the performances of concretes. This paper reported the study carried out on the suitability of the polyethylene terephthalate (PET), rubber crumb and coconut shell as fine aggregate replacement in concrete. The performances of the concretes were assessed through its com-pressive strength and water absorption. In this study the fine aggregate was replaced by PET, rubber crumb and coconut shell at 10, 20 and 30 % by weight of binder and tested for 7, 28 and 60 days of curing. The overall compressive strength of concrete decreased when fine aggregate was replaced with PET, rubber crumb, coconut shells and rubber crumb with either PET or coconut shells. The results showed that by increasing the replacement of PET in higher proportion (up to 15 %), rubber crumb (up to 10 %) and coconut shells (up to 20 %), the compressive strength of concretes decreased, while the water absorption of concretes increased with the increase of PET, rubber crumb and coconut shell replacements. However, generally it can be concluded that the PET, rubber crumb and coconut shell can be utilized in replacing fine aggregates in concrete production.

Keywords Polyethylene terephthalate (PET) · Rubber crumb · Coconut shell · Fine aggregate · Compressive strength · Water absorption

A.R. Norhana (✉) · K. Kartini (✉) · M.S. Hamidah
Faculty of Civil Engineering, Universiti Teknologi MARA, Shah Alam, Malaysia
e-mail: ann_trace@yahoo.com

K. Kartini
e-mail: ce_kartini2002@yahoo.com

1 Introduction

In recent years, one of the most crucial environmental issues talked about all around the world is the disposal problems of waste materials either from the industrial by-products and agricultural. The growing amount of the waste materials resulted in environmental problems and represents a waste of useful resources. Thus, the modification of concrete properties by the addition of appropriate materials becomes popular in concrete research nowadays. It is attributed to factors such as versatility, ease of raw materials obtainment, low cost, ease of fabrication, high mechanical strength, impermeability to water, great durability and for sustainability [1]. Previous researches [2–6] showed that the use of waste materials and by-product as substitution in concrete is becoming more popular. According to the past researches [7–9], the successful utilization of these materials gave benefits to reduction of environmental load, cost of concrete production and waste management cost, besides improving the properties of the concrete. Industrial by-products and agricultural wastes should be considered as potentially valuable resources merely awaiting appropriate treatment and applications. In responding to these matters, this study focuses on utilization of polyethylene terephthalate (PET), rubber crumb (RC) and coconut shell (CS) as an alternative material for partial replacement of fine aggregate with the objective to determine the optimum replacement of PET, RC and CS to fine aggregate in making concrete.

2 Experimental Method

2.1 Material Preparations

The PET was obtained from Jupiter Previlege Sdn Bhd, North Port Klang. It is a residue produced from shredded plastic bottles. The size of PET used was up to 5 mm. The RC was obtained from Yong Fong Rubber Industries, Port Klang. This RC is manufactured by special mill where scrap rubber tyre is ground and screened into smaller particles. The RC used was up to 5 mm. The CS was obtained from local sources mainly from market. The CS was dried in open air for 7 days approximately with the temperature of 25–30 °C in order to remove moisture content and copra residual. The half part of CS is then crushed into small pieces which are approximately 5–6 pieces manually by using hammer prior to grinding process. These materials used in this study were sieved with maximum size of 5 mm sieve.

The other materials used in the concrete mixture were ordinary portland cement (OPC) type 1. The fine aggregate used was mining sand with maximum size of 5 mm, while the coarse aggregate used was crushed granite passing through 20 mm and retained on 10 mm sieve. Sodium hydroxide (NaOH) was used in this study to increase the hydrophilicity of the rubber particle surface. The RC was soaked into 0.1 N NaOH for 20 min. The rubber was filtered and air dried at ambient

temperature before adding into the concrete mixture. The tap water which is free from contamination was used for the mixing and curing purposes.

2.2 Mix Proportions

In brief, the strength behaviour of PET concrete, RC concrete, CS concrete, rubberized-PET and rubberized-coconut shell concretes were assessed by compressive strength test and the durability behaviour was assessed by water absorption test. Twenty eight series of blended specimens which comprises of three different replacement levels of PET, RC and CS, that are 10, 20 and 30 % were prepared using 0.5 w/b ratio. The series for 10, 20 and 30 % replacement of fine aggregate with PET, RC and CS were designated as 10P, 20P, 30P, 10R, 20R, 30R, 10C, 20C and 30C, respectively. The concrete mix was designed by using DOE method [10]. Summary of concrete mix design for control mix, PET concrete, RC concrete, CS concrete, rubberized-PET concrete and rubberized-CS concrete are shown in Table 1.

The amount of water added was kept constant to ensure its consistency. For the use of other materials , the amount depends on the replacement of PET, RC and CS to fine aggregate.

2.3 Sample Preparations

Size of cube specimens were $100 \times 100 \times 100$ (mm^3) for compressive strength test, while for water absorption test the cylindrical specimen 50×100 mm were used. All concrete specimens were placed in water curing tank at room temperature and the specimens were taken out for testing at 7, 28 and 60 days. The method and procedure used for curing are in accordance to BS 1881: Part 111: 1983 [11].

3 Test Methods

3.1 Sieve Analysis

The British Standard BS 812-103:1:1985 [12] was used in determining the particle size distribution of fine and coarse aggregates. The grading curves of the fine and coarse aggregate conform and satisfied the grading requirement of BS EN 12620:2002 [13]. This is important as well graded aggregates can reduce the quantity of water and cement in concrete mix, whereby the smaller particle can fill the voids between the large particles. The fineness modulus of fine aggregate

Table 1 Mix proportion of PET, RC and CS in concrete

Mixes	Cement (kg/m^3)	Water (kg/m^3)	CA (kg/m^3)	FA (kg/m^3)	PET (kg/m^3)	RC (kg/m^3)	CS (kg/m^3)
Control	380	190	1190	670	–	–	–
10P	380	190	1190	603	67	–	–
20P	380	190	1190	536	134	–	–
30P	380	190	1190	469	201	–	–
10R	380	190	1190	603	–	67	–
20R	380	190	1190	536	–	134	–
30R	380	190	1190	469	–	201	–
10C	380	190	1190	603	–	–	67
20C	380	190	1190	536	–	–	134
30C	380	190	1190	469	–	–	201
10P10R	380	190	1190	536	67	67	–
20P10R	380	190	1190	469	134	67	–
30P10R	380	190	1190	402	201	67	–
10C10R	380	190	1190	536	–	67	67
20C10R	380	190	1190	469	–	67	134
30C10R	380	190	1190	402	–	67	201
10P20R	380	190	1190	469	67	134	–
20P20R	380	190	1190	402	134	134	–
30P20R	380	190	1190	335	201	134	–
10C20R	380	190	1190	469	–	134	67
20C20R	380	190	1190	402	–	134	134
30C20R	380	190	1190	335	–	134	201
10P30R	380	190	1190	402	67	201	–
20P30R	380	190	1190	335	134	201	–
30P30R	380	190	1190	268	201	201	–
10C30R	380	190	1190	402	–	201	67
20C30R	380	190	1190	335	–	201	134
30C30R	380	190	1190	268	–	201	201

obtained was 3.45 which describes that the fine aggregates were mainly of 600 μm size. The fineness modulus of the coarse aggregate is found to be 3.26. It means that the coarse aggregate used in this study is an average size of 14 mm.

3.2 Slump Test

Slump test on the fresh concrete was conducted to determine the workability of the concrete which was in accordance to BS EN 12350-2:2000 [14]. The slump values obtained were shown in Fig. 1.
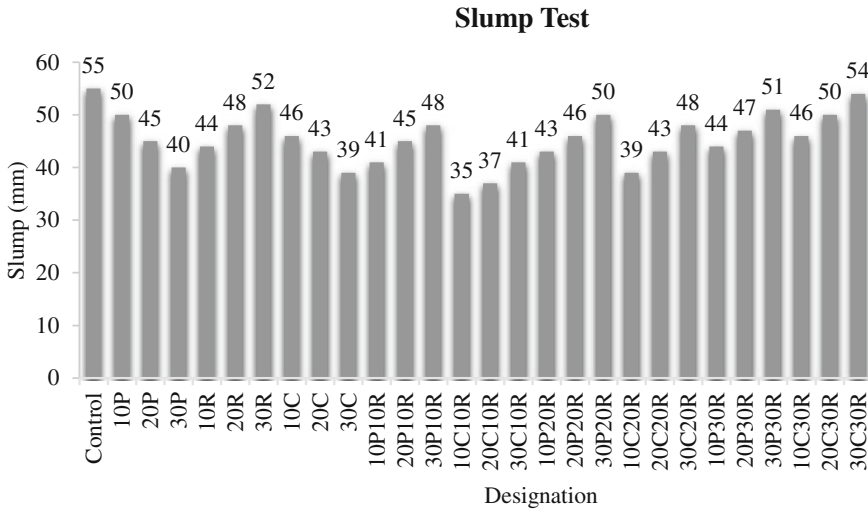
Fig. 1 Slumps for control, PET, RC, CS, rubberised-PET and rubberized-coconut shell fresh concretes

3.3 Compressive Strength

The compressive strength test on specimens of 100 mm^3 was conducted on the control, PET, RC, CS, rubberized-PET and rubberized-coconut shell concretes as in accordance to BS EN 12390-4:2000 [15]. The test was conducted on the cube specimens taken at ages of 7, 28 and 60 days of water curing.

3.4 Water Absorption

The measurement of the water absorption was determined based on BS 1881-122:2011 [16]. At the age of 7, 28 and 60 days, the cylindrical specimens of 50 Ø by 100 mm height were oven dried to constant mass at 105 ± 5 °C for 72 ± 2 h. The specimens were stored in the airtight containers before subjected to test. The specimens were immersed in water for 30, 60, 120 and 240 min.

4 Results and Discussion

4.1 Workability

In this study, the values of slump were determined as an indication of workability of fresh concrete. Figure 1 shows the slump values of concrete containing PET, RC

and CS as partial replacement of fine aggregate. Based on the result, it shows that the values of slump for all mixes are within the slump design. It shows that the increasing of percentage replacement level of PET, RC and CS affected the workability of the concrete. The slumps decreased as the replacement level of PET and CS increased. This reduction can be attributed to the fact that PET and CS have nonuniform shapes resulting in less fluidity. The slumps of RC increased as the replacement level of RC increased. The slumps obtained for control mix was 55 mm. For 10P, 20P and 30P concretes mixes, the slump recorded was 50, 45 and 40 mm, respectively. The past researchers [17, 18] have proven that the slump is prone to decreasing sharply with increasing of the PET ratio. The inclusion of NaOH to the rubber crumb before mixing is to increase the hydrophilicity of the rubber particle surface. The slump recorded for 10R, 20R and 30R was stated as 44, 48 and 52 mm, respectively. Rubberized concrete has been found to be less workable than conventional concrete as the rubber content increases [19]. For CS concrete mixes, the slump is recorded as 46, 43 and 49 mm for 10C, 20C and 30C, respectively.

4.2 Compressive Strength

Figure 2 shows the compressive strength of 28 series of control, PET, RC, CS, rubberized-PET and rubberized-coconut shell concrete specimens tested at 7, 28 and 60 days of curing.

It can be seen that the compressive strength of control concrete was higher compared to rubberized-PET and rubberized-coconut shell concretes. This might be
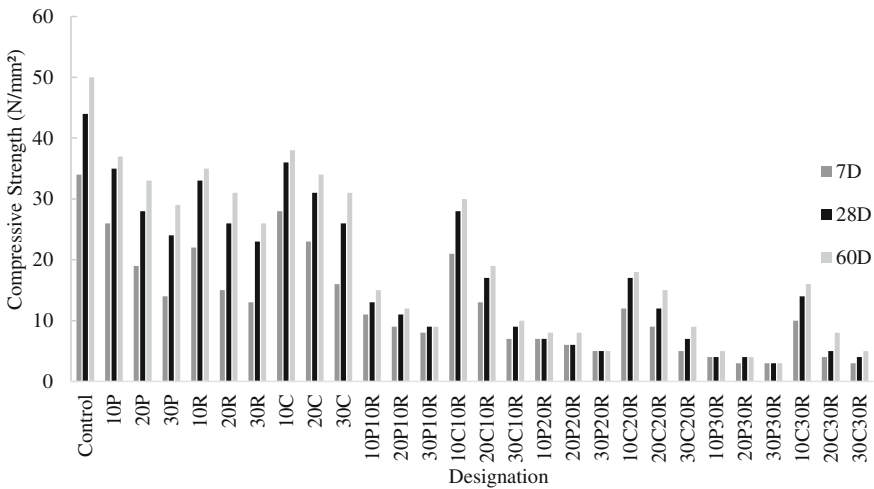
Fig. 2 Compressive strength taken at 7, 28 and 60 days of curing

due to the fineness of fine aggregates which is higher compared to rubberized-PET and rubberized-coconut shell concretes which resulted in higher strength. Studies conducted by past researchers [20, 21] indicated that the fineness of the material have some influences in which it increases the compressive strength of hardened concrete. It can also be seen that for all concrete, the increasing of curing days for 7, 28 and 60 days showed increase in strength, i.e. for control concrete the compressive strength was 34, 44 and 50 N/mm^2, respectively. The compressive strength of 10P, 20P and 30P ranges from 14 to 37 N/mm^2. For 10R, 20R and 30R the compressive strength ranges from 14 to 37 N/mm^2. Meanwhile, the compressive strength for 10C, 20C and 30C taken on 7, 28 and 60 days ranges from 16 to 38 N/mm^2. For the combination of PET rubberized concretes and coconut shells rubberized concretes, the compressive strength decreased with increase of PET, rubber crumb and coconut shells. PET rubberized concretes recorded the lower strength compared to coconut shells rubberized concretes.

4.3 Water Absorption

Figure 3 shows the percentage of water absorption of twenty eight series of control, PET, RC, CS, rubberized-PET and rubberized-coconut shell concrete specimens tested at 7, 28 and 60 days of curing.

It can be seen that the water absorption for control concrete was lower compared to the rubberized-PET and rubberized-coconut shell concretes. The percentage of water absorption of control concrete recorded was 4.82, 4.47 and 3.18 % for 7, 28 and 60 days, respectively. The percentage of water absorption of 10P, 20P and 30P taken on 7, 28 and 60 days ranges from 4.95 to 5.43 %, 5.19 to 5.89 % and 5.43 to
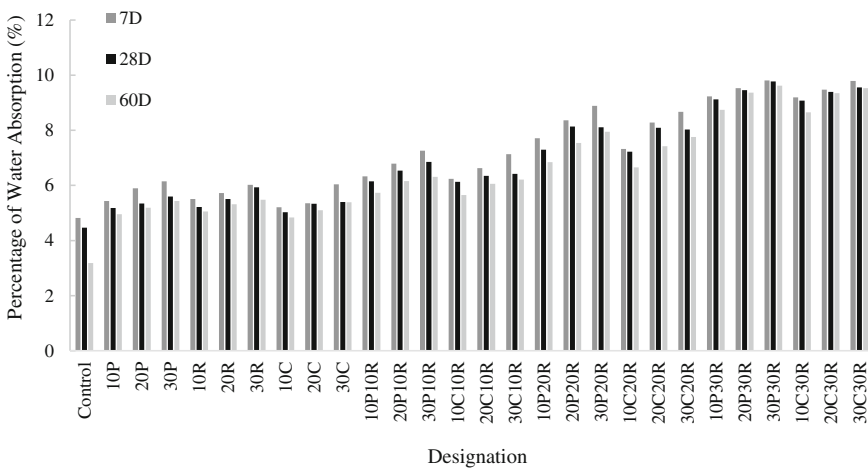
Fig. 3 Water absorption taken at 7, 28 and 60 days of curing

6.15 %, respectively. For 10R, 20R and 30R taken at 7, 28 and 60 days ranges from 5.05 to 5.51 %, 5.32 to 5.72 % and 5.48 to 6.02 %, respectively. Meanwhile, the percentage of water absorption for 10C, 20C and 30C taken on 7, 28 and 60 days ranges from 4.84 to 5.21 %, 5.1 to 5.35 % and 5.39 to 6.04 %, respectively. These showed that the percentage of water absorption of rubberized concretes have higher water absorption followed by PET concretes, CS concretes and control concrete. This might be due to the particle size of PET, RC and CS that influences the percentages of water absorption in concrete. Furthermore, the weight of fine aggregate passing 600 μm sieve that was used in this research study was higher compared to PET, RC and CS. According to sieve analysis that have been conducted, the weight of fine aggregate passing 600 μm sieve was 47.82 % while 43.94, 39.90 and 40.2 % for PET, RC and CS, respectively. A previous research [22] reported that, smaller size particles of fine aggregate make the particles to fill up the capillary pores structures that reduced water absorption in concrete; however, in this study the particle size of PET, RC and CS are coarser.

For the combination of rubberized-PET concretes and rubberized-coconut shells concretes, the percentage of water absorption increased with increased of PET, RC and CS. Thus, these showed that the durability of concrete decreased with increased PET, RC and CS percentages in rubberized-PET and rubberized-coconut shell concrete. Based from the graphs, it shows that water absorption for all mixes were higher than control mix concrete. Thus, very high CS and CR content in concrete affected water absorption in concrete as it restricted and unable the cement paste to bond together that allow the increment of pores sizes.

However, the replacement of PET, RC and CS with 10, 20 and 30 % for all mixes still achieved the required absorption of good quality concrete as the percentage of water absorption was below 10 % by mass. Previous research [23] stated that, the performance of good quality concrete should be less than 10 % absorption by mass. Figure 3 shows that the percentage of water absorption decreases with the increase in curing days because the voids of original water space in concrete were replaced with gel, thus, water absorption in concrete became lower.

5 Correlation Between Compressive Strength and Water Absorption

Figure 4 shows that the correlation between the compressive strength and water absorption exists through power graph. It shows that as the compressive strength decreases, the water absorption increases. The graph of regression shows that the correlation of rubberized-PET was good as the coefficient magnitude, R^2, recorded was 0.9512 which is close to unity. The correlation of rubberized-coconut shell concrete showed that the coefficient magnitude, R^2, recorded was 0.5885.
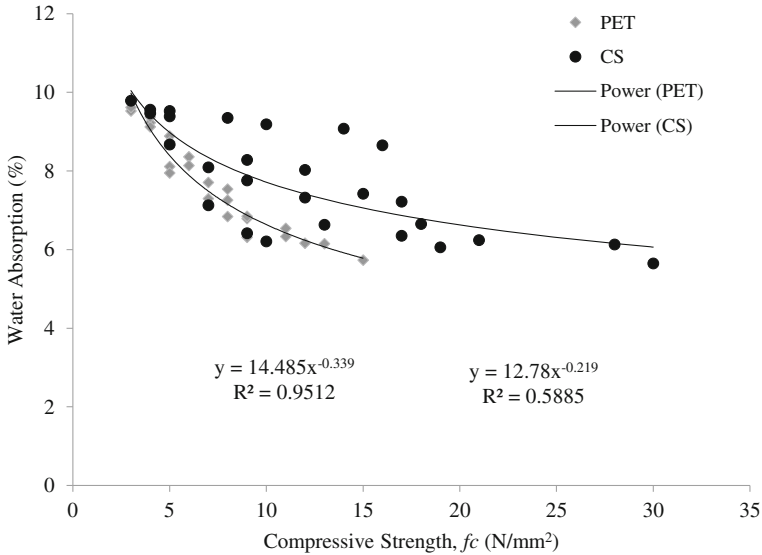
Fig. 4 Relationships between the compressive strength and water absorption

6 Conclusions

From the investigation carried out, the following conclusions were made:

- The slump values decreased with the increasing replacement of PET and CS in the concrete, however, slump increased with increasing of RC replacement level.
- Replacement of fine aggregate with PET, RC and CS at all replacement levels reduces the compressive strength. The compressive strength increased with age of curing. The optimum replacement of PET, RC and CS chosen was 10, 10 and 20 % taken at 28 days of curing.
- The percentage of water absorption increases with the replacement of fine aggregate with PET, RC and CS. However, all the values of water absorption taken at all curing days satisfy the requirements of good quality concrete, i.e. less than 10 % absorption by mass.

References

 1. Fernando Pelisser, Nilomar Zavarise, Tiago Arent Longo, Adriano Michael Bernadin, "Concrete Made with Recycled Tire Rubber: Effect of Alkaline Activation and Silica Fume Addition", Journal of Cleaner Production, Vol. 19, pp. 757–763, 2011.
 2. Rao G.A., "Influence of Silica Fume Replacement of Cement on Expansion and Drying Shrinkage", Journal of Elsevier, Cement and Concrete Research, Vol. 28, No. 10, pp. 1505–1509, 1998.
 3. Chindaprasirt P., Homwuttiwong S. and Sirivivatnanon V., "Influence of Fly Ash Fineness on Strength Drying Shrinkage and Sulfate Resistance of Blended Cement Mortar", Journal of Science Direct, Cement and Concrete Research, Vol. 34, Issue 7, pp. 1087–1092, 2004.
 4. Alabadan B.A., Olutoye M.A., Abolarin M.S. & Zakariya M. "Partial Replacement of Ordinary Portland Cement (OPC) with Bambara Groundnut Shell Ash (BGSA) in Concrete". Leonardo Electronic Journal of Practices and Technologies, Issue 6, 2005, pp. 43–48.
 5. Hanifi Binici, Orhan Aksogan, Ismail H. Catgatay, Mustafa Tokyay, Engin Emsen, "The Effect of Particle Size Distribution on the Properties of Blended Cements Incorporating GGBFS and Natural Pozzolan (NP)", Journal of Science Direct, Power Technology, Vol. 177, pp. 140–147, 2007.
 6. Kartini K., Mahmud H.B., Hamidah M.S., "Absorption and Permeability Performance of Selangor Rice Husk Ash Blended Grade 30 Concrete", Journal of Engineering Science and Technology, School of Engineering, Taylor's University College, Vol. 5, No.1, pp. 1–16, 2010.
 7. Marta Kosior-Kazberuk And Malgorzata Lelulsz, "Strength Development of Concrete with Fly Ash Addition", Journal of Civil Engineering and Management, Vol. XIII, No 2, pp.115–122, 2007.
 8. Raman S.N, Zain M.F.M, Mahmud H.B, Tan K.S., "Suitability of Quarry Dust as Partial Cement Replacement Material for Sand in Concrete", Department of Civil Engineering, Universiti Malaya, Kuala Lumpur, 2005.
 9. Shannag M.J., "High Strength Concrete Containing Natural Pozzolan and Silica Fume", Journal of Science Direct, Cement & Concrete Composites, Vol. 22, pp. 399–406, 2000.
10. Department of Environment, Design of Normal Concrete Mixes, Building Research Establishment, U.K., 1998.
11. British Standard Institution, BS 1881:111:1983, Testing Concrete, Methods of Normal Curing of Test Specimens.
12. British Standard Institution, BS 812–103:1:1985. Testing Aggregates. Methods for Determination of Particle Size Distribution. Sieve tests, 1985.
13. British Standard Institution, BS EN 12620: 2002. Aggregates for Concrete, 2002.
14. British Standard Institution, BS EN 12350-2:2000. Testing Fresh Concrete: Slump Sest, 2000.
15. British Standard Institution, BS EN 12390-4:2000. Testing Hardened Concrete: Compressive Strength. Specification for Testing Machines, 2000.
16. British Standard Institution, BS 1881-122:2011, Testing concrete, Method for Determination of Water Absorption, 2011.
17. Soroushian P., Mirza F., Alhozaimy A., "Permeability Characteristics of Polypropylene Fiber Reinforced Concrete", ACI Materials Journal, Vol. 92, No. 3, pp. 291–295, 1995.
18. Ismail Z.Z., Al-Hashmi E.A., "Use of Waste Plastic in Concrete Mixture as Aggregate Replacement." Waste Management, Vol. 28, No. 11, pp. 2041–2047, 2008.
19. Khatib, Z.K., and Bayomy, F.M., "Rubberized Portland Cement Concrete", Journal of Material Civil Engineering, ASCE, Vol. 11, No. 3, pp. 206–213, 1999.
20. Shimizu, G. and Jorillo, P. JR., "Study on the Use of Rough and Unground Ash From an Open Heaped-up Burned Rice Husk as a Partial Cement Substitute", Proceedings of The 2nd RILEM Symposium on Vegetable Plants and Their Fiber as Building Materials, Brazil, Editor: Sobral, H.S., Chapman and Hall, London, pp. 321–333, 1990.

21. Chopra, S.K., Ahluwalia, S.C. and Laxmi, S., "Technology and Manufactured of Rice Husk Ash Masonry (RHAM) Cement", Proceeding of ESCAP/RCCT 3rd Workshop on Rice-Husk Ash Cement, New Delhi, 1981.

22. Sikontasukkul, P., & Wiwatpattanapong, S.,"Lighweight Concrete Mixed with Superfine Crumb Rubber Powder Part 1: Insulation Properties". The Journal of KMUTNB, Vol. 19, 2009.

23. Neville A.M., Properties of Concrete, Fourth & Final Edition, ISBN 978-0-582-23070-5, Pearson Education Limited, England, pp. 488-493, 2002.

Comparative Study of Seismic Behavior of Tunnel Form Building Between Experiment and Modeling

S.A. Anudai, N.H. Hamid and M.H. Hashim

Abstract It is important to validate the hysteresis loops between the experimental results while modeling using HYSTERES program in Ruaumoko 2-D. One-third scale three-storey double unit tunnel form building was designed using BS8110, and constructed and tested under in-plane lateral cyclic loading. Parameters such as ultimate lateral load, stiffness, ductility, and equivalent viscous damping (EVD) were calculated using the experimental hysteresis loops. The analytical result from the modeling of hysteresis loops was compared with experimental results for validation purposes. The modeling of hysteresis loops was developed using Modified SINA hysteresis rule in the HYSTERES program. This type of hysteresis rule was selected because it is most similar to the hysteresis loops obtained from experimental work. The comparison results show good correlation as the percentage difference is less than 5 % for all parameters.

1 Introduction

A one-third scale double unit tunnel form building (TFB) was designed using BS 8110 (non-seismic code of practice) and constructed and tested subject to in-plane lateral cyclic loading [1]. This specimen was constructed with three-floor level using a single layer of BRC wire mesh for slab and wall components. The experimental

S.A. Anudai (✉) · N.H. Hamid · M.H. Hashim
Faculty of Civil Engineering, Universiti Teknology MARA,
40450 Shah Alam, Selangor, Malaysia
e-mail: shamilahanuar@yahoo.com

N.H. Hamid
e-mail: norha454@salam.uitm.edu.my

M.H. Hashim
e-mail: hisbany@salam.uitm.edu.my

work was performed to determine the performance of TFB in terms of its lateral strength, stiffness, ductility, and energy absorption. Then, the specimen was repaired and retrofitted using additional 50 mm thickness of RC wall, steel angle, and CFRP [2]. Experimental results showed that the repaired specimen had higher values for lateral strength capacity, ductility, and equivalent viscous damping compared to before retrofitting [2, 3].

The modeling of hysteresis loops for single unit of tunnel form building was made using Modified Takeda Hysteresis model in the HYSTERES program [4]. Another modeling of hysteresis loops of corner beam-column joint using Pampanin Hysteresis with Reloading Slip Factor was performed [5]. Both the modeling hysteresis loops have a similar shape and pattern as the experimental hysteresis loops. The chosen modeling of hysteresis loops will be used for prototype buildings of Ruaumoko 2D program. This software utilizes the finite element system to produce time-history response of nonlinear analysis of two- and three-dimensional buildings subjected to ground acceleration of time differ force excitations [6]. The output from Ruaumoko 2D program can be used to plot the hysteresis loops, mode shape, damage indices, energy absorption, and moment rotation. Moreover, the wide range of modeling system applied in Ruaumoko 2D program can produce the mass of the structure, damping, and stiffness factors [7]. Various modeling systems have been studied by previous researchers in validation and prediction of seismic performance of beam column connection, RC frame system, and tunnel form building. Kalkan and Yuksel [8] used 3D nonlinear finite element models to validate their experimental result of 1/5 scale down 3-storey RC tunnel form building with analysis result. They found that the seismic performance of TFB can be enhanced by providing an adequate vertical reinforcement ratio and boundary reinforcement bar. Meanwhile, Jun et al. [9] developed a simple lumped-parameter model to represent the complex high rise structure. They used ZEUS-NL to predict the dynamic response history analysis for the complex behavior and interaction of RC high-rise buildings. Meanwhile, Mostofinejad and Talaeitaba [10] studied the nonlinear FE analysis to model the RC connections strengthened by FRP composites. They found that the predicted model gives good accuracy after analyzing seven different strengthening techniques. Lee and Woo [11] modeled three-storey RC frame using IDARC-2D to determine the correlation between earthquake simulation and pushover test with analysis. They found that the prediction model using IDARC-2D is more reliable for global response rather than local response.

The utilization of each type of modeling software depends on the ability, accessibility, and reliability of the selected program. In this paper, the HYSTERES program in Ruaumoko 2D software is applied to model the seismic performance of retrofitted double unit TFB. The accuracy of the experimental result is verified through comparisons with modeling results. The main objective of this paper is to model the load versus displacement curve (hysteresis loops) of retrofitted double unit TFB using Modified SINA hysteresis rules. The seismic parameters such as maximum lateral strength, stiffness, ductility, and equivalent viscous damping (EVD) are compared between experimental and analytical results.
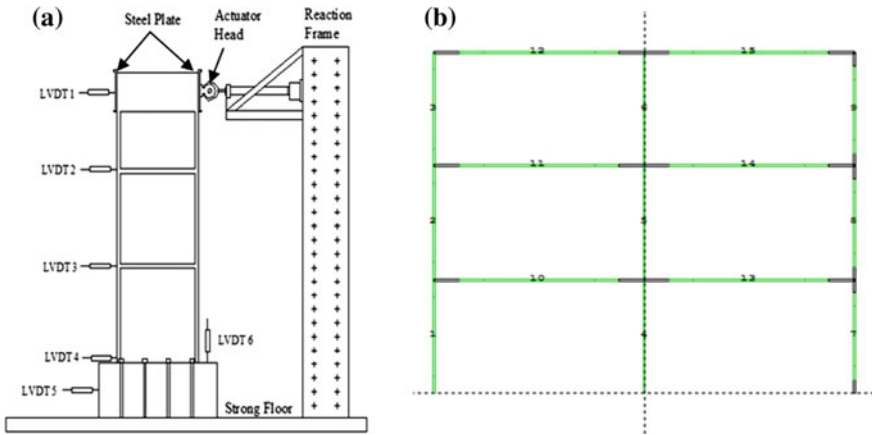
Fig. 1 **a** Experimental setup conducted in heavy laboratory and **b** modeling the double unit TFB using Ruaumoko 2D program

2 Experimental Setup and Modeling Approach

Figure 1a shows the experimental setup of double unit tunnel form building together with six LVDTs performed in Heavy Structural Laboratory, Universiti Teknologi Mara Malaysia. The prototype specimen was bolted to a strong floor using high threaded bolt at the foundation beam. The specimen was loaded in-plane direction which is directly in front of the frame interface. Figure 1b shows the modeling of double unit TFB using Ruaumoko 2D program together with nodes and elements. The double unit TFB was modeled using the RUAUMOKO 2D program using nonlinear elastic Giberson frame members. The model was tested with displacement control at the top node to represent the in-plane lateral cyclic loading.

3 Development of Hysteresis Loops Using Hysteres Program

The HYSTERES program is used to model the hysteresis loops based on the data obtained from the experimental work. The prototype specimen was modeled as a Giberson Component Beam Model and acts as a frame member. The characteristic of the element was defined according to the local axis system for the element where the x-axis runs along the length of the element. The type of hysteresis loop was chosen from the 56 hysteresis model as attached in the RUAUMOKO 2D Appendices [6]. The model follows a similar pattern of hysteresis loops as the experiment result, which is Modified SINA degrading Tri-linear hysteresis by
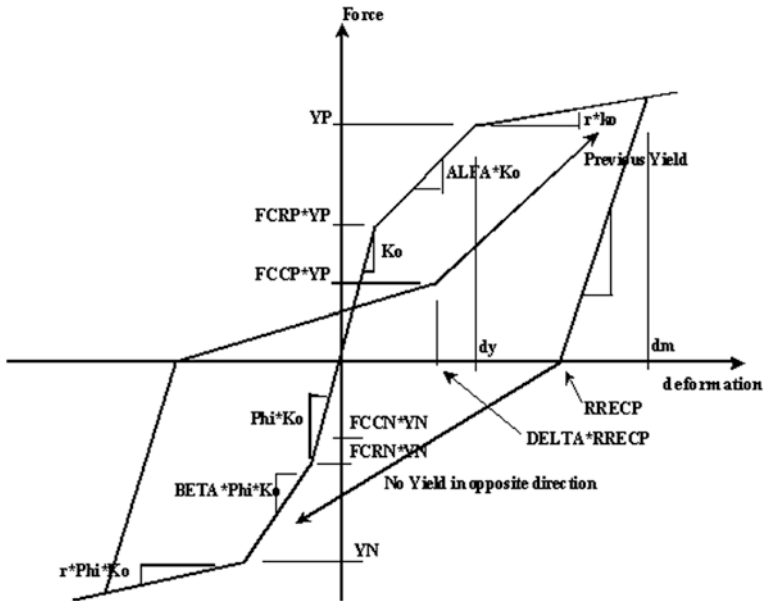
Fig. 2 Modified SINA degrading tri-linear hysteresis

Saidi [12]. Figure 2 shows the Modified SINA degrading hysteresis which has similar hysteretic characteristics as experiment hysteresis loops of the repaired double unit tunnel form building.

During the development of the hysteresis loops using RUAUMOKO 2D, the HYSTERES.EXE file was selected under Executable folder. The input data such as initial stiffness and tri-linear factor were calculated using Eqs. (1) and (2), respectively, based on raw data from the experimental results.

$$K_O = \frac{(Y_2 - Y_1)}{(X_2 - X_1)} \tag{1}$$

$$r = \frac{(Y_2 - Y_1)}{(X_2 - X_1)} \times \frac{1}{K_O} \tag{2}$$

where K_O represents the initial stiffness and r represents the tri-linear factor. Meanwhile, Y_1 represents the coordinate at node 1 in y-y direction and Y_2 represents the coordinate at node 2 in y-y direction. Furthermore, X_1 and X_2 represent the coordinate at nodes 1 and 2 in x-x direction respectively. Since the prototype specimen is symmetrical, the symmetric moments such as FCRP = FCRN and Alfa = Beta are required,. The bilinear factor is taken as the tri-linear factor which acts as a part of the basic member section data. Several parameters that are required to be inserted are shown in Fig. 3.

ALFA	Bi-linear factor (positive cracking to yield)	(0.2 ≤ **ALFA** ≤ 0.9)
BETA	Bi-linear factor (negative cracking to yield)	(0.2 ≤ **BETA** ≤ 0.9)
GAMMA	Unloading power factor	(0.0 ≤ **GAMMA** ≤ 0.5)
DELTA	Pinching Factor	(0.0 ≤ **DELTA** ≤ 0.8)
PHI	Ratio of Compression to Tensile Stiffness	(0.1 ≤ **PHI** ≤ 10.0)
	If PHI = 0.0 then PHI reset to 1.0	
FCRP	Cracking action as ratio of Positive Yield	(0.3 ≤ **FCRP** ≤ 0.9)
FCRN	Cracking action as ratio of Negative Yield	(0.3 ≤ **FCRN** ≤ 0.9)
FCCP	Crack closing action as ratio of Positive Yield	(0.1 ≤ **FCCP** ≤ 0.7)
FCCN	Crack closing action as ratio of Negative Yield	(0.1 ≤ **FCCN** ≤ 0.7)
IOP	=0; Cracking and yield deformations set at static analysis	
	=1; Cracking and yield deformations set at first cracking	
	=2; Cracking and yield deformations set at first yield or when axial force falls outside range of **PMIN** to **PMAX**	
PMAX	Maximum (Most tensile) axial force to set deformation limits.	
PMIN	Minimum (Most compressive) axial force to set deformation limits.	

Fig. 3 Input interface stiffness degradation parameters

4 Comparison of Hysteresis Loops Between Experimental and Modeling

The hysteresis loops were plotted based on experimental data obtained from the laboratory work. Modified SINA hysteresis was adopted in this model as its pattern has the most fitting hysteresis loops from experimental results. The output from the HYSTERES program is imported to the Microsoft Excel software. The hysteresis loops from the model are superimposed to the experimental hysteresis loops in order to compare their behavior subjected to lateral cyclic loading. Figure 4 shows the comparison of hysteresis loops between experimental and modeling for double unit TFB. The modeling hysteresis loops in dark chocolate color seem to have a similar pattern as the experimental hysteresis loops.

Fig. 4 The comparison of hysteresis loops between experimental and analysis
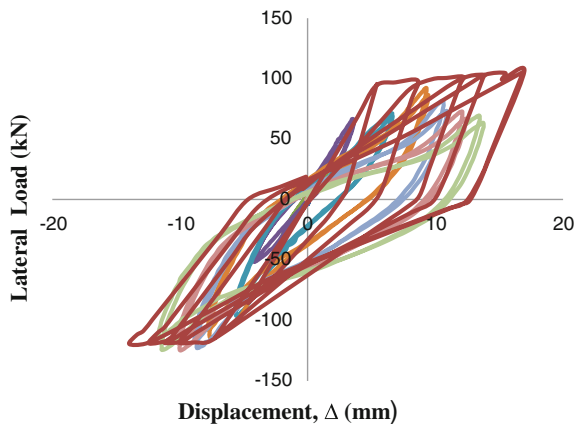
Table 1 Comparison of tested parameters between experiment and modeling

Parameter	Comparison of results		
	Experiment	Modeling	Percentage different (%)
Strength (max load)	92.39	95.7	3.31
Stiffness	1.00	1.06	0.06
Ductility	3.12	3.24	0.12
EVD	19.29	21.9	2.62

Table 1 shows the comparison of maximum lateral load, stiffness, ductility, and equivalent viscous damping (EVD) between experimental and modeling of hysteresis loops in terms of percentage difference. The value seems to give good correlation between experimental and modeling results as the percentage difference is less than 5 %. The maximum lateral strength is 3.31 %, which differs between experimental and modeling work. It may be caused by a loss of kinetic energy to friction energy during the push and pull forces. Meanwhile, stiffness and ductility are 0.06 and 0.12 %, respectively, which differs between experimental and modeling. These values exhibit good deals with each other.

5 Conclusion

Accuracy determination of experimental result was performed by comparing the raw data obtained from experimental work with the modeling result using the HYSTERES program. The percentage difference of the maximum lateral strength, stiffness, ductility, and equivalent viscous damping (EVD) were investigated by comparing both experimental and modeling work. The comparison was conducted by plotting load versus displacement curve (hysteresis loops) for both experimental and modeling work. After that, both hysteresis loops were superimposed in a single graph in order to see the similarity between each other. Based on the investigation, it can be concluded that the compared results were acceptable and demonstrated the effectiveness of the Ruaumoko program in validating both results. However, further analysis is still under investigation utilize the related software in Ruaumoko program in order to give clear differences for both modeling and experimental work. Furthermore, it is recommended for validation between experiment and modeling to be conducted using software such as SAP, Staad Pro, Orion, and others in order to see different seismic behaviors.

References

1. H. Nor Hayati, M. S. Saleha, and A.A. Shamilah, "Seismic Performance of Double Unit Tunnel Form Building Under In-plane Lateral Cyclic Loading," Structures under shock and impact XIII, 141, 467, 2014
2. H. Nor Hayati, A.A. Shamilah, and A. Nur Liyana, "Retrofitting of a Double Unit Tunnel Form Building Using Additional RC Wall, Steel Angle and CFRP", Applied mechanics and materials, 661, pp. 123–127, 2014
3. H. Nor Hayati, A.A. Shamilah, and A. Nur Liyana, "Retrofitting of a Double Unit Tunnel Form Building Using Additional RC Wall, Steel Angle and CFRP", Applied mechanics and materials, 661, pp. 123–127, 2014
4. H. Nor Hayati, and A. A. Shamilah, "Modeling of a Tunnel Form Building Using Ruaumoko 2D Program"; Advanced engineering and technology, pp.77–81, 2014
5. G. Kay Dora, and H. Nor Hayati, "Modeling Hysteresis Loops of Corner Beam-Column Joint Using Ruaumoko Program," Advanced engineering and technology, pp. 115–119, 2014
6. A.J. Carr, "RUAUMOKO Manual," (volume 1: Theory), University of Canterbury, Christchurch, New Zeland, 2007.
7. G. Kay Dora, H. Nor Hayati, and M. S., Jaafar, "Load Versus Displacement Validation between Ruaumoko Hysteresis Program and Experimental Work on CFRP Retrofitted Precast Beam-Column Exterior Joint", Key Engineering Materials Vols. 594–595, pp. 390-394, 2014
8. E. Kalkan, and S. Bahadir Yuksel, " Pros and Cons of Multistorey RC Tunnel Form (Box-Type) Buildings", The structural design of tall and special buildings, struct. Design tall spec. build. Pusblish online in Wiley Intersicence (www.interscience.wiley.com). DOI: 10.1002/tal.368, 2007 in press.
9. J.I. Jun, A.S. Elnashai, D.A. Kuchma, "An Analytical Framework For Seismic Fragility Analysis of RC High-rise Buildings," Engineering structures 29, pp. 3197–3209
10. D. Mostofinejad, and S.B. Talaeitaba, "Finite Element Modeling of RC Connections Strengthened with FRP Laminates', Iranian Journal of Science & Tachnology, transaction B. Engineering, vol. 30, No. B1, 2006
11. L. Han-Seon, and W. Sung-Woo, "Seismic Performance of a 3-storey RC Frame in A Low-Seismicity Region", Enineering structures 24, pp. 719–734, 2002
12. Saidi and Sozen,'Simple and Complex Models for Nonlinears Seismic Responsed Concrete Structures, UILU 79–2013, 1979

Part IV
Construction Project Management

A Look into Poor Marketing Strategy on the Issue of Abandoned Housing Projects in Malaysia

Sunitha V. Doraisamy and Zainal Abidin Akasah

Abstract The issue of abandoned projects is something very common that is happening around the world. It is considered a serious issue, which paints a negative image of the country's construction industry, and is an absolute downfall of the country's economy as well. Due to this issue various causes and effects have been studied and identified by researches worldwide. This is also the same for Malaysia, and steps have been taken to overcome this issue. At the moment most of the abandoned projects in Malaysia are in planning and in the process of revival. From the many causes identified pertaining to this issue, improper management of its other contributing causes has been highlighted as the main cause, where this paper focuses on one of the contributing causes among others, that is, poor marketing strategy. Poor marketing strategy contributing to noneffective sales of property is known to have an understandable impact on the issue of abandoned projects in Malaysia. This paper also looks into the concepts and aspects of property marketing to know and to have a better understanding of property marketing. Apart from that, current statistics on the development of new projects, and also abandoned projects from the Ministry of Housing and Local Government are laid out here to have a proper outlook of the current situation of the construction industry as well. By conducting this paper, the aspects of property marketing along with the strategies were viewed and co-jointly its impact on projects. Lastly the lacking of a strategy is also considered to contribute to the issue of abandoned projects.

Keywords Abandoned projects · Property · Marketing · Strategy · Revival

S.V. Doraisamy · Z.A. Akasah (✉)
Faculty of Civil & Environmental Engineering, Universiti Tun Hussein Onn Malaysia,
Parit Raja, 86400 Batu Pahat, Johor, Malaysia
e-mail: drzainalakasah@gmail.com; drzainal@gmail.com

S.V. Doraisamy
e-mail: suni7624@yahoo.com

1 Introduction

Property marketing or real estate economics is the application of economic techniques to real estate markets. It tries to describe, explain, and predict patterns of prices, supply, and demand [1]. Marketing is the management process which is useful in identifying, anticipating, and satisfying customer's needs to make profit [2]. Marketing is the utmost priority of the manager in any sort of management. As for the aspects of management, it should not just focus on the financial ability, but should also give importance to the type of product sold, to whom it is sold, and whether it will be a successful type of business. The basic functions of management are planning, organizing, executing, and controlling [3], which also enhances the functions of marketing.

Property marketing is something that is happening worldwide, to enhance the quality of life among people and society everywhere. Property marketing actually develops satisfaction among people in terms of consumption. It provides maximum production, employment, and wealth. Investing a certain amount of money in a property gives self-satisfaction to people knowing that their money is safe in something that is ensuring and profitable, in a long term to come [4].

In Malaysia, and in some other countries as well, the desire to own a property at the moment is being compromised with the issue of abandoned projects, which is happening on quite a large scale. In Malaysia, it is reported by the Ministry of Housing and Local Government (MHLG) that up to January 2015, a total of 215 projects, which comprises about approximately 60,000 unit houses had been abandoned in Peninsular Malaysia. The Ministry of Housing and Local Government is therefore seriously looking into this matter and the government has invested a vast amount of money in reviving these abandoned projects, where it is also reported in [5] that approximately 40,000 people have purchased these abandoned properties. With the purpose to find the reasons behind such issues, poor marketing strategy has been highlighted as one the causes behind abandoned projects, not only in Malaysia, but in other countries as well. Looking into the proper concepts and aspects of property marketing and management is something essential that be come useful in the long run in the effort of curbing the issue of abandoned projects in the coming future.

2 Basic Problems in Property Marketing

Marketing a property comes along with a certain process, which starts with identifying and knowing what people want, which is usually obtained through complaints or suggestions given by them. This would lead to a more efficient marketing process by knowing their needs, rather than assuming what they want. Marketing a property is not just based on the type of building, but also by taking into account the surrounding of the property which could attract the interest and anticipation of

people towards the specific property. Marketing a property should always look into the profitable basics of it, where a buyer always sees if the amount of money that is invested is something profitable in the years to come. If it is so, then marketing such property and selling it would not be much of a problem.

According to Iman [2], there are two basic problems that could be categorized, (1) basic economy problems and (2) problems in delivering products to consumers. He has explained the basic economic problems in property marketing common in economic studies, where the quantity and the type of real estate products and services has to be known, how, by whom, in what manner it could be produced, and lastly, the suitable targets for these products or services and how to reach them. In [2] it is further elaborated that these problems could be solved by two approaches based on the marketing functions, which first of all is the macro approach, which treats national economy as the basic unit and then investigates marketing as a part of a bigger whole. Secondly, the micro approach where marketing is looked into from the individual business point of view and its function toward the economy. He further stated that in the marketing strategy the second viewpoint is the most commonly and widely adopted. This is because the people or target groups are easier to handle, and the whole operation is convenient to be evaluated and comprehended.

The next problem mentioned is the problems in delivering products to consumers, problems that could be related to economic, social, governmental, and technical in nature. When it comes to problems in delivering products to consumers, therefore the marketing strategy applied here is always questionable. The marketing channel and product positioning are difficult aspects in the marketing strategy. Since real estate products and services are not something that could be moved from one place to the other, the marketing channel therefore becomes a major concern. This is the same in the case of product positioning, where the effectiveness of the promotional strategies used guarantees an effective sale [6].

Overall, what can be seen here is that real estates is something that cannot be moved around and is best described as immobile. It is something that is built and established statically or in situ, long-lasting, produced with a large amount of money, legally bonded, have limited markets, and not easy to be disposed, as elaborated by [7]. When it comes to marketing a property, location suitability, promotional activities, and loan facilities are some of the main characteristics that have a great role and impact on marketing on the whole.

3   Abandoned Housing Projects in Malaysia

When it comes to abandoned housing projects, the end-users are those who are affected and suffer the most. In the desire to own a property or a house, end-users invest a large amount of their savings, and go through procedures through banks to obtain a loan with the intention of purchasing the desired property. It is indeed a great worry to them when the construction work of these properties have

discontinued and completely stopped, resulting in its abandonment. In fact, monthly payments on their housing loans with interests have to be carried out by them although they are yet to occupy their new houses. Even if the housing project is long abandoned, the monthly payments have to be honored, failing to do so will result with them being fined or sued.

Browsing the Ministry of Housing and Local Government's records from 1990 till 2005, we find that the problem of abandoned housing projects is indeed serious. From 1990 to 2005, the Ministry of Housing and Local Government's records show that 261 projects involving 88,410 houses in Peninsular Malaysia were abandoned [8]. A total of 58,685 buyers were affected by this problem. Selangor had the most number of abandoned projects, with a total of 63 projects involving 32,987 houses affecting 22,480 buyers. Although with such issue the demand for houses, be it low-cost, medium-cost or high-cost, has not decreased as well. Table 1 shows the current statistics of abandoned projects with its number of houses abandoned and the number of buyers affected.

There have been many causes identified by researches over the years on the issue of abandoned projects. Among these causes, improper management has been highlighted as the main purpose or cause for abandoned projects. The identification of the causes was done based on a comparison matrix that was established based on these causes, where improper management stands out with the most percentage of 61 % as the reason behind abandoned projects. From some of the contributing and underlying causes in improper management, poor marketing strategy is also a noticeable factor which contributes toward projects abandonment, as shown in Fig. 1.

With the existing issue of abandoned projects still plaguing the country, there are still new housing projects that have been approved for development and are in fact under construction. According to Ministry of Housing and Local Government [9], there is an estimation of more than 50 % of buyers existing for these projects. The update on the development of new housing projects is shown in Table 2.

Table 1 Statistics of abandoned housing projects according to states up to December 2014 [5]	States	Project	Unit houses	Buyers
	Selangor	25	12,077	8,834
	Johor	11	4,104	3,084
	Negeri Sembilan	5	1,165	999
	Pulau Pinang	2	1,550	1,337
	Kedah	3	860	209
	Perak	6	822	425
	Pahang	2	414	299
	WP Kuala Lumpur	2	1,070	573
	Kelantan	1	39	29
	Melaka	1	554	502
	Terengganu	–	–	–
	Perlis	–	–	–
	Total	58	22,655	16,291

Fig. 1 Causes contributing to improper management [8]

Improper Management → Lack of communication on project goals

Lack of project team promise

Improper project timing & scheduling

Improper project planning & design

Incompetent project manager

Leadership instability

Improper project controlling & monitoring

Improper project financing

Poor marketing strategy

Table 2 Total of unit houses approved for development, January–March 2014 [9]

Month	Low cost	Medium low cost	Medium cost	High cost	Total
January	0	15	12	6,832	6,859
February	64	24	220	9,209	9,517
March	133	149	371	7,464	8,117
Total	197	188	603	23,505	24,493

Table 3 Status of private housing projects according to states in Peninsular Malaysia [9]

States	Smooth development			Late			Sick		
	Total projects	Units built	Units sold	Total projects	Units built	Units sold	Total projects	Units buil	Units sold
Johor	620	84,839	65,716	19	3,999	2475	28	6,495	3,961
Kedah	211	16,586	8,040	9	323	235	12	2,133	1,219
Kelantan	159	9,520	5,322	4	330	284	12	1,066	768
Melaka	160	21,747	10,463	0	0	0	2	145	135
Negeri Sembilan	162	23,830	12,114	1	16	15	10	1,186	916
Pahang	303	9,151	3,485	1	8	2	11	866	496
Perak	482	23,387	16,457	2	421	343	44	4,018	2,417
Perlis	30	1,914	391	1	21	19	0	0	0
Pulau Pinang	372	33,470	17,717	2	29	8	15	1,123	977
Selangor	1,015	162,294	85,493	17	3,604	2,759	81	14,248	8,370
Terengganu	50	1,991	1,247	0	0	0	8	1,057	849
WP Kuala Lumpur	209	45,019	29,517	7	2,369	1,592	3	903	461
Total	3,773	433,748	255,962	63	11,120	7,732	226	33,240	20,569

Table 3 is the status of private housing projects that are undergoing smoothly, late and sick, according to states in Peninsular Malaysia.

Although it seems here that before a certain project is abandoned, there are some success rates on selling these projects, hence looking at the number of units sold.

There are various causes contributing toward the issue of abandoned projects, where the construction works or activities are stopped or discontinued along the way. Poor marketing strategy also seems to be one of the contributing factors to this issue, according to a report issued by Ministry of Housing and Local Government [5], where the unsuccessfulness of marketing the property shows the noneffectiveness of the sales, which indirectly fails or stumbles on the part of financial adequacy of the whole project.

4   Conclusion

Every organization developing property for sale should have a marketing plan, preferably before the project starts. The most appropriate question that an organization should impose on itself before going ahead with a project are (1) to whom the product/property will be sold?, (2) what do they want?, (3) how will you reach them?, and (4) what is your competition? All of these questions are important when i comes to crafting the price, product, and promotion strategies for the purpose of having an effective property sale.

It is fair enough to say that all the necessary considerations and decisions were made in marketing a property, but yet due to some reasons the strategy used seemed to fail leading towards unprofitable sales and lastly the property being abandoned. Therefore, it is reasonable to state here that an efficient marketing strategy should be put in place right before a projects starts. Putting forward a well-versed property marketing strategy is also likely to define a proper management process of the whole project development that is intended. Consequently, the effort of curbing the issue of abandoned projects could also be achieved, where it has been mentioned earlier, that based on the comparison matrix on the causes of abandoned projects identified by many researches from various countries including Malaysia, and also referring to the report issued by the Ministry of Housing and Local Government, 2014, improper management has been rated as the main cause behind abandoned projects.

Some suggestions on having a good and effective property marketing strategy are (1) knowing the basic components of the intended marketing plans, (2) conducting a quick market research on the type of market it is intended to be sold on, (3) understanding the marketing goals so that a clear picture on what is focused on and when it is actually needed is known, (4) identifying the target markets which could help to achieve the marketing goals, (5) analyzing the possible benefits that could be obtained from the product, in this case the property, and from here identify the refinements that could be made to the product or property, and lastly, (6) measuring the effectiveness or success of the marketing strategy used, which could allow to determine what is working and not working, ultimately saving a lot of time and money.

Having a proper understanding of the types of causes contributing toward abandoned projects, in which poor marketing strategy is focused here, are

reasonable efforts in solving the problem. Knowing and understanding the impacts and effects of abandoned projects, suitable efforts should be made in solving this issue and avoiding it from happening to other projects which are under development. Looking into the poor property marketing strategy, which seems to be one of the contributing causes for this issue, it is also a step in curbing the problem and making proper mitigations to solve it.

Therefore, it is important to have a suitable and proper property marketing strategy, and in fact having an evaluation of the strategies used, helps in achieving the goals of the whole project, and lowering the chances of a project to be discontinued or even abandoned.

References

1. Robert, E., "Consumer and business credit management", Homewood: Irwin. pp. 123–128. ISBN 0-256-13948-2, 1995.
2. Iman, A., "An Introduction to Property Marketing", Universiti Teknologi Malaysia, 2002.
3. Kaplan, A., "European Management and European Business Schools: Insights from the History of Business Schools", European Management Journal, 2014.
4. An, K., "Making Profitable Marketing Decisions", 20th. June, 2014.
5. Ministry of Housing & Local Government, "Statistic for Abandoned Housing Projects in Malaysia", Putrajaya, Kuala Lumpur, 2014.
6. Nielsen, L., "Product Positioning & Differentiation Strategy", Hearst Newspapers, 2015.
7. Iman, A., "Basic Aspects of Property Market Research", Universiti Teknologi Malaysia, 2006.
8. Ministry of Housing & Local Government, "Problem Based Housing Projects in Malaysia", Putrajaya, Kuala Lumpur, 2011.
9. Ministry of Housing & Local Government, "Statistical Report for First Tribal Year 2014", Putrajaya, Kuala Lumpur, 2014.
10. Doraisamy, S.V and Akasah, Z.A, "Incorporating Rehabilitation Management towards the Restoration of Abandoned Housing Projects", Journal of Civil Engineering & Environmental Technology (JCEET), vol. 2, no. 1, pp. 7–13, New Delhi, India, 24th & 25th January 2015.

Conflict, Complexity, and Uncertainty in Building Refurbishment Projects

Adel Noori, Masran Saruwono, Hamimah Adnan and Ismail Rahmat

Abstract Building refurbishments involve improvement, upgrading, renovation, retrofit, and repair of existing buildings. It is an important sector of the construction industry. Building refurbishment projects are characterized by a high level of complexity and uncertainty which often involves factors such as change in design, inadequate and unavailable information which may initiate conflicts. The aim of this paper is to investigate how the factors cause conflicts. A comprehensive literature review was carried out as part of on-going Ph.D. research program. The review reveals that building refurbishment projects are more uncertain than new building projects and that the uncertainties tend to increase conflicts. This paper concludes that knowledge relating to complexity and uncertainty in refurbishment projects and the factors that cause conflict has to be managed systematically to enable successful project implementation.

Keywords Building refurbishment · Complexity and uncertainty · Conflict

1 Introduction

Building refurbishment works involve improvement, upgrading, renovation, expansion, and repair of existing building [1, 2]. The benefits of refurbishing existing building have recently been brought into focus along side the concern on environmental impacts of buildings [3]. This is due to the fact that existing buildings constitute the majority of the total building stocks for years to come and hence will remain responsible for the majority of greenhouse gas emissions in the environment [3]. Also, building refurbishment works have received increasing

A. Noori · M. Saruwono · H. Adnan · I. Rahmat (✉)
Faculty of Architecture, Planning and Surveying, Universiti Teknologi MARA (UiTM),
40450 Shah Alam, Selangor, Malaysia
e-mail: ismail046@salam.uitm.edu.my

A. Noori
e-mail: Adel.noori61@gmail.com

Table 1 The growth of building refurbishment projects in Malaysia, 2011–2014

Type of refurbishment projects	Number of refurbishment projects			
	2011	2012	2013	2014
Upgrading	513	516	612	435
Expansion	176	179	146	92
Repair	241	247	401	281
Renovation	300	337	291	220
Total	1230	1279	1450	1028

Source Malaysia, CIDB (2014)

Table 2 Total number of new projects in Malaysia, 2011–2014

Type of work	Number of new projects			
	2011	2012	2013	2014
New building	6160	6229	6289	4539

Source Malaysia, CIDB (2014)

attention and grown hugely in the past decade; because of the change in economic conditions and the emphasis on sustainable development [4]. In Malaysia, building refurbishment works have become an important sector in the construction industry. This is due to increased number of aged buildings and rapidly changing technology that requires the existing buildings to be altered to accommodate the current building needs [5]. In recent years, the numbers of building refurbishment projects have been increasing rapidly. Data in Table 1 shows a growth in the number of building refurbishment projects from 2011 to 2014. However, due to downturn in the construction industry, these numbers have been slightly decreased in 2014 (Table 2).

It should be considered that many building refurbishment projects have not been reported during these years, especially those that have been done by building owners. Therefore, the value of building refurbishment projects could be higher.

The first objective of this paper is to identify the factors that make building refurbishment projects complicated and uncertain. The second objective is to establish the extent to which these factors cause conflicts.

Changes in design, inadequate and unavailable information, difficulty of access to the site, difficulty of matching new materials with the old ones, limited space available for working, and storage of material are common factors that cause complication and uncertainty in building refurbishment projects [6–11].

Therefore, it is important to do further research to establish the factors that contribute to the complexity and uncertainty of building refurbishment projects.

In construction industry, complexity and uncertainty is one of the main factors that cause conflicts [12–14]. Also, conflicts are more likely to occur in building refurbishment projects which are noted with a high level of complexity and uncertainty [8].

Rahmat and Ali [15] states that complexity and uncertainty cause conflict in building refurbishment projects. Thus, the aim of this paper is to overview the factors that cause complexity and uncertainty in building refurbishment projects and to show how these factors cause conflicts in the projects.

2 What is Complexity and Uncertainty in Building Refurbishment Projects?

Baccarini [16] defined project complexity as consisting of interconnected parts and can be operationalized in terms of differentiation and interdependency, and this definition can be applied to any project dimension relevant to the project management process, such as organization, technology, environment, information, decision-making, and systems.

Uncertainty may have different meanings in different fields. In psychology, uncertainty is defined as a state of mind characterized by a conscious lack of knowledge about the outcomes of an event [17]. However, in project management, uncertainty is defined as an event or condition that, if occurs, has a positive or negative effect on at least one project objective, such as time, cost, scope, or quality [18]. Also, [19] in a simplest and most comprehensive expression which defined uncertainty as difference between information required for the decision and the information available.

In addition, there is a relationship between complexity and uncertainty: with increasing complexity, uncertainty also decreases [20]. As business systems become more complex, it is difficult for managers to be certain of anything [20]. By the same token, [21] believe that the more complex the undertaking, the greater the likelihood of surprise, because more factors can interact in unforeseen ways. So, there is a strong correlation between complexity and uncertainty.

The complexity and uncertainty variables in building refurbishment projects are many, such as unforeseen site conditions [22, 23], site access [12, 22, 24, 25], lack of space [13, 24, 26], availability of material [24, 26–29], design change [8, 30–32], defective design and plan [6, 25, 29], and lack of information during design stage [11, 31, 33]. However, [8] found that unavailability of design information and changes in design during construction had the greatest impact on project performance, and arguably, on the level of conflicts. Therefore, this paper focuses on these two variables of building refurbishment projects, complexities, and uncertainties.

The second cause of complexity and uncertainty is design change, which 'is inevitable' in construction [14]. Change is the act or an instance of making or becoming different, an alteration or modification. Changes in construction projects are mainly due to changes due to site conditions, changes due to client requirement, and changes due to design errors. [34], incomplete design information [11, 30, 35, 36], insufficient condition data, inadequate information on building condition, and ineffective communication between the client and contractors [35].

Changes in building refurbishment projects are exacerbated by unforeseen site conditions [11]. Unforeseen site conditions are defined as an unanticipated or unexpected circumstance or situation that affects the price, time and quality of project [37]. For instance, information about building services is normally very limited and is one of the major elements of unforeseen building conditions [11]. This is mainly due to the fact that the majority of services components such as electrical wiring and piping are embedded in walls or ceilings [11]. Unforeseen site conditions could occur because of the demolition work involved in the building refurbishment projects [38]. Demolition works involve tearing down, breaking up, and razing whole buildings or parts of buildings and includes the removal of machinery or equipment from buildings [39]. The demolition of a building can be total or partial. Total demolition is, in general, aimed at the recovery of the area for subsequent reuse, while partial demolition is aimed at the recovery of the building for refurbishing or rebuilding [40].

Apart from design changes, building refurbishment projects are more challenging, especially when dealing with historical buildings, because in such projects, the availability of design information is limited due to the absence of "as-built" document [41, 42]. According to [11], much of the necessary information is not available at the required time. Furthermore, in some building refurbishment projects, the designers face problems in matching up the old and new materials because many materials are no longer in production. This contributes to a complexity and uncertainty in building refurbishment projects [43].

Ali et al. and Egbu [5, 10] have provided evidence of the problems of building refurbishment projects. This is most commonly due to the lack of design information available to perform a task, especially during the initial stages of the design process [11]. By the same token, [11] believed that, the problem in the design process is further compounded by complicated nature in building refurbishment projects, mostly due to the unavailability of design information.

The changes occurred in design often due to indecisiveness of the client came to certain realizations during a specific phase of the project, or changing requirements that the company has of the building [28]. These design changes frequently conflict with completed work, and thus force the design team to alter the designs. Consequently, client induced design changes caused unplanned delays depending on the severity of the design change [28].

3 How Complexity and Uncertainty Cause Conflict

Bin Rahmat [8] noted that, conflicts are more likely to occur in building refurbishment projects with a high level of complexity and uncertainty; therefore are often considered.

As one of the main reasons for construction projects is conflict [13, 32, 44]. According to [45], conflict is defined as opposition, struggle, or disagreement between two or more individuals or groups. Meanwhile, there are three basic forms

Table 3 Sources of conflict

Area	Discipline	Sources of conflict
Complexity and uncertainty	*External*	Design change, variations, environmental concerns, social impacts, economics, political risks, weather, regulations, and unforeseen site conditions
	Internal	Incomplete scope definition, errors in design, lack of design information, construction methods, and workmanship

Source Ng et al. (2007)

of conflict that occur in teams and within an organization: process conflict, task conflict, and relationship conflict [46–48]. Process conflict occurs when the parties agree on the goals and content of the project, but disagree on how to achieve the goals and actually do the works (conflict about how to do a project), task conflict refer to conflict regarding the goals and content of the project (conflict about the substance of an issue or project), and relationship conflict occurs when the parties have interpersonal issues (also known as emotional conflict) [49–51].

Ng et al. [22], prepared a table to show complexity and uncertainty as a source of conflict in design and construction projects, as shown in Table 3 design change, unforeseen site condition, errors in design, and lack of design information are factors that cause both external and internal complexity and uncertainty

According to [38], design information for building refurbishment projects did not often correspond with the existing conditions, because relevant information (e.g., dimensions) is not available until the construction phase begins. In this situation, the design is in conflict with the existing conditions, which makes design change and cause conflict between owner and contractor. By the same token, [8, 28, 30, 31] believed that design changes are one of the main causes of conflict in building refurbishment and new built projects.

Some construction conflicts are unavoidable, to contractually accommodate changes because of unforeseen project conditions or unavoidable changes in client's priorities. While such conflicts may be settled amicably, the prior presence of unhealthy conflict can trigger degeneration into unnecessary disputes [34].

Yates [31] mentioned that the underlying causes of conflict are identified as inaccurate design information, inadequate design information of client's requirements, changes in design due to changes in client's requirements; in construction projects, design change was characterized as a root causes of conflict by [52], and as problem areas by [33]; also it was characterized as a causes of conflict by [53].

According to [2], building refurbishment projects involve a high level of complexity and uncertainty that are likely to cause asymmetric information between contractors and residents which will cause conflicts between them. Definition of information asymmetry is a situation in which one party in a transaction has more or superior information compared to another. Potentially, this situation could be harmful because one party can take advantage of the other party's lack of knowledge [54].

On the other hand, there are many issues relating to building refurbishment project, and also there are many studies about the conflict or causes and roots of conflict in new building such as researches done by [13, 14, 55, 56]. However, the study on conflict in building refurbishment is limited. Only in some of the studies, the authors have a brief mention about conflict or causes of conflict in building refurbishment projects [8, 9, 30].

4 Conclusion

The review presented in this paper showed that refurbishment projects are tend to be complicated and uncertain. The factors that cause complexity and uncertainty are unforeseen site conditions, site access, lack of space, availability of material, design change, defective design and plan, lack of information during design stage. It was also found that conflicts are prevalent in refurbishment projects. The complexity and uncertainty factors that causes conflict are design changes, unforeseen project conditions, inaccurate design information, errors in design, and lack of design information. The findings presented in this paper would help the refurbishment managers to reduce conflicts in refurbishment projects.

References

1. C. O. Egbu, B. A. Young, and V. B. Torrance, "Refurbishment management practices in the shipping and construction industries — lessons to be learned," *Build. Res. Inf.*, vol. 24, no. 6, pp. 329–338, Nov. 1996.
2. Y.-K. Juan, Y.-H. Perng, D. Castro-Lacouture, and K.-S. Lu, "Housing refurbishment contractors selection based on a hybrid fuzzy-QFD approach," Autom. Constr., vol. 18, no. 2, pp. 139–144, Mar. 2009.
3. B. Sodagar, "Sustainability Potentials of Housing Refurbishment," Buildings, vol. 3, no. 1, pp. 278–299, Mar. 2013.
4. N. Kohler and U. Hassler, "The building stock as a research object," Build. Res. Inf., vol. 30, no. 4, pp. 226–236, Jul. 2002.
5. A. S. Ali, S. N. Kamaruzzaman, and H. Salleh, "The characteristics of refurbishment projects in Malaysia," Facilities, vol. 27, no. 1/2, pp. 56–65, 2009.
6. S. O. Cheung and K. H. Y. Pang, "Anatomy of Construction Disputes," no. January, pp. 15–23, 2013.
7. A. S. Ali and I. Rahmat, "Methods of coordination in managing the design process of refurbishment projects," J. Build. Apprais., vol. 5, no. 1, pp. 87–98, 2009.
8. I. Bin Rahmat, "The Planning and Control Process of Refurbishment Projects.," University College London, 1997.
9. Chew Lee Fuan, "FACTORS AFFECTING TIME PERFORMANCE OF REFURBISHMENT PROJECTS IN SINGAPORE," UNIVERSITY OF MALAYA, 2012.

10. C. O. Egbu, "Perceived degree of difficulty of management tasks in construction refurbishment work," Build. Res. Inf., vol. 23, no. 6, pp. 340–344, Nov. 1995.
11. A. Ali, "Design information in managing refurbishment projects in Malaysia," *Int. J. Phys. Sci. …*, vol. 5, no. June, pp. 768–773, 2010.
12. P. Mitropoulos and G. Howell, "Model for understanding, preventing, and resolving project disputes," *J. Constr. Eng. …*, no. JUNE, pp. 223–231, 2001.
13. N. Jaffar, A. H. A. Tharim, and M. N. Shuib, "Factors of Conflict in Construction Industry: A Literature Review," *Procedia Eng.*, vol. 20, pp. 193–202, Jan. 2011.
14. G. Ofori, "Conflict in Construction," Constr. Manag. Econ., vol. 31, no. 5, pp. 497–501, May 2013.
15. I. Rahmat and A. Ali, "The involvement of the key participants in the production of project plans and the planning performance of refurbishment projects," J. Build. Apprais., vol. 5, no. 3, pp. 273–288, 2010.
16. D. Baccarini, "The concept of project complexity—a review," International Journal of Project Management, vol. 14, no. 4. pp. 201–204, 1996.
17. George L. Head, "an alternative to defining risk as uncertainty," J. Risk Insur., vol. 34, No. 2, pp. 205–214, 1967.
18. Project Management institute, *A Guide to the Project Management Body of Knowledge, Third Edition (PMBOK Guides)*. Project Management Institute, 2004.
19. J. K. Galbraith, *The age of uncertainty*. Houghton Mifflin, 1977.
20. G. T. Friedlob and L. L. F. Schleifer, "Fuzzy logic: application for audit risk and uncertainty," Apr. 2013.
21. E. Woodhouse, *The Future of Technological Civilization | Ned Woodhouse - Academia.edu*. 2013.
22. H. Ng, F. Peña-Mora, and T. Tamaki, "Dynamic conflict management in large-scale design and construction projects," *J. Manag. …*, no. April, pp. 52–66, 2007.
23. J. Diekmann and M. Girard, "Are contract disputes predictable?," *J. Constr. Eng. …*, no. December, pp. 355–363, 1995.
24. N. K. Acharya, Dai Lee Young, and Man Im Hae, "Conflicting factors in construction projects: Korean perspective," Eng. Constr. Archit. Manag., vol. 13, no. 6, pp. 543–566, 2006.
25. N. K. Acharya, Y. D. Lee, and J. K. Kim, "Critical construction conflicting factors identification using analytical hierarchy process," KSCE J. Civ. Eng., vol. 10, no. 3, pp. 165–174, May 2006.
26. T. Vaaland and H. Håkansson, "Exploring interorganizational conflict in complex projects," Ind. Mark. Manag., vol. 32, no. 2, pp. 127–138, Feb. 2003.
27. K. M. J. Harmon, "Conflicts between Owner and Contractors: Proposed Intervention Process," J. Manag. Eng., vol. 19, no. 3, pp. 121–125, Jul. 2003.
28. S. J. Meijers, T. Hartmann, and G. P. M. R. Dewulf, "Conflict Management in Concurrent Engineering, a Case Study," *ASCE*, 2010.
29. J. Newstrom, *Organizational Behavior: Human Behavior at Work*. McGraw-Hill/Irwin, 2010.
30. O. Daoud, "The architect/engineer's role in rehabilitation work," *J. Constr. Eng. Manag.*, no. March, pp. 1–5, 1997.
31. D. Yates, "Conflict and disputes in the development process: A transaction cost economics perspective," pp. 1–14, 1998.
32. A. Yusof, S. Ismail, and L. Chin, "Procurement Method as Conflict and Dispute Reduction Mechanism for Construction Industry in Malaysia," *… Int. Conf. Constr. …*, vol. 15, pp. 215–219, 2011.
33. E. H. W. Chan and H. C. H. Suen, "Dispute resolution management for international construction projects in China," Manag. Decis., vol. 43, no. 4, pp. 589–602, Jan. 2005.
34. M. Kumaraswamy, "Conflicts, claims and disputes in construction," *Eng. Constr. …*, pp. 95–111, 1997.
35. Y. Lee and J. . Gilleard, "Collaborative design: a process model for refurbishment," Autom. Constr., vol. 11, no. 5, pp. 535–544, Aug. 2002.

36. S. Kemmer and L. Koskela, "DEVELOPING A LEAN MODEL FOR PRODUCTION MANAGEMENT OF REFURBISHMENT PROJECTS," *iglc20.sdsu.edu*, 2012.
37. G. Kelley, "Differing Site Conditions," *Constr. Law An Introd. Eng. ...*, no. 215, 2008.
38. R. Krizek, W. Lo, and A. Hadavi, "Lessons learned from multiphase reconstruction project," *J. Constr. Eng. ...*, no. 7965, pp. 44–54, 1996.
39. R. Diven and M. R. Taylor, "Demolition Planning," pp. 1–12, 2006.
40. J. Miller, Protecting Potential Landmarks Through Demolition Review. Washington, D.C.: The National Trust for Historic Preservation, 2007.
41. L. K. Quah, "Comparative variability in tender bids for refurbishment and new build work," Constr. Manag. Econ., vol. 10, no. 3, pp. 263–269, May 1992.
42. A. Ali and C. Au-Yong, "The designer in refurbishment projects: implications to the compatibility of design," *Struct. Surv.*, 2013.
43. A.-S. Ali and C.-P. Au-Yong, "The designer in refurbishment projects: implications to the compatibility of design," Struct. Surv., vol. 31, no. 3, pp. 202–213, 2013.
44. D. Ilter, "Identification of the relations between dispute factors and dispute categories in construction projects," Int. J. Law Built Environ., vol. 4, no. 1, pp. 45–59, 2012.
45. J. R. Gordon, *Organizational Behavior: A Diagnostic Approach (7th Edition)*, 7th ed. Prentice Hall, 2001.
46. T. L. Simons and R. S. Peterson, "Task conflict and relationship conflict in top management teams: the pivotal role of intragroup trust.," J. Appl. Psychol., vol. 85, no. 1, pp. 102–11, Feb. 2000.
47. E. Martínez-Moreno, P. González-Navarro, A. Zornoza, and P. Ripoll, "Relationship, task and process conflicts on team performance: The moderating role of communication media," Int. J. Confl. Manag., vol. 20, no. 3, pp. 251–268, 2009.
48. F. J. Medina, L. Munduate, M. a. Dorado, I. Martínez, and J. M. Guerra, "Types of intragroup conflict and affective reactions," J. Manag. Psychol., vol. 20, no. 3/4, pp. 219–230, 2005.
49. R. Pinkley, "Dimensions of conflict frame: Disputant interpretations of conflict.," *J. Appl. Psychol.*, 1990.
50. K. a. Jehn, "A Multimethod Examination of the Benefits and Detriments of Intragroup Conflict," *Adm. Sci. Q.*, vol. 40, no. 2, p. 256, Jun. 1995.
51. R. W. Griffin and G. Moorhead, *Organizational Behavior*, 10th ed. Cengage Learning, 2011.
52. S. O. Cheung, T. W. Yiu, A. Yee, T. Leung, and O. K. Chiu, "Catastrophic Transitions of Construction Contracting Behavior," no. December, pp. 942–952, 2008.
53. P. Cakmak and E. Cakmak, "An Analysis of Causes of Disputes in the Construction Industry Using Analytical Hierarchy Process (AHP)," *ascelibrary.org*, pp. 94–102, Apr. 2013.
54. P. Xiang, J. Zhou, X. Zhou, and K. Ye, "Construction project risk management based on the view of asymmetric information," *... Eng. Manag.*, no. November, pp. 1303–1311, 2012.
55. P. Fenn, D. Lowe, and C. Speck, "Conflict and dispute in construction," Constr. Manag. Econ., vol. 15, no. 6, pp. 513–518, Nov. 1997.
56. J. Whitfield, *Conflict in Construction*. John Wiley & Sons, 2012.

Part V
Geotechnical Engineering

Bioengineering Stabilization Method to Counter Rainfall-Induced Slope Failure

Abdul Samad Abdul Rahman, Juhaizad Ahmad and Mohd Ikmal Fazlan Rozli

Abstract The application of vegetation as part of slope stability and to control erosion has proved to be cost-effective for stabilizing the surface of the slope. This research describes the unique characteristics of Vetiver grass and *Vetiveria Zizanioides Nash* and it is the potential use for stabilizing slopes and erosion control. This study refers to the past research on the generic characteristics of Vetiver grass. Also, reports on the laboratory tests that had been conducted determine the strength of Vetiver grass roots at an existing slope. It concludes that in the basis of tests are success and effectiveness over many years that the grass and its associated applications can be effective, durable, and low cost method of vegetative stabilization of slopes under tropical and extreme conditions.

Keywords Multistage · Shear strength · Unsoaked · Soaked

1 Introduction

One of the important, interesting, and challenging aspects of civil engineering is evaluating the stability of slopes in soil. Concerns with slope stability have driven some of the most important advances in our understanding of the complex behaviour of soils. According to Duncan [1], there are two reasons that are important to understand the agents of instability in slopes. First, for purposes of designing and constructing new slopes, it is important to be able to anticipate the changes in the properties of the soil within the slope that may occur over time and the various loading and seepage conditions to which the slope will be subjected over the course of its life. Second, for purposes of repairing failed slopes, it is important to understand the essential elements of the situation that lead to its failure, so that repetition of failure can be avoided.

A.S.A. Rahman (✉) · J. Ahmad · M.I.F. Rozli
Faculty of Civil Engineering, Institute for Infrastructure Engineering
and Sustainable (IIESM), 40450 Shah Alam, Selangor, Malaysia
e-mail: kempass@hotmail.com

By the ability of the plant life growing on slopes to both promote and hinder the stability of the slope, it can be said that vegetation and slope stability are interrelated. The relationship is a complex combination of the type of soil, the rainfall regime, the plant species present, the slope aspect, and the steepness of the slope. A major underlying aspect of understanding how vegetation can alter the stability of the slope is the knowledge of underlying slope stability as a function of the soil type, its age, horizon development, compaction, and other impacts [2].

Furthermore, the application of vegetation on a slope surface is one of the ways to controlling slope erosion and landslide from occurred. This is because the plant growth serves two purposes. The leaves can absorb rainfall energy and reduce the size of drops impacting the soil surface which will infiltrate to the ground. At the same time, it can reduce runoff of rainfall. To have the optimum effect, the greatest ground must be realized during periods of maximum rainfall.

The name of "vetiver" comes from the Tamil word "vettiver". In Reunion Island the name of vetiver then changes to be "vetivert". There are twelve known varieties of Vetiver grass, where the most important is Vetiveria zizanioides (L) Nash [3]. Vetiveria zizanioides is a member of family Poaceae commonly known as the Khas-Khas, Khas or Khus grass in India. Vetiver grass grows wild widely in many states such as Haryana, Uttar Pradesh, Rajastan, Gujarat, Bihar, Orissa Madhya Pradesh, and throughout South India. Vetiver grass is a perennial grass with thick fibrous adventitious roots which are aromatic and of high value [4]. For this reason, for centuries, the oil extract from the roots of Vetiveria zizanioides has been used in India in the industry of fragrant oil, screens, mats, hand fans, baskets, and also as traditional medicine (Fig. 1).

Unlike other grass, Vetiver grass is considered as a special grass. Architecturally, it looks like lemongrass and its leaves are like sugarcane but smaller in size. The stem acts like the backbone of the erosion control barrier as strong, hard, and lignified as in bamboo. When they are planted on contour across hill slope, they act like a wooden palisade [6].

Furthermore, these grass have unique characteristics because it can grow fast and erect, acts as a stiff barrier hedge, has vigorous, strong, long, and massive fibrous root system, perennial requiring minimum maintenance, even its seed does not germinate, nor does not spread by stolons or rhizomes to become a 'weed', its crown is below the surface, protecting from fire and overgrazing. Other than that, it also

Fig. 1 Sketch of a Vetiver plant [5]

A - Silt-loaded runoff being slowed down by the plant
B - Silt dropping out of the water behind the plant
C - Sediment free water continuing on down the slope
D - Dense spongy root system that binds the soil together to a depth up to 3 m
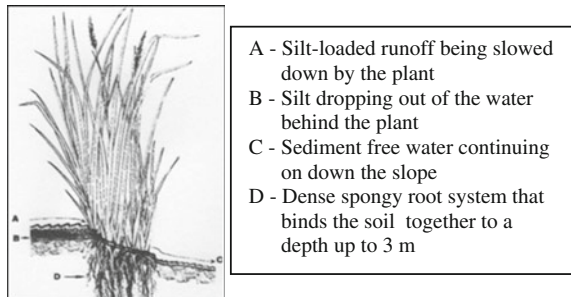
does not harbour rodents, snakes, and other pests, grows under xeric and hydric soil conditions and hence able to survive both drought and flood.

Vetiver grass can survive in a wide range of soil conditions such as low fertility, acidity, alkalinity, salinity, and in high aluminium content. Also, it grows across a wide climatic range and can stand in mean annual rainfall of 300–6,000 mm (Fig. 2).

Vetiver roots are very strong with high mean tensile strength of 75 MPa or approximately 1/6 of mild steel strength. The dense and massive root networks which act in unison; therefore, they resemble the soil nails. With its innate power to penetrate through hardpans or rocky layers, the action of Vetiver roots is analogically likened to 'living soil nails' [7] (Table 1).

Fig. 2 Vetiver grass after a few months [3]

Over time, a natural terrace forms
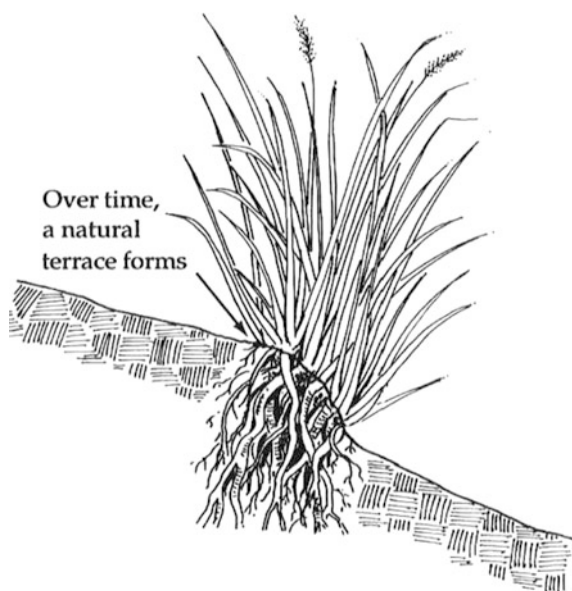
Table 1 Diameter and tensile strength of root of various herbs [7]

Grass	Avg. diam. of roots (mm)	Avg. tensile strength (MPa)
Late juncellus	0.38 ± 0.43	24.50 ± 4.20
Dallis grass	0.92 ± 0.28	19.74 ± 3.00
White Clover	0.91 ± 0.11	24.64 ± 3.36
Vetiver grass	0.66 ± 0.32	85.10 ± 31.20
Common Centipede grass	0.66 ± 0.05	27.30 ± 1.74
Bahia grass	0.73 ± 0.07	19.23 ± 3.59
Manila grass	0.77 ± 0.67	17.55 ± 2.85
Bermuda grass	0.99 ± 0.17	13.45 ± 2.18

2   Methodology

This research is focused on the analysis of root reinforcement on Vetiveria Zizanioides at the selected slope which in this case is at the area of Chamang, Bentong, and Pahang. In order to complete the task, proper planning is required in order to make sure that the study can be completed within the given time. Therefore, the research methodology has been divided into four stages, i.e., problem identification, data collection, data analysis, and conclusion, as shown is Fig. 3.

Samples were collected at the specific slope locations near Air Terjun Chamang, Bentong, and Pahang. The slope was planted with Vetiveria Zizanioides grass and in order to collected the samples, hand auger were used. This is to determine the physical test for disturbed samples. Among the tests that were carried out are moisture content, particle size, particle density, and liquid and plastic limit. Soils with and without Vetiveria Zizanioides grass roots are cut into square shape with depth of 300 mm in order to determine the shear strength using direct shear box test machine. Figure 4 shows the sample that has root reinforcement underneath the soil and how the sample will be taken from its original condition.

Figure 5 shows how the sample was put in a compartment of direct shear box test to determine the shear strength with the root reinforcement into the soil.

A popular apparatus to determine the shear strength parameters is shear box or also known as direct shear test. This test is useful when a soil mass is likely to fail along a thin zone under plane strain conditions [8]. Shear box consists of a square metal box that is split into two halves horizontally. To determine the shear strength of a sample, a rectangular prism is carefully cut from a soil sample and fitted into the shear box apparatus. In the standard type of apparatus, the box is 60×60 mm but for testing coarse soils and fissured clay, a larger version is used. For this sample in which the soil consists of clay, a larger box dimension of 100×100 mm was used.

With the halves of the box together, the soil specimen is sandwiched within the box between ridged metal plates and porous ceramic stones. In addition, a pressure pad is placed on the top and the box itself is placed in an outer box which runs horizontally on roller bearings. A vertical load is then applied to the specimen by means of a static weight hanger. After removing the screw holding the two halves of the box together, the soil is shear by applying a horizontal force at a constant rate of strain. The magnitude of shearing force is measured by means of a proving ring or electronic load cell.

This procedure is repeated to the other two specimens of the same soils. Value of normal stress (σn) and shear stress (τ) on the failure plane are computed and plotted by using a computer. From that values plotted, the shear strength envelopes corresponding to peak and ultimate stresses (σn, τ) can be seen clearly.
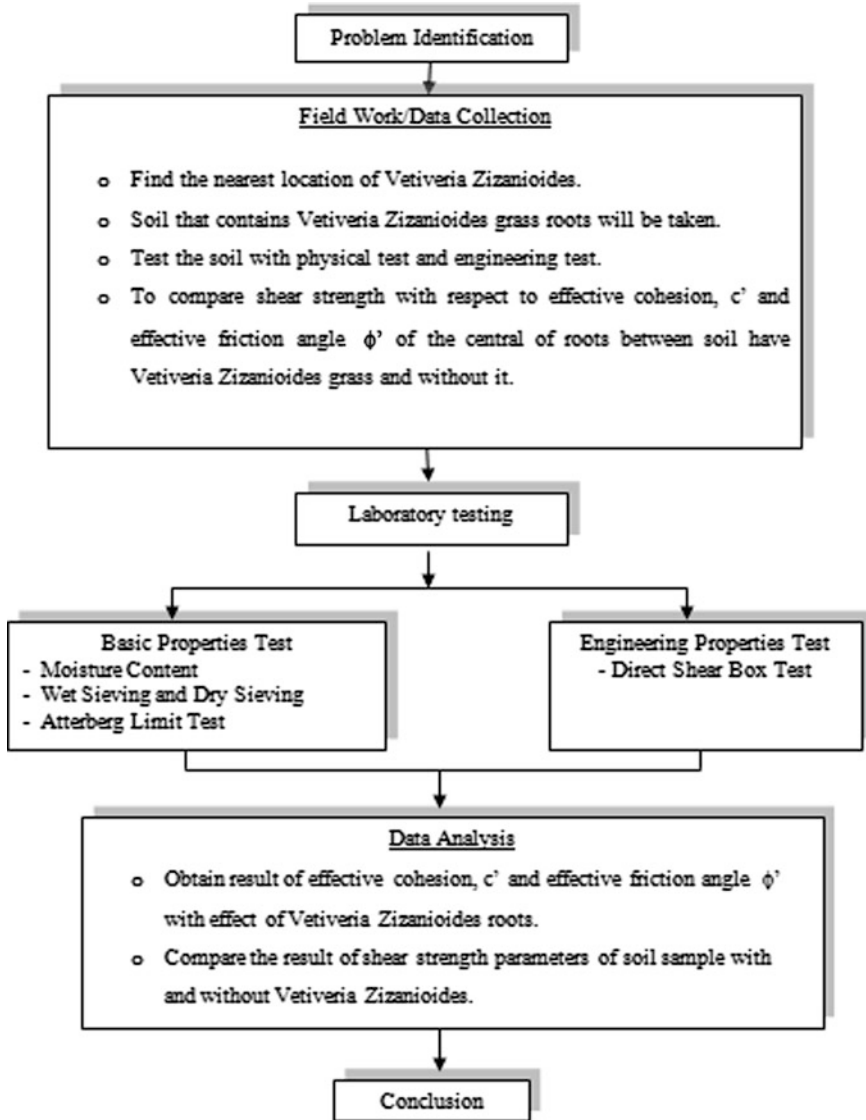
Fig. 3 Flow chart of research methodology

Fig. 4 Sample with the root reinforcement

Fig. 5 Sample preparation
for shear box tests

3 Experimental Results and Discussion

One of the physical tests conducted were the moisture content test of the samples. About four samples were tested as shown in Table 2. Result shows that the average moisture content of the samples were at 18.2 %.

Table 2 Moisture content test of the samples

Samples/container no.	1	2	3	4
Mass of container (g)	16.56	16.70	17.01	13.81
Mass of wet soil + container (g)	95.04	99.59	110.58	87.12
Mass of dry soil + container (g)	82.83	86.75	96.52	75.74
Mass of water (g)	12.21	12.84	14.06	11.38
Mass of dry soil (g)	66.27	70.05	79.51	61.93
Water content, %	18.42	18.33	17.68	18.37
Average water content, %	18.20			

To determine the engineering properties of the sample, the related tests were carried out according to BS1337: Part8: 1990. It will determine the effective cohesion, c' and effective internal friction angle, ϕ' of the in situ soil consists of with and without Vetiveria Zizanioides root reinforcement. The shear strength tests have been conducted using direct shear box test. To execute direct shear test, the disturbed samples were collected at the slope area of Air Terjun Chamang, Bentong, and Pahang. Four samples, namely, Sample A (Control Sample), Sample B, Sample C, and Sample D were tested at vertical effective stress of 30, 60, and 120 kPa. For Sample A (Control), the soil condition is without Vetiveria Zizanioides root reinforcement while the other three samples were tested with the existing Vetiveria Zizanioides root reinforcement.

Figure 6 shows the maximum value in stress–strain plane for Sample A (Control). Finding shows that the maximum values for applied load 30 kPa was 49.6 kPa, while for 60 kPa was 85.4 kPa and for 120 kPa was 122.2 kPa.
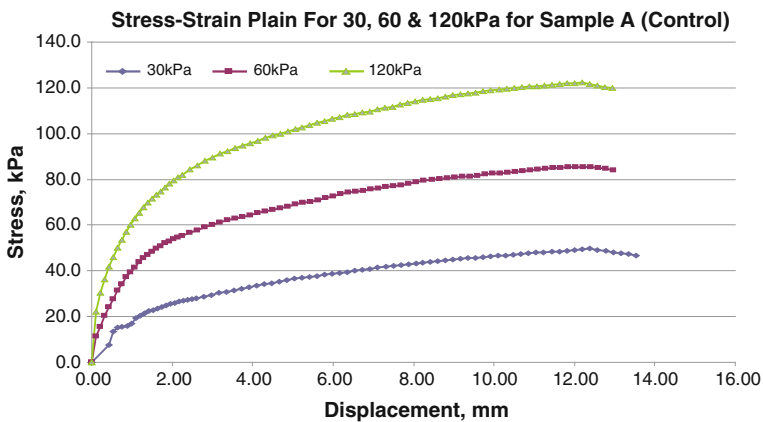
Fig. 6 Stress–strain plane of 30, 60, and 120 kPa for sample A (control)

While Fig. 7 shows the shear strength linear envelope for Sample A at an applied load of 30, 60 and 120 kPa. Result shows that the effective friction angles developed was 23° and effective cohesion was 30 kPa.

Figure 8 shows the maximum value in stress–strain plane for Sample B with root reinforcements. Finding shows that the maximum values for applied load 30 kPa was 35.5 kPa, while for 60 kPa was 74.0 kPa and for 120 kPa was 124.9 kPa while in Fig. 9 shows that the shear strength linear envelope was about 28° in effective friction angle and 17 kPa in effective cohesion.

Figure 10 shows the maximum value in stress–strain plane for Sample C with vetiver grass root reinforcement. Finding reveal that the maximum values for applied load of 30, 60 and 120 kPa was 48.0, 72.9 and 131.0 kPa consecutively.
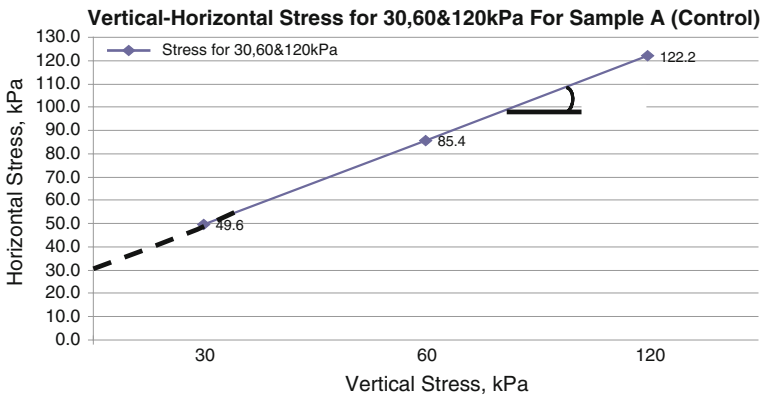
Fig. 7 Shear strength linear envelope at 30, 60, and 120 kPa for sample A (control)
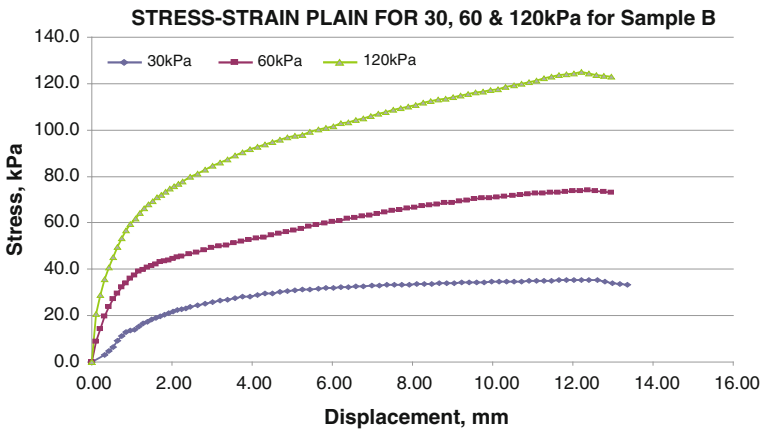
Fig. 8 Stress–strain plane of 30, 60, and 120 kPa for sample B
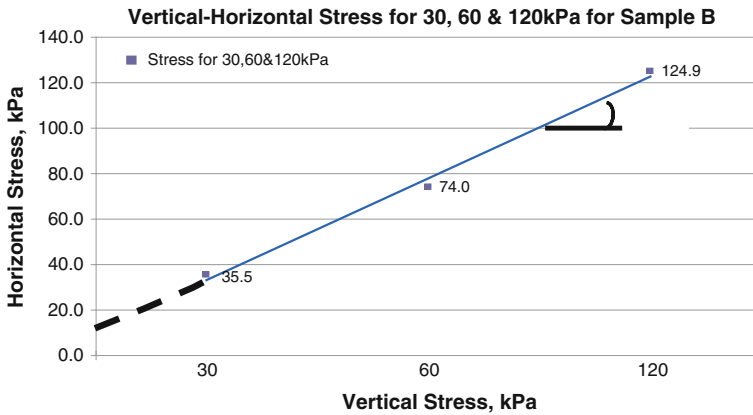
Fig. 9 Shear strength linear envelope at 30, 60, and 120 kPa for sample B
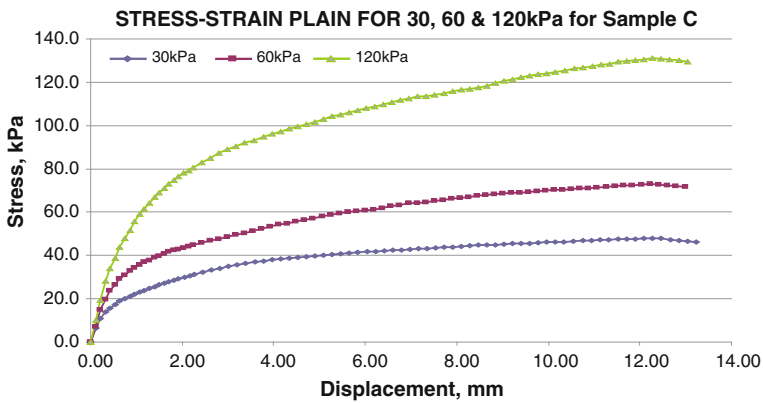
Fig. 10 Stress–strain plane of 30, 60, and 120 kPa for sample C

Figure 11 shows the shear strength linear envelope for Sample C at an applied load of 30, 60 and 120 kPa. Result shows that the effective friction angles developed was 26° and effective cohesion was 20 kPa.

For Sample D, the maximum value of stress–strain at 30 kPa was 48.4 kPa, for 60 kPa was 80.2 kPa and for 120 kPa was 139.8 kPa as shown in Fig. 12. Furthermore, when plotted in shear stress plane, the failure envelope developed was at 25° in effective friction angle while in effective cohesion was 20 kPa as in Fig. 13.

Table 3 shows the summarized results for all the samples with respect to maximum stress, effective cohesion, and effective friction angle.

In addition, all the data were analysed based on the average of effective cohesion, c', and effective friction angle. It shows that for effective cohesion, c' for sample B, C, and D was at 19.0 kPa while for control samples (Sample A) was 30 kPa as shown in Table 4.

Vertical-Horizontal Stress for 30,60&120kPa for Sample C

Fig. 11 Shear strength linear envelope at 30, 60, and 120 kPa for sample C
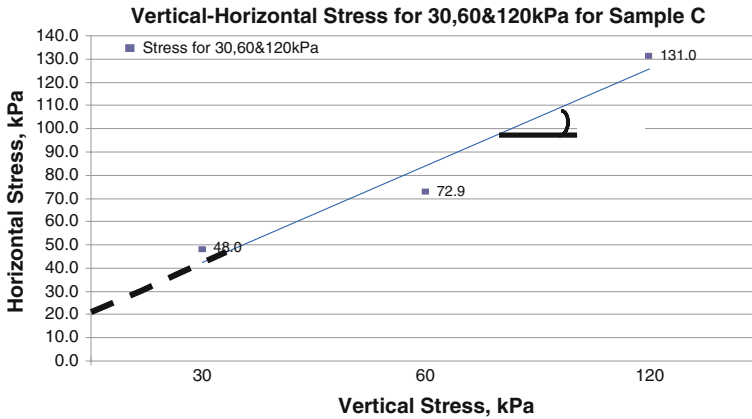
Stress-Strain Plane For 30, 60 & 120kPa for Sample D
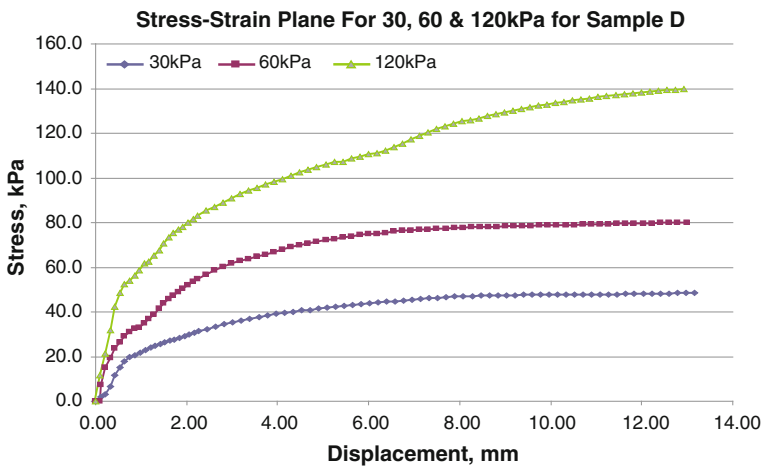
Fig. 12 Stress–strain plane of 30, 60, and 120 kPa for sample D

Findings reveal that there are drastic decreases in effective cohesion, c' for the samples that have Vetiveria Zizanioides root compared to control sample. Meanwhile, the average for effective friction angles, ϕ' for sample B, C, and D was 26° while for control samples (Sample A) it was 23°. It shows that in conjunction to effective friction angles, ϕ' there are slight increases of values between samples that have Vetiveria Zizanioides root and samples that do not have Vetiveria Zizanioides root.

It also shows that sample with Vetiveria Zizanioides root have higher value of effective friction angles ϕ', which the roots help to reinforce the soil surrounding it and thus increase the shear strength. It shows that with the existence of root reinforcement, it will help to strengthen in term of shear strength of the soil especially
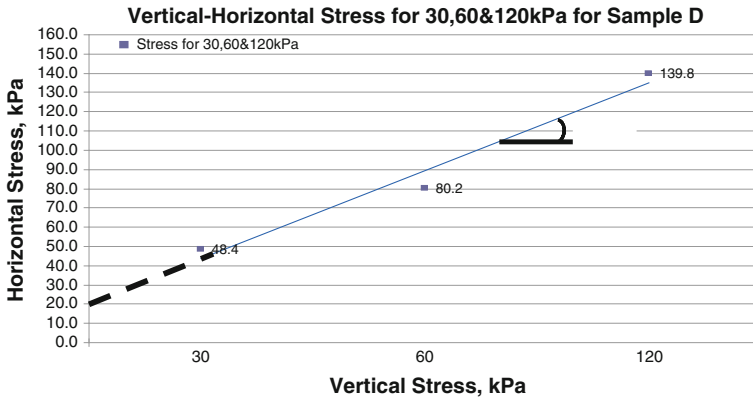
Fig. 13 Shear strength linear envelope at 30, 60, and 120 kPa for sample D

Table 3 Summarized values for maximum stress, effective cohesion, and friction angle for all samples

Sample	Max. stress, kPa			Effective cohesion, c' kPa	Effective friction angles, ϕ'
	30	60	120		
A	49.6	85.4	122.2	30	23°
B	35.5	74.0	124.9	17	28°
C	48.0	72.9	131.0	20	26°
D	48.4	80.2	139.8	20	25°

Table 4 Average of effective cohesion, c' and effective friction angle for Sample A, B, C, and D

No. of sample	A (Control)	B	C	D	Average
Effective cohesion, c' (kPa)	30	17	20	20	19
Effective friction angles, ϕ'	23°	28°	26°	25°	26°

when located in slope areas. Thus, planting Vetiveria Zizanioides in slope areas is one of the methods that can stabilize the slope condition.

On the other hand, there are slight changes in decreasing of effective cohesion, c' of the sample with and without Vetiveria Zizanioides. The result shows that for sample condition that does not have root reinforcement was 30 kPa while for sample having root reinforcement was 19 kPa. The existing of Vetiveria Zizanioides root in the sample will loosen the bonding between soil skeletons in respect to interaction between the soil particles. Channels made by the root in the soil sample will result in loose and weaker the bond interaction.

Furthermore, during rainfall, the roots of Vetiveria Zizanioides will trap the moisture when the water infiltrate into the soil and thus it will weaken the interaction bonding between the soil skeleton. Water that gathered along the roots will

create a barrier between the soil and thus the effective cohesion, c' will become smaller compared to soil that is without root. This explains why the effective cohesion, c' for soil that have root, decreases compared to soil that are without root.

In addition, there is slight increase by 12 % of effective friction angle, ϕ' between sample having Vetiveria Zizanioides root and sample without it. The value of effective friction angles, ϕ' for sample having Vetiveria Zizanioides root is 26° while sample without it is 23°. For effective cohesion, c', the value decreases by 37 %. Study shows that even though the effective friction angles, ϕ' increase but in the same time it would affect the value of effective cohesion, c' decrease rapidly. Nevertheless, the effective friction angles, ϕ' and effective cohesion, c' are the two critical parameters that would reflect the overall shear strength of the soil.

4   Conclusions

The effective cohesion, c' for Sample A (Control) is higher compared to other samples which Sample B, C, and D that have Vetiveria Zizanioides root. It shows that the moist trap along the roots will weaken the bonding between soil particles which will decrease the effective cohesion, c'. In addition, the effective friction angles, ϕ' for Sample A (Control) is slightly lower compared to other samples which Sample B, C, and D that have Vetiveria Zizanioides root. It means in the same time, the existence of root will increase the shear strength with respect to friction angles.

Nevertheless, at low stress level, applied stress of 30 and 60 kPa, the value for Sample A (Control) is slightly higher compared to other samples that have root while for applied stress of 120 kPa, the value for Sample A (Control) drastically decreases compared to other samples that have root. It shows that at low stress level, the soil particles being oriented to fill up the gap in the void along the root and when it reach to applied stress 120 kPa, shear strength of samples that have root will increase rapidly.

The main purpose of this study is to determine the shear strength while linear shear strength envelope incorporates the existing of Vetiveria Zizanioides root reinforcement and sample without root. However, before this research is implemented into practice, several issues need further development and refinement which first, to carry out unconfined compression test (UCT) in order to define the shear strength parameters at zero cell pressure and second, to carry out shear box test in order to determine the shear strength parameters at zero applied loads. Specimens have to be saturated first before the process of shearing took place. The result would give better understanding on the behaviour of the specimens with respect to shear strength in zero loads.

References

1. Duncan, J.M. and Wright, S. G., (2005). "*Soil strength and slope stability*." Canada: John Wiley & Sons.
2. Mattia, C.; Bishetti, G. & Gentile, F. 2005, *Biotechnical characteristics of root systems of typical Mediterranean species*, Plant and Soil, vol. 278, no. 1, pp. 23–32.
3. Worldbank, (1993). *Vetiver grass: a hedge against erosion*, Worldbank, Washington, DC, ISBN 0-8213-1405-X.
4. Rao, R.R. and Suseela, M.R. (1989), *Vetiveria Zizanioides (Linn.) Nash A Multipurpose Eco-Friendly Grass of India*. National Botanical Research Institute Lucknow, India, 439.
5. Carey, B., (2006). *Monto vetiver grass for soil and water conservation*, Natural Resources Sciences, Queensland Government.
6. National Research Council (1993). *Vetiver Grass: A Thin Green Line Against Erosion*. National Academy Press, Washington, D.C.
7. Hengchaovanich, D. (1998). *Vetiver grass for slope stabilization and erosion control*, Tech. Bull. No. 1998/2, Pacific Rim Vetiver Network (PRVN), Bangkok, Thailand, ISBN 974-7773-71-6.
8. Budhu, M. (2007). *Soil Mechanics and Foundations*, John Wiley & Sons, Inc., U.S.A, 2nd edition.

Seismic Refraction Investigation on Limestone Area in Gopeng, Perak

Nurul Huda Abdullah and Haryati Awang

Abstract Seismic refraction method is one of the most commonly used geophysical methods in civil engineering that is able to provide detailed information on the distribution and thickness of subsurface layer with characteristics seismic velocities. By necessity, it also could be a support to the interpretation of geological data. Two-dimensional (2D) seismic refraction tomography is one of the surface geophysical methods used in determining the continuous subsurface profile of ground damage with particular reference to geo materials based on P-wave (Primary velocity, v_p) results. This method was used in this study in purpose to determine the subsurface profile from the study area. ABEM Terraloc MK6 seismograph was used to record data from P-wave data acquired. Using OPTIM software package, the subsurface profile based on linear and delay time analysis would be investigated. Based on the study, it was found that overall strata along the study area were reasonable with the previous geological data by using the P-wave seismic velocity. Thus, this study helps in reducing the cost of site investigation significantly.

Keywords Geophysical · Seismic refraction · P-wave seismic velocities · Borehole data

1 Introduction

In identifying layers or soil strata in subsurface area, there are lots of methods that can be used. Geophysical method is one of them. It also consists of many minor sections, such as seismic refraction and reflections, electrical resistivity, ground

N.H. Abdullah (✉)
Faculty of Civil Engineering, Universiti Teknologi MARA,
40450 Shah Alam, Selangor, Malaysia
e-mail: nurulhuda2801@gmail.com

H. Awang
Institute for Infrastructure Engineering and Sustainable Management,
Faculty of Civil Engineering, Universiti Teknologi MARA, 40450 Shah Alam,
Selangor, Malaysia

penetration radar, and electromagnetic. The discipline of geophysics has developed for use in many fields such as environment, engineering, mining, and archeology where the depth of investigation required is relatively shallow (usually less than 100 m). According to [1–3], seismic is most the favorite method in the field of geophysics to determine the internal distribution of materials within a slope, water effect on slope, identifying sliding surface geometry, mass movement, and geo materials features for rehabilitation and mitigation purposes.

In Malaysia, as well as elsewhere, seismic refraction is the most popular geophysical technique in engineering application. The seismic refraction method was carried out to obtain the subsurface profile of the rock mass. It also is one of the effective methods applied in shallow exploration, including determining the depth of bedrock and the subsurface structural features, such as cracks in the rock bodies. Besides that, an attractive target for shallow seismic refraction was used in environmental investigation, such as to investigate lateral or vertical changes in lithology [4]. Additionally, it is the technique mainly used to investigate near surface geological structures.

Seismic is a technique using the concept of the waves propagated through the geo materials beneath the earth. It is generated by sources which created the seismic waves by free drop weight (geograft and dinoseis) and vibroseis technique [5]. Many researchers have used the seismic refraction technique to determine the characteristics of the site [6–8]. Besides, the advantages of seismic refraction are a cost effective manner within a reasonable time frame and also has the ability to acquire information about the subsurface over a substantial area.

For this study, the seismic refraction method was carried out to determine overburden on both soil and rock distribution analysis. The aim of the study is to determine the information of the subsurface layers in tropically weathered sedimentary rock area.

2 Literature Review

2.1 Seismic Wave Velocity

Generally, the seismic method utilizes the propagation of waves depending upon the elastic properties of the rocks. The waves were created by controlled source and propagated through the earth. The solid body can be changed by applying force in terms of size and shape. But, the body regains to its original condition when the external forces are removed.

The seismic refraction method is utilized such that the seismograph data obtained help to determine the precise depth to weathered basement and overburden thickness such that the different lithologies within the subsurface can easily be predicted [9]. The first arrivals on the seismic signals derived from the seismic refraction method are plotted against shot distances to determine depth information.

At the same time, seismic refraction survey can determine the seismic velocity of a geologic horizon and calculated a relatively precise estimate of the depth to different acoustic interfaces (which may be related to a geologic horizon).

Seismic wave velocity has been widely applied to the investigation of the subsurface geology and to improving our general understanding of fault behavior. While, [10, 11] used similar seismic techniques to observe small-scale (local) geological phenomena, and [12] used porosity and permeability as indices for predicting micro earthquakes on the basis of a one-dimensional poroelastic model. Both the P- and S-waves velocities are the most basic kinds of seismic waves used empirically to evaluate the elastic modulus and geotechnical parameters.

2.2 Seismic Refraction Tomography

Seismic refraction tomography is aimed at providing a representative seismic wave velocity distribution of the subsurface through the inversion of first arrival travel times from multiple sources and receivers. It should be noted that seismic tomography generation is not limited to using first arrival travel times as input only, but some algorithms utilize both refracted and reflected travel times [13]. Tomography is a technique where measurements are made of energy that has propagated through a medium. As stated in [14], the properties of the medium were propagated using the energy received. Several tomographic techniques have been applied to seismic first arrival travel time data [15–17].

Furthermore, the seismic acquisition cable length determines the maximum depth of investigation that will be observed in the refraction tomography results. Accordingly, the far offset shots recorded during the data acquisition are valuable in illuminating deep targets in the study area. Seismic refraction tomography develops. As specific by the modeler, the seismic refraction tomography gives the velocity models by iteratively comparing different velocity structures with observed data to a degree of resolution. The method is also easily applied and well topography. Moreover, the advantage of tomography is the minimum curve ray path in the inversion defines a maximum depth of investigation, whereas only estimates of the investigation depths are possible using more traditional methods.

3 Research Methodology

3.1 General Geology

The study area takes place at the Kota Bharu Estate, Gopeng, Perak is shown in Fig. 1. It is a small town which is approximately 7 km away from the larger town of Mukim Teja, Gopeng. Gopeng in the northern state of Perak, is a town steeped in
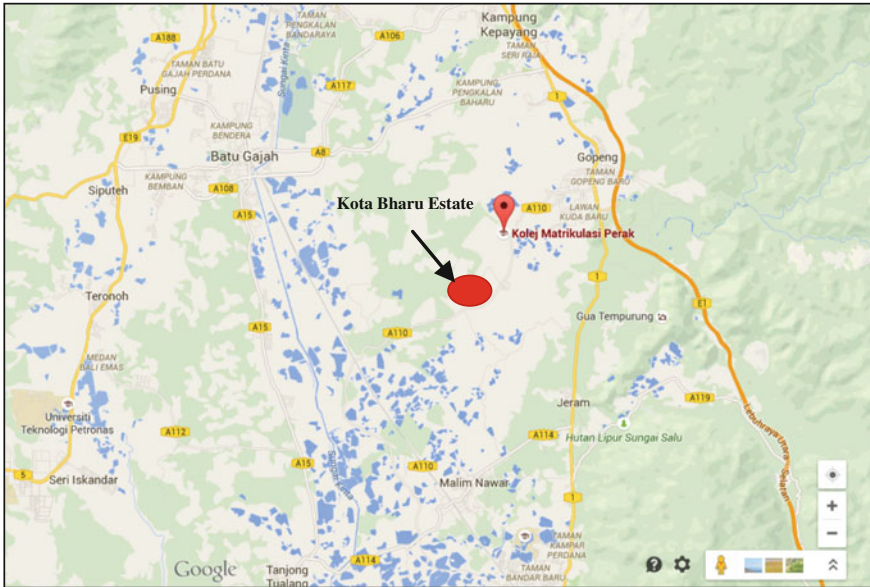
Fig. 1 Location map of study area

tin mining history and the spirit of entrepreneurship. Geologically, the study area is said to be underlain by Kinta Formation. The land use of the study area is mainly covered by forest which especially has oil palm plantations.

According to the geological map in Fig. 2 [18], the bedrock geology of the study area comprises sedimentary and metamorphic rocks. The sedimentary rocks consist predominately of limestone and sandstone. Most of the sedimentary rocks in the valley are Devonian in age which include of phyllite, schist, and slate. Kinta Limestones mostly comprise very pure, massive crystalline marble [19]. The formation consists of massive and pure calcitic limestone that is gray when fresh and weather to a chalky white surface patina [20].

The main primary tin ore mineralization occurs in veins and is related to granites in contact with the sedimentary cover [21]. Beneath the tin rich alluvial deposits Devonian limestones with karst topography are widespread [22]. The investigations of [22] showed that the tin mineralization and the associated mineral composition of the limestones are remarkably different than those in the underlying politic series. In marbles of contact metamorphic origin the tin is associated with tourmaline, fluorite, calcite, and calcic garnet due to metasomatism.
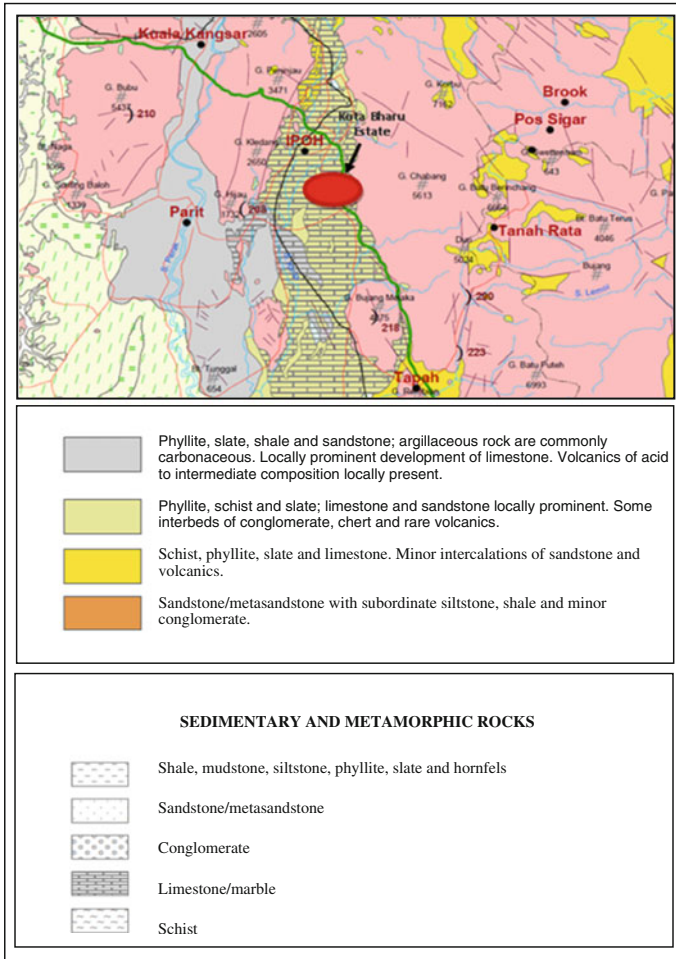
Fig. 2 Geological map of the study area (*source* mineral and geoscience department)

3.2 Seismic Refraction Survey

Throughout the study area surveyed, there are two lines of seismic namely, spread line 1 (SL1) and spread line 2 (SL2). The location of the both spread lines was shown in Fig. 3. All the spread lines were determined based on the suitability condition in the study area.

There are several main equipments that need to be set up properly as to obtain the data for the seismic refraction survey displayed in Fig. 4. It has three main components which are seismic energy source, seismic receiver, and seismic record. The seismic energy source was generated by various methods such as the vibrator, the hammer hitting at the plate, and explosive. Those methods applied by
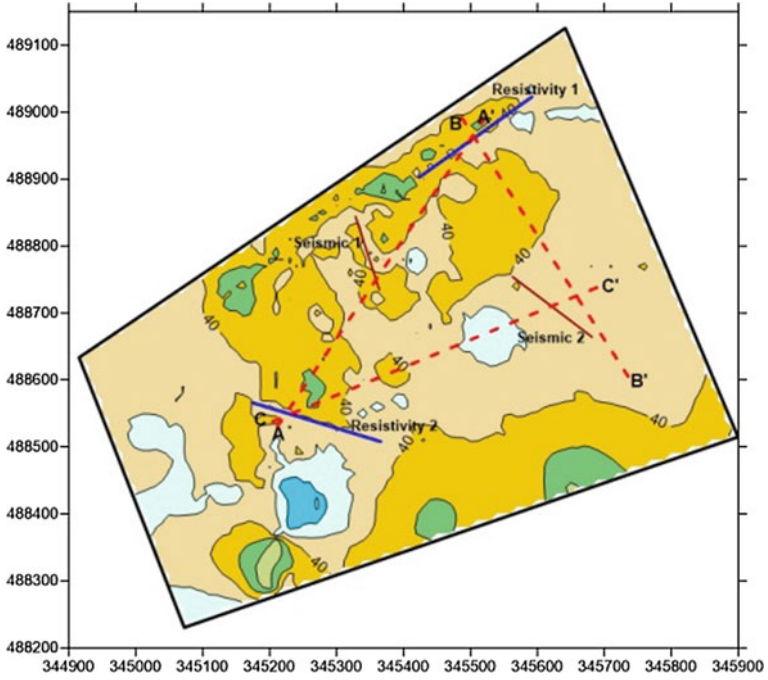
Fig. 3 Location of boreholes and spread lines in the study area

Fig. 4 Seismic refraction survey equipments

depending on the situation to be conducted, for example, the explosive can produce high seismic energy, and thus, the wave produce can travel deeper into the deeper layer compared to the hammer hitting at the plate and the vibrator. The deeper the layer which is wanting to explore, the higher the energy of seismic source is
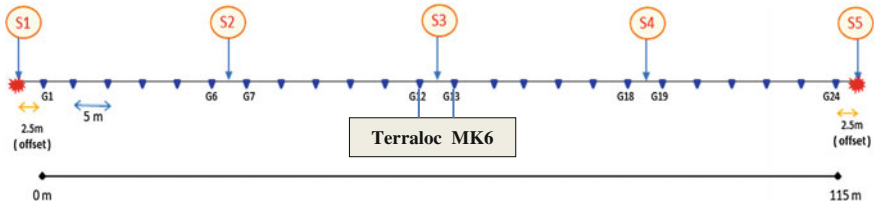
Fig. 5 Geophone layout for the seismic refraction data acquisition along spread line

needed. Mauritsch et al. [2] had to switch from a sledgehammer to explosives in order to impart enough energy in the ground. The wave in the study was generated using a hammer as sources of energy to be acquired in the target area and five numbers of hammer stacking were performed. It depends on the noise surrounding area to get an accurate value during data acquisition.

Geophone is one of the devices that can detect the seismic wave and receiving the wave without storing the data will be useless and no analysis can be made. The device which can store the data obtained from geophones is the seismogram. The entire detected would be recorded and the data obtained would be transferred into the seismograph.

By collecting data acquisition, the seismic refraction line setting out as illustrated as Fig. 5. Five sets of readings were taken along the spread line including one in the middle, two in the forward, and two in the reverse. Then, two seismic cable connectors were connected with twenty-four number of 28 Hz geophones fixed on the ground surface area. The connection of all the devices should be connected in a proper manner in order to obtain the most precise results.

This study applied five numbers of shot points along the spread line with two offset shots at both ends and three center shots were executed at geophone to obtain subsurface profile. It is more efficient processing. A spread line was conducted with a total length of 120 m for the interval 5 m between.

Interference from surrounding and intermitted background noise such as noise caused by direct air wave, ground roll, wind noise, rain noise, traffic, and heavy machinery could be reduced by stacking signals from several strikes at each shot point. Kearey et al. [23] stated that the effects of the wind and source-generated noise should be reduced. It is because the useful signals were generated by lesser frequencies than the wind noise. Thus, the noise has minimized its effects by simple frequency filtering. The seismic signals pick up by the linear array of geophones connected to 24 channels seismograph ABEM Terraloc MK6. The critically refracted wave from seismic sources was considered. It travels down and along the different refractor boundaries. After that, it was converted to digital signals before storing in the stacking memory. Thence, the seismograph digital data from ABEM Terraloc MK6 would be transferred to the hard disk computer was called data processing.

The data analysis was obtained by the available software, namely OPTIM software which consists of SeisOpt Picker and SeisOpt@2D processing. It was used in generating subsurface profile model. SeisOpt Picker was acquired to pick the first

arrival (P-wave). While, the SeisOpt@2D software was used to generate the velocity distribution representing the subsurface profile model based on the depth and velocity calculated. This method is used by on the interpretation of the first arrivals in the seismic signals and assumed that the velocity increases with depth [24].

4 Result and Discussion

The seismic refraction in the study had been carried out along two spread lines and the result is shown in Figs. 6 and 7. During the data acquisition stages, two spread lines called spread line 1 (SL1) and spread line 2 (SL2) with a total length of 240 m were conducted. Based on the SL1, it was transverse from Southeast to Northwest of the study area. From the previous researcher, the various P-wave velocities (v_p) related to the study area for different mediums were given in Table 1.

The seismic tomogram in Fig. 6 considered as approximate representations of geological sections along the seismic refraction survey that has varying velocity. The thickness of the soil layer along SL1 varies between 100 and 500 ms^{-1} of the seismic velocity below 10 m from existing ground level. Below this layer of the

Fig. 6 Velocity model for spread line (SL1)
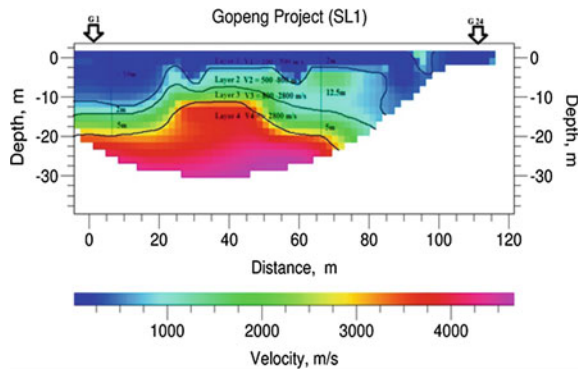
Fig. 7 Velocity model for spread line (SL2)
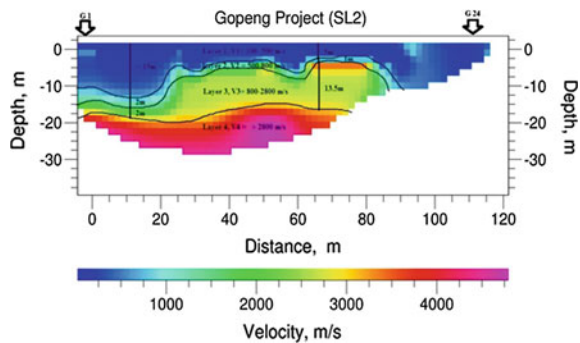
Table 1 Typical primary (v_p) velocities of some of the earth materials [25–27]

Material	v_p (m/s)
Air	330
Water	1450–1530
Soil	100–500
Shales	1200–3000
Sandstone	1400–4500
Limestone (soft)	1700–4200
Limestone (hard)	2800–7000
Rock, weathered, fractured or partly decomposed	610–3048

velocity range from 500 to 800 ms^{-1} showing the highly weathered limestone area having a thickness between 2.0 and 12.5 m. The seismic velocity in the third layer along this line is in the range of 800–2800 ms^{-1} indicating the highly fractured limestone area with 8.0 and 19.5 m depth. The bottom of the subsurface profile in SL1 was mapped by limestone bedrock, average seismic velocity above 2800 ms^{-1} and having the thickness between 12 and 25 m from existing ground level.

Meanwhile, SL2 was transverse from Northwest to Southeast of the study area. The seismic tomogram was illustrated in Fig. 7. The thickness of the soil layer along SL1 varies between 100 and 500 ms^{-1} of the seismic velocity below 15 m from existing ground level. The seismic velocity in the second layer is in the range 500–800 ms^{-1} indicating the highly weathered limestone area with 1.0–12.5 m depth. Below this layer, having a thickness from 2.0 to 19.5 m showing the highly fractured limestone area of the velocity range between 800 and 2800 ms^{-1}. Limestone bedrock mapped below this layer varies between 12 and 25 m with an average seismic velocity of above 2800 ms^{-1}.

Based on results of seismic tomogram for SL1 and SL2, it was presented that there were four main layers of seismic velocity. In summary, there were four types of geo materials with possible different characteristics. These show that the first layer along these lines was covered by overburden soil. The second layer was indicating with highly weathered.

Limestone area. The highly fractured limestone area was mapped below this layer. Thence, the forth layer showing the limestone bedrock area suggestive of a good rock mass, thus is good enough for laying civil foundation for structures. Seismic velocity in the layer gradually increases downwards suggesting that the bedrock quality improves with depth. The results of seismic velocity value along two spread lines as obtained from the seismic refraction survey were summarized as per Table 2 below.

The result of this P-wave seismic velocity exploration was validated with borehole data as shown in Figs. 8, 9 and 10. So the findings showed that intrusive drilling method from borehole data was almost the same with the seismic subsurface profile of the study area.

Table 2 Typical primary (v_p) velocities for different materials of the study

Layer	v_p (m/s)	Thickness (m)	Description
1	100–500	<15 m from existing ground level	Overburden soil
2	500–800	1–12.5 m thickness	Highly weathered limestone
3	800–2800	2–13.5 m thickness	Highly fractured limestone
4	>2800	<15–20 m from existing ground level	Limestone bedrock
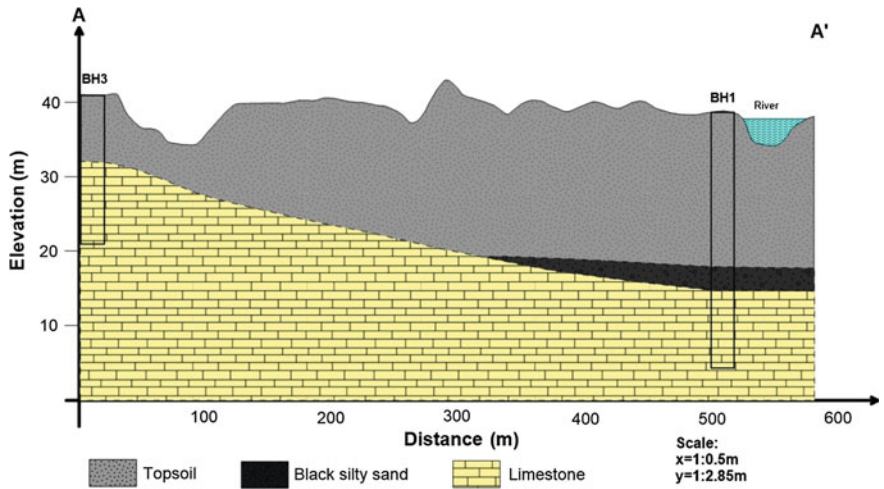
Fig. 8 A subsurface cross section based on borehole result at profile A–A′
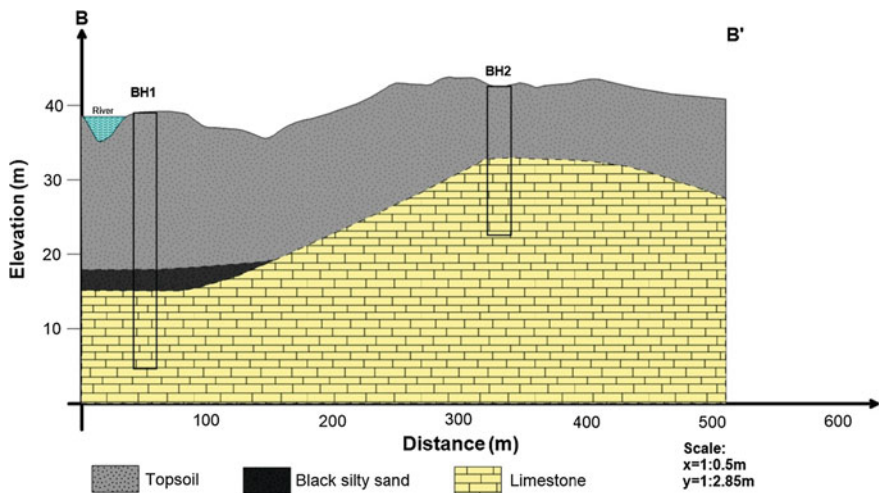
Fig. 9 A subsurface cross section based on borehole result at profile B–B′
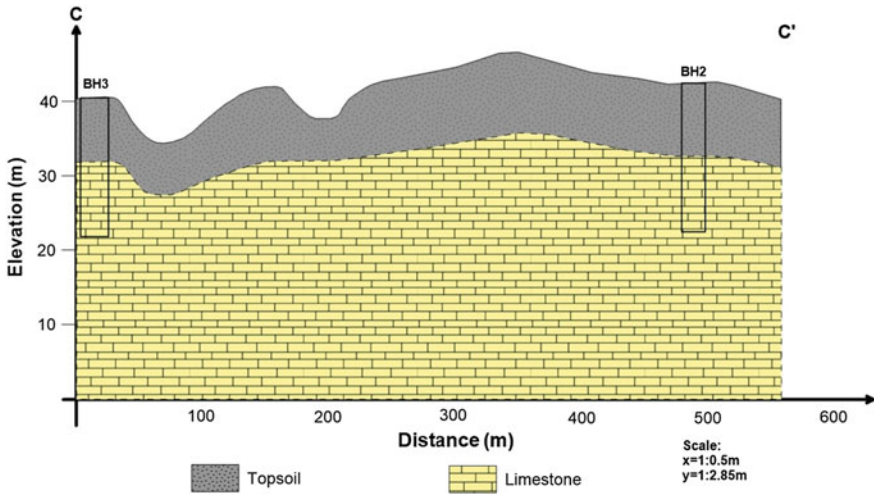
Fig. 10 A subsurface cross section based on borehole results at profile C–C′

5 Conclusion and Recommendation

From these data, it appears that P-wave velocity can determine the soil and rock interface and also the subsurface layers. It will be supported by the drilling method for the confirmation. Then, it can be concluded that overall strata along the study area where reasonable with the previous geological data. But, drilling rather expensive and usually the information between the boreholes are merely based on interpretation and correlation. Therefore, the seismic refraction survey has the ability to produce comprehensive continuous subsurface profile in a short duration and at relatively low cost. However, it can be tried for other areas with different weather conditions and latitude region whereby both conditions are expected to affect the weathering rate of rock. The magnitude of parameters obtained will be influenced by the surrounding conditions.

References

1. G. Gokturkler, C. Balkaya and Z. Erhan, Geophysical investigation of a landslide: The Altundag landslide site, Izmir (western Turkey). Journal of Applied Geophysics, 65, 2008, pp 84–96.
2. H.J. Mauritsch, W. Seiberl, R. Arndt, A. Romer, K. Schneiderbauer and G.P. Sendlhofer, Geophysical investigations of large landslides in the Carnic Region of southern Austria. Engineering Geology, 56, 2000, pp 373–388.
3. D.M. MCann and A. Forster, Reconnaissance geophysical methods in landslide investigations. Engineering Geology, 29, 1990, pp 59–78.

4. G.T. Al-Anezi, A.M. Al-Amri, H. Zaman, Investigation of the weathering later using seismic refraction and high-resolution seismic reflection methods, NE of Riyadh city. 2011, DOI 10.1007/s12517-011-0290-y.

5. A.R. Samsudin, GEOFIZIK, Konsep dan Penggunaan. Dewan Bahasa dan Pustaka, Kuala Lumpur, 1990, pp 222–256.

6. K.T. Kilty, R.A. Noriss, W.R. McLamore, K.P. Hennon and K. Euge, Seismic refraction at Horse Dam. An application of the generalized reciprocal method. Geophysics 51, 1986, pp 266–272.

7. N.P. Dutta, Seismic refraction method to study the foundation rock of a Dam. Geophys Prospect 32, 1984, pp 1103–1110.

8. P.J Hatherly and M.J. Neville, Experience with the generalized reciprocal method of seismic refraction interpretation for shallowseismic engineering site investigation. Geophysics, 51, 1986, pp 276– 288.

9. D.J. Tearpock and R.E. Bischke, Applied subsurface geological mapping. Prentice-Hall PTR Press, Englewood Cliffs, NJ., USA., 1991, pp 94–96.

10. Y. Xu, Z. Li, R. Huang and Y. Xu, Seismic structure of the longmen shan region from S-wave tomography and its relationship with senchuan Ms 8.0 earthquake on 12 May 2008, Southwestern China. Geophysics Res. Lett, 37, 2010.

11. C. Sanchez-Valle, S. Ghosh and A.D. Rosa, Sound velocities of ferromagnesian carbonates and the seismic detection of carbonates in eclogites and the mantle, Geophysics Res. Lett, 38, 2011.

12. C.A. Zelt and R.B. Smith, Seismic travel time inversion for 2-D crustal velocity structure. Geophysical Journal International, 108, 1992, pp 16–34.

13. R.R. Stewart, Exploration seismic tomography: fundamentals. Society of Exploration Geophysicists, Tulsa, OK, 1991, pp 1–1.

14. C. J. Ammon and J. E. Vidale, Tomography without rays. Bulletin of the Seismological Society of America, vol 83, 1993, pp 509–528.

15. J.L. Simmons and M.M. Backus, Linearized tomographic inversion of first arrival times, Geophysics, vol. 57, no. 11, 1992, pp 1482–1492.

16. K. Vasudevan, W.G. Wilson and W.G. Laidlaw, Simulated annealing statistics computation using an order-based energy function. Geophysics, vol. 56, no 11, 1991, pp 1831–1839.

17. Mineral and Geoscience Department, Geological Map of Perak, 2004.

18. J. Crowther, Magnesium and calcium concentration in limestone groundwaters, Peninsular Malaysia. Bulletin of Geological Society Malaysia, 23, 1989, pp 59–83.

19. C.S. Hutchison and N.K. Tan, Geology of Peninsular Malaysia. vol. 1, 2009, pp 72–73.

20. C.S. Hutchison, Geological evolution of South-East Asia. Geological Society of Malaysia, Kuala Lumpur [paperback reprint of Hutchison, 1989a], 1986, pp 72–73.

21. R. Krahenbuhl, Magmatism, tin mineralization and tectonics of the Main Range, Malaysian Peninsular: Consequences for the plate tectonic model of Southeast Asia based on Rb-Sr, k-ar and fission track data. Buletin of the Geological Society of Malaysia, 29, 1991, pp 14–17.

22. F.M. Campbell, A. Kaiser, H. Horstmeyer, A.G. Green, F. Ghisetti, A.R. Gorman, M. Finnemore, D.C. Nobes, Processing and preliminary interpretation of noisy high resolution seismic reflection/refraction data across the active Ostler Fault zone, South Island, New Zealand. Journal of Applied Geophysics 70, 2010, pp 332–342.

23. P. Kearey, M. Brooks and I. Hill, An introduction to geophysical exploration. 3rd edition, Blackwell, Oxford, 2002, pp 262.

24. H. Kohnen, The temperature dependence of seismic waves in ice. Journal of Geology, 13, 1974, pp 144–147.

25. H.R. Burger, A.F. Sheehan and C.H. Jones, Introduction to Applied Geophysics: Exploring the Shallow Subsurface. New York. W. W. Norton and Company, 2006.

26. D.F. McCarthy, Essentials of Soil Mechanics and Foundations: Basic Geotechnics. 7th ed. New Jersey; Pearson International Edition, 2007.

27. R.B. Peck, W.E. Hanson and T.H. Thornburn, Foundation Engineering. New York; Wiley, 1974.

The Effect of Cyclic Stress on the Strain and Microstructure of Weathered Granite

**Nurul Ainain Mohd Salim, Zainab Mohamed
and Mohamad Nor Berhan**

Abstract This paper elaborates the effect of cyclic stress on tropically weathered granite of grade II, grade III, and grade IV. The specimens were tested under cyclic loading with frequency of 1 Hz, under constant sinusoidal waveform and identical stress ratio of 0.17. The test was setup under maximum stress of 70, 80, and 90 % of its ultimate strength. The compressional wave velocity, shear wave velocity, and uniaxial compressive strength were recorded before and after cyclic load testing in order to observe the post-cyclic effect on rock properties. Petrographic analysis using SEM and thin-section images were also captured to investigate the change in rock microstructure under cyclic load. Result reveals that when specimen is loaded at 70 and 80 % of its ultimate strength, eight out of nine specimens are able to withstand the one million cycles. However, at 90 % of the ultimate strength, only two out of nine specimens were failed before reaching one million cycles. SEM images were evidently showing the presence of abundance microcracks due to cyclic load.

Keywords Weathered rock · Cyclic load · Post behavior

1 Introduction

Investigations on weathered rock have been gaining attention since researchers are now realizing the importance of assessing the weathered rock quality in the tropic. The effect of cyclic load on weathered rock performance is a challenging exercise

N.A.M. Salim · Z. Mohamed (✉)
Institute for Infrastructure Engineering and Sustainable Management,
Faculty of Civil Engineering, Universiti Teknologi Mara, Shah Alam, Malaysia
e-mail: 2010486472@isiswa.uitm.edu.my

N.A.M. Salim
e-mail: nurulain2@yahoo.com

M.N. Berhan (✉)
Faculty of Mechanical Engineering, Universiti Teknologi Mara, Shah Alam, Malaysia
e-mail: 2010486472@isiswa.uitm.edu.my

since it is hard to control the variables of weathered rock specimens. However, effort must be done to scrutinize this type of rock condition since in tropical country constructions were made on weathered rock. According to [1] chemical weathering on rock minerals is aggressive in tropical country and the effect of weathering may occur up to 100 m down from the ground surface [2]. Furthermore, weathered rock is known to be weaker than fresh rock in terms of its strength.

The response on intact and fresh rock under cyclic loading has been conducted by many researchers [3–9]. However, there are also investigations made on jointed rock under cyclic loading [10, 11]. Jointed rock is said to have more obvious effect under cyclic load such as the increase of joint density as well as crack opening. Jointed rock may refer as rock having all sorts of discontinuities like cracks, fissures, joint, faults, and bedding plane. Such discontinuities caused the rock to be weaker and more deformable [12]. This jointed rock may have similar behavior like weathered rock; however weathered rock in the tropical climates much differs from the cool climates. This is due to the fact that in tropical climates, chemical weathering is so intense where quartz mineral are typically the only component of the rock that remains unaltered. Quartz relatively unaltered because the mineral has great resistant to chemical attack [13].

Cyclic load investigation on weathered rock is strongly required to recognize the rock behavior especially when subjected to cyclic activities such as earthquakes, blasting, traffic-loading, and drilling. The most fundamental investigation in order to understand the behavior of weathered rock under cyclic loading is to know the strength degradation using cyclic uniaxial compression loading. Therefore, this paper is intended to investigate the effect of cyclic load on the weathered granite post-cyclic behavior.

2 Sample Preparation and Experiment Setup

2.1 Selecting Rock Specimen

In this study, cylindrical rock specimen of height-to-diameter ratio (h/d) of 2 is used throughout the test. The specimen preparation is generally based on [14]. The test is conducted on grade II, III, and IV granite specimen and the weathering degree of each specimen is determined using Schmidt rebound number. The weathering grade classification of hand-sized specimen is referred to [15]. Twenty seven of granite specimens were used and prepared for the cyclic loading test. Specimens were grouped in three for each weathering grade, namely grade II, III, and IV for each test. Each specimen is equipped with two strain gages in order to monitor its axial strain and radial strain.

Rock specimen is labeled as in Fig. 1. GR refers to as types of rock in this case granite, followed by number of specimen and at the end is for rock weathering grade (e.g., grade II, grade III, or grade IV). However, the weathering grade is written in standard numbering instead of roman.

Fig. 1 Rock specimen

2.2 Experiment Setup

Cyclic loading test is conducted using UTM-IPC 1000 kN digital servo-control testing machine. The equipment consists of hardware components and software applications that provide direct closed-loop digital servo-control and the test setup is illustrated as in Fig. 2. The machine has the capacity of 1000 kN which enable to run cyclic loading up to 3 Hz.

In this study, the test was performed using frequency of 1 Hz, constant sinusoidal wave, and similar stress ratio of 0.17 on all specimens. Maximum stress for the test is set at 70, 80, and 90 % of the specimen static ultimate strength which later in this paper will be introduced as 0.7, 0.8, and 0.9 σu, respectively.

This applied maximum stress used to investigate the fatigue life of weathered rock. Previous researches have revealed that the fatigue life of rock is between 60 and 80 % of their static ultimate strength [5, 6] also reveals that it is not less than 81.5 %.

The additional detail on the test loading condition is provided in Table 1. The mean rebound number, R is written in parentheses.
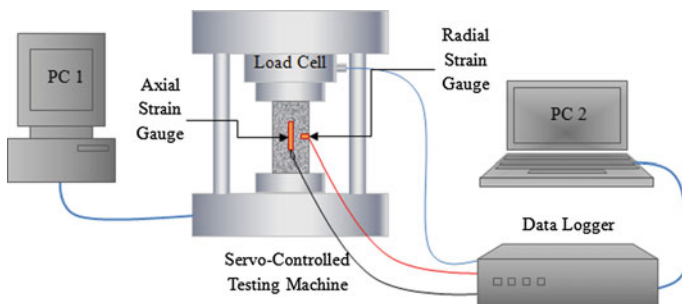
Fig. 2 Cyclic loading test setup

Table 1 Cyclic loading test condition

Weathering grade	No. of specimen	Ultimate strength σu (MPa)	Loading condition		
			Max stress at.% σu	Applied maximum stress (MPa)	Applied minimum stress (MPa)
II (46)	3	81.915	70	57.340	9.747
	3		80	65.532	11.140
	3		90	73.723	12.532
III (36)	3	52.982	70	37.087	6.304
	3		80	42.386	7.205
	3		90	47.634	8.097
IV (17)	3	23.286	70	16.300	2.771
	3		80	18.629	3.166
	3		90	20.957	3.562

The stress ratio which defines the ratio of minimum stress to maximum stress is kept similar throughout the test. It is meant to control the result discrepancy between each set of specimens based on its weathering grade. The number of cycles is also limited to one million cycles for most engineering purposes; the infinite is taken to be 1 million cycles. As for materials which do not exhibit a fatigue limit, tests are usually terminated between 10^7 and 10^8 cycles, and the concept of an endurance limit at either 10^7 or 10^8 cycles defined [16]. Beyond this subtopic, the uniaxial compressive stress will be written as UCS.

3 Test Results

3.1 Engineering Properties of Weathered Granite Specimen

Prior executing the cyclic loading test, the engineering properties for each weathered specimen is recorded. This is to observe the change in specimen properties before and after subjected to cyclic load. A total of 27 specimens were tested. However, not all specimens able to withstand the one million cycles and therefore only four specimens were able to have the properties recorded after subjected to cyclic load.

Unfortunately, for grade II and grade III, the data is unable to record during the test conducted and the specimens were destroyed just after completing the one million cycles. There are two possibilities of this problem to occur: one is due to power rectification done in the course of conducting the test and two the specimen fatigue life occurred approximately at one million cycles. Only for grade IV specimens of 0.8 and 0.9 σu were able to record their properties after subjected to cyclic load.

The engineering properties include compressional wave velocity, V_p, shear waves velocity, V_s and ultimate compressive strength (UCS). Both V_p and V_s were

Table 2 Engineering properties before and after cyclic load

Specimen description	Engineering properties (mean value)					
	Before cyclic load			After cyclic load		
	V_p (m/s)	V_s (m/s)	UCS (MPa)	V_p (m/s)	V_s (m/s)	UCS (MPa)
GR41G4 (At 0.8 σu)	3121	1213	23.286	4231	1665	–
GR32G4 (At 0.8 σu)	2024	1265	23.286	3907	1892	88.173
GR58G4 (At 0.9 σu)	2917	1274	23.286	3667	1586	75.239
GR48G4 (At 0.9 σu)	3494	1168	23.286	4154	1375	63.315

determined using the FFRC test; the test procedure and specimen setup can be found in [17]. The engineering properties comparison before and after subjected to cyclic load is tabulated in Table 2.

From Table 2, all four specimens show an increment for all properties after being subjected to cyclic load. For GR41G4, the UCS after cyclic load is unable to record since the specimen is damaged due to some technical problem during executing the test.

Based on the result, it seems that all four specimens become stiffer as refer to the increase of V_p and V_s result. The percentage increase of V_p is 35 and 93 % for specimen of 0.8 σu while for specimen of 0.9 σu is about 19 and 25 %. As for V_s, the percentage increase for specimen of 0.8 σu is 37 and 49 % while for 0.9 σu is 18 and 24 %.

Furthermore, the uniaxial compressive strength of rock was also increased. The reason is when the rock is under compression loading primarily it started with the closing of cracks [18]. The closing of cracks in rock may contribute to the compactness of rock thus increase the velocity as well as the strength of the rock. Since the applied maximum stress used in this test is lower than the specimen ultimate stress; it is expected that the specimen fatigue limit possibly beyond one million cycles. It is reflected in the result of UCS after subjected to cyclic load; where the strength is significantly increased. For GR32G4 (0.8 σu), the strength increased at 278 %, while for GR58G4 (0.9 σu) and GR48G4 (0.9 σu) the strength increased approximately at 223 and 173 % accordingly.

3.2 Axial Strain of Weathered Specimen Under Cyclic Load

Nine representative specimens of grade II, III, and IV granite are selected to undergo cyclic loading test. Each set of specimen was tested for different maximum stresses as mention in Sect. 2.2. The details of the rock type, specimen number, weathering grade, including number of cycles to failure is tabulated in Table 3. Graph of axial strain versus number of cycles were plotted to observe the changes on specimen strain subjected to cyclic load are shown in Figs. 4, 7 and 8.

From Fig. 3, there are eight out of nine specimens survived the one million cycles; however, only one specimen, GR157G3, failed at 510,606 cycles. From the

Table 3 Description of specimens under cyclic load

No.	Specimen no.	Weathering grade	Loaded at. % σu (%)	Cycles at failure
1	GR42G2	II	70	1×10^6
2	GR22G2			1×10^6
3	GR38G2			1×10^6
4	GR157G3	III		510,606
5	GR68G3			1×10^6
6	GR136G3			1×10^6
7	GR21G4	IV		1×10^6
8	GR14G4			1×10^6
9	GR17G4			1×10^6
10	GR99G2	II	80	1×10^6
11	GR102G2			1×10^6
12	GR98G2			1×10^6
13	GR147G3	III		1×10^6
14	GR23G3			1×10^6
15	GR132G3			1×10^6
16	GR42G4	IV		1×10^6
17	GR32G4			1×10^6
18	GR52G4			1×10^6
19	GR38G2	II	90	24
20	GR51G2			30
21	GR88G2			1
22	GR82G3	III		40
23	GR73G3			1
24	GR114G3			1
25	GR48G4	IV		1×10^6
26	GR43G4			1
27	GR58G4			1×10^6

Fig. 3 Specimen loaded at 70 % of ultimate strength
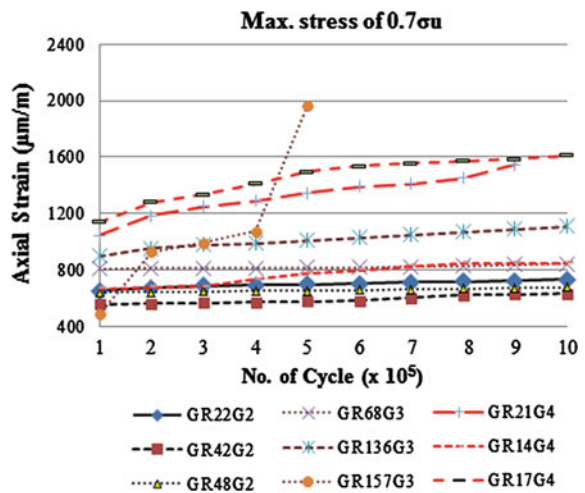
graph, it can be seen that the strain is dramatically increased at 1969 µm/m before failure occurred. It is expected that the specimen was failed due to fatiguing considering that the specimen was burst during testing and the rock fragment was greater and varied from big pieces to dust size pieces as explained by [19, 20]. The image of the fail specimen was captured as evidenced in Fig. 4.

Specimens showed a slow increase in strain when reaching one million cycles except for GR21G4. The specimen is started to show the sign of failure at approximately 900,000 cycles. The specimen is found cracked after completing one million cycles. With regards to weathering grade, all specimens grade II, III, and IV are showing the similar trend and no significant difference can be seen through the graph.

Scanning Electron Microscope (SEM) image was captured to analyze the microscopic damage suffered by the specimen. Using magnification of 5000×, the presence of cracks can be seen clearly as shown in Fig. 5. Presence of abundance of cracks was seen from the fragment of GR157G3; all cracks are found interconnecting to each other. The image suggested that these cracks are propagated during the cyclic load. The propagated cracks resulted in the instability of rock structure thus contributing to the failure of GR157G3.

At 0.8 σu, all specimens were able to complete the one million cycles and no specimens showing any sign of crack and fail. However, Fig. 6 shows that the axial strain is gradually increased with a number of cycles for all specimens (weathering grade II, III, and IV). The strain is positively increasing and there is a potential that those specimens may fail beyond one million cycles.

Fig. 4 Specimen of GR157G3 fails due to fatigue
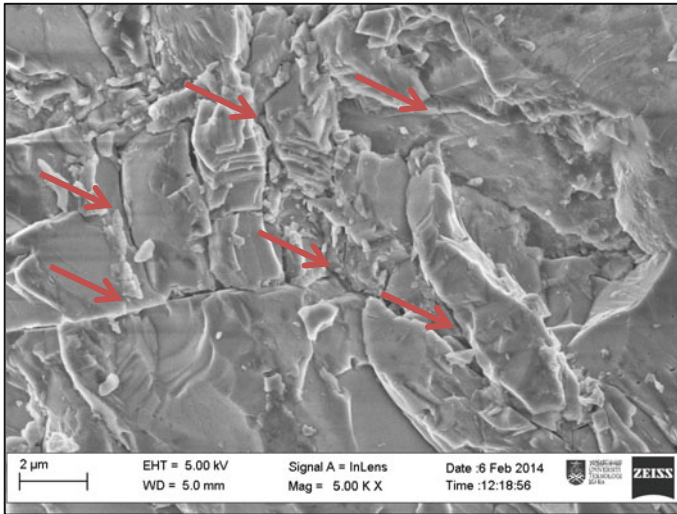
Fig. 5 SEM image of GR157G3

Fig. 6 Specimen loaded at
80 % of ultimate strength
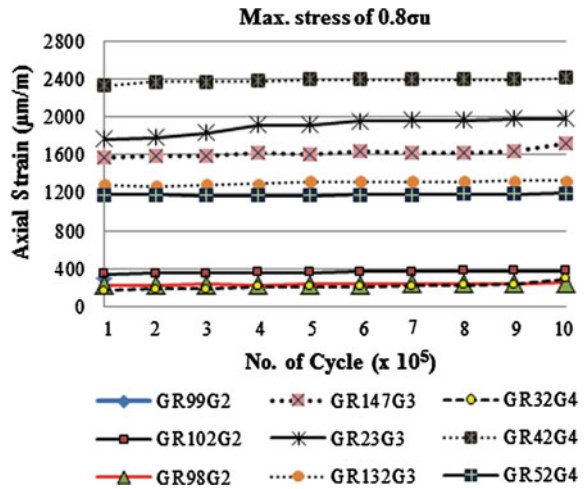
At 0.9 σu only two out of nine specimens are able to complete the cycle, while others were fail less than 100 cycles as shown in Fig. 7. Sudden increase in strain can be seen at the end of cycles for the two specimens. Near the end of the cycle, strain gage detected high strain in specimen due to the accumulation of microcracks in the specimen as well as on the surface of the specimen as shown in Fig. 8. The presence of microcrack is analyzed using SEM images.

In order to supplement in investigating the failure of rock, SEM images were captured before and after cyclic load. Using the same magnification of 1000×,

Fig. 7 Specimen loaded at 90 % of ultimate strength
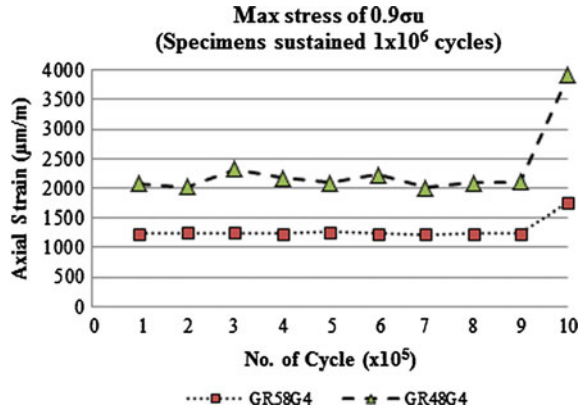
Fig. 8 Crack presence on specimen surface

Fig. 9 shows no apparent crack present in unloaded specimen which differ from Fig. 10. There is abundance of cracks build up in GR48G4 specimen and the cracks seem to interconnect to each other. Petrographic analysis using thin-section method shows that the microcracks were transgranular and intergranular. Most of the intergranular cracks found in feldspar (Fs), while transgranular cracks were found in biotite (Bi) and quartz (Qz) as shown in Fig. 11. As explained by [21], long intergranular cracks were found primarily in cyclic load near failure and it will lead to fatigue process.

Thus it shows that the increased amount of intergranular and development of microcracks causes the strain to increase which lead to fatigue failure. Since only a
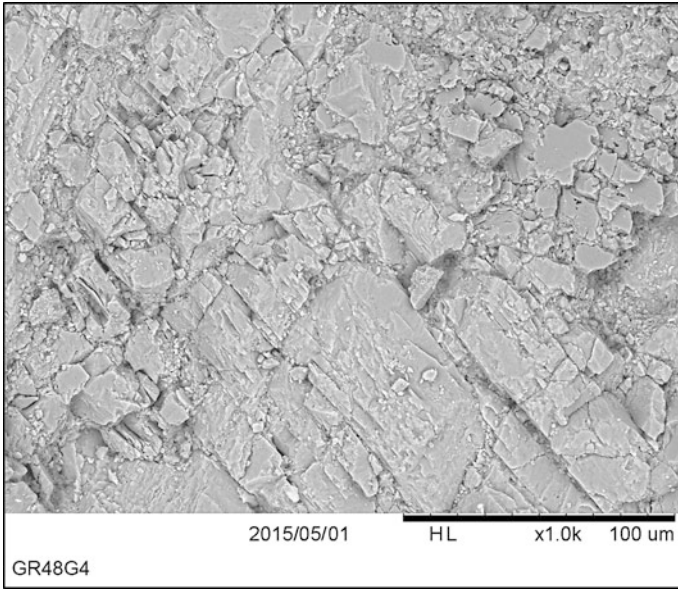
Fig. 9 SEM image of typical grade IV specimen (before cyclic load)
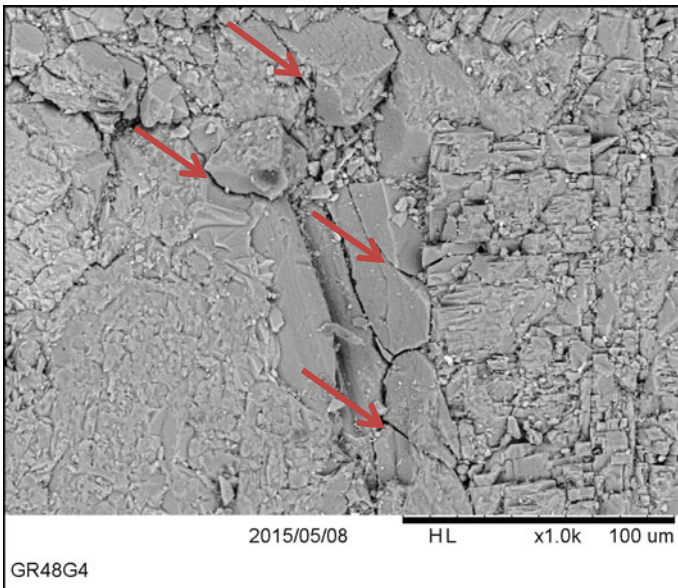
Fig. 10 SEM image of GR48G4 (after cyclic load)

Fig. 11 Microphotograph of microcrack present in granite under cyclic loading
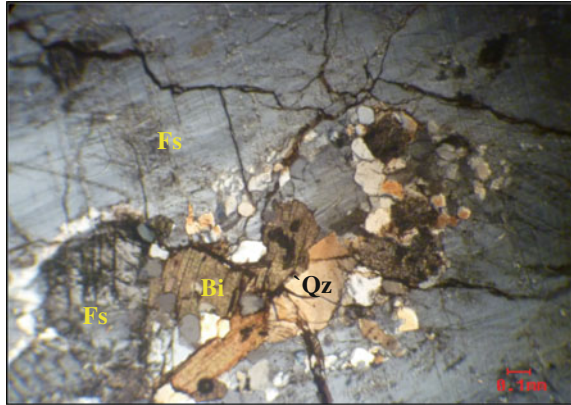
small number of specimen survived when loaded at 0.9 σu, it can be considered that the fatigue life of weathered rock is approximately near 90 % of its static ultimate strength.

4 Discussion

When different maximum stresses under cyclic loading are used, the result shows that there is a significant effect on weathered rock specimen; especially when specimen is loaded at 0.9 σu. The effect experienced by the specimens can be observed through its axial strain result. Specimens which are going through the fatigue process will have sudden increase in strain before fatigue failure.

Seventeen out of eighteen specimens that are loaded at 0.7 and 0.8 σu were able to sustain the one million cycles of cyclic load. However, only a specimen which is GR157G3 (at 0.7 σu) is failed at 510,606 cycles. The specimen strain shows rapid increase with number of cycles. As for specimen GR21G4, the axial strain is increasing due to crack development before reaching the final cycles.

Despite the fact that no specimen fails at 0.8 σu, the probability of the specimen to fail over one million cycles is high due to the steady increase in strain observed in each specimen. As for specimens loaded at 0.9 σu, only two grade IV specimens survived while others failed in less than 50 cycles.

5 Conclusion

From the result, conclusion has been made as following:

1. Specimen properties such as V_p, V_s, and UCS are increased after subjected to cyclic load. The closing of microcracks in rock under cyclic loading may

contribute to the compactness of rock thus increase the velocity as well as the strength of the rock.

2. Axial strain for the specimens sustain under one million cycles was slowly increasing; however, the axial strain of rock which failed rapidly increases near fatigue failure. One specimen failed out of nine specimens when loaded at 0.7 σu, while no specimen failed when loaded at 0.8 σu. However, only two out of nine specimens survived when loaded at 0.9 σu.

3. SEM images proven that during the process of fatigue, there is abundance of microcrack present in specimens; which include transgranular and intergranular cracks. Most of the intergranular cracks found in feldspar where transgranular cracks were found in biotite and quartz. Long intergranular cracks were primarily exhibited in cyclic load near failure.

Hence, it shows that weathered rock could not sustain under the maximum stress of 0.9 σu especially for grade II and III specimen. Thus, it is concluded that the life of weathered rock is nearly at 90 % of its static ultimate strength.

References

1. Kassim, A., & Mohamad, E.T. (2007). Laboratory study of weathered rock for surface excavation works. Report under Research Management Centre Universiti Teknologi Malaysia (UTM).
2. Komoo, I. (1995) Geologi Kejuruteraan: Perspektif Rantau Tropika Lembap. Syarahan Perdana UKM. ISBN 967–942-325-5 70F.
3. Burdine NT. (1963). Rock failure under dynamic loading conditions. *Society* Petroleum Engineering Journal, 3, 1–8.
4. Attewell P.B., & Farmer I.W. (1973). Fatigue behaviour of rock. *International* Journal of Rock Mechanics & Mining Science, 10, 1–9.
5. Ishizuka Y., Abe T., & Kodama J. (1990). Fatigue behaviour of granite under cyclic Loading. ISRM international symposium, 136–146.
6. Lee J.U, Rhee C.G, Kim J. and Kim Y.S. (1992). A study on the fatigue behaviour of Cheon-Ho Mt. Limestone under cyclic loading. Journal of the Korean Nuclear Society, 24(1), 98–109.
7. Eberhardt E., Stead D., & Stimpson B. (1999). Quantifying progressive pre-peak brittle fracture damage in rock during uniaxial compression. *International Journal of Rock Mechanics and Mining Sciences,* 36, 361–380.
8. Ray S.K., Sarkar M., & Singh T.N. (1999). Effect of loading and strain rate on the mechanical behaviour of sandstone. International Journal of Rock Mechanics & Mining Sciences, 36, 543–549.
9. Dubey R.K., & Gairola V.K. (2000). Technical Note: Influence of structural anisotropy on the uniaxial compressive strength of pre-fatigued rocksalt from Himachal Pradesh, India. *International Journal of Rock Mechanics and Mining Sciences,* 37, 993–999.

10. Li N., Chen W., Zhang P., & Swoboda G. (2001).Technical note: The mechanical properties and fatigue damage model for jointed rock masses subjected to dynamic cyclical loading. *International Journal of Rock Mechanics & Mining Sciences,* 38, 1071–1079.
11. Li N., Zhang P., Chen Y., & Swoboda G. (2003). Technical note: Fatigue properties of a cracked, saturated and frozen sandstone samples under cyclic loading. *International Journal of Rock Mechanics & Mining Sciences,* 40, 145–150.
12. Agrawal A. "Study on Strength and Deformation Characteristic of Jointed Rock Mass," Degree Disertation, Department of Civil Engineering, National Institute of Technology Rourkela, Odisha, India. 2009.
13. Veena. (2009). *Understand Geology.* New Delhi: Discovery Publishing.
14. ISRM. 1981, Rock characterization, testing and monitoring-ISRM suggested methods,.E.T. Brown ed. Pergamon Press, Oxford.
15. E.W. Brand, & H.B. Phillipson, Site investigation and geotechnical engineering practice in Hong Kong. Geotechnical Engineering, 1984, 15, 97–153.
16. J. Pelleg, (2013). "Cyclic Stress– Fatigue," in Mechanical Properties of Materials. vol. 190, ed: Springer Netherlands, 2013, pp. 339–447.
17. N. A. M. Salim, Z. Mohamed, and M. N. Berhan, "The Influence of Cyclic Load to the Properties of Weathered Granite," in *InCIEC 2013*, R. Hassan, M. Yusoff, Z. Ismail, N. M. Amin, and M. A. Fadzil, Eds., ed: Springer Singapore, 2014, pp. 477–487.
18. Bieniawski, Z. T., 1976, Rock mass classification in rock engineering. Proceedingsof the Symposium on Exploration for Rock Engineering: Johannesburg, South Africa, Vol. 1, pp. 97–106.
19. D. Malovichko, G. van Aswegen, and R. Clark, "Mechanisms of large seismic events in platinum mines of the Bushveld Complex (South Africa)," *Journal of the Southern African Institute of Mining and Metallurgy,* vol. 112, pp. 419–429, 2012.
20. Erarslan N, and Williams D. J. (2012), "Investigating the Effect of Fatigue on Fracturing Resistance of Rocks" *Journal of Civil Engineering and Architecture*, Volume 6, No. 10 (Serial No. 59), pp. 1310–1318.
21. Chen Y, Watanabe K, Kusuda H, Kusuda E, Mabuchi M. Crack growth in Westerly granite during cyclic loading test. *Engineering Geology*, 2011, 117 (3/4): 189–197.

The Shear Strength Characteristics of Kota Samarahan Sedimentary Soil

Applying the Nonlinear Envelopes Concept in the Soil Shear Strength Determination

Ahmad Zaidi Hampden, Mohd. Jamaludin Md. Noor, Pooya Saffari and Basharuddin Abdul Hadi

Abstract The current approaches and practices for determination of shear strength of soil that widely used in Malaysia is Mohr–Coulomb failure envelope theory. This theory states that the failure envelope is linear to the effective stress on the shear strength versus effective stress graph. The problem with this current approach when the linear envelope is produced and the shear strength at low stresses was extrapolated by the higher level of stresses. By applying the nonlinear method with a slight curve envelope when approaching the origin of the graph seems to show that the nonlinear failure envelope takes into consideration the value of shear strength at a very low level of stresses.

Keyword Nonlinear failure envelope

1 Introduction

There are lots of incidence of slope failures that have been claimed associated by rainfall in Malaysia. If we reflect the normal practices that are being conducted in the industry, the shear strength determination is by applying the shear strength

A.Z. Hampden (✉) · Mohd.J.Md. Noor · P. Saffari
Faculty of Civil Engineering, Universiti Teknologi MARA (UiTM),
Shah Alam, Malaysia
e-mail: zaidihampden@yahoo.com

Mohd.J.Md. Noor
e-mail: mohdjamaludinmdnoor@yahoo.com

P. Saffari
e-mail: safari.pooya@gmail.com

B.A. Hadi
Faculty of Civil Engineering, Universiti Teknologi MARA (UiTM),
Bukit Mertajam, Malaysia
e-mail: basha_uitma@yahoo.co.uk

model of Terzaghi [1] and Fredlund et al. [2] in quantifying landslide. In this case, we tend to overestimate the value of the shear and thus suggesting the soil could sustain a higher amount of load. In the end, the soil at the slopes still fails.

2 Background

2.1 Slope Failures

Slope failure is a general term used to describe the significant downward and outward movement of soil or rock on the slope. Related phenomena such as mudflows, earthflows, and rockfalls are natural events that would occur with or without human activities. It can occur on the natural slope or man-made fill or cut slope during or after implementation of developing projects, may be either its infrastructure or building construction. However, both human use and interest have led to an increase in some of these events. Often slope failures on hillside developments are worsened by over steeping slopes.

An understanding of the possible modes of failure is important to the prediction of slope instability. The mode of possible failure depends on the influence of the geological materials and groundwater conditions. The geological structure that permits the agents of weathering to detach rock from the face of a slope will facilitate rockfalls [3].

During a prolonged intense rainfall in the monsoon seasons, slope failures also frequently occur on natural slopes that are untouched by any human activity. For that reason, natural slopes should never be assumed to be naturally stable or safe although the slope may have been in existence for years. However, the reduction of slope failures can be achieved by means of stabilizing structures or techniques on naturally sensitive slopes [4].

2.2 Rainfall Induced Landslide

A landslide is a geological phenomenon which includes a wide range of ground movement, such as rockfalls, deep failure of slopes, and shallow debris flows which can occur in offshore, coastal, and onshore environments. Although the action of gravity is the primary driving force for a landslide to occur, there are other contributing factors affecting the original slope stability. Typically, preconditional factors build up specific subsurface conditions that make the area/slope prone to failure, whereas the actual landslide often requires a trigger before being released.

Abbot [5] indicates that the landslide is a down slope movement of large volume of material under the gravity pull. Matthew and Doyle [6] simplified it as down

slope mass movement of soil, sediment, and rocks. The occurrences of the shallow failures and the mass movements always occurs during the period of intense rainfall [7, 8]; thus it is then referred to as "rainfall induced landslides" [9].

2.3 Shallow Landslide

Shallow landslides can often happen in the slope areas with high permeable soils on top of the low permeable soil. The low permeable bottom soils trap the water in the shallower, high permeable soils creating high water pressure in the top soils. As the top soils are filled with water and become heavy, slopes can become very unstable and slide over the low permeable bottom soils. Figure 1 shows a schematic diagram to differentiate shallow landslide from a deep-seated slope failure.

It has been stated in previous section that these landslides triggered by prolong intense rainfall during a period of time. However, some researchers stated that the shallow failures could also be contributed by short intense storms which bring heavy rains [10, 11].

The depth of this shallow type of slope failure vary between 3 and 4 m [7] and it creates limitations as it could not be modeled when the role of negative pore water pressure or suction in the partially saturated zone above ground water table is neglected [12].

Shallow mode of failure is also a typical attribute for rainfall infiltration-induced failure. A definition of shallow landslides as given by Santacana et al. [13] is considered that it is a shallow landslide which has the ratio of depth to the length of the convex failure shape less than 0.1, while Giannecchini [14] states that it is less than 1.0. Another definition of shallow landslides is referred to slides less than 5 m thick referring to the failure being above the toe according to Fell et al. [15].

Fig. 1 Schematic diagram of a shallow landslode and a deep-seated slope failure
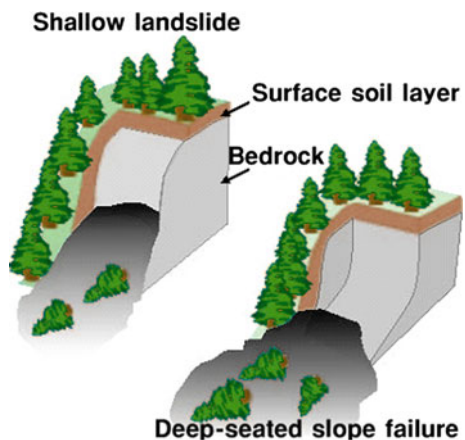
Usually in a case of tropical residual soil in Malaysia, the ground water table is very deep and usually it is unaffected by the intense rainfall regardless of the rainfall duration. The effect of surface water infiltration on the stability by raising the ground water table was used to be a normal practice in conventional approach, although it is not actually the mechanism that triggered this failure.

This type of considerations usually produces a deep type of failure in theoretical and modeling, but in contrast it do not reflect the actual shallow failure as obtained in the field. The difference between the modeled and the actual failure can be misleading when the model is applied in slope construction design. There it is relatively essential to fully aware and understand the relationship between moisture content, suction, and shear strength.

In order to understand the mode of shallow slope failure, it is very important to model the failure base on the actual mechanism that triggered the failure. During the process of infiltration, the wetting front advances downward and it is anticipated that factor of safety must be decreasing since this mechanism is responsible for slope failure after a heavy prolonged rainfall in the tropics. A particle level investigation is conducted to identify the changes in the effective stress and suction which in turn governs the change in shear strength. The change in shear strength is anticipated according to the reported shear strength behavior with respect to suction and net stress.

The effect of suction influencing the shear strength needs to be incorporated where with the presence of suction in the partially saturated zone then elevates the shear strength from the shear strength at saturation and contributes toward stabilizing the slope. The infiltration from the rainfall surface runoff reduces the suction and brings down the shear strength to the saturated shear strength. The first soil shear strength equation that considers this is the extended Mohr–Coulomb model of Fredlund et al. [2] and the first slope stability method that incorporates the role of suction is by Fredlund and Rahardjo [12]. All these help to explain the occurrence of slope failure due to rainfall.

A further enhancement in the knowledge is when the shear strength behavior at low stress levels is actually nonlinear which demonstrated a steep drop in shear strength as the depth approaches the surface Md. Noor and Hadi [16]. This study had also been supported by Gan and Fredlund [17] and Toll et al. [18].

2.4 Limitation of the Conventional Slope Stability Practice

Conventional slope stability methods always assumed that the unit weight of the soil being constant despite it getting heavier with increase in moisture content. This is the aspect that the failure disturbing variable increases with rain water infiltration. Omitting this feature in analysis is neglecting the aspect that the soil has increased its tendency to fall when it becomes heavier when wetted.

By neglecting these important characteristics that contribute toward failure (i.e., lost in strength and greater tendency to fall when weight increases), the

Fig. 2 Plane envelope shear strength model of Fredlund et al. [2]
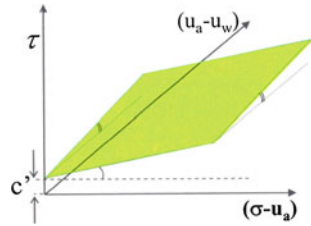
conventional slope stability methods do not replicate the true mechanism of shallow rainfall induced failure. Hence the resultant slope stability factor would not be realistic.

Another weakness with the conventional slope stability method is that it cannot be back analyze to achieve the shallow failure. This problem arises when the actual mechanism of failure is not replicated in the analysis.

The advantage of applying the shear strength behavior of Fredlund et al. [2] as shown in Fig. 2 is that it considers the reduction in shear strength when the soil is wetted as well as the effect of net stress, $(\sigma - u_a)$ or effective stress, $(\sigma - u_w)$. Net stress is the stress state variable in partially saturated condition while effective stress is the stress state variable when the condition turns saturated. The latter is considering the increase in shear strength with depth.

2.5 Nonlinear Failure Criterion in Slope Stability Analysis

It has been stated in the main source of the civil engineering handbook which gave us information such that drained test conducted on an over consolidated clay will not give a high apparent cohesion value through the fitted straight line envelope. Neither the drained test is conducted on normally consolidated clay where the apparent cohesion is zero via the fitted straight line envelope. Instead, the envelope is actually "curved" and value of the apparent cohesion is more than zero but relatively the value is considered small (Fig. 3). In this case, it has been shown that there is an ample room to explore on the shear characteristics of soil with respect to the curvilinear characteristics.

The nonlinear shear strength behavior has a strong influence on the shallow rainfall induced failure. The feature depicts steep drop in shear strength when water infiltrates. Shear strength is the only slope failure resisting variable. Losing its magnitude may be detrimental to the slope. Thus, the application of the actual shear strength decreasing behavior with degree of wetness is very important in order to achieve the true variation of stability factor with regards to rainfall. The stability factor is a dynamic number which vary according to the amount of moisture content or depth of water infiltration.

In addition, slope stability analysis ignoring the presence of suction in the zone above groundwater table would indicate failure for a standing slope [20]. These
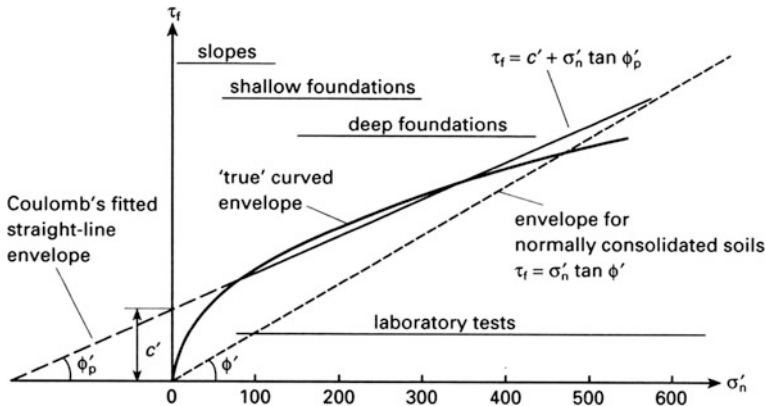
Fig. 3 Coulomb's equation and failure envelope [19]

contribute to the difficulty of understanding the behavior of landslide. Previous research has proven the advantages on applying the real curvilinear shear strength behavior relative to effective or net stress as shown by Bishop [21] and Md. Noor and Anderson [22].

In addition, the nonlinear shear strength behavior relative to suction has been conducted by Gan and Fredlund [17] and Toll et al. [18] in replicating the shallow mode of infiltration-induced landslide. The nonlinear shear strength behavior relative to effective stress at low stress levels with zero cohesion intercept was realized for both fine-grained and coarse-grained soil as early as 1966 (Bishop). This is in fact very relevant for the modeling of shallow rainfall induced failure since the stress involved falls within the lower range (less than 100 kPa).

3   Laboratory Results and Discussions

The soil is derived from a sedimentary residual soil located in Kota Samarahan, Sarawak. A series of triaxial testing has been conducted where all samples are tested for consolidated drained tri axial test. The series of comparison of result is discussed in this chapter especially the comparison of linear envelope and nonlinear envelope that represent the shear strength of the soils studied. The series of shear strength test is used to develop the shear strength against effective stress graph. This graph is important in determination of shear strength and the behavior of soils. From the result obtained, the comparison can be made between the current approaches in determination of the shear strength behavior with the actual shear strength behavior of the soil.

3.1 Stress–Strain Relationship

Four samples have undergone the consolidated drained test using a standard triaxial machine, whereas each sample is tested under the effective stress of 50, 100, 200, and 300 kPa using a multistage method. Figure 4 shows the stress–strain relationship of the first soil sample, i.e., soil 1.

Table 1 shows the maximum deviator stress for every effective stress applied to all the three soil samples. This information and data of maximum deviator stress obtained is really important to develop the shear strength versus effective stress graph. Therefore, this data is needed to ensure the graph can be plotted and the failure envelope can be developed to investigate the shear strength behavior of the soil.
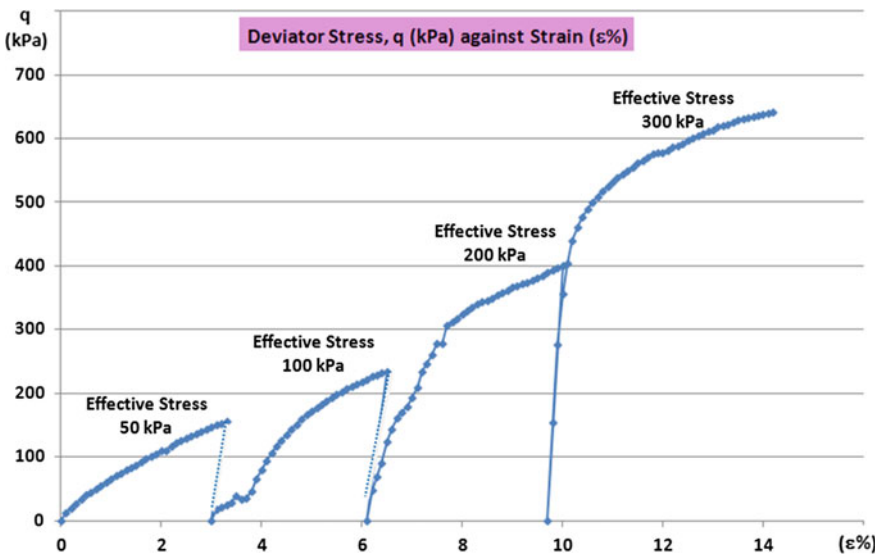
Fig. 4 Stress–strain relationship curve on a multistage consolidated drained tri axial test for soil 1

Effective stress (kPa)	Maximum deviator stress (kPa)			
	Soil 1	Soil 2	Soil 3	Soil 4
50	155.5	248.6	175.5	219.1
100	234.6	335.2	250.2	305.3
200	400.1	434.3	463.2	417.6
300	641.9	594.8	655.3 k	518.3

Table 1 Maximum deviator stress for each effective stress stages for the four soil samples

3.2 Linear Failure Envelope

All three linear envelopes (Figs. 5, 6, and 7) show a well-fitted line thus the envelope do touches the Mohr circle at the 50 kPa low stress effective stress accept for the last one (Fig. 8) where it is obvious that the value of the apparent shear strength is extrapolated, thus becomes bigger. The apparent cohesion and the angle of internal friction values are summarized in Table 2.
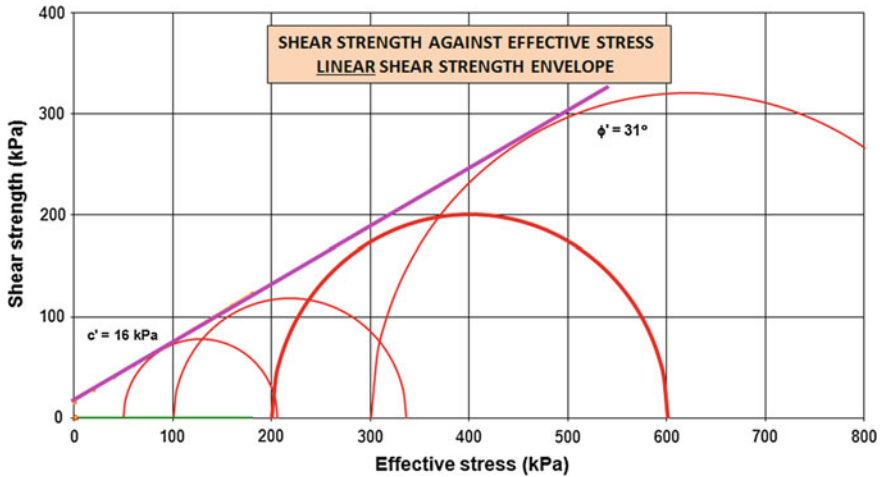
Fig. 5 Shear strength against effective stress for the linear failure envelope for soil 1
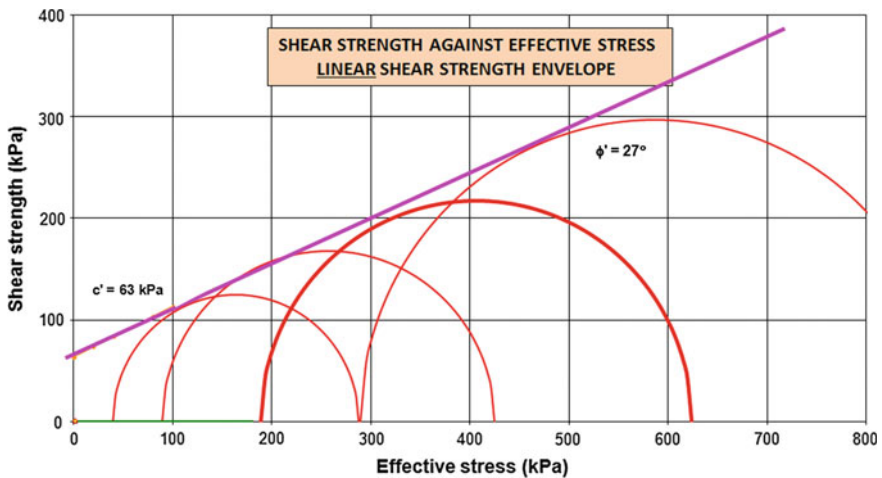
Fig. 6 Shear strength against effective stress for the linear failure envelope for soil 2
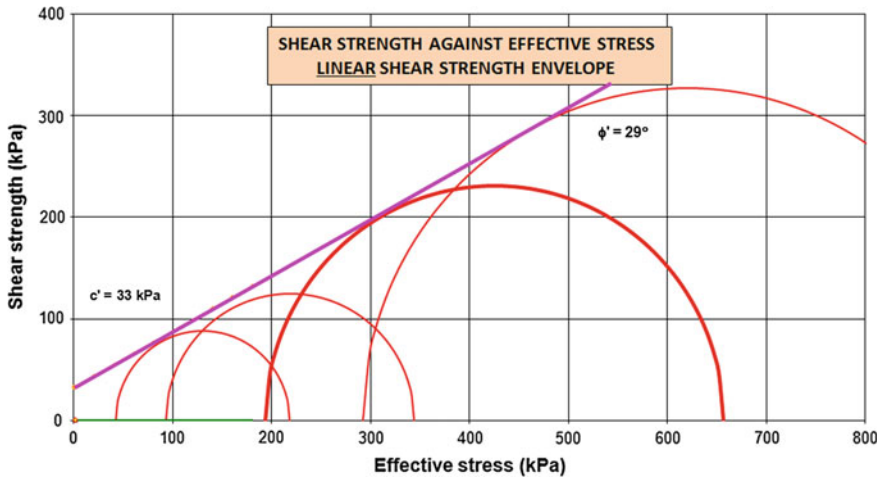
Fig. 7 Shear strength against effective stress for the linear failure envelope for soil 3
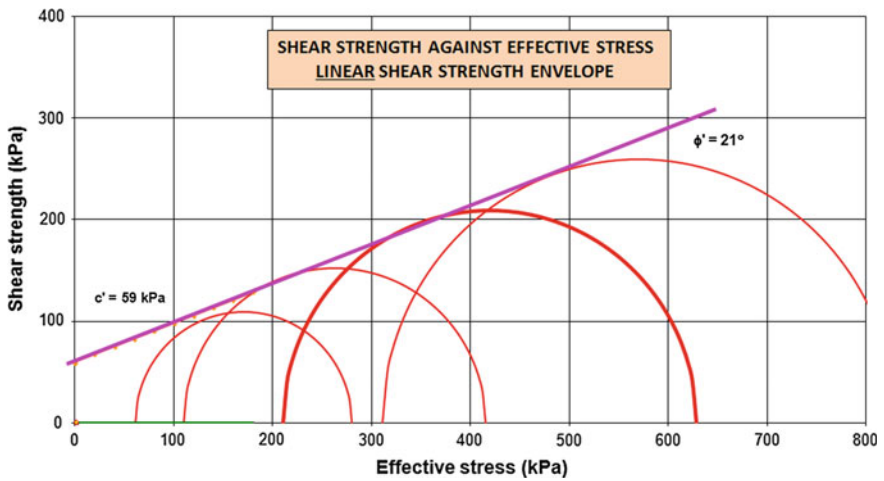
Fig. 8 Shear strength against effective stress for the linear failure envelope for soil 4

Table 2 Aparent cohesion value and angle of shearing resistance for linear failure envelope

Parameter	Sample			
	Soil 1	Soil 2	Soil 3	Soil 4
Aparent cohesion, c' (kPa)	16	63	33	59
Angle of shearing resistance, ϕ'	31°	27°	29°	21°

3.3 Nonlinear Failure Envelope

The nonlinear envelope is the failure envelope produced for this study which explains that envelope is the one that has curve line toward the origin. The envelope is intercept at the origin. This means that the failure envelope have no value of cohesion value.

According to Noor and Derahman [16], this nonlinear failure envelope is the failure envelope that has consideration on the stress at very low level. According to Noor and Derahman [16], as shown in Eqs. 1, 2, and 3, both Eqs. 1 and 2 are applicable from effective stress zero up to transition-effective stress, while Eq. 3 is applicable for any effective stress that equal or greater than transition-effective stress.

$$\tau_F = \frac{(\sigma - u_w)}{(\sigma - u_w)_t} \left[1 + \frac{(\sigma - u_w)_t - (\sigma - u_w)}{N(\sigma - u_w)_t} \right] \tag{1}$$

$$N = \frac{1}{1 - \left[(\sigma - u_w)_t \frac{\tan \varphi'_{\min_f}}{\tau_t} \right]} \tag{2}$$

$$\tau_f = (\sigma - u_w) \tan \varphi'_{\min_f} + \left[\tau_t = (\sigma - u_w) \tan \varphi'_{\min_f} \right] \tag{3}$$

where

$(\sigma - u_w)$ Net Stress/Effectine Stress
$(\sigma - u_w)_t$ Transition Effectine Stress
τ_t Transition Shear Strength
$\varphi'_{\min_f}$ Minimum Friction Angle at Failure

The parameters obtained from nonlinear failure envelope are transition-effective stress, transition shear strength, and minimum friction angle at failure. These three parameters are important to calculate the shear strength of the soil. The parameters needed can be obtained and extracted from the nonlinear failure envelope of shear strength versus effective graph.

Figures 9, 10, 11, and 12, shows that the nonlinear envelope that consist of curve line when approaching the origin is fitted nicely on Mohr circle for effective stress at 50 kPa. This situation shows that there are no extrapolated of shear strength at low stresses by the high level of stresses.

The transition shear strength can be obtained from the value of shear strength at point of where the transition between the curve line envelope and the linear line envelope meet each other. The transition-effective stress is where the value of effective stress at point of where the transition between the "curve line envelope" and "linear line envelope" meet each other. For the minimum friction angle at failure, the parameter can be obtained by measure the angle at linear line envelope.
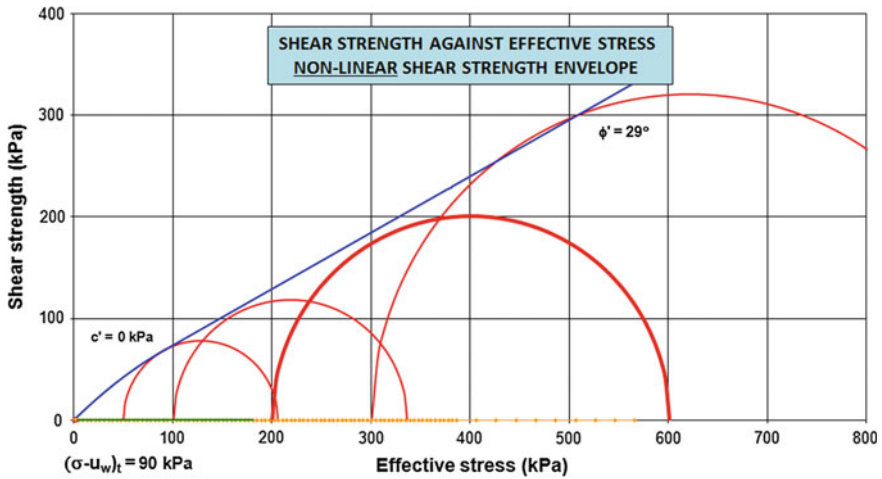
Fig. 9 Shear strength against effective stress for the nonlinear failure envelope for soil 1
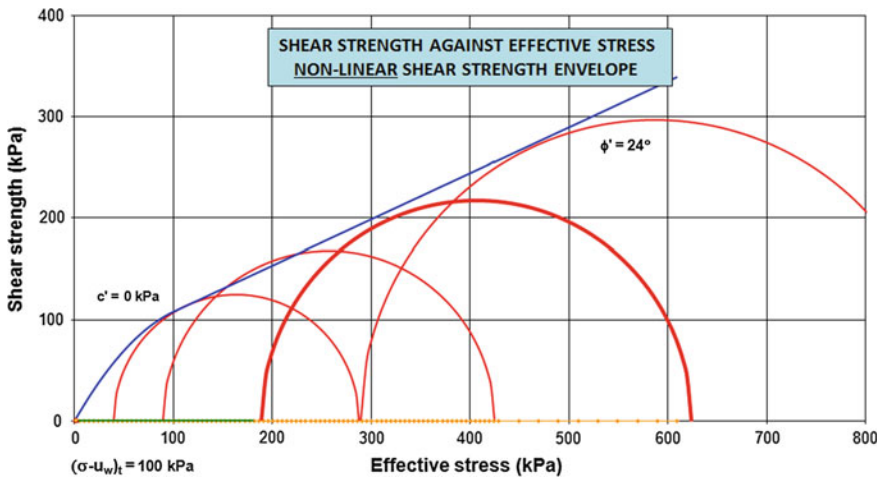
Fig. 10 Shear strength against effective stress for the nonlinear failure envelope for soil 2

Table 3 shows the transition shear strength value, transition-effective stress value, and minimum friction angle at failure value for the soil samples.

The nonlinear failure envelope provides parameters such as shear strength transition, effective stress transition, and minimum friction angle at failure is the actual shear strength behavior of the soil. There is no apparent cohesion value such as in Mohr–Coulomb failure theory is needed when using this actual shear strength determination theory.
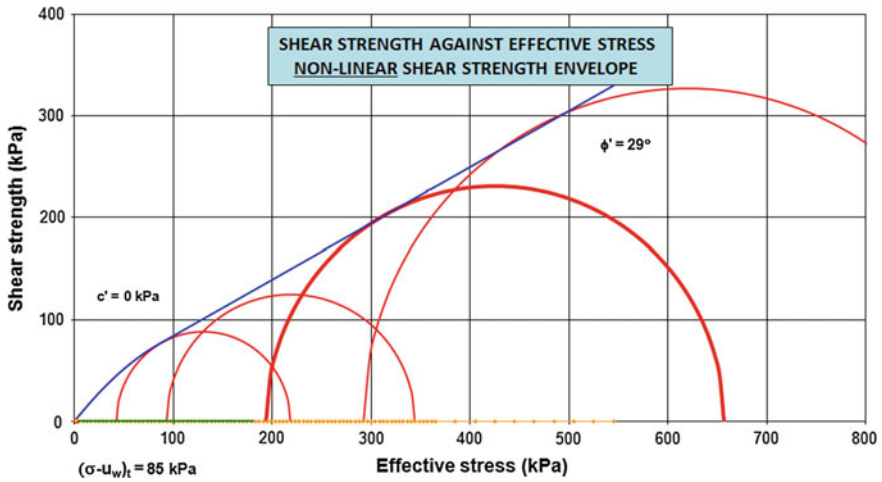
Fig. 11 Shear strength against effective stress for the nonlinear failure envelope for soil 3
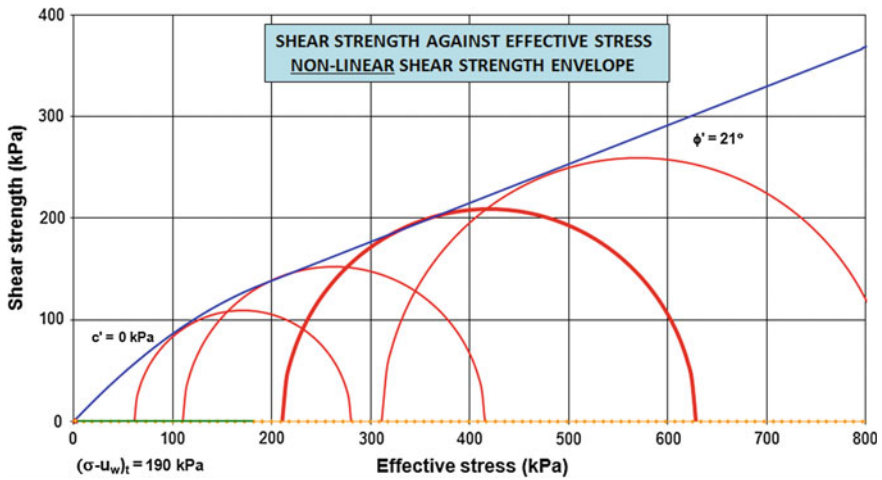
Fig. 12 Shear strength against effective stress for the nonlinear failure envelope for soil 4

Table 3 Parameter of the nonlinear failure envelope

Parameter	Sample			
	Soil 1	Soil 2	Soil 3	Soil 4
Transition-effective stress (kPa)	90	100	85	190
Transition shear strength (kPa)	68	108	76	135
Minimum friction angle at failure	29°	24°	29°	21°

Although the linear envelope shows that the curve fitting envelope do touches the low stress level, the nonlinear envelope provide an actual shear strength of the soil. If the apparent cohesion is to be selected, then surely gives huge differences in designing the geotechnical structure and any structural work because most structure and building are built on the soil in comparison to the actual shear strength. Thus, the apparent cohesion gave an over rated value to the soil shear strength.

Since the actual shear strength is the one with nonlinear envelope, so that the equations used to determine the shear strength are Eqs. 1 and 2 for shear strength lower than transition-effective stress, while Eq. 3 for shear strength equal or higher than transition-effective stress. All these three equations are applicable to soil studied with parameters obtained which are transition shear strength, transition-effective stress, and minimum friction angle at failure.

Apart from nonlinear method that has been shared above, Maksimovic [23] also had done numerous studies and applied the nonlinear method and thus came out also with his equation:

$$\tau_f = c' + \sigma'_n \tan\left(\phi'_B + \frac{\Delta\phi'}{1 + \sigma'_n/P_N}\right) \tag{4}$$

where

c' Cohesion

ϕ'_B Basic angle friction

$\Delta\phi'$ Maximum angle difference

P_N Median angle of normal stress

The equation could be presented easily in a geometrical and graphical manner as shown in Fig. 13.

Fig. 13 Graphical and geometrical parameters for nonlinear envelope [23]
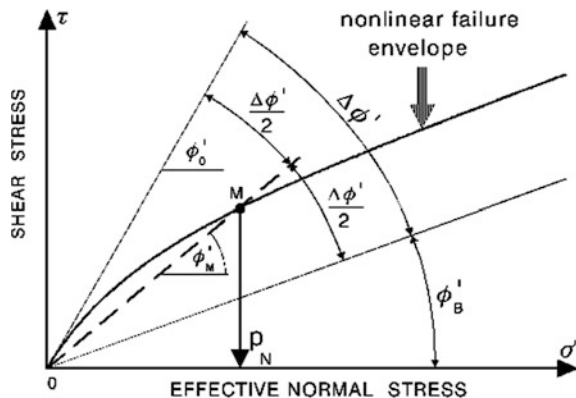
Maximum angle difference is the difference between the initial angle, when the normal stress tends to zero, and the asymptotic basic angle of friction, when the stress level tends to infinity.

The median angle pressure is the stress level at which the angle of the shearing resistance is equal to the mean of the initial and basic angle, or in other words the basic angle plus one half of the maximum angle difference and corresponds to point M.

The failure envelope has a tangent in the origin inclined at angle which is the sum of the basic angle and the maximum angle difference.

Basic angle of friction is the total angle of shearing resistance tends toward the lower constant limiting value.

The equation by Maksimovic involves a lot of graphical plots and angles in which becomes the entity in its equation. The same results from all the four soil samples have been used in order to reconstruct the nonlinear curve by Maksimovic. By right, the nonlinear curve should give a similar pattern especially the linear section similar to the linear envelope. But instead, the angles obtained from the graphical plot do not show the same character.

Figures 14 and 17 show the nearly fitted Maksimovic's nonlinear envelope, but in Figs. 15 and 16 the Maksimovic's nonlinear envelope portrays a hefty amount of increased in the angle of shearing resistance. Thus, it could not fit in well to the Mohr circle plots.
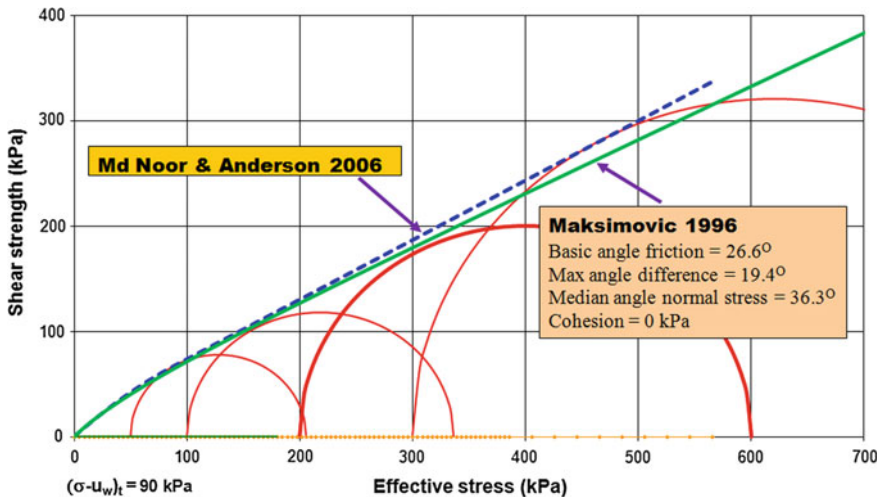
Fig. 14 Comparison between the Maksimovic [23] nonlinear envelope and the Md. Noor Anderson [22] nonlinear envelope for soil 1
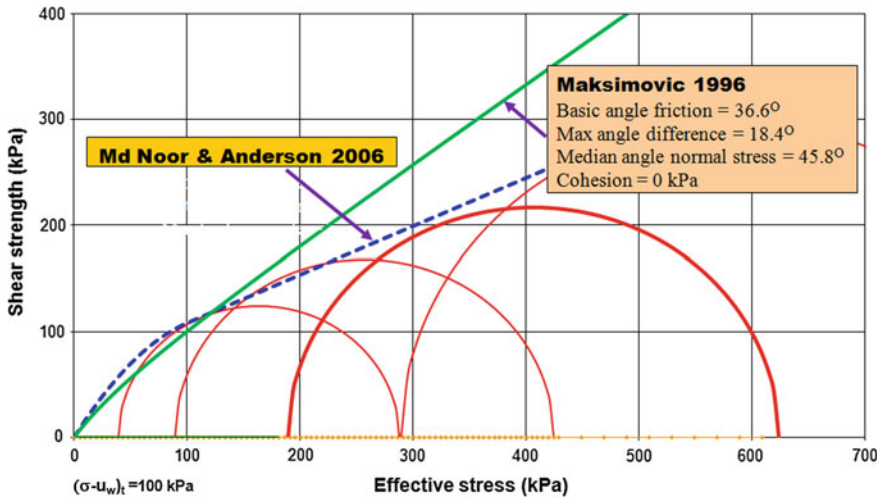
Fig. 15 Comparison between the Maksimovic [23] nonlinear envelope and the Md. Noor Anderson [22] nonlinear envelope for soil 2
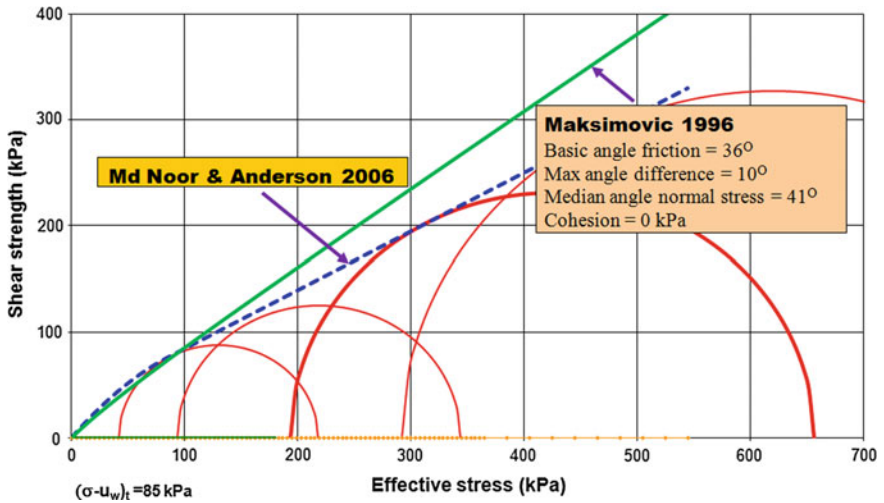
Fig. 16 Comparison between the Maksimovic [23] nonlinear envelope and the Md. Noor Anderson [22] nonlinear envelope for soil 3
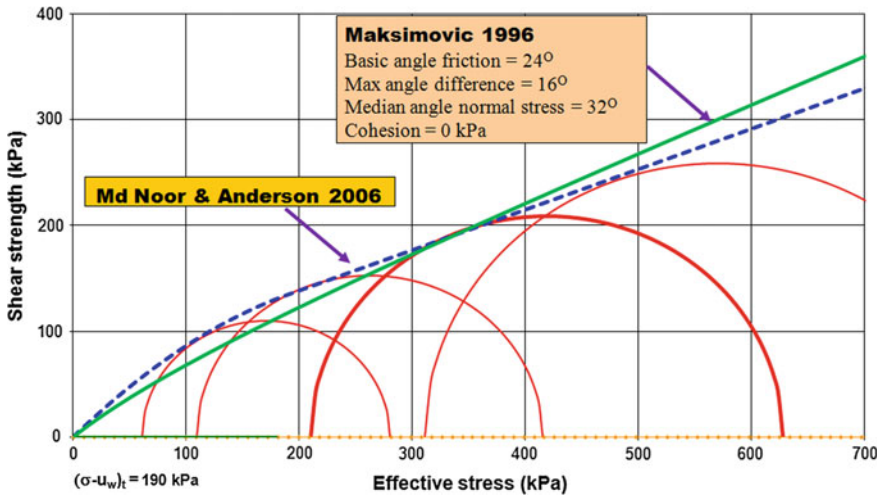
Fig. 17 Comparison between the Maksimovic [23] nonlinear envelope and the Md. Noor Anderson [22] nonlinear envelope for soil 4

4   Conclusions and Recommendation

The differentiation between the linear and the nonlinear shear strength theories is very significant. On the linear failure envelope, the shear strength at low stresses has been extrapolated by the higher level of stresses, while for nonlinear failure envelope the curve line when approaching the origin where the shear strength at very low stresses been considered.

By referring the result and discussion, the results of the experimental and laboratory works show that the actual shear strength of the soils studied is the shear strength with the nonlinear failure envelope. This proves that the nonlinear shear strength is the shear strength behavior of the soils studied.

A more ample amount of study could be done in the future to look into the various existing equations on the nonlinear envelopes.

References

1. Terzaghi, K. (1936). "The shear resistance of saturated soils." Proceedings for the 1st. International Conference on Soil Mechanics and Foundation Engineering (Cambridge, MA),
2. Fredlund, D. G., Morgenstern, N. R. and Widger R. (1978). "The shear strength of unsaturated soils." Canadian Geotechnical Journal, 15(3), pp. 313–322.

3. Omar, H. (2002). Development of risk assessment and expert systems for cut slopes. PhD thesis, Universiti Putra Malaysia (unpublished).
4. Edward A.K. (1992). Environmental Geology. University of California, Santa Barbara, USA.
5. Abbot, P.L (2002). Natural Disaster, Boston, McGraw-Hill.
6. Matthew, B.R. and Doyle, P. (1997). Environmental Geology–Geology and the Human Environment., Chicester: John Wiley and Sons Ltd.
7. Brand, E.W. (1989). "Occurance and Significant of Landslides in Southeast Asia." International Geological Congress: Symposium on Landslides, Washington D.C.
8. Tarolli P., Marco Borga M., Kang, T.S and Shou, H.C. (2011). Modeling shallow landsliding susceptibility by incorporating heavy rainfall statistical properties. Geomorphology Volume 133, Issues 3–4, 15 October 2011, Pages 199–211.
9. Md. Noor, M.J. and Derahman, A. (2011), Curvi-linear shear strength envelope for granitic soil grade VI, *Unsaturated Soils: Theory and Practice 2011,* 1–6.
10. Brand, E.W., Premchitt, J., Phillipson, H.B., (1984). Relationship between rainfall and landslides in Hong Kong. Proc. of the IV International Symposium on Landslides, Toronto, vol. 1, pp. 377–384.
11. Flentje, P., Chowdhury, R.N. and Tobin, P., (2000). Management of landslides triggered by a major storm event in Wollongong, Australia. Proc. of the II International Conference on Debris-Flow Hazards Mitigation, Mechanics, Prediction and Assessment, Taipei, pp. 479–487.
12. Fredlund, D. G. and Rahardjo, H. (1993). Soil Mechanics for unsaturated soils., John Wiley and Son.
13. Santacana N, Baeza B, Corominas J, Paz A.D. & Marturia, J. (2003). "A GIS-Based Multivariate Statistical Analysis for Shallow Landslide Susceptibility Mapping in a Pobla de Lolled Area (Eastern Pyrenees, Spain)". Natural Hazards 30: 281–295.
14. Giannecchini, R. (2006). "Relationship between rainfall and shallow landslides in the southern Apuan Alps (Italy)." Nat. Hazards Earth Syst. Sci., 6, 357–364.
15. Fell R, Hungr O., Leroueil, S. and Riemer, W. (2000). Keynote Lecture- "Geotechnical Engineering of the Stability of Natural Slopes, and Cuts and Fills in Soil." Proc of An International Conference on Geotechnical and Geological Engineering (GeoEng 2000). Melbourne, Australia.
16. Md. Noor, M. J. and Hadi, B.A. (2010). "The role of curved-surface envelope Mohr-Coulomb model in governing shallow infiltration induced slope failure". http://www.ejge.com/2010/JourTOC15B.htm.
17. Gan, K .J. M. and Fredlund, D. G. (1995). "Shear strength behaviour of two saprolitic soils." Proc. 1st. Int. Conf. Unsaturated Soils, 1: 71–76. Rotterdam, Balkema.
18. Toll, D. G., Ong, B. H., and Rahardjo, H. (2000). "Triaxial testing of unsaturated samples of undisturbed residual soil from Singapore." Proceedings of the Unsaturated soil for Asia., Singapore: 581–586.
19. Whitlow, R. (2004). Basic Soil Mechanics 4th eds. Prentice Hall, London.
20. Othman, M.A. (1989). "Highway cut slope instability problems in West Malaysia". Ph.D. Thesis, Department of Geography, University of Bristol, United Kingdom. (Unpublished).
21. Bishop, A.W. (1966). "The strength of soil as engineering materials", Geotechnique, 16, No. 2, pp 91–128.
22. Md. Noor, M J and Anderson, W.F. (2006) "A comprehensive shear strength model for saturated and unsaturated soils". Proc. 4th Int. Conf. on Unsaturated Soils, ASCE Geotechnical Special Publication No. 147, Carefree, Arizona, Vol. 2, pp 1992–2003 ISBN 0-7844-0802-5.
23. Maksimovic, M. (1996). A Family of Nonlinear Failure Envelopes for Non-Cemented Soils and Rock Discontinuities. http://www.ejge.com/1996/Ppr9607/Abs9607.htm.

Strength of Treated Peat Soil with Pond Ash—Hydrated Lime Subjected to Soaking Time

Zeety Md. Yusof and Kamaruzzaman Mohamed

Abstract Rapid development in Malaysia has encroached to the area which are considered as problematic ground like peat land. However, strength characteristics of natural peat soil need some improvement with the introduction of economical, efficient and sustainable methods. The used of byproduct material in stabilizing of peat soil become more reliable and expanded. In this paper, the physical properties of the peat soil were classified and identified accordingly. Peat treated with pond ash (PA) and hydrated lime (HL) in seventeen (17) different types of mixtures were prepared. Each mixture was prepared using PVC molds with a diameter of 50 mm and a height of 100 mm and then soaked in water for ten (10) different soaking period. The strengths of Unconfined Compressive Strength (UCS) were comparatively investigated. The results have shown that the peat becomes stronger when the percentage of PA-HL and soaking period increased. Of the investigation, the results show the strength characteristics of peat treated with PA-HL against soaking time. Peat with a mixture of 15 and 20 % of PA in various compositions of HL and soaking period exceeding 60 days have presented a great unconfined compressive strength. These findings indicate that the PA and HL is potentially as a stabilizer for peat soil, which experience a high water table.

Keywords Unconfined Compressive Strength (UCS) tests · Pond ash · Hydrated lime · Peat soil · Strength behavior

Z.Md. Yusof (✉) · K. Mohamed
Faculty of Civil Engineering, Universiti Teknologi MARA (UiTM),
Shah Alam, Selangor, Malaysia
e-mail: zeetyyusof@gmail.com

K. Mohamed
e-mail: kamar164@salam.uitm.edu.my

1 Introduction

According to [1], Malaysia, especially in parts of Peninsular Malaysia, contributes about 8 % or 3 million hectares of the 23 million hectares of peatlands in Southeast Asia. However, not all of the peat land areas are suitable for development purposes. It depends on the type and physical properties of the peat soil [2]. Naturally, peat soil is a weak material and considered as a problematic ground. As stated by [3], peat has a very high compressive strength, low shear strength, high water content, high permeability, low specific gravity and low bearing capacity.

Due to these characteristics, civil engineers always face problems to design and construct suitable structures on it [4], unless a better solution were introduced by redesigning the peat soil itself before it can be used as a support ground. Various ideas and technologies have been introduced by researchers and practitioners in their attempts to improve the strength of peat soil. By then, the most economic and most effective method is seeking [5].

Nowadays, issues in sustainability have been raised up everywhere. A lot of solid waste and byproduct materials have been produced and stockpiled for example the byproduct of coal fired power station which is known as pond ash. PA has a potential used in Geotechnical engineering, especially for road construction [6] and the ground layer of the building structure [7]. Meanwhile, [8] has investigated that soaking time plays to promote the strength of the peat soil with an increase of PA after a few days soaked.

Besides using the PA alone, a few attempts have been carried to mix it with other material. Chand and Subbarao [9] mentioned that combination of PA and lime can produce a suitable material for engineering applications. For soil stabilization [10] explained that PA particles need the HL admixture as stabilizing agent. A study by [11] showed that PA–lime admixture had strengthened the soil structure. The presence of HL and reaction with water provides a good cementing agent to the soil [12–15].

Therefore, in this study, the peat soil was treated by applying a specific composition of PA and HL and kept under water for a specific duration. The strengths were then investigated accordingly.

2 Materials and Method

2.1 Material Sampling

Samples of peat soils were taken from Rejo Sari road at Senggarang in Batu Pahat, Johor. The selection of the site will be due to the potential of that area to be developed in the future. By a visual observation, the samples are dark brown in color. Disturbed samples were collected by hand digging whereby the undisturbed samples were carefully extracted using a thin wall sampler of 100 mm diameters

and preserved accordingly as stipulated in British Standard BS1377 (1990)-1 and ASTM standard. The undisturbed peat soil was prepared for the required physical properties test while the disturbed peats were oven dried at 105 ± 5 °C for more than 24 h. Samples of PA were collected from the disposal field at Jimah Energy Venture Thermal Power Plant, Negeri Sembilan. It was extracted about 0.3–1 m below the ground surface. The samples were oven-dried, sieved and collected for the size of particles passing the 2 mm sieve. While, samples of HL, in the forms of powder were obtained from the local supplier factory.

2.2 Physical Properties of Materials

A preserved natural peat soils were prepared accordingly for a series of physical properties determination such as natural moisture content, degree of decomposition, loss of ignition, plastic limit, specific gravity, pH, and maximum dry density and optimum moisture content (Standard Proctor test). All tests are in accordance with British Standard BS 1377: 1990. Physical and chemical properties of PA and HL were provided by the supplier company respectively.

2.3 Preparation of Treated Samples

A dried peat soil, PA, and HL in predetermined composition were mixed together with the optimum water content of peat (42.31 %). These mixed materials were assembled and compacted in 50 mm split PVC molds with 100 mm height. As shown in Fig. 1a, a PVC pipe has been cut in such a way to facilitate the extraction of soil sample. PA contents were constantly adopted in 5, 10, 15 and 20 %, while the HL contents for each percentage of PA were varied in four different compositions of 3, 6, 9 and 12 %. A typical sample features are shown in Fig. 1b, c.

Each mix was labeled as 'A' until 'Q' and prepared accordingly to accommodate ten (10) different soaking time, namely 0, 3, 7, 14, 21, 28, 60, 90, 120 and 150 days.

Fig. 1 a PVC mold b Untreated peat sample and c Treated peat sample
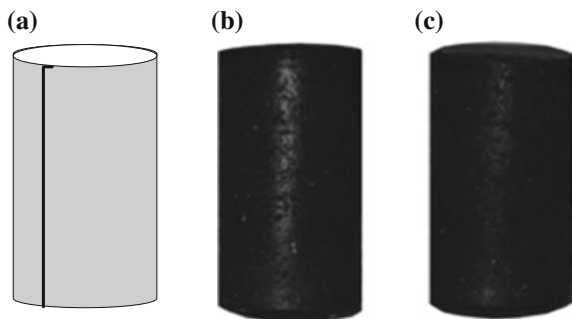
The application of soaking is to simulate the condition of treated peat soil when expose to the real high water content of natural peat soil at the site. For each soaking time, three (3) specimens of the same mixed are required. All together, four hundred eighty three (483) specimens were developed as indicated is shown in Table 1. The soaked samples were then carefully extruded and readily prepared for the UCS test.

2.4 Unconfined Compressive Strength Test

Each specimen was placed and tested under unconfined compressive loading. The maximum load experienced by the sample was recorded as an unconfined compressive strength of the treated peat soil. A typical stress-strain curved developed from UCS test is shown in Fig. 2. Since there are three specimens were tested for each mix and soaking time, only an average of the three values are presented as results.

3 Result and Discussion

Physical and engineering properties of the untreated or natural peat soil are presented in Table 2.

The mineralogical composition of the PA sample was mainly quartz, mullite, hermatite and calcite as shown in Table 3. According to the ASTM D 618–94 [16], the PA sample in this study falls in the category of Class F. While the HL contain of calcium hydroxide (Ca $(OH)_2$) [17].

The results of the UCS test provide substantial stress–strain curves for various types of treated peat soil. However, only a maximum stress or unconfined compressive strength of each sample was plotted and presented according to their specific soaking time, namely 0, 3, 7, 14, 21, 28, 60, 90, 120 and 150 days as shown in Fig. 3a, j respectively.

Obviously, the strength of a treated peat soil, increase with increase of PA-HL in peat soil as exhibited in all samples for each soaking time. Figure 3a shows the unconfined compressive strength (UCS) of samples at 0 day soaking time. It is shown that with increase of PA and HL, the strength of the samples increases from 22 to 102 kPa.

Figure 3b shows the unconfined compressive strength (UCS) of samples at 3 days. The UCS increases up to 103 kPa. Meanwhile, for 7 and 14 days' sample, as shown in Fig. 3c, d respectively it increases up to 113 kPa. These increments are about five times on the untreated peat's strength (sample B).

In Fig. 3e, samples with 21 days soaking time exhibited strength increment up to 146 kPa which is 6.6 times of untreated peat strength. Meanwhile, in Fig. 3f, samples with 28 days soaking time, the strengths were increased up to 167 kPa,

Table 1 Types, composition and soaking time of samples

Label	Types of sample	Composition		Soaking time (days)									
		Pond ash (PA) (%)	Hydrated lime (HL) (%)	0	3	7	14	21	28	60	90	120	150
				No. of specimens									
A	PEAT	0	0	3	–	–	–	–	–	–	–	–	–
B	5PA3HL	5	3	3	3	3	3	3	3	3	3	3	3
C	5PA6HL		6	3	3	3	3	3	3	3	3	3	3
D	5PA9HL		9	3	3	3	3	3	3	3	3	3	3
E	5PA12HL		12	3	3	3	3	3	3	3	3	3	3
F	10PA3HL	10	3	3	3	3	3	3	3	3	3	3	3
G	10PA6HL		6	3	3	3	3	3	3	3	3	3	3
H	10PA9HL		9	3	3	3	3	3	3	3	3	3	3
I	10PA12HL		12	3	3	3	3	3	3	3	3	3	3
J	15PA3HL	15	3	3	3	3	3	3	3	3	3	3	3
K	15PA6HL		6	3	3	3	3	3	3	3	3	3	3
L	15PA9HL		9	3	3	3	3	3	3	3	3	3	3
M	15PA12HL		12	3	3	3	3	3	3	3	3	3	3
N	20PA3HL	20	3	3	3	3	3	3	3	3	3	3	3
O	20PA6HL		6	3	3	3	3	3	3	3	3	3	3
P	20PA9HL		9	3	3	3	3	3	3	3	3	3	3
Q	20PA12HL		12	3	3	3	3	3	3	3	3	3	3

Fig. 2 Typical stress–strain
curves of UCS test
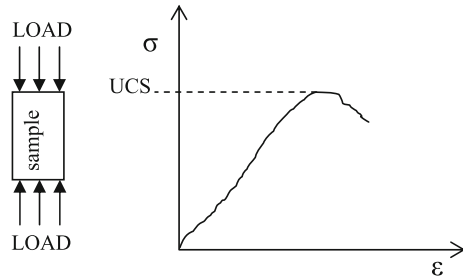
Table 2 Physical and Eng.
properties of peat soil

Physical properties	Values
Moisture content (w) (%)	811–856
Degree of decomposition	H3–H6
Loss of ignition (N) (%)	78.163
Organic content (H) (%)	77.289
Plastic limit	Non plastic
Specific gravity (Gs)	1.39
pH	3.35–3.82
OMC	42.31 %
MDD	0.62 Mg/m^3
UCS (untreated)	22 kPa

Table 3 Chemical and
Physical composition of Pa

Major element	Value
SiO_2	46.3 %
Al_2O_3	34.5 %
Fe_2O_3	9.88 %
MgO	0.91 %
CaO	0.73 %
TiO_2	5.95 %
SO_3	0.31 %
P_2O_5	0.05 %
Alkalis ($Na_2O + K_2O$)	(0.098 + 0.84) %
$SiO_2 + Al_2O_3 + Fe_2O_3$	90.68 %
Specific gravity	2.15
Bulk density	720 kg/m^3

which is 7.6 times on the untreated strength. Similar for samples 60 days soaking
time in Fig. 3g and 90 days soaking time in Fig. 3h, the strengths were increased up
to 188.4 and 195 kPa, respectively. These increments are about 8.5 and 8.9 times on
the untreated strength. Further soaking had caused the strength increased up to 189
and 183 kPa for 120 days (Fig. 3i) and 150 days (Fig. 3j) respectively. These are
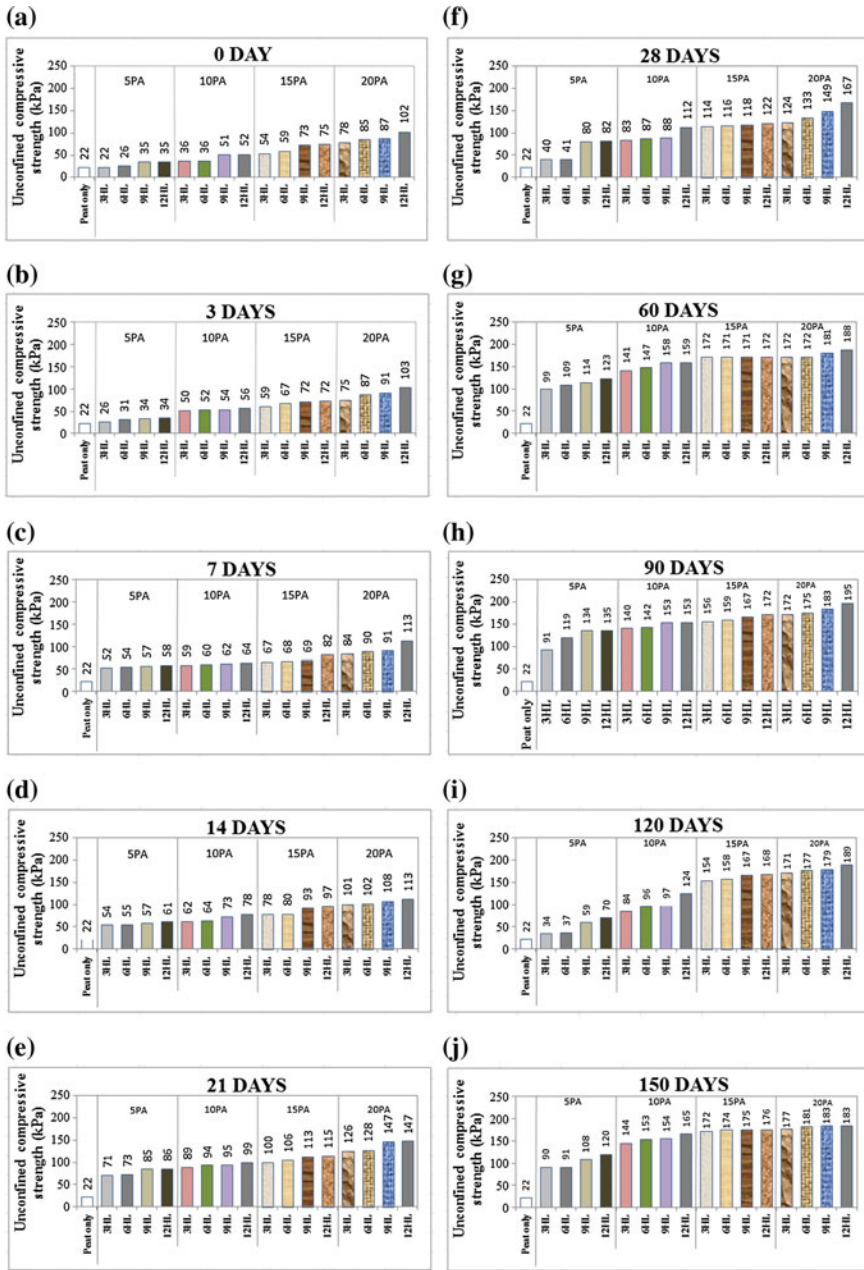
Fig. 3 **a** Effect of different admixture on UCS at 0 day. **b** Effect of different admixture on UCS at 3 days. **c** Effect of different admixture on UCS at 7 days. **d** Effect of different admixture on UCS at 14 days. **e** Effect of different admixture on UCS at 21 days. **f** Effect of different admixture on UCS at 28 days. **g** Effect of different admixture on UCS at 60 days. **h** Effect of different admixture on UCS at 90 days. **i** Effect of different admixture on UCS at 120 days. **j** Effect of different admixture on UCS at 150 days

about 8.6 and 8.3 times on the untreated strength. It showed that the presence of PA as a granular material and HL as an additive has promoted a better strength of the peat soil. By comparing the duration of soaking, the magnitude of strengths reveals good improvement with longer soaking time. It showed a very significant effect on the strength of treated samples. Presence of PA has provided a good granular material in peat. Then the presence of HL has provided a good cementation material that conglomerated peat and PA to form a stiffer material.

In order to observe the strength characteristics of each sample against duration of soaking, a series of graph was derived in four different plots, according to their PA contents. Figure 4 shows strength characteristics of samples B, C, D and E which contain 5 % of PA. Figure 5 shows strength characteristics of samples F, G, H and I with 10 % of PA. Meanwhile Fig. 6 shows strength characteristics of samples contain 15 % of PA which represented by sample J, K, L and M. The strength characteristics of sample with highest PA content (20 %) were shown in Fig. 7. It was represented by sample N, O, P and Q.

In Fig. 4, sample B exhibits some improvement of strength at an early stage of soaking. The strength has increased by 18, 102, 4 and 32 %, before it drops by 43 % at 28 days. Further soaking had caused the strength to increase by 147 % before it slightly drop by 8 and 63 %, then increase again by 16 % at 150 days. The maximum strength was achieved by the sample B at 60 days soaking which is 91 kPa. Sample C also exhibits a similar trend, but achieving a maximum strength
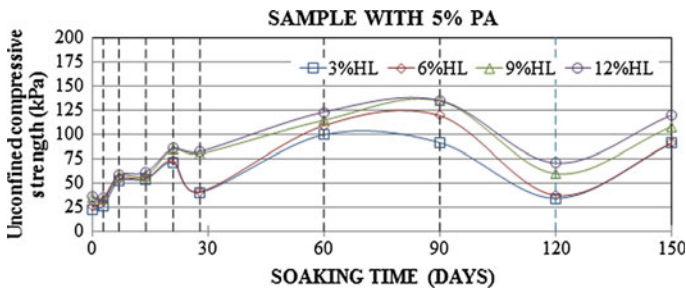
Fig. 4 Strength characteristic of treated peat (5 % PA) subjected with soaking time
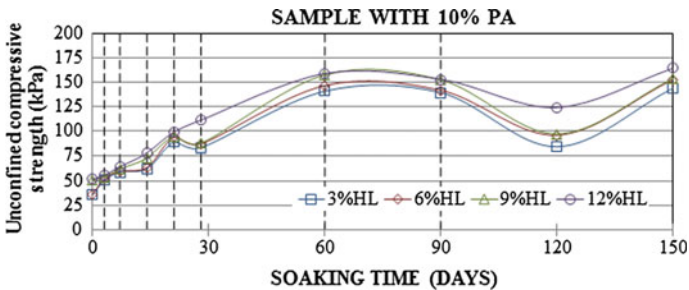
Fig. 5 Strength characteristic of treated peat (10 % PA) subjected with soaking time
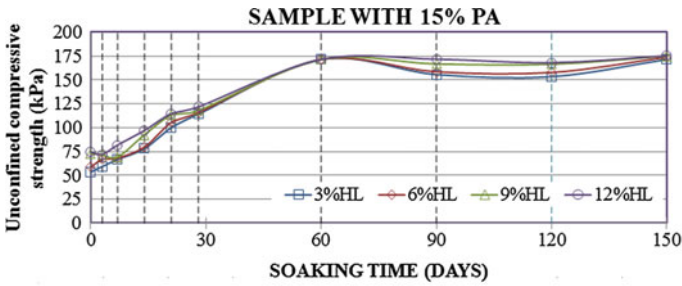
Fig. 6 Strength characteristic of treated peat (15 % PA) subjected with soaking time

at 90 days which is 119 kPa. Sample D experiences a slight drop by 3 % before it increase by 70, 1 and 48 % at 21 days. The strength was dropped by 6 % before it increase by 43 and 18 % until drop by 56 % at 120 days. The strength was then increased against by 81 % for further soaking. The maximum strength of 143 kPa was achieved in 120 days. Sample E also exhibits the same trend as sample D but with slightly different percentage. The maximum strength of 135 kPa was recorded by the sample at 120 days.

In Fig. 5, sample F and G show a closely similar pattern of characteristics. It started with the increment of 42, 16, 7 and 47 % before drop by 6 %. At 60 days soaking, the strength of both samples increase by 69 %, which is 141 and 147 kPa respectively. The strength for sample F decrease by 1 and 40 % before increase by 71 %. The maximum strength of 144 kPa was achieved in 150 days soaking. Meanwhile, strength of sample G drop by 3 and 32 % before increase by 59 %. The maximum strength was recorded as 153 kPa at 150 days soaking. Sample H also follows the same trend of characteristics. It increases by 6, 16, 18 and 30 % before drop by 7 %. In 60 days, the strength increase drastically by 79 % and then drops by 3 % before increase again by 36 and 58 %. The maximum strength of 158 kPa was recorded in 60 days. The sample I portray a good strength improved by 8, 16, 21, 27 and 43 % before drop by 4 and 19 %. The strength is then increased by 19 % and achieved a maximum value of 165 kPa at 150 days soaking.

In Fig. 6, sample J exhibits some improvement of strength at an early stage of soaking. The strength has increased by 11, 13, 17, 28, 14 and 50 %, before it drop by 9 and 1 % then increase again by 12 % on the final stage. The maximum strength of 172 kPa was recorded by the sample at 90 and 150 days. Sample K also exhibits a similar trend, but achieving a higher strength at 150 days which is 174 kPa. Sample L experiences a slight drop by 2 and 3 % before increase by 34, 22, 4 and 45 % and achieved the maximum strength of 171 at 90 days soaking. With further soaking, the strength was dropped by 3 % and stagnant at 150 days. Sample M exhibits a little drop by 3 % at an early stage before increase by 13, 19, 18, 6, 41 and 0 %, then drop another 2 %. It increases again by 4 % on the final stage. The maximum strength of 176 kPa was achieved in 150 days.

In Fig. 7, strength of sample N is slightly dropping by 3 % before increase by 11, 21, 25 %, then drop again by 2 %. At 60 days, it increases by 39 % and consistent at
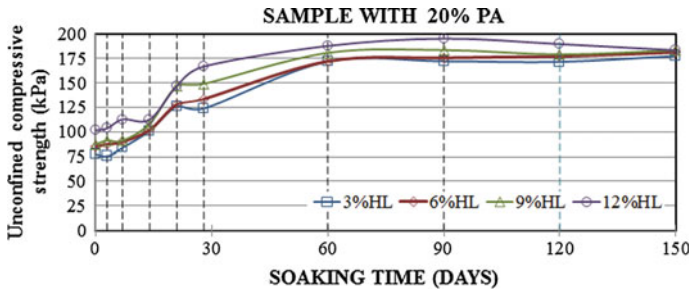
Fig. 7 Strength characteristic of treated peat (20 % PA) subjected with soaking time

90 and 120 days before slightly increase by another 3 %. Soaking for 150 days has given the maximum strength of the sample which is 177 kPa. For sample O, the strength was increased by 3, 3, 13, 26, 4, 29, 2, 1 and 2 % consecutively. The maximum strength of 183 kPa was achieved at 90 and 150 days soaking. Sample Q which contains the maximum composition of PA and HL, exhibits the highest strength characteristic among the all samples. Starting with 102 kPa, the early stage of soaking has increased the strength by 2, 9, 0, 30, 13, 13 and 4 % before slightly drop by 3 % and followed by another 3 % drop at the final stage. The maximum strength of 185 kPa was achieved in 90 days.

By comparing all the samples, sample with less composition of PA tend to achieve the maximum strength at 60 days soaking and start to drop with further soakings. The strengths were then increased close to maximum strength at the final stage. Sample B with lesser PA-HL content exhibits low strength characteristics. However, samples with 15 and 20 % behave more consistently in terms of strength improvement.

The maximum strength was almost achieved in 60 days and further soaking shown insignificant effects on the strength of treated soil samples. Practically, a good strength of soil after treatment will provide a good bearing capacity, hence increase the capability of the soil like peats to sustain more loads.

4 Conclusion

Peat soil stabilized with a higher percentage of pond ash and hydrated lime and soaked for 60–90 days has promoted the highest strength which is nine times on the strength of original peat soil. It is believed that the sample has already achieved the maximum strength. It can be concluded that hydrated lime chemical reaction needs time to bond together with particles.

Further soaking does not allow a significant increment to the strength of treated peat because the pozzolanic process has already completed when it approached 90 days.

Furthermore, attempts to use more pond ash with an appropriate percentage of hydrated lime should be studied to determine the strength of treated peat in another composition.

The findings suggest that the pond ash, which is a byproduct material along with hydrated lime, can be used as an additives and stabilizing agents for treatment of peat which is known as a problematic ground.

References

1. Akol, K., Stabilization of peat soil using lime as a stabilizer, Degree dissertation UTP, Perak, 2012.
2. Adon, R., Bakar, I., Wijeyesekera, D. C. and Zainorabdin, A., Overview of the sustainable uses of peat soil in Malaysia with some relevant Geotechnical assessments, Int. J,. of Integrated Eng., Vol. 4, No. 3, pp. 38–46, 2012.
3. Kalantari, B. and Huat, B. B. K., Precast stabilized peat columns to reinforce peat soil deposits, EJGE, Vol. 14, pp. 1–15, 2009.
4. Kalantari, B. and Huat, B. B. K., Effect of fly sh on the strength values of air cured stabilized Tropical peat with cement, EJGE, Vol. 14, pp. 1–4, 2009.
5. Makusa, G. P., Soil stabilization methods and materials (In engineering practice). PhD student, Lulea University of Technology, Sweden, 2012.
6. Sharan, A., Strength characteristics of fibre reinforced compacted pond ash, Master thesis, National Institute of Technology, Rourkela, 2011.
7. Swain, A. and Nayak, S. R., Geotechnical properties of fiber reinforced pond ash, Degree Thesis, National Institute of Technology, Rourkela, 2012.
8. Kolay, P. K., Sii, H. Y. and Taib, S. N. L., Tropical peat soil stabilization using class F pond ash from coal fired power plant, Int. J. Of Civil & Env. Eng., Vol. 3, No. 2, pp. 79–83, 2011.
9. Chand, S. K. and Subbarao, C., Strength and slake durability of lime stabilized pond ash, J. Of Mat. In Civil Eng., Vol. 19, pp. 601–608, 2007.
10. Raj, P., Compaction characteristics and shear parameter of pond ash, Degree Thesis, National Institute of Technology, Rourkela, 2010.
11. Said, J. M. and Taib, S. N. L., Peat stabilization with carbide lime, UNIMAS E-J. of Civil Eng., Vol. 1, pp. 1–5, 2009.
12. Saride, S., Chikyala, S. R., Pippala, A. J. and Harris, P. J., Effects of organics on stabilized expansive subgrade soils, GoeShan. Int Conf, pp. 155–164, 2010.
13. Pokhrel, D. R. and Godiwalla, A., Performance evaluation of lime fly-ash stabilization as pozzolanic stabilizer for airfield pavement used at Houston airport systems, EJGE, Vol. 17, pp. 1391–1406, 2012.
14. Yusof, Z. M., Harris, S. N. M. and Mohamed, K., Compressive strength improvement of stabilized peat soil by pond ash – hydrated lime admixture, Applied Mechanics and Materials, Vol.747, pp. 242–245, 2015.
15. Huat, B. B. K., Prasad, A., Asadi, A. and Kazemian, S., Geo of organic soils and peat, CRC Press, 2014.
16. ASTM C 618, Specification for Coal Fly Ash and Raw or Calcined Natural Pozolanic for Use as a Mineral Admixture in Portland Cement Concrete, *Annual Book of ASTM Standards*, ASTM, Philadelphia, USA, 1994.
17. National Lime Association, Lime – Treated Soil Construction Manual, Lime Stabilization & Lime Modification, 2004.

A Study on the Effectiveness of Soil–Root Matrix of Vetiver Grass and Bermuda Grass as Soil Slope Reinforcing System

M.N. Noorasyikin and M. Zainab

Abstract A study on the characteristic and effectiveness of the vegetation roots as soil slope reinforcing system to mitigate soil erosion and slope failure was carried out. The two types of grasses, namely Vetiver grass and Bermuda grass were used as slope vegetation cover. This study is to examine the root matrix strength of these grasses. The in situ grass root pull out test was carried out on the residual soil slopes. Then the root matrix system was characterized and tested for its tensile strength. Initial result showed that the resistance of Bermuda grass root system in clay loam is higher that Vetiver grass root matrix. Meanwhile, in sandy loam the Vetiver grass root has higher resistance than Bermuda grass root. The results indicated that the functionality of these grasses was mainly influenced by grass root matrix properties, soil type, and its bonding characteristics.

Keywords Pull out · Tensile strength · Root matrix

1 Introduction

Slope failure is a common problem in tropical countries. Despite many stabilization techniques applied to date none are able to provide an absolute solution, therefore continuous study is vital. Over the years, the application of vegetation cover as soil slope protection is continuously enhancing as it is a more friendly bioengineering technique. The vegetation root matrix system plays the major role as slope stabilization elements are believed to act as root reinforcement to the soil slope [2].
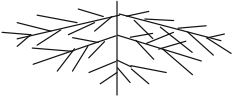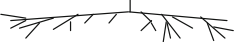
M.N. Noorasyikin (✉)
Institute of Infrastructure Engineering and Sustainable Management,
University Teknologi MARA, Shah Alam, Malaysia
e-mail: shecan83us@gmail.com

M. Zainab
Faculty Civil Engineering, Institute of Infrastructure Engineering and Sustainable
Management, University, Teknologi MARA, Shah Alam, Malaysia
e-mail: zaina556@perak.uitm.edu.my

Table 1 Root morphology types (*Sources* [1, 7])

Root morphology	Structure pattern
Heart root system (Fibrous root system)	
Tap root system (horizontal and vertical root system)	
Plate root system (horizontal root system)	

It was stated that the root matrix system of vegetation provides immediate mechanical shear strength for slope remedial and long-term beneficial effects. Meanwhile similar study revealed that the vegetation root matrix system had a similar reinforced behavior as soil nailing where the root supposed to anchor into the soil [5]. However, the grass root soil matrix varies by the types of grass root morphology [9]. The grass root morphology is an architecture, shape, or structure of vegetation root system [1]. Previous studies stated that there are three types of root morphology which were classified as heart, tap, and plate types as shown in Table 1. The tap root system was found to be more efficient as soil reinforcing system against landslide followed by heart root system and plate root system [7]. Furthermore, the root–soil strength is lower as the size of the root increases [8]. Subsequent study found that the root grows well in pores soil masses or sandy texture [9]. There were initial studies to understand the vegetation root resistance against pull out failure. Table 2 shows some findings on the pull out resistance value for various grass root systems [3]. It was reported that grass root strength of 6.00–49.7 N was able to resist soil mass surface erosion due to rainfall surface water erosion energy [6]. Another study found that the pull out resistance of Vetiver grass roots ranged from 190 to 620 N was able to anchor and resist the soil and water flow forces.

Hence this study shall further investigate the engineering characteristics of root morphology which is purposely classified as primary root system, secondary root system, and tertiary root system as shown in Fig. 1. The primary root represents the vertical root system, secondary represented by horizontal root and tertiary root represented by fibrous root system. The Vetiver grass and Bermuda grass were selected since these types were commonly recommended for soil slope surface cover in engineering practices for soil slope stabilization in Malaysia tropical climate. However, its effectiveness and function ability as engineering solution is yet to be fully understood.

Table 2 Previous studies of grass root pull out resistance findings for slope stabilization (*Source* [3, 6])

Grass species	Root pull out resistance (N)	Findings
Boehmeria spicata	49.7	The species with deep rooted with lateral spreading have shown greater pull out resistance and considered to be suitable species to prevent landslides against surface erosion
Erigeron Canadensis	27.6	
Solidago altissima	44.4	
Artemisia indica	37.6	
Trifolium repens	17.0	
Equisetum arvense	23.2	
Houttuynia cordata	13.2	
Miscanthus senensis	34.7	
Carex lanceolata	24.6	
Anthenoron filiform	24.0	
Rubus minusculus	42.4	
Achyranthus aspera	36.5	
Boehmeria cylindrical	28.8	
Sphenomeris chinensis	31.7	
Ambrina ambrosioides	28.0	
Hydrocotyle ramiflora	6.00	
Athyrium nipocium	45.2	
Vetiver grass	190–620	The Vetiver grass root strength able to withstand runoff and act as barrier to the movement of water and soil

Fig. 1 New concept of root matrix system was introduced in this study
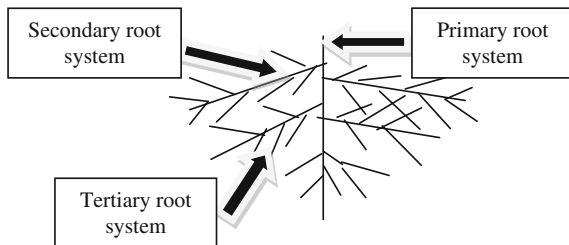
2 Materials and Methods

2.1 Site Characteristics and Grass Species

Three sites were selected to carry out the in situ pull out tests. The residual soil slopes along highway at Temerloh, Maran, and Gambang have an average slope gradient of 45° which were planted by Vetiver and Bermuda grass. The respective root and soil samples were taken to the laboratory for further study.

Fig. 2 A new fabricated
in situ root pull out test
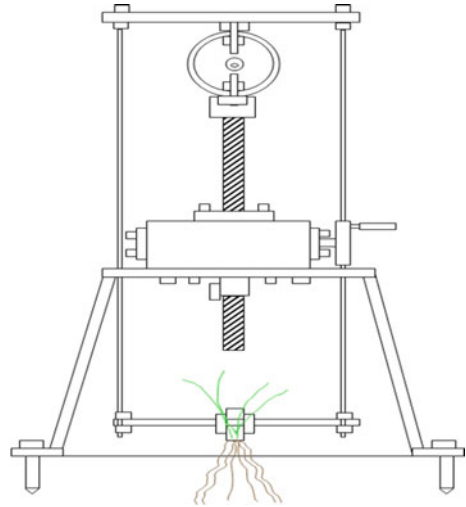
2.2   In Situ Root Pull Out Test

A new pull out test equipment was designed and fabricated for this study as shown
in Fig. 2. The challenges were to determine the capacity and function ability of the
mechanical equipment and its setup that is suitable to grass root system.

The equipment was fabricated with manual operated mechanical jack system;
pull out attachment with wedge and steel frame. The equipment was designed in
such a way that the pull out test can be carried out on horizontal slope surface or
sloping ground. The load ring and transducer were set on the upper part of the steel
frame to measure load and displacement in a vertical direction. The load and
displacement gauges were set to zero before starting the test. The grass root crown
was gripped using material named as epoxy to ensure root can easily be clamped
and no slippage during the measurement.

Mechanical jack system was rotated manually at clockwise direction in order to
generate force pulling out the root at the rate of 2 mm/min. The force was applied
until the load and a displacement reading was constant or reduces. The peak value
record is the maximum force or pull out load. The sampled grass was first identified
and classified by its well grown, moderately grown, and poorly grown grasses.

2.3   Root Tensile Strength Test

The Bermuda grass and Vetiver grass root system from in situ test was classified
and selected for its tensile strength. The root tensile strength test was carried out
using Shimadzu Universal Testing Machine as shown in Fig. 3. The root tensile

Fig. 3 Root tensile strength test using Shimadzu Universal testing machine
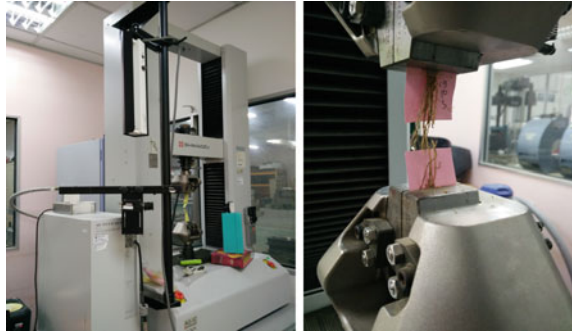
strength was carried out on individual primary root, a group of 5, 10, and 15 roots. Also individual secondary roots, a group of 5, 10, and 15 roots were also tested. The root diameter was measured and fixed at the length of 100 mm. The tensile strength of root sample was measured in MPa (MN/m^2).

3 Results and Discussion

3.1 Field Observation and Root Characteristics

Based on field observations, it was found that the Bermuda grass is able to grow well in sandy loam and clay loam comparatively to Vetiver grass as shown in Fig. 4. It is based on observation of successful growth rate which was estimated and measured by percentage growth area. The planted Vetiver grass at Temerloh site was observed poorly grown in clay loam which is at Berm 1 about 30 % and at Berm 2 roughly about 80 %. Meanwhile at Maran site, the Vetiver grass grows moderately with Bermuda grass in sandy loam. At Gambang area, the Bermuda grass was found well grown with clay loam.

Previous study stated that the root will grow through large pore if the soil has granular structure or sandy texture [9]. The sandy soil is more porous and able to hold a huge capacity of water and then became waterlogged. Due to this clarification, the root of Vetiver grass and Bermuda grass was able to grow greener with Sandy Loam. In clay loam soil, the Vetiver grass was observed to grow poorly at Temerloh site area. Meanwhile, the Bermuda grass was found to grow well in clay loam at Gambang area.

Previous study claimed that the Vetiver grass has massive and deep root matrix system where the root may grow vertically 2–3 m in the first year and ultimately can reach to 5 m length in wet tropical environment [4]. While for Bermuda grass, generally this grass is well known among engineers and grows at the surface of soil slope only. Thus, it can be revealed that the root of this grass is not able to grow as deep as Vetiver grass. The clay soil is different from sandy soil, where it is also able to hold a huge amount of water but without waterlogged. Generally, the root of
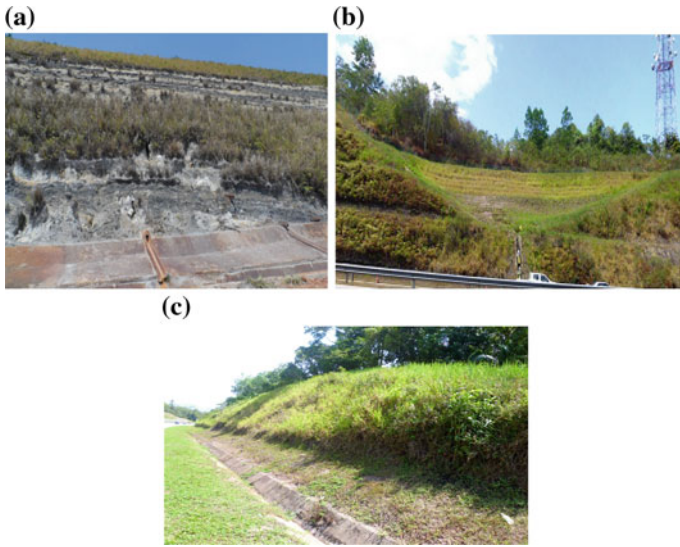
Fig. 4 Field observation. **a** Temerloh—Vetiver grass grow poorly [Clay Loam]. **b** Maran–Bermuda grass and Vetiver grass grow moderately [Sandy Loam]. **c** Gambang–Bermuda grass well grown [Clay Loam]

vegetation requires water as their nutrient to grow. Although the moisture of clay soil is easily reduced, the Bermuda grass is able to survive because it was planted on soil surface only for short-term time. While, the root of Vetiver grass cannot grow vertically as well as the moisture content is reduced. The longer the root length and larger root diameter of Vetiver grass, the smaller the strength of clay soil.

The typical root morphology of Vetiver grass and Bermuda grass is as shown in Table 3. The root system of both grasses is of fibrous in nature and characterized as heart root system.

Table 3 Root morphology of Vetiver grass and Bermuda grass

Grass types	Root morphology
Vetiver grass	Heart root system (Fibrous)
Bermuda grass	Heart root system (Fibrous)

3.2 Root Profile of Pull Out Resistance for Vetiver Grass and Bermuda Grass

3.2.1 Vetiver Grass

The in situ pulls out test have been implemented at two site areas, Temerloh (Clay Loam) and Maran (Sandy Loam) area.

(a) Temerloh—Fig. 5 shows the graph pull out resistance versus vertical displacement for Vetiver grass in clay loam soil. The average of the pull out resistance increases drastically until reached at peak value with vertical displacement −51.18 mm (primary root) and the gradient of pull out resistance 8.004 N. It can be seen from the graph, the pull out resistance has small range values which from 0 to 8.004 N as the displacement increases. It is mainly because of clay soil texture. Clay soil usually has small discontinuity pores and this kind of soil is capable of holding a huge quantity of water thus often waterlogged especially during raining season. Thus, when the surface is dried up extremely, the soil became cracking and peeling. It slowly decreases the nutrient level of soil which inhibits the grass growth.

(b) Maran—Fig. 6 shows the graph pull out resistance versus vertical displacement for Vetiver grass with sandy loam soil. The average of the pull out resistance increases drastically at the first stage of the test, which at the small vertical displacement below than −20.00 mm. The resulting force–distance diagrams showed a 45° of slope until reached at the maximum pull out resistance of 295.81 N (peak value) with vertical displacement −21.79 mm (secondary root). It was observed that there is another peak value of pull out resistance which is at 237.452 N (secondary root). In nature, the root
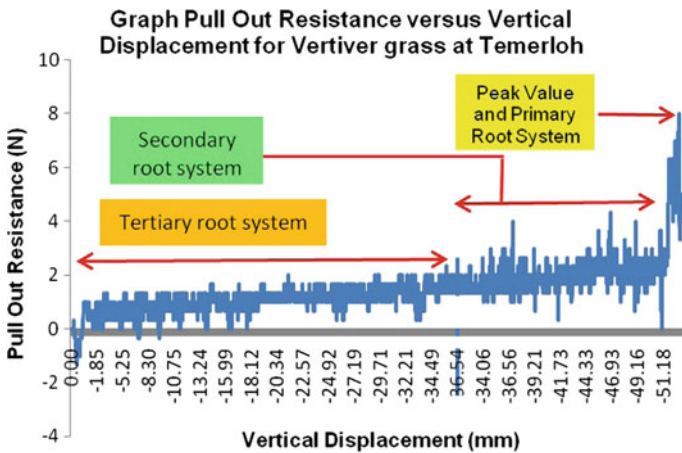
Fig. 5 Graph pull out resistance versus vertical displacement for Vetiver grass at Temerloh— (Clay Loam)
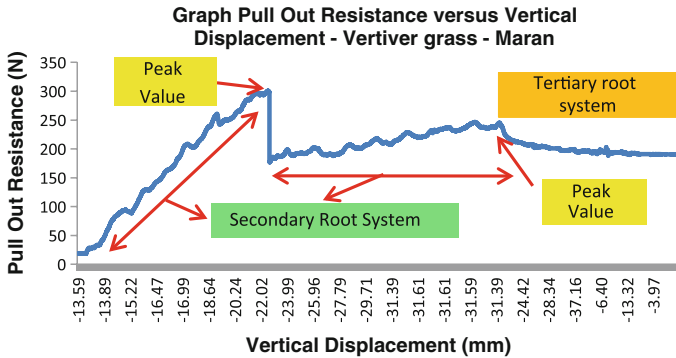
Fig. 6 Graph pull out resistance versus vertical displacement for Vetiver grass at Maran—(Sandy Loam)

morphology of Vetiver grass is in fibrous root system and most of them grow with large diameter, thus with sandy loam soil it is possible that this is the second maximum value of force where it required to pull out the root from the soil. Subsequently, the gradient of pull out resistance decreases gradually and begins to drop until at vertical displacement −4.05 mm (tertiary root).

3.2.2 Bermuda Grass

The in situ pulls out test have been implemented at two site areas, Maran (Sandy Loam) and Gambang (Clay Loam) area.

(a) Maran—The average of the pull out resistance increases drastically at the first stage of the test, which at the small vertical displacement below than −20 mm as shown in Fig. 7. The resulting force–distance diagrams showed a 45° of slope until reached at peak value of pull out resistance at 220.44 N (primary root) with vertical displacement −19.87 mm. Subsequently, the gradient of pull out resistance decreases gradually and begins to drop until at vertical displacement −49.15 mm (tertiary root). Based on the graph, it can be seen that the root of grass is easy to pull out until reached at maximum force. Although the root of Bermuda grass grow with fibrous system, the large pore space of sandy loam texture and the root grow on the surface of soil slope made the reason why the root is easy to pull out.

However, the peak value of resistance is still in large value which can be said that the root is well grown with this kind of soil type.

(b) Gambang—The average of the pull out resistance increases drastically until reached at peak value of pull out resistance 72.3695 N (secondary root) which at the vertical displacement −19.317 mm as shown in Fig. 8. However, there are another two peak values which are 68.034 N (tertiary root) and 88.044 N (primary root).
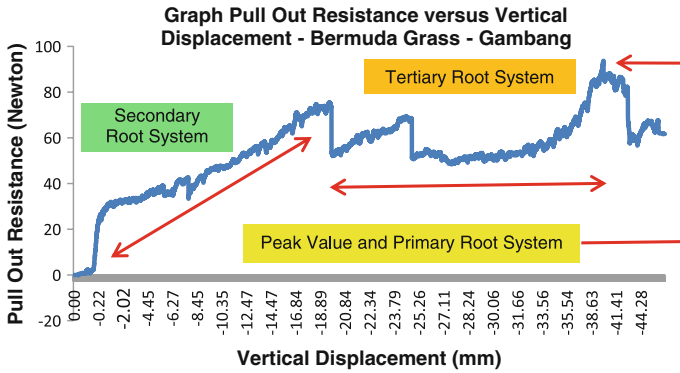
Fig. 7 Graph pull out resistance versus vertical displacement for Bermuda grass at Maran—(Sandy Loam)
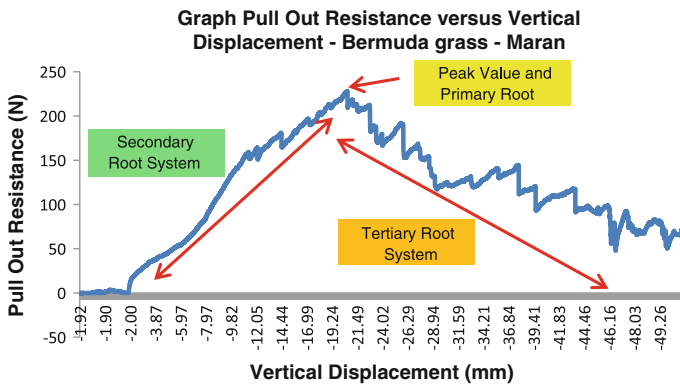
Fig. 8 Graph pull out resistance versus vertical displacement for Bermuda grass at Gambang—(Clay Loam)

The pull out resistance findings for each grass was tabulated in Table 4. The pull out resistance of grass at Temerloh was found obtained a small value as compared to other site location with maximum root diameter 2 mm and minimum 1 mm, maximum root length 60 mm and minimum 30 mm. The heart root system of Vetiver grass was found able to act as root reinforcement to the sandy loam soil compared with clay loam soil. However, for Bermuda grass it shows contrarily where it was able to grow in both soil types. The graphs of pull out resistance versus vertical displacement at Maran area show similar trend which the in situ pull out test were conducted at slope angle 45°, meanwhile the graphs at Gambang and Temerloh present flat trend because the pull out test was conducted at flat surface near to the slope face. The Vetiver grass which grows in well condition exhibits high value of pull out resistance than Bermuda grass. Although the Vetiver grass is not able to grow well with clay loam soil, the minimum root diameter contained

Table 4 Root characteristics of grasses

Bil	Site location	Grass type	Max pull out resistance (Newton)	Soil type	Root diameter (mm)		Root length (mm)	
					Max	Min	Max	Min
1	Temerloh	Vetiver grass	8.004	Clay loam	2	1	60	30
2	Maran	Vetiver grass	295.81	Sandy loam	3	1	90	40
3	Maran	Bermuda grass	220.44	Sandy loam	3	0.2	110	60
4	Gambang	Bermuda grass	72.3695	Clay loam	2.1	0.1	120	40

high value as compared with Bermuda grass. It shows that the heart root system of Vetiver grass is more efficient than heart root system of Bermuda grass.

Based on the results obtained, it shows that the soil type may be the major factor that influences the grass root growth. The clay has a good water holding capacity, thus it is confined to cracks when it turns to dry. The root of grass was not able to anchor well into these soil types. On contrary, the sandy soil is able to hold a huge water thus waterlogged. Therefore, there is a pore space between the soil textures where the nutrient level of soil is sufficient for root of grass to grow. On the other hand, root morphology also influences the strength of soil between the roots. According to the previous researcher findings from Table 2, it can be considered that the root of Vetiver grass and Bermuda grass in sandy loam soil is able to act as root reinforcement to the soil slope. However, with clay loam soil it shows otherwise. So, it can be summarized that the Bermuda grass and Vetiver grass were a good choice of bioengineering technique for slope stabilization works especially with sandy loam soil.

3.3 Root Tensile Strength of Vetiver Grass and Bermuda Grass

The tensile strength test has been carried out on 5 primary root, 10 primary root, 15 primary root, 5 secondary root, 10 secondary root, and 15 secondary root of Vetiver grass and Bermuda grass. The comparison can be seen from Fig. 9. It was observed that the Vetiver grass require maximum force rather than Bermuda grass to pull the root with results obtained; 5 primary root (181.12 Mpa), 10 primary root (339.14 MPa), 15 primary root (460.74 MPa), 5 secondary root (181.91 MPa), 10 secondary root (238.52 MPa), and 15 secondary root (367.26 MPa) respectively represent by red bar from the graph. Meanwhile, for Bermuda grass the tensile strength is ranged from 52.98 to 431.07 MPa.
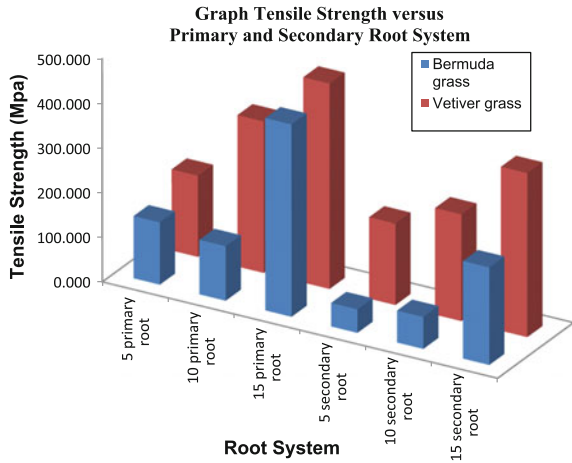
It can be summarized that the root of Vetiver grass is more strengthen compared to root of Bermuda grass. Previous study found that the tensile strength of Vetiver grass is ranged from 40 to 120 MPa. [4]. But, the number of root tested did not mention. However, in this study the tensile strength value of Vetiver grass root was represented by different root system which is ranged from 181.12 to 460.74 MPa.

4 Conclusion

The new fabricated equipment designed for grass root pull out test has function effectively and the test was carried out successfully. The root–soil matrix reinforcing properties planted on the soil slopes was pulled out gradually and the pull out load was measured from the pull out test. The Vetiver grass and Bermuda grass roots had similar trend resistance to the pull out test. In sandy soil, the grass root–soil matrix has higher anchoring resistance than in clay root matrix. The Bermuda grass and Vetiver grass were found a good choice of bioengineering technique for slope stabilization works especially with sandy loam soil. However, the pull out resistance of Vetiver grass exhibit higher value then Bermuda grass. In addition, the tensile strength obtained for Vetiver grass also required maximum force to pull the root. The result strongly revealed that heart root system of Vetiver grass has a good root bonding properties than the heart root system of Bermuda grass and it could be the most choice to mitigate slope failure. Two types of main factors were found gave major contribution toward grass root growth, there are soil type and root morphology. However, further study is needed to test the individual root strength to conclude these findings.

References

1. Bibalani,G,H., Golshani,A.A., Zahedi,S.S and Bazhrang,Z. (2007). Soil Stabilizing Characteristics of Rangelands Vegetation in Northwest Iran (Misho Rangelands Protected Location of Shabestar). *Asian Journal of Plant Sciences*. 6 (6). pp 1020–1023. ISSN: 1682-3974.
2. Bujang, B.K.H & Sina, K. (2010). Study of Root Theories in Green Tropical Slope Stability. *Electrical Journal of Geotechnical Engineering.* Vol. 15 [2012]. Bund Q.
3. Devkota,B.D., Omura,H.,Kubota,T.,Paudel,P & Inoue,S. (2006). Revegetation condition and morphological characteristics of grass species observed in landslide scars, Shintategawa watershed,Fukuoka, Japan. *Journal of Applied Science.* 6(10):2238–2224.
4. Diti,H. (1999). *15 Years of Bio-Engineering in the Wet Tropics*. First Asia-Pacific Conference on Ground and Water Bio-engineering. Manila, April 1999.
5. Hallett,P.D.,Bengough,A.G,Hamzah,O., Bransby,M.F., Davies,M.C.R and Halpin,C. (2003). Plant root biomechanics and slope stabilization. Environment Article.
6. Mickovski,S.B., Van Beek,L.P.H & Salin,F. (2005). Uprooting of Uprooting Resistance of Vetiver Grass. *Plant and Soil Journal.* 278:33–41. DOI 10.1007/s 11104-005-2379-1.
7. Nomessi,K., Thierr.F., Kouami.K., Kouma,N., & Lac,P. (2006). Disaster Mitigation of Debris Flows, Slope Failures and Landslides. Universal Academy Press Inc Tokyo Japan, pp 561–569.
8. Sasan,M., Bujang, B.K.H., & Vahed, G. (2009). Evaluation on Root Theories and Root Strength Properties in Slope Stability. *European Journal of Scientific Research. Vol.30 No.4.*594–607. ISSN 1450-216X.
9. Yoav,W., Amran,E & Uzi, K. (2002). Plant Roots The Hidden Half. Third Edition. ISBN: 0-8247-0631-5.

A Correlation Between P-Wave Velocities and Standard Penetration Test (Spt-N) Blows Count for Meta-Sedimentary Soils of Tropical Country

Haryati Awang and Mohamad Nazly Nasir Mohamad

Abstract The conceptual foundation design acquires geotechnical parameters such as stiffness, elastic, strength, etc. As such, geophysical method such as seismic refraction may assist in providing parameters for geotechnical analysis and design. Using seismic methods, the information on the stiffness of the ground can be obtained. This study has been carried out to develop the correlation between P-waves velocity from seismic refraction method against Standard Penetration Test (SPT) N value from existing borehole data. The study area was located at Bandar Country Homes, Rawang, Selangor which was believed to be underlained by Terolak Formation, a geological formation consisting of meta-sedimentary rock. Three seismic lines were conducted across six numbers of existing boreholes with the aim of characterizing the subsurface of the study area. Interval of each geophone was set to 5 m with the total length of each seismic line 120 m. The seismic sources were used by 12 lbs sledge hammer and steel plate, then seismograph data received by geophones (24 Hz) and saved in ABEM Terralock MK6 as seismogram. The high quality data obtained was then processed using SeisOpt Picker and SeisOpt@2D software to produce a seismic tomography section for each survey line. The correlation was made between seismic velocities and SPT-N value at the same depth. The findings from this study, a linear regression was found to enhance the relationship between Vp and SPT-N value. Also, the subsurface information together with depth of each geomaterial at the study area could be determined. Thus, this study may assist engineers for estimating and predicting the properties of the subsurface geomaterials in meta-sedimentary soils especially in reducing the

H. Awang (✉)
Institute for Infrastructure Engineering and Sustainable Management (IIESM),
Faculty of Civil Engineering, Universiti Teknologi MARA (UiTM),
Shah Alam, Selangor, Malaysia
e-mail: harya406@salam.uitm.edu.my

M.N.N. Mohamad
Faculty of Civil Engineering, Universiti Teknologi MARA (UiTM),
Shah Alam, Selangor, Malaysia
e-mail: nazlynasir@gmail.com

cost of site investigation and enhance the knowledge of understanding earth's subsurface characterizations physical parameters.

1 Introduction

Geotechnical site investigation (S.I.) is the utmost compulsory tool to gather detailed subsurface information and evaluation of the geological characteristics. It has played the vital role prior execution of any construction on the ground. The aim of the site investigation is to characterize the nature parentheses, following the example. Some components, such as multi-leveled equations, graphics, and tables are not prescribed, although the various table text styles are provided. The formatter will need to create these components, incorporating the applicable criteria that follow and distribution of the geotechnical properties of the site to permit the acceptable design, construction and operation of the proposed works. The investigation should endeavor to achieve the required technical standards of good practice with maximum economy. Hence, the conceptual design can be provided in reliable, economic and safe foundation structures in timely manner at minimum cost for the effort needed. A good planning and management of site investigation is a key of success factor to obtain sufficient and correct site information. No matter what the approach to a project is, it invariably adheres to the BS 5930:1999 'Code of practice for site investigations' [3] and the BS 10175:2001 'Investigation of potentially contaminated sites [4]—Code of practice'.

Geophysical method was an alternative method in geology and civil engineering discipline for detecting subsurface information. The concept of applied physics is used to measure subsurface characteristics and ground properties to develop strata profile. It comes with several techniques in terms of wave velocity, electrical resistivity, radioactivity and gravity, electromagnetometric, and magnetometric concept. The techniques which can be used in ground and aquatic medium are called seismic technique. In oil exploration, the concept of seismic reflection had been used to determine the geological structures such as salt dome, fault trap, folding plane, etc. At normal condition, the crude oil had trapped inside these geological structures. Seismic reflection is suitable for deep exploration under the ground for subsurface profiling. Meanwhile, seismic refraction has been used for shallow subsurface investigation up to 30 m. Seismic refraction is a cost-effective means to obtain generalized subsurface information for geotechnical characterization over large area [1]. By performing seismic refraction tomography, the bedrock structure, velocity distribution, and depth underlying can be obtained in more details [1]. Seismic refraction method is a commonly used traditional geophysical technique to determine depth to-bedrock, competence of bedrock, depth to the water table, or depth to other seismic velocity boundaries [7].

The complexity of subsoil profile especially in karstic formation lead geotechnical engineers in misinterpretation of the data. The exploratory holes carried out during this rock formation are inadequate for geotechnical engineers to come out with conceptual design. Borehole data only provide discrete information to the geotechnical engineers. In karstic formation, the adjacent borehole sometimes shows the variance of subsoil profile. To overcome this problem, extra borehole will be located in order to obtain better information which increases cost and time of site investigation. It comes into pictures that the usage of geophysical technique especially seismic refraction method becomes an alternative technique. Seismic method is one of the effective and inexpensive methods to be carried out for subsurface profiling either in shallow or deep exploration. Recently, there was lack of studies with regards to P-wave velocity and standard penetration test blows count (SPT) in meta-sedimentary soils of tropical country. The study might help geotechnical engineers to interpret subsurface information based on seismic refraction method data. As such, the cost for exploratory holes will be minimized and in addition to avoid any destruction of the study area.

The study has established the relationship between P-waves velocity and SPT-N blows count from existing boreholes data. Then, it also determined the subsurface profiling using seismic refraction survey method at the proposed study area. Finally, it has obtained the velocities and depth of each layers of geomaterial at the study area.

2 Location and Geology of the Study Area

The study took place at Bandar Country Homes Rawang, Selangor Darul Ehsan. The global position systems (GPS) is latitude $3°19'55.89''$ N and longitude $101°32'13.55''$ E as shown in satellite image as per Fig. 1.

Fig. 1 Satellite image of study location
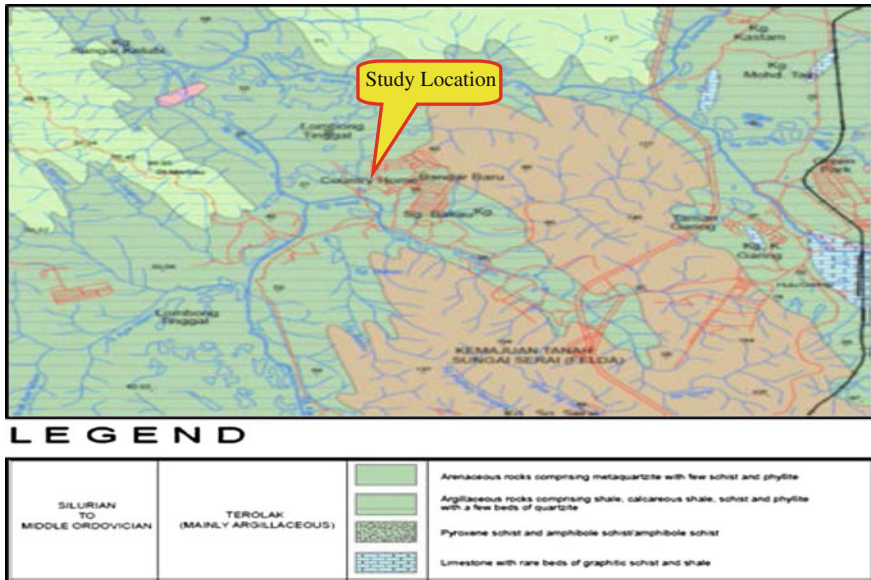
Fig. 2 Geological map of the study area (Department of Mineral and Geosciences Malaysia, Sheet 85.)

Based on geological map of Rawang, Selangor (Fig. 2) published by Department of Minerals and Geoscience Malaysia, Sheet No. 85, and Scale 1: 63,360, [6] the study area was underlained by Terolak Formation which consists of argillaceous rocks comprising of phyllite, schist, shale, calcareous shale also few beds of quartzite and sometimes with occurrence of limestone. The age of this meta-sedimentary rock was believed to be from Silurian to Middle-Ordovician.

3   Methodology

The study involved analysis of standard penetration test (SPT) taken from existing borehole data (secondary data) available. Six (6) numbers of boreholes were carried out at the study area (Fig. 3). The groundwater level during site investigation was recorded as per Table 1. The study involved seismic refraction data acquisition followed by data processing and tomography interpretation (primary data). The data acquisition was performed using 24 channel ABEM Terraloc MK6, the multi-channel digital seismograph with internal PC compatible computer 386 Hz CPU, 80–250 MB Hardisk, a 3.5 in. storage disk high density (1.44 MB) and a standard VGA graphic display. Total of three (3) numbers of seismic refraction lines were conducted across each of boreholes as shown in Fig. 3. Each of the lines has twenty-four (24) numbers of 28 Hz geophones traverse along the spread lines.
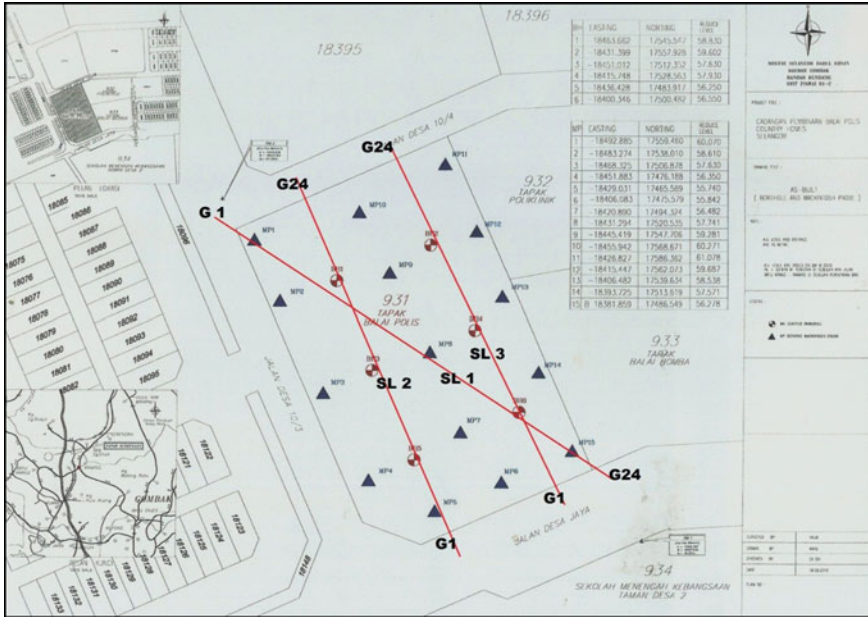
Fig. 3 Location of boreholes and seismic lines of study location

Table 1 Ground water level (GWL) inside borehole

BH	1	2	3	4	5	6
GWL (m)	6.0	10.5	12.0	9.0	9.8	11.0

Then, each geophone was slotted at five (5) m interval excluding offset points used as 2.5 m (half of interval) at both ends of the spread line. There were five (5) shot points conducted as sources for each spread line. The numbers of shot point must have mirror image numbers for both sides of each spread line. The numbers of shot point can be more than five (5) shot points. Then, each shot point has five (5) numbers of hammer stacks performed during data acquisition. The schematic diagram was illustrated as shown in Fig. 4.
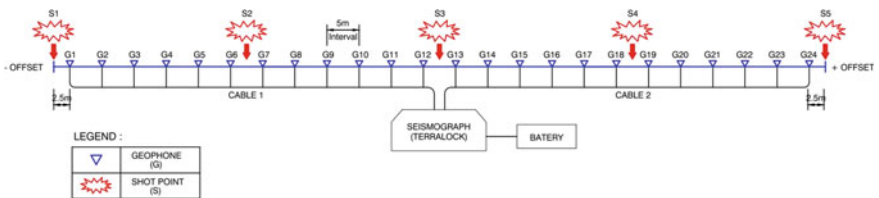
Fig. 4 Layout of geophones and shoot points along the seismic spread line

4   Result and Discussion

In this study, the author used seismic refraction survey to locate the exact value of seismic velocities which can correlate with SPT-N value from boreholes data set. The seismic tomography results had processed using SeisOpt software such as SeisOpt Picker and SeisOpt@2D. The seismic was interpreted by author based on color indication in the seismic tomogram. Each color represents the velocity of each geomaterial. Then, the velocity for each layer was compared with the research of previous researcher (Table 2). As a result, the seismic tomography for three spread lines are shown in Figs. 5, 6, 7.

Based on results of seismic tomogram for Seismic Line 1 (SL1), Seismic Line 2 (SL2), and Seismic Line 3 (SL3), it can be concluded that the study area consists of three layers. Layer 1 has velocity below 500 ms^{-1} and the depth of layer one from existing ground level up to 13 m. The layer one was identified as soil layer [5], mostly gravelly Sandy SILT. Meanwhile, layer 2 has velocity between 2200 and 3000 ms^{-1}. The depth of layer 2 is about 13 m from existing ground level up to 18 m. Layer 2 was determined as sand (water saturated, loose) [5]. Whereas, layer 3 which has velocity above 3000 ms^{-1} and the occurrence approximately more than 18 m from existing ground level. This layer was predicted as sandstone (bedrock)

Table 2 Various velocities for different material (after Kohnen 1974)	Material	Vp (m/s)
	Air	330
	Water	1450–1530
	Soil	100–500
	Sand (loose)	200–2000
	Sand (dry, loose)	200–1000
	Sand (water saturated, loose)	1500–2000
	Sand and gravel (near surface)	400–2300
	Sand and gravel (at 2 km depth)	3000–3500
	Clay	1000–2500
	Sandstone	1400–4500
	Limestone (soft)	1700–4200
	Limestone (hard)	2800–7000
	Dolomites	2500–6500
	Shale	2000–4100
	Granites	4600–6200
	Basalt	5500–6500
	Gabbro	6400–7000
	Gneiss	3500–7600
	Disturbed soil	180–335

Note Kohnen 1974. The temperature dependence of seismic waves in ice
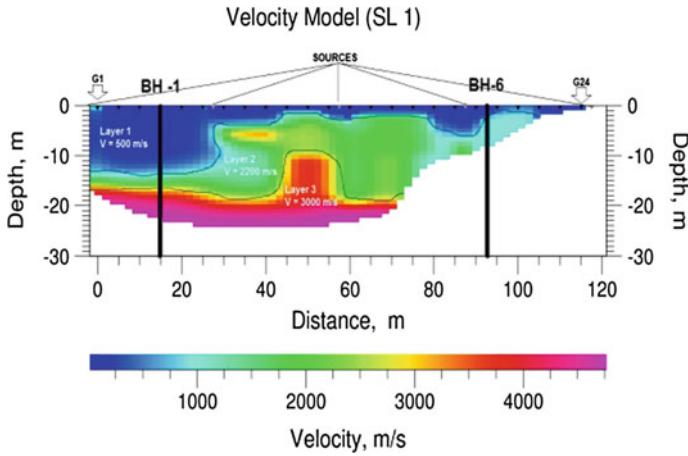
Fig. 5 Velocity model for spread line (SL1)
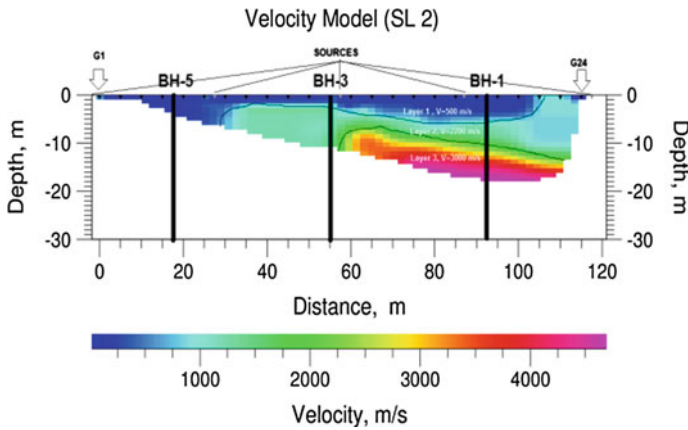
Fig. 6 Velocity model for spread line (SL2)

[5]. Table 3 shows the summary of this study and the subsurface profiling is illustrated as per Fig. 8.

Afterwards, the seismic tomogram and subsurface profile for SPT-N value then correlated with the same depth location (Table 4). Based on correlation made between SPT-N blows counts known as independent variable and P-Wave velocities known as dependent variable for all the boreholes, the relationship between this engineering parameter for meta-sedimentary soil was found as simple linear regression. The outlier points have been deleted from the graph due to an error during reading the data. As such, the positive linear regressions indicate that P-wave velocity in meta-sedimentary soils increases gradually with depth reflecting the SPT-N value increasing with depth (Fig. 9).
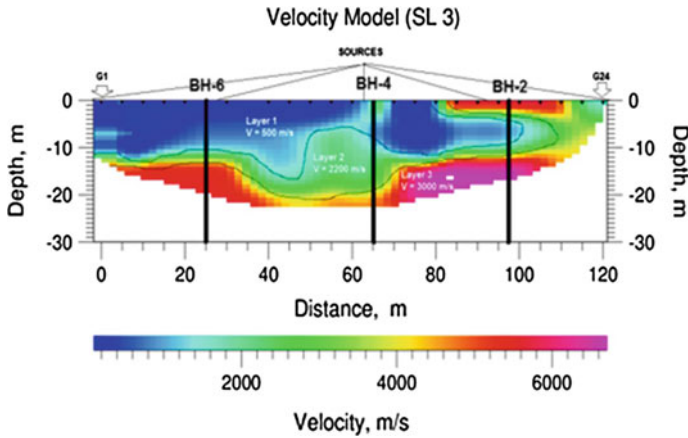
Fig. 7 Velocity model for spread line (SL3)

Table 3 Summary of this study

Layer	Velocity (ms^{-1})	Depth	Description
1	Below 500	Below 13 m from existing ground level	Soil (gravelly sandy SILT)
2	Between 2200–3000	Between 13 and 18 m	Sand (water saturated, loose)
3	Above 3000	Above 18 m from existing ground level	Sandstone (bedrock)
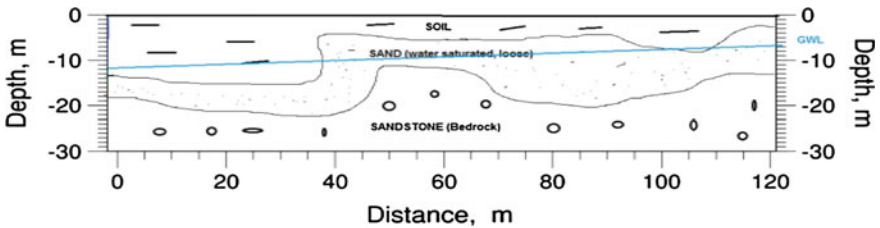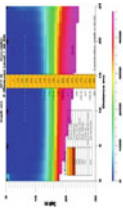
Fig. 8 Subsurface profiling of study area

The empirical correlation between seismic velocity and SPT-N value for tropical granitic rock is Vp = 23.605(N)–160.43 and regression value is R2 = 0.9315 or 93.15 % [2]. As mentioned earlier in introduction section, there is no study with regards to correlation SPT-N value with P-wave velocity in meta-sedimentary soils in tropical country. As such, the comparison between these findings and previous researchers cannot be highlighted.

However, these findings can demonstrate new discovery for study of meta-sedimentary soils and SPT-N value. The data found was unsatisfactory during

Table 4 Correlation between SPT-N and seismic velocity

BH	Depth (m)	SPT–N	Seismic velocity (m/s)	Cross section area
BH-1	1.5–3.0	7	150	
	3.0–4.5	10	150	
	4.5–6.0	35	160	
	6.0–7.5	39	200	
	7.5–9.0	43	330	
	9.0–10.5	21	460	
	10.5–12.0	29	920	
	12.0–13.5	16	1500	
	13.5–15.0	22	1900	
	15.0–16.5	36	2640	
	16.5–18.0	41	3290	
	18.0–19.5	43	3550	
	19.5–21.0	49	4000	
	21.0–22.5	22	4360	
	22.5–24.0	20	4400	
	24.0–25.5	15	End of data	
	25.5–27.0	21	SL 1	
	27.0–28.5	45		
	28.5–30.0	49		
	30.0–31.5	50		
	31.5–33.0	50		
	33.0–34.5	50		
	34.5–36.0	50		
	36.0–36.09	50		

(continued)

Table 4 (continued)
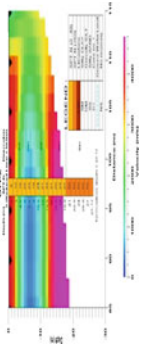
BH	Depth (m)	SPT–N	Seismic velocity (m/s)	Cross section area
BH-2	1.5–3.0	8	1580	
	3.0–4.5	10	1760	
	4.5–6.0	15	1780	
	6.0–7.5	22	2060	
	7.5–9.0	23	2280	
	9.0–10.5	19	3000	
	10.5–12.0	24	3370	
	12.0–13.5	21	4100	
	13.5–15.0	33	4680	
	15.0–16.5	31	4910	
	16.5–18.0	20	5320	
	18.0–19.5	23	5430	
	19.5–21.0	27	End of data	
	21.0–22.5	50	SL 3	
	22.5–24.0	50		
	24.0–25.5	50		
	25.5–27.0	50		
	27.0–27.165	50		

Fig. 9 The relationship between P-wave velocities and SPT-N blows count for meta-sedimentary soil
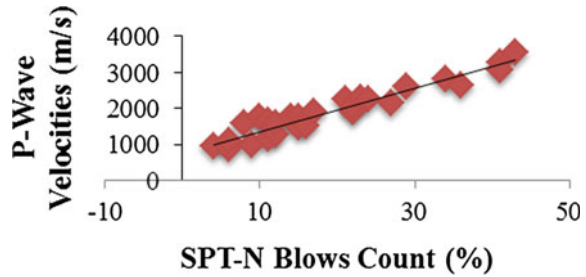
the study because seismic refraction method has some limitation. During field data acquisition, noise and vibration has affected the efficiency of the results because seismic method is very sensitive due to many disturbance at field. To determine seismic velocity in geomaterial, the velocity should increase gradually by increasing the depth. The deeper the seismic wave propagates through the sub-surface material, the higher velocity obtained. The existence of hidden layer which has low velocity between two layers, identification of such geomaterial becomes imprecise. It can be justified by SPT-N value where the value suddenly decreases by increasing the depth.

5 Conclusion

This study had investigated correlation between P-waves velocity and SPT-N value in meta-sedimentary soils for tropical country. The primary data were obtained using seismic refraction method whereas secondary data were obtained from soil investigation report. As mentioned earlier, the objective of this study was to determine the subsurface profiling, to obtain the velocities and depth of geomaterials, and finally to correlate the results of P-wave velocity with SPT-N value from the existing borehole data.

The following conclusions can be drawn based on the findings of the study;

(a) The subsurface profiling was determined by seismic tomogram as shown in Fig. 8.
(b) The first layer has velocity below 500 ms^{-1} and the depth is below 13 m from existing ground level. Second layer was identified as velocity between 2200 and 3000 ms^{-1} and the depth is between 13 m up to 18 m from existing ground level. Meanwhile, third layer was detected at velocity above 3000 ms^{-1} and it was formed above 18 m from existing ground level.
(c) The relationship between P-wave velocity and SPT-N value was determined as simple linear regression.

The results of this study may give some ideas to geotechnical engineers to assume geotechnical parameters with regards to meta-sedimentary soils in tropical

country. Hence, the cost for exploratory holes and destruction of area will be reduced and minimized. However, this established correlation limited to meta-sedimentary soils in Terolak Formation was only because the study area was underlained by Terolak Formation. The extension of study could focus on other meta-sedimentary soils from adjacent formation such as Kenny Hill Formation and Belata Formation. As such, the empirical correlation of P-wave velocities versus SPT-N value for all meta-sedimentary soils could be derived.

References

1. Azwin, I.N., Saad, R. and Nordiana, M., (2013). Applying the Seismic Refraction Tomography for Site Characterization. APCBEE Procedia,5, pp 227–231.
2. Bery, A.A. and Saad, R. (2004). Correlation of seismic P-wave velocities with engineering parameters (N-value and rock quality) for tropical environmental study. International Journal of Geosciences, 2012, 3, pp 749–757.
3. British Standards Institute: BS 5930 (1999). Code of Practice for Site Investigation Work, London, British.
4. British Standards Institute: BS 10175 (2001). Code of Practice for the Investigation of Potentially Contaminated Sites, London, British.
5. Kohnen, H., (1974). The temperature dependence of seismic waves in ice. Journal of geology,13, pp 144–147.
6. Mineral and Geo-sciences Department, Geological Map of Rawang Selangor.
7. Northwest Geophysical Associates, Inc., 2002, Technique-Seismic Refraction and Reflection, Geophysical Services, Corvallis.

Landslide Mapping Using LiDAR in the Kundasang Area: A Review

Syed Omar, Zainab Mohamed and Khamarrul Azahari Razak

Abstract Kundasang has been identified as one of the major geological hazardous area in Malaysia. This is due to the existence of numerous landslides occurrences at some locations in the Kundasang area. The occurrence of landslide has resulted substantial damaged to the building structure, access road, telecommunication towers and agriculture orchards. Several studies and attempts of landslide investigation have been conducted in the Kundasang area using various methods such as localized drilling method, geodynamic mapping and a regional geological structure mapping. These methods have not gathered sufficient information which is considered important in developing a complete landslide inventory to assess landslide susceptibility due to constraint of time and cost. This paper presents a critical review to determine the potential use of light detection and ranging (LiDAR), specifically airborne laser scanning (ALS) for landslides mapping to assess landslide susceptibility of the Kundasang area. Several researchers found that the usage of light detection and ranging (LiDAR) such as airborne laser scanning (ALS) has been a successful technique in landslides mapping. Availability of this new technology for identification and mapping of landslides will assist in obtaining of landslide inventory in term of providing clear, complete and accurate information to investigator for the process of interpretation. With such comprehensive information, landslide susceptibility assessment can be conducted precisely. Most likely the usage of ALS may be a way forward for investigating the landslide phenomena in Malaysia.

S. Omar (✉)
Faculty of Civil Engineering, Universiti Teknologi Mara, Shah Alam, Malaysia
e-mail: syed_omar@jmg.gov.my

Z. Mohamed
Institute for Infrastructure Engineering and Sustainable Management,
Universiti Teknologi Mara, Shah Alam, Malaysia
e-mail: zaina556@salam.uitm.edu.my

K.A. Razak
UTM Razak School of Engineering and Advanced Technology,
Universiti Teknologi Malaysia, Kuala Lumpur, Malaysia
e-mail: khamarrul.kl@utm.my

1   Introduction

Kundasang has been identified as one of the major geological hazardous area in Malaysia. This is due to the existence of numerous landslides occurrences at some locations in Kundasang. The occurrence of landslide has resulted substantial damaged to building structure, access road, telecommunication towers and agriculture orchards which directly caused in high economic losses to the government and residents in Kundasang (Fig. 1).

Fig. 1 a Building and **b** Pavement were badly damaged by landslide occurrence in Kundasang

According to [1, 2], Kundasang area is located in geohazard zone which consist of numerous geological structures including active faults and generally weak geomaterials with highly jointed rocks. These are among the major factors that are identified which greatly influenced the occurrence of landslide in Kundasang. Seismic activity usually referred to earthquake occurrence and appeared to be related to existence of major active faults. These major active faults namely, the Mensaban and the Lobou-Lobou faults were identified as the likely cause of the local earthquakes in the respective areas [3]. According to [4], in 1991 there was an earthquake of 5.1 Mb magnitude which occured at 18 km SE of Ranau and caused minor damage to the Principal's house of SMK Kundasang school and also aggravated soil movement. Recently, on 5th June 2015 there was an earthquake with magnitude 5.9 which occurred at the Kundasang and some other locations nearby. This is considered as the strongest earthquake ever recorded in Malaysia. Many landslides are detected due to the earthquake event (Fig. 2). Therefore, it is strongly believed that earthquake is considered as one of the important triggering factor identified for several landslides occurrence in Kundasang. Actually many other factors would contribute to landslide occurrences in Kundasang such as geological, ground water, slope gradient, vegetation and human activities.

Several researchers, namely [1, 5, 2], conducted studies to determine probable causes of landslides and massive creep movements in the Kundasang area using various methods such as localized drilling method, geodynamic features mapping and a large scale of structural geology mapping. In general using of sub-surface drilling technique was considered as acceptable approach. However, many bore-holes are required in order to obtain sufficient information which would increase the cost and time of the investigation. A limitation while using the technique is that, the information from each borehole will represent only single borehole information at the specific drilling location. Thus the sub-surface interpretation between boreholes to evaluate the sub-surface profile and ground conditions may involve some degree of uncertainty especially in a large, complex and sensitive geological area. Geodynamic features mapping and structural geology mapping also have some degree of limitation on surface information which can only be identified by a visible

field observation survey based on existing geodynamic features caused by ground instability. Thus, it clearly showed that all the above applications have some degree of limitation when involving landslides investigation in a large area in Kundasang.

Due to frequent occurrences and widespread distribution of landslides in Kundasang, it is a great challenge to detect and map its actual boundary zone in the field. It is important to gather detailed inventory and information such as distribution, types, lithology, geological structure and many more which is considered important in producing landslide susceptibility map of the area. Insufficient of landslide distribution and abundant information will hamper the effort to determine landslide susceptibility at the regional scale such as Kundasang. Hence, it is important to adopt the application of detailed landslides mapping through a new approach by using light detection and ranging (LiDAR) particularly airborne laser scanning (ALS) and aided by field mapping to assess landslide susceptibility of the Kundasang area. Since Kundasang is located within the active faults zone (refer Fig. 3), it is expected that numerous landslide incidents have occurred. These including seismically induced landslides, old landslides and landslides covered by vegetation which are not being detected and mapped by conventional method of landslides mapping during previous investigations due to the constraint of time, cost and availability of new advanced remote sensing technology. To date, there is no detailed landslides susceptibility assessment that has been conducted in the

Fig. 3 Kundasang (*square*) located at the intersection of two major active faults, the Mensaban and Crocker Fault Zones (*source* from [2])

Kundasang area. Therefore, it is important to conduct detailed landslides mapping in Kundasang using LiDAR in order to produce a complete inventory of landslides which subsequently will be used for analysis of the characteristics and identifying the mechanism of landslides within the active faults zone area. Eventually, landslide susceptible area will be identified which will be presented in the form of susceptibility map. Landslide susceptibility map is broadly useful for the development planning and management of regional area where it can provide useful information to reduce possible landslide risk in future. It is expected that a comprehensive information obtained from landslides mapping will be assisted certain party, especially local authority to structure a development plan in a sustainable way.

2 Factors Affecting Landslide Occurrences in Kundasang

According to [2], ground instability in Kundasang is caused by: (1) The existence of Oligocene submarine weak deposits in Trusmadi Formation (2) Location of Kundasang within Mensaban fault zone, (3) Uplifting of Kinabalu pluton which affected the surrounding stability and led to local normal faulting as adjustment. Basically, Kundasang area is underlain by Trusmadi Formation, Crocker Formation, igneous rock, Pinosuk Gravels, alluvium and sand. Based on previous study by [1, 5–7], there were numerous slope failures identified not only in Trusmadi Formation but also in Crocker Formation and Pinosuk Gravel deposit. Therefore, it clearly showed that there are some other factors that also contribute to ground instability rather than earth material of the Trusmadi Formation alone. It is undeniable that landslides occurred not only due to a single factor but usually due to combination of several factors. In general, landslide hazard factors (LHF) can be classified into two categories; internal and external causes [6]. Internal factors refer to reduction of shear strength on slope because of changes in some factors which influenced engineering properties of the geomaterial. Among factors are topographic, climate, geologic setting and processes, groundwater condition and engineering characteristics. External factors are refer to the increase of shear stress on slope, which are usually induced by human activities such as slope cutting, forest clearing, vehicles loading or vibration and artificial changes or natural phenomenon such as tremors. According to [1], ground instability and the extent of damage on several man-made structures in Kundasang are caused by the movement of two large scale landslide systems which form a part of the large Kundasang Landslide Complex. The large scale landslides refers to the movement of huge land masses in natural slopes that have moved in the past and still retain the original slope form without completely collapsing as in ordinary slope failures. In assessing the landslide susceptibility, it is important to deal with old landslides especially a large scale landslide.

Apart from Mensaban fault zone, based on gathered evidence from previous study by [3], a second major fault zone is identified crosses the Kundasang area and named as the Crocker fault zone (CFZ). Two major regional faults in Kundasang

were formed during complex tectonic history which involved multiphase deformations [8]. It is believed that the engineering properties of the rock and soil are reduced by tectonic complexity which subsequently affected the ground stability. For instance in Trusmadi Formation, the existing of highly fractured and sheared rock indicates the result from long history of tectonic activities [9]. Apart from two major active faults, there were several localized faults which associated with major faults and influenced the ground stability in certain location. The widespread mass movements of the Kundasang area can be partially attributed to active movements on the Crocker and Mensaban fault zones that intersect in Kundasang area [2]. The Mensaban and the Lobou-Lobou fault zones (part of Crocker fault zone) in Kundasang, Ranau, are considered active which could generate earthquakes in this area which have caused and continue to cause, damage to the infrastructure and certain buildings in the area [10]. Earthquake which is generated by active faults in Kundasang and Ranau area also triggered landslides occurrences in some locations. Therefore, it is important to consider seismic factor in assessing landslides susceptibility within active fault zone area where the identification of seismically induced landslides must be conducted.

As Kundasang is located in complex geological area, it is compulsory to assess comprehensively geological factors that influenced occurrences of landslides. Roslee et al. [9] found out six geological inputs as main parameters in transforming the Trusmadi Formation slopes prone to landslide occurrences; (1) local and regional geology, (2) hydrological and geohydrological, (3) mineralogical and micro structures, (4) local discontinuities structures, (5) physical and engineering properties of geomaterial and (6) geomorphological processes. All six geological inputs mentioned above could be significant in contributing of landslide occurrences in Trusmadi Formation but in order to assess more accurately in Kundasang area, it is suggested that some other parameters have to be considered because other geological formations such as Crocker Formation and Pinosuk Gravel deposit also existed in Kundasang and exhibited differently in term of geological and engineering characteristic and behaviour. Other part in Kundasang which underlain by Pinosuk Gravel deposit also experienced ground movement. According to [5], soil samples taken from Pinosuk Gravel deposit showed the tested soil strength from laboratory testing is generally greater than the gradient of the surrounding terrain. Theoretically, the subsoil shall have sufficient strength to withstand the gravity force of the sloping soil masses against slope instability. Since the ground instability also detected in Pinosuk Gravel deposit, this implied that there would be other important geological factor influenced the ground instability in Pinosuk Gravel deposit. Other geological factor identified in inducing landslides in the Crocker and Trusmadi Formations are lineament density [7]. Based on the study, both formations showed similar susceptibility to landsliding due to the presence of high lineament density although both formations have different types of lithology. From the previous study mentioned above, it clearly showed that lineament density play a major role in inducing landslides occurrence. Thus it is important to quantify or determine lineament density in landslide susceptibility mapping.

In order to accomplish landslides susceptibility assessment in Kundasang, several aspects have to be evaluated. Considering the geological complexity in Kundasang, great emphasize on geological input is needed during assessment. With detailed geological input and other factors, landslide susceptibility assessment will be more precise and meaningful. In other words, the final output of the susceptibility map will be fit to purpose and benefited to certain party especially local authority for structuring a development plan in a sustainable way.

3 Conventional Methods of Landslides Mapping

As a preliminary step toward landslides susceptibility assessment, it is compulsory to conduct landslide mapping and prepare landslide inventory maps. Landslides mapping can be conducted using variety of techniques and tools. Conventional methods that usually used for landslide mapping are (i) geomorphological field mapping [11], and (ii) visual interpretation of stereoscopic aerial photographs [12]. There are certain degrees of limitation when landslides mapping is conducted in the field. The most common limitation is difficulty to cover within short time when involved a large area such as Kundasang. Ordinary practice of field mapping is the geologist or geomorphologist will map the area that can be accessed either through roads or stream. For the remote area, usually the extension of geological boundary is based on assumption. Another limitation is difficulty in detecting old landslides in the field because most of old landslides and its features are often located under dense vegetation. In addition, old landslides and its features often disappeared due to the presence of other recent landslides, erosion processes and human activities such as agricultural activities. Informations regarding old landslides are vital in assessing the level of susceptible to landsliding in particular area. Another factor which hampered landslides mapping in the field is the size of landslides often too large for the investigator to identify some parts of the landslides. Insufficient of any important informations will lead to wrong interpretation in later stage. According to [13], there is a misconception which stated that landslides field mapping is more precise than landslide mapping using remote sensing technology (e.g. using aerial photographs, satellite images, very high resolution DEMs). This is particularly not true because landslides mapping in the field sometimes could not determine the exact boundary of a landslide and parts of landslides such as the scarp, lateral edges, deposit and toe due to hummocky topography and dense vegetation. Therefore it is a great challenge to map landslides in the field. The whole picture and landscape of the landslide can possibly be seen at the distant from a certain angle of view. Thus, the application of new method in landslides mapping is considered very important to overcome the previous challenge in landslides investigation.

Visual interpretation using stereoscopic aerial photographs still considered as the most common method to map the occurrence of landslides. Geographical evolution of landslides with time can be investigated with availability of various sets of aerial photograph for the same area [14]. The most important factor required in

interpretation of aerial photograph is a well-trained and experienced geomorphologist. The type, quality and characteristics of the particular stereoscopes used for visual interpretation of aerial photographs also influenced accuracy of landslide inventory [13]. The high quality result will be achieved with better stereoscopes. For instance, [15] used Abrams Model CB-1 pocket stereoscopes to carry out interpretation of more than 2000 aerial photographs to obtain an inventory for New Mexico, USA. When using stereoscopic aerial photographs, it will involve many series of images in order to complete an inventory. This process needs a longer time to produce landslides inventory map. It is not advisable to solely dependent on the visual interpretation of aerial photograph during landslides mapping. Hence, the field validation should be carried out or performed if there is any uncertainty encountered during interpretation.

Both conventional methods above which used for obtaining landslide inventory are acceptable, however, these methods require a lot of time and many human resources. Currently, method which could produce the quickest result with high quality and precise output seem to be preferable. Therefore with the availability of new remote sensing technologies such as LiDAR especially ALS for landslides mapping, it may assist the production of landslide inventory in term of providing clear, complete and accurate information to investigator for the process of interpretation.

4   Application of LiDAR in Landslide Mapping

The main purpose of using LiDAR in landslide investigation is to obtain accurate and precise high resolution digital elevation models (HRDEM) in raster grids or triangulated irregular networks (TINs), which are 2.5D representations of the topography, or in true 3D point clouds with a high density of information [16]. With the availability of the terrain 3D information and high spatial resolution data from LiDAR, it is expected that landslide mapping will produce more comprehensive and accurate result that can be used for landslide susceptibility assessment at the later stage. Recently ALS considered as one of the most effective tools for remote geospatial data acquisition [17]. ALS application in landslides mapping has improved the acquisition of terrain data by collecting comprehensive topographic data over a large area with great accuracy within short time. Advantage of ALS compared to other tools of landslides mapping is ability to enter the space between vegetation foliage and its independence of solar incidence which could generate a high resolution digital terrain model (DTM) in forested terrain [18]. Mapping and classifying landslides beneath equatorial mountainous forests can be conducted using the ALS-derived DTMs which could lead to a better knowledge about hazardous geomorphic problems in tropical countries [19]. Thus, with the above reasons ALS is highly recommended to be used for landslides mapping in Kundasang which dominated by forested terrain. It is expected that more landslides will be detected in Kundasang with ALS compared to the previous mapping methods (Fig. 4).
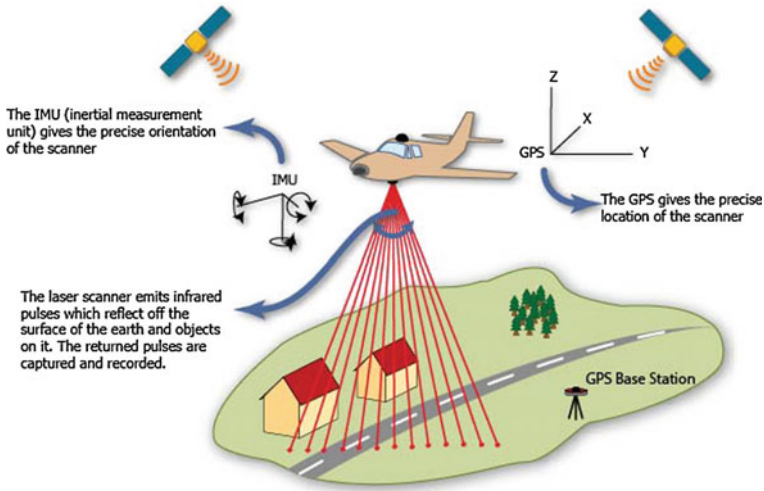
Fig. 4 Basic principle of airborne laser scanning operation (*source* from https://www.google.com)

In general, laser scanning was divided into two methods depending on the position of the sensor; airborne-based for airborne laser scanning (ALS) and ground-based for terrestrial laser scanning (TLS). ALS and TLS can be applied for various types of investigation such as (1) Landslide identification and characterization; (2) Hazard evaluation and susceptibility mapping; (3) Modelling; (4) Monitoring [16]. The application of ALS and TLS in the landslide inventory mapping can greatly assist in the process of producing landslide inventory maps which eventually used in assessing landslide susceptibility of the particular area. ALS could provide a space for improvement in the landslide inventory mapping especially for geological mapping by increasing the resolution of the landslide contours which allow the investigator to identify important features of landslides.

In recent years, LiDAR particularly ALS has become a popular technique for obtaining information about the terrain surface topography which required for construction of digital terrain models (DTM). According to study conducted by [20], using ALS data for landslides mapping in Roznow Lake Vicinity, Poland, DTM has clearly been proved as an important tool for landslides mapping and interpretation. From the study it is also concluded that the LiDAR DTM appears to be a significant support for geological interpretation and landslide detection especially on steep and forested slopes. Thus, based on reasons above, it is strongly recommended to use ALS in landslides mapping in the Kundasang area in order to improve previous data collection in landslides mapping. It is expected that numerous landslides can be detected within the Kundasang area which were not detected in the previous studies. The effectiveness and quality of landslides mapping using ALS depend on quality of LiDAR data. Therefore it is important to choose a suitable LiDAR sensor in order to obtain a very high quality image for landslides mapping purpose.

The advantage of using ALS data in landslides mapping is capability to retrieve terrain (i.e. bare Earth) point measurements despite under forest cover, allowing the generation of digital terrain models (DTMs) with a high degree of automation, which is not possible with old methods such as field mapping and photogrammetry [18]. It is undeniable that old landslides will be located under dense forest cover especially in tropical region. Therefore it is inevitable to test and evaluate the effectiveness of ALS data for detecting old landslides existence in the Kundasang area. Based on previous literature regarding airborne LiDAR, it is clearly shown that airborne LiDAR acted as beneficial source of data and information for expert to enhance the understanding of geomorphological processes, distribution and spatial extent which has not been possible before [21] (Figs. 5 and 6).

Morphologic features of a large landslide can be identified and observed through bare earth lidar maps without the camouflage presented by vegetation [22]. In this sense, lidar could provide clear informations related to landslides occurrence in the thick forest compared to aerial photographs which are not possible to produce image under dense vegetation. Landslide detection and classification in forested terrain can be improved significantly using ALS-derived DTM as compared to optical images [23]. Since most of the Kundasang area is covered by vegetation, it is essential to use ALS data to detect and recognize landslides type which present under tree coverage. It is believed that some of landslides in forested terrain in the Kundasang are not detected from the previous landslides mapping. Landslides inventory in forested terrain is compulsory for landslide susceptibility assessment.

Basically the application of ALS in landslide mapping does not replace the whole conventional field mapping but it changes the culture of fieldwork where time spent in the field will be reduced significantly. Field mapping still considered necessary and important as validation process of the landslide inventory which is produced by ALS data (Table 1).
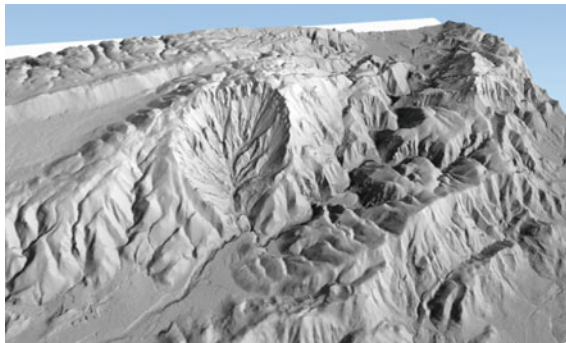
Fig. 5 Example of 3D digital terrain model (DTM) which constructed from LiDAR data (*source* from https://www.google.com)
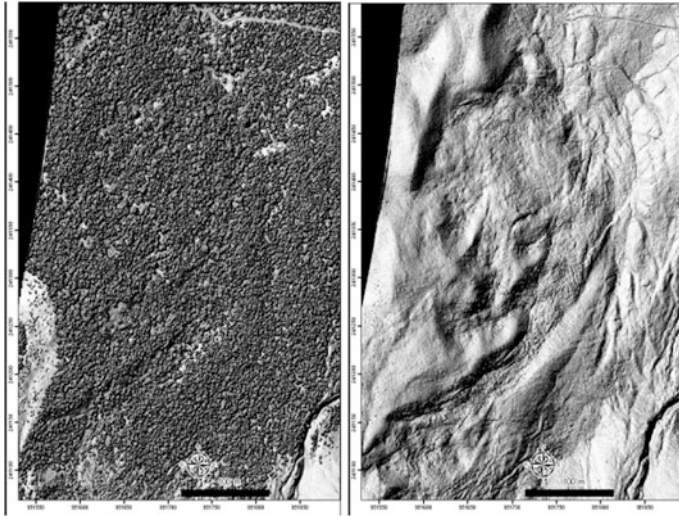
Fig. 6 Digital terrain model can be generated despite under forest cover using LiDAR data (*source* from UTM Razak School of Engineering and Advanced Technology, UTM Kuala Lumpur)

Table 1 Summary of comparison between conventional method and LiDAR application for landslides mapping

	Conventional method	LiDAR application
Method usually used for landslides mapping	Geomorphological field mapping and visual interpretation of stereoscopic aerial photographs	Airborne laser scanning (ALS) and terrestrial laser scanning (TLS)
Mapping a large area	Difficult to map a large area within a short time	A large area can be mapped with great accuracy within a short time
Creating images under tree coverage	Less effective creating images under dense vegetation	Images can be created under forest cover
Detecting old landslides	Difficult to detect old landslides in forested enviroment	LiDAR DTMs could provide significant support for old landslides detection in forested environment
Identifying some landslides features	Difficult to identify some parts of landslides if the size of landslides are too large, hummocky topography and dense vegetation	Important features of landslides can be identified by increasing the resolution of ALS application
Temporal and geographical evolution of landslides	Can be investigated with availability of multiple sets of aerial photographs of the same area	Can be investigated precisely with availability of LiDAR data within a certain period
Interpretation	Require well-trained and experienced geomorphologist	Require well-trained and experienced geomorphologist
High quality results	Influenced by type, quality and characteristics of the stereoscopes	Influenced by type of LiDAR sensor

5 Conclusion

The number of literature reviews discussing the application of LiDAR in landslides investigation indicated a promising research gap for the introduction of LiDAR as a new tool in landslides mapping for landslide susceptibility assessment in the Kundasang area. Availability of this new technology for the identification and mapping of landslides may strongly facilitate the production of landslide inventory maps in terms of providing clear, complete and accurate informations to investigator for the process of interpretation. With such comprehensive informations, landslide susceptibility assessment can be conducted precisely. Landslide susceptibility map is useful for the development planning and management of regional area. Most likely the usage of LiDAR may be a way forward for investigating the landslide phenomena in Malaysia.

References

1. Komoo I, Lim C.S, (2003). Kundasang Landslide Complex: Detailed Mapping at Sekolah Menengah Kebangsaan Kundasang. Geological Society of Malaysia, Bulletin 46 May 2003; pp.387–392
2. Tjia H.D. 2007. Kundasang (Sabah) at the intersection of regional fault zones of Quarternary age. Geological Society of Malaysia, Bulletin 53, June 2007, pp. 59–66
3. Yan A.S.W, Suratman S, Liau A, Hamzah M, Ramli M.Y, Ariffin H, Abd Manap M, Mat Taib M.B, Ali A, Tjia H.D, 2006. Report on Geological and Seismotectonic Of Malaysia. ISBN: 978-983-43449-0-0
4. Yan A.S.W, Liau A, Hamzah M, Ramli M.Y, Mat Taib M.B, Ali A, Ariffin H, Ismail B, 2008. Report on the monitoring Of active faults in the Kundasang-Ranau area, Sabah. ISBN: 983-43449-3-1
5. Liew S.S, Gue S.S, (2001). Massive Creep Movement of Post-Glacial Deposits in Kundasang Areas. GSM-IEM Forum: Engineering Geology & Geotecnics of Slopes, 23rd October 2001 Kuala Lumpur, Malaysia
6. Roslee. 2004. *Study of Mass Movement along Bundu Tuhan to Kundasang Highway, Sabah, Malaysia.* MSc Thesis. Unpublished. Universiti Malaysia Sabah.
7. Simon N, Roslee R, Lian Marto N, Mat Akhir J, Rafek A.G, Lai G.T, 2014. Lineaments and their association with landslide occurrences along the Ranau-Tambunan Road, Sabah. EJGE vol.19 (2014), Bund. C
8. Roslee R, Tahir S, S.Omang S.A.K, Laming A, (2011). Survey of slope failures (SFS) along the Bundu Tuhan Kundasang Highway, Sabah, Malaysia. Borneo Science 29 September 2011
9. Roslee R, Tahir S, Musta B, S.Omang S.A.K, (2011). Geological inputs for landslide hazard identification (LHI) in the Trusmadi Formation Slopes, Sabah, Malaysia. Borneo Science 29 September 2011
10. MOSTI (2009). Seismic and Tsunami Hazards and Risks Study in Malaysia
11. Brunsden, D, (1985). Landslide types, mechanisms, recognition, identification. In: Morgan, C. S. (Ed), Landslides
12. Brunsden, D, (1993). Mass movements; the research frontier and beyond: a geomorphological approach. Geomorphology 7, 85–128.
13. Guzzetti F, Mondini A, Cardinali M, Fiorucci F, Santangelo M, Chang KT, (2012). Landslide inventory maps: New tools for an old problem. Earth-Science Review 112 (2012) 42–66

14. Guzzetti F, (2005). Landslide Hazard & Risk Assessment (Dissertation) 33–64
15. Cardinali, M., Guzzetti, F., Brabb, E.E., 1990. Preliminary map showing landslide deposits and related features in New Mexico. U.S. Geological Survey Open File Report 90/293, 4 sheets, scale 1:500,000
16. Jaboyedoff M, Oppikofer T, Abellan A, Derron M, Loye A, Metzger R, Pedrazinni A, (2010). Use of LIDAR in landslide investigation: a review. Nat Hazards DOI 10.1007/s11069-010-9634-2
17. Petrie, G., Toth, C.K., 2008. Introduction to laser ranging, profiling, and scanning. In: Shan, J., Toth, C.K. (Eds.), Topographic Laser Ranging and Scanning: Principles and Processing. CRC/Taylor & Francis, Boca Raton, pp. 1–27.
18. Kraus, K. & Pfeifer, N. (1998): Determination of terrain models in wooded areas with airborne laser scanner data.—ISPRS J. Photogramm. and Rem. Sens. **53** (4): 193–203.
19. Razak K.A, Santangelo M, Van Westen C.J, Straatsma M.W, de Jong S.M, (2013). Generating an optimal DTM from airborne laser scanning data for landslide mapping in a tropical forest environment. Geomorphology 190 (2013) 112–125
20. Borkowski, A, Perski, Z, Wojciechowski, T, Jozkow, G, Wojcik, A (2011). Landslides Mapping In Roznow Lake Vicinity, Poland Using Airborne Laser Scanning Data. Acta Geodyn. Geomater., Vol. 8, No. 3 (163), 325–333, 2011
21. Hoflfle, B & Rutzinger, M. (2011): Topographic airborne LiDAR in geomorphology: A technological perspective-Zeitschrift für Geomorphologie Vol. 55, Suppl. 2, 1–29
22. Roering, J et al (2013): 'You are HERE': Connecting the dots with airborne lidar for geomorphic fieldwork- Geomorphology 200 (2013) 172–183
23. Razak K.A, Straatsma M.W, van Westen C.J, Malet J.P, de Jonget S.M, (2010). Airborne laser scanning of forested landslides characterization: Terrain model quality and visualization-Geomorphology 126 (2011) 186–200

Polyurethane Foams in Soil Stabilization: A Compressibility Effect

N. Sidek, K. Mohamed, I.B. Mohd Jais and I.A. Abu Bakar

Abstract The use of polyurethane foam is so-called as a low cost technique in soil stabilization. The workable characteristic of polyurethane foam suits the construction needs which increase the strength performance while reducing the compression index. The research permits a reliable prediction of compressibility effects of stabilized soils in which the polyurethane foam contents are the variables. The unstabilized soils are taken from the current residential projects and the physical properties are investigated. The research is performed by an experimental work in accordance with BS 5930. The compressibility effects of stabilized (with the addition of polyurethane foams) and unstabilized soils are presented by the percentage of compression and swelling indices. These indices reduce between 40–50 % and the void ratio is also reduced between 30–50 % with the addition of polyurethane foams. The research also presents the physical and engineering properties of the stabilized and unstabilized soils.

Keywords Polyurethane foams · Compressibility effects · Compression index · Swelling indices · Soil stabilization

1 Introduction

Many countries are confronted with unstable soil conditions, especially Malaysia, which causes an increment in construction costs for the treatment of unstable soil. It is essential to encounter the unstable soil in construction for safety and economical purposes. A proper analysis needs to be carried out to ensure the safe structure is free from settlement or collapse due to the compressibility of soil [1, 2].

N. Sidek (✉) · K. Mohamed · I.B. Mohd Jais · I.A. Abu Bakar
Faculty of Civil Engineering, Universiti Teknologi MARA, Shah Alam, Selangor, Malaysia
e-mail: norbayasidek@gmail.com

The recent ground improvement techniques used have significantly shortened the time consumption for new land opening and secured the economic viability of many projects [3, 4]. The alternative methods of soil stabilization such as surface reinforcement, preloading, chemical stabilization, sand or stone column, prefabricated vertical drains, and pile constructions are well discussed by Noto [5] and Kazemian [6]

There are two primary methods used in soil improvement wherein mechanical and chemical approaches [7]. The mechanical approach involves the compaction of soil and the addition of lime and other chemical additives are referred to the chemical approach. These chemical additives improve the load bearing capacity of the existing soil.[8]

Polyurethane foams are available in the forms of flexible or rigid foams, solid elastomers (or rubbers), coatings, adhesives and sealants [9]. The versatility of polyurethane foams depends on their chemical contents. For instance, urethanes commonly behave as thermosets and thermoplastic at certain grades of urethanes [10, 11].

Urethanes are prepared by mixing the polyols and isocyanates liquids in certain ratio. In the form of elastomers, polyurethanes offer abrasion resistance and toughness. The commonly used of isocyanates for manufacturing polyurethane foams are toluene diisocyanate, methylene diphenyl isocyanate, and polymeric isocyanates. These isocyanates are extracted by phosgenation of polyamines through the condensation of aniline with formaldehyde. Polyols (with hydroxyl groups) are macroglycols, which are either polyester or polyether-based. Polyurethane elastomers and resins take the form of liquid castings systems, thermoplastic elastomers and resins, microcellular products, and millable gums [12–14].

2 Material and Methodology

This research is conducted to determine the compressibility effects using polyurethane foams for soil stabilization. A specific specification has been carried out to test the suitability of the selected soil types and polyurethane foams. The physical properties test has been conducted as codified in BS 5930: Method of soil investigation (1999).

The evaluated physical properties are moisture content, particle density, plastic limit, liquid limit, dry density, particle size distribution and shear strength of the selected soil. JKR Probe test is conducted on site for soil investigation [15–17].

Chemical solution used in the study is polyurethane with 1:1 ratio [18]. Polyurethane is produced by the reaction of a polyol (R–OH) and isocyanate (R1–NCO) in the presence of catalyst and additives.

Moisture content test conducted by placing the container with wet sample in the oven and then soil been dry for overnight (12 h) at the temperature 110 °C to ensure all water in soil sample are removing until the weights remain constants [19].

Particle size is an easy parameter to measure and controls many aspect of the engineering behavior of a soil. Sand and gravel are cohesionless particles that pose no interparticle bond. Clay and silts are usually cohesive [20].

Atterberg limit described an amount of water content at certain limit or critical stages in soil behavior. The test been conducted to determine Atterberg limit by using cone penetration test. This method is more preferable compared to casagrande method because the apparatus is easier to maintain in correct adjustment and the test is less dependent on the operator [21].

3   Result and Discussion

3.1   Introduction

In this section, we quantify the physical and engineering properties of stabilized soils (with the addition of polyurethane foams) and unstabilized soils that play an important role in influencing the compressibility effects.

3.2   Physical Properties

3.2.1   Moisture Content

The moisture content of unstabilized soil is 14.88 %. It is evident that the unstabilized soil consists a lot of sand due to a low moisture content obtained.

3.2.2   Particle Size Distribution

Based on the wet sieving and hydrometer analysis, the unstabilized soil consists 9.25 % of gravel, 49.45 % of sand and 41.29 % of fines grained (27.13 % silt and 14.16 % clay). It is concluded that the soil type is very clayey sand of low plasticity (CL). Particle size distribution of unstabilized soils is presented in Fig. 1.

3.2.3   Specific Gravity Investigation

Small pycnometer method is used to determine the particle density of the unstabilized soil as indicated in Table 1. The average value of specific gravity is 2.76 Mg/m^3. It can be classified that the soil sample is silty clay which ranges between 2.70–2.80 $Mg/m^{3.}$
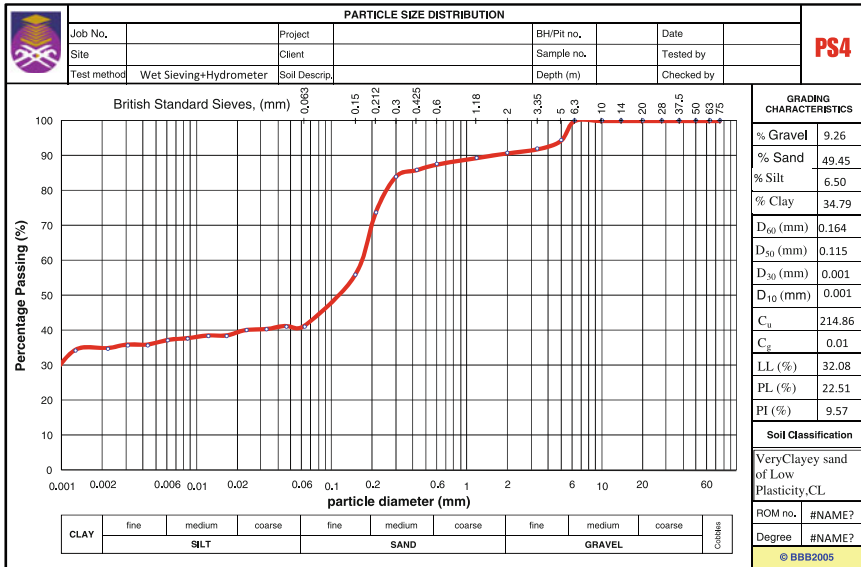
Fig. 1 Particle size distribution chart

Table 1 Specific gravity

Preparation method	Test method	Small pyknometer		
Density bottle no.	No.	1	2	3
Mass of density bottle + stopper (gm)	M_1	31.2	32.01	31.19
Mass of density bottle + stopper + dry soil (gm)	M_2	46.43	46.32	46.81
Mass of density bottle + stopper + soil + water (gm)	M_3	90.88	91.02	90.05
Mass of density bottle + stopper + full of water (gm)	M_4	81.56	80.98	81.05
Mass of dry soil used (gm)	M_2–M_1	15.23	14.31	15.62
Mass of water used (gm)	M_3–M_2	44.45	44.70	43.24
Mass of water to fill density bottle (gm)	M_4–M_1	50.36	48.97	49.86
Temperature (°C)	T_x			
Particle density of soil (Mg/m^3)	r_s	2.58	3.35	2.36
Average particle density (Mg/m^3)	r_s	**2.76**		

3.2.4 Atterberg Limit

According to Fig. 2, the liquid limit (LL) of the soil at 20 mm penetration is less than 32 % and it is evident that the unstabilized soil is a clay of low plasticity (CL), see Table 2. The plastic limit (PL) of the unstabilized soil is approximated 23 % whilst the plasticity index is 9.57 % (Fig. 3).
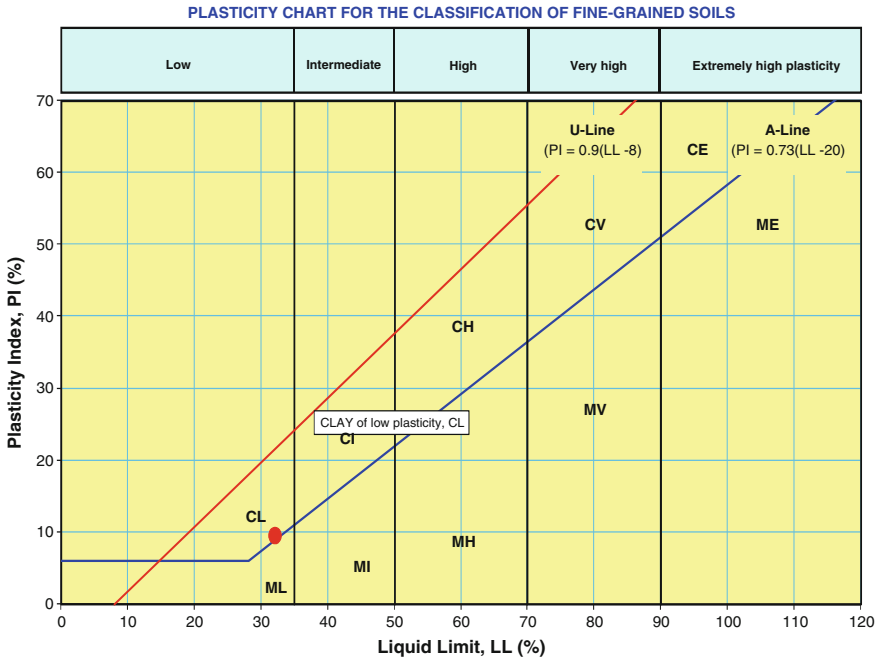
Fig. 2 Plasticity chart for the classification of fine-grained soils

Table 2 Five degrees of plasticity based on percentage of liquid limit

Liquid limit (%)	Plasticity
Less 35	Low plasticity
35–50	Intermediate plasticity
50–70	High plasticity
70–90	Very high plasticity
More 90	Extremely high plasticity

Fig. 3 Graph of compaction curve (dry density vs. moisture content)
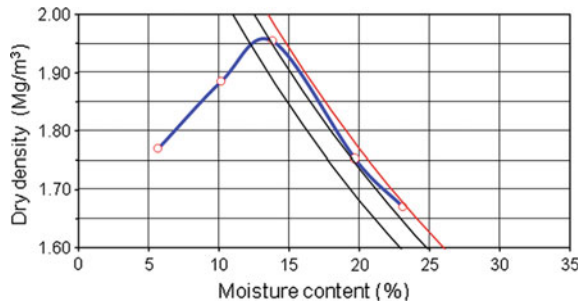
3.2.5 Compaction Test

Compaction is the process of densification of soil mass by reducing air voids. The purpose of laboratory compaction test is to determine the proper amount of water at which the weight of the soil grains in a unit volume of the compacted a maximum, the amount of water is thus called the optimum moisture content (OMC). In the laboratory different values of moisture contents and the resulting dry densities, obtained after compaction are plotted both to arithmetic scale, the former as abscissa and the latter as ordinate. The points thus obtained are joined together as a curve. The maximum dry density and the corresponding OMC are measured from the curve [22, 23].

3.3 Engineering Properties

The compressibility effect of a soil relates with the amount and rate of settlements which are usually determined by a consolidation test using an oedometer [24]. The specimen that needs to be tested is soil specimen, cut from an undisturbed sample, polyurethanes with the ratio 1:1 (polyol: isocyanate) and a soil that has been stabilized with polyurethanes. There are two stages of loading series applied in this test which are compression (loading) and recompression (unloading). The sets of loading to be used were 10, 20, 40, 80, 160, 320, and 640 kPa was applied and unloading series of 80 and 10 kPa.

3.3.1 Void Ratio

A standard consolidation test was conducted to get the compressibility characteristic of the soil. The data obtain from this test was used for comparison between soil sample and soil after injected with Polyurethanes. The results of void ratio are summarized in Table 3.

3.3.2 Coefficient of Volume Compressibility, m_v

The amount of volume compressibility (m_v) represents the amount of change in unit volume due a unit increase in effective stress. m_v is not constant with stress (or depth) and it should always be calculated at the stress (depth) range of interest.

Table 4 shows the coefficient of volume compressibility (m_v). The coefficient of volume compressibility (m_v) decreases with the increase of pressure for both stabilized and unstabilized soils. The unstabilized soil shows higher m_v results as compared to the stabilized soil. Table 4 represents that the m_v values reduce with the addition of PU at 40 %. The stabilized soil underwent an overstressed state at the pressure of 640 kPa and dropped to 320 kPa after the recompression state.

Table 3 The results of void ratio for unstabilized soil and stabilized soil with polyurethane foams (PU)

Load (kPa)	Sample								
	Soil			PU			Soil + PU		
	S1	S2	S3	PU1	PU2	PU3	S + PU1	S + PU2	S + PU3
10	3.465	2.140	1.870	1.650	1.655	0.7525	0.995	1.0S0	0.185
20	0.730	0.981	1.238	0.635	0.651	0.762	0.626	0.637	0.461
40	0.976	0.929	0.557	0.954	0.993	0.481	0.526	0.511	0.224
80	0.499	0.352	0.399	0.282	0.326	0.319	0.343	0.262	0.265
160	0.209	0.209	0.202	0.171	0.253	0.355	0.133	0.186	0.187
320	0.247	0.127	0.164	0.128	0.188	0.188	0.147	0.114	0.112
80	0.018	0.017	0.015	−0.036	−0.006	−0.004	0.026	0.025	0.011
10	0.335	0.336	0.332	0.231	0.366	0.341	–	–	–
320	0.125	0.147	0.141	0.103	0.144	0.140	0.042	0.034	0.028
640	0.117	0.108	0.126	–	–	–	0.136	0.123	0.121

Table 4 Coefficient of volume compressibility (m_v)

Pressure (kPa)	Soil sample					
	Soil 1	Soil 2	Soil 3	S + PU1	S + PU2	S + PU3
10	0.6437	0.5849	0.637	0.4748	0.4482	0.4362
20	0.6317	0.5693	0.6167	0.4656	0.439	0.4295
40	0.5999	0.5402	0.5987	0.4501	0.4243	0.4321
80	0.568	0.5185	0.5732	0.4303	0.4094	0.408
160	0.5418	0.4931	0.5478	0.4151	0.3885	0.387
320	0.4807	0.4628	0.5071	0.3818	0.363	0.3621
80	0.4871	0.4686	0.5126	0.3903	0.374	0.3659
10	0.5219	0.5032	0.5478	–	–	–
320	0.4628	0.4345	0.48	0.3763	0.3599	0.3567
640	0.3508	0.3319	0.3575	0.3136	0.3064	0.3042

The results shown in Fig. 4 indicate that the initial void ratio has reduced by approximately 40 % than the natural soil and the modified soil has reduced the swelling index to almost rigid and elastic. The comparison between natural soil and soil that has been modified are clearly proven in compaction curve, where the compression characteristics can be determined based on the consolidation curve shown in Fig. 4.

There is a minimal volume change and settlement in the stabilized soils compared to the unstabilized soils. This depicts that the addition of PU foams significantly improves the soil structures and is suitable for rehabilitation work. With the addition of PU foams, we could reduce the operational and maintenance costs. In addition, PU foams are lightweight materials and efficiently react after 2–3 h of injection to the respective areas.

Fig. 4 The consolidation curves of stabilized soils and unstabilized soils
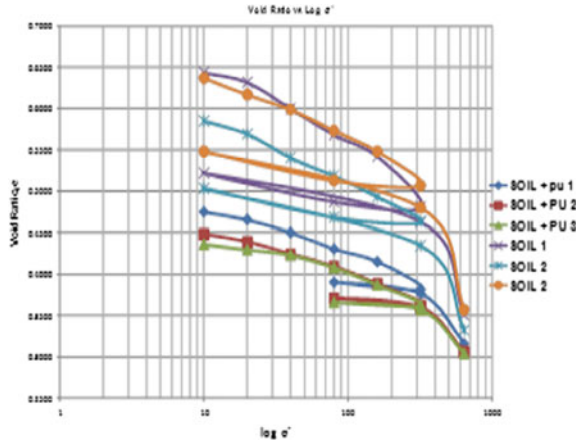
4 Conclusion

This research has presented an experimental work to evaluate the significance of PU foams' addition in soil stabilization through the compressibility effects. The moisture content, particle size distribution, specific gravity, and Atterberg limit are conducted to evaluate the physical properties of unstabilized and stabilized soils. The engineering properties are tested via void ratio and coefficient of volume compressibility evaluations. The physical and engineering properties are conducted to give a better understanding on the compressibility effect with and without the addition of PU foams. It has been proved that this approach has provided cost effective and reliable results. Overall, an understanding of the designation mechanisms of PU foams is beneficial for soil stabilization, which comprehends investigation of the relationships between the compressibility effects of stabilized and unstabilized soils.

References

1. Craig, R. F. (1992). **Soil Mechanics. 6th Edition**. Spon Press. London.
2. Das. B. M, (2003)," **Principle of Geotechnical Engineering**, London, 7th Edition.
3. G. Archibald, J.F., (2003), **Effectiveness of Conventional Support Systems and Polymer Spray-on Liners for Reducing Hazards Associated with Rockbursting**. Presented at the Mining Health and Safety Conference 2003, Sudbury, Ontario, April, 2003.
4. Atkinson et al. (1986), "**The mechanics of Soil, An Introduction to Critical State soil Mechanics**", Mc Graw- Hill Book Company Limited, p 239.

5. Noto, S. (1991). **Peat Engineering Handbook**. Civil engineering Research Institute Hokkaido development Agency, Prime Minister's Office, Japan.

6. Kazemian. S, and Huat, B.B.K, 2009, **A Review of Stabilization of Soft Soil by Injection of Chemical Grouting**. Australian J, Basic Application, Sci, 4(12):p5862–5868.

7. Terzaghi, K & Peck. R.B, (1969). **Soil Mechanics in Engineering** Practice. New York, 2nd Edition. John Wiley and Son, New York, 1967, 729 p.

8. Karol R. H. (1990), **Chemical Grouting**, Marcel Dekker, Inc., New York, 2nd edition, 465 pp.

9. Vinson, T. S., and Mitchell, J. K. (1970), "**Foamed Plastic Chemical Systems for Lunar Soil Stabilization Applications**," Lunar Surface Engineering Properties Experiment Definition, Final Report presented to NASA George C. Marshall Space Flight Center, V o l. I of IV, Jan. 1970.

10. Y. Yorozu, M. Hirano, K. Oka, and Y. Tagawa, "Electron spectroscopy studies on magneto-optical media and plastic substrate interface," IEEE Transl. J. Magn. Japan, vol. 2, pp. 740–741, August 1987 [Digests 9th Annual Conf. Magnetics Japan, p. 301, 1982].

11. M. Young, The Technical Writer's Handbook. Mill Valley, CA: University Science, 1989.

12. Eason, B. Noble, and I.N. Sneddon, "On certain integrals of Lipschitz-Hankel type involving products of Bessel functions," Phil. Trans. Roy. Soc. London, vol. A247, pp. 529–551, April 1955. (*references*)

13. J. Clerk Maxwell, A Treatise on Electricity and Magnetism, 3rd ed., vol. 2. Oxford: Clarendon, 1892, pp.68–73.

14. I.S. Jacobs and C.P. Bean, "Fine particles, thin films and exchange anisotropy," in Magnetism, vol. III, G.T. Rado and H. Suhl, Eds. New York: Academic, 1963, pp. 271–350.

15. Edil, T.B. (2003). **"Recent advances in geotechnical characterization and construction over peat and organic soils"** Proceedings 2nd International Conference on Advances in Soft Soil Engineering and Technology. (Eds). Malaysia: Putrajaya, pp: 3–25.

16. Gopalakrishnana, S and Sujathaa. R. (2011). "**Research Journal of Pharmaceutical, Biological and Chemical Sciences**" "Ageing studies of cardanol based polyurethanes. Volume 2 Issue 3 Page No. 1069

17. Huang, G.H., Zhang, R.D, 2005**." Evaluation of soil water retention curve with the pore–solid fractal model"**. Geoderma 127, 52–61.

18. Sidek et al., "Environmental And Sustainable Technology Using Polyurethane Foam," 2014. A. Conference and C. Engineering, "Annual Conference on Civil Engineering and Engineering (March 14–16 Phuket, Thailand) A1403-436," pp. 1–9

19. Whitlow, (2001), "**Basic Soil Mechanics**", Fourth Edition by Pearson Education South Asia Pte. Ltd.

20. Mitchell, J.K, **Fundamentals of Soil Behaviour**, Second Edition, John Wiley & Sons Inc., New York, 1993, ch. 3.

21. Kazemian, S. and Huat, B.B.K, 2010 "**Assessment of Stabilization Methods for Soft Soils by Admixtures**," 2010 International Conference on Scientific & Social Science Research (CSSR 2010), Malaysia.

22. Brady, N., Weil, R.R., (2002)**. The Nature and Properties of Soils**, 13th edition, Prentice-Hall, Upper Saddle River, NJ, 960 pp.

23. Ball, B.C. (2000)**. Soil Compatibility In Relation To Physical and Organic Properties** at 156 sites in UK. Soil Tillage Res. 57, 83–91.

24. Bowles, J. E. (1979). **Physical and geotechnical Properties of Soils**. Mc Graw Hill. United States of America.

25. Skempton, A. W. (1954) "**Notes on the Compressibility of Clay**", Quarterly Journal of the Geological Society of London, Vol.100, No 2.

Engineering Characterisation of Kuala Lumpur Granite and Limestone

Haryati Awang and Norhanisah Abdul Karim

Abstract Rock properties are key elements that should be taken into account in designing substructures especially for underground structures such as tunnel and pile. For this reason, rock should be tested directly in the laboratory to measure the properties of the material particularly the physical and mechanical properties. This study is about investigating the quality of granite and limestone from Kuala Lumpur area for engineering purposes. As Kuala Lumpur is having a rapid development in urbanisation, construction in and on rock mass is an important element that cannot be avoided. Being part of tropical region, the quality of rock should be measured thoroughly because of deterioration and decaying of the material due to weathering. Referring to the problems encountered with rocks in tropical country, this study was carried out to characterise the engineering properties of granite and limestone found in the Kuala Lumpur area. Samples of granite and limestone were taken from a number of places where the borehole drilling for site investigation works is on progress. A finding of this study hopefully is useful in providing information of engineering properties of granite and limestone from Kuala Lumpur for technical communities.

Keywords Engineering properties · Granite · Limestone · Characterisation · Kuala Lumpur

1 Introduction

Rapid developments in capital of Malaysia, Kuala Lumpur, are encroaching the whole area of the city. Many of the engineering structures are built upon rock mass such as high rise buildings, railways and highways for transportation systems and tunnelling for raw water supply. Since, many substructures are constructed on rock

H. Awang (✉) · N.A. Karim
Faculty of Civil Engineering, Universiti Teknologi MARA,
40450 Shah Alam, Selangor, Malaysia
e-mail: harya406@salam.uitm.edu.my; haryatiawang@yahoo.co.uk

masses; it is very essential to have a proper knowledge for technical communities who involve in the projects on the engineering properties of the material found in the structures in Kuala Lumpur.

Geologically, there are two main types of rocks that are mostly found in Kuala Lumpur which are granite and limestone. In Kuala Lumpur, about one third of the area is on limestone formation. The geologic setting of Kuala Lumpur and Ipoh (city in the state of Perak) is strikingly similar where the granite intruded the sedimentary formation of limestone [1]. The limestone is dominantly found at the centre of Kuala Lumpur city meanwhile, granite mostly bounded at the eastern area of Kuala Lumpur towards the Main Range of Peninsular Malaysia. The design and construction in limestone area have various problems to geotechnical engineers due to karstic features of limestone such as steeply inclined bedrock, cavities, slump zones and sink holes. The construction problem is mostly due to piling works.

Granite is the rock that is considered as having a massive structure, and is often assumed as stable and suitable for any construction projects. In Malaysia, incident of rock slides may have happened several times in the past but they were not too obvious as the Bukit Lanjan rock slide which blocked the nearby highway and caused the closure for 6 months [2]. The problem faced by granitic rock is when it is exposed to weathering that causes rock material to decay and deteriorate. Slopes and terrains are the most risky area for granite formation. Examples of such failure include the highland Tower tragedy in 1993, rockslide at Bukit Lanjan in 2003 and landslide at Bukit Antarabangsa in 2008. All these cases involve construction on granite on hill slopes.

This research was carried out to provide information on engineering properties and characteristics of Kuala Lumpur granite and limestone. This research study was conducted based on the ongoing highway project connecting Sungai Besi to Ulu Kelang in Kuala Lumpur city. The main objective of this research work is to determine the physical and geological properties of limestone and granite through a series of testing conducted on the rock samples. The findings from this laboratory testing will be used to determine the physical and mechanical properties of limestone and granite; and to characterise the geology of limestone and granite by petrography study. The engineering characterisation of rocks from Kuala Lumpur significantly provides information to the geotechnical practitioners, rock mechanics society and engineering geology communities on this natural material from a place in tropical region.

2 Materials and Methods

The rock samples for this study were provided by a site investigation contractor who is responsible to report the result of engineering properties from Kuala Lumpur area to the consultant of the project (Fig. 1). All laboratory tests were conducted in Universiti Teknologi MARA Rock Mechanics Laboratory. A total of 64 numbers of
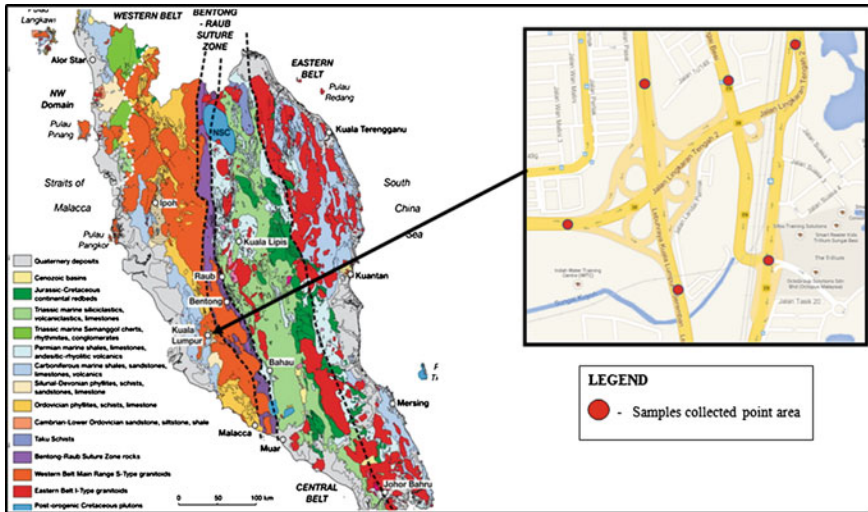
Fig. 1 Samples from borehole locations

rock samples from 32 boreholes were collected during site investigation works using borehole drilling method. The tests were referred to the Standard of Rock Characterisation Testing from International Society of Rock Mechanics manual (ISRM) [3]. In this research, there were five laboratory tests that were conducted to measure the engineering parameters of granite and limestone rock materials. The tests were divided into two groups which are the determination of physical and mechanical properties of rock. Physical properties identification was done by petrography description while determination on mechanical properties was conducted by several tests including uniaxial compression strength (UCS), point load test (PLT), Brazilian test and slake durability test.

3 Result and Analysis

Upon completing the laboratory tests, results were recorded and classified based on the types of tests.

3.1 Uniaxial Compressive Strength (UCS)

The uniaxial compression test is the main test in the laboratory for the rock samples. This is a destructive test that was performed on cylindrical rock specimen by compressing or loading them to get the maximum load to fail. Upon failure, the

rock specimen usually fractures by axial, brittle splitting or fails in shear, depending on the specimens affected by the platens of testing machine and the surface quality of the particle, Tables 1 and 2 indicate the results for granite and limestone of UCS.

Table 1 Result of UCS for granite

Sample	Diameter (mm)	Height (mm)	Weight (g)	Area (m²)	Max load (kN)	UCS (Mpa)
P513	51.88	103.76	560.4	0.00211	140.993	66.69
P514	51.89	103.78	562.9	0.00212	113.313	53.58
P515	51.59	103.18	557.0	0.00209	106.15	50.77
P516	51.75	103.50	566.9	0.00210	134.847	64.10
P517	51.25	102.50	565.2	0.00206	120.952	58.62
P518	51.47	102.94	552.1	0.00208	136.986	65.83
P519	51.83	103.66	555.8	0.00211	89.9760	42.64
P521	51.6	103.20	571.7	0.00209	137.638	65.23
P522	51.11	102.22	557.9	0.00205	131.775	61.78
P523	51.80	103.60	563.7	0.00211	40.2110	19.55
P524	51.68	103.36	547.4	0.00210	33.4790	15.96
P525	51.75	103.50	552.0	0.00210	193.670	92.07
P526	52.08	104.16	566.0	0.00213	93.5590	43.91
P527	51.89	103.78	566.5	0.00212	82.0630	38.80
P528	51.70	103.40	552.3	0.00210	160.628	76.51
STN13/1	52.01	104.02	534.4	0.00212	220.664	103.85
STN13/2	51.89	103.78	566.5	0.00212	89.3580	42.33
P483	52.24	104.48	588.3	0.00214	135.782	63.34
P484	52.19	104.38	605.1	0.00214	70.4180	32.91
P485	51.75	103.50	551.2	0.00210	111.760	53.13
P486	52.20	104.40	565.8	0.00214	67.1150	31.38
P487	52.31	104.62	602.8	0.00215	41.3740	19.25
P482	52.29	104.58	588.7	0.00215	97.4030	45.35
P481	51.93	103.86	564.9	0.00212	73.1790	34.55
P479	52.07	104.14	586.1	0.00213	104.142	48.90
P480	51.97	103.94	584.0	0.00212	115.703	54.54
P478	52.05	104.10	592.9	0.00213	80.6290	37.89
P477	51.63	103.26	563.3	0.00209	77.206	36.87
P476	47.41	94.82	436.7	0.00177	65.905	37.33
P475	51.66	103.32	545.6	0.00210	55.985	26.71
P473	51.77	103.54	596.5	0.00211	72.791	34.58
P465	51.49	102.98	579.7	0.00208	80.42	38.62
P490	52.07	104.14	533.7	0.00213	19.044	38.11
P502	51.88	103.76	568.5	0.00211	15.268	24.55

Table 2 The result of UCS for limestone

Sample	Diameter (mm)	Height (mm)	Weight (g)	Area (m^2)	Max load (kN)	UCS (Mpa)
P421	51.88	103.76	578.0	0.00211420	63.151	29.87
P425	53.30	106.60	630.4	0.00223152	26.540	11.89
P426	53.40	106.80	601.2	0.00223990	13.370	5.97
P427	53.50	107.00	627.4	0.00224830	21.151	9.41
P428	51.73	103.46	558.4	0.00210199	120.496	57.32
P429	52.04	104.08	615.5	0.00212726	195.246	91.78
P430	52.20	104.40	596.9	0.00214036	62.883	29.38
P431	51.74	103.48	555.3	0.00210281	13.554	6.45
P432	53.80	107.60	598.7	0.00227358	63.849	27.92
P433	52.78	105.56	592.9	0.00218819	98.168	44.86
P434	52.05	104.10	602.9	0.00212808	167.323	78.63
P435	51.58	103.16	609.0	0.00208982	148.687	70.41
P436	52.94	105.88	623.1	0.00220148	116.193	52.78
P437	51.65	103.30	574.4	0.00209550	8.852	4.21
P438	52.86	105.72	623.2	0.00219483	111.649	50.87
P439	53.24	106.48	600.4	0.00222650	95.977	43.11
P440	51.60	103.20	609.1	0.00209144	183.798	87.88
P441	52.90	105.80	600.1	0.00219815	103.988	47.31
P442	51.77	103.54	614.6	0.00210524	73.114	34.73
STN 11/1	51.53	103.06	555.9	0.00208577	47.626	22.83
STN 11/2	51.88	103.76	593.2	0.00211420	120.909	57.19
P443	51.75	103.5	544.2	0.00210362	110.007	52.29
P415L	51.62	103.24	574.8	0.00209306	8.723	4.17
P415R	51.64	103.28	583.9	0.00209468	62.041	29.62
P416	51.51	103.02	591.9	0.00208415	104.787	50.28
P449	52.16	104.32	585.7	0.00213708	49.466	23.15
P418	51.71	103.42	577.7	0.00210037	88.339	42.06
P414L	51.28	102.56	581.2	0.00206558	42.081	20.37

3.2   Point Load Strength

Point load test is another simple index test for rock material. It gives the standard point load index, Is(50) that was calculated from the point load at failure and the size of the specimen, with size correction to an equivalent core diameter of 50 mm. The result is tabulated in Tables 3 and 4 for granite and limestone, respectively.

Table 3 Results of point load for granite

Sample	D (mm)	H (mm)	Wt (g)	Force, P (kN)	Equivalent diameter, De² (mm)	Point load strength index, is (MPa)	Correlation factor, F	Point load index is (50) (MPa)
S1G	51.92	51.06	284.7	26.71	3375.40	7.91	1.07	8.46
S2G	52.07	51.96	284.4	9.93	3444.82	2.88	1.07	3.08
S3G	51.97	51.32	297.5	16.682	3391.94	4.92	1.07	5.26
S4G	52.10	51.84	285.7	10.43	3438.85	3.03	1.07	3.24
S5G	51.35	51.29	286.3	19.285	3353.58	5.75	1.07	6.15
S6G	52.31	52.28	294.6	17.361	3482.01	4.99	1.08	5.39

D Diameter; H Height; Wt Weight

Table 4 Results of point load for limestone

Sample	D (mm)	H (mm)	Wt (g)	Force, P (kN)	Equivalent diameter, De² (mm)	Point load strength index, is (MPa)	Correlation factor, F	Point load index is (50) (MPa)
S1	51.91	50.02	284.7	11.244	3374.97	7.91	1.07	8.46
S2	51.85	52.3	317	7.96	3452.27	2.31	1.08	2.49
S3	52.45	52.28	275.2	1.834	3491.33	0.53	1.08	0.57
S4	51.9	51.4	309.7	1.916	3396.57	0.56	1.07	0.6
S5	51.96	52.03	314.3	8.608	3441.51	2.5	1.07	2.68
S6	51.29	51.14	289.9	6.186	3340.32	1.85	1.07	1.98

D Diameter; H Height; Wt Weight

3.3 Tensile Strength

Brazilian test is interpreted as indirect method to determine the tensile strength of the rock. The test is to measure the weakest point of rock specimen due to tensile load. Result of tests is Tabulated in Tables 5 and 6. The tensile strength of the rock

Table 5 Result for Brazilian test of granite

Sample	Diameter (mm)	Thickness (mm)	Weight (g)	Max load, P (kN)	Tensile strength (MPa)
S1G	47.48	23.7	111.4	16.473	9.31
S2G	52.29	25.9	136.8	17.912	8.41
S3G	52.2	26.5	134.5	5.227	2.4
S4G	52.04	26.3	148.5	31.653	14.7
S5G	51.78	25.08	141.2	8.646	4.23
S6G	51.97	25.5	125.6	8.776	4.21

Table 6 Result for Brazilian test of limestone

Sample	Diameter (mm)	Thickness (mm)	Weight (g)	Max Load, P (kN)	Tensile strength (MPa)
8					
S1	51.75	25.87	149.4	11.76	5.59
S2	52.44	26.22	150	12.88	5.96
S3	51.93	25.96	157.3	5.798	2.74
S4	51.75	25.88	163.2	5.483	2.6
S5	51.88	25.94	145.6	22.286	10.53
S6	51.95	25.97	155.4	21.65	10.21
S7	51.98	25.99	148.4	20.493	9.65

is calculated from failure load (P), specimen diameter (D) and specimen thickness (t) by the following formula:

$$\text{Tensile strength} = \frac{0.636P\,(100)}{Dt} \tag{1}$$

where
P Load of failure (N)
D Diameter of specimen (mm)
t Thickness of specimen (mm)

3.4 Slake Durability

The slaking process involves two groups of different rocks which are granite and limestone. The purpose is to measure the differences in durability between granite and limestone from the same place of taking. Table 7 shows the slake durability index of granite and limestone throughout the slake process.

Table 7 Slake durability of granite and limestone

Sample	Empty drum mass (g)	Sample and drum mass (g)	Dried sample and drum mass (g)	Slake durability cycle				Slake durability index	
				Cycle 1 (g)	Cycle 2 (g)	Cycle 3 (g)	Cycle 4 (g)	Id$_1$ (%)	Id$_2$ (%)
Limestone	1801.45	2249.37	2247.33	2242.12	2239	2237.16	2235.17	98.74	98.04
Granite	1791.33	2298	2196.15	2285.17	2278.24	2273.03	2138.6	97.82	96.45

3.5 *Petrographic Analysis*

3.5.1 Granite

The mineral in thin section are seen by Plan Achro FP 10X/0.25. In granite, feldspars and quartz are major constituent minerals. Feldspars can be divided into two types which are alkali feldspars and plagioclase feldspars that consist of 25 % of mineral constituent, respectively. Alkali feldspars are more common than plagioclase, because they are more resistant to chemical weathering. Simple twinning as seen in Fig. 2 is very common in monoclinic alkali feldspar and this serves to distinguish them from plagioclases since the latter usually shows lamellar twinning as well as simple twinning.

Quartz is also the most abundant grain in granite with 40 % mineral constitution. The matrix between the quartz and feldspar grains contains dark minerals such as biotite, olivine or hornblende commonly present in granite constitute 10 % of the thin section specimen of granite.
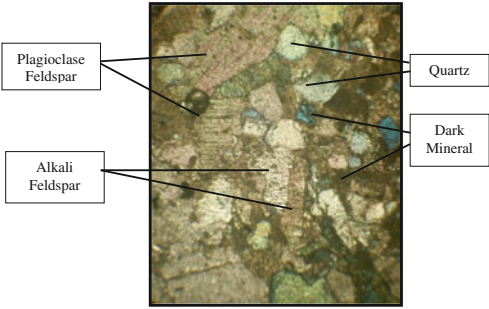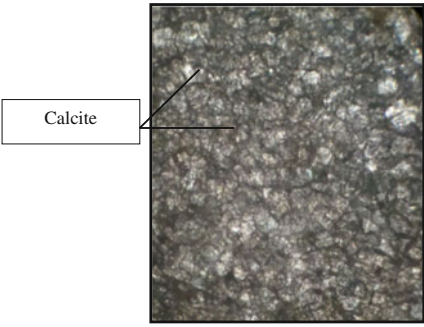
Fig. 2 Microscopic image of granite and limestone

3.5.2 Limestone

Calcite cement is usually fairly coarse grained and constitutes 100 % in the limestone rock as it is originated from calcium carbonate mineral based such as shell brachiopod. Occasionally they are so coarse resulting in a poikilitic texture. Figure 2 shows sandstone in which the detrital grains are subangular to surrounded quartz. The cement is calcite of such a grain size that there are only a few crystals in the field of view shown.

4 Discussions

Based on the result of the engineering properties for granite and limestone of this study, there are two types of characteristics which are physical and mechanical characteristic. For mechanical characteristic, four types of tests have been conducted which are UCS, point load test, Brazilian test and slake durability test. The value that obtained from UCS is 15.96–103.85 MPa for granite and 4.17–87.88 MPa for limestone. Then for the point load test, the value for the granite is 3.0–8.5 MPa and for the limestone is 0.5–8.5 MPa. For the third test which is Brazilian test, the result was 2.4–9.4 MPa for granite while 2.6–10.6 MPa for limestone. The result for slake durability test is indicating in percentage which is different from other test. The result

Table 8 Summary of engineering characterisation of granite and limestone of Kuala Lumpur

	Engineering properties	Granite		Limestone		Rock quality compared to standard value	
Mechanical characteristic	Unaxial compression strength (MPa)	15.96–103.85		4.17–87.88		Granite	Limestone
						Bieniawski [4]	
						Vey low–high strength	Vey low–high strength
	Point load index (MPa)	3.0–8.5		0.5–8.5		Bieniawski [4]	
						Medium–high strength	Very low–high strength
	Tensile strength (MPa)	2.4–9.4		2.6–10.6		–	
	Slake durability (%)	98.0–99.0		96.4–97.9		Hasani and Scoble [5]	
						High quality	High quality
Physical characteristic	Petrographic description (mineral composition)	Mineral	%	Mineral	%	–	–
		Feldspar (Alkali)	25	Calcite	100		
		Feldspar (Plagioclase)	25				
		Quartz	40				
		ark mineral	10				

is 98.0–99.0 % for granite and 96.4–97.9 % for limestone. The physical characteristic test was conducted by petrography study. The mineral content found in granite are feldspar, quartz and a little of dark minerals. The percentage of each mineral is different due to the origin of granite during crystallisation and cooling process. Calcite was only mineral found in limestone sample in the study. The summary of the engineering characterisation of granite and limestone from Kuala Lumpur is shown in Table 8.

The results were compared with the established value of each strength categories to remark the quality of the rock [4, 5].

5 Conclusions

It can be concluded that this study has provided significant information of the engineering characterisation for granite and limestone from Kuala Lumpur. The strength quality of UCS for granite and limestone varies from very low to high strength, meanwhile for point load index, the quality is from medium to high strength and very low to high strength for granite and limestone, respectively. The wide range of strength quality is may be caused by weathering and dissolution of both the types of rock. However, most of the samples have high durability index.

References

1. Hutchison, C.S., Tan, D.N.K. (Eds.). (2009). Geology of Peninsular Malaysia, University of Malaya/Geological Society of Malaysia, Kuala Lumpur.
2. Gue, S.S. & Cheah, S.W. (2008), "Geotechnical Challenges in Slope Engineering of Infrastructures", International Conferences on Infrastructures Development, Putrajaya Mariott Hotel, 7–9May 2008.
3. Rock Characterization, Testing and Monitoring, ISRM Suggested Methods, ed. E.T. Brown, Pergamon, Oxford, (1985)
4. Bieniawski, Z. T. (1975), The point load test in Geotechnical Practice. *Engineering Geology 9*, 1–11.
5. Hassani, F.P., Scoble, M.J. & Whittaker, B.N. 1980. Application of slake durability index test to strength determination of rock and proposals for new size-correction chart. *Proc. 21st U.S. Symp. Rock Mechanics, Rolla*, Md.:.543–564.

Prediction of Stress–Strain Response for Malaysian Granitic Residual Soil (Grade VI) in a Range of Effective Stresses, According to Rotational Multiple Yield Surface Framework

Pooya Saffari, Mohd Jamaludin Md Noor, Yasmin Ashaari and Ahmad Zaidi Hampden

Abstract The conventional soils volume change models which are based on the effective stress concept are not accurate to model true volume change behavior of unsaturated soil solely. It seems that the effect of shear strength in interaction of effective stress is essential to be incorporated in these frameworks. Rotational multiple yield surface framework (RMYSF), which introduced by Md.Noor and Anderson (16th South East Asian Geotechnical Conference Kuala Lumpur, 2007) [21] is developed based on the concept. In this paper, the framework has been examined for Malaysian granitic residual soil grade VI. With the aim of this process, the stress–strain curves were predicted using the framework. Beside that, the stress–strain curves have been obtained from consolidated drained triaxial tests under various effective stresses and then the results were compared with the predicted ones. The result shows a good agreement between the laboratory stress–strain curves and predicted ones from the framework.

Keywords Unsaturated soil · Effective stress · Volume change · Rotational multiple yield surface framework · Mobilized shear strength · Stress–strain response

1 Introduction

On the nature and construction fields, normally the ground water table is at a deep level of the ground surface and soil is in unsaturated condition except after a rain. In tropical countries like Malaysia due to heavy rainfall, the soil condition is always changing from unsaturated to saturated condition and vice versa. This alternate wetting and drying of the soil causes a lot of geotechnical problems such as shallow slope failure or inundation settlement (wetting collapse) in the fields.

P. Saffari (✉) · M.J. Md Noor · Y. Ashaari · A.Z. Hampden
Department of Civil Engineering, Universiti Teknologi Mara, Shah Alam, Sarawak, Malaysia
e-mail: pooya_sa2002@yahoo.com

The conventional soil volume change models like [1–3] were established based on Terzaghi effective stress concept [3]. According to these models, settlement is always related with an effective stress increment. Either pore water pressure is driven away or total stress rises, effective stress will increase and settlement will take place. The settlement also can occur when the water table drops triggered an increase in effective stress. This happened in Mexico city after water was pumped for domestic consumption and ground water level dropped significantly [4].

However, some researchers like [5–7] have reported the occurrence of settlement during the wetting process of the soil which is under constant load. This settlement is popularly known as wetting collapse. First, the soil is in partially saturated condition and pore water pressure is negative. Soils particles are pushed together by the surface tension force which provides suction [8]. After Infiltration, the pore water pressure changes from being negative to positive within the soil mass and causes an ensuing drop in the effective stress due to the Terzaghi effective stress concept as Eq. 1.

$$\sigma' = \sigma - u_w \tag{1}$$

Hence, wetting collapse occurs due to effective stress reduction and cannot be characterized solely by any of conventional settlement models which are based on Terzaghi effective stress concept. It seems a second factor rather than effective stress must be involved in soil volume change of unsaturated soils. This is the reason that geotechnical researchers consider wetting collapse as a complex soil volume change behavior.

In addition, there are some more soil volume change behavior problems with soil in unsaturated conditions such as massive settlement while soil is near to saturation [9] or greater wetting collapse at low net stress compared to higher net stress [10], which makes the volume change behavior of unsaturated soil more complicated. In fact, it is not just increasing of effective stress, which influences the volume change behavior of soil. It can also be influenced by the reduction in shear strength. This is reported first time by [11].

This paper first, reviews some soil volume change models and their limitation briefly in unsaturated soils. In addition, the rotational multiple yield surface framework (RMYSF) which is based on the concept of effective stress and shear strength is verified for Malaysian granitic residual soil grade VI. The capability of the framework to model the wetting collapse and loading collapse is also examined.

2   Volume Change Models in Unsaturated Soils

Characterizing of all strange volume change behavior in unsaturated conditions needs a framework which can replicate them in a model without any compromise. This model needs to consider the important role of shear strength in addition by

effective stress in governing the settlement. However, to incorporate the concept of shear strength and effective stress interaction in a volume change framework is not easy.

The earlier framework for volume change behavior of unsaturated soils was introduced by [12]. He assumed that soil is isotropic and behaves linear elastic. According to his model the deformation of unsaturated soils is related to the soil structure and water face. Later on [13] in terms of experimental studies on the oedometer test and all existing compression tests conducted on saturated and unsaturated soils, reported that there is no unique relationship between effective stress and volume change for most soils either in saturated or unsaturated condition. They suggested that best analyzed for the volume change behavior of unsaturated soils is based on stress, $(\sigma - u_a)$, and suction, $(u_a - u_w)$. These two variables, as stress variables, also had suggested earlier by [14–16] in determining of unsaturated soil volume change behavior.

Reference [9] introduced a soil settlement model for unsaturated soil base on critical state models which was an extension of modified cam clay model presented by [17] (Fig. 1). In this model, there are four stresses variable applied, which are net stress, p', deviator stress, q, specific volume, v and suction, s. The model allows to predict settlement of a soil either subjected to wetting or stress. Later, Wheeler and Sivakumar refined the model twice on 1993, and 1995, [11, 18].

However, the model was refuted by [19]. They proved that the model failed to define soil volume change behavior of unsaturated soils in alternate drying and wetting by referring to the performance of the model reported by [20].

Fig. 1 Semiempirical model presented by [9]
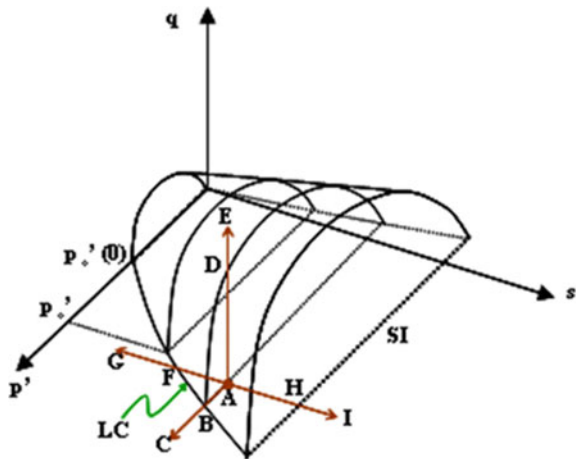
2.1 Rotational Multiple Yield Surface Framework

In 2007, Md. Noor and Anderson [21] introduced an anisotropic soil volume change model, named rotational multiple yield surface framework (RMYSF). The model is based on the extended concept of the interaction between effective stress (or net stress) and mobilized shear strength. According to this concept, settlement can be related to an increase in effective stress (known as loading collapse) or a reduction in shear strength (known as wetting collapse).

The framework is developed from soil stress–strain response and is able to model correct soil elastic-plastic response. RMYSF model is able to predict settlement either for loading collapse or wetting collapse from a combination of theoretical concept and laboratory observations and is considered as a semiempirical model. The state of stress for the saturated condition is considered as effective stress and for unsaturated condition is considered as net stress and is presented by Mohr circles. The stress state is considered as driving variables. In other hand, the state of the mobilized shear strength acts as resisting variable in the soil mass and represented by the curved surface mobilized shear strength envelope (Fig. 2).

According to the model, the settlement takes place while stress (effective or net) extends beyond the mobilized shear strength envelope. In this case, the driving variable becomes greater than resisting variable. During the compression process, soils particles move to a denser state. The mobilized shear strength resists against this rearrangement by providing the frictional resistance and rotate anticlockwise about the origin toward the mobilized shear strength envelope at failure. This is marked as an increase in the shear strength of the soil. This process will continue until the driving and resisting variables reach an equilibrium state. At the equilibrium state if the Mohr circle is placed in a lower position than mobilized shear strength, it means driving variable is smaller than resisting variable and soil is stable. However, if the Mohr circle is placed in a position beyond the mobilized shear strength, it means soil mass is not stable and it undergoes settlement.

Fig. 2 The Mohr circle representing the state of applied stress and the curved surface envelope representing the state of shear strength [24]
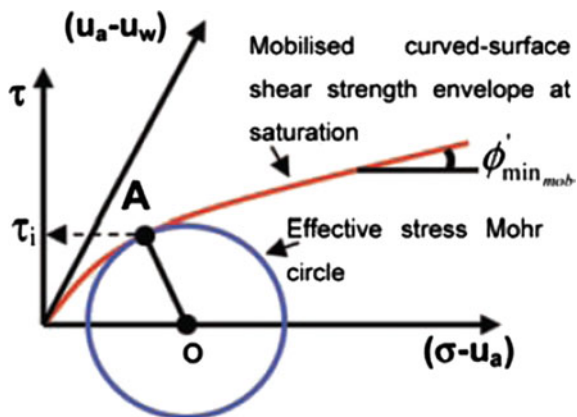
Fig. 3 Enlargement of Mohr circle and rotation of mobilized shear strength during the compression (loading collapse)
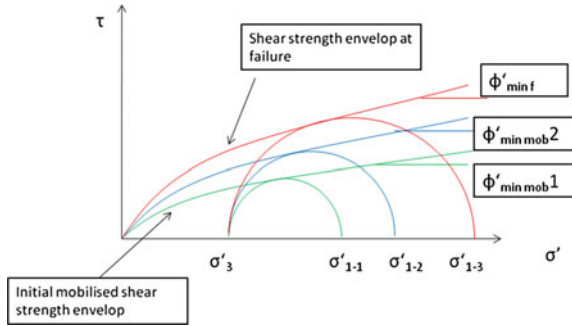
The rotation of mobilized shear strength toward the mobilized shear strength at failure is shown in Fig. 3. The position of mobilized shear strength envelope at each stage is presented by minimum mobilized friction angle, $\emptyset'_{min\ mob}$. In Fig. 3, first the soil is under initial minor and major effective stresses of σ'_3 and σ'_{1-1}, respectively. The initial mobilized shear strength is in a position with $\emptyset'_{min\ mob\ 1}$. During the compression the major effective stress increases to the new value shown as σ'_{1-2} and mobilized shear strength also rotates toward the mobilized shear strength envelope at failure ($\emptyset'_{min\ mob\ 2}$) to resist against this increase. The soil will be stable since Mohr circle has not reached the shear strength envelope at failure. While the Mohr circle extends due to increase of major effective stress to σ'_{1-3} the soil becomes unstable and fails. This is known as loading collapse.

However, as mentioned in part one, settlement can occur under constant effective stress and due to inundation of water within the soil mass. Figure 4 illustrates the displacement of Mohr circle and rotation of mobilized shear strength during the inundation. In the initial stage, the soil mass is under minor and major net stress of σ'_3 and σ'_1, respectively. The apparent shear strength due to initial suction is shown by c'_1 and the minimum friction angle of mobilized shear strength is $\emptyset'_{min\ mob1}$. During the inundation, suction is reduced and Mohr circle is driven toward the frontal plane (zero suction or fully saturated plane). However, the size of the Mohr
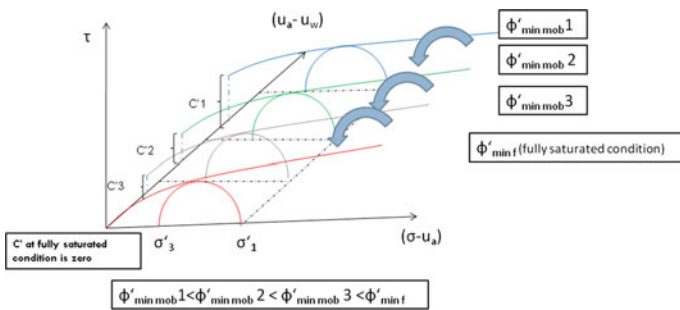
Fig. 4 The displacement of Mohr circle and rotation of mobilized shear strength during the inundation

Fig. 5 The unique relationship $\emptyset'_{\min \text{mob}} - \varepsilon_a$ for the compression of saturated and partially saturated specimens [24]
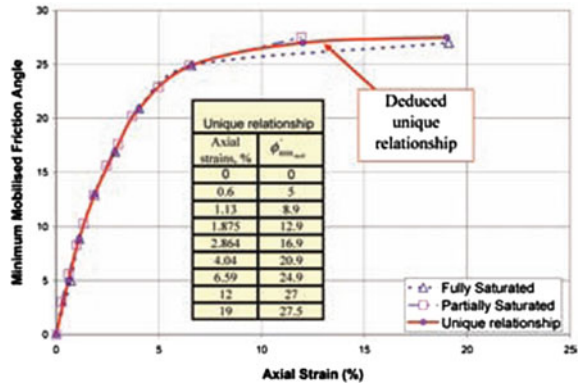
circle remains constant since the reduction in suction does not have any effect on the value of net stresses. Reduction in suction leads a nonlinear reduction in apparent shear strength [22] to the new value of c′2. In this manner, if the Mohr circle extends above the mobilized shear strength envelope, settlement will take place and forces the mobilized shear strength envelope to rotate in a new position with a greater mobilized friction angle, $\emptyset'_{\min \text{ mob2}}$. If the inundation continues and suction approaches zero, soil will be faced with a steep drop in apparent shear strength c′3 and as a result a massive settlement will trigger. This is the reason of massive settlement near saturation which has reported by [9].

Reference [23] have reported that there is a unique relationship between the minimum mobilized friction angle, $\emptyset'_{\min \text{ mob}}$ and axial strain, ε_a. In other words, during applying the deviator stress, the mobilized shear strength rotates in accordance with axial strain, either for saturation or unsaturation condition regardless of the value of net stress or effective stress. The existence of this unique relationship is the basis of the RMYSF model. It helps to predict stress–strain response of a specific soil at any effective stress or net stress just by determining a series of mobilized shear strength envelopes. Figure 5 shows this unique relationship for the compression of saturated and partially saturated specimens reported by [24].

3 Mobilized Shear Strength Envelopes and the Unique Relationship for Malaysian Granitic Residual Soil Grade VI

The soil tested in this study was granitic residual grade VI from Rawang, Selangor, Malaysia. The specimen consists of 48.83 % sand, 21.90 % gravel, 20.68 % silt, and 8.59 % clay and classified as a very silty gravely SAND. Consolidated drained triaxial tests in fully saturated condition were conducted on specimens with 50 mm diameter and 100 mm height according to *BS1337: part8: 1990*. The soil was tested
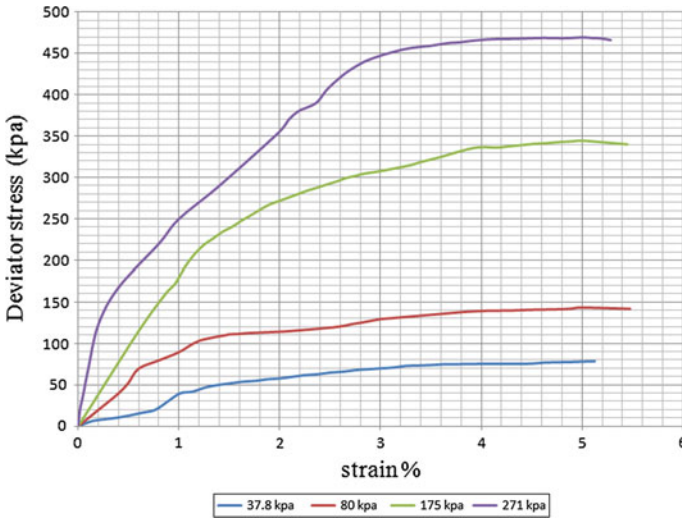
Fig. 6 The stress–strain curves for granitic residual soil grade VI in saturated condition

at effective stresses of 37.5, 80, 175, and 271 kPa. From the result of shearing stage the stress–strain curves was plotted as shown in Fig. 6.

The magnitude of axial strain in the graph presents the specimen axial deformation subjected to the related deviator stress. For example, for 2 % strain at 175 kPa effective stress, the magnitude of deviator stress is 270 kPa. It means if the specimen subjected to 270 kPa deviator stress at 175 kPa effective stress, it would settle 2 % of its initial height. During the shearing stage, the deviator stress increased and compressed the soil structure in a denser position and caused the extension of Mohr circle. The maximum deviator stress (deviator stress at failure) was approached at 5 % axial strain.

Figure 7 presents the mobilized shear strength envelopes in various axial strains obtained from the stress–strain curve in Fig. 6. Mohr circles were drawn under
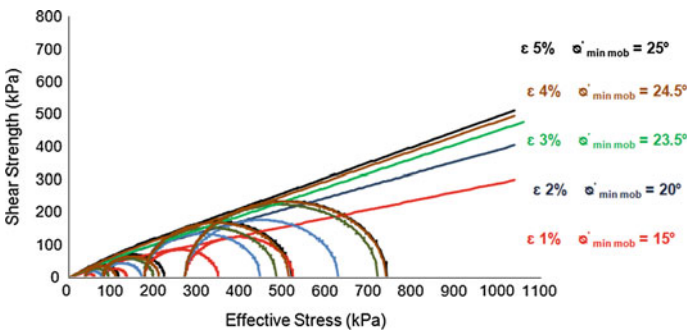
Fig. 7 Mobilized shear strength envelopes for granitic residual soil in various axial strains
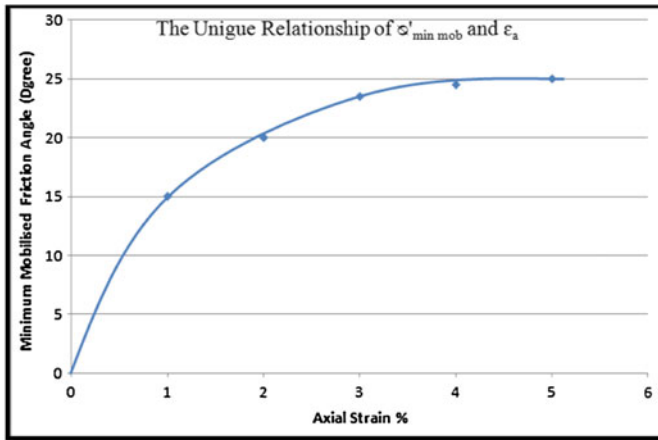
Fig. 8 The unique relationship for $\varnothing'_{min\ mob}$ and ε_a of granitic residual soil

effective stress of 37.5, 80, 175, and 271 kPa and their related deviator stress, in 1, 2, 3, 4, and 5 % axial strain. From the Mohr circles, the mobilized shear strength envelopes and their mobilized friction angles in different axial strains were plotted.

It can be observed from Fig. 7 in which there is a unique relationship between each axial strain and $\varnothing'_{min\ mob}$. In other words, the position of mobilized shear strength presents a specific amount of axial strain without any regard of effective stress. This is same as the unique relationships which has described by [23]. This unique relationship for soil tested is given in Fig. 8.

4 Prediction of Soil Stress–Strain Response Using Rotational Multiple Yield Surface Framework

The most advantage of the unique relationship between mobilized friction angle and axial strain is the ability of the graph to predict the soil strain–stress behavior at any specific net or effective stress. The stress–strain curves obtained from triaxial test (Fig. 6) were predicted, according to RMYSF model and the result was compared.

Mobilized shear strength envelopes, presented in Fig. 7, are a natural property of the soil. They are valid for the whole range of net and effective stresses and can be utilized to predict the stress–strain response of the soil at any net or effective stresses. In the aim of this prediction, first Mohr circles are plotted in beginning at required σ'_3. Each Mohr circle has to touch its specific mobilized shear strength envelope. As a result, the amount of σ'_1 can be determined. From σ'_3 and σ'_1, the Mohr circle can be drawn. The diameter of the Mohr circle presents the corresponding deviator stress, $\Delta\sigma$. At the end, each specific deviator stress is linked to the corresponding axial strain that mobilized shear strength presents.

Figures 9, 10, 11, and 12 shows the mobilized shear strength envelopes and predicted Mohr circles related to them under 37.5, 80, 175, and 271 kPa effective stresses, respectively.

Figure 13 illustrates a comparison between the experimental results of the consolidated drained triaxial test with predicted deviator stresses and the corresponding axial strains. It can observe that, the predicted deviator stresses which are indicated by dotted data points represent an acceptable agreement with the experimental data.
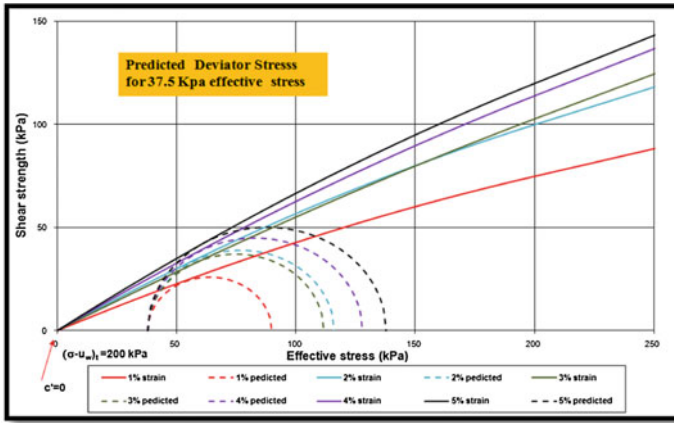
Fig. 9 Predicted Mohr circles under 37.5 kPa effective stress
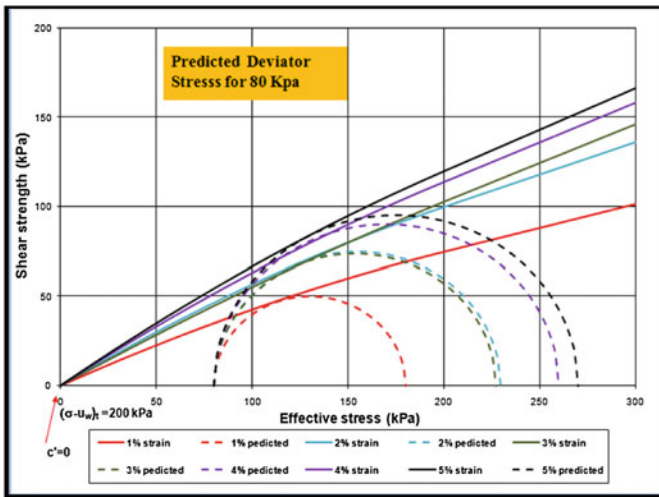
Fig. 10 Predicted Mohr circles under 37.5 kPa effective stress
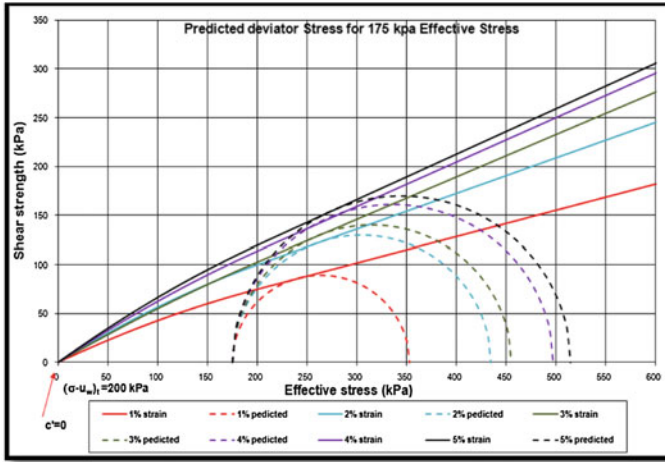
Fig. 11 Predicted Mohr circles under 175 kPa effective stress
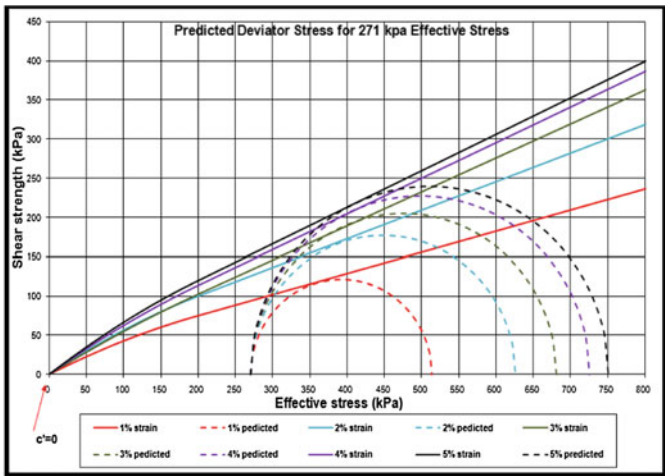
Fig. 12 Predicted Mohr circles under 271 kPa effective stress
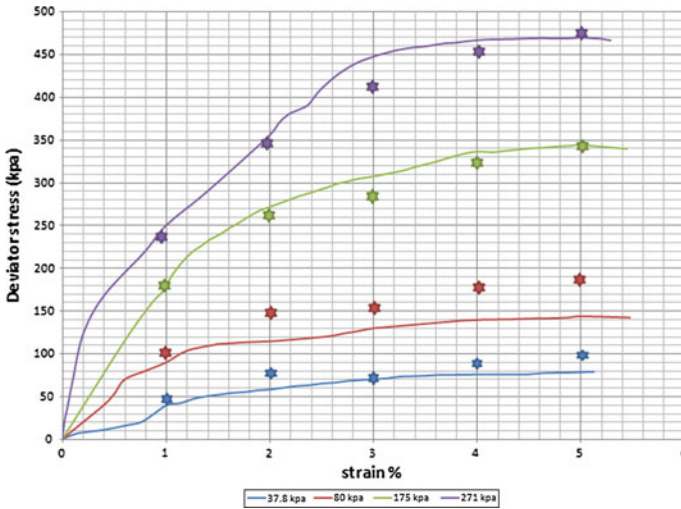
Fig. 13 The comparison between experimental results with predicted deviator stresses and the corresponding axial strain

5 Conclusion

The following conclusion can be determined from this study:

- The conventional soil volume change models which are based on the effective stress concept are not accurate to model true volume change behavior of unsaturated soil solely. The effect of shear strength in governing the volume change behavior of the unsaturated soil needs to be considered at volume change frameworks.
- It is very difficult to have a volume change model which can model all the strange behaviors of unsaturated soils like inundation settlement or massive settlement close to saturation stage. Models which are based on critical state theories can model inundation settlement, but they fail to simulate volume change behavior of soils in alternate drying and wetting.
- The RMYSF is obviously a perfect soil volume change model which is based on the concept of interaction between effective stress and mobilized shear strength. The framework is able to model the occurrence of wetting collapse as well as loading collapse. Most importantly, the model is capable to explain the massive settlement while suction approaches zero.
- Stress–strain curves can be predicted at any range of effective or net stresses by applying RMYSF model based on the unique relationship between minimum mobilized friction angle and axial strain. The results from Malaysian granitic residual soil grade VI shows a good agreement between the experimental and predicted result.

References

1. N. Janbu, L. Bjerrum, and B. Kjaernsli, "Veiledning ved løsning av fundamenteringsoppgaver," 1956.
2. J. H. Schmertmann, P. R. Brown, and J. P. Hartman, "Improved strain influence factor diagrams," Journal of the Geotechnical Engineering Division, vol. 104, pp. 1131–1135, 1978.
3. K. Terzaghi, *Theoretical soil mechanics* vol. 18: Wiley New York, 1943.
4. T. Strozzi and U. Wegmuller, "Land subsidence in Mexico City mapped by ERS differential SAR interferometry," in *Geoscience and Remote Sensing Symposium, 1999. IGARSS'99 Proceedings. IEEE 1999 International*, 1999, pp. 1940–1942.
5. R. Blanchfield and W. Anderson, "Wetting collapse in opencast coalmine backfill," Proceedings of the ICE-Geotechnical Engineering, vol. 143, pp. 139–149, 2000.
6. J. Jennings and J. Burland, "Limitations to the use of effective stresses in partly saturated soils," Géotechnique, vol. 12, pp. 125–144, 1962.
7. R. Tadepalli, H. Rahardjo, and D. G. Fredlund, "Measurements of matric suction and volume changes during inundation of collapsible soil," Geotechnical Testing Journal, vol. 15, pp. 115–122, 1992.
8. Bishop and A. Wilfred, *The principles of effective stress*: Norges Geotekniske Institutt, 1960.
9. E. E. Alonso, A. Gens, and A. Josa, "A constitutive model for partially saturated soils," Géotechnique, vol. 40, pp. 405–430, 1990.
10. M. Md.Noor, R. Jidin, and M. Hafez, "Effective Stress and Complex Soil Settlement Behavior," EJGE, vol. 13, 2008.
11. S. Wheeler and V. Sivakumar, "An elasto-plastic critical state framework for unsaturated soil," Géotechnique, vol. 45, pp. 35–53, 1995.
12. M. A. Biot, "General theory of three-dimensional consolidation," Journal of applied physics, vol. 12, pp. 155–164, 1941.
13. D. G. Fredlund and H. Rahardjo, *Soil mechanics for unsaturated soils*: John Wiley & Sons, 1993.
14. G. D. Aitchison and J. A. Woodbum, "Soil Suction in Foundation Design," presented at the 7th Int. Conf. Soil Mech. Found. Eng, Mexico, 1969.
15. I. Brackley, "Partial collapse in unsaturated expansive clay," in *Proceedings of 5th African Reg. Conf. on Soil Mech. and Found. Engrg*, 1971, pp. 23–30.
16. G. D. Aitchison and R. Martin, "A Membrane Oedometer for Complex Stress-Path Studies in Expansive Clays," in 3rd Int. Conf. Expansive Soils, Haifa, Israel, 1973, pp. 83–88.
17. K. H. Roscoe and J. Burland, "On the generalized stress-strain behaviour of wet clay," 1968.
18. S. Wheeler and V. Sivakumar, "Development and application of a critical state model for unsaturated soil," in *PREDICTIVE SOIL MECHANICS. PROCEEDINGS OF THE WROTH MEMORIAL SYMPOSIUM, 27–29 JULY 1992, ST CATHERINE'S COLLEGE, OXFORD*, 1993.
19. S. Wheeler, R. Sharma, and M. Buisson, "Coupling of hydraulic hysteresis and stress–strain behaviour in unsaturated soils," Géotechnique, vol. 53, pp. 41–54, 2003.
20. E. Alonso, A. Lloret, A. Gens, and D. Yang, "Experimental behaviour of highly expansive double-structure clay," in *PROCEEDINGS OF THE FIRST INTERNATIONAL CONFERENCE ON UNSATURATED SOILS/UNSAT '95/PARIS/FRANCE/6–8 SEPTEMBER 1995. VOLUME 1*, 1995.
21. M. J. Md.Noor and W. F. Anderson, "A Qualitative Framework for Loading and Wetting Collapses in Saturated and Unsaturated Soils," in 16th South East Asian Geotechnical Conference, Kuala Lumpur, Malaysia, 2007.

22. M. J. Md.Noor and W. Anderson, "A comprehensive shear strength model for saturated and unsaturated soils," in Unsaturated Soils 2006, 2006, pp. 1992–2003.
23. I. B. Mohamed Jais and M. J. Md.Noor, "Establishing Unique Relationship between Minimum Mobilised Friction Angle and Axial Strain for Anisotropic Soil Settlement Model," presented at the Asia Pacific Conference on Unsaturated Soil, Newcastle, Australia, 2009.
24. M. J. Md.Noor and I. B. Mohamed Jais, "Rotational multiple yield surface framework and the prediction of stress-strain response for saturated and unsaturated soils," in *5th International conference on unsaturated soils* Barcelona, Spain, 2010.

Quantifying Cavity Through Volumetric Study by Resistivity Images

Haryati Awang, Yunika Kirana Abdul Khalik and May Raksmey

Abstract The complexity of karst system, referring to its geological and hydrological characteristics can be categorized among the most fragile and vulnerable environments in the world. Karst voids are commonly a major engineering risk associated with construction in areas underlain by carbonate rocks. Due to karst unique characteristics to exhibit sudden change in subsurface conditions, extensive geotechnical exploration is needed in order to achieve the best geotechnical results. A site investigation that can provide clearer picture of the overall underground condition should be carried out in order to overcome the problems related to karst void, such as cavity profiling. This study anticipated to determine the subsurface profile and investigate the underground cavities in limestone areas by electrical resistivity method and using the simulation of Voxler software. An electrical resistivity test was conducted at a proposed site at Jalan Sultan Ismail, Kuala Lumpur. The subsurface profile of the selected study area was successfully analyzed and determined from 2-D resistivity images, including identification of potential cavities and voids. The 2-D resistivity images and 2-D oblique images (sliced images from 3-D model) show similar subsurface profile indicating that the Voxler software is suitable and flexible to model the 2-D resistivity images to 3-D images. The potential cavity volume calculation was also successfully calculated.

Keywords Cavity · Volumetric study · Resistivity images

H. Awang (✉) · Y.K.A. Khalik (✉) · M. Raksmey (✉)
Faculty of Civil Engineering, Universiti Teknologi MARA,
40450 Shah Alam, Selangor, Malaysia
e-mail: harya406@salam.uitm.edu.my

Y.K.A. Khalik
e-mail: yunikakirana@gmail.com

M. Raksmey
e-mail: may_raksmey@salam.uitm.edu.my

1   Introduction

Dominating almost total volume of calcareous sedimentary rock in Malaysia, limestone composed largely of the minerals calcite and aragonite, which are different crystal forms of calcium carbonate ($CaCO_3$). Most of the limestone is composed of skeletal fragments of marine organisms such as coral or foraminifera. Certain limestone does not consist of grains at all and are formed totally by the chemical precipitation of calcite or aragonite. Karst landscapes are one of the formations developed by the solubility of limestone in water and weak acid solution, in which water erodes the limestone over thousand millions of years. The complexity of karst system, referring to its geological and hydrological characteristics can be categorized among the most fragile and vulnerable environments in the world. Karst voids are commonly a major engineering risk associated with construction in areas underlain by carbonate rocks. Several problems related to the subsurface karstic voids are road and highway subsidence, building foundation collapse, and dam leakage [1].

Due to karst unique characteristics to exhibit sudden change in subsurface conditions [2], extensive geotechnical exploration is needed in order to achieve the best geotechnical results. A site investigation that can provide clearer picture of the overall underground condition should be carried out in order to overcome the problems related to karst void, such as cavity profiling. The adaption of geophysical methods for engineering purposes signifies an important contribution to the improvement of site investigation methodology. As important as it is to obtain accurate subsurface profile from the conventional site investigation method such as using borehole, auger drilling or cone penetration tests, it is in many cases hard to generate continuous yet accurate subsurface profile from the little, disconnected data that come out of the detailed geotechnical investigations. Nevertheless, combining conventional site investigation and geophysical methods can help achieve a more reliable subsurface profiling [3].

Erosion of the limestone mass has created deep cavities and underground caverns, which, if not discovered beforehand, can pose extensive danger for the design estimation and construction works. Failure to identify karst terrain features, such as rock pinnacles and large soil-filled cavities in rock, will pose great uncertainties and difficulties during foundation design and construction [2]. These rock cavities may increase in size under favorable hydrological conditions, thus resulting in a sudden collapse since carbonate rocks are soluble. Large void formation in a karst environment may lead to sudden and catastrophic pavement failure, while fine particles' slow migration from the subbase may cause gradual ground subsidence [1].

This study was carried out to give better subsurface profile, where it provides clearer picture of the overall underground condition using 2-D resistivity images and 3-D Voxler images. By estimating the potential cavity beneath using 3-D simulation, the shape, location, and volume calculation can be identified. This can

help not only designers during the design stages but also the contractors during the construction stages. From this study, future problems especially related to geotechnical engineering can be forecast and prevention action can be taken.

2 Methodology

2.1 *Resistivity Field Survey and Data Collection*

Electrical resistivity imaging system was carried out with a multielectrode resistivity meter system where the electrodes were laid out in a straight line with a constant spacing. Forty one numbers of stainless steel electrodes, with 2.5 m interval were embedded into the ground with a total length of 100 m along each line. In this study, the array configuration applied was Wenner-Schlumberger Array. Figure 1 shows the resistivity line locations chosen for this study.

Fig. 1 Resistivity line locations
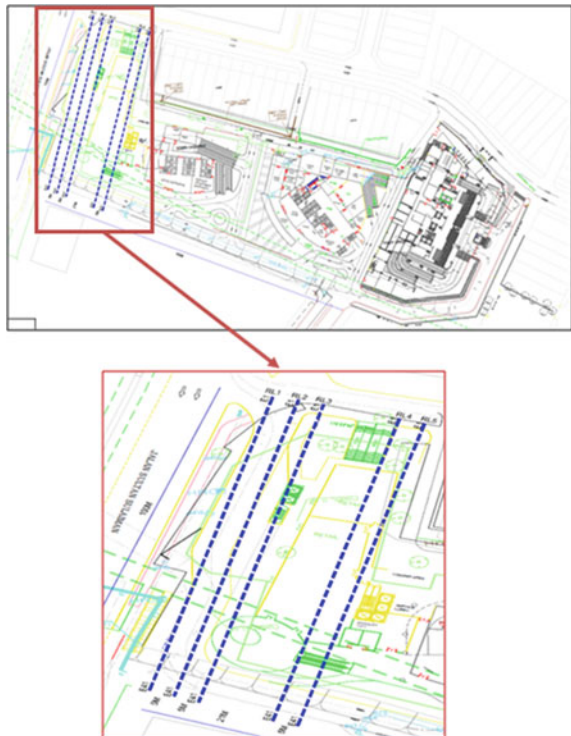
2.2 Data Transferring, Data Conversion, Data Processing and Data Inversion

The collected resistivity data inside the ABEM Terrameter SAS 4000 were first imported to laptop or computer using SAS 4000 software. The file will be in .S4 K format. Then this file was converted where the output data will be in .DAT format. To obtain two-dimensional (2-D) inverse resistivity model of the subsurface profile, the data were processed and inverted using RES2DINV software. RES2DINV used inverse process to get the actual subsurface resistivity. The inverse model resistivity sections were presented together with topographic data and geological interpretation of the resistivity and other data. RES2DINV of software will produce three different pseudosections. The first pseudosection was produced from raw data results from the field. The second pseudo-sectional resistivity material was produced from the software calculation. The third pseudosection was produced the resistivity model.

2.3 Data Analysis and Interpretation

The image of 2-D resistivity was analyzed and interpreted based on the resistivity value used by previous researches in order to determine the subsurface profile. The range of resistivity value is represented by each color indicated at the bottom of the image.

2.4 3-Dimensions Image Using Voxler Software

For a more comprehensive visualization of the electrical resistivity imaging data file inversions, the results were used as input into Voxler. Voxler is a three-dimensional scientific visualization program oriented primarily toward volumetric rendering and three-dimensional data display. The benefit of reimaging the inversion results in Voxler is that multiple data files may be viewed at one time. Viewing multiple data files gives the ability to see clearly the subsurface resistivity structure [4]. From here, the potential cavities location can be determined. The cavity volume can also be calculated using this software.

3   Result and Analysis

3.1   Resistivity Images Analysis and Interpretation

Electrical resistivity measurements have continuous information over areas or in sections and volumes, where this certainly benefits and becomes the main contribution in geotechnical site investigation. This method can help to characterize the initial extent of different geological units and the heterogeneity of the geology. From this, a continuous resistivity model will be generated where it provides a possibility of reliable interpolation of, such as, geotechnical design parameters. Changes in porosity, clay content, water content, and grain size distribution can also be revealed from the resistivity results variation [3].

The resistivity value of natural geological materials such as soils and rocks varies widely. The values depend much on the constituent of the material. As we are acquainted with, soil consists of solid, water, and air void. Variation of water content and dissolved ions in the water mainly influences the resistivity [5]. Material type, properties, porosity, and density also contribute to the resistivity values. Theoretically, dense and compact solid will have higher resistance compared with loose solid. Rocks, dry sand, dry clay, compacted soil and air (void) have high resistivity values which are usually relatively high to the surroundings. High resistivity values indicate that the subsurface material delayed or hardly allow electric current to flow through it. Meanwhile, low resistivity value indicates that the subsurface material easily allow electric current to flow through it. As for instance, water and soil with high moisture content have low resistivity value. Loose and porous materials which are able to trap more water between its particles also have low resistivity. This is due to the fact that water is a very good electric conductor, thus it allows current to flow through it easily. But it will be different for pure/distilled water since it that has no ion present in it; therefore it might have higher resistivity values. The high conductivity of salty water is the salt ions but water has in any case an amount of ions.

The results of 2-D resistivity images of this study can be interpreted as the distribution of areas of high resistivity (red–purple) and areas of low resistivity (blue). The resistivity values were then referred to the resistivity index published by previous researchers. The value is then summarized in Table 1 for data analysis. Referring to the index provided, it helps to interpret and classify the subsurface according to their material and composition. From the analysis, the potential cavity areas can be predicted.

3.1.1   Interpretation of Line 1

Figure 2 shows the result of data inversion processing for Line 1. The image shows the range of resistivity along the traverse profile to a depth of 20 m. According to the result, beginning from 25 to 60 m (horizontal distance), 3 m depth from the

Table 1 Resistivity summary of earth material for this site

Indicator	Resistivity (Ω m)	Descriptions
	<50	Saturated zone (fresh groundwater/clay/water filled cavities)
	50–200	Wet soil (saturated sand and gravel/clay sand and gravel mixture)
	200–1000	Consolidated sediment (hard soil/material/weathered limestone)
	>1000	Rock (limestone)
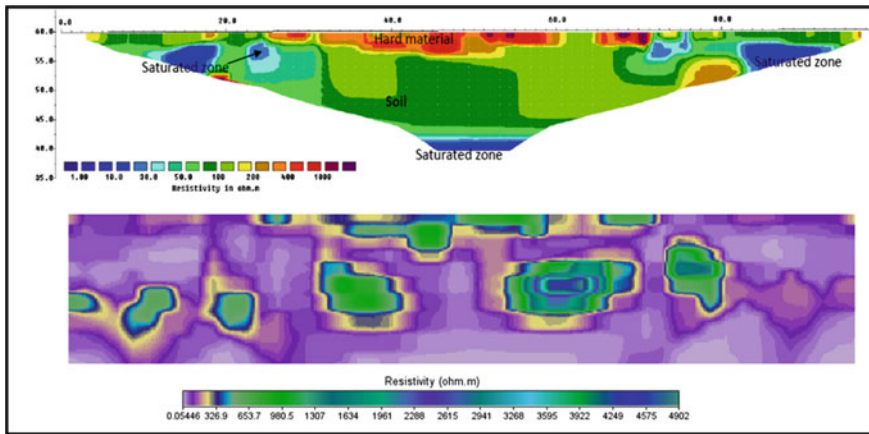
Fig. 2 2-D resistivity image versus 2-D voxler oblique image at line 1

surface ground level, the resistivity value ranges from 200 to 1000 Ω m predicted as hard soil or perhaps weathered limestone. It also applies from 65 to 72 m horizontally. Several locations show higher resistivity values represented by dark red to purple color interpreted as limestone. The green to yellow color zone encountered in the middle and at both ends, having resistivity values of 50 to 200 Ω m, is interpreted as saturated sand and gravel or clay sand and gravel mixture. Three locations of saturated zone can be seen in the image, ranging from 0 to 50 Ω m. The lighter blue is interpreted to represent fresh groundwater or clay while the dark blue having lower resistivity could have represented clay or possibly water filled cavities.
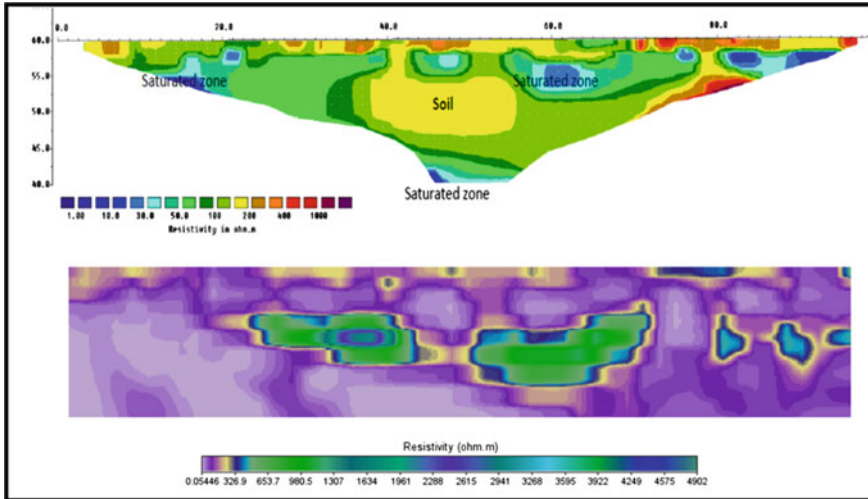
Fig. 3 2-D resistivity image versus 2-d voxler oblique image at line 2

3.1.2 Interpretation of Line 2

2-D electrical resistivity model along Line 2 profile is shown in Fig. 3. This model indicates that the resistivity values ranged from 0 Ω m to more than 1000 Ω m. A very clear green zone can be seen dominating the subsoil profile, extended 17 m deep from the ground surface. This green zone has moderate resistivity values ranging from 50 to 200 Ω m which is interpreted as saturated sand and gravel or clay sand and gravel mixture. Located at several locations at the surface area, having resistivity values of 200–1000 Ω m, the orange to red zone represents as hard material or possibly potential weathered limestone. Saturated (blue color) zone located at 15, 20, 48, 60, and 80–95 m in horizontal distances was interpreted as saturated zone such as fresh groundwater or clay. The dark blue zone having lower resistivity response below 30 Ω m is predicted as potential cavity.

3.1.3 Interpretation of Line 3

From the inverse resistivity image at Line 3 (Fig. 4), it is found that the resistivity values ranges from 1 Ω m to more than 1000 Ω m. The image shows a majority of blue color zone ranging from 0 to 50 Ω m interpreted as fresh groundwater or clay or possibly water filled cavities. This line shows that it has the largest potential cavities underneath having resistivity values lower than 30 Ω m. As for 50–200 Ω m, located from the surface until 2 m depth at 0–30 m horizontally, it is predicted as saturated sand and gravel or perhaps clay sand and gravel mixture. It can also be seen at 5 m depth, 15 m from horizontal direction. At several locations
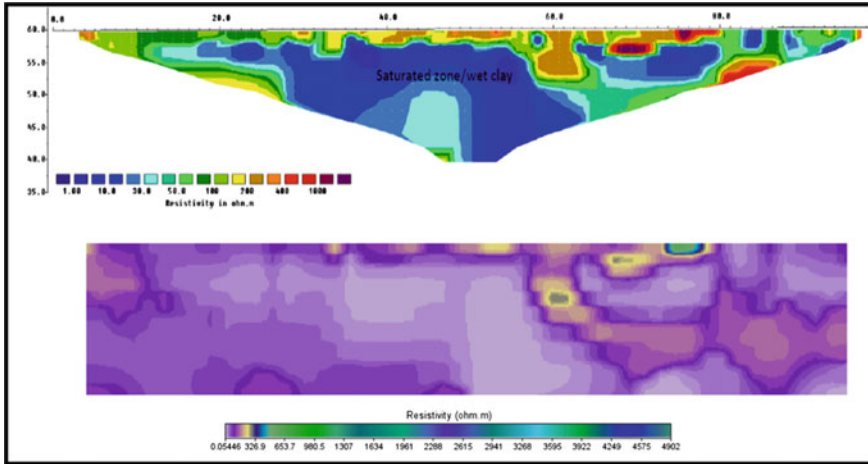
Fig. 4 2-D resistivity image versus 2-d voxler oblique image at line 3

from the ground surface, weathered rock (limestone) or hard soil was detected, ranging from 200 to 1000 Ω m. Two locations indicated as limestone with higher resistivity values were discovered at 70 and 75 m in horizontal direction.

3.1.4 Interpretation of Line 4

Figure 5 shows the resistivity result for Line 4. The image shows the range of resistivity along the traverse profile to a depth of 20 m. Based on the result, saturated zone can be seen at several locations encountered at 2–10 m depth traversing from 15 to 25 m horizontally. The largest saturated zone can be seen at the center of the image. At 25–30 m in horizontal direction, hard material or possibly weathered limestone was detected having resistivity values of 200–1000 Ω mm. The outer region of the orange to red color zone has less resistivity values ranging from 200 to 400 Ω m interpreted as hard material. Green to yellow zone can be seen in the image interpreted as saturated sand and gravel or maybe clay sand and gravel mixture.

3.1.5 Interpretation of Line 5

Figure 6 shows the result of data inversion processing for Line 5. The resistivity values ranges from 1 Ω m to more than 1000 Ω m. Orange to red color zone can be seen at 30–40 m and from 70 to 80 m in horizontal direction. This is interpreted as weathered limestone. Green to yellow color zone covers large area of the subsurface
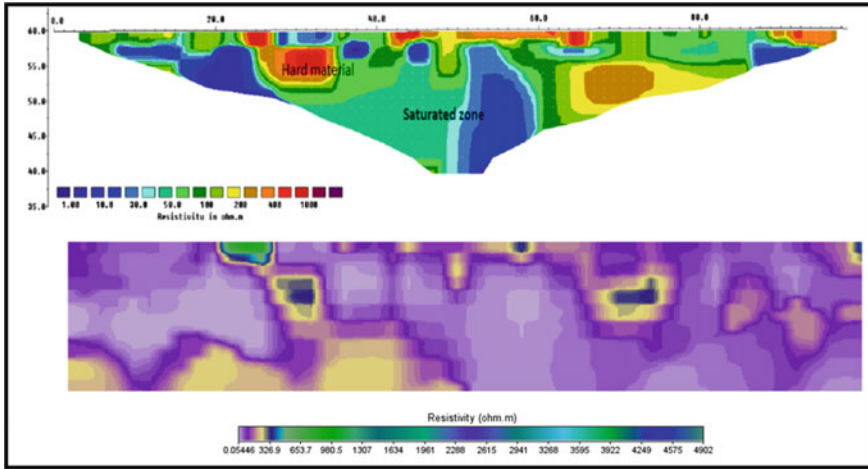
Fig. 5 2-D resistivity image versus 2-d voxler oblique image at line 4
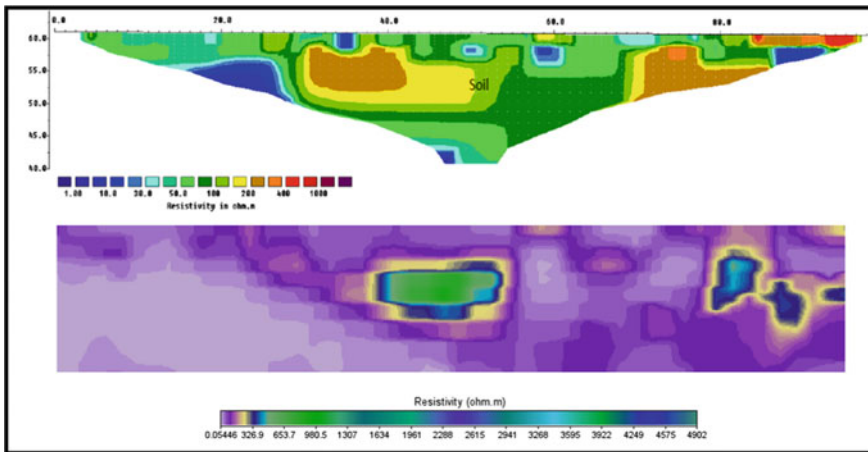
Fig. 6 2-D resistivity image versus 2-d voxler oblique image at line 5

as shown in the image. The resistivity values ranges from 50 to 200 Ω m defined as saturated sand and gravel or possibly clay sand and gravel mixture. Saturated zone was identified at several locations as shown in the resistivity image. Lying about 20 m in horizontal direction and 6 m in vertical direction, lies the largest blue color zone having resistivity values from 1 to 40 Ω m. The outer blue region is identified as fresh groundwater and the inner part is interpreted as water filled cavity.

3.2 Resistivity Image versus Voxler Oblique Image

Figures 2, 3, 4, 5, and 6 show the comparison of 2-D resistivity images with 2-D Voxler oblique images. Oblique images are the sliced images from the 3-D model. Generally, the model generated by Voxler Software shows similar profile to the image produced by Res2Dinv software. This is due to the fact that the Voxler used the *x*, *y*, and *z* values extracted from the resistivity image.

However, for the Voxler model, the data which were not provided from the resistivity method were interpolated using trilinear interpolation. As an example, for Line 1 (Fig. 2), the resistivity image only shows trapezoidal/triangle shape of the subsurface when the Voxler image shows rectangular shape. This means that the data which are not covered in resistivity were interpolated by the Voxler software to predict and estimate the subsurface profile where no original data points exist.

In terms of subsurface profile interpretation and classification, it is nonetheless easier to analyze using the 2-D resistivity image since it gives clearer color region compared to the oblique images. The interpretation of 2-D resistivity images will analyze the resistance distribution of areas of high resistivity (red–purple) and areas of low resistivity (blue).

3.3 Potential Cavity Identification and Volume Estimation

As mentioned earlier, the study was conducted to identify the potential cavities and determine its volume. The benefit of reimaging the inversion results in Voxler is that multiple data files may be viewed at one time. Viewing multiple data files gives the ability to see clearly the subsurface resistivity structure. The isosurface module can visualize the expected cavities area in 3-D form, where it gives clearer pictures of the sizes, shapes, locations, and extension of the cavities in the subsurface. The volume computation was calculated automatically by the software, fairly by setting the isovalue as desired. It was really fast and easy. After several research, analysis, and interpretation, the isosurface selected for potential cavity is less than 30 Ω m. Figure 7 shows the results of the isosurface model showing the potential cavities in the study area.

Fig. 7 The isosurface model showing the existence of cavities in the limestone area
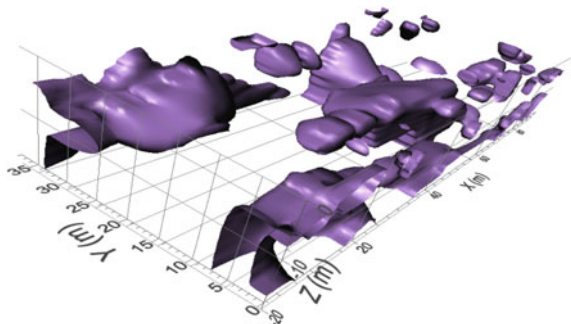
Table 2 Volume computation

The total volume of the survey area	61431.84 m^3
Volume of cavities in the survey area (resistivity values less than 30 Ω m)	10114.95 m^3
Percentage of cavities in the survey area	$= \dfrac{10,114.95 \text{ m}^3}{61431.84 \text{ m}^3} \times 100$ $= 16.47\%$

From the isosurface model, we can identify the potential cavities that lie in the subsurface between Line 1 and Line 5. However, since Line 3 and Line 4 have 31 m distances between each line, the Voxler loses lot of input data for that particular area so it needs to interpolate and predict the data. This may lead to inaccuracy since we know that the nature of subsurface may differ even in 1 m, especially in limestone areas. However, the limitation was that the resistivity line could not be arranged nearer due to an existence of building on top of the ground. According to the iso-surface model, the largest cavity volume can be found 5 m from the surface until 20 m depth at 35–60 m horizontally. It is located 10–20 m in y direction, in between Line 3 and Line 4. Another large cavity can be seen 5–20 m depth, 5–30 m in horizontal direction, and 20–35 m in y direction, where it lies in between Line 3 and Line 5.

Based on the volume calculation, the total volume for the subsurface profiles involved is about 61431.84 m^2. The predicted potential cavity volume is 10114.95 m^3 where the isosurface selected is 30 Ω m. In overall, the cavity covers 16.47 % of the total volume of the survey area. The table below shows the volume computation (Table 2).

4 Conclusions

The results presented in this paper illustrate that the subsurface profile of the selected study area can be successfully analyzed and determined from 2-D resistivity images, including identification of potential cavities and voids. The 3-D images were successfully modeled from 2-D resistivity data. The 2-D resistivity images and 2-D oblique images (sliced images from 3-D model) show similar subsurface profile. This indicates that the Voxler software is suitable and flexible to model the 2-D resistivity images to 3-D images. Isovalue of less than 30 Ω m was selected and it indicates the presence of potential cavities. This study was also able to provide volume calculation for the predicted cavities using Voxler software. This software helps user in estimating the volume by setting the isovalue where the software will automatically calculate the volume of cavities required. The predicted potential cavity volume is 10114.95 m^3.

References

1. Farooq, M., Park, S., Song, Y.S., Kim, J.K., Tariq, M., Abraham, A.A., 2012. Subsurface Cavity Detection in a Karst Environment Using Electrical Resistivity (ER): A case study from Yongweol-ri, South Korea. *Earth Sciences Research Journal, Vol.16, No.1, June,* pp. 75–82.
2. Ramakrishna, A., 2011. Characterization of Karst Terrain using Electrical Resistivity Imaging Technique. *Geo-Frontiers 2011 © ASCE 2011,* pp. 2514–2523.
3. Wisen, R., Christiansen, A. V., Dahlin, T. & Auken, E., 2008. Experience of Two Resistivity Inversion Techniques Applied in Three Cases of Geotechnical Site Investigation. *Journal of Geotechnical and Geoenvironmental Engineering © ASCE,* pp. 134: 1730–1742.
4. Golden Software. [Online] Available at: http://www.goldensoftware.com/products/voxler
5. ABEM, 2014. *ABEM*. [Online]Available at: http://www.abem.se/

Case Study on Geophysical and Geotechnical Assessment on Rock Subsurface: Road Construction

Haryati Awang and Sabira Abdul Samad

Abstract Most of the site investigation (SI) works for geotechnical design parameters are still using conventional methods such as borehole drilling, mackintosh probe, hand auger and others. For projects at hilly, marshy and jungle areas, site investigation work is harder to implement because of the difficulty in getting water resources, oil, food and others. Also, soil profile interpretation by borehole data sometimes cannot determine the location and size of boulders. Combination of two types of tests, borehole drilling and 2D electrical resistivity test, is able to get more accurate ground profile and the location of boulders and bedrock level can be determined. This will help engineers to design accurately and minimize other risks, avoiding under estimation project cost and thus, construction could be completed according to plan. This paper presents finding of a study that was carried out in rock subsurface material. The main objective is to compare subsurface profiles between resistivity and boreholes. The results showed that the resistivity image allows large areas to be covered in a short period of time whenever borehole results are limited to a single point. Besides that, borehole drilling cannot be implemented in all areas due to difficulty in mobilization of drilling machine as the study area is in hilly areas and high cliff. The resistivity image and boreholes profile give alike result. However, the result shows some irregularities due to several aspects, namely, level of ground water table where the water table is high and the resistivity is low. Resistivity image has to compliment with advancing boreholes for interpretation as the range of resistivity value to differentiate the material is very wide. Also, in order to identify relationships between resistivity and engineering properties a correlation between resistivity value and SPT N-value was developed.

H. Awang
Institute of Infrastructure Engineering & Sustainable Management, Faculty of Civil Engineering, Universiti Teknologi MARA, 40450 Selangor, Shah Alam, Malaysia
e-mail: harya406@salam.uitm.edu.my

S.A. Samad (✉)
Faculty of Civil Engineering, Universiti Teknologi MARA, 40450 Selangor, Shah Alam, Malaysia
e-mail: sabira@jkr.gov.my

1 Introduction

Most of the site investigation (SI) works for geotechnical design parameters are still using conventional methods such as borehole drilling, mackintosh probe, hand auger and others. For projects at hilly, marshy and jungle areas, site investigation work is harder to implement because of the difficulty in getting water resources, oil, food and others. The mobilization is also complicated and the cost to perform the SI work usually is a bit higher. Moreover, site clearance has to be made in hilly and jungle area and as for swamps and sea area, staging or pontoon is required for machine setup.

The most troubling example of the construction at rock formation is the actual position of boulders or bedrock is usually unknown. Soil profile interpretation depends on the designer. If the borehole results obtained indicate no boulders or bedrock, designer will prepare design and construction drawings without taking into consideration about the boulders, such as allocating extra cost for blasting works. In the event of work that requires piling works, designer might choose the wrong type of piles. RC pile or spun pile is only suitable/can penetrate at the area that has cobbles not more than 100 mm in size. More than this, the pile has a potential to fail. The best piles chosen for rock formation that has boulders are borepile and micropile, but borepiles are limited to boulders size not more than 1000 mm [1]. Figure 1 shows some piling problems in rock formation.

Apart from geotechnical consultant, many contractors or consultants still did not include SI costing in project estimation. Too little or none SI cost will increase costs of construction, such as variation order (VO) and extension of time (EOT). More SI work will reduce the total cost of project and cost of construction. However, too many SI work does not give any changes in design and cost of construction but will
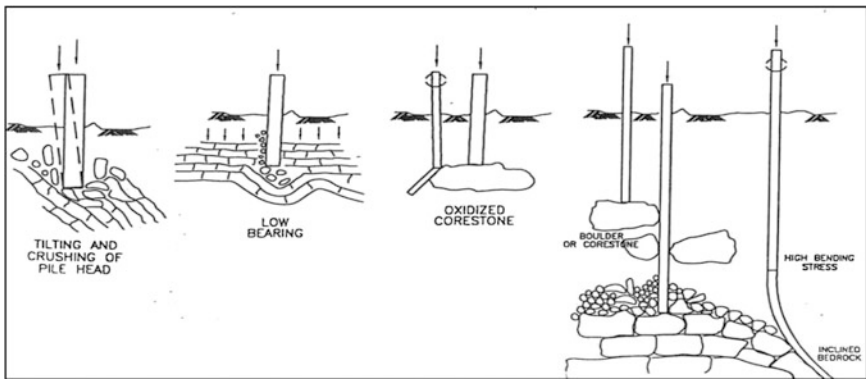
Fig. 1 Piling problems in rock formation [1]

only increase the total cost of construction. That is why it is critical to plan and allocate relevant amount for SI work, according to the project necessity.

2 Study Area

2D electrical resistivity test was conducted at a road project from Kampung Chennah to Kampung Esok started from Chainage CH3775 to CH9045. For this study, resistivity data were collected from CH8675 to CH9045 together with ten
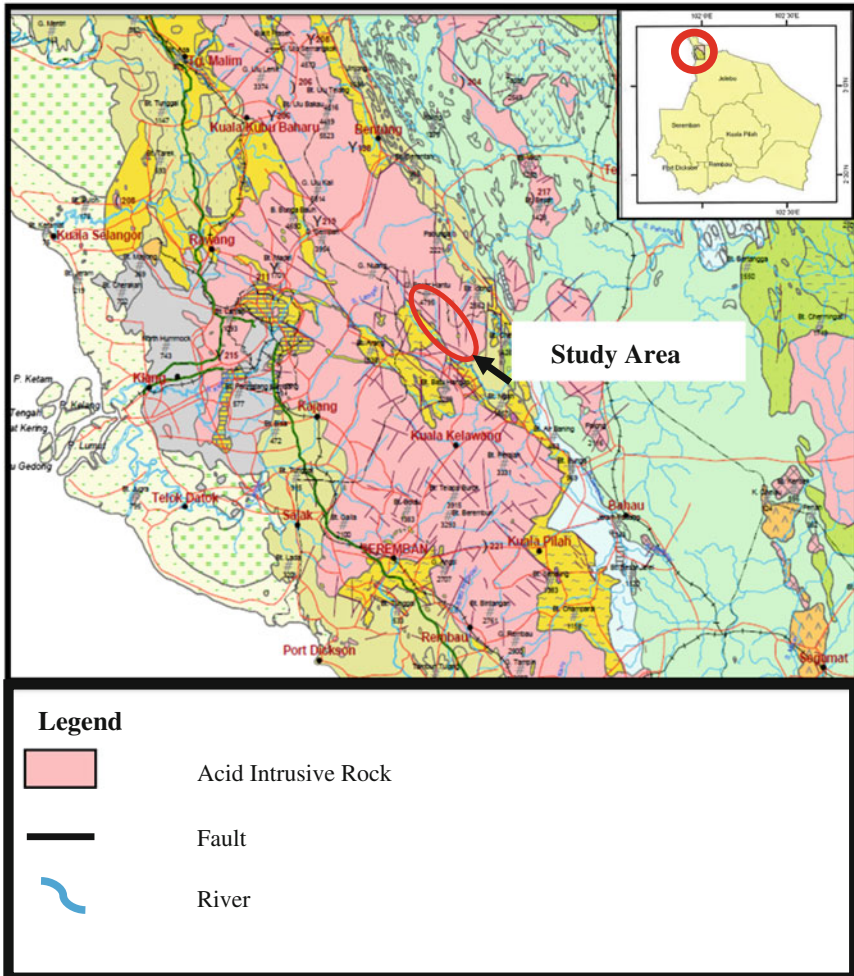
Fig. 2 Geological map of Peninsular Malaysia (Mineral and Geoscience Department 1985)

borehole drillings, which were located on that chainage, namely, ABH1 until ABH10. Figure 2 shows the geological map of the study area. Geologically, this area is founded by granite bedrock of acid intrusive rock class. A few fault lines strike the rock formation. The study is located at the northern town of Kuala Kelawang, a district of Negeri Sembilan State where the site is on hilly and high cliff. A new road is to be constructed through this village.

3   Subsurface Exploration

Geophysical and geotechnical testings are two ways of subsurface exploration. In this study, geotechnical testing used is borehole drilling and geophysical testing is electrical resistivity test.

The objectives of borehole drilling are to obtain geotechnical information at the site, to obtain disturbed and undisturbed soil sample, to determine the physical parameters of the soil, to obtain shear strength values on soft soil and to measure the ground water table at the site.

Electrical resistivity techniques are active geophysical methods as electric energy is directed into the ground through two electrodes and the potential difference is measured across a second pair of electrodes at suitable locations. These techniques are used extensively in the search for suitable groundwater sources [2]. In engineering surveys this technic was used to locate subsurface cavities, geologic strata, faults and fissures, permafrost, mineshafts [3]; to determine the suitability of the soil as foundation support for engineering structures [4]; and also to image underground geological structures [2]; in archaeology used for mapping out the areal extent of remnants of buried foundations of ancient buildings and direct detection of gem-bearing gravel [5]; and in geo-environmental engineering for detection and delineation of subsurface contaminants among many other applications [3].

4   Integrated Resistivity Survey and Geotechnical Properties

The integrated geophysical and geotechnical investigations carried out in this study are useful in characterizing the earth material. The geophysical results revealed the presence of four subsurfaces including topsoil, weathered layer, fractured basement and the fresh bedrock [4].

Electrical resistivity surveys have been used for locating and mapping buried gravel deposits since the 1950s. In general, the applicability of electrical methods to gravel exploration is based on the high resistivity of coarse-grained materials, in contrast to surrounding clay, silt or soil [6]. According to [4], the low resistivity

value composed of type of clay, sandy clay, clayey sand and laterite. Also, the electrical resistivity parameter is highly dependent on the porosity, water content and conductivity of the fluid and the percentage of clay minerals [5].

Resistivity value is correlated with grain size distribution. When grained size increases, the bulk resistivity of soil will increase. Below than ground water table, the soils are saturated and resistivity value is low [7].

5 Result and Analysis

5.1 Interpretation of Electrical Resistivity Image

A result of the resistivity survey at CH8675 to CH9045 is presented in image as shown in Fig. 3. The image was interpreted to describe the subsurface based on the range of resistivity value which is represented by each colour as indicated in Table 1.

In principle, low resistivity value indicates that the subsurface material easily allows electric current to flow through. As for example, water and soil with high moisture content have low resistivity value. Meanwhile, high resistivity value indicates that the subsurface material retards or hardly allows electric current to flow through. Rocks, dry sand, dry clay, compacted soil, coarse grained and air (void) have high resistivity value.
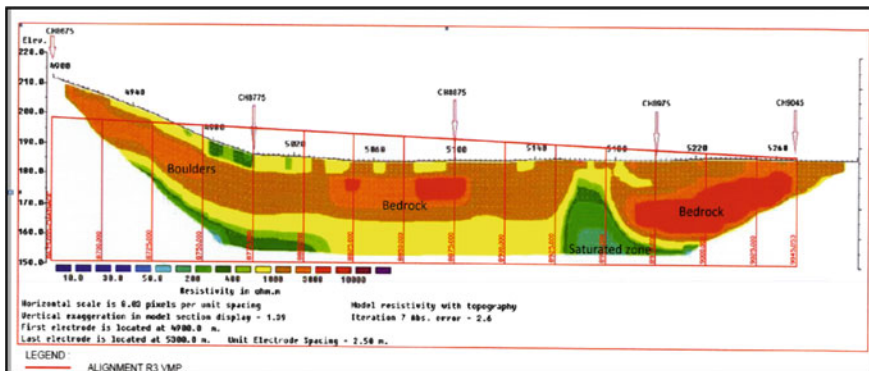
Fig. 3 Resistivity image of subsurface profile from CH8675 to CH9075

Table 1 Different types of soil with colour

Material	Saturated Zone	Soil	Hard material/Rock
Resistivity (Ohm.m)	<100	100- 500	>500

The resistivity image in Fig. 3 shows a subsurface profile of resistivity line from CH8675 to CH9075. The resistivity trapezoidal image covers reduced level from 190 to 155 m, approximately 35 m deep.

From CH8750 to CH8775 there is a pocket of soil materials which the value of resistivity ranges from 100 to 500 Ω m. It appears in the images as green colour. The depth of material is approximately 10 m below the existing ground level.

For the first 10 m depth along the resistivity line, it is found that resistivity value ranges fro m 500 to 2000 Ω m. Based on Table 1, the material is interpreted as hard material. It appears in the image as yellow colour.

From CH8675 to CH8750, CH8810 to CH8885 and from CH8960 to CH9045, the resistivity value ranges from 2000 to 10,000 Ω m. It appears in the images as orange and red colour, respectively. The materials can be interpreted as boulders, approximately 10 m thick due to the size and shape.

From the resistivity image, it is possibly a layer of boulder. The thickness of the boulder from the existing ground level is 20 m thick. It appears in the resistivity image as brown colour.

Below the boulders layer, the resistivity value ranges from 500–1000 Ω m. Based on Table 1, the materials are interpreted as hard materials.

Generally, the subsurface under this line is almost covered by boulder and hard layers. Boulders possibly exist between CH8675 and CH8800. Possible saturated zones were suspected to present around CH8950 at less than 20 m from the surface.

There are three significant types of material found which are hard layer (boulders), soil and rock identified by resistivity value. It was found that most of the subsurfaces were covered by high resistivity value (>500 Ω m).

5.2 Boreholes Profile

Soil profiles from 10 borehole drilling logs (ABH1–ABH10) were used for analysis. The sample and SPT were taken at every 1 m interval for the first 6 m depth and 1.5 m interval above 6 m. The detailed soil profile from ABH1 to ABH 10 as shown in Fig. 4 includes SPT N-value and ground water table.

Generally, most of the soils were identified as non-cohesive soil, boulders and rock. Soil profiles from ABH1 to ABH2 show that from the ground level to 5–6 m depth the soil can be described as hard soil with SPT N-value 50 and from 6 m depth and below, it is a weathered rock. In ABH3 and ABH4, rock was identified at layer 3–5 m. ABH4 represents soil with SPT N-value 50 below than the spotted rock. However, in ABH3 it has higher RQD value below the spotted rock but at level 10.8 m, the value of RQD decreases.

It shows that the soil profile was similar from ABH5 to ABH7. From ground level until 4–5 m depth, SPT N-value is smaller than 10; however, from 5 m depth, it drastically changes to hard soil with SPT N-value 50. At the depth of 10 m, rock was found with high RQD, showing similar profile as ABH 3. However, as the depth of drilling penetration increases, the value of RQD decreases.
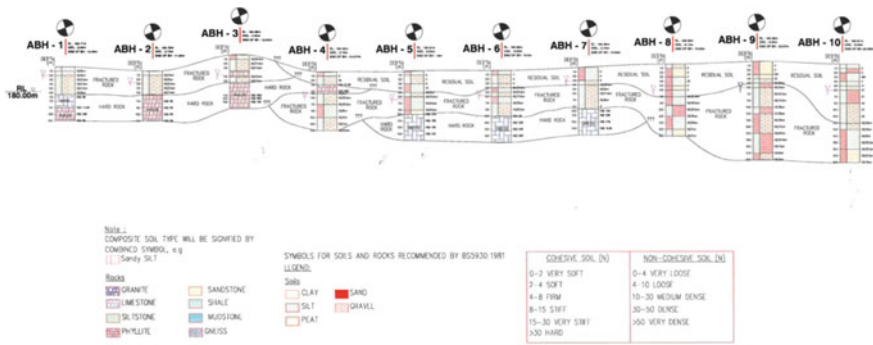
Fig. 4 Borehole profile from ABH1 to ABH10

For the first 5 m depth from ABH8 to ABH10, it was more or less 50 % of cohesive soil and 50 % of non-cohesive soil and some of gravel. The SPT N-value is less than 25. Below 5 m depth, it is identified as hard layer with SPT N-value 50 except in BH10 where hard soil started at depth 13.5 m. There is no rock founded in these boreholes.

From the soil profile generated from the ten numbers of boreholes, it was found that the major types of residual soil are gravels, silts and sand with SPT N-value less than 50. Since the value of SPT N-value of the soil materials is more than 50 (SPT N-value >50), it is categorized as fractured rock. All types of rock with rock quality designation (RQD) percentage ranges from as low as 0 to 80 % and it is categorized as hard rock.

5.3 Correlation Between Electrical Resistivity Image and Borehole Profile

Based on Fig. 4, the materials were classified into three types which are residual soil represented as green colour, fractured rock represented in yellow colour and hard rock represented in brown colour, and hence, Fig. 5 was generated. Level of ground water table shown in the figure plays an important role of resistivity value. Table 2 shows the colour range for simplified boreholes.

Figure 6 shows the comparison between soil profiles generated from boreholes with resistivity image to get clearer picture of the soil profile.

For better and clearer soil profile comparison, it was divided into four sections, namely, Section A, Section B, Section C and Section D, respectively. The comparison also being made based on depth.

Section A, having depth between 0 and 6.5 m with the resistivity value of more than 500 Ω m (yellow colour), is classified as hard material or rock. Soil profile generated from boreholes with SPT N-value >50 is showed as fractured rock
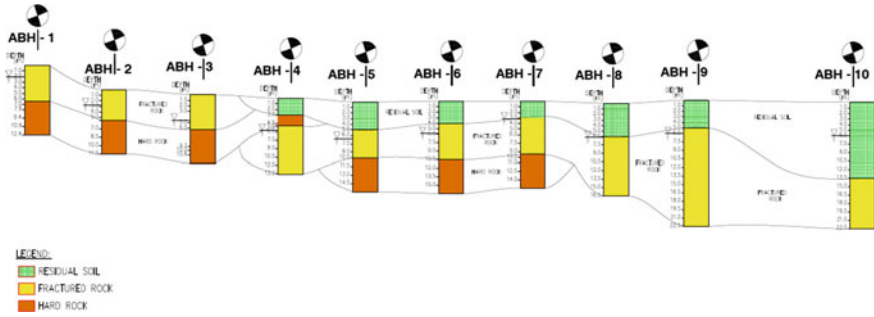
Fig. 5 Simplified borehole profile from ABH1 to AB10

Table 2 Colour range for simplified boreholes

Types of materials	SPT N-value/RQD %	Colour range
Residual soil	<50	Green
Fractured rock	>50	Yellow
Hard rock	Starting from 0 % RQD	Brown
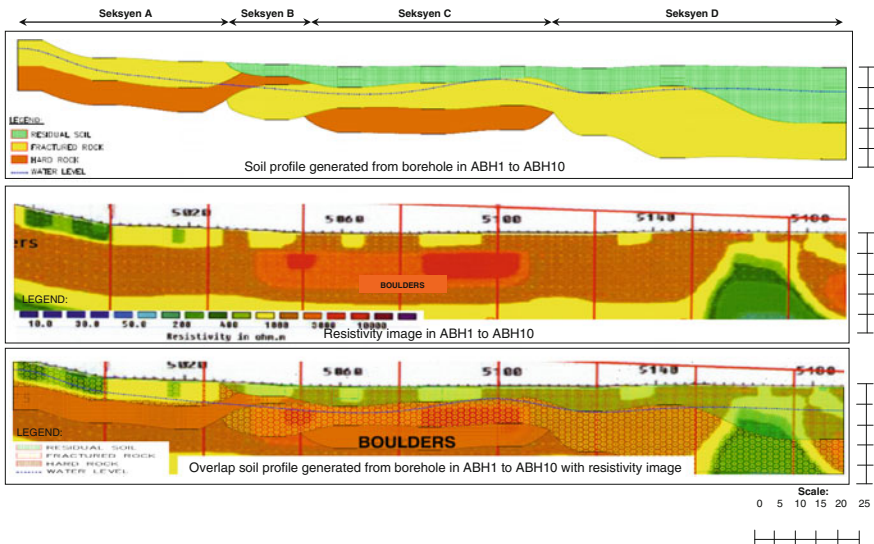
Fig. 6 Comparison between soil profiles generated from boreholes and resistivity image

(yellow colour). Both profiles show similarities. However, there is a pocket of residual soil that appears in resistivity image. This is maybe due to the presence of high water table at level 2 m. Underneath 6 m depth, both profiles show similarity, which is classified as hard rock.

While for Section B, soil profile generated from boreholes shows a residual soil (green colour) at top 3 m. However, resistivity image is showed as hard materials (yellow colour). The value of resistivity is maybe high because of lower table which is at the depth of 5.75 m, and thus the soil is in dry condition. Below 3 m depth, the resistivity value is shown as hard material or rock. Both profiles show similarity classified as a hard material or fractured rock. However, resistivity image cannot differentiate the type of material either hard material or rock. Since the resistivity image covers large area, therefore, the value of resistivity is taken in big range.

In Section C, for the first 5 m depth, borehole profile shows residual soil which contains silt, sand and gravel known as coarse grain soil. From particle distribution test, gravel is the dominant particle having SPT N-value less than 50. However, resistivity image shows hard material or rock with resistivity value more than 500 Ω m. Shallow ground water table might be the reason of the non-similarity where the level of ground water is 6 m. Below 6 m depth, it shows the similarity of both profiles, where it is classified as fractured rock (borehole profile) and hard material or rock (resistivity image). At 10 m depth, hard rock was found in borehole profile and it is similar to resistivity image.

In Section D, referring to borehole profiles, it represents as residual soil in varied depth between 5 and 13.5 m which contains sand and silt with some gravel, while the resistivity image shows that it is classified as hard material or hard rock. It is represented as hard material because of its materials and shallow ground water table (6 m). As it goes deeper, fractured rock and no hard rock are found in this section. In resistivity image, it shows that the deeper it goes, it is represented as residual soil. Both profiles show similar profile.

From Section A to Section D analyses, the overall summary of Kuala Kelawang formation is as classified in Table 3.

Referring to Table 3, the resistivity range of residual soil with SPT N-value <50 is 500–1000 Ω m. Fractured rock with SPT N-value 50 has resistivity value ranging from 500 to 3000 Ω m, while hard rock ranges from 500 to 10,000 Ω m.

Borehole data can determine types of soil and obtain design parameters. However, it could not produce accurate soil profile. This can be improved using electrical resistivity imaging where it can provide overall soil profile. Resistivity will provide results in wide range. Therefore, for interpretation works it could not be used independently. It really relies on boreholes result. Ground water table and soil material are among the most important aspects in resistivity interpretation.

Table 3 Summary of resistivity range in this study area

Types of soil	Resistivity value (Ω m)				
	Section A	Section B	Section C	Section D	Range
Residual soil (SPT < 50)	–	–	500	500–1000	500–1000
Fractured rock (SPT 50)	500	500–1000	1000–3000	500–1000	500–3000
Hard rock (RQD%)	1000–3000	500–1000	1000–10,000	–	500–10,000

Correlations of resistivity values and SPT N-values are not similar at different formations and areas. For example, in hilly terrain rock formation area, it has large resistivity range. Thus, the presence of fine grain could not been detected by the resistivity image. For saturated soil area, where it has high clay particles, the resistivity value range will be low due to high moisture content and it can be clearly seen in the image.

Resistivity could be used as guidance but could not be used directly for identifying material types and for design work. Result from boreholes is important in obtaining parameters for design work, supported by resistivity data for soil profile.

6   Conclusions

Based on the analysis and discussion done, the subsurface profiles between the resistivity and boreholes were successfully compared. The correlation of resistivity value and engineering properties such as SPT N-value is accomplished. The resistivity image and boreholes give alike result. However, the result shows some irregularities due to several aspects namely level of ground water table and soil grain. Where the water table is high and coarse grained, the resistivity is low. Resistivity image has to compliment with advancing boreholes as the range of resistivity value to differentiate the material is very wide.

References

1. Aik, I. N. C., 1998. Design and Construction of Pile foundations. s.l.:s.n.
2. Jung, Y., Ha, H. & Lee, Y., n.d. Application of Electrical Resistivity Imaging Techniques to Civil & Environmental Problems. *Use of Geophysical Methods in Construction.*
3. Yeung, A. T. & Akhtar, A. S., 2007. Use of a Circuit Simulator in Electrical Resistivity Analysis. *Innovative Applications of Geophysics in Civil Engineering,* Issue GSP164.
4. O., O. & Tolulope, O. T. H., 2014. Integrated geophysical and geotechnical assessment of the permanent site of Adekunle Ajasin University, Akungba Akoko, Southwestern, Nigeria. *Advances in Applied Science Research,* Volume 5(2):, pp. 199–209.
5. Chenrai, P., Charusiri, P. & Galong, W., 2010. One Dimensional Resistivity Sounding for Resolving Gem-bearing Gravel Layer: A Comparison of Sclumberger with Wenner Techniques at Bo Rai, Eastern Thailand. *Bulletin of Earth Sciences of Thailand.*
6. Abu-Hassanein, Z. S., Benson, t. C. H. & Blotz, a. L. R., 1996. Electrical Resistivity Of Compacted Clays. *Journal Of Geotechnical Engineering,* Volume 122, pp. 397–406.
7. Sudha, K., Israil, M. & S. Mittal, J. R., 2009. Soil characterization using electrical resistivity tomography and geotechnical investigations. *Journal of Applied Geophysics,* Volume 67, pp. 74–79.

Alternative Ground Improvement Solution with Polyurethane Foam/Resin

I.B. Mohamed Jais, M.A. Md. Ali and H. Muhamad

Abstract Polyurethane (PU) foam/resin consists of two categories namely, hydrophobic PU and Hydrophilic PU. Hydrophobic PU is water resistant whereby the liquid form reacts and expels water from the voids in the soil. Hydrophilic PU reacts with the presence of water to form a gel and hardens to form flexible PU. The use of PU foam/resin has been explored in Europe, Korea, and Japan since the soil condition is likely to expand as water seeps into the voids and creates fissures and fractures within the soil body. The PU foam/resin is injected into the voids to fill in the gaps and creates bonding effect to the soil particles, enhancing the strength and reducing the permeability significantly. In Malaysia, the behavior of partially saturated soil is complex where the presence of suction in the microstructure influences the shear strength behavior of the soil. However, when the soil becomes fully saturated, where the suction drops to zero, collapse settlement occurs, which cause voids to increase within the soil body. Grouting methods either compaction, hydro fracturing, permeation, or compensation are used to inject the PU foam/resin into weak subsoil, hence increase the engineering characteristics of the soil. The objective of this implementation is (i) to increase the bearing resistance of the soil without increasing the weight or overburden of the soil; (ii) to shorten the time of implementation and eliminate the excavation process. Based on the results, the engineering characteristics of the soil have improved and the bearing resistance has increased to the desired values. The in situ tests conducted also show that the PU foam/resin becomes impenetrable and the strength of the soil has improved significantly. This paper presents the cases where hydrophobic PU foam/resin was injected to enhance the engineering characteristics of different soil types.

I.B.M. Jais (✉)
Institute for Infrastructure Engineering and Sustainable Management (IIESM),
Universiti Teknologi MARA, Shah Alam, Malaysia
e-mail: ce_ismacahyadi@yahoo.com

M.A.Md.Ali · H. Muhamad
Progrout Injection Sdn Bhd, Shah Alam, Malaysia
e-mail: alistar_ent@yahoo.com

H. Muhamad
e-mail: hnsbersatu@yahoo.com

1 Introduction

Peninsular Malaysia is a tropical country experiencing variable soil conditions causing an increase in construction cost for treatment. The need for rapid solution of treatment, repair, and remediation for variable soil conditions was studied for the safety and economy of the project.

Polyurethane (PU) foam/resin injection is a technique of rapid ground repair and remediation without the process of excavation and replacement. The objective of this system is to remediate and repair problematic foundation soil by injecting lightweight polyurethane foam/resin at high pressure. This system consists of injecting hydrophobic polyol and isocyanate mix using hydraulic power packs into problematic subgrade producing polyurethane foam-resin, filling the void space during the expansion of the polyurethane foam-resin mix. This system reduces the time of setting and curing, eliminates the cost of excavation and replaces road subgrade. With recent issues relating to pavement defects, depression, and high maintenance cost, PU foam/resin injection provides an alternative to rapid ground remediation work, free from excavation and the foam can be produced within hours compared to conventional techniques.

1.1 PU Foam/Resin Characteristics

Polyurethane is a chemical name of a polymer within the carbamate groups (–NHCOO) and is referred to as urethane groups, in their backbone structure. Polyurethane is obtained by the reaction of a diisocyanate with macroglycol, a so-called polyol, or with a combination of a macroglycol and a short chain glycol extender. In the latter case, segmented block copolymer is produced. The macro-glycots are based on polyethers, polyesters, or a combination of both [1] as shown in Fig. 1.
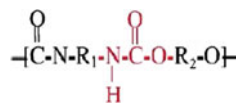
Fig. 1 The chemical structure of polyurethane, where R_1 represents the isocyanate structure, R_2 represents the polyol structure, and the urethane linkage is shown in *red*

Polyurethane (PU) foam is a cellular rigid solid polymer consisting of areas of PU polymer separated by voids [2]. PU foams may be discriminated in terms of their mechanical properties, if the samples are large enough. For example, large or bulk foam samples may be subjected to mechanical tests to determine the stress required to cause the material to fracture [3].

1.2 Types of PU Foam/Resin

There are two (2) types of polyurethane foam/resin namely, hydrophobic and hydrophilic polyurethanes. Hydrophilic polyurethane is not suitable for ground repair since this grout reacts with water, absorbs it, and cures to become flexible foam or gel. When it is in contact with water, the hydrophilic polyurethane only expands up to five (5) to seven (7) times from its original liquid volume.

Hydrophobic polyurethane is suitable for ground repair and remediation since the rate of expansion is six (6) to 20 times from its liquid volume. Yu et al. [4] refer hydrophobic polyurethane as foam where it has an accelerator to control the curing time. The advantage of using this foam is that it can expel water during expansion before it stabilizers the soil. Polyurethane is a lightweight material with high insulation quality, high expansion rate, quick reaction time and only uses a small diameter injection holes. Figure 2 shows the reaction of polyol and isocyanate to form PU foam/resin.

Fig. 2 After contact with water, liquid hydrophobic polyurethane grout expands up to 20 times (Joyce 1992)

2   Case History of PU Foam/Resin as Ground Remediation

Three (3) different locations were included in this paper to show their problems and what are the outcomes from the repair and remediation solutions. In situ and laboratory tests were conducted to determine the initial and remediated conditions after PU foam/resin injection was conducted. The soil samples before and after injection process were taken from site and tested for verification of the natural and modified properties of the soil.

2.1   *PETRONAS (Chemicals) MTBE, Gebeng, Kuantan, Pahang*

PETRONAS (Chemicals) MTBE, Gebeng, Kuantan, Malaysia was under siege, when 39 of their concrete sleepers supporting three (3) gas pipes were experiencing massive settlement due to inundation collapse of the fill as shown in Fig. 3. The solution was to inject lightweight polyurethane foam-resin that has sufficient strength and additional buoyancy effect, which could assist to support the sleepers. Therefore, three (3) injection points per sleeper were proposed, acting as artificial roots to support the existing structure, enhance the engineering properties of the soil and provide buoyancy to the ground with less overburden effect. The work was carried out less than two (2) months and settlement monitoring was conducted within the period of one (1) year. The borehole and soil profile are given in Fig. 4.

Fig. 3 PETRONAS (Chemicals) MTBE, Gebeng kuantan, Pahang

Section A-A   Section B-B
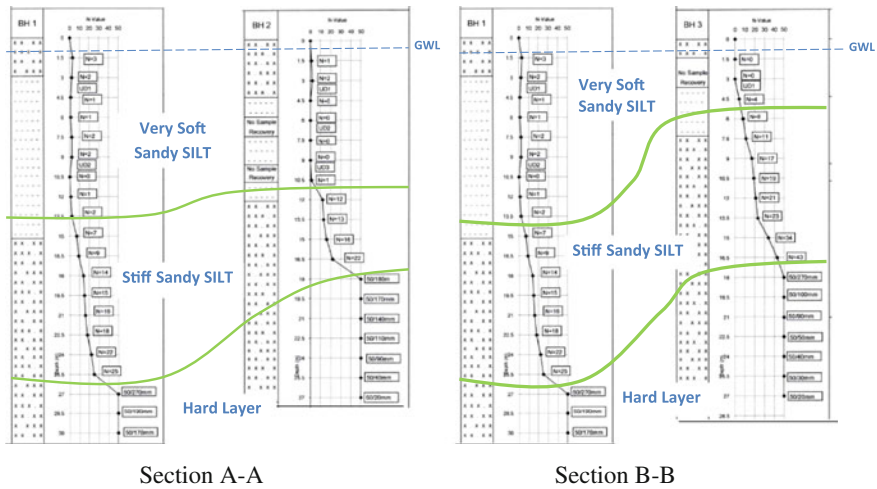
Fig. 4 Soil profile from borehole obtain at PETRONAS MTBE site

2.2   KM 88.78 Both Bound, North South Expressway, Ayer Hitam, Johor

A recent case history of approach settlement was also recorded at the North South Expressway, Ayer Hitam, Johor Bahru, Malaysia. At km 87.88 on the main line expressway, the transition zone between the fill and the slab embankments experienced massive depression causing riding discomfort to the expressway users. Therefore, this solution was adopted by the method of compensation grouting, increasing the bearing resistance and recompacts the existing soil with polyurethane foam/resin. With the injection of lightweight polyurethane foam/resin into the problematic foundation soil, there is no additional overburden pressure; and primary consolidation of the foundation soil was minimized.

2.3   KM 48.7 East Bound, Kuala Lumpur-Karak Expressway, Karak, Pahang

The heavy vehicle lane experienced massive depression for about 200 m stretch as shown in Fig. 5. Kuala Lumpur-Karak Highway was originally built in the 1970s by the government of Malaysia as an alternative for the winding, narrow Federal Route, which runs from Gombak in Kuala Lumpur to Bentong, Pahang. The highway included a 900 m tunnel at Genting Sempah, which became Malaysia's first highway tunnel ever constructed. The highway was officially opened to traffic in 1977. The project involves remedial works to be performed to rehabilitate the

Fig. 5 Depression of the
HMA pavement at km 48.7,
KL-karak expressway

settlement of the expressway by injecting polyurethane foam/resin into the ground,
increasing the strength of the surrounding soil and filling the voids that are present
due to scouring.

3 Proposed Injection Works and Testing Program

Based on the projects explained in the previous section, injection of expansion
foam/resin was used which is the dense polyurethane rapid (PUR) for densification.
Blowing agent was incorporated into the resin to ensure the expansion factor could
reach up to 15 times. However, additional agent (nitrogen based catalyst) was added
to improve the expansion of the foam.

Curing time of the expansion foam starts about 15 min after each injection and
the packer was removed. The holes were then grouted with cementitious mortar.
Any diffused and spilled PUR were removed from the points and backfilled with
suitable material. Figure 6 shows a typical injection procedure implemented on one
of the sites mentioned above. The methods of injection introduced are

Fig. 6 Typical injection
procedure using hydraulic
power packs

- Drilling of the hole for installing the packer was conducted using mechanical drill with drill bit of 32 mm diameter. Depth of the hole varies for various sites from the ground surface.
- The Depth of drilling was inspected by measuring the penetration of the drill bit.
- The packers of 32 mm diameter were installed together with the mixing head.
- Installation of packer was then incorporated.
- A metal tubing for resin to flow in the horizontal and vertical directions was installed.
- Dense PUR part A and part B were used with mix ratio of 100/100. Both parts were injected simultaneously to obtain the proper expansion.
- Hydraulic or pneumatic two part pumping unit with proper ratio were used for densification and uplifting.
- Injection of PUR commenced after all connections were securely tighten and continuously pumped until reaching various PSI of pressure depending on the ground conditions.
- Diffused PUR was then removed after fully set and holes were then grouted with cementitious mortar.

Typical method employed is tabulated in Table 1 for determining the geotechnical assessment of the rehabilitation works include:

- Collection of soil sample—this method includes sample extraction and in situ probing. The soil samples were then taken to the laboratory for testing.
- Laboratory test and analysis—this method includes testing of natural soil and remediated soil samples obtained from site for physical properties, strength, and compressibility.

Table 1 Typical test program for classification and engineering properties

No.	Types of tests	No of samples
1	Moisture content test (3 spc/set)	1
2	Particle density test (3 spc/set)	1
3	Sieve analysis	1
4	Hydrometer test	1
5	Atterberg limits (LL and PL tests)	1
6	Consolidated undrained triaxial test	1 (UD)
7	Unconfined compression test	2 (UD)
8	One dimensional consolidation test	2 (UD)
9	Cone penetrometer test[a]	4
10	Plate bearing test[b]	4

[a]Test conducted at PETRONAS MTBE, Gebeng, Kuantan, Pahang only
[b]Test conducted at Ayer Hitam, Johor site only

4   Results of Remediation

Details of the results will be discussed in this section. The results included initial condition of the soil for each site and the laboratory test results obtained after the grouting was executed. In situ and soil sampling were conducted for both conditions, which are before remediation and after remediation of the three (3) sites, explained previously. The modified properties obtained are the strength, stiffness, compression characteristics, bearing resistance, and recorded settlement.

4.1   *Initial Soil Condition*

Table 2 presents the physical properties of the soil at three (3) locations described in the previous section. For Karak site, the soil was described as well graded silty gravelly SAND, whereas for Ayer Hitam and PETRONAS MTBE sites, the soils were classified as very silty gravelly SAND. It is interesting to note that there is significant clay content for Ayer Hitam and PETRONAS MTBE sites which can cause further depression due to the absorption properties of the clay.

The initial strength and compressibility characteristics of the soil from each site were also examined. Typically, the soil characteristics show similar behavior; therefore the strength and compressibility showed some resemblance as presented in Table 3. Since the coarse particles were dominant for the Karak site, the friction angle was high and the fill material was derived from the parent igneous formation present. For the PETRONAS MTBE soil sample, the compression index was very high due to the higher fines content. Therefore, if the sample was fully saturated, the capacity to expel water from the voids was more and could cause serious deformation if the fill was inundated.

Table 2 Initial soil characteristics from three (3) different locations

Soil properties	PETRONAS MTBE	Ayer Hitam km 88.78	Karak km 48.7
Gravel content	19.86 %	24.86 %	42.80 %
Sand content	40.69 %	40.25 %	51.20 %
Silt content	26.88 %	29.99 %	5.76 %
Clay content	12.58 %	4.90 %	–
Specific gravity	2.60	2.51	2.65
In situ moisture content	18.92 %	38.42 %	26.20 %
Liquid limit	44.0 %	31.0 %	–
Plastic limit	34.0 %	24.0 %	–
Plasticity Index	10 %	7 %	–
Consistency	Intermediate plasticity silt	Low plasticity silt	–

Table 3 Initial strength and compressibility characteristics

Site location	Strength characteristics				Compressibility characteristics			
	c (kPa)	c'	ϕ (°)	ϕ' (°)	e	P_c (kPa)	c_c	c_s
PETRONAS MTBE	35	0	17	19	0.96	180	0.919	0.006
Ayer Hitam km 88.78	35	0	17	19	0.91	85	0.103	0.107
Karak km 48.7	70	0	32	40	0.25	58	0.066	0.006

4.2 Modified Strength and Stiffness Using Unconfined Compression Test Before and After Remediation

Figures 7, 8 and 9 show the unconfined compressive strength conducted on the natural soil sample and the sample after remediation has taken place. During sample extraction, the soil is fully saturated since the water table is just below the crusher run. The natural soil specimens are designated as **NS** and the specimens extracted after the remediation process is designated as MS.

Based on the natural specimens extracted from site and tested in the laboratory, the maximum compressive stress observed was the specimen located in the middle of the sampling tube. This finding shows that the soil was compacted to the density specified but the top and bottom specimens experienced similar compressive stress as they were rather loose as presented in Table 4.

The unconfined compressive stress of the soil specimens after remediation has shown an increase of up to twice the stresses it can sustain. The soil behavior was slightly modified from an elasto plastic behavior to elastic brittle failure. Hence the
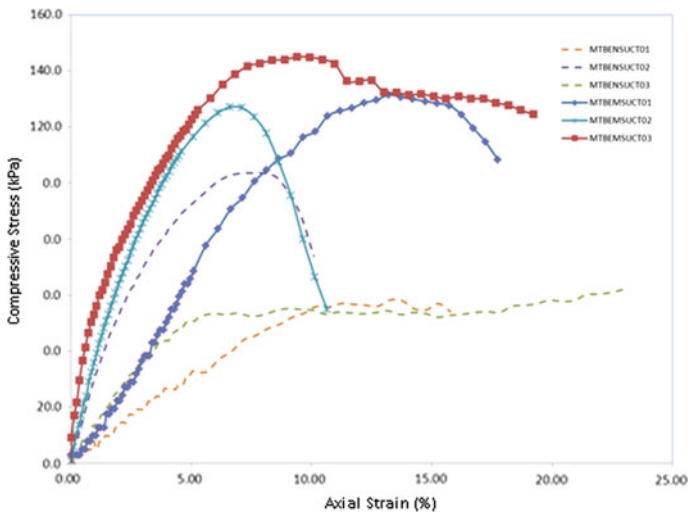
Fig. 7 Unconfined compressive stress of natural samples and samples after remediation obtained from PETRONAS MTBE site
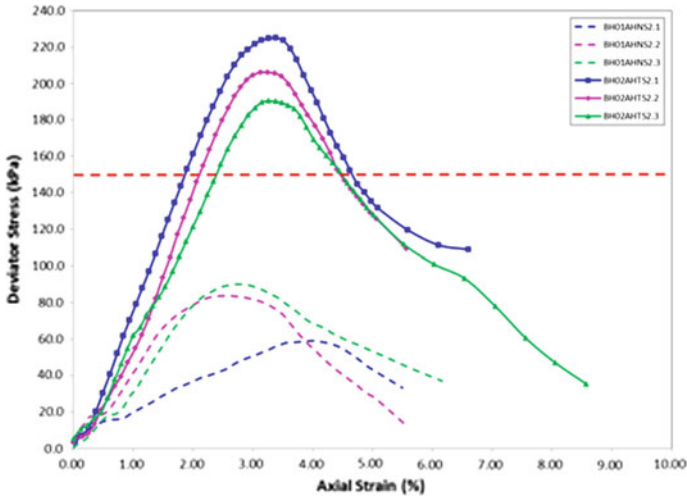
Fig. 8 Unconfined compressive strength of natural samples and samples after remediation obtained from Ayer Hitam km 88.78 site
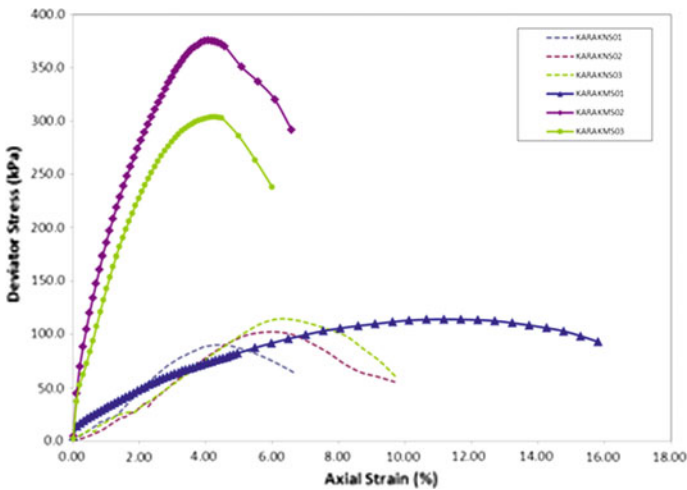
Fig. 9 Unconfined compressive strength of natural samples and samples after remediation obtained from Karak km 48.7 site

undrained shear strength of the natural soil was within loose state. However, when the PU foam/resin was injected into the ground, the undrained shear strengths have increased, which were within the medium state. Table 4 presents the natural and remediated soil strength properties obtained from the test for all three (3) sites. Though the PU foam/resin is lightweight, its additional stiffness property has modified the soil stiffness.

Table 4 Unconfined compression test data for natural and modified soils

Site Location	Sample no.	Unconfined compressive stress (kPa)	Undrained stiffness, E_u (kPa)	Strength classification
PETRONAS MTBE	NSUCT01	58.4	666	Loose
	NSUCT02	91.0	3,000	Loose
	NSUCT03	62.1	1,333	Loose
	MSUCT01	131.5	4,000	Medium
	MSUCT02	126	1,200	Medium
	MSUCT03	145	7,000	Medium
Ayer Hitam km 88.78	NS2.1	59.1	2,500	Loose
	NS2.2	83.7	5,000	Loose
	NS2.3	90.1	4,000	Loose
	MS2.1	225.0	8,000	Medium
	MS2.1	206.1	7,000	Medium
	MS2.1	190.4	6,667	Medium
Karak km 48.7	NS01	90.2	2,500	Loose
	NS02	102.3	2,000	Medium
	NS03	114.8	2,000	Medium
	MS01	114.4	2,500	Medium
	MS02	375.4	30,000	Dense
	MS03	303.6	25,000	Dense

4.3 Modified Compressibility Characteristics

Figures 10 and 11 illustrate the consolidation curve obtained from the oedometer test to determine the compressibility characteristics of the natural and remediated soils taken from the Ayer Hitam, km 88.78 and Karak km 48.7 sites. The soil has high void ratio and since the void spaces during consolidation were filled with water, therefore when water was expelled from the soil sample, massive volume change of the soil occurs, hence settlement was high as seen in most loose soils with the presence of significant fines.

The initial void ratio, e_o observed has reduced and the preconsolidation pressure obtained from Casagrande's method has a slight increase. This showed that the soil has significant reduction to the void ratio after the remediation process and a slight increase of the preconsolidation pressure. This was due the fact that the voids between the particles were cemented with the PU foam/resin, creating an additional bond, hence reducing the voids in the soil. Therefore, the remediated soil underneath the bituminous pavement has experienced lower compressibility characteristics since the voids were filled with PU foam/resin with a reduction of initial void ratio by almost 15 %.
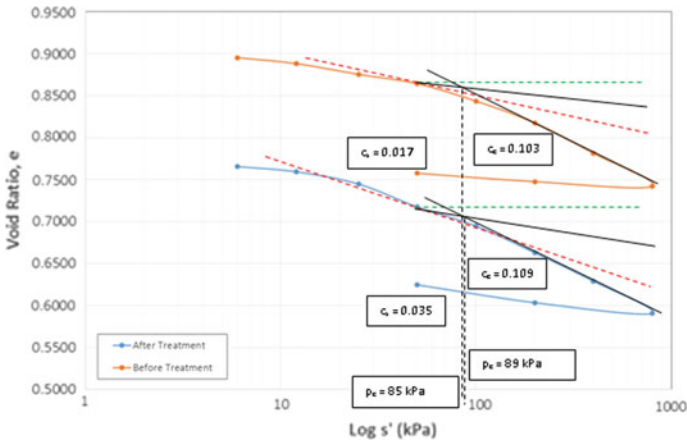
Fig. 10 Consolidation curve for natural and remediated soil samples obtained from Ayer Hitam km 88.78 site
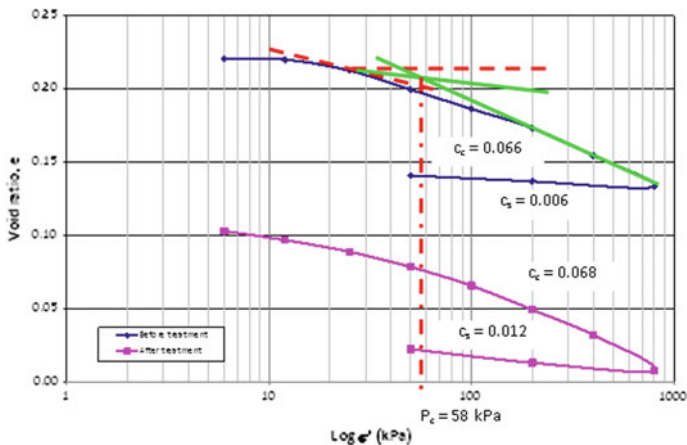
Fig. 11 Consolidation curve for natural remediated soil samples obtained from karak km 48.7 site

4.4 In Situ *Strength and Plate Bearing Test*

The cone penetrometer was conducted at PETRONAS MTBE site after sample extraction next to the borehole to determine the in situ strength of the soil after injection of the PU foam/resin. The length of the cone penetrologger rod is 800 mm therefore at natural condition, the cone penetrologger managed to penetrate down to 800 mm. Point 1 represents the cone resistance for borehole at natural condition whereas point 2 represents the cone resistance for borehole modified with PU foam/resin. Figure 12 shows the results for the test where at point 1, the cone
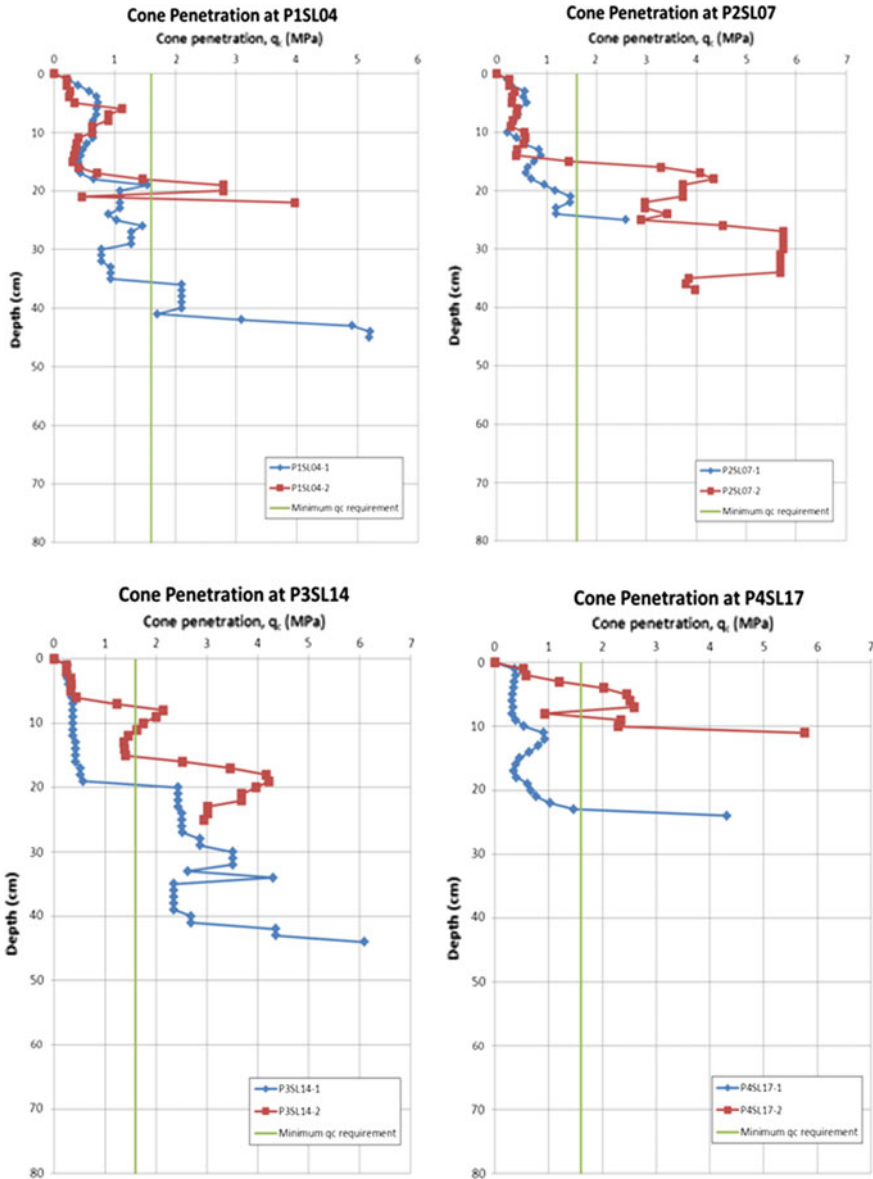
Fig. 12 Cone penetration from P1SL04 to P4SL17 at PETRONAS MTBE site

penetrologger can be easily pushed into the borehole. However, once the soil has been injected with PU foam/resin; the cone penetrologger has difficulties in penetrating into the modified soil.
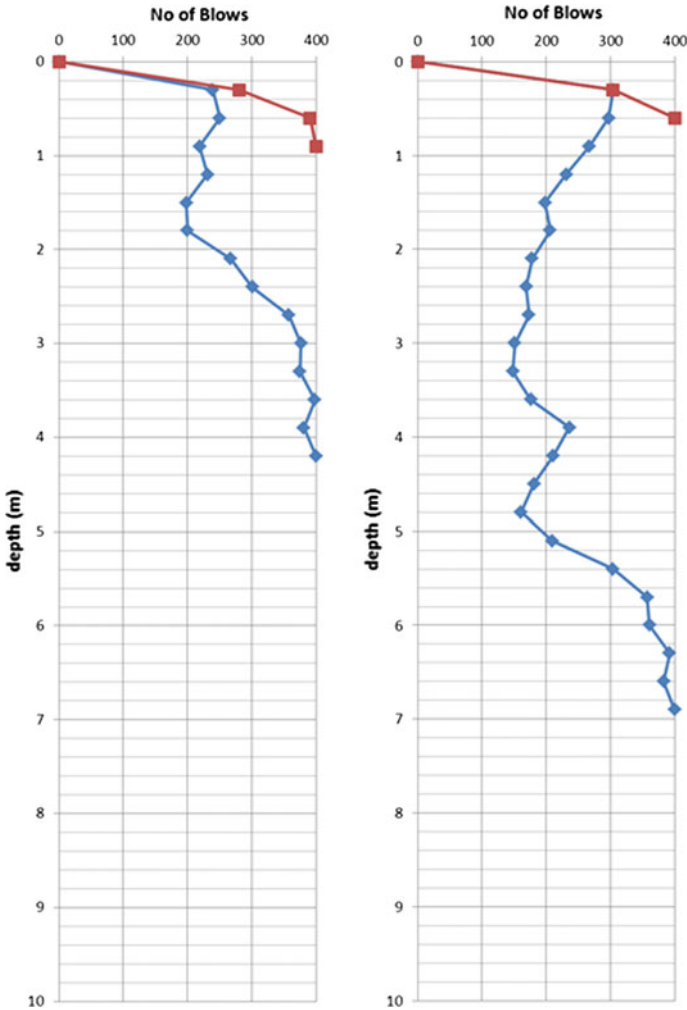
Fig. 13 JKR/Mackintosh probe before and after remediation using PU foam/resin at Karak km 48.7 site

JKR/Mackintosh probe was conducted after sample extraction based on the MP location proposed to determine the in situ strength of the soil after modification using PU foam/resin at Karak km 48.7 site. Figure 13 presents the JKR/Mackintosh probing with respect to depth. From the plots for before and after injection, it was seen that the number of blow counts per 300 mm penetration was more than 300 after PU foam/resin injection. These plots showed strength increase of the sub grade before 600 mm, whereas before injection, the JKR/Mackintosh probe could penetrate easily until it reached 100 numbers of blows to a maximum depth of 9 m BGL. This proves that shallow injection of PU foam/resin could restabilize and

Fig. 14 Displacement against
bearing pressure for North
and South bounds of the Ayer
Hitam km 88.78 expressway
before and after remediation

Fig. 14 Displacement against bearing pressure for North and South bounds of the Ayer Hitam km 88.78 expressway before and after remediation
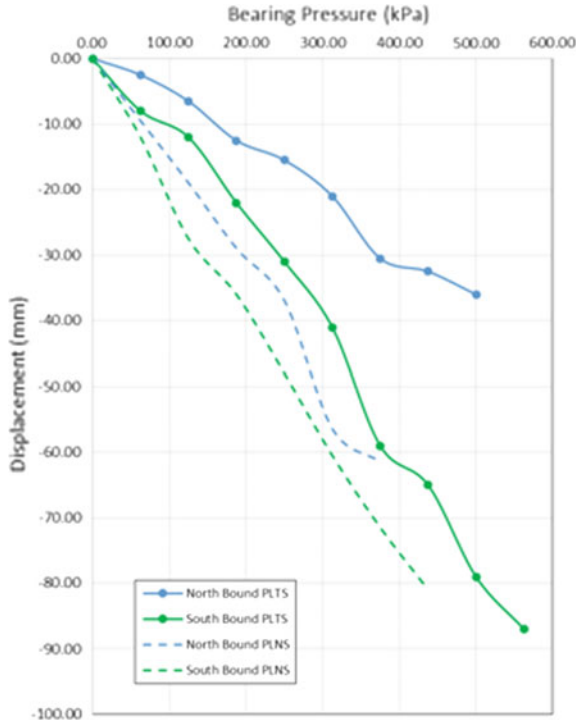
restrengthen the sub grade layer which has experienced massive depression in the past.

The plate loading test was conducted for both bound before and after remediation at Ayer Hitam km 88.78 site. This test was to determine the bearing pressure that the soil experience in its initial state and after remediation has taken place. The test on both bounds was designated as PLNS indicating plate loading on natural ground conditions whereas PLTS indicates plate loading on treated ground conditions. The bearing pressure increases for north and south bounds as shown in Fig. 14. For 40 mm criteria in coarse fill material, the bearing pressures increased to more than twice (2) the criteria set by the public works department (PWD) of 150 kPa.

5   Conclusions

From the in situ and laboratory tests conducted on the samples of natural and remediated soils taken from the PETRONAS MTBE, Ayer Hitam km 88.78 and Karak km 48.7 remediation sites, it can be concluded that:

- the strength and stiffness of the fill have increased and the fill has been rehabilitated to ensure that volume change of the modified soil or settlement can be reduced, and hence increases the bearing pressure of the foundation layer.
- the compressibility characteristics have also increased and void ratio has reduced significantly. This shows that the PU foam/resin has filled part of the void consisting of air and water, thereby enhancing the compressibility characteristics of the problematic sub grade.
- the PU foam/resin is water repellent; therefore the roots flow into the void space filled with water, hence pushing the water out of the voids during injection.

References

1. Chun, B. & Ryu, D, "A study on application of polyurethane injection material for ground improvement", 4, 2000, pp 113–118.
2. Gibson, L. L. & Ashby, M. F., "Cellular solids. Structure & properties". Pergamon Press, Oxford 1988.
3. Callister, William.D, "Material Science and Engineering", 7th edition, 2007.
4. Yu, L., Wang, R. & Skirrow, R, "The application on polyurethane grout in roadway settlement issues". Geo Montreal, 2013.

Evaluation of Physical and Mechanical Properties of Tsunami Deposit Soils

Yuta Tada, Nozomu Kotake and Minoru Yamanaka

Abstract An enormous amount of disaster debris was generated by the 2011 Great East Japan Earthquake. The tsunami deposit soils have not been effectively utilized for earthworks because they contain wood chips and other organic materials mixed in the treatment process although the post-earthquake revival has been strongly required. In this study, physical and compaction properties of the sampled tsunami deposit soils were investigated, and large-scaled direct box shear tests were conducted for the purpose to evaluate the applicability of the soils as earthwork material. In order to assess the influence of inclusion of wood chips, two types of soil were prepared for the mechanical tests: one was "wood-chip mixed soil" that was sampled from the sites and another was artificially made "wood-chip removed soil." It was seen from the compaction test results that the maximum dry density clearly increased by removal of wood chips. However, a clear effect of removing wood chips did not appear in the shear strength obtained from the direct shear test results while deformation characteristics were somehow improved.

Keywords Tsunami deposit · Wood chip · Direct shear test · Compaction properties

1 Introduction

An enormous amount of disaster debris was generated by the 2011 Great East Japan Earthquake. The amount of disaster debris was estimated to be about 23 million tons and had passed to a very wide area across six damaged prefectures. In some tsunami-flooded areas, marine sediments were left onshore after the inundation

Y. Tada · N. Kotake (✉)
Department of Civil Engineering, National Institute of Technology,
Kagawa College, 355, Takamatsu, Kagawa 761-8058, Japan
e-mail: kotake@t.kagawa-nct.ac.jp

M. Yamanaka
Faculty of Engineering, Kagawa University, 1-1, Takamatsu,
Kagawa 760-8521, Japan

phase, and are referred to as "tsunami deposits." The amount of the tsunami deposits was estimated to be approximately 11 million tons. Separation treatment of tsunami deposits ended in all areas except Fukushima in March 2014, and the large amount of soil fraction, hereafter referred to as "tsunami deposit soil," were kept at temporary stockyards. Figure 1 shows the status of temporary storage of tsunami deposit soils in Iwate and Miyagi Prefectures as of March 2014.

Ministry of the Environment published "Guideline on the Treatment of Tsunami Deposits" [1] that promoted a policy of effective utilization of tsunami deposits as earthwork materials for reconstruction. Also, research studies have been carried out on the physicochemical properties of the tsunami deposit soils (ex. [2, 3]). Then, a part of the tsunami deposit soils had been already used for construction of embankments and others applications. However, most of the tsunami deposit soils have not been effectively utilized as earthwork materials. The primary reason is that they contain wood chips and other organic materials mixed in the treatment process, and that the size of contained wood chips and mixture degree differs depending on separation method. In addition, the tsunami deposit soils are different physically from site to site due to the difference of the original soil properties, and the influence of wood chips on the mechanical characteristics of soils has not been known. Therefore, in the present situation as described above, the use of tsunami deposit soils for post-disaster reconstruction has been rather difficult.

In this study, for the purpose to examine the applicability of tsunami deposit soil as earthwork material, the soil properties and compaction characteristics of sampled soils were examined, and the shear strength characteristics were evaluated by large-scaled direct shear tests in relation to the effect of contained wood chips.

2 Soil Properties of Tsunami Deposit Soils

In the present study, soil samples were collected from five tsunami-damaged areas in Iwate and Miyagi Prefectures. The soils were separated by sieving from tsunami deposits that were collected from damaged areas. They were considered to be classified into ordinary soils because they had relatively small fraction of other mixed materials according to the manual published by the local government [4]. Figure 2 shows an example of sampled tsunami deposit soil, and Fig. 3 shows contained wood chips larger than 2 mm.
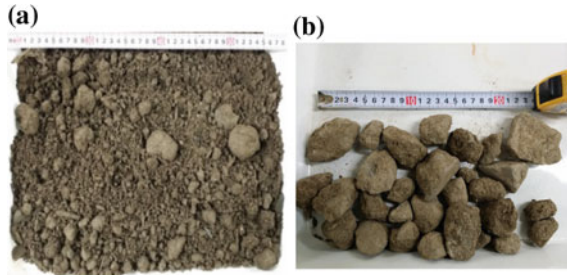
Fig. 2 Example of tsunami deposit soil (Soil C), **a** sampled soil, **b** contained gravel

Soil A Soil B Soil C

Fig. 3 Contained wood chips

Determining the engineering properties of the tsunami deposits is important to ensure the stability of geotechnical structures. Table 1 summarized soil properties obtained from soil tests on five samples, A to E. The specific density of soil particle was in a range similar to that of ordinary soils while a couple of them were slightly smaller possibly due to the contained wood chips.

Figure 4 shows grain size distribution curves of the sampled soils. The maximum grain size of the soils ranged from 19 to 37.5 mm, and coefficient of uniformity $U_c = 39$–228 and curvature coefficient $U_c' = 0.5$–5.1. All of the soils were classified into sand with fine fraction {SF} in triangular diagram (JGS0051) [5]. Considering the physical soil properties as described above, the sampled tsunami deposit soils seem to belong to the category of geomaterials suitably used for earth works.

The wood chips contained in the tsunami deposit soils had been mixed with soils during the process of collecting and carrying, and not able to be removed in the treatment process by sieving. The wood chips as seen in Fig. 3 were the mixture of 4–5-cm-long, slender small fragments derived from wood building materials, small parts of plant roots, and other organic materials.

The wood chip contents of more than 850 μm and 2 mm were in the range of 0.3–1.3 % and 0.1–0.9 %, respectively, as shown in Table 1. The distribution of wood chip content for each sampled soil was examined by sieve analysis using 850 μm to 37.5 mm sieves. Here, the wood chip content was defined as the percentage of the dry weight of wood chips to that of the respective tsunami deposit

Table 1 Soil properties of sampled tsunami deposit soils

Soil property	Soil sample				
	A	B	C	D	E
Soil particle density ρ (g/cm^3)	2.62 (2.68)*	2.59 (2.63)*	2.58 (2.64)*	2.53	2.65
Maximum grain (mm)	19.0	26.5	37.5	19.0	19.0
Gravel fraction (%)	17.1	26.1	30.9	11.1	36.7
Sand fraction (%)	51.5	46.9	40.7	55.3	39.4
Fine fraction (%)	31.4	27.1	28.5	33.7	23.9
Uniformity coefficient U_c	216.7	160.5	76.2	38.7	227.3
Coefficient of curvature $U_{c'}$	5.1	3.0	0.5	0.8	2.0
Soil classification	Sand with fine fraction	Sand with fine fraction	Sand with fine fraction	Sand with fine fraction	Sand with fine fraction
Ignition loss Li (%) 2 mm passing	6.3	9.4	11.8	9.4	6.8
9.5 mm passing	4.7 (3.7)*	5.3 (5.2)*	11.8 (10.7)*	–	–
Wood chip content more than 850 μm	0.40	0.80	1.29	0.29	0.57
more than 2 mm	0.31	0.61	0.88	0.13	0.46

*The values in () denote test results of wood-chip removed soils

Fig. 4 Grain size distribution
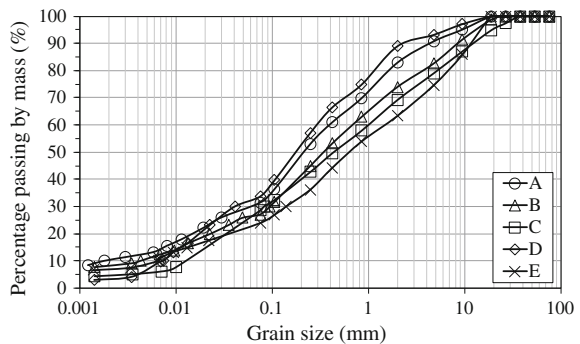
soil. Figure 5 shows the results of sieve analyses on wood chips. The results suggest that the wood chip contents differ from site to site due to the different processing methods and the properties of original soils.

Ignition loss is an index to express the content of organic matter including wood chips, and the soils with high content of organic matter are generally considered unsuitable for earthworks. It has been concerned that tsunami deposit soil may

Fig. 5 Results of sieve analysis on wood chips
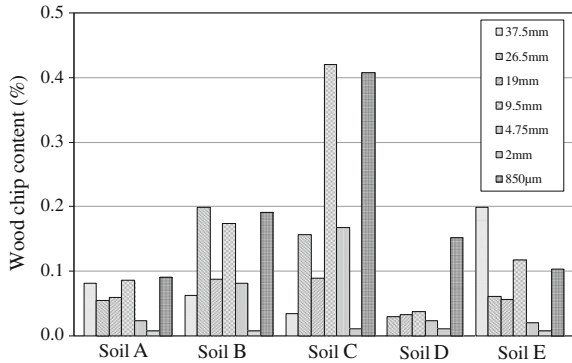
shrink in volume associated with decomposition of wood chips when used as embankments. Thus, ignition loss is one of the important factors to determine tsunami deposit soil since it can be used as an index of the potential of long-term settlement according to the local government manual [4]. Ignition losses under 650 °C (JGS0221) [6] were $L_i = 6.3–11.8$ % that were obtained from the five sample soils passing 2 mm sieve. In addition, the sample soils passing 9.5 mm were crushed to 2 mm particles and their ignition losses were tested so as to evaluate the effect of wood chip fraction with the size larger than 2 mm on the ignition loss. Ignition losses of sample soils passing 9.5 mm sieve were smaller than those of 2 mm as seen in Table 1 since the former had the resultant larger content of sand and gravel. Figure 6 shows the relationship between wood chip content and ignition loss. It is seen that the wood chip content was smaller than the ignition loss. Therefore, it can be estimated that the tsunami deposit soil contains small amount of organic matter that cannot be removed by sieving or manually.

Fig. 6 Relationship between wood chip content and ignition loss
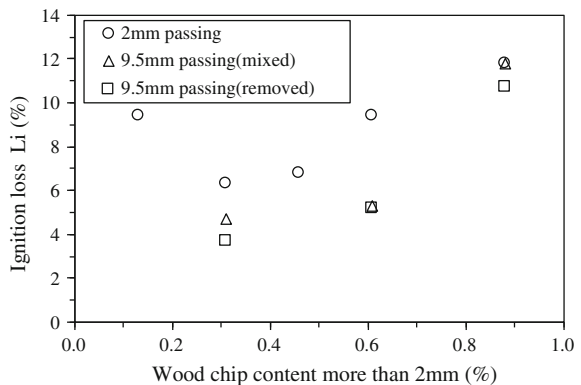
3 Compaction Properties of Tsunami Deposit Soils

3.1 Test Method

Procter compaction properties were examined on five sampled tsunami deposit soils (Soils A to E). Compaction test method was determined due to the allowable maximum grain size according to JIS A1210 [7]. That is, for the sampled soils (Soils A, D and E) having the maximum grain size less than 19 mm, a 10-cm-diameter mold and a 2.5 kg rammer were used and the soils were tamped 25 times per layer in 3 layers to complete compaction (A-a Method, JIS A1210). For the sampled soils (Soils B and C) having the maximum grain size greater than 19 mm and less than 37.5 mm, a 15-cm-diameter mold and a 2.5 kg rammer were used and the soils were tamped 55 times per layer in 3 layers (B-a Method, JIS A1210). In the present test, the water content of soil was adjusted by drying at a constant temperature of 40 °C in an incubator when decreasing, and by adding water and leaving for more than 12 h so as to make the wood chips absorb water when increasing.

3.2 Sampled Soils (Wood Chip Mixed Soils)

Compaction curves obtained from the compaction tests on five sampled soils are shown in Fig. 7, and the maximum dry density ρ_{dmax} (g/cm^3) and the optimal water content w_{opt} (%) are shown in Table 2. It is seen that the shape of the compaction curves seems to be relatively flat, and that the maximum dry density varied widely $\rho_{dmax} = 1.44$–1.82 (g/cm^3) although the sampled soils were classified into the same category, i.e., sand with fine fraction.

Fig. 7 Compaction curves of sampled tsunami deposit soils
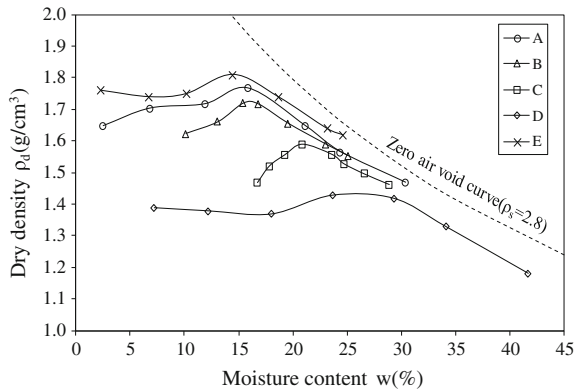
Table 2 Results of compaction tests on wood-chip mixed soil

Soil	A	B	C	D	E
Method	A-a	B-a	B-a	A-a	A-a
ρ_{dmax} (g/cm^3)	1.769	1.722	1.592	1.442	1.817
W_{opt} (%)	16.2	16.2	21.4	25.7	15.3

3.3 Effects of Wood Chip Removal

In the present study, for the purpose to examine the effects of wood chip inclusion on the engineering soil properties, the "wood-chip removed soils" were made by processing the grain size less than 19 mm and removing wood chips more than 2 mm by sieving and picking out manually for three sampled soils from A to C. The compaction test results of the wood-chip removed soils are shown in Table 3. Figure 8 shows compaction curves of the wood-chip removed soils in comparison with the respective sampled wood-chip mixed soils. The clear tendency is observed that the maximum dry density ρ_{dmax} increased and the optimal water content w_{opt} decreased due to wood chip removal in each soil. Particularly, Soil A showed a large increase in maximum dry density. On the other hand, relatively small increase in the maximum dry density was seen in Soils B and C. It may be attributed that the gravels greater than 19 mm were also removed from the originally sampled soils to conduct the similar test method of A-a.

Figure 9 shows the relationship between soil particle density and the maximum dry density obtained from the compaction tests. It is noted that the physical

Table 3 Results of compaction tests on wood-chip removed soil

Soil	A	B	C
ρ_{dmax} (g/cm^3)	1.972	1.788	1.634
W_{opt} (%)	11.6	15.4	20.6

Fig. 8 Compaction curves of wood-chip-mixed and wood-chip-removed soils
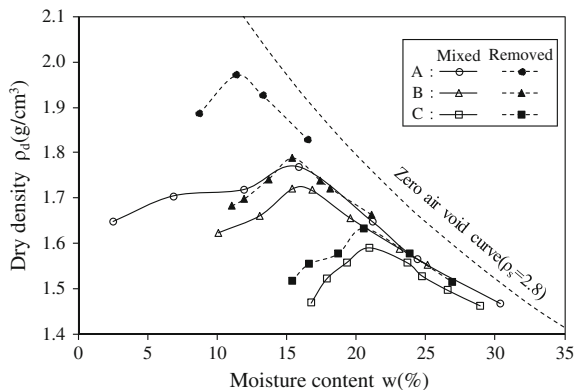
Fig. 9 Relationship between
the soil particle density and
the maximum dry density
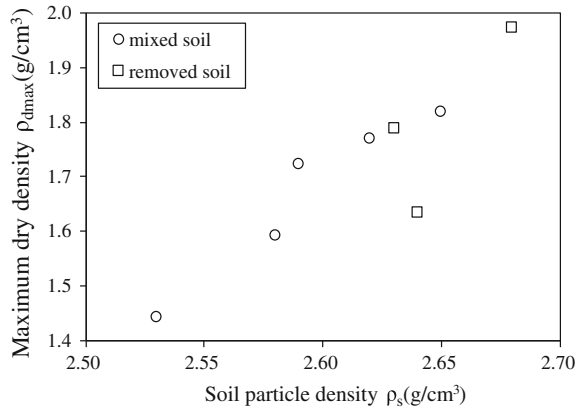
properties have high correlation, and that the wood-chip removal can lead to increase in soil particle density and have the effect to make the more densely compacted condition as well.

4 Direct Shear Test on Tsunami Deposit Soils

4.1 Test Method

In the present study, consolidated constant pressure direct box shear test (JGS 0561) [8] was conducted using the apparatus as shown in Fig. 10. For the purpose to use the wood chips as they were actually mixed in the sampled tsunami deposit soils, the large size shear box was selected to have the dimension of 200 mm in diameter and 100 mm in height.

The apparatus has the structure in which normal force is applied from the upper loading plate, and shear force is applied to the movable lower box while the upper

Fig. 10 Large-scale direct
box shear test apparatus
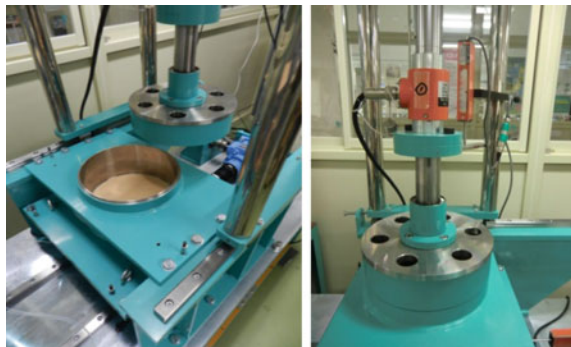
box is fixed. Also, both of the normal forces applying at the loading side (upper side) and the reaction side (lower side) can be measured to control the test conditions. Consolidation pressure was specified as σ = 50, 100, 150 kN/m^2 that was kept constant and applied as normal stress in the subsequent shearing process. Shear force was applied by prescribing the shear displacement control of 0.66 mm/min until the displacement attained δ = 23 mm. The constant normal pressure during shearing process was determined by controlling the normal pressure at the reaction side to be a specific amount. Here, the normal stress applying at the shearing plane was defined as the mean value of the normal stress measured at the upper loading plate and the lower reaction, respectively. The mean value becomes larger than that of the lower reaction stress that is controlled to be a constant prescribed value as seen later in the stress paths (Fig. 12c). This is because the friction at lateral surface acts upward when the specimen is compressed.

4.2 Specimen Preparation

The shear deformation and strength characteristics of the sampled wood-chip mixed soil were examined in comparison with the wood-chip removed soil regarding Soils A, B, and C. The soils were adjusted to have the optimal water content and compacted in the shear box to satisfy more than 90 % of degree of compaction D_c. A layer of 20 mm thickness was made by tamping 150–200 times using 1.0 kg rammer fallen from 10 cm above the specimen surface. Then, this procedure was repeated 5 times to make a 100-mm-height specimen. The energy per unit volume used to compact the specimen in this fashion was E_c = 230–310 kJ/m^3 that was approximately half of the energy E_c = 550 kJ/m^3 defined for A and B methods in JIS A1210.

The degree of compaction D_c of the specimens was more precisely evaluated after the direct shear tests, using the volume after consolidation and the water content of specimen measured after the shear tests; the results were D_c = 96.6–99.3 % (Mean: 97.8 %) for Soil A, D_c = 95.4–98.8 % (Mean: 97.0 %) for Soil B, and D_c = 92.8–95.9 % (Mean: 94.0 %) for Soil C. Thus, the degrees of compaction of the specimens under shearing were mostly more than 95 % except for some cases of Soil C.

4.3 Test Results and Discussions

(1) *Compression properties*

Figure 11 shows time-settlement relations measured in the consolidation stage for wood-chip mixed and removed soils of Soil C under the normal pressure of σ = 50, 100, 150 kN/m^2. The specimens were consolidated for 60–120 min until the settlement rate became sufficiently small although approximately 90 % of the total

Fig. 11 Time-settlement relations in the consolidation stage (Soil C)
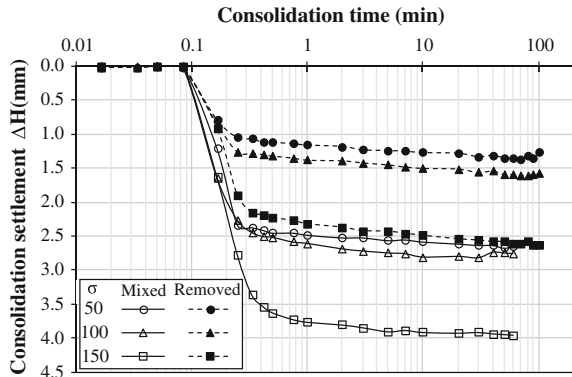
settlement generated in the initial 0.5 min. It is understood from Fig. 11 that the wood-chip mixed soils were more compressive than the respective wood-chip removed soils. Similar tendency was observed in the test cases of Soils A and B.

(2) *Shear strength characteristics*

The deformation and strength characteristics are described below focusing the different behaviors due to containing wood chips. The experiment results on Soils C are shown in Fig. 12 in terms of (a) relations between shear stress τ and shear displacement δ, (b) relations between normal displacement ΔH and shear displacement δ, and (c) stress paths with respect to shear stress τ and normal stress σ and Coulomb's expression of shear failure.

It is seen from the relations between shear stress τ and shear displacement δ (Fig. 12a) that the shear stress in the wood-chip removed soil was more largely mobilized in the initial shear stages of up to $\delta = 10$ mm compared to that of the wood-chip mixed soil. Also, it is seen that the initial stiffness became greater due to removal of wood chips. The tendency as described above may mainly attribute to the increase of soil density and resulting increase in internal friction angle by removal of wood chips.

It is seen from the relations between vertical displacement ΔH and shear displacement δ (Fig. 12b) that the specimen shrank in the early stage of shearing and showed clear dilatancy afterward under low normal pressure of $\sigma = 50$ kN/m². On the contrary, under higher normal pressure of $\sigma = 100, 150$ kN/m², the specimen remained almost in the similar state or dilated slightly. Irrespective of soil type, the dilatancy was more clearly observed in the wood-chip removed soils.

In the stress path with respect to shear stress τ and normal stress σ (Fig. 12c), it is seen that there is no clear difference due to removal of wood chips. The Coulomb's expression of shear failure in each soil is drawn respectively in Fig. 12c, and the strength parameters of wood-chip mixed and removed soils for Soils A to C are summarized in Table 4. It can be described from the present experiments that the shear strength of wood-chip mixed soils could not be improved clearly by the removal of wood chips.

Fig. 12 Results of direct
shear tests (soil C),
a relationship of shear stress
and shear displacement,
b relationship between
vertical displacement and
shear displacement, **c** shear
stress and normal stress paths
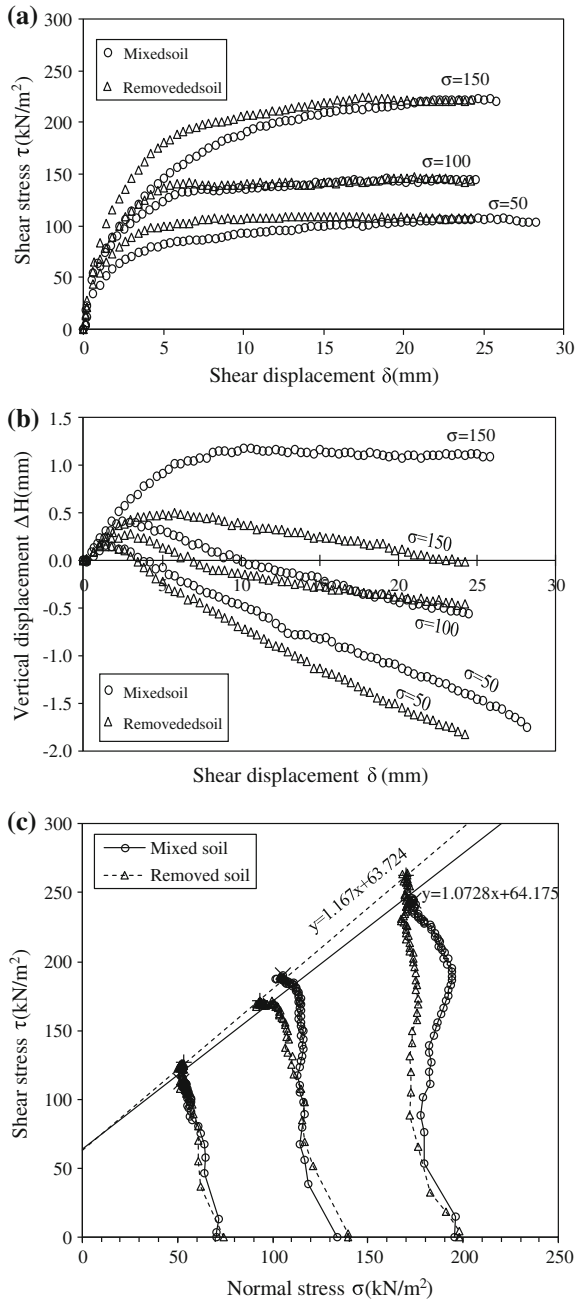
Table 4 Strength parameters of tsunami deposit soils

Strength	Soil					
	A		B		C	
	Mixed	Removed	Mixed	Removed	Mixed	Removed
c (kN/m^2)	37.0	49.6	51.7	46.8	64.2	63.7
φ (°)	43.3	42.0	46.3	46.1	46.8	49.4

5 Conclusion

In this study, for the purpose to examine the applicability of tsunami deposit soils as earthwork material, the physical and compaction properties of the sampled soils were examined, and the shear strength characteristics were evaluated by large-scaled direct shear tests in relation to the effects of contained wood chips. The findings from the present study are described as follows:

(1) The contents of wood chips in the sampled tsunami deposit soils varied by a site possibly due to the different processing methods and the properties of original soils.
(2) The wood chip removal can lead to the increase in density of soil particles and resultantly make the soils more densely compacted.
(3) The effects of wood chip removal did not appear clearly in the shear strength, while deformation characteristics were somehow improved in the present direct shear tests. The results may suggest the tsunami deposit soils can be used for earthworks at least when the soil strength is not particularly required.
(4) More studies will be required including long-term stability in relation to the decomposition of wood chips to determine the applicability of the tsunami deposit soils for earthworks.

References

1. Ministry of the Environment (MOE), "Guideline on the Treatment of Tsunami Deposit," 2011 (in Japanese). Available from: http://www.env.go.jp/jishin/attach/sisin110713.pdf (accessed 15 July, 2015).
2. T. Katsumi, A. Takai, K. Omine, M. Kazama, T. Inui, "Physical and chemical properties of tsunami deposits collected in the flooded area, Miyagi Prefecture," Proceedings of the Annual Symposium on Groundwater and Geo-environment. The Research Committee of Groundwater and Geo-environment, pp. 83–90, 2011 (in Japanese).
3. N. Kotake, M. Yamanaka, Y. Tada and S. Yamauchi, "Evaluation of shear strength of soils separated from tsunami deposit using large type direct shear test," Proceedings of the 11th JGS symposium on Environment Geotechnics, Fukushima, Japan, July 2015 (in Japanese).

4. Iwate Prefecture, "Detailed Plan for the Disaster Debris Treatment in Iwate Prefecture (Revised)," 2013 (in Japanese).
5. Japan Geotechnical Society (JGS), "Method of Classification of Geomaterials for Engineering Purposes, JGS0051," 2009.
6. Japan Geotechnical Society (JGS), "Test method for ignition loss of soils, JGS0221," 2009.
7. Japanese Industrial Standard (JIS), "Test method for soil compaction using a rammer," JIS A1210.
8. Japan Geotechnical Society (JGS), "Method for consolidated constant pressure direct box shear test, JGS 0561," 2009.

Part VI
Innovative Construction
Materials & Structures

Magnetorheological Elastomer Performances with the Presence of Carbon Black

Nurul Husna Rajhan, Hanizah Ab Hamid, Azmi Ibrahim and Rozaina Ismail

Abstract This paper deals with the isotropic magnetorheological elastomers (MRE) samples which compounded in the absence of magnetic field. Two types of MRE composites with and without the addition of carbon black were fabricated. The mechanical properties through tensile test were obtained by using an Instron Tensile Machine. Morphological characterization test of these MRE samples was conducted by using a scanning electron microscopic (SEM). From the experimental study, it can be concluded that, the addition of carbon black in MRE increases tensile strength, decreases the elongation of the break and also cure time. Thus, this study demonstrated that carbon black has a significant improvement on the mechanical properties of MRE. This method of fabrication of MRE is useful for the further research on rubber bearing application.

Keywords Magnetorheological elastomer · Carbon black · Mechanical properties · Microstructures · SEM

N.H. Rajhan (✉) · H.A. Hamid · A. Ibrahim
Faculty of Civil Engineering, Universiti Teknologi Mara UiTM,
Shah Alam, Malaysia
e-mail: nunurajhan@yahoo.com

H.A. Hamid
e-mail: hanizah696@salam.uitm.edu.my

A. Ibrahim
e-mail: azmi716@salam.uitm.edu.my

R. Ismail
Institute for Infrastructure Engineering and Sustainable Management (IIESM),
Universiti Teknologi Mara UiTM, Shah Alam, Malaysia
e-mail: rozaina_fka_uitm@yahoo.com

1 Introduction

Interest in magnetorheological elastomers (MREs) has increased due to their potential applications in smart systems. MRE belongs to a group of smart material, whose mechanical and magnetic properties can be controlled continuously, rapidly, and reversibly under the application of an external magnetic field [1–6]. Based on the literatures, MRE has focused on several areas in engineering applications such as adaptive tunable vibration absorber [7–9], sensors [10, 11], noise barrier system [12], dampers [13], seismic isolator [14–16], etc.

MREs are solid analogs of magnetorheological fluids, in which the fluid component is replaced by a cross-linked material such as rubber or gel. MREs are a new member of the magnetorheological family, where it is the solid analog of magnetorhelogical fluids and may be a good solution to overcome the disadvantages of magnetorhelogical fluids. The obvious advantages of MRE are that the particles are not prone to setting with time and so there is no need for containers to keep the MR material in a fixed place [2, 5, 17, 18].

MREs compromise to offer great potential devices as base isolators with high magnetorheological effect, good mechanical properties, and low damping ratio. In addition, increasing the large numbers of magnetic particle content will deteriorate the damping characteristics [19].

Over the past few years, researchers have been focusing on improving the MR effect by using soft matrix and increasing the magnetic particle content [20]. Nevertheless, modifying soft matrix such as silicone rubber decreases the mechanical performance of MRE compared to MRE with natural rubber.

Limited researches have been conducted regarding the influence of carbon black in the development of MRE. Till date, only Chen et al. [21] studied the effect of carbon in order to increase the MRE performances by using natural rubber as matrix based. On contrast, Nayak et al. [22] analyzed the characterization of isotropic MRE with and without carbon black in the absence of magnetic field by using silicone rubber. Both of these studies demonstrated that the addition of carbon black led the enhancement on the mechanical performances of MRE, even they used different methods to fabricate the MRE. Commonly, carbon black has been used as a reinforcing agent for many rubber applications, because carbon has a significant role in polymer engineering [21].

Thus, this present study was conducted to study the effect of carbon black on the mechanical properties of isotropic MRE. This study was organized as follows. At first, two compounds of MREs were developed with and without presence of carbon black. The mechanical properties through tensile strength were obtained. After that, the morphological characterization of MRE samples was observed.

2 Experimental

2.1 Preparation of MRE Materials

Figure 1 presents the ingredients that were used in compounding MRE composites. Elastic matrix and magnetic particles are the main ingredients of MRE. In order to conduct the work, carbonyl iron particles, type C3518 were purchased from Sigma-Aldrich Sdn. Bhd. (Malaysia). The diameter and the density of the iron particles are in the range of 6–9 μm and 7.86 g/cm^3, respectively. Natural rubber SMR L was supplied by Rubber Research Institute of Malaysia, (RRIM). The reinforcing filler that was manipulated was carbon black, ISAF N220.

Ingredients such as zinc oxide, stearic acid, and sulfur are important in compounding a vulcanized rubber. Sulfur is the main vulcanizing agent in most rubber cases. Zinc oxide acts as activator and stearic acid acts as coactivator. Both of them need to be added together to increase the speed of vulcanization. N-cyclohexyl-2-benzothiazole sulphenamide (CBS), antioxidant, and tetramethylthiuram disulphide (TMTD) were additives that were chosen to improve the properties of elastomers. All ingredients were commercial grades and supplied by Sigma-Aldrich Company Sdn. Bhd.

In this present study, the formulations of MRE composites are presented as in Table 1. Each has a specific function. However, each is capable to function in more than one manner. Generally, the formulation of elastomer is given in a specific amount based on a total 100 parts of rubber (pphr). Rubber compounds in most rubber products use a basic composition of carbon black within the range of 20–50 pphr [23]. Thus, 40 pphr of carbon black was chosen to study the effect of the carbon black on MRE. The MRE composite with carbon black was named as CB40, whereas the MRE without carbon black was named as CB00.

The fabrication of MRE consists of three major steps same as the fabrication of conventional rubber compound; i.e., mixing, preconfiguration and curing. The

Fig. 1 MRE ingredients arranged in order

Table 1 Formulation of MRE composites

Ingredients (pphr)[a]	Samples	
	CB00	CB40
Natural rubber (SMR L)	100	100
Carbon black ISAF N220	0	40
Carbonyl iron powder	30	30
Zinc oxide (ZnO)	5	5
Stearic acid	2	2
Antioxidant	2	2
Sulfur	1.5	1.5
CBS	0.5	0.5
TMTD	0.5	0.5

[a]Part per hundred of rubber

Fig. 2 Two-roll mill

mixing process was conducted carefully to get the finest MRE compound. A two-roll mill as shown in Fig. 2 was used to mix the ingredients with the natural rubber homogeneously. Figure 3 shows the process of compounding the MRE composites with the presence of carbon black. The MRE composites were left for 24 h before the vulcanization process.

Figure 4 represents the photo of the rheometer 100 that was used to determine the cure time of the MRE. The rheometer sample tests were cut about 10 g and ran for up to 60 min at 150 °C. After obtaining the results with the specific cure time, the MRE would go through the vulcanization process, where the MRE final samples were compressed in a hot press machine (Refer Fig. 5). The MRE samples were vulcanized in square shape molding and about 60 g from each sample was required.

Fig. 3 The compounding process of MRE by using a two-roll mill
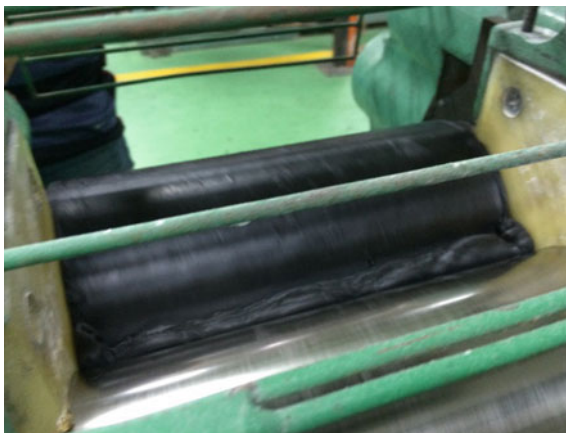
Fig. 4 Rheometer 100

2.2 Tensile Properties

Tensile test is one of the most applied tests in order to determine the mechanical properties of rubber-based material. The standard method for determining the tensile properties is according to BS ISO 37:2011 [24]. The samples were cut to the

Fig. 5 Hot press machines

Fig. 6 Dumbbell shape of tensile test pieces with addition of carbon black

dumbbell shape as shown in Fig. 5. Method of tensile properties measurements is detailed in [25]. The Tensile Instron Machine used to conduct this experiment is shown in Fig. 7 (Fig. 6).

2.3 Morphological Characterization

Morphological characterization between the interparticles of rubber matrix, carbonyl iron powder, and carbon black fillers can be investigated by observing the microstructure of MRE. These samples were cut into pieces with surface of 5 mm × 5 mm. Figure 8 illustrates each surface of the sample that was coated with a

Fig. 7 Tensile Instron Machine for polymer and latex

Fig. 8 The samples are coated with a thin layer of gold
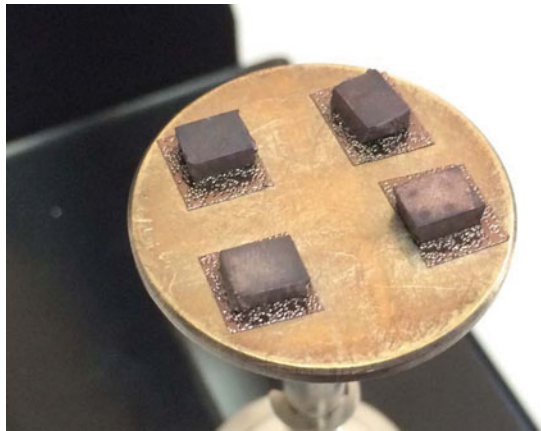
thin layer of gold prior to the SEM observations. The coating process was made by using a Sputter Coater as shown in Fig. 9. The microstructure of the samples was observed at an accelerating voltage of 10–15 kV depending on the sample. Through the microstructural observation, the interactions between rubber and magnetic particles were obtained. The microstructure observations of MRE samples were carried out using a scanning electron microscopy (SEM).

Fig. 9 Sputter coater

3 Results

3.1 Cure Characteristics

The measurements of cure time of MRE were referred to BS ISO 3417:2008 [26]. The cure characteristics of each MRE composites with and without carbon black were recorded as in Table 2. From the results, Table 2 shows MRE composite with carbon black, CB40 has shorter cure time, which is 4.0 min. Meanwhile CB00 took 5.0 min to cure.

3.2 Tensile Properties

Mechanical performances in terms of tensile strength were measured and compared. Tensile strength is related to the stress distribution within the rubber and the effective increase in the rupture path. Strong interaction between filler particles and rubber matrix will capitalize the dispersion, which led to achieve higher result of tensile strength [27]. From Table 3, it can be seen that the results of tensile strength and elongation at break of MRE compounds with and without the addition of carbon black. The tensile strength of CB40 increased by 0.57 % compared to CB00. However, the elongation at break (E_b) of MRE composite decreased with the

Table 2 Rheological measurements

Test sample	CB00	CB40
torque$_{max}$	54.5	71.9
torque$_{min}$	11.5	14.8
Δt	43.0	57.1
$t_{c'(90)}$ (min)	5.0	4.0

Table 3 Tensile strength and elongation at break

Sample	CB00	CB40
Tensile strength (MPa)	22.97	23.10
Elongation at break (%)	801.32	319.89

addition of carbon black. This can be proved when E_b of CB40 is decreased to 319.89 %.

3.3 SEM

Generally, it was expected that the addition of carbon black could improve the mechanical properties of MRE. Scanning electron microscopy was used to provide the microstructure of MRE with and without the addition of carbon black. For MRE without the addition of carbon black, the dispersion of iron particles is homogeneously distributed as shown in Fig. 10. In Fig. 11, the gaps between iron particles can be seen clearly which indicate where the carbon black takes place.

Figure 12 depicts the magnified picture of MRE with the addition of carbon black. Unfortunately, the mechanism of interaction between iron particles and carbon black cannot be detected. These results are firmly supported by Chen et al. [21]. Even though the interparticles of iron particles and carbon black are not clear, the addition of carbon black significantly gives effect to the microstructure of MRE.

Fig. 10 SEM image of morphology of MRE without carbon black
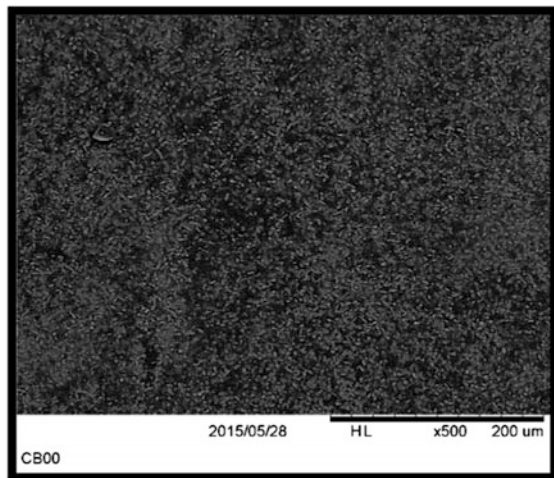
Fig. 11 SEM image of morphology of MRE with carbon black
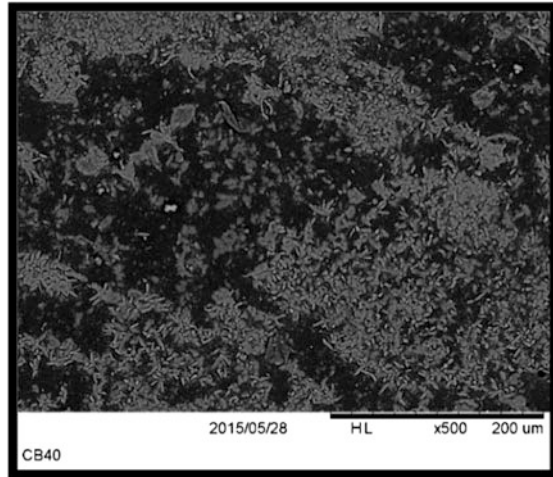
Fig. 12 Magnification of Fig. 10 at ×3.0 k
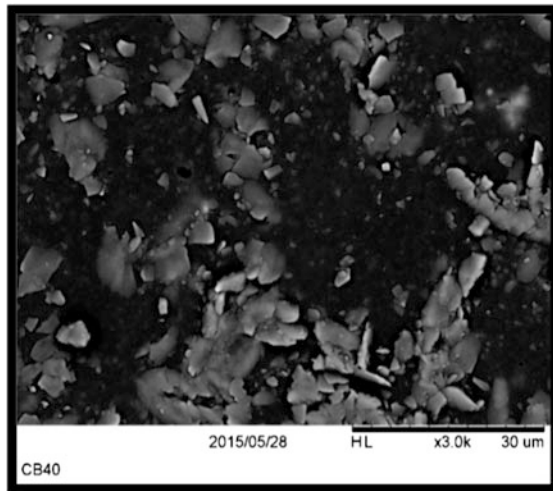
4 Conclusion

From this present study, it can be concluded that the addition of carbon black has shorten the cure time of MRE. The dispersion of carbon black in the samples was observed from SEM. The results prove that carbon black fill up the spaces between the interparticles interaction of rubber matrix-carbonyl iron powder, thus slightly improving the tensile properties of MRE composite. Also, the addition of carbon black decreases the elongation of break of MRE. Further exploration can be extended by varying the percentages of carbon black in order to find the optimum

volume in MRE. Other than that, the morphology characterization of MRE can be studied by using an advance tool to observe the interparticles interaction between rubber, carbonyl iron particles, and carbon black.

References

1. M. R. Jolly, J. D. Carlson, and B. C. Munoz, "A model of the behaviour of magnetorheological materials," *Smart Mater. Struct.*, vol. 5, pp. 607–614, 1996.
2. M. Kallio, "The elastic and damping properties of magnetorheological elastomers," VTT Publications, 2005.
3. M. Rowlinson, C. R. Herd, G. Moninot, N. Thomas, and J. A. Ayala, "The Effect of Carbon Black Morphological Characteristics on Tear Propagation In Rubbers," *Kautschuk Gummi Kunststoffe*, vol. 52, no. 12, pp. 830–835, 1999.
4. A. Boczkowska and S. Awietjan, "Microstructure and Properties of Magnetorheological Elastomers," 2012.
5. B. X. Ju, M. Yu, J. Fu, X. Zheng, and Q. Yang, "Study on the properties of porous magnetorheological elastomers under shock effect," *J. Phys. Conf. Ser.*, vol. 412, p. 012039, Feb. 2013.
6. N. H. Rajhan, H. A. Hamid, A. Ibrahim, and R. Ismail, "Magnetorheological Elastomers: A Review," *Appl. Mech. Mater.*, vol. Vol 695, pp. 255–259, 2015.
7. H. X. Deng and X. L. Gong, "Adaptive Tuned Vibration Absorber based on Magnetorheological Elastomer," *J. Intell. Mater. Syst. Struct.*, vol. 18, no. 12, pp. 1205–1210, Dec. 2007.
8. H. Deng and X. Gong, "Application of magnetorheological elastomer to vibration absorber," *Commun. Nonlinear Sci. Numer. Simul.*, vol. 13, no. 9, pp. 1938–1947, Nov. 2008.
9. X. Dong, M. Yu, C. Liao, and W. Chen, "A new variable stiffness absorber based on magneto-rheological elastomer," *Trans. Nonferrous Met. Soc. China*, vol. 19, no. 20070420719, pp. s611–s615, Dec. 2009.
10. W. Li, K. Kostidis, X. Zhang, and Y. Zhou, "Development of a force sensor working with MR elastomers," in *IEEE/ASME International Conference on Advanced Intelligent Mechatronics*, 2009, pp. 233–238.
11. T. F. Tian, W. H. Li, and G. Alici, "Study of magnetorheology and sensing capabilities of MR elastomers," *J. Phys. Conf. Ser.*, vol. 412, p. 012037, Feb. 2013.
12. M. Farshad and A. Benine, "Magnetoactive elastomer composites," *Polym. Test.*, vol. 23, no. 3, pp. 347–353, May 2004.
13. A. Sarrafan, S. H. Zareh, A. A. Khayyat, and A. Zabihollah, "Performance of an Offshore Platform with MR Dampers Subjected to Wave," pp. 242–247, 2011.
14. H.-J. Jung, S.-H. Eem, D.-D. Jang, and J.-H. Koo, "Seismic Performance Analysis of A Smart Base-isolation System Considering Dynamics of MR Elastomers," *J. Intell. Mater. Syst. Struct.*, vol. 22, no. 13, pp. 1439–1450, Jul. 2011.
15. S. H. Eem, H. J. Jung, and J. H. Koo, "Seismic performance evaluation of an MR elastomer-based smart base isolation system using real-time hybrid simulation," *Smart Mater. Struct.*, vol. 22, no. 5, p. 055003, May 2013.

16. J. Li, Y. Li, W. Li, and B. Samali, "Development of adaptive seismic isolators for ultimate seismic protection of civil structures," in *Sensors and Smart Structures Technologies for Civil, Mechanical, and Aerospace Systems*, J. P. Lynch, C.-B. Yun, and K.-W. Wang, Eds. San Diego, California, USA: SPIE, 2013, pp. 1–12.
17. C. Ruddy, E. Ahearne, and G. Byrne, "A review of Magnetorheological Elastomers: Properties and Applications," Belfield, Dublin 4, Ireland., 2007.
18. W. Li and X. Zhang, "Research and Applications of MR Elastomers," *Recent Patents Mech. Eng.*, vol. 1, no. 3, pp. 161–166, Nov. 2008.
19. L. Chen, X. L. Gong, and W. H. Li, "Damping of Magnetorheological Elastomers," 2008.
20. M. Lokander and B. Stenberg, "Improving the magnetorheological effect in isotropic magnetorheological rubber materials," *Polym. Test.*, vol. 22, no. 6, pp. 677–680, Sep. 2003.
21. L. Chen, X. L. Gong, and W. H. Li, "Effect of carbon black on the mechanical performances of magnetorheological elastomers," *Polym. Test.*, vol. 27, no. 3, pp. 340–345, May 2008.
22. B. Nayak, S. K. Dwivedy, and K. S. Murthy, "Fabrication and characterization of magnetorheological elastomer with carbon black," *J. Intell. Mater. Syst. Struct.*, pp. 1–10, 2014.
23. A. Samsuri, *An Introduction to Polymer Science and Rubber Technology*. Shah Alam: Pusat Penerbitan Universiti, Universiti Teknologi MARA, 2009.
24. British Standards: Rubber, vulcanized or thermoplastic-Determination of tensile stress-strain properties (BS ISO 37:2011).
25. N. H. Rajhan, R. Ismail, H. A. Hamid, and A. Ibrahim, "Influence of Different Fillers on the Tensile Properties of 50/50 NR/NBR Blend," in *International Civil and Infrastructure Engineering Conference 2014*, pp767–777, 2015.
26. British Standards: Rubber-measurement of vulcanization characteristics with oscillation disk curemeter (BS ISO 3417: 2008).
27. H. H. Hassan, E. Ateia, N. A. Darwish, S. F. Halim, and A. K. A. El-aziz, "Effect of filler concentration on the physico-mechanical properties of super abrasion furnace black and silica loaded styrene butadiene rubber," *Mater. Des.*, vol. 34, pp. 533–540, 2012.

TFGM a New Composite Material with Palm Oil Fuel Ash

Zalipah Jamellodin, Hamidah Mohd Saman, Suraya Hani Adnan, Noor Shuhada Mohammad and Wan Yuslinda Wan Yusof

Abstract Textile fine grained mortar (TFGM) is a composite construction material which provides another alternative to strengthen and repair existing concrete structures. TFGM is a combination of fine grained mortar (FGM) made of waste material with textile fabrics. The strengthening approach significantly increases both the ultimate load carrying capacity and the serviceability. FGM is a special binder matrix with maximum grain size of 600–1 mm. Therefore, less than 2 mm mortar thickness is needed between the textile layers due to the small aggregate size. In addition, 10 % of cement content in FGM is replaced by palm oil fuel ash (POFA) as a waste material. The utilization POFA can reduce the carbon dioxide emission generated by cement, which can be harmful to the environment In this study, plain concrete prism with size of 100 mm × 100 mm × 500 mm was produced. Specimens were strengthened by using alkali resistant (AR) glass fabrics impregnated with FGM. Four levels of strengthening consisting of 2, 4, 6 and 8

Z. Jamellodin (✉) · N.S. Mohammad · W.Y.W. Yusof
Faculty of Civil and Environmental Engineering,
University Tun Hussein Onn Malaysia, Batu Pahat, Johor, Malaysia
e-mail: zalipah@uthm.edu.my

N.S. Mohammad
e-mail: shuhadamohammad89@gmail.com

W.Y.W. Yusof
e-mail: yuslinda89@gmail.com

H.M. Saman
Faculty of Civil Engineering, University Technology MARA,
Shah Alam, Selangor, Malaysia
e-mail: hamid929@salam.uitm.edu.my

S.H. Adnan
Faculty of Engineering Technology, University Tun Hussein Onn Malaysia,
Batu Pahat, Johor, Malaysia
e-mail: suraya@uthm.edu.my

layers fabric were used on three replicate specimens in each category. Strengthened concrete prisms were subjected to monotonic load with three-point bending test to determine the effect of the strengthening process and the number of fabric layers on the behaviour of concrete prism. The recorded measurements on the test specimens were evaluated for the ultimate flexural strength and deflection. TFGM significantly contributed on the flexural load carrying capacity and ductility of concrete prisms. The contribution of these composites varies according to the number of fabric layers. The flexural capacity increased about threefold from unstrengthened plain concrete prism.

1   Introduction

Nowadays, there are a lot of problems occurring on the building structure such as collapse, cracking, and others due to the concrete structure weakness under flexural loads and tend to be brittle [1]. It may also be due to the low tensile capacity and low porosity in concrete which is the designing of concrete structure before are emphasize the relation of compressive stresses only [2]. Thus, the strength of a material is a very important factor to consider in the production of good quality construction due to demands on higher loads, degradation, reconstruction and others which there is for repair or strengthening of existing beams structures [3].

Nevertheless, the potential of industrial wastes such as POFA also known pozzolan materials is important to enhance the properties such as workability, flow ability and mechanical properties in mortar [4]. The main point for using pozzolan material is to prevent the carbon dioxide contamination, low mechanical strength, low resistance to the sulphate attack, low porosity, low modulus of elasticity and thus gear toward sustainable development [5, 6]. So, it is no wonder that pozzolan material becomes more popular and is widely used in the construction industry. On the other hand, most of the researchers [7, 8] agreed to verify that the alternative method in modern concrete designing use fibres in order to increase the strength of concrete. The utilization of fibre as a second reinforcement is important to overcome the existing deficiencies in cementitious material [7].

Incorporation of POFA as a partial cement replacement in mortar has gained considerable importance because of the requirements of environmental safety. This application will reduce construction cost of concrete components and also reduce CO_2 gas pollution. It is concluded that all pozzolanas act as filler that will provide a positive effect on the compressive and flexural strength of mortar.

2 Strength of Fine Grained Mortar

Fine grained mortar is special binder systems obtained using a small maximum grain size of 0.6–1 mm. FGM mixture showed flowable consistency which offers good penetration on textiles. FGM also has high binder content, by adding pozzolanic additives and high performance plasticizers [8–12].

Due to the small diameter of grain size, it is possible to get new, very thin concrete elements as applications for new materials [8, 13]. With a compressive strength similar to that of ordinary mortar, FGM produces a lower Young's modulus The results of the investigation in tensile strength and fracture mechanical properties clearly indicate that less ductile behaviour bearing on FGM makes a more homogeneous structure than ordinary mortar [14].

Generally the use of FA with low calcium content enhances the properties of mortar [15] and also increases the workability [16]. The content of the cement in mortar can be reduced by using FA as a substitute for cement. Furthermore, the combination of FA and superplasticizer will produce a very good flowability in mortar [17].

The replacement of FA with cement increases the porosity and the average pore size is reduced making it less permeable [18]. The interface zone between aggregate and matrix also increased as a result of the use of FA [19, 20].

However, different result was found by Turk [21], the compressive and flexural strengths of the control mortar performed better than those of mortars containing FA. This is because the use of FA with a relatively low surface area causes the slow rate of mortar hardening.

The compressive strength of mortars containing POFA with various water/binder ratio investigated by Sata [22]. They found that the higher the water/binder ratio, the lower the compressive strength of mortar due to the hydration reaction.

Because of that, this study focuses on the utilization of POFA as a cement replacement in FGM. The behaviour of compressive strength of mortar with different fineness of POFA was reported by Tangchirapat [23] and Kroehong [24]. When POFA was ground to reasonable fineness, the rate of compressive strength was significantly improved due to rapid hydration process and pozzolanic reaction. Besides that, the results indicated that unground POFA is not suitable for the use as a pozzolanic material.

The higher the percentage of replacement of portland cement, the lower the compressive strength of mortar. Thus, mortar containing POFA with high fineness was more homogeneous and denser, which improved the compressive strength of the mortar. POFA with high fineness can be used as a good pozzolana as a portland cement replacement up to 20 % [18].

In recent years, it is necessary to find the suitable improvement in terms of sustainability and speed of execution because many concrete structures are exposed to damaging, such as suffering from various deteriorations, which may be attributed to cracks and large deflection. Generally, many researchers discovered about the usefulness of POFA in concrete but there are few practicing the utilization of POFA

in mortar, whereas it is an important part of any project because mortar can give the protection to the surface and structure of building. The strength, durability and other characteristic of mortar depends on the properties of content and proportions of mixture.

Based on previous research [23], it was expressed that the increasing of POFA fineness with the longer curing time gives the higher compressive strength at 10–20 % and improve the sulphate resistance. It was also found that the utilization of unground POFA is a slightly reduced with the low compressive strength. Besides that, the effect of particle size plays the main role in terms of strengthening and quality of mortar. The utilization of sand is less than 1 mm when compared with normal mortar that is 5 mm due to the change in the particle size of the air flow, compressive strength and mortar voids content. Therefore, the performance of POFA combined with fine sand gives the highest strength in both compressive and flexural strength at 10 % of POFA replacement [4].

In the selection of building materials, the application of the fibres has more effect on the microcracking, workability of beams and subjected to axial compression [25]. Furthermore, the utilization of textile fibres has known to be effective in reinforced concrete but still is lacking in mortar. The properties of textile fibres, also known as textile reinforcement, contain more than 15 % of zircon in order to resist the corrosive alkaline in the concrete [26]. Textile fibres are specifically used in concrete or mortar due to the high elastic modulus with 70–80 GPa, tensile strength with 2–4 GPa and also the great properties on brittle stress with 2.5–4.8 % elongation at break [27]. In terms of technology and the sustainable development, the studies on properties of concrete with textile fibres was continuously revealed which can increase the strength. According to previous researcher [28], the utilization of textile fibres (basalt-based textile) with mortar for reinforced concrete beams was enhanced the flexural capacity about 39–91 % increment. Also, the 4 layers are the effective layers due to the higher shear loading capacity without delamination which is about 30 % compared to unstrengthened beam [8].

So that, it is necessary to apply AR glass as textile reinforcement with the combination of POFA and fine sand in FGM in order to increase the performance of TFGM in terms of flexural strength.

3 Materials and Method

3.1 Materials

POFA was collected from small power plant for the palm industry in Kluang, Johor. POFA was oven dried at 105–110 °C for 24 h. Then it was ground by grinder until 95 % of the particles could pass trough sieve number 325 (45 μm) complying the requirement of ASTM C618 [29]. Particle size distribution was measured by laser particle size analyzer (CILAS 528). Ordinary portland cement (OPC) and sand with maximum grain size of 600 mm were used. The chemical composition of OPC and

Fig. 1 Textile fabric for strengthening
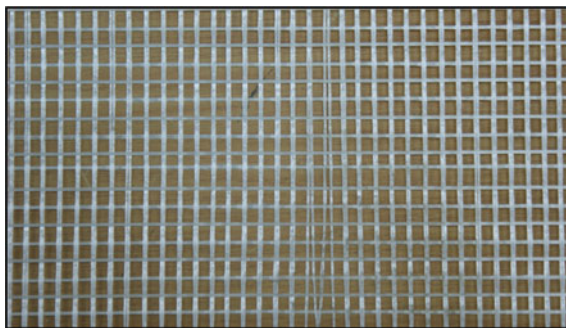
POFA was determined by X-ray fluorescence analysis (XRF). Analysis was conducted using Bruker AXS S4 Spectra Plus.

Textile fabrics used are from Nippon Electric Glass Co. Ltd. type TD 5 × 5 made of glass fibre, which contains the largest content of zirconium dioxide (ZrO_2) as shown in Fig. 1.

3.2 Mix Proportions of FGM

Five (5) series of mix FGM were prepared. OPC is partially replaced with POFA at the dosage of 0, 10, 20, 30 and 40 % by weighing cementitious materials, sand to binder ratio of 2 by weight, and water to binder (w/b) ratio of 0.45. Workability of FGM was adjusted by adding superplastisizer (SP) to maintain the mixes with similar penetration based on BS 4551 [30]. The FGM mix proportions are given in Table 1.

3.3 Flexural and Compressive Strength of FGM

Prism specimens of dimension 40 × 40 × 160 mm were used to test flexural and compressive strength. All specimens were prepared and tested according to BS EN 196-1 [31]. Flexural and compressive strengths of mortar specimens were

Table 1 FGM mix proportions

Mix No.	Symbol	OPC	POFA	SP	Fine grained sand	Water/Binder
M1	OPC	1	–	0.010	2	0.45
M2	POFA10	0.90	0.10	0.010	2	0.45
M3	POFA20	0.80	0.20	0.010	2	0.45
M4	POFA30	0.70	0.30	0.010	2	0.45
M5	POFA40	0.60	0.40	0.010	2	0.45

Fig. 2 Compressive and flexural testing of FGM

determined at ages of 7, 28 and 90 days of curing. The prism specimens were covered with damped cloth and were demoulded at the age of 1 day. Next, the prism specimens were cured in water until the test aged. The reported results are the average of three samples for flexural strength. Flexural testing was done with used three point loading method. Compression test was carried out using the prism broken from flexural test. It is means that the compressive strength is mean of six made of three prism. If one result within six individual results varies by more than ±10 % from the mean, result was discarded and five remaining results were calculated. Figure 2 shows the compressive and flexural testing of FGM. The optimum mix proportion of FGM was selected as a binder material with AR glass textile fibre to produce composite materials TFGM.

3.4 Plain Concrete Prism

The fifteen plain concrete prisms with size of $100 \times 100 \times 500$ mm were produced and then were cured in water for 28 days. The compressive strength of plain concrete was 30 MPa after 28 days casting concrete. Table 2 shows details of the fifteen plain concrete prisms. The twelve of these beams were strengthened using AR glass embedded in FGM. Then the plain concrete prisms strengthened by TFGM were held in water for cure for 28 days after hardening.

Table 2 Details of plain beam specimens

Beam No.	Symbol	No. of textile layers	No. of specimens
1	BC	–	3
2	BPOFA2	2	3
3	BPOFA4	4	3
4	BPOFA6	6	3
5	BPOFA8	8	3

3.5 Laminating FGM onto Plain Concrete Prism

The concrete plain prisms were roughened by sandblasting to ensure an adequate bond between the existing concrete plain prisms. FGM paste in thickness 2–3 mm was firstly laid and the fabrics with cement paste were mounted to the bottom face of beam with respect to the flexural load layer by layer. The laminating process of TFGM is shows in Fig. 3.

3.6 Experimental Test Set Up

This experiment is based on the specification in BS. EN 196-1 [32]. The aim of the experiment was to determine the flexural strength of the plain concrete prisms that is not strengthened and strengthened with TFGM. Universal testing machine (UTM) is used in this experiment. Figure 4 shows the three points bending testing on strengthened plain concrete prism. The distance between the rollers is 300 mm was adjusted in order to reach the ±1.0 mm of accuracy. In the three point bending test, the deflection of the plain concrete prism was measured using linear variable differential transducers (LVDT). During the running test, load was applied gradually for plain concrete prism with TFGM layers. Three specimens were tested under monotonic flexural loads for each number fabric layers.

4 Results and Discussion

4.1 Strength of FGM

Tables 3 and 4 show the results of compressive and flexural of FGM containing POFA. As expected for all mortar mix, an increase in the curing age of FGM leads to an increase in the strengths of FGM. This clearly shows that the replacement of portland cement to POFA is about 10 %, increases the strength. Substitution of POFA acts as a filler effect due to the fine particles.
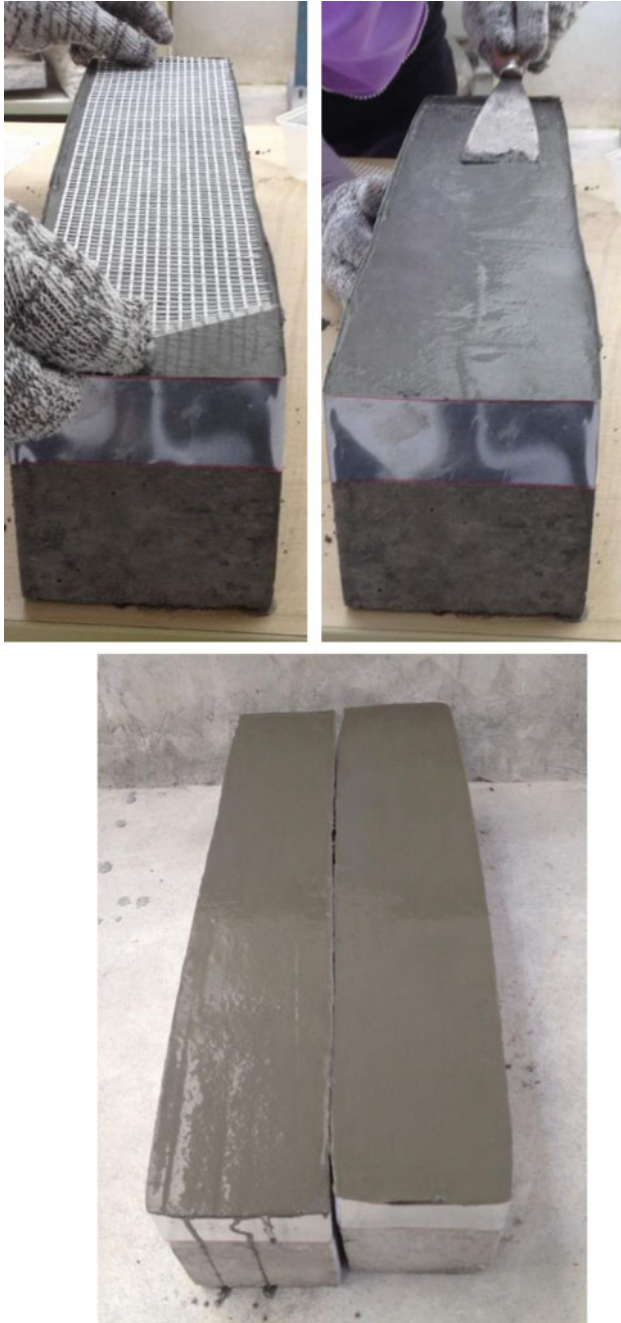
Fig. 3 Laminating process of TFGM onto plain concrete prism
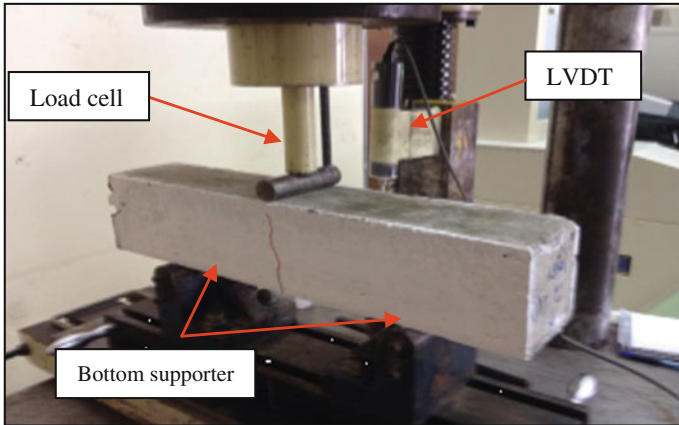
Fig. 4 Three point bending test on strengthened plain concrete prism

Table 3 Compressive strength of FGM

Mix No.	Symbol	Compressive strength (MPa-*normalized*)					
		7 days		28 days		90 days	
M1	OPC	38.25	−100	67.34	−100	66.49	−100
M2	POFA10	39.00	−102	69.87	−104	70.10	−105
M3	POFA20	36.50	−95	65.31	−97	67.12	−101
M4	POFA30	32.10	−84	63.58	−94	66.89	−101
M5	POFA40	30.20	−79	62.88	−93	66.50	−100

Table 4 Flexural strength of FGM

Mix No.	Symbol	Compressive strength (MPa-*normalized*)					
		7 days		28 days		90 days	
M1	OPC	8.55	−100	10.82	−100	11.00	−100
M2	POFA10	8.69	−102	11.1	−103	11.48	−104
M3	POFA20	8.22	−96	10.73	−99	10.55	−96
M4	POFA30	7.43	−87	9.58	−89	9.45	−86
M5	POA40	6.87	−80	9.11	−84	9.28	−84

An increasing number of substitution of POFA from 20 to 40 % reduces the strength of FGM in the early stages. However, the compressive and flexural strength on day 90 is slightly higher than the OPC. This shows that both the pozzolanic materials and the reaction rate in the early stages of POFA is slow. The strength of mortar depends on the cement paste cohesion, adhesion between aggregate particles and aggregate strength itself [33]. Depending on that, by a proper utilization of POFA it can be able to produce both high strength and high performance mortar.

Based on the result, 10 % replacement of POFA was selected as a binder material with AR glass textile fibre to produce composite materials TFGM.

4.2 Flexural Strength of Plain Concrete Prism Strengthened with TFGM

The flexural load-deflection curves of the strengthened concrete prism are presented in the Fig. 5. Based on a graph, unstrengthened plain concrete prism shows the lowest strength about 9346 N. From the observation, plain concrete prism can carry a little more flexural load when strengthened by TFGM. The strengthening with 2 layers of AR glass shows the increasing of loads by about 42 % compared to unstrengthened concrete prism, followed by an increase in the flexural strength of 4 and 6 layers, 82 and 118 % respectively.

When the plain concrete prism is strengthened by 8 layers of AR glass fabric, the flexural load carrying capacity of the strengthened prism is extremely enhanced by about threefold more than unstrengthened plain concrete prism as well as high strength.

This indicates that the layers of TFGM effect on increasing the load carrying capacity and serviceability. The increasing in strength was due to the response of cementitious composite in FGM which means the fineness of POFA and sand in the cement mixture provides a strong bond between the particles and achieves greater strength. Other than that, the pozzolanic reaction produced the calcium silicate hydrate (C-S-H) gel in order to fill the voids completely.

Also, the plain concrete prism characteristic that is well known is weak and brittle under the flexural loads [1]. So that, with the elasticity features of AR glass fabric that is great on brittle stress give more durability and ability as a structure
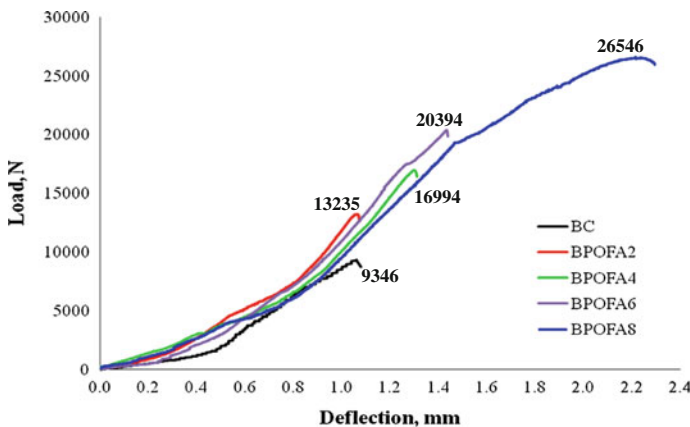
Fig. 5 The variations of flexural load versus deflection of specimens under monotonic loads

components to bear the high ultimate load capacity and serviceability. Thus, it can increase the lifespan of the structure.

Therefore, the more TFGM layers strengthened on plain concrete prism, the strength provided by textile fibres can increase. However, by using a lot of textile layer it is not effective to be used as a mortar due to the allowed maximum thickness of mortar which does not exceed 10 mm [34].

5   Conclusion

From results obtained on this study, the following conclusion was drawn out:

(1) The alternative method to repair the existing deficiencies in modern concrete was successfully developed by TFGM.
(2) TFGM is effective in increasing the flexural strength on plain concrete prism because the ultimate load carrying capacity of the strengthened beams is higher compared to unstrengthened plain concrete prism.
(3) AR glasses have great properties on brittle stress due to the increasing of flexural behaviour.

References

1. M. Gencoglu, "Monotonic and cyclic flexural behavior of plain concrete beams strengthened by fabric-cement based composites," pp. 1961–1966, 2005.
2. T. Tysmans, S. Adriaenssens, H. Cuypers, and J. Wastiels, "Structural analysis of small span textile reinforced concrete shells with double curvature," *Compos. Sci. Technol.*, vol. 69, no. 11–12, pp. 1790–1796, Sep. 2009.
3. T. Blanksvärd, L. Tech, and P. D. Student, "Strengthening of concrete structures with cement based bonded composites," *Nord. Concr. Res.*, vol. 2, pp. 133–154, 2008.
4. W. Y. W. Yusof, S. H. Adnan, Z. Jamellodin, and N. S. Mohammad, "Strength Development of Fine Grained Mortar Containing Palm Oil Fuel Ash as a Partial Cement Replacement," vol. 774, pp. 964–968, 2015.
5. P. Chindaprasirt, S. Homwuttiwong, and C. Jaturapitakkul, "Strength and water permeability of concrete containing palm oil fuel ash and rice husk–bark ash," *Constr. Build. Mater.*, vol. 21, no. 7, pp. 1492–1499, Jul. 2007.
6. M. R. Karim, M. F. M. Zain, M. Jamil, and F. C. Lai, "Significance of Waste Materials in Sustainable Concrete and Sustainable Development," in *International Journal of Biotechnology and Environmental Management*, 2011, vol. 18, pp. 43–47.

7. E. T. Dawood and M. Ramli, "Properties of High Strength Flowable Mortar Reinforced With Different Fibers .," vol. 2, no. December, pp. 315–325, 2011.

8. A. Brückner, R. Ortlepp, and M. Curbach, "Textile reinforced concrete for strengthening in bending and shear," *Mater. Struct.*, vol. 39, no. 8, pp. 741–748, Sep. 2006.

9. T. Brockmann, "Mechanical and Fracture Mechanical Properties of Fine Grained Concrete for Textile Reinforced Composites," RWTH Aachen, 2005.

10. J. Hartig, U. Häußler-Combe, and K. Schicktanz, "Influence of bond properties on the tensile behaviour of Textile Reinforced Concrete," *Cem. Concr. Compos.*, vol. 30, no. 10, pp. 898–906, Nov. 2008.

11. M. Butler, V. Mechtcherine, and S. Hempel, "Experimental investigations on the durability of fibre–matrix interfaces in textile-reinforced concrete," *Cem. Concr. Compos.*, vol. 31, no. 4, pp. 221–231, Apr. 2009.

12. R. Ortlepp, U. Hampel, and M. Curbach, "A new approach for evaluating bond capacity of TRC strengthening," *Cem. Concr. Compos.*, vol. 28, no. 7, pp. 589–597, Aug. 2006.

13. B. Banholzer, T. Brockmann, and W. Brameshuber, "Material and bonding characteristics for dimensioning and modelling of textile reinforced concrete (TRC) elements," *Mater. Struct.*, vol. 39, no. 8, pp. 749–763, Jul. 2006.

14. J. Hegger and S. Voss, "Investigations on the bearing behaviour and application potential of textile reinforced concrete," *Eng. Struct.*, vol. 30, no. 7, pp. 2050–2056, Jul. 2008.

15. K. Erdogdu and P. Tucker, "Effect of Fly Ash Particles Size on Strength of Portland Cement Fly Ash Mortars," *Cem. Conrete Res.*, vol. 28, no. 9, pp. 1217–1222, 1998.

16. S. Xu and M. Krüger, "Bond characteristics of carbon, alkali resistant glass, and aramid textiles in mortar," *J. Mater. Civ. ...*, no. May 2012, pp. 356–364, 2004.

17. J. Hegger, N. Will, O. Bruckermann, and S. Voss, "Load–bearing behaviour and simulation of textile reinforced concrete," *Mater. Struct.*, vol. 39, no. 8, pp. 765–776, Jul. 2006.

18. P. Chindaprasirt, C. Jaturapitakkul, and T. Sinsiri, "Effect of fly ash fineness on compressive strength and pore size of blended cement paste," *Cem. Concr. Compos.*, vol. 27, no. 4, pp. 425–428, Apr. 2005.

19. M. Kuroda, T. Watanabe, and N. Terashi, "Increase of bond strength at interfacial transition zone by the use of fly ash," *Cem. Concr. Res.*, vol. 30, no. February 1999, pp. 253–258, 2000.

20. Y. Wong, L. Lam, C. Poon, and F. Zhou, "Properties of fly ash-modified cement mortar-aggregate interfaces," *Cem. Concr. Res.*, vol. 29, no. 1999, pp. 1905–1913, 1999.

21. K. Turk, "Viscosity and hardened properties of self-compacting mortars with binary and ternary cementitious blends of fly ash and silica fume," *Constr. Build. Mater.*, vol. 37, pp. 326–334, Dec. 2012.

22. V. Sata, J. Tangpagasit, C. Jaturapitakkul, and P. Chindaprasirt, "Effect of W/B ratios on pozzolanic reaction of biomass ashes in Portland cement matrix," *Cem. Concr. Compos.*, vol. 34, no. 1, pp. 94–100, Jan. 2012.

23. W. Tangchirapat, C. Jaturapitakkul, and K. Kiattikomol, "Compressive strength and expansion of blended cement mortar containing palm oil fuel ash," *J. Mater. Civ. Eng.*, no. August, pp. 426–431, 2009.

24. W. Kroehong, T. Sinsiri, C. Jaturapitakkul, and P. Chindaprasirt, "Effect of palm oil fuel ash fineness on the microstructure of blended cement paste," *Constr. Build. Mater.*, vol. 25, no. 11, pp. 4095–4104, Nov. 2011.

25. M. Ramli and E. T. Dawood, "High-strength flowable mortar reinforced by steel fiber," *Slovak J. Civ. Eng.*, vol. 0, no. 3, pp. 10–16, 2011.

26. W. Brameshuber, *Report 36: Textile Reinforced Concrete-State-of-the-Art Report of RILEM TC 201-TRC. Vol. 36.* RILEM publications, 2006.

27. S. M. Harle, "Review on the Performance of Glass Fiber Reinforced Concrete," vol. 5, no. 3, pp. 281–284, 2014.

28. H. M. Elsanadedy, T. H. Almusallam, S. H. Alsayed, and Y. A. Al-Salloum, "Flexural strengthening of RC beams using textile reinforced mortar—Experimental and numerical study," *Compos. Struct.*, vol. 97, pp. 40–55, Mar. 2013.

29. ASTM International, "Standard Specification for Coal Fly Ash and Raw or Calcined Natural Pozzolan for Use," 2013.
30. British Standard, "BS 4551:2005-Mortar—Methods of test for mortar—Chemical analysis and physical testing," 2005.
31. British Standard, "BS EN 196-1:2005. Methods of testing cement—Part 1: Determination of stength," 2005.
32. British Standard, "BS EN 196-3:2005. Methods of testing cement—Part 1: Determination of setting times and soundness," 2005.
33. A. M. Neville, *Properties of Concrete*, 5th ed. England: Pearson Education Limited, 2011.
34. R. S. Ravindrarajah and M. Mansour, "Current Practices on Cement Rendering in Australia," no. 979, pp. 21–22, 2009.

Axial Compression Behaviour of Plastered Wood-Wool Cement Composite Panel Wallettes

M.S. Md Noh, Z. Ahmad, A. Ibrahim and P. Walker

Abstract Wood-wool cement composite panel (WWCP) is a wood-based product which is produced from renewable materials, lightweight and low carbon emission. WWCP is currently available for the construction industry in Malaysia, especially for wall element in building construction. However, the installation of WWCP as the walling unit is still not well established. Therefore, this paper presents the axial compression behaviour of plastered wallettes fabricated using wood-wool cement composite panel (WWCP). Two different configurations of wallettes were designed and denoted as W1 and W2. Each wallettes of dimensions 600 mm × 600 mm were plastered with 16 and 20 mm mortar thicknesses. A total of 18 wallettes were prepared accordingly and tested under axial compression load. The results indicated that, the application of surface plaster significantly increases the load capacity of wallettes. However, the increase of plaster thickness marginally increases the loading capacity of both types of wallettes.

M.S. Md Noh (✉) · A. Ibrahim
Faculty of Civil Engineering, Universiti Teknologi Mara,
40450 Shah Alam, Selangor, Malaysia
e-mail: soffi@uthm.edu.my

A. Ibrahim
e-mail: Azmii716@yahoo.com

Z. Ahmad
Institute for Infrastructure Engineering and Sustainable Management,
Universiti Teknologi Mara, 40450 Shah Alam, Selangor, Malaysia
e-mail: zakiah@salam.uitm.edu.my

P. Walker
Department of Architecture and Civil Engineering, University of Bath,
Bath BA2 7AY, UK
e-mail: P.Walker@bath.ac.uk

1 Introduction

Sustainability in building technology has brought new materials to be used as a wall element in building construction. Wood is an important building material and widely available to the construction industry [1]. Wood-wool cement composite panel (WWCP) is one of wood-based products that were produced from renewable material, lightweight, easy to process and fabricate and can be an alternative to replace the conventional brick wall and concrete masonry in building construction [2]. In Malaysia, WWCP are manufactured by compressing a mixture of wood-wool and cement paste in a specific size of wooden mould. When hardened, the resulting WWCP are stable and have a density range from 300 to 500 kg/m^3 [3]. The mechanical properties of wood-wool cement board or panel made from different timber species have been studied by several researchers [3–5]. Ashori et al. [4] studied the mechanical properties of wood-wool cement board made from eucalyptus and poplar species and found that the boards produced using poplar wood-wool had better properties compared to board with eucalyptus and mixed wood-wool. Ahmad et al. [3] studied the mechanical properties of wood-wool cement composite board made from Malaysian fast grown timber species known as Kelampayan and the results indicated that the boards made from smallest wood-wool sizes and less thicker board performed well in mechanical properties. Soffi et al. [5] experimentally compared the mechanical properties of 50 and 100 mm thickness of WWCP which are also made from Kelampayan species. They highlighted that the increase of panel thickness decreased the density and strength properties of the panels. For structural application purposes, all boards produced should satisfy the minimum requirement specified in the ISO and DIN 1101 standards.

The applications of WWCP not only can be used as a wall element, but its use as a permanent formwork for reinforced concrete structure has also been explored. Nursafarina et al. [6] investigated the structural performance of reinforced concrete column with wood-wool cement board (WWCB) as permanent formwork and the results showed that the column with WWCB permanent formwork increased about 30 % load carrying capacity of the column. Ahmad et al. [7] further investigated the fire resistance performance of reinforced concrete column embedded with WWCB as a permanent formwork and the result indicated that the insulation and integrity of the WWCB after two hours fire exposure had satisfied the requirement of BS 476: Part 22: 1987. In another study [5], authors had previously investigated the structural behaviour of wallettes constructed using WWCP with the different panel arrangement and joint techniques. The wallettes then were tested under axial compression load without surface plaster. The results revealed that the new proposed panel arrangement technique bonded with 15 mm mortar thickness recorded

a higher loading capacity compared against all tested wallettes. This paper is a continuation of the research work reported in the previous paper, however the effect of surface plaster on both sides with two different thicknesses is explored.

Surface plaster is an important element for wall in building construction. It can be either for aesthetic purposes or enhance the structural performance of the wall. On the other hand, surface plaster also can prevent the wall from severe weather condition and fire resistance [7]. Previous studies have shown that the application of surface rendered or plastered significantly increased load carrying capacity and stiffness of the wall [8–10]. Therefore, this study experimentally investigated the behaviour of plastered WWCP wallettes under axial compression load.

2 Materials and Methods

2.1 Materials

Wood-wool cement composite panel (WWCP) used in this study is made from wood-wool that has been shredded from a cut of local fast grown timber species known as Kelampayan [5]. WWCP is factory made and manufactured by Duralite (M) Sdn. Bhd., produced in standard panel size of 600 mm width, 2400 mm in length and varying from 25 to 100 mm thicknesses (Fig. 1). There are two types of panel thicknesses considered in this study, which are 50 and 100 mm. The strength properties of WWCP are shown in Table 1.

Fig. 1 Wood-wool cement composite panel (WWCP)

Table 1 Material properties of wood-wool cement composite panel [5]

WWCP thickness (mm)	Density (kg/m^3)	Bending properties		Compressive strength		Tensile strength (N/mm^2)
		MOE (N/mm^2)	MOR (N/mm^2)	Perpendicular (N/mm^2)	Parallel (N/mm^2)	
50	328	444	1.15	0.84	1.00	0.060
100	272	239	0.40	0.30	0.30	0.018

Table 2 Material properties of EMACO R1 mortar mix at age 28 days

Application of mortar	Mix ratio (Dry mix (kg): Water (kg))	Flexural strength (N/mm^2)	Compressive strength (N/mm^2)
Adhesive	5:1	12.44	26.02
Plaster	5:1	6.55	27.11

In the fabrication process of wallettes, the pre-mix mortar namely *EMACO R1* has been used as a bonding agent and surface plaster. This pre-mix mortar is manufactured by BASF (M) Sdn. Bhd. The mix ratio and strength properties of hardened mortar are shown in Table 2.

2.2 Fabrication of Wallettes Specimens

The fabrication process of W1 and W2 are similarly described in Soffi et al. [5] where, W1 is the currently practiced technique while W2 is the new proposed
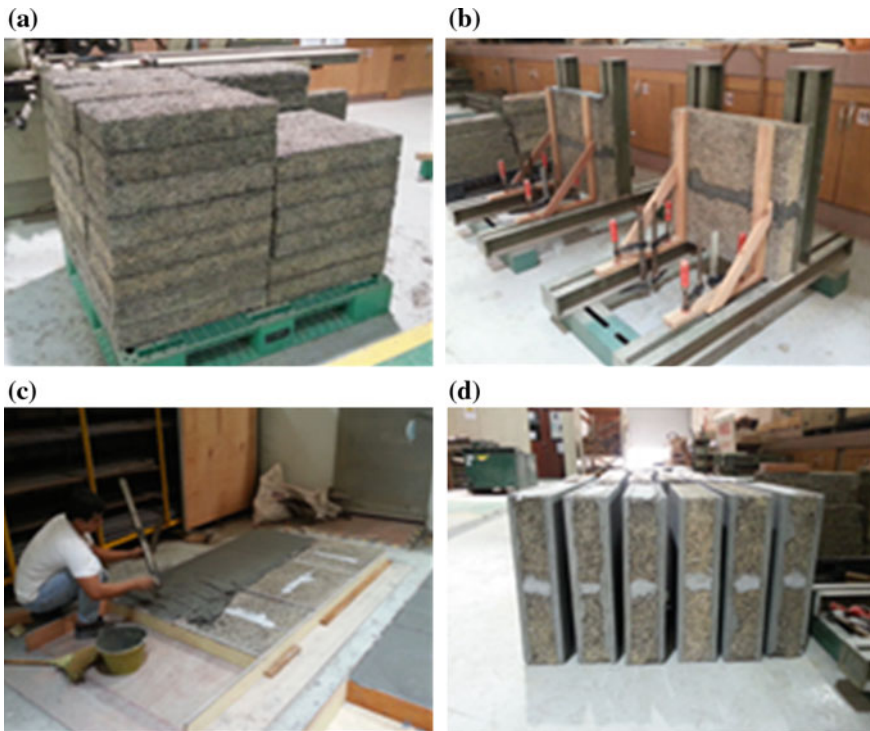
Fig. 2 Fabrication process of wallettes type 1 (W1). **a** Preparation 100 mm thick cut panel for W1. **b** Vertical stacking the cut panel for W1. **c** Plastering of W1. **d** Curing of W1
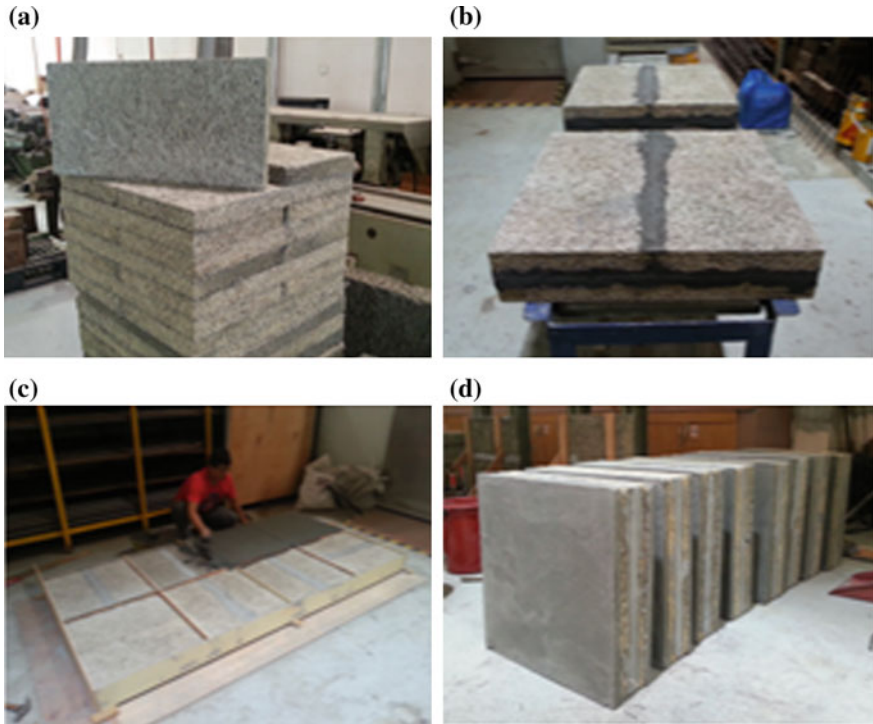
Fig. 3 Fabrication process of wallettes type 2 (W2). **a** Preparation 50 mm thick cut panel for W2. **b** Horizontal laying of cut panel for W2. **c** Plastering of W2. **d** Curing of W2
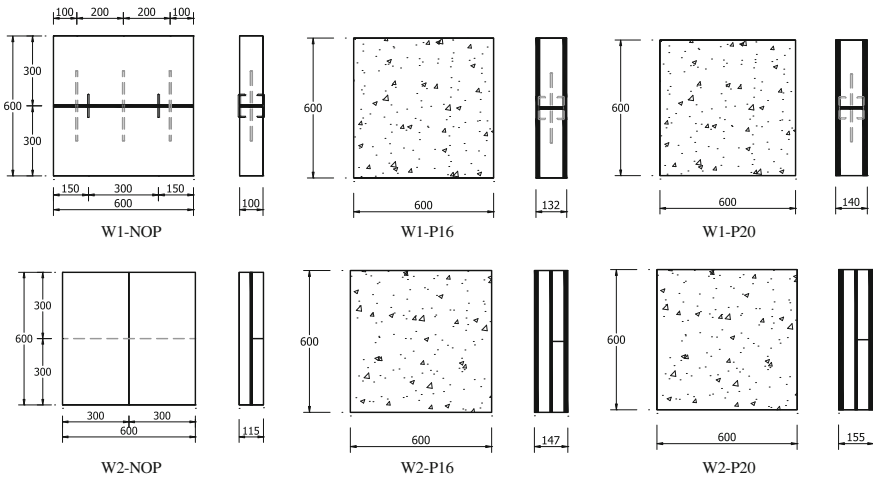
Fig. 4 Details of wallettes fabricated using wood-wool cement composite panel (all units in millimetres)

technique for wall construction using WWCP. For W1, the 100 mm thickness of WWCP were used and cut into size of 600 mm × 300 mm. Then, the cut panels vertically stacked in two layers and bonded together using 10 mm mortar thickness. To hold stacked panel in their position, three 8 mm steel bars were inserted between panel and two U-nails have been clamped on each side of wallettes. Meanwhile, for W2 the 50 mm thickness of WWCP was used and also cut into size of 600 mm × 300 mm. The cut panels were then horizontally laid in two layers at different panel orientation (longitudinal and transverse direction) and bonded together using 15 mm mortar thickness. This wallettes can be seen as a sandwich panel where the panels are the covering sheet and the mortar mix is the core. Both wallettes were then plastered by hand on both sides with two different plaster thickness and denoted as P16 for 16 mm and P20 for 20 mm plaster thickness. Three replicates were prepared for each wallettes specimen. The fabrication process of W1 and W2 are described in Figs. 2 and 3, and details of wallettes specimen are shown in Fig. 4.

2.3   Testing Set-up and Procedures

In the axial compression load test, a total of 18 wallettes were tested under axial compression load after 28 days of fabrication. The wallettes were carefully placed on a testing rig as shown in Fig. 5b. The 600 kN hydraulic jack was used to apply uniformly distributed load on top of wallettes specimens. The testing set-up was instrumented with three LVDTs, where LVDT 1 is used to measure the vertical displacement and LVDT 2 and 3 are used to measure the horizontal displacement of the wallettes. The position and straightness of the specimens were checked using a

(a)

Load Cell

LVDT 1

Spreader Beam

LVDT 2 & 3

600 mm

Specimen

Steel Beam

(b)
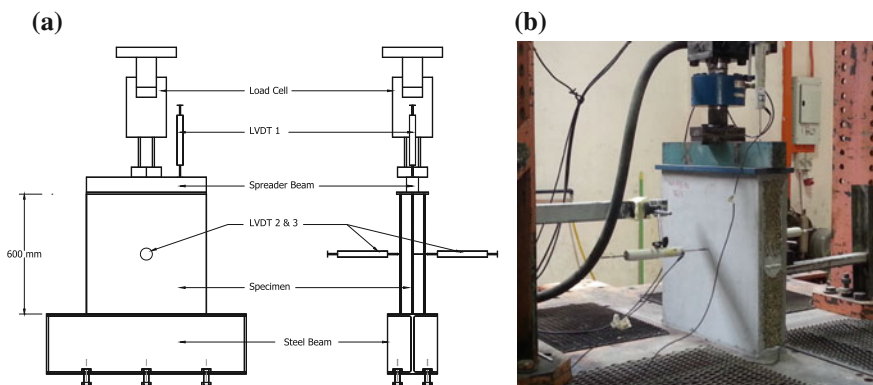
Fig. 5 Axial compression load testing set-up of WWCP wallettes. **a** Illustrated testing set-up. **b** Actual testing set-up

spirit level to avoid load eccentricities. The load was then applied at a uniform rate of 0.005 mm/s up to failure [10]. The failure load, maximum displacement at peak and the failure mode were observed and recorded [11].

3 Results and Discussions

This section presents the results of the axial compression load test of wallettes fabricated from WWCP. The wallettes types W1 and W2 without surface plaster and plastered with 16 and 20 mm mortar thicknesses have been observed in terms of maximum load carrying capacity, load-vertical displacement behaviour and failure mode of each wallettes type.

3.1 Axial Compression Load Capacity of Wallettes

A summary of maximum load and displacement at the maximum applied load of wallettes W1 and W2 is shown in Table 3. From the testing results of wallettes W1, it can be seen that the maximum axial load of wallettes without surface plaster (W1-NOP) was very low (10.18 kN) compared to plastered wallettes. This shows that the 100 mm panel thickness used as a wall panel alone without surface plaster did not show a good performance probably due to poor bonding condition within the composites. However, the axial compression load capacity of wallettes W1 significantly increased when they were plastered with 16 mm (W1-P16) and 20 mm (W1-P20) mortar which up to 164.84 kN and 166.17 kN, respectively. This shows that the application of surface plaster effectively improved compressive strength of wallettes W1.

It also can be seen that the axial compression load capacity of wallettes W1-P20 marginally higher than wallettes W1-P16 is about 0.8 %. It was noticed that the increase in plaster thickness did not affect the strength of this type of wallettes.

For W2 wallettes, the results show that the wallettes without surface plaster (W2-NOP) achieved the maximum load of 157.04 kN. For wallettes plastered with 16 mm mortar, the axial compression load capacity significantly increased about 17 % to the maximum load of 184.32 kN and 20 % increased to the maximum load of 188.71 kN for wallettes plastered with 20 mm mortar. In terms of plaster thickness effect, similarly as W1, the increase of plaster thickness from 16 to 20 mm did not affect the strength of the wallettes which only increased about 2.40 %. These results indicated that the new panel arrangement technique (W2) which fabricated using two layers of 50 mm panel thickness and bonded with 15 mm thickness of mortar shows a good performance in terms of load carrying capacity even when tested without surface plaster.

Table 3 Maximum load and vertical displacement of wallettes W1 and W2 under axial compression load

Wallettes types	Plaster thickness (mm)	Number of specimens	Specimen name	Maximum load (kN)	Vertical displacement (mm)	Maximum load (Mean) (kN)	Vertical displacement (Mean) (mm)
W1	0	3	W1-NOP-1 V	9.77	4.95	10.18	4.09
			W1-NOP-2 V	8.35	3.76		
			W1-NOP-3 V	12.42	3.56		
	16	3	W1-P16-1 V	175.93	2.15	164.84	2.17
			W1-P16-2 V	220.60	2.43		
			W1-P16-3 V	97.98	1.94		
	20	3	W1-P20-1 V	212.70	1.91	166.17	2.00
			W1-P20-2 V	121.44	2.14		
			W1-P20-3 V	164.38	1.45		
W2	0	3	W2-NOP-1 V	133.05	4.08	157.04	4.60
			W2-NOP-2 V	164.66	4.48		
			W2-NOP-3 V	173.30	5.25		
	16	3	W2-P16-1 V	218.04	3.90	184.32	4.78
			W2-P16-2 V	165.85	4.39		
			W2-P16-3 V	169.06	6.06		
	20	3	W2-P20-1 V	224.49	7.19	188.71	7.71
			W2-P20-2 V	156.43	6.55		
			W2-P20-3 V	185.22	9.38		

3.2 Load-Displacement Behaviour of Wallettes

The load and vertical displacement behaviour of wallettes W1 under axial compression load test is shown in Fig. 6. For wallettes W1 without surface plaster (W1-NOP), the load-displacement of selected curve shows that the load relatively flat increased up to very low compression load due to weakness of 100 mm panel thickness. After reaching the maximum load of an average 10.18 kN, the displacement was recorded on an average of 4.09 mm, a gradual drop in the applied load was observed and this shows that the wallettes continued to resist the load before its final failure. For wallettes W1 with 16 and 20 mm thicknesses of surface plaster, the plots shows that the wallettes plastered with appropriate mortar strength was able to prevent the crushed failure of 100 mm WWCP and consequently contributed the wallettes to resist a higher applied load. The vertical displacement increases almost linearly with the load up to a maximum applied load, however, the load was observed to suddenly drop to final failure after reaching the maximum applied load and the wallettes were considered to not resist anymore loads beyond this point.

Figure 7 shows the load-vertical displacement behaviour of wallettes W2 without surface plaster and plastered with 16 and 20 mm mortar thicknesses. As can be seen that the applied axial load of wallettes W2-NOP increased nonlinearly with vertical displacement up to maximum load on average of 157.04 kN at the displacement of 4.60 mm. After this load, the applied load was observed to drop in, however, it can be seen that the wallettes W2-NOP continued to resist the load until its final failure. A high applied load and displacement recorded from this type of wallettes without surface plaster proved that the panel arrangement technique proposed for W2 wallettes is the best solution for prefabricated wall construction using WWCP. For wallettes W2 with surface plaster which are W2-P16 and W2-P20, the load-displacement behaviour exhibited the similar pattern if compared against wallettes without surface plaster. The increment of maximum applied load and vertical displacement was observed for both plastered wallettes. The highest

Fig. 6 Axial load—vertical displacement response for wallettes W1
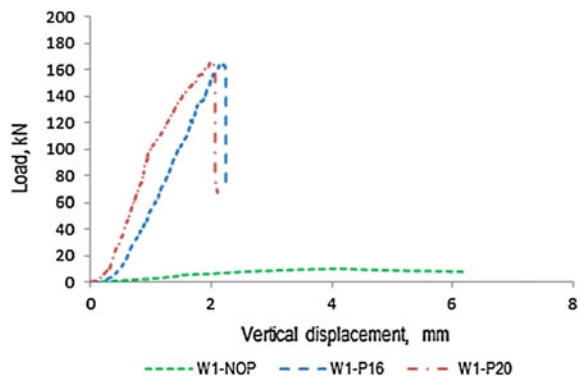
Fig. 7 Axial load—vertical displacement response for wallettes W2
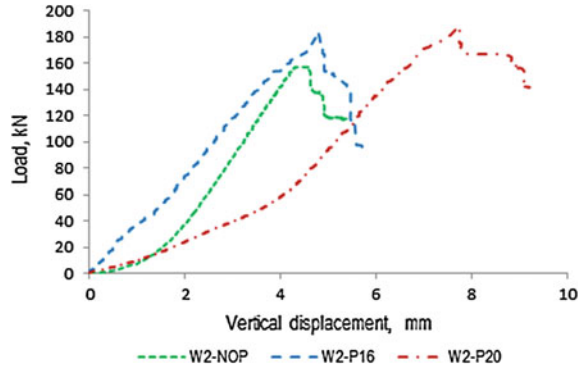
applied load and vertical displacement were recorded for wallets W2 with 20 mm plaster thickness.

3.3 Failure Behaviour of Wallettes

Figure 8 shows the failure behaviour of wallettes W1 and W2 under compression load test. Based on the observation, the crack of wood-wool panels was observed as a main cause of the failure of the wallettes. The failure mechanism observed for wallettes W1-NOP was started with the crushing of the panel and transverse crack appeared along the panel (Fig. 8a). There was no failure along the connexion and finally the vertical crack was observed in the cross section of the wallettes. For plastered W1 wallettes (Fig. 8c, e), it can be seen that when the load was continued, the vertical crack was seen to appear and grow in the WWCP up to final failure. The load was suddenly dropped after the failure of wood-wool panel occurred. There is no crack or failure observed on the plaster surface on both wallettes and this proved that the surface plaster prevents the panel against crushing failure as occurred on wallettes without surface plaster.

For wallettes W2, the failure behaviour of wallettes was identical for all wallettes either plastered or without surface plaster (Fig. 8b, d, f). As can be seen that when the applied load increases up to the maximum, the vertical crack of wood-wool panel was observed to propagate along the height of wallettes. After the post peak load, the crack panel started to split out vertically in adjacent to the mortar joint which caused the debonding failure of the 50 mm wood-wool panel.
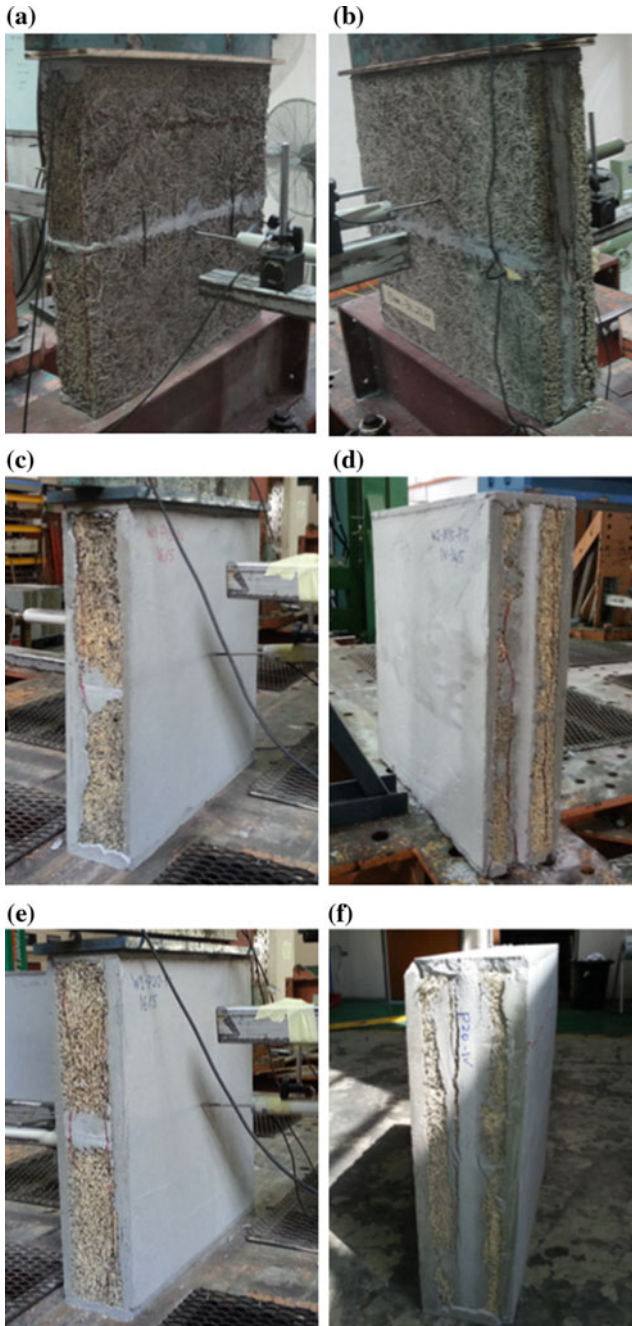
Fig. 8 Failure behaviour of wallettes W1 and W2 under compression load test. **a** W1-NOP, **b** W2-NOP, **c** W1-P16, **d** W2-P16, **e** W1-P20, **f** W2-P20

4   Conclusion

The following conclusions may be drawn from this study,

- The wallettes W1 without surface plaster demonstrated very low in axial compression load capacity, however the axial compression load capacity of wallettes W1 significantly much higher increased when plastered with 16 and 20 mm mortar thicknesses. This indicated that the provision of surface plaster gave additional restraint to effectively utilise the compressive strength of 100 mm thickness wood-wool panel.
- The experimental results of wallettes W2 show a good performance in terms of axial load carrying capacity even tested without surface plaster and moreover, after being plastered with 16 and 20 mm the load carrying capacity increased approximately 17 % and 20 %, respectively.
- The increase in plaster thickness from 16 to 20 mm did not show significant difference on the load carrying capacity of the wallettes W1 and W2.
- The failure mechanism of wallettes indicated that the damage of wood-wool panel by the formation of vertical crack on the web is the main failure cause of wallettes under axial compression load.
- The wallettes W1 and W2 with 16 mm plaster thickness will be used as guidance for future research of prefabricated wall constructed using wood-wool cement composite panel (WWCP).

References

1. Okino, E. Y., Souza, M. R. d., Santana, M. a., Alves, M. V. d. S., Sousa, M. E. De, & Teixeira, D. E. . Cement-bonded wood particleboard with a mixture of eucalypt and rubberwood. Cement and Concrete Composites, 26(6) (2004), 729–734.
2. Goverse, T., Hekkert, M. P., Groenewegen, P., Worrell, E., & Smits, R. E. H. . Wood innovation in the residential construction sector; opportunities and constraints. Resources, Conservation and Recycling, 34(1) (2001), 53–74.
3. Ahmad, Z., Wee, L. S., & Fauzi, M. A. . Mechanical Properties of Wood-wool Cement Composite Board Manufactured Using Selected Malaysian Fast Grown Timber Species. ASM Science Journal, 5(1) (2011), 27–35.
4. Ashori, A., Tabarsa, T., Azizi, K., & Mirzabeygi, R. . Wood–wool cement board using mixture of eucalypt and poplar. Industrial Crops and Products, 34(1) (2011), 1146–1149.
5. Mohammad Soffi Md Noh, Zakiah Ahmad, Azmi Ibrahim. Axial compression behaviour of wallettes constructed using wood-wool cement composite panel. Advanced Materials Research, 1051 (2014), 671–677.
6. Nursafarina Ahmad, Zakiah Ahmad, Azerai Ali Rahman, Hanizah Ab Hamid, & Mohd Azrizal Aziz Fauzi . Increasing the capacity of concrete column with integrated permanent

formwork using wood-wool cement board. Applied Mechanics and Materials, 325–326 (2013), 1305–1309.

7. Ahmad, Z., Ahmad, N., Ali, Rahman, A., Abdul, Hamid, H., & Md, Noh, M. S. . Fire resistance performance of reinforced concrete column with embedded permanent formwork using wood-wool panel. Applied Mechanics and Materials, 661 (2014), 111–117.

8. Lawrence, M., Drinkwater, L., Heath, A., Walker, P. . Racking shear resistance of prefabricated straw-bale panels. Proceeding of the Institute of Civil Engineers: Contruction Materials, 162(3) (2009), 133–138.

9. Vardy, S. and MacDougall, C. Concerntric and eccentric compression experiments of plastered straw bale assemblies. Journal of Structural Engineering, 139 (3), (2013), 448–461.

10. F. L. De Oliveira and J. B. De Hanai. Axial compression behaviour of concrete masonary wallettes strengthened with cement mortar overlay. IBRACON Structures and Materials J., 1 (2) (2008), 158–170.

11. Manalo, A. . Structural behaviour of a prefabricated composite wall system made from rigid polyurethane foam and Magnesium Oxide board. Construction and Building Materials, 41 (2013), 642–653.

Waste Paper Sludge Ash (WPSA) as Binder in Solidifying Water Treatment Plant Sludge (WTPS)

I. Nurliyana, M.A. Fadzil, H.M. Saman and W.K. Choong

Abstract Water treatment plant sludge (WTPS) is pathogen and heavy metals that can harm human health and the environment. As strict regulation had been implemented, WTPS is advised and must be treated before the waste is transported to landfill. Therefore, this research is conducted to solidify WTPS with an alternative waste material. The waste material so called as waste paper sludge ash (WPSA) was chosen as binder to be used to solidify WTPS. WPSA is a waste that is produced in bulk at the recycled paper factories. Somehow, its potentiality, especially as cement replacement materials is unknown. The objective of this research is to investigate the possibility of using WPSA as an alternative replacement material of cement in solidifying the WTPS. WPSA was used in proportions of 10, 20, 30, and 40 % as cement replacement by volume along with WTPS in fixed quantity. An additional mix without WPSA solidifying WTPS is also prepared. The effectiveness of WPSA in solidifying WTPS was determined based on the compressive strength achieved on 1, 3, 7, and 28 days of curing. High replacement amount of WPSA with at least 0.34 N/mm^2 compressive strength will be selected as the best mix. Based on results obtained, the compressive strength of solidified WTPS increased with increasing curing days for all mix types. The smallest particle size and highest surface area of WPSA had contributed to the condition. Although, the compressive strength of solidified WTPS decreases with increasing WPSA percentage replacement. In addition, WPSA used in this research

I. Nurliyana (✉) · H.M. Saman
Faculty of Civil Engineering, Universiti Teknologi MARA, Shah Alam, Malaysia
e-mail: nurliyana_ismail@ymail.com

H.M. Saman
e-mail: hmohdsaman@salam.uitm.edu.my

M.A. Fadzil
Institute of Infrastructure Engineering and Sustainable Management (IIESM),
Faculty of Civil Engineering, Universiti Teknologi MARA, Shah Alam, Malaysia
e-mail: fadiil2013@yahoo.com

W.K. Choong
Department of Civil Engineering, University of Nottingham, Nottingham, Malaysia
e-mail: Choong.WeeKang@nottingham.edu.my

was a non-pozzolanic material with very porous surface area and irregular shape. In conclusion, a mix of 40 % WPSA labeled as W5 is a more sustainable mix binder in solidifying WTPS. Although, W2 with 10 % of WPSA substitution had passed the landfill acceptable limit at 0.34 N/mm^2.

1 Introduction

Water Treatment Plant Sludge (WTPS) is the end product which was produced together during processing of drinking water resources in a typical water treatment facility. The production of WTPS is increasing parallel to the demand of the quantity and quality of potable water. Whereby, with the increase number of population, it is expected that 10,000 tons of WTPS will be increasingly generated globally [1].

The main source of WTPS is the drainage from sedimentation tank. Commonly, the moisture content of the WTPS is about 99.7 % [2]. In addition, WTPS contains pathogen and heavy metals although it is usually found at low level of concentration [3, 4]. Unfortunately, the majority of WTPS is still disposed to landfill [5–8]. To reduce the long-term accumulation of heavy metals in landfill as well as protecting the environment, a sustainable solution to deal with the WTPS must be looked into.

Solidification can be categorized as the best method in dealing with sludge. It is due to its simplicity and economical view of point. In a study conducted by Montañés et al. [9], it was shown that solidification/stabilization process using cement was successfully applied to tannery sludge chromium. The chromium concentration decreases as the relative amount of cement and water increases. However, the method highly depends on the type of binder used. Thus, waste paper sludge ash (WPSA) is introduced as binder in this research for solidifying WTPS. WPSA is a problematic waste material that mainly consists of calcium, silica, alumina, and organic compound which calcined in temperature range of 700–800 °C [10].

WPSA is believed to pose the desired solidifying function as well as meeting the environmental requirement on the concentration of heavy metals. WPSA was found to be used as partial cement replacement, can act either as supplementary material or binder material.

A considerable amount of the literature has been published on WPSA. A study by Wong et al. [11] involved waste paper sludge ash in developing hydrophobic concrete. Ferrándiz-Mas et al. [12] also used paper sludge as supplementary cementitious material to develop lightweight cement mortars with good thermal insulation properties. Vegas et al. [13] revealed that the addition of activated paper sludge in the ternary cements gave good effects on strength development. Based on

these previous studies, it can be concluded that WPSA has potential in producing solid products. In other words, WPSA is able to transform the stage form of waste. However, there is yet no research usingWPSA as binder in solidifying WTPS.

Therefore, this research aims to experimentally evaluate the potential of WPSA, to act as cement replacement material to solidify the WTPS. To do so, WPSA was utilized 10–40 % cement replacement by volume with purpose to solidify WTPS. A binder with 100 % of ordinary portland cement (OPC) was then used as control in order to solidify WTPS. The effectiveness of the WPSA in solidifying WTPS was evaluated based on the compressive strength value identification at various days of curing. Now, this is a part of the author's research. A research on various types of sludge utilizing WPSA in the developed binder is still ongoing.

2 WTPS and Binder Materials

2.1 WTPS Source and Compositions

WTPS was obtained from a local drinking water treatment plant located in Perak, Malaysia. WTPS contains 20.72, 26.73, and 0.17 % of Al_2O_3, SiO_2, and CaO, respectively, as the major chemical compositions in the sludge. In addition, high content of iron in the raw water resource is the main issue for this treatment plant. Therefore, the predominant component of metals in WTPS is iron with 7.25 %. Other components of WTPS to meet the waste acceptance criteria are tabulated in Table 1. The percentage of the other components was determined based on the leachability test of the untreated WTPS in order to allow WTPS acceptable for direct landfill disposal. As there is stringent concern on accumulation of heavy metals in landfill, by solidifying WTPS, the leachability of the component of metals stopped.

2.2 Binders Source and Compositions

Ordinary portland cement (OPC) confirming to MS 522:Part 1:1989 was a main binder used. While, the replacement materials used in this research was WPSA. WPSA was collected from a paper factory in Selangor, Malaysia. The quantity of OPC

Table 1 The WTPS components to meet waste acceptance criteria

Components	WTPS (mg/L)	Waste acceptance criteria (mg/L)
Cadmium (Cd)	0.003	<0.2
Lead (Pb)	0.004	<2
Nickel (Ni)	0.004	<3
Copper (Cu)	0.01	<10
Chromium (Cr)	0.02	<0.5

Table 2 Chemical compositions of OPC and WPSA

Chemical compositions	OPC (%)	WPSA (%)
CaO	63.0	50.67
SiO_2	20.0	13.96
Al_2O_3	5.70	9.36
MgO	0.99	4.23
Fe_2O_3	2.90	–
SO_3	3.50	–
Na_2O	0.08	–
K_2O	1.20	0.22
LOI	2.63	–
Others	–	21.56

Table 3 OPC:WPSA mix types to solidify WTPS

Mix types	OPC:WPSA	WTPS (g)
W1	100:0	200
W2	90:10	200
W3	80:20	200
W4	70:30	200
W5	60:40	200

used was based on weight-to-weight ratio by volume of WPSA replacement. The chemical compositions were tested prior to mixing in the cement paste to solidify WTPS and shown in Table 2 respectively. The chemical analysis was done to determine the silica, alumina, calcium oxide, and magnesium contents in the both ash.

Volume replacement is adopted in this research as the relative weight of WPSA is lower than OPC. Four mix types were produced with partial substitution of WPSA by volume into OPC in various percentages of 10 % (W2), 20 % (W3), 30 % (W4), and 40 % (W5) as shown in Table 3. W1, control mix types using 100 % OPC is used to discover the influence of WPSA substitution in solidifying the WTPS. The water content was between 0.5–0.8. 200 g of WTPS was used for each mix types and prepared in triplicate. All the specimens were cast into 50 mm × 50 mm × 50 mm cubes for compressive strength. All the cubes were cast in standard steel molds. After 24 h of casting, the specimens were removed from the molds and cured. The cubes were tested for compressive strength accordance to BS 1881: Part 1: 1983 at 1, 3, 7, and 28 days using universal testing machine (UTM).

3 Results and Discussions

As seen in Table 4 and Fig. 1, the compressive strength increases with increasing curing days for all mix types. Overall, these results indicate that the addition of WPSA as cement replacement can effectively enhance the compressive strength of

Table 4 Compressive strength of solidified WTPS at different curing days

Mix types	OPC:WPSA	Compressive strength (N/mm^2)			
		1	3	7	28
W1	100:0	0.77	0.99	1.26	1.43
W2	90:10	0.69	0.84	0.95	1.16
W3	80:20	0.65	0.72	0.81	1.01
W4	70:30	0.59	0.69	0.78	0.92
W5	60:40	0.58	0.65	0.75	0.84
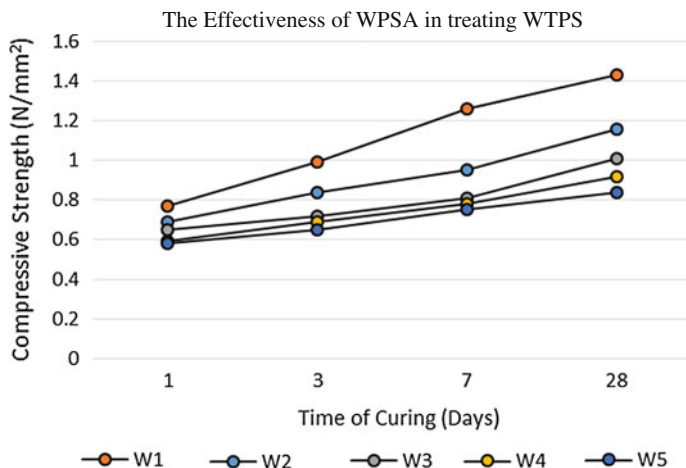
Fig. 1 The compressive strength development of solidified WTPS using WPSA

solidified WTPS but in long-term condition. These results seem to be consistent with those of Sharipuddin et al. [14] who stated that the addition of WPSA as cement replacement could effectively enhance the compressive strength. Hence, it could conceivably be hypothesized that high content of calcium oxide (CaO) in WPSA assists in sustaining the strength development throughout the curing periods [15].

Further analysis showed that, the compressive strength decreased with increasing WPSA in the mix types. W3, W4, and W5 showed the decreasing trends after the substitution of 20, 30, and 40 % replacement of WPSA, respectively, in order to solidify WTPS. W2 contains 10 % of WPSA replacement and achieved highest compressive strength compared to the strength achieved by W2, W3, and W4. The compressive strength values of W2 for days 1, 3, 7, and 28 were 0.69, 0.84, 0.95, and 1.16 N/mm^2, respectively.

What is interesting in this data is the compressive strength of control mix, which is W1, is still the highest compared to other mix types. W1 contains 50 % of OPC without any partial replacement of WPSA. The compressive strength achieved at days 1, 3, 7, and 28 were 0.77, 0.99, 1.26, and 1.43 N/mm^2, respectively.

A similar trend has been reported by other researchers [16–18]. The researchers revealed that the compressive strength in the presence of WPSA was lower than those of control specimens. Similarly, Anuar et al. [19] reported that the amount of WPSA should not be too high (<10 % by weight of cement). This is due to the fineness and water adsorption capability of WPSA. The specific gravity and particle size of WPSA is about 1.65 and 99.92 % of fine or silt size, respectively [20]. Thus, the utilization of more than 10 % WPSA can only achieve limited compressive strength.

Furthermore, a pozzolanic material hardens with water only after activation with an alkaline substance such as lime (CaO) [21]. Unfortunately, the WPSA used in this research is not considered as pozzolanic material as the total percentage of the three major combined oxides is less than 50 %. The three major combined oxides are silicon dioxide (SiO_2), aluminum oxide (Al_2O_3), and ferric oxide (Fe_2O_3). Therefore, this condition effects the strength development to evaluate the effectiveness of WPSA in solidifying WTPS.

Although this research focuses on compressive strength of solidified WTPS, the findings may well have a bearing on the particle size of WPSA. WPSA also has very porous surface area and irregular in shape [22]. Smallest particle size and highest surface area of WPSA will generate more calcium silicate hydrate (C-S-H) in cement matrix [23–25]. This condition leads to highest number of links interparticles of the matrix produced, hence contributing to strength development of solidified WTPS.

Returning to the hypothesis posed at the beginning of this research, it is now possible to state that WPSA is potential to be used as binder in solidifying WTPS. Therefore, it can be concluded that W5 (40 % of WPSA substitution) is the favorable percent for cement replacement in solidifying WTPS. The mix also satisfied the landfill acceptable limit of 0.34 N/mm^2. Taken together, these findings suggest a role for WPSA in promoting the proper management of sludge through solidification method. Since this research was limited to solidification of WTPS, it was not possible to evaluate the potentiality of WPSA in stabilizing the heavy metals in the sludge.

4   Conclusion

The following conclusions can be drawn from the present research:

1. The compressive strength increased with increasing curing days for all mix types.
2. The compressive strength decreases with increasing WPSA percentage replacement.
3. W2 can gain strength at landfill acceptable limit which is at least 0.34 N/mm^2 although it needs a minimal (10 %) WPSA substitution to solidify water treatment plant sludge (WTPS).

4. W5 achieved compressive strength exceeded the minimum landfill acceptable limit and can be considered as the most economical and environmental mix types as W5 utilized 40 % WPSA in order to solidify the WTPS.
5. WPSA can significantly affect the compressive strength of solidified WTPS due to chemical composition that is high in CaO content about 50.67 %.
6. The physical characteristics of WPSA such as particle size and porosity can influence the development of strength in solidifying WTPS. Utilization of more than 10 % of WPSA will reduce the compressive strength of solidified WTPS.

Further studies regarding the role of WPSA would be worthwhile interesting if:

1. The inner structure of treated WTPS solidified by binder substituting WPSA into ordinary portland cement (OPC) is investigated using scanning electron microscope (SEM).
2. The effect of WPSA by varying the sludge types is considered.
3. The properties of mix made of WPSA are compared with other mix incorporated with other waste materials.

References

1. I. Fabrizi, B. Jefferson, S.A. Parsons, A. Wetherill, and P. Jarvis, "The role of polymer in improving floc strength for filtration," Environment Science Technology, vol. 44(16), pp. 6443–6449, 2010.
2. Q.H. Wang, and J.I. He, "Determination of sludge yield and selection of relevant parameters in water treatment plant," China Water Wastewater, vol. 18(8), pp. 64–66, 2002.
3. A. Hanim, P. Thanalechumi, and M.Y. Abdull Rahim, "Charaterization of alum sludge for reuse and disposal," Malaysian Journal of Fundamental & Applied Sciences, vol. 8(4), pp. 209–213, 2012.
4. M.B. Aminudin, "Study on characteristic, treatment and disposal of drinking water treatment plant residue," Proceedings of Water Malaysia 2009: International Conference on Industry Best Practice (ICIBP2009), Kuala Lumpur, Malaysian Water Association (MWA), May 19–21, 2009.
5. A. Simpson, P. Burgess, and S.J. Coleman, "The management management of potable water treatment sludge: present situation in the UK," Journal of the Chattered Institution of Water and Environmental Management, vol. 16 (4), pp. 260–263, 2002.
6. A.O. Babatunde, and Y.Q. Zhao, "Constructive approaches toward water treatment works sludge management: an international review of beneficial reuses," Critical Review Environmental Science Technology, vol. 37, pp. 129–164, 2007.
7. Y.L. Chen, M.S. Ko, Y.C. Lai, and J.E. Chang, "Hydration and leaching characteristics of cement pastes made from electroplating sludge," Waste Management, vol. 31, pp. 1357–1363, 2011.

8. J. Keeley, P. Jarvis, and S.J. Judd, "An economic assessment of coagulant recovery from water treatment residuals," Desalination, vol. 287, pp. 132–137, 2012.

9. M.T. Montañés, R. Sánchez-Tovar, and M. S. Roux, "The effectiveness of the stabilization/solidification process on the leachability and toxicity of the tannery sludge chromium," Journal of Environmental Management, vol. 143, pp. 71–79, 2014.

10. J. Pera, and A. Amrouz, "Development of highly reactive metakaolin from paper sludge," Advance Cement Based Material, vol. 7, pp. 49–56, 2008.

11. H.S. Wong, R. Barakat, A. Alhilali, M. Saleh, and C.R. Cheeseman, "Hydrophobic concrete using waste paper sludge ash," Cement and Concrete Research, vol. 70, pp. 9–20, 2015.

12. V. Ferrándiz-Mas, T. Bond, E. García-Alcocel, and C.R. Cheeseman, "Lightweight mortars containing expanded polystyrene and paper sludge ash," Construction and Building Materials, vol. 61, pp. 285–292, 2014.

13. I. Vegas, J.J. Gaitero, J. Urreta, R. Garcia and M. Frias, "Aging and durability of ternary cements containing fly ash and activated paper sludge," Construction and Building Materials, vol. 52, pp. 253–260, 2014.

14. S.S. Sharipuddin, A.R.M. Ridzuan and H.M. Saman, "The effect of FRCA and WPSA on the strength properties of foamed concrete," Journal Intelek, vol. 6(1), 2009.

15. C.Y. Yin, W.S.W. Ali, and Y.P. Lim, "Oil palm ash as partial replacement of cement for solidification/stabilization of nickel hydroxide sludge," Journal of Hazardous Materials, vol. 150, pp. 413–418, 2008.

16. J. Bai, A. Chaiparich, J.M. Kinuthia, M. O'Farrell, B.B. Sabir, S. Wild, and M.H. Lewis, "Compressive strength and hydration of wastepaper sludge ash-ground granulated blastfurnace slag blended pastes," Cement Concrete Research, vol. 33(8), pp. 1189–1202, 2003.

17. E. Mozaffari, J.M. Kinuthia, J. Bai, and S.S. Wild, "An investigation into the strength development of wastepaper sludge ash blended with ground granulated blastfurnace slag, Cement and Concrete Composites (Article in Press), 2009.

18. E. Mozaffari, M. O'Farrell, J.M. Kinuthia, and S.S. Wild, "Improving strength development of wastepaper sludge ash by wet-milling," Cement and Concrete Composites, vol. 28(2), pp. 144–152, 2006.

19. K.A. Anuar, A.R.M. Ridzuan, and S. Ismail, "Strength characteristics of geopolymer concrete containing recycled concrete aggregate," International Journal of Civil & Environmental Engineering, vol. 11(1), pp. 59–62, 2011.

20. N. Khalid, M. Mukri, F. Kamarudin, and M.A. Fadzil, "Clay soil stabilized using waste paper sludge ash (WPSA) mixtures," Electronic Journal of Geotechnical Engineering, vol. 17, pp. 1215–1225, 2012.

21. ASTM C618-08: Standard specification for coal fly ash & raw or calcined natural pozzolan for use in concrete, 2008.

22. R. Vigil de la Villa, M. Frias, M.I. Sanchez de Rojas, I. Vegas, and R. Garcia, "Mineralogical and morphological changes of calcined paper sludge at different temperatures and retention in furnace," Applied Clay Science, vol. 36, pp. 279–286, 2007.

23. A.N. Givi, S.A. Rashid, F.N.A. Aziz, and M.A.M. Salleh, "Assessment of the effects of rice husk ash particle size on strength, water permeability and workability of binary blended concrete," Construction and Building Materials, vol. 24, pp. 2145–2150, 2010.

24. P. Chindraprasirt, C. Jaturapitakkul, and T. Sinsiri, "Effect of fly ash fineness on compressive strength and pore size of blended cement paste," Cement and Concrete Composites, vol. 27, pp. 425–428, 2005.

25. S. Goñi, M. Frias, I. Vegas, R. Garcia, and R. Vigil de la Villa, "Effect of ternary cements containing thermally activated paper sludge and fly ash on the texture of C-S-H gel," Construction and Building Materials, vol. 30, pp. 381–388, 2012.

Bond Strength of Bar Connector Performance in Male-Female Interlocking Panel (M-FiP)

Mohd Suhelmiey Sobri, Siti Hawa Hamzah and Ahmad Ruslan Mohd Ridzuan

Abstract In this paper, the bond strength characteristic between reinforcement bar and cement grout as a wet joint connection mechanism in male-female interlocking panel (M-FiP) was investigated. The bond strength result depended on cement grout strength respectively. Total eight (8) specimens were constructed with grout strength as variables. Recycled aggregate with size 10 and 20 mm has been used as replacement normal aggregate in concrete production Grade 30 of male and female panel. The 12 Ø reinforcement bar size was used and installed vertically for all M-FiP specimens. The test result demonstrated that the average bond strength for all different days with cement grout strength about 58.70, 64.50, 64.70, and 90.60 N/mm^2 is 3.80, 3.93, 3.99, and 4.29 N/mm^2, respectively. From this result, it can be seen that the bond strength was influenced by material strength that has been used surrounding the reinforcement bar. The percentage increment of bond strength in different cement grout strength is 3.4, 5, and 12.9 % when compared with bond strength for 7 day M-FiP specimens. The high strength of cement grout provided greater bearing resistance against slippage between cement grout key and steel reinforcement bar. In fact, longer development length embedded in cement grout added the numbers of key that resist the slippage and directly increased the bond strength. The pullout failure occurred to all M-FiP specimens when concrete surrounding steel reinforcement bar ribs or called as concrete key is weak and other concrete at surrounding steel reinforcement bar is strong.

M.S. Sobri (✉) · S.H. Hamzah · A.R. Mohd Ridzuan
Faculty of Civil Engineering, Universiti Teknologi MARA (UiTM),
Shah Alam, Selangor, Malaysia
e-mail: suhelmiey_sobri@yahoo.com

S.H. Hamzah
e-mail: shh@salam.uitm.edu.my

A.R. Mohd Ridzuan
e-mail: ahmad299@salam.uitm.edu.my

1 Introduction

The use of reinforcement bar in reinforced concrete construction is widely applied to increase the concrete strength in terms of tensile and bending strength. Therefore, the reinforcement bar needs sufficient tensile properties and must be well performed under direct load application on reinforced concrete structures. There are two types of reinforcement bar usually used in reinforced concrete construction which is hot rolled mild steel and high yield steel with characteristic strength (f_y) 250 and 460 N/mm^2, respectively. Reference [1] have been studying the effect of reinforcement bar on the structural performance of hollow concrete block masonry under compression load. The study found that masonry structures construction needs to use reinforcement bar to increase ductility, to increase ultimate strength capacity due to axial load, and to resist tensile strength. Reference [2] indicated that the characteristic of deformed bars with ribs on surface promotes positive effect on bond strength between reinforcement bar and concrete. Reference [3] investigated the bond behavior between reinforcement bar and recycled aggregate concrete (RAC) was investigated. In their experiment, different percentage replacement of RAC was used in the concrete mix with 0, 50, and 100 %. The plain and deformed reinforcement bar has been used to study the influence of reinforcement bar surface on bond strength capacity. In fact, the bond strength capacity between concrete and reinforcement bar in reinforced concrete construction is important as an indicator value to determine the reinforced concrete strength. However, the replacement percentage of RAC in concrete using 50 and 100 % has influenced the plain rebar bond strength by reducing 12 and 6 %, respectively. Meanwhile, the bond strength deformed steel rebars is 100 % more than bond strength plain rebars between normal and recycled aggregate concrete. The result concluded that the bond between recycled aggregate concrete and deformed steel rebars is higher due to better mechanical anchorage and friction resistance. On the other hand, the bonding strength for plain steel rebar is lower because it mainly depends on the adhesion between surrounding steel and recycled aggregate concrete only, which is also depending on the percentage replacement of RAC.

2 Finding from Previous Research

Reference [4] investigated the bond performance and behavior between steel rebars and recycled aggregate concrete (RAC). They conducted 60 samples of pullout test using 12, 16, 20, and 25 mm diameter size of deformed steel rebars embedded in recycled aggregate concrete with different percentage replacement. In their

investigation, 0, 25, 50, 75, and 100 % degree of RAC replacement was used in the concrete mix to study the behavior of bond strength due to different percentage replacement. They indicate that the bonding between steel rebar and surface concrete which is to transfer the axial force between these materials is an important indicator in structural component property. They also reported that the study of bond behavior with normal concrete and steel rebars has been widely studied by previous researcher but limited study on bond behavior between deformed steel rebars and concrete with recycled coarse aggregate. In these studies, the result from bond stress-slip relationship of the deformed bars was used in proposing an empirical formula of bond stress-versus-slip relationship when using recycled aggregate concrete instead of normal concrete. By assuming a same bond stress distribution along the embedded length of deformed steel rebars in RCA concrete, the nominal bond strength formula is given in Eq. 1. The result shows that the behavior of bond development and deterioration between RCA concrete and normal concrete showed similar pattern criteria. The result of the study also shows that the increase of RCA replacement in concrete mix has increased the bond strength for all size of deformed steel rebars, the higher bond strength of RCA concrete is due to similar elastic modulus of RCA, and cement paste from recycled aggregate concrete.

$$\tau_{\max} = \frac{P_{\max}}{\pi d l} \tag{1}$$

where

$\tau_{\max}$ the peak bond stress (MPa) between concrete and steel rebar or termed as the nominal bond strength

$P_{\max}$ the peak load (N)

d is the nominal rebar diameter (mm)

l is the embedded length (mm) taken equal to 5d in this investigation

Reference [5] they tested the pullout and beam to investigate the bond behaviour between corroded steel bars and normal aggregate concrete (NAC) and recycled aggregate concrete (RAC). In this study, the effect between corroded steel bars and concrete in terms of bond strength performance and behavior was investigated. They indicate that the bonding performance between steel bars in reinforced concrete structures is important to ensure the reinforced concrete durability due to load applications. The study found that there are three major components that influence the bond strength between reinforced steel rebars and concrete surface. The components are shear stress due to adhesion along the surrounding rebars, the bearing stresses against mechanical interlock facing steels rebars of ribs, and friction between steel rebars rib and the surrounding concrete. However, the mechanical interlock from steel rebar ribs showed the greatest contribution to bond strength performance. In other result, the bond strength between deformed steel rebars and recycled aggregate concrete has increased when percentage replacement of recycled coarse aggregate increased.

2.1   Pullout Test of Steel Reinforcement Bar

Reference [4] reported that the pullout test is mostly used to determine the bond strength behaviour due to ease of fabrication and simple procedure during the test. The specimens were tested normally in cube and cylinder dimension according to standard requirement. Figures 1 and 2 show the detailed test setup for cylinder and cube specimens' pullout test. The standard state that bonded length must be five
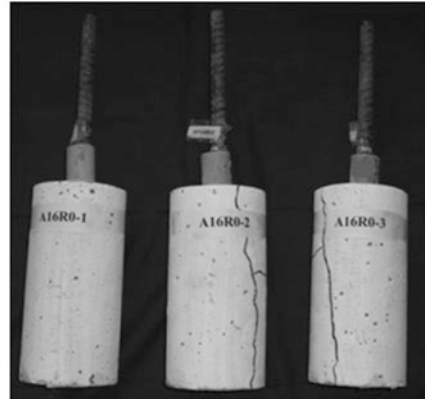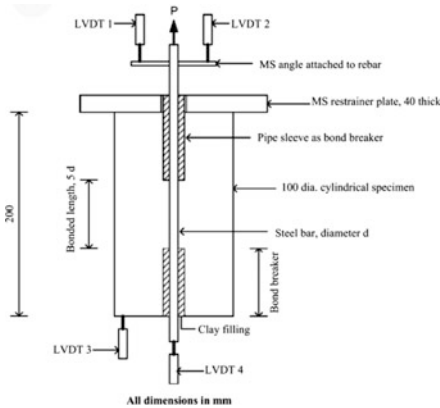
Fig. 1 Cylinder pullout specimens test setup configuration and typical pullout test specimens [4]
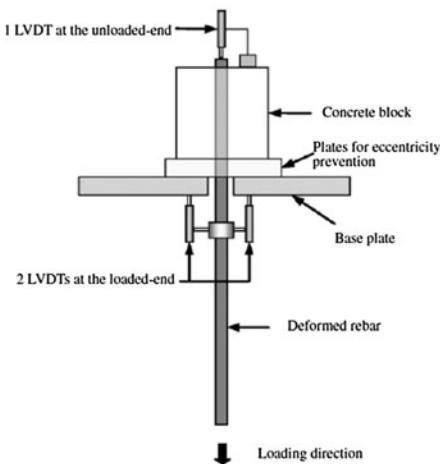
Fig. 2 Cube pullout specimens schematic and detailed test setup [2]

times the rebars' diameter and has been selected to protect yielding of the deformed steel rebars under pullout ultimate load.

2.2 Bond Stress-Slip Relationship

Reference [4] was discussed in detail about bond stress-slip relationship between deformed steel rebars and concrete surface. The researcher concluded their observation in two phase graph relationship named as Phase I and Phase II. Figure 3 shows the bond-slip relationship curves for the deformed rebars with size 12 mm diameter. The Phase I graph shows the obvious relationship between load-slip behaviour with increment sharply and increases in linear pattern up to 60–70 % of the ultimate load with small slip. In Phase I, steep slope indicates that the load and slip has increased linearly in small and no obvious slip occurs. However, Phase II has increase in load due to internal cracking by adhesion mechanism for bond resistance was exhausted has encourage the resulted in slip of the deformed steel rebars. On the contrary, in Phase II, the bond strength increased in small increment but rate of slip greatly increased and became nonlinear pattern as shown in graph until maximum load was reached at peak value P_{max} before the sample totally failed.

Reference [4] has been carried out. No different trend for the effect on reinforcement bar diameter, types of concrete, or replacement level on slip at peak bond stress result. It was observed that the crack started at inner to outer surface of concrete cylinder in splitting mode for all specimens tested as shown in Fig. 4. This observation was expected due to high stress concentration on surrounding reinforcement bar surface when pullout test was conducted. The detailed summary experimental result of pullout test is shown in Table 1. The specimens using 12 mm diameter of rebar and 100 % recycled aggregate replacement in concrete mix (A12R100) was referred in detail due to similar condition with this study. Reference [5] reported that the load-slip curve showed in similar pattern between concrete by recycled aggregate or normal aggregate with steel reinforcement bar. However, the

Fig. 3 Bond-slip curves for the deformed bars [4]
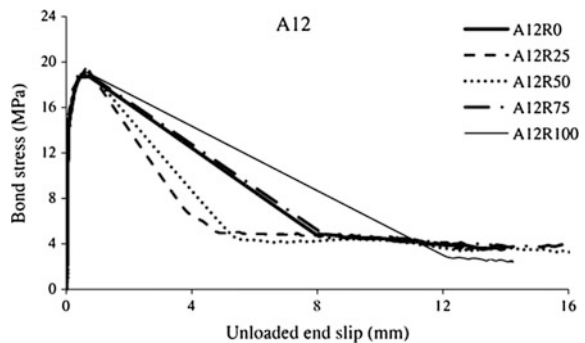
Fig. 4 Splitting mode of
bond failure in the specimens
[4]
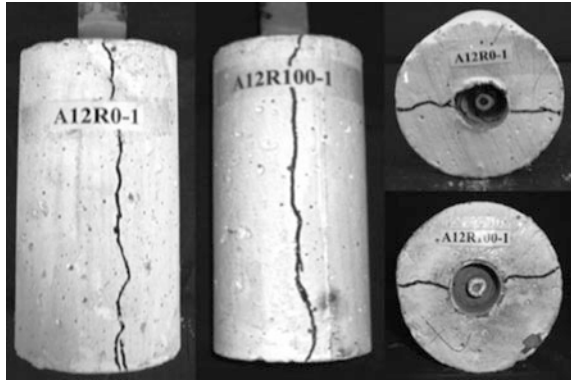
Table 1 Pullout specimens result [4]

Specimens	f_c' (MPa)	P_{max} (kN)	τ_{max} (MPa)	Slip, s (mm)	$\tau_{r.max}$ (MPa$^{0.5}$)	Failure mode
A12R0	36.9	42.2	18.7	0.561	3.1	Splitting
A12R25	28.9	44.2	19.5	0.651	3.6	Splitting
A12R50	24.0	42.7	18.9	0.657	3.9	Splitting
A12R75	26.2	43.0	19.0	0.710	3.7	Splitting
A12R100	24.7	43.2	19.1	0.636	3.8	Splitting

bond strength result between RAC and steel reinforcement bar was not affected by
recycled aggregate replacement percentage. It was supported by their result when
using replacement ratio about 50 % of RAC showed similar pattern to normal
aggregate concrete due to bond stress-slip relationship behaviour. The use of 100 %
recycled aggregate in reinforced concrete wall panel production was presented in
similar performance and behaviour with panel using natural aggregate (Na) in terms
of ultimate load carrying capacity [6].

3 Methodology

Normally, the bond strength between steel reinforcement bar and concrete is an
important criterion on the performance of reinforced concrete structures. Therefore,
male-female interlocking panel (M-FiP) specimens were prepared to determine the
structural behavior and performance of male-female wet joint connection. The
purpose of the pullout test in this study is to determine the bond-slip relationship
between steel reinforcement bars and cement grout as wet joint connection. It also
studies the bond's behavior, mode of failure, and crack pattern on specimens under
pullout load.

Table 2 Concrete mixture proportion

Constituents	Mix (kg/m^3)	Mix per sample (kg)
Cement	373	2.80
Sand	638	4.79
CCwA (10 mm)	395	2.96
CCwA (20 mm)	789	5.92
Water	205	1.54

3.1 Male-Female Interlocking Panel Specimens Preparation

A total eight (8) set M-FiP were prepared and casted for pullout testing. The concrete mix used was concrete crushed waste aggregate (CCwA) of size 20 and 10 mm as normal coarse replacement. The concrete strength was designed for Grade 30 in male and female specimens. Table 2 shows the concrete mix proportion per male and female specimens. Crescent-ribbed deformed steel bars with nominal tensile strength equal to 500 MPa of diameter 12 mm were used in the pullout tests. The dimension of each specimen was 75 mm × 500 mm × 200 mm (Thickness: Height: Length). Figure 5 shows the schematic diagram with details of the dimensions of male and female specimens. The grouting hole of 35 mm in size was constructed in the middle of M-FiP as a part of jointing mechanism.

3.2 Male and Female Specimens Formwork Preparation

Preparation of the formwork of the male and female specimens faced difficulty due to complicated design and the need for accurate construction to avoid problems during jointing process. The formwork was prepared at Fabrication Laboratory using soft plywood of 10 mm thick. Plywood was cut into pieces according to the dimension that was designed. The eight (8) set of male and female formwork were constructed for casting the specimens. Figure 6 shows the schematic diagram with
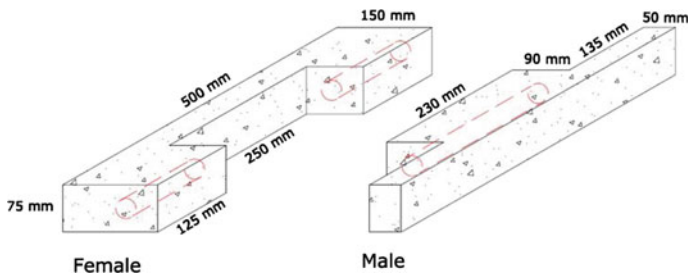
Fig. 5 Male-Female panel dimension details
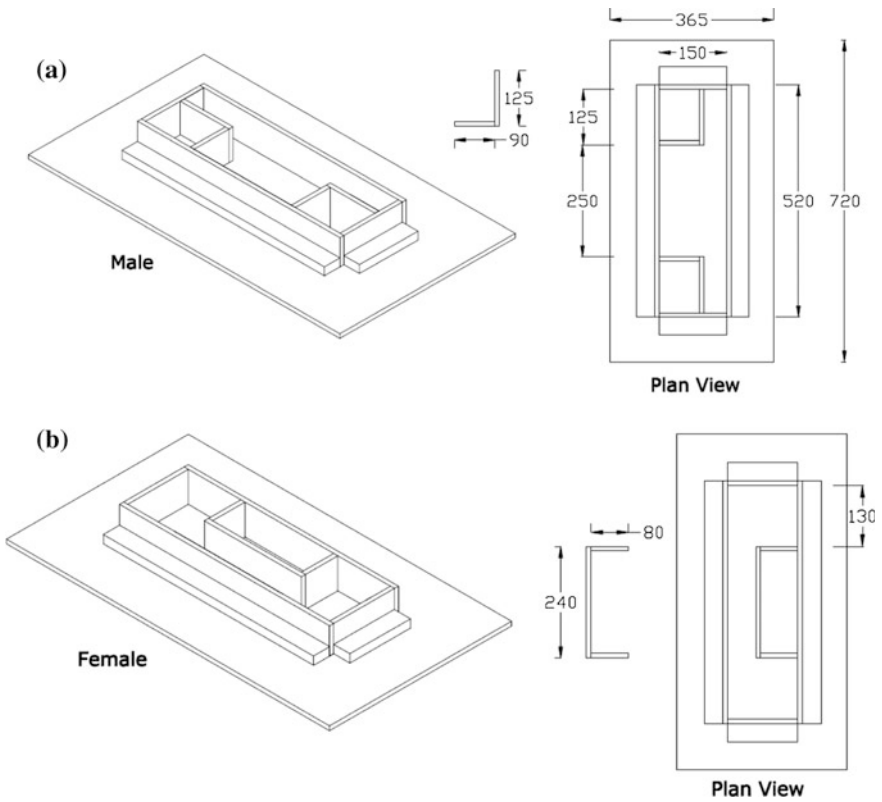
Fig. 6 Specimens formwork schematic diagram

Fig. 7 Specimens formwork

the detailed dimension of the specimens' formwork. Before casting the specimens, formwork must be prepared by installing the corrugate plastic ducting as permanent mould to construct a hole for grouting process. Figure 7 shows the complete male and female specimens formwork ready for concrete casting.

3.3 Male-Female Specimens Casting Preparation

The male and female specimens were cast using formworks that have been prepared using soft plywood as stated before. Surface oiling was applied on the surrounding of the formworks for easy removal of male-female concrete specimens. Concrete was mixed using pan mixer machine at the laboratory. After concrete mixing has been completed, concrete was poured into the formworks. Pouring process was done in three layers, each layer needs to be compacted using vibration table machine to remove all void in fresh concrete. Figure 8 shows the vibration process. After the concreting process was completed, all specimens were assembled on flat surface as shown in Fig. 9. The specimens were remolded and cleaned after 24 h of casting. Figure 10 shows the specimens after removing the formworks. All specimens were cured in water at a temperature of 20 ± 2 °C in curing tank until the test day was conducted. The curing of specimens was performed in accordance to Malaysian Standard [7]. After curing process was done, male and female panels were taken out from curing tank for jointing process. The male and female specimens were combined together to be M-FiP specimens. The space between male and female specimens was filled by cement mortar. Figure 11 shows the jointing
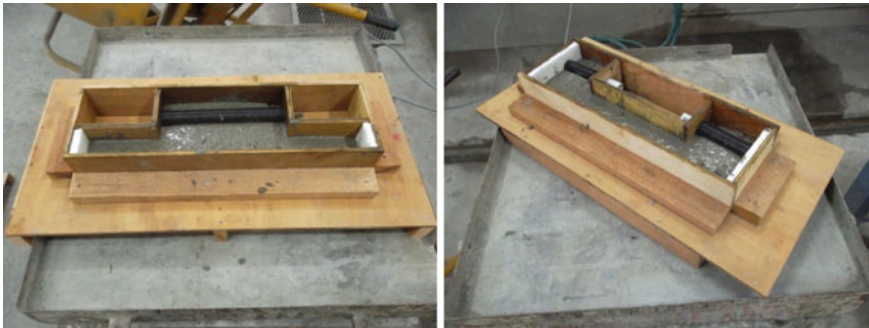
Fig. 8 Specimens on vibration process

Fig. 9 Specimens casting process

Fig. 10 Specimens after removing formwork

Fig. 11 Specimens male-female jointing process

process of the male and female specimens. The steel reinforcement bar of 1000 mm in length was installed vertically into the specimens' holes and cement grout was poured into the holes of specimens undergoing pullout test.

3.4 M-FiP Pullout Test

This test was conducted in order to determine the pullout strength by measuring the force required to pull the deformed steel bar embedded in the hardened cement grout on M-FiP specimens. The purpose of this test was also to investigate the performance of M-FiP connection and its effect on the connection mechanism. The methods and procedures of the pullout test were performed in accordance to ASTM [8]. Based on this test, maximum pullout strength load, slip, and failure mode for each specimen was carried out and discussed. From this pullout test result, the bond stress-slip relationship was studied according to the formula provided.

3.5 Direct Pullout Test Specimens

Eight (8) M-FiP specimens for pullout test were constructed and prepared. The specimens were tested in different days at 7, 14, 28, and 56 days of hardened cement grout. Table 3 shows the detailed test specimens. The pullout test was carried out using M-FiP specimens connection of 200 mm width and 500 mm height with concentric rebar placement. The specimens were placed in a horizontal position in the laboratory using timber formwork during casting and subsequent compaction. The steel reinforcement bars T12 were placed in hollow position with concrete grout. Figure 12 shows the detailed schematic diagram of pullout test specimens. The concrete was mixed in the laboratory using a tilting drum-type concrete mixer poured into the moulds and compacted using a vibrating table. To prevent excessive evaporation of the fresh concrete, the specimens were covered with a plastic sheet after the casting was completed. The specimens were remolded 24 h after casting following which they were moist-cured in the laboratory for a nominal period of 7, 14, 28, and 56 days by immersion in a curing tank where water was changed every week.

Table 3 Grout compressive strength

Specimens no.	Testing days	Grout strength (N/mm^2)
1	7	58.70
2		
3	14	64.50
4		
5	28	64.70
6		
7	56	90.60
8		

Fig. 12 Detail schematic diagram for pullout test specimens
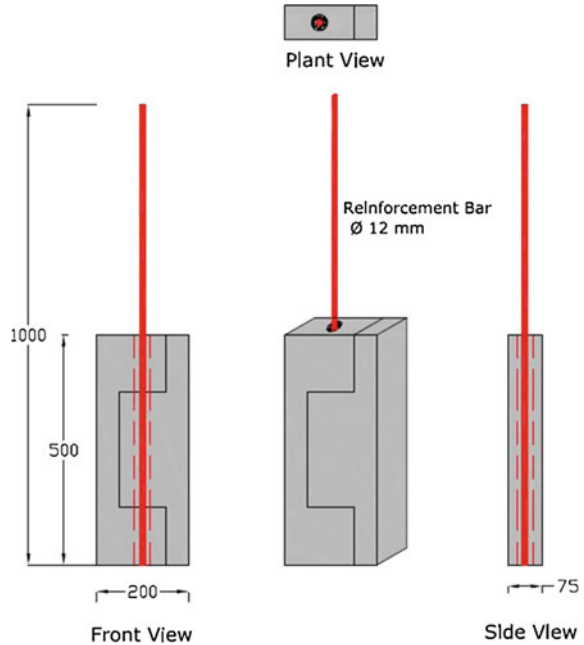
3.6 Pullout Instrumentation and Test Setup

The pullout test was conducted using Universal Testing Machine (UTM-1000) frame load with a capacity of 1000 kN. The specimens were installed vertically gripped rigidly at the upper end actuator and 20 mm thick steel plate was placed at top surface of M-FiP to prevent the specimens while the testing was conducted. On the other hand, top surface of the specimens need to ensure in smooth horizontally which removes debris and abnormalities to ensure the flat bearing surface perpendicular with steel reinforcement bar. If specimens were prepared in not flat surface condition, some grinding work need to conduct for provides smooth flat horizontal surface. The UTM-1000 machine was operated by moving upper actuator frame vertically while bottom frame actuator was fixed rigidly. The actuator was performed by pulling the embedded rebar in cement grout upward while recording the applied load. Figure 13 shows the detailed pullout test instrumentation and setup. The test was loaded using displacement control of 3 mm/min which allowed the observation process on the specimens during testing. The preparation and testing was performed in accordance to ASTM [8]. When reaching maximum load or failure stage, the specimens were unloaded automatically by the testing machine. The result from pullout test was recorded and discussed in detailed.
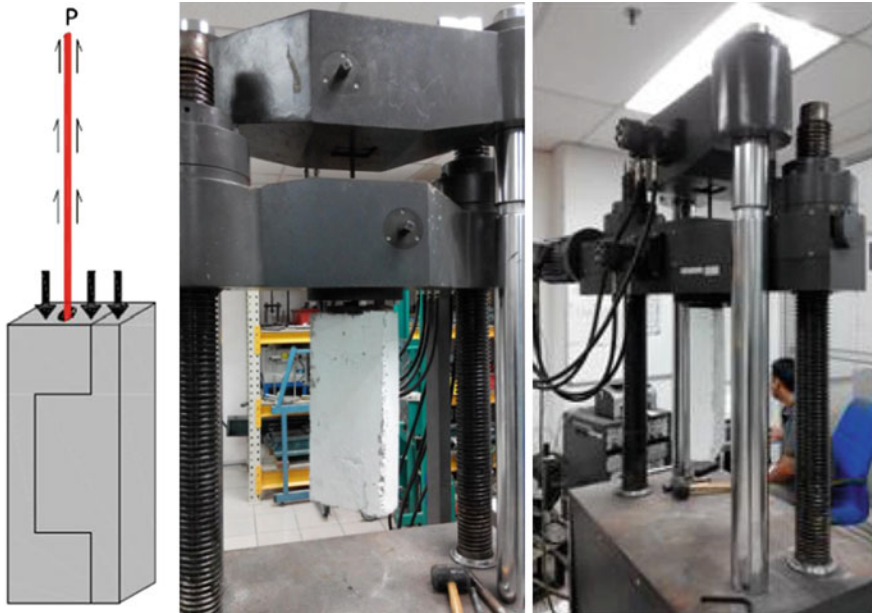
Fig. 13 Pullout instrumentation and test setup

4   Result and Discussion

The effectiveness of male-female interlocking panels depend on the bond behavior between cement grout, steel reinforcement bar, and concrete panel component. The result of bond behavior of this simple joint connection was presented in ultimate bond strength (τ), slip displacement (s), male-female connection performance, and mode of failure. Figure 14 shows the rate of strength development of concrete male-female interlocking panels. The increment of concrete strength showed a similar pattern to the concrete mix production for M-FiP samples. On the other hand, the compressive strength of cement grout was recorded at 7, 14, 28, and

Fig. 14 Compressive strength of interlocking concrete specimens
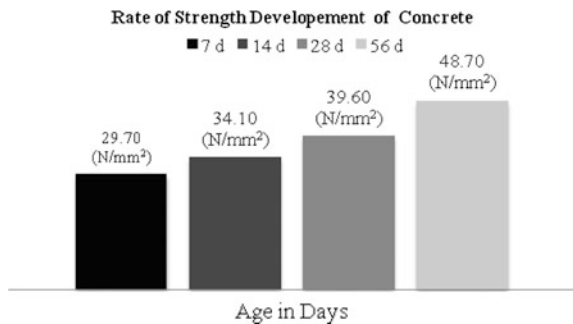
56 days. Identification of grout strength of different ages was important to study the behavior and performance of interlocking joints under pullout load test. The influence of cement grout strength on bond strength was discussed in detailed in this part. Apart from that, the slip performance for each age was also studied due to different cement grout strength.

4.1 Influence of Grout Strength on Bond Strength

The result of bond strength between reinforcement bar and cement grout was obtained from ultimate pullout load by conducting pullout test on M-FiP specimens. Reference [9] reported that, the compressive strength self-compacting concrete (SCC) directly influenced the behavior and performance of bond strength. A study concluded that SCC specimens generated higher bond strength compared to normal concrete specimens. Therefore, the influence of grout strength on bond strength was discussed in this study based on previous researches. The bonding strength development of reinforcing bar in cement grout on interlocking joint specimens is summarized in Table 4. The average bond strength was recorded due to the different grout strength depending on the age. However, the average bond strength was calculated based on ultimate pullout load result from the experimental testing. Thereby, the average bond strength for each age with cement grout strength of about 58.70, 64.50, 64.70, and 90.60 N/mm^2 was 3.80, 3.93, 3.99, and 4.29 N/mm^2 respectively. From this result, it showed that bond strength was influenced by the strength of the material used surrounding the reinforcement bar. The percentage increment of bond strength in different cement grout strength was 3.4, 5, and 12.9 % when compared with the bond strength of M-FiP specimens on the 7th day of age. However, on the 14th and 28th day, the average bond strength recorded was around the same value with only 1.5 % increase. The slow development of compressive strength and bond strength in cement grout at early age was due to the reaction process stage between water and cement grout. This result gave an

Table 4 Bond strength result

Specimen no.	Days	f_{cu} Concrete (N/mm^2)	f_{cu} Grout (N/mm^2)	P_{max} (kN)	Average, P_{max} (kN)	τ (N/mm^2)	Average τ (N/mm^2)
1	7	29.70	58.70	69.10	71.60	3.66	3.80
2				74.10		3.93	
3	14	34.10	64.50	74.44	74.06	3.95	3.93
4				73.68		3.91	
5	28	39.60	64.70	74.96	75.15	3.98	3.99
6				75.35		4.00	
7	56	48.70	90.60	79.94	80.85	4.24	4.29
8				81.76		4.34	
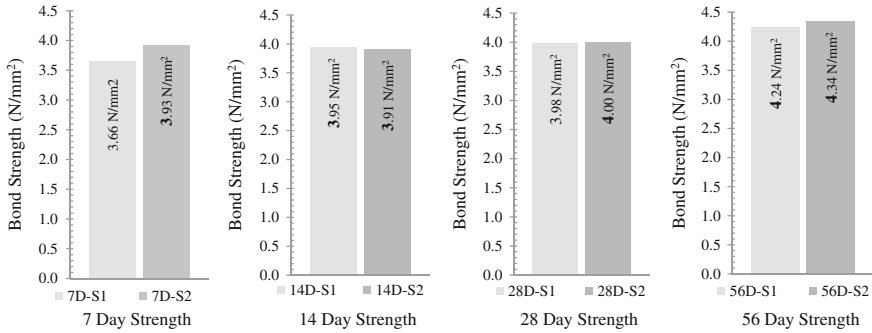
Fig. 15 Ultimate bond strength result from experimental testing

indication that bond strength directly depended on the compressive strength of materials attached surrounding the steel reinforcement bar. The higher strength of cement grout provided greater bearing resistance against slippage between cement grout key and steel reinforcement bar. In fact, longer development length embedded in cement grout was an extra factor in resisting the slippage and directly increasing the bond strength. Figure 15 shows the development of ultimate bond strength result from experimental testing. However, some specimens might not be in the assigned dimensions due to human error during casting process. Similarly, different material properties strength might have been used in each specimen prepared. The experimental setup might also influence the difference in bond strength result between the experiment due to mechanical error and human factor.

4.2 Mode of Failure

In normal pullout test on cube or cylinder, two types of failures usually occurred which were pullout failure and splitting failure. Pullout failure occurred when concrete surrounding the steel reinforcement bar ribs or called as concrete key, was weak while the other concretes surrounding the steel reinforcement bar were strong. The failure in this type occurred due to heavy stress on the rib surface at ultimate pullout load. On the contrary, splitting failure occurred when concrete key on rib surface was crushed due to circumference generating around radial tensile stresses between concrete and steel reinforcement bars' surface. From the observation, similar crack patterns occurred on the surface of all M-FiP specimens. The line crack appeared along the specimens starting from the top surface to the bottom part due to high concentrated load at ultimate pullout load. Figure 16 shows the failure characteristic behavior on interlocking panel specimens for each day they were tested. From the analysis, the crack pattern was more concentrated at the top of the interlocking panel due to higher stress on that location coming from ultimate pullout load increment. Meanwhile, a small crack also occurred at the top surface

| 7 Day | 14 Day | 28 Day | 56 Day |
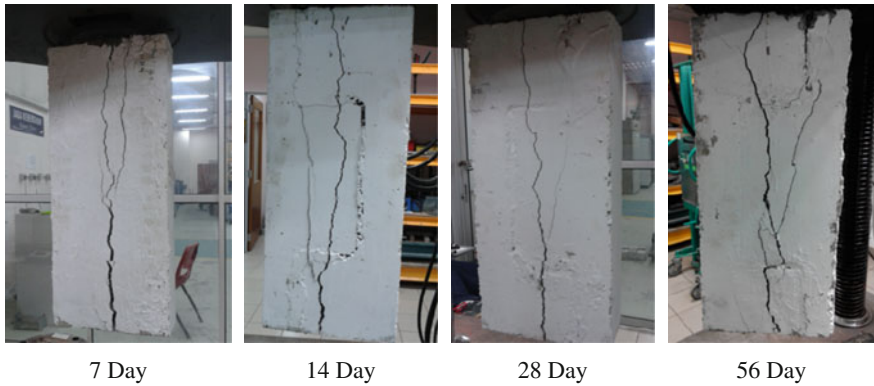
Fig. 16 Failure characteristic behaviour of interlocking panel specimens under pullout test
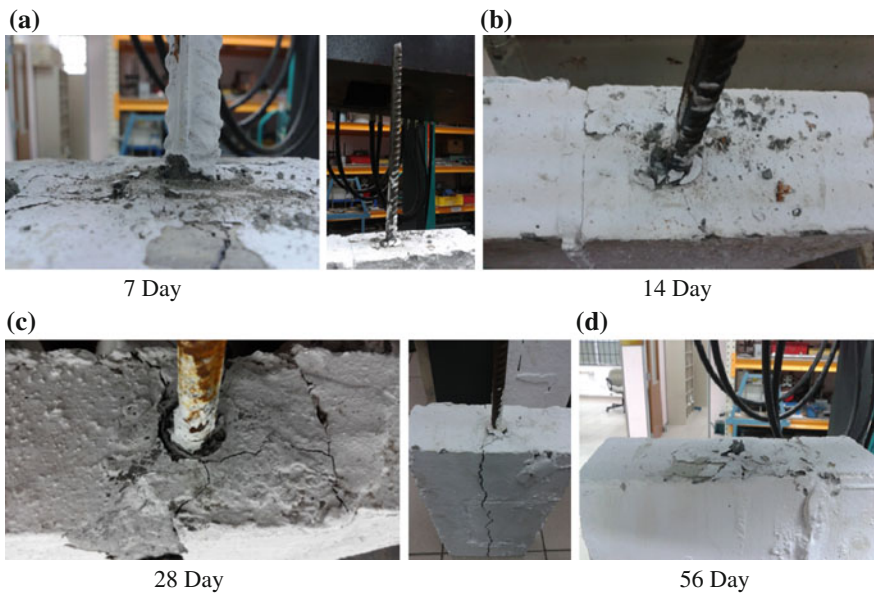
Fig. 17 Failure characteristic behaviour on reinforcement bar of interlocking panel specimens under pullout test

near the joint connection of the model due to weaker location from mortar component part. The failure on steel reinforcement bar embedded in cement grout as joint connection mechanism in M-FiP specimens was also observed. Conversely, when M-FiP was tested vertically under bending condition, the first crack started at bottom part of joint connection due to weakest area location. Nevertheless, after increment of load the major crack was clearly appeared at mid male and female joint [10].

Figure 17 shows the failure characteristic behaviour on steel reinforcement bar. The test result demonstrated that the reinforcement bar for all M-FiP specimens failed in splitting failure due to high bond strength on reinforcement bar and cement grout. However, for specimens using cement grout of the 56th day of age, the steel reinforcement bar was broken into two pieces as shown in Fig. 17d. This situation happened due to good bonding strength between the steel reinforcement and the cement grout. In addition, the corrugated plastic ducting that was used also provided more resistance on the cement grout from failure by splitting. It happened when cement grout filled the void between corrugated plastic ducting during casting process and hardened until the 56th day.

5 Conclusion

In this chapter, the experimental result on bond strength of reinforcement bar embedded in different strength of cement grout as wet joint connection mechanism in M-FiP was carried out and discussed in detail. Based on these experimental results the following conclusion can be described:

1. It was found that the bond strength between reinforcement bar and cement grout in M-FiP joint connection increased linearly with grout strength.
2. The bond strength is directly depending on compressive strength of material attached surrounding the steel reinforcement bar. The high strength of cement grout provided greater bearing resistance against slippage between cement grout key and steel reinforcement bar.
3. The pullout failure occurred on most of M-FiP specimens when cement grout surrounding steel reinforcement bar ribs or called as concrete key is weak and other concretes at surrounding steel reinforcement bar are strong.
4. The test result demonstrated that the reinforcement bar for all M-FiP specimens failed in splitting failure due to high bond strength between reinforcement bar and cement grout.
5. Recycled coarse aggregate in concrete mix production of male and female specimens showed similar performance with normal aggregate (NA) in terms of concrete strength due to same design mix.

References

1. R. Sandeep, M.V. Mnajunath, and S. Somanath, "Influence of reinforcement of the behaviour of hollow concrete block masonry prism under compression- An experimental and analytical approach", International Journal of Research in Engineering and Technology, 106–110, 2013.
2. S.W. Kim, and H.D. Yun, "Influence of recycled coarse aggregates on the bond behaviour of deformed bars in concrete", Engineering Structures, 48, 133–143, 2013.
3. J. Xiao, and H. Falkner, "Bond Behaviour between recycled aggregate concrete and steel rebars" Construction and Building Materials, 21, 395–401, 2007.
4. M.J.R. Prince, and B. Singh, "Bond behaviour of deformed steel bars embedded in recycled aggregate concrete", Construction and Building Materials, 49, 852–862, 2013.
5. Y. Zhao, H. Lin, K. Wu, and W. Jin, "Bond behavior of normal recycled concrete and corroded steel bar", Construction and Building Materials, 48, 348–359, 2013.
6. S. Mohd Suhelmiey, H. Siti Hawa, and M.R. Ahmad Ruslan, "Ultimate strength of steel fabric reinforced concrete short wall panel using crushed concrete waste aggregate (CCwA)", International Journal of Civil and Environmental Engineering", IJCEE-IJENS, vol. 11 no 01, pp.64–80, 2011.
7. MS EN 12390, "Testing hardened concrete - Part 2: Making and curing specimens for strength test (Second Revision)". Malaysian Standard Institution. Malaysia, 2012.
8. ASTM C900, "Pullout Strength of Hardened Concrete". ASTM International, West Conshohocken PA, United States, 2013.
9. A. A. Foroughi, S. Dilmaghani and H. Famili, "Bond strength of reinforcement steel in self-compacting concrete", International Journal of Civil Engineering. Vol. 6, No. 1, March 2008, 24–33, 2008.
10. S. Mohd Suhelmiey, H. Siti Hawa, and M.R. Ahmad Ruslan, "Bending strength of Male-Female interlocking joint in RC wall panel", Colloquium on Humanities, Sciences and Engineering (CHUSER 2014), 193–197, 2014.

Finite Element Analysis: Displacement of Eccentric Loaded SFRC Ribbed Wall Panel

Mohd Maiziz Bin Fishol Hamdi, Siti Hawa Binti Hamzah and Mohd Hisbany Bin Mohd Hashim

Abstract This finite element study was carried out to investigate the steel fiber reinforced concrete with three (3) ribbed wall (SFRC-3RW) panel containing reinforced wire mesh (BRC) subjected to axial and eccentric loading, also its load bearing response behavior. A ribbed wall with steel reinforced was modeled with finite element analysis software LUSAS 14.7 using three dimensional modeling and nonlinear finite element analysis. The SFRC-3RW panel was subject to axial and eccentric loading to observe and investigate its buckling effect, the load bearing response behavior, and compare with SFRC plain wall (PW). The SFRC-3RW and PW was using concrete grade 30 with 0.5 % steel fiber content. The SFRC-3RW ultimate load bearing is 581 kN with maximum compression vertical and lateral displacement by 2.36 and 6.16 mm, respectively, compared to SFRC-PW with eccentric loading (SFRC-PWe) 577 kN with maximum compression vertical and lateral displacement by 2.31 and 8.24 mm. The reduction in concrete volume and ultimate load capacity were 20 and 0.33 % from SFRC-PWe in which SFRC-3RW save the concrete amount and gave higher load capacity compared to SFRCPWe. It can be concluded that the load bearing capacity for SFRC-3RW with BRC is acceptable and can withstand vertical pressure also reducing the amount of concrete usage.

Keywords Compressive axial load · Finite element analysis · Industrialized Building System · Load bearing capacity · Steel fiber reinforced concrete

M.M.B.F. Hamdi (✉) · S.H.B. Hamzah · M.H.B.M. Hashim
Faculty of Civil Engineering, Universiti Teknologi MARA,
Shah Alam, Selangor, Malaysia
e-mail: mohd.maiziz@gmail.com

S.H.B. Hamzah
e-mail: shh@salam.uitm.edu.my

M.H.B.M. Hashim
e-mail: hisbany@salam.uitm.edu.my

1 Introduction

The construction projects today are far more complicated than before. It involves larger capital investments, embraces several disciplines, widely dispersed project participants, tighter schedules, and stringent quality standards. The changing construction environment is also influenced by factors other than the project management requirements. The Malaysian Construction Industry has been urged to use innovative construction technique and to shift from monolithic RC buildings to Industrialized Building System (IBS) construction as shown in Fig. 1. Since 2008, IBS is made compulsory in public building project especially in the residential project, where 70 % of components in the construction to be IBS. One of the IBS components is the load bearing wall. Reinforced concrete wall panels are widely used as load bearing components within the core of high-rise buildings and in tilt-up construction [1].

Over the years, reinforced concrete wall have gained greater acceptance by practicing engineers, as load carrying structural members. Some of the load bearing also is designed to withstand high in-plane lateral forces at low displacement level making them particularly suitable for earthquake resisting purpose [2]. Thus, the maximum load capacity shall parallel with the size of the wall using high amount of concrete and difficulties in moving together with installation of the member.

One of the proposed prefabricated wall panels used in the construction is ribbed wall. The required rigidity of the panel is provided with perimeter ribs. Previous study concluded that the load bearing capacity of the wall with ribbed profile decrease towards the additional number of ribs [3]. Therefore, there are more need to establish the behavior of steel Fiberfiber reinforced concrete—ribbed wall (SFRC-RW) in order to gain better understanding of the failure mechanism and appropriate design approach. This research will add engineering and technological knowledge on the rib effect on SFRC with BRC as the load bearing wall panel under axial load and eccentric loading. The three ribbed SFRC with BRC are also

Fig. 1 IBS precast wall in building constructions

expected to function as load bearing wall and robust structural component that can withstand vertical pressure.

The application and utilization of steel fiber in concrete mixture to improve concrete ductility was accepted widely by practicing engineers. The presence of steel fiber having adequate tensile strength and being well distributed throughout the concrete mixture introduces the term maximizing potential of the buckling behavior and toughness in concrete, thus enhancing the post-crack stage before failure [4]. With addition of BRC, the load bearing capacity of the wall can be improved. In the end, this research aims that three ribbed SFRC with BRC wall panel can perform in withstanding the axial compressive and eccentric loading also to ensure the light weight by reducing the amount of concrete.

This study was done through the analysis of axially loaded SFRC-RW by Finite Element Method (FEA) analysis. The finite element software used was LUSAS version 14.7. The structural performance of the wall panel such as ultimate strength load, load-displacement relationship, and mode of failure was determined. The steel fiber concrete grade used was Grade 30 normal OPC concrete with the mixing of 0.5 % hooked end steel fiber by volume fraction. The height, length, and thickness of each wall model are 1500, 1000, and 75 mm, respectively. There are two types of wall; plain wall and ribbed wall. For ribbed wall, it contains three ribs in which each rib has 200 mm width and 37.5 mm thick.

The design of SFRC-ribbed wall essentially involves a conceptual design, approximate analysis, preliminary design and optimization, to safety carrying lateral and eccentric loading. The three ribbed SFRC with BRC are also expected to function as load bearing wall and robust structural component that can withstand vertical pressure and also reducing the amount of concrete usage. Therefore, the aim of structural engineer is to study the structural behavior and to satisfy the expectation. Five (5) different wall panels were modeled and analyzed.

2 Research Review

2.1 Steel Fibers Concrete

Plain unreinforced concrete is a brittle material, with a low tensile strength, and a low strain capacity. The tensile strength of concrete is normally 8–15 % of the compressive strength resulting in cracking, at low tensile stress levels [5]. The role of randomly distributed discontinuous steel fibers is to bridge across the cracks that provides some post-cracking ductility. If the steel fibers are sufficiently strong, sufficiently bonded to material, and permit the SFRC to carry significant stresses over a relatively large strain capacity in the post-cracking stage [6]. In certain specific circumstances, steel fibers can entirely replace traditional steel reinforcement bar in reinforced concrete (Fig. 2).
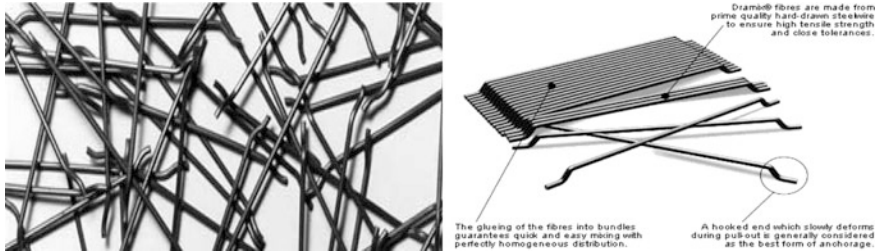
Fig. 2 Hooked-end steel fiber

One of the important properties of steel fibers reinforced concrete (SFRC) is its superior resistance to cracking and crack propagation. As a result of this ability to arrest cracks, fiber composites possess increased extensibility and tensile strength, both at first crack and at ultimate. Steel fibers improved mechanical properties of the concrete such as modulus of elasticity, tensile strength, compressive strength, and uniaxial peak strain of concrete [7].

2.2 Load Bearing Wall

The precast building systems are mainly categorized into load bearing wall structure system and frame and skeletal structure system. The structural element of load bearing wall structure system consists of load bearing walls and floors while the structural elements of frame and skeletal structure systems consists of column, beams, and floors. The load bearing wall structure are suitable for apartment buildings, nursing homes, dormitories, and hotel. Wall element of a building can be constructed using precast system. A precast wall system can be comprised of flat or curved panels (solid, hollow core, or insulated), window or mullion panel, ribbed panels, or a double tee [8]. This is due to their structural capability as load bearing elements are often overlooked

When the walls are slender, they are capable of buckling and which is normally not a design consideration in conventional concrete member. The design considers wall as restrained at the bottom and top, with free vertical edges, when carrying vertical loads [9]. It is shown in Fig. 3 the one-way action by uniaxial curvature in the direction of loading. However, axially loaded walls can behave in two-way action, where biaxial curvature will occur in the directions parallel and perpendicular to that of loading. Figure 3 also shows a typical example of two-way action on a wall loaded axially. This research will emphasize on the behavior of reinforced concrete ribbed wall panel in one-way action to provide a clear overview on future laboratory work.

Fig. 3 One-way and
two-way action wall panel
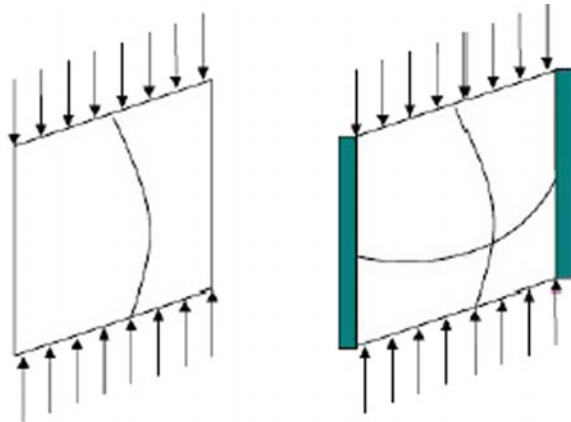
Freedman [10] conducted an extensive test on normal and high strength solid concrete wall panel in one-way and two-way action with slenderness ratios (H/tw) varying from 25 to 40. Equations 1 and 2 show the effective height determination of wall panel.

$$\beta = 1 \qquad H/t_w < 27, \text{ and}$$
$$\beta = \frac{18}{\left(\frac{H}{t_w}\right)^{0.88}} \quad H/t_w \geq 27 \tag{1}$$

For two-way action, the effective height factor;

$$\beta = \alpha \frac{18}{1 + \left(\frac{H}{L}\right)^2} \quad \text{for } H \leq L,$$
$$\beta = \alpha \frac{L}{2H} \qquad \text{for } H > L \tag{2}$$

2.3 LUSAS Nonlinear Analysis

All materials that are linear elastic in behavior and that deformation are small enough to not significantly affect the overall structure shall be assumed as linear finite element analysis. However, this description applies to very few situations with a few restrictions and assumption linear analysis that will suffice for the majority of engineering application.

Thus, nonlinear FEA is required in situations such as permanent deformation, gross changes in structural geometry, buckling, structural cracks, and stresses beyond yield stress. There are three types of nonlinear analysis available in LUSAS software but only two were used for the research:
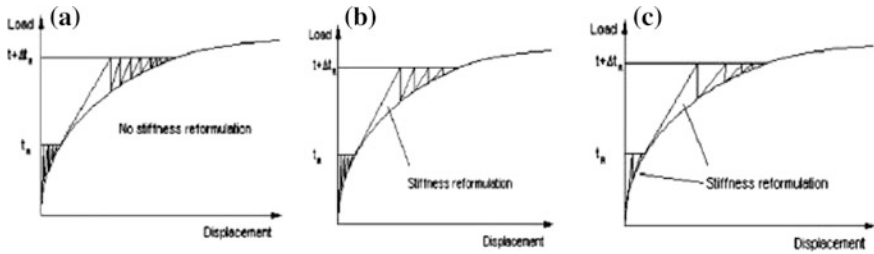
Fig. 4 Forms of iteraion

(a) Material Nonlinearity

The analysis specifies nonlinear effects which has disproportionate stresses and strains. A nonlinear material model is one that does not follow a linear relation between strain and stress and does not have constant modulus of elasticity.

(b) Geometric Nonlinearity

Geometric nonlinearity occurs when there is significant change of the structural configuration during loading. Due to the deformation, it changes the structure matrix. Consequently stiffness does not remain constant throughout the process of deformation due to the applied load. The stiffness therefore is to be calculated by the software along the process of incremental load application.

(c) Boundary Nonlinearity

Deformation dependent boundary condition models account for the modifications to the external restraints resulting from support lift-off, or smooth or frictional contact within an analysis.

LUSAS applies the modified Newton-Raphson iteration in the nonlinear static analysis. Newton-Raphson iteration converges quadratically and stable, provided an initial estimation which is close enough to the solution available [11]. With the modified Newton iteration, the current tangent stiffness matrix is replaced with previous stiffness matrix. This method will reduce the number of iteration as the factorization of the tangent stiffness matrix is not required for each iteration as shown in Fig. 4.

3 Material and Method

In order to meet the research objectives, the modeling of SFRC-PW and SFRC-3RW are done using LUSAS version 14.7. In the finite element analysis (FEA) the structure is modeled by the assemblage of small pieces of structure. These pieces with simple geometry are called finite elements. In the finite element analysis (FEA), the variation of the field variable on the element is approximately

by the simple functions, such as polynomials. The actual variation on the elements is almost certainly more complicated, so FEA provides an approximate solution. However, the solution can be improved using more elements to represent the structure.

Finite element analysis were done by calculating the response of a complex shape to any of external load by dividing the complex shape into lots of smaller simpler shapes. The shape of each element is defined by the coordinates of its nodes. Adjoining elements with common nodes will interact. The real engineering problem responds in an infinite number of ways to external forces. The manner in which the finite element model will react is given by degrees of freedom, which are expressed at the nodes. Since the response of a single finite element to a known stimulus building up a model for the whole structure by assembling all of the simple expression into a set of simultaneous equation with the degrees of freedom at each nodes as the unknown. These are then solved using a matrix solution technique.

Five models were analyzed with different position of eccentricity loading in this research. The models cross-section dimensions in x and y axes vary and are shown in Fig. 5. The height of each respective model is 1500 mm and the entire model containing BRC.

The concrete body of the SFRC-PW and SFRC-3RW is represented by volume geometry. And BRC will be represented as a lines element. Element aspect ratio should always be a consideration in order to establish an accurate model. The increase of aspect ratio may result unsimilarity value of the analysis. Therefore, the proper partition especially at the location of the neutral axis towards the unribbed section will be done.

Meshing is the process where SFRC-PW and SFRC-3RW models are defined in terms of geometry features which are sub-divided into finite elements for analysis. Volumes are meshed using regular mesh pattern. In order to generate a regular mesh pattern the number of mesh divisions on opposite faces of the volume must match. The HX20 (3D solid continuum element) is a three dimensional solid hexahedral element which is regularly used in LUSAS to model fully three dimensional structures. The element is shown as Fig. 6. SFRC-PW and SFRC-3RW modeling
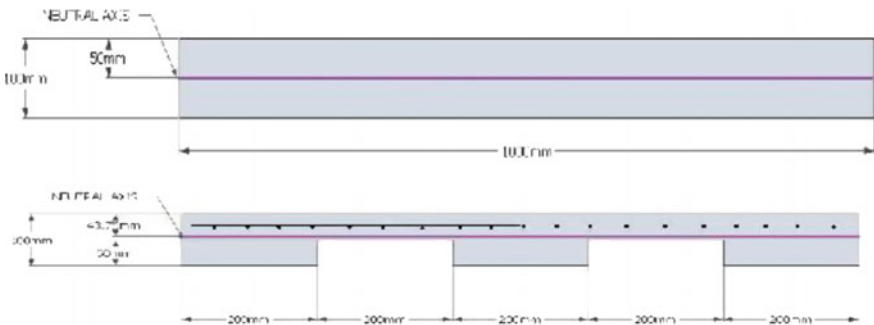
Fig. 5 Dimension of the wall panels
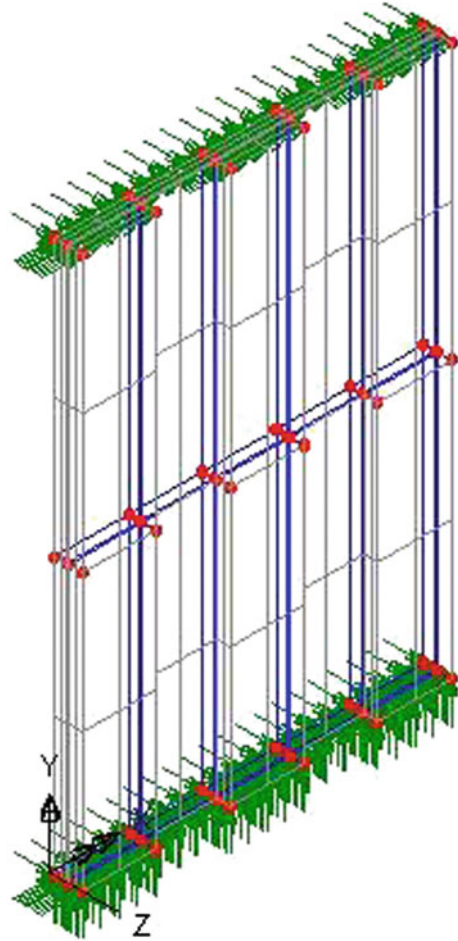
results are based in an increase of element numbers which has resulted in longer
time taken for the analysis to be completed. Therefore, the local numbers of divi-
sions were set as 4 for local X, Y, and Z axes.

For concentrated load, model is applied with global distributed load where the
load is concentrically at the neutral axis of each respective model in y direction. For
the eccentricity load, model is applied with discrete patch load. The load is con-
centrically at the location needed based on the axis required for assign. For
SFRC-PW, the (+e) positive eccentric and (−e) negative eccentric loading is similar.
This is due to similar shape between front and backward of the wall except with
SFRC-3RW. For SFRC-3RW, the positive eccentric loading is where loading
located at ribbed area and negative eccentric is where loading located at plain area as
shown in Fig. 7. For initial loading, models were applied with 1 Newton (N) along

Fig. 7 Loading applied on wall models
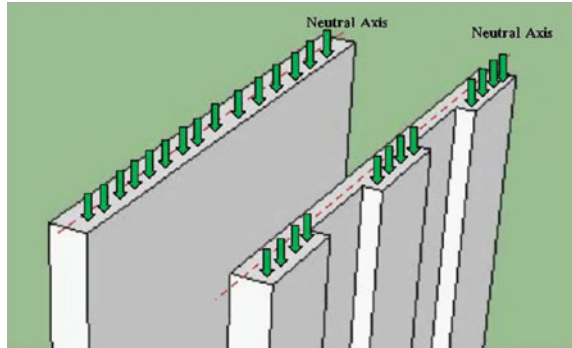
Table 1 Wall samples summary

Eccentricity value	Plain wall	3-Ribbed wall
e = +t/5	PWe	3RW+ve
e = 0	PW	3RW
e = −t/5	Nil	3RW−ve

the neutral axis (Appendix B). Five models were summarized in Table 1 based on different wall type and different location load applied.

Nonlinear analysis control properties are defined by a loadcase. Newton–Raphson procedures are applied by LUSAS nonlinear analysis. Each time of iteration, the stiffness matrix (KT) are being updated. This is known as an incremental iterative method where the total load is applied in a number of increments. Within each increment, linear prediction of nonlinear response is established and subsequent iterative corrections are performed to restore equilibrium by the elimination of the residual forces.

Nonlinear option is selected on nonlinear and transient method approach of analysis. And the incrementation were set as automatic with starting load factor as 0.1 and maximum change in load factor as 10 kN. Iteration per increment is set as four number and maximum number of iteration as twelve. When the increment of the load factor failed to converge, the nonlinear analysis is terminating the calculation. In the nonlinear option of nonlinear and transient property features, set of the total lagrangian are used for the geometry nonlinearity.

To decide the suitable mesh density of the models, validation for mesh density is being analyzed. The same kind of model with more refined mesh and higher order elements were used to bring the model analysis close to the experimental result in the future and some of the case studied. Results from different density of mesh were compared and variance of the result is expected to be zero. The accurate results are important and to avoid study result is far away from predicting the experimental model shape due to limitation of the LUSAS or poor on the element shape.

4 Results and Discussion

4.1 Load and Displacement

The modeling of wall panel was differentiated between ribbed and plain profile. The positioning of the loading was also different between those wall panels either at the neutral axis or eccentricity of the wall. Therefore, the comparison point was chosen at the top-center of the outer face of the wall panel. These comparisons were established by the plotting load versus displacement in y direction at the selected nodes of the models developed.

The load versus displacement profile in Fig. 8 of the selected node shows the influence of the BRC on the load carrying capacity of the SFRC-3RW panels.

Based on Fig. 8, the elastic region was recorded at about 1.5 mm vertical compression displacement for each wall panel except SFRC-3RW−ve. However, due to the variety of load location on sample, the maximum load capacity differs due to the different location of load applied and nonlinearity in each wall panel respectively. The SFRC-PW (control) panel maximum load capacity and vertical compression displacement was 1200 kN and 3.10 mm, respectively, while the SFRC-3RW (three Ribs) panel maximum load capacity and vertical compression displacement was 581 kN and 2.36 mm, respectively The vertical compression displacement of the wall panel with ribbed profile was then compared to the control wall panel at every respective ultimate load bearing capacity. This is shown in Table 2.

The vertical compression displacement of control wall panel was significantly small compared to wall panels with ribbed profile at their respective ultimate loads. At each wall panel ultimate loads, the control wall panel was still in its elastic region resulting in small displacement. Thus, the ribbed wall is near to 50 % of its buckling resistance capability compared to control panel.

Figure 9 shows the vertical and lateral displacement of the SFRC-3RW model. At ultimate load of 581 kN, the model has shown maximum value of vertical

Fig. 8 Loading and displacement correlation of wall panel models
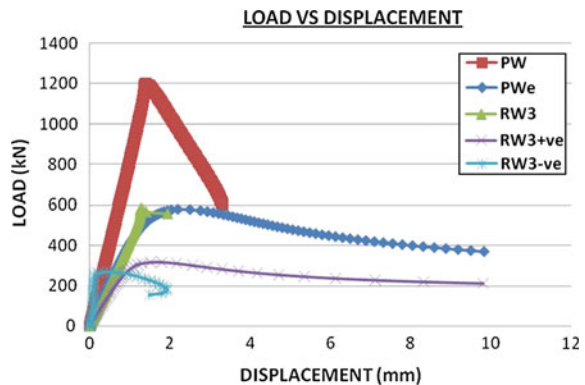
Table 2 Vertical displacement and difference percentage

Panel	Ultimate load (kN)	Vertical displacement (mm)	Difference percentage (%)
PW	1200	3.1	0
PWe	577	2.31	69.3
3RW	581	2.36	69.5
3RW+ve	317	1.85	78.9
3RW− ve	270	1.96	83.2
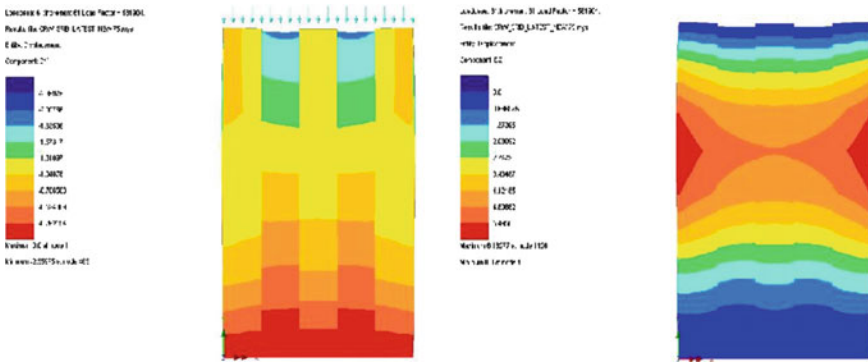
Fig. 9 Displacement contour of 3RW wall panel model

compression displacement of 2.36 mm along the region of the unribbed section where the load was applied. The ribbed profile was capable to reduce the vertical displacement towards the applied load. The vertical displacement decreases towards the lower end of the model due to support restraint. At ultimate load, the model buckles laterally towards its weak axis. At 0.8 height (1200 mm from bottom) and has resulted in single curvature profile with the maximum value of 6.18 mm away from the z-axis. The ribbed profile was capable to reduce the lateral displacement. The lateral displacement is minimal towards the upper and lower end of the model due to support restraint

4.2 Deformation Mesh and Crack Pattern

The mode shapes of the deformed mesh due to vertical and lateral displacement were shown in Fig. 10. It was shown that the buckled for SFRC-PWe and SFRC-3RW are at the same area. The weak axis for the both wall also indicates at the same place which occur at 0.7 height of the wall. The possibility of crack pattern for the wall also has been established for estimation. The most development crack for plain wall and ribbed wall are located at the 0.7 height of the wall up to the top
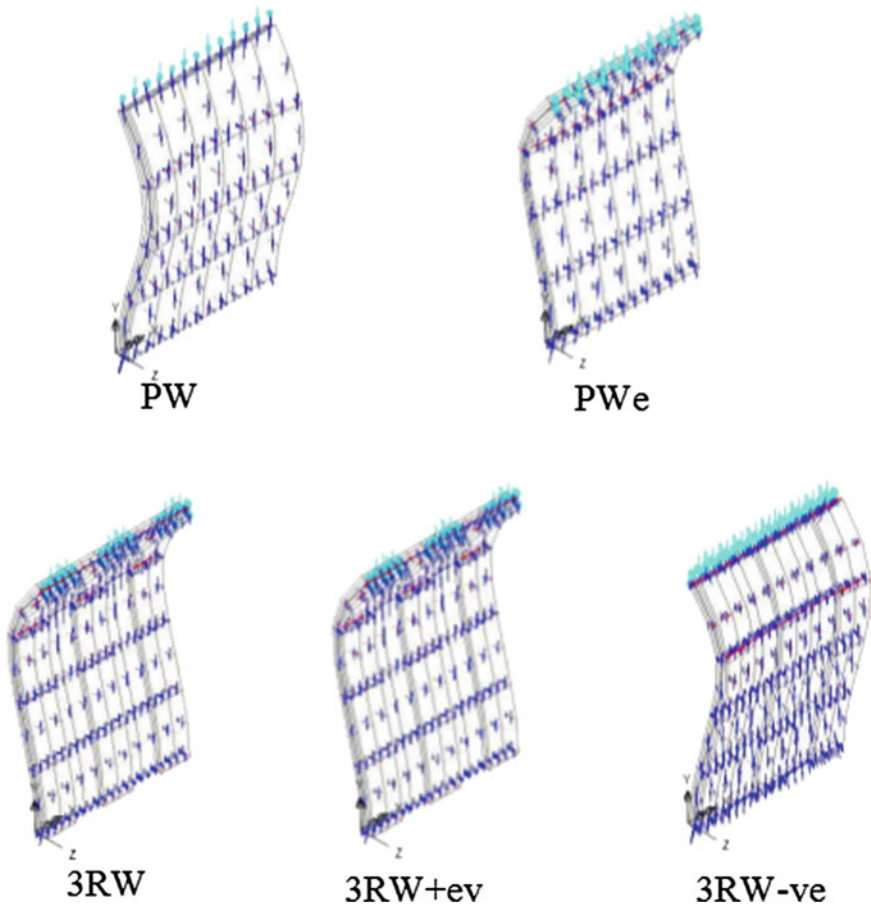
Fig. 10 Deformation pattern of wall panel models

of the wall. For ribbed wall, the critical cracks occur on the unribbed area together with the ribbed area. Therefore, the SFRC-RW was expected to fail due to buckling of the wall which was mostly located 0.7 height of the wall

The wall panels showed maximum vertical displacement at about 2–3 mm with respect to the ultimate load capacity of each wall panel. The SFRC-PW showed distorted profile at both side of the wall face while the remaining SFRC-RW panels showed buckling at about 1.2 m height of wall. The analysis shows single curvature deformation profile where the maximum lateral displacement was mostly at 0.7 height of the wall.

It seems the lateral displacement is spreading up to 0.8 height of the wall to 0.6 wall height for control panel. But for SFRC-3RW and SFRC-3RWve, the lateral displacement is minimizing to the center of the wall. And for the vertical displacement, the maximum displacement is located at upper unribbed area which

Table 3 Maximum vertical and lateral displacement of wall panels

Panel	Ultimate load (kN)	Vertical displacement (mm)	Lateral displacement (mm)
PW	1200	3.1	9.27
PWe	577	2.31	8.24
3RW	581	2.36	6.18
3RW+ve	317	1.85	6.70
3RW−ve	270	1.96	7.80

Fig. 11 Lateral displacement profile of wall panel models
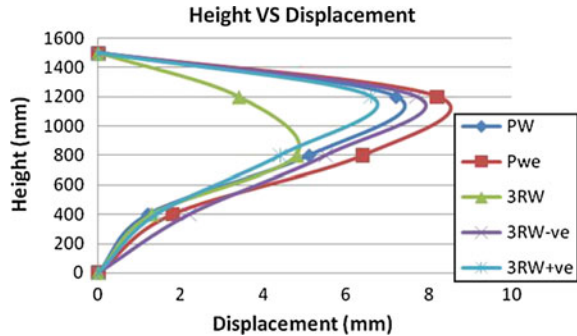
concrete cover is much thicker there. From the contour also, its shows ribbed area transmitting the displacement equally to vertical axis compared with lateral axis by plain wall. Value for ultimate load bearing, maximum vertical displacement and lateral displacement of the wall is shown in Table 3.

The SFRC-PW and SFRC-3RW above in Fig. 11 shows a single curvature profile as plotted and it failed by buckling due to design slenderness ratio of 15 (more than 12). Based on visual observation on the wall condition, it was found that the 0.7 height from top end are suffering excessive crack and crush all along its length. For the SFRC-3RW, the minimal displacement is shown compared to SFRC-PWe. It happens due to channeling the load and displacement equally to the bottom. Compared to plain wall, even though the maximum capacity load is higher the graph indicates it has major displacement compared to ribbed wall.

The experiment also shows that the buckling curves justify with the Euler buckling theory where it happens at the 0.7 H of the wall. Then, the curve pattern showing constant profile displacement indicates that the steel fiber helps load distribution to be widely spread across its concrete composite, thus preventing crack propagation toward bottom end of the wall. The addition of steel fiber in the mix for WSF wall helps concrete to dissipate energy around its matrix.

5 Conclusion

It can be concluded that ribbed wall effectively transmits the load imposed on it if the load is applied to the neutral axis. Thus the load bearing capacity of the ribbed wall panel increases if the load is applied nearer to the neutral axis and away from the negative (−ve) eccentricity of the ribbed wall. The ribbed wall also gives lesser displacement compared to plain wall due to consistently transmitting the load below to the ground. As a conclusion, it seems that SFRC-3RW could be considered as an alternative in place of other frequently used conventional wall due to its capability to reduce the amount of concrete used and weight of the building. Thus, the objectives of this research were achieved.

References

1. Guan, H., Lee, D. J., & Cooper, C.,"Ultimate Strength Analysis of Normal and High Strength Concrete Wall Panels with Varying Opening Configurations", Journal of Engineering Structures Vol. 32, 1341–1347, 2010.
2. Koncz, T. "New Technology Spurs Market for Large Panel Precast Concrete Buildings." Journal of Precast/Prestressed Concrete Institute, 30–42, 2002.
3. Syed Alif Iskandhar bin Syed Zainal Abidin. "Finite Element Analysis: Axially Loaded Steel Fiber Reinforced Concrete Ribbed Wall", Master of Engineering (Civil-Structure) Research Report, Universiti Teknologi Mara Malaysia, 2012.
4. Nguyen Van Chanh. "Steel Fiber Reinforced Concrete", Ho Chi Minh City University of Technology, 2001.
5. Shah, S. P., Swartz, S. E., & Ouyang, C. "Fracture Mechanics of Concrete". New York: John Wiley & Sons, Inc.,1999.
6. Thomas, J., & Ramaswamy, A.. Mechanical Properties of Steel Fibre Reinforced Concrete. ASCE Journal of Materials in Civil Engineering, 33–37, 2011.
7. Nataraja, M. C., Dhang, N., & Gupta, A. P.. "Stress-strain Curves for Steel Fiber Reinforced Concrete Under Compression". Journal of Cement & Concrete Composite, Vol. 21, 383–390, 2001.
8. Oberlender, G. D., and Everard, N. J., "Investigation of Reinforced Concrete Walls," ACI JOURNAL, Proceedings V. 74, No. 6, pp. 256–263, June 1998.
9. D.J. Lee, H.Guan, J.H. Doh, & S. Fragomeni. "Finite Element Analysis of Reinforced Concrete Walls with Openings in One- And Two- Way Action". Griffith School of Engineering, 2011.
10. Freedman, S., "Load Bearing Architectural Precast Concrete Wall Panels", PCI Journal Vol. 44, No.5, 92–115, 2004.
11. Chandrupatla, Tirupathi, R., & Belegundu, A. D. Introduction to Finite Elements in Engineering 3rd Edition. USA: Prentice Hall, 2002.

Investigation of Intercity Train Loading on Prestressed Concrete Sleeper

**I. Sharul Nizam, A.B. Afidah, H. Siti Hawa
and R. Mohd Ikmal Fazlan**

Abstract In order to provide better alternative for road users, Malaysian rail industry has developed tremendously over the last decade. The old intercity trains which transported passengers had lower number of passengers compared to nowadays in which number of passengers increased rapidly from day-to-day parallel to the economy growth of the country. Moreover, as well as increased interest in high and higher speed passenger rail development, demand is increasing on railway infrastructure and its components. Thus, the research work presented in this study was carried out to know the value of maximum stress limit and maximum displacement after fatigue and static test being applied. A major part of the laboratory investigation is covered on the preparation of the sleeper itself and compliance to design requirements. This laboratory works preliminary data come from constant amplitude spectrum from previous study.

Keywords Prestressed concrete sleeper (PCS) · Maximum stress and displacement

I. Sharul Nizam · A.B. Afidah · H. Siti Hawa
Faculty of Civil Engineering, Universiti Teknologi MARA,
40450 Shah Alam, Selangor, Malaysia
e-mail: sharulchong_08@yahoo.com

A.B. Afidah
e-mail: afida3342@salam.uitm.edu.my

H. Siti Hawa
e-mail: shh@salam.uitm.edu.my

R. Mohd Ikmal Fazlan (✉)
Faculty of Civil Engineering, Universiti Teknologi MARA,
13700 Permatang Pauh, Pulau Pinang, Malaysia
e-mail: ikmal601@ppinang.uitm.edu.my

1   Introduction

Transportation is very important for the growth of economy and society of any country. Nowadays, railway system provides the best and safest result for transportation of either freight or passenger [1]. The railways were originally developed to have ability to carry heavy load compared to the roads. The major component of railway infrastructure is the railway sleeper. Some of the requirements and functions of sleeper are to give a support for rails and fastenings. Next, transfer rail forces to the ballast bed. Then, to preserve rail inclination and track gauge and give adequate electrical insulation between both rails. Lastly, to be resistant to mechanical influences and weathering over a long time periods. The material of railway sleeper can be steel, timber, and concrete [1]. Railway structure timbers are the first system used, but it is replaced with precast concrete sleeper in order to reduce cost and maintenance. Prestressed concrete sleeper have another advantages which is longer service life [2]. During World War II blockades, the shortage of good quality of timber forced the United Kingdom to develop and use prestressed concrete sleepers. Since then, several countries had invented prestressed concrete sleepers as standard in the railway tracks [3]. Railway system also can help in economy.

For intercity train, it can help in terms of tourism. When public transportation like railway is good, our country will become attractive to the tourist. Tourist will feel easy to move from one place to another. In order to ensure that railway will be first choice of transportation for public, the conditions of railway need to be in safe and good in condition. Prestressed concrete is one type of reinforced concrete. There are a few advantages when using prestressed concrete as sleeper. Some of the main advantages are to reduce deflections of reinforce concrete element which are under service loads, fatigue resistance is considerably raised, segmental forms of construction can be applied, very high strength steel used to form the tendons, and sections of reinforced concrete element are smaller mainly due to the capacity to reduce reflection. Nowadays designers have approached the design of prestressed concrete sleepers based on permissible stress design, whereas the structural behavior or deformations are kept within the elastic range. Static or static quasi load is the design load of structural design. Static or quasi static load can be ascribed to a dynamic impact factor multiplying with the wheel load [4]. In fact, the railway track condition loading is somewhat time dependent.

There is cyclic loading involved in this prestress concrete sleeper due to wheel train. Cyclic load is known when engineers discovered that if you repeatedly subjected loading onto material or subject then remove a nominal load [5]. The part may break after some cycles of load and unload, although the highest maximum cyclic stress level subjected is much less than the ultimate tensile stress (UTS) and actually less than Yield Stress. When the magnitude of cyclic test was reduced, the part can maintain more before breaking. The term that have been used to this behavior is known as "Fatigue" because it describes that the sleeper behavior became weary or exhausted. It can be summarized that when loaded was subjected

to ductile metal and load is increased moderately from zero to maximum, final result of the material will give very large strains. Despite that, when repeated loads were applied on the same material, failure resulted from elastic limit is higher than stress and plastic deformation does not exist in the area of the fractures. There indicated that no prior is in existing of failure. Fatigue damage can be lead by compressive and tensile stress. This study has lead to determine stress limit and maximum displacement for this type of train due to cyclic loading as explained further in methodology.

2   Methodology

Prestressed concrete sleeper widely used are designed based on AS1085.14 [6]. A rail seat repeated load test was conducted on the prestressed concrete sleeper by universal testing system machine located at the Heavy Structure Laboratory Fakulti Kejuruteraan Awam, UiTM Shah Alam. The prestressed concrete sleeper was subjected to repeating cyclic loads as typical loading were from intercity train of 12 coaches loading to attain the maximum displacement and stress limit. The data used in the test to form the loading were taken from the previous study [7]. Table 1

Table 1 Constant amplitude data for intercity loading train [7]

Coaches	Constant amplitude average			Frequency, F
	Loading, P	Stress, σ	Cycle, N	
N1	−87.10	−805.74	1.17	11.86
N1	−63.94	−591.49	1.17	11.86
N1	−40.78	−377.24	1.17	11.86
N1	−63.94	−591.49	1.17	11.86
N2	−60.52	−559.85	5.32	2.15
N2	−43.23	−399.91	5.32	2.15
N2	−25.94	−239.96	5.32	2.15
N2	−43.23	−399.91	5.32	2.15
N3	−80.54	−745.05	1.15	11.62
N3	−61.70	−570.77	1.15	11.62
N3	−42.86	−396.49	1.15	11.62
N3	−61.70	−570.77	1.15	11.62
N4	−69.55	−643.39	2.80	4.87
N4	−49.75	−460.22	2.80	4.87
N4	−29.95	−277.06	2.80	4.87
N4	−49.75	−460.22	2.80	4.87

Table 2 Simplify data from previous study [7]

Block	Load, P (kN)	Cycle, N	Frequency, F
N1	$P_{max} = 87$	129,600	3 Hz
	$P_{min} = 41$		
N2	$P_{max} = 61$	43,200	1 Hz
	$P_{min} = 26$		
N3	$P_{max} = 81$	129,600	3 Hz
	$P_{min} = 43$		
N4	$P_{max} = 70$	43,200	1 Hz
	$P_{min} = 30$		

Fig. 1 Location of the block at the train [7]
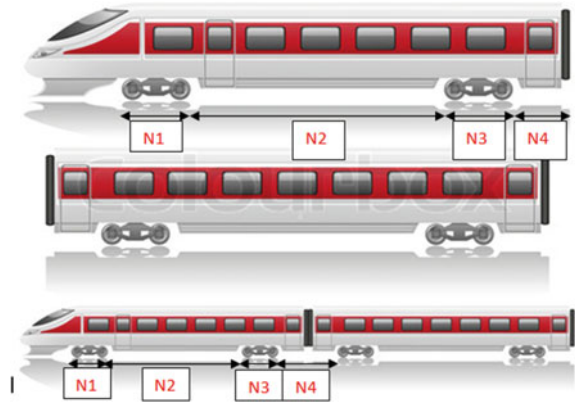
shows the data used in the test. The data have been collected during working hours for 4 days at alongside Bangi to Kajang. This data were taken with the cooperation from KTMB. The location was chosen to get an optimum speed of freight train nearby Selangor. The raw data collected were divided into four blocks as shown below. Fatigue test was done for this sample for almost 2 days and every parts of N are about 12 h based on their cycle and frequency. Post-fatigue test is taken over after this fatigue test has been done. Table 2 shows the simplify data from Table 1 for this laboratory test.

Figure 1 gives a simple picture to locate the real partition of N. This will show how classification of load cycles determined. N1 front wheel. There are two wheels for the front wheel. Next, N2 is the distance between front wheel, N1 and back wheel, N3. N3 is back wheel and consists of two wheels. Finally, N4 is distance from back wheel, N3 of the coaches to front of the wheel, N1 for the next coaches. The coordination of sample and point during the test conducted is shown in Fig. 2 [6] and Fig. 3. While Fig. 4 shows the real picture installation in laboratory test.
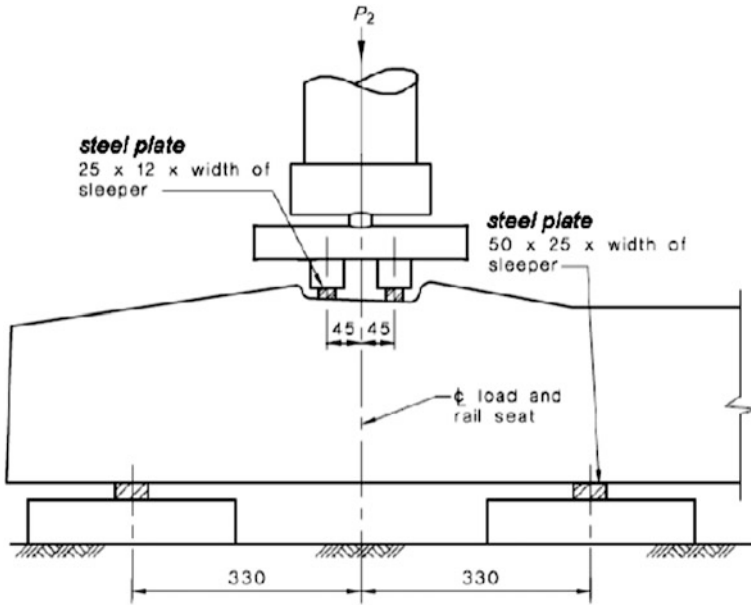
Fig. 2 Rail seat for fatigue test positioning [5]
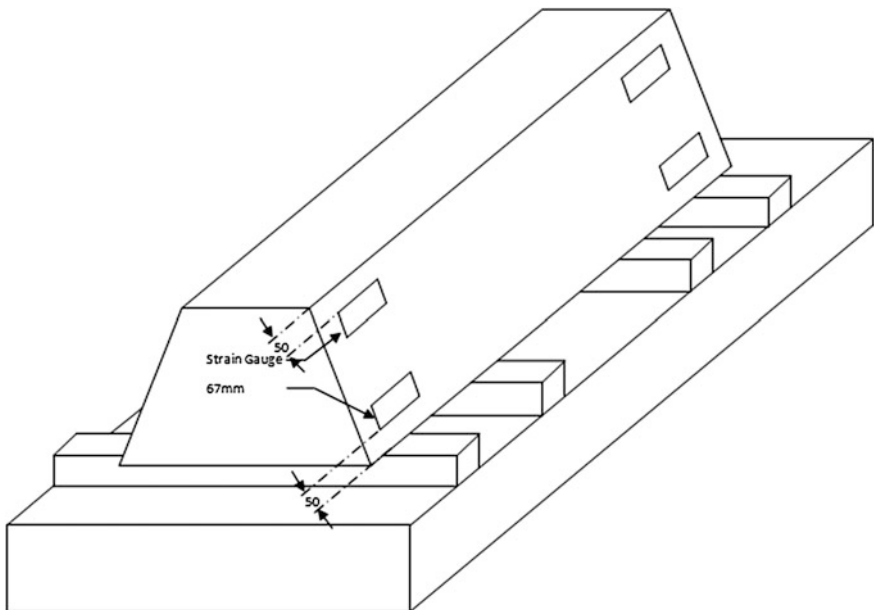
Fig. 3 Installation sample to UTS machine
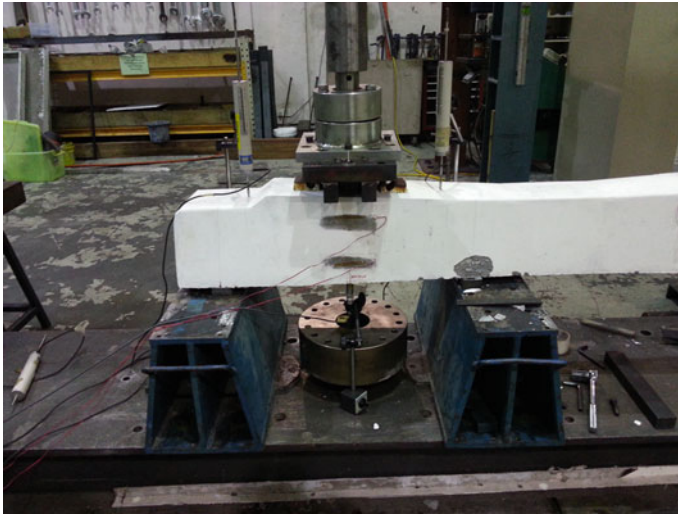
Fig. 4 Installation sample to UTS machine

3 Result

Stress and strain relationship were obtained from the fatigue test. Strain gauges were installed at two points of the sleeper which are at the bottom and top of the samples. Strain gauge at the bottom was used as observation because theoretically failure of sample was started at the bottom. The value of the strain depended on the
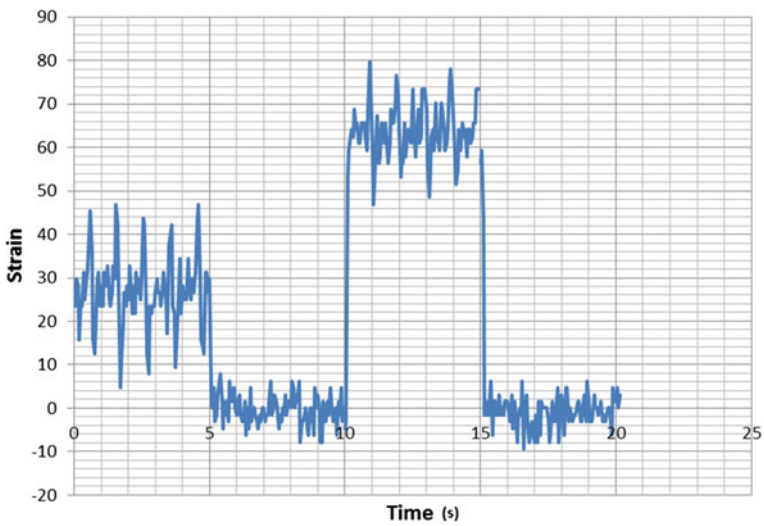
Fig. 5 Strain versus time

load applied to the sample. The data show the pattern of strain on every block which is presented in Fig. 5.

The value of stress can be determined by using the formula $E = \delta/\varepsilon$. $E =$ Young Modulus of elasticity (50 GPa), $\delta =$ Stress, and $\varepsilon =$ Strain. Figures 6, 7, 8 and 9 show the relationship of stress and strain on every load cycles which is from N1 until N4. Then from the graph obtained the maximum strain and stress of each part as in Table 3.

After fatigue test was done, sample had through the post-fatigue test. Figure 10 shows load versus displacement graph under post-fatigue test. This test has achieved the ultimate load at 418kN. Figures 11 and 12 show condition of the sample after post-fatigue was conduct. Post-fatigue test was done after run full fatigues test.

Fig. 6 Stress versus strain for block number one
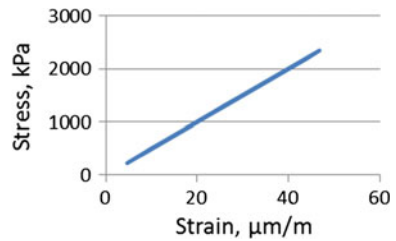
Fig. 7 Stress versus strain for block number two
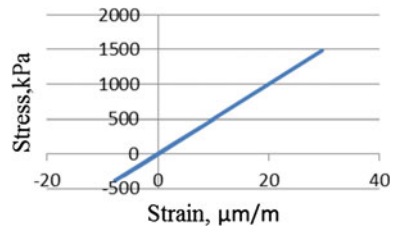
Fig. 8 Stress versus strain for block number three
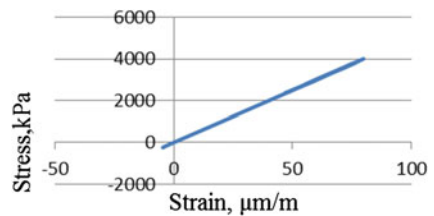
Fig. 9 Stress versus strain for block number four
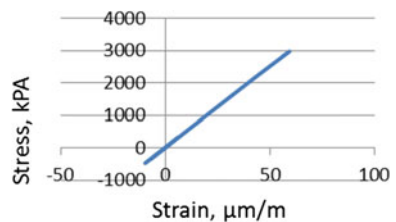
Table 3 Maximum value of stress on every block

Block	Strain (μm/m)	Stress (kPa)
N1	46.8750	2343.75
N2	29.6875	1484.38
N3	79.6875	3984.38
N4	59.3750	2968.75
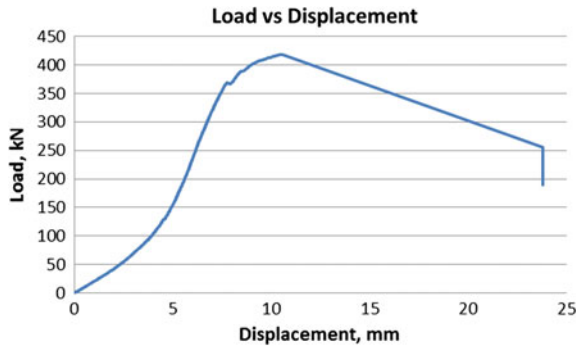
Fig. 10 Load versus displacement under post-fatigue test

Fig. 11 Sample after failure post-fatigue test
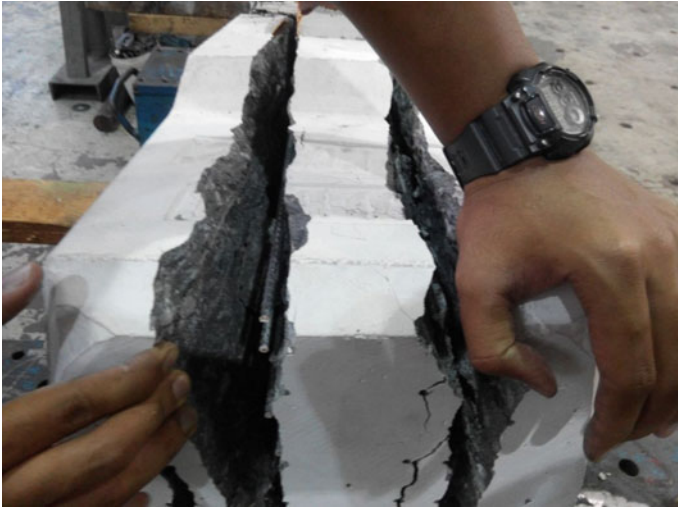
Fig. 12 Sample after failure post-fatigue test

4 Conclusion

Based on the interpreted result and discussion, the stress limit of prestressed concrete sleeper after variable load being implemented was achieved. It can be seen by the result of the stress limit from stress–strain relationship. The value of the highest stress limit is 3984.38 kPa. The prestressed concrete sleeper under this maximum stress limit can still perform without failure. Therefore, the prestressed concrete sleeper still can be designed based on the existing standard.

Through the interpret result, the maximum displacement of prestressed concrete sleeper after static load being applied is determined by running the post-fatigue test. Maximum displacement achieved when loading was optimum and experienced elastic phase which is when the load applied is directly proportional to displacement. The value of the maximum displacement in this experiment was 10.59 mm.

References

1. A. M. Remennikov and S. Kaewunruen, "Resistance of railway concrete sleepers to impact loading," 2007.
2. M. R. Salim, A. Abu-Bakar, and A. A. Shariff, "Investigation on simulation of train loading on prestressed concrete sleepers," *Applied Mechanics and Materials,* vol. 157, pp. 666–670, 2012.
3. M. M. Shokrieh and M. Rahmat, "On the reinforcement of concrete sleepers by composite materials," *Composite structures,* vol. 76, pp. 326–337, 2006.
4. D. Edmund, A. Abu-Bakar, S. H. Hamzah, and R. M. I. F., "Flexural and Cylces Determination of Prestressed Concrete Sleeper (PCS) Subjected to Train Wheels Movement by Using Rainflow Method," Curtin University of Technology Science and Engineering International Conference 6 November 2012.
5. S. Ariduru, "Fatigue Life Calculation By Rainflow Cycle Counting Method," p. 119, 2004.
6. A. Remennikov, M. H. Murray, and S. Kaewunruen, "Conversion of AS1085. 14 for prestressed concrete sleeepers to limit states design format," *Faculty of Engineering-Papers,* p. 400, 2008.
7. N. I. Sharul, E. Dozier, A. Afidah, H. Siti Hawa, and R. Mohd Ikmal Fazlan, "Loading Capacity of Prestressed Concrete Sleeper Under Harmonic Function," in *Applied Mechanics and Materials*, 2014, pp. 118–122.

Serviceability of Construction Materials Under Tropical Climate Effects

Nauwal Suki, Mohd Hisbany Mohd Hashim and Afidah Abu Bakar

Abstract The key aspect discussed in this study is the serviceability of the construction materials namely concrete and steel under the tropical climate effects. The environmental effects such as the temperatures, chemicals from the rain, and particles brought by the wind can cause corrosion on the concrete surface and thus may affect a structure's performance. Through this study, the extent durability of the construction materials was investigated in order to know how far the strength can be affected by the nature. Fifteen concrete cubes and fifteen numbers of steel rods were prepared and placed in two different areas; one is an area which has room temperature surrounding while the other is exposed to the tropical climate for a period of 3, 6, 9, and 12 months. Once the exposure time has lapsed, compression test was done to test the mechanical properties of the concrete cubes while the steel reinforcement underwent the tensile test. After the test was done, it was shown that the control samples of both concrete cubes and steel reinforcements are more durable and stronger compared to its counterpart that was placed in the exposed areas.

Keywords Concrete · Steel reinforcement · Compression test · Tensile test · Tropical climate effects

N. Suki · M.H.M. Hashim (✉) · A.A. Bakar
Faculty of Civil Engineering, Universiti Teknologi MARA,
40450 Shah Alam, Selangor, Malaysia
e-mail: hisbany@salam.uitm.edu.my

N. Suki
e-mail: nauwal@gmail.com

A.A. Bakar
e-mail: afida3342@salam.uitm.edu.my

1   Introduction

Based on the observations done by past researchers, it was found that the deterioration and failure of a structure occurred due to many factors namely the temperature changes between seasons, effects from the rain water and particles carried by the wind as well as polluted air [1], heavy loads of snow on the building and tougher climate condition [2], chemical reactions that are accelerated by increased temperature and are also influenced by the humidity [3].

The mechanical properties and serviceability of a hardened concrete can adversely be affected by a high temperature in the tropics [4]. The environmental attacks thus cause corrosion on the concrete surface. The concrete surfaces affected by the effects from the nature will gradually erode and may expose the steel reinforcements inside. It is known that the steel reinforcement faces the problem of corrosion if not properly covered and protected by the concrete and thus may affect the structure's performance.

Climate change also contributed to the uncertainty of the environmental load estimation in the future, in turn raises questions of the need to modify the existing structural design [5]. Deterioration and failure of a structure cost a lot of money and it is a clear reminder on how vulnerable the effects of climate are. Aware of the signals, the climatologists around the world started to find ways to detect and control changes in extreme weather [6]. It is suggested to implement the climate adaptation in order to reduce the vulnerability of the built infrastructure to changing climate. This includes improvements of the design standards, retrofitting the existing structures, utilization of alternative materials, and regular maintenance [7]. Strengthening the structures can also be done in order to overcome the effect of environmental deterioration [8].

The main issue focused in this study is the extent durability of the two mostly used construction materials which are concrete and steel reinforcement under tropical climate effects. It is hoped that the results produced shall prepare for the problems that may arise in the future as the additional knowledge that can help studies in this area is limited.

2   Materials and Methods

2.1   Concrete Cubes

Fifteen concrete cubes grade 30 were cast in this study with the size of 150 mm × 150 mm × 150 mm and were used according to BS 1881-116:1983 [9]. The concrete were cast and left to harden. As it is hardened, the concrete cubes were cured in a curing tank for a period of 28 days. After 28 days, the control sample were directly tested for compression while the excess cubes were removed from the curing tank and placed in the area exposed to the tropical climate for the periods of 3, 6, 9, and 12 months. Three samples were prepared for each condition. After the

Fig. 1 Compression test

exposed time has lapsed, these cubes were tested until failure using a 3000 kN compression machine as shown in Fig. 1.

2.2 Steel Reinforcements

Fifteen steel rods were prepared in accordance to BS4449:1997 [10]. The steel rods were divided into two different functions namely the control samples and exposed samples which were exposed for a period of 3, 6, 9, and 12 months. Three samples were prepared for each condition. All the steel rods have a diameter of 12 mm with a tensile strength of 460 N/mm^2. These steel rods were cut 750 mm in length. They were then tested using the 1000 kN Universal Testing Machine (UTM) as shown in Fig. 2.

3 Results and Discussions

3.1 Compression Test

Concrete strength is commonly being determined through compression test as the test is able to give a view of the concrete's quality in its hardened state. Table 1 shows the tabulated data for compression test for both control and exposed samples.

Fig. 2 Tensile test
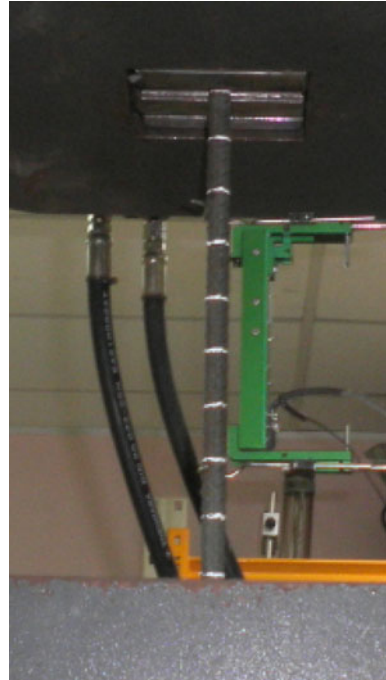
Based on the data, the concrete is seen to have properly developed in proportion to the period of 28 days it takes to cure. It was found that the compressive strength for the exposed samples did reduce compared to the samples placed in room temperature condition but did not reduce from the original grade (grade 30). In brief, the tropical climatic effects contributed to the strength reduction but did not provide extreme effects to the concrete's stiffness.

The curve for compression strength versus months was plotted in Fig. 3.

Through the physical observation, Fig. 4a shows the concrete cubes which were exposed for 3 months as presented has the same physical attributes compared to the cubes placed in room temperature settings. Figure 4b–d show the concrete cubes that were exposed to tropical climate for 6, 9, and 12 months, respectively. There were slight color changes in certain areas and small stone spillage at the edges of the exposed cubes and the condition worsened as time went by.

Table 1 Compressive strength of concrete cubes

Condition	Compressive strength, f_{cu} (N/mm^2)				
	28 Days	3 Months	6 Months	9 Months	12 Months
Control	31.50	–	–	–	–
Room Temp.	–	36.79	36.82	39.39	39.64
Exposed	–	33.97	35.54	35.73	35.93
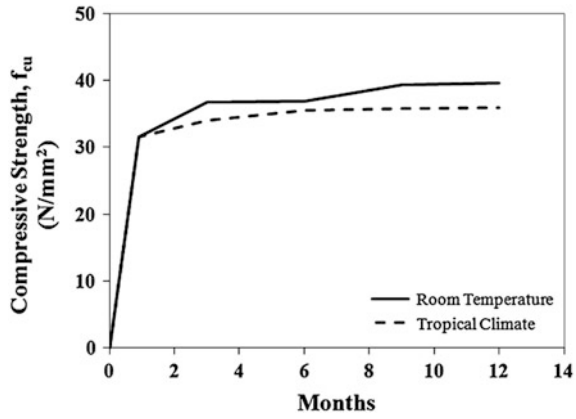
Fig. 3 Compressive strength versus months
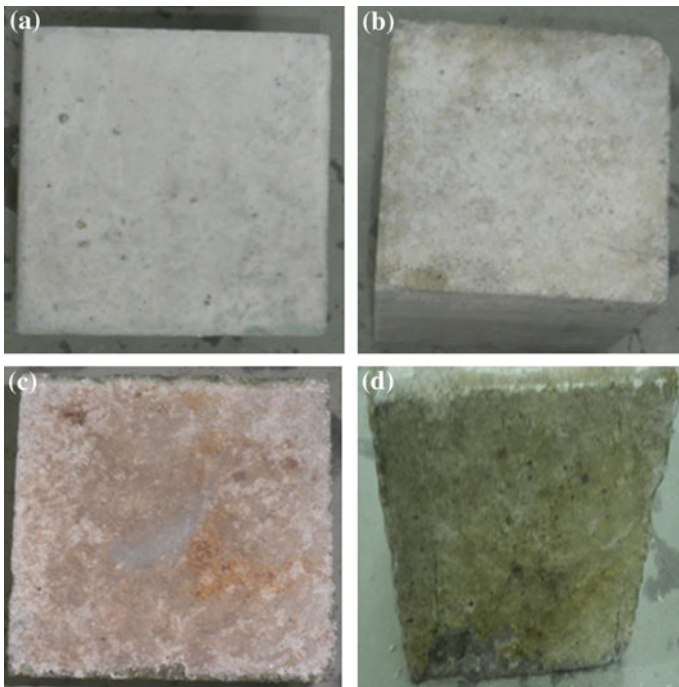
Fig. 4 Concrete cubes exposed to the tropical climate. **a** 3 months exposed, **b** 6 months exposed, **c** 9 months exposed, **d** 12 months exposed

3.2   Tensile Tests

The mechanical properties of the steel reinforcements were determined through the tensile test. Table 2 tabulates the average data for tensile strength of the reinforcement bars. It was found that after being exposed, the tensile strength was seen to reduce.

Figure 5 illustrated the load versus deformation curves for both control and exposed samples. It was found that after being exposed, the load was seen to reduce. Moreover, the elongation of steel at rupture was seen to be longer.

Figure 6 shows steel failure at rupture. All steel rods faced ductile failure. Figure 6a shows the control sample while Fig. 6b–e were the steel exposed for 3, 6, 9, and 12 months, respectively. As time goes by, it can be seen that the oxidization process becoming worse. The steel exposed for 3 months was partially oxidized. The steel exposed for 6 months was almost completely oxidized while the steel exposed for 9 and 12 months were completely oxidized.

Table 2 Tensile strength of the steel reinforcement

Condition	Tensile strength, f_y (N/mm^2)				
	Control	3 Months	6 Months	9 Months	12 Months
Control	762.45	–	–	–	–
Exposed	–	756.89	740.29	661.62	541.81

Fig. 5 Load versus deformation curves
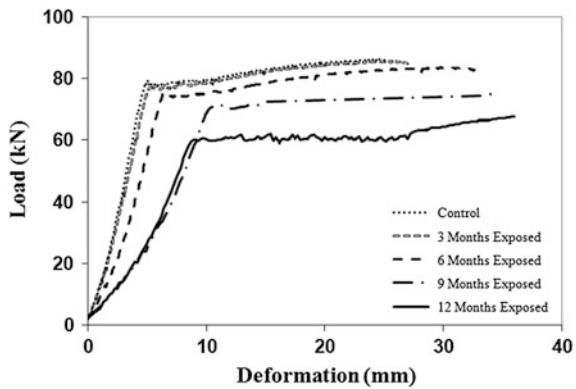
Fig. 6 Control and exposed samples of the reinforcement steels. **a** Control, **b** 3 months exposed, **c** 6 months exposed, **d** 9 months exposed, **e** 12 months exposed
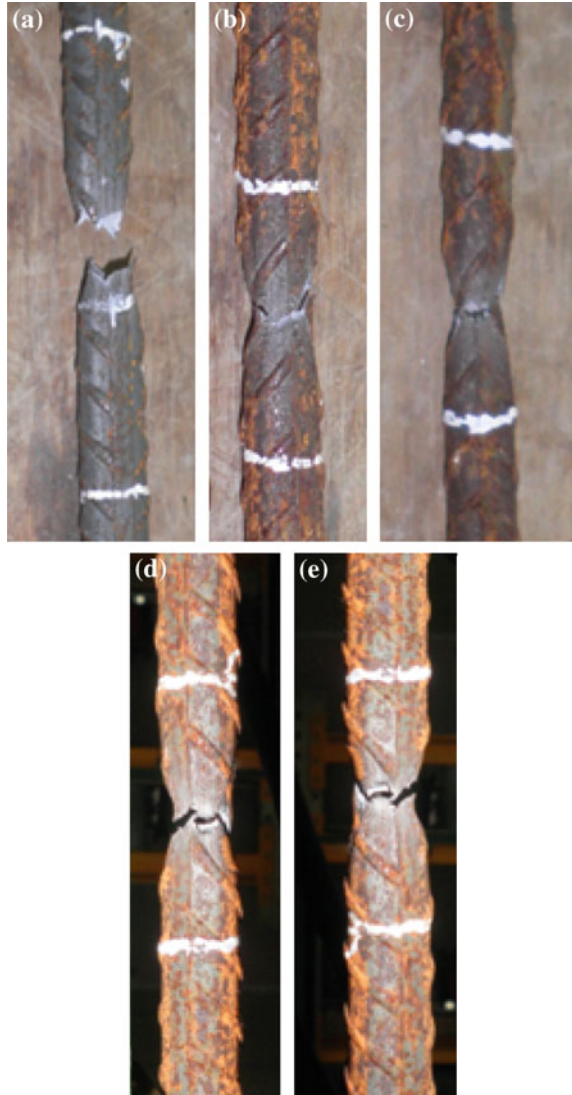
4 Conclusions and Recommendations

Steel reinforcement is used in construction to withstand the tensile load thus avoiding the concrete from cracking. To ensure that the combination of the steel reinforcement and concrete remains strong, both materials need to support each other. The results show that the strength of steel was reduced as it is affected by the tropical climate effects. To avoid the unwanted condition to happen, the concrete needs to properly protect the steel. Maintenance needs to be done to ensure concrete

spillage due to tropical climate effects does not increase and the concrete can properly protect the steel within its expected lifetime. With consideration of the climate effects, the combination of these two materials can produce a structure that can withstand various conditions if it is designed and maintained properly.

References

1. E. Yaldiz, "Climate Effects on Monumental Buildings," 4th International Scientific Conference on Water Observation and Information System for Decision Support (BALWOIS 2010), vol. May 2010, pp. 1–10, May 2010.
2. K. R. Lis, and N. Year, "Effects of Climate Change on Built Environment," Norwegian Building Research Institue (NBI), pp. 2000–2002, 2005.
3. J. Skalny, J. Marchand, and I. Odler, Sulfate Attack on Concrete (Modern Concrete Technology), SPON Press, 2001.
4. K. A. Soudki, E. F. Salakawy, and N. B. Elkum, "Full Factorial Optimization of Concrete Mix Design for Hot Climate," Journal of Materials in Civil Engineering, vol. 13, no. 6, pp. 427–433, 2001.
5. F. T. Lombardo, and B. Ayyub, "A Plan for Characterizing Uncertainties in Extreme Environmental Loads with Climate Change Considerations: Wind Speed and Wave Height as Case Studies," Vulnerability, Uncertainty and Risk, vol. 1, pp. 1363–1372, 2014.
6. F. W. Zwiers, and X. Zhang, "Towards Regional Scale Climate Change Detection," Journal of Climate, vol. 16, pp. 793–797, 2003.
7. M. G. Stewart, and X. Deng, "Climate Impact Risks and Climate Adaptation Engineering for Built Infrastructure," Risk Uncertainty Engineering System (Part A: Civil Engineering), vol. 1, pp. 1–12, 2015.
8. M. H. M. Hashim, A. R. M. Sam, and M. W. Hussin, "The Future of External Application of Fiber Reinforced Polymer in Civil Infrastructure for Tropical Climate Region," International Journal of Mechanical and Materials Engineering (IJMEE), vol. 6, no. 2, pp. 147–159, 2011.
9. "BS 1881-116: 1983 Testing Concrete (Part 116: Method for Determination of Compressive Strength of Concrete Cubes)," British Standard, 1983.
10. "BS 4449: 1997 British Standard: Specification for Carbon Steel Bars for the Reinforcement of Concrete," British Standard, 1997.

Strength, Water Absorption and Carbonation Depth of Micro Fine Quarry Dust Concrete Grade 60

A.R. Nur Hanani, K. Kartini and M.S. Hamidah

Abstract An alternative material (pozzolanic) needs to be looked into, in order to reduce the usage of cement in the concrete, since the demand for cement is quite high in developing countries owing to rapid infrastructural development. Pozzolanic material, also known as a cement replacement material, has been introduced as substitutes for cement in concrete. Several types of materials are in common use, some of which are by products from other industrial processes and hence their use may have economic advantages. Micro fine quarry dust (MFQD) is a by product from the quarry in a form of white material that is introduced to replace cement. The introduction of quarry dust (QD) seems acceptable since the study on the chemical composition shows that the QD can be classified under category mineral admixture Class N (pozzolan). This paper deals with the utilization of MFQD as a partial replacement of cement in the concrete. The aim of this study is to determine the compressive strength, water absorption and carbonation depth of hardened concrete Grade 60 at replacement level of 3, 5, 10, 15 and 20 % taken at 7, 28, 60, 90, 180 and 365 days of age. The results lead to the conclusion in which MFQD is suitable to be used as a partial cement replacement with the percentage replacement of cement up to 15–20 %, while the carbonation depth increased as the percentage replacement level increased, in which at 28 days, the carbonation depth increased from 1.25 to 2.44 mm. The results show that the decision reached in enhancing the suitability of MFQD as a partial cement replacement thus will reduce not only demand for cement but also the environmental problem.

Keywords Pozzolanic material · Micro fine quarry dust · Compressive strength · Water absorption · Carbonation depth

A.R. Nur Hanani (✉) · K. Kartini · M.S. Hamidah
Faculty of Civil Engineering, Universiti Teknologi MARA, 40450 Shah Alam, Selangor, Malaysia
e-mail: nanierahim14@ymail.com

1   Introduction

In the year 2006, about 1.8 Giga tonnes of carbon dioxide (CO_2) emission was produced [1]. Wang et al. [2] stated that about 15 % of total greenhouse gas (GHG) emissions was in China, which is the biggest cement producer and carbon dioxide emitter in the industry. The percentage increase of GHG with increasing cement production is expected due to the extensive use of concrete in construction industry. Overall, Malaysia presents significant potential increased in cement demand due to growing population as well as scope for growth in gross domestic product per capita which stimulate the needs for better infrastructure. However, cement production poses problems in many areas with respect to its availability of natural resources, cost and environmental impact such as emission of airborne population due to dust, gases, noise and vibration when operating machine and during the blasting process in quarries.

According to Wan Zulasmin in 2007 [3], for the year 2006, Malaysia produced 33 million tonnes of limestone where 21.2 million tonnes were used in the manufacture of cement. Hudson [4] stated that the utilization of quarry dust (QD) in the industrialized country such as Australia, France, Germany and UK have reached more than 60 % of its total production. The QD has been accepted as a building material for the past three decades which is known as manufactured sand [5]. The utilization of micro fine quarry dust (MFQD) in concrete mixes as partial cement replacement has been gaining importance since the study on MFQD as partial cement replacement showed the potential use [6].

Quarry rock dust (QRD) is a fine particle having size less than 4.75 mm which is defined as residue, tailing or other non-valuable waste material obtained after extraction and processing of rock at quarry site [7]. David [8] defined QD as the material used in construction industry having size less than 4 mm. The introduction of QD to the concrete mixes as pozzolanic material is limited due to its high fineness. The addition of QD in fresh concrete may increase the water demand and the cement content in order to give workability and thus strength of the concrete [9].

Through reaction of concrete admixtures, QD improved the pozzolanic reaction and concrete durability and thus improved the strength of the concrete [10]. On the other hand, Shahul Hameed et al. [10] also reported that due to efficient micro-filling ability and pozzolanic activity, the combination of QRD and marble sludge powder present an excellent performance.

In order to determine the classification of MFQD, the sum of SiO_2, Al_2O_3 and Fe_2O_3 was calculated and it achieved almost 70 % in the QD [6, 7, 10] which can be classified as mineral admixtures under categories of class N and classified as pozzolanic material according to ASTM C 618-2003 [11]. Meaning that, MFQD is suitable to be used as an alternative material for partial cement replacement. According to the Boonleangubpathum et al. [12], QD can be used in construction work and thus the natural resources would be used efficiently and can minimize the cost for the construction materials.

However, there are still limited studies on the concrete properties with different percentage replacement of MFQD. Therefore, this paper reported the study on the strength, water absorption and carbonation depth of MFQD concrete grade 60 at different percentage replacement of OPC.

2 Experimental Methods

2.1 MFQD Materials and Its Production

QD is defined as the fine particle having size less than 4.75 mm. This powder is quite similar to the size of sand. In order to produce MFQD, 5 kg of QD was grinded in Los Angeles Machine for 24,000 revolutions with a speed of 33.3 rpm with 16 nos. of ball bearings (427 $\pm$ 5 g of each) placed inside the machine. After grinding, the powder was sieved using 90 µm sieve in order to produce MFQD.

2.2 Mix Proportion

In this study, the mix design of concrete Grade 60 was prepared based on the designated mix design [13]. The OPC (CONTROL) and five series of MFQD concrete which are designated at different levels of percentages, i.e. 3, 5, 10, 15 and 20 % named as 3MFQD, 5MFQD, 10MFQD, 15MFQD and 20MFQD, respectively, as partial cement replacement were prepared. The water binder (w/b) used in this concrete mix design was 0.3.

2.3 Testing Procedure

2.3.1 Slump Test

Workability can be defined as properties of fresh concrete which are able to manipulate a freshly mixed with minimum loss of homogeneity. Workability of the fresh concrete was tested by conducting the slump test. This test was conducted in accordance with British European Standard BS EN 12350-2:2009 [14]. The objective of this test is to ensure that the fresh concrete achieved the targeted slump that has been designated. The targeted slump of this study was 30–60 mm for the concrete mixes.

2.3.2 Compressive Strength

The compressive strength is the ratio of breaking load to the transversal section of the specimen [15]. The compressive strength test was conducted based on British European Standard BS EN 12390-3:2009 [16]. The machine used was compression test auto test with pace rate of 3 kN/s and load capacity 3000 kN. This test was subjected on $100 \times 100 \times 100$ mm cube specimens and tested at 7, 28, 60, 90, 180 and 365 days of curing. The specimen was placed centrally on the lower platen and the load was applied continuously until the maximum loading was achieved. The compressive strength of the specimens was expressed by using formula as in (1) according to British European Standard BS EN 12390-3:2009 [16] as calculated below:

$$fc = P/A \tag{1}$$

where, fc is compressive strength (N/mm^2), P is total maximum load (N) and A is area of loaded surface (mm^2).

2.3.3 Water Absorption

The water absorption test was conducted in order to determine the water absorption of concrete specimens of size 50 dia $\times$ 100 mm. This test was complied to British Standard BS 1881-122:2011 [17]. The specimens were tested at 7, 28, 60, 90, 180 and 365 of curing days. The specimens were placed in the well ventilated drying oven for 72 ± 2 h at 105 ± 5 °C and cooled in the air tight vessel for 24 ± 0.5 h and the readings were recorded for every 30 min for 240 min after immersed in the water. The water absorption of the specimen was computed as increase in mass as percentage of dry mass by using formula as in (2) which prescribed in British Standard BS 1881-122:2011 [17] as follow:

$$W = \frac{w_t - w_i}{w_i} \times 100 \tag{2}$$

where, W is water absorption after immersion (%), w_i is the weight of specimen after dried in the oven (g) and w_t is the weight after immersed in water at specific time (g).

2.3.4 Carbonation Depth

This test was carried out on the specimens of size 150 dia $\times$ 150 mm complying with British European Standard BS EN 14630:2006 [18]. All the specimens were

exposed in the concrete laboratory, Faculty of Civil Engineering, Shah Alam with average temperature of 30 $\pm$ 1 °C and 69 $\pm$ 2 % RH for 7, 28, 60, 90, 180 and 365 days. The specimens were divided into two halves sections and the 1 % phenolthalein solution was sprayed on the broken surface. The specimen surfaces turn into purple colour if it retains alkaline and no colour changes if carbonation has taken place.

3 Result and Discussion

3.1 Properties of MFQD

3.1.1 Physical Properties

Table 1 shows the physical properties of OPC and MFQD with respect to fineness, specific gravity, standard consistency and soundness. The result of fineness test shows the fineness of OPC (98.6 %) was higher than MFQD (92.1 %). The MFQD is 6.5 % coarser than OPC. According to [19], the fineness of the cementitious material is very important in determining the compressive strength of the concrete, in which higher fineness resulted in an increased compressive strength [19]. The fineness of OPC and MFQD as a partial cement replacement may affect the rate of hydration, hydrolysis and development of strength in concrete. The fineness test was carried out based on British European Standard BS EN 196-6:2010 [20].

The specific gravity test complying to British Standard BS 1377-2:1990 [21] was conducted and the result shows that the specific gravity of OPC (3.24) is higher than MFQD (2.56), which indicated that MFQD is lighter than OPC. The specific gravity of MFQD obtained by Mahendrana et al. [22] and Felekoglu [23] was in the range of 2.54–2.60.

The result of standard consistency shows that OPC paste required more water (32 % of standard consistency) compared to MFQD paste (16 % of standard consistency) which indicated that MFQD does not absorb water in the mixed. The test procedure and the result complied to British European Standard BS EN 196-3:2005+A1:2008 [24].

The soundness of the paste was determined according to British European Standard BS EN 196-3:2005+A1:2008 [24]. According to British Standard BS

Physical properties	OPC	MFQD
Fineness	98.6 %	92.1 %
Specific gravity	3.24	2.56
Standard consistency	32 %	16 %
Soundness	0.27	0.07

Table 1 Physical properties of OPC and MFQD

6610:1996 [25], the limit expansion for pozzolanic material is 10 mm. For this study, the result of soundness test shows the expansion of blended OPC and MFQD paste was in the range of 0.07 to 0.27 mm.

3.2 Chemical Composition

In order to identify the chemical composition of OPC and MFQD, the Shimadzu X-ray Fluorescence Spectrometer (XRF) was conducted and the result is shown in Fig. 1. From the Fig. 1, the sum of the SiO_2, Al_2O_3 and Fe_2O_3 in MFQD achieved almost 70 % and according to ASTM C618-2003 [11], MFQD can be classified as a mineral admixture under categories of class N.

In addition, OPC contained high calcium oxide (CaO) which is 72.17 % compared to MFQD about 1.84 %. It is known that when $Ca(OH)_2$ with MFQD mixed together, it will produce C-S-H gel and less portlanite and will enhance the strength of the hardened concrete and thus resistant to carbonation, penetration and acid attack.

The sulphur trioxide (SO_3) also known as gypsum found in the MFQD was only 0.20 % compared to OPC which was around 2.90 %. According to Neville [26], due to high reactivity of C_3S, the function of SO_3 is to retard the setting time of concrete. Similar to OPC, MFQD contained almost 1.32 % of loss of ignition (LOI) while OPC contained almost 1.33 %, respectively. Neville [26] also stated that the loss of ignition shows the extent of carbonation and hydration of free lime and free magnesia due to the exposure of cement to the atmosphere. Referred to the ASTM C150-2007 [27], the maximum loss on ignition (at 100 °C) is 3 % whereas 4 % is acceptable for cement in the tropics and it was permitted by British Standard BS 12:1991 [28]. The MFQD satisfies the requirement of ASTM C 618: 2003 [11].
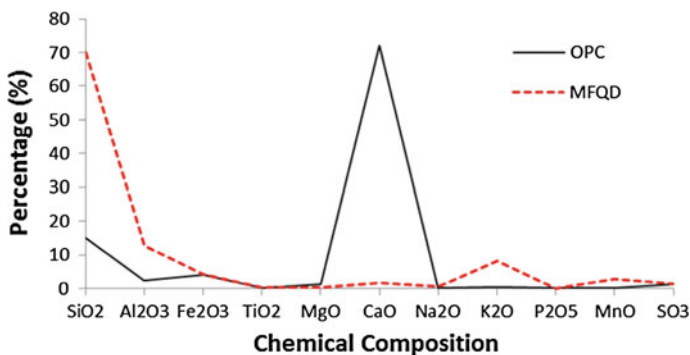
Fig. 1 Chemical composition of OPC and MFQD

3.3 Workability

From Fig. 2, CONTROL mixes were recorded at 32 mm slump, while MFQD mixes were recorded between 32–37 mm slumps. CONTROL mixes show a minimum slump compared to MFQD mixes. This might be because the CONTROL mixes required more water (32 % of standard consistency) compared to MFQD mixes (16 % of standard consistency). According to Raman et al. [29], a minimum slump produced minimum air content in order to ensure excellent workability of the fresh concrete. Thus, from the test result, it shows that the MFQD mixes still maintain the excellent workability as the slump between 32–37 mm.

3.4 Compressive Strength

The compressive strength is expressed by the power of the concrete to resist destruction by the action of stresses due to the compression load [30]. Figure 3 showed the results of the compressive strength for CONTROL concrete and 5 series of MFQD concrete taken at ages 7, 28, 60, 90, 180 and 365 days of water curing. From Fig. 3, for the CONTROL, 3MFQD, 5MFQD, 10MFQD, 15MFQD and 20MFQD, the compressive strength of concretes increased from 7 to 365 days of water curing. The compressive strength increased from 64.72 to 88.90 N/mm^2 (CONTROL), 63. 77 to 87.10 N/mm^2 (3MFQD), 63.52 to 85.88 N/mm^2 (5MFQD), 63.21 to 84.21 N/mm^2 (10MFQD), 63.08 to 83.98 N/mm^2 (15MFQD) and 58.87 to 82.64 N/mm^2 (20MFQD).

It can be observed that prolonged period of curing resulted in an increased compressive strength for all replacement of MFQD concrete. This is in line with Ramezanianpour [31], who stated that concrete moist cured improved in strength as
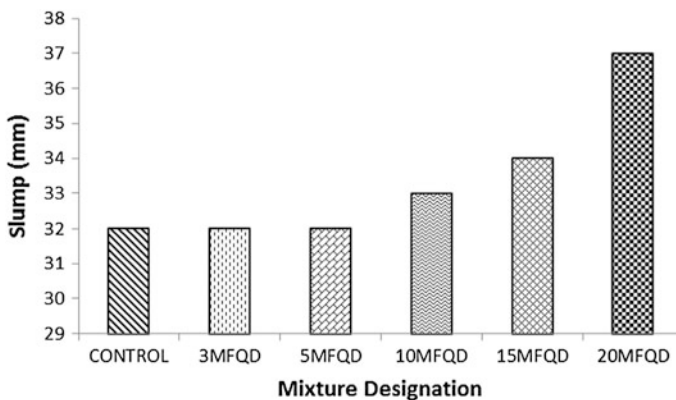
Fig. 2 Slump of CONTROL and MFQD fresh concrete
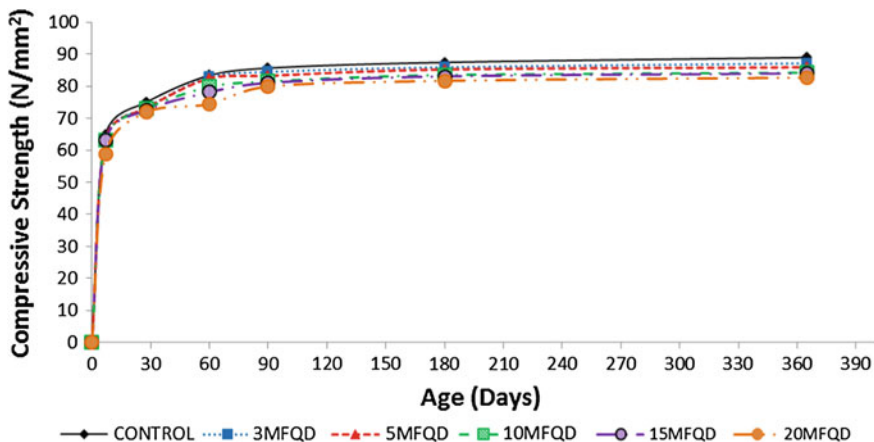
Fig. 3 Compressive strength versus age of CONTROL and MFQD concrete at different percentages of replacement level

compared with concrete without any curing. This was also agreed by Mamlouk and Zaniewski [32] who quoted that compressive strength increased with increasing days of curing.

From Fig. 3, the compressive strength of CONTROL concrete was slightly higher than the compressive strength of MFQD concrete. It also can be seen that the compressive strength slightly decreased with increased percentages replacement of cement. This might be because of higher fineness of OPC compared to MFQD which resulted in higher compressive strength of OPC concrete. As it can be seen, the fineness of OPC was 98.6 %, while MFQD was 92.1 %.

Figure 4 shows the results of CONTROL and MFQD concrete in which it is observed that all replacement achieved targeted strength at 28 days. It is widely accepted that strength at 28 days is consider as governing strength for concrete mix design. The good compressive strength is attributed from proper hydration of cement and reduction in voids in the presence of pozzolanic material. This statement was agreed by Pamnani Nanak et al. [33].

3.5 Water Absorption

Figure 5 shows the water absorption for CONTROL, 3MFQD, 5MFQD, 10MFQD, 15MFQD and 20MFQD at w/b ratio 0.3 taken at 7, 28, 60, 90, 180 and 365 days. It shows that the water absorption decreased with prolonged curing period. From Fig. 5, the water absorption decreases from 3.30 to 2.34 %—CONTROL, 3.44 to 2.41 %—3MFQD, 3.78 to 2.53 %—5MFQD, 4.15 to 2.72 %—10MFQD, 4.41 to 2.78 %—15MFQD and 4.43 to 2.89 %—20MFQD. This might be due to the transformation of large pores to fine pores as a consequence of the pozzolanic
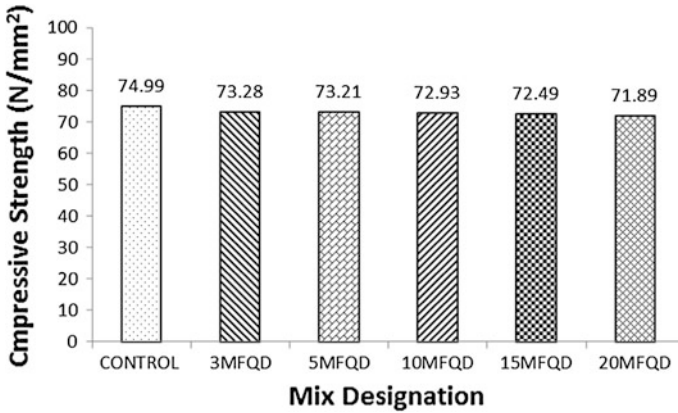
Fig. 4 Compressive strength versus mix designation of CONTROL and MFQD concrete at 28 days of curing

reaction between OPC and MFQD and also might be due to the discontinuity of capillary pores.

Figure 5 also shows the absorptive level of MFQD concrete is higher than the CONTROL concrete for all ages of curing; however the values are still lower than 10 % of mass as stipulated in the British Standard BS 1881-122:2011 [34]. While in term of percentage replacement, the water absorption of MFQD concrete was higher than CONTROL concrete. This might be because of the presence of the higher capillary pores and voids in the concrete. According to Sutan et al. [35], the capillary pores and voids increase resulted in higher absorption characteristic [35]. This is also in line with the statement made by Norhana and Kartini [6], in which they stated that the increased percentage replacement of cement increased water absorption.

3.6 Carbonation Depth

Figure 6 shows the carbonation depth of CONTROL and MFQD concretes. In Fig. 6, the results illustrated that with increasing percentage replacement of cement resulted in increasing carbonation depth from 1.04 to 2.23 mm (7 days), 1.25 to 2.44 mm (28 days), 1.81 to 3.23 mm (60 days), 2.48 to 4.44 mm (90 days), 3.53 to 5.02 mm (180 days) and 4.89 to 6.45 mm (365 days), respectively. In other words, the higher the percentage replacement of cement, the higher the depth of carbonation.

It can be seen that, the depth of carbonation might be because of the presence of pozzolanic material, moisture content and thus the porosity of the concrete. This is agreed by Sisomphon and Franke [36] which found that pozzolanic as replacement
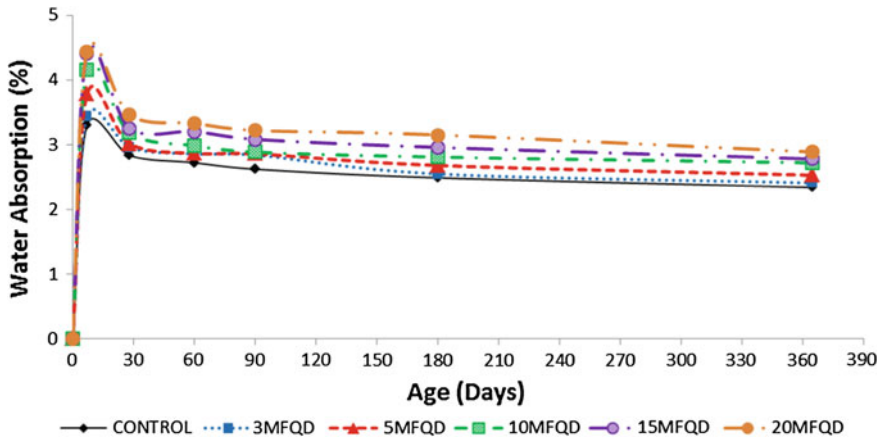
Fig. 5 Water absorption versus age of CONTROL and MFQD concrete at different percentages of replacement level
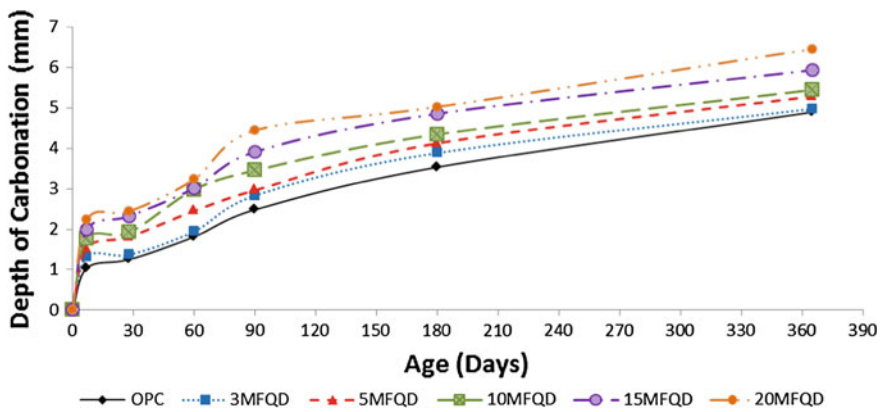
Fig. 6 Carbonation versus age of CONTROL and MFQD concrete at different percentages of replacement level with average temperature of 30 ± 1 °C and 69 ± 2 % RH

material in concrete has affected the depth of carbonation which concerns both binding capacity of CO_2 and its porosity. Neville [26] stated that the rate of carbonation depends on the moisture content of the concrete and its porosity [37]. Study by Hewlet [38] stated that concrete with pozzolanic material is less capable of resisting carbonation than OPC concrete. The extended of chemical interaction which bind the CO_2 will be reduced compared to CONTROL concrete [39]. From Fig. 6, it can be found that the greater the amount of pozzolanic material in concrete, the depth of carbonation becomes deeper. This phenomenon might be due to the reduction of the alkali content in the cementitious material. This is in line with

Park [40] who stated that the calcium silicate hydrate formed from the pozzolanic reaction absorbs more alkali ions hence the pH in the concrete reduced.

In conducting the carbonation test, the specimens were exposed in the concrete laboratory with average temperature of 30 ± 1 °C and 69 ± 2 % RH. However, Sisomphon and Franke [36] reported that the carbonation process under the natural condition is low due to the concentration of CO_2 in the environment which is only about 0.03–0.04 % by volume. On the other hand, the factors controlling carbonation might be because of the reactivity of the concrete with the CO_2 and the diffusivity of CO_2. A study conducted by Xiao-Yong and Han-Seung [41] found that the diffusivity of CO_2 depends on the exposure condition and pore system of the hardened concrete which is controlling the carbonation depth.

According to Al-Khaiat and Fattuhi [42], carbonation depth also depends on the w/b ratio. For this study, since the w/b ratio is 0.3, it is expected that the carbonation process is lower. As explained by Song and Sulapha [43, 44], lower carbonation process enhances the carbonation resistance of concrete. Thus, it can be predicted that with lower w/b ratio, the carbonation depth also will be lower.

4   Conclusion

Based on above discussion, following conclusions are drawn:

1. According to ASTM C 618-2003 [11], MFQD can be classified as a mineral admixture under categories of class N (pozzolan).
2. The fineness of MFQD passing the 90 µm sieve was 92.1 % and specific gravity was 2.56. The standard consistency was 16 % while the soundness of OPC-MFQD paste was in the range of 0.28 to 1.51 mm.
3. The strength of MFQD concrete grade 60 reduced as the amount of replacement increased. However, the strength of the MFQD concretes obtained achieved the targeted strength of grade 60. The optimum replacement of MFQD can be considered up to 15 %.
4. The water absorption of the MFQD concrete with w/b ratios 0.3 decreased as the percentage replacement of cement increased. However, the MFQD concretes can be classified as a good quality concrete as the percentage of water absorption was below than 10 % by mass with optimum replacement up to 20 %.
5. The higher the percentage replacement of cement with MFQD, the higher the depth of carbonation. The carbonation depth increased from 1.04 to 2.23 mm (7 days), 1.25 to 2.44 mm (28 days), 1.81 to 3.23 mm (60 days), 2.48 to 4.44 m (90 days), 3.53 to 5.02 mm (180 days) and 4.89 to 6.45 mm (365 days), respectively.

References

 1. D.J. Barker, S.A. Turner, P.A. Napier-Moore, M. Clark and J.E. Davison, "CO_2 Capture in the Cement Industry", Proceeding of the 9th International Conference on Greenhouse Gas Control Technologies, GHGT-9, Washington DC, United State, 2009, Vol.1, Issue 1, pp. 87–94
 2. Y. Wang, Q. Zhu and Y. Geng, "Trajectory and Driving Factors for GHG emissions in the Chinese Cement Industry", Journal of Cleaner Production, 2013, Vol. 53, pp. 252–260
 3. W.I. Wan Zulasmin, "Towards a sustainable quarry in Malaysia, Jurutera (Bulletin)", The Institution of Engineers, Malaysia, 2007, pp. 22–25 http://dspace.unimap.edu.my/dspace/bitstream/123456789/14622/1/feature%20sustain%20quarry%203p.pdf (Date of Retrieved: 8 April 2014).
 4. B.P. Hudson, "Manufactured Sand for Concrete", The Indian Concrete Journal, 1997, pp. 237–240
 5. M. Nisnevich, G. Sirotin and Y. Eshel, "Lightweight Concrete Containing Thermal Power Station and Stone Quarry Dust", Magazine of Concrete Research, 2003, pp. 313–320
 6. A.R. Norhana and K. Kartini, "Quarry Dust Fine Powder as Sustainable Material for Cement", Malaysia Science Technology Congress 'Scaling New Height in S&T for Sustainable Development' (MSTC). Crystal Crown Hotel Petaling Jaya, Malaysia. 7–11 November 2010, pp. 104–105
 7. R. Ilangovan and K. Nagamanib, "Application of Quarry Rock Dust as Fine Aggregate in Concrete Construction", National Journal on Construction Management: NICMR. Pune, 2005, pp. 5–13.
 8. M. David, "Exploitation and Use of Quarry Fines", MIRO-FINAL REPORT, Report No.087/MIST2/DACM/01. MIST Project Reference: MA/2/4/003, 2004, p.10.
 9. B. Felekoglu, "Utilization of High Volumes of Limestone Quarry Waste in Concrete Industry (Self-Compacting Concrete Case)", Department of Civil Engineering, Dokuz Eylul University, Izmir, Turkey, 2007, pp. 770–791
10. M. Shahul Hameed and A.S.S. Sekar, "Properties of Green Concrete Containing Quarry Dust and Marble Sludge Powder as Fine Aggregate", ARPN Journal of Engineering and Applied Science, Vol. 4, No. 4, pp. 83-89
11. ASTM C 618:2003. Specification for Coal Fly Ash and Raw of Calcined Natural Pozzolan for Use in Concrete
12. Boonleangubpathum and Ch. Choopanich, Standard Methods For Testing Aggregate and Concrete, 2000, p.101
13. BS EN 206-1:2013. Concrete. Specification, performance, production and conformity
14. BS EN 12350-2:2009. Testing fresh concrete. Slump-test
15. B. Mezghiche, "Laboratory Testing of Construction Materials", Algerie: Publication Universitaire Biskra; 2005, p. 120
16. BS EN 12390-3:2009. Testing hardened concrete. Compressive strength of test specimens
17. BS 1881-122:2011. Testing concrete. Method for determination of water absorption
18. BS EN 14630:2006. Products and systems for the protection and repair of concrete structures. Test methods. Determination of carbonation depth in hardened concrete by the phenolphthalein method
19. G. Shimizu and P. Jr. Jorillo, "Study on the Use of Rough and Underground Ash from an Open Heaped-Up Burned Rice Husk as a Partial Cement Substitute", Proceedings of the 2nd RILEM Symposium on Vegetable Plants and their Fiber as Buildings Materials. Brazil. Editor: Sobral, H.S. Chapman and Hall, London, 1990, pp. 321–333.

20. BS EN 196-6: 2010. Method of Testing Cement. Determination of Fineness.
21. BS 1377-2:1990. Method of Test for Soil for Civil Engineering Purposed. Classification Test
22. N. Mahendrana, R. Ilangovana and K. Nagamarib, "Strength and Durability Properties of Concrete Containing Quarry Dust as Fine Aggregate", Department of Civil Engineering, PSNA College of Engineering, 2008, vol.3(5)
23. B. Felekoglu, "Utilization of High Volumes of Limestone Quarry Waste in Concrete Industry (Self-Compacting Concrete Case)", *Department of Civil Engineering, Dokuz Eylul University*, Izmir, Turkey, 2007, pp.770–791
24. BS EN 196-3:2005+A1:2008. Methods of testing cement. Determination of setting times and soundness
25. BS 6610:1996. Specification for Pozzolanic pulverized-fuel ash cement
26. A.M. Neville, "Properties of Concrete*", 4$^{\text{th}}$ Edition. ISBN 0-582-23070-5. Longman. England, 2002, pp. 1-632
27. ASTM C 150-2007. Specification for Portland cement
28. BS 12:1991. Specification for Portland cement
29. S.N. Raman, M.F.M. Zain, H.B. Mahmud and K.S. Tan, "Influences of Quarry Dust and Fly Ash on the Concrete Compressive Strength Development", 2005, Department of Civil Engineering. http://eprints.um.edu.my/524/1/PTS3-3-8.pdf. (Date of Retrieved: 28 March 2011).
30. M. Rabehi, B. Mezghiche and S. Guettala, "Correlation Between Initial Absorption of The Cover Concrete, The Compressive Strength and Carbonation Depth", Construction and Building Materials 45, 2013, pp. 123–129
31. A.A. Ramezanianpour, "Effect of curing on the compressive strength, resistance to chloride-ion penetration and porosity of concrete incorporating slag, fly ash or silica fume Cement & Concrete Composites", 1995, 80 (1), pp. 125–133
32. M. Mamlouk and J. Zaniewski, "Materials for Civil and Construction Engineers", Addison Wesley Longman, Inc, 1999
33. J. Pamnani Nanak, A.K. Verma and R. Bhatt Darshana, "Comparison Between Mechanical Properties of M3O Grade Self Compacting Concrete For Conventional Water Immersion and Few Non-Waterbased Curing Techniques", International Journal of Engineering and Advanced Technology (IJEAT) ISSN:2249-8958, 2013, Volume 3, Issue 2, pp. 265–272.
34. BS 1881-122:2011. Testing concrete. Method for determination of water absorption
35. M.M. Sutan, S. Hamdan and E.C.C Jin, "The Influence of Porosity to the Accuracy of Ultrasonic Pulse velocity Method", Faculty of Engineering, Universiti Malaya Sarawak, 2002, 7(11), p. 1
36. K. Sisomphon and L. Franke, "Carbonation rates of concretes containing high volume of pozzolanic materials", Cement and Concrete Research, Volume 37, Issue 12, December 2007, pp. 1647–1653
37. I. Soroka, "Corrosion of Reinforcement", Concrete in Hot Weather, 1993, p.207
38. P.C. Hewlett, "Lea's Chemistry of Cement and Concrete", (4th Edition.) St. Edmundsbury Press Ltd., UK, 1998
39. M.D.A. Thomas, J.D. Matthews, "Carbonation of fly ash concrete", Magazine of Concrete Research, 44 (160) (1992), pp. 217–228
40. G.K. Park, "Durability and carbonation of concrete" Magazine of the Korean Concrete Institute, 1995;7: pp. 74–81
41. W. Xiao-Yong and L. Han-Seung, " A Model for Prediciton The Carbonation Depth of Concrete Containing Low-Clcium Fly-Ash", Construction and Building Materials 23, 2009, pp. 725–733
42. H. Al-Khaiat and N. Fattuhi, "Carbonation of Concrete Exposed to Hot and Arid Climate", Journal of Materials in Civil Engineering, 2002, 14 (2), pp. 97–107
43. H.W. Song, "Predicting carbonation in early-aged cracked concrete", Cement and Concrete Research, 2006, 36 (5), pp. 979–989
44. P. Sulapha, "Carbonation of Concrete Containing Mineral admixtures", Journal of Materials in Civil Engineering, 2003, 15 (2), pp. 134–143

Effect of Heat Treatment on Mechanical Properties of Ternary Blended Eco-friendly UHPFRCC

A.Q. Sobia, M.S. Hamidah, I. Azmi and S.F.A. Rafeeqi

Abstract The rapid expansions in economic development, urbanisation and above all population have been accompanied by an upsurge in the accidental fire hazard. The fire redundancy of buildings can decrease the risk of damage and injury by improving the safety of residents and also by enhancing the reusability of buildings. In the recent decades, investigations on elevated temperature resistant passive fire protection layers have been progressing with the use of several environmental friendly materials. However, there is an inadequate information on the effect of heat treatment on the ultra-high performance fibre-reinforced cementitious composites (UHPFRCC) containing high-alumina cement (HAC), ground granulated blast furnace slag (GGBS) and fly ash (FA) in conjunction with hybrid fibres (basalt and polypropylene fibres), which could be a potential fire resisting UHPFRCC for the structural members. The effect of heat treatment on the compressive strength and flexural strength of UHPFRCC, made of ternary blend and hybrid fibres, was investigated in this study. Besides control sample, five other UHPFRCC samples were prepared. After 28 and 56 days of normal curing, each of the samples was held at room temperature as well as exposed to 400, 700 and 1000 °C, then tested. Examination of results disclosed that the UHPFRCC with the replacement of 25 %

A.Q. Sobia (✉) · M.S. Hamidah · I. Azmi
Faculty of Civil Engineering, Universiti Teknologi MARA (UiTM),
Shah Alam, Malaysia
e-mail: sobiaqazi@ymail.com

M.S. Hamidah
e-mail: hamid929@salam.uitm.edu.my

I. Azmi
e-mail: azmii716@salam.uitm.edu.my

S.F.A. Rafeeqi
Department of Civil Engineering, NED University of Engineering & Technology,
Karachi, Pakistan
e-mail: srafeeqi@yahoo.com

of fly ash with GGBS, in conjunction with hybrid fibres, possessed highest residual compressive strength in the temperature range of 28–900 °C with 48 % of RCS value at 900 °C after 56 days of curing. However, in the range of 28–1000 °C, UHPFRCC with PP fibre and hybrid fibre performed almost equally well with the residual flexural strength value of 36 % at 1000 °C after 28 days of curing.

Keywords Eco-friendly/green material · Ground granulated blast furnace slag (GGBS) · Heat treatment · High-alumina cement · Ternary blend · UHPFRCC

1 Introduction

The rapid expansions in economic development, urbanisation and above all population have been accompanied by an upsurge in the accidental fire hazard. The fire redundancy of buildings can decrease the risk of damage and injury by improving the safety of residents and also by enhancing the reusability of buildings. A high-rise building, as compared to the low-rise building, is a massive enclosed space, making the extinguishing of fire and evacuation of people even more challenging. Besides the loss of life, possible long-term disruption of the building operation is another concern. In order to fireproof a building, generally, passive fire protection layer (PFP) is applied. Normally, PFP comprises of cement as its main component, which is believed to be a vital source of carbon dioxide emission. Carbon dioxide is the main cause of global warming. The annual global cement production of 1.6 billion tonnes corroborates for about 7 % of the emission of carbon dioxide into the atmosphere and approximately 1 tonne of carbon dioxide is emitted from the manufacture of 1 tonne of cement [1]. Consequently, there is a huge concern towards the reduction of the cement content of fireproof coatings. In the recent decades, investigations on elevated temperature resistant construction materials have been progressing with the use of several environmental friendly materials [2–13]. In this study, the formulation of an eco-friendly fireproof ultra-high performance fibre-reinforced cementitious composite (UHPFRCC) is devised, suitable for various concrete structures. Also the behaviour of UHPFRCC under elevated temperature is studied.

In this study, instead of normal Portland cement, high-alumina cement was selected due to its refractoriness and resistance to aggressive medium. Nevertheless, ground granulated blast furnace slag (GGBS) and fly ash (FA) were incorporated due to its complimentary effects on residual mechanical properties of composites at high temperature [14, 15]. GGBS and fly ash are industrial by-products that are abundantly produced almost all over the world and are considered as environmental pollutants. In conjunction with HAC, GGBS and FA, different dosages (0.5, 1, 1.5 % of total weight of mix) of basalt fibres (BF) and fixed amount (1 kg/m^3) of polypropylene (PP) fibres were also used. Basalt fibres possess high operating

temperature resistance in the range of −269 to 700 °C [16] whereas PP fibres curb the phenomenon of explosive spalling in high performance cementitious composites [12, 17–20].

2 Test Program

2.1 Test Materials

High-alumina cement (HAC), utilised in this study, is also recognised as calcium aluminate cement, which was acquired from CALUCEM branded as 'ISTRA 40'. The oxide content of HAC is shown in Table 1. HAC meets the requirements of EN 14647 and its oxide content is shown in Table 1. Very fine silica sand containing 99 % SiO_2 was used and graded according to ASTM C136-06. Aggregate and cement paste act like a thermal shield within UHPFRCC therefore very fine aggregates were used in order to prevent weak interface [21].

YTL cement Sdn. Bhd. provided ground granulated blast furnace slag (GGBS) and fly ash (FA) complying with BS EN 450-1995 and MS EN 15167-1:2010, respectively. Chemical composition is shown in Table 1. Basalt fibres and polypropylene (PP) fibres were complimentarily provided by Kamenney Vek and Maccaferri, respectively. Physical properties of fibres are given in Table 2. Tap water was used in all the mix conforming to ASTM C1602/C1602 M−12, without any types of silt, chloride, oils, harmful chemicals, etc.

Table 1 Oxide content and physical properties of HAC, FA and GGBS used in present study

Oxides	HAC (%)	FA (%)	GGBS (%)
SiO_2	<6	56.39	32.9
Al_2O_3	38–42	17.57	14.1
Fe_2O_3	13–17	9.07	–
CaO	37–40	11.47	43.1
MgO	<1.5	0.98	4.8
SO_3	<0.4	0.55	0.3
TiO_2	–	–	0.48
Mn_2O_3	–	–	0.3
Na_2O	–	1.91	0.16
K_2O	–	1.98	0.27
LOI	–	–	1.8
Specific gravity	3.2–3.3	2.3–2.8	2.9
Fineness (m^2/kg)	320–370	243	–
Bulk density (kg/m^3)	–	–	–

Table 2 Physical properties of basalt and polypropylene fibres

Fibre type	Diameter (μm)	Length (mm)	Specific weight (g/cm³)	Melting point (°C)	Ignition point (°C)	Elastic modulus (GPa)	Tensile strength (MPa)	Break elongation (%)	Thermal conductivity (W/m°K)
Polypropylene fibres	18	6	0.91	160	360	38	400	>20	0.15
Basalt fibres	13	12.7	2.67	1450	–	100–110	4000–4300	3.15	0.031–0.038

2.2 Mix Proportion

Mix proportion was designed by keeping in view the previous research study by [22, 23]. Detailed mix proportion is given in Table 3. Sand-binder ratio is same for all mixes i.e. 0.8. In the mix proportion, effect of replacement of GGBS with FA was studied. Control mix (C) was prepared using 50 % HAC and 50 % GGBS. However, in the subsequent two mixes, i.e. CP and CB1, in addition to the former materials, PP fibres (1 kg/m^3) and PP plus basalt fibres were respectively added to the mix. In the following mixes (F1B1, F2B1, F3B1), GGBS was replaced by fly ash in three different dosages (10, 15, 25 % of GGBS). In all of the mixes, amount of HAC, sand-to-cement ratio, water-to-binder ratio, PP fibres and basalt fibres were set to the constant value.

2.3 Mixing

Mixing of UHPFRCC was done using SPAR high-speed mixer. Firstly, all dry materials were put in the mixer and mixed for about two and a half minute at slow speed (99 rotation per minute (rpm) of planetary shaft) after that water was added to the mixture and then further mixed for 1 min at the same speed, followed by hand mix. Afterwards, PP fibres were added and mixed for one minute with the mixture and mixed for 1 minute followed by the addition of basalt fibres and mixed for one more minute at intermediate speed (176 rpm of planetary shaft). Finally, the speed was set to the highest level (320 rpm of planetary shaft) and the mixture was mixed for one and a half minute.

2.4 Casting of UHPFRCC Specimen

After mixing, the casting of the specimens was done for each mix. For residual compressive strength and residual flexural strength testing, prism shape specimens of

Table 3 UHPFRCC mixture proportions

Mix	Total binder			PP fibre (kg/m^3)	Basalt fibre (%)	W/B	S/C
	HAC (%)	GGBS (%)	FA (%)				
C	50	50	0	0	0	0.38	0.8
CP	50	50	0	1	0		
CB1	50	50	0	1	0.5		
F1B1	50	40	10	1	0.5		
F2B1	50	35	15	1	0.5		
F3B1	50	25	25	1	0.5		

dimensions 40 mm × 40 mm × 160 mm were cast according to ASTM C348-08 as also used in past research studies [10, 12, 24]. All together, specimens were cast for 28 and 56 days of testing at room and elevated temperatures for each mix. Right after casting, specimens were kept into the conditioning room (details are reported in Sect. 2.5).

2.5 Method of Curing

After casting, for 24 h, all specimens were kept in the conditioning room (60 % relative humidity at 20 ± 2 °C) followed by de-moulding and curing in the usual water tank for 28 and 56 days. Specimens were kept in the conditioning room in order to keep the hydration temperature low, which could give rise to the formation of C_3AH_6 (responsible for conversion) [25]. In addition to that, HAC emits 2.5 times more heat of curing as compared to ordinary Portland cement (OPC), which may cause cracking and strength reductions [26]. After de-moulding, standard curing was carried out for all specimens in the water basin at an average temperature of 28 °C. Curing was done for 28 and 56 days.

2.6 Exposure to High Temperature

UHPFRCC specimen was heated to the temperature of 400, 700 and 1000 °C. Heating was done at the average rate of 5 °C/min till it reached the required temperature and after that the achieved temperature was sustained for 1 h in order to achieve the steady state. At each curing age (28 and 56 days), set of three prisms of specimen was placed, at elevated temperature, in a gas furnace, available at Ceramic Workshop, Faculty of Art and Design, Universiti Teknologi MARA (UiTM).

2.7 Testing Methods

Prior to the mechanical testing, three identical specimens from each mix were weighed before and after exposure to elevated temperatures in order to measure the average mass loss at each temperature point (400, 700 and 1000 °C) with respect to their mass at room temperature. Subsequently, compressive and flexural strength testing was performed for each mix (three identical specimens each) after 28 and 56 days of curing according to ASTM C349-08 and ASTM C348-08, respectively. Universal testing machine was used for testing. After each curing age, three identical specimens of each mix were exposed to the elevated temperatures of 400, 700 and 1000 °C and afterwards used to calculate residual compressive strength (RCS) and residual flexural strength (RFS), using Eqs. 1 and 2, respectively. Before being exposed to elevated temperatures, all specimens were kept in the open

atmosphere for almost 24 h in order to release excessive water. Specimens were allowed to cool down before residual strength is determined. Following are the equations used to calculate residual compressive strength (RCS) and residual flexural strength (RFS):

$$\text{RCS } (\%) = 100 - [(C_i - C_f)/C_i] * 100 \qquad (1)$$

whereas,

C_i = Compressive strength at room temperature at the specific curing age
C_f = Compressive strength at respective elevated temperature at the specific age

$$\text{RFS}(\%) = 100 - [(F_i - F_f)/F_i] * 100 \qquad (2)$$

whereas,

F_i = Flexural strength at room temperature at the specific age
F_f = Flexural strength at respective elevated temperature at the specific age

3 Results and Discussions

3.1 Mass Loss in UHPFRCC Specimens Due to Heating

Due to the moisture loss from matrix, cementitious composites tend to lose their weight as the temperature elevates [27]. This phenomenon was also obvious in the UHPFRCC specimens. When the 28 days cured specimens were exposed to 400 °C, specimen F1B1 experienced the highest mass loss (10.9 %) whereas control sample showed the lowest mass loss value of 7.2 %, due to the release of capillary and gel water. As compared to the control specimen, the specimen containing PP fibres showed a slight more loss in mass as compared to the control specimen same as also experienced by [28]. Alternatively at the exposure temperature of 700 °C, the highest mass loss was indicated again by F1B1 i.e. 21.1 % and the lowest value was shown equally by CP and F3B1 with 19.7 % owing to the loss of chemically bound water from the matrix. Among all exposure temperatures, the highest mass loss (24.1 %) was depicted by the control specimen after being exposed to 1000 °C. The best performance was shown by CB1 with the lowest mass loss value of 22.4 % after exposure to 1000 °C, which was almost the same after 56 days of curing.

3.2 Compressive Strength of UHPFRCC Specimens

Room temperature compressive strength of specimens is tabulated in Table 4. The addition of polypropylene (PP) fibres to the control mixture caused the

Table 4 Room temperature compressive strength of specimens

Mix code	Compressive strength (MPa)	
	28 days	56 days
C	60.00	80.41
CP	50.60	54.91
CB1	57.97	71.59
F1B1	73.31	74.65
F2B1	72.32	70.85
F3B1	42.67	42.67

significant drop in the compressive strength due to the lower elastic modulus of PP fibres.

However, with the addition of basalt fibre in conjunction with PP fibre (specimen CB1) the compressive strength was increased because of their high elastic modulus value of 89 GPa [29] and the good bonding of fibres with the cementitious matrix and also due to the good dispersion of fibres among the matrix [30]. Results of the investigation implied that the highest room temperature compressive strength was marked by F1B1 after 28 days of curing i.e. 73.31 MPa, and after 56 days of curing, control sample marked the highest value i.e. 80.41 MPa.

Except specimen F2B1 and F3B1, the entire specimens sustained the escalation in compressive strength between 28 and 56 days of curing but control specimen portrayed the highest increase in compressive strength. The increase in compressive strength after longer curing age is corroborated with the slow reactivity of GGBS as reported elsewhere [25]. Specimen F2B1 showed a slight decrease of strength, i.e. around 2 %, after 56 days of curing that is almost negligible, however, specimen F3B1 marked the strength equal to that was achieved after 28 days of curing. The latter is the indication of the fact that 25 % of GGBS was consumed after 28 days of curing along with 25 % of FA and therefore there was no further increment in the strength beyond 28 days of curing.

Compressive strength of all the specimens relative to the control specimen at each temperature point is graphically compared with the compressive strength of control sample shown in Fig. 2. For instance, compressive strength of UHPFRCC–CP (with PP fibres only) was exposed to 400 °C. It was found that after 28 days of curing (Fig. 2a), at the exposure temperature of up to 400 °C, F1B1 bore the highest relative compressive strength i.e. 179.84 %.

However at 700 and 1000 °C, F1B1 and CB1 (equal) and CP attained the higher relative compressive strength value, i.e. 108 % and 119 %, respectively. It is interesting to note that F1B1 also showed the highest moisture loss (Fig. 1a) up to 700 °C in conjunction with highest relative strength which complies with the phenomenon that if more water is evaporated from the composites during the heating process, more heat is consumed, hence the matrix and the fibres are less deteriorated resulting in the better performance at elevated temperature [31]. This also interprets the over all positive effect of replacement of GGBS with fly ash as compared to the specimen with GGBS only at elevated temperature. On the
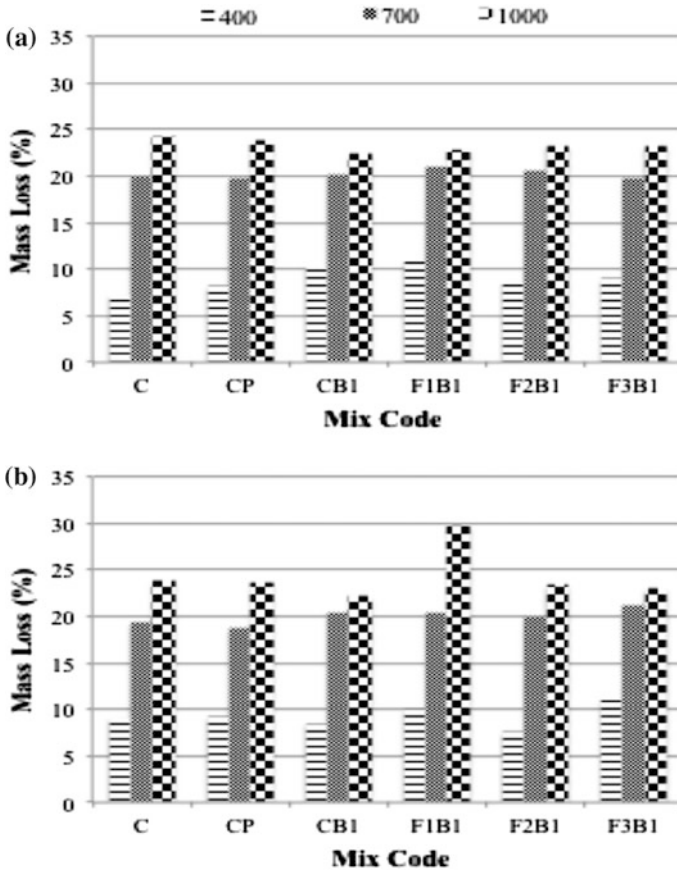
Fig. 1 Graphical comparison of mass loss of UHPFRCC specimen after heat treatment. **a** 28 days of curing. **b** 56 days of curing

contrary, after 56 days of curing (Fig. 2b), relative compressive strength of F3B1 was reported the best among all specimens with the value of 90 % at the exposure of 400 °C. At the exposure of 700 °C, F2B1 stood out with approximately 104 % of relative compressive strength whereas at 1000 °C, only CB1 maintained the highest relative compressive strength value of 109 %.

3.3 Flexural Strength of UHPFRCC Specimens

In Table 5, room temperature flexural strength of specimens is listed. After 28 and 56 days of curing, CB1 (with PP fibres + 0.5 % basalt fibres) and CP (with PP fibres only) manifested highest flexural strength, which is substantiated with the zero
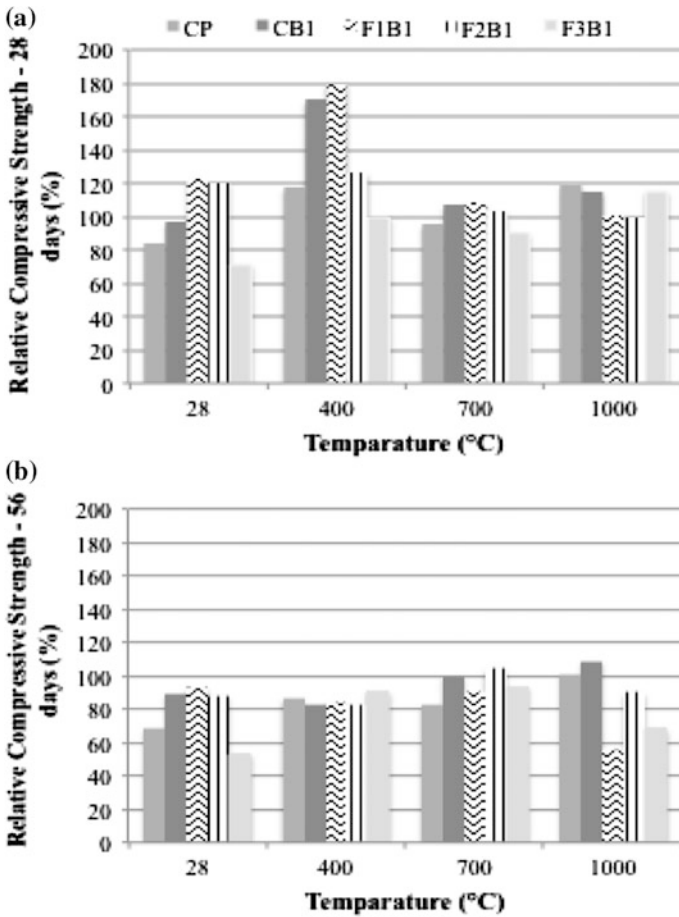
Fig. 2 Graphical comparison of relative compressive strength of UHPFRCC specimen before and after heat treatment

Table 5 Room temperature flexural strength of specimens

Mix code	Flexural strength (MPa)	
	28 days	56 days
C	8.33	7.14
CP	9.31	15.96
CB1	14.27	14.09
F1B1	11.94	9.80
F2B1	9.16	10.36
F3B1	8.83	9.52

effect of FA on the room temperature flexural strength of PP fibre-based UHPFRCC. Alternatively, control specimen indicated the lowest flexural strength that was also obvious in former research study [32].

In order to compare all the specimens with the control sample at each temperature point, relative flexural strength has been computed as graphically shown in Fig. 3. Figure 3a clearly shows that, CB1 (with PP fibres + 0.5 % basalt fibres) signifies the best relative flexural strength of 177 % and 124 % at 400 °C and 700 °C, respectively after 28 days of curing.

Moreover, CP bore the significant relative flexural strength value of 163 % when exposed to 1000 °C. Furthermore, after 56 days of curing, F2B1 showed the highest relative flexural strength value of 123 and 111 % at 400 and 700 °C. Although at 1000 °C, CB1 and F2B1 equally marked the highest relative flexural strength of 118 %. Therefore, overall F2B1 performed the best during heat treatment after 56 days of curing owing to the effectiveness of 15 % replacement of GGBS with FA.
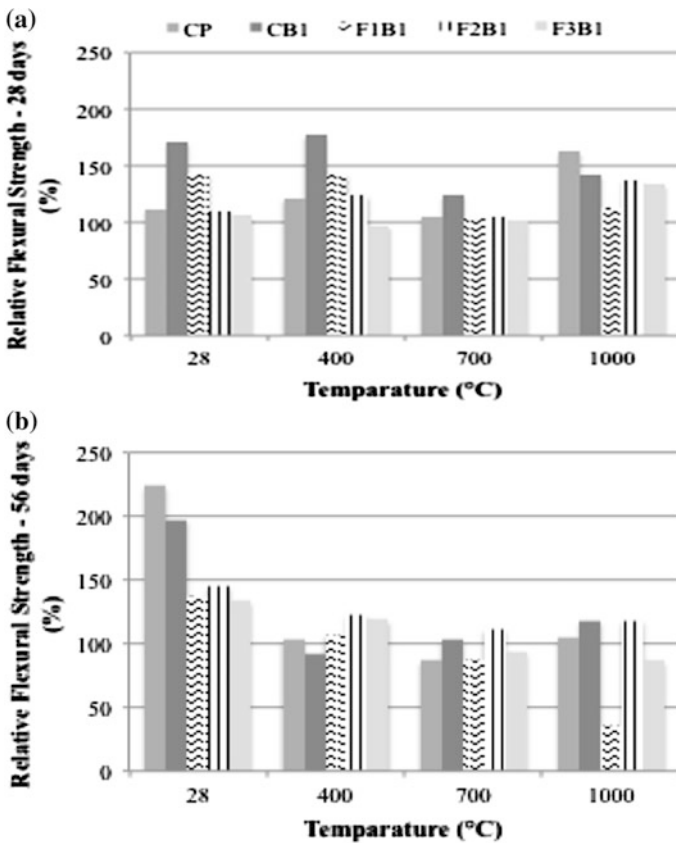
Fig. 3 Graphical comparison of relative flexural strength of UHPFRCC specimens before and after heat treatment. **a** 28 days of curing. **b** 56 days of curing

3.4 Residual Compressive Strength

Compressive strength test was performed for both room temperature specimens (C_i) and heated specimens (C_f). Formula for calculating residual compressive strength (RCS) for each mix at specific age is given in Eq. 1. Experimental results of residual compressive strength are graphically represented in Fig. 4. Results show that after 28 days of curing, CB1 (with PP fibres + 0.5 % basalt fibres) performed the best in the range of 28–700 °C and marked the highest RCS value of 93.34 % when exposed to 400 °C and 52.96 % at 700 °C (almost equal to UHPFRCC with PP fibre only (CP)). However, afterwards there was a significant drop in RCS value of CB1 (with PP fibres + 0.5 % basalt fibres) in comparison with CP (with PP fibre only) specimen. Finally, CP depicted the lowest strength drop in the range of 700–1000 °C with the
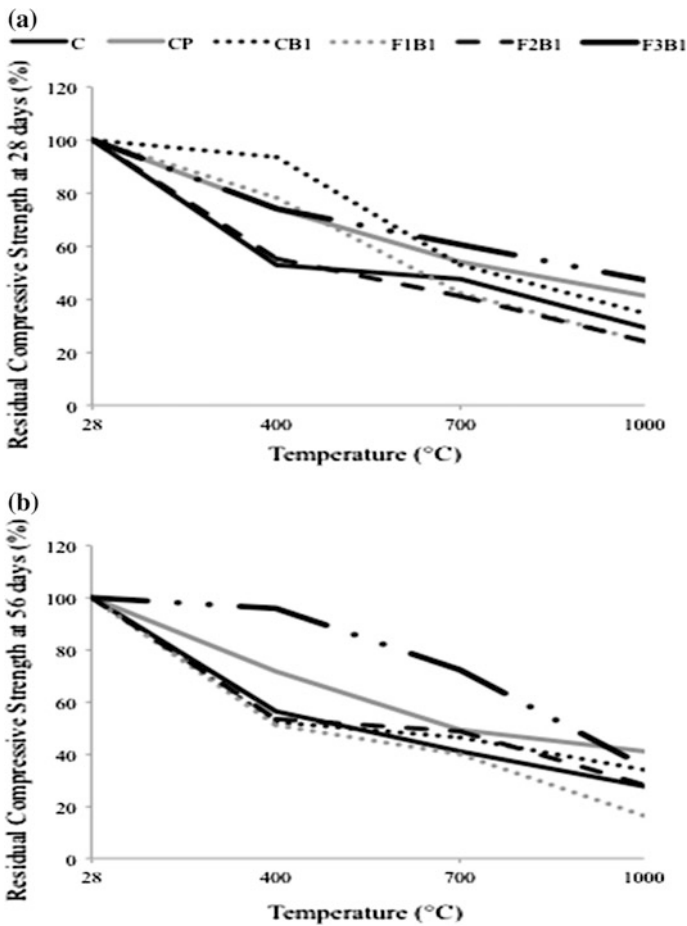
Fig. 4 Graphical comparison of residual compressive strength of UHPFRCC specimens before and after heat treatment. **a** 28 days of curing. **b** 56 days of curing

highest RCS value of 41.31 % at 1000 °C. This may be due to the melting of PP fibres in the UHPFRCC, which leaves behind the micro-channels to mitigate the vapour tension in the capillaries resulting in the improved residual compressive strength [33]. The quasi-linear decrease in the residual compressive strength, at temperatures higher than 400 °C, might be translated due to the removal of bound water from the specimen.

After 56 days of curing, F3B1 possessed highest RCS value in the temperature range of 28–900 °C as compared to other mixes. Only beyond 900 °C, CP performed around 14 % better than F3B1 which is not much significant. Therefore, the replacement of 25 % of GGBS with FA resulted in the improved residual compressive strength, even better than that of concrete [34, 35].
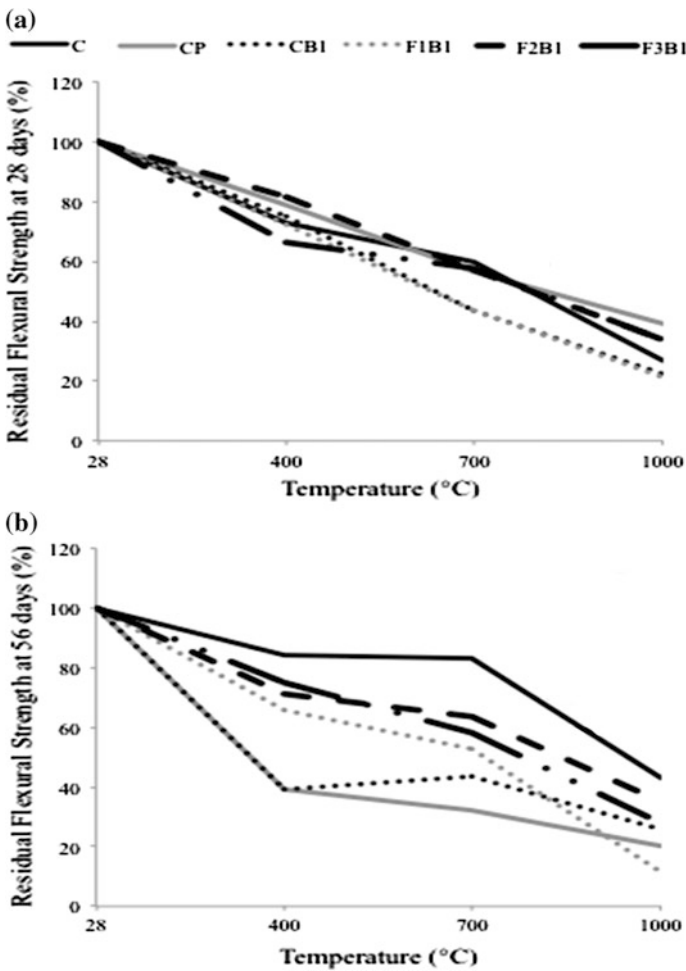
Fig. 5 Graphical comparison of residual flexural strength of UHPFRCC specimens before and after heat treatment. **a** 28 days of curing. **b** 56 days of curing

3.5 Residual Flexural Strength

Residual flexural strength was computed using the flexural strength of unheated (F_i) and heated specimens (F_f). Residual flexural strength (RFS) of specimens was calculated using the Eq. 2.

Laboratory results show that after 28 days of curing (Fig. 5a), in the range of 28–700 °C of exposure temperature, CP and F2B1 performed equally well and residual strength dropped from 100 % to about 56.5 %. However, after heating at 700 °C, CP was insignificantly better than F2B1 with the average residual value of 36 %. Therefore, the replacement of 15 % of GGBS with FA showed improved results as compared to the specimens containing only GGBS in conjunction with HAC [36].

Figure 5b illustrates the RFS value of specimens after exposed to elevated temperature after 56 days of curing. Results depict that the control specimen performed the best throughout the course of heat treatment after 56 days of curing. The reason could be that after 56 days of curing, most of the GGBS was consumed resulting in the increase of flexural strength as also described elsewhere [37]. Nevertheless, it is very unusual for a non-fibre cementitious composite to reach 1000 °C without any sign of spalling. Among hybrid fibre specimen, F2B1 showed the best performance. Specimen F1B1 performed the least after 56 days of curing like those after 28 days of curing.

4 Conclusions

Following conclusions could be derived based on the experimental results:

- Highest room temperature compressive strength (73 MPa) was marked by the UHPFRCC (F1B1) enclosing hybrid fibres (1 kg/m^3 of PP fibres + 1.5 % of basalt fibres) after 28 days of curing. Nevertheless, beyond 56 days of curing, control specimen illustrated the highest compressive strength i.e. 80 MPa.
- Optimum room temperature flexural strength (14.27 MPa) was marked by UHPFRCC—CB1 with hybrid fibres (1 kg/m^3 of PP fibres + 1.5 % of basalt fibres) and UHPFRCC—CP (15.96 MPa) containing polypropylene fibres only after 28 and 56 days of curing, respectively.
- GGBS replacement with fly ash in UHPFRCC resulted in the effective performance at elevated temperature after 56 days of curing. Specifically specimen F3B1 (25 % GGBS replacement with FA) possessed highest residual compressive strength in the temperature range of 28–900 °C with 48 % of RCS value at 900 °C.
- In the range of 28–1000 °C, CP and F2B1 performed almost equally well with the residual flexural strength value of 36 % when heated at 1000 °C after 28 days of curing. However, control sample possessed highest RFS value (i.e. 43 % at 1000 °C) in the range of 28–1000 °C after 56 days of curing without undergoing any spalling.

In conclusion, inclusion of ternary blend (HAC, GGBS and FA) and hybrid fibres (polypropylene + basalt fibres) can yield a UHPFRCC, which bears good mechanical properties as well as improved resistance against thermal load up to 1000 °C. Such UHPFRCC is a promising eco-friendly fire protection material for RC structures.

References

1. P. K. Mehta, "Reducing the environmental impact of concrete," *Concrete International*, pp. 61–66, 2001.
2. L. Sarvaranta and E. Mikkola, "Fibre mortar composites under fire conditions: effects of ageing and moisture content of specimens," *Mater. Struct.*, vol. 27, no. 9, pp. 532–538, 1994.
3. M. M. Shoaib, S. a. Ahmed, and M. M. Balaha, "Effect of fire and cooling mode on the properties of slag mortars," *Cem. Concr. Res.*, vol. 31, no. 11, pp. 1533–1538, 2001.
4. M. S. Cülfik and T. Özturan, "Effect of elevated temperatures on the residual mechanical properties of high-performance mortar," *Cem. Concr. Res.*, vol. 32, no. 5, pp. 809–816, 2002.
5. C. Leiva, L. Vilches, J. Vale, and C. Fernandezpereira, "Influence of the type of ash on the fire resistance characteristics of ash-enriched mortars," *Fuel*, vol. 84, no. 11, pp. 1433–1439, 2005.
6. S. Aydin and B. Baradan, "Effect of pumice and fly ash incorporation on high temperature resistance of cement based mortars," *Cem. Concr. Res.*, vol. 37, no. 6, pp. 988–995, 2007.
7. S. Aydin, "Development of a high-temperature-resistant mortar by using slag and pumice," *Fire Saf. J.*, vol. 43, no. 8, pp. 610–617, 2008.
8. H. Wang, "The effects of elevated temperature on cement paste containing GGBFS," *Cem. Concr. Compos.*, vol. 30, no. 10, pp. 992–999, 2008.
9. D. Bentz, M. Peltz, A. Duran-Herrera, P. Valdez, and C. Juarez, "Thermal properties of high-volume fly ash mortars and concretes," *J. Build. Phys.*, vol. 34, no. 3, pp. 263–275, 2010.
10. J. Formosa, J. M. Chimenos, A. M. Lacasta, L. Haurie, and J. R. Rosell, "Novel fire-protecting mortars formulated with magnesium by-products," *Cem. Concr. Res.*, vol. 41, no. 2, pp. 191–196, 2011.
11. S. Djaknoun, E. Ouedraogo, and A. Ahmed Benyahia, "Characterisation of the behaviour of high performance mortar subjected to high temperatures," *Constr. Build. Mater.*, vol. 28, no. 1, pp. 176–186, 2012.
12. R. K. Ibrahim, R. Hamid, and M. R. Taha, "Fire resistance of high-volume fly ash mortars with nanosilica addition," *Constr. Build. Mater.*, vol. 36, pp. 779–786, Nov. 2012.
13. J.-P. Won, H.-B. Kang, S.-J. Lee, and J.-W. Kang, "Eco-friendly fireproof high-strength polymer cementitious composites," *Constr. Build. Mater.*, vol. 30, no. 2012, pp. 406–412, May 2012.
14. J. Xiao and H. Falkner, "On residual strength of high-performance concrete with and without polypropylene fibres at elevated temperatures," *Fire Saf. J.*, vol. 41, no. 2, pp. 115–121, Mar. 2006.

15. S. Donatello, C. Kuenzel, A. Palomo, and A. Fernández-Jiménez, "High temperature resistance of a very high volume fly ash cement paste," *Cem. Concr. Compos.*, vol. 45, pp. 234–242, Jan. 2014.

16. H. L. Wang, X. L. Yang, Q. C. Ren, and P. Dong, "Research Progress Basalt Fiber in Civil Engineering," *Appl. Mech. Mater.*, vol. 71–78, pp. 1484–1487, Jul. 2011.

17. P. Raivio and L. Sarvaranta, "Microstructure of fibre mortar composites under fire impact-effect of polypropylene and polyacrylonitrile fibres," *Cem. Concr. Res.*, vol. 24, no. 5, pp. 896–906, 1994.

18. I. Hager and P. Pimienta, "The Impact Of The Addition Of Polypropylene Fibres On The Mechanical Properties Of High Performance Concretes Exposed To High Temperatures," in *6th RILEM Symposium on Fibre-Reinforced Concretes (FRC)*, 2004, pp. 575–582.

19. J. Komonen, V. Penttala, and B. M. Technology, "Effects of High Temperature on the Pore Structure and Strength of Plain and Polypropylene Fiber Reinforced Cement Pastes," *Fire Technol.*, vol. 39, pp. 23–34, 2003.

20. W. Khaliq and V. Kodur, "High Temperature Mechanical Properties of High-Strength Fly Ash Concrete with and without Fibers," *ACI Mater. J.*, vol. 109, no. 6, pp. 665–674, 2013.

21. S. Qazi, M. S. Hamidah, A. Ibrahim, S. F. A. Rafeeqi, and S. Ahmad, "State-of-the-art review-Behaviour of thin high performance cementitious composites (THPCC) at elevated temperatures," in *11th International Conference on Concrete Engineering and Technology 2012 (CONCET2012)*, 2012, vol. 2012, no. June, pp. 83–89.

22. A. Q. Sobia, A. Shyzleen, M. S. Hamidah, I. Azmi, S. F. A. Rafeeqi, and S. Ahmad, "Post Elevated Temperature Effect on the Strength and Microstructure of Thin High Performance Cementitious Composites (THPCC)," *World Acad. Sci. Eng. Technol.*, no. 74, pp. 1–6, 2013.

23. A. Q. Sobia, A. Shyzleen, M. S. Hamidah, I. Azmi, S. F. A. Rafeeqi, and S. Ahmad, "The Effect of Elevated Temperature on HAC-based THPCC with GGBS Addition," in *Concrete Institute of Australia's Biennial National Conference*, 2013.

24. L. Tanaçan, H. Y. Ersoy, and Ü. Arpacıoğlu, "Effect of high temperature and cooling conditions on aerated concrete properties," *Constr. Build. Mater.*, vol. 23, no. 3, pp. 1240–1248, Mar. 2009.

25. Y. Fu, F. Ding, and J. Beaudoin, "Temperature dependence of compressive strength of conversion-inhibited high alumina cement concrete," *ACI Mater. J.*, vol. 94, no. 6, pp. 540–544, 1997.

26. D. J. D. Naus, "The Effect of Elevated Temperature on Concrete Materials and Structures-a Literature Review.," Washington, DC, 2006.

27. W. Zheng, H. Li, and Y. Wang, "Compressive behaviour of hybrid fiber-reinforced reactive powder concrete after high temperature," *Mater. Des.*, vol. 41, pp. 403–409, Oct. 2012.

28. P. Kalifa, G. Chene, and C. Galle, "High-temperature behaviour of HPC with polypropylene fibres: From spalling to microstructure," *Cem. Concr. Res.*, vol. 31, no. 10, pp. 1487–1499, 2001.

29. R. Parnas, M. Shaw, and Q. Liu, "Basalt Fiber Reinforced Polymer Composites," Connecticut, 2007.

30. M. Butler, "Report of Material Testing on Basalt Fibres 4 Series 1 A: Basic material properties of cement mortar with 3 types of basalt fibres with length of 6 mm," Moscow, Russia, 2010.

31. Z. Li, X. Zhou, and B. Shen, "Fiber-cement extrudates with perlite subjected to high temperatures," *J. Mater. Civ. Eng.*, vol. 16, p. 221, 2004.

32. F. J. Chu, H. W. Liu, Z. Bin Yang, and H. M. Dai, "Bending Performance of Basalt Fiber Reinforced Cement," *Adv. Mater. Res.*, vol. 332–334, pp. 2142–2145, Sep. 2011.

33. B. Chen and J. Liu, "Residual strength of hybrid-fiber-reinforced high-strength concrete after exposure to high temperatures," *Cem. Concr. Res.*, vol. 34, no. 6, pp. 1065–1069, Jun. 2004.

34. M. Bastami, F. Aslani, and M. Omran, "High-Temperature Mechanical Properties of Concrete," *Int. J. Civ. Eng.*, vol. 8, no. 4, pp. 337–351, 2010.

35. A. Knaack, Y. Kurama, and D. Kirkner, "Compressive Strength Relationships for Concrete under Elevated Temperatures," *ACI Mater. J.*, vol. 107, no. 2, pp. 164–175, 2010.

36. A. Q. Sobia, M. S. Hamidah, S. Ahmad, and S. Alam, "Residual Mechanical Properties Of HAC-GGBS Based UHPFRCC After Exposed To Elevated Temperature," in *International postgraduate seminar*, 2013, pp. 1–13.
37. R. Siddique and M. I. Khan, *Supplementary Cementing Materials*, vol. 37. Berlin, Heidelberg: Springer Berlin Heidelberg, 2011.

Effect of Longitudinal Reinforcement Ratio on Shear Capacity of Concrete Beams with GFRP Bars

Noor Azlina Abdul Hamid, Azmi Ibrahim, Rendy Thamrin and Hanizah Abdul Hamid

Abstract This paper evaluates the shear capacity of concrete beams longitudinally reinforced with glass fiber-reinforced polymer (GFRP) bars. All beams were provided with steel stirrups as shear reinforcement within shear region with spacing, 150 mm. The effect of longitudinal reinforcement ratios, ρ_f is discussed and compared with conventional beams reinforced with steel. The test results were compared with predictions recommended by ACI 440.1R-06 design guidelines and by other references. Other performance in terms of tensile strength and stresses in reinforcement bars was analyzed. Based on the findings of test results, it is shown that the shear resistance of GFRP RC beam is influenced by modulus elasticity of GFRP bars that resulted in low shear strength compared to conventional beams. Moreover, due to specific properties of GFRP materials, shear behavior of beams with GFRP bars is different to that of beams with steel. The current design guideline (ACI 440.1R-06) was found to be very conservative compared with experimental results.

Keywords GFRP bar · Steel stirrup · Shear strength · Reinforced concrete beam

N.A.A. Hamid (✉) · A. Ibrahim · H.A. Hamid
Faculty of Civil Engineering, Universiti Teknologi Mara (UiTM), Shah Alam, Selangor, Malaysia
e-mail: azlinah@uthm.edu.my

A. Ibrahim
e-mail: azmii716@yahoo.com

H.A. Hamid
e-mail: hanizah696@salam.uitm.edu.my

R. Thamrin
Department of Civil Engineering, Universiti Andalas, Padang, Indonesia
e-mail: rendy@ft.unand.ac.id

1 Introduction

Fiber-reinforced polymer or commonly known as FRP has become as an alternative reinforcement to solve the corrosion problems of steel. Nevertheless, due to the differences between FRP and steel associated with their low modulus of elasticity and brittle failure of FRP bars, the total replacement of steel with FRP bars is not possible and not fully explored. The use of FRP materials with combination of conventional reinforcing materials in concrete structures has been started since 1990 [1–3]. Several studies have been conducted to investigate the performance of FRP and steel as combination reinforcement materials in beams [4–7]. However due to low modulus of elasticity of FRP bars, the shear capacity of beams reinforced with FRP bars especially made of glass (GFRP) is significantly lower than the beams reinforced with steel bars [4, 8–10]. Although glass fiber-reinforced polymer (GFRP) had lower tensile modulus of elasticity about 40–55 GPa, it still offers higher tensile strength and potential as reinforcement bars in concrete structures [11]. In addition, the cost of using GFRP bars as reinforcement in concrete member can be much lower compared with the use of steel bars.

Similar as steel RC beams, FRP RC beams which are designated as under-reinforced sections tend to fail on flexural while beams with over-reinforced sections failed on shear [12]. Test results [8, 13] indicate that the longitudinal reinforcement ratio of FRP bars has not significantly influenced the shear capacity of the beams. However, other studies showed that the effect of reinforcement ratio can be seen in beams with beam depth greater than 300 mm and by shear span ratio [10, 14, 15]. Similar behavior also exhibited in concrete slabs such that the shear strength increased as the reinforcement ratio increased [16]. Moreover, beams provided with shear reinforcement enable to increase the shear capacity of the beams due to increasing concrete contribution and confinement of shear cracks formation [7, 17].

The prediction using existing design guidelines as recommended by ACI 440.1R-06 [18] gave conservative predictions of beams reinforced with FRP. Thus, this paper investigates the effect of an amount of longitudinal reinforcement on the shear strength GFRP RC beams with steel stirrups. In addition, the accuracy of current shear strength equations concerning FRP as reinforcement bars is examined.

2 Shear Strength Design Provision

Table 1 summarizes the existing shear design provisions (V_{cf}) for predicting concrete contribution to the shear resistance of FRP RC beams. The shear resistance for conventional steel RC beams is the basic provision which

Table 1 Concrete shear strength equations

Reference	Shear provisions $\left(V_{cf}\right)$
ACI 440.1R-06 [18]	$V_{cf} = \frac{2}{5}\sqrt{f_c}bc$ where $c = kd$ (1) $k = \sqrt{2\rho_f n_f + \left(\rho_f n_f\right)^2} - \rho_f n_f$ $\rho_f = \frac{A_f}{bd}$
Wegian and Abdalla [9]	$V_{cf} = 2\left(f_c \frac{\rho E_f}{E_s}\frac{d}{a}\right)^{1/3}bd$ (2)
Kim and Jang [19]	$V_{cf} = \beta_f \frac{1}{6}\sqrt{f_c}bd$ (3) where, $\frac{a}{d} \leq 2.5$; $\beta_f = 3.944 + 0.256\frac{E_f}{E_s} - 1.472\frac{a}{d}73.886\rho_f$

$$V_{cf} + V_s = V \tag{4}$$

$$V_s = \frac{A_s f_y d}{S_v} \tag{5}$$

is adopted from ACI 318-08 [20] as in Eq. (1), while the shear resistance for beams reinforced with GFRP bars in Eq. (2) is adopted from ACI 440.1R-06 [9, 18]. The other equation which consider the effect of modulus of elasticity and shear span ratio have been proposed [19] as in Eq. (3). Basically, the shear design provisions for FRP RC beams are adopted from equations used for steel RC beams. The summation of concrete shear strength equations (V_{cf}) and contribution strength from steel stirrups (V_s) as written in Eqs. (4) and (5) was used to predict the shear carrying capacity of GFRP RC beams. Furthermore, the accuracy of those equations to GFRP RC beam was analyzed and compared with experimental results.

3   Experimental Program

3.1   Material Properties

A type of sand-coated glass fiber-reinforced polymer (GFRP) bars was used as longitudinal reinforcement for the compression and tension bars of the beam are shown in Fig. 1. The sand-coated type is used to enhance the bond characteristics between GFRP bar and surrounding concrete. The bar was produced by Concrete Protection Products Inc. North Carolina, USA using pultrusion process. The GFRP bar was made of continuous E-glass fibers, approximately 83 % fiber content impregnated in a vinylester resin. In this study, only one size of longitudinal reinforcement bars (d_b = 16 mm) of GFRP and deformed steel bar was used. As shown in Table 2, the mechanical properties of GFRP and steel bar were obtained by performing tensile test. The tensile strength, f_f of GFRP bar was 771 MPa with modulus elasticity, E_f of 57 GPa. The deformed steel bars (d_b = 16 mm) with yield strength, f_y of 512 MPa and modulus of elasticity, E_s of 207 GPa were used for

Fig. 1 GFRP bars as
longitudinal reinforcement

Table 2 Reinforcement material properties

Reinforcing material	Diameter (mm)	Tensile strength (Mpa)	Modulus of elasticity (Gpa)	Ultimate strain
Glass FRP	16	771	57.3	0.013
Steel	16	512	207	0.0026
Steel	8	440	162	0.0028

control beams. The plain steel bars (d_b = 9 mm) with the yield strength, f_{yv} of
440 MPa and modulus of elasticity, E_s of 162 GPa were selected to fabricate the
steel stirrup in all beams. Figure 2 shows the detailed configurations of closed steel
stirrups with sufficient bend and anchorage length which shall not be less than $4d_b$
as suggested to resist from slippage due to high shear stresses at shear span [20].

The beams were cast from two different batches of ready-mix concrete of normal
compressive strength, f_{cu} of 24 and 36 N/mm^2 with a maximum size crushed
aggregate of 20 mm. The slump test measurement was medium workability mixes
of 50 mm. All beams were provided with closed rectangular steel stirrups with
sufficient spacing of 150 mm within shear span zone. The variables considered in

Fig. 2 Details of steel stirrup
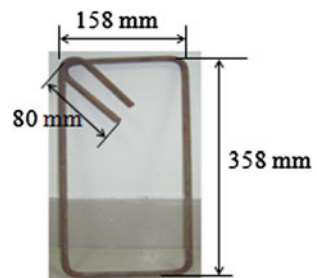
this experimental program were the longitudinal reinforcement ratios with contribution of steel stirrups in resisting shear strength of concrete beams.

3.2 Test Setup and Instrumentation

Totally six large-scale concrete beams were constructed and tested up to failure as shown in Table 3. The beam specimen consisted two control beams that were reinforced with conventional steel bars and identified as BSS beams. Meanwhile, four concrete beams reinforced with longitudinal GFRP bars and were denoted as BGS and BGD beams according to their reinforcement ratio. The identification of beams such that the second letter S and G refers to reinforcement types of steel and GFRP, respectively. While the third letter S and D indicates that a single or double layered of longitudinal tension bars provided. To investigate the effect of reinforcement ratio on shear strength, the GFRP RC beams were reinforced with different reinforcement ratios of 0.6, 0.8, 1.2, and 1.5 %. As compared, the control beams were reinforced with reinforcement ratios of 0.6 and 0.8 %. To obtain the failure mode of the beam sections, the actual reinforcement ratio, ρ_{act}, and balanced reinforcement ratio, ρ_{bal} are compared by considering the equilibrium of internal forces and strain compatibility as given by ACI 440.1R-06 [18] as follow,

$$\rho_{\text{act}} = A_f/bd \tag{6}$$

$$\rho_{\text{bal}} = 0.85\beta_1 \frac{f_c'}{f_{fu}} \frac{E_f \varepsilon_{cu}}{E_f \varepsilon_{cu} + f_{fu}} \tag{7}$$

where f_c' = compressive strength of concrete (MPa), β_1 = factor taken as 0.85 if $f_c' \leq 28$ MPa but the factor reduced continuously at a rate of 0.05 per each increasing 7 MPa of f_c', but is not taken as less than 0.65 while, f_{fu} = tensile strength of the FRP bars (MPa), E_f = modulus elasticity of the FRP bars (MPa), and ε_{cu} = ultimate strain in concrete. Due to different properties, the total replacement of steel bars with an equivalent reinforcement ratio of GFRP bars does not govern the similar failure mode conditions.

By comparing the reinforcement ratio, the balanced reinforcement ratio of GFRP RC beams is significantly lower than steel RC beams provided with higher reinforcement ratio. This is due to low modulus elasticity of GFRP bars that may lead to severe deflection and cracking. In fact, if the reinforcement ratio is smaller than the balanced reinforcement ratio ($\rho_{\text{act}} < \rho_{\text{bal}}$), the rupture of GFRP bars may occur [18]. Hence in order to avoid brittle failure, the GFRP RC beam is designated as over-reinforced section where concrete crushing governs at failure. Moreover, with respect to modulus of elasticity, E_f and area of longitudinal bars A_f, show that the value of axial stiffness of GFRP RC beam is significantly lower than that of steel

Table 3 Details of test specimens

Test specimen	Shear span ratio (a/d)	Steel stirrup spacing (mm)	Longitudinal reinforcement					Axial stiffness, $E_f A_f$ ($N \times 10^6$)
			Types	Area reinforcement, A_f (mm²)	ρ_{act} (%)	ρ_{bal} (%)	ρ_{act}/ρ_{bal}	
BSS-03	1.5	150	Steel	402.1	0.6	1.6	0.3	80.4
BSS-04	1.5	150	Steel	603.2	0.8	1.6	0.5	120.6
BGS-03	1.5	150	GFRP	402.1	0.6	0.4	1.4	22.7
BGS-04	1.5	150	GFRP	603.2	0.8	0.4	2.1	34.1
BGD-03	1.6	150	GFRP	804.2	1.2	0.6	2.0	45.5
BGD-04	1.6	150	GFRP	1005.3	1.5	0.6	2.4	56.8

Fig. 3 Details of test setup
and dimensions

| 250 mm | 550 mm | 200 mm |
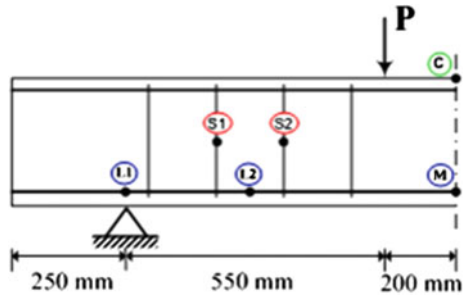
RC beams though they had high amount of GFRP bars, which in turn, reflects the
flexure stiffness of the beam.

All tested beams had shear span-to-effective depth ratio, a/d less than 2.5 with
250 mm overhang length on both sides of the beam in order to provide sufficient
anchorage length from bonding failure. As shown in Fig. 3, the beams were
instrumented with one pair of electrical-resistance strain gages that were bonded on
top of concrete surface and denoted as C. Strain gages on longitudinal reinforce-
ment bars were bonded at three locations of support (L1), middle of shear span
(L2), and middle of beam span (M). The strain gages on steel stirrups were attached
at mid-height of stirrup and denoted as S_η ($\eta = 1, 2, 3…\eta + 1$).

For deflection measurements, totally three linear variable differential transducers
(LVDT) with a 50 mm stroke were installed at mid-span and under two load
positions. During loading, any crack formations on both sides of the beam were
marked and labeled according to its load increment. Meanwhile, careful observa-
tions on the behavior of beam failure were recorded using tape. As a comparison,

Fig. 4 Cross-sectional beam
of BSS, BGS, and BGD beam

BSS and BGS beam
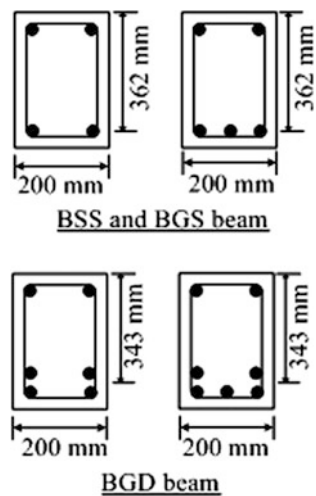
BGD beam

the design of GFRP RC beams as in the case of BGS and BGD beams is shown in Fig. 4 in which the effect of increasing reinforcement ratio in the range of 0.6–1.5 % is analyzed. The beams were tested monotonically using 1000 kN closed-loop MTS actuator at a stroke-controlled rate of 0.3 mm/min. The load was distributed evenly onto two concentrated loads of 0.4 m/apart through steel I-beam.

4 Results and Discussion

The experimental results of the beam in terms of failure mode, shear capacity, and maximum deflection are summarized in Table 4. As expected, all beam failed in shear due to over-reinforced section of GFRP RC beams and fewer amount of steel stirrups within short shear span. Higher deflection clearly indicates in beams reinforced with GFRP bars especially in beams with higher reinforcement ratio. Hence, low flexural stiffness exhibits in all GFRP RC beams compared to steel RC beams due to low axial stiffness, $E_f A_f$ that is attributed to the low modulus elasticity of GFRP bars.

Furthermore, the shear strength predictions based on Eq. (4) revealed that the code of ACI 440 in Eq. (1) is conservative for GFRP RC beams with mean value of 1.19 and standard deviation of 0.2. While, Eq. (3) unconservatively predicted the shear capacity of beams with mean value of 0.85 that account for the effect of shear span-effective depth and modulus ratio. The equation suggested by Wegian and Abdalla [9] that account for the modulus ratio of GFRP and steel, $\frac{E_f}{E_s}$ gives more accurate results with mean value of 1.02. The effect of reinforcement ratio on shear strength can be seen in Fig. 5. Based on the graph, it clearly shows that the shear capacity of GFRP beam was lower than that steel RC steel beam which is in good agreement with other test results [9].

Moreover, similar performance was indicated with increasing reinforcement ratio from 0.6 to 0.8 %, the shear strength increased. No significant effect can be obtained when the reinforcement ratio increases more than 0.8 %. This may be attributed to the shear transfer mechanism within uncracked concrete, reinforcement bars, and also due to increases in dowel action capacity. From observation, the diagonal shear crack of GFRP RC beams occurs within the shear span. Upon loading, more progressive cracks propagate toward the concentrated load which eventually forms approximately 45° of cracks at one side of the beam either on the left or right side as typically shown in Fig. 6. The beam was failed by severe diagonal cracks associated with concrete crushing (Fig. 7).

In beam BGD-03 designated with double layers of longitudinal GFRP bars failed on shear by critical diagonal cracks within shear span. More importantly, the steel stirrup at the middle of shear span breaks away from bend location. Similar results had been reported on FRP stirrup which suddenly ruptured away from bend location in beams reinforced with multilayers of longitudinal steel bars rather than single layer of bars [21]. Accordingly, better performance of steel stirrup is obtained

Table 4 Test results

| Beam | Concrete strength, f_c (Mpa) | Experimental results | | | | ACI 440.1R-06 (2006) | | Wegian and Abdalla (2005) | | Chung Ho Kim (2013) | |
		Experimental shear load, V_{exp} (kN)	Maximum deflection (mm)	$exp/\sqrt{fc.b.d}$	Failure mode	V_{pred} (kN)	V_{exp}/V_{pred} (kN)	V_{pred} (kN)	V_{exp}/V_{pred} (kN)	V_{pred} (kN)	V_{exp}/V_{pred} (kN)
BSS-03	24	195.5	13.66	0.55	Shear	–	–	–	–	–	–
BSS-04	24	223.3	11.15	0.63	Shear	–	–	–	–	–	–
BGS-03	24	139.0	12.63	0.39	Shear	157	0.89	177	0.79	211	0.66
BGS-04	24	181.3	16.08	0.51	Shear	161	1.13	183	0.99	218	0.83
BGD-03	36	179.3	8.73	0.44	Shear	133	1.35	157	1.14	194	0.92
BGD-04	36	190.8	18.01	0.47	Shear	136	1.40	162	1.18	202	0.95
					Mean		1.19		1.02		0.85
					Standard deviation		0.20		0.18		0.13

Fig. 5 Normalized shear strength versus reinforcement ratio
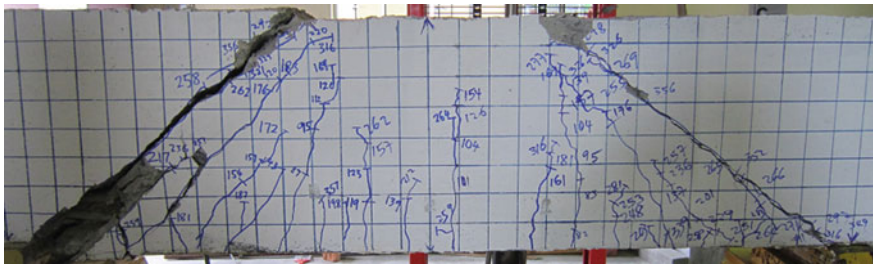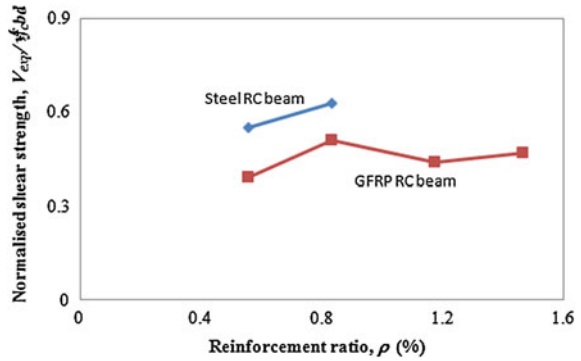
Fig. 6 Diagonal shear failure of GFRP RC beam

Fig. 7 Stirrup broken at failure in beam BGD-03
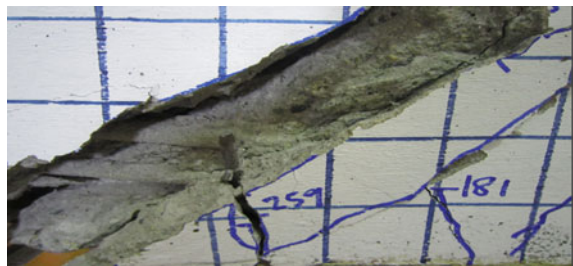
in GFRP RC beams with multilayers of longitudinal bars such that bend location is the weakest part of stirrup. It also revealed that the amount of steel stirrups also influenced the shear performance of GFRP RC beams.

Figure 8 shows the typical distribution of tension forces on longitudinal reinforcement bars at the support (S), middle of shear span (M), and middle of beam span (SS). This clearly shows that the tension force at the middle of shear span and at the middle of beam span increased after the first flexural cracks occurred. The increasing load resulting the tensile force at the support increased after the

Fig. 8 Tension force of
longitudinal bars
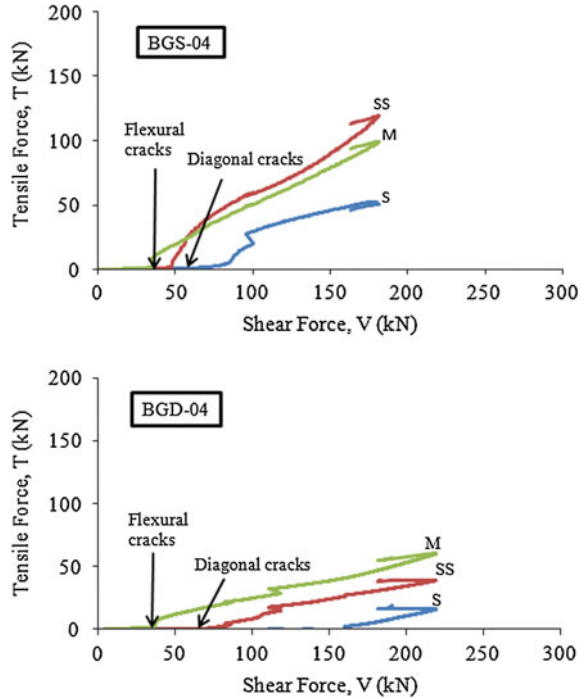
occurrence of diagonal cracks. Similar distribution also developed in beams rein-
forced with steel bars. In the case of beam with double layers of bar as in beam
BGD-03 and BGD-04, no differences of tension force were observed between
bottom and top layers of longitudinal bar. Besides, the tension force increases as the
amount of longitudinal bars increases.

5 Conclusion

The shear performance of GFRP RC beams with different longitudinal reinforce-
ment ratios was investigated. Based on the experimental result of six beams, the
following conclusions can be drawn:

1. The shear strength of beams reinforced with GFRP bars is significantly lower
   than the equivalent beam reinforced with steel bars.
2. Beams reinforced with lower reinforcement ratio tend to fail in flexure failure,
   while beams with higher reinforcement ratio tend to fail in shear with critical
   diagonal cracks.

3. The steel stirrup breaks away from the bend location in beam with multilayers of longitudinal reinforcement bars, which provides better performance in resisting high shear stresses in stirrup.
4. High reinforcement ratio of longitudinal GFRP bars influenced the shear capacity of GFRP RC beams but low flexural stiffness is obtained.
5. The tensile forces of longitudinal bars considerably increased with an increasing amount of reinforcement bars.
6. The ACI 440.1R-06 equations conservatively predict the shear strength of GFRP RC beams. The equation proposed by Wegian and Abdalla that account for the modulus ratio of reinforcement bar provides better prediction for beams with shear span less than 2.5. The equation suggested by Kim and Jung unconservatively predicts the shear capacity of GFRP RC beams.

References

1. L. C. Hollaway, "The evolution of and the way forward for advanced polymer composites in the civil infrastructure," *Constr. Build. Mater.*, vol. 17, pp. 365–378, Sep. 2003.
2. L. C. Hollaway, "A review of the present and future utilisation of FRP composites in the civil infrastructure with reference to their important in-service properties," *Constr. Build. Mater.*, vol. 24, pp. 2419–2445, Dec. 2010.
3. Task Group 9.3, "FRP Reinforcement in RC Structures," 2007.
4. N. A. A. Hamid, R. Thamrin, and A. Ibrahim, "Shear Capacity of Non-Metallic (FRP) Reinforced Concrete Beams with Stirrups," vol. 5, no. 5, pp. 593–598, 2013.
5. N. A. A. Hamid, R. Thamrin, A. Ibrahim, and H. A. Hamid, "Strain Distribution on Reinforcement of Concrete Beams Reinforced with Glass Fiber Reinforced Polymer (GFRP) Bars," vol. 595, pp. 812–817, 2014.
6. R. Thamrin and T. Kaku, "Tension Force Model of Longitudinal Reinforcement at the Support of RC Beam with Hanging Region," in *Proc. of FIB Symposium Keep Concrete Attractive, Budapest, Hungary*, 2005, pp. 613–618.
7. E. A. Ahmed, E. F. El-Salakawy, and B. Benmokrane, "Fibre-reinforced polymer composite shear reinforcement: performance evaluation in concrete beams and code prediction," *Can. J. Civ. Eng.*, vol. 37, no. 8, pp. 1057–1070, Aug. 2010.
8. J. R. Yost, S. P. Gross, and D. W. Dinehart, "Shear Strength of Normal Concrete Beams Reinforced with Deformed GFRP Bars," *omposites Constr.*, vol. 5, no. 4, November, pp. 268–275, 2001.
9. F. M. Wegian and H. A. Abdalla, "Shear capacity of concrete beams reinforced with fiber reinforced polymers," *Compos. Struct.*, vol. 71, pp. 130–138, 2005.
10. N. A. A. Hamid, A. Ibrahim, T. Rendy, and Hamid, "Experimental Investigation on the Shear Behaviour of Concrete Beams Reinforced with GFRP Reinforcement Bars," *Adv. Mater. Res.*, vol. 626, pp. 559–563, Dec. 2012.
11. B. Benmokrane, O. Chaallal, and R. Masmoudi, "Glass fibre reinforced plastic (GFRP) rebars for concrete structures," *Constr. Build. Mater.*, vol. 9, no. 6, pp. 353–364, 1995.

12. A. F. Ashour, "Flexural and shear capacities of concrete beams reinforced with GFRP bars," *Constr. Build. Mater.*, vol. 20, pp. 1005–1015, 2006.
13. S. P. Gross, J. R. Yost, D. W. Dinehart, E. Svensen, and N. Liu, "Shear Strength of Normal and High Strength Concrete Beams Reinforced with GFRP Bars," *Bridg. Mater.*, pp. 1–12, 2001.
14. M. S. Alam and A. Hussein, "Experimental investigation on the effect of longitudinal reinforcement on shear strength of fibre reinforced polymer reinforced concrete beams," *Can. J. Civ. Eng.*, vol. 38, no. 3, pp. 243–251, Mar. 2011.
15. A. K. El-sayed, E. F. El-salakawy, and B. Benmokrane, "Shear Strength of FRP-Reinforced Concrete Beams without Transverse Reinforcement," *ACI Struct.*, no. 103–S25, pp. 235–243, 2006.
16. A. El-Sayed, E. El-Salakawy, and B. Benmokrane, "Shear Strength of One-Way Concrete Slabs Reinforced with Fiber-Reinforced Polymer Composite Bars," *J. Compos. Constr.*, vol. 9, no. 2, pp. 147–157, Apr. 2005.
17. E. A. Ahmed, E. F. El-salakawy, and B. Benmokrane, "Performance Evaluation of Glass Fiber-Reinforced Polymer Shear Reinforcement for Concrete Beams," *ACI Struct.*, no. 107–S06, pp. 53–63.
18. American Concrete Institut (ACI), "Guide for the Design and Construction of Structural Concrete Reinforced with FRP Bars (440-1R-06)." p. 44, 2006.
19. C. H. Kim and H. S. Jang, "Concrete Shear Strength of Normal and Lightweight Concrete Beams Reinforced with FRP Bars," pp. 2–10, 2013.
20. American Concrete Institut (ACI), "Building Code Requirements for Structural Concrete (ACI 318-08) and Commentary. American Concrete Institute, Farmington Hills (MI)." p. 465, 2008.
21. E. C. Bentz, L. Massam, M. P. Collins, and M. Asce, "Shear Strength of Large Concrete Members with FRP Reinforcement," no. December, pp. 637–646, 2010.

Autogenous Healing Mortar Made of Alginate-Encapsulated *Geobacillus Stearothermophilus*

M.A. Raden Maizatul Aimi, K. Khalilah, H. Noor Hana and M.S. Hamidah

Abstract The autogenous healing by microbial induced calcite precipitation (MICP) has become significant interest in sustainable approaches on concrete repair and maintenance. Alginate-encapsulated *Geobacillus stearothermophilus* is introduced as a new smart material for self-healing concrete. Its effects on concrete performance were evaluated with regard to strength enhancement and healing efficiency. The aim of this study was to optimize bacteria cell concentration and alginate-encapsulated *Geobacillus stearothermophilus* (AE-GS) composition in the concrete mixture in order to obtain the maximum healing capacity by using response surface methodology approach. Verification tests have shown the successful relation developed by statistical treatments; due to the potential of *Geobacillus stearothermophilus* immobilized into sodium alginate gels that can act as a guideline in the mixture proportion of autogenous healing concrete in a future.

Keywords Autogenous healing · Crack · *Geobacillus stearothermophilus* · Sodium alginate gel beads · Microbial $CaCO_3$

M.A. Raden Maizatul Aimi (✉) · M.S. Hamidah
Faculty of Civil Engineering, Universiti Teknologi MARA (UiTM), Shah Alam, Selangor, Malaysia
e-mail: raden.amy@gmail.com

M.S. Hamidah
e-mail: hamid929@salam.uitm.edu.my

K. Khalilah · H. Noor Hana
Faculty of Applied Sciences, Universiti Teknologi MARA (UiTM), Shah Alam, Selangor, Malaysia
e-mail: khali552@salam.uitn.edu.my

H. Noor Hana
e-mail: noorhana88@salam.uitm.edu.my

601

1 Introduction

Previous studies on the ureolytic bacteria, confirmed their capabilities in producing urease enzyme that leads to biomineralization process and has shown promising results in sustainable concrete repair methodology. Some bacterial species such as *Bacillus megaterium, Bacillus licheniformis and Bacillus flexus* [1], *Bacillus cohnii* [2], *Bacillus pasteurii/Spocarcina pasteurii* [3–6], *Bacillus sphaericus* [7–10], and *Bacillus subtilis* [11] have proven their ability in enhancing concrete performance. However, the methodological limitation of the bacteria used in such method exhibits temporal activity and shorter lifetime of bacteria when embedded or mixed up directly to the concrete due to the increasing of pH (>12) [2, 4].

Due to the high temperature during concrete hydration, the exploration of bacteria dragged into the type that can resist heat and at the same time capable to produce endospore. The *Geobacillus stearothermophilus* was selected as a highlight in this study. The *Geobacillus stearothermophilus* is a high resistant bacteria and a thermophilic type bacterium due to its capability thriving high temperature (30–75 °C) that can be found in geothermal heated region or high temperature ambient such as hot spring [12, 13]. The *Geobacillus stearothermophilus* is capable to produce endospore when depriving for nutrients. The morphology and resistance properties of *Geobacillus* enable them to be mobilized in the atmosphere and transported long distances [14]. In addition, the longevity of *Geobacillus stearothermophilus* enables them to lie quiescent but viable for long periods of time in extreme condition, accumulating gradually over time to achieve surprisingly high population densities.

Suitable carrier is necessary to encapsulate the bacteria and protect it from the destruction of bacterial cells. The embedment of bacteria in the carrier ensures the bacteria being dormant but viable in the concrete matrix that will aid to the potential of self-healing. For instance, the use of the hydrogel encapsulated carbonate as bacteria carrier [7] and the embedment of bacteria with their food as nutrient supply in clay capsules [15] before mixing in the concrete has proven its effectiveness in concrete matrix.

This study was designed to observe the effect of incorporating *Geobacillus stearothermophilus* into sodium alginate gel beads as vehicle protector prior mixing process. Different cell concentrations of bacteria (BC) with the percentage replacement of alginate (AE) to become alginate-encapsulated *Geobacillus stearothermophilus* (AE-GS) was adopted and were designed as such to optimize the healing capacity by *Geobacillus stearothermophilus*. The result obtained would demonstrate the feasibility of using alginate-encapsulated *Geobacillus stearothermophilus* (AE-GS) to heal cracks in cementitious matrix that would be beneficial in varying capabilities of bacteria in concrete maintenance and repairs.

2 Materials and Methods

The materials used for producing alginate-encapsulated *Geobacillus stearother-mophilus* (AE-GS) mortar mixes are described in the following subsections.

2.1 Bacterial Strain

Geobacillus stearothermophilus (ATCC 12978) was used in this study. Living cells were grown in the sterile nutrient broth (NB) consisting of beef extract (3.0 g/L) and peptone (5.0 g/L). The pH of the medium was adjusted to 7.0. The culture was incubated at 65 °C, and centrifuged at 110 rpm for 24 hours. The cells were harvested by centrifuging the culture (8000 rpm, 4 °C) for 5 min. The centrifuged cells remained, called as pellet, were washed twice with sterile distilled water before being used for encapsulation process.

2.2 Encapsulation Process

The encapsulation processes was prepared to protect the bacteria on its way as inert material. The encapsulation occurs by cross-linking process in which the calcium ion in the solution crosslinked the polymers in the alginate which attached them at many points resulting in gel beads. For each series of alginate beads, 15 g/l sodium alginate $(C_6H_8O_6)_n$ as gelling agent, while 33.3 g/l yeast extract, 33.3 g/l urea (CH_4N_2O), and 20 g/l calcium lactate $(C_6H_{10}CaO_6)$ as a nutrient source of bacteria are required with 11.1 g/l calcium chloride $(CaCl_2)$ for cross-linker.

2.3 Optimisation of Alginate-Encapsulated Geobacillus Stearothermophilus (AE-GS) in Mortar

The optimization of bacterial concentration (BC, cfu/ml) replacement percentage of alginate encapsulation (AE, %) in mortar was designed by response surface methodology (RSM)—Design–Expert software (Version 8.0.7.1). The RSM is used to optimize product where several factors (coefficients) were chosen. In this study, two (2) factors which are bacterial concentrations and also replacement of alginate hydrogel to encapsulate *Geobacillus stearothermophilus* were adopted.

RSM capable as an optimization tool due to the fact it explicates experimental data and sufficiently yields elucidation of experimental data as a conclusive result [16]. An augmented factorial design namely central composite design (CCD) has been chosen for the optimisation. There are three (3) general steps in RSM namely

experiment design, model fitting and validation, and an optimisation. Only the experimental design step is entailed in the following subsection while the remaining model fitting and an optimization are described under statistical analysis and evaluation.

2.3.1 Experimental Designs

Under central composite design (CCD) approach, face centered (CCF) rules were selected to represent all the combination factors. The lowest and higher bacterial concentration used in this experiment design selected were 1×10^3 and 1×10^{11} cfu/ml, respectively. Meanwhile, alginate-encapsulated *Geobacillus stearothermophilus* used was ranged from 3 % to 15 % from the total of mortar mass. Under two (2) factors selected, the numbers of batches were 13 runs with 4 factorial, 4 axial, and 5 centers. Table 1 shows the two (2) chosen coefficients and trial batches produced by RSM.

2.3.2 Determination of Mortar Mix Proportion and Casting Process

The weight of mortar materials was based on the optimization range calculated by Design–Expert Software. The mortar mix design was based on the ratio of cement and fine aggregate (sand) which was 1:3 respectively with water cement ratio of 0.5. Thirteen (13) batch were used and the mix proportion is shown in Table 2. Alginate-encapsulated *Geobacillus stearothermophilus* (AE-GS) was prepared earlier prior mixing process as described in Sect. 2.2. Dry mix was prepared by mixing

Table 1 Optimization of bacterial concentration and alginate-encapsulated *Geobacillus stearothermophilus*

Run	Type	Encapsulation (AE, %)	Bacterial concentration (BC, cfu/ml)
1	Factorial	3	1×10^3
2	Axial	3	5×10^{10}
3	Factorial	3	1×10^{11}
4	Axial	9	1×10^3
5	Center	9	5×10^{10}
6	Center	9	5×10^{10}
7	Center	9	5×10^{10}
8	Center	9	5×10^{10}
9	Center	9	5×10^{10}
10	Axial	9	1×10^{11}
11	Factorial	15	1×10^3
12	Axial	15	5×10^{10}
13	Factorial	15	1×10^{11}

Table 2 Mix proportion of mortar with alginate-encapsulated *Geobacillus stearothermophilus*

Run	AE-GS (%)	BC (cfu/ml)	Alginate-encapsulation[a]					Mortar[b]			Σ Total weight (kg)
			Σ dH²O (ml)	Sodium alginate (gram)	Urea (ml)	Yeast extract (ml)	Calcium lactate (ml)	Cement (kg)	Sand (kg)	Water (liter)	
1	3	1×10^3	1039	20	80	80	133.2	10.8	32.3	5.4	44.4
2	3	5×10^{10}	1039	20	80	80	133.2	10.8	32.3	5.4	44.4
3	3	1×10^{11}	1039	20	80	80	133.2	10.8	32.3	5.4	44.4
4	9	1×10^3	3116	60	240	240	399.6	10.1	30.3	5.1	44.4
5	9	5×10^{10}	3116	60	240	240	399.6	10.1	30.3	5.1	44.4
6	9	5×10^{10}	3116	60	240	240	399.6	10.1	30.3	5.1	44.4
7	9	5×10^{10}	3116	60	240	240	399.6	10.1	30.3	5.1	44.4
8	9	5×10^{10}	3116	60	240	240	399.6	10.1	30.3	5.1	44.4
9	9	5×10^{10}	3116	60	240	240	399.6	10.1	30.3	5.1	44.4
10	9	1×10^{11}	3116	60	240	240	399.6	10.1	30.3	5.1	44.4
11	15	1×10^3	5194	100	400	400	666	9.4	28.3	4.7	44.4
12	15	5×10^{10}	5194	100	400	400	666	9.4	28.3	4.7	44.4
13	15	1×10^{11}	5194	100	400	400	666	9.4	28.3	4.7	44.4

[a]The encapsulation composition for alginate-encapsulated *Geobacillus stearothermophilus* for every batch
[b]The material constituents of mortar for every batch

cement and sand followed by incorporation of alginate-encapsulated *Geobacillus stearothermophilus.*

2.4 Experimental Methods

2.4.1 Compressive Strength

Compressive strength was carried out in accordance with BS EN 12390-3:2009. The compressive strength of the specimens was conducted for the specimens at 7, 28, and 60 days of ages. The specimens size is 50 mm × 50 mm × 50 mm. Compressive machine was operated at a pace rate of 3.0 kN/s and the specification refers to BS EN 12390-4:2000.

2.4.2 Autogenous Healing—Quantification

The evaluation of autogenous healing was done by creating realistic cracks to the specimens. Cylinder with 40 mm diameter and 100 mm length were used to perform this experiment. The realistic cracks were made by driving the controlled applied load using universal testing machine (UTM) Type 1000. The specimen is placed in the machine between the grips and a suitable jig to create crack placed above the table load. The high pace rate that fixed at (15 %, 0.083 kN/s) compression load, was applied for all specimens to create multiple realistic cracks widths. Every specimens were done in triplicate ($n = 3$). Visualization of crack filling was performed using portable stereomicroscope Dino Lite Camera (Dino Capture 2.0, AnMo Electronics, Taiwan). After crack creation, 6 positions were marked on each crack of the specimens distributed homogeneously along the crack length. Initial images and final images (after 7, 28 and 60 days of incubation under wet–dry cycles) were taken with the markers in the center of the images. In each image, crack widths at two locations nearby the marker were analyzed by the Dino Lite. Cracked specimens were also prepared for ambient curing (dry curing) to measure the extent of healing properties for controlled purposes. The healing ratio by the width decreasing was calculated using Eq. (1) [7].

$$\text{Healing} \% = (Cw_i - Cw_f)/Cw_t \times 100 \tag{1}$$

where Cw_i is the initial crack width, Cw_f is the final crack width, and Cw_t is the total initial crack width. The result was analyzed and taken as average for further analysis latter using RSM.

2.5 Statistical Analysis and Evaluation

2.5.1 Response Surface Methodology (RSM)

RSM was predetermined to optimize response selected by meeting a set of specifications consisting of compressive strength and autogenous healing quantification with regards to the curing days (7, 28, and 60 days). A total of 13 runs of the CCD experimental design and responses based on the experimental runs are shown in Table 2. Eight experiments were enhanced with five replications to assess the pure error. The optimum predictor quadratic model Eq. (2) was used to determine the optimum condition of the responses [17, 18].

$$Y = \beta_0 + \sum_{i=1}^{k} \beta_{ii} X_i + \sum_{i=1}^{k} \beta_{ii} X_i^2 + \sum_{i_{i \leq j}}^{k} \sum_{j}^{k} \beta_{ij} X_i X_j + e_i \tag{2}$$

where Y is the predicted response, X_i, and X_j are the coded values of the preparation variables, i is the linear coefficient, j is the quadratic coefficient, β is the regression coefficient, k is the number of factors studied and optimized in the experiment, and e is the random error.

2.5.2 Model Fitting and Validation

The ANOVA was performed to select the appropriate type of model (linear, quadratic, etc.). Once the model fitting was performed, residual analysis was further evaluated to validate the assumptions used in the ANOVA. This analysis includes calculating case statistics to identify outliers and examining diagnostic plots such as normal probability plots and residual plots. If these analyses are satisfactory, the model is considered adequate and response surface plots can be generated. Contour plots were used for interpretation and optimisation.

2.5.3 Optimisation

After establishing the appropriate model, several responses were optimized simultaneously. Optimization was performed by selecting mathematically (numerical). Numerical optimization needs level of reflection in terms of minimum or maximum desirability to define an objective function. In this study, the maximum compressive strength and the maximum quantification healing derived by AE-GS were selected for optimization.

2.5.4   Verification of Optimised Condition and Predictive Model

The Design–Expert software used searches for a combination of factor levels that simultaneously satisfy the requirements placed on each of the responses and factors. Optimization requires that goals are set for the variables and response where all goals then get combined into one desirability function. Two (2) different responses namely maximum compressive strength and maximum healing efficiency were set for optimization. The importance of setting the goals to meet the requirement due to the fact that this conducted study would able to yield the performance of *Geobacillus stearothermophilus* in cementitious material as an autogenous healing type bacteria. A list of solutions appeared after all the analyses were performed. It will be verified by comparing the results using predicted value and observed value of AE-GS mortar to ensure that the model is a good fit through experimental data.

3   Results

The following tests were performed to investigate the capability of *Geobacillus stearothermophilus* in enhancing the strength of mortar and maximizing its healing capacity using RSM software.

3.1   Statistical Analysis and Validation

3.1.1   Compressive Strength

Cubes sizes of 50 mm were tested to investigate the compressive strength of alginate-encapsulated *Geobacillus stearothermophilus* (AE-GS). The specimens were tested at 7, 28, and 60 days as shown in Table 3 and Fig. 1. In the present study, the discussion was in three (3) phases namely AE-GS replacement in mortar, influence on bacterial concentration towards strength development, and also curing effect towards AE-GS mortar.

First phase involved on replacement of AE-GS into mortar at 3, 9, and 15 %. Higher compressive strength is always associated with the first group at 3 % replacement of alginate-encapsulated *Geobacillus stearothermophilus* (AE-GS1–AE-GS3), which is in the range of (34–54 MPa). Moderate and lower compressive strength are associated with the second group at 9 % replacement (AE-GS4–AE-GS10) and the third group at 15 % replacement (AE-GS11–AE-GS13), which are in the ranges of (32.7–49.7 MPa) and (27.5–38 MPa), respectively. It was found that the highest compressive strength between replacement percentage in Group I and Group II was found declined at 8 % while 23 % declined was observed at compressive strength result between Group II and Group III.

Table 3 Findings obtained in all experiments by RSM

Exp. no	Batch		CCD (actual variables)		Responses					
					Compressive strength			Healing efficiency		
			BC	AE	CS-7d	CS-28d	CS-60d	HE-7d	HE-28d	HE-60d
			(cfu/ml)	(%)	(MPa)	(MPa)	(MPa)	(%)	(%)	(%)
1	G(I)	AE-GS1	1×10^3	3	34.0	44.8	47.0	4.5	10	41
2		AE-GS2	5×10^{10}	3	36.0	46.3	50.1	10	21.5	48
3		AE-GS3	1×10^{11}	3	37.7	48.0	54.0	17	33	54
4	G(II)	AE-GS4	1×10^3	9	32.7	41.2	42.4	13	41	62
5		AE-GS5	5×10^{10}	9	33.9	42.8	46.3	25.8	49	65
6		AE-GS6	5×10^{10}	9	33.2	43.6	49.0	24	50	69
7		AE-GS7	5×10^{10}	9	32.6	43.0	47.0	22.6	54	67
8		AE-GS8	5×10^{10}	9	33.5	44.9	48.9	28	58	64
9		AE-GS9	5×10^{10}	9	32.9	42.7	46.0	27.5	58	66
10		AE-GS10	1×10^{11}	9	34.0	44.5	49.7	36	67	78
11	G(III)	AE-GS11	1×10^3	15	27.5	31.1	34.0	17	59	87
12		AE-GS12	5×10^{10}	15	27.9	34.0	36.3	28	62	95
13		AE-GS13	1×10^{11}	15	28.4	35.0	38.0	41.0	80	100
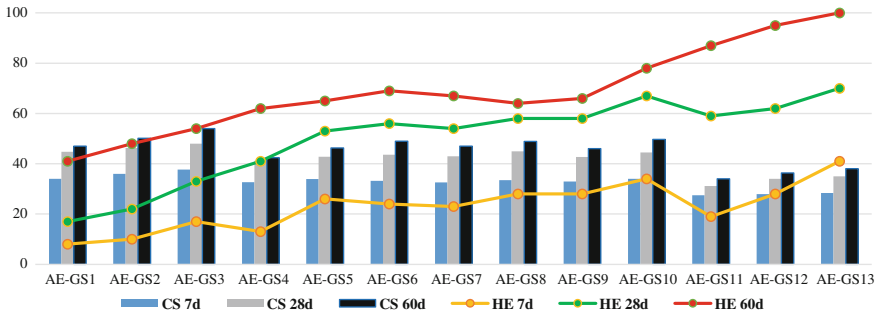
Fig. 1 Compressive strength (CS) development and healing efficiency (HE) by AE-GS mortar

The second phase involved on the curing effect towards strength development, the result on 28 and 60 days curing was found to obtain strength satisfactorily on mortar compared to the strength at 7 days. For analysis on third phase considering bacterial concentration on strength development of AE-GS mortar, bacterial concentration gives small effect on the strength development. Among the AE-GS mortar batch in each group, the mix design with higher concentration, 1×10^{11} cfu/ml obtained slightly higher strength from lowest bacterial concentration at 1×10^3 cfu/ml with the range between 3–13 %. Based on the above discussion, it has been predicted that higher replacement of AE-GS leads to reduction on strength development due to the fact that alginate gel beads are not supplementary cementation materials or natural pozzolans.

The optimization effects would give clear picture on the right mix constituents for compressive strength. Therefore, the suitable ranges for compressive strength were mix design in Group I and II at 28 or 60 days of curing at higher bacterial concentration of 1×10^{11} cfu/ml.

3.1.2 Autogenous Healing—Quantification

As shown in Table 3 and Fig. 1, the Group II and Group III obtained medium to higher healing efficiency respectively as compared to Group I. It can be seen that mortar with higher replacement of AE-GS (15 %) obtained higher degree of healing efficiency as compared to the lowest replacement of AE-GS mortar (3 %). 100 % of healing efficiency was observed on mix design of AE-GS 13 (1×10^{11} cfu/ml, 15 %) which indicate higher bacterial concentration and higher replacement level at 60 days of curing. Based on 60 days of curing, the minimum healing efficiency was found at AE-GS1 (1×10^3 cfu/ml, 3 %). The crack width range from 0.13–0.76 mm and only meant for calculation on healing efficiency. The quantification emphasize on healing effect with regards to bacterial concentration and healing level as shown clearly on Fig. 2.

0 days

7 days

28 days

60 days
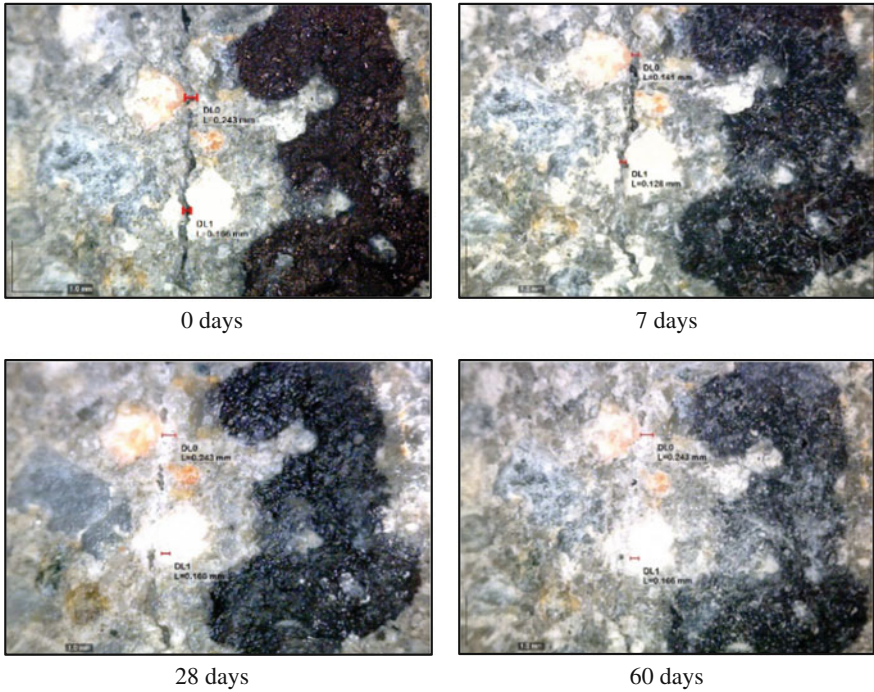
Fig. 2 Maximum crack width healed in the specimen AE-GS 12

3.1.3 Response Surface Methodology (RSM)

RSM was used for obtaining a relationship between factors and the response (response surface, contour plot, and analysis) for optimizing the response of compressive strength and healing capability of *Geobacillus stearothermophilus.*

3.1.4 Model Fitting and Validation

The data design matrix of the variables (in the actual units) with the experimental values of responses is shown in (Table 3). By using the analysis of variance (ANOVA), the interaction and relationship between the process factors (BC and AE) within the responses (compressive strength (CS) and healing efficiency (HE)) were determined. The R^2 has been used to measure the quality of the quadratic prediction model. In order to assess the model terms, confidence level at 95 % of the probability (*P*-value) and 5 % significance level of statistical significance test (*t*-test) indicating ($P < 0.05$) were used. Based on the CCD as shown in Table 3, the mathematical prediction equations were developed. The results obtained from experiments were evaluated as (*Y*) (2) in a function of BC (cfu/ml) and AE (%).

These are calculated as the sum of a constant, two first-order effects (terms in B_C and A_E), one interaction effect ($B_C A_E$), and two second-order effects (B_C^2 and A_E^2) based on Eq. (1). The insignificant terms were excluded to modify the performance of the prediction equations. To establish the prediction model of the compressive strength and healing efficiency, the response average on 60th day was used.

The ANOVA results for the response compressive strength and healing efficiency parameters respectively were demonstrated at Tables 4 and 5. The P values less than 0.05 illustrate that all models were significant at the 5 % confidence level. Furthermore, the large P values for lack of fit (>0.05) for both responses demonstrate that the F value was not significant, implying significant model correlation between the variables and process responses [17].

The empirical relationship between the responses (CS and HE) and the variables is expressed by the following second-order polynomial Eqs. (3) and (4):

$$60\text{-Days strength} = 45.09569 + 1.11293 \times 10^{-10} B_C \\ + 0.70852 A_E - 0.098467 A_E^2 \tag{3}$$

$$60\text{-Days healing} = 33.30603 + 8.06897 \times 10^{-11} B_C + 2.36973 A_E \tag{4}$$

Table 4 Analysis of variance (ANOVA) for compressive strength

Response: compressive strength (60 days)						
Source	Sum of squares	df	Mean square	F value	p-value prob > F	
Model	411.59	5	82.32	53.33	<0.0001	Sign.
B_C (cfu/ml)	55.82	1	55.82	36.16	0.0005	Sign.
A_E (%)	305.31	1	305.31	197.79	<0.0001	Sign.
A_E^2	34.71	1	34.71	22.48	0.0021	Sign.
Residual	10.81	7	1.54	–	–	–
Lack of fit	2.67	3	0.89	0.44	0.738	Not sign.
Pure error	8.13	4	2.03	–	–	–
Cor total	422.4	12	–	–	–	–

Table 5 Analysis of variance (ANOVA) for healing efficiency

Response: healing efficiency (60 days)						
Source	Sum of squares	df	Mean square	F value	P-value prob > F	
Model	3560.9	5	712.18	146.53	<0.0001	Sign.
B_C (cfu/ml)	294	1	294	60.49	0.0001	Sign.
A_E (%)	3220.2	1	3220.2	662.53	<0.0001	Sign.
Residual	34.02	7	4.86	–	–	–
Lack of fit	19.22	3	6.41	1.73	0.2982	Not sign.
Pure error	14.8	4	3.7	–	–	–
Cor total	3594.9	12	–	–	–	–

Table 6 Model validation for both responses

	Compressive strength (MPa)	Healing efficiency (%)
Std. dev.	1.24	2.2
Mean	45.28	68.92
Coefficient of variance	2.74	3.2
Press	34.28	163.85
R^2	0.9744	0.9905
Adjusted R^2	0.9561	0.9838
Predicted R^2	0.9188	0.9544
Adequate precision	24.129	40.282

Aldahdooh et al. [17] reported that a high R^2 value close to 1, is satisfactorily desirable with the adjusted R^2, indicating a satisfactory adjustment of the quadratic model to the experimental data. The adequate precisions were 24.129 and 40.282 for both responses, which were higher than 4 indicating a desirable model for predicted value and confirm that the predicted models can be used to navigate the design space defined by the CCD. Generally, the models can be considered a reproducible model if its coefficient of variance is less than 10 % [18]. By referring to Table 6, the reproducibility of both models was successful.

Figure 3 presented diagnostic plots, such as the normal plot of residual and the predicted versus actual values plot. The diagnostic plots aid in judging the model's adequacy and satisfactoriness [17, 18]. The predicted versus actual values plots and the normal plots of residual are shown in Fig. 3A(a) and B(a), respectively, for compressive strength, and Fig. 3A(b) and B(b), respectively, for healing efficiency. Figure 3a shows that the predicted values of both responses (compressive strength and healing efficiency) from the models with the observed values are well accorded. In addition, satisfied result was obtained on the constructing plots of studentized residual versus the normal % of probability (Fig. 3B). The results were achieved by approximation of compressive strength and healing efficiency residual plots to the straight lines. Therefore, the design space can be navigated using both predicted models.

3.1.5 Process Analysis

The comparative effect of BC (cfu/ml) and AE (%) on intensifying the compressive strength and healing efficiency was clarified by the perturbation plots as shown in Fig. 4A(a) and (b), respectively. In comparison of curvature for AE (B, %) and BC (A, cfu/ml), AE (B, %) curves are much sharper in both the tests (compressive strength and healing efficiency), showing that compressive strength and the healing efficiency were more responsive to AE (%) in this mortar mix design.

Furthermore, the 3D surface response plots are used to demonstrate the effects of the experimental conditions of BC (cfu/ml) and AE (%) on compressive strength

(A)

(B)
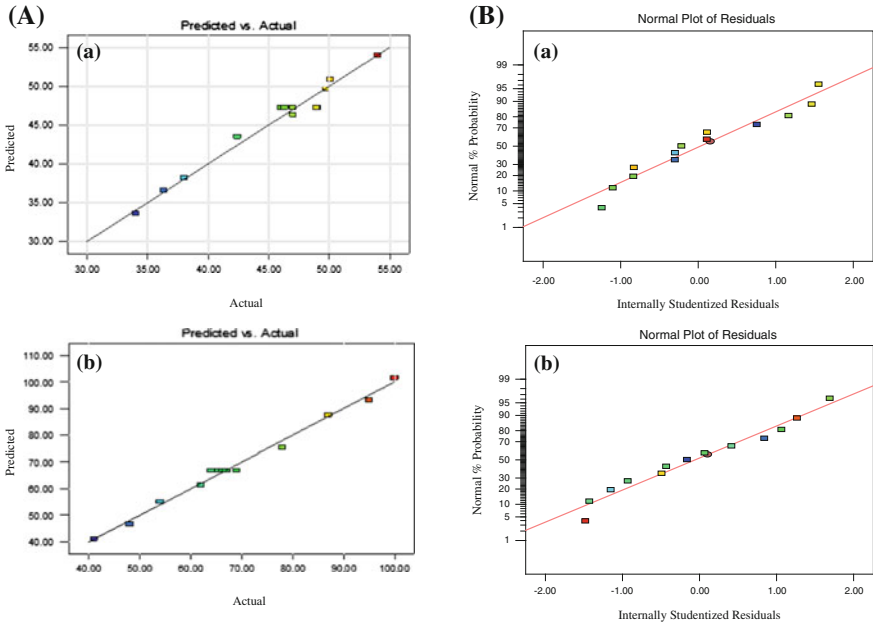
Fig. 3 **A** Diagnostics plots, predicted versus actual values plot for **a** compressive strength (MPa) and **b** healing efficiency (%); **B** normal plot of residual for **a** compressive strength (MPa) and **b** healing efficiency (%)

(A)

(B)
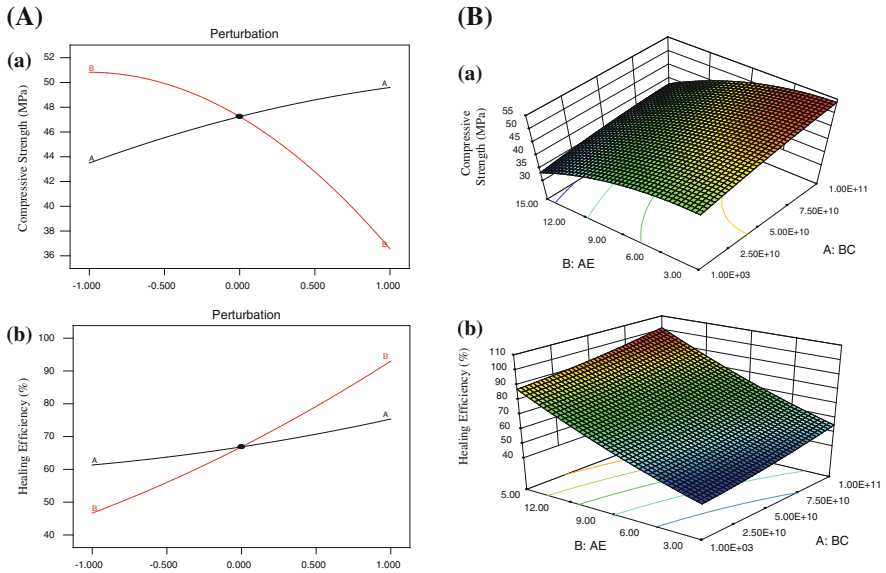
Fig. 4 **A** Perturbation plots for **a** compressive strength (MPa) and **b** healing efficiency (%); **B** response surface plots **a** compressive strength (MPa) and **b** healing efficiency (%)

and performance of healing efficiency as shown in Fig. 4B(a) and (b), respectively. The figures show that by increasing the replacement levels of AE (%), the compressive strength was decreased while it enhanced the healing efficiency of alginate-encapsulated *Geobacillus stearothermophilus* mortar.

Figure 4B(a) shows that the fitting ranges of AE (%) for enhancing the compressive strength should be in the range of 3–9 %. In addition, Fig. 4B(b) shows that the highest healing efficiency (100 %) was observed at 1×10^{11} (cfu/ml) and of 15 % AE (%). Due to the fact that higher healing efficiency indicates lowest compressive strength. The optimize value was analyzed by RSM.

3.1.6 Optimization by Multiple Response

It is noticed that compressive strength was more responsive to AE (%) based on observation at Fig. 4. The highest compressive strength was associated with the lowest HE (%) at 3 % in this mixing procedure. Design–Expert software was used for maximizing the BC (cfu/ml) and keeping the AE (%) within the range, taking into consideration the healing efficiency that derived by higher replacement of AE (%) into mix design.

To find the process variables, the equations of the model were solved simultaneously. Figure 5 shows the ramp function graph of BC (cfu/ml) and AE (%) for optimum compressive strength and healing efficiency and the prediction based on desirability function of 0.678 at the optimum condition. The BC (cfu/ml) was 10×10^{10} cfu/ml and AE (%) was 9.96 % with 48.2474 MPa of the compressive strength and 79.1201 % healing efficiency, respectively.

Using value of 10×10^{10} cfu/ml (BC) and 9.96 % (AE), the mixing batch was designed accordingly as in Table 7. The compressive strength samples were tested after 60 days where the average gained compressive strength was up to 47.9 MPa
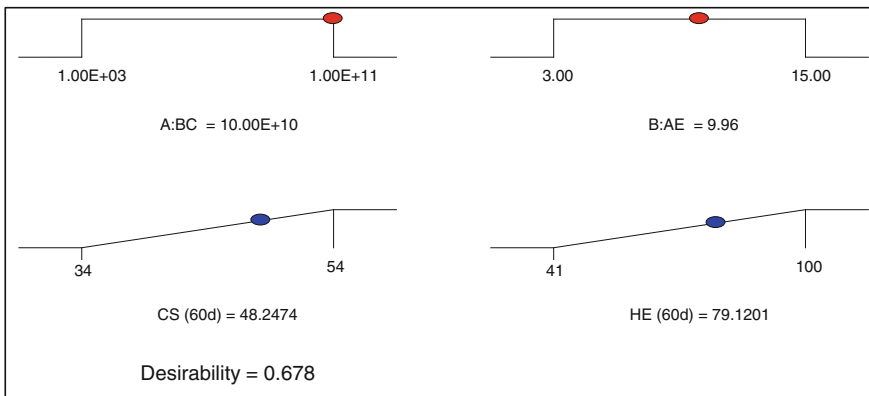
Fig. 5 Ramp function graph for the BC (cfu/ml) and AE (%) for optimum compressive strength at 60 days and healing efficiency

Table 7 Detail of the optimal AE-GS mix proportion and properties based on RSM

| | AE-GS (%) | BC (cfu/ml) | Alginate-encapsulation | | | | | Mortar | | | Σ Total weight (kg) |
			dH$_2$O (ml)	Sodium alginate (gram)	Urea (ml)	Yeast extract (ml)	Calcium lactate (ml)	Cement (kg)	Sand (kg)	Water (liter)	
Composition (kg/m^3)	9.96	10×10^{10}	3418	66	263	263	438	10	30	5	44.4
Time 60 days											

Table 8 Optimum response results from the model prediction and laboratory experiments

Compressive strength				Healing efficiency			
Observed	Predicted	Error (%)	Desirability	Observed	Predicted	Error (%)	Desirability
47.9	48.3	0.83	0.678	78.5	79.1	0.76	0.678

and the healing efficiency was up to 78.5 % as described in Table 8. By referring on the model prediction and laboratory experiment in Table 8, good agreement of the responses values were obtained. The good agreement was approved as the reliability of the optimum combination and the accuracy of the model. The compressive strength and healing efficiency predicted values were 48.3 MPa and 79.1 %, respectively.

4 Conclusions

The optimum bacteria cell concentrations were 10×10^{10} cfu/ml and replacement rate at 9.96 % of alginate cell composition shall be used to obtain maximum healing capacity without neglecting the properties of mortar. The best optimum rate for compressive strength and healing efficiency were given at 48.3 MPa and 79.1 %, respectively. The response values obtained for compressive strength and healing efficiency were 47.9 MPa and 78.5 %, respectively.

There are many factors to determine the capacity of bacteria in self-healing concrete. The selection of bacteria having capability to thrive in concrete harsh environment is vital to ensure its longevity by capability on producing endospore. In the other hand, the specialty of bacteria to evolve by mutation process if favorable conditions change might incur new bacterial properties that are time consuming to study its new behavior . *Geobacillus stearothermophilus* was successfully encapsulated into sodium alginate gel beads to form alginate-encapsulated *Geobacillus stearothermophilus* (AE-GS). The benefit of using AE-GS into mortar was demonstrated by improvement on healing efficiency in the amount on crack filling and strength.

The response surface method is a reliable tool in designing, mathematical modeling, statistical testing, and optimization of the maximum replacement levels of alginate-encapsulated *Geobacillus stearothermophilus* to develop an autogenous healing mortar. Theoretically, the type of bacteria used in the recent study has shown promising result in healing capacity. Higher concentration of bacteria produces maximum healing effect as compared to lower concentration, but due to the size of the AE-GS being produced, the unification of both bacterial concentration and nutrient sources in AE-GS influence the outcome result of healing efficiency. This can be seen that higher concentration of bacteria does not really develop results as desired. Therefore, the usage of RSM for optimization was needed.

The present investigation shows that the compressive strength is largely dependent on the replacement of AE-GS into mortar. Higher strength is obtained on the lowest replacement of AE-GS. The amount of microcapsules was observed giving the best result at the addition of 3 % where the same condition occurs by higher replacement of AE-GS into mortar. By increasing the replacement of AE-GS content, the strength was decreased as compared with the design strength. This condition occurred due to the fact that AE-GS is neither a supplementary cementitious material (SCM) nor natural pozzolans. Hence, the reduction of strength was expected earlier. However, the contradiction of result occurs with higher replacement of AE-GS capable to induce higher degree of healing that can clearly be seen through crack filling and closure of the crack path.

As *Geobacillus stearothermophilus* is a new type of bacteria being explored as a self-healing inducer, further investigation need to be carried out in order to explore the potential of *Geobacillus stearothermophilus.* In summary, the positive potential of *Geobacillus stearothermophilus* with sodium alginate gel beads offers an interesting approach for crack remediation technique using autogenous healing concept.

References

1. S. Krishnapriya, D. L. Venkatesh Babu, and G. Prince Arulraj, "Isolation and identification of bacteria to improve the strength of concrete," *Microbiological Research,* vol. 174, pp. 48–55, 16/03/2015 2015
2. H. M. Jonkers and E. Schlangen, "Development of a bacteria-based self healing concrete," *Proc. int. FIB symposium,* vol. 1, pp. 425-430, 2008.
3. N. Chahal, R. Siddique, and A. Rajor, "Influence of bacteria on the compressive strength, water absorption and rapid chloride permeability of fly ash concrete," *Construction and Building Materials,* vol. 28, pp. 351–356, 2012.
4. P. R. Patel and S. K. Patel, "Microbial Concrete: The Pioneering Work On Repairing Concrete," *International Journal of Pharmaceutical Sciences and Research* vol. 2, pp. 825–828, 2011.
5. S. K. Annamalai, K. D. Arunachalam, and K. S. Sathyanarayanan, "Production and characterization of Bio Caulk by Bacillus pasteurii and its remediation properties with carbon nano tubes on concrete fractures and fissures," *Materials Research Bulletin,* vol. 47, pp. 3362–3368, 2012.
6. V. Achal and X. Pan, "Characterization of Urease and Carbonic Anhydrase Producing Bacteria and Their Role in Calcite Precipitation," *Current Microbiology,* vol. 62, pp. 894–902, 01/03/2011 2011

7. J. Y. Wang, D. Snoeck, S. Van Vlierberghe, W. Verstraete, and N. De Belie, "Application of hydrogel encapsulated carbonate precipitating bacteria for approaching a realistic self-healing in concrete," *Construction and Building Materials,* vol. 68, pp. 110–119, 10/15/2014

8. J. Wang, N. De Belie, and W. Verstraete, "Diatomaceous earth as a protective vehicle for bacteria applied for self-healing concrete," *Journal of Industrial Microbiology & Biotechnology,* vol. 39, pp. 567–577, 2012.

9. W. De Muynck, K. Verbeken, N. De Belie, and W. Verstraete, "Influence of urea and calcium dosage on the effectiveness of bacterially induced carbonate precipitation on limestone," *Ecological Engineering,* vol. 36, pp. 99–111, 2010.

10. W. De Muynck, D. Debrouwer, N. De Belie, and W. Verstraete, "Bacterial carbonate precipitation improves the durability of cementitious materials," *Cement and Concrete Research,* vol. 38, pp. 1005–1014, 2008.

11. S. Sunil Pratap Reddy, M. V. Seshagiri Rao, P. Aparna, and C. Sasikala, "Performance of ordinary grade bacterial (Bacillus subtilis) concrete," *International Journal of Earth Sciences and Engineering,* vol. 3, pp. 116–124, 2010

12. G. McMullan, J. M. Christie, T. J. Rahman, I. M. Banat, N. G. Ternan, and R. Marchant, "Habitat, applications and genomics of the aerobic, thermophilic genus Geobacillus," *Biochemical Society Transition,* vol. 32, 2004

13. T. Watanabe, S. Furukawa, J. Hirata, T. Koyama, H. Ogihara, and M. Yamasaki, "Inactivation of Geobacillus stearothermophilus Spores by High-Pressure Carbon Dioxide Treatment," *Applied and Environmental Microbiology,* vol. 69, pp. 7124–7129, December 1, 2003

14. D. R. Zeigler, "The Geobacillus paradox: why is a thermophilic bacterial genus so prevalent on a mesophilic planet?," *Microbiology,* vol. 160, pp. 1–11, January 1, 2014

15. H. M. Jonkers, A. Thijssen, G. Muyzer, O. Copuroglu, and E. Schlangen, "Application of bacteria as self-healing agent for the development of sustainable concrete," *Ecological Engineering,* vol. 36, pp. 230–235, 2010.

16. R. Rhea and W. O. Andres, "Application of Response Surface Methodology : Optimum Mix Design of Concrete with Slag as Coarse Aggregate," *DLSU Research Congress 2014,* 6–8 March. 2014

17. M. A. A. Aldahdooh, N. Muhamad Bunnori, and M. A. Megat Johari, "Development of green ultra-high performance fiber reinforced concrete containing ultrafine palm oil fuel ash," *Construction and Building Materials,* vol. 48, pp. 379–389, 2013.

18. M. A. A. Aldahdooh, N. Muhamad Bunnori, and M. A. Megat Johari, "Evaluation of ultra-high-performance-fiber reinforced concrete binder content using the response surface method," *Materials & Design,* vol. 52, pp. 957–965, 2013.

Discovery of Used Cooking Oil as Foaming Agent Admixture for Lightweight Foamed Concrete

M.M.A. Hafiz, A.R. Mohd Ridzuan, M.A. Fadzil and J. Nurliza

Abstract This study is to observe the ability and potential of used cooking oil as foaming agent admixture in lightweight foamed concrete. The intention is to utilize the waste materials derived from food industry which is known as used cooking oil. Due to this aim, several scientific observations and testings should be performed in order to observe the morphology of used cooking oil foam and used cooking oil foamed concrete. Other physical test has been performed to measure the viscosity and stability of used cooking oil foam. From the result, the morphology of used cooking oil foam was well developed and able to show their foam characteristic. Meanwhile, to compare the treated used cooking oil also having the viscosity value of about 88 cP which is proven to have good foam ability behaviour. Apparently the viscosity value of this used cooking oil showed that it had good stability compared with cooking oil foam.

1 Introduction

Cooking oil is the main component in food production, especially for fried food. In Malaysia, the use of palm oil in cooking activities is quite popular. It is believed that, abundant supply of palm cooking oil is to induce the food industries and production [1]. Since there is an increase in food production, the use of palm oil is

M.M.A. Hafiz (✉) · A.R. Mohd Ridzuan · M.A. Fadzil · J. Nurliza
Institute of Infrastructure Engineering and Sustainable Management (IIESM)
Faculty of Civil Engineering, Universiti, Teknologi MARA,
40450 Shah Alam, Selangor, Malaysia
e-mail: mohdhafizmdali@gmail.com

A.R. Mohd Ridzuan
e-mail: ruslanridzuan@yahoo.co.uk

M.A. Fadzil
e-mail: fadiil2013@yahoo.com

J. Nurliza
e-mail: nurlizajasmi@salam.uitm.edu.my

also increased. Due to this reason, the waste product also keeps increasing. The waste produced from the frying activities is so-called used cooking oil that is forever a portion of the waste that has to be discarded. In line with the reuse of used cooking oil, this waste product is familiarly involved with fuel engine combustion. One of this study's intentions to utilize the waste of used cooking oil to become others new becomes green product is significant. To be particular, in this study, the aims are to observe the morphology characteristic of the foam produced by utilizing used cooking oil. The foam generally is thermodynamically unstable and usually influent with the drainage effect due to the gravity attraction [2]. Other than that, the coalescence makes the foam rupture and collapses to become liquid form. This situation makes the foam structure become less stable and easy to self-denature in foam structure. Another factor such as chemical added, the viscosity of the solution, mechanical forces, type blowing agents and type of surfactants also contribute to the stability and foamability of foam [3]. The constancy of the foam can be measured by cylindrical method and the viscosity is considered as major ingredient that finds out the foam stability.

2 Materials

The several raw materials required in this study such as used cooking oil, cooking oil, blowing agent, binder ordinary Portland cement, OPC, fine silica sand, water where the materials important to fulfil this study's aims and objectives. The main material was used cooking oil that was needed for the making of used cooking oil foaming agent. Used cooking oil was collected at nearest restaurant within Seksyen 7 Shah Alam.

3 Method

3.1 Treatment

First step for used cooking oil to become foam is formulation. Since used cooking oil contains a lots of impurities such as debris, solid, lipids and oxide materials, a treatment is required to treat used cooking oil to reduce the impurities and favourable to proceed for foam formulation. This task of treating the used cooking oil is known as filtration process. The process is done by double filtration as function to separate the impurities from used cooking oil.

3.2 Formulation

The treated used cooking has been collected and made ready to be formulated to become foaming agent. For foam formulation, the blowing agent is required to induce the entrapment gas production. This blowing agent is alkaline-based and will react with used cooking oil with the presence of water. The reaction between blowing agent and used cooking oil produces bubbles and then it produces more bubbles until the foamy structure forms.

3.3 Morphology Observation

The foam structures will determine the characteristic of the foam. This morphology observation was done by light microscope (model OLYMPUS CH20). The sample of the foam will be placed into the petri dish and then directly observed under light microscope. The camera for capturing the image has been installed at the top of the microscope's lens. Magnification of this microscope is 10× and remains constant for entire observation.

3.4 Viscosity Measurement

Viscosity is the other factor that will influence the stability and foamability of the foam. The value of viscosity of used cooking oil will be measured by Viscometer DV-I-Prime BROOKFIELD. The viscosity measured by this equipment is in centipoise cP unit. One sample of used cooking oil will be continued with different rpm starting from 10 until 100. The time taken of three different times (minute) have been selected. Lastly, the average result of viscosity will be calculated and tabulated in table form.

3.5 Stability Measurement of Used Cooking Oil and Cooking Oil Foam

The stability of foam from used cooking oil will be measured using cylindrical measurement. This examination has been performed to measure two types of foams that were derived from used cooking oil foam and was compared with palm oil cooking foam. This experiment of stability testing starts at time (m) zero until the measurement of the foam volume in mL gets constant reading

4 Result and Discussion

4.1 Treatment of Used Cooking Oil

Untreated used cooking oil is difficult without treatment process due to presence of impurities. These impurities are strictly to be removed to ensure that the only component of used oil could be the main ingredient instead of other materials such blowing agent and water. The presence of impurities will disturb the reactions and makes the foam become less stable. In order to prevent all the possible impurities that might interfere during the formulation process of used cooking oil foam, treatment by filtration is the best way and most economical. Figure 1 shows the untreated used cooking oil and treated used cooking oil. Apparently, untreated used cooking oil is yellow-dark in colour. Whereas, treated used cooking oil is darker compared with untreated. The presence of yellowish colour in untreated might due to the high concentration of lipid compounds and greases that resulted from the food preparation.

Figure 1 shows picture of untreated used cooking oil (left) ant treated used cooking oil after treatment (right).

4.2 Formulation Used Cooking Oil Foam

For ensure that the used cooking oil becomes foam, blowing agent is needed to induce the foamability of this foam. Treated used cooking oil plays an important role for this formulation instead of adding several chemical into the solution. The reaction between used cooking oil and blowing agent was initiated by the presence
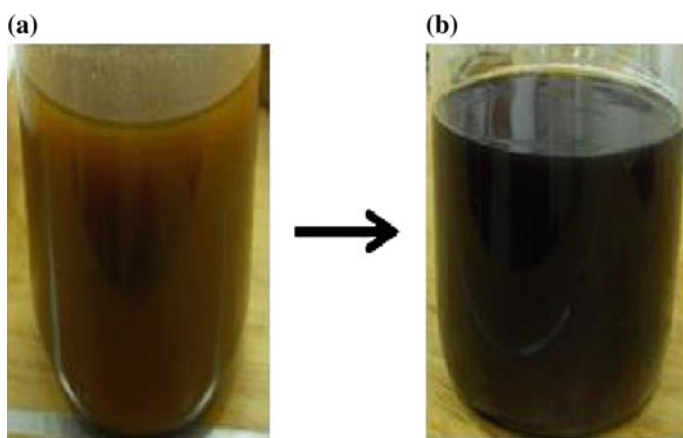
Fig. 1 The changes of untreated used cooking oil (**a**) and (**b**) treated used cooking oil

of water. Water will help the effectiveness of blowing agent to react with lipid and others compounds present in treated used cooking oil. Figure 2 shows the process of formulation of used cooking oil foaming agent that will function as an admixture in lightweight concrete. The unique characteristic of this foam is self-rising foam. Here, the usage of machinery was not required and energy consumption starts reducing. This is to promote the invention of environmental friendly and green products (Fig. 3).

4.3 Morphology Observation

Foam is produced from single bubble that emerges with others bubbles to form one structure of foam. This continues to form the structure of foam that makes it stable

Fig. 2 The transition of used cooking oil begin formulated become foam

Fig. 3 The morphology structure of used cooking oil foam by using light microscope at ×10 magnification
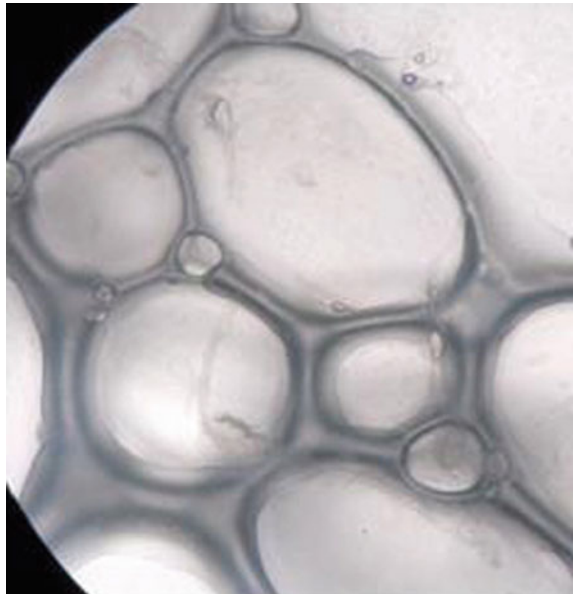
and rigid. The connection from one bubble to other bubble will form bond among each bubble that is known as plateau border [4]. Structure of foam is formed due to the assembling of surfactant that line up toward each other to become rigid structure until the foam structure is shaped. This is where the concentration of surfactant plays important role in determination of stability of foam achieved [5]. The void in the middle of the foam is filled by air to ensure that the foam is lighter and much in volume. Several phenomena were identified which have contributed to the stability of the foam such as drainage effect and coalescence [6]. The shape of single structure of foam is considered as polygonal and some have hexagonal structural. The shape of single foam structure is one of the other factors that will be contributed to the foam stability.

4.4 Viscosity Measurement

Viscosity is one of the factors to be concerned in order to achieve stable foam. This special foam is being utilized as used cooking oil in which the viscosity is the main factor that contributes to the stable foam. From the basic theory that has been stated the high viscosity will contribute to the foam stability and foamability. Due to this reason, viscosity measurement of treated used cooking oil is required. Table 1 shows that the highest revolution per minute, rpm was contributed to the highest viscosity value, centipoise cP within minute of time. Results for rpm 10 showed the highest viscosity value which is 125 centipoise cP and the lowest viscosity value is 71 centipoise cP at 50 rpm. This experiment was conducted in laboratory under room temperature (21 °C ± 2). Whereas, the viscosity of waste cooking oil measured by Chhetri et al. [7] is 72 mm^2/s at room temperature (Table 1).

4.5 Stability Measurement of Used Cooking Oil and Palm Cooking Oil Foam

The stability of used cooking oil and palm cooking oil has been done by cylindrical method. This method is to measure the expansion of the foam starting from zero 0th

Table 1 The tabulated data from the viscometer of used cooking oil sample

Time (minute)				
RPM	1	2	3	Centipoises (cP)
10	125	125	125	125.00
20	87.5	87.5	87.5	87.50
50	71	71	71	71.00
100	68.5	68.5	68.5	68.50
Total average				88.00

time (minute) until it gets stable and remains constant in volume. Both treated used cooking oil and palm cooking oil have been measured and for the result is shown in Fig. 4 as the volume (mL) versus time (minute). Apparently, as shown in the graph plotted start time is zero until at 60 min both foam.

That vigorously gets reacted with blowing agent and in the presence of water.

The bubbling keeps increasing until the volume of foam was expanded to the max. The expansion of the foam was showed for the optimum at time 60 for both type of foam. The maximum volume for used cooking oil foam is 400 mL and 200 mL. Reflect to the theory of viscosity and its viscosity value, used cooking oil was the highest viscous compared to palm cooking oil. Meaning that, the most viscous will be contributed to the most stable foam. The foam shows the stable foam when it remains constant in volume at time 60. Whereas, cooking oil foam is identified as less stable when it starts decreasing in volume after time 60. This is due to the drainage effect by gravity. The cooking oil foam collapsed when the time was increased. The volume of cooking oil foam kept decreasing and remained constant at time 120.

5 Application of Cooking Oil Foaming Agent in Concrete

Foam derived from this method has been applied as admixture in the production of lightweight foamed concrete. The foamed concrete could vary in it properties and the strength depends on the mix proportion that has been designed and the target strength. Somehow, the percentage of the Fuscof to be added is by volume which in order induces the air entrainments in foamed concrete (Fig. 5).

Fig. 4 The graph of volume (mL) versus time (minute) for stability measurement of used cooking oil and palm cooking oil foam
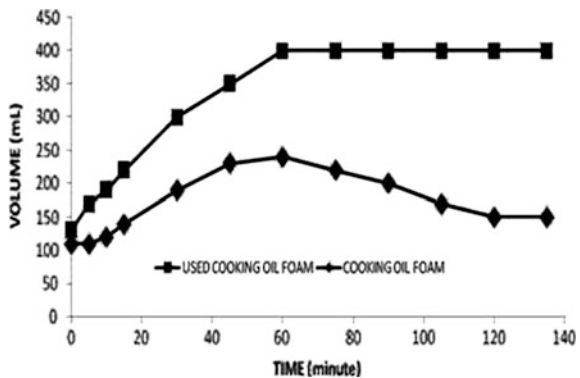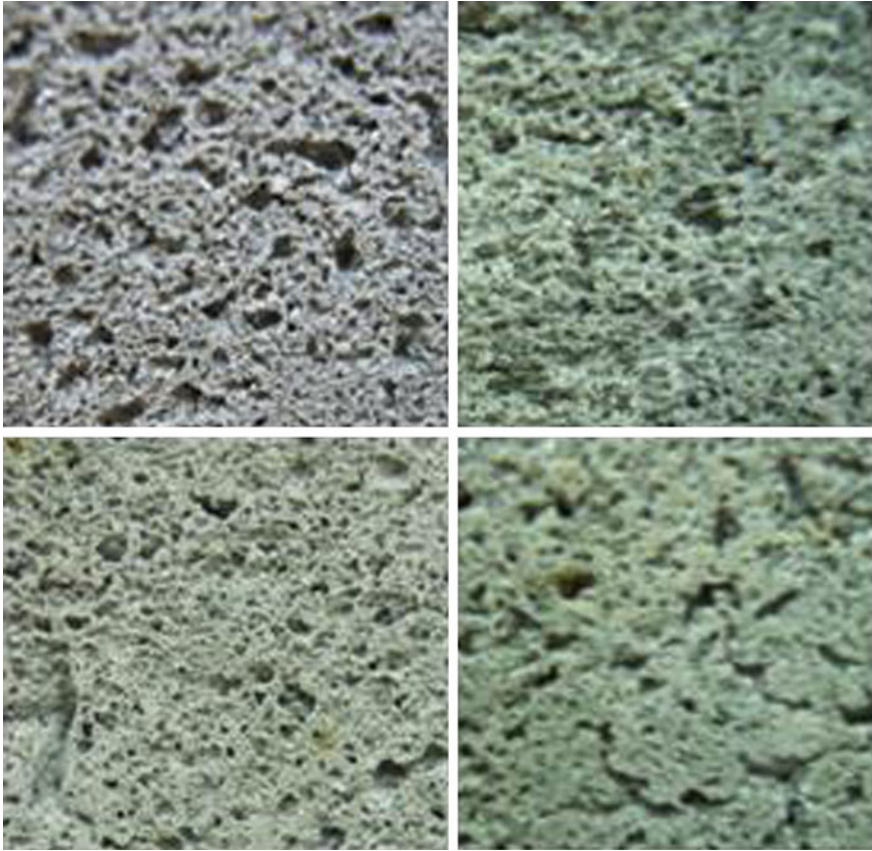
Fig. 5 The used cooking oil foamed concrete that has been added as mixture in the application of lightweight foamed concrete

6 Summary

In general, the used cooking oil was proven to have a potential to become foaming agent admixture in lightweight foamed concrete. This foaming agent was shown to have good stability and foamability behaviour. Moreover, this foaming agent has unique characteristic which is self-rising, cost effective, green product and environmental friendly.

References

1. R. Tanaka, S. Hirose, and H. Hatakeyama, "Preparation and characterization of polyurethane foams using a palm oil-based polyol.," Bioresour. Technol., vol. 99, no. 9, pp. 3810–6, Jun. 2008.
2. W. Xie, S. J. Neethling, and J. J. Cilliers, "A novel approach for estimating the average bubble size for foams flowing in vertical columns," Chem. Eng. Sci., vol. 59, no. 1, pp. 81–86, Jan. 2004.
3. W. Drenckhan and D. Langevin, "Monodisperse foams in one to three dimensions," Curr. Opin. Colloid Interface Sci., vol. 15, no. 5, pp. 341–358, Oct. 2010
4. O. Pitois, C. Fritz, and M. Vignes-Adler, "Liquid drainage through aqueous foam: study of the flow on the bubble scale.," J. Colloid Interface Sci., vol. 282, no. 2, pp. 458–65, Feb. 2005.
5. L. K. Shrestha, R. G. Shrestha, S. C. Sharma, and K. Aramaki, "Stabilization of nonaqueous foam with lamellar liquid crystal particles in diglycerol monolaurate/olive oil system.," J. Colloid Interface Sci., vol. 328, no. 1, pp. 172–9, Dec. 2008.
6. a. Saint-Jalmes, M.-L. Peugeot, H. Ferraz, and D. Langevin, "Differences between protein and surfactant foams: Microscopic properties, stability and coarsening," Colloids Surfaces A Physicochem. Eng. Asp., vol. 263, no. 1–3, pp. 219–225, Aug. 2005
7. A. B. Chhetri, K. C. Watts, and M. R. Islam, "Waste Cooking Oil as an Alternate Feedstock for Biodiesel Production," Energies, vol. 1, no. 1, pp. 3–18, Apr. 2008.

Monitoring of Precast Prestressed Concrete Beam due to Static Load by Using Pundit Equipment

Nurul Huda Suliman, Afidah Abu Bakar and Siti Hawa Hamzah

Abstract The vast growt of population now increases the usage of buildings and infrastructures especially for concrete bridge. Prestressed concrete was introduced to be used in most concrete bridge superstructures. Predetermination of concrete strength ensures the condition of precast prestressed concrete structures. Testing of precast concrete is crucial in order to find its capabilities before commencing construction. Conventional method of testing usually takes a lot of time and is very costly. The aim of this study is to find the speed of the sound wave passing through the precast prestressed concrete beam. This study also identifies the shear modulus and the elastic modulus of precast prestressed concrete beam after the application of bending test on the two rectangular beams of 4 m length each. The test result indicates the condition of the beam, before and after loading condition. The ultrasonic pulse velocity (UPV) method is an ideal tool to show whether concrete structure is in good condition. This method can be used for those still been constructed and on existing structures. Interpretation of velocities using UPV method could easily determine the grading in terms of its uniformity and strength. The velocities indicate the occurrence of voids inside the beam which relates to the tendency of initial failure. Decreases in ultrasonic waves speed over time can reveal the onset of damage before visible deficiencies become evident. This allows inspectors and engineers to implement repair recommendations before minor deficiencies become safety hazards.

Keywords Monitoring · Prestressed concrete · Beam · Ultrasonic pulse velocity · Static load

N.H. Suliman (✉) · A.A. Bakar · S.H. Hamzah
Faculty of Civil Engineering, Universiti Teknologi MARA, Shah Alam, Malaysia
e-mail: huda_4606@yahoo.com

A.A. Bakar
e-mail: afida334@salam.uitm.edu.my

S.H. Hamzah
e-mail: shh@salam.uitm.edu.my

1 Introduction

Conventional destructive testing is very costly and time consuming. A flexural test on a big beam requires construction of it and after that destruction. In order to reduce the cost and time in doing data gathering for engineering purpose, ultrasonic pulse velocity is introduced [1, 2]. This nondestructive method will enable assessing the prestressed concrete beams without damaging it and faster than conventional destructive method.

Often engineers decide whether the material used is according to specification needed. The higher the specification needed the more risk that an engineer has to evaluate especially in terms of strength and durability. The uniformity of a prestressed concrete beam could be determined by using ultrasonic sound wave where the voids, placements of aggregates, and tendons in concrete will be visible via wave's velocities. The difference in sound wave velocities may locate these elements inside the prestressed concrete beams. The velocities will indicate the occurrence of voids which greatly influence the condition of concrete [3].

Monitoring and maintaining covers on the ways of detections of problems which often seen after failure are initiated. Often the structures such as bridge will only undergo checking after large failure is seen. The condition of any structures in terms of its strength and durability can be checked regularly without getting the structures to fail first [4]. These parameters such as shear modulus and elastic modulus can be determined by using ultrasonic pulse velocity testing.

Therefore, this research study carried out to determine uniformity of precast prestressed concrete beam and shear modulus before and after flexural test.

1.1 Objectives of Study

The main objective of this study is to determine the velocity of which the pulses moving from one point to another. From this analysis, the velocities will determine the uniformities of unloaded prestressed concrete beam, the determination of shear modulus in precast prestressed concrete beam under static load, and the determination of its elastic modulus with the relationship of shear modulus and Poisson's ratio, v.

The approach of this study is to use the static load testing results and to find the connection between those results of statics to the need of implementing them into the shear modulus and elastic modulus formulas in order to obtain the study's objectives.

The two beams underwent static load tests in order to get the prior velocities and after fracture velocities. The location of failure was estimated by the difference of prior velocities and after velocities comparison.

The Poisson's ratio, v is taken as 0.2 for uncracked concrete while the density of concrete is 2400 kg/m^3 [5].

Calculation of the shear modulus, G:

$$G = r \times V^2 \tag{1}$$

where, V = velocity in m/s.

Calculation for Elastic Modulus, E:

$$E = 2G \times (1 + v). \tag{2}$$

1.2 Scope of Study

The specimens are two identical prestressed concrete beams, having the same concrete cross section, span length, prestressed strands of tendons, and its purposes of loading arrangements [6]. The dimensions of the beams are shown in Figs. 1 and 2.

The design of specimens used is not the ordinary design where the depth of beam is shorter than the width of it. This study will ensure that the performance and serviceability of this type of prestressed concrete beam are up to its standard need. In doing monitoring prestressed concrete beam due to static, the improvement of design emphasized on reducing cost will greatly help the construction industry of going forward.

The monitoring and data gathering using nondestructive test will ensure minimum wastage of materials and time consumption. The performance of the prestressed concrete beams based on its uniformity before testing, crack initiation
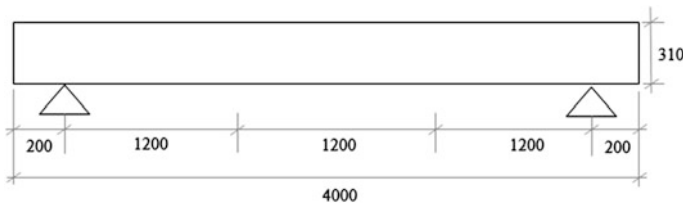
Fig. 1 Dimension of prestressed beam

Fig. 2 Cross section dimension
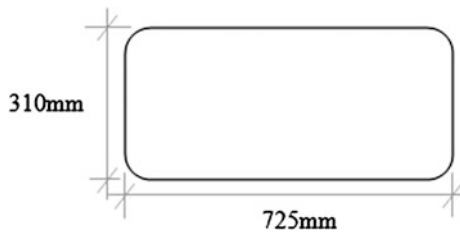
during and after testing will help in understanding more on its behavior, as well as the determination of its shear modulus and elastic modulus.

The limitation of using this equipment is the availability of only one in UiTM. The ability of translating the data from PUNDIT equipment is very critical for it to become reliable for interpretation.

2 Experimental Study

2.1 Testing Procedure

Both beams were assigned for constant amplitude loadings and both of these specimens were tested to obtain their respective load capacity after static loadings [6]. Ultrasonic pulse velocity equipment was used to obtain the variables needed to identify the uniformity before loadings and study of their respective cracks initiation and propagation.

The arrangement of the transducer will be placed directly facing the receiver on opposite surface on the specimen. The width of the beam is the distance between the transducers. The ultrasonic wave will be transferred directly and this will ensure maximum interaction between the transducer and receiver. These nine pre-decided surfaces location were cleaned and smoothened (See Figs. 3 and 4). It may be smoothened up by using carborundum stone. The surfaces were thinly pasted with petroleum jelly to ensure the maximum contact to the transducer and receiver [7].

Transducers were then pressed against the concrete surface and held manually. It is important that only a very thin layer of coupling medium separates the surface of the concrete from its contacting transducer. The distance between the measuring points should be accurately measured. Repeated readings of the transit time were observed until a minimum value was obtained.
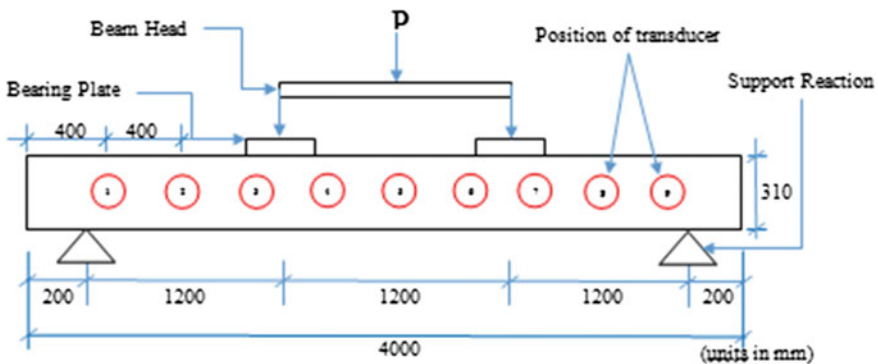
Fig. 3 PUNDIT testing points

Fig. 4 Transmitter and receiver transducer
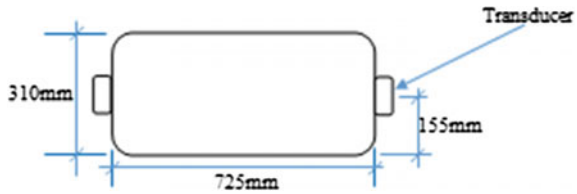
2.2 Data Collection

There were two data collections in this study, the first was taken prior before load was applied (i.e., no crack occurrence) and the other was taken after loading was applied on the sample. At the elevation of the beam (left and right), nine points for the transducer to be placed were marked with increment of 400 mm. After that, grease was applied on the transducer and on the points that were established earlier. Switch on the equipment (PUNDIT Plus) and the velocity measurement was selected. The path length was input into the equipment. The transducer was put at each point and at least three readings were taken to average the data. After that, the load was applied incrementally until 300 kN or until the crack length was not half of the height of the sample. Then, when the load was removed, the transducer was put back at each and again four readings were taken to average the data points.

3 Result

From the ultrasonic pulse velocity testing, the values of velocities were obtained for the determination of uniformity before the load testing and also to identify the location of cracks in the sample beams.

According to the uniformity level the sample is determined by the following Table 1.

3.1 Prior Velocity Before Bending Test

The results were used to determine the parameters of shear modulus and the elastic modulus. Velocities results from the unloaded beam are shown in Fig. 5, and then

Table 1 Quality of concrete as a function of UPV [8]

Pulse velocity by cross probing	Concrete quality grading
>4500	Excellent
3500–4500	Good
3000–3500	Medium
<3000	Doubtful
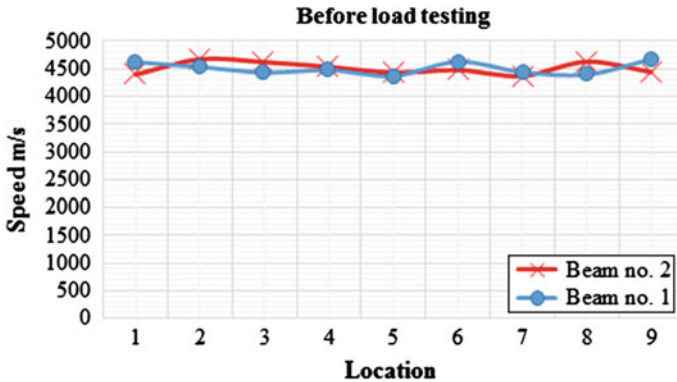
Fig. 5 UPV speed for beams before bending test

Table 2 Shear modulus and elastic modulus before loading

Point	1	2	3	4	5	6	7	8	9
G	49	51	50	49	47	50	47	49	50
E	117	122	118	117	112	119	112	117	120

the shear modulus and the elastic modulus were determined. Note that all shear modulus and elastic modulus are in GPa, see Table 2.

As an example, for point 1 of beam no. 1 (Fig. 5), the value of velocity, V is 4622.67 m/s Therefore,

$$G = 2400 \times 4623^2 \, \text{kg/m/s}^2 = 51.293 \, \text{GPa}$$

Then, the relationship of elastic modulus, $E = 2G(1 + v)$, where Poisson's ratio v is taken as 0.2:

$$E = 2 \times 51.293 \times (1 + 0.2) = 123.10 \, \text{GPa}$$

3.2 Subsequent Velocity After Bending Test

After the testing was done, the pattern of the crack initiation falls on the middle of those beams. The uniformity of the beams at both conditions was good except for the middle of the location of the crack.

The lower the speed of the velocities from, the UPVT showed the occurrence of cracks in terms of void enlargement and changes in transfer medium. Solid behavior of concrete provides better pulses medium than the air (voids and cracks). The velocity, shear modulus, and elastic modulus are shown in Fig. 6 and Table 3.
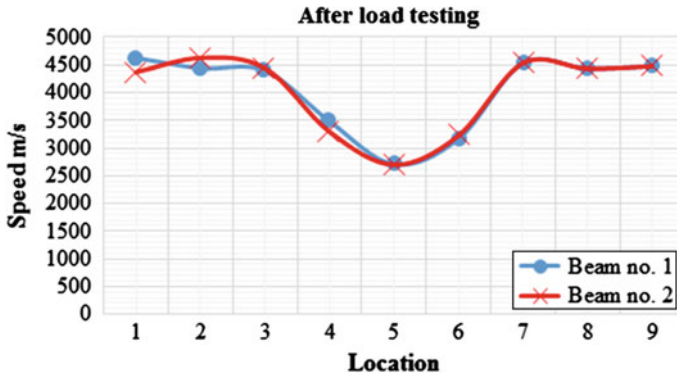
Fig. 6 UPV speed for beams after bending test

Table 3 Shear modulus and elastic modulus after loading

Point	1	2	3	4	5	6	7	8	9
G	49	49	47	28	18	25	49	47	48
E	117	117	112	66	42	59	117	113	116

3.3 Comparison

The average readings of velocities before and after the tests of beam are shown in the graph (Fig. 7).

From Fig. 8, it shows that the weakest strength of those beams were located at the middle of their spans. By taking the average of shear modulus, G before the loadings, the value is 48.837 GPa, while the failure shear modulus is taken at location 5 after loading which is 17.535 GPa.
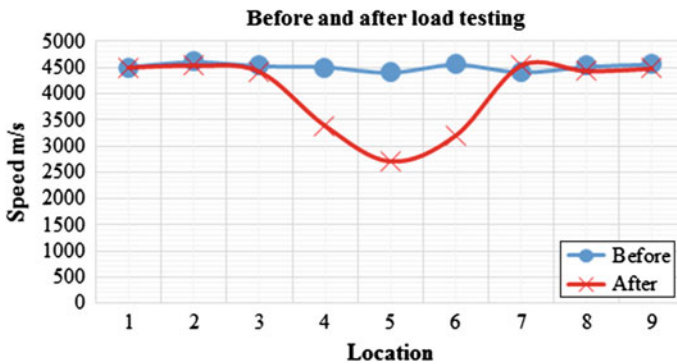
Fig. 7 Comparison of UPV speed for beams before and after bending test
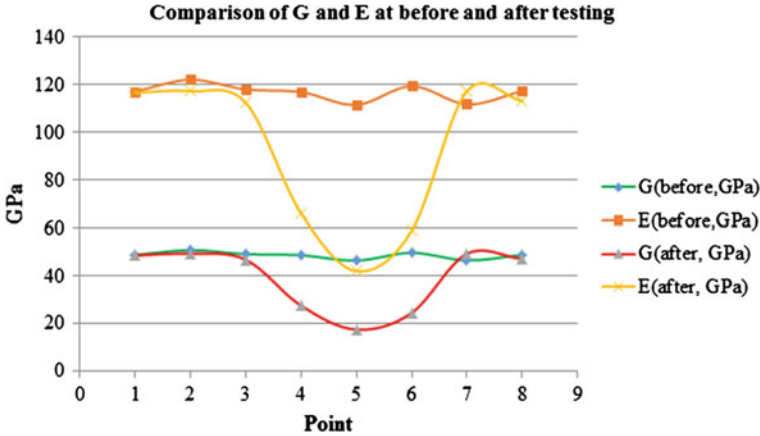
Fig. 8 Comparison of shear modulus and elastic modulus for beams before and after bending test

The value of elastic modulus, *E* is calculated by taking the average values of *E* before the loading, which is 117.21 GPa, while the failure elastic modulus is taken at location 5 after the loading which is 42.08 GPa.

4 Discussion

The grades of those unloaded beams were excellent in terms of its uniformity checking. The values are overall above 4500 m/s. This is due to the fact that those beams were well precasted and designed prestressed concrete. Factory made concrete structure with high grade of strength requires high uniformity to achieve its specifications.

The location of failure happened at the middle span of the beams because of the arrangement of simple supports. The maximum moment should occur at the middle span and the most probability of failure should always happen at the middle of span.

The cracks and voids inside the precast prestressed concrete beam were detected through the difference velocities. The quality of the precast prestressed concrete beam are compared where the concrete is good before loading but changed to doubtful quality when the beam failed after loaded. The relationship between velocities, Poisson ration, density, shear modulus, and elastic modulus were taken from Eurocodes.

According to Eurocodes, the value of elastic modulus of a C50 concrete grade is 30–35 GPa, while the value of steel strand of diameter 12.9 mm is 200 GPa. These values do not consider the composite relationship where the effect of bonding between steel strands and concrete. Taking the maximum value of elastic modulus as 200 GPa, this experiment should only reach 30–40 % of its value [5]. This value

is known as the static elastic modulus. So, for 40 % of 200 GPa, the value of static modulus is 80 GPa. From this experiment, the static elastic modulus is 117.21 GPa, so the value exceeds the normal G value by 32 %.

5   Conclusion

After doing this study, it can be concluded that the UPV method of testing could easily determine the velocities data required to achieve the objectives. Interpretation of velocities indicates the condition inside precast prestressed concrete beams even if crack cannot be seen. From this experimental study, the following conclusions are made.

The uniformity of precast prestressed concrete beam was determined and it showed that concrete had an excellent grade.

The shear modulus before and after testing identified which are 48.837 and 17.535 GPa, respectively.

The elastic modulus was determined by the relationship of shear modulus and Poisson's ratio which is 117.21 GPa. At cracked region, the elastic modulus dropped by 64.1 %.

References

1. ASTM C597-09, *Standard test method for pulse velocity through concrete*. West Conshohocken: ASTM Internasional, 2009
2. BS EN12504-4:2004, *Testing concrete. Recommendations for measurement of velocity of ultrasonic pulses in concrete*. BSI, 2004
3. B. Raj, T. Jayakumar, and M. Thavasimuthu, *Practical non-destructive testing*, Third edit. India: Alpha Science International Ltd., 2007.
4. F. Federal Highway Administration, "System Conditions," in *2010 Status of the Nation's Highways, Bridges and Transit: Conditions and Performance*, United States Department of Transportation, 2010, pp. 2–28
5. EN1992-1-1, "BS EN 1992-1-1:2004 Design of concrete structures - Part 1-1: General rules and rules for buildings," *Eurocode 2*, vol. 1, no. 2004, 2004
6. N. Huda, Afidah, S. Hawa, and Norliyati, "Bending Strength of Pre-tensioned (PRT) Concrete," 2009
7. M. Zaid, *Non-destructive testing of pre-stressed concrete beam by using portable ultrasonic non-destrictive difgital indicating tester*. Shah Alam: University Thesis, 2014
8. BS1881, *BS1881:Part 203, 1986: Recommendations for measurement of velocity of ultrasonic pulses in concrete*. London: British Standard Institution, 1986

Self-healing Shape-Memory Alloy (SMA) in Reinforced Concrete Structures: A Review

Nur Aliah Mohd Khairi, Hanizah Ab Hamid and Azmi Ibrahim

Abstract The presence of shape-memory alloy (SMA) in civil engineering fields was an eye-opener for researchers to develop better technology which can aid in various related aspects. The superiority of SMA over others is that it has a special capability where it remembers the previous shape and is able to return back to its original shape after being heated. The usage of SMA is tremendous in other applications such as in medical, dentistry, and also in automotive and robotic. However, SMA in structural applications can be considered as new and is still in research mode. Construction fields are always thirsty for new and fresh ideas to make improvements in existing technology. As the construction field has to face the possibility of natural disasters such as landslide, earthquake, and others, technologies are needed to reduce the total damages when such natural disasters occur. The existence of SMA as a new material in construction field gives positive vibes to researchers in creating a new technology. This paper explains the ability of SMA as a self-healing material and its unique properties of shape-memory effect and super-elasticity that are helpful in structural applications. The use of SMAs in reinforced concrete structures has been reviewed to clearly understand its mechanism processes. Comparison between SMAs and regular reinforced concretes were made to distinguish the performance of SMA-reinforced structures. Other recognized issues related to SMA, which is seismic protection of buildings are also presented in this paper.

N.A. Mohd Khairi (✉) · H. Ab Hamid · A. Ibrahim
Faculty of Civil Engineering, Universiti Teknologi Mara (UiTM),
40450 Shah Alam, Malaysia
e-mail: nuraliah4889@gmail.com

H. Ab Hamid
e-mail: Hanizah696@salam.uitm.edu.my

A. Ibrahim
e-mail: Azmi716@salam.uitm.edu.my

1 Introduction

Cracks in building structures are of concerned problem, especially when natural disasters such as landslide, earthquake, and others arise. There are many ideas and ways that have been adopted to overcome the problem. The implementation of SMAs in structural applications seems to be a good idea in improving and maintaining the structures serviceability.

Shape-memory alloy (SMA) is a unique material which has a self-healing feature that make it remember its original shape. When SMA has been deformed to another shape, with the help of heat, SMA is able to regain back to its previous shape [1–5]. This characteristic makes SMA very valuable and worthwhile to be used in various applications, eventhough the cost is quite high.

Other applications that are synonymous with the use of SMAs are in medicine, dentistry, robotic, and also consumer goods [6]. In civil engineering fields, SMA is still considered as a new item despite the material being discovered for decades before. It is perceived that usually civil engineering fields require heavy and large components to be used in constructions. However, usage of SMA is still inconvenient in terms of manufacturing cost and limited knowledge about the material itself. Various studies have been carried out on the use of SMAs in structural applications. Most of the research works are focused on the implementation of SMAs in RC structures.

2 Concepts of SMA

2.1 History

It is recorded that SMA was first discovered in year 1932 by the Swedish Physicist, Arne Olander. He found a super-elastic behavior in the gold cadmium (Au–Cd) alloy. Later, the shape-memory effect was revealed to be SMA capability by Vernon in 1941 who used SMAs in his polymeric dental material. In the early 1960s, the greatest discovery of SMA was done by Buehler where he and his colleagues discovered SMA with the name Nickel Titanium in the U.S. Naval Ordnance Laboratory. It is reported that Buehler and his colleagues found shape-memory phenomena in an equiatomic alloy of nickel and titanium accidently when they were studying the corrosion and heat resistance of the correlated alloy. They named the alloy as Nitinol related to the NiTi Naval Ordnance Laboratory [2, 7, 8].

NiTi has been recognized as the finest alloy among SMA groups. As verified by Debbarma and Saha [4], there are more than 30 types of different SMAs recorded, but only 3 types of SMAs are widely known due to their ability in commercial interest. Those SMAs are nickel titanium (NiTi), copper zinc aluminum (CuZnAl)

and copper aluminum nickel (CuAlNi). However, among these three SMAs, NiTi is the most commonly used since it has the best properties and is suitable for most applications, eventhough copper-based alloys are low in cost and commercially available. The discovery of NiTi made SMA popular and gain interest for commercialization in the industries. The unique properties of SMA such as shape-memory effects and super-elastics make SMA completely different from other conventional metal alloys.

2.2 Heat Transformations

SMA is recognized due to its capability in changing shape to its original state after being deformed with the aid of heats. SMA exists in two conditions of heat transformations. They are austenitic phase (high temperature) and martensitic phase (low temperature). In the martensitic phase, SMA is found to be in two forms which are called twinned and detwinned [9–11]. The different forms of SMA according to heat transformations are provided in Fig. 1 and the graph due to temperature changes of SMAs are shown in Fig. 2.

The transformation characteristic of temperature changes in SMA are defined as follows:

- M_s: Martensite start temperature upon cooling. The temperature at which the phenomenon starts.
- M_f: Martensite finish temperature upon cooling. The temperature at which martensite is again completely reverted.
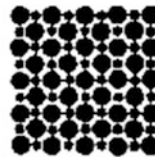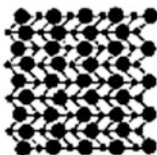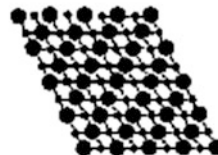
Fig. 1 Different forms of SMAs according to heat transformations
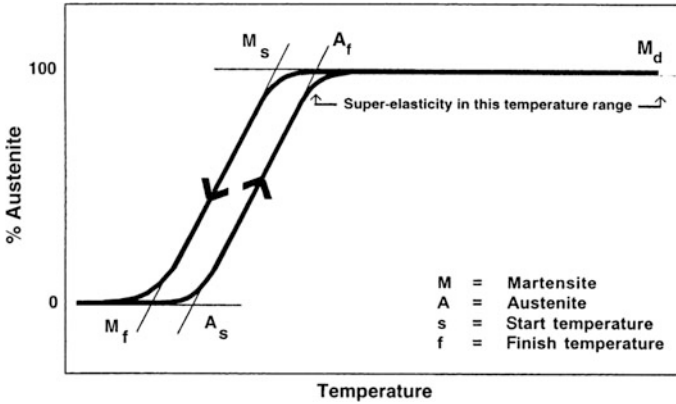
Fig. 2 Temperature changes of SMA

- A_s: Austenite start temperature upon heating. Reverse transformation start temperature at which the phenomenon starts.
- A_f: Austenite finish temperature upon heating. Reverse transformation finish temperature at which the phenomenon is completed.

SMA exhibits two different types of behaviors which are shape-memory effects and superelasticity. These two behaviors have their individual characteristics that highlight the capability of SMA as a different alloy.

2.3 Shape-Memory Effects

The memorizing parts in SMA are representative of the shape-memory effects (SME). SME is identified in SMA when there is a recovery process of apparent plastic strain given at a temperature below A_s by heating to a temperature above A_f [5, 12]. This phenomenon shows the reversible martensitic transformation. There are two categories of SME which are one-way SME and two-way SME. One-way SME only remembers the shape in the low-temperature state. This differs with the two-way SME where it is able to remember two different shapes which are at low-temperature state and at high-temperature state [5]. The movements of one-way and two-way SME are described in Fig. 3.

The descriptions of the movements of one-way and two-way SME shown in Fig. 3 are explained as follows:

- At a, the movement starts from martensite state for both one-way and two-way.
- At b, a reversible deformation is applied for one-way and a severe deformation with an irreversible amount is applied for two-way.
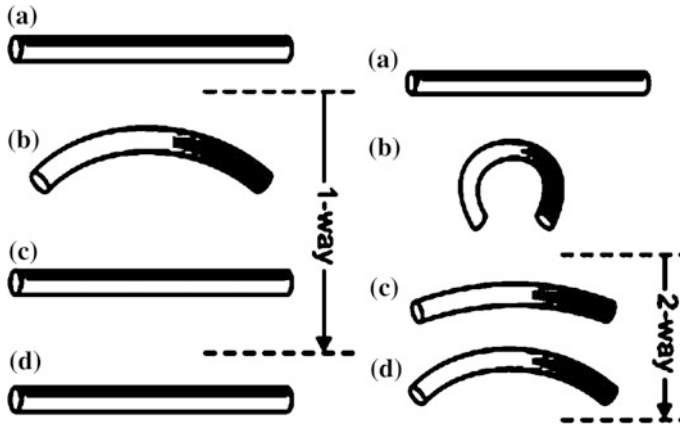
Fig. 3 The movements of one-way and two-way SME

- At c, the specimens are heated for both one-way and two-way.
- At d, finally both specimens are being cooled again.

When the materials are cooling from high temperature, for one-way effect, the change in macroscopic shape does not occur; but for two-way effect, the shape changes since the material remembers two different shapes which are at low temperature and at high temperature. The reason is because the material of two-way effect has been trained to behave in certain ways. In a normal situation, SMA will remember its shape in the high-temperature state and immediately forget its shape in low-temperature state while going through the recovery process. However, SMAs can be trained to remember to leave some reminders of the deformed low-temperature condition at the high-temperature phase.

2.4 Superelasticity

Superelasticity is one of the SMA properties. It is a mechanical process that occurs in SMA when the alloy is strained above its transformation temperature. Superelasticity is caused by stress, so it differs from shape-memory effect where it is created by temperature [13]. According to Stoeckel [14], when a wire is loaded at a temperature above A_f but below M_d, the wire can be elongated to approximately 8 % strain after reaching the first yield point with no significant stress increases. The completed process of superelasticity is provided in Fig. 4.

Fig. 4 The completed
process of superelasticity
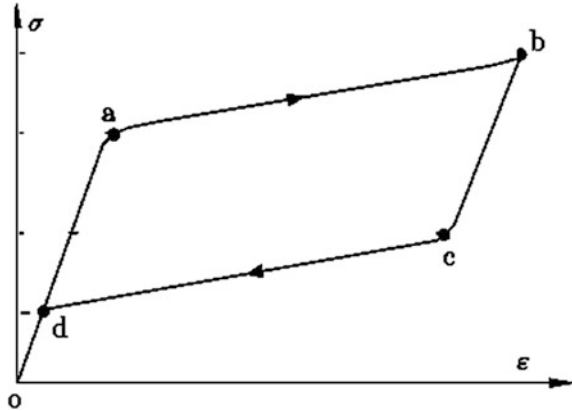
The completed superelasticity process as shown in Fig. 4 are explained as
follows;

- o–a: An elastic distortion of the austenitic lattice starts to occur when a unidi-
  rectional stress is applied to an austenitic specimen within a temperature range
  between A_f and M_d ($M_d > A_f$); See Fig. 2.
- a–b: Austenite becomes unstable at position (a) which is a critical value and a
  transformation from austenite to stress-induced martensite takes place. Then, the
  deformation proceeds and the stress remains almost constant until the material is
  completely transformed. The two phases coexist during this stage.
- b–c: The elastic unloading of the detwinned martensite takes place when stress
  is removed. Martensite becomes unstable below a critical stress at (c). As the
  unloading process continues, a reverse transformation occurs.
- c–d: At a lower stress plateau, detwinned martensite reverts back to austenite.
  Material is completely transformed at parent phase (d) but further unloading will
  follow the initial loading path with full recovery if the temperature is greater
  than A_f.

This whole superelasticity process is translated by an energy-absorption capacity
with zero residual strain [5].

3 Self-rehabilitation of Reinforced Concrete Structures

3.1 Self-healing Effects

The problem with reinforced concrete structures is that cracks due to shrinkage and
external loading are common. Microcracks are obviously unavoidable in reinforced
concrete structures. Corrosion of the reinforcing steel adds to the problem. If this
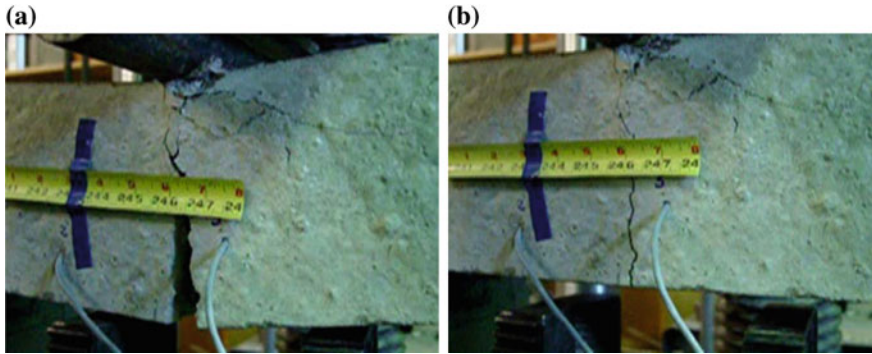
Fig. 5 a Cracks at the bottom surface during a loading test **b** Cracks close up after applying electrical currents

problem is ignored or not taking seriously, it will affect the durability of the structures, hence decreases the service life of the structures.

The characteristics of SMA that consume self-healing effects and high resistance to corrosion make SMA seem useful to be approached in structural applications. Besides that, the superelasticity behavior of SMA can adequately handle micro-sized cracks in structural applications [15]. Debbarma and Saha [4] had summarized some other SMA properties that are applicable in civil structures, such as;

- SMA has the capability to repeatedly absorb large amount of strain energy without permanent deformation.
- Damping characteristic of SMA is great at temperature below the transition temperature range.
- SMA is nonmagnetic in nature.
- SMA has high resistance to fatigue under large strain cycles.
- SMA has low density.

SMA can be used as reinforcement bars in RC structures and is placed especially at critical locations such as at plastic hinge region, where the area is disposed to more damages during an earthquake [16]. Song et al. [8] demonstrated the use of smart materials in the concept of an intelligent reinforced concrete structure. They used Nitinol-type SMA in the form of wire cables reinforced inside beam structures. A maximum strain up to 5 % was experienced by cables as suggested ceiling value for repeated situations to imitate the real situations that give large cracks to concrete structures such as earthquakes or explosions. By heating the SMA cables electrically at 90 °C, it closed-up the crack. The experimental works are pictured as in Fig. 5.

Abdulridha et al. [17] has evaluated the compatibility of SMAs as alternative reinforcement in RC structures. They concluded that SMA has shown structural characteristics such as exhibits yielding and strain hardening while sustaining large

displacement ductility. Deng et al. [18] had performed experimental works for actuated SMA wires in concrete beams. The results show that a large recovery force can be obtained from heated SMA wires.

After all, SMA has the potential characteristics to be substituted reinforcement for reinforced concrete structures as it has significant enhancement in crack recovery capacity compared to steel reinforcing bars.

3.2 Seismic Approach

Natural disasters such as landslide, earthquake, and many others are unavoidable events. There must be a way to defend these from severely affecting structural buildings. Seismic protections are important to make the buildings able to withstand seismic forces. Some of the SMA features that can be integrated into seismic applications are excellent resistance to fatigue under large strain cycles, highly corrosion resistance, great durability, and no degradation due to aging [19].

Research by Alam et al. [20] focused on the seismic performance of RC frames that used SMAs as reinforcement. They found out that when seismic actions have been applied onto structures, SMA reinforcement in hinge locations of beams and columns can dissipate the seismic energy and also can restore the original shape of such members. More importantly, Fukuta and Liba [21] mentioned that SMA bars are needed to be used as tension members in structures as they show super-elasticity behavior in tension not in compression. Moreover, the use of SMA bar as a tension member can efficiently control a displacement response of a structure and is able to return its lateral drift to zero after occurring of an earthquakes.

3.3 SMA Damper

SMA is known to have a good damping property as it has high damping capacity and the ability to have fully reversible strain after removing the stress.

Ren et al. [22] came out with a recentering damping device that uses SMA strands. The device shows an excellent result where it can eliminate the residual displacement and reduce the interstory displacement of structures that are subjected to earthquakes. It has been reported by Song [8] that as SMA cables elongated along the widen cracks of structures, SMA cables are able to increase the damping of the structures by absorbing the external energy created during the process. It is mentioned by Mortazavi et al. [23], that in order to have a good damper for use in passive control, the damper should have the properties of good dissipating capacity and unique recentering capability. SMA dampers have that quality as proven by Dolce and Cardone [24] and Shrestha et al. [25] where the recentering and the

Fig. 6 Prototype model of earthquake effects using SMA damping
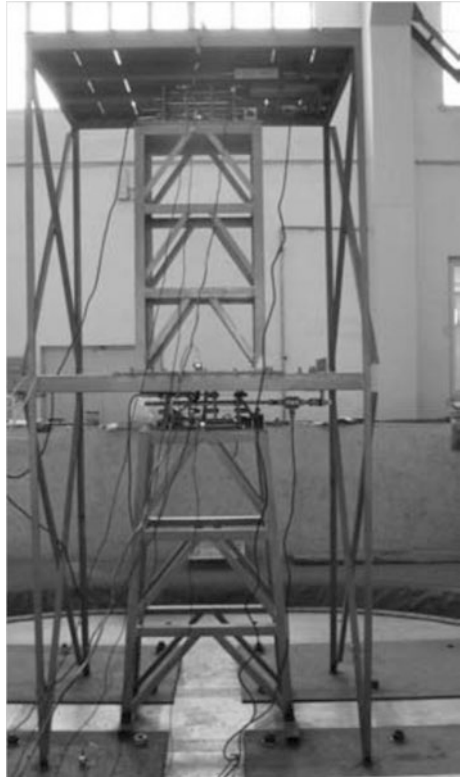
energy dissipating of SMA dampers can be easily obtained. It is important for a damper to have the recentering capability to make sure the structure return to its original geometry at frequent times during excitation. This will prevent the structure from accumulation of inelastic deformations. Meanwhile, the dissipating capability is good to decrease the demand on the main structural systems and decrease the plastic deformations of structure member. The prototype model of earthquake effects using SMA damping shown in Fig. 6.

In 1996, a specific research project on exploring the potentials of SMA in seismic protection named MANSIDE (Memory Alloys for New Seismic Isolation and Energy Dissipation Devices) was funded by the European Commission. MANSIDE has summarized the requirements that SMA should satisfy in order to be effectively used in seismic applications [24]. The study conducted on different types of SMAs including NiTi, CuZnAl, CuAlNi, FeMn, MnCu, and NiTiNb. It is confirmed that NiTi has the best features among the others due to its excellent superelasticity that can undergo large recoverable strains and high resistance to corrosion [26]. The requirement that SMA should satisfy in order to be effectively used in seismic protection devices are summarized by MANSIDE in Table 1.

Table 1 Requirement of SMA to be used in passive control devise

Martensite	Austenite
High energy dissipation	Superelasticity
High fatigue resistance Low sensitivity to temperature in the range 5–35 °C for buildings and 5–45 °C for bridges	
Low sensitivity to strain rate or to frequency in sinusoidal vibrations, in the range 0.4–1 Hz, for seismic isolation techniques and 1–10 Hz, for energy dissipation techniques	
Stability of cyclic behavior: $0.9 \leq \sigma_{1,1}/\sigma_{1,I} \leq 1.1$, $0.9 \leq \sigma_{2,1}/\sigma_{2,i} \leq 1.1$ where i is the number of the cycle produced by an earthquake	
No degradation for environmental actions or as low as possible (applications on buildings are much less sensitive than applications on bridges)	
$\varepsilon_2 \geq 6$ %, $\gamma_2 \geq 12$ % or as large as possible	
$\varepsilon_4/\varepsilon_2 \geq 2$, $\gamma_4/\gamma_2 \geq 2$ or as large as possible	
$E_2 \leq 0{:}10\ E_1$ or as low as possible	
$E_3 \leq 0{:}5\ E_1$ or as low as possible	
$E_1 \geq 30{,}000$ MPa (as large as possible)	$E_1 \geq 70{,}000$ MPa (as large as possible)
$\sigma_1 \geq 300$ MPa or as large as possible	$\sigma_1 \geq 500$ MPa or as large as possible
$\sigma_3/\sigma_1 \leq 1.5$ or as low as possible	
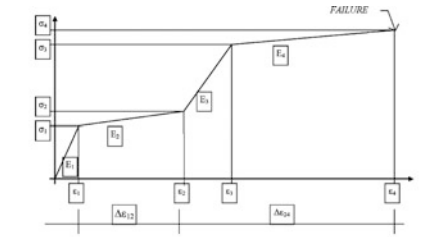
4 Conclusions

This paper explains the ability of SMA as a self-healing material and its unique properties of shape-memory effect and superelasticity. The applications of SMA in civil engineering fields, especially in reinforced concrete structures and seismic protection buildings are reviewed. From the review, it is convinced that SMA is a valuable material for use in civil engineering applications where it has several useful properties that can be adopted such as repeated absorption of large amounts of strain energy under loading without permanent deformation can be used to produce an excellent SMA damper. Furthermore, embedding SMA into concrete structures can increase the life span of the structures due to the continuous self-repairing through the times. Even though the costs of implementation of SMA in structural applications are a main restraining factor. Large scale civil engineering requires considerable use of SMA and the difficulty in processing high-strength

SMA increases the manufacturing cost. Despite that the decreasing price of SMAs especially of NiTi type of SMA are recorded. Over the last 10 years, the price reduced from 1000 USA/kg to below 100 USD/kg at the present [27]. Although the price can still be claimed as high at the moment, with the high demand of SMA in industry, it is expected that the manufacturing costs of SMA will decrease and no longer will be a constraint to construction industry.

References

1. K. Otsuka and C. M. Wayman, "Shape Memory Materials," in *Cambridge University Press*, 1998
2. J. M. Jani, M. Leary, A. Subic, and M. A. Gibson, "A review of shape memory alloy research, applications and opportunities," *Mater. Des.*, vol. 56, pp. 1078–1113, Apr. 2014.
3. G. Song, N. Ma, and H. N. Li, "Applications of shape memory alloys in civil structures," *Eng. Struct.*, vol. 28, no. 9, pp. 1266–1274, Jul. 2006.
4. S. R. Debbarma and S. Saha, "Review of shape memory alloys applications in civil structures, and analysis for its potential as reinforcement in concrete flexural members," *Int. J. Civ. Struct. Eng.*, vol. 2, no. 3, pp. 924–942, Feb. 2012.
5. J. Chopade, R. Barjibhe, and B. Kumar, "Critical review on shape memory alloy," *Int. J. Eng. Res. Technol.*, vol. 2, no. 2, pp. 1–6, 2013.
6. Q. Meng, H. Yang, Y. Liu, T. Nam, and D. Favier, "Ti–50.8at.% Ni wire with variable mechanical properties created by spatial electrical resistance over-ageing," *J. Alloys Compd.*, vol. 577, pp. S245–S250, Nov. 2013.
7. K. Otsuka and C. M. Wayman, *Shape Memory Materials*. Cambridge University Press, 1998
8. G. Song, Y. L. Mo, K. Otero, and H. Gu, "Health monitoring and rehabilitation of a concrete structure using intelligent materials," *Smart Mater. Struct.*, vol. 15, no. 2, pp. 309–314, Apr. 2006.
9. S. Nemat Nasser, J. Yong Choi, W. G. Guo, J. B. Isaacs, and M. Taya, "High strain-rate, small strain response of a NiTi shape-memory alloy," *J. Eng. Mater. Technol.*, vol. 127, no. 1, p. 83, 2005
10. S. Nemat Nasser, J. Y. Choi, W. G. Guo, and J. B. Isaacs, "Very high strain-rate response of a NiTi shape-memory alloy," *Mech. Mater.*, vol. 37, no. 2–3, pp. 287–298, Feb. 2005
11. S. Nemat Nasser and W. G. Guo, "Superelastic and cyclic response of NiTi SMA at various strain rates and temperatures," *Mech. Mater.*, vol. 38, no. 5–6, pp. 463–474, May 2006
12. W. Tang and R. Sandstrom, "Property database on shape memory alloys for engineering design hysteresis," *Am. Soc. Test. Mater.*, vol. 4, pp. 85–95, 1995.
13. N. K. Paul and R. P. Nanda, "Shape memory alloy as retrofitting application in historical buildings and monuments - A review in Indian perspective," *Int. J. Civ. Eng. Technol.*, vol. 4, no. 1, pp. 117–125, 2013.
14. D. Stoeckel, "The Shape Memory Effect - Phenomenon, Alloys ans Applications," 1995
15. Y. Kuang and J. Ou, "Self-repairing performance of concrete beams strengthened using superelastic SMA wires in combination with adhesives released from hollow fibers," *Smart Mater. Struct.*, vol. 17, no. 2, p. 025020, Apr. 2008.
16. A. H. M. Muntasir Billah and M. Shahria Alam, "Seismic performance of concrete columns reinforced with hybrid shape memory alloy (SMA) and fiber reinforced polymer (FRP) bars," *Constr. Build. Mater.*, vol. 28, no. 1, pp. 730–742, Mar. 2012.

17. A. Abdulridha, D. Palermo, S. Foo, and F. J. Vecchio, "Behavior and modeling of superelastic shape memory alloy reinforced concrete beams," *Eng. Struct.*, vol. 49, pp. 893–904, Apr. 2013.
18. Z. Deng, Q. Li, and H. Sun, "Behavior of concrete beam with embedded shape memory alloy wires," *Eng. Struct.*, vol. 28, no. 12, pp. 1691–1697, Oct. 2006.
19. S. Alvandi and M. Ghassemieh, "Application of Shape Memory Alloys in Seismic Isolation : A Review," *Civ. Enigineering Infrastructures J.*, 2014
20. M. S. Alam, M. Moni, and S. Tesfamariam, "Seismic overstrength and ductility of concrete buildings reinforced with superelastic shape memory alloy rebar," *Eng. Struct.*, vol. 34, pp. 8–20, Jan. 2012.
21. T. Fukuta and M. Iiba, "Experimental results on stress-strain relation of Ti-Ni shape memory alloy bars and their application to seismic control of buildings." 2002
22. W. Ren, H. Li, and G. Song, "An innovative shape memory alloy damper for passive control of structures subjected to seismic excitations," in *World Conference on Earthquake Engineering*, 2008
23. S. M. R. Mortazavi, M. Ghassemieh, and S. A. Motahari, "Seismic control of steel structures with shape memory alloys," *Int. J. Autom. Control Eng.*, vol. 2, no. 1, pp. 28–34, 2013.
24. M. Dolce and D. Cardone, "Mechanical behaviour of shape memory alloys for seismic applications 2. Austenite NiTi wires subjected to tension," *Int. J. Mech. Sci.*, vol. 43, no. 11, pp. 2657–2677, Nov. 2001.
25. K. C. Shrestha, Y. Araki, T. Nagae, Y. Koetaka, T. Suzuki, T. Omori, Y. Sutou, R. Kainuma, and K. Ishida, "Feasibility of Cu–Al–Mn superelastic alloy bars as reinforcement elements in concrete beams," *Smart Mater. Struct.*, vol. 22, no. 2, p. 025025, Feb. 2013.
26. R. Desroches and B. Smith, "Shape Memory Alloys in Seismic Resistant Design and Retrofit : A Critical Review of their Potential and Limitations," vol. 7, no. 3, pp. 1–15, 2003
27. M. S. Alam, M. A. Youssef, and M. L. Nehdi, "Exploratory investigation on mechanical anchors for connecting SMA bars to steel or FRP bars," *Materials and Structures*. 2010

Energy Dissipation and Strain Recovery of Pseudo-Elastic Shape Memory Alloy Ni-Ti Wire

Nubailah Abd Hamid, Hanizah Ab Hamid, Azmi Ibrahim, Azlan Adnan and Muhammad Hussain Ismail

Abstract Shape Memory Alloy (SMA) is classified as a novel functional material characterized by pseudo elastic and shape memory effect and has caught the interest across many research disciplines recently. Owing to its wide properties, originated from reversible austenite to martensite phase transformation, this alloy has been used widely in many applications from medical, aerospace and civil applications. The discoveries of SMAs to be exploited as intelligent materials have become the sparked research to be addressed for their prospective use as seismic resistant design and retrofit. Highlighting the unique properties of pseudo-elastic wire, it is not only have the ability to reverse macroscopically inelastic deformation during earthquake by stress removal to recover their original shape but also have significant promises to dissipate energy, large elastic strain capacity, hysteretic damping, excellent high, low-cycle fatigue resistance, re-centering capabilities and excellent corrosion resistance. Hence, this study evaluates the cyclic properties of pseudo elastic Ni–Ti shape memory alloys to assess their potential for seismic applications. An attempt is devoted to correlate the influence of annealing temperatures to the hysteretic behavior of Ni-Ti alloys in terms of fatigue resistant in cyclic loading, mechanical properties at ambient temperature, loading history, equivalent damping, energy dissipation and recovery stress were investigated experimentally. The sample of

N.A. Hamid (✉) · H.A. Hamid · A. Ibrahim · M.H. Ismail
Faculty of Civil Engineering, University Technology Mara,
40450 Shah Alam, Malaysia
e-mail: nubailah_hamid@yahoo.com; bellehafiz@gmail.com

H.A. Hamid
e-mail: hanizah_ah@yahoo.com

A. Ibrahim
e-mail: azmii716@yahoo.com

M.H. Ismail
e-mail: muhammadhussain_ismail@yahoo.co.uk

A. Adnan
Faculty of Civil Engineering, University Technology Malaysia,
81310 Johor, Malaysia
e-mail: azlanadnan@utm.my

Ni-Ti wire of 0.127 mm diameter of as received wire had a nickel to titanium ratio of 0.49:0.51 and were heat treated to produce pseudo-elastic response at room temperature. Based on the experimental findings, the pseudo-elastic properties of as received wires have found to be in a good agreement in terms of their ability to dissipate energy through repeated cycling without significant degradation or permanent deformation and better response for seismic application to be optimized. The tensile cyclic test obtained demonstrated a rounded loading curve based on a 0.2 % offset. The as-treated has improved the energy dissipation, but has reduced in pseudo-elasticity. This is due to the formation of martensitic phase upon heating. It is evident from the XRD results, the presence of both austenite and martensite at room temperature. The improvement in energy absorption could be resulted from the greater enthalphy for the phase transition. This is due to pseudo elastic is highly sensitive to the temperature. Extreme temperature can completely eliminate the superelastic effect due to the formation of martensite and unwanted secondary phases such as Ni_4Ti_3 and and Ti_2Ni. The experimental results show potential for the use of SMAs in seismic applications and provide areas for continued research.

1   Introduction

The shape memory effect (pseudo plastic) and super elasticity also known as pseudo-elasticity is a novel functional material properties that distinguish SMAs from other metals and alloys [1] that make them ideal contender and significant attention nowadays due to their excellent properties such as exhibits stable pseudo elasticity above a reverse transformation finish temperature, able to recover inelastic deformation during earthquake, hysteretic damping, energy dissipation through hysteresis of response, excellent resistance to corrosion [2], high fatigue resistance, high strength, large elastic strain capacity, recentering capabilities, strain hardening at large strains and stress plateau [3]. These properties, can be integrated in civil engineering structures as seismic design resistant and retrofit and promising a good prospective for rehabilitation in order to address the problem of deteriorating civil structures.

SMAs are a unique class of materials that have the ability to spontaneously recover strain of up to 8 %. The behavior of SMAs subjected to seismic applications can be dictated by stress strain under cyclic response [4]. Since there is limited understanding about the potential and limitations about the properties for Shape Memory Alloys for seismic applications, therefore previous of researches have focused on mechanical properties and mechanical characterization. Study by [4] demonstrated that recentering properties can be negligible because of nearly ideal pseudo-elastic obtained for wires and bars. However, the strength and damping properties of wires is higher than bar but equivalent damping decreases when

loading rates increases. McCormick et al. [5] revealed that the equivalent viscous and recentering capability decreases with increasing of the bar sizes. Study by Tyber et al. [6] confirmed that heat treatment causing temperature transformation temperatures which then influences the degree of hardness but not the diameter of the bar.

Research works on material properties for Shape Memory Alloy were performed by [7–9]. The recent experimental investigations on material characterization to understand the response of SMA elements such as wires, bars and plates under various loading conditions were described by [10] in a state-of-the-art review. Mechanical behaviour of Shape Memory Alloys for seismic applications for Martensite and Austenite NiTi bars subjected to torsion and Austenite NiTi wires subjected to tension can be referred to [11, 12] respectively. While experimental study on with regard to its Shape Memory Alloy, stress-strain property towards application of self-restoration for structural members can be obtained from [13]. The relation between the SMAs mechanical properties and cyclic deformation mechanism and correlation between engineering stress-strain and true stress-strain curve, can be established from [14, 15]. Heat treatment is required to increase the ductility of the alloy and produce pseudo-elastic response at room temperature according to [16, 17].

The existing number of researches provides the analytical and experimental studies focusing on the effect of strain rate and temperature effects to the shape memory alloy [19]. However, the influence of heat treatment to the hysteretic behavior of Ni-Ti alloy, energy dissipation and the recovery stress are scanty in the literature. Hence, this study this study is to evaluate the cyclic properties of pseudo elastic Ni–Ti shape memory alloys to correlate the influence of heat treatment to the hysteretic behavior of Ni-Ti alloy in terms of energy absorption and recovery stress were experimentally investigated.

2 Fundamental of Shape Memory Alloy and Energy Dissipation

Tensile cyclic loading protocols depict the full picture of cyclic nature of an earthquake and fatigue resistance of NiTi SMAs, disclose the information associated to the specific forward cyclic properties [7] as the key information needed by structural engineers in regards to the cyclic properties of pseudo elastic Ni-Ti instead of monotonic test.

Figure 1 illustrates the key properties which are important for structural application of pseudo elastic NiTi SMAs such as the forward transformation stress, σ_L; reverse transformation stress, σ_{UL}; initial elastic modulus, E_i; residual strain, σ_R; and the equivalent viscous damping, ξeq. The forward transformation stress refers to the stress at which the Martensite phase transformation initiates reverse transformation stress, σ_{UL}, initial elastic modulus, E_i, residual strain, ε_R, and the equivalent viscous damping, ξ_{eq}. The first set of provides the key properties which

Fig. 1 SMA properties for structural applications [7]
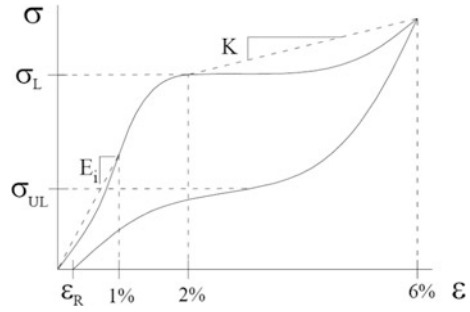
are important for superelastic SMAs when considered in structural applications: forward transformation stress, σ_L; reverse. The forward transformation stress refers to the stress at which the Martensite phase transformation initiates.

Recentering denotes as the capacity to return to its original undeformed shape upon unloading recoverable strain after the imposed deformation. Plastic deformation due to the accumulation of permanent inelastic strain during cycling or maximum recoverable strain attained after the imposed deformation demonstrates as re-centering capability measurement for residual strain. The equivalent viscous damping can be expressed through Eqs. (1) or (2). Figure 2 shows the graph for computation of the equivalent viscous damping ratio for a random cycle—adapted from [20].
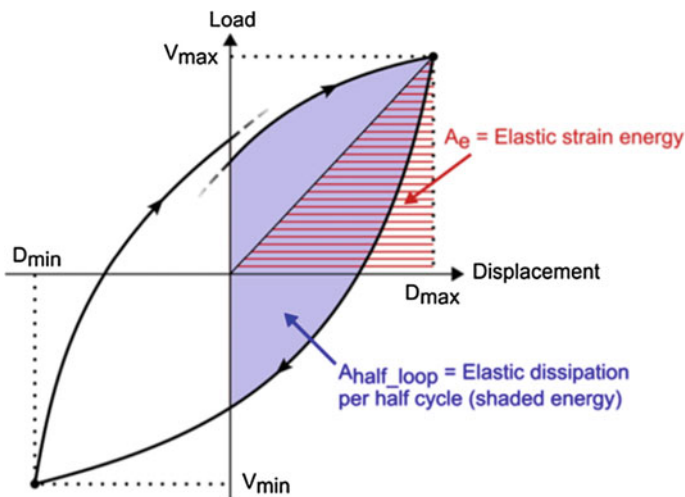
Fig. 2 Graph for the computation of the equivalent viscous damping ratio for a random cycle—adapted from [9]

$$\xi_{eq} = \frac{1}{4\pi} \frac{E_D}{E_{so}}$$

(1)

where E_{So} refers to the strain energy per cycle and E_D refers to the energy dissipated per cycle

or

$$\xi_{eq} = \frac{1}{4\pi} \frac{A_h}{A_e}$$

(2)

where A elastic is the elastic strain energy for a complete cycle and A hysteresis represents the area under the stress-strain curve [12].

3 Experimental Programs

The 0.127 mm diameter of Austenitic wire with composition percentage of nickel 54.56 % and titanium 45.54 % was heat-treated in a Tube Furnace carbolite CTF16/75 & 3/89/347 using argon gas to exhibit pseudo elastic response at room temperature as shown in Figs. 3 and 4 at a temperature of 600 °C in 5°/min for 1 h duration. The chemical composition of Nickel-Titanium alloy wire used in this study and phase transformation temperature of Nickel and Titanium are depicted in Tables 1 and 2 respectively.

In order to implement and optimize the pseudo elastic NiTi into structural systems for seismic mitigation, Tensile Cyclic test was implemented using Instron Universal Testing apparatus model 5982 as shown in Fig. 5a. A pair of wire grip fixtures made of mild steel was used in the test.

Round specimen wedges were used to grip the wires with flat specimen wedges being used for wire as demonstrated in Fig. 5b. The gauge length for the specimen was 280 mm for each specimen respectively. The above mentioned loading protocol

Fig. 3 Austenitic wire of 0.127 mm diameter

Fig. 4 Electrical Furnace for heat treatment

Table 1 Chemical composition, diameter and gauge length of SMA wire used for both samples

Samples	Diameter (mm)	Length (mm)	Gauge length (mm)	Weight (%)	
				Ni	Ti
As-received	0.127	280	280	54.46	45.54
Heat-treated	0.127		280	54.46	45.54

Table 2 Phase transformation temperature of the Austenic wire used for the experiment

Austenitic wire	Transformation temperature (°C)					
	A_s	A_p	A_f	M_s	M_p	M_f
As-received	−47.5	10	17.5	19.2	10	−35
Heat-treated	−45	34.2	65.8	19.2	3.33	−28.33

(a)   **(b)**
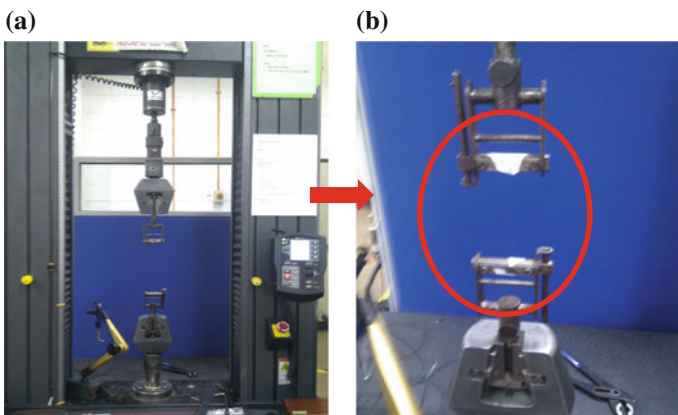
Fig. 5 a Instron Universal Tensile, **b** grip fixtures used for machine

was input using Blue Hill 3 software which use strain output to control the movement of the actuator. The specimens were loaded and unloaded with the loading rate of 1 mm/min and compliance to ASTM F2516-07 (Standard Test Method for Tension Testing of Nickel-Titanium Super elastic Materials 2007).

4 Results and Discussion

The yield point was based on a 0.2 % offset, and the loading plateau stress, total elongation and permanent set after 6 % strain for as-received Ni-Ti based on specifications provided by the manufacturer was compared with the experiment samples as shown in Table 3. The result obtained from the manufacturer is not much different with the result obtained from the manufacturer.

The stress–strain cyclic responses of the 0.127 mm pseudo elastic wire for both as-received and heat-treated sample illustrated in Figs. 6 and 7 respectively, demonstrate rounded loading curves. Both figures show that the number loading cycles, N, that would be considered are in the range of 5–15 which is 13 for as-received wire and heat-treated pseudo elastic wire. Thus, the pseudo elastic response shows that it is suitable for seismic design mitigation. The forward transformation (austenite to martensite) stress and the reverse transformation (martensite to austenite) are decreased for increasing cyclical loading. Both samples are able to recover from plastic deformation.

The as-received material shows good pseudo elasticity with a narrow stress hysteresis as compared to heat-treated wire. The results show that the stiffness of the sample is slightly varied in this stage, where the heat-treated sample exhibits slightly higher stiffness.

Table 4 shows the cyclic properties for as-received and heat-treated austenitic wires. The residual strains provide a clear differentiation between the heat treated and as received samples. During the last loading cycle, the as-received Ni-Ti wire was strained to 12.2 %, and upon unloading, the residual strain was 0.0015 %, representing a 99.99 % strain recovery capacity. While the deformed or heat-treated wire was subjected to a comparable strain of 7.7 % during the last loading cycle. The resulting residual strain was approximately 0.65 %, representing a strain recovery of 91.6 % of strain recovery. Stress–Strain Hysteresis of pseudo Ni-Ti wire repeated cyclical loading leads to gradual increases in the residual strains demonstrates repeated hysteretic damping.

Table 3 Specification by the manufacturer

Samples	Loading plateau stress @ 3 %(min)	Total elongation (min) (%)	Permanent set after 6 % strain (max) (%)
Manufacturer	60,000 psi	10.0	0.5
As-received	52,000 psi	10	0.22
Heat-treated	78,000 psi	13	1.84
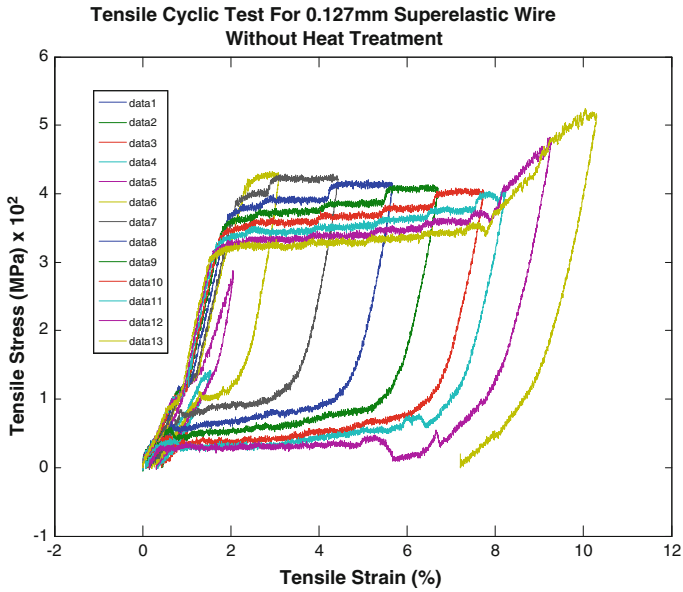
Fig. 6 Tensile Cyclic test for as received 0.127 mm pseudo elastic wire
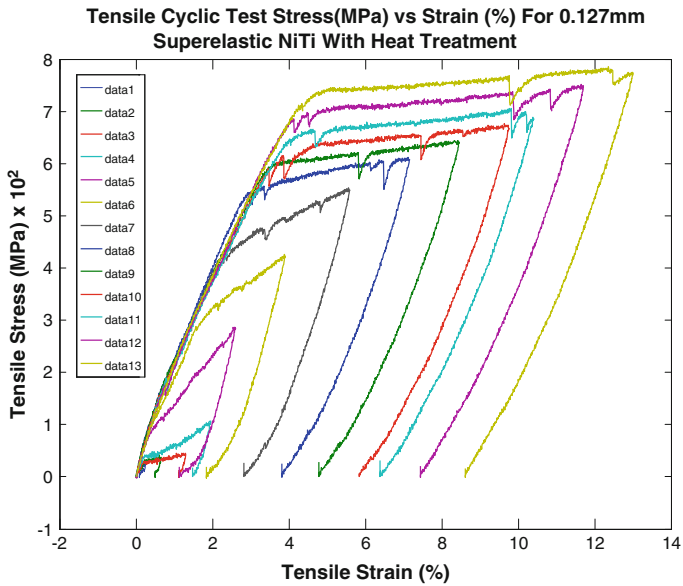
Fig. 7 Tensile Cyclic result for 0.127 mm superelastic wire with heat treatment

Table 4 Cyclic properties for as-received and heat-treated austenitic wires

Specimen	Total elongation (%)	Residual strain %	Strain Recovery %
As-received	10	0.0015	99.99
Heat-treated	13	0.07	99.46

Figure 8 shows cyclic deformation on the stress-strain curves of as received Ni-Ti alloys and subjected to heat treatments. Purple lines indicate shape recovery of as received wire while the red lines demonstrate the shape recovery by heat-treated of pseudo elastic wire. The residual strain increased when heat
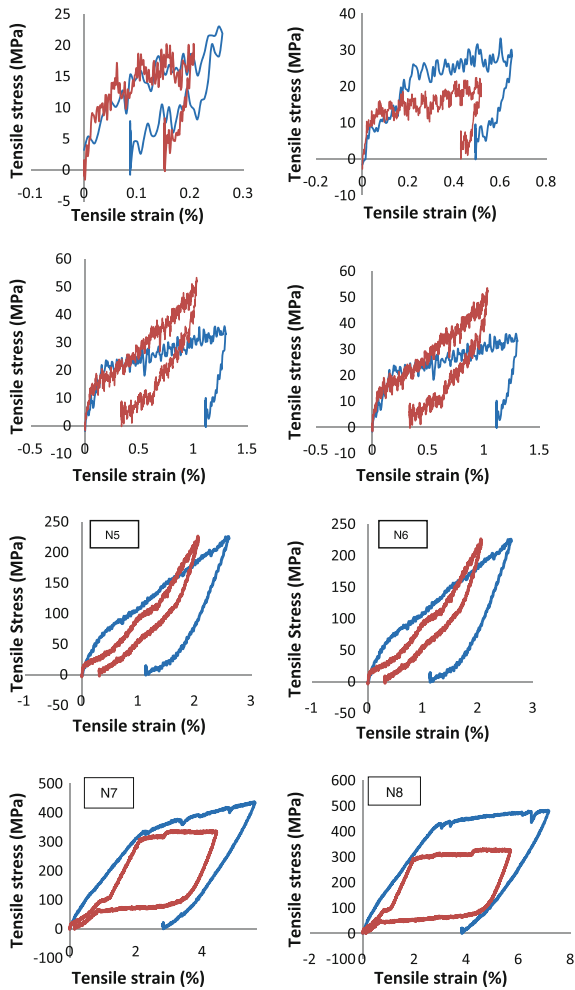
Fig. 8 Cyclic deformation on the stress-strain curves of as received Ni-Ti alloys and subjected to heat treatments
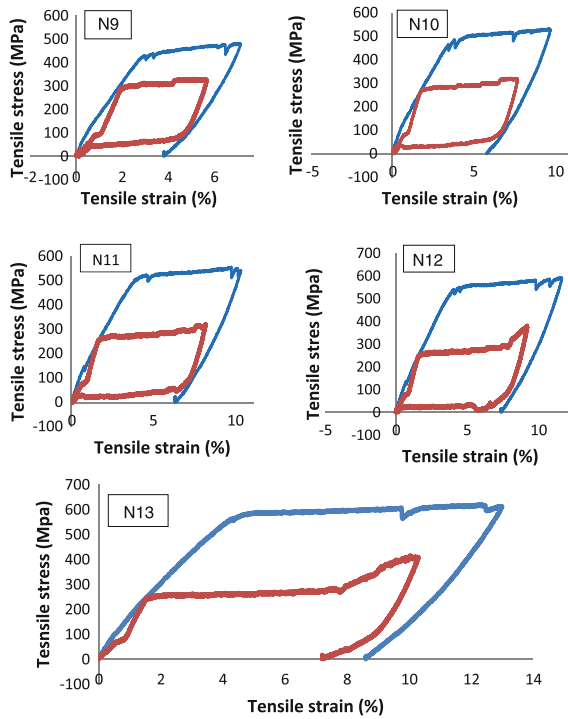
Fig. 8 (continued)

treatment is applied. In particular, as-received wire exhibits superior super elasticity where the residual strains were almost completely recover without heating and increased with applied strain until 8 %.

While the result in Fig. 9 shows a decrease in the hysteresis and energy dissipation of the specimen. In both cases, the energy dissipated (as measured by the

Fig. 9 Energy dissipation for as received and heat-treated wire
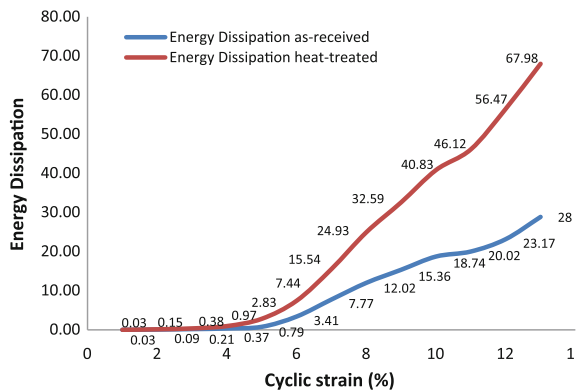
area under the stress-strain diagram) using the MATLAB slightly increased for increasing strain rates. However, the as-treated has improved the energy absorption, however reducing in pseudo elasticity. This is due to the formation of martensitic phase upon heating. Both set of results found that increased loading rates led to reductions in hysteresis and energy dissipation of the SMAs. It is generally believed that the rate effects subjected to cyclic loading are due to the heat generated while going through the transformation. The reduction in the reverse transformation is less than that in the forward phase transformation. This causing the hysteresis and energy dissipation of the samples decreased.

In order to get a better results a proper method of heat treatment should be introduced in vacuum to avoid the pick-up of impurity elements and avoid brittle secondary phases especially oxygen and carbon.

5 Conclusion

Based on the experimental findings, there are some conclusions to be drawn:-

- The properties of pseudoelastic for as received wires have found to be in good agreement with previous studies in term of their ability to dissipate energy through repeated cycling without significant degradation or permanent deformation and better response for seismic application to be optimized.
- The tensile cyclic test obtained demonstrated graphd with rounded loading curves based on a 0.2 % offset. The as-treated sample has improved the energy absorption, however reducing in pseudo elasticity. This is due to the formation of martensitic phase upon heating.
- The residual strains were almost completely recover until 8 percent strain while residual strain increases when the as received wire was heat treated.

References

1. S. R. Debbarma and S. Saha, "Review of Shape Memory Alloys applications in civil structures, and analysis for its potential as reinforcement in concrete flexural members," *Int. J. Civ. Struct. Eng.*, vol. 2, no. 3, pp. 924–942, Feb. 2012.
2. O. E. Ozbulut, S. Hurlebaus, and R. Desroches, "Seismic Response Control Using Shape Memory Alloys: A Review," *J. Intell. Mater. Syst. Struct.*, vol. 22, no. 14, pp. 1531–1549, Aug. 2011.
3. R. Desroches and B. Smith, "Shape Memory Alloy In Seismic Resistant Design and Retrofit : A critical Review of Their Potential and Limitations," *J. Earthq. Eng.*, vol. 8, no. 3, pp. 415–429, 2004.

4. R. DesRoches, J. McCormick, and M. Delemont, "Cyclic Properties of Superelastic Shape Memory Alloy Wires and Bars," *J. Struct. Eng.*, vol. 130, no. 1, pp. 38–46, Jan. 2004.

5. R. Desroches, M. Asce, J. Mccormick, and M. Delemont, "Cyclic Properties of Superelastic Shape Memory Alloy Wires and Bars," vol. 130, no. 1, pp. 38–46, 2004.

6. J. Tyber, J. Mccormick, S. M. Asce, K. Gall, R. Desroches, M. Asce, H. J. Maier, and A. E. A. Maksoud, "Structural Engineering with NiTi. I : Basic Materials Characterization," *J. Eng. Mech.*, p. 10, 2007.

7. J. Mccormick, S. M. Asce, J. Tyber, R. Desroches, M. Asce, K. Gall, and H. J. Maier, "Structural Engineering with NiTi. II : Mechanical Behavior and Scaling," no. September, pp. 1019–1029, 2007.

8. S. Cai, J. E. Schaffer, M. R. Daymond, C. Yu, and Y. Ren, "Effect of heat treatment temperature on nitinol wire," *Appl. Phys. Lett.*, vol. 105, no. 7, p. 071904, Aug. 2014.

9. M. Drexel, G. Selvaduray, and A. Pelton, "The Effects of Cold Work and Heat Treatment on the Properties of Nitinol Wire," pp. 114–120.

10. J. Kłaput, "Studies of selected mechanical properties of nitinol – shape memory alloy," vol. 10, no. 3, pp. 155–158, 2010.

11. D. V. Ě. Ch, "Influence of Heat Treatment of Shape Memory NiTi Alloy on Its Mechanical Properties," in *Influence of Heat Treatment of Shape Memory NiTi Alloy on Its Mechanical Properties*, 2010, no. 18. - 20. 5. 2010, Roznov pod Radhostem, Czech Republic, Eu Influence, pp. 2–6.

12. D. Fugazza, "Experimental Investigation On The Cyclic Properties Of Superelastic NiTi Shape Memory Alloy Wires and Bars," 2005.

13. M. Dolce and D. Cardone, "Mechanical behaviour of shape memory alloys for seismic applications 1. Martensite and austenite NiTi bars subjected to torsion," vol. 43, pp. 2631–2656, 2001.

14. M. Dolce and D. Cardone, "Mechanical behaviour of shape memory alloys for seismic applications 2. Austenite NiTi wires subjected to tension," *Int. J. Mech. Sci.*, vol. 43, no. 11, pp. 2657–2677, Nov. 2001.

15. T. Fukuta and M. Iiba, "Experimental Results on Stress-Strain Relation of Ti-Ni Shape Memory Alloy Bars and their Application to Seismic Control of Buildings".

16. A. Gloanec, G. Bilotta, and M. Gerland, "Relation between cyclic deformation mechanisms and mechanical properties in a TiNi shape memory alloy Abstract :," pp. 1–6.

17. I. Faridmehr, M. H. Osman, A. Bin Adnan, A. F. Nejad, and R. Hodjati, "Correlation between Engineering Stress-Strain and True Stress-Strain Curve," pp. 53–59.

18. A. Abdulridha, D. Palermo, S. Foo, and F. J. Vecchio, "Behavior and modeling of superelastic shape memory alloy reinforced concrete beams," *Eng. Struct.*, vol. 49, pp. 893–904, 2013.

19. S. Nemat-Nasser and W.-G. Guo, "Superelastic and cyclic response of NiTi SMA at various strain rates and temperatures," *Mech. Mater.*, vol. 38, no. 5–6, pp. 463–474, May 2006.

20. R. Crambuer, B. Richard, N. Ile, and F. Ragueneau, "Experimental characterization and modeling of energy dissipation in reinforced concrete beams subjected to cyclic loading," *Eng. Struct.*, vol. 56, no. 2013, pp. 919–934, Nov. 2013.

Part VII
Micro and Nano Technology in Constructions and Civil Engineering

Thermal Gravimetric Analysis (Tga) of Kenaf Core and Its Cellulose for Membrane Fabrication

Sharifah Abdullah and Ramlah Mohd Tajuddin

Abstract Membranes can be fabricated using three main materials, namely solvent, polymer, and additives. The function of the solvent is to dissolve the polymer so it becomes homogenous with another material that is required to form the membrane layer. Various types of additives can be used to enhance the surface of the membrane layer. Examples of commonly used additives in membrane are polyethylene glycol (PEG), monosodium glutamates, sulfonated poly(ether ether ketone), and polyvinylpyrrolidone (PVP). However, these are synthetic additives; therefore, there is a need to search for a sustainable organic additive that would be greener for the environment, such as cellulose from suitable plants. In this study, cellulosic material was extracted from kenaf core, to be used as the organic additive for membrane formation. In order to investigate the suitability of this material, thermal gravimetric analyses (TGA) were performed in two parts. The first TGA was done on the kenaf core to determine the amount of cellulose that can be extracted from it. Then, a second TGA was done on a sample of the extracted cellulose to determine its weight and quantified loss of water, loss of solvent, loss of plasticizer, decarboxylation, pyrolysis, oxidation, decomposition, weight % filler, amount of metallic catalytic residue remaining on carbon nanotubes, and weight percentage of ash. TGA results on cellulose from kenaf core have shown that the crystalline melt was defined by the peak temperature at 333.07 °C. After the melt transition, the baseline had returned to a slightly lower position than the premelt baseline. The slope of the post-melt baseline had changed as the sample began to decompose. Meanwhile, TGA has extrapolated the onset temperature to 421.61 °C as the sample decomposes.

Keywords Kenaf core · Cellulose · Thermal gravimetric analysis

S. Abdullah (✉) · R.M. Tajuddin
Faculty of Civil Engineering, Universiti Teknologi MARA,
40450 Shah Alam, Selangor, Malaysia
e-mail: shaz6466@gmail.com; sharifah.abdullah@salam.uitn.edu.my

Fig. 1 Kenaf

Fresh kenaf   Kenaf core   Kenaf fiber

1 Introduction

Kenaf pulps were harvested from a plantation registered with the National Kenaf and Tobacco Board (NKTB) in Kelantan with the code name V36. Cellulose from kenaf was found to be suitable as an additive for membrane formation. Figure 1 shows images of fresh kenaf, kenaf core, and kenaf fiber. Kenaf core was used in this study.

Kenaf, or *Hibiscus cannabinus*, is considered as one of the most important commercial sources of fiber. It has been proven to be better than wood fibers in producing textiles, paper, pressed wood materials, etc. Cellulose was first discovered in tissues of plants in 1838 and was used to produce fibrous materials. Since then, cellulose is generally accepted as a polymer that consists of d-anhydroglucose units bonded with α-1, 4-glycosidic [1]. Cellulosic kenaf fibers are renewable and recyclable, thus have been used in the production of ethanol fuel additives and butanol. Kenaf core consists of 46.1 % cellulose, 29.7 % hemicellulose, and 22.1 % lignin [2]. Edeerozey et al. [3] have reported that kenaf stalks have an inner wood core and an outer fibrous bark that surrounds it, which is also known as the bast fiber. This fiber has high tensile strength and is said to be an alternative for glass fiber. The objective of this research is to investigate the suitability of this cellulosic material by analyzing the kenaf core and kenaf core cellulose using TGA.

2 Literature Review

Thermal Gravimetric Analysis (TGA) is a substance monitoring procedure, as a function of time or temperature in a controlled area/space. While heating a sample, TGA can observe whether its weight was decreasing or increasing. TGA can measure a sample's weight and quantifies the loss of water, loss of solvent, loss of plasticizer, decarboxylation, pyrolysis, oxidation, decomposition, weight % filler, amount of metallic catalytic residue remaining on carbon nanotubes, and weight the percentage of ash [4]. These quantifiable characteristics can be detected upon heating of a sample but there are some experiments where information may be obtained upon cooling. TGA is widely used to characterize and verify materials in various industries such as environmental, food science, pharmaceutical, and petrochemical [5]. Production of kenaf fibers has helped these industries in terms of

protecting the environmental ecosystem. Kenaf can replace the usage of wood in the paper industry as well as help to reduce damages to the tropical rainforest. Kenaf is a fast-growing plant that matures in 5–6 months and requires less fertilizer compared to other fibrous plants. Products made from kenaf include paper, mat, hand phone casing, plywood, car indoor panels, and packing material.

Previous studies related to membrane technology have shown that membranes have been fabricated using various materials but none have used cellulose from kenaf core. Idris et al. [6] have reported that suitable increment of monosodium glutamate in dope solution of dialysis membrane has improved its performance. Bowen et al. [7] have found that sulfonated poly(ether ether ketone) (SPEEK)has improved a membrane's surface condition. However, Kim and Lee [8] found that increasing the ratio of polyethylene glycol (PEG) will result in the casting solution becoming thermodynamically less stable. Patterson et al. [9] have used nanofil-tration membranes to treat public drinking water in Ohio and Minnesota by checking the color and total organic carbon (TOC) in the drinking water. These researches have proven that membrane technology encompasses numerous areas of research, such as materials to use, systems of membranes and also, the purpose of such investigations. Furthermore, wastewater that has been treated efficiently can be reused for another purpose. The concept of reusing and recycling can help various industries achieve better green management goals. Therefore, this research aims to develop a new membrane formulation and fabrication using a sustainable and low cost material. The optimum percentage of cellulose extracted from the kenaf core was determined for the fabrication of nanofiltration membrane.

3   Material and Research Method

The materials used in this study include kenaf core and chemicals, such as N, N-Dimethylacetamide (DMAc), polysulfone resin (PSF), sodium chloride (NaCl), anthraquinone, sodium hydroxide, hydrochloric acid, and chlorine dioxide. Kenaf core was separated from the kenaf fiber using a water retting system and was dried in an oven at a temperature of not higher than 60 °C for 24 h. Then, the dried and cleaned kenaf cores were grounded and sieved into 0.25 cm uniform samples for the microcrystalline cellulose process (ASTM E 11-09). Before proceeding with the cellulose extraction process at the Forestry Research Institute of Malaysia (FRIM), the grounded sample of the kenaf core underwent thermal analysis. This procedure, known as the Thermal Gravimetric Analysis (TGA), was done at the Nano-SciTech Centre, Universiti Teknologi Mara (UiTM) to estimate the amount of kenaf cores needed for extracting certain amount of cellulose. A rotary digester was used to heat, wash, and clean the samples from the reagent used. In order to obtain a fine-sized cellulose, the digestion method was repeated several times until the selected sizes were obtained. The percentage of chemical used and the repetitions depended on the characteristics of the samples. Raw materials from the kenaf cores, which have been grounded into smaller pieces, underwent the pulping process. This step required the

raw materials to be mixed with a certain amount of chemical and heated at 170 °C for a few hours until the samples were completely mixed and homogenous. The pulps were then washed and bleached several times until the pulps were white in color. After cellulose has been extracted from the kenaf core, a sample was sent to the Faculty of Chemical Engineering for the TGA test. In this study, cellulose from the kenaf core was formulated with polymer and solvent to fabricate membranes.

In this research, the pulps underwent five rounds of bleaching, in a process called the elementary chlorine free (ECF), using chlorine dioxide (D) and alkaline extraction (E). Table 1 shows the bleaching conditions of this process. Each set of bleaching process consisted of 100 g oven-dried pulps (OD). The bleaching process was repeated until the pulps were observed to be white in color.

The microcrystalline process required the use of 1 N hydrochloric acid (HCl) with the ratio of 1:20 to bleached pulps, which were mixed together in the rotary digester for 1 h at 70 °C. Then, the mixed pulps were refluxed for another hour. This step was repeated until the required texture and color of the pulps were achieved. Finally, the hydrolyzed cellulose was washed with distilled water and dried using the dry milling and sieving method. The extracted microcrystalline cellulose from kenaf core is shown in Fig. 2.

Membrane formation began with the titration process. During this process, polysulfone resin (polymer) was added to N,N-Dimethylacetamide (solvent). This mixture was stirred continuously until the polymer had dissolved in the solvent. Cellulose was added to this mixture, which was stirred in a controlled temperature

Table 1 Bleaching conditions		D1	E1	D2	E2	D3
	Chemical and charge (%)	ClO_2	NaOH	ClO_2	NaOH	ClO_2
		3 %	2 %	3 %	2 %	3 %
	Pulp consistency (%)	10	10	10	10	10
	Time (min)	120	60	90	60	90
	Temperature (°C)	70	70	70	70	70

ClO_2 = Chlorine dioxide, NaOH = Sodium hydroxide

Fig. 2 Microcrystalline cellulose, extracted from kenaf core

Fig. 3 Flat-sheet membrane

Fig. 4 Pneumatically controlled flat-sheet membrane casting unit (Model: TR31-A)

of 60 °C until homogeneous. This final mixture is called a dope. The dope was placed in a water bath sonicator for 24 h to remove air bubbles. Examples of kenaf core cellulose membranes are as shown in Fig. 3. These membranes were fabricated using the fabricating machine shown in Fig. 4. This pneumatically controlled flat-sheet membrane casting unit (Model: TR31-A) was used to fabricate membranes, during the wet-dry immersed membrane process as well as for flux permeate and slat rejection tests.

4 Results and Discussion

Cellulose from kenaf core is a very fine material, which has been used to fabricate nanofiltration membranes in this research. The first stage of this process was to formulate the membrane. The formulation had involved material selections, as well as determining the percentage of materials to be used and parameters to be tested. In this research, the selected materials include polysulfone resins (PSF) as the polymer, N,N-Dimethylacetamide (DMAc) as the solvent, and kenaf core cellulose as the additive. These materials were blended homogenously with several formulations and then, analyzed with a number of parameters and selected tests. Formulations of membrane in this study are as listed in Table 2a, b.

For comparison purposes, the first formulations were made using a commercial cellulose acetate (Agros), as shown in Table 2a. Parametric analyses have shown that cellulose acetate membranes failed when applied with high pressure, whereas the membranes formulated using kenaf core cellulose were more resistant to higher pressure, as shown in Table 3. Based on these findings, the focus of this research was shifted toward using cellulose from kenaf core as the new material for fabricating membranes. Polymer, as the main material for membrane fabrication, was

Table 2 Formulation of Membrane

(a) Using cellulose acetate			
Dope	DMAc %	Polysulfone %	Cellulose Acetate %
D1	78.66	20.34	1
D2	77.66	20.34	2
D3	76.66	20.34	3
D4	75.66	20.34	4
D5	74.66	20.34	5
D6	73.66	20.34	6
D7	72.66	20.34	7
D8	71.66	20.34	8
D9	70.66	20.34	9
(b) Using cellulose from kenaf core			
Dope	DMAc %	Polysulfone %	Cellulose from Kenaf Core %
K1	78.66	20.34	1
K2	77.66	20.34	2
K3	76.66	20.34	3
K4	75.66	20.34	4
K5	74.66	20.34	5
K6	73.66	20.34	6
K7	72.66	20.34	7
K8	71.66	20.34	8
K9	70.66	20.34	9

Table 3 Maximum pressure applied on membranes

Membrane	Max pressure (bar)	Membrane	Max pressure* (bar)
D1	3	K1	6
D2	3	K2	6
D3	3	K3	6
D4	3	K4	6
D5	3	K5	6
D6	3	K6	6
D7	3	K7	6
D8	3	K8	6
D9	3	K9	6

D—membrane formulate with cellulose acetate
K—membrane formulate with cellulose from kenaf core
*indicates the available maximum pressure in the laboratory

selected to be the constant parameter for the formulation of membrane. Solvent concentration and kenaf core cellulose were the variables in this part of the research, as shown in Table 2b.

In this research, TGA was used to analyze the characteristics of the kenaf core and the results are shown in Fig. 5. The curves have indicated that kenaf core can handle a maximum of 598.37 °C of heating temperature. However, the inflection point for the sample was at 316.41 °C with residue of 6.2634 mg. The initial weight of the sample was 20 mg, and the weight loss was approximately 68.7 %. Based on this result, it was concluded that approximately 4 kg of dried kenaf core was needed to extract 1 kg of cellulose. A sample of dried kenaf core was sent to FRIM and processed with anthraquinone, sodium hydroxide, hydrochloric acid, and chlorine dioxide to extract cellulose.

The extracted cellulose from the kenaf core was also verified using thermal analysis. A sample of the extracted cellulose was sent to the Faculty of Chemical Engineering to be analyzed with the thermogravimetric analyzer. Parameters for this analysis are listed in Table 4.

The cellulose sample was characterized using the STAR SW9.30. Results from the TGA, as seen in Fig. 6, have shown that the thermal curve was a descending curve, which indicates that weight loss of the kenaf core cellulose has occurred. Based on this curve, it is clear that several diffusion controlled reactions have occurred. The cellulose was also observed to be melting during the TGA process. The shape of the TGA curve was also indicative of other gravimetric effects, such as drying by desorption and sublimation. The first stage of the TGA process has shown that the sample's weight had decreased from 20 to 17.7 mg (88.5 % residue), which has the right limit temperature of 116.9 °C and inflected point of 52.61 °C. The next step of this process has shown that the cellulose was burned up to a higher temperature of 421.61 °C with its weight decreasing to 7.1 mg (35.4 % residue). At this stage, the inflected point was 333.07 °C. The shape of the TGA curve has indicated that some of the cellulose material was melting at this stage. The curve kept
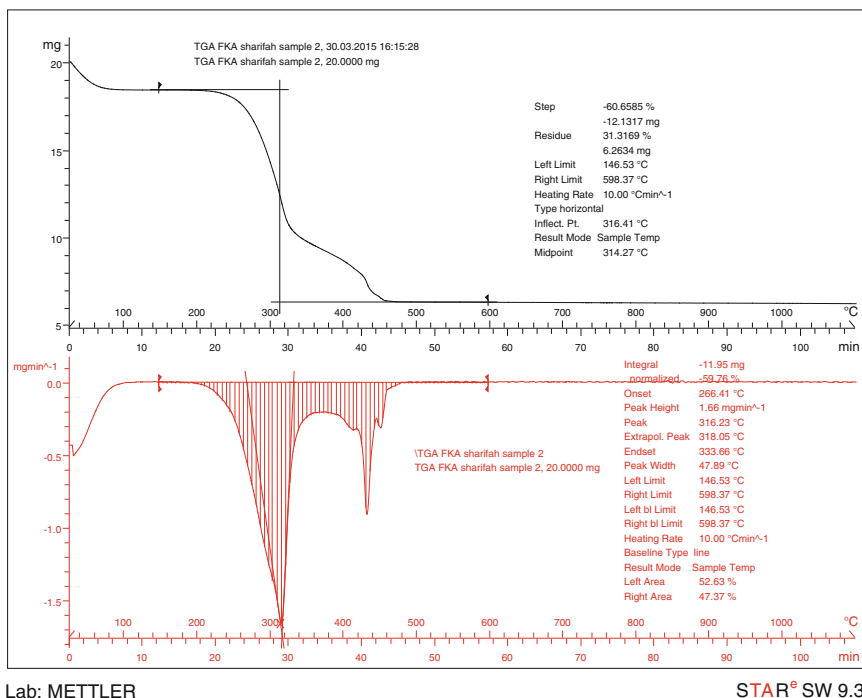
Fig. 5 TGA of kenaf core

Table 4 TGA parameters for kenaf cellulose

Parameter for TGA analysis	
Gas	Compressed air
Flow rate gas	50 ml/min
Start Temp.	25 °C
End Temp.	1100 °C
Heating rate	10 °C/min

descending and finally stopped when the cellulose's weight was down to 2.95 mg, which was 14.76 % residue with the inflection point of 545.65 °C. By comparing the TGA data between cellulose and kenaf core, we have noticed that the cellulose can withstand the lower temperature due to the extraction process. The red Differential Scanning Calorimetry (DSC) thermal curve and the blue TGA weight loss curve are as displayed in Fig. 6. This sample is a free base, small-molecule crystalline powder. The DSC curve indicates that there was a crystalline melt, as defined by the peak temperature at 333.07 °C. After the melt transition, the baseline returned to a slightly lower position than the pre-melt baseline. The slope of the post-melt baseline changed when the sample began to decompose. The DSC exothermic decomposition peak at 421.61 °C corresponded to the TGA extrapolated onset temperature of
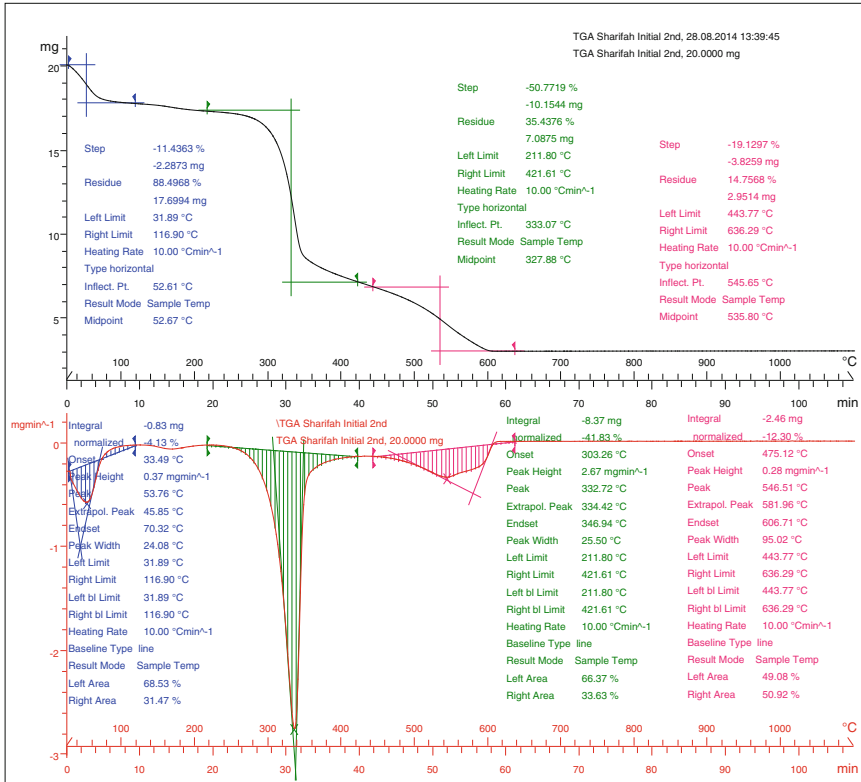
Fig. 6 TGA of kenaf cellulose

Fig. 7 Permeate flux of kenaf core cellulose membrane
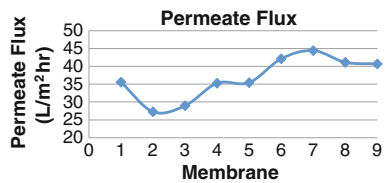
421.61 °C when this sample began to decompose. The fabricated membranes in this study were tested with permeate flux using pure water to verify their characteristics. The average permeate flux were found to be in the range of 27.2–44.4 L/m^{2}hr with the highest flux given by K7 membrane, as shown in Fig. 7.

Results from the permeate flux were also compared with the results of NaCl rejection test. NaCl testing is a salt rejection test to determine the capability of the membrane in restraining salt. The results of the NaCl test are shown in Fig. 8.

Fig. 8 NaCl rejection test
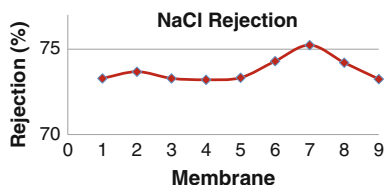
Based on these results, it was concluded that the membranes' rejection values ranged between 73.24–75.23 %, with membrane K7 giving the highest rejection result.

5 Conclusion

As a conclusion, TGA can be a medium to investigate the characteristics of any material, such as weight loss, maximum temperature, melting point, decomposition peak, and drying by desorption. The kenaf core sample has a maximum heating temperature of 598.37 °C but its inflection point was at 316.41 °C with residue of 6.2634 mg (31.3 %). Meanwhile, the remaining cellulose weighed at 2.95 mg (14.76 %) residue with the inflection point of 545.65 °C. In this study, TGA was used to verify the amount of raw materials to be prepared before the extraction process, which has helped to manage the limited sources of raw materials. The fabricated membrane (K7) using kenaf core cellulose has given the highest flux of 44.4 L/m^{2}hr and NaCl rejection of 75.23 %.

The characteristics of kenaf core cellulose can be determined using various procedures or methods but the most popular method is by using TGA. While heating a sample, TGA can observe whether its weight decreases or increases; in this case, it found that after final stage, the residue was only 15 % of the initial sample. Thermal gravimetric analysis on kenaf core cellulose has shown that its melting point was at 333 °C and exothermic decomposition peak was at 421.61 °C.

References

1. Lee, S. A., & Eiteman, M. A. (2001). Ground kenaf core as a filtration aid. *Industrial Crops and Products*, *13*(2), 155–161. http://doi.org/10.1016/S0926-6690(00)00062-5
2. Gan, S., Zakaria, S., Chia, C. H., Kaco, H., & Padzil, F. N. M. (2014). Synthesis of kenaf cellulose carbamate using microwave irradiation for preparation of cellulose membrane. *Carbohydrate Polymers*, *106*, 160–165. http://doi.org/10.1016/j.carbpol.2014.01.076
3. Edeerozey, A. M. M., Akil, H. M., Azhar, A. B., & Ariffin, M. I. Z. (2007). Chemical modification of kenaf fibers. *Materials Letters*, *61*(10), 2023–2025. http://doi.org/10.1016/j.matlet.2006.08.006

4. Wu, C., Zhang, S., Yang, D., & Jian, X. (2009). Preparation, characterization and application of a novel thermal stable composite nanofiltration membrane. *Journal of Membrane Science*, *326*, 429–434. http://doi.org/10.1016/j.memsci.2008.10.033

5. Li, B., Chen, G., Zhang, H., & Sheng, C. (2014). Development of non-isothermal TGA–DSC for kinetics analysis of low temperature coal oxidation prior to ignition. *Fuel*, *118*, 385–391. http://doi.org/10.1016/j.fuel.2013.11.011

6. Idris, A. N. I., Kee, C. M., & Ahmed, I. (2008). Effect of Monosodium Glutamate Additive on Performance of Dialysis Membrane. *Journal of Engineering Science and Technology*, *3*(2), 172–179.

7. Bowen, W. R., Doneva, T. A., & Yin, H. (2002). The effect of sulfonated poly(ether ether ketone) additives on membrane formation and performance. *Desalination*, *145*(1–3), 39–45. http://doi.org/10.1016/S0011-9164(02)00364-8

8. Kim, J.-H., & Lee, K.-H. (1998). Effect of PEG additive on membrane formation by phase inversion. *Journal of Membrane Science*, *138*(2), 153–163. http://doi.org/10.1016/S0376-7388 (97)00224-X

9. Patterson, C., Asce, M., Anderson, A., Sinha, R., Muhammad, N., Ph, D., & Pearson, D. (2012). Nanofiltration Membranes for Removal of Color and Pathogens in Small Public Drinking Water Sources. *Journal of Environmental Engineering ASCE*, *138*(January), 48–57. http://doi.org/10. 1061/(ASCE)EE.1943-7870.0000463.

Effect of Clay as a Nanomaterial on Corrosion Potential of Steel Reinforcement Embedded in Ultra-High Performance Concrete

M.J. Mohd Faizal, M.S. Hamidah, M.S. Muhd Norhasri and I. Noorli

Abstract The effect of clay as nanomaterial or nanoclay (NC) on corrosion potential of steel reinforcement embedded in ultra-high performance concrete (UHPC) due to the early age properties of UHPC was investigated. In this present research, ordinary Portland cement (OPC) was partially replaced by NC at 1, 3, and 5 % by weight of cement to produce the nanoclayed UHPC. It is well recognized that the corrosion of steel reinforcement would affect the service life of the reinforced concrete structure performance. To overcome this problem, UHPC was benefited due to its superior characteristic in term of density and durability as compared to OPC concrete itself. In this present research, half-cell potential (HCP) was used to monitor and measure the corrosion potential of steel reinforcement embedded in UHPC and nanoclayed UHPC. Meanwhile, weight loss of corroded steel reinforcement and pH values of hardened UHPC and nanoclayed UHPC were also conducted as follows to the specific procedures. All the samples were immersed in 3 % sodium chloride solution up to 91 days of exposure. The results revealed that the corrosion activity of steel reinforcement embedded in UHPC with 5 % NC recorded the lowest corrosion potential readings compare to those UHPC. It is also shows that the pH value of concrete and weight loss of corroded steel reinforcement in UHPC alone is highest compared to UHPC

M.J. Mohd Faizal (✉)
Faculty of Civil Engineering & Earth Resources, Universiti Malaysia Pahang,
Lebuhraya Tun Razak, 26300 Gambang, Pahang, Malaysia
e-mail: faizaljaafar@ump.edu.my

M.S. Hamidah · M.S. Muhd Norhasri
Faculty of Civil Engineering, Universiti Teknologi MARA,
40450 Shah Alam, Selangor, Malaysia
e-mail: hamid929@salam.uitm.edu.my

M.S. Muhd Norhasri
e-mail: norhasri@gmail.com

I. Noorli
Faculty of Civil & Environmental Engineering, Universiti Tun Hussien Onn Malaysia,
86400 Parit Raja, Batu Pahat, Johor, Malaysia
e-mail: noorli@uthm.edu.my

incorporating different levels of NC. As regards to the results, it is revealed that replacing NC as a replacement to cement significantly enhanced the chloride penetration of nanoclayed UHPC. It is also indicated that the corrosion potential decreased with the increase of NC and as a result delayed the corrosion initiation.

1   Introduction

Concrete is a unique composite material that provides a high degree of protection to the reinforcing steel against corrosion under high alkalinity and thus steel remains passivated [1]. However, concrete is a porous material and therefore easy to be penetrated into by some aggressive substances, especially chloride ions in seawater or de-icing salts. The potential risk of steel corrosion in a structure is unpredictable and cannot be detected visually. Thus, the damage due to corrosion of steel in concrete structures has become a large field of research interest until today. Corrosion of steel embedded in concrete structure becomes a worldwide problem in construction. In general, chloride contamination is the main cause concerning corrosion of the reinforcement and premature failure of reinforced concrete structures [2–4]. Corrosion can be defined as rust formation and/or loss in cross-section of steel rebar [5, 6]. In addition, the steel corrosion also depends on several factors such as concrete mix proportion, temperature, water/cement ratio, cement type and content, relative humidity, and blended materials [7]. On the other hand, pH of concrete pore solution also influences the steel corrosion. Normally, the steels remain passive when the pH values of concrete are about 12.5–13.5 [8, 9]. Previous researches noticed that the lowering of pH in the concrete under certain circumstances would disrupt the passive film of steel reinforcement [10–13].

For conventional concrete, the porous nature is an avoidable. Through the pores, the chloride penetrates easily and initiates corrosion of steel reinforcement. At this point of view, ultra-high performance concrete (UHPC) has been announced as a solution for corrosion problem in RC structures due to its durable, dense solid density, and reduced pore size [14]. UHPC also can achieve strength five times greater than conventional concrete [15, 16]. Nowadays, the usage of UHPC is increasing because of demand of high-strength concrete that can be used in constructing dams, high-rise tower, wide-span girders and bridges. The achievement of such of high-strength concrete has been possibly through the introduction of pozzolanic material such as silica fume, fly ash, rice husk ash, palm oil fuel ash, and other by-product materials. Recently, the development of nanotechnology to produce the nanomaterial has been growth rapidly. A nanomaterial has been introduced as an alternative material as cement replacement to produce high-performance concrete. Nanomaterial can be referred as nanoparticles which have the smallest size ranges from 1 to 100 nm in size [17]. Due to the nano size of particles, the surface area becomes larger and able to

facilitate the chemical reactions to produce a dense cement matrix with more calcium silicate hydrate (C-S-H) and less calcium hydroxide [18]. In addition, this will refine the overall performance of UHPC. Therefore, it is also proved that nanomaterials can affect chloride penetration within concrete pore solution.

In spite of this, there are several types of nanomaterial available in the market and one of it is nanoclay (NC). In this present study, NC was incorporating into UHPC to investigate its influence to the resistance of chloride penetration. As a consequence, it lead to the corrosion of steel reinforcement in concrete. The NC is a new supplementary cementitious material in producing UHPC. NC is a smallest particle and very reactive due to pozzolanic reactivity, and thus improves the strength. In comparison with previous research, this study aimed to evaluate the corrosion activity of ultra-high performance concrete (UHPC) incorporating different levels of NC as cement replacement at the early age of UHPC strength.

2 Methodology

2.1 Materials

This research was conducted to investigate the influence of nanoclay (NC) as a cement replacement to the corrosion potential of steel reinforcement embedded inside ultra-high performance concrete (UHPC). The cement used is ordinary Portland cement (OPC) Type I provided by local supplier. The control concrete mix (UHPC) was prepared using OPC while the UHPC incorporating NC were prepared by replacing the OPC amount with different levels of NC from the total weight of OPC used. The crushed gravel was used as the coarse aggregate with a nominal size of 14 mm. Meanwhile, fine aggregate passing 600 μm were used as sand. In order to obtain a workability of UHPC and nanoclayed UHPC, the hyper-superplasticizer namely Glenium ACE 389 SURETEC supplied by BASF (M) Sdn. Bhd. was necessarily used to apply high-range water-reducing. In this research, NC also known as bentonite was supplied by Aldrich (M) Sdn. Bhd. The molecular weight of NC is 80 g/mol. Before using NC, the raw NC was subjected to calcination process. The calcination process was done by heating the raw NC in furnace at 700 °C for 3 h.

2.2 Mix Designation and Samples Fabrication

Three identical series of UHPC that contain different levels of NC were prepared. The OPC where replaced with NC at 1, 3, and 5 % from the total weight of cement. The mix proportion was identified as control UHPC (0 % NC) and remaining nanoclayed UHPC incorporating 1, 3, and 5 % NC was labeled as UHPC-NC1, UHPC-NC3, and UHPC-NC5, respectively. All the samples were casted in cylinder with a dimension of 100 and 200 mm in diameter and length, respectively.

The UHPC and nanoclayed UHPC samples for corrosion measurement were obtained by embedding the steel bar in concrete with a cover depth of ±20 mm. In this present research, the conventional steel reinforcement namely high-yield tensile strength steel of ∅12 mm was used. The initial weight of steel reinforcement was weighted before it was embedded centrally inside the concrete. The steel reinforcement used was in new condition (no corrosion). After the concrete samples hardened, the samples were cured in water for 7 days. Thus, the concrete samples immediately immersed into 3 % sodium chloride (NaCl) solution for accelerates the corrosion. Before immerse, the samples were sealed at the top and bottom using waterproofing membrane. This is to prevent chloride ingress at the top and bottom of samples. The 3 % NaCl expose process takes up to 91 days. Meanwhile, the exposed steel reinforcement (outer from concrete sample) was also protected using thin plastic.

In order to measure the corrosion potential of the steel reinforcement embedded in UHPC and nanoclayed UHPC, half-cell potential (HCP) was used to record the potential readings. The corrosion potential of steel bar was monitored up to 91 days. Meanwhile, those parameters were measured at 3, 7, 28, 56, and 91 days. Table 1 displays the mix designation of the UHPC and UHPC-NC concrete were used. The water to cement factor used was constant at 0.20.

2.3 Testing Procedures

In this research, the testing method can be divided into three tests comprises of corrosion potential monitoring of steel bar embedded in UHPC and UHPC-NC, weight loss of embedded steel bar and pH value of UHPC and UHPC-NC samples. For corrosion potential monitoring, the nondestructive technique namely half-cell potential (HCP) were used to record the corrosion potential. The test procedure is outlined in the ASTM C876: Standard test method for half-cell potential of reinforcing steel in concrete. The copper/copper sulfate electrode (CSE/CSE) was used as a reference electrode. Furthermore, the potential readings recorded by HCP were taken every day for 2 months and were continued weekly after that period up to 91 days. The reading of HCP that pass the threshold at −350 mV shows the steel reinforcement experienced corrosion. The corrosion classification can be identified in Table 2.

Table 1 Mix proportion of UHPC and nanoclayed UHPC concrete

Mix design	Raw materials (kg/m³)					
	Cement	NC	Agg.	Sand	Water	Glenium
UHPC	800	0	433	800	160	11.55
UHPC-NC1	797	8	433	800	160	6.38
UHPC-NC3	776	24	433	800	160	6.98
UHPC-NC5	760	40	433	800	160	7.60

Table 2 Half-cell potential measurements according to ASTM C876

Corrosion condition	Half-cell potential (-mV) (CSE/CSE)
Severe corrosion	<−500
High (<90 % risk of corrosion)	<−350
Intermediate corrosion risk	−350 to −200
Low (10 % risk of corrosion)	>−200

On the other hand, the weight loss for corroded steel bar embedded in UHPC and nanoclayed UHPC were measured at 7, 28, 56, and 91 days. The sample was split into two parts by using hydraulic pressure machine. Accordingly, the corroded steel bar was taken out from the concrete sample to measure its weight. Before measure the weight loss, the corroded steel bar was cleaned using Die grinders (MK-505) to remove all the corrosion products. The weight loss of corroded steel bar was measured immediately by using digital weight balance. In order to determine the pH value of hardened UHPC and nanoclayed UHPC, the concrete powder was obtained from the broken samples. The samples were drilled at three different points at the top, middle, and bottom of the concrete samples. The depth required to drill is about ≤50 mm from the surface where the steel reinforcement was embedded. The test procedures for determining the pH value are adopted from [19].

3 Result and Discussion

The results of corrosion potential, weight loss of corroded steel, and pH value of hardened ultra-high performance concrete (UHPC) and nanoclayed UHPC are presented. The result on the relationship of corrosion potential and days of exposure for all UHPC mixes is illustrated in Fig. 1. It is demonstrated that the evolution of corrosion potential measured on the steel bar in UHPC and nanoclayed UHPC increase as the duration of exposure was prolonged. Moreover, although the half-cell potential (HCP) for all UHPC samples randomly fluctuate throughout the expose days. A decreasing corrosion potential with the increased content of NC can be generally observed after the steel corrosion is initiated.

At the early age, the chloride can be penetrated in the concretes to attack the steel bar owing to their slow diffusion. A relatively more negative potential have been detected after 30 days. This is happen may be attributable to the rather higher concentration of dissolved oxygen in the concrete at the early age to promote the steel corrosion [3]. Within a few days of exposure, the corrosion of steel bar for UHPC alone has been detected to corrode and follows by UHPC-NC1 at 50 days of exposure. The corrosion initial time for steel reinforcement to corrode is verified when the chloride threshold limit is below −350 mV$_{CSE}$ whereas over 90 % risk of corrosion [20]. Previous research also reported that the more negative readings of potential generally considered a higher probability of steel corrosion [21].
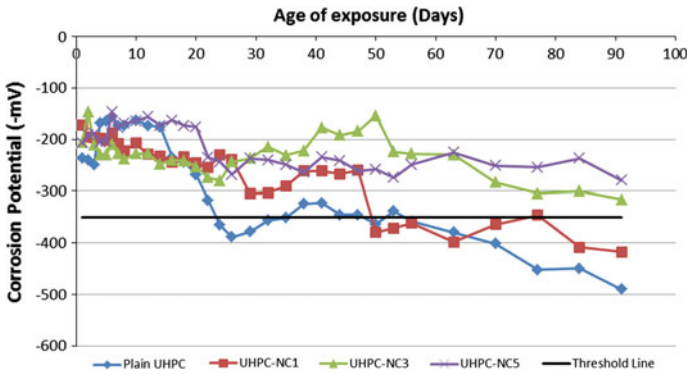
Fig. 1 Corrosion potential of steel reinforcement in UHPC and nanoclayed UHPC

It can be also found that the corrosion potential readings of steel embedded in UHPC incorporating 3 and 5 % NC showed the embedded steel rebar without showing any signs of corrosion up to 91 dyas. It is reveals that the alteration of UHPC with NC takes a longer time to take place the corrosion initiation than that of UHPC alone. Although the application of cement replacement with 5 % NC have been recognized as one of the potential and excellent parameters to resist the chloride penetration. This is also claimed by [22] who are found that concrete incorporating silica fume (SF), pulverized fuel ash (PFA), and ground granulated blast furnace slag (GGBS) as partial cement replacement were performed to reduce the corrosion initiation of steel reinforcement in concrete. On the other hand, the combination of the pozzolanic reaction namely NC makes a contribution to produce a dense microstructure of cement matrix in the long term. Therefore, the resistance to the chloride penetration into the nanoclayed UHPC is enhanced and delay the corrosion initiation. As well-documented in [3] that concrete containing SF and PFA restricts the access of oxygen and water and thus the corrosion potential are kept at a lower after corrosion initiation.

On the other hand, Fig. 2 shows the results on weight loss percentage of rusted embedded steel reinforcement in UHPC alone and nanoclayed UHPC. All the steel reinforcement embedded in concrete samples were exposed to 3 % NaCl solution at 3, 7, 28, 56, and 91 days. The figure demonstrates that there were little differences in the propagation percentage of weight loss of rusted embedded steel reinforcements during the first 91 days of NaCl exposure (early age of concrete strength). This research also found that the steel inside nanoclayed UHPC samples are significantly superior to the UHPC alone. But, it is shows that steel embedded in UHPC-NC5 experienced least weight loss after expose at 91 days. From the results, it is realized that by increasing the percentage of NC in UHPC, the weight loss percentage of rusted embedded steel can be minimized. It is revealed that UHPC incorporating 5 % NC is good quality concrete that provides excellent protection for steel reinforcement.

This showed that the weight loss of rusted embedded steel reinforcement occurred when there is a chloride present that contributed to the corrosion.
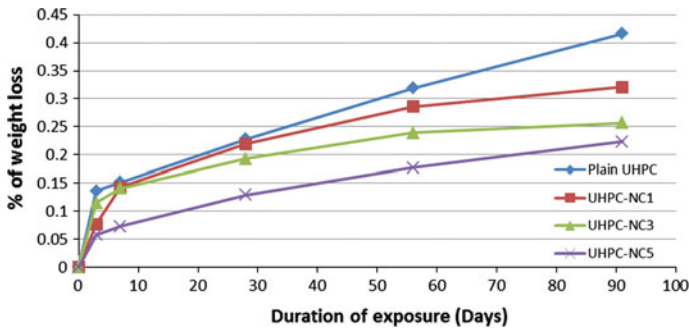
Fig. 2   Weight loss of embedded rusted steel in UHPC and nanoclayed UHPC

However, high NC content in UHPC provides better pozzolanic reactions that improve the concrete pore size in concrete matrix. Previous researchers also claimed that concrete containing high amount of fly ash resulted in less chloride penetration in the pore solution of concrete [20]. This finding, also agreed by [23], stated that NC filled the pore space inside the concrete and thus concrete will be denser and can protect form chloride ions penetration. On the other hand, it is revealed that the percentage of weight loss for all rusted embedded steel recorded at early age of concrete strength could be barely observed and can be defined as time for corrosion initiation. This is because the percentage of rusted weight loss obtained is lower than 2 % from the initial weight of steel. As well-documented in [4, 20] also noticed that the prediction of initial corrosion on steel reinforcement was occupied approximately at ranging 0–2 % deterioration.

The pH of UHPC alone and nanoclayed UHPC at 3, 7, 28, 56, and 91 days of exposure is shown in Fig. 3. Overall, it was found that the pH of concrete decreasing with increased of age of exposure. However, by replacing the levels of NC in UHPC alone show that the pH of hardened nanoclayed UHPC significantly affects the pH levels. It is also found that the pH value of UHPC alone drop
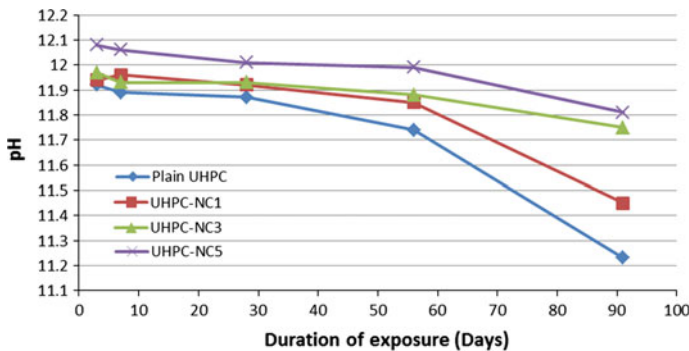
Fig. 3   pH values of hardened UHPC and nanoclayed UHPC

drastically after exposure at 56 days. It can be noted that the use of nanoclay as cement replacement can increase the alkalinity level of the pore solution of concrete. As known, NC incorporates more alkalis into hydration products than they release to the pore solution. It resulted in a lower pH value in the pore solution.

Other than that, the pore solution in concrete was acting as an electrolyte which was absorbed into pores of concrete physically and it contained various ions such as sodium, calcium, potassium, and sulfate [24]. These ions were neutralized by forming carbonates and sulfates and at the same time reducing the pH value. Normally, pH of pore solution for normal concrete was approximately 12.5–13.5. However, most of previous researchers noted that the pH of concrete is commonly depends on the types of cement used as reviewed in [4]. The figure reveals that at 28 days, the pH value for UHPC alone and nanoclayed UHPC samples were slightly decreased than the pH for new concrete. This showed that steel reinforcement will corrode even though the initial pH value was high with respect to the present certain chloride amount in pore solution.

4 Conclusions

From this finding, the conclusions can be accessible as follows:

1. It is revealed that there was a reduction on corrosion potential recorded by half-cell potential for nanoclayed UHPC compared to UHPC alone. It is obtained that the optimum for replacement of nanoclay (NC) into UHPC was 5 % of level replacement.
2. It is realized that the presence of NC material was able to resist chloride penetration. 5 % NC in producing UHPC has been proved to be lower percentage of weight loss of rusted embedded steel.
3. It is demonstrated that inclusion of different levels of NC content would increase the pH value on nanoclayed UHPC. It is also found that UHPC that contained 5 % NC (UHPC-NC5) showed highest pH value than that UHPC and nanoclayed UHPC.
4. It can also be concluded that NC significantly had a potential to be used in UHPC to slow the chloride penetration in concrete.

References

1. Y. Xizhen and Y. Wu, "Thermodynamics of metal corrosion," Chemical Industry Press, 1996, Beijing, Chap. 3.
2. L. Samples and J. Ramirez, "Methods of corrosion protection and durability of concrete bridge decks reinforced with epoxy-coated bars, phase I," FHWA/IN/JTRP-98/15. Purdue University, IN, 1999.

3. J. Xu, L. Jiang, W. Wang, Y. Xu and Y. Jiang, "Chloride threshold value for reinforcement corrosion in concrete with additions of silica fume or fly ash," Magazine of Concrete Research, 2011, vol. 63 (12), pp. 905–913.

4. X. Shi, N. Xie, K. Fortune and J. Gong, "Durability of steel reinforced concrete in chloride environments: An overview," Construction and Building Materials, 2012, vol. 30, pp. 125–138, doi:10.1016/j.conbuildmat.2011.12.038.

5. P. Schiessl, "Corrosion of steel in concrete," RILEM Technical Commitee, 1988, 60-CSC, Chapman & Hall, New York.

6. B. Elsener, "Corrosion and environmental degradation," 2000, vol.2, M. Schutze (Ed.), Willey-VCH, Weinheim, p. 389.

7. W. Cao, X. Wan and T. Zhao, "Influencing parameters analysis of chloride threshold value on reinforcements embedded in concrete," Advanced Materials Research, 2011, vol. 250–254, pp. 202–206, doi:10.4028/www.scientific.net/AMR.250-253.202.

8. G. Qiao and J. Ou, "Corrosion monitoring of reinforcing steel in cement mortar by EIS and ENA," 2007, Electrochimica Acta, vol. 52, pp. 8008–8019.

9. B. Junyig, A. Hongmei and L. Puguang, "Effect of oxygen ions diffusion on steel corrosion in concrete," Key Engineering Material, 2011, vol. 477, pp. 398–403. doi:10.4028/www.scientific.net/KEM.477.398.

10. W. H. Hartt and J. Nam, "Effect of cement alkalinity on chloride threshold and timeto-corrosion of reinforcing steel in concrete," Corrosion, 2008, vol. 64 (8), pp. 671–80.

11. H.A.F. Dehwah, M. Maslehuddin and S.A. Austin, "Effect of cement alkalinity on pore solution chemistry and chloride-induced reinforcement corrosion," ACI Material Journal, 2002, vol. 99 (3), pp. 227–35.

12. M. Mareno, W. Morris, M.G. Alvarez and G.S. Duffo, "Corrosion of reinforcing steel in simulated concrete pore solutions—effect of carbonation and chloride content," Corrosion Science, 2004, vol. 46, pp. 2681–2699.

13. M. Ismail, B. Muhammad and E. Hamzah, "Corrosion behaviour of dual-phase and galvanized steels in concrete," Anti-Corrosion Methods and Materials, 2012, vol. 59 (3), pp. 4–4.

14. M. Schmidt and E. Fehling, "Ultra-high-performance concrete: research, development and application in Europe," Special Publication, 2005, vol. 228, pp. 51–78.

15. P. Richard and M. Cheyrezy, "Composition of reactive powder concretes," Cement and Concrete Research, 1995, vol. 25 (7), pp. 1501–1511.

16. M. Schmidt, E. Fehling, E. Glotzbach, C. Frohlich and S. Piotrowski, "Ultra-high performance concrete and nanotechnology in construction," 2012, Kassel: Kassel University Press.

17. Klefenz, "Nanobiotechnology: From molecules to systems," Engineering in Life Science, 2004, vol. 4 (3), pp. 211–218.

18. K. Patel, "The use of nanoclay as a construction material," International Journal of Engineering Research and Applications (IJERA), 2012, vol. 2 (4), pp. 1382–1388.

19. O. S. B. Al-Amoudi, Rasheeduzzafar and M. Maslehuddin, "Carbonation and corrosion rebars in salt contaminated OPC/PFA concretes," Cement and Concrete Research, 1991, vol. 21 (1), pp. 38–50.

20. T. Cheewaket, C. Jaturapitakkul and W. Chalee, "Initial corrosion presented by chloride theshold penetration of concrete up to 10 years-results under marine site," Construction and Building Materials, 2012, vol. 37, pp. 693–698

21. G. Ping and J. J. Beaudoin, "Obtaining effective half-cell potential measurements in reinforced concrete structures," Construction Technology Updates, 1998, vol. 18, National Research Coucil of Canada, July 1998, ISSN: 1206–1220

22. K. Y. Ann and H. W.Song, "Chloride threshold level for corrosion of steel in concrete," Corrosion Science, 2007, vol. 49, pp. 4113–4133.

23. M. Morsy, S. Alsayed and M. Aqel, "Effect of nano-clay on mechanical properties and microstructures of ordinary portland cement mortar". International Journal of Civil & Environmental Engineering IJCEE-IJENS, 2010, vol. 10 (1), pp. 23–27.

24. G. Song and A. Shayan, "Corrosion of steel in concrete: cause and detection," State-The-Art-Review, 1998, pp. 11–21.

Characteristic and Strength Properties of Nano Metaclayed UHPC

M.S. Muhd Norhasri, M.S. Hamidah, A. Mohd Fadzil and M.J. Mohd Faizal

Abstract Nanometal clay formerly known as nanoclay was a product from kaolin. Nanoclay considered as layered silicate mineral and potentially can be used as supplementary material in concrete study due to kaolinite compound in its chemical composition which is similar to metakaolin. In this study, formulation of nano metaclay where used as additives from 0, 1, 3, 5, 7, and 9 % in ultra-high performance concrete mix. This paper aims to study the effect of nano metaclay in morphology which includes XRF, SEM, and XRD analysis, characteristics of nano metaclay UHPC mix in workability, and also to see the hardened properties by means of compressive strength behavior and micrograph image of UHPC. All nano metaclayed UHPC mix will be compared to normal UHPC mix. As a conclusion, nano metaclay ball-forming structure provides a new knowledge on nano materials in concrete. Due to its clay properties, water demand is higher and decrease in fresh state occurred. Finally, addition of nano metaclay UHPC improves compressive strength of UHPC mix by acting as nano filler and promoting nucleation process in cement grain.

Keywords Nano metaclay · Nanoclay · Kaolinite · Additive · Ultra-high performance concrete

M.S. Muhd Norhasri (✉) · M.S. Hamidah · M.J. Mohd Faizal
Faculty of Civil Engineering, University Technology MARA, Shah Alam, Malaysia
e-mail: norhasri@gmail.com

M.S. Hamidah
e-mail: Hamid929@salam.uitm.edu.my

M.J. Mohd Faizal
e-mail: faizal@ump.edu.my

A. Mohd Fadzil
Institute of Infrastructure and Sustainability Management, Faculty of Civil Engineering, University Technology MARA, Shah Alam, Malaysia
e-mail: fadiil2013@yahoo.com

1 Introduction

Since the new millennium, design of concrete structure becomes more rigid and sophisticated. Most of the design requires materials that can carry heavy load more than 100 MPa, medium weight and easy to construct at adequate cost. Consequently, a new concrete called Ultra-High Performance Concrete (UHPC) was created. UHPC was the solution for special-type concrete that needs very high load application. Examples of UHPC structure are nuclear plant, dams, bomb shelter, and special-type building. Till now, there is no specific design for UHPC and for mix proportion, rigid and selective materials have to be applied. High cement content normally more than 1000 kg/m^3 is required, special aggregates such as pure silica-based aggregates to contribute strength, very low water content, hyperplasticizers, and also silica fume [1–3]. As mentioned earlier, mix proportion of UHPC requires very strict design and controlled and thus creates problem in terms of high cost materials due to special type of materials such as silica-based aggregates, silica fume which is expensive in certain country. Preparing the UHPC from start to finish is difficult due to low water content thus affecting the workability [4–6]. Despite the poor handling of UHPC mix, advantages of UHPC are many. First, higher strength performs by UHPC will reduce the structure size, weight, transportation, and is easy to handle [7, 8]. Second, by proper controlling of raw materials and handling, resulting in very dense concrete and automatically high-elastic concrete be performed and thus structure deformation is reduced by increasing stiffness and stability [9]. Finally, low-maintenance cost due to superb durability to discrepancies and destructive agent such as chemical attack [10].

Having nanoparticles in concrete component proves to contribute improvement and advantages to existing concrete. The most impact by performing stronger structure and improve permeability of liquid and gases in concrete [11, 12]. Other effect of nanoparticle is improving packing density of concrete thus can be a solution to the existing UHPC mix. The term nano concrete is created by Sobolev, and the nano material used in nano concrete must less than 500 nm [13–15]. Nano concrete improves packing model of concrete component and resulting in ultra-dense concrete. In conclusion, nano concrete will enhance concrete performance by increasing strength and durability of concrete thus reducing the size of structure member by eliminating or reducing the reinforcement system. From that concrete cost will be optimized and the consumer will benefit on having a quality concrete at affordable price and durable structure.

Till now, the utilization of nano metaclay in concrete is not revealed. Due to the potential of kaolin as supplementary cementitious materials, with the inclusion of nano metaclay it will produce a durable and increased strength concrete. Moreover, nano metaclay can offer more improvement in concrete and also as an alternative to other nano materials. The addition from this research also will contribute on the knowledge and availability of nanoclay-based materials in the market. It is believed that nano metakaolin can perform better or equal to the existing nanomaterials such as nano silica, nano alumina, and others.

2 Experimental Programme

2.1 Characteristics of Nanoclay and Nano Metaclay

Nanoclay is procured from Sigma Aldrich (M) Sdn Bhd. Since raw nanoclay is not active chemically, calcination process is done to activate the nanoclay. For calcination of nanoclay, temperature and duration was fixed to 700 °C and time of calcined is 3 h [16]. After calcined, nanoclay is transformed into nano metaclay. To characterize the nanoclay sample, chemical composition of nanoclay and nano metaclay is done using X-Ray Fluorescence (XRF) analysis. Next, microscopic analysis is done using Scanning Electron Microscope (SEM). Difference in chemical composition and image of nanoclay and nano metaclay samples is compared to those of OPC and metakaolin.

2.2 Setting Time Analysis and Compressive Strength of Nano Metaclay Cement Paste

Seven (7) series of nano metaclay UHPC are prepared and the mix proportion is shown in Table 1. Inclusion of nano metaclay as additive incorporated in UHPC is fixed from 0, 1, 3, 5, 7, and 9 %. Ten percent of metakaolin as cement replacement material is included in all nano metaclay UHPC specimens. Nano metaclay UHPC is compared to those of plain UHPC and metakaolin UHPC.

2.3 Preparation for Compressive Strength Testing

Due to low water content which causes poor workability, cement, water, and additive are added first in the mix. The superplasticizer is included, so that the paste

Table 1 Mix proportion of UHPC specimens

Mix	Cement (kg/m^3)	Fine (kg/m^3)	Coarse (kg/m^3)	SP (kg/m^3)	Water (kg/m^3)	Metakaolin (kg/m^3)	Nano metaclay (kg/m^3)
OPC	800	433	800	16	160	0	0
MK10	720	433	800	16	160	80	0
NMCA1	720	433	800	16	160	80	8
NMCA3	720	433	800	16	160	80	24
NMCA5	720	433	800	16	160	80	40
NMCA7	720	433	800	16	160	80	56
NMCA9	720	433	800	16	160	80	72

is uniform and homogenous. Superplasticizer used for this research is supplied by BASF (M) type Glenium ACE Suretec 389. The process to blend paste took around 10 min. While mixer is running, fine aggregate is poured and the mixer continued to rotate for about 6 min. Finally, coarse aggregate is added and mixed for 5 min. The total duration for mixing UHPC mix is around 25 min. Then slump test is performed to determine the workability of UHPC and molded into 100-mm cube for compressive strength test, respectively. Determination of compressive strength is confirmed by taking average from three identical cubes at every age of testing.

3 Result and Discussion

3.1 Characteristics of Nanoclay and Nano Metaclay

Table 2 shows the chemical composition of OPC, kaolin, metakaolin, nanoclay and nano metaclay. The chemical composition is confirmed by using X-ray Fluorescence (XRF). Nano metaclay records the highest content of silica oxide (SiO_2) compare to other samples. Silica compound found in nano metaclay reaches almost 65 % and followed by nanoclay which records almost 60 %. The highest silica content is recorded by metakaolin with 75 % and followed by kaolin at 70 % silica component. Meanwhile, OPC records the lowest content of silica which is less than 15 %. Based on the total content of the SiO_2, CaO, and Al_2O_3 more than 65 %, metakaolin and nano metaclay are considered as a pozzolanic material. Next, important element is alumina (Al_2O_3). The effect of alumina in concrete is to control setting of concrete. With higher content of alumina, concrete will set immediately and strength is achieved earlier compared to that of low alumina content cement. Another influence of alumina is to perform liquidation effect during heat treatment. Alumina reacts with heat and dilutes the particles of nano metakaolin by pushing the layered particles of nano metakaolin apart from one to another. Thus, resulting increase in surface area. For this research, metakaolin and

Table 2 Chemical composition for OPC, kaolin, metakaolin, nanoclay, and nano metaclay

Chemical composition	Mass percentage (%)				
	OPC	Kaolin	Metakaolin	Nanoclay	Nano metaclay
SiO_2	11.6	70.3	74.3	63.9	65.9
Al_2O_3	2.2	14.2	10.2	14.0	12.1
CaO	75.17	0.8	2.4	4.8	4.3
TiO_2	0.4	0.65	1.45	1.01	0.9
Fe_2O_3	5.38	0.76	1.82	13.41	11.4
K_2O	0.43	1.62	4.64	0.27	0.24
Remaining constituent	4.82	11.67	4.28	2.61	2.42
Total compound	100	100	100	100	100

nano metaclay recorded less than 15 % of alumina content as compared to those of OPC.

The micrograph of nanoclay and nano metaclay is shown in Figs. 1 and 2. Rounded shape and smooth surface is illustrated by nanoclay and nano metaclay specimen. The difference between before and after calcined for nanoclay and nano metaclay, is portrayed by smaller particles created after heat is applied. Heats applied during calcination liquidize the alumina content of in nanoclay. Due to liquidation, smaller rounded particle of nano metaclay is created. It shows that calcination not only reactivates the crystal of nanoclay but also reduces the particle of nanoclay into smaller size of nano metaclay.

Compressive strength for UHPC incorporated by nano metaclay is portrayed in Fig. 3. Inclusion of nano metaclay at every level addition, shows slow strength development as compared to those of OPC and metakaolin mix. Initially, from day 3 until 90 days of age-compressive strength incorporated by nano metaclay

Fig. 1 Micrograph image of nanoclay
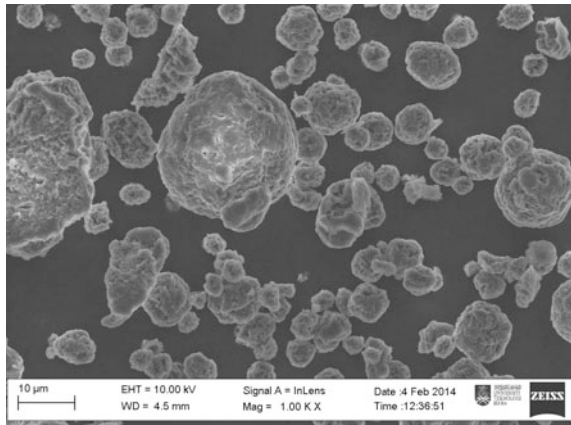
Fig. 2 Micrograph image of nano metaclay
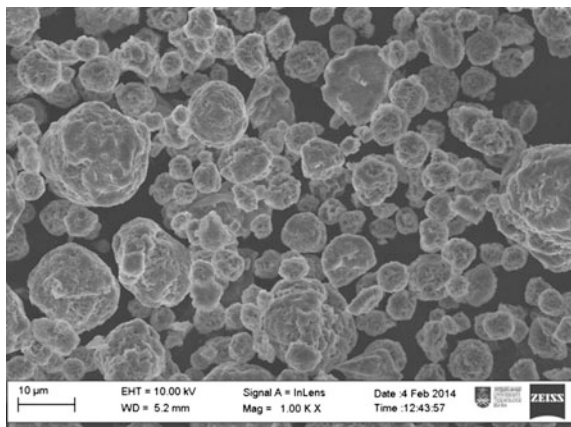
Fig. 3 Compressive strength of UHPC incorporated with nano metaclay
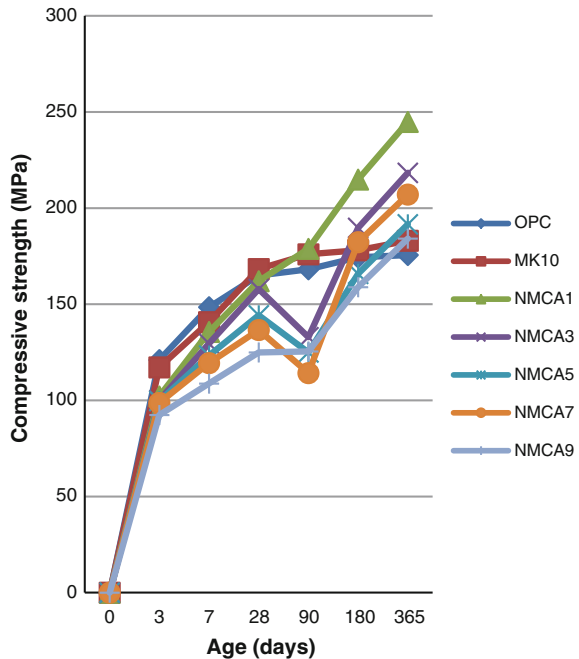
recorded lower than OPC and metakaolin mix. This phenomena is caused by dilution effect and also low silica and alumina component that delayed the pozzolanic reaction in UHPC. The delay in pozzolanic reaction is because there is not enough silica and alumina to react with compact component of UHPC. In UHPC, high cement content with smaller particles of aggregate is difficult to nano metaclay reacted with cement. During this period, addition of nano metaclay performs filling effect and densifies the microstructure of UHPC only. However, after 90 days of age-compressive strength of nano metaclay, UHPC started to develop and shows better result to those of OPC and metakaolin UHPC. Strength increment continues until period of 1 year. The highest compressive strength recorded is 244 MPa at 1 % inclusion of nano metaclay designated by NMCA1 mix. Metakaolin and OPC mix recorded strength at 183 and 175 MPa. Reason on this matter is nucleation of nanoparticles performed by nano metaclay creating and additional formation of C–S–H gel. Those additional gel created helps UHPC to gain strength at later ages. Formation of nucleation occurs with the addition of nano metaclay proves that strength of UHPC can be extended with the help of nanoparticles. Nucleation only occurs in the C–S–H gel and only nanoparticle can perform the densifying effect in the C–S–H system. With the occurrence of nanoparticles, microstructure of C–S–H gel is improved due to the densifying process in the void between C–S–H matrix components [17, 18]. Although highest strength is performed by NMCA1, other

nano metaclay UHPC mix also recorded higher compressive strength better than those OPC and metakaolin UHPC mix. It shows that nucleation process for nano metaclay improved the strength of UHPC at later ages. However, strength recorded by other types of nano metaclay UHPC specimens as compared to those OPC and metakaolin UHPC is minimal. Packed UHPC component makes nano metaclay difficult to create pozzolanic reaction. Thus, strength growth for nano metaclay is affected.

Discussion on Fig. 3 is supported by relative strength analysis performed in Fig. 4. It was clear that strength development of nano metaclayed UHPC only started at age 90 and strength development keep on continue until 365 days of age. The highest relative strength recorded at 365 days is performed by NMCA1 with 140 % more than OPC and metakaolin UHPC. From this analysis, concluded that addition of nano metaclay in UHPC performs a late strength affect as compared to those of OPC and metakaolin UHPC. At early age, nano metaclay only works as filler in densifying UHPC but the pozzolanic reaction and nucleation is seen after 90 days of age. It is confirmed that the strength of nano metaclayed UHPC will keep on increasing if duration of testing is prolonged. With the reaction that comes from nano metaclay, UHPC component is refined producing a more compact and less void which contributes to the increases in strength and also durability.

Fig. 4 Relative strength for UHPC incorporated by nano metaclay
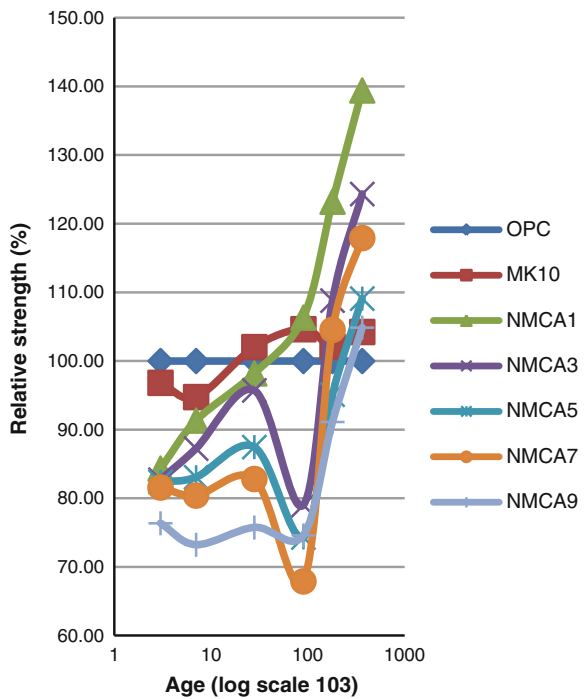
4 Conclusions

From this research, conclusions are drawn as follows:

1. Calcination process is the process use to activate the nanoclay crystal. With the appropriate temperature and time, the crystal of nanoclay is improved and transformed into nano metaclay. From calcination also, particles of nano metaclay is reduced as compared to those of nanoclay due to liquidation of alumina which break the rounded particle of nanoclay into smaller particle of nano metaclay.
2. Rounded and smooth surface and texture of nanoclay and nano metaclay is the criteria of nanoclay as compared to those OPC and metakaolin.
3. Inclusion of nano metaclay as an additional approach in UHPC, provides a late strength effect to UHPC. Delay in compressive strength occurred due to densifying process of nano metaclay in UHPC and also delay in dilution process is due to the compact component of UHPC. However, prolonged age strength of nano metaclay UHPC is improved and recorded higher than those of OPC and metakaolin. Nucleation process is extended by good filler process creating an additional C–S–H gel.

References

1. Khurana, R., R. Magarotto, and S. Moro, *User Friendly Ultra High Performance Concrete (UHPC)*, 2010.
2. Yazıcı, H., et al., *Utilization of fly ash and ground granulated blast furnace slag as an alternative silica source in reactive powder concrete.* Fuel, 2008. **87**(12): p. 2401–2407.
3. Richard, P. and M. Cheyrezy, *Composition of Reactive Powder Concretes.* Cement and Concrete Research, Vol. 25, No. 7, pp. 1501–1511, 1995.
4. Ferraris, C.F., K.H. Obla, and R. Hill, *The influence of mineral admixtures on the rheology of cement paste and concrete.* Cement and Concrete Research, 2001. **31**(2): p. 245–255.
5. Megat Johari, M.A., et al., *Influence of supplementary cementitious materials on engineering properties of high strength concrete.* Construction and Building Materials, 2011. **25**(5): p. 2639–2648.
6. Kovler, K. and N. Roussel, *Properties of fresh and hardened concrete.* Cement and Concrete Research, 2011. **41**(7): p. 775–792.
7. Wang, C., et al., *Preparation of Ultra-High Performance Concrete with common technology and materials.* Cement and Concrete Composites, 2012. **34**(4): p. 538–544.
8. Tafraoui, A., et al., *Metakaolin in the formulation of UHPC.* Construction and Building Materials, 2009. **23**(2): p. 669–674.
9. Yazıcı, H., et al., *Mechanical properties of reactive powder concrete containing mineral admixtures under different curing regimes.* Construction and Building Materials, 2009. **23**(3): p. 1223–1231.
10. Matte, V. and M. Moranville, *Durability of Reactive Powder Composites: Influence of Silica Fume on the leaching properties of very low water/binder pastes.* Cement and Concrete Composites 21, pp. 1–9, 1999.

11. Crainic, N. and A.T. Marques, *Nano - composites: a state of the art review.* Key Engineering Materials Vols. 230–232 pp 656-0, 2002.
12. Li, H., et al., *Microstructure of cement mortar with nano-particles.* Composites Part B: Engineering, 2004. **35**(2): p. 185–189.
13. Mehta, K.P. and P.J.M. Monteiro, *Concrete: Microstructure, Properties and Materials*1993: Taylor & Francis.
14. Maholtra, V.M. and P.K. Mehta, *POZZOLANIC AND CEMENTITIOUS MATERIALS*1996: TAYLOR & FRANCIS.
15. Cabrera, J.G. *Bringing the Concrete Industry into A New Era of Sustainable Development.* in *Proceedings of Mario Collepardi Symposium on Advances in Concrete Science and Technology*. 1997. Rome 8 October 1997, pp. 49–67.
16. Morsy, M.S. and S.A. Alsayed, M., *Effect of Nano-clay on Mechanical Properties and Microstructures of Ordinary Portland Cement Mortar.* International Journal of Civil & Environmental Engineering IJCEE-IJENS Vol: 10 No: 01, 2010.
17. Hou, P., et al., *Effects of the pozzolanic reactivity of nanoSiO2 on cement-based materials.* Cement and Concrete Composites, 2015. **55**: p. 250–258.
18. Yu, R., P. Spiesz, and H.J.H. Brouwers, *Effect of nano-silica on the hydration and microstructure development of Ultra-High Performance Concrete (UHPC) with a low binder amount.* Construction and Building Materials, 2014. **65**: p. 140–150.

Part VIII
Timber Engineering

Effect of Embedded Rod Length on Kempas and Keruing Timber Beam Jointed Using Bonded-in Pultruded Rods

Z. Nurul Izzatul Lydia, A. Zakiah and I. Azmi

Abstract Most common failure in timber structure is mainly caused by improper connection design, construction detail or serviceability. Selection of a connection fastener for a specific design application depends on the type of connection and the required strength capacity. One of the connecting method is by using adhesive bonded joint which give few advantages such as high local force transfer, distribute stresses more evenly, enhance joint stiffness and improve aesthetics of the timber beam. A successful connection can be determined when it was able to transfer load from member to member without failing the connector material and without damaging members it joint. There are lot of research on bonded-in timber connection that has been explored quite extensively in European countries using their type of timber species; however, there are still no publications available using Malaysia tropical timbers. This study investigates the effect of embedded length of the pultruded rods on Malaysian timber species, specifically Kempas and Keruing timber beam jointed using bonded-in adhesive method. Two timber members are connected using bonded-in glass fibre reinforced polymer (GFRP) rods by varying the embedded length. The capacity of the bonded-in joint was determined by bending shear test. Influence of the embedded length is clearly seen as the embedded length increases, the shear strength also increase. However after the rod embedded length had reached half of the timber length, the shear strength seem to decrease. The presence of bonded-in rod can also improve the ductility of the beam.

Keywords Timber structure · Bonded-in · Timber connection · GFRP

Z.N.I. Lydia (✉) · I. Azmi
Faculty of Civil Engineering, Universiti Teknologi Mara (UiTM),
40450 Shah Alam, Selangor, Malaysia
e-mail: lydia85@live.com

A. Zakiah
Institute for Insfrastructure Engineering and Sustainable Management (IIESM),
Universiti Teknologi Mara (UiTM), Level 3, Block 1, Engineering Complex,
40450 Shah Alam, Selangor, Malaysia

1 Introduction

Connections are the most important criteria to produce optimum design in wood structure, however, it was least understood component. Selection of a connection fastener for a specific design application depends on the type of connection and the required strength capacity. Each connection must be designed to transmit forces adequately and provide satisfactory performance for the life of the structure without causing splitting, cracking, or excessive deformation of the wood members.

Common methods of connection timber member are mechanical joint and adhesive joint. One of the examples that combine both of the joint is the bonded-in joint. It have been used for approximately 30 years in Nordic countries for joining and anchoring glulam members, rocks anchors, holding down bolts in concrete [1] and as rods to secure wooden turbine blades [2]. Bonded-in joints are formed when holes were drilled in the both part of timber block and rod is embedded into the holes by using bonding agent such as adhesive to produce connection. Bonded-in joint could be a tool to improve the competitiveness of wood as a structural material and potential as preferred choice of connection because it has seen to be more efficient as compared to the conventional connection. It also offer better stiffness and strength, better fire resistance and improvement in appearance. These techniques hopes can be used for allowing the utilization of weaker species of timber and creating a more efficient use of the timber supply.

The applications of bonded-in connection are still limited in the construction industry. This is because the performance of bonded-in connection are affected by many variable such as adhesive type, timber species, embedded length, rod types, rod diameter, rod length, etc. There are also no specific standards in the production of bonded-in rod except the general specification produced by the adhesive manufacture and as stated in Eurocode 5—Design of timber structure—Part 2: bridges as well as in European project report title "*GIROD-Glued in Rods for Timber Structure, 2003*". Eventhough there are general specification, the information is very limited as it only considered steel as the rod material and using overseas type of timber. Study on the varying embedded length of the pultruded rods is still not yet quantified as most of the studies were performed on low-density timber or softwood type timber. In fact, in Malaysia, none of the higher institution of higher learning and other centre has done any test on bonded-in connection. The application of bonded-in rod into the beams using Malaysian tropical timber by directly following the published data will be questionable. Therefore this study investigated one of the parameters that affects the performance of the bonded-in timber connection by seeing the effect of the rod embedded length.

2 Literature Review

Bonded-in connection is a method of joining structure together that eliminates some, or all, of the cost and weight of mechanical fastener. High strength adhesive was used to produce concealed timber connection and to transfer forces between structural elements, such as in a frame corner, or into a structure such as in a column foundation joint. The aim in connecting timber is to achiev a connection which at least as strong as the timber itself and must be able to transfer load from member to member without failing the connector and without damaging the timber member itself [3]. Few foreign researchers have explored the performance of timber connections by looking at the effect of few parameters by varying glueline thickness, bonded length, rod surface preparation, rod diameter, adhesive type, moisture content and grain orientation.

Bonding of rods into timber members has been widely investigated by Broughton and Hutchinson [4] using both experimental and numerical technique. They explored the key effect parameters (adhesive types and performance, rod embedded length, rod diameter, annular bondline thickness, multiple rods and rods spacing) on bonded-in joint performance and found out that pull-out strength can be significantly improved through careful selection and optimization of the joint geometry.

Harvey [5] have done pull-out test using Laminated Veneer Lumber (LVL), Oak and Ash timber. In the study, bonded-in rods (which include the use of bolts, rods and dowels) are used with high strength resins to investigate the performance of the bonded-in joint. As in the finding, the pull-out failure load of the joint increases as the bonded length increases. This is mainly because of the increasing surface area of the rod and timber which contact with the adhesive.

There are also research done by Pizzi and Van Leemput [6] that compare the performance of the threaded steel rod and smooth steel rods in order to achieve sufficient adhesion between the timber surface and the adhesive. To disperse stress concentrations under tensile loading, threaded rods of different length, which is shorter on the outside of the beam member, are recommended by Gaunt [7]. Hamad [8] optimizing the rib geometry of steel reinforcing bars to enable shorter bonded-in lengths for a given load. As alternative to steel rod, the use of FRP such as Glass Fibre Reinforced Plastic (GFRP) are quiet popular as it will improve resistance to corrosion which is useful in a humid or acid environment, lower weight of connection, easier, faster handling and installation and it is more compatible with resin and timber. Tingley and Gai [9] suggested that the GFRP composite reinforcement is more compatible than traditional steel that includes factors such as the strain at yield, the differential stiffness, the thermal expansion coefficient and the environmental resistant.

Other than that, adhesive is one of the important factors in bonded-in pultruded rods. Adhesive used will transmit load from one member of a joint to another with a more uniform distribution although the failure tends to be more brittle than

mechanical fasteners joined [4]. The choice of adhesive, design of the connection, production methods and quality can be defined by the Swedish National Type Approval 1396/78. Beside that, there are standard on design of timber (Eurocode 5 —Design of timber structure—Part 2: Bridge) has been drafted and contains an informative annex on the subject. According to informative annex, the minimum bonded length, $L_{b,\min}$, of the maximum between two values achieve from Eq. (1)

$$L_{b,\min} = \max\{0.4\mathrm{d}_r^2 \text{ or } L_{b,\min} = \max\{8\mathrm{d}_r \tag{1}$$

where dr is the diameter of rod in mm. However, this recommendation is made based on steel rods which may not be applicable for other alternative rod.

3 Materials and Research Method

3.1 Material and Test Method

- Materials

Two selected timbers used in this study, which are from a medium hardwood species, namely, Kempas (*Koompassia malaccensis*), from strength group 2 with a density of 900 kg/m^3 and Keruing (*Dipterocarpus* spp.) from strength group 5 with density of 1800 kg/m^3.

Glass fibre-reinforced plastic (GFRP) rods with diameters 8 were used with a modulus of elasticity of 150,000 N/mm^2. GFRP rods were sandpapered using coarse sand paper, and degreased with ethanol to aid bonding with the adhesive.

The adhesives used in this study were Sikadur®-30 which was supplied by Sika Sdn. Bhd, Malaysia. It is a gap-filling, thixotropic and structural two-part adhesive, based on a combination of epoxy resins and a special filler, designed for use at normal temperatures between +8 and +35 °C.

- Specimens Preparation and Test Method

The bending shear specimens were prepared from timber with dimension 500 mm × 100 mm × 50 mm. Two types of bending shear specimens were prepared which are controlled specimens that consist of a single timber member with no jointing while the bonded-in specimens using GFRP rods to connect two timber members with different length of embedded rods, L_b.

For jointed specimens, the beams were prepared with properties as shown in Table 1 with the information on the adhesive type, glueline thickness, t_g, type of rods and diameter of rods and illustrated in Fig. 1. Two holes were drilled into the beam parallel to grain using drill machine. The adhesive was then injected into the hole using application gun and the rods were inserted into the hole and were left for 10 days to allow the adhesive to cure at room temperature. Then the two parts were connected.

Table 1 Bending shear specimens properties

Items	Properties
Adhesive	Sikadur
Glueline thickness, t_g	2 mm
Main rod diameter, dr	8 mm
Embeded length, L_b	100, 150, 200, 300 mm
Beam dimension	500 mm × 100 mm × 50 mm
Timber species	Keruing and Kempas

Fig. 1 Specimen for bending test
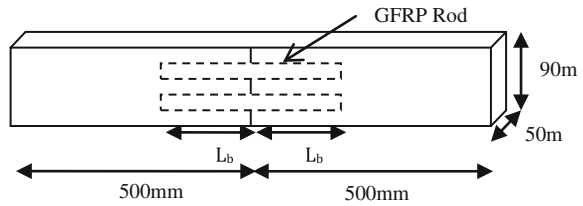
100 ton capacity universal testing machine (UTM) UTS-348 was used in this laboratory test. Axial loads were applied with a crosshead of 5 mm/min for the four point bending test as shown in Fig. 2. The deflection curve was recorded on as *xy* recorder up to maximum load. The deflection was measured by the movement of the movable crosshead of the testing machine using two linear variable differential transformers (LVDT) setup at the bottom of specimens. The mode of failure was also recorded.

Fig. 2 Four point bending test
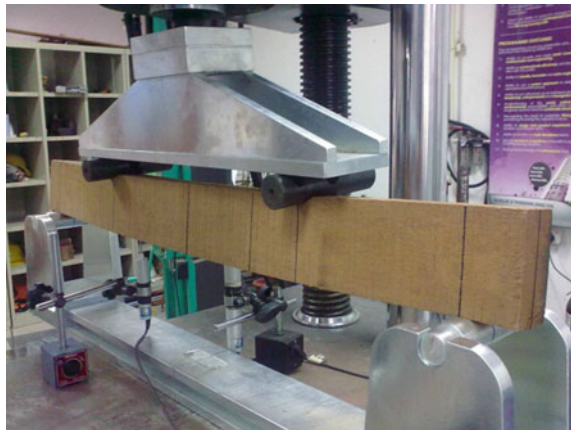
4 Result and Discussion

4.1 Effect of Timber Species on the Bending Shear Strength Properties of Controlled Specimens

As shown in Table 2, Kempas specimens achieved bending shear strength of 61.4 Mpa while Keruing achieved 62.3 Mpa.

There are differences in the typical load-displacement graph for both type of timber (Fig. 3). These plots show that for both timber species the initial curve is fairly linear up to a load roughly between 30–40 kN. After this point the behaviour of the joint is no longer linear as it approaches the failure load of the joint. For Kempas species, after achieving the failure load, the load continued to decrease slowly compared to Keruing species, the load building up again up to a point where the load suddenly drops again and the behaviour is repeated until further damage in the timber. These show that Kempas is more ductile than Keruing due to bigger deformation in which the beam can sustain before totally failed.

4.2 Failure Mode for Controlled Specimens

All of three specimens for Kempas and Keruing controlled specimens were failed due to splitting of the timber. Initial cracking sounds were heard in the timber as the failure load reached around 7–8 kN but there was no visible damage. As soon as the failure load reached, loud cracking sound was heard and sometimes there are few of timber pieces that came out from the timber.

Figure 4 shows the differences in failure modes for Kempas and Keruing timber. For Kempas specimens, the failure initiated at the lower section (Tension zone) of

Table 2 Shear strength of controlled timber beam

Timber type	τmax (N/mm^2)
Kempas	61.4
Keruing	62.3

Fig. 3 Typical load-displacement graphs for controlled specimens

(a)

(b)
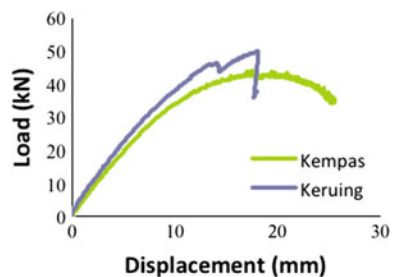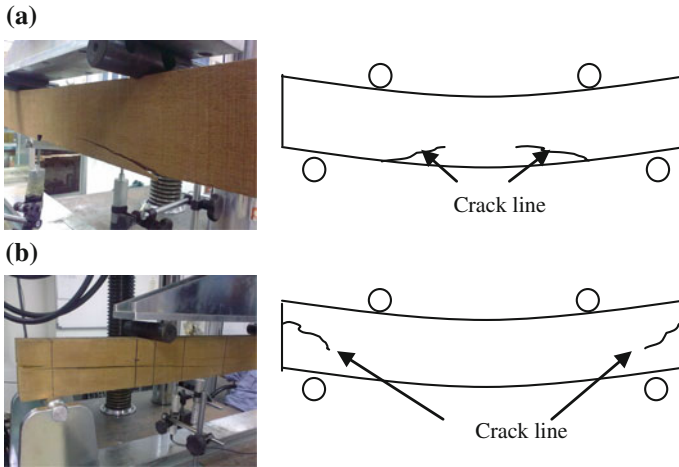
Fig. 4 Failure modes for controlled specimens **a** Kempas **b** Keruing

the beam while for Keruing specimens, failure tend to be at the side of timber member which is shear failure.

According to Bodig and Jayne [10] the mode of failure and the stress distribution in a defect free beam are largely determined by the stress–strain relationship in tension and compression parallel to the grain. Failure in a beam due to the compression will tend to have lower strength value compared to the beam with tension failure. This is because the maximum crushing strength of compression parallel to the grain is about 25–33 % of the ultimate tensile strength parallel to the grain. Therefore it is a good indicator as the Kempas beam failed in tension mode which allows for better deformation even though the ultimate strength has no significant different than Keruing (see also Fig. 3) which explained the higher ductility. Meanwhile, Keruing beam failed in shear as seen in Fig. 4b which may indicate that the beam contained internal checks even though the timbers were graded standard and better.

4.3 Effect of Bonded-in Length on the Bending Shear Properties of Timber Beam

The effects of rods embedded length on the shear strength of jointed member are shown in Fig. 5. It can be seen that as the embedded length increases the shear strength increased and optimum when the embedded length is at 250 mm. Later when the embedded length reached 300 mm, the strength was decreased. The shear strength for Kempas is 26 % lower than Keruing except at 150 mm embedded length, where Kempas achieve higher shear strength than Keruing (12.3, 10.8 N/mm^2, respectively).

Fig. 5 Average shear stress
for bonded-in joint bending
test
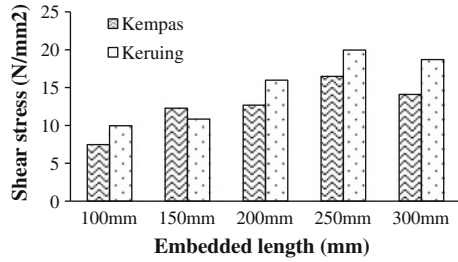
Fig. 6 Average shear stress
for controlled and bonded-in
specimens
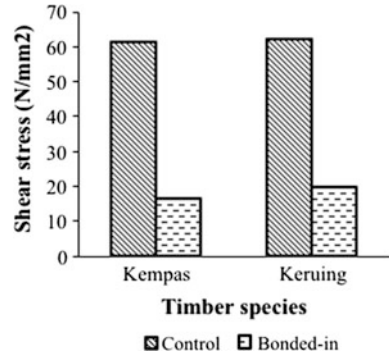
The high shear strength in Keruing compared to Kempas is consistent with the result of controlled specimen (Table 2) but with further enhancement in the strength values, the shear strength of beam with embedded length of 250 mm (about half of the specimen's length) has decreased the shear strength of Kempas and Keruing by 73 and 68 %, respectively, compared to controlled beams as shown Fig. 6.

Load-displacement curve for bonded-in specimens are shown in Fig. 7 and it can clearly be seen that the plot between these two types of timbers is in the same trend. The initial curve of the load is fairly linear before it achieved the maximum failure load and suddenly drops. After the initial drop in the load, the load will then build
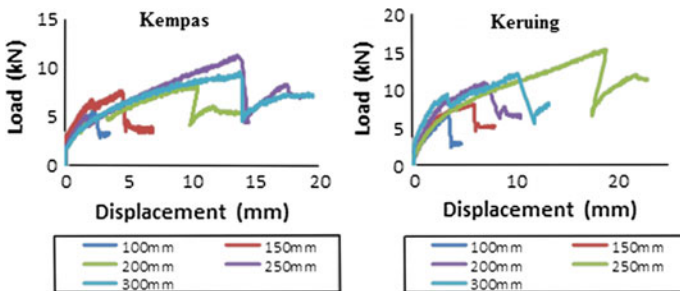
Fig. 7 Typical load-displacement graphs for bonded-in specimens

Fig. 8 Prediction equation for Kempas and Keruing timber
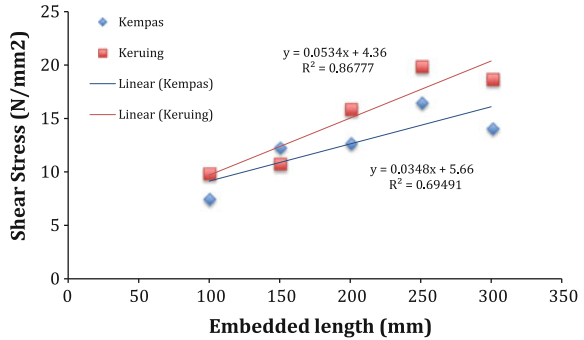
up again to a point where the load was suddenly drop again. The plot was continued until the timbers are totally damaged. This indicates improvement in the ductility which explained the enhancement in strength of bonded-in jointed beams. The graphs also showed that as the embedded length is longer, the deformation is also bigger and gives higher ductility.

Multiple linear regression analysis was used to develop a model for predicting the average of shear stress from various bonded-in length (Fig. 8). For Kempas, the prediction equation for shear stress is $y = 0.0348x + 5.66$ while for Keruing is $y = 0.0534x + 4.36$.

4.4 Failure Mode for Jointed Specimens

There is common visible mode of failure in the surface of the timber close to the position of the bonded-in rods as shown in Fig. 9. The specimens began to split at line A as the test load increased where the timber members end against each other in compression. As the load increased line B slowly appeared and the cracks were more visible and began to separate. However, when the specimens are continued to loaded, the specimens still can hold on with some load. This happened as the rods restrained the bending of the timber. GFRP rods have a greater flexural stiffness than the timber therefore it allowed the increase in ductility and enhanced the strength. In fact the failure mode is mainly in shear failure.

This is due to the bearing pressure of the rod on the timber which leads the longitudinal split as shear failure. It can also be seen that the crack at lower section

Fig. 9 Failure mode of bonded-in joint timber
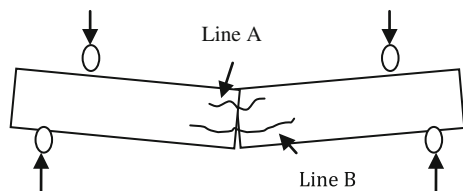
is longer than the upper section. This is due to the bearing pressure that is likely to be more concentrated in the lower rod as the crushing at line A reduces the bearing pressure on the upper rod. This phenomenal has made the rod as an additional function as strengthening material. Therefore by this method of jointing, provided additional advantage which is a strengthening material compared to other method of jointing.

5   Conclusions

- No significant difference on average shear strength for both timber species for controlled specimens.
- For control Kempas specimens, the failure initiated at the lower of the beam while for control Keruing specimens, failures tend to start at the end of timber member producing shear failure.
- The shear strength of Kempas is lower compared to Keruing by 1.5 %.
- Influence of the embedded length is clearly seen as the embedded length increases, the shear strength also increases. However, after the rod embedded length had reached half of the timber length, the shear stress seems to decrease.
- The shear strength of bonded-in joint beam decreased by 73 and 68 % from the controlled specimens for Kempas and Keruing, respectively, however the presence of bonded-in rod has improved the ductility of the beam.

References

1. H. Lee, and K. Neville, Handbook of Epoxy Resin. New York: McGraw-Hill, 1st edition.
2. H. Riberholt, and P. Spoer "Design of the Inglued Rods that are used for the Wingblade Root Section on Nibemolt-B." Seri R-Denmarks Tekniske Hojskole, Afdelingen for Baerende Konstructioner, 1983, No. 167.
3. J.S. Stalnaker, and E.C. Harris, Structural Design in Wood. Chapman and Hall, USA, 1997.
4. J.G. Broughton, and A.R. Hutchinson, "Efficient timber connection on bonded-in GFRP rods." Composite construction, Figueiras et al., (ed.), A Balkema, Rotterdam, ISBM 90-5809-260-7, 275-280., 2001.
5. K. Harvey, "Improved timber connection using bonded-in GFRP rods." PHD thesis. University of Bath. United Kingdom, 2003.
6. C.J. Pizzi, and M. Van Leemput, COST – Action E1 Wood Adhesion and Wood Product. Satee of Art Report. Working Group 2. Glued Wood Products, 2002.
7. D.J. Gaunt, "Joint in Glulam using groups of Epoxy Grouted Steel Bars plus an Alternative to Epoxy Bonding." Proceeding: 5th World Conference on Timber Engineering Montreux, Switzerland, Vol. 1, pp 281–288, 1998.
8. B.S. Hamad, "Bond strength improvement of Reinforcing Bars with specially designed rib geometries." ACI structural Journal (American Concrete Institute), Jan – Feb, Vol.92, No.1, pp. 3–13, 1995.

9. D.A. Tingley, and C. Gai, "FRP Reinforced Glulam performance: A case study of the lighthouse bridge", Proceeding: 5th World Conference on Timber Engineering, Montreux, Switzerlandm Vol 2, pp 177–181. 1998.
10. J. Bodig, and B.A. Jayne, Mechanics of wood and wood composites. Van Nostrand, New York., 1993.

Evaluation on the Thermal Performance of Selected Tropical Timber Species

Raihana binti Mohamad Hata, Rohana Hassan and Fadzil Arshad

Abstract Heat gain for buildings is a common incident and is inevitable as building is exposed to surrounding climate. Positive thermal heat balance within building and specially building materials are an important means in search of thermal indoor comfort. Buildings consist of different materials which have its own different characteristics in terms of thermal conductivity, thermal resistivity, specific heat, and thermal diffusivity. In this study, the effect of heat on selected timber species was investigated based on data collected from KD2 Pro thermal analyzer at unsteady-state. The study has been done on selected tropical timber species from strength group two, four, five, and seven from MS 544 Table 3: Strength Groups. The aim of this study is to examine the relationship of thermal properties with different timber species.

Keywords Thermal conductivity · Building material · Timber species

1 Introduction

The increase of awareness in global warming issues has made green building requirements one of the most crucial criteria that every party involved in construction industry need to follow. According to Malaysian Green Building Index (GBI), six key criteria of GBI are energy efficiency (EE), indoor environmental quality (EQ), sustainable site planning and management (SM), material and resources (MR), water efficiency, and innovation. GBI promotes the optimizing energy consumption and thermal indoor comfort. Hence GBI also requires the use of environmental friendly materials sourced from sustainable sources [1].

People living or working in a confined spaces need thermal indoor comfort for them to have the personal satisfaction. Air conditioning system is the most common and reliable solution that can provide thermal indoor comfort. However air

R.M. Hata (✉) · R. Hassan · F. Arshad
Faculty of Civil Engineering, Universiti Teknologi MARA,
Shah Alam, Selangor, Malaysia
e-mail: raihana106@gmail.com

conditioning consumes a large portion of building's energy consumption [2]. One of the way to promote energy efficiency in building is the application of passive cooled building through natural means as opposed to the use of electrical or mechanical devices [1]. Timber technology in construction industry is one of the solutions to overcome energy usage in building. In some country for example Italy, the trend of new timber residential building has been increasing since year 2008–2015 as timber provide better insulation especially in Mediterranean climate [3].

Study on materials thermal properties is important to find the suitable materials for every building to compensate the building climate location and it amenities. Research on thermal effect on masonry for example bricks and blocks had been done by Jalilluddin et al. [4]. Jalilluddin study on the addition of kenaf fiber is on sand–cement block. Research was done using hot-box method in the steady-state condition. The result from the research summarizes the thermal conductivity with various portion of sand-kenaf. Authors conclude that the sand-kenaf portion gave good thermal conductivity characteristic to the samples. Md Din et al. [5], study the thermal effect of brick, concrete, granite and white concrete tiles. The author runs the test on existing building and study the actual impact of thermal to the surrounding. From the research author conclude that brick absorbs more heat than the others three materials. Ozel [6], consider the effect of different insulation location for normal brick wall with cement plaster. The results show that the best thermal performance obtained when the insulation is placed at the most outer of the wall. Hence, research on the major materials use in building construction which is concrete had been done by Huang and Tsai [7]. Authors explained that the sunshades effect could cut down heat transparency. Furthermore, studies on thermal effect on wood or timber had been done by Kairys et al. [8], Kehrer and Schmidt [9], Harijaona et al. [10], Kruger et al. [11], Kruger and Adriazola [12]. Kairys et al. and Harijoana had done the research on wooden wall while Kruger focus more on test cell made from timber and subjected on transient method. On the other hand Kehrer take into account all heat impact subjected to wooden flat roof. Timber was used as it is the most environmental friendly material and the only material that absorb carbon during its live span whereas other material emitted carbon [13].

There are various method and device that can be used to determine thermal conductivity such as calibrated hot-box method and guarded hot plate method. Each of these method and devices should be choose according to our samples types and characteristic. Asdrubali et al. suggested hot-box method to be used to analyses low thermal resistance samples [14]. However in this paper, KD2 Pro Thermal Analyzer is used to determine thermal properties for selected timber materials. KD2 Pro was choose due to it availability during the testing period. KD2 Pro is compliance to ASTM D5334-08 and IEEE 442-03.

The objective of this paper is to determine the thermal conductivity, thermal resistivity, specific heat, and thermal diffusivity of selected timber species prior to their strength. This research used thermal needle probes KD2 Pro thermal analyzer manufactured by Decagon to identify the thermal properties. Results collected will give an information on suitable timber species specially for building sector.

2 Overview of Timber

Basically the use of timber is divided into two, structure purposes and for esthetic purposes [15]. For either of the purposes, timber needs to be chosen and classify accordingly. Timber are considered as a sustainable buildings materials as growing of trees absorb Carbon dioxide (CO_2) compares to others building materials [10]. Timber is truly renewable building materials as new trees can be planted to replace those that harvested. Furthermore planting and harvesting trees contribute positively to environmental through the cycle of "absorb-and-lock" of CO_2 atmosphere.

Research on thermal energy for different timber species has been done before by Akapabio et al. [16]. Author takes into consideration of six types of Nigerian timber species. Outcomes of the research proof that wood with highest thermal diffusivity and lowest absorptivity are suitable for passive cooled building. Furthermore wood with low thermal conductivity and high thermal resistivity are good for thermal insulation. Authors suggested the wood to be used as ceiling panels, doors, and windows and other padded building design.

The four types of selected tropical timber in this research are;

a. Kempas (*Koompassia malaccensis*) from strength group two. Kempas is a medium hardwood. This timber is extremely strong and very easy to treat with preservatives. The timber when treated with preservatives is suitable for heavy constructional works, posts, beams, joists, bridges, wharves, railway, sleepers, and power transmission poles. The untreated Kempas is suitable for covered structures, such as parquet and strip flooring, paneling, rotary peeled veneers, and charcoal manufacture and very suitable for timber pile manufacture.
b. Merpauh (*Swintonia* spp. Anacardiaceae) from strength group four is a medium hardwood and considered as strong wood. The attractive textures of Merpauh make it suitable for high-class joinery, furniture, and for interior finishing paneling, partitioning, and flooring. The timber is suitable for under covered light and medium construction.
c. Keruing (*Dipterocarpus* spp. Dipterocarpaceae) from strength group five is a medium hardwood and generally strong. The timber are suitable for heavy construction, posts, beams, joists, rafters, truck body construction, container flooring. Treated Keruing are suitable for railway sleepers, harbor works, bridges, power line poles and telegraph poles.
d. Sesendok (*Endospermum* spp. Euphorbiaceae) from strength group seven is a light hardwood and is a weak timber (Strength group D). The timber is non-durable but is extremely easy to treat with preservatives. Due the characteristic this timber is suitable for match splints, boxes, drawing board, trays, plywood, crates, toys, and chopsticks manufacture [17].

Table 1 stated the strength group, class, species, density, and specific gravity for the selected timber from Malaysian Standard (MS 544).

Table 1 Strength group of selected timber species, density and specific gravity (MS 544 Part 2 2001: Code of practice for structural use of timber: Part 2: Permissible stress design of solid timber, 2001) [18]

Strength group	Class	Timber species	Density at 19 % moisture content (kg/m³)	Specific gravity (MS 544)
2	Medium hard wood	Kempas	910	0.74
4		Merpauh	780	Not mention
5		Keruing	830	0.64
7	Light hardwood	Sesendok	550	0.46

3 Thermal Needle Probes

Thermal needle probe in this research are from Decagon KD2 Pro thermal analyzer. The dual needle (SH-1) is use for this research due to its compatibility with most solid and granular materials (Fig. 1). The theory behind KD2 Pro is heat is applied to the needle for a set time, t_h and temperature are then measured during heating and during cooling period following heating. Ambient temperature are then subtract by ambient temperature at time 0 and multiplying by 4π and dividing by the heat per unit length, q. Nonlinear least squares procedure are used at final two third of heating and cooling data to determines the thermal conductivity hence removing the effect of temperature drift during computation [19].

$$T^* = b_0 t + b_1 E_i\left(\frac{b_2}{t}\right) \tag{1}$$

$$T^* = \frac{4\pi(T - T_0)}{q} \tag{2}$$

where E_i is exponential integral and b_0, b_1, and b_2 are the constant need to be fit. T_0 is the temperature at the start of measurement and q is the heat input. Equation 1 is

Fig. 1 KD2 Pro handheld thermal analyzer by Decagon Devices

used of the first t_h seconds when heat is applied and Eq. 2 was when the heat was off.

Further thermal conductivity was calculated using Eq. 3 and thermal diffusivity using Eq. 4.

$$k = \frac{1}{b_1} \tag{3}$$

$$D = \frac{r^2}{4b_2} \tag{4}$$

Thermal conductivity and diffusivity was calculated by substituting Eq. 1 into transform data and the value of b_0, b_1, and b_2 the one that minimize the sum of squares error in the equation [20].

4 Methodology

The KD2 Pro by Decagon devices is a handheld device to measure thermal properties for various materials. The sensor used for this research is a dual needle sensor which can measure thermal conductivity, resistivity, volumetric specific heat capacity, and diffusivity. The dual sensor is 1.3 mm diameter × 3 cm long with 6 mm spacing. The specific thermal conductivity are 0.02–2.00 W/m K, thermal resistivity 50–5000 °C cm/W, diffusivity 0.1–1.0 mm^2/s and volumetric specific heat 0.5–4.0 mJ/m^3 K.

5 Sample Preparation and Testing

Samples are cut to 100 mm × 100 mm × 25 mm. The samples edge was cleaned to provide smooth and safe testing work and to minimize the differences in density for every samples. Two holes with 1.5 mm diameter was drilled using drilling machine at the middle of the samples for the dual needle sensor penetration. Twelve samples were prepared for each sample (Fig. 2).

Testing was done at University Teknologi MARA Civil Engineering Laboratory to minimize the effect of humidity and unpredictable outdoor event such as rain. However, humidity value is neglected in this experiment as research applied unsteady state condition. The needle probes were inserted in the prepared holes. For every samples, the KD2Pro took around 2–5 min to read the thermal conductivity, thermal resistivity, volumetric specific heat, and thermal diffusivity (Fig. 3).

The temperature of the samples are kept as constant as possible during the measurement by allowing at most 15 min for the samples and sensors to come to temperature equilibrium before the measurement start for every samples. Contact

Fig. 2 Samples dimensions

Fig. 3 Needle probes was
inserted into center of samples
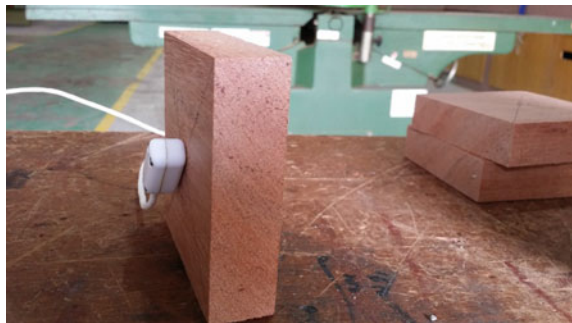
resistance can happen if there is gap between needle and samples because hole has
been drilled to accommodate the needle. To minimize this contact resistance, the
sensor was fit tightly in the hole or thermal grease provided by the manufacturer can
be applied to the sensor prior to inserting.

6 Result Analysis

The thermal properties of four types of solid timber were tested at a range of
strength group and density. The four timbers comprised; Kempas, Merpauh,
Keruing, and Sesendok. Results of the thermal conductivity, thermal resistivity,
volumetric specific heat and thermal diffusivity are stated in Table 2.

The Err value is the relative error for the reading. The good data gives error value
below 0.0100. Therefore, the data collected shows a good fit of the needle probes to
the samples hole. The relationship between thermal conductivity and thermal
resistivity and thermal diffusivity are shown in Figs. 4 and 5. From Fig. 4 the thermal
conductivity was observed to be inversely proportional to the thermal resistivity. The
value of thermal resistivity and conductivity for sample Kempas and Merpauh are
almost identical compare to Keruing and Sesendok. Thermal diffusivity value
against thermal conductivity value shows almost zero relationship. Thermal con-
ductivity is not affected by the thermal diffusivity.

Table 2 Summary of the results of thermal properties

Sample ID	Thermal conductivity K (W/m K)	Thermal resistivity Rho (°C cm/W)	Volumetric specific heat C (MJ/m^3 K)	Thermal diffusivity D (mm^2/s)	Err	Temperature at t_0 (°C)	Density
SG2 Kempas	0.250	400.800	1.806	0.140	0.001	29.508	852.083
SG4 Merpauh	0.274	365.992	1.845	0.152	0.001	29.679	857.927
SG5 Keruing	0.235	427.275	1.860	0.128	0.001	29.095	738.637
SG7 Sesendok	0.149	672.533	1.017	0.150	0.001	29.614	445.983
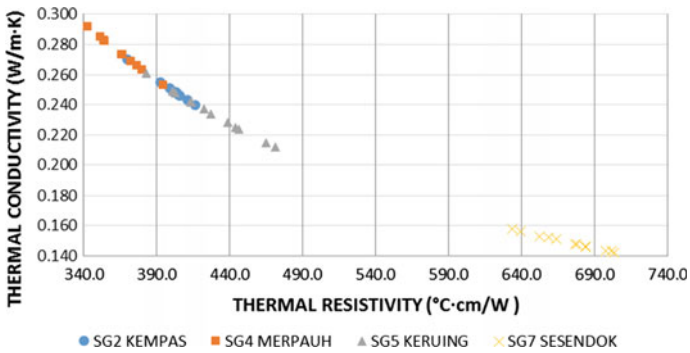
Fig. 4 Thermal conductivity against thermal resistivity for Kempas, Merpauh, Keruing and Sesendok
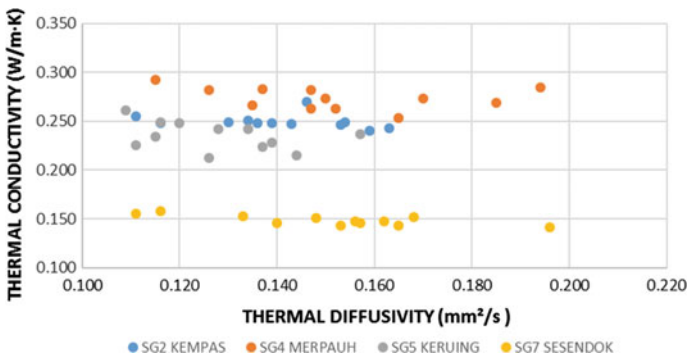
Fig. 5 Thermal conductivity against thermal diffusivity for Kempas, Merpauh, Keruing and Sesendok

Figure 6 clarified the thermal conductivity of the four selected timber species. Sample Merpauh shows the highest thermal conductivity value with 0.274 w/m K and Sesendok has the lowest thermal conductivity of 0.149 w/m K. On the other hand, Fig. 7 simplified the thermal resistivity.

Sesendok have the highest thermal resistivity with 672.533 °C cm/W and Merpauh has the lowest thermal resistivity with 365.992 °C cm/W.

There is a big difference on volumetric specific value for the selected timber samples. Referring to Fig. 8, Sesendok is 0.843 less value then Keruing which has the highest value with 1.860 MJ/m³ K. This can be related to the density value for Sesendok from Table 2 that are far lower than others samples. Figure 9 displays the

Fig. 6 Thermal conductivity against timber species
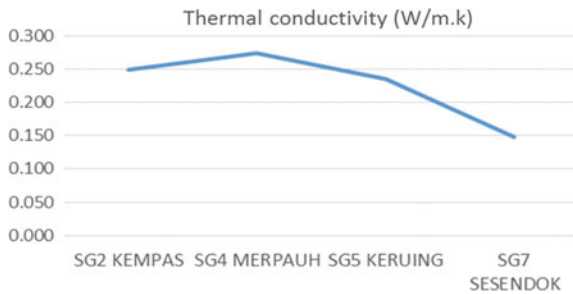
Fig. 7 Thermal resistivity against timber species
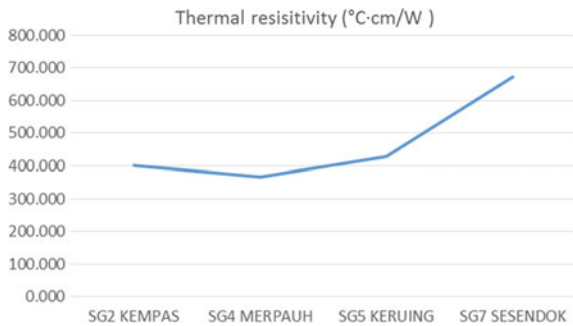
Fig. 8 Volumetric specific heat against timber species
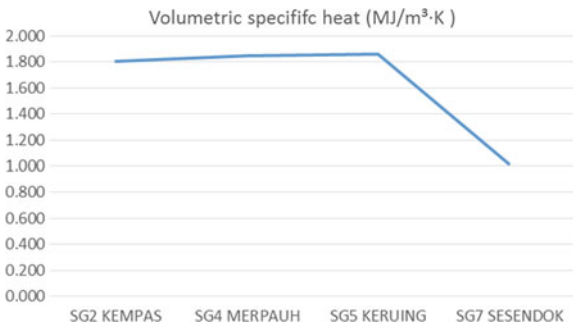
Fig. 9 Thermal diffusivity against timber species
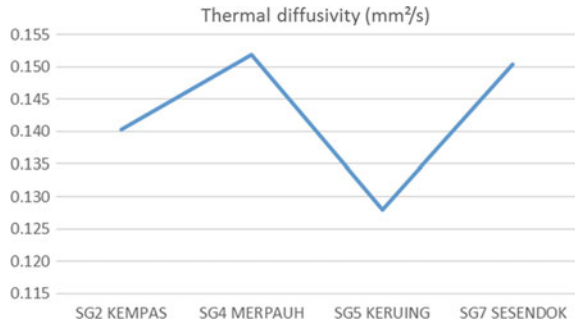
thermal diffusivity pattern for selected timber species. From the value recorded and from graph, it is quite difficult to explain the relation between timber species and the thermal diffusivity value. This is because Merpauh and Keruing have the most identical characteristic with both come from medium hard wood and conductivity and volumetric heat value are almost identical. But the value for diffusivity is far different with highest value is Merpauh 0.152 and lowest value is Keruing 0.128 MJ/m^3 K.

7 Conclusion and Recommendation

1. There are pattern of thermal characteristic with different timber strength group. Different timber strength gave different value of thermal properties. Others criteria such as density, moisture content, could add a further information in further study.
2. KD2 Pro is a suitable needle probes testing devices for analyzing timber thermal properties in uncontrolled surrounding environment. However, the result does not represent any certain room temperature. Hence result could be varied in different room temperature and furthermore in outdoor surrounding temperature.
3. The lowest thermal conductivity and the highest thermal resistivity was recorded by Sesendok. However Sesendok is a nondurable and weak timber and are not suitable structures wise. However the Sesendok can be applied for esthetic uses, for example flooring. The second lowest thermal conductivity and second highest thermal resistivity is Keruing. Keruing is a medium hard and strong wood. There is a possibility of this wood to be used in building structures, architecture work and also for passively cooled building timber.
4. There is a relationship between density and specific heat. High density usually indicates high specific heat and vice versa.

This research has a lot of potential as there are many others timber species from the seven of the strength group which has not been tested. There are many others ways in defining thermal conductivity in steady-state, unsteady-state, and transient method.

References

1. "GBI index," no. December, 2013.
2. N. H. Abdul Halim, N. Z. Zakaria, and A. Zain Ahmed, "Thermal and Energy Performance of Pitch and Wall Insulation for Air-Conditioned Buildings in Malaysia," *Appl. Mech. Mater.*, vol. 209–211, pp. 1766–1769, Oct. 2012.
3. C. Tonelli and M. Grimaudo, "Timber buildings and thermal inertia: Open scientific problems for summer behavior in Mediterranean climate," *Energy Build.*, vol. 83, pp. 89–95, Nov. 2014.
4. A. M. Jalilluddin, S. M. Ayop, and K. Kamaruddin, "Evaluation on the Thermal Conductivity of Sand-Cement Blocks with Kenaf Fiber," *Adv. Mater. Res.*, vol. 626, pp. 485–489, Dec. 2013.
5. M. F. Md Din, H. Dzinun, M. Ponraj, S. Chelliapan, Z. Zainun Noor, D. Remaz, and K. Iwao, "Investigation of thermal effect on exterior wall surface of building material at urban city area," *Int. J. Energy Environ.*, vol. 3, no. 4, pp. 531–540, 2012.
6. M. Ozel, "Effect of insulation location on dynamic heat-transfer characteristics of building external walls and optimization of insulation thickness," *Energy Build.*, vol. 72, pp. 288–295, 2014.
7. C. H. Huang and S. Y. Tsai, "Effects of Exterior Sun Shades on Heat Transfer by Solar Radiation," *Adv. Mater. Res.*, vol. 935, pp. 61–65, May 2014.
8. L. Kairys, V. Stankevièius, and J. Karbauskaitë, "Heat flux through the timber walls under summer climate conditions in eastern Europe," *J. Civ. Eng. Manag.*, no. June 2014, pp. 37–41, 2006.
9. M. Kehrer and T. Schmidt, "Radiation effects on exterior surfaces," *Proc. 8th Symp. Build. Phys. Nord. Ctries.*, vol. 1, pp. 207–212, 2008.
10. Z. Harijaona, R. Cantin, and G. Guarracino, "Numerical modeling of impact of radiation exchanges between wood and building thermal comfort," *2009 Int. Conf. Adv. Comput. Tools Eng. Appl.*, pp. 249–254, Jul. 2009.
11. E. L. Krüger, M. Adriazola, a. Matoski, and S. Iwakiri, "Thermal analysis of wood-cement panels: Heat flux and indoor temperature measurements in test cells," *Constr. Build. Mater.*, vol. 23, no. 6, pp. 2299–2305, 2009.
12. E. L. Krüger and M. Adriazola, "Thermal analysis of wood-based test cells," *Constr. Build. Mater.*, vol. 24, no. 6, pp. 999–1007, 2010.
13. A. Kadir, B. Marsono, and A. T. Balasbaneh, "Combinations of building construction material for residential building for the global warming mitigation for Malaysia," *Constr. Build. Mater.*, vol. 85, pp. 100–108, 2015.
14. F. Asdrubali, G. Baldinelli, F. Bianchi, a Libbra, and a Muscio, "Comparative Analysis of Different Methods To Evaluate the Thermal Conductivity of Homogenous Materials," 2010.
15. "Step by Step Guide to specifying timber," *Malaysian timber Counc.*, 2004.
16. G. T. Akpabio, N. J. George, A. E. Akpan, and I. Obot, "Thermal response of some select wood samples for a passively cooled building design," *Arch. Appl. Sci. Res.*, vol. 2, no. 3, pp. 267–276, 2010.
17. T.M. Wong, *A Dictionary of Malaysian Timbers. Malayan Forest Records No. 30*. 2002.
18. MS 544 : Part 2: 2001 Code of practice for structural use of timber : Part 2 : Permissible stress design of solid timber, 2001.

19. D. Barry-Macaulay, a. Bouazza, R. M. Singh, B. Wang, and P. G. Ranjith, "Thermal conductivity of soils and rocks from the Melbourne (Australia) region," *Eng. Geol.*, vol. 164, pp. 131–138, 2013.
20. D. Devices, "KD2 Pro Thermal Properties Analyzer, Operator's Manual," p. 68, 2012.

Dowel-Bearing Strength Properties of Glulam with and Without Glue Line Made of Mengkulang Species

Nurul Atikah Binti Seri, Mohamad Faizal Bin Nurddin and Rohana Binti Hassan

Abstract The lateral connection of wood design strength performance to fastener bending can be estimated by dowel-bearing strength. The value from the dowel-bearing strength can be used in resolving the European Yield Model (EYM) theory. This study focus on determination the dowel-bearing strength properties of glulam with and without glue line made of Mengkulang species on the effect of two (2) different bolt diameters using 16 and 20 mm dowel diameters. The dowel-bearing strength of glulam also compared according to 5 % diameter offset and maximum load by using ASTM 5764-97a (2013) and BS 383:1993, respectively. The mean value of dowel-bearing strength, Fe using 5 % diameter offset of load for with glue line of glulam made of Mengkulang species using 16 mm dowel diameter is 11.21 N/mm^2 and 20 mm is 8.88 N/mm^2. The mean value of dowel-bearing strength, Fe for without glue line of glulam made of Mengkulang species using 16 mm dowel diameter is 13.33 N/mm^2 and 20 mm is 11.52 N/mm^2. The percentage differences of dowel-bearing strength, Fe due to effect on increasing dowel diameter for with glue line specimens is reduced 21 % and without glue line specimens is reduced 14 %. It is shown the dowel-bearing strength decreased when the dowel diameter increased. The percentage differences of dowel-bearing strength, Fe of same dowel diameter between with and without specimens using 16 mm dowel diameter is 19 % and 20 mm dowel diameter is 30 %, respectively. The results shown the dowel-bearing strength of glulam without glue line are better and higher compared to the with glue line specimens. The mean value of dowel-bearing strength, Fh using maximum load method of glulam with glue line made of Mengkulang species using 16 mm dowel diameter is 17.02 N/mm^2 and 20 mm is 12.74 N/mm^2. The mean value of dowel-bearing strength, Fh of glulam

N.A.B. Seri · M.F.B. Nurddin · R.B. Hassan (✉)
Faculty of Civil Engineering, Universiti Teknologi MARA, Shah Alam, Malaysia
e-mail: rohan742@salam.uitm.edu.my

N.A.B. Seri
e-mail: nurulatikahseri@yahoo.com

M.F.B. Nurddin
e-mail: faizalnurddin@gmail.com

without glue line made of Mengkulang species using 16 mm diameter is 20.37 N/mm^2 and 20 mm is 18.36 N/mm^2. The percentage differences between 5 % diameter offset and maximum dowel-bearing strength for with glue line specimens using 16 mm dowel diameter is 52 % and 20 mm is 43 %. The percentage differences for without glue line specimens using 16 mm dowel diameter is 53 % and 20 mm is 59 %.

1 Introduction

Dowel-bearing strength also referred as embedment strength of wood. It is the one of the properties that is used to estimate the lateral connection of wood design strength performance to fastener bending strength [1]. The dowel-bearing strength is a critical component of wood connection design and is based on the interaction of the bending resistance of the fastener and the crushing resistance of the wood around the fastener. The dowel-bearing strength value is use in resolving the European Yield Model (EYM) theory. In order to be able promote the application of glulam in Malaysia on the timber connection, this study is conducted to determine the dowel-bearing strength properties of glulam with and without glue line made of Mengkulang species on the effect of two (2) different bolt diameter sizes that are 16 and 20 mm. The main purpose of this study is to determine the dowel-bearing strength properties of glulam with and without glue line made of Mengkulang species on the effect of two (2) different bolt diameters. In order to achieve that, the dowel-bearing strength properties of Mengkulang species for glulam with and without glue line using 16 and 20 mm dowel diameters is determined. The dowel-bearing strength of glulam due to effect of the different dowel diameter for with and without glue line are also compared and analysed. Lastly the dowel-bearing strength using 5 % diameter offset load, *Fe* and dowel-bearing strength using maximum load, *Fh* of glulam with and without glue line is compared.

2 The Dowel-Bearing Strength

Many previous researchers relate the dowel-bearing strength to the fastener or wood characteristics. The fastener characteristic is such as dowel diameter and dowel types (nails, bolts and screws) [2]. Dowel dowel-bearing strength was also being studied for the engineering wood materials such as glue laminated, laminated veneer lumber and plastic wood composite [1]. Dowel-bearing strength is a critical characteristic of wood connection design. The connection design strength is based

on yield theory that relates connection performance to fastener bending strength and dowel-bearing strength [3]. According to American Society for Testing and Materials [4], the dowel-bearing strength is the 5 % diameter offset load obtained from the load-displacement curve of a dowel-bearing test divided by the dowel diameter and specimen thickness. The dowel dowel-bearing strength can be determined using full hole or the half-hole test. According to Awaludin et al. [5] studied in the half-hole method, the dowel uniformly loaded along its length producing a uniform stress distribution through the projected bearing. This is because the uniformly distributed of bearing stress under the dowel and the dowels are fit tightly as possible in the hole. It is mean all ends of dowels are free to rotate and load-displacement behaviour of wood and wood-based products laterally loaded by a fastener where the fastener does not bend during loading. Whereas, for full-hole method although it include bending properties of connection, the uniform stress is not projected under the dowel which is important when using EYM.

3　Research Methodology

The experimental work of dowel-bearing strength properties of glulam with and without glue line made of Mengkulang species has been conducted at UiTM Shah Alam laboratory and carried out using universal test machine (UTM) with capacity of 1000 kN. Dowel-bearing strength tests in this study were performed in accordance with [4] that is using half-hole test method. This method allows full exposure of the specimens during testing, thus detail observations on the specimens during the test such as appearance of cracks or any failure pattern shall be observed. Figure 1 shows the illustration of half-hole specimen. All tests are loaded parallel to the grain directions.

Table 1 shows the total specimens prepared for testing on determination the dowel-bearing strength properties. The total numbers of (60) sixty specimens of each are prepared for with and without glue line. Figure 2a, b shows the example of specimen of half-hole with and without glue line. Figure 3 shows the arrangement for dowel-bearing test procedure using Universal Testing Machine (UTM).

Dowel-bearing strength capacities are determined from 5 % diameter offset load in Fig. 4. The first step of procedure is to fit a straight line to the initial linear portion of the load-displacement curve. Then, offset this line by a deformation equal to 5 % of the diameter. After that, select the load at which the offset line intersects the load-displacement curve. In those cases, the maximum load shall be used as the 5 % offset load if the offset line does not intersect the load-displacement curve. The maximum or ultimate load is when the load head touch the block specimens or the load of each bearing stress before the block split or cracks. At this point the dowel material is considered bearing in full.

According to ASTM-57 64-97a (2013), the following equation calculates the dowel-bearing strength from the experiment (FE) using 5 % diameter offset load:
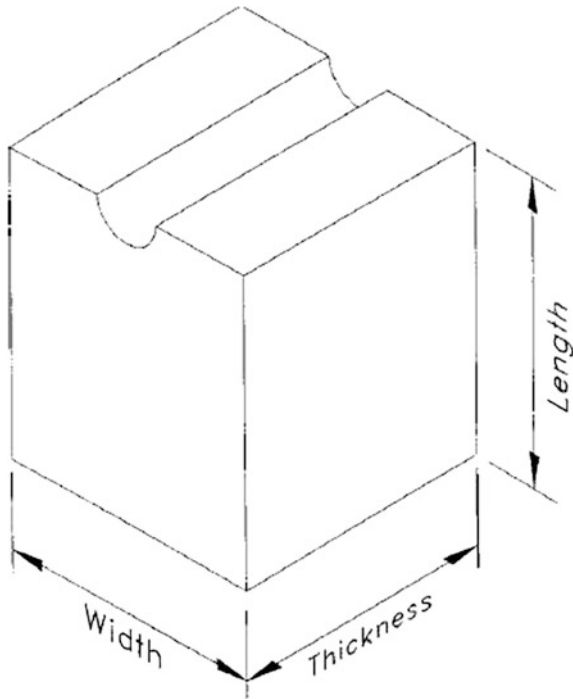
Fig. 1 Illustration of half-hole specimen [4]

Table 1 Total specimens for testing

Specimens	Dowel (mm)	Size of specimens ($W \times L \times T$)	Specimens without glue line (Nos)	Specimens with glue line (Nos)
Mengkulang	16	64 × 64 × 38	30	30
	20	80 × 80 × 40	30	30
		Total	60	60
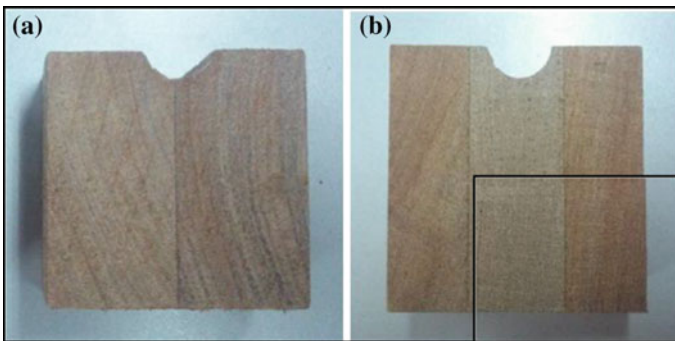
Fig. 2 Specimens of half-hole with and without glue line

Fig. 3 The arrangement for dowel-bearing test procedure using UTM Machine

Fig. 4 Definition of load obtained from load-displacement curve [4]
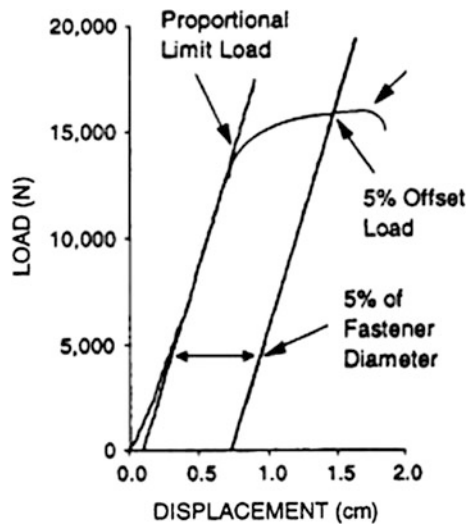
$$Fe = \frac{F5\%}{d \cdot T} \tag{1}$$

If the offset line does not intersect the load-displacement curve, the maximum load to be used to calculate the dowel-bearing strength (*Fe*):

$$Fe = \frac{F\text{max}}{d \cdot T} \tag{2}$$

where $F5\%$ is a 5 % diameter offset load from the test, Fmax is a maximum load from the test, d is a bolt/dowel diameter and T is a thickness of dowel-bearing specimens. In accordance with BS EN 383:1993, the following equation should be calculated for determination of the dowel-bearing strength (Fh):

$$Fh = \frac{F\text{max}}{d \cdot T} \tag{3}$$

where Fmax is a maximum load from the test, D is a dowel diameter and T is the thickness of the test specimen.

4 Result and Discussion

4.1 Dowel-Bearing Strength, Fe Properties of Glulam Made of Mengkulang Species for with and Without Glue Line Using 16 and 20 mm Bolt Diameters

This dowel-bearing strength study involved four types of specimens such as with glue line using steel dowel size 16 and 20 mm diameters and without glue line using steel dowel size 16 and 20 mm diameters. Table 2 shows the summary of dowel-bearing strength, Fe properties of glulam with and without glue line using 16 and 20 mm dowel diameter. The dowel-bearing strength, Fe is calculating and determines using 5 % diameter offset load data where has been determined using Eq. 1. Table 2 is the summary of dowel-bearing strength, Fe properties of glulam.

From Table 2 shows the dowel-bearing strength, Fe for with glue line for 16 mm dowel diameter is 11.21 N/mm^2 and for 20 mm dowel diameter is 8.88 N/mm^2. While the dowel-bearing strength, Fe for without glue line for 16 mm dowel diameter is 13.33 N/mm^2 and for 20 mm dowel diameter is 11.52 N/mm^2.

Table 2 Summary of dowel-bearing strength, Fe properties of glulam with and without glue line using 16 and 20 mm dowel diameter

Specimens	Dowel (mm)	Fe (N/mm^2)	SD	COV (%)	mc (%)	ρ (kg/m^3)
With glue line	16	11.21	1.44	13	13.39	646
	20	8.88	1.51	17	13.29	665
Without glue line	16	13.33	2.02	15	12.62	652
	20	11.52	0.93	8	13.12	688

4.2 Dowel-Bearing Strength, Fe of Glulam due to Effect of the Different Dowel Diameter for with and Without Glue Line

The comparison and analysis of dowel-bearing strength due to effect of the different dowel diameter for with and without glue lines as shown in Fig. 5, the relationship between dowel-bearing strength of glulam with and without glue line specimens using 16 and 20 mm dowel diameter.

The relationship between dowel-bearing strength in the terms of trend is found similar to [1, 6–8] where all mean values of dowel-bearing strength decreased when the dowel diameter increased. It shows the dowel-bearing strength of timber is influence by dowel diameter. Also, the dowel-bearing strength for without glue line or solid timber specimens are higher compared to with glue line specimens. Table 3 shows the percentage differential of dowel-bearing strength for with and without glue line specimens.

From Table 3, it is shown the differences of dowel-bearing strength due to effect of different dowel diameter for with glue line specimens is reduced 21 % from 11.21 to 8.88 N/mm^2 and without glue line specimens is reduced 14 % from 13.33 to 11.52 N/mm^2. An analysis of using same dowel diameter also shows the dowel-bearing strength for without glue line specimens is higher compared to the with glue line specimens. The different of dowel-bearing strength using 16 mm dowel diameter is 19 % and 20 mm dowel diameter is 30 %.

Fig. 5 Relationship between dowel-bearing strength of glulam with and without glue line specimens
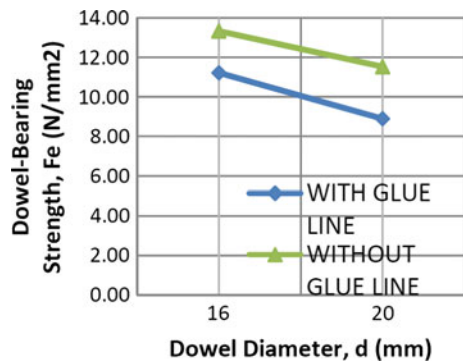
Table 3 The percentage differences of dowel-bearing strength, *Fe* for with and without glue line specimens

Specimens	Dowel diameter (mm)		Differences (%)
	16	20	
With glue line	11.21 N/mm^2	8.88 N/mm^2	21 %
Without glue line	13.33 N/mm^2	11.52 N/mm^2	14 %
Differences (%)	19 %	30 %	–

4.3 Comparison Between Dowel-Bearing Strength (Fe and Fh) of Glulam with and Without Glue Line Using 5 % Diameter Offset Load and Maximum Load

According to BS EN 383:1993, the dowel-bearing strength, Fh is calculating and determines using maximum load data where has been determined using Eq. 3. Table 4 shows the summary of actual dowel-bearing strength, Fh value for with and without glue line specimens using 16 and 20 mm dowel diameter.

Table 5 shows the percentage differences between dowel-bearing strength (Fe and Fh) of glulam with and without glue line using 5 % diameter offset load and maximum load.

From Table 5, it is shown the percentage differences between dowel-bearing strength (Fe and Fh) of glulam for with glue line specimens using 16 mm dowel diameter is 52 % and 20 mm is 43 %, respectively. The percentage differences for without glue line specimens using 16 mm dowel diameter is 53 % and 20 mm is 59 % respectively. In this study, the without glue line of glulam made of Mengkulang species specimens is similar to the solid timber specimens. Previously, Jumaat et al. [7] studied on the determination of the embedment strength of Mengkulang species. The embedment strength tested using three (3) different sizes of 6, 8, and 12 mm dowel diameters. All the dimensions of the specimen test procedure were in accordance with BS EN 383:1993 and done using full-hole test method. Table 6 shows the comparison between dowel-bearing strength, Fh for Mengkulang species by Jumaat et al. [7] using 6, 8, and 12 mm dowel diameter and the mean value of dowel-bearing strength, Fh obtained from this study using 16 and 20 mm dowel diameter.

Table 4 Summary of dowel-bearing strength, Fh for with and without glue line using 16 and 20 mm dowel diameter

Specimens	Dowel (mm)	Fh (N/mm^2)	SD	COV (%)
With glue line	16	17.02	2.34	14
	20	12.74	2.26	18
Without glue line	16	20.37	1.00	5
	20	18.36	1.96	11

Table 5 The percentage differences between dowel-bearing strength (Fe and Fh)

Specimens	Dowel (mm)	Fe (N/mm^2)	Fh (N/mm^2)	Differences (%)
With glue line	16	11.21	17.02	52
	20	8.88	12.74	43
Without glue line	16	13.33	20.37	53
	20	11.52	18.36	59

Table 6 Comparison of dowel-bearing strength, Fh for Mengkulang species

Species	Dowel (mm)	Fmax (kN)	Fh (N/mm^2)	ρ (kg/m^3)	MC (%)
Mengkulang	6[a]	4.41	61.29	663.14	12.43
	8[a]	7.59	59.28	637.93	12.21
	12[a]	17.06	59.23	677.82	11.05
	16	12.39	20.37	651.68	13.29
	20	14.69	18.36	688.41	13.12

Note [a]Embedment strength data from [7]

From Table 6, the mean of maximum load, Fmax are increased when the dowel diameter increased. The dowel-bearing strength, Fh is decreased when the dowel diameter increased. Also, the density of the specimens is in the range of 625–895 kg/m^3 air dry.

5　Conclusion

Therefore the conclusions for this study are concluded as the mean value of dowel-bearing strength, Fe using 5 % diameter offset of load for with glue line of glulam made of Mengkulang species using 16 mm dowel diameter is 11.21 N/mm^2 and 20 mm is 8.88 N/mm^2. The mean value of dowel-bearing strength, Fe for without glue line of glulam made of Mengkulang species using 16 mm dowel diameter is 13.33 N/mm^2 and 20 mm is 11.52 N/mm^2. The percentage differences of dowel-bearing strength, Fe due to effect on increasing dowel diameter for with glue line specimens is reduced 21 % and without glue line specimens is reduced 14 %. It is shown the dowel-bearing strength decreased when the dowel diameter increased. The percentage differences of dowel-bearing strength, Fe of same dowel diameter between with and without specimens using 16 mm dowel diameter is 19 % and 20 mm dowel diameter is 30 %, respectively. The results shown the dowel-bearing strength of glulam without glue line are better and higher compared to the with glue line specimens. The mean value of dowel-bearing strength, Fh using maximum load method of glulam with glue line made of Mengkulang species using 16 mm dowel diameter is 17.02 N/mm^2 and 20 mm is 12.74 N/mm^2. The mean value of dowel-bearing strength, Fh of glulam without glue line made of Mengkulang species using 16 mm diameter is 20.37 N/mm^2 and 20 mm is 18.36 N/mm^2. The percentage differences between 5 % diameter offset and maximum dowel-bearing strength for with glue line specimens using 16 mm dowel diameter is 52 % and 20 mm is 43 %. The percentage differences for without glue line specimens using 16 mm dowel diameter is 53 % and 20 mm is 59 %.

Bakar and Dr. Ranga Rao Krishnamoorthy. Special appreciation recorded to all staff of UiTM for the themes and information during the course of preparation this dissertation. The author would also like to thank all lecturers and friends and everyone who had contributed in the completion of this dissertation. Last but not least, the author would like to express the deepest appreciation to our family.

References

1. Hassan R., Azmi I. and Zakiah A. (2014). Dowel-Bearing Strength Properties of Two Tropical Hardwoods. Proceedings of the International Civil and Infrastructure Engineering Conference 2013 (InCIEC 2013). ISBN No.: 978-981-4585-01-9 (Print), p. 27–36.
2. Maclain T.E. and Thangjitham S. (1993). Bolted Wood-Joint Yield Model. Journal of Structural Engineering (ASCE). 109(8), p. 1820–1835.
3. Hassan R., Azmi I. and Zakiah A. (2008). Effect of Different Dowel Material on Koompassia Malaccensis Bearing Strength. Proceedings of the National Conference on Forest Products 2008: Towards Competitiveness and Sustainability: Kuala Lumpur (Malaysia), 29–31 Oct 2008, p. 114–125.
4. American Society for Testing and Materials, ASTM D5764-97a (2013). Standard Test Method for Evaluating Dowel-Bearing Strength of Wood and Wood-Based Products, 2013.
5. Awaludin A., Smittakorn W. and Hirai T. (2007). Bearing Properties of Shorea Obtusa beneath a laterally loaded bolt. J Wood Science 53(3), 204–210.
6. Rammer D.R. (1999). Parallel-To-Grain Dowel Bearing Strength of Two Guatemalan Hardwoods. Forest product Journal, 49 (6), 77–87.
7. Jumaat M.Z., Bakar A.A., Razali F.M., Rahim A.H.A. and Othman J. (2006). The Determination of the Embedded Strength of Malaysian Hardwood. Proceedings of the 9th World Conference on Timber Engineering. WCTE, Portland or USA, 6–10 Aug 2006 (126p).
8. Steffen F. and Pierre Quenneville (2010). Embedding Behaviour of LVL and Radiata Pine. Proceeding of 11th World Conference on Timber Engineering (WCTE), Italy, 2010.

Light Organic Solvent Preservative Behavior on Bending Strength of Mengkulang (*Heritiera* spp.) Glulam

Syarifah Hanisah Bt Syed Mokhtarruddin, Zakiah Bt Ahmad, Rohana Bt Hassan and Zaidon B. Ashaari

Abstract The purpose of this study was to determine the behavior of LOSP on the bending strength of glulam manufactured using Malaysian tropical timber namely Mengkulang. Timber preservatives are used to prevent from degradation which can be due to some extend weathering, fungi, or insects. Therefore, the use of quality preservatives is essential in determining the performance of timber under such conditions. An experiment was carried out to determine the effect of using preservative to the performance of Mengkulang (*Heritiera* spp.) glued laminated timber (glulam) treated using light organic solvent preservative (LOSP). LOSP was chosen due to its more environmental friendly chemical ingredient. Ten specimens of Mengkulang manufactured at a factory in Selangor, Malaysia which followed the Malaysian Standard, MS 758 were divided into one group of five timber beams treated with LOSP prior to gluing and another group of five untreated timber beams. This paper only reported the effect of LOSP on the bending strength properties. The static bending test under four-point loading was carried out based on American Standard for Testing and Material, ASTM D 198. The results showed that LOSP-treated Mengkulang glulam had higher values of modulus of rupture (MOR) and modulus of elasticity (MOE) compared with untreated Mengkulang glulam by 4 % and 6 %, respectively. Since most researches have so far focused on temperate softwood species, the findings of this study are significant as the specimens were from tropical timber species and the study employed experimental

S.H.B.S. Mokhtarruddin (✉) · R.B. Hassan
Faculty of Civil Engineering, University Technology MARA, Shah Alam, Malaysia
e-mail: syarifahhanisah89@gmail.com

R.B. Hassan
e-mail: rohana742@yahoo.com

Z.B. Ahmad
Institute of Infrastructure Engineering and Sustainable Management (IIESM), University Technology MARA, Shah Alam, Malaysia
e-mail: zakiah@salam.uitm.edu.my

Z.B. Ashaari
Faculty of Forestry, University Putra Malaysia, Serdang, Malaysia
e-mail: zaidon@putra.upm.edu.my

design. It can be concluded that LOSP has the quality to improve the bending strength of Mengkulang glulam thus increasing its performance.

Keywords Malaysian tropical timber · Light organic solvent preservative (LOSP) · The bending strength

1 Introduction

Timber is well recognized as a unique material due to the potential of readily available, renewable by plantation, good in ecological evaluation, and can be easily fabricated [1]. However, if environmental conditions are conducive to the development of wood-degrading organisms within the timber, protection is therefore required during processing, merchandising, and use.

Timber used for the manufacturing of glued laminated timber (glulam) normally are of low grade and low density so that the benefit of making glulam can be fully utilized besides having good bonding due to easy penetration of glue. Glulam is an engineered wood product manufactured from layers of graded sawn timber glued together using weatherproof resin. Studies have shown that by making glulam, the quality of timber can be improved two grades higher [2]. Malaysian timber of low grade and low density is not naturally durable. To enhance the usage of these timbers and extend the service life of wood products, preservative treatment is recommended [3].

Preservatives commonly used in the treatment of timber are aimed at improving resistance to fungi, insect, and to some extend weathering [4]. Numerous studies have reviewed the performance of treated glued timber [5–10]. For instance, Raknes [9] carried out experimental work using beech wood treated with waterborne preservative (CC and CCA). The clamping pressure used in his study was 0.69 and 2.07 N/mm^2 for 12 h. In his conclusion, it was emphasized that tension in beech wood treated with waterborne preservatives was satisfactory when bonded with PRF and RF adhesives even at high retention rates of preservatives. The author also found that higher curing temperature had negative effect on the clamping pressure.

In another study, Vaughn and Morrell [7] reported on the effects of post-layup ammoniacal copper zinc arsenate (ACZA) treatment on appearance and flexural properties of Douglas-fir glued laminated beams. This study revealed that (ACZA) treatment did not have significant effect on the modulus of rupture (MOR), modulus of elasticity (MOE), and glue-line shear. They concluded that timber treatment using waterborne preservatives subsequently affect the appearance of beam but not the loading properties. Yang et al. [11] used ammoniacal copper quaternary compound (ACQ) preservative to treat glulam samples made of three specimens of hardwood lumber to evaluate the effects of preservative treatment on the mechanical properties of hardwood glulam. The results showed that the MOE value

of lumber decreased after ACQ preservative treatment. However, there was no significant difference between untreated and ACQ-treated group.

Despite numerous studies which have reviewed the performance of treated glued timber; few have studied the behavior of preservatives treatment on the performance of glulam from Malaysia tropical timber. List of preservatives for pressure treatment can be found in American Wood Preservers' Associations [12]. Examples of preservatives commonly used in Malaysia are chromate copper arsenate (CCA) and boron. Nevertheless, these chemicals are inorganic preservatives and may be harmful to the environment if not handled properly. Therefore, the more environmental friendly chemical preservatives such as light organic solvent preservatives (LOSP) should be used. LOSP are widely used for glulam preservation in New Zealand and Australia and being applied to treatment of softwood species.

Bending strength, or specifically, its modulus of rupture (MOR), of a beam measures the load that the beam can carry which relates to its strength while the modulus of elasticity (MOE) relates to its resistance to bending which is also known as the stiffness of a beam. These two parameters are important mechanical properties used for the selection of timber materials [13] and they are equally important for designing timber structures. Therefore, it is crucial to study the effects of preservatives on mechanical properties of Malaysian timber especially glulam as they may interfere with bonding properties.

The purpose of this study was to determine the behavior of LOSP on bending properties of glulam manufactured using Malaysian tropical timber, namely, Mengkulang. Mengkulang is one of 3,000 known timber species of Malaysian Tropical Timber. Mengkulang is classified under hardwood timber that belongs to Strength Group (SG) 5, based on the Malaysia Standard [14]. This timber species can be found to be distributed throughout Southeast Asia. Mengkulang is widely used as material in heavy structure and joinery based on its ability to achieve good gluing characteristics [15].

2 Timber Preservatives

2.1 Wood-Degrading Organism

The principal organisms that can degrade wood are fungi, insects, bacteria, and marine borers. Most of the damages to timber in the Malaysia are caused by fungi. Molds, most sapwood stains, and decay are caused by fungi, which are microscopic, thread-like microorganisms that thrive on organic material. For some of these microorganisms, timber offers the required food supply. Most of the timber that decay in service has to be replaced, much of it primarily from improper use and care. Added to this base raw material cost would be, in many cases, the costs for processing, fabricating, finishing, merchandising, and assembly or replacement operations [16].

Fig. 1 Typical
load-deflection curve parallel
to grain [22]
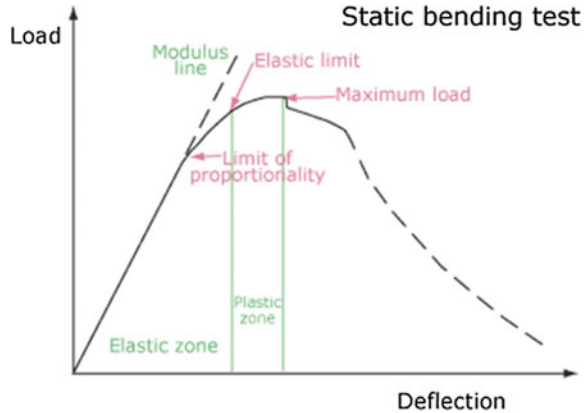
2.2 Bending Performance

Wood is an orthotropic material with three perpendicular property directions: tangential, radial, and longitudinal. In tension, the weakest direction for wood is perpendicular to the grain. A piece of wood that has a large knot in it will be weaker in bending or tension at the location of the knot. Thus, bending performance can be analyzed by constructing a static bending test. Two main properties can be obtained from the test, namely, modulus of rupture (MOR) and modulus of elasticity (MOE) [17–21]. These two properties can be easily understood by referring to typical load-deflection curve (Fig. 1: typical load-deflection curve parallel to grain [22]).

This study was conducted to achieve the main goal of improving the quality of the bending strength of Mengkulang glulam which included the maximum load data, MOR, and MOE of LOSP-treated Mengkulang glulam by comparing it with that of untreated Mengkulang glulam of the same type of timber beams. The typical pattern of graph was compared and failure mode was observed.

3 Materials and Methods

3.1 Glulam

Mengkulang (*Heritiera* spp.) glulam was manufactured at a glulam factory in Selangor, Malaysia. The manufacturing process followed the Malaysian Standard, MS 758 [15]. The lamellas were treated with LOSP prior to gluing. The total number of specimens of Mengkulang glulam was 10, where five beams were treated with LOSP and another five were untreated and used as control specimens. Mean density of LOSP-treated Mengkulang glulam was 721 kg m^{-3}, while untreated Mengkulang glulam was 731 kg m^{-3}.

3.2 Bending Test

All timber beams with 50 mm in width, 60 mm in depth, and 1200 mm in length were tested under four-point loading in accordance with ASTM D198 with the span-to-depth ratio of 18 [23] (Fig. 2).

The test was carried out in a universal testing machine (UTM) equipped with a 2500 kN load cell. The test was conducted to fail between 5 and 10 min with a loading rate of 1.5 mm/min. The experimental design was performed based on the schematic diagram as shown in Fig. 3. The data acquisition was collected through the data loggers.

The MOR and MOE in four-point bending were analyzed using simple beam theory as shown in (1) and (2) [22]. Slope of load displacement, *m* (3) was calculated from the graph.

Modulus of Rupture (MOR);

$$\text{MOR} = \frac{PL}{bh^2} \ (\text{MPa}) \tag{1}$$

Fig. 2 Four-point bending test
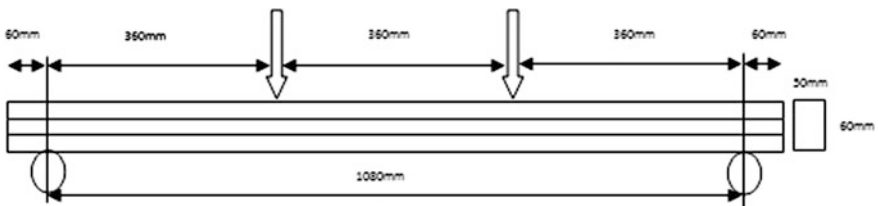
Fig. 3 The schematic diagram of test setup

Modulus of Elasticity (MOE);

$$\text{MOE} = \frac{P'a(3L^2 - 4a^2)}{4bh^3\Delta'} \text{ (MPa)} \tag{2}$$

where,

b Width of the specimen (mm)
h Depth of the specimen (mm)
P' Load at the proportional limit (N)
Δ' Deflection at the proportional limit (N)
L Length of the span (mm)
A Half shear span (mm)

$$m = \frac{P'}{\Delta'} \tag{3}$$

4   Result and Discussion

4.1   LOSP Behavior on Bending Strength Properties of Glulam

All of the 10 specimens were tested for strength performance which included both the LOSP-treated Mengkulang glulam and the untreated Mengkulang glulam. The overall strength performance results are shown in Table 1 including the calculated MOE and MOR together with standard deviation (STD) and coefficient of

Table 1 Mean bending strength data: LOSP-treated Mengkulang glulam versus untreated Mengkulang glulam

Specimen	LOSP-treated Mengkulang glulam				Untreated Mengkulang glulam			
	Max load (N)	P' (kN)	Δ' (mm)	m (N/mm)	Max load (N)	P' (kN)	Δ' (mm)	m (N/mm)
1	16,190	3.94	11.56	340.83	16,880	1.41	14.62	131.65
2	16,190	4.11	9.37	438.63	16,140	4.47	11.63	384.35
3	16,880	4.04	9.41	429.33	16,880	3.25	8.10	401.23
4	16,880	4.42	11.95	369.87	12,250	3.04	6.91	439.94
5	16,300	5.65	13.51	418.21	17,200	4.58	8.68	527.65
MOR (MPa)	98.928				95.22			
STD	1.94				11.06			
COV (%)	1.97				11.61			
MOE (MPa)	8720.45				8163.79			
STD	2897.24				3887.24			
COV (%)	33.22				47.62			

Fig. 4 Average MOR of LOSP-treated and untreated Mengkulang glulam
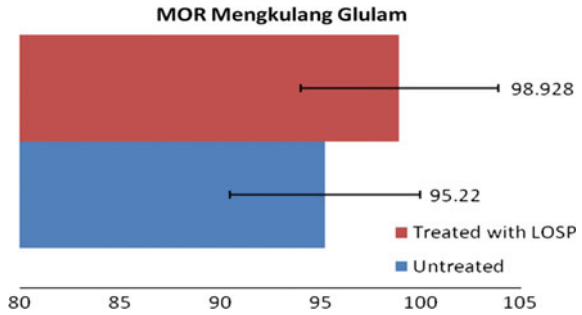
Fig. 5 Average MOE of LOSP-treated and untreated Mengkulang glulam
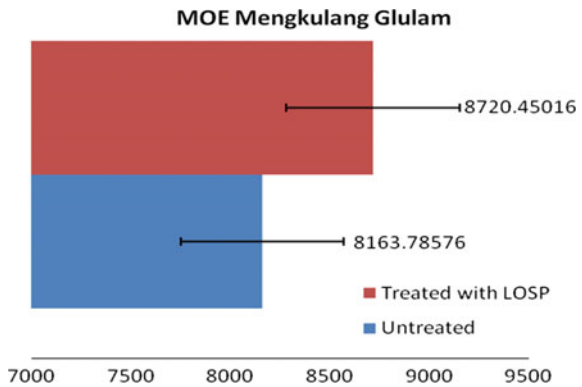
covariance (COV). The COV values for all specimens tested under four-point bending were in the range of 1–35 %. In specific data calculated, COV for LOSP-treated Mengkulang glulam was less than 10 % while for untreated Mengkulang glulam, the value was more than 10 % but still considered small for timber products.

Figures 4 and 5 show the histograms of the MOR and MOE of the tested beams. It can be seen that the MOR and MOE of LOSP-treated Mengkulang glulam were higher than those of untreated Mengkulang glulam by 4 % and 6 %, respectively. This shows that LOSP were not only effective in protecting the timber due to decay, attacks from fungi and insects and weathering effect but LOSP were also effective in improving the stiffness MOR and MOE.

4.2 Bending Behavior of Mengkulang (Heritiera spp.) Glulam

The bending behavior of LOSP-treated Mengkulang glulam and that of the untreated Mengkulang glulam were combined into one typical load versus deflection graph as shown in figure.

Fig. 6 Typical
load-displacement curve for
Mengkulang glulam
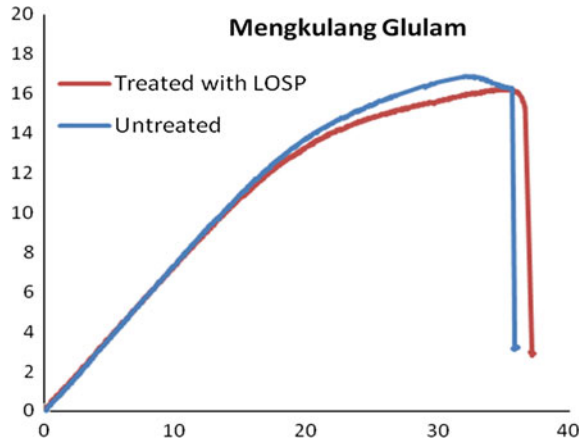
These illustrations are only representatives of the general behavior of load versus displacement. Generally, both types of specimens showed similarities in the shape of the linear portion to reach the maximum point and then in form of abrupt fall of the load in the nonlinear portion of the graph as illustrated in Fig. 6. However, there was a slight drop in the observed values of the untreated Mengkulang glulam as a result of small cracking during testing until untreated specimen reached total failure stage. In contrast, LOSP-treated Mengkulang glulam showed uniformity in bending behavior until failure occurred when compared with the untreated Mengkulang glulam.

4.3   Failure Mode Characteristics

This section analyzes the failure mode characteristics of LOSP-treated Mengkulang glulam and untreated Mengkulang glulam under four-point bending test as shown in Figs. 7 and 8.

Fig. 7 Failure mode
characteristics of
LOSP-treated Mengkulang
glulam under bending; **a** cross
grain tension, **b** horizontal
shear
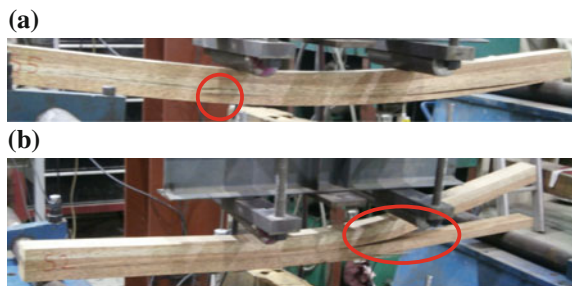
Fig. 8 Failure mode
characteristics of untreated
Mengkulang glulam under
bending; **a** simple tension,
b horizontal shear

(a)

(b)

The LOSP-treated Mengkulang glulam mainly failed in horizontal shear but in timber (Fig. 7a) it was not along the glue-line and only some samples failed in horizontal shear along the glue-line (Fig. 7b). For untreated Mengkulang glulam, there was a combination of failure modes. Some beams failed in true bending with tension failure at the tension zone (Fig. 8a) while the other beams showed failure in horizontal shear (Fig. 8b). This explains the small variation (low COV values) in the MOR and MOE for treated glulam since almost all of the LOSP-treated Mengkulang glulam beam specimens failed only in horizontal shear as compared to the untreated Mengkulang glulam beam specimens which failed in a combination of modes.

5 Conclusion

This study was conducted to determine the bending strength of LOSP-treated and untreated Mengkulang (*Heritiera* spp.) glulam. The maximum load carrying capacity, the modulus of rupture (MOR), and modulus of elasticity (MOE) were observed for both groups of glulam beam specimens. LOSP-treated Mengkulang glulam had higher MOR and MOE values compared to those of the untreated Mengkulang glulam beams by 4 % and 6 %, respectively. The treatment using LOSP was therefore effective in the improving the bending strength of glued laminated timber (glulam) from tropical timber such as Mengkulang (*Heritiera* spp.). The findings of the present study are significant as the specimens were from tropical timber and the study employed experimental design.

In addition, the failure mode characteristics of the glulam specimen were also observed in the study. It was found that LOSP-treated Mengkulang glulam beams mainly failed in horizontal shear test while the untreated beams failed in combination modes, namely, in tension and horizontal shear tests. Therefore, more research is needed to gain new knowledge and understanding of the potential uses of LOSP in improving the quality of the overall performance of glulam especially with regard to tropical timber species such as Mengkulang (*Heritiera* spp.).

References

1. D. Sandberg, and P. Navi, "Introduction to thermo-hydro-mechanical (THM) wood processing," School of Technology Design. Report, No 30. Växjö University, Växjö Sweden, pp. 167, 2007.
2. W. H. W. Mohamad, M. A. Razlan, and Z. Ahmad, "Bending strength properties of glued laminated timber from selected Malaysian hardwood timber," International Journal of Civil & Environmental Engineering, August 2011, vol: 11, no: 04.
3. S. Lebow, "Leaching of wood preservative components and their mobility in the environment," Summary of pertinent literature, Gen. Tech. Rep. FPL–GTR–93, Madison, WI: U.S., Department of Agriculture, Forest Service, Forest Products Laboratory, 36 p, 1996.
4. S. Sandeep Nair, "Effectiveness of copper-boron diffusion treatments for wood," Thesis for Master of Science, University of Idaho, 2006.
5. B. P. Lisperquer, and P. H. Backer, "Strength and durability of phenol-resorcinol-formaldehyde bonds to CCA-treated radiata pine wood," *For. Prod. J*, vol. 55, no. 12, pp. 113–116, 2005.
6. L. Podgorski, and G. Legrand, "Paintability and gluability of wood treated with asernic-free and chromium-free preservative treatments," in *The international Research Group on Wood Protection*, 2006.
7. J. J. Vaughn, and J. Morrell, "Effects of post-layup ammoniacal copper zinc arsenate treatment on appearance and flexural properties of Douglas-fir glued laminated beams," *Eur. J. Wood Wood Prod.*, pp. pp. 1–4, 2012.
8. Y. S. Yildiz UC, A. Temiz, and E. D. Gezer, "Effects of wood preservatives on mechanical properties of yellow pine (Pinus sylvestris L.) wood," *Build. Environ.*, vol. Volume 39, no. Issue 9, pp. 1071–1075, 2004.
9. E. Raknes, "Gluing of wood pressure-treated with water borne preservative and flame retardant," *Inst Wood Sci*, pp. 22–44, 1963.
10. S. M. Truax TR, and J.O Blew, "Production of preservative-treated laminated timber," in *AWPA Granbury*, 1953, pp. 113–123.
11. T. H. Yang, C. H. Lin, and S. Y. Wang, "Effects of ACQ preservative treatment on the mechanical properties of hardwood glulam," *Eur. J. Wood Wood Prod.*, vol. Volume 70, no. Issue 5, p. pp 557–564, 2012.
12. American Wood-Preservers Association, "List of Timber Preservatives," Annual book of standard, Grabbury, TX, 2003.
13. J. G. Haygreen, and J. L. Bowyer, " Forest products and wood science an introduction," USA: Iowa State University; 1989, p. 500. ISBN 0-8138-1801-X.
14. Malaysia Standard, "Code of practice for structural use of timber: Part 2: Permissible Stress Design of Solid Timber," Malaysia, MS544:2, 2001.
15. Malaysia Standard, "Glued laminated timber: performance requirements and minimum production requirements," First Revision, Malaysia, MS758, 2001.
16. A. Robert Zabel, and J. Jeffry Morrel, "Wood microbiology: decay and its prevention," Academy Press, Inc. San Diego, C A, pp. 476, 1992.
17. T. Takeda, and T. Hashizume, "Effective Sampling Method For Estimating Bending Strength Distribution Of Japanese Larch Square-Sawn Timber," *Journal Wood Science, 46*, Japan, 350–356, 2000.
18. H. Heräjärvi, "Static bending properties of Finnish birch wood," *Wood Science Technology* 37, 523–530, 2004.
19. J. Branco, H. Varum, and P. Cruz, "Structural Grades of Timber by Bending and Compression Tests," *Materials Science Forum* Vols. 514–516, Portugal, pp 1663–1667, 2006.
20. M. Frese, and H. J. Blaß, "Characteristic Bending Strength of Beech Glulam," *Materials and Structures*, Germany 40, 3–13, 2006.
21. W. David Green, E. Jerrold Winandy, and E. David Kretschmann, "Mechanical Properties of Wood," Forest Product Laboratory, Madison Wiscinson, Chapter 4, 1999.

22. D. Gardiner, "Typical load-deflection curve parallel to grain bending specimen," Retrieved on 3 September 2015, http://flysafe.raa.asn.au/scratchbuilder/wood_strength_values.html.
23. American Standard for Testing and Material, "Standard test methods for static tests of lumber in structural sizes," ASTM: D 198, 2009.

Wood Properties and Bonding Shear Strength of Hardwood Glulam After Fire Exposure

Abdul Wahab Mohd Jamil, Jabar Khairul Azmi and Seok Sean How

Abstract Highlights on glued laminated timber (glulam) of tropical hardwoods have attracted both local and foreign businesses. However, knowledge and technology regarding Malaysian timbers for the glulam application are still very limited. To improve the knowledge on structural performance of tropical timber glulam in fire occurrence, mechanical tests of burned glulam beams were conducted. The study focused on the effect of fire exposure to the mechanical properties of wood and bonding shear strength of the lamination. Based on the results of mechanical test of a selected species, strength and stiffness of timber were reduced due to the exposure to fire. Bonding shear strength of the lamination was also reduced.

Keywords Engineered timber · Fire test · Mechanical properties

1 Introduction

In recent years, positive attention is gained from local practitioners for the technological development of glued laminated timber (glulam) application. Previously, a few attempts were made by local experts to introduce structural glulam products using Malaysian hardwoods [1, 2]. To date, numerous studies of native timber for

A.W. Mohd Jamil (✉)
Timber Engineering Laboratory, Forest Research Institute Malaysia (FRIM),
Kepong, Malaysia
e-mail: mohdjamil@frim.gov.my

J. Khairul Azmi
Fire Protection Laboratory, Forest Research Institute Malaysia (FRIM),
Kepong, Malaysia
e-mail: khairulazmi@frim.gov.my

S.S. How
Wood Lamination Laboratory, Forest Research Institute Malaysia (FRIM),
Kepong, Malaysia
e-mail: howss@frim.gov.my

glulam application have been conducted [3–5] and the number of professionals trained in the glulam syllabus has increased [6, 7].

Nevertheless, this progress is only recent, and thus, we are many decades behind from the current glulam technology. In reality, only a few Malaysian timbers have been scientifically evaluated for glulam application (presumably less than 10 timber groups), while many others remain to be considered. There are more than 2500 timber species in the nation; each is sizable enough as a plank-producing species. Besides, focus was mostly given to the lamination issue, while the performance of glulam of Malaysian hardwoods related to fire, fatigue, mechanical creep, outdoor and exposed condition, etc., are still unknown.

In general, research on glued laminated timber requires good knowledge in wood mechanics as well as knowledge in adhesive behavior. These subjects are necessary to ensure an accurate process of glulam fabrication and a reliable structural performance of finished products. Through proper design, there is a potential to fabricate glulam from tropical hardwoods whose strength is equivalent to a solid beam of structural size [8]. However, when combustion element is added, additional knowledge concerning the interaction between wood, adhesive, and heat is critical.

Sik et al. [9] conducted a study on the mechanical properties of tropical hardwoods dried at elevated temperatures. They reported that modulus of rupture and modulus of elasticity of rubberwood were affected by drying temperatures. The results showed that modulus of rupture of rubberwood dried at 150 °C was 8.5 % lower compared to rubberwood dried at 60 °C. Based on the similar comparison, modulus of elasticity was 2.3 % lower.

A study by Gan et al. [4] demonstrated that fire performance of keranji glulam was considerably improved than the solid timber itself. Based on the physical observation, failure was due to deformation and twisting of the samples. They concluded that the stability of keranji glulam against fire was probably enhanced with finger jointing and lamination techniques. The effect is, however, contrary to other species such as balau, red balau, kekatong, and kempas. The results of fire test between solid and glulam samples of these timbers showed no significant differences. Gan et al. also found that the charring rate of glulam fabricated from high density timbers such as kekatong and kempas were higher than those of lower density timbers such as red balau and keranji. The results indicated that besides density, other characteristics may influence the fire resistance of glulam. They concluded that glulam made from higher density timbers may not necessarily perform better in fire.

It is stated in Clause 213 of Uniform Building By-Laws (UBBL) that every structural component must be built with a clear indication of the fire resistance rating. Materials intended for any load-bearing application should fulfill the minimum rate requirement. Thus, to use timber glulam as a structural component of building, the fire performance of glulam beam must be properly justified.

Therefore, to improve our knowledge of the performance of timber glulam against heat, we conducted fire and mechanical tests on glulam beams. The samples were fabricated from a selected tropical hardwood species. This paper focuses on the effect of fire exposure to the mechanical properties of wood and bonding shear strength of the glue lamination.

2 Materials and Methods

2.1 Preparation of Test Samples

Glulam beams were fabricated from balau (*Shorea* spp.) timber boards of 25 mm × 125 mm cross-section size. The boards were finger-jointed to a final length of 1500 mm using phenol resorcinol formaldehyde. Each beam consisted of 3 lay-ups, laminated using resorcinol formaldehyde. The nominal dimensions of the beams are 75 mm (width), 125 mm (thickness), and 1500 mm (length). A total of 10 glulam beams were prepared for fire exposure test and 5 beams as control samples.

2.2 Fire Test

The main test setup consisted of a closed room, horizontal gas-fired furnace. The frame was made of concrete blocks. Test samples were exposed to fire in the furnace for 15 min. The range of temperature inside the furnace was measured between 730 and 745 °C. Figure 1 shows the arrangement during fire test of glulam beams. A total of 10 samples were tested, namely Beam 1 to Beam 10.

The charring rate, R, (mm/min) was calculated using Eq. 1, based on Fig. 2. Five consecutive points through the length of each beam were marked before and after the fire test.

Fig. 1 Arrangement of fire exposure test

Fig. 2 Calculation of charring rate
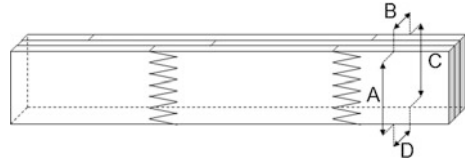
Fig. 3 Flexural test of glulam beam
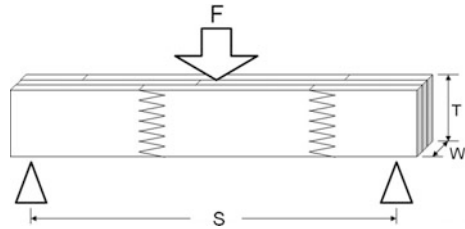
$$R = \frac{\left[\dfrac{\sum_1^n ((A-a) + (B-b) + (C-c) + (D-d)/4)}{n} \right]}{t} \qquad (1)$$

where A, B, C and D are the dimensions before fire test (mm), a, b, c and d are the dimensions after fire test (mm), n is the number of consecutive measurement point through the length of the beam and t is the duration of fire exposure (min).

2.3 Flexural Test of Beam

Test arrangement for the determination of maximum load capacity of each beam is illustrated in Fig. 3. Flexural test was conducted based on three-point static bending principle. Center point loading of 6.6 mm/min was applied over a span (S) of 1371 mm. A total of 10 samples of glulam beams that have been exposed to fire (Beam 1–10) were tested. For comparison, 5 control samples (unburned) were tested based on the similar method. A Shimadzu universal testing machine and Trapezium software were used to record the maximum load of every beam.

2.4 Mechanical Properties Test

Mechanical test was conducted to determine the modulus of rupture (MOR) and modulus of elasticity (MOE) of timber after exposure to fire. Comparison between the specimens cut from burned samples and the specimens of control samples was made. Free-char, small clear specimens of 20 mm × 20 mm × 300 mm were cut

from the remnant of the beams. A total of 28 specimens of burned samples (Beam 1–10) and 35 specimens of control samples were tested. Small specimen bending test was conducted based on the BS373:1957 method.

The MOR was calculated based on the equation:

$$\text{MOR} = 3P_{\text{max}}l/2bd^2 \tag{2}$$

where P_{max} is maximum applied load (N), l is bending span (mm), b is width of the specimen (mm) and d is depth of the specimen (mm).

The MOE was calculated using the following equation:

$$\text{MOE} = \Delta Pl^3/4\Delta\delta bd^3 \tag{3}$$

where ΔP is increment of load below the limit of proportionality (N), l is bending span (mm), $\Delta\delta$ is increment of deflection corresponding the load (mm), b is width of the specimen (mm) and d is depth of the specimen (mm).

2.5 Bonding Shear Test

Bonding shear test was conducted by setting the adhesive layer as the planar surface of shear failure (Fig. 4). Twenty millimeter cube specimens having adhesive layer at center were cut from glulam samples. Shearing force of 0.6 mm/min was applied to determine the bonding shear stress. Shearing stress at maximum load, τ_{max} was calculated using the following formula:

$$\tau_{\text{max}} = F_{\text{max}}/A \tag{4}$$

where F_{max} is the maximum shear load (N) and A is the plane area of the glue layer (mm^2), which is equal to $l \times w$. A total of 83 specimens cut from burned samples and 72 specimens of control samples were tested.

Fig. 4 Test arrangement of bonding shear
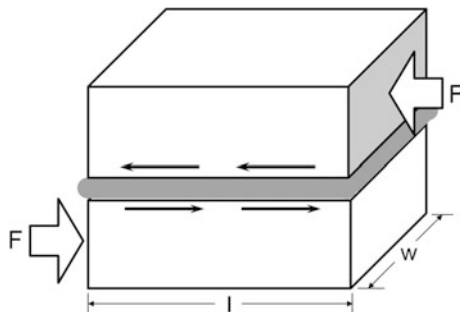
3 Results and Discussion

Flame distribution through the length of the samples was uniform. Char formation was observed on the whole surface of the glulam beams. Figure 5 shows the picture of a glulam beam after fire test. Charring rates of Beams 1–10 are shown in Table 1. The average charring rate was 0.435 mm/min. The lowest and highest charring rates were 0.281 and 0.683 mm/min respectively. Abdul Rashid [10] reported that the charring rates of some Malaysian timbers were between 0.525 and 0.600 mm/min. In another study, tropical timber species were reported with charring rates between 0.360 and 0.580 mm/min [11]. Based on samples of 6 tropical timber groups, they found that charring rate decreases when density of the timber increases.

Results of flexural test of burned glulam beams are shown in Table 2. Mean values showed a slight reduction in the maximum load capacity of burned samples. In summary, the glulam beams lost 8 % of their maximum load capacity after being

Fig. 5 Glulam beams—before and after fire test

Table 1 Charring rate of balau glulam

Sample number	Charring rate (mm/min)
Beam 1	0.366
Beam 2	0.399
Beam 3	0.460
Beam 4	0.467
Beam 5	0.683
Beam 6	0.430
Beam 7	0.369
Beam 8	0.448
Beam 9	0.451
Beam 10	0.281
Average	*0.435*
Minimum	*0.281*
Maximum	*0.683*

Table 2 Flexural test results of balau glulam

Burned		Control	
Sample number	Max. load (kN)	Sample number	Max. load (kN)
Beam 1	25.4	Control 1	28.9
Beam 2	24.3	Control 2	39.3
Beam 3	26.9	Control 3	30.6
Beam 4	24.3	Control 4	23.3
Beam 5	24.8	Control 5	35.7
Beam 6	31.1		
Beam 7	31.6		
Beam 8	41.6		
Beam 9	34.0		
Beam 10	25.8		
Mean	*29.0*	*Mean*	*31.6*
SD	*5.6*	*SD*	*6.2*

Table 3 Average modulus of rupture and modulus of elasticity after fire exposure

Sample (n)	MOR (N/mm^2)	MOE (N/mm^2)	Specific gravity
Control (35)	152	16902	0.896
Burned (28)	144	16644	0.839

exposed to fire for 15 min. This is reasonable since the combustion reduced the effective dimension of the beams.

However, these values do not indicate the effect of fire exposure to the mechanical properties of timber material. Thus, specimens were cut from remnants of burned glulam samples to evaluate the properties of the wood itself. The results are summarized in Table 3. Slight reductions of MOR and MOE were observed from burned specimens. The timber lost 5 and 2 % of strength and stiffness respectively. Similarly, a lower specific gravity of 6 % reduction was obtained.

The comparison of MOR and MOE between burned and control specimens are presented as cumulative functions in Figs. 6 and 7. The differences shown in both graphs are trivial. However, as the number of specimen increases, the differences become obvious. Although the variations are generally small, these proved the effect of fire exposure to the structural performance of glulam timber.

In general, three different modes of fracture of small clear specimen test were observed as splintering, cross-grained, and simple tension. Pie charts representing fracture modes of burned and controls specimens are shown in Fig. 8. The rates of fracture modes between burned and control specimens were generally the same.

Although study reported that timber develops into brittle characteristic due to elevated temperature, this occurrence was not demonstrated in the present study. Brittle wood is characterized by an abrupt breakage across the grain without
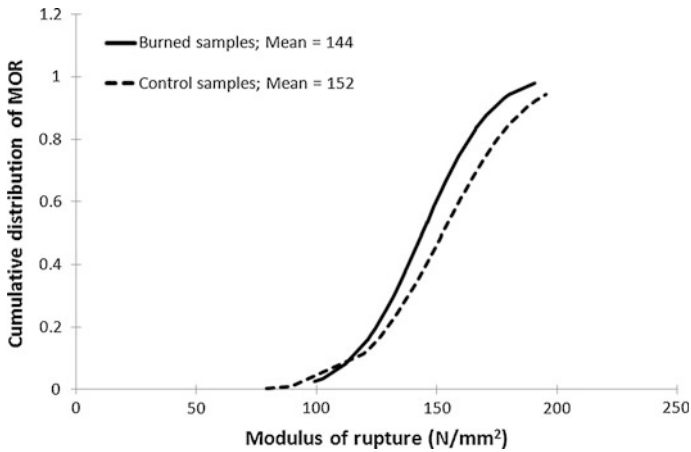
Fig. 6 Cumulative distribution of MOR
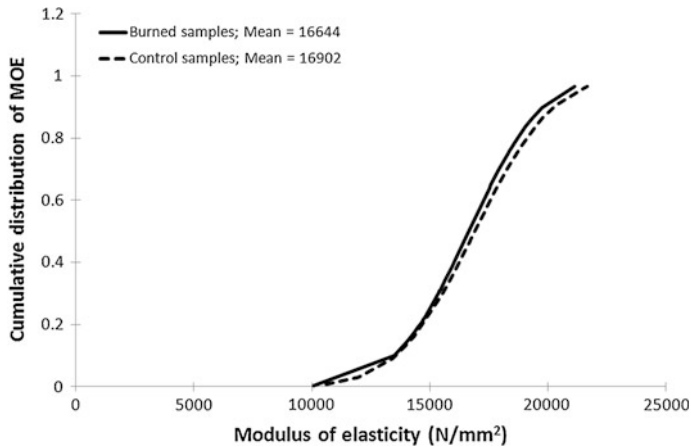
Fig. 7 Cumulative distribution of MOE

splinters [12]. It is usually indicated by brash tension fracture or simple tension fracture at maximum stress during static bending test.

Bonding shear test was conducted to evaluate the effect of fire to the bonding shear of adhesive layer. Similarly, lower bonding shear strength was obtained from specimens of burned samples. The results of bonding shear test are summarized in Table 4. Shear strength of burned specimens was 10 % lower than control samples. Based on the existing data of Malaysian hardwoods, shear strength of balau timber is 15.0 N/mm^2 at 15.6 % moisture content [13]. The value is considerably higher than the bonding shear strength of the adhesive. Thus, when load was applied to glulam beam, failure due to shearing force was expected to occur at the lamination plane.

Fig. 8 Pie charts showing the
rates of fracture modes
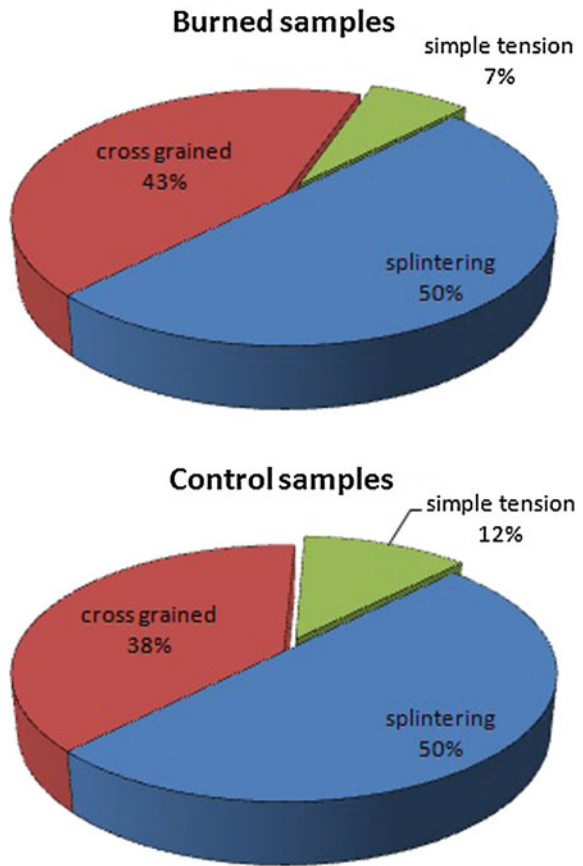
Table 4 Average bonding shear strength after fire exposure

Sample (n)	Shear stress (N/mm^2)	Standard deviation (N/mm^2)
Control (72)	12.3	2.6
Burned (83)	11.1	2.2

These results were obtained from glulam samples of one selected hardwood species. Hence the outcome may probably vary among other species. Based on the present assessment, modulus of rupture and modulus of elasticity of timber were affected after fire exposure. In addition, bonding shear strength of the lamination was reduced. Further research on glulam of other tropical hardwoods and their effect against fire is recommended.

The evaluation was limited to the modulus of rupture and modulus of elasticity values. Although MOR and MOE are generally adequate to indicate the overall structural performance of timber material, other mechanical properties such as

hardness, compressive stress, shear stress, tensile stress, etc., are also important for future research. Additionally, fire test of glulam made from medium density timber such as *Acacia mangium* and merawan will be an added advantage in promoting plantation species for structural applications.

4   Conclusions

The average charring rate for the glulam beams was 0.435 mm/min. In average, the results showed that the beams lost 8 % of their maximum load capacity after being exposed to fire for 15 min. Slight reductions were observed in the MOR and MOE values of the specimens from burned samples. The timber lost 5 and 2 % of its strength and stiffness respectively. Similarly, a lower specific gravity of 6 % reduction was obtained from the specimens of burned samples. Relatively, the fracture modes between burned and control specimens were the same. The effect of brittle wood development on remnants of burned samples was not observed. Likewise, bonding shear strength of the adhesive of burned samples was 10 % lower than control samples.

References

1. Mohd Hamami S, "The glue joint strength of laminated timber decking made from three Malaysian hardwood species," Pertanika 7(3): 131–136, 1984.
2. Tan YE, Mohd Zaini U and Komatsu M, "Effect of moisture content and sawing pattern on the gluing of meranti tembaga (Shorea leprosula)," Journal of Tropical Forest Science 5(1): 44–53, 1992.
3. Wan Hazira WM, Mohd Azran R and Zakiah A, "Bending strength properties of glued laminated timber from selected Malaysian hardwood timber;" International Journal of Civil & Environmental Engineering 11(4): 7–12, 2011.
4. Gan KS, Khairul Azmi J, Zairul Amin R, Pang SK, Tan YE, Lau LH, Mohd Adawi TO and Zaihan J, "Fire performance of timber door frames," Journal of Tropical Forest Science 25(3): 429–436, 2013.
5. Norshariza MB, Zakiah A, Afidah AB and Paridah MT, Ultimate strength of kekatong glued laminated timber railway sleepers. Proceedings of the International Civil and Infrastructure Engineering Conference 2013. Springer, 2014, pp 97–106.
6. Ong CB, Prediction of Beam Stiffness for Structural Glued Laminated Timber. Master Thesis, Universiti Putra Malaysia, 2004.
7. Dalila K, The behaviour of glulam beam strengthened using fibre reinforced polymer. Master Thesis, Universiti Teknologi Malaysia, 2007.
8. Suhaimi AB, Abd Latif S and Zainai BM, "Factors affecting ultimate strength of solid and glulam timber beams," Jurnal Kejuruteraan Awam 16(1): 38–47, 2004.

9. Sik HS, Choo KT, Sarani Z, Sahrim A, How SS and Mohamad Omar MK, "Influence of drying temperature on the physical and mechanical properties of rubberwood," Journal of Tropical Forest Science 21(3): 181–189, 2009.

10. Abdul Rashid AM, Guidelines in Manufacturing Timber Fire Door. Timber Digest No. 83. Forest Research Institute Malaysia, Kepong, 1987.

11. Njankouo JM, Dotreppa JC and Franssen JM, "Experimental study of charring rate of tropical hardwoods," Fire Material 28: 15–24, 2004.

12. Highley TL and Scheffer T, Controlling decay in waterfront structures. Research paper FPL-RP-494. Forest Product Laboratory, Madison, 1989.

13. Lee YH, Engku ARC & Chu YP. 1993. The Strength Properties of Some Malaysian Timbers. Timber Trade Leaflet No. 34. Malaysian Timber Industry Board, Kuala Lumpur.

Evaluation of Density for Malaysian Hardwood Timber Treated by Heat: The Case of *Pauh Kijang* (*Irvingia* spp.) and *Kapur* (*Dryobalanops* spp.)

N.I.F. Md Noh and Z. Ahmad

Abstract Heat treatment is one of the environmental friendly ways to treat timber that will lead to the improvement of timber natural quality and equip the timber with new properties. It is an eco-friendly and alternative treatment method that will modify the properties of timber by using high temperature instead of using chemical preservatives as common practice. This paper presents the effect of heat treatment on physical properties which is density for two types of Malaysian hardwood namely *pauh kijang* and *kapur*. Specially, design electronic furnace was used as an oven for the heat treatment process. The result shows a reduction in density after heat treatment, however, the difference is not merely significant. Reduction in density indicates a weight loss which is theoretically caused by moisture content loss thus leading to the increment of movement stability.

Keywords Heat treatment · Environmental friendly · Timbers · Physical properties · Density

1 Introduction

Timber is one of the oldest building materials which are being used to build man's shelters. In construction industry, timbers are useful to build a structure such as building, bridge, boats, and the other civil engineering works [1]. However, there is a limit on timber usage based on its properties and characteristics. This limit has defined timber as a material that is not, under all conditions, an appropriate building

N.I.F. Md Noh (✉)
Faculty of Civil Engineering, Universiti Teknologi Mara (UITM),
Shah Alam, Selangor, Malaysia
e-mail: nurilyafarhana@yahoo.com

Z. Ahmad
Institute of Infrastructure Engineering and Sustainable Management (IIESM),
Universiti Teknologi Mara (UITM), Shah Alam, Selangor, Malaysia
e-mail: zakiah@salam.uitm.edu.my

material [2]. Most of timber species with natural durability such as Kekatong and Resak are expensive and are being supplied from nonrenewable forest resources. Due to this problem, the use of timber with natural durability has been decreasing and an alternative to encounter this problem has been found out which is by using timber species with nonnatural durability [3]. However, this timber needs to be modified or treated to help improve its durability properties. In Malaysia, timber that will be used in construction industry is usually treated by using a water-based chemical preservatives. The allowed preservative to be used in this treatment is copper chromium arsenic (CCA) [4]. The most common method of treatment for timber is by using chemical preservatives known as Copper Chromium Arsenic (CCA) [5]. It is a world most widely used wood preservatives including Malaysia. It has been proven that CCA can help to improve timber properties and can also help to prolong the life of a timber species from few years to 30 years or more [4].

Due to the usage of chemical preservatives that are toxic, there are many issues that arise related to CCA. One of the issues is related to human where CCA can give a threat to their health. EC Scientific Committee on Toxicity, Eco-toxicity, and the Environment (CSTEE) had announced that CCA is both genotoxic and carcinogenic. CCA may give a risk of cancer especially in lung, bladder, kidney, and liver. CCA also damages mucus membrane, produces peripheral nervous system disturbances, degeneration hearing loss, and also skin ulcer. CCA will suppress and attack the immune system of a human body [6]. CCA also give bad and negative impact to the environment and ecological system. When it is raining, CCA leaches out of timber that is being treated until the arsenic, chopper, and chromium from the treated timber can be washed off into the river or soil below. This situation will kill the aquatic organisms in the river or sea because they are very sensitive to CCA exposure [7]. Based on these issues, many countries have put restriction and banned on the usage of CCA for treating timbers such as Canada, US, Japan, Denmark, Switzerland, Vietnam, and Indonesia [8]. US also had banned CCA where the US Environmental Protection Agency (EPA) announced that starting from January 2004, timber treated by using CCA can no longer be manufactured [9]. However, Malaysia still allows CCA to be used for treatment.

In light of this issue, alternative treatment method need to be explored and made available in Malaysia. One of the possible methods of treatment is heat treatment which using heat rather than chemicals. Heat treatment is the most environmental friendly way to treat a timber species that will be an alternative way to replace CCA. This method of treatment will alter the substrate of a timber species by using high level of temperature, not by using chemical preservatives. The usage of high level temperature will lead to chemical changes that will reduce the hygroscopicity of the timber [10]. This will lead to improvement of natural quality and properties of the timber that being treated and may equip it with new physical, mechanical and chemical properties. This study is conducted with objective to achieve which is to analyze the effect of heat treatment on the physical properties; density of timber in strength groupings SG3 and SG4 which is Kapur by varying temperatures from 150 to 210 °C and time exposure is 1 h duration.

As stated in Malaysian Standard MS544: Part 2: 2001, *pauh kijang* is listed under SG3 while *kapur* is listed in SG4 timber which required treatment to improve its properties and durability. The objective of this study is to identify the effect on the density of *pauh kijang* and *kapur* which has been treated by heat at temperature level 150 °C.

2 Literature Review

2.1 *Heat Treatment*

Heat treatment is one of the methods of treatment to alter and improve the properties of timbers by using a high level temperature which also finally can equip the timbers with new properties [11]. It is an environmental friendly way to improved and alters the timber's structures and components [12]. Differs from Copper Chromium Arsenic (CCA) which widely used in Malaysia, heat treatment is an eco-friendly way of treating timber because there is no chemicals or preservatives used during its process. Based on previous researches, heat treatment may affect the physical, mechanical, and chemical properties of timbers. Therefore, the next section reviewed the effects of heat treatment on physical, chemical, and mechanical properties of timbers.

According to Militz [13], the heat treatment process involves exposing wood to an elevated temperatures ranging from 160 to 260 °C in an atmosphere with low oxygen content to avoid the wood from burning due to the high temperature. The temperature and duration for heat treatment generally vary from 180 to 280 °C and 15 min to 24 h, respectively, depending on the process, wood species, sample size, moisture content of the sample, the desired mechanical properties, resistance to biological attack, and dimensional stability of the final product. The extent of the change in timber properties during heat treatment is determined by the method of thermal modification, the wood species and its characteristic properties, the initial moisture content of the wood, the surrounding atmosphere, the treatment temperature and time. It is reported that temperature has a stronger effect on timber properties than the amount of time the timber was exposed to heat. Treating wood at lower temperature for longer time periods does not produce the desired properties. Syrjänen and Oy [14] found that temperature over 150 °C alter the physical and chemical properties of wood gradually.

Heat treatment reduces certain mechanical properties, but the dimensional stability and the biological durability of wood increases through heat treatment. Yildiz [15] said that heat treatment also resulted in changes in the physical properties of the wood including reduced shrinkage and swelling, low equilibrium moisture content, enhanced weather resistance, a decorative dark color, and better decay resistance. Therefore, heat treated wood is an eco-friendly alternative to impregnate wood materials, and heat treated wood can be used for garden, kitchen, and sauna

furniture, cladding on wooden buildings, bathroom cabinets, floor material, ceilings, inner and outer bricks, doors, and window joinery, and a variety of other outdoor and indoor wood applications.

Based on [16], most of the earlier experiments showed that heat treatment reduces the equilibrium moisture content (EMC), and thickness swelling and slow down water absorption (WA) and wet ability of wood. However, heat treatment actually increased the WA of pine sapwood heat treated at 170, 190, 210 °C. Rousset et al. [17] said that heat treatment significantly reduces the ability of bound water to migrate through the wood sample due to the chemical modification of the cell wall, but the permeability value did not change significantly.

2.2 Physical Properties of Timber

Physical properties of timber are related to the natural characteristics of the timber such as color, smell, moisture content, durability, density, and dimensional stability [18]. Treatment or modification on timber could affect the properties of timber. Heat treatment also will modify and give effect to properties of timber including physical properties of timber.

2.3 Density

Density is one of the physical properties of timber that might be affected by heat treatment. It can be defined as weight per unit volume of timber itself. It can be expressed in kilogram per cubic meter (kg/m^3) [19].

3 Experimental Works

This study utilized the solid hardwood timber namely *Pauh Kijang* (*Irvingia* spp.) and Kapur (*Dryobalanops* spp.). Temperature of 150, 170, 190 and 210 °C were determined for the heat treatment. 15 samples of green (wet) timbers with moisture content (MC) more than 20 % and size of 50 × 90 × 1800 mm were prepared, respectively, for the mentioned heat treatment temperatures. All samples were weighted prior to the test. The heat applied on the samples with four different temperatures as stated before for one hour duration of treatment.

Those samples were stored in the conditioning room for 2 weeks prior to the heat treatment process. The conditioning room has 65 % of relative humidity with temperature level of 24 °C as shown in Fig. 1.

Heat treatment was then executed on the samples after the conditioning process, which was conducted at Margin Heat Treatment and NDT Services Sdn Bhd, Shah

Fig. 1 **a** Conditioning room,
b samples arrangement in
conditioning room for 2
weeks before heat treatment
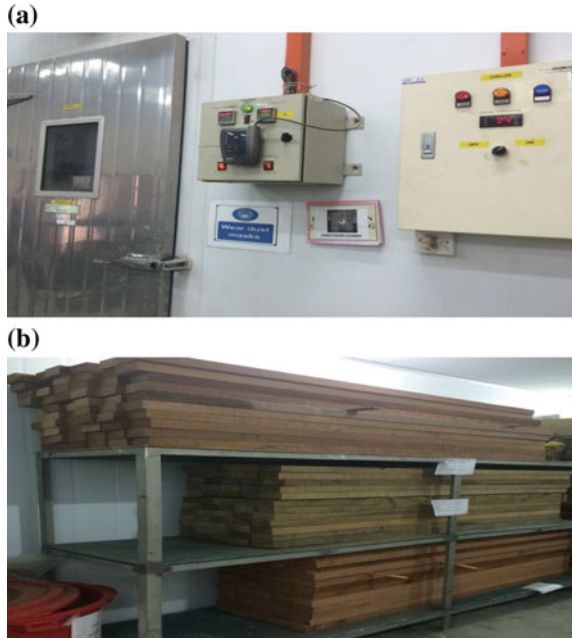
Alam. The heat treatment was performed within one hour duration under steam and
atmospheric pressure in an oven which will provide 16 different treatment condi-
tions. A special electrical furnace acted as an oven and was designed and prepared
according to the size and numbers of the samples as shown in Fig. 1 (Fig. 2).

The samples were then weighted again once the heat treatment process was
done. Figure 3 showed the timber samples after been treated. In determining the
density of the timber samples, [20] was referred. Calculation of the density was
done by using Eq. 1 and expressed as kg/m^3. The density of the hardwood timber
was determined for each samples before taken into average, for each type of
hardwoods and temperature of heat treatment, then compared between before and
after heat treatment.

$$\rho = \frac{m}{v} \tag{1}$$

in which m mass of the sample in kg and v volume of the sample in m^3.

4   Results and Discussion

Table 1 shows the result on density on hardwood *kapur* before and after heat
treatment.

Fig. 2 Specially designed
electrical furnace and the
arrangement of samples inside
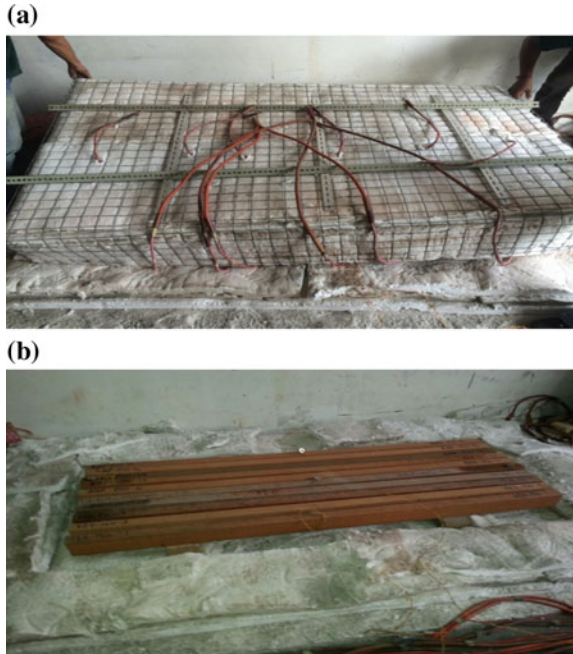
Fig. 3 **a** Heat treated *pauh
kijang* samples, **b** heat treated
kapur samples
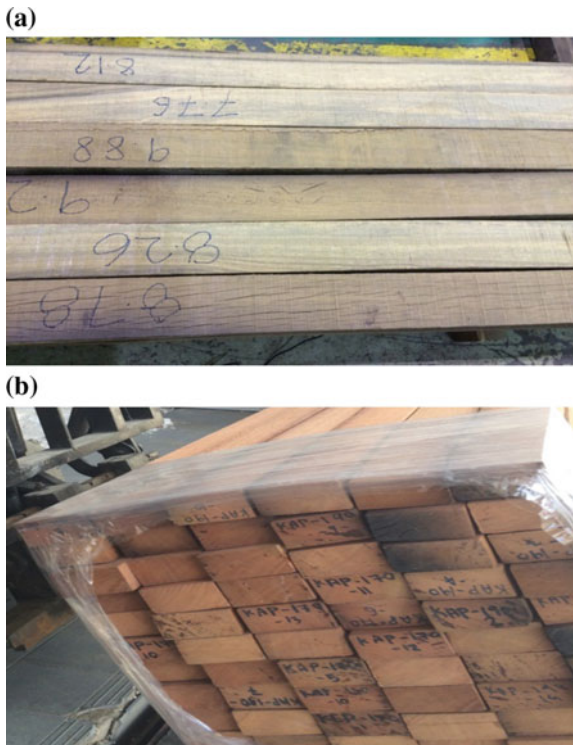
Table 1 Density value before and after heat treatment for hardwood timber *kapur*

Temperature of heat treatment (°C)	Average density (kg/m^3)		Percentage of reduction (%)
	Before heat treatment	After heat treatment	
150	798.189	768.395	3.73
170	806.831	776.132	3.81
190	791.28	752.92	4.85
210	811.03	767.74	5.34

Table 2 t-test analysis of difference in density before and after heat treatment for *kapur*

	Before heat treatment	After heat treatment
Mean	801.8313	766.2963
Variance	78.09277	94.03038
Observations	4	4
Hypothesized mean difference	0	–
df	6	–
tStat	5.417095	–
$P(T \leq t)$ one-tail	0.000819	–
tCritical one-tail	1.94318	–
$P(T \leq t)$ two-tail	0.001637	–
tCritical two-tail	2.446912	–

The density seems to reduce once treated by heat, and the percentage of reduction does increase with the increase of temperature. The t-test analysis by Excel in Table 2 shows that the tStat = 5.417 > tCritical two-tail = 2.447 which is can be said that the density before and after heat treatment differ significantly.

The same condition goes to hardwood *pauh kijang* which has reduction of density after heat treatment as shown in Table 3. Reduction in density indicates reduction in weight which might not be a positive indication. However the difference of density before and after heat treatment is not merely significant, as shown by the t-test analysis of Excel in Table 4 as the tStat = 2.067 is larger than tCritical two-tail = 2.570 which can be conclude that null hypothesis is accepted.

The t-test had shown that there is significance different of density value for heat treated *kapur* but there is no significance different for *pauh kijang*. Even though

Table 3 Density value before and after heat treatment for hardwood timber *pauh kijang*

Temperature of heat treatment (°C)	Average density (kg/m^3)		Percentage of reduction (%)
	Before heat treatment	After heat treatment	
150	1132.675	1093.004	3.5
170	1094.486	1054.815	3.63
190	1115.885	1067.325	4.35
210	1069.959	998.848	6.65

Table 4 t-test analysis of difference in density before and after heat treatment for *pauh kijang*

	Before heat treatment	After heat treatment
Mean	1103.251	1053.497942
Variance	736.8592	1580.102401
Observations	4	4
Hypothesized mean difference	0	–
df	5	–
tStat	2.067239	–
$P(T \leq t)$ one-tail	0.046784	–
tCritical one-tail	2.015048	–
$P(T \leq t)$ two-tail	0.093568	–
tCritical two-tail	2.570582	–

both of the density value of *kapur* and *pauh kijang* were decreased after been treated by heat, but it is not significantly affected the density properties of *pauh kijang* compared to *kapur*. This might be due to the different strength group of these two species of timber samples where pauh kijang is located in high strength group SG3 compared to kapur SG4.

Reduction in density indicates the reduction of the weight. However, theoretically, weight loss of hardwood is caused by the loss of moisture content which might lead to the increment of the movement stability. Based on [16], most of earlier experiments showed that heat treatment reduces the equilibrium moisture content (EMC), and thickness swelling and slow down water absorption (WA) and wet ability of wood. However, heat treatment actually increased the WA of pine sapwood heat treated at 170, 190, 210 °C.

Treatment on Malaysian hardwood timber is vital and heat treatment is another alternative way. Density of Malaysian hardwood timber seems to decrease caused by heat treatment but the difference of before and after heat treatment is not that significant. Reduction in density indicates the weight loss. However, theoretically, weight loss of hardwood is caused by the loss of moisture content which might lead to the increment of the movement stability. Increment in movement stability will give better result for hardwood in term of shrinkage and dwelling. Furthermore, it still cannot be concluded either heat treatment will give negative or positive affect to *kapur* and *pauh kijang* through density value only, there are another properties need to be study if they are affected or not to the high temperature level of heat treatment.

5   Conclusion

Heating of Malaysian Hardwood Timber significantly reduced its density. Both density of *kapur* and *pauh kijang* were affected by the different level of heating temperature after been treated. The percentages of reduction for these two species density were increasing with the increment of the temperature level. As *pauh kijang*

is in higher strength group of timber compared to *kapur*, there is no significance different of density value reduction for *pauh kijang* after been treated by heat while there is significance different for *kapur* density reduction value. Lower density might lead to lower moisture content which can help to improve the timber movement stability which is good for construction industry materials. Heat treatment research is important for the purpose of finding a smarter and better alternative to treat material for construction works. The heat treatment might give an acceptable effect on the physical properties. This will allow timbers in the future to be treated without using chemicals and become materially more appropriate in many applications especially in construction and structural use.

References

 1. Al-nagadi, E. M., Saudi Arabia – Concrete Construction Industry – Cement Based Materials And Civil Infrastructure (CBM & CI), 2012.
 2. Patel, K. V., Construction Materials Management On Project Sites. In *National Conference on Recent Trends in Engineering & Technology*, 2011.
 3. Hall, N. L., & Beder, S., Treated Timber , Ticking Time bomb, (February), 2005.
 4. Tong, H. L., Treatment Of Timber For Trusses. *Malaysian Wood Preserving Association (MWPA)*, 2005.
 5. Hardin, R. A., & Beckermann, C.,. Simulation of Heat Treatment Distortion, (3), 2005.
 6. Hedley, M. D., An assessment of risks associated with use of CCA-treated timber in sensitive environments and options for its substitution with alternative timber materials. 1997.
 7. Barrie, D. E., Copper Chromium Arsenate (CCA) In The Environment, 2000.
 8. Read, D.,. *Report on Copper , Chromium and Arsenic (CCA) Treated Timber*, 2003.
 9. Arsenic Timber Treatments (CCA And Arsenic Trioxide), *Authority, Australian Pesticides and Veterinary Medicines*, 2003.
10. Korkut, S., Alma, M. H., & Elyildirim, Y. K., The effects of heat treatment on physical and technological properties and surface roughness of European Hophornbeam (Ostrya carpinifolia Scop .) wood, *8*(20), 5316–5327, 2009.
11. Sundqvist, B., Colour Changes and Acid Formation, 1402–1544, 2004.
12. Heat Treatment of Timber, *Calu Technical Notes*, (July), 2005.
13. Militz, "Thermal treatment of wood: European processes and their background.", Cardiff-Wales: IRG/WP 02-40241 33rd Annual Meeting, 2002.
14. Syrjänen, T., & Oy, K., *Production And Classification Of Heat Treated Wood In Finland*, 2000.
15. Yildiz, "Physical, mechanical, technological and chemical properties of beech and spruce wood treated by heating." *Ph*.D. dissertation, Karadeniz Technical University, 2002.
16. Petrissans, "Wettability of heat treated wood", Holzforchung, 301–307, 2003.
17. Rousset et al., "Modification of mass transfer properties in polar wood (P. robusta) by a heat treatment at high temperature", Holz als Roh-und Werkstoff, 377–386, (2004).
18. Timber Structures Design 8.1., *DelDOT*, (April), 1–30, 2008.
19. Azlan, H. M., *Bending Behavior of Timber Beams Strengthened Using Bonded In Plates*, 2013.
20. MS 1787: PART 5., *Wood Based Panel- Part 5: Determination of Density*, 2004.

Effect of Different Diameter of Glulam Dowel-Bearing Strength Made of Mengkulang Species

Amirah Ali Chew, Nurul Fatin Alia Puasa and Rohana Hassan

Abstract Timber is one of the construction materials to construct sustainable construction. Mengkulang species are one of the timber that widely used nowadays. It is suitable for flooring, interior finishing, furniture and paneling. In order to improve the ability of timber as structural components, its value is added through innovation in timber engineering such as glulam. Dowel-bearing strength is the maximum load capacity that the specimen or structural component can cater. In this study, the load bearing test was conducted using universal testing machine (UTM). The physical properties such as moisture content, density and specific gravity also had been determined. The dowel-bearing strength of 16 mm bolt diameter for $Fe_{5\%}$ and $Fe_{\max}$ is 0.018 and 0.02 kN/mm^2, respectively. For 20 mm bolt diameter, average value of $Fe_{5\%}$ and $Fe_{\max}$ are 0.015 and 0.018 kN/mm^2, respectively. From the result, it can be concluded that the smaller the bolt diameter, the higher the dowel-bearing strength. The record of bearing strength for Mengkulang species is not yet available. Therefore, this study can help in order to enhance the understanding of load bearing strength of this species.

Keywords Dowel bearing strength · Different diameter of bolt · Glulam · Mengkulang species · Physical properties of timber

1 Introduction

In Malaysia, the use of timber in building construction has started long time ago. Most of the Malaysian houses were built using timber and still standing until now. Malaysian timbers are classified as tropical timber and are divided into seven

A.A. Chew (✉) · N.F.A. Puasa · R. Hassan
Faculty of Civil Engineering, Universiti Teknologi Mara, UiTM,
Shah Alam, Selangor, Malaysia
e-mail: meyna.1623@gmail.com

R. Hassan
e-mail: rohan742@salam.uitm.edu.my

769

(7) strength of groups which are S.G.1 to S.G.7 as classified in MS 544: Part 2: 2001. Mengkulang species is a medium hardwood and the density range from 625–895 kg/m^3 air dry [1].

Nowadays, timber industry in many countries introduced new timber innovation, the glued-laminated timber namely 'glulam'. Glulam structural timber product is produced by gluing as one piece of dimensioned and strength graded timber under strict and hard producing condition [2]. 'Galeri Glulam' is the first completed glulam building from various type of strong timber species which the wood usage exceed 80 % of bearing load structure to set off design concept of the glulam representative building.

Bearing strength is one of the properties that is used to determine the load carrying capacity of connection. Besides that, dowel-bearing strength (Fe) of glulam for tropical timber has not yet been published especially for Heritiera Borneensis (Merr.) Kosterm, (Mengkulang) species. The information about effect of different diameter of glulam dowel-bearing strength made of Mengkulang species is limited. There is no data on the dowel-bearing strength of Malaysian glulam timber available as there are no study been conducted locally which emphasize in this area. Hence, this study is to determine the effect of different diameter of glulam dowel-bearing strength made of Mengkulang species. In this research, the dowel-bearing strength for the specimen with parallel to grain direction.

1.1 Glued-Laminated Timber (Glulam)

Glulam is specifically designed as an engineered laminated structural element [2]. The timber laminations range from 19 to 50 mm. There are two forms of glulam lamination which are horizontal and vertical lamination lay-up. The lamination for horizontal glulam is glued perpendicular to the length of cross section while the laminations are glued perpendicular to the short length of cross section for the vertically laminated glulam [2]. Figure 1 shows the orientation of horizontal and vertical laminated beam.

Fig. 1 Horizontal and vertical laminated beam timber [2]
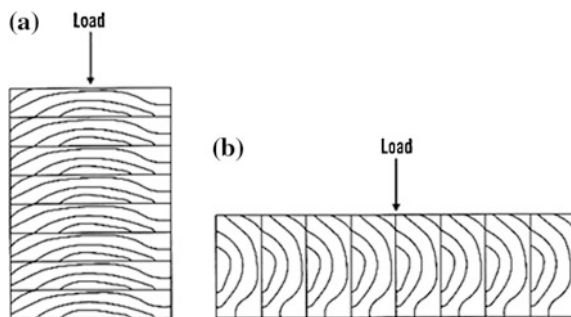
1.2 Mengkulang Species

Mengkulang species or known as *Heritiera* spp. (light species) is the type of tropical timber that is used in this research. There are two types of timber texture explained in [1] which are slightly to moderate coarse and straight to shallowly interlocked grain. Mengkulang is listed in group B wood strength and have a good nailing property. Reference [1] also stated that the color of sapwood was lighter and not clearly defined like reddish brown of heartwood color. However, the timber is susceptible to lyctus and beetle attacks. They are not durable in exposed condition but can be easily treated with preservatives [1]. According to Malaysian standard, MS 544: Part 2: 2001, Mengkulang has been categorized in strength group of five.

1.3 Dowel-Bearing Strength

Dowel-bearing strength is the maximum load capacity that the specimen or structural component can cater [3]. Reference [4] defined the property of wood that influence nominal design value, Z of a nail, bolt or lag bolt known as embedded strength with the notation of F_e. It is correlated to the crushing strength of the timber member under loading from a dowel subjected to a shear load. The load deformation performance of wood or wood base products is dowel-bearing behavior where the fastener will not bend during loading while the dowel bearing strength is the yield load from the load deformation curve divided with dowel diameter and specimen thickness [5].

Additionally, by proper fitting of a straight line to the initial linear proportion of the load deformation curve, the dowel-bearing yield load or relative limit load can be obtained. Then, it is balance by a deformation equal to 5 % of the fastener diameter [6]. Reference [6] reported that Wilkinson defined the 5 % offset stress as strength.

Reference [7] published a research on the Shorea obtuse bearing properties, one of the ASEAN famous tropical timber under a laterally loaded bolt and the rate of compression used in this researched was 1.2 mm/min. Five different angle of grain loading was used to carried out the full configuration. Result obtained showed that the average value of dowel-bearing strength parallel to grain was 7.25 % lower than prediction of Eurocode 5 while dowel-bearing strength perpendicular to grain was different from the early prediction by the standards or previous studies because there is no definite maximum load was determined within its range [7].

Reference [8] published a research focuses on determining the relationship of dowel-bearing strength to different dowel material using parallel and perpendicular grain loading for Kempas species. The tests were conducted on solid timber. The percentage difference of dowel-embedment strength compressed by the wood dowel is lower than GFRP dowel. However, the dowel-bearing strength compressed by the steel dowel is higher compared to both wood and GFRP dowel.

1.4   Dowel Type Fasteners

There are many different types of joint and variety type of fastener that can be used in timber connections. According to Porteous and Kermani [3], the critical design of the structure in timber engineering is the design of joint because the connection strength is established from the structure strength. Mechanical connections are when structural members are joined with fasteners or some other type of hardware [4]. Dowel such as screws, nails, bolts, and others transfer load applied to the whole block is called metal dowel type fastener to fasten members in timber frame construction is nailing.

Nails are available in an assortment of lengths, straight slender fasteners, cross-sectional shapes and areas and usually pointed and headed. Nailed connections are simple to form from relatively thin members and suitable for simple structures. It is used in almost simple light loads and easy elements in construction such as wall, decks, floors and others.

Wood screws are used in the applications that required higher capacities and greater withdrawal capacity. There are three methods that are suitable for joints to use screw connection, which are timber-to-timber, steel-to-timber and panel-to-timber joints [3]. Wood screws that are most commonly used which are countersunk head, round head, and coach screw. Screws must should not hammered into its position but be fixed by being threaded into the timber [3].

Dowel is a cylindrical shape of rods and made up of steel. The surface of dowels is smooth and striated and available from 6 to 30 mm of diameter size. Bolts have a range size of 6–30 mm in diameter and threaded dowels with hexagonal nuts and hexagonal or semi-spherical heads. Both dowels and bolts are usually used for high load carrying capacity in connections. In axially loaded tension connections, dowels cannot be used while bolts can be used [9]. The most familiar type of connection is two, three or more members in a multiple shear arrangement [3].

1.5   Effect on Dowel Diameter

The dowel-bearing strength differs with the specific gravity of the timber and the size of the dowel diameter. For example, the angle of load influences the dowel-bearing strength for large diameter fasteners [4]. Reference [10] used 'Spring Theory' in the evaluation of dowel-bearing strength for wood dowel using Kempas species instead of European wood. 'Spring Theory' is the combination result of steel block compressed with wood dowel and steel dowel compressed the wood block. The results of the research were to prove the capability of the 'Spring Theory' in predicting the dowel-bearing strength of Kempas. The combination results of both shows that the 'Spring Theory' is valid to obtain the dowel-bearing strength of Kempas compressed with 12.7 mm wood dowel [11]. Reference [12] did a study on Kempas, Mengkulang and Pulai species bearing strength which

comes from different strength group and densities. Each species represent heavy, medium and light hardwood. He found that the bearing strength decreased when diameter of dowel increased.

1.6 European Yield Model

European Yield Model (EYM) which was proposed by Johanson [13] is broadly used in estimation of the yield strength of joints. The dowel-bearing strength of timber and yield moment of the dowel affect the properties for validate the strength of the joints [13]. In order to determine the yield point on load-displacement graph, the 5 % offset method is used. The 5 % offset value obtained by draw a line parallel to the initial elastic region on load-displacement plot. The yield point is between these two lines. The correlation between EYM and 5 % offset value comes for the dowel-bearing strength and bolt bending yield test [14].

Other than that, the maximum load that the specimen can cater is determined from the graph of load displacement where the highest load before the specimen becomes crack or brittle. There are two method of testing based on ASTM which is full-hole or half-hole test. For half-hole test, bolt is uniformly loaded along its length and uniform stress distribution throughout the projected bearing area is produced [7]. The dowel-bearing strength in this research is a test according to ASTM D5764-9a by using the half-hole method. The details inspection on the specimen throughout the test such as cracks or any failure pattern is observed.

1.7 Moisture Content, Specific Gravity, and Density

The solid part of wood is made of a complex cellulose-lignin compound which contains the framework of the cell walls and the lignin cements and binds the cells together. Wood contains moisture and it is held within wood in two ways. The water enclosed in the cell cavity is called as free water while water enclosed within cell walls is known as bound water [4]. It is important that all glulam members take into account the expected moisture content during service and their connection with other elements in the completed structure [15]. Moisture content is an important property of wood as it affects the strength of wood. The ratio of the density of wood to the density of water of 1000 kg/m^3 at a specific temperature known as specific gravity. Specific gravity or relative density is an evaluation of timber's solid material and commonly conveyed as the ratio of the dry weight to the weight of an equal volume of water [16]. Density is a major factor in determining the strength of timber. Density of timber is the mass per unit volume. It is one of the important properties of timber and calculated with oven-dry weight condition of timber.

2 Materials and Research Method

2.1 Sample Preparation

The specimens are prepared based on the ASTM 5764-97a standard based on half-hole testing setup. The wood that has been selected in this experiment is Mengkulang species and the bolts are a steel material. The specimen is tested based on parallel loading grain and satisfy the specific dimension. The dimension of the specimen is 64 mm × 64 mm × 38 mm for 16 mm bolt diameter while for 20 mm bolt diameter specimen dimension is 80 mm × 80 mm × 40 mm. Each bolt diameter has thirty (30) specimen that make a total of sixty (60) specimens. Bolt that been used to determine the maximum load as in Fig. 2.

Drilling of specimen is done after the specimen cut to dimension required. Two specimens are clamped together and the lead hole then drilled in between the two pieces with hole larger than the dowel diameter (Fig. 3).

2.2 Testing Process

The testing was conducted by placing the rectangular glulam wooden block with half hole on the UTM machine. A steel load was placed in the half hole to press the dowel into specimen. The test used the load rate of 1 mm/min within one (1) to ten (10) minutes of time according to ASTM 5764-97a. The reading deformation is measured at the start of load application and the reading was taken at satisfactorily frequent load intervals to permit establishment of an adequate load deformation curve (ASTM D5764-9a, 2007). Figure 4 shows the arrangement of the test setup.

The general behavior of the specimen, mode of failure, maximum load, and other significant details were recorded and observed. The dowel-bearing strength capacities are determined from 5 % offset load or from the maximum load obtained from the experiment. In this research, both method were used and compared. When the load head had a contact with the block specimens or the load of each

Fig. 2 Steel bolt with different diameter
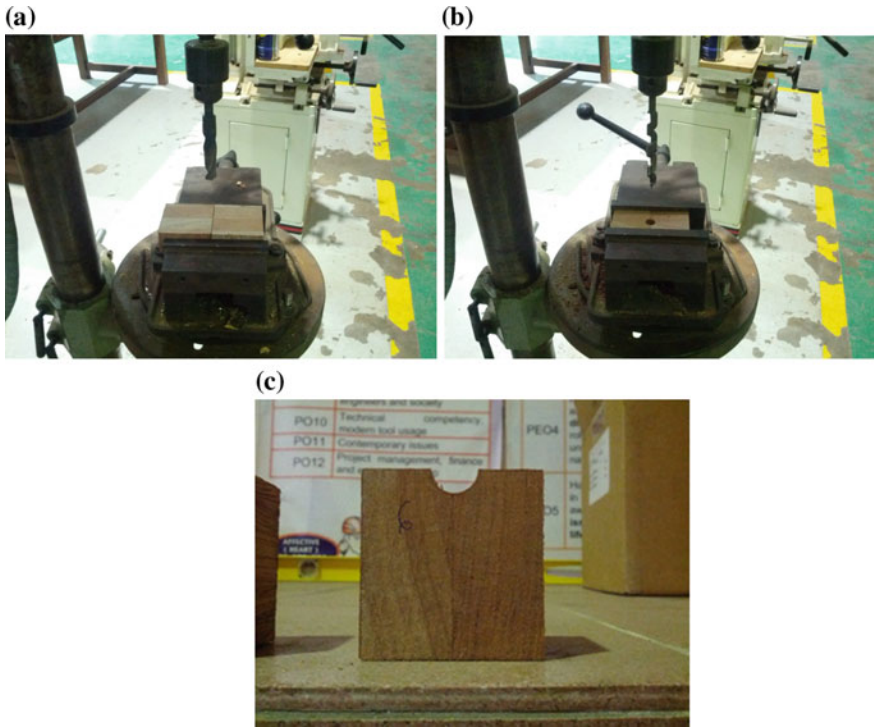
Fig. 3 The step of drilling the specimen where **a** the specimen are clamped together, **b** the specimen is drilled at the center by avoiding the glue lines using radial drilling machine and **c** the specimen is cut into two using radial arm saw

Fig. 4 The arrangement for dowel-bearing test procedure using UTM machine

Fig. 5 The specimens were left in the oven for 24 h

dowel-bearing stress before the block split or cracks is known as ultimate load. At this point the dowel material is considered as full bearing.

Other than that, oven-dry specific gravity and moisture content test of the specimen also been tested. The specimen then heated in the oven of 100 °C for 24 h and takes the final reading. Figure 5 shows the specimens were left in the oven.

3   Result and Discussion

3.1   Moisture Content

The moisture content obtained is 11.21 for 16 mm diameter of bolt and 11.51 for 20 mm bolt diameter. Both values are almost the same and the difference of moisture content in term of percentage is 0.30 %. The moisture content for glulam timber with 20 mm bolt diameter is higher and it shows that the bigger the size of sample, the higher the percentage of moisture content of the glulam timber.

3.2   Density

Mengkulang is a medium hardwood and have a density range of 625–895 kg/m^3 air dry [17]. From the result, the range of density for glulam timber made of Mengkulang species is between 630.3 to 704.7 kg/m^3.

3.3   Specific Gravity

The mean value of specific gravity is 0.68 and the value acquired from the test is 0.652 and 0.688 for 16 and 20 mm bolt diameter, respectively. Therefore, the specific gravity of the glulam timber made of Mengkulang species is in range.

Fig. 6 Typical graphs of load versus deformation of a 16 mm bolt diameter
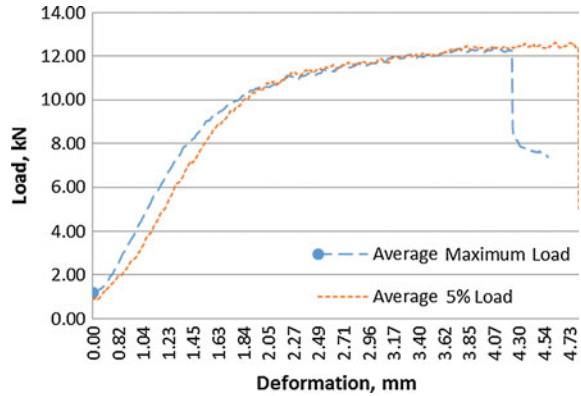
3.4 Dowel-Bearing Strength

3.4.1 16 mm Bolt Diameter

The yield stress of 16 mm bolt diameter and 20 mm bolt diameter were obtained from bearing tests using universal test machine (UTM). It is calculated based on BS 383: 1993 standard and by using the 5 % offset load from the graph.

The average value for 16 mm dowel-bearing strength of 5 % offset is 0.018 kN/mm^2 while the average dowel-bearing strength from maximum load is 0.020 kN/mm^2. The average dowel-bearing strength of both values does not have much different. The typical graphs established from the tests are represented by the load versus deformation graph. The typical graph for 16 mm bolt diameter is in Fig. 6 that show the average maximum load and average 5 % offset load. Figure 7 shows on how the 5 % offset load were determined and the sample failure is shown. The differences in percentage for the $Fe_{5\%}$ in this study with the dowel-bearing strength by Jumaat et al. [12] is 67 %. The percentage different is higher regardless the dowel diameter.
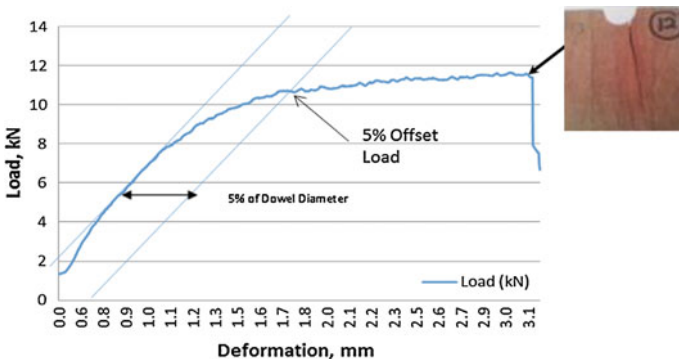
Fig. 7 Five percent (5 %) offset load and the sample failure pattern

Fig. 8 Typical graphs of load
versus deformation of a
20 mm bolt diameter
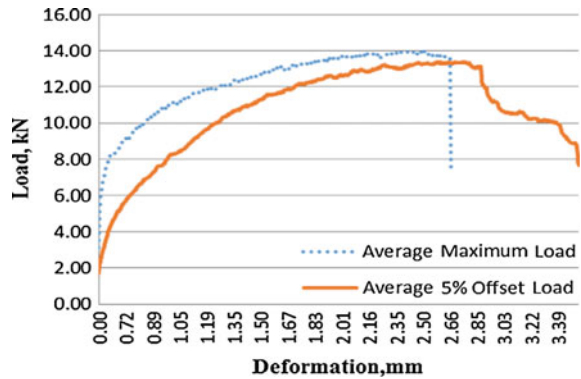
3.4.2 20 mm Bolt Diameter

The average value of Fe_{max} for 20 mm diameter of bolt is 0.018 kN/mm^2 while the
average value of $Fe_{5\%}$ is 0.015 kN/mm^2. From previous study by Hassan et al. [11],
for parallel to grain loading, the dowel-bearing strength decreased slightly as the
dowel diameter increased. The grain loading used in this study is parallel to grain as
stated earlier. Figure 8 shows typical graphs that represent the 20 mm diameter of
bolt for average maximum load and average 5 % offset load. Difference in per-
centage of both $Fe_{5\%}$ and Fe_{max} for 20 mm bolt diameter is twenty percent (20 %).

Therefore, the average dowel-bearing strength for 5 % offset and average
dowel-bearing strength of maximum load is 0.015 and 0.018 kN/mm^2, respectively.
Reference [18] found that the effect of diameter on dowel-bearing strength is
apparently minimal. However, Ref. [8] found that with dowel diameter of 19.1 mm,
the dowel-bearing strength is 28.69 kN/mm^2 for Kempas species. The
dowel-bearing strength obtained by Hassan et al. [8] is higher compared with this
study which is 0.015 kN/mm^2. The reason of the high difference is Kempas is in
strength grade 2 (SG2) while Mengkulang species is strength grade 5 (SG5) as in
MS544: Part 2:2001. Therefore, Kempas is much more stronger when compared to
Mengkulang.

3.5 Comparison of Dowel-Bearing Strength for 16 and 20 mm Bolt Diameter

Figure 9 shows the relationship between dowel-bearing strength and bolt diameter for
16 and 20 mm bolt diameter. It is obvious that all average values decreased as the bolt
diameter increased. Therefore, this study has supported the finding made by Hassan
et al. [8]. They stated that the higher the bolt diameter, the lower the dowel-bearing
strength. Other than that, the bearing strength of timber parallel to grain decreased
somewhat as the bolt diameter increased without considering any species [8].

Fig. 9 Relationship between dowel-bearing strength and bolt diameter for 16 and 20 mm bolt diameter
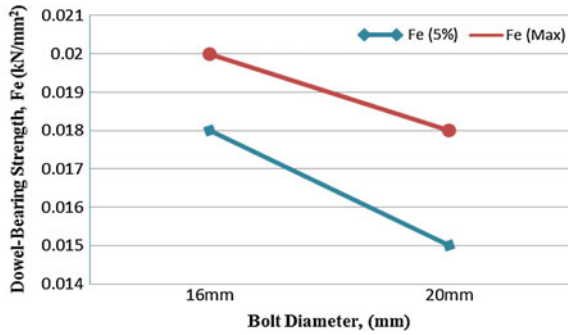
Fig. 10 Bar chart of average dowel-bearing strength for 16 and 20 mm bolt diameter
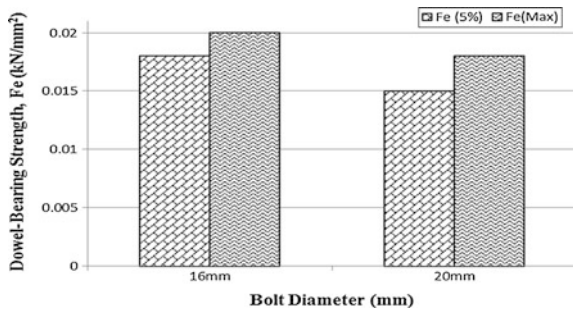
This finding is also similar to the [12] which the bearing strength decreased while the dowel diameter increased. However, the dowel-bearing strength for five percent (5 %) offset load is decreased slightly as the dowel diameter increased compared to the dowel-bearing strength of maximum load. The relations between both dowel-bearing strength and bolt diameter also can be seen from bar chart on Fig. 10.

In addition, Ref. [19] also found that the 5 % offset bearing strength and dowel diameter affiliation shows that the data of bearing strength is decreasing with increasing of dowel diameter. The differences can be seen in the Fig. 9 where the dowel-bearing strength influenced by the size of bolt diameter. Therefore, it can be concluded that dowel-bearing strength is affected by the different dowel diameter. The dowel-bearing strength value obtained in this study is a slightly lower compared to the code evaluation report of dowel-bearing strength with a value of 0.053 kN/mm^2 from the national design specification (NDS).

3.6 Failure Modes

The most mutual causes of failure in the timber structural systems are insufficiency of formation in relation to the actions, both static and dynamic loading; besides slenderness, instability, defects of the wood laid in place, simple biotic damages,

Fig. 11 Split failure mode

Fig. 12 Crack failure mode

and accidental factors [20]. Failure mode is the failure pattern that been observed after the test or to be precise when the load reaching its maximum and the changes that happened to the samples. There are two (2) modes of failure which are crack and split. Figures 11 and 12 show the two examples of failure modes, which are crack and split failure modes.

Since the specimens are made of glulam timber, therefore the failure mode is also observed on the glue lines failure. In this study, it is found that there is no effects of bearing shape on the glue lines since no failure were found falls on the glue lines itself.

4   Conclusion

The physical properties namely, moisture content, density and specific gravity are; 11.21 %, 651.68 kg/m^3 and 0.652, respectively for 16 mm bolt diameter. On the other hand, a 20 mm diameter of bolt attained 11.51 %, 687.67 kg/m^3, and 0.688 for moisture content, density and specific gravity, respectively. The dowel-bearing strength of 16 mm bolt diameter for $Fe_{5\%}$ and Fe_{max} is 0.018 and 0.02 kN/mm^2, respectively. For 20 mm bolt diameter, average value of $Fe_{5\%}$ and Fe_{max} are 0.015 and

0.018 kN/mm^2, respectively. The dowel-bearing strength significantly influenced by the dowel diameter although the comparison of 16 and 20 mm bolt diameter is slightly small. The percentage differences for 16 and 20 mm bolt diameter for $Fe_{5\%}$ is 11 % while the percentage difference for 16 and 20 mm bolt of Fe_{max} is 20 %. From the result, it can be concluded that the smaller the bolt diameter, the higher the dowel-bearing strength. The failure modes of the samples are various and it is also noticed that no failure falls on the glue lines.

References

1. T. M. Wong, "A Dictionary of Malaysian Timber," Kuala Lumpur: The Forest Department, 1982.
2. S. Rajan, Y. E. Tan, Z. Ahmad, H. Abdullah, and R. Idris, "GLULAM: Freedom of Shape and Design," Kuala Lumpur: Malaysian Timber Industry Board, 2010.
3. J. Porteous, and A. Kermani, "Structural Timber Design to Eurocode 5," United Kingdom: Blackwell Publishing, 2007.
4. D. E. Breyer, K. J. Fridley, D. G. Pollock, and K. E. Cobeen, "Design of Wood Structures – ASD," United States of America: McGraw Hill, 2003.
5. *ASTM International*. (2007, July 1). Retrieved March 12, 2014, from Standard Test Method for Evaluating Dowel-Bearing Strength of Wood and Wood-Based Products: www.astm.org.
6. J. R. Church, and B. W. Tew, "Characterization of Bearing Strength Factor in Pegged Timber Connections," Journal of Structural Engineering, 326–332, 1997.
7. A. Awaludin, W. Smittakorn, T. Hirai, and T. Hayashikawa, "Bearing Properties of Shorea obtusa Beneath a Laterally Bolt," Wood Science, 204–210, 2006.
8. R. Hassan, A. Ibrahim, and Z. Ahmad, "Effects of Different Dowel Material on Kompassia Malaccensis Bearing Strength," Forest Research Institute Malaysia (FRIM), p. 114–125, 2009.
9. V. S. Perry, "Single Shear Strength of Kempas in Influence of Dowel Diameter," Shah Alam, Selangor: Universiti Teknologi Mara, 2012.
10. R. Hassan, A. Ibrahim, Z. Ahmad, and M. Yusoff, "Dowel Bearing Strength Properties of Two Tropical Hardwoods," Proceedings of the International Civil and Infrastructure Engineering Conference 2013, pp. 27–36, Singapore: Springer Science, 2014.
11. R. Hassan, S. Hamid, N. A. Mohammad Amini, and T. A. Raja Hussin, "Evaluation of Dowel Bearing Strength for Wood Dowel Using 'Spring Theory'," 2013.
12. M. Z. Jumaat, A. Abu Bakar, F. Mohamad Razali, A. H. Abdul Rahim, and J. Othman, "The Determination of the Embedded Strength of Malaysian Hardwood," Proceedings of the 9th World Conference of Timber Engineering, WCTE, 126, 2006.
13. K. W. Johanson, "Theory of timber Connections," International Association for Bridge and Structural Engineering, 249–262, 1949.
14. R. D. Theilen, D. A. Bender, D. G. Pollock, and S. G. Winistorfer, "Lateral Resistance of Ring-shank Nail Connections in Southern Pine Lumber," Transaction of the ASAE, 41 (2):465–472, 1998.
15. Anonymous, "*Glulam*," Retrieved from Manufacturing Process: http://www.glulam.co.uk/specGuide_brochure/specGuide04.htm, 2006.
16. D. Kamaruzaman, "The Behavior of Glulam Beam Strengthened using Fibre Reinforced Polymer," Universiti Teknologi Malaysia, 127, 1983.

17. M. T. Council, "*Mengkulang*," Retrieved from Wood Wizard: http://woodwizard.my/report. asp?AttrID=8&ItemID=71, n.d.
18. T. L. Wilkinson, "Dowel Bearing Strength," Research Paper, 1–9, 1991.
19. K. Hwang, and K. Komatsu, "Bearing Properties Of Engineered Wood Products I: Effects Of Dowel Diameter And Loading Direction," The Japan Wood Research Society, 48:295–301, 2002.
20. G. Tampone, "Mechanical Failures of The Timber Structural Systems," ICOMOS IWC – XVI, International Symposium, 21, 2007.

A Conceptual Review of Structural Performance of Mengkulang Laminated Veneer Lumber (LVL) Roof Trusses

N.A. Muhammad, A. Ibrahim and Z. Ahmad

Abstract In Malaysia, the development of engineered timber product (ETP) such as laminated veneer lumber (LVL) and glued laminated timber (glulam) in manufacturing and construction has not been encouraged, due to limited data either on the data for engineering properties or data on the structural behaviour. This paper presents the overview of earlier research done about roof trusses behaviour, forming the basis of the conceptual framework of the proposed research, namely the structural performance of roof trusses constructed using Mengkulang LVL. Mengkulang (*Heritiera* spp.) in strength grouping 5 (SG5) according to Malaysian strength grading groupings that are commonly and suitably used for nonstructural applications. By converting lower grade timber into LVL, it has been shown that the strength improves into two grades higher. This paper reviewed the literature from previous research in investigating the behaviour of roof truss structure in terms of its load-carrying capacity and the stiffness of the joints. Also, the requirement of mechanical properties of timber data by performing series of tests namely bending, bending shear, tension and compression were discussed. A literature review was also made to identify the method of numerical analysis using finite element and experimental. As a conclusion, it is expected that LVL from tropical hardwood timber can safely be used as roof truss system.

Keywords Laminated veneer lumber · Roof trusses · Tropical timber · Finite element · Mechanical properties · Timber joint

N.A. Muhammad (✉) · A. Ibrahim
Faculty of Civil Engineering, Universiti Teknologi Mara (UiTM),
Selangor, Malaysia
e-mail: norazizah@jkr.gov.my

A. Ibrahim
e-mail: azmi716@gmail.com

Z. Ahmad
Institute for Infrastructure Engineering and Sustainable Management (IIESM),
Universiti Teknologi Mara (UiTM), Selangor, Malaysia
e-mail: zakiah@salam.uitm.edu.my

1 Introduction

Prefabricated timber and steel cold formed roof trusses are two types of structural systems typically used in Malaysian construction industry at present. The demand for the timber truss construction industry is relatively low particularly in the government projects due to factors such as the quality of timber and in some cases of timber roof truss failures had happened before. Nevertheless, a couple of incidents involving the collapse of prefabricated steel cold formed roof structure happened in Terengganu in 2013, had drawn some attention to the government to look into a good building practice which includes standard of procedures, human capital, alternative materials and enforcement as well.

To gain confidence in the usage of timber as structural components or roof trusses, the timber industry has to look into more reliable timber products. As the world is making an initiative towards green construction, sustainable or "green building", there is a need for Malaysian construction industry to use timber as green materials more efficiently. The application of engineered timber products (ETP) such as glued laminated timber (glulam) and laminated veneer lumber (LVL) as roof trusses in Malaysia's construction industry is a possible choice as these products are available in Malaysia. In other countries such as Australia, North America and New Zealand, LVL is used extensively as a roof truss structure. Unlike solid timber, LVL roof truss can be designed for the larger span. However, the application of LVL as structural members in Malaysia trusses is not yet materialized due to lack of transfer technologies, established engineering data and competition with other materials such as concrete and steel in construction industry.

Based on some research into tropical timber conducted previously, the strength of the ETP timber can achieve higher strength grade than the grade of its parent timber. H'ng [1] investigated the mechanical properties of LVL made from few tropical hardwood species, namely yellow meranti (*Shorea* spp.), kedondong (*Canarium* spp.), Bintangor (*Calophyllum* spp.), white meranti (*Shorea* spp.) and Keruing (*Dipterocarpus* spp.) and found that the grade stresses of LVLs from those species are at least one grade higher than the same species of solid timber as published in MS 544. Whereas, Wahab [2] also reported that by converting solid Rubberwood into LVL has improved the strength significantly. LVL is also more dimensionally stable.

To promote the usage of LVL roof trusses, more research needs to be conducted to identify suitable species for LVL manufacturing, its mechanical properties and structural performance. This research is proposed to investigate the potential of medium hardwood tropical timber, such as Mengkulang (*Heritera* spp.) to be used as LVL for roof trusses in terms of its mechanical properties, behaviour of the truss structure and stiffness of the connections, by performing numerical analysis and experimental validation. Therefore, the purpose of this paper is to attain the conceptual review of previous research done by others that associated with the proposed research.

2 Literature Review

2.1 Introduction

Timber had been traditionally used as building material and is remarkable for many reasons: its beauty, versatility, strength, durability, workability and flexibility. Besides, it also possesses strength-to-weight ratio, can withstand a short period of overloading, having lower electrical and thermal conductance and performs well at low temperature. Timber roof truss system is one of the important parts of a building structure that need to be properly design and constructed by taking into account the quality and safety. Nowadays, the use of ETP as frame structures and trusses is developing due to its advantages such as selection of sizes and dimensions, shapes and span that are better than solid timber. The engineered timber structures were also proved to perform well both in life safety, and serviceability during the Canterbury earthquakes happened in September 2010 and February 2011 [3].

2.2 Laminated Veneer Lumber (LVL)

Basically, laminated veneer lumber or LVL, is part of the structural composite lumber (SCL), which looks similar to plywood and is made from thin veneers that are glued together using exterior structural adhesives to form structural-size members [4]. These engineered products have many advantages when compared with sawn timber and also have been improved by manufacturing and adhesive technologies [5]. Some of the advantages include various usages for structural and nonstructural applications; higher strength properties than its parent species; good performance in adverse condition and suitability for large structural members [1]. While Table 1 shows a typical advantage of using ETP in term of labour efficiencies [5].

There was also a local research being conducted which proved these engineered products, made from tropical timber hardwoods had better performance and strength

Table 1 Labor efficiencies when using engineered timber (wood) product [5]

Application	Conventional solution	Engineered wood product solution
Headers (i.e., for garage doors)	Two 2′ × 10′ timber nailed together	One LVL beam
Floor system	Conventional floor with 133 pieces	LVL I-system with 80 pieces (40 %) less
Main beams	Three or four 2′ × 12′ timber nailed together	One LVL beam (89 mm)
Roof truss	Roof truss with metal plates and conventional timber members with high grades	Roof truss with metal plates and LVL manufactured using lower grade timber

than solid timber. Chee [6] investigated the properties of Rubberwood LVL and initiated that the strength of Rubberwood LVL increased to higher grade (from SG5 to SG4) and compatible to Resak and Kapur. Moreover, its bending strength properties were found to be higher than LVL made from Radiata Pine. Apparently, Chee also concluded that Rubberwood LVL could be an alternative material for prefabricated roof truss.

Whereas, Wahab [2] also proved from her research that the compressive strength of Rubberwood LVL was higher than its parent material. Some studies also were carried out to evaluate the mechanical properties of LVL made from tropical hardwood species as well. It was verified LVL manufactured with mixed species from low and high density gave better performance than the LVL manufactured with single species [5]. H'ng et al. [5] also reported that research by others on tropical hardwoods (*Dipterocarpus* spp. and *Havea bransiliensis*), and thinning from forest plantation (*Acacia mangium, Paraserinthes falcataria, Gmelina arborea* and *Eucalyptus deglupta*), have also been successfully converted into LVL with satisfactory physical and mechanical properties.

While H'ng [1] in his research identified, by using different densities of wood species, to manufacture LVL as the density of the wood veneer increases, the strength of the LVL increased only slightly as oppose to that made from low density wood. H'ng et al. [7] and Hoover et al. [8] also suggested that species and number of layers had a significant effect on all properties like bending and shear properties.

2.3   Mengkulang LVL as a Potential ETP for Roof Trusses

According to the Malaysian Standard, MS 544:Part 2:2001 [9], sawn timbers in Malaysia are grouped into the strength group of SG1 to S57 based on its physical properties and strength. timbers from SG1 to SG4 group are suitable for structural applications as outlined by Malaysian Standard.

Similarly, the requirements set out in the Specifications for Building Works by Public Works Department of Malaysia (JKR) [10], which specify that the strength for the timber roof structures should be at least of SG4. Mengkulang (*Heritera* spp.), is classified into the strength group of SG5 (Table 2, MS 544:2:2001), can be identified by its colour of red-brown to dark red-brown, non-durable and requiring treatment.

The species is from a medium hardwood with a density of 800 kg/m^3 at 19 % moisture content and specific gravity of 0.55. They are widely used in nonstructural applications including plywood manufacture, interior finishing, flooring, furniture and other nonstructural application. With the plentiful supply in the local market and relatively competitive price, Mengkulang timber can be commercialized as the ETP for structural usage. As reported in the Mas Kayu, Volume 1 of January 2015 [11], the average price of Mengkulang sawn timbers is the lowest among the other species of medium hardwood timbers. Since the strength of LVL from the lower grade of timber can be upgraded to the higher grade, further research into this

Table 2 Grade stresses for the strength group of SG4, SG5 and Mengkulang [9, 12]

Grade stresses	Grade stresses (N/mm^2)		
	SG4	SG5	Mengkulang
Bending parallel to grain	13.2	9.5	14
Tension parallel to grain	7.9	5.7	11.1
Compression parallel to grain	11.1	8.5	10.6
Compression perpendicular to grain	1.65	1.14	1.88
Shear parallel to grain	1.19	1.23	1.71
Modulus of elasticity (mean)	11,000	9100	10,900
Modulus of elasticity (minimum)	7600	6300	6700

timber can be beneficial to the local timber industries. The dry grade stresses for the strength group of SG4, SG5 and Mengkulang are shown in Table 2. These grade stresses indicate the basic working stresses and stiffness to be used for structural design purposes.

To date, the design properties of LVL from tropical timber are not fully developed yet due to ongoing research. The grade stresses for structural LVL as tabulated in Table 1, MS 544: Part 12 [12] are based on basic working stress from a dry standard of solid timber in MS 544: Part 2. Hence, in order to extend the use of Mengkulang LVL to load bearing structural uses, it is important to identify its mechanical strength particularly modulus of rupture (MOR), tension parallel to grain, compression parallel to grain and modulus of elasticity (MOE) beforehand.

Additionally, these mechanical properties will subsequently be adopted in roof truss design and as input parameters for finite element analysis FEA of this research as well.

2.4   Structural Performance of Timber Roof Trusses

The structural performance of timber roof truss is related to the deformation of a truss under applied loadings, joint's displacement and mode of failure as well. When a truss structure is subjected to axial or gravity loads, the web members will experience either compression or tension. There will be combined compression and bending of the top chord member while the bottom chord member undergoes a combination of tension and bending. The design of the truss members also considers those four conditions. However, current standards available do not take into account the bending moment in the design of the joint.

There are various types of mechanical fasteners or connectors being used for trusses; bolts, split rings, nailed on plywood, metal gusset plates and metal plate connectors (MPC). MPC for roof trusses and floors have been used in light-frame residential, industrial and commercial construction since more than 50 years ago due to economic values and less labour usage [13]. In Malaysia, most of the

fabricators of prefabricated timber roof trusses are also using MPC for the truss connections system.

It is essential to evaluate the failure and strength of the connection with mechanical fasteners precisely if possible. The evaluation includes both the ductile and the brittle failures. Most of the standards acknowledged the use of European yield model (EYM) to determine the ductile failure strength. The EYM is also an incredibly precise model that outlines the fundamental of the European timber standard Eurocode 5, EN 1995-1-1:2004 (CEN, 2004) [14]. The fastener yield moment and embedment strength are the main parameters of EYM. The fastener yield moment capacity is depending on the ultimate tensile strength of the steel of the fastener, and can be adopted from the Eurocode 5 formulas. The embedment strength values can be determined by performing embedment test according to EN 383:1993 (CEN, 1993). The other standards, ASTM D 5764-97a (ASTM International, 2007) and ISO/DIS 10984-2 (ISO, 2008) are also available for the test but with different procedures that were discussed by Franke and Quenneville [14] in their research.

In early studies of truss connections, the focus was more on investigations of tensile connections through testing and modelling to evaluate modes of failures, strength and stiffness of joints, load-slip characteristics, and also to identify variables that affect the joints behaviour.

Güntekin [15] had summarized in his research that some variables can influent the joints behaviour including size and numbers of teeth; plate thickness and its orientation; the pressing force used to fix the plate at the joint; and the time between fabrication and testing. While the timber properties such as species, moisture content and specific gravity orientation and loading direction were also reported to have influences on the behaviour of joints.

Subsequently, the following research showed interest in the other types of connections subjected to various types of loading conditions and modelling. Moura et al. [16] investigated the influence of timber density on metal plate connectors (MPC) which subjected to static and cyclic loading. The results of the investigation initiated that high-density timber joints could withstand loads of 30 % higher than low-density timber. Timber density was also found to have no significant effect on the mechanical behaviour of connections.

The semi rigidity behaviour of joints was also studied by Gupta and Gebremedhin [17] by performing destructive tests on MPC of timber truss joints including tension splice, heel and the web to bottom chord. The results of the test showed that the heel joint failure was a ductile failure, whereas the tension splice and the web possessed brittle failures. Apparently, the truss joints were identified to have failures in material and tooth plate. Figure 1 shows the load-displacement curves for the respective joints. Figure 2 indicates the tabulation of average ultimate load, deflection, stiffness and their failure modes. Stiffness in the table is obtained by the ratio of the design load and the deflection at the design load, whereas the design load equals to the ultimate load divided by a factor of three, which included a load duration factor for load test duration of 12 min and a factor of safety.
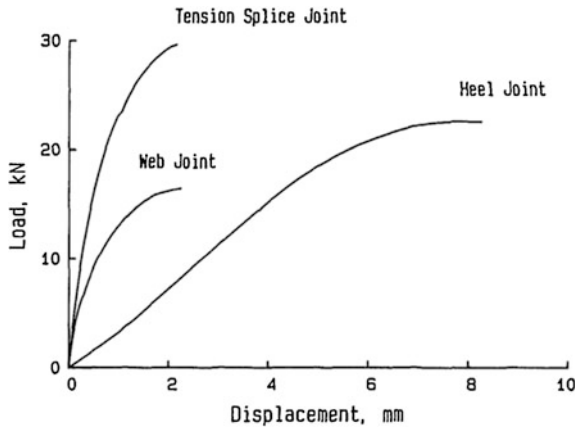
Fig. 1 Load-displacement curve for three types of joints using metal plate connector [17]

TABLE 2. Means and Coefficients of Variation of Ultimate Strength, Deflection at Failure, and Stiffness and Failure Modes for Three Types of Joints Tested

Joint type (1)	Mean ultimate load (kN) (2)	Deflection at failure (mm) (3)	Stiffness (kN/m) (4)	Failure mode (5)
Tension	27.0 (52, 17.6%)	1.91 (52, 22.1%)	5.28×10^4 (50, 18.3%)	Wood tearing and teeth failure
Web	16.7 (55, 17.1%)	2.23 (53, 28.1%)	4.12×10^4 (50, 52.0%)	Teeth failure at the tension web
Heel	22.7 (56, 06.7%)	7.60 (45, 09.4%)	0.38×10^4 (44, 10.4%)	Teeth failure at the bottom chord

Note: Numbers in parentheses are number of observations and coefficient of variation, respectively.

Fig. 2 Tabulated values of mean ultimate load, deflection at failure and stiffness with respective mode of failure [17]

While research by Franke and Quenneville [14] to investigate bending moment capacity of MPC splice joints manufactured using red pine lumber had identified that the type of loading, the size of plate and orientation of tooth have effects on the capacity of bending moment. For joints that were tested in the edgewise position, they were found to have higher bending moment capacity than that of flatwise position.

The performance of bolted connections in structural composite timber namely parallel strand lumber (PSL) and LVL in comparison with solid timber and glulam had also been investigated by Davis and Claisse [18]. The tests were performed according to BS EN 26891 and the results from the load-deformation response showed that the strength and stiffness properties of bolted connections in PSL and LVL and solid timber of the same density are comparable. Besides, the joint's performance was not affected by the bolts position on the glue-line of a glulam member.

However, the embedment strength of the structural timber composites improved better than both the solid timber and glulam.

Adhesively bonded joints, another approach of innovative connections were testified to demonstrate higher capacities and stiffness than dowel type mechanical fasteners [19]. Vallee and his coresearchers had conducted numerical analysis and experimental investigations on a full-scale adhesively bonded timber trusses and joints, in which adhesive bonds were compared to doweled connections. The results showed the adhesively bonded trusses achieved significantly higher failure load and stiffness. Figure 3 shows load-displacement curves of the corresponding joints. Another research to investigate truss performance was carried out by Chen et al. [20] which pointed out the global failure of glulam bamboo truss was due to the failure of MPC. The truss failed by brittle fracture.

The failure mechanisms between timber and cold formed roof truss may differ due to many factors. Several researches demonstrated that the failure of a roof truss

Fig. 3 Load-displacement curves **a** bonded and dowelled joints, **b** bonded and dowelled truss [19]
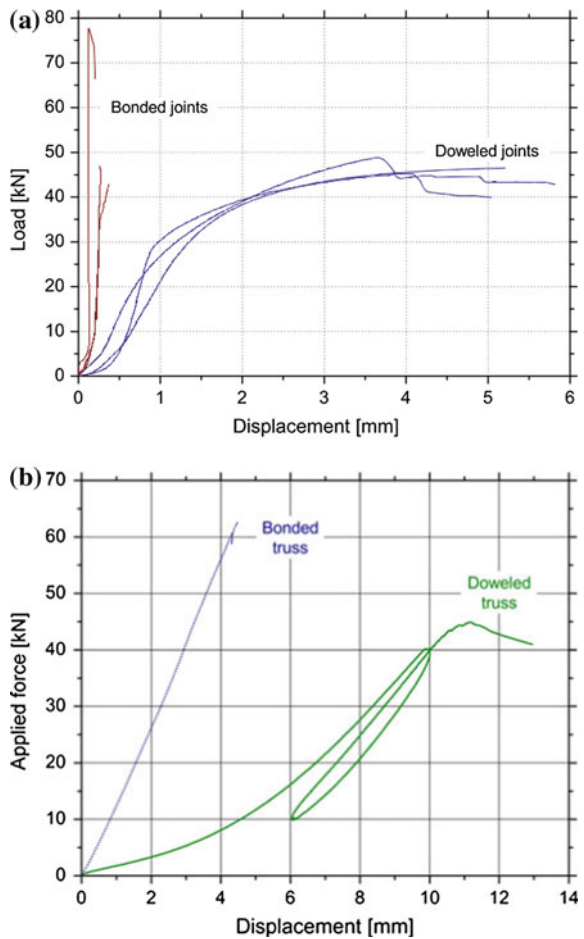
system was mainly caused by the failure of the connections rather than the failure of the timber members. Research by Arya and Jain [21] found that from the engineering analysis of the timber truss system of destroyed property caused by a storm, the truss connectors have failed in resisting the wind loads. Otherwise, the designed truss members were still capable of carrying the storm loads.

Conversely, Wood and Dawe [22] investigated the failure of cold formed roof truss and pointed out that the local buckling of the top chord member is the primary mechanisms of failure. Despite numerous researches have been carried out to understand the behaviour of roof truss and its joints, we still lack studies concerning the roof truss manufactured from LVL tropical timber. Therefore, it is important to carry out this research to understand the actual behaviour of this material.

3　Methodology

3.1　Material Preparation

The fabrication of LVL in Malaysia must conform to the Malaysian Standard MS 2209:2009. For the proposed research, the LVL panels will be fabricated at the timber and LVL factory in Perak. All timber species should be supplied from one source of a supplier to ensure the secure test material with not having many variations in strength properties that could arise from different timber growth conditions.

The veneers of 0.5 mm thick will be bonded together with phenolic resorcinol formaldehyde resin. Previous research had also suggested that phenolic resin can influence the properties of LVL by increasing its bending and compression, but reducing tension strength, toughness and dynamic properties [5]. The quality of LVL can also be influenced by the manufacturing process. Adequate time of required pressure, number of veneer laminations, defects size and distribution, veneer end joints efficiency, the strength of the clear timber and the depth and frequency of knife checks were reported by H'ng [1] that can significantly control the quality.

3.2　Determination of Mechanical Properties of LVL

According to H'ng et al. [5], the mechanical properties of a material refer to the strength and resistance of material to deformation. Strength is the ability of a material to undertake applied loads, whereas resistance to deformation is determined by the amount a material can be compressed, distorted or bent due to applied loads. The mechanical properties values are required in the derivation of basic working stress and stiffness of LVL which to be used for structural design purposes. The standards applicable to determine the mechanical properties are namely, BS EN 408, BS EN 14374, ASTM D198. Based on BS EN 408, the minimum of 32

specimens of various sizes are required for each of the related test involved including static bending test (flatwise and edgewise), tension test and compression test. The bending properties are measured by strength and stiffness which represent modulus of rupture (MOR) and modulus of elastic (MOE), respectively. While for tensile and compressive strength, the tension parallel to grain, the compression parallel to grain and compression perpendicular to grain will be determined.

After the test, at least, two numbers of test pieces should be taken from each of the tested specimens for the determination of the moisture content and density. Methods required for the tests of moisture content and density must conform to BS EN 322 and BS EN 323, respectively.

The modification of mechanical properties to fifth-percentile value due to the moisture contents variations is also required for LVL fabricated from tropical hardwood species [5].

3.3 Numerical Analysis of Roof Trusses and Joints

Figure 4 shows the schematic drawing of the designed truss of the proposed research. To determine the member size, manual calculation will be carried out and the design will be in accordance to MS 544: Part 12 and BS EN 1995. For connection design, MS 544: Part 3 and BS EN will be referred. A roof truss is usually designed as a simple two dimensional (2D) truss assuming the end supports are pinned at one end and roller at the other end.

The axial forces are determined by assuming that the members end is pinned. The moments for the top chord are obtained by assuming the ridge and the heel joint of top the chord are pinned but continuous over the web connections. The web members are considered to take axial forces only, and the bottom chord is continuous with pinned jointed at both ends of the supports. However, in building construction, the assumption does not represent the actual behaviour because both ends of the trusses are always fixed to the wall plate [23].

According to Arya and Jain [21], it is impractical to model the roof truss connection a semirigid joint, but for pinned or rigid joint, the modelling is more convenient and easier. Nevertheless, it was also proven by previous research that
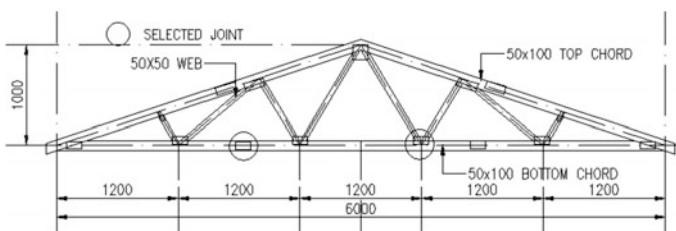
Fig. 4 Designed fink truss

roof trusses connected by metal plate connectors behave as semirigid joints. A semirigid joint tends to tolerate for the members' movement in either axial direction; translation or rotation resulted from the concentric or eccentric loadings and deformation of the joint which contribute to the extensive bending of the structure [17]. Thus, the numerical analysis using finite element method is significant in understanding the behaviour and stiffness of the truss.

Ellegard [24] had pointed out different models of finite element analysis for semirigid joints of MPC from other researchers. In his paper, he also discussed the basic concepts of beam element, nail element, plate element and contact element as well. Using the toolbox named TrussLab (under the Technical Computing Language Programme, MATLAB); and with some modification of these elements and adopting Foschi approach, Ellegard found out that there were good agreement between the models and experiments for the splice joints, except for slight overestimation of stiffness at the knee joints that might be caused by the cracks development in the timber. Likewise, the research conducted by Masse and Salinas [25] into the semi rigidity of multi-laminated nailed joints also found the good agreement between the theoretical analysis of the joint stiffness and the experimental results.

The later of study utilized commercial programme packages like ABAQUS and ANSYS to generate FE-models of the roof trusses and the truss joints [17, 26]. Method of modelling the 2D slotted in nailed wood to steel joints of a glulam truss structure was explained in detail by Ellegaard [24]. The load was applied as force increments to the model until failure of one nail occured.

3.4 Full-Scale Tests of Roof Trusses and Truss Joints

The Laboratory tests on the full-scale members, connections and trusses are very important to understand the real behaviour of the load transfer and the internal forces. In some cases, the full-scale tests of roof trusses or joint tests were conducted to validate the results obtained from the numerical analysis. Otherwise, the finite element analysis was carried out after performing the experimental investigations. Vallee et al. [19] had considered the second approach to making comparison between adhesively bonded timber trusses and traditional dowelled connections. Similarly, Stehn and Borjes [26] applied the same methodology.

The test for the truss joints will be conducted according to BS EN 26891. Transducers fixed to the joint will measure displacements due to the load increment and the load-displacement curve will be plotted from the readings. For the ultimate load test, the load will be increased up to ultimate failure. The structure is defined as failed when a sudden large displacement occurs under a small increment of load. The above observations for the whole structures and its connections will be checked and recorded at every increment as well as the condition of the truss and connection details at ultimate failure. Figure 5 indicates the conceptual framework of this research.
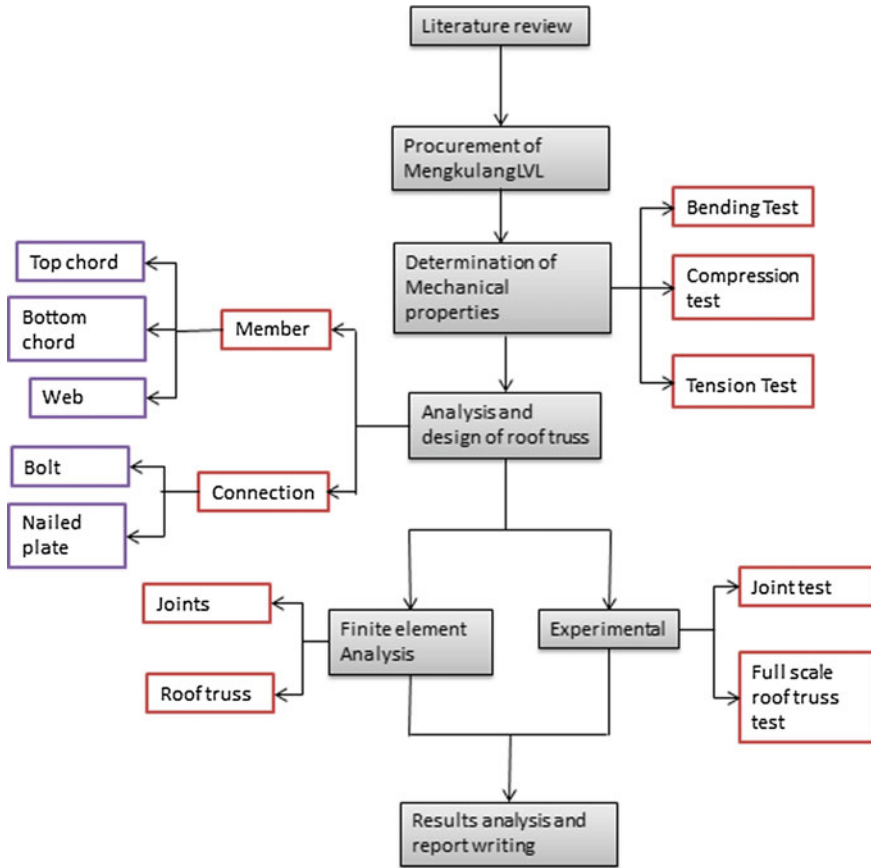
Fig. 5 Conceptual framework of the proposed research

4 Expected Outcomes

Expected outcomes of the proposed research are stated as below:

a. LVL properties including MOE, MOR, shear modulus, tension parallel to grain and compression parallel to grain needed for structural design and finite element analysis will be obtained from the mechanical tests.
b. From the experiment, it is expected that the mechanical properties of Mengkulang LVL will be improved and the strength grade of timber will increase from SG5 to SG4.
c. From the results of the full-scale of roof truss test, the truss capacity of carrying load is expected to satisfy and validate the numerical analysis. The mode of failure is expected to be at the joints rather than the failure of the material.

d. The load-deflection characteristics of the joints tested are expected to be non-linear. The characterisation of joint's failure will be either ductile or brittle. Bonding failure of the material may also be observed. The experimental results for strength and stiffness of the joints will validate the numerical analysis.

5 Conclusion

The proposed research on the structural performance of Mengkulang LVL roof trusses is expected to give contribution of new data for LVL manufactured using medium density hardwood timber in SG5 so that in future any timbers in SG5 with good bondability characteristics become more appropriate material in much more applications especially in construction and structural use. It is expected from the research that by converting lower grade timber into LVL will give acceptable effect on the physical and mechanical properties and dimensional stability. The LVL manufacturing will help improve the quality of lower grade timber in the eco-friendly way, thus providing a better alternative for construction material.

The research also will help to give basic data on the joint performance of LVL using selected metal connectors for later use of practicing engineers in their design. The structural analysis of roof trusses using finite element model will provide basic information for predicting the performance of roof trusses using LVL. It is also expected that this modelling will able to optimize appropriate connection systems as well as the design of LVL roof trusses which will enhance the usage of engineered wood products that meet the concept of industrialised building system (IBS), green building and sustainable constructions material.

References

1. P. S. H'ng, "Basic engineering properties of laminated veneer lumber (LVL) produced from tropical hardwood species," unpublished, Universiti Putra Malaysia, Selangor, Malaysia, 2003.
2. E. S. Wahab, "Compressive strength properties of full-sized laminated veneer lumber (LVL) made from Rubberwood (*Hevea brasiliensis*)," unpublished, Universiti Teknologi Mara, Selangor, Malaysia, 2005.
3. A. Buchanan, D. Carradine, & J. Jordan, "Performance of engineered timber structures in the Canterbury earthquake," *Earthquake Engineering*, *44*(4), 394–401, 2011.
4. F. Lam and B. A. Craig, "Shear strength in structural composite lumber," *J. Mater. Civ. Eng.*, vol. 12, no. 3, August, pp. 196–204, 2000.
5. P.S. H'ng, Z. Ahmad and P. Md. Tahir, "Laminated veneer lumber from Malaysian tropical timber," Shah Alam, UiTm Press, 2012.

6. Y.S. Chee, "Structural Rubberwood LVL: An Engineering Wood Product For Prefabricated Timber Roof Truss," unpublished, Universiti Putra Malaysia, Selangor, Malaysia, 2003.

7. P.S. H'ng, P. Md. Tahir, and K.L. Chin, "Bending properties of laminated veneer lumber produced from Keruing (Dipterocarpus s.p) reinforced with low density wood species," *Asian Journal of Scientific Journal*, 3(2), 118–125, 2010.

8. W.L. Hoover, "Material design factors for hardwood-laminated-veneer-lumber," *Forest Product Journal*, 37(9), 15–23, 1987.

9. MS 544 Part: 2, "Code of Practice for the Structural Use of Timber Part 2: Permissible Stress Design of Solid Timber, " Shah Alam, Malaysia, Sirim Berhad, 2001.

10. "Standard Specifications for Building Works 2014", Malaysia, Jabatan Kerja Raya Malaysia, 2014.

11. "MAS KAYU 2015: Vol.1, January", Malaysia, MTIB, 2015.

12. MS 544 Part: 12, "Code of Practice for the Structural Use of Timber Part 2: Laminated Veneer Lumber for Structural Aplications," Shah Alam, Malaysia, Sirim Berhad, 2006.

13. R. Gupta, M. Vatovec, and T. H. Miller, "Metal-plate-connected wood joints : A literature review," Research Contribution No: 13, Forest Research Laboratory, Oregon State University, Corvallis, USA, 1996.

14. S.Franke and P. Quenneville, "Bolted and dowelled connections in Radiata pine and laminated veneer lumber using the European yield model, " *Aust. J. Struct. Eng.*, vol. 12, pp. 13–27, 2011.

15. E. GÜNTEKIN, "Bending moment capacity of metal plate connected wood-splice joints constructed with Red Pine (Pinus brutia Ten.) lumber," *Turk J Agric For*, 31, 207–212, 2007.

16. Moura, J.D.D., C. Bastian, G. Duchanois, J.M. Leban and P. Triboulot. "The influence of wood density on metal-plate connector mechanical behavior under cyclic loading," *Forest Products Journal*. 45: 74–82, 1995.

17. R. Gupta and K. G. Gebremedhin, "Destructive testing of metal plate connected wood truss joints," *J. Struct. Eng.*, vol. 116, no. 7, pp. 1971–1982, 1990.

18. T. J. Davis and P. A. Claisse, "Bolted joints in glulam and structural timber composites," *Constr. Build. Mater.*, vol. 14, no. November 1999, pp. 407–417, 2000.

19. T. Vallée, T. Tannert, and S. Hehl, "Experimental and numerical investigations on full-scale adhesively bonded timber trusses," *Mater. Struct.*, vol. 44, no. 10, pp. 1745–1758, 2011.

20. G. Chen, Y. Xiao, and B. Shan, "Experimental Studies on Glue-laminated Bamboo Trusses," vol. 640, pp. 757–762, 2013.

21. B. Arya and A. Jain, "Prefabricated wood truss roof failure under wind induced loads," *Forensic Eng. 2012*, pp. 1228–1237, 2013.

22. J. V Wood and J. L. Dawe, "Full-scale test behavior of cold-formed steel roof trusses," *J. Struct. Eng.*, vol. 132, no. April, pp. 616–623, 2006.

23. R. Gupta and P. Limkatanyoo, "Practical approach to designing wood roof truss assemblies," *Pract. Period. Struct. Des. Constr.*, vol. 13, August, pp. 135–146, 2008.

24. P. Ellegaard, "Finite-element modeling of timber Joints with punched metal plate fasteners," *J. Struct. Eng.*, vol. 132, no. 3, pp. 409–417, 2006.

25. D. I. Masse and J. J. Salinas, "Analysis of timber trusses using semi-rigid joints," *Can. Agric. Eng.*, no. May 1987, pp. 111–124, 1988.

26. L. Stehn and K. Börjes, "The influence of nail ductility on the load capacity of a glulam truss structure," *Engineering Structures*, vol. 26, no. 6. pp. 809–816, 2004.

Effect of Adding Cement to the Mechanical Properties of Red Gypsum Particleboard Made of Kelempayan Wood

A.A.G. Halim, H. Shaharin, N.S. Aini and M.A. Fadzil

Abstract Gypsum particleboard has many disadvantages such as low water resistivity and low mechanical properties compared to cement-bonded particleboard. The properties of gypsum particleboard can be improved by adding cement. To analyze the improvement of the properties of the particleboard, a series of mechanical tests were conducted. The compatibility of Kelempayan wood species in manufacturing of the particleboard was also determined by referring to the strength of board obtained from the mechanical test. Experimental results showed that particleboard with more cement has better mechanical properties compared to particleboard with less cement. However, the properties decrease after a certain quantity of cement. The results show how the properties of the board change positively and negatively when cement is added. Thus, the amount of cement added must be optimal, which means not too less and not too much. Thus, the properties of cement-gypsum particleboard were successfully improved when cement is added at 2 %.

A.A.G. Halim · H. Shaharin (✉) · N.S. Aini
Faculty of Civil Engineering, Universiti Teknologi MARA (UiTM),
Shah Alam, Selangor, Malaysia
e-mail: shaharin.ir@gmail.com

A.A.G. Halim
e-mail: abdhalim.g@gmail.com

N.S. Aini
e-mail: aein86@yahoo.com

M.A. Fadzil
IIESM, Universiti Teknologi MARA (UiTM), Shah Alam, Malaysia
e-mail: fadiil2013@yahoo.com

1 Introduction

Nowadays, the amount of treated wood products is increasing dramatically. It is forecast that the number of treated wood will reach up to 18 million m^3 in 2020. This has become a serious issue in terms of environmental impacts and difficulties in disposing the treated wood product, as landfills are becoming less acceptable to deal with this issue. Thus, the development of cement particleboard which is produced together with the wood product can become one of the solutions to this problem. The practice of using wood waste in constructing the particleboard makes wood-cement composites attractive and greener to the environment.

Wood-cement panels (WCPs) are material with various excellent properties. They are good in terms of fire resistance, wet and dry rot resistance thermal insulation, and acoustic insulation. Because of this, their applications in the construction field have been highly accepted in many countries [1]. However, despite these positive characteristics, some disadvantages still exist, which have become barriers to the development of wood-cement composites. These include high variation in the compatibility of wood species mixed with cement due to soluble sugar and extracts and the effective chemical additives required to overcome the inhibitory properties of wood [2]. The effect and presence of soluble sugar and extractives in wood will make the board strength really sensitive to the change in wood species. Another problem is the tendency of the boards to become moist and decay due to insects.

Although wood-cement boards have been long established and acknowledged all over the world, wood-cement-gypsum boards have finer property than WCPs. This is because inorganic binders (gypsum) are used in a high proportion in contrast to wood.

Gypsum is cheaper compared to Portland cement or magnesia, takes less time to harden, and is also easily available. Yet, gypsum does not have much resistance to moisture compared to Portland cement. The moisture resistance of gypsum can be altered and repaired by combining it with Portland cement. The use of gypsum can help in reducing the production costs, while the use of Portland cement in a small amount will recover the strength and moisture resistance of the inorganic-bonded wood composite boards. The hardening of calcium sulfate hemihydrates ($CaSO_4 \cdot H_2O$), which is the main component of gypsum, is mostly because of the formation of dehydrate crystals ($CaSO_4 \cdot 2H_2O$) and this occurs during the hydration reaction. In contrast, the Portland cement hardening process for most of the part is due to the formation of silicate and aluminates hydrates [3].

Gypsum has low resistivity against water. The gypsum particleboard (GPB) tends to show low mechanical properties and high thickness swelling when absorbing water. However, after investigating the effects of adding cement on the physical and mechanical properties of GPB, it is shown that the physical and mechanical properties of GPB were improved greatly after adding cement [4].

The main objective of this study is to evaluate the feasibility of Malaysian fast grown wood particles, which is Kelempayan wood flakes with cement and with a mixture of red gypsum and Portland cement to show the improvement when cement is added.

2 Materials and Methods

2.1 Materials

Commercial Ordinary Portland Cement (OPC) was used as the basic cementitious material. The reference cement used was the type CEM 1 42, R according to the BS EN 197-1:2000 [5]. The OPC was supplied by Tasek Cement Bhd and red gypsum was supplied from Tioxide Malaysia Sdn. Bhd. The wood particles were chosen from the Kelempayan timber species, which is from Malaysian fast grown timber species scientifically known as *Anthocephalus Chinensis*. Currently, the timber species are considered as a less utilized species. They grow wild in the gaps of selective felling and also by the logging roads.

2.2 Production of Red Gypsum Particleboard

The materials' proportion was prepared on the basis of the dry mass of powders. This is done in order to raise the moisture resistance of the binder. Fundamentally, the ratio of inorganic binder: wood: water is maintained at 2.5:0.7:1. However, the ratio of gypsum: OPC is varied at 30:70, 20:80 and 10:90. This mixture is used for the manufacturing of board. The density for the boards is targeted at 1.4 g/cm^3 and board size of 450 × 450 × 13 mm was produced. The mixed proportions for preparation of gypsum particleboard are as shown in Table 1.

Table 1 Mixed proportion for preparation of red gypsum particleboard

Mix type	Inorganic binder		Kelempayan wood	Water
	Gypsum	OPC		
M1	0 %	2.5 %	0 %	1 %
	0 kg	6 kg	0 kg	2.4 kg
M2	0 %	2.5 %	0.7 %	1 %
	0 kg	5 kg	1.4 kg	2 kg
M3	0.25 %	2.25 %	0.7 %	1 %
	0.5 kg	4.5 kg	1.4 kg	2 kg
M4	0.50 %	2.00 %	0.7 %	1 %
	1 kg	4 kg	1.4 kg	2 kg
M5	0.75 %	1.75 %	0.7 %	1 %
	1.5 kg	3.5 kg	1.4 kg	2 kg

2.3   Measurement of Mechanical Properties of Red Gypsum Particleboard

All the red gypsum particleboard was mixed and casted in a mold of size of 450 mm × 450 mm. Demold process was conducted after 24 h and exposed to air for 28 days. The mechanical properties were identified as proposed by ASTM D1037-96a [6], recorded, and analyzed to determine the effect of added cement to the red gypsum particleboard made of Kelempayan wood.

3   Results and Discussion

3.1   Effect of Added Cement to the Red Gypsum Particleboard Made of Kelempayan Wood to Bending Test and Tensile Test

Figure 1 and Table 2 show the effect of added cement to the bending strength value of red gypsum particleboard made of Kelempayan wood. The value of strength keeps increasing from M1 until M2 before it fluctuates from M3 to M5. The strongest value of bending strength is from M2, which is 27499.5 kPa, while the lowest reading given is from M1, which is 17553.5 kPa.

Figure 2 and Table 3 show the effect of added cement to the tensile strength value of red gypsum particleboard made of Kelempayan wood. For the tensile test, the pattern is similar to the bending test. The value of tensile strength increases from M1 till M2 before but fluctuates for the next three mixes, M3, M4, and M5. The
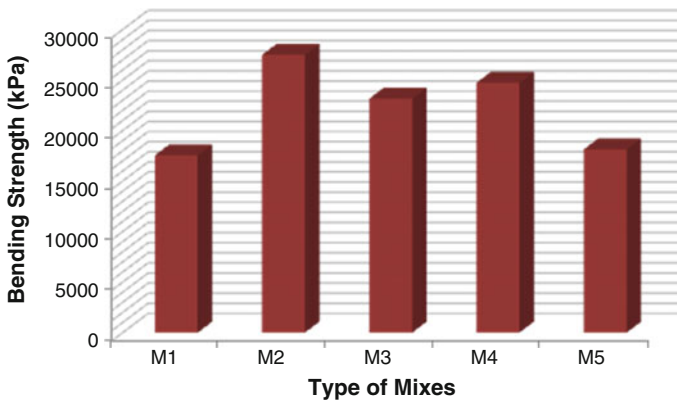
Fig. 1 Bending test of red gypsum particleboard made of Kelempayan wood with the effect of cement added

Table 2 Bending test value

Type of mixes	Bending strength (kPa)
M1	17553.50
M2	27499.50
M3	23165.50
M4	24739.00
M5	18140.00
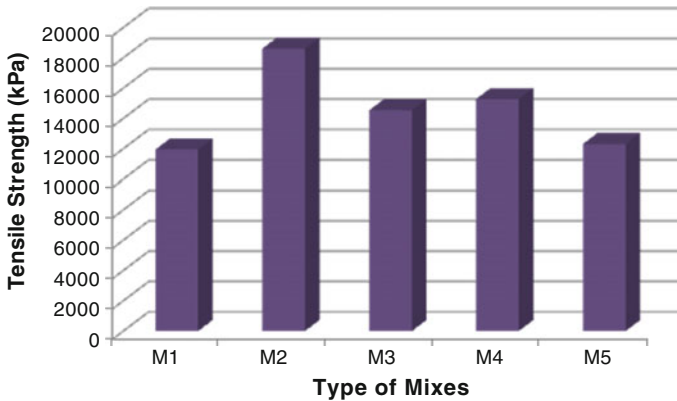
Fig. 2 Tensile test of red gypsum particle board made with Kelempayan wood with the effect of cement added

Table 3 Tensile test value

Type of mixes	Tensile strength (kPa)
M1	11944.44
M2	18611.11
M3	14537.04
M4	15277.78
M5	12314.48

highest tensile strength obtained from the test is 18611.11 kPa, which is given by M2, and the lowest strength is 11944.44 kPa, which comes from M1.

OPC as we all know gives high bonding strength between particles when it cures in the appropriate condition. When the particleboard is produced by adding a suitable amount of cement, the OPC contributes to increase the bonding strength of the board. When the board is not casted in the appropriate amount of OPC, the bonding is not perfect but is weak. So, the mixture of gypsum and OPC which is used as adhesive agent will not produce good bonding strength between particles. Therefore, it will not provide the board with high strength but will just weaken the board. A good mix of these two adhesive agents will make them become perfect reinforcing material for the board.

Hence, we see that M2 gives the highest value of bending and tensile strength. This happens because M2 is the most appropriate mix that uses the optimal amount of ingredients in constructing the particleboard. The key here is the optimal amount of OPC and gypsum as they will determine the strength of the board. The amount of cement in M2 is optimum for manufacturing the board; it is not too much and not too less. If the amount is lesser such as in M1, the OPC will be insufficient and will not be able to provide strength as it should.

For the bending and tensile test, we can observe that the strength of the particleboard is improved by adding cement, especially improvement from M1 to M2. However, the properties only keep increasing and improve until it reaches the optimum strength. After that, the strength decreases even though the cement is continuously increased.

By observing the increase or decrease compared to the control mix, we can also say that the properties of board are improved. For M2, the bending strength increases by 9359.5 kPa (51.5 %), which is improved by half the value compared to the control mix. The same goes for the tensile strength. The tensile strength increases by 51.1 % from the control mix. Therefore, we observe here that the Kelempayan wood used here is compatible with the particleboard mix. This results in increase of strength by almost half the value compared to the control mix, which did not contain any wood particle in it. So the Kelempayan wood species is suitable for use in the manufacturing of this particleboard.

3.2 Effect of Added Cement to the Red Gypsum Particleboard Made of Kelempayan Wood to Compression Test

Figure 3 and Table 4 show the effect of added cement to the compressive strength value of red gypsum particleboard made of Kelempayan wood. For compression test, the value of compressive strength keeps decreasing from M1 to M3, which is from 2156.24 kPa for M1, 1298.62 kPa for M2, and 945 kPa for M3. The strength increases during M4 which gives the strength value of 7331.60 kPa and is also the highest value of compressive strength compared to other mixes used in this research. After that, the strength slightly decreases to 6678.67 kPa for M5.

As we all know, the high amount of OPC contributes greatly to the compressive strength. This theory is similar to the concept of concrete. One of the best properties of concrete is that it can withstand high amount of compression load. This concept also applies to the composite board. Cement can give the board great strength in terms of compression, especially if the hydration process is complete. Mix 5 did not give the highest value of compression. This is because this mix does not contain wood composite necessary to help the cement to bind more perfectly so that the board can become a strong board. Mixes 1, 2, and 3 have a lower value of compressive strength compared to mixes 4 and 5 because mixes 1, 2, and 3 have a lower
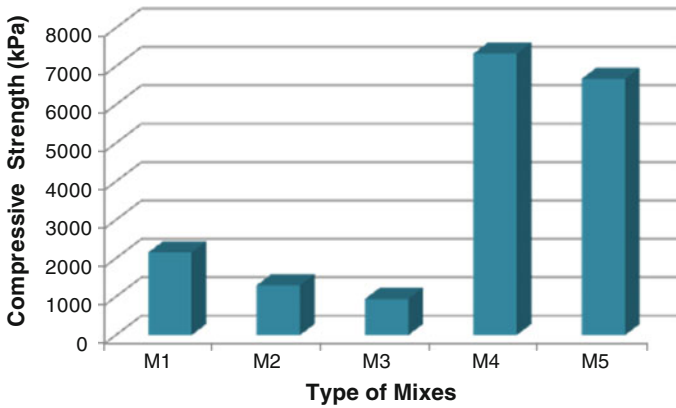
Fig. 3 Tensile test of red gypsum particle board made of Kelempayan wood with the effect of cement added

Table 4 Compressive strength value

Type of mixes	Compressive strength (kPa)
M1	2156.24
M2	1298.62
M3	945.00
M4	7331.60
M5	6678.67

amount of OPC. Although they have more amount of gypsum that does not really help in contributing to the compressive strength.

Basically, increasing the cement also increases the strength of the board. However, at some point, it also acts negatively. This is because excess cement will cause more hydration and thus give more heat due to the reaction. This high temperature is the cause for reduction in the strength of the board. If there is an excess of cement, the mix will be too packed and crowded. The hydration process cannot occur completely because of this condition. This causes low strength of the board due to incomplete process of hydration. The amount of OPC cannot be excessive because it will affect the curing of gypsum.

3.3 Optimum Performance of Red Gypsum Particleboard Made of Kelempayan Wood to Mechanical Properties

In Figs. 1, 2 and 3, we can see the relationship between bending and tensile strength. This is because the bending and tensile strength is related to the modulus of rupture. Modulus of rupture is the ability of material to resist deformation under

load. This bending, tensile, and compressive strength will depend on the quantity of cement. In addition, the bending strength of a composite board will be equal to tensile strength if the materials are homogeneous. A material is homogeneous if it is uniform in composition or character. For the compression value, it is quite low compared to the bending and tensile strength. This is due to the presence of wood particles that result in the decrease in density of the board. OPC is replaced with the wood particle and hence the compressive strength is reduced.

Based on the results, we can say that the best mix that can be used to manufacture this cement–gypsum particleboard is M2. This is because M2 gives the highest bending strength and also the tensile strength compared to other mixes. Although the compressive strength is not high which is 1298.62 kPa, it is negligible. This because most of the time, the particleboard is applied in the industry as partition board, ceiling finishing, and also as wall finishing. All these features do not require high compressive strength. However, they do require high bending strength and also tensile strength.

4   Conclusion

In conclusion, the mechanical properties of particleboard such as bending, tensile, and compression were successfully ascertained. In fact, it is clear in this research that the mechanical properties can be greatly improved by adding cement. The best mix is mix 2 which gives the bending strength of 27499.5 kPa, tensile strength of 18611.11 kPa, and compressive strength of 1298.62 kPa.

In addition, the effect of wood particles of Kelempayan timber species which is fast grown toward the properties of cement-gypsum composites board is perfectly analyzed. Based on the research, the Kelempayan timber species can be said to be compatible for manufacturing of the board, as it really affects the mix and helps to increase the strength of the board.

References

1. Frybort, Stephan, Mauritz, Raimund, Teischinger, Alfred, & Müller, Ulrich, "Cement bonded composites—a mechanical review". BioResources, 3(2), 602–626, 2007.
2. Wei, Yi Min, Zhou, Yia Guang, & Tomita, Bunichiro, "Study of hydration behavior of wood cement-based composite II: effect of chemical additives on the hydration characteristics and strengths of wood-cement composites". Journal of Wood Science, 46(6), 444–451, 2000.

3. Fratini, Emiliano, Ridi, Francesca, Chen, Sow-Hsin, & Baglioni, Piero, "Hydration water and microstructure in calcium silicate and aluminate hydrates". Journal of Physics: Condensed Matter, 18(36), S2467, 2007.
4. Yuhe Deng, T. F, "Improvement on the properties of gypsum particleboard by adding cement". The Japan Wood Research Society Journal, 98–102, 1998.
5. British Standard Institution, BS EN 197: Part 1, "Cement: Part 1: Composition, specifications and conformity criteria for common cements", 2000.
6. American Standard Testing Methods, "Standard Test Methods for Evaluating Properties of Wood-Base Fiber and Particle Panel Materials", 2006.

Perpendicular Glue Line Dowel-Bearing Strength Properties of Mengkulang Glulam

Nor Jihan Abd Malek, Rohana Hassan, Adrian Loh Wai Yong and Haslin Idayu Amaruddin

Abstract Dowel-bearing strength also known as embedment strength is a significant parameter for the wood connection design. The wood connection design is still referring to the European Yield theory which predicts the load capacities of the connection under lateral load. Bolt has been extensively used for the wood connection due to ease of assembly and able to reassemble for variation of member size. Glulam is an engineered wood product which has good strength to weight ratio and is able to design to meet the required design strength. Existing data provided in the Malaysian Standard (MS 544: 2001) is only applicable for the solid timber, therefore it is insufficient. Research on determining the dowel-bearing strength of Malaysian tropical hardwood is ongoing; more information is required in order to enhance the application of the Glulam Malaysian tropical timber. This study determined the dowel-bearing strength of Glulam Malaysian tropical hardwood, Mengkulang also known as *Heritiera* spp. loaded perpendicularly to glue line using two different bolt diameter 16 and 20 mm. Dowel-bearing strength test is performed in accordance to the ASTM-D5764-97a using the half-hole test method. Dowel diameter is found to have influenced the dowel-bearing strength, where dowel-bearing strength increased 20.82 % when the dowel diameter increased from 16 to 20 mm. Both standard ASTM D 5764- and BS EN 383 are commonly used in determining the dowel-bearing strength. Comparison of dowel-bearing strength using the ASTM D5764-97a standard based on the 5 % offset load and BS EN 383 standard based on the maximum load is made and found to have higher value using the BS EN 383 standard, 12.27 % higher for specimens using 16 mm dowel diameter and 10.29 % higher for specimens using 20 mm dowel diameter.

Keywords Dowel-bearing strength · Wood connection design · Glulam · Mengkulang · Half-hole test

N.J.A. Malek (✉) · R. Hassan · A.L.W. Yong · H.I. Amaruddin
Faculty of Civil Engineering, Universiti Teknologi MARA, Bandar Pusat Jengka, Pahang, Malaysia
e-mail: norjihan.abdmalek@gmail.com

1   Introduction

Timber has been extensively used as construction material since the ancient time. Wood grows natural and unique, its structural properties is widely different as the wood strength is highly dependent on the environmental conditions [1]. Defects found in the wood can affect the strength of the wood. As timber has good strength to weight ratio and many benefits such as less carbon emission during the manufacturing process, enhancement has been done to it in order to promote the use of timber. Glued laminated timber (Glulam) is an engineered wood product which is made from numbers of timber lamina bonded together with an adhesive [2]. There are two type of glued laminated member, one is the horizontal Glulam in which the timber layer is glued horizontally while the other is vertical Glulam in which the timber layer is glued vertically [3]. Performances of the Glulam member can be improved by placing the greater strength timber layer in the regions of higher stress [4]. Developed countries such as America, Japan, and Europe have been widely using the Glulam timber in the construction of commercial building, sport complex, residential houses, and church. However, the extensive use of Glulam timber in Malaysia has is to be seen due to the lack of research and data provided regarding it. Mengkulang is one of the Malaysian tropical timber species which is often used in furniture, flooring, paneling, and glue-lamination [5].

The weakest part in the timber is the joint connecting the large structural system. Mechanical fastener such as nails, screws, dowel, and bolts are often used to enhance the performance of timber connection. Bolt is commonly used in the construction and to connect the Glulam timber member due to its ability to resist high lateral shear force [6]. European Yield Model (EYM) theory proposed by the Johansen in 1949 has been often used in prediction of the ultimate load capacities of the wood connection with fasteners. This theory has been extensively used and been revised over the years but still remains the basic concept same as Johansen proposed. Theory of connection design stated in the Eurocode 5 and National Design Specifications are based on the EYM.

Dowel-bearing strength is one of the important parameter for the design of wood connection. Wood connection performances rely upon the fastener bending strength and the dowel-bearing strength [7]. According to ASTM D 5764-97a, dowel-bearing strength is the yield load obtained from the load-displacement curve using the 5 % offset method of a dowel-bearing strength test over the dowel diameter and specimen thickness. There are two methods with which the full-hole test and half-hole test can be adopted in determining the dowel-bearing strength. Studies showed that the half-hole test provides uniform load along the dowel fastener length, and fastener does not bend during the loading process, where full-hole test method load is only acting at the both end of the dowel, bending might occur during the loading process [8]. ASTM D 5764-97a and BS EN 383 are two different standards of test which are commonly used to determine the dowel-bearing strength. ASTM D 5764-97a is usually based on the half-hole test method where BS EN 383 is based on the full-hole test method. Several researches have been done

the using the half-hole test method such as research done by Wilkinson [9], Rammer [10, 11], Eratodi et al. [12], and Schmidt [13]. While the other researchers such as Hubner [14], Sawata and Yasumura [15], and Ivan [16] applied the full-hole test method in their study. The previous study done on the dowel-bearing strength for Malaysian tropical hardwood species is done and published by Jumaat et al. [17, 18], Awaludin et al. [19], and Hassan et al. [20, 21]. However, there is still lack of data emphasized on the effect of different dowel diameter loaded perpendicular tn the glue line of Mengkulang glulam. In order to enhance the current information and data on the dowel-bearing strength to promote the use of Malaysian tropical timber, more research and study are required. Therefore, the main objective of this study is to investigate the effect of two dowel diameters loaded perpendicularly to the glue lines of glulam made of Mengkulang species. The observation is also being made with two different code of practice which is the ASTM D 5764-97a and BS EN 383 in determination of the dowel-bearing strength. The effect of moisture content and density of the Mengkulang glulam species to the dowel-bearing strength is also being observed.

2　Materials and Method

Dowel-bearing strength was conducted on the Glulam Malaysian tropical hardwood Mengkulang (*Heritiera* spp.) species loaded perpendicularly to the glue line. Two different dowel diameter 16 and 20 mm of bolt (see Fig. 1) were used to determine the dowel-bearing strength of Glulam Mengkulang species with glue line embedded on the half-hole specimen (see Fig. 2). Specimens dimension and the test procedure is in accordance to the ASTM D 5764-97a, 2007. For specimens using 16 mm dowel diameter, the dimension is 64 mm × 64 mm × 38 mm, where specimens using 20 mm dowel diameter the dimension is 80 mm × 80 mm × 40 mm. Total sixty (60) specimens were tested, thirty (30) specimens using 16 mm dowel diameter, and thirty (30) specimens using 20 mm dowel diameter. The dowel-bearing strength test was tested with the universal testing machine (UTM) at

Fig. 1 Steel bolt 16 and 20 mm diameter

Fig. 2 Half-hole specimen

Fig. 3 Dowel-bearing
strength test set up

a constant rate of 1 mm/m (0.02 mm/s) for each specimen. Figure 3 shows the
dowel-bearing strength test set up on the UTM. Moisture content and density were
determined using the dry-oven method according to ASTM D 4442 standard. Initial
weight of specimens is first weighted and dried in the oven at 103 °C for 24 h and
then dry weight of the specimens is recorded.

Load-deformation curve is plotted after the dowel-bearing strength test.
According to ASTM D 5764-97a, 2007, 5 % offset method is used to determine the
yield load from the load-deformation curve. Yield load were determined by drawing
a straight line fit into the initial linear portion of load-deformation curve. Then,
offset the line by 5 % dowel diameter. Load at which the offset line intersects with
the load-deformation curve is selected as the yield load. Dowel-bearing strength
using ASTM D 5764-97a is computed using the Eq. (1) which is based on the 5 %

offset load and dowel-bearing strength using BS EN 383 is computed using the Eq. (2) which is based on the maximum load.

$$F_y = \frac{F_5}{d \cdot t} \tag{1}$$

$$F_h = \frac{F_{max}}{d \cdot t} \tag{2}$$

where F_5 is the 5 % offset load, F_{max} is the maximum load, d is the dowel diameter, and t is the thickness of specimen.

3   Results and Discussions

Figures 4 and 5 show the load-deformation curve of one of the specimens using 16 and 20 mm dowel diameter respectively.

Table 1 shows the mean dowel-bearing strength, standard deviation value, and coefficient of variance for the specimens using 16 and 20 mm dowel diameter. Table 2 shows the mean moisture content and density value of the specimens using 16 and 20 mm dowel diameter. Moisture content of specimens using 16 mm dowel diameter ranges from 9.52 to 12.03 % and moisture content of specimens using 20 mm dowel diameter ranges from 9.43 to 11.92 %. Density of the specimens using 16 mm dowel diameter ranges from 552.27 to 785.20 kg/m³ and density of specimens using 20 mm dowel diameter ranges from 665.47 to 791.33 kg/m³.

Figure 6 shows the mean dowel-bearing strength of specimens using 16 and 20 mm dowel diameter against the dowel diameter. It shows that the dowel-bearing strength is influenced by the dowel diameter. When the dowel diameter increases, dowel-bearing strength will also increases. This trend is found to be similar with the

Fig. 4 Example of load-deformation curve for specimens using 16 mm dowel diameter
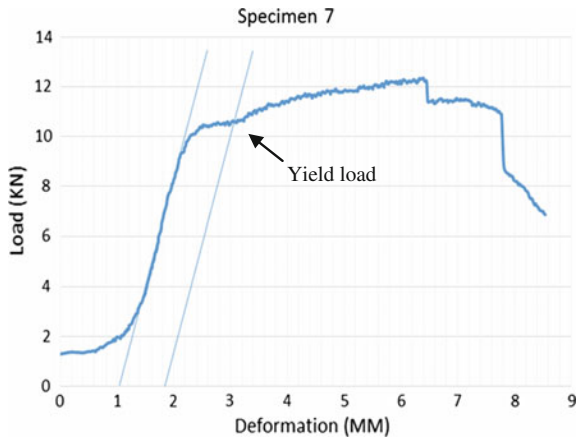
Fig. 5 Example of
load-deformation curve for
specimens using 20 mm
dowel diameter
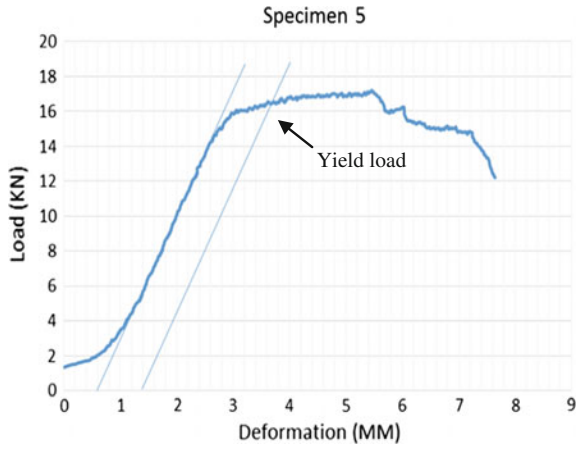
Table 1 Summary of the test results for specimens using 16 and 20 mm dowel diameter

Specimens (Nos)	Dowel diameter (mm)	Mean dowel-bearing strength, F_y (N/mm^2)	Standard deviation (SD)	Coefficient of variance (CV) (%)
30	16	17.77	1.12	6.30
30	20	21.47	1.79	8.34

Table 2 Mean moisture content and density value of specimens using 16 and 20 mm dowel diameter

Specimens (Nos)	Dowel diameter (mm)	Mean moisture content (%)	Mean density (kg/m^3)
30	16	10.82	648.52
30	20	10.86	722.56

Fig. 6 Dowel-bearing
strength versus dowel
diameter
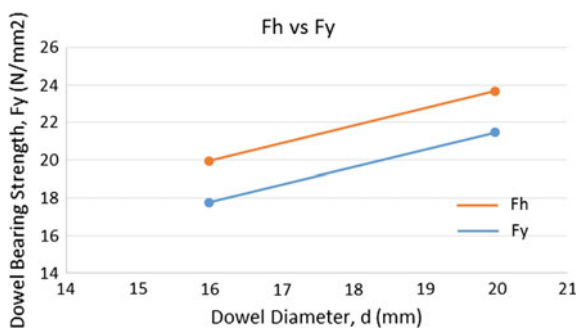
Fig. 7 Typical failure of the specimens using 16 mm dowel diameter

Fig. 8 Typical failure of the specimens using 20 mm dowel diameter
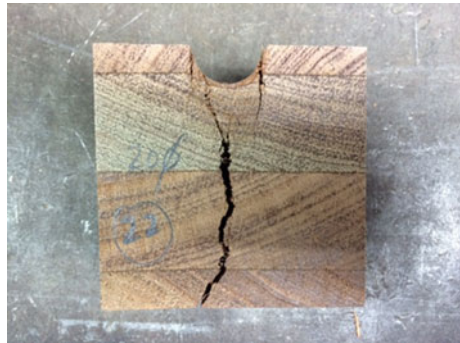
trend from the study by Jumaat et al. (2008) for Mengkulang solid timber species. Percentage differences of the dowel-bearing strength, F_y for Glulam Mengkulang with glue line species using 16 and 20 mm dowel diameter is 20.82 %.

Figures 7 and 8 shows the typical failure of the specimens using 16 and 20 mm dowel diameter. Both specimens are split perpendicular to the glue line. However, there are minor specimens observed in which the crack line is towards the glue line, this failure is due to lack of bonding of the adhesive between the timber layers on the specimens.

Table 3 shows the mean dowel-bearing strength, F_h is higher than the mean dowel-bearing strength, F_y. Percentage difference of mean dowel-bearing strength (F_y and F_h) for specimens using 16 mm dowel diameter is 12.27 %. Percentage

Table 3 Mean dowel-bearing strength (F_y and F_h) of specimens using 16 and 20 mm dowel diameter and percentage differences

Specimens (Nos)	Dowel diameter (mm)	Mean dowel-bearing strength, F_y (N/mm^2)	Mean dowel-bearing strength, F_h (N/mm^2)	Percentage differences (%)
30	16	17.77	19.95	12.27
30	20	21.47	23.68	10.29
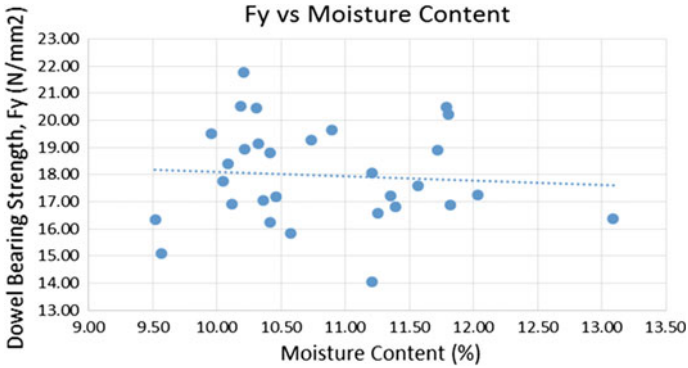
Fig. 9 Dowel-bearing strength versus moisture content (specimens using 16 mm dowel diameter)
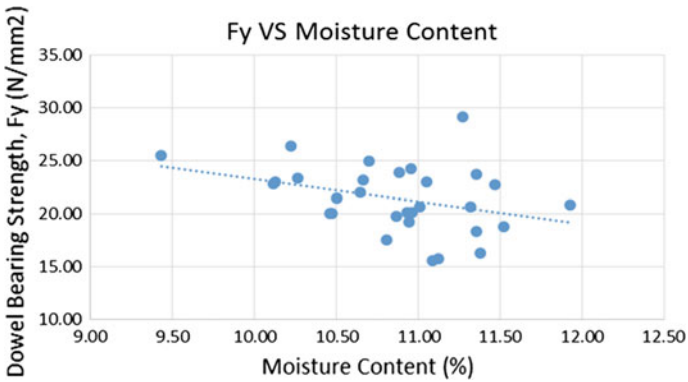
Fig. 10 Dowel-bearing strength versus moisture content (specimens using 20 mm dowel diameter)

difference of mean dowel-bearing strength (F_y and F_h) for specimens using 20 mm dowel diameter is 10.29 %.

Figures 9 and 10 show the relationship between moisture content and dowel-bearing strength of Glulam Mengkulang with glue line species. It is found that moisture content have a significant influence to the dowel-bearing strength. Dowel-bearing strength decreased when moisture content increased. These results agreed with the results from the study by Rammer in the year 2001. This is due to moisture content which causes the wood to shrink and expand, therefore degrading the strength of the wood.

Figures 11 and 12 show the relationship between density and dowel-bearing strength of Glulam Mengkulang with glue line species. It is found that density has a significant influence to the dowel-bearing strength. Dowel-bearing strength increased when density increased. This is because the wood fiber is more compacted in the wood specimens resulting in the value of mass over the higher
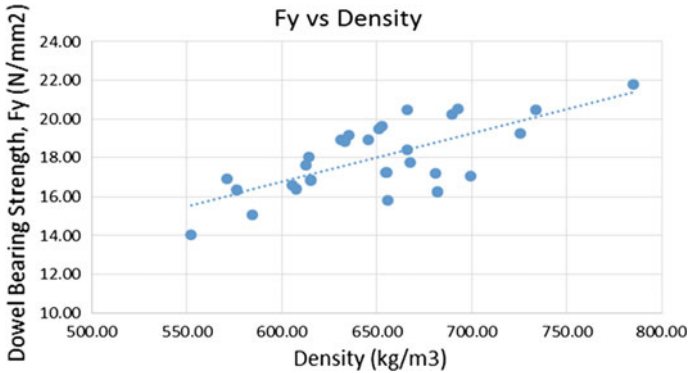
Fig. 11 Dowel-bearing strength versus density (specimens using 16 mm dowel diameter)
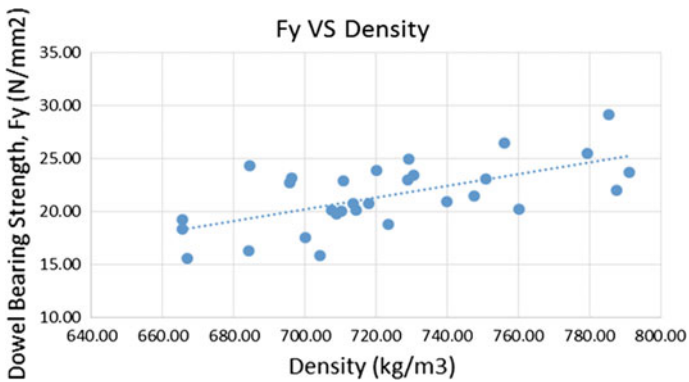
Fig. 12 Dowel-bearing strength versus density (specimens using 20 mm dowel diameter)

specimen volume. The results in terms of relation between dowel-bearing strength and density is similar with the results from Sawata and Yasumura (2002), Hubner (2008), and Ivan (2012).

4 Conclusion

Dowel-bearing strength of the Glulam Malaysian tropical timber, Mengkulang (*Heritiera* spp.) loaded perpendicularly to the glue line has been determined using 5 % diameter offset method according to ASTM 5764-97a, 2007. Dowel diameter is found to have influenced the dowel-bearing strength. When the dowel diameter increased from 16 to 20 mm dowel-bearing strength also increased. Percentage differences between the dowel-bearing strength using 16 and 20 mm dowel diameter is 20.82 %. Dowel-bearing strength obtained using BS EN 383 is found to

have higher value than the value obtained from the ASTM D 5764-97a. Density and moisture content of the Glulam Mengkulang with glue line species is found to have significant influence on the dowel-bearing strength.

References

1. A. Aghayere, J. Vigil, Wood Properties, Species and Grades: Factors Affecting Wood Strength. Structural Wood Design: A Practice-Oriented Approach, John Wiley & Sons, Inc., Hoboken, New Jersey, pp.12–16 (2007).
2. T.H. Yang, S.Y. Wang, C.J. Lin, M.J. Tsai, Evaluation of the Mechanical Properties of Douglas-Fir and Japanese Cedar Lumber and its Structural Glulam by Nondestructive Techniques. Construction and Building Materials 22 487–493 (2008).
3. E.C. Ozelton, Glulam Beams. Timber Designers Manual Third Edition, Blackwell Science Ltd, Oxford, pp.123–152 (2006).
4. W.H.W. Mohammad, M.A. Razlan, Z. Ahmad, Bending Strength Properties of Glued Laminated Timber from Selected Malaysian Hardwood Timber', International Journal of Civil & Environmental Engineering IJCEE-IJENS, Vol: 11 No: 04 (2011).
5. T.M. Wong, S.C. Lim & R.C. Chung, A Dictionary of Malaysian Timbers, Forest Research Institute Malaysia, Malaysia, Kuala Lumpur (2002).
6. G. Coste, The Assessment and Applications of a New Connector Type for use in Timber Structural Systems', Degree of Doctor Thesis, Edinburgh Napier University (2010).
7. R. Hassan, S. Ismail, A.A. Siblamurisi, I.A.A. Bakar, C.M.M. Isa, Effectiveness of Glass Fibre Reinforced Plastic (GFRP) for Dowel-Type Timber Connections, University Teknologi MARA (2009).
8. Awaludin, Ali, Smittakorn, Watanachai, Hirai, Takuro, Hayashikawa, Toshiro, Bearing Properties of Shorea Obtusa beneath a Laterally Loaded Bolt, Journal of Wood Science, 53(3), 204-210 (2007).
9. T.L. Wilkinson., Dowel Bearing Strength Technology MARA. (2014), Res.Pap. FRL-RP-505 Madison, WI: U.S. Department of Agriculture, Forest Service, Forest Products Laboratory, 9p. (1991).
10. D.R. Rammer, and S.G. Winistorfer, Effect of Moisture Content on Dowel -Bearing Strength, Wood and Fiber Science 33(1), pp.126-139 (1999).
11. D.R. Rammer, Effect of Moisture Content on Nail Bearing Strength, Res.Pap. FRL-RP-591. Madison, WI: US. Department of Agriculture, Forest Service, Forest Products Laboratory, 22p. (2001).
12. I.G.L.B. Eratodi, A. Triwiyono, A. Awaludin, T.A. Praytino, The Effect of Specific Gravity on Embedding Strength of Glued-Laminated Bamboo: Numerical Analysis and Experiment, Department of Civil and Environmental Engineering, Gadjah Mada University (2012).
13. R.J. Schmidt, Timer Pegs: Considerations for Mortise and Tenon Joint Design, Structure Magazine (2006).
14. U. Hubner, Embedding Strength of European Hardwoods, Graz University of Technology, Austria (2008).
15. K. Sawata, and M. Yasumura, Evaluation of Yield Strength of Bolted Timber Joints by Monte-Carlo Simulation (2002).
16. G. Ivan, Embedment Test on Wood for Dowel-Type Fasteners, Wood Research 57(4), 639-650 (2011).

17. Jumaat et al., The Determination of the Embedment Strength of Malaysian Wood, Department of Civil Engineering, University of Malaya (2006).
18. Jumaat et al., Development of Limit State Design Method for Malaysian Bolted Timber Joints, Department of Civil Engineering, University of Malaya (2008).
19. Awaludin et al., Bearing Properties of Shorea Obtusa beneath a Laterally Loaded Bolt, Journal of Wood Science,53(3),204-210 (2007).
20. Hassan et al., Effectiveness of Glass Fibre Reinforced Plastic (GFRP) for Dowel-Type Timber Connections, University Technology MARA (2009).
21. Hassan et al., Effects of Different Dowel Materialon Koompassia Malaccensis Bearing Strength, Faculty of Civil Engineering, University Technology MARA (2014).

Post-fatigue Behaviour of Kekatong Glued Laminated Timber Railway Sleepers

Norshariza Mohamad Bhkari, Zakiah Ahmad, Afidah Abu Bakar
and Paridah Md Tahir

Abstract The availability of good quality timber log is limited as well as the depleting supply of wide width and long-length structural-grade timbers caused increase in price. However, the usage of timber sleeper is significant to certain location in the track system. Consequently, alternative to replace existing timber sleepers to another timber product is vital and glued laminated timber (glulam) has a potential. Numerous researchers on glulam timber sleeper are focusing on the performance of static flexural study. However, the performance of glulam sleepers under the flexural fatigue is less known. Thus, this study leads to conduct flexural fatigue test in order to identify fatigue resistance of timber sleepers and investigate its behaviour. In addition, this study is carried out to determine the residual strength of timber sleepers after imposed with cyclic loading. A series of test were

N.M. Bhkari (✉)
Faculty of Civil Engineering, Universiti Teknologi MARA Pahang,
26400 Bandar Tun Abdul Razak Jengka, Pahang, Malaysia
e-mail: nshariza@pahang.uitm.edu.my

Z. Ahmad
Institute Infrastructure Engineering and Sustainable Management,
Universiti Teknologi MARA Malaysia, 40450 Shah Alam, Selangor, Malaysia
e-mail: zakiah@salam.uitm.edu.my

A.A. Bakar
Faculty of Civil Engineeering, Universiti Teknologi MARA Malaysia,
40450 Shah Alam, Selangor, Malaysia
e-mail: afida334@salam.uitm.edu.my

P.M. Tahir
Institute of Tropical Forestry and Forest Product (INTROP),
Universiti Putra Malaysia, 43400 Serdang, Selangor, Malaysia
e-mail: parida@putra.upm.edu.my

819

performed to determine the fatigue performance in accordance with the America Railway Engineering and Maintenance-of-Way (AREMA) Manual. The results showed that the *Kekatong* glulam sleepers complied with the requirement set by the AREMA Manual and the fatigue performance and behaviour are comparable to the solid timber sleepers.

Keywords Fatigue · Glulam · Heavy hardwood · Timber sleeper

1 Introduction

Timber sleeper has an effective and reliable performance in the railway track environment. There are more than 2.5 billion timber sleepers installed worldwide [1]. In Malaysia, as reported by Malaysian railway authority, *Keretapi Tanah Melayu Berhad* (KTMB), 26.4 % from a total track length of 1724.5 km has been laid with timber sleepers [2]. Timber sleepers are in high demand in USA with 13 million timber sleepers in service [3]. Other European countries, Asian countries and Australia, the use of timber sleepers are recorded but the figures are less compared to other sleeper materials [4].

There are certain sections in the railway track systems required to use these timber sleepers such as at bridges, tunnels, stations, yard and industrial lines and at the soil area contributing extreme shocks and excessive force to locomotives and sleepers [5, 6]. In these locations, the sleepers will be subjected to very high vibration compared to other location. At the pumping soil area, the ground base for the sleepers is soft and induced extra vibration. Meanwhile at yard, industrial line and station, the train is slowing down and produces high vibration due to the weight of the locomotives and the resistance of the brake. Timber is good in absorbing the vibration that comes from locomotives compared to steel and concrete.

However, the uses of solid timber sleepers in Malaysia are reduced mainly due to inconsistency supply of timbers. There are limited resources of the required naturally durable which comes from high grade hardwood timber namely, strength group 1 (SG1) and SG2. The existing solid timber sleepers require big section and the timber must be of *select and better* grade for naturally durable hardwood and *standard and better* grade for non-durable hardwood [7]. Hence from one timber log, only few sleepers can be obtained and these processes cause lot of wastages. Consequently, the solid timber railway sleepers are increasing in price because of depleting supply in large timber log. Thus, the alternative to replace the solid timber sleeper is necessary and the use of engineered timber product which is glued laminated timber or glulam is recommended.

The strength of glulam timber sleeper can be designed and controlled by removing or dispersing timber knot within layers or lamellas. With appropriate lamella configuration, the glulam timber sleepers are more homogeneous and

stronger with reliable properties compared to the existing solid timber sleepers. As in [8], the strength of glulam beam has been proven to improve into two grades higher from the original strength grade of medium hardwood timber. Although for naturally durable heavy hardwood timber, the strength of glulam timber is expected at least at par with the value of solid timber sleeper [2].

Studies in flexural test of glulam timber sleepers have shown that the performance is good compared to solid timber sleeper [9, 10]. However, there is an issue concerning the applications of glulam in their behaviour on fatigue [11] where glulam timber railway sleepers are subjected to millions of live load cycles over their design life. Glulam strength is generally assumed to be unaffected by fatigue in any structural design, but as railway sleepers it is not compromised. Thus, this study is aimed to assess the post-fatigue behaviour of *Kekatong* glulam timber sleepers after certain cyclic loading. The fatigue performance is determined after the flexural fatigue performance test had been conducted. This is required in evaluation of sleepers compliance set by the American Railway Engineering and Maintenance-of-Way Association (AREMA) Manual [12].

2 Fatigue Design Parameters

Fatigue can be determined as a failure that normally occurs after sufficiently high cyclic loading stresses [13]. In order to understand the performance under repeated or cyclic loading, fatigue testing is carried out on the structural components or materials. In fatigue testing, fatigue properties such as type of loading, frequency of cyclic, repetition and reversal of loading, number of load application cycles, temperature, moisture content and specimen size are important factors to observe the fatigue strength and the fatigue life, which contributed to the performance of the structural component [14].

Notable studies on fatigue performance of timber sleepers are limited. Therefore, some reviews on fatigue parameters for timber and timber composite are conducted. Reference [15] has studied the fatigue performance of solid timber railway sleepers. Eight numbers of treated Douglas fir timber sleepers are assessed in varies axle loads value with the cyclic frequency between 0.5 to 2 Hz. Test for every sleeper was conducted until failed and the S-N curve for the particular timber sleeper species was constructed. In [16], fatigue study was conducted in four-point flexural of two metres long of Nordic spruce glulam beam. The constant amplitude displacement with stress ratio, $R = 0.1$ and loading frequency of 10 Hz is performed in order to measure the fatigue performance for different angle of grain alignment that varied $0°–12°$. The test was stopped at two million load cycles or at the total rupture of beam. Sloping grain was shown to remarkably decrease in fatigue life of the beam.

Reference [13] summarised the fatigue life data of dried solid timber. However, the species of tested samples were not mentioned in the summary table. Two million cycles with 60 % of estimated ultimate static capacity was loaded into

four-point flexural test beam. The stress ratio for the test is 0.1 with the loading frequency of 8.33 Hz. For centre-point flexural test setup, the reverse loading, $R = -0.1$ with 40 Hz loading frequency and four million cycles is applied to the tested beam. The beam was loaded with 30 % from the ultimate static capacity.

In [17], the study was conducted for 6.7 m long Douglas fir composite-reinforced glulam beam applied at bridge girder. The beam was setup under four-point flexural loading and tested at 1–2 Hz loading frequency up to two million cycles. The stress ratio for the test is, $R = 0.33$. From the results, the beam girder with full-length and confined partial-length reinforced beam has adequate fatigue resistance and has favourably residual strength compared to the expected strength.

3   Material

Kekatong (*Cynometra* spp.) species were selected as prototype of glulam timber sleepers. The timbers are naturally durable, untreated and suitable for outdoor environment conditions having in SG2 [18]. The glulam sleepers were manufactured at a glulam factory in Johor Bahru. The timbers were visually graded in accordance with [19] by certified grader. Only timbers in HS grade were chosen and the production of glulam was done in accordance with [20]. The test specimens were graded again by certified grader as a function of railway sleepers and the grading is based on Section E in [7].

Two numbers of each *Kekatong* solid and glulam timber sleepers with size of 254 mm × 127 mm × 2000 mm length [21] were prepared for metre gauge [7]. The production of glulam sleepers were taken from normal and controlled manufacturing processes and the grain for all timber pieces are parallel to the longitudinal axis of the sleeper. Phenol-resorcinol formaldehyde (PRF) adhesive was used as recommended in [20]. All the test specimens were in dried condition and the study was conducted in normal room temperature.

4   Experimental Works

4.1   The Flexural Fatigue Performance Test of Kekatong Solid and Glulam Timber Railway Sleepers

The performance test is a test required to assess whether the sleepers comply with the requirements set by AREMA Manual [12]. There is specific section in this referred standard for the performance requirement for engineered timber sleeper. However, the detailed procedures for flexural fatigue performance test as in Sect. 2.2.4, AREMA Manual [12] for timber sleeper and engineered timber sleeper

are absent. Thus, the test procedures and setup for prestressed monoblock sleepers were modified and suited to the timber sleepers [22].

A series of the ultimate static flexural tests at rail seat were conducted on the timber sleepers before the flexural fatigue test is performed [2]. Table 1 shows the summary of the test results. These data are applied in the flexural fatigue test henceforward.

The centre-point flexural fatigue test was setup as accordance with AREMA Manual [12]. The fatigue test was conducted at the rail seat of sleepers under positive moment as shown in Fig. 1.

Figure 2 shows the schematic test setup at the rail seat of sleeper. In the procedures of flexural fatigue test, the pre-cracked static test is required before conducting the flexural fatigue test as mentioned in [12]. Fatigue failure is considered to occur in three phases where the first phase is crack initiation followed by crack propagation and finally failure takes place [23]. As the aim of flexural fatigue test is to assess the ability of sleepers to resist the repeated load, generally, the sleeper is recommended in the condition of pre-cracked. Thus, the sleeper can be examined under initiated cracked and observed the life of sleeper to survive the cyclic load.

The elastomeric supports are used during the pre-cracked static test and then replaced by the 8 mm thick plywood strips before conducting the flexural fatigue

Table 1 Summary of average ultimate flexural static test of Kekatong timber sleeper at rail

Type of sleepers	P_{ult} (KN)	Δ_{max} (mm)	P_y (KN)	Δ_y (mm)	MOR (N/mm^2)	Density (kg/m^3)	Moisture content (%)
Kekatong solid	407.96	22.39	284.69	13.50	106.23	988.00	16.53
Kekatong glulam	431.04	15.92	389.65	13.00	112.24	1041.92	9.98

Fig. 1 Flexural fatigue test setup at rail seat of sleepers
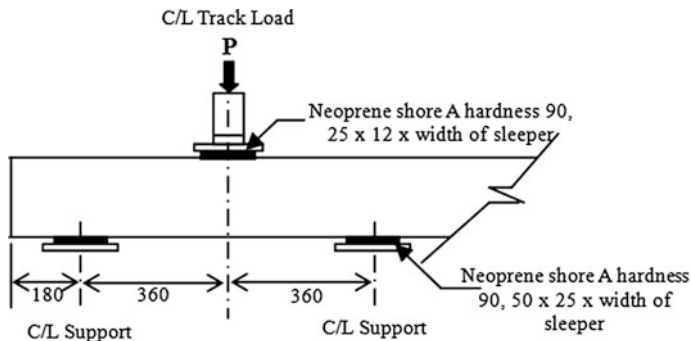
Fig. 2 Schematic diagram of test arrangement (in mm)

test. One 50 mm transducer was placed at mid-span of sleeper in order to measure the central displacement. The other two transducers were placed vertically near the both end of the sleeper for monitoring misalignment during the test. In the case of glulam sleeper, two 10 mm transducers were located horizontally at edge of sleeper in order to monitor misalignment of lamellas in tension and compression zones. All transducers were connected to the Kyowa UCAM 60B for pre-cracked static test Kyowa EDX-100A for flexural fatigue test.

For pre-cracked static test, the test was performed under a displacement control at a constant rate of 0.02 mm/s. The load was applied until the first crack occurred in the sleeper. Values for displacement and loads were then recorded. After removing the pre-cracked static load, the plywood strips were inserted at the supports replacing the elastomeric loading pads. The test rate for flexural fatigue test was set based on load control as discussed below. Further cracks were inspected and marked on the sleeper.

(1) *Determination of load spectrum*

In [23], two approaches were recommended in designing the load spectrum for the flexural fatigue test which is by determining from the highest load of actual static strength of sleeper or employing the maximum wheel load from the train types. Since there are no field measurement data on the actual train load, the load spectrum for this study was based on ultimate static load done in [2] as in Table 1. The flexural fatigue test was conducted in a load control setup where in each sinusoidal the maximum cyclic load is $1.1P$ [12]. The value of P was taken as 60 % from the ultimate static strength ($0.6\ P_{ult}$). Besides, the minimum cyclic load for this test was 10 % from the maximum cyclic load. Thus, the stress ratio was calculated as $R = 0.1$ where this study simulated the repetitive train loading pattern.

(2) *Number of load cycles*

In order to construct the S-N curve for the particular glulam data, the sleeper should be tested until failure. However, this approach was not feasible in this study because of limitations of the hydraulic testing equipment and took

longer time. In the absence of flexural fatigue study for the sleeper, a related timber and timber product studies were referred. Many researchers adopted the two million load cycles such in [13, 16, 17]. Thus, the tested sleeper was loaded for a maximum of two million load cycles. The S-N curve was not developed in this study and the results are based on the fatigue resistance under two million load cycles.

(3) *Cyclic loading frequency*

Previous studies have expressed the safe loading frequency for fatigue study in timber product as 1–5 Hz [14]. In Ref. [15], study on the bridge solid timber sleepers is conducted with 2 Hz. Other researchers performed 2 Hz cyclic loading frequency in their glulam and solid timber beam studies [13, 17]. According to AREMA Manual, the cyclic loading shall not exceed 600 cycles per minute [12]. Hence, the flexural fatigue in this study was conducted with 2 Hz for two million cycles and the estimated test duration is approximately 12 days and 12 hours.

4.2 The Ultimate Post-fatigue Load Test

The static test was conducted after the flexural fatigue test. In AREMA Manual, the sleeper would comply with the performance test if the sleeper can support the rail seat load of $1.1P$ without crack after the application of two million cycles [12]. However, this standard has not described duration of time for sleeper to support the required rail seat load. Hence, the AS1085.14:2003 is referred where the sleeper should be able to sustain the load at least for 3 min [24].

In order to determine the residual strength of sleeper after flexural fatigue, the ultimate static test was carried out for sleeper that survived in flexural fatigue test. Similar procedures are followed as in [2]. The load was applied until the sleeper had totally failed. Structural cracks were inspected and marked and the corresponding values of displacement and load were recorded.

4.3 Moisture Content and Density of Kekatong Glulam and Solid Timber Railway Sleepers

The moisture content and density of sleeper were determined by the oven-dry method. The sleeper was cut from the full crosssection with a thickness of 25 mm [25] after the ultimate post-fatigue load test.

5   Results and Discussions

5.1   The Flexural Fatigue Performance Test

In this flexural fatigue performance test, two (2) sleeper prototypes, each of solid and glulam timber railway sleepers were used. According to the test procedures in AREMA Manual, both types of timber sleepers complied with the performance requirement where the sleepers are able to sustain the required static load after imposed with two million load cycles. All sleepers were observed with no further crack from the earlier pre-crack. Thus, these sleepers are required for further investigation in order to determine the residual strength of sleeper after undergoing fatigue test.

5.2   Post-fatigue Behaviour of Kekatong Solid and Glulam Timber Railway Sleepers

The strength performances were compared between solid and glulam timber sleepers at the rail seats. Table 2 provides a comparison of the residual ultimate strength of the fatigued and non-fatigued sleepers. Solid timber railway sleeper shows a higher ultimate load for fatigued sleeper with 15 % greater than non-fatigued sleeper. However, for glulam timber sleeper the ultimate load for fatigued sleeper shows a small percentage of difference with 7 % lower than the non-fatigued sleeper. Consequently, the two million loading cycles did not cause any significant fatigue damage for glulam sleeper.

The ultimate post-fatigue strength for solid timber sleeper is 17 % higher compared to glulam timber sleeper. However, the glulam timber sleeper has 10 % load allowance before reaching the maximum load from the first cracked load compared to solid timber sleeper by 3 % load allowance. As an alternative to solid timber sleeper, the percentage difference of glulam timber sleeper is possibly

Table 2 Summary of average ultimate static of Kekatong timber sleepers at rail seat

Type of sleepers		P_{ult} (kN)	Δ_{max} (mm)	P_y (kN)	Δ_y (mm)	MOR (N/mm^2)	Density (kg/m^3)	Moisture content (%)
Kekatong solid	Without fatigue	407.96	22.39	284.69	13.50	106.23	988.00	16.53
	With fatigue	483.14	21.38	468.27	19.17	125.81	945.50	15.08
Kekatong glulam	Without fatigue	431.04	15.92	389.65	13.00	112.24	1041.92	9.98
	With fatigue	401.90	14.11	366.19	12.01	104.66	965.24	12.13

accepted. The manufacturing processes for glulam timber sleeper are required to improve as the good quality glulam production can provide better strength. In addition, further study on wood anatomy is feasible to understand the wood structure under densification after fatigue.

The modulus of rupture (MOR) for solid timber sleeper is slightly higher than glulam timber sleeper with percentage difference of 17 % after fatigue. The lower in MOR for glulam timber sleeper is possibly due to the numerous finger joints along the span. However, both types of sleepers showed that the MOR values exceeded the performance requirement of AREMA Manual with MOR of 66.9 N/mm^2 [12].

Table 2 presents the maximum displacement (Δ_{max}) and the displacement (Δ_y) at the first cracked load, P_y, at the rail seat. The maximum displacement under non-fatigued and fatigued condition is not significantly different for both types of sleeper. Figure 3 shows the graph of load and mid-span displacement of sleepers after applied with cyclic loading. Displacement under the 120 kN designed wheel load for normal train loading [6] is obtained from the regression line representing the solid and glulam timber sleeper. These displacements were compared with the average first cracked load displacements, Δ_y. It was found that the displacement for solid timber sleeper (9 mm) is higher than the displacement for glulam timber sleeper (2.7 mm). The displacement at first cracked load, P_y for solid and glulam timber sleeper are reached about 53 % and 76 % higher than displacement at designed wheel load, respectively. As a result, both timber sleepers in fatigue condition are marginally safe for designed wheel load before reaching the first crack. This behaviour is similar to the ultimate static test for the non-fatigue sleeper as discussed in [26].

The area under the graph as in Fig. 3 illustrated the ability of timber sleeper to absorb the energy before failure. Solid timber sleeper has larger area under the ultimate strength compared to glulam timber sleeper which indicates that the solid timber sustained a longer time before it failed. Glulam timber sleeper is expected to be brittle due to crack initiated in the finger joint during static test. Regression relationship for solid timber sleeper as given in (1) and glulam timber sleeper as in

Fig. 3 The flexural static strength after imposed by cyclic loading

Load versus Displacement for Kekatong Solid and Glulam Timber Railway Sleeper at Rail Seat

Glulam Timber Sleeper
Solid Timber Sleeper

$y = 0.554x^2 + 43.64x$
$R^2 = 0.993$

$y = -0.061x^3 + 2.293x^2 - 2.958x$
$R^2 = 0.996$

Wheel Load = 120kN

Load (kN)

Rail Seat Displacement (mm)
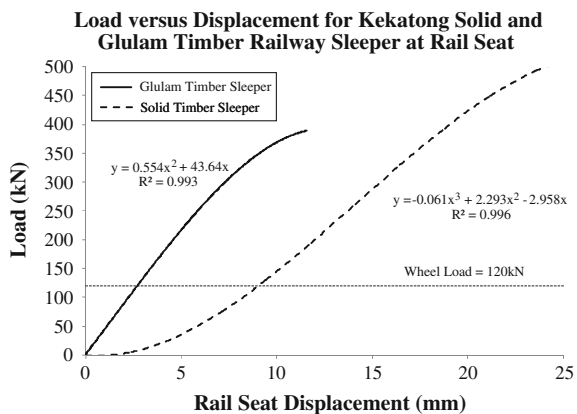
(2) are calculated based on the typical load (y) and displacement (x) data in static strength after fatigue and will be useful for further analysis.

$$y = -0.061x^3 + 2.293x^2 - 2.958x \qquad (1)$$

$$y = 0.544x^2 + 43.64x \qquad (2)$$

5.3 The Crack Pattern of Post-fatigue

Figures 4 and 5 show the crack patterns of solid timber sleeper and glulam timber sleeper respectively. For solid timber sleeper, the pre-crack occurred at the soffit of sleeper as in Fig. 4a at load of 471.68 kN. After two million cycles, there is no

Fig. 4 Condition of solid Kekatong timber at the rail seat
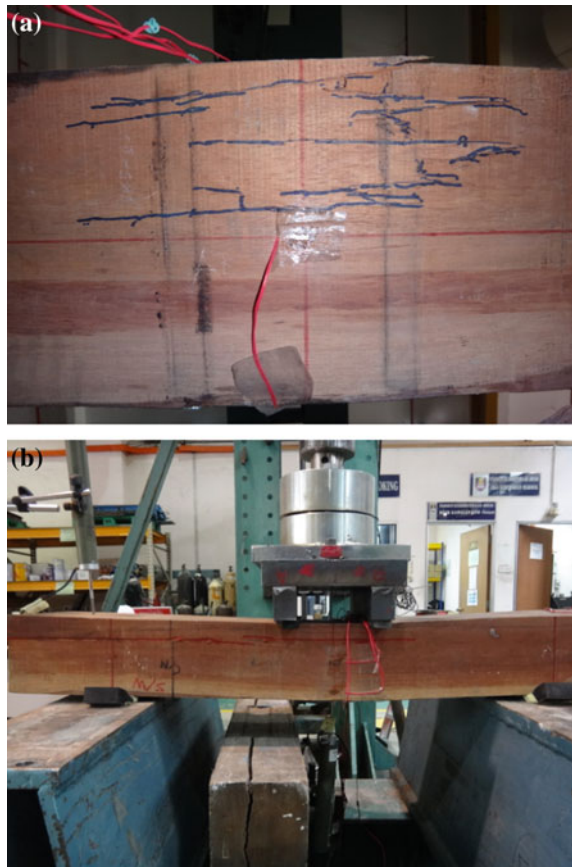
Fig. 5 Crack lines at rail seat of glulam Kekatong timber sleeper
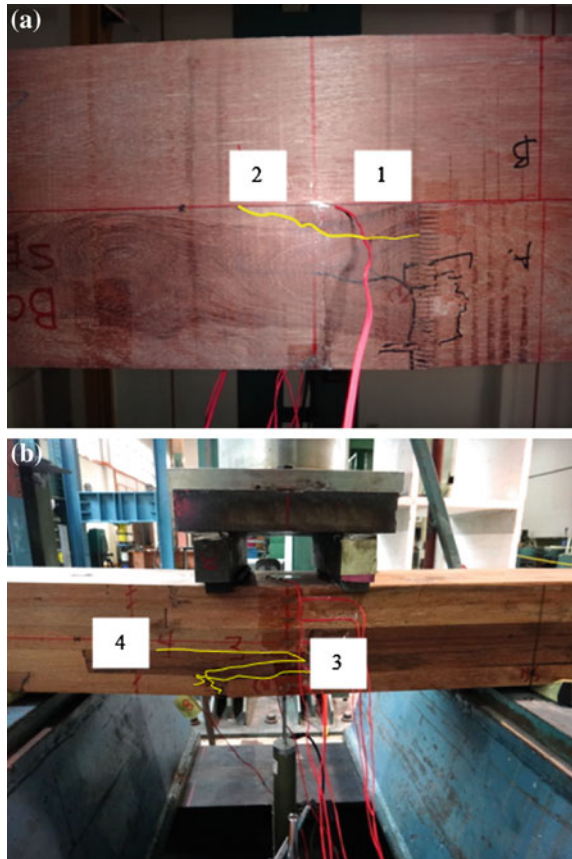
further crack observed. Figure 4b shows crack initiated at compression zone below the loading head and propagated to the end of sleeper in the ultimate static test.

For glulam timber sleeper, the pre-crack initiated at the finger joint located at outer lamella in the tension zone. Figure 5a shows the pre-crack with black mark. After the flexural fatigue test, no further cracks were observed and the sleeper was required for ultimate static test. In this test, the crack propagated from the pre-crack as marked with number 1 and continued to marking number 2 (refer Fig. 5a). Mark number 3 shows the crack at finger joint continued from the pre-crack at soffit of sleeper. This crack propagated to the second lamella as marked with number 4.

6 Conclusions

From the study, the following conclusions can be drawn;

1. In the flexural fatigue performance test, both types of timber sleeper show that no cracks occurred and complied with the performance requirement. The MOR values after flexural fatigue test for both types of sleeper exceeded the requirement set by AREMA Manual.
2. There is slight difference in percentage for ultimate load in glulam timber sleeper before and after fatigue indicating that the two million cyclic loading did not produce any significant fatigue damage.
3. The strength of glulam timber sleeper can be improved by controlling the quality of production.
4. Both types of timber sleepers surpassed the designed wheel load of 120 kN with higher percentage difference in displacement before reaching the first cracked load.

Further analysis will be conducted using the regression relationship for solid and glulam timber sleeper.

References

1. Ets Rothlisberger SA, "History and development of the wooden sleeper," 2008. [Online]. Available: www.corbat-holding.ch.
2. M. B. Norshariza, Z. Ahmad, A. A. Bakar, and P. Tahir, "Ultimate Strength of Kekatong Glued Laminated Timber Railway Sleepers," in *The International Civil and Infrastructure Engineering Conference 2013*, 2013, pp. 97–105.
3. "International Federation for Structural Concrete. fib bulletin 37: Precast concrete railway track systems, state-of-art report," Stuttgart, 2006.
4. W. Ferdous and A. Manalo, "Failures of mainline railway sleepers and suggested remedies - Review of current practice," *Eng. Fail. Anal.*, vol. 44, pp. 17–35, 2014.
5. International Union of Railways (UIC), "Sustainable wooden railway sleepers," France, 2013.
6. A. R. Mohamed, "Engineer of Permanent Way, KTMB in personal communication," 2012.
7. The Malaysian Timber Industry Board, *The Malaysian Grading Rules for Sawn Hardwood Timber*. Kuala Lumpur: Malaysian Timber Industry Board (MTIB), 2009.
8. W. H. Wan Mohamad, M. A. Razlan, and Z. Ahmad, "Bending strength properties of glued laminated timber from selected Malaysian hardwood timber," *Int. J. Civ. Environ. Eng.*, vol. 11, No.4, no. August, pp. 7–12, 2011.

9. E. V. M. Carrasco, L. B. Passos, and J. N. R. Mantilla, "Structural behavior evaluation of Brazilian glulam wood sleepers when submitted to static load," *Constr. Build. Mater.*, vol. 26, no. 1, pp. 334–343, Jan. 2012.

10. M. Gong, S. Delahunty, Y. H. Chui, and L. Li, "Use of low grade hardwoods for fabricating laminated railway ties," *Constr. Build. Mater.*, vol. 41, pp. 73–78, Apr. 2013.

11. M. C. Richie, "Fatigue Behaviour of FRP-Reinforced Douglas-Fir Glued Laminated Bridge Girders," The University of Maine, 2003.

12. AREMA, "Chapter 30, Volume 1 - Ties, The American Railway Engineering and Maintenance-of-Way Association (AREMA) Manual for Railway Engineering," USA: Washington, 2012.

13. Forest Products Laboratory, *Wood Handbook - Wood as an Engineering Material*, Centennial. Wisconsin, USA: United States Department of Agriculture Forest Service, 2010.

14. M. B. Enam, "Fatigue evaluation of structural composite lumber (SCL) T-beam bridge girders," Florida State University, 2008.

15. K. A. Soudki, S. H. Rizkalla, and A. S. Uppal, "Performance of bridge timber ties under static and fatigue loading," *J. Bridg. Eng.*, vol. 4, no. 4, pp. 263–268, 1999.

16. L. P. Hansen, "Experimental investigation of fatigue properties of laminated wood beams," in *The International Timber Engineering Conference London*, 1991.

17. W. G. Davids, E. Nagy, and M. C. Richie, "Fatigue Behavior of Composite-Reinforced Glulam Bridge Girders," *J. Bridg. Eng.*, vol. 13, no. 2, pp. 183–191, 2008.

18. MS 544: Part 2, "Code of practice for structural use of timber - Permissible stress design of solid timber," Malaysia: Department of Standards Malaysia, 2001.

19. MS 1714, "Specification for visual strength grading of tropical hardwood timber," Malaysia: Department of Standards Malaysia, 2003.

20. MS 758, "Glued laminated timber - Performance requirements and minimum production requirements (First revision)," Malaysia: Department of Standards Malaysia, 2001.

21. KTMB, "Technical Specifications," Malaysia: Keretapi Tanah Melayu Berhad, 2005.

22. S. H. Hamzah and K. Din, "Appraisal of used wooden railway sleeper," *J. Eng. Sci. Technol.*, vol. 3, no. 3, pp. 224–233, 2008.

23. A. A. Bakar, "Fracture mechanics analysis of prestressed concrete railway sleepers containing fibres," Universiti Teknologi MARA Malaysia, 2010.

24. Standards Australia, *Railway track material. Part 14: Prestressed concrete sleepers*. Australia: Standard Australia International, 2003.

25. MS 837, "Solid timber - Determination of moisture content (First revision)," Malaysia: Department of Standards Malaysia, 2006.

26. M. B. Norshariza, Z. Ahmad, A. Abu-Bakar, and P. Tahir, "Structural behaviour of Kekatong glued laminated timber railway sleepers under 'Sleepers static performance test,'" in *The 4th International Conference on Green Building, Materials and Civil Engineering (GBMCE) 2014*, 2014, pp. 45–49.

A Review on Structural Response of Hybrid Glulam-Cold-Formed Steel Roof Trusses

S. Ismail, A. Ibrahim and Z. Ahmad

Abstract The use of glulam technology, not only to enhance the strength of timber properties but also long span roof truss can be constructed. Long span timber structures can be quite heavy especially if using high density tropical timber. One possible way to reduce the weight of glulam roof trusses may be by combining or hybriding it with other materials such as steel. In order to predict the structural performance of this hybrid roof truss, finite element modeling will be used and validated using reduced-scale testing of 6.0 m hybrid roof truss and the values will be used to establish the design criteria. This paper presents the review on the related works and proposal of research work on hybrid roof trusses by means of glulam manufactured using Malaysian tropical timber which will focus on the assessment of the mechanical response of a bolted connection for hybrid glulam cold-formed steel roof trusses. The outcomes of the result would be useful as a reference for further research and the design of hybrid truss system using glulam and cold-formed steel section.

Keywords Hybrid truss · Structural response · Glulam · Joints system · Malaysian tropical timber

S. Ismail (✉) · Z. Ahmad
Faculty of Civil Engineering, Universiti Teknologi Mara (UiTM),
Shah Alam, Selangor, Malaysia
e-mail: sarina.jkr@1govuc.gov.my; sarinaisma@gmail.com

Z. Ahmad
e-mail: azmii716@salam.uitm.edu.my

A. Ibrahim
Institute for Infrastructure Engineering and Sustainable Management (IIESM),
Universiti Teknologi Mara (UiTM), Shah Alam, Selangor, Malaysia
e-mail: zakiah@salam.uitm.edu.my

833

1 Introduction

Currently, there are two types of prefabricated roof trusses namely prefabricated timber roof trusses and prefabricated steel roof trusses. Nowadays the usage of prefabricated roof truss system gives more challenges to the construction industry because of the materials used for the roof truss systems either for timber or steel cold-formed. This problem is added with the lack of quality assurance practiced for both of prefabricated roof trusses which can be seen by a few incidents of roof collapses in the country. With the collapse experiences and depleting supply of timbers, there is a need for the industry to use more reliable timber product.

Currently, the limited supply of high grade timber has been scarce due to depletion and reduction of timber supply from the natural forest [1]. For structural components, the timbers used need to at least come from strength grouping 4 (SG4) based on Malaysian Public Works Department for roof trusses specification. With tight supply and rising demand, this would require sustainably sourced timber to be considered as the primary construction material. Timbers in lower strength groupings are cheaper and easily available as they can be harvested much earlier than higher grade timber. In order for these timbers to be used as structural members, they have to be engineered to enhance the strength properties. This can be done using Engineered Timber Product (ETP) technology such as glued laminated timber (glulam) or laminated veneer lumber (LVL).

At present, in Malaysia, these two types of ETP are available. Structural ETP have been extensively used in developed countries particularly America, Europe, UK, Australia, Canada, New Zealand, China, and Japan. However, in Malaysia these products have not been applied widely even as roof truss system. In fact, a few researches have been carried out locally showing that these products are more homogenous, dimensionally stable, and the strength of these products are higher than the solid timber of the same species [2–4]. Study by Wan Mohamad et al. [5] on the glulam beam from Malaysian hardwood timber showed that the performance of glulam has improved two grades higher than the solid timber. For example, when solid timber is in strength, grouping SG6 was used to make glulam; the strength grade of glulam can go into SG4. However, the previous research only studied on the mechanical properties made of hardwood timber but none of them studied the performance of glulam as roof truss system.

Other researchers using softwoods proposed with other material such as fiber and plate as composite structure in order to modify the initial properties and performance of the structure [6]. Timber can be very flexible under loads, keeping strength while bending, and is incredibly strong when compressed vertically. Timber is much weaker in compression perpendicular to the grain than in compression parallel to the grain. Timber exhibits its greatest strength in tension parallel to the grain. Cross grain of any kind materially reduces the tensile strength of timber, since the tensile strength perpendicular to the grain is only a small fraction of that parallel to the grain. In general, tensile strengths in tangential and radial directions are very low compared to the longitudinal strength, about 3 and 5 %,

respectively [7]. By converting solid timber into glulam, not only to improve the performance of the timber but also to obtain large span structure without jointing with metal connectors. Therefore, glulam usually used for large span structure such as for roof trusses for sport complex or convention center.

Roof trusses system can be built in steel, timber, aluminum alloy, in spans up to 60 m, even more when required. To reduce area of roof to be covered and prevent excessive internal volume, the pitch is designed in low height for very large spans of roof [8]. Vandenberg [9] claimed that trussed rafters have a span up to 10 m, fink truss up to 10 m, double fink truss between 5 and 14 m. When the span for the roof trusses is long and carries roof load, the glulam trussed members can be deep and thick, hence heavy. One of the ways to reduce the weight of trussed structure is by combining with light material which is steel for the webs and this system is called hybrid truss. The combination of glulam and light steel would give better performance than single material. This can be done by placing glulam as top and bottom chords and steel as webs [10].

Generally, a truss construction consists of top chord, bottom chord, and webs. Truss chords are generally subjected to a combination of bending and compression or bending and tension stresses. Moreover, designing the same cross-section using hardwood glulam for all members in truss system will lead to a heavier truss system. This is due to the density of the tropical timber which is higher than softwood timber being used in the foreign countries. According to Budio et al. [11] the weight of light steel roof truss is lighter than the timber roof truss. Therefore, in order to reduce the weight of glulam roof trusses, by hybriding it with steel web may solve the problem. According to Fridley [12], the flexibility of timber, together with the special characteristics of other materials can significantly create economical and efficient hybrid structure. Before this, hybrid system can be introduced to the construction industry, testing needs to be done on the stability and integrity of the system, as well design values need to be established.

The hybrid truss in this research will be defined as two different material combined together to form a truss system, which is top and bottom chord made of glulam section whereas cold-formed steel section will be used as web members. All members in the truss system are connected to each other by metal plates or bolts. Currently designed connection system is crucial and the information of this connection is still lacking. Therefore, there is a need to study and observe the performance of hybrid ETP roof truss system. This research is conducted to achieve specific objectives as follows:

(i) To analyze behavior of hybrid truss joints in isolation for web member to chord arrangements for bolts and nuts connection, using Finite Element (FE) analysis.
(ii) To investigate experimentally the behavior of limited joints in isolation for web member to chord arrangements for bolts and nuts connection.
(iii) To determine the performance of hybrid roof truss using FE method for full scale and reduced scale.
(iv) To evaluate experimentally the performance of reduced-scale hybrid roof truss assemblies.

2 Literature Review

2.1 *Introduction*

Prefabricated roof trusses is a triangular timber structures, which are built in a factory then shifted to construction site. Nowadays, there are two types of prefabricated roof trusses available in local market. Solid timber and steel prefabricated roof trusses. They are installed using crane after the building's wall has been framed. Nowadays 80 % buildings construction used prefabricated roof trusses instead of traditional rafters. The greatest benefits of using prefabricated roof trusses are cost saving, construction speed, and ease of installation. In recent years, the use of prefabricated roof trusses are becoming popular because they allow flexibility and complexity in designing of roof structures.

The use of light gage construction material has been recently highlighted by Public Works Department Malaysia, especially in replacing timber for roof truss system for most of the government projects. Therefore, cold formed steel section, which has proven to be efficient and widely used in developed countries is a good alternative to traditional timber truss system. Consequently, the used of cold formed section have shown tremendous increase in demand.

2.2 *Glulaminated Timber (Glulam)*

Glulam is manufactured by bonding up together graded sawn timber laminations using structural adhesives. The thickness of each layer of the laminations may not exceed 50 mm, glued together under pressure using structural adhesives. Normally, a commercially graded timber has the limitation in its length, however by converting it into glulam timber, the shorter length of timber can be joined to any required length. In Malaysia, the process of glulam manufacturing may follow MS 758:2001 and the design is in accordance of MS544 Part 3:2001.

Structural glulam member and element have been largely used in developed countries namely America, Europe, Canada, and Japan. The building constructed including sports complexes, commercial buildings, churches, bridges arch, and houses used glulam members either in straight or curved form. In Malaysia, glulam just started to gain interest to be used in the construction. However, the Crops for Future (CropFur) building construction fully utilizes glulam in the country. At present, the building built using glulam are Galeri Glulam and Masjid FRIM. However, the unique design of Galeri Glulam in Johor Bahru has been acknowledged by the Malaysia Book of Records as the first building completed using glulam.

Glulam has an advantage of virtually unlimited flexibility in shape and size. Beside the flexibility in its shape and size, glulam member can also be manufactured in horizontally laminated with loadings applied to the wide face of

laminations, or vertically laminated. However, the horizontal method is easier to produce curved member. This method disperses timber defects more efficient and also allowing higher design stresses [13]. Moreover, for bending member that have a higher stress on the top and bottom member, glulam timber has the advantage in enhancing its strength. This can be achieved by replacing part of the upper and lower member with layer from higher strength of timber species [4].

A few studies on Light Red Meranti has been made by Ahmad [14], who reported on the suitability for making structural members such as beam. The manufacturing of glulam beams made from Light Red Meranti is suitable and could be used as structural component in heavy construction. This research has been done to investigate the various properties, factors affecting ultimate strength, method of preparation, and testing of glulam. However, very few studies have been done to evaluate the mechanical and physical properties of glulam beam using local species. Abu Bakar et al. [4] ha carried out the researches regarding the factor affecting the ultimate strength of solid and glulam timber beams made up of Meranti Rambai Daun and Dark Red Meranti. Although the researchers used different species of timber, for example, the use of White Meranti (*Shorea* spp.) and Kedondong (*Canarium* spp.), the researches of glulam done were on the beams. None of the researches were done in roof truss system.

2.3 Hybrid Roof Truss

Hybrid construction refers to the method of combining one or more material to another material [10]. However, the hybridization techniques can be done at component level or at the building level. For examples, hybrid construction at component levels is hybrid slab, hybrid beam, hybrid column, and hybrid post tension joint. Building level are hybrid frames, hybrid steel and wood frames, and hybrid trusses. When combining glulam and steel, designer should consider the advantages and limitation of each material and optimally utilize them. However, in this study the focus is only on the hybrid glulam cold formed roof trusses. Some advantages of hybrid timber-steel construction are enhanced seismic performance, better fire resistance, cost savings, and increase in sustainability [10].

However in-depth understanding of the properties of each material is essential for designing a hybrid roof truss structure. The designer should know and understand the properties of each material and in what context each of them perform better. Timber is green and oldest structural materials, non-homogeneous, and orthotropic biological material. The strength of timber is due to the direction of load transfer relative by the direction of the grain. Since timber is naturally occurring, its structural properties are virtually important to practice engineer in evaluate the structural behavior and strength of timber member and elements. Table 1 shows the approximate material properties for Cold-formed C-channel and Mengkulang-Glulam to be used in finite element model.

Table 1 Material properties for glulam and cold-formed to be used in *Fe* model

Item	Material properties for glulam and C-channel		
	Properties	Mengkulang-glulam	Cold formed C-channel
1	Elastic modulus (N/mm^2)	17276.50	200000
2	Poison's ratio	0.2	0.3
3	Yield strength (Mpa)	–	350
4	Density (kg/m^3)	693	7800
5	Young's modulus (N/mm^2)	8.164E3	–

Timber is an anisotropic and nonhomogeneous material. The strength behavior of timber is linear elastic depending on the direction of the load applied. The strength of timber is represented in three directions of the member that are longitudinal, radial, and tangential. The longitudinal direction is equal to the parallel to grain direction, and the tangential and radial directions are both referred to as the perpendicular to grain direction. Timber is strongest when a load is applied in a direction parallel to the direction of timber grain, and weakest when the load is perpendicular to the direction of the timber grain. The strength of timber in compression parallel to the grain is normally stronger than compression perpendicular to the grain and has a zero strength in tension perpendicular to the grain. According to Slavid tensile strengths in tangential and radial directions are about 3 and 5 %, and approximately very low compared to the longitudinal strength [7]. The approximate compressive strength of steel in the range of 400–1000 N/mm^2 and concrete in the range of 20–40 N/mm^2. Steel is isotropic material, due to this fact its properties are same in any direction. Steel performs well in tension [10].

The strength of timber largely depends on its moisture content. Moisture content is referred to as the percentage amount of moisture in a piece of timber. As the moisture content increases up to certain level where all the free water has been dissipated, the timber strength decreases and when the moisture content decreases, the timber strength increases. The loses of moisture content are depending on the environmental conditions to where the timber member is exposed. Although this increases and decreases of moisture content may cause some strength reduction due to shrinkage of the timber fibers. The extent of shrinkage condition may effects changes in dimension and the presence of water in combination with other conditions can cause decay.

2.4 Roof Truss Jointing System

Jointing system for any structure is usually very small portion relative to the supported member, but they are a very critical. The dowel-type fasteners (bolt, nail, dowel) are one of the most popular types of joints in timber construction since they are easy to use, relatively cheap, and available everywhere. In order to apply

dowel-type joints efficiently the important thing to understand is their mechanical behavior when undergoing the load. The mechanical response and behavior of timber joints involved in flexibility and rigidity is governed by a number of geometric, material properties, and loading parameters [15]. In general, timber joints system greatly depends on dowel type, timber density, and properties and arrangement of loading.

According to Aghayere and Vigil [16] there are three basic options for connection: use a pre-engineered connector; use the design equations and use the connector capacity tables. Several types of connectors are available, but only bolts connector will be covered in this research. Bolts have the highest strength but required most labor. Moreover, bolts connection is one of the example of mechanical fastener that forms timber joints through a laterally loaded dowel action. However, Trayer examined the bolted joints and different joints configuration on the several timber species [17]. Finally, this result has been addressed as a basis of the empirical design data for UK permissible stress design codes. In 1949, Johansen [18] published his major work on the numerical simulation for predicting the yield and ultimate load of doweled joints. Whale and Smith [19] extended this work by performing an extensive testing program into the load-embedment response of doweled joints. They concluded that there was a good correlation between the embedment response and density of timber. Similar experimental techniques have been employed shall be integrated into current testing that will be adopted for this research.

Johansen had reported a new and convenient model to examine the yield strength of joints which is called European Yield Model (EYM). Due to this model, the strength of the joints greatly depends on embedment strength of timber and yield moment of the dowels. The completed research and investigation on the embedment strength of softwood, hardwood, plywood, and tempered hardboard with nails and bolts are done by Smith et al. [19]. In 1991, Wilkinson [20] had pointed the effect of the specific gravity, a diameter of the dowel, and direction of the loading. His research focused on bolts and nails of various diameters with several hardwood and softwood species. Rammer had demonstrated the embedment strength based on an analysis of variance [21]. Davis and Claisse [22] performed the embedment test on bolted joint to solid timber, glulam, parallam, and microlam. Effect of moisture content on the embedment strength had also been studied [23]. Japanese Pine and diameter offset test method are being conducted by Sawata and his co-workers and reported that the differences are between 5 %. The nonlinear model based on Johansen theory gives the approximate strength of bolted joints [24]. Although, various researches have performed the investigation on the embedment strength and characteristics of timber with dowel-type fasteners, but this study does not fully extensive to Malaysian hardwood timber.

Although the research is popular worldwide, the scenario in Malaysia is different. Only one research on the embedment strength of Malaysian timber is available as they are conducted locally. The embedment strength tests were conducted on three species of Malaysian hardwoods from various joints groups and densities, i.e., Kempas (*Koompassia malaccencis*), Mengkulang (*Heritiera* spp.),

Table 2 The embedment strength and dowel diameter for malaysian hardwood timber [25]

Dowel φ	Embedment strength for Mengkulang		
	Percentage different (%)	f_h, Eq. (1) (N/mm^2)	f_h, exp (N/mm^2)
6	2.16	62.64	61.29
8	2.63	60.88	59.28
12	3.30	57.34	59.23

and Pulai (*Alstonia* spp.) [25]. Surprisingly, none of the research is done on the embedment strength of glulam using Malaysian hardwood species.

Bolted joints has been largely used in modern glued laminated timber (glulam) structures, such as column-beam structures, glulam frames, glulam trusses, glulam arches, cable-glulams, and so on. However, bolted joints in structural timber composites had the capacity to give strength and stiffness properties at least comparable to a solid timber of similar density. The positioning of a bolted connection on the glue line of a glulam member does not affect the joint. In contrast, Davis and Claisse [22] concluded that the embedment strength of timber materials that is used in the design of timber joints greatly depends on the timber density.

According to Jumaat et al. [25] the equation of the embedment strength for Malaysian hardwood is $f_h = 0.103(1 - 0.013d)\rho$ ([25] Eq. (1)). Table 2 shows the summary of the embedment strength and dowel diameter for Malaysian hardwood species Mengkulang. The glulam and solid timber results are comparable, so that the embedment strength for Mengkulang (Table 2) can be used as a guideline in design stage. However, this behavior needs further investigation since the embedment strength of timber materials that is used in this research is largely dependent on timber density and dowel diameter. Moreover Davis and Claisse [22] also had concluded that the glue line had no major effect on joint strength or stiffness, in fact the stiffness, and slip at maximum load was much less variable in the glulam.

The flexibility of the joints in timber trusses depends greatly on the selected type of connections. Since the flexibility of bolts differs from the flexibility of nails or dowels, the complete joint flexibility largely depends on the selected type of fastener. While fastener dimensions (diameter, length) represent a second factor, the number and disposition of the fasteners in the connection constitute a third one. According to Masse and Salinas [26], the truss was analyzed for three types of joint conditions: joints assumed pinned, joints assumed rigid, and joints assumed to have some axial and rotational stiffness. Masse and Salinas claimed that a good correlation was obtained between the theoretical and experimental joint stiffness behavior, and between the analog model using semi-rigid joints and the full-scale truss tests. Due to this fact the truss member forces were obtained from the calculation that exactly represented the actual member forces.

The behavior and mechanical properties of single-bolted steel-glulam-steel joint subjected to a load parallel to the grain had been studied by Stehn and Börjes [27]. He found that the failure modes, stiffness, ductility, and bearing capacity of the single-bolted steel-glulam-steel joints under the load parallel to the grain are mainly influenced by the thickness of the glulam and the diameter of the bolt. The failure

mode of the joints changes with the variation of the glulam thickness and the bolt diameter. According to this fact, the bearing mode should be suitably selected in design according to the thickness of the glulam and the diameter of the bolt.

According to Claisse and Davis [26], the use of high performance jointing systems has the potential to reduce the volume of timber used in structures such as roof trusses. He had studied four different jointing systems which are suitable for large timber sections which is bolted joints, resin-injected doweled joints, shear-plate connector joints, and GRP reinforced joints. Claisse and Davis also recommended the shear plates and the glass-reinforced joints as the best and high performance jointing system. Bolted joints and shear-plate connector easy to produce, but this joint does need special cutter.

Stehn and Börjes [27] had studied the effect of the ductility of the connection on the load-carrying capacity of the glulam roof trusses. Finally, they proposed a method how to calculate load-carrying capacity of truss from the appearance of a nail load-displacement curve. In timber structures, the directions of bending cannot be considered to act as a ductile material. Therefore, this is important for practice engineers to design connections carefully to avoid brittle failure modes. The ability of connection to deform and redistribute loads to other members commonly called as ductility. The ductility for a statistically indeterminate structure largely depends on the failure mode of the connection and its ability to generate plastic hinges in the dowels and embedding failure in the timber. This means that more ductile behavior, up to a certain level, will produce a higher load-carrying capacity. Haller pointed that the relationship between strong and ductile behavior is consistent with the requirements for a timber connection design with optimized load-carrying capacity and ductility [28].

Vallee et al. had considered the numerical Finite Element Analysis (FEA) and experiment approach for doweled and bonded joints timber roof trusses [29]. The experimental results showed that the bonded trusses are much stiffer and higher, and the capacity increases with the embedment length. Figure 1 shows the load-displacement curves of timber-steel joints for embedment length 120 mm in

Fig. 1 Load-displacement curves of bonded timber-steel joints (embedment length 120 mm) in comparison to doweled timber joints [29]
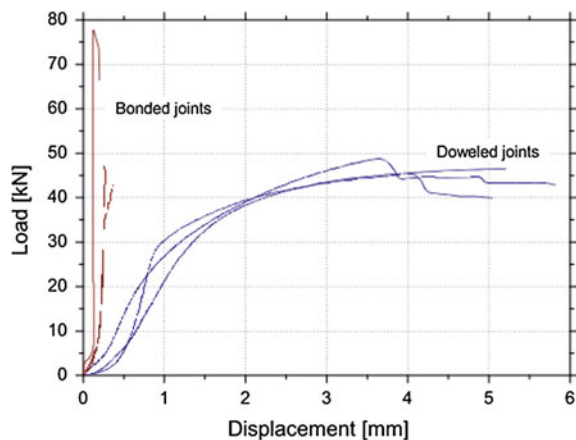
Fig. 2 Typical stress pattern around a dowel, for a doweled timber joints [29]
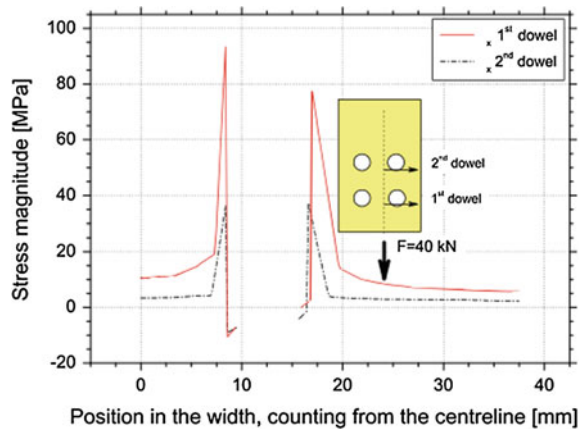
comparison to doweled timber joints. FEA which allowed the stress-strain state of the structure and approved that the stress pattern induced by the mechanical fastener leads to generate the peaks stress, as shown in Fig. 2. They highly recommended for a complex system such as joints and trusses to be investigated by using FE software packages. Due to this fact the hybrid roof truss in this research will be investigated by using Finite Element software and validation by the experiment of 6 m reduced-scale hybrid roof truss.

3 Methodology

This research will investigate the performance of a hybrid glulam truss which is expected to reduce the self-weight of roof truss system and investigate the performance of a hybrid glulam roof trusses as a structural element. The hybrid roof truss is obtained by combining a glulam section with cold-formed steel in the truss system as shows in Fig. 3. This research will assess and evaluate the mechanical response of structural members using theoretical and laboratory testing. The experimental values will be corroborated using finite element analysis and then will be used to construct the design criteria. Reduced-scale tests on the truss will be made to verify the numerical analysis, and consequently the analysis model will be develop using different parameters such as span of the truss and the arrangement of bolts on the connection. The overall procedure of the research is represented in flow chart (Fig. 4) comprises of main stages as described below: FEA analysis of joint, testing of joint connection, model validation, reduced-scale testing and analysis, FEA analysis of full-scale hybrid truss.
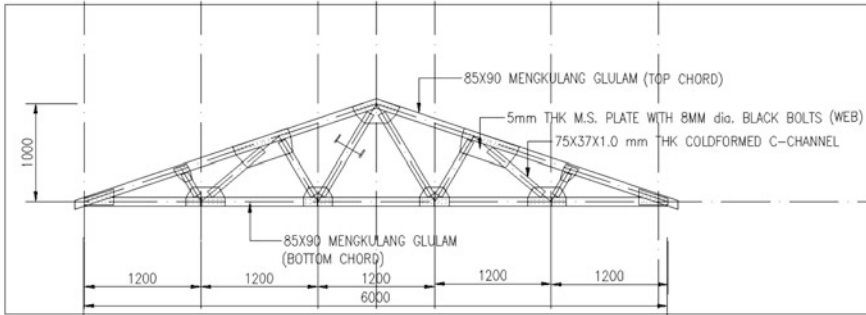
Fig. 3 The hybrid roof truss configuration
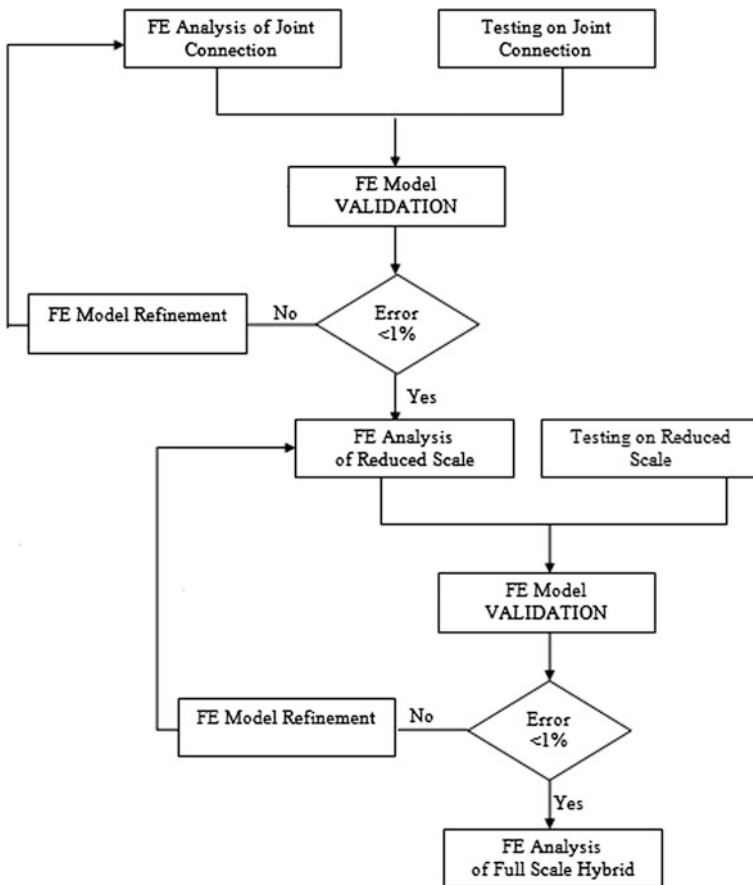
Fig. 4 Flowchart of research methodology and testing

4   Expected Outcome

This research is expected to give contribution of new data for preparation of design manual for a hybrid glulam cold-formed steel truss. This research will give opportunities and flexibility in designing roof trusses with a combination more than one material in truss system. It is expected from the research that it will provide significant information and performance such as strength and jointing system which can contribute to the preparation of hybrid glulam roof trusses manual. It is expected from the research that good agreement between numerical simulation and experiment in terms of load-displacement curves indicated that the simulation is an accurate and effective way of evaluating the mechanical properties of the hybrid roof truss system. This will increase the products that meet the concept of industrialized building system (IBS), green building, sustainable constructions material, and also as an alternative to replace existing prefabricated roof truss.

5   Conclusion

Hybrid construction is the method of combining one or more material to another material. When combining glulam and steel, designer should understand the properties, behavior, and limitation of each material and consider the advantages of each material in the design stage. However, in-depth understanding the properties and also jointing system are essential for designing a hybrid roof truss structure. The undetermined of the overall behavior of hybrid or composite timber roof trusses can result in incorrect in design, conservation of structural component and most frequently, on their replacement. So that Hybrid roof truss needs a more precise knowledge of the real response and behavior to determine internal loads and loads path.

References

1. Maskayu, MTIB, 2012.
2. Ahmad, M. Glue laminated timber beam from light red meranti (Shorea Spp) Research paper. Institut Teknologi Mara.1997.
3. H'ng, P.S. Basic engineering properties of laminated veneer lumber from tropical timber species. Ph.D. Thesis, Faculty of Forestry, Universiti Putra Malaysia, 2003.
4. Abu Bakar, S., Abd Latif, S., Zainai, M. Factor affecting Ultimate strength of solid and glulam beams. Journal Kejuruteraan Awam. Universiti Teknologi Malaysia, 2004, 16(1), 38–47.

5. Wan Mohamad, W.H, Ahmad, Z., Tan, Y.E., Abd Jalil, A. Bending strength of glulam from selected Malaysian hardwood timber, World Conference of International Journal of Civil Engineering, 2012.
6. Issa, C, Ziad, K. Advanced wood engineering glulam beams. Journal of Material in Civil Engineering, 2005, 14(2),91–96.
7. Slavid. R. Wood Architecture, London Laurence King Publishing Ltd, 2005, pp 239.
8. Foster, J. S. Structure and Fabric, Part 1 and Part 2, The Mitchell Publishing Company Limited, London, 1983.
9. Vandenberg, M. AJ Handbook of Building Enclosure, The Architectural Press, London, 1974.
10. Khorasani, Y. Feasibility study of hybrid wood steel structures, Master of Applied Science dissertation, Faculty of Graduate Studies, University of British Columbia, 2011.
11. Budio, S.P., Cahya, I., Wibawa, K.G. Selection on roof structure model of timber, lightweight steel and conventional steel due to gravity load. International Journal of Academic Research, 2011, 3(4), 487–489, Baku. Azerbaijan.
12. Fridley, K.J. Wood and wood-based materials: Current status and future of a structural material. Journal of Materials in Civil Engineering, 2002, 14(2), 91–96.
13. Abbot, A.R and L.R.J Whale. An overview of the use of glued laminated timber (glulam) in UK. Journal of Construction & Building Material, 1987, 2, 104–110.
14. Ahmad, M. Glue laminated timber beam from light red meranti (Shorea Spp). Research paper. Institut Teknologi Mara. 1997.
15. Santos, C.L., de Jesus, A.M.P., Morais, J. J.L., Lousada, J.L.P.C., 2010: A comparison between the EN 383 and ASTM D 5764 test methods for dowel-bearing strength assessment of wood: Experimental and numerical investigations. Strain 46(2): 159–174.
16. Agheyere, A and Vigil, J. Structural wood of design, A practice-oriented approach using the ASD method. Book. John Wiley & Son New Jersey. 2007.
17. Trayer, G. W. 1932. The bearing strength of wood under bolts. Technical bulletin No. 332. USDA Forest Serv., Forest Prod. Lab., Madison, WI.
18. Johansen, K.W., 1949: Theory of timber connections. International Association for Bridge and Structural Engineering. Bern, Switzerland, Publication No. 9: 249–262.
19. Smith I., Hilson, B. O. Whale. L. R. J. and Pope, D. J., Characteristic Properties of Nailed and Bolted Joints under Short-term Lateral Load. Part 3: Analysis and interpretation of embedment test data in terms density and related trends. Journal of Institute of Wood Science, 1987, 11(2), pp. 65–71.
20. Wilkinson, T. L., Dowel Bearing Strength. Research Paper FPL-RP-505. USDA Forest Service, Forest Product Laboratory, Madison, WI, 9 pp. 1991.
21. Rammer, D. R.. Parallel-to-grain Dowel-Bearing Strength of Two Guatemalan Hardwoods. Forest Product Journal, 1999,49(6) pp. 77–87.
22. Davis, T.J, Claisse, P.A. Bolted joints in glulam and structural timber composites. Construction and Building Materials, 2000,14, 407–417.
23. Rammer, D. R. and Winistorfer, S. G.,. Effect of Moisture Content on Dowel-bearing Strength. Journal of Wood and Fiber Science, 2001, 33(1), pp. 126–139.
24. Sawata, K. and Yasumura, M. Estimation of Yield and Ultimate Strengths of Bolted Timber Joints by Nonlinear Analysis and Yield Theory. Journal of Wood, 2003.
25. Jumaat, M. Abu Bakar, A. Mohamad Razali, F. Abdul Rahim, A.F. Othman, J. The Determination of the Embedment Strength of Malaysian Hardwood, Research Paper, University Of Malaya, 2003.
26. Massse, D.I, Salinas, J.J. Analysis of timber trusses using semi-rigid joints. Canadian Agricultural Engineering, 1987, 111–124.

27. Stehn, L., Börjes, K,. The influence of nail ductility on the load capacity of a glulam truss structure. Engineering Structures, 2004, 26(6), 809–816.
28. Haller, P. Progress in timber joint development and modelling Proceedings of 5th World Conference on Timber Engineering, Montreux, Switzerland, 1998, 1. 336–43.
29. T. Vallée, T. Tannert, and S. Hehl, "Experimental and numerical investigations on full-scale adhesively bonded timber trusses," *Mater. Struct.*, vol. 44, no. 10, pp. 1745–1758, 201.

The Joint Strength of Timber Connected with Adhesively Bonded-in GFRP Rod

Zakiah Ahmad and Reza Andasht Kazeroon

Abstract This paper reports the investigation made on the timber beam jointed with adhesively bonded-in pultruded rod into timber by using a various parameters such as different types of timber (Keruing and White Meranti) and number of rods. The aim of this study is to determine the best configuration of the joint by varying the number of rods. Pull-out tests of bonded-in rod specimens were conducted (at parallel and perpendicular to grain) in order to determine the shear strength capacity of the adhesively bonded-in joint. Meanwhile the tensile tests of jointed beam were conducted for determining the joint strength of the beam jointed with adhesively pultruded rods. The tests were conducted in accordance with ASTM D5764: 1995. The limitations of this study are; rod size is 8 mm and glueline thickness is 2 mm based on previous study. The shear strength of the bonded joint increases as the density increases. For tensile test, the results show that as the number of connectors increase, the joint capacity also increases.

Keywords Jointed strength of timber · Adhesively bonded-in rod · GFRP rod · Keruing · White Meranti · Tropical hardwood

1 Introduction

One of the important aspects in the design part of every single structure whether is made of concrete, steel or timber is the connection between members, which is to link up and to carry a function of distribution key of load. In timber structures, joints,

Z. Ahmad
Institute for Infrastructure Engineering and Sustainable Management (IIESM),
Universiti Teknologi Mara, Shah Alam, Selangor, Malaysia
e-mail: zakiah@salam.uitm.edu.my

R.A. Kazeroon (✉)
Faculty of Civil Engineering, Universiti Teknologi Mara,
Shah Alam, Selangor, Malaysia
e-mail: reza.andasht@gmail.com

and connections frequently represent the weakest points. An inadequate design is responsible for their mechanical behavior and many failures in structure, in particular their stiffness, which plays a crucial role in stress distribution in the structure. Timber joints are often less effective than corresponding joints in steel. For example, timber joint has relatively low embedding strength and low strength of wood in shear, particularly in tension perpendicular to grain [1]. The selection of connections is based on type of joint, type of materials, required strength capacity, and many more. The design of connection must achieve the safe limit or satisfaction without causing splitting, cracking, or excessive deformation of structure components.

In timber structure, the common connection comes in two types which are mechanical joint and adhesive joint. Mechanical joint is widely used as connection which is divided into two general fastener types which are dowel and bearing type connection. Dowels which transmit either lateral load or withdrawal load present such as nails, screws, and bolts while bearing type present when there is existence of shear plate and split ring connectors whereby it is able to transmit shear forces through bearing on the connected part of a structure.

Timber connected with dowel type fasteners is usually made of steel. The disadvantages of steel are not only it reduces the volume of the fastener, but also chemically deteriorates the adjacent wood due to corrosion or oxidation while reducing its strength [2]. The degradation of metallic fasteners is still a problem and it is for this reason, among others, that nonmetallic fasteners as well as adhesive bonding are becoming increasingly attractive for joining timber.

There is a lack of information with little publications available of bonded-in timber connections manufactured using Malaysian tropical timber but joint using steel dowel has been well established. Since the use of steel as fastener has introduced problems in the timber joint, there is a need to look at alternative materials. This study is exploring the potential of glass fiber reinforced plastic (GFRP) rod as the dowel but embedded it with adhesive. This type of joint is called adhesively bonded-in rod. The usage of sustainable materials has been taken with great initiative for the implementation in the design and construction works. There are many researches that have been explored very extensively in European countries, United Kingdom, and Canada which investigating more on their timber. A little knowledge of this method is mainly on strengthening of timber beams by using steel plate and fiber plate. They have found that GFRP rods are able to replace the steel dowel type connection and this will reduce the dependency on steel [3]. In order to use GFRP dowels as connector, adhesive has to be used. The adhesive is used to improve the stiffness and the strength of connection and also to prevent the connected timber from squeaking [4].

Glueline thickness is an important parameter because it allows the performance increment for a better strength [3]. The effect of glueline thickness has been studied by Harvey [5] towards connection strength. The dispersion of stress developed in the glueline is caused by the size of adhesive or wood interface increase where the pull-out failure load of the joint increases as the glueline thickness increases. Harvey [5] recommended that 2 mm glueline thickness gives the best result for epoxy adhesive.

There are many parameters set in order to carry out an investigation of timber member jointed with adhesively bonded-in GFRP rod into timber such as timber species, adhesive types, embedded length, rod diameter, rod length, and glue line thickness. Hence, more studies can be carried out to identify the behavior of the timber member connected with the rod. In this study, timber beams connected with bonded-in rods by varying the timber species and number of rods were constructed in order to evaluate the effectiveness of the connection.

2 Experimental Procedures

2.1 Material

Keruing and White Meranti from strength group 5 (SG5) in accordance with Malaysian grading rule were used for this study. The timbers are sponsored by Malaysia Timber Industry Board (MTIB). The timbers have been visually graded as select and better by MTIB's grader. The timbers have been cut using horizontal bend saw machine and drilled using radial drilling machine according to specified test required.

The rod used was glass fiber reinforced plastic (GFRP) rod supplied by Sika Malaysia. The diameter of the rods was 8 mm and the length was cut for 120 mm as shown in Fig. 1. The rods were sandpapered using coarse sandpaper and degreased with ethanol to remove the contamination such as dirt and oil from machinery and human hands in order to have a good bonding between the adhesive and rods.

Sikadur-30 was used as adhesive to create bonding between timber and rod. It is a viscous polymer modified which is self-leveling, fast drying cementitious screed. The adhesive was prepared according to the manufacturer's instruction. It was a two-part resin based adhesive (Part A) and hardener (Part B). Mixture of Part A and Part B was manually mixed until well blended for about 5 min using steel knife at a constant rate to avoid air bubble entrapment.

Fig. 1 Schematic diagram of pull-out samples with dimension; **a** perspective view, **b** side view
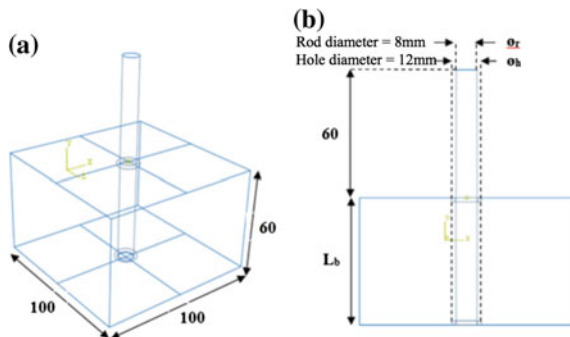
Fig. 2 Pull-out specimens for
Keruing and White Meranti
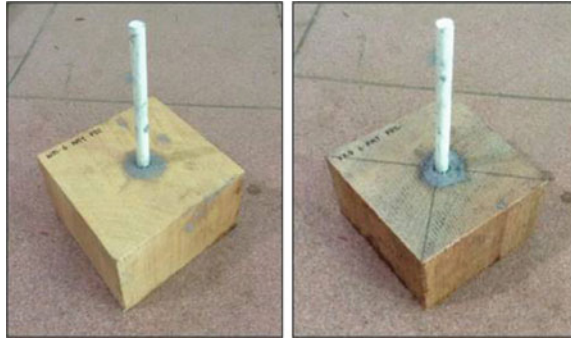
2.2   Sample Preparation for Pull-Out Test

Timber specimens for pull-out test were prepared in the size of $100 \times 100 \times 60$ mm. The blocks were cut in two grain orientations, parallel and perpendicular to grain to determine the effect of grain orientation on the shear strength of bonded-in rod into timber. Hole was drilled in the block at parallel to the grain and perpendicular to the grain with a diameter of 12 mm to insert 8 mm rod with 2 mm glueline thickness which is the best performance of the study stated by Harvey [5]. The hole was lightly clean to remove any wood residue. The adhesive prepared earlier was injected into the hole using a gun. Then, the rod was slowly pushed in and gently rotated to squeeze out the adhesive without causing the air void. Two O-rings were placed at the bottom and top of the hole to keep the rods in center. All specimens were cured in a temperature control room at 28 °C for 10 days. Figure 2 shows the prepared pull-out specimens.

2.3   Sample Preparation for Timber Beam Jointed with Bonded-in Rod

Figure 3 shows the specimens' dimensions for timber joint with bonded-in rod and actual specimen to test. Two specimens for timber jointed with bonded-in rods were prepared by connecting two pieces of timber in size of $50 \times 100 \times 500$ mm using one and two bonded-in rod of 8 mm diameter, respectively. The length of rods was 140 mm. 12 mm holes were drilled into the timbers to allow 2 mm glueline.

2.4   Pull-Out Test Method

The pull-out block specimens were placed in the jig as shown in Fig. 4 and gripped using universal testing machine (UTM). The load was applied to pull out the rods with the rate of crosshead of 1 mm/min according to ASTM D5764: 1995. Ten

Fig. 3 Dimension of specimen for timber joint with bonded-in rod; **a** side view, **b** top view with one rod, **c** top view with two rods, **d** actual specimen with one rod
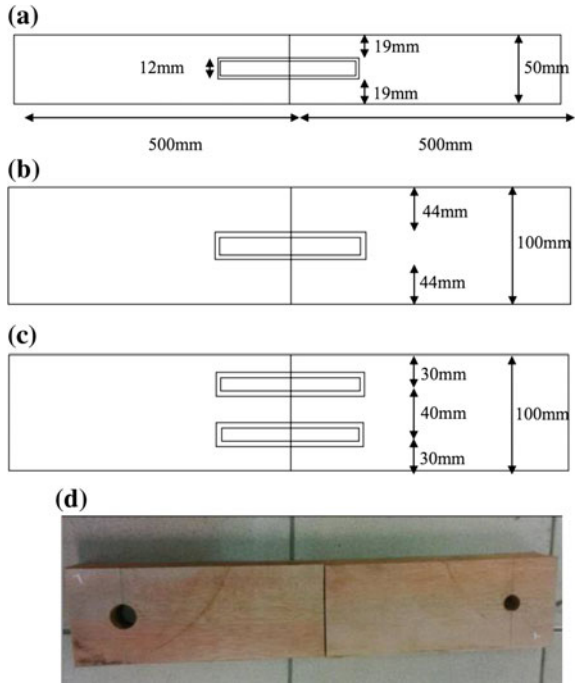
Fig. 4 Pull-out test setup for timber block with bonded-in rod

specimens for each species, Keruing and White Meranti were prepared for two different orientations.

Since there were different interface areas, the shear strength was calculated based on shear surfaces. Shear strength or pull-out strength for adhesive to timber interface is denoted as τ_{ta} and shear strength for adhesive to rod interface is denoted as τ_{ra}.

The pull-out strength or shear strength of bonded-in rod into timber was calculated by the following equations.

Timber to Adhesive interfaces;

$$\tau_{ta} = \frac{P_{max}}{\pi L \phi_{hole}} \tag{1}$$

Rod to Adhesive interfaces;

$$\tau_{ra} = \frac{P_{max}}{\pi L \phi_{rod}} \tag{2}$$

2.5 Tensile Test Method for Timber Beam Jointed with Bonded-in Rod

The jointed beam samples were subjected to axial load in tension parallel to the grain. The tests were performed using universal testing machine equipped with 1000 kN load cell for timber jointed with bonded-in rods as shown in Fig. 5.

Fig. 5 Test setup for tensile test on timber jointed with bonded-in rod

Both ends of the specimens were drilled to insert the steel rod of size 18 mm in order to grip the specimens with the clamp. The load was applied at a constant rate of 1 mm/min until failure according to ASTM D5764: 1995. The design or permissible pull-out strength is given in EN 1995-2: 1997 is depend on the density of the timber, bonded length, rod diameter, and holes diameter as shown in Eq. 3.

$$R = \pi \, d_{\text{equ}} l_i f_v \tag{3}$$

where,

d_{equ} min $(d_{\text{hole}} 1.25 \, d_{\text{rod}})$
l_i glued-in length
f_v Shear strength of wood-adhesive interface
      $= (1.2 \times 10^{-3})(d_{\text{equ}-0.2})(\rho^{1.5})$
ρ density of timber

Based on Eq. 3 which stated earlier, the shear strength of pull-out rod is calculated as bellow:

where,

d_{equ} min $(d_{\text{hole}} 1.25 \, d_{\text{rod}})$ = min (12, 10) = 10 mm
l_i 60 mm

For Keruing,
ρ 830 kg/m^3
f_v $(1.2 \times 10^{-3})(d_{\text{equ}-0.2})(\rho^{1.5})$ = 18.105
R 34.127 kN

For White Meranti,
ρ 700 kg/m^3
f_v $(1.2 \times 10^{-3})(d_{\text{equ}-0.2})(\rho^{1.5})$ = 14.023
R 26.433 kN

2.6 Moisture Content

As the properties of timber are very much dependent on the moisture content (MC) of timbers, the moisture content of the specimens at the time of test was determined. The MCs were determined in accordance with MS837. Each specimen was cut into 50 × 50 × 50 mm in size with five replicates. All specimens were weighed to obtain the initial weight put into the oven with temperature of 100 °C. All specimens were left in the oven for 24 h then, they are weighed to obtained dry

weight. The moisture content percentages were obtained using the formula stated in equation.

$$\text{Moisture content} = \frac{\text{Moist weight} - \text{Dry weight}}{\text{Dry weight}} \times 100\,\% \qquad (4)$$

3 Results and Discussions

3.1 Shear Strength of Timber Bonded-in with GFRP Rods Parallel and Perpendicular to the Grain

The pull-out strength of bonded-in rods was used to investigate the shear strength of bonded-in rod timber connections. This test most closely simulates a bonded-in connection under load. All specimens failed in adhesive failure at rod-adhesive interface as shown in Fig. 6.

The average shear stresses at the adhesive to timber and rod to adhesive interfaces were calculated using Eqs. 1 and 2 stated earlier and the results are shown in Tables 1 and 2 for various orientation of timber.

For pull-out test parallel to grain, the shear strength for Keruing is higher than White Meranti by 44 %. Keruing and White Meranti are in the same strength group

Fig. 6 Failure mode of pull-out test specimen
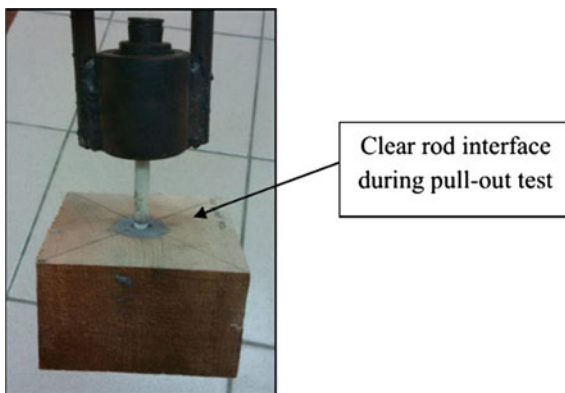
Table 1 Pull-out strength for GFRP rod parallel to the grain of timber

Type of timber	P_{max} (kN)	Shear stress, τ_{ta} (MPa)	Shear stress, τ_{ra} (MPa)
Keruing	9.66	4.3	6.4
White Meranti	5.43	2.4	3.6

Table 2 Pull-out strength for GFRP rod perpendicular to the grain of timber

Type of timber	P_{max} (kN)	Shear stress, τ_{ta} (MPa)	Shear stress, τ_{ra} (MPa)
Keruing	14.05	6.2	9.3
White Meranti	10.64	4.7	7.1

Fig. 7 Load versus displacement for GFRP rod parallel to the grain
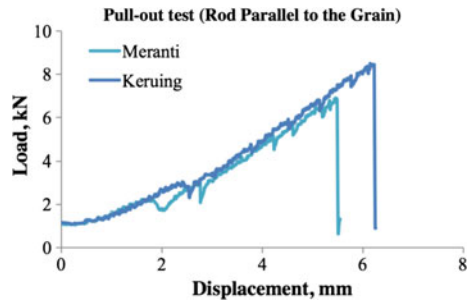
but with the different densities of timber. The result of shear strength shows a relationship between density and shear strength of timbers. It seems that the timber with higher density has higher shear strength. The shear strength of bonded-in rod for perpendicular to the grain also showed the same trend. The shear strength of Keruing is higher than the shear strength of White Meranti by 24 %.

Figures 6 and 7 show the behavior of shear strength of pull-out test through load versus displacement graph in different orientations of timber. These figures show the same trend for both Keruing and White Meranti except that the maximum load and displacement which Keruing shown is higher than White Meranti. This illustrated that the area under the graph of Keruing is bigger than the area under the graph of White Meranti. This indicated Keruing requires more energy to pull out the rod from the timber, which means it has higher shear strength compared to White Meranti (Fig. 8).

Fig. 8 Load versus displacement for GFRP rod perpendicular to the grain
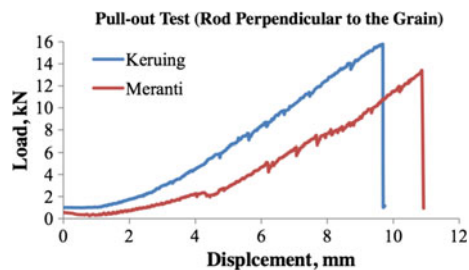
Table 3 Joint capacity for 1 embedded GFRP rod connection

Type of timber	Density (kg/m^3)	MC (%)	P_{max} (kN)	F_{adm} (kN)
Keruing	32.0	11.1	8.6	34.1
White Meranti	26.4	11.4	6.2	26.4

Fig. 9 Load versus displacement for 1 embedded GFRP rods connection
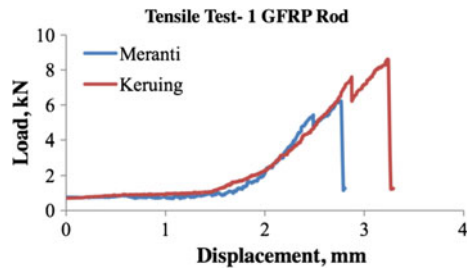
3.2 Joint Capacity of Timber Jointed with Bonded-in Pultruded Rod

3.2.1 Bonded-in One Rod

Table 3 shows the joint capacity of timber jointed with one bonded-in pultruded GFRP rod together with the design value. For Keruing, the value of joint capacity shows 30 % higher than the joint strength of White Meranti which reflected well with the load versus displacement graph (Fig. 9). On the other hand, the joint capacity for both species jointed with one bonded-in rod is lower by 75 and 77 % of design joint capacity.

3.2.2 Bonded-in Two Rods

Table 4 shows the joint capacity for two embedded GFRP rods connection meanwhile the Fig. 10 shows the load versus displacement graph for timber jointed with two bonded-in rods joint.

For this joint, there are no much differences in the joint capacity of both timbers. The load versus displacement graph (Fig. 10) also shows that the area under the graph is about the same with the graph of Keruing shifted to the right. The joint

Table 4 Joint capacity for 2 embedded GFRP rods connection

Type of timber	Density (kg/m^3)	MC (%)	P_{max} (kN)	F_{adm} (kN)
Keruing	32.0	11.1	13.5	17.1
White Meranti	26.4	11.4	13.3	13.2

Fig. 10 Load versus
displacement for 2 embedded
GFRP rods connection
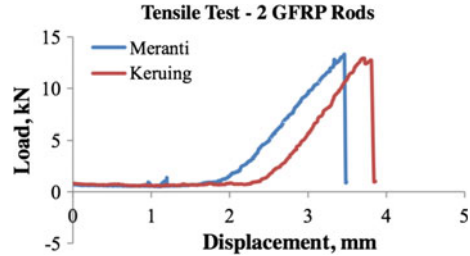
Tensile Test - 2 GFRP Rods

capacity for Keruing was 21 % lower than the permissible load. However, the joint capacity for White Meranti has similar values as the permissible joint capacity.

The results show that Keruing and White Meranti samples with bonded-in one rod have 57 and 71 % less joint capacity, respectively, compared to the case of using two number of pultruded rods. As the number of rods increases the joint capacity increases. At this point of investigation, it seems the number of rods play important role in increasing the joint capacity and not the density.

3.3 Failure Modes of Jointed Timber

The failure mode of the specimens was observed for tensile tests. The failure mode of tensile test specimens was also same with the failure mode of pull-out test. The failures were found clearly at the interface of the rods. The photos of the failure were not shown here.

It can be seen that there was weak adhesion between the adhesive and GFRP rod even though surface preparation has been made to aid bonding with GFRP rod. However, to achieve sufficient adhesion between rod and adhesive, threaded rods can be used rather than smooth rods which are clearly stated by Johansson et al. [4].

4 Conclusions

The result of this research can enhance the understanding on the joint strength properties of Malaysian tropical timber jointed with bonded-in rod. The results are summarized as follows;

- For pull-out test parallel to grain, the shear strength for Keruing is higher than White Meranti by 44 and 24 % higher when the rod is embedded perpendicular to the grain. In this case, density plays an important role.
- For timber beam jointed with one bonded-in pultruded GFRP rod results in Keruing achieved 30 % higher strength compared to White Meranti but both strengths are lower design joint capacity by 75 and 77 %, respectively.

- For timber beam jointed with two embedded GFRP rods there are no much differences in the joint capacity of both timbers. The joint capacity for Keruing was 21 % lower than the permissible load. However, the joint capacity for White Meranti has similar values as the permissible joint capacity.
- Keruing and White Meranti timber beams bonded-in one rod have 57 and 71 % less joint capacity, respectively, compared to the case of using two number of pultruded rods. As the number of rods increase the joint capacity increases. At this point of investigation, it seems that the number of rods play an important role in increasing the joint capacity and not the density.

References

1. H. J. Larsen, "Introduction: Fasteners, Joints and Composite Structures," In: Thelandersson S, Larsen H J - Timber Engineering. Ed. by S. Thelandersson, H.J. Larsen, Wiley & Sons, Chichester, 2003.
2. W. S. Thompson, "Adverse environments and related design consideration – chemical effect in Structural uses of wood in adverse environments," Edited by R.W. Meyer and R.M. Kellog. Van Nodtrand Reinhold Company, New York. pp. 117–130, 1982.
3. C. R. Walker, F. S. Fonseca, J. P. Judd and P. R. Thorley, "Tensile Capacity of Timber-Frame Mortise and Tenon Connections," 10th World Conference on Timber Engineering (WCTE), Miyazaki, Japan. 2008.
4. C. J. Johansson, T. Pizzi and M. Van Leemput, "Wood adhesion and glued products," Working group 2: Glued wood products. State of the art report. Glued wood products. COST Action E13, 1st Edition, 2002.
5. K. Harvey, "Improved timber connection using bonded-in GFRP rods. PHD thesis, University of Bath, United Kingdom. 2003.
6. Z. Ahmad, "Nano- and Micro-particle filled epoxy-based adhesive for in-situ timber bonding," PHD thesis, University of Bath, United Kingdom. 2007.
7. G. Mays and A. R. Hutchinson, "Adhesive in engineering," Cambridge University Press, Cambridge. 1992.
8. G. Davis and C. J. Mettem, "The use of resin adhesives in the repair of structural timber members," Structural studies, repair and maintenance of historical buildings, S. Sanchezbeitia and C. A. Barebbia (ed.), Advances in Architecture Series 3, Comp. Mech. Ltd, Southampton, pp. 531–540. 1997.
9. M. Davis and D. Bond, "Principles and practices of adhesive bonded structural joints and repairs," Int. J. Adhesion and Adhesives, pp. 19, 91–105. 1999.
10. L. J. Hart-Smith, "Design of adhesively bonded joints," In joining Fibre-Reinforced Plastics, F. L. Mattews, (ed.), Elsevier Applied Science Publishers Ltd. 1987.
11. R. J. Bainbridge, C. Mettem, K. Harvey and M. Ansell, "Bonded-in rod connections for timber structures- Development of design methods and test observation," International Journal Adhesion and Adhesives, pp. 22, 47–79. 2002.
12. R. J. Bainbridge and C. J. Mettem, "Bonded-rods for timber structures," Towards a European basis for structural design. Adhesive in timber systems, Society of Chemistry Industry, London. 1990.

13. G. P. Anderson, S. J. Bennet and K. L. De Veries, "Analysis and testing of adhesive bonds," Academic Press, New York. 1997.
14. J. G. Broughton and A. R. Hutchinson, "Effect of timber moisture content on bonded-in rods," Construction and Building Materials. pp. 15, 17–25. 2001.
15. J. G. Broughton and A. R. Hutchinson, "Efficient timber connection using bonded-in GFRP rods," Composite Construction, Figueiras et al., A Balkema, Rotterdam, ISBN 90-5809-260-7, pp. 275–280. 2001.
16. E. Gehri, "Ductile behaviour and group effect of glued-in steel rods," In: S. Aicher, H.W. Reinhardt - Joints in Timber Structures, RILEM Publications, Paris, pp. 333–342. 2001.
17. J. L. Hart-Smith, "Further developments in the design and analysis of adhesively-bonded structural joints," Doughlas Aircraft Report No. 6922, Long Beach, CA, USA. 1980.

The Effect of Span Lengths on the Bending Strength Properties of Glued Laminated Timber Beam

**Reza Andasht Kazeroon, Zakiah Ahmad
and Norshariza Mohamad Bkhari**

Abstract This paper presents the effect of span length on the bending strength properties of glued laminated (glulam) timber beam using tropical hardwood timber namely Mengkulang (*Heritiera* spp.). The timbers have been visually graded according to MS 1714:2003 and the glulam manufacturing followed MS 758:2001. Four-point bending tests were conducted according to ASTM D198:2009. The moisture content and specific gravity of the test pieces were investigated following MS 837:2006. The failure characteristics were also analysed and reported. The results showed that the modulus of elasticity increases as the span length increases. The failure occurred mostly at the finger joints.

Keywords Bending strength properties · Glued laminated timber · Glulam · Mengkulang · Tropical hardwood

1 Introduction

Glued laminated timber, generally known as Glulam, is a type of structural timber products including numerous layers regarding dimensioned timber bonded combined with durable, moisture-resistant structural adhesives. Individual pieces superbly selected using dimensioned and also strength ranked timber within controlled production conditions, the grain for many pieces essentially parallel towards longitudinal axis from the member [1–3].

R.A. Kazeroon (✉) · N.M. Bkhari
Faculty of Civil Engineering, Universiti Teknologi Mara,
Shah Alam, Selangor, Malaysia
e-mail: reza.andasht@gmail.com

Z. Ahmad
Institite for Infrastructure Engineering and Sustainable Management (IIESM),
Universiti Teknologi Mara, Shah Alam, Selangor, Malaysia
e-mail: zakiah@salam.uitm.edu.my

Glulam construction has an extended lifestyle throughout European union given that early 1826 specifically throughout Britain, France, Germany, Sweden and Switzerland as well as accompanied by United States throughout 1934 and later by other western countries [4]. Glulam has been used as a heavy structure material on the manufacturing of bridge, stadium and dome structure [4–7] in some developed countries such as United States and Japan; since then, many research works have been done related to this industry.

Glulam offers many advantages if compared to solid-sawn timber. By combining small components of solid timber, the larger cross section and also the longer length involving structural grade timber could be manufactured. In architectural perspective, glulam solid timber provides free of charge column space and has aesthetic price either throughout straight in addition to curve order, and most often left exposed to be a decorative element in building construction. In comparison with solid wood, glulam demonstrates many advantages for instance improved strength and stiffness properties [8].

Glulam has been used in many applications, including headers or support beams in residential framing to major structural elements in roof framing of domed stadiums with span length over 500 ft (150 m). Glulam might be produced in any size and desired shape, including large, long-span straight beams to complex curved-arch configurations [9].

It has been accepted that the beam apparent strengths are influenced by timber sizes or dimensions. Bohannan [10] investigated the effect of beam size and derived the size factor based on Weibull weak link theory. This theory relates the apparent strength of a beam to its volume and assumes beam strength is governed by tension failure.

Studies have shown that the tensile strength of defect-free specimens decreases strongly with increasing length of the specimens [11–14]. Their findings indicate that the strength depends on the cross-sectional area rather than span length. For clear bending specimens, the strength was reduced by the size effect [15, 16].

Chudziński [13] tested beams with different lengths, resulting in higher bending strength values for longer beams. Schneeweiß and Felber [17] reported the work done by [10] whom investigated the effect of length of using 343 and 210 Douglas fir beams tested with centre point loading at span lengths of 36 and 46 mm, respectively, and resulted in average bending strength values of 91.4 and 92.1 N/mm^2. According to [15], in general the bending strength decreases with increasing span length which is independent of the loading configuration (centre loading, two-point loading, and third-point loading).

In the design of timber structures, there is adjustment factor for this effect. At present, the size effect for timbers either solid or glulam as stated in Malaysian standard adopted British standard which is based on softwood with no validation when using Malaysian hardwood timbers. This may introduce error in the design. Therefore, this study investigated the effect of span lengths on bending strength of glulam using Malaysian tropical timber.

2 Experimental Procedures

2.1 *Manufacturing of Glulam Sample*

The glulam beams were manufactured at a glulam factory in Selangor, Malaysia in accordance with MS 758:2001 [18]. The timber species used was Mengkulang (*Heritiera* spp.) and has been visually graded prior to the glulam manufacturing. The glulam pieces were graded visually in accordance with MS 1714:2003 [19] and classified into hardwood structural (HS) grade. Timbers used were dried to the required moisture content in the range of 8–15 %.

Phenolic resorcinol formaldehyde (PRF) Prefere 4001 with slurry hardener Prefere 5837 W obtained from Dynea NZ Limited was used to join the finger joints and laminate the glulam beams. PRF is a durable liquid–liquid system suitable for the manufacturing of structural finger joints and laminates the glulam species. The properties of Prefere 4001/5837 W are shown in Table 1. As recommended by the manufacturer, the mix ratio of adhesive is 2.5 parts resin to 1 part hardener slurry by weight.

A series of beams with different lengths were prepared. The dimension of the beams is shown in Table 2. Five replicates were prepared for each beam.

2.2 *Test Method*

Bending tests on full size Mengkulang glulam beams were performed at the Civil Faculty of Universiti Teknologi Mara. The experiment was carried out with large

Table 1 Properties of Prefere 4001/5837 W

Appearance	Viscosity at 25 °C	Specific gravity at 25 °C	Solid content	pH
Red-brown liquid, free from foreign material	16,000–20,000 mP	1.145–1.165	56–60 %	9–10

Table 2 Dimension of glulam beams

Beam length (m)	Dimension (mm)	
	Width, b	Depth, h
6	100	300
	130	300
8	100	400
	130	400
10	100	500
	130	500
12	100	600
	130	600

NOTED: T1, T2 and T3 are transducers
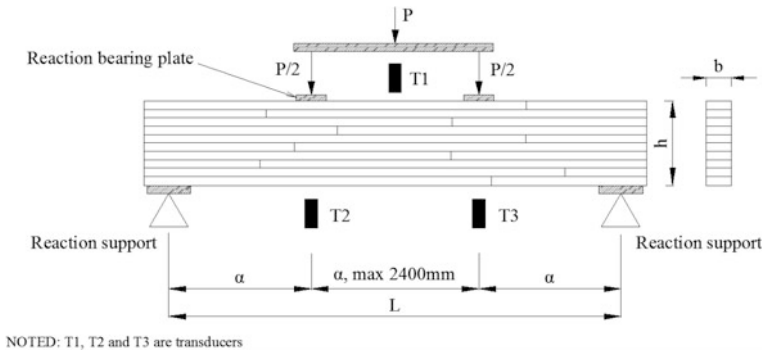
Fig. 1 Schematic diagram of bending test setup

dimension of the Mengkulang as shown in Table 2 for the beams with two different widths (100 and 130 mm) according to ASTM D198:2009 [20] by applying 1000 kN at two-point loading, using universal testing machine (UTM). The machine was set for cross-head position with rate of 0.001 mm/s to apply load perpendicular to the wide face of laminations. The deflection was measured by the movement of testing machine movable cross-head using linear variable differential transformer (LVDT) transducer. The details of the bending test are shown in Fig. 1. All tests were conducted until the beams failed completely.

The bending properties, modulus of rupture (MOR) and modulus of elasticity (MOE) are calculated using (1) and (2) respectively:

$$\text{MOR} = (P_{\text{max}}L)/(\text{bh}^2) \qquad (1)$$

$$\text{MOE} = \text{Pa}(3L^2 - 4a^2)/(4\Delta\text{bh}^3) \qquad (2)$$

where

P_{max} maximum load on beam,
h depth of beam,
b width of beam,
L span of beam = 18 h [20],
a distance from reaction to nearest load point (1/2 shear span),
Δ Increment of deflection of beam's neutral axis measured at mid-span,
P Increment of applied load below proportional limit

The following bending test was accomplished; test pieces for moisture content and also specific gravity measurements were cut off near the point of fracture. The size of three test pieces (cross section × 25 mm) from every single sample as well as the method to look for the moisture content and specific gravity is in accordance to MS 837: 2006 [21]. The pieces were dried using oven at 103 ± 2 °C.

3 Results and Discussions

3.1 Effect of Span Lengths on the Bending Properties

The bending properties, modulus of rupture (MOR) and modulus of elasticity (MOE) of glulam beams are tabulated in Table 3 as well as the characteristic shapes of the load–displacement graph of the bending members are illustrated in Figs. 2 and 3, respectively.

Table 3 shows that changes in the bending strength or modulus of rupture (MOR) of the glulam beams for different cross sections were small. However, it can still be seen that as the cross section increases, the MOR increases. When comparisons were made on the effect of span lengths on MOR, it was found that the MOR decreases as the span length increases. These results are contradicting with the findings of [13] but supported the report by [15]. For modulus of elasticity, it can be seen that the MOE values of specimens are almost improved by the

Table 3 Bending strength properties of glulam beams with different span lengths

Beam length (m)	Dimension (mm)		MOR		MOE	
	Width, b	Depth, h	Mean (N/mm^2)	STDEV	Mean (N/mm^2)	STDEV
6	100	300	47.6	5.62	14751.6	499
	130	300	42.7	2.76	16967.3	876
8	100	400	36.6	8.16	16974.0	717
	130	400	46.9	7.78	18032.0	498
10	100	500	28.8	5.47	17276.5	435
	130	500	35.8	7.45	17044.4	365
12	100	600	29.3	7.90	16160.5	1663
	130	600	34.9	7.44	17350.2	84.9

Fig. 2 Load versus deflection graph for glulam beams with 100 mm width
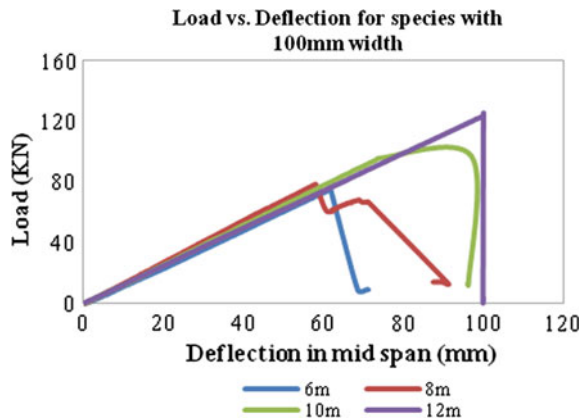
Fig. 3 Load versus deflection graph for species with 130 mm width
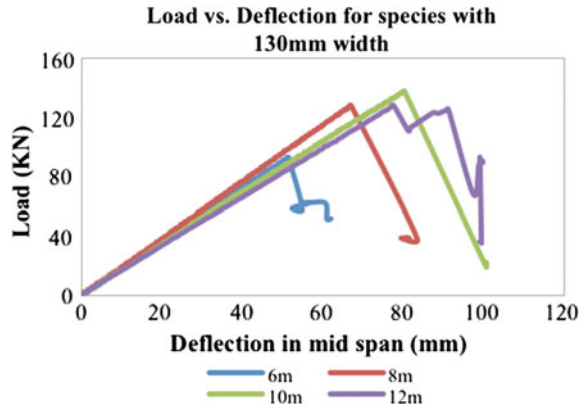
increment of beam span lengths (14751.6, 16,974 and 17276.5 N/mm^2 for 6, 8 and 10 m, respectively).

The load versus displacement graphs were also analysed for different beam widths. Figure 2 shows 100-mm-width beam and Fig. 3 shows 130-mm-width beam. The graphs were plotted using the graph that has almost similar value with the average values of the replicates. The graphs show similar pattern but with different optimum and deflection values. This indicates that the manufacturing process is quite consistent since the stiffness is not significantly different. Stiffness is the material properties.

3.2   Failure Mode Characteristics

This section analyses the failure mode characteristics of Mengkulang glulam beams under bending. The different failure modes that occurred during the testing of Mengkulang glulam beams with different widths (100 and 130 mm) and spans (6, 8, 10 and 12 m) are shown in Figs. 4, 5, 6, 7 and 8. From the figures, it shows that the

Fig. 4 Failure mode of Mengkulang glulam, failed in timber

Fig. 5 Failure mode of Mengkulang glulam, the timber failure at finger joint (indicates good manufacturing process)

Fig. 6 Failure mode of Mengkulang glulam, failure start at tension zone

Fig. 7 Failure mode of Mengkulang glulam, the beam failed in ductile manner

cracks originated at the bottom of the tension zone and progressed with the application of load for all the glulam beams. The fractures of the glulam timbers began to tear the wood fibres until it reached the next weaker point, which reflected in high bending strength. Typical weaker zone for glulam is at finger joint areas. The failed surface, which is in timber, indicates that the glulam was adequately manufactured where the failure is in timber rather than at the glue line.

Fig. 8 Failure mode of
Mengkulang glulam, **a** the
crack proceed to weaker zone
which is finger joint, **b** failure
at finger joint area
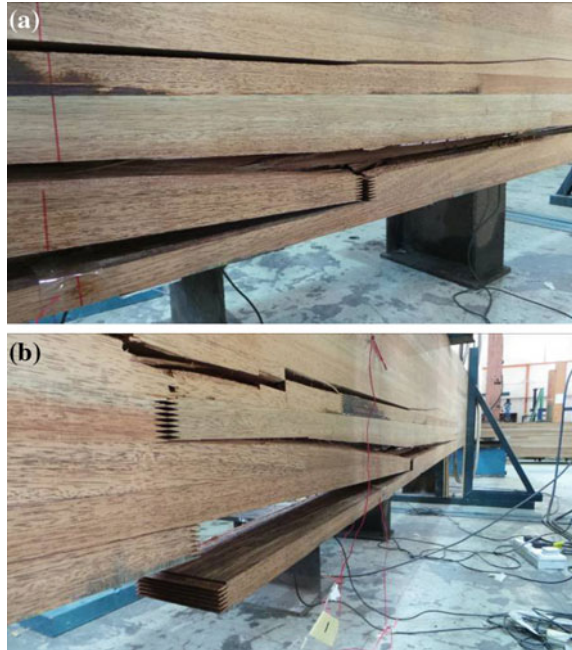
4   Conclusions

The bending characteristics and behaviour of glulam manufactured using
Mengkulang with different spans were investigated and the following conclusion
has been acquired:

- As the cross-sectional area of replicates increases, the value of MOR increased.
  On the other hand, MOR decreased as the span length of replicates increases.
- As the span length of replicates increases, the value of MOE might be improved.
- Generally, the failure mode of Mengkulang glulam for all replicates showed
  almost same crack patterns. This crack pattern indicates that the glulam was
  adequately manufactured where the failure is in timber rather than in glue lines.
  Observation on finger joint also showed that the failure occurred in timber not in
  glue line.

References

1. N. M. Bhkari, A. A. Bakar, P. M. Tahir and Z. Ahmad, "Flexural strength of glued laminated timber beam from selected Malaysian tropical hardwood," Proceeding the 6th Civil Engineering Conference in Asia Region: Embracing the Future through Sustainability, *ISBN* 978-602-8605-08-3. 2012.
2. Anon, Forestry Statistic for the Year 2011, 2011, Retrieved from www.forestry.gov.my
3. ASTM International, "Standard practise for establishing allowable properties for structural glued laminated timber (glulam) (ASTM D3737: 2009)," 2009.
4. A. Bakar, S. Saleh, A. Latif and M. Zainai, "Factors affecting ultimate strength of solid and glulam timber beams," Jurnal Kejuruteraan Awam, 16 (1), pp. 38–47, 2004.
5. J. K. Natterer, "Modern timber construction: from new simple techniques to high tech construction," The 7th World Conference on Timber Engineering. Shah Alam, Malaysia. 2002.
6. Forest Product Laboratory, Wood Engineering Handbook. New Jersey: Prentice Hall. 1990.
7. T. Haruji, M. Shyouhe and Y. Arata, "Innovative large timber buildings–Design of semi rigid hanging roof structure composed of glulams and steel plate," The 7th World Conference on Timber Engineering. Shah Alam. 2002.
8. G. Fink, J. Kohler and A. Frangi, "Bending tests on glued laminated timber beams with well-known material properties," Institute of Structural Engineering, no. 350, Zurich, July 2013.
9. R. Moody, R. Falk and T. Williamson, "Strength of glulam beams-volume effects," In: Sugiyama, Hideo, ed. Proceedings of the 1990 International timber engineering conference; 1990 October 23–25; Tokyo. Tokyo: Steering Committee of the International Timber Engineering Conference: 1990, Vol. 1. pp. 176–182.
10. B. Bohannan, "Effect of size on bending strength of wood members," Research Paper FPL 56. Madison, Wisconsin: U.S. Forest Products Laboratory. 1966.
11. R. Brandner and G. Schickhofer, "Length effects on tensile strength in timber members with and without joints," Materials and joints in timber structures, RILEM book series, 2014, vol. 9. pp. 751–760.
12. K. Sumiya and H. Sugihara, "Size effects in the tensile and bending strength of wood," J. Japan Wood Res. Soc., 3(5): 1957, pp. 168–173.
13. Z. Chudziński, "Strength Properties Determined by Different Testing Procedures for Solid Pinewood, Veneer-, Fibre-, Chip-, and Flax-Boards," Holztechnologie, 5(4): 1964, pp. 233–240.
14. R. H. Kunesh and J. W. Johnson, "Effect of Size on Tensile Strength of Clear Douglas-fir and Hem-fir Dimension Lumber," For. Prod. J., 24(8): 1974, pp. 32–36.
15. B. Madsen and A. H. Buchanan, "Size effects in timber explained by a modified weakest link theory," Can. J. Civ. Eng., 13(2): 1986, pp. 218–232.
16. B. Madsen, "Size effects in defect-free Douglas fir," Can. J. Civ. Eng., 17(2): 1990, pp. 238–242.
17. G. Schneeweiß and A. Felber, "Review on the bending strength of wood and influencing factors," American journal of material science, 3(3): 2013, pp. 41–54.
18. Malaysian Standard, "Glued laminated timber—Performance requirements and minimum 219 production requirements," 2001, MS 758:2001.
19. Malaysian Standard, "Specification for visual strength grading of tropical hardwood timber," 221 2003, MS 1714:2003.
20. ASTM International, "Standard test method of static tests of lumber in structural size (ASTM 210 D198:2009)," 2009.
21. Malaysian Standard, "Solid Timber—Determination of moisture content (First Revision)" 2006, MS 837:2006

Bending Strength Properties of Malaysian Tropical Timber in Structural Size

M.B.F.M. Puaad, Z. Ahmad and S.A.K. Yamani

Abstract Malaysian standard (MS 544: Part 2) adopted is BS528 for design code. However, the data in MS 544: Part 2 were developed by testing small sample without defect known as small clear sample, whereas the data published in BS5268 were tabulated based on large size tested samples. Therefore, this study investigated the bending strength properties of selected timber of different strength groupings (SG), namely Resak (SG 4), Kapur (SG 4), Merpauh (SG 4), Bintangor (SG 5), White Meranti (SG 5) Jelutong (SG 6), Sesendok (SG 7), and Kelampayan (SG 7) using structural size timbers. Small clear specimens were also tested for bending strength which was used to correlate with data from large size specimens. Bending tests were performed in accordance with BS 373: 1957 and ASTM D-198, respectively. The results showed that the groupings of the timber have been changed when using large size specimens.

Keywords Bending strength · Malaysian tropical timber · Small clear specimen · Structural size

1 Introduction

The code of practice MS 544: Part 2: 2001 [1] gives the recommendations for the structural use of Malaysian timbers. The mechanical properties presented in this code were obtained from testing small pieces of wood known as clear specimen, which means they did not contain strength reduction characteristics such as knots, cross-grain, checks, and splits. Therefore, in design, these stresses have to be

M.B.F.M. Puaad (✉) · S.A.K. Yamani
Faculty of Civil Engineering, Universiti Teknologi MARA Pasir Gudang,
81750 Bandar Seri Alam, Masai, Malaysia
e-mail: bfaliq86@gmail.com

Z. Ahmad · S.A.K. Yamani
Institute of Infrastructure Engineering and Sustainable Management (IIESM),
Universiti Teknologi MARA, 40500 Shah Alam, Malaysia

modified by certain modification factors to reflect the defect permitted in the structure size member and the different durations of loading actually subjected to the structures. The high safety factor also needs to be introduced to overcome the uncertainties.

Therefore to design economically, the strength data should be derived from structural size specimens. In BS 5268 [2] (permissible stress design) and European Code 5 (limit state design), the strength data available in these standards are based on structural size timber. Previously, the strength data in BS 5268: 1996 were also based on small clear specimens and this standard has been reviewed (BS 5268: 2002) and incorporated data from structural size specimens. MS 544: Part 2:2001 adopted the BS 5268: 1996 by placing strength data of Malaysian tropical timber based on small clear specimens and the design is based on permissible stress design. However, until today those data have not been changed. Therefore, there is a need to change those data based on structural size specimens. This is because full size in-grade structural timber and clear wood specimen have been shown to have a quite different behavior in most cases [3].

Natural defects in structural size cause reduction in timber strength and make it more brittle than small clear specimen wood [4]. This reduction of the strength depends on number of defects on timber specimen. In other words many defects cause huge reduction on timber strength. Hence, data of the small clear specimen cannot be applied in designing structural size timber.

Fonselius [5] and Piter [6] stated that the bending strengths for the structural specimens have lower strength when compared with the strength of the specimen that is smaller in size in the same grade. However, the result produced by Branco [7] and San [8] showed that the bending strength of structural size timber is much higher than the small clear specimen, but it must take into notice that [8] used the structural size LVL rather than solid structural timber. As for modulus of elasticity, MOE, [5, 9, 6] obtained similar results where they found that the MOE produced by the structural size timber can be considered the same with the result produced by small clear specimen. But, Branco found that the MOE of full-scale specimen is much lower than small-scale specimen. The contradiction of results of other findings in comparison of small clear specimen and structural size specimen shows the importance of the needs of data produced by the structural timber rather by depending on the small clear specimen data. Therefore, it is important to determine the bending strength of timber in structural size in order to have more reliable data for design timber structural member.

This paper reports the study conducted on the bending strength properties of selected timber using in-grade testing. Bodig and Jayne [10] stated bending strength is one of the strength properties that are considered important in timber design.

Bending properties can be determined using the static bending test where the material is deformed under the constant load until it fails where modulus of elasticity (MOE) and modulus of rupture (MOR) are the two main properties that were determined.

2　Methodology

2.1　Materials

Eight timber species were used in this experimental study (Table 1). All timber materials used in this project were selected on one occasion in order to obtain a test material without too high a variation in strength which could be arisen from different growth conditions. The timbers used for this study were sourced from reserved forest in UiTM Jengka. Based on MS 544: Part 2, these species are in different strength groups. The total number of specimens in structural size was 160 (20 sample for each species) and the total number of specimens for small clear was 240 (30 sample for each species). These specimens were kiln dried to attain dried timber condition as according to the Malaysian standard, it must have moisture content less than 19 %.

2.2　Specimen Preparations and Measurements

2.2.1　Sample Preparation

The specimens were planned on four sides to the size of 50 mm × 90 mm × 1800 mm (structural size) and 20 mm × 20 mm × 400 mm which were prepared according to ASTM D-198 and BS 373: 1957. Then the specimens were visually stress graded for standard and better grade in accordance with MS 1714.

2.2.2　Testing Procedure

(a)　Structural size specimens

All timber beams were tested under four-point loading where the half shear span-to-depth ratio (a/h) should be between 5 and 12 in accordance with ASTM D198, 2009. The distance between the two applied loads was restricted to 0.54 m.

Table 1 Timber species

Species	Family	Strength Grouping (SG)
Kapur	Dipterocarpaceae	SG 4
Merpauh	Anacardiaceae	SG 4
Resak	Dipterocarpaceae	SG 4
Bintangor	Guthiferea	SG 5
White Meranti	Dipterocarpaceae	SG 5
Jelutong	Apocynaceae	SG 6
Kelampayan	Rubiaceae	SG 7
Sesendok	Euphorbiaceae	SG 7
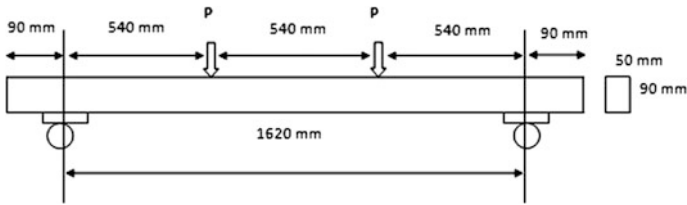
Fig. 1 The dimension for static bending structural specimen

One-half of the shear span, *a*, was 0.54 m. Therefore, the one-half shear span-to-depth ratio, *a/h*, for the 50 mm × 90 mm beam was 6 which is larger than 5 to avoid shear failure. Figure 1 shows the test setup for bending strength properties.

IPC testing instrument equipped 2500 kN load cell used to applied load at a crosshead rate of 0.06 mm/min. Four linear variable differential transducers (LVDT) were attached in vertical position to the timber beam and moving crosshead to monitor the deflection. LVDT were connected to the data logger to receive and record the reading during testing.

(b) Small clear specimen

As for small clear specimen, the bending load is applied using the Instron 3383 testing instrument equipped 100 kN load cell. The specimens were subjected to three-point loading in general conformance with British Standard BS 373: 1957 as shown in Fig. 2 and the load was applied with crosshead of 0.11 mm/s. The loading data were recorded by the chart recorder.

The bending properties were determined using equations as follows:

(i) Modulus of rupture, MOR,

$$MOR = \frac{PL}{bh^2}, N/mm^2$$

(ii) Modulus of elasticity, MOE

$$MOE = \frac{P'a(3L^2 - 4a^2)}{4bh^2\Delta'}, GPa$$

Fig. 2 The dimension for small clear specimen
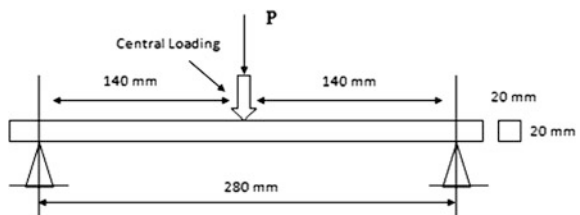
where

b   Width of the specimen (mm)
h   Depth of the specimen (mm)
P′   Load at the proportional limit (*N*)
Δ′   Deflection at the proportional limit (*N*)
L   Length of the span (mm)
a   Half shear span (mm).

3   Results and Discussions

3.1   Failure Characteristics (Small Clear Specimen)

Specimens under bending can be failed in tension, compression, shear, or combinations. The failure patterns found in this study were recorded for each specimen as shown in Fig. 3 and summarized in Table 2. By referring to Table 2 it can be seen that 100 % failure occurred at tension zone and only one that failed in combination
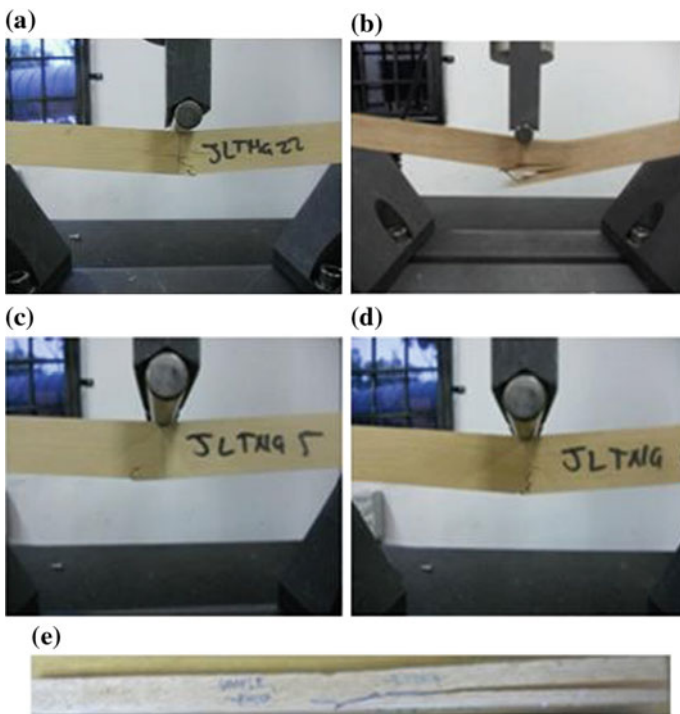
Fig. 3 Bending failure: **a** simple tension, **b** splintering, **c** cross-grain tension, **d** brash, **e** horizontal shear

Table 2 Summary failure characteristic for bending parallel to grain

Species	Percentage of failure modes (%)		
	Tension	Compression	Horizontal shear
Kapur	100	–	–
Merpauh	100	–	–
Resak	100	–	–
Bintangor	90	–	10
White Meranti	100	–	–
Jelutong	100	–	–
Kelampayan	100	–	–
Sesendok	100	–	–

of tension and horizontal shear (Fig. 3e) and this is may be due to the internal checks and shakes of the specimens [10].

From Fig. 3 it was found that there were four different types of tension failure modes, namely simple tension (Fig. 3a), splintering (Fig. 3b), cross-grain tension (Fig. 3c), and brash (Fig. 3d).

According to Bodig, the mode of failure and the stress distribution in a defect-free beam are largely determined by the stress–strain relationship in tension and compression parallel to the grain. Failure in a beam due to the compression will tend to have the lower bending strength value compared to the beam with tension failure. This is because the maximum crushing strength of compression parallel to the grain is about 25–33 % of the ultimate tensile strength parallel to grain. There it a good indicator as the entire specimens are failed in tension mode except for Bintangor. Hence, all the data found in these experiments can be taken in the determination of bending strength.

3.2 Bending Failure Characteristics (Structural Size)

It can be seen that there are three different types of failure mode produced after tested. Table 3 shows the summary of failure characteristics for bending parallel to grain for structural size specimens.

In this study, generally the beams failed in tension except for Merpauh, Kelampayan, and Sesendok. The examples of tension failures are shown in Fig. 4a, b, horizontal shear in Fig. 4c, d. The obvious defects on the specimen are observed in Fig. 4e, f, even though through the visual grading conducted these defects were considered small since these timbers were graded as standard and better.

Bodig stated that an usual complex distribution of stresses in the material that are due to internal inhomogeneities in other word called defects is responsible for this behavior and causes the deficiency in mechanical properties in timber, which is for sure will cause the reduction of mechanical properties. This is also true for Kelampayan where there are 40 % failures due to defects.

Table 3 Summary failure characteristic for structural size specimens under bending parallel to grain

Species	Percentage of failure modes (%)			
	Tension	Compression	Shear	Presence of defects
Kapur	100	–	–	–
Merpauh	90	–	–	10
Resak	100	–	–	–
Bintangor	100	–	–	–
White Meranti	100	–	–	–
Jelutong	100	–	–	–
Kelampayan	60	–	–	40
Sesendok	95	–	5	–

The small clear specimens were taken from the same batch of timbers for structural size. The failure modes for bending test specimens for structural size were found to have more failure patterns than small clear specimen because of the existence of defects in structural size.

3.3 Bending Strength Properties

Tables 5 and 6 show the bending strength properties of small clear specimens and large size specimens. An analysis of variance (ANOVA) at 0.05 % probability was performed to determine if there were differences in the mean modulus of rupture and modulus of elasticity values among species. The ANOVA analysis revealed that there were significant differences in the MOR and MOE values (p value < 0.05). DUNCAN multiple comparisons were performed for MOR as shown in Table 5. It can be seen MOR for (Merpauh and Resak) > Kapur > Bintangor > White Meranti > (Jelutong, Kelampayan, and Sesendok). This result also suggested that Merpauh and Resak should be in the same group as well as Jelutong, Kelampayan, and Sesendok. The result of MOE also follows the same but the Duncan multiple comparison was not shown here.

As for large size specimens, there are also significant differences in the MOR and MOE values. From Table 5, it can be seen that there is no significant difference in the MOR values for Merpauh, Kapur, and Bintangor and also there is no significant difference in the mean value for Kelampayan and Jelutong. The MOR values are in the order of Resak > (Kapur, Merpauh, and Bintangor) > White Meranti > Sesendok > (Jelutong and Kelampayan). This result also suggested that Bintangor, Merpauh, and Kapur should be in the same strength group and at the same time Jelutong and Kelampayan also should be in the same strength group. The result of MOE also follows the same order as MOR except for Bintangor (Table 4).

Table 4 Summary statistics for bending strength properties of small clear specimens and large size specimens

Species	Small clear specimen			Large size specimen			MS 544		MC (%)	Estimated strength group
	Bending strength		MOE (GPa)	Bending strength		MOE (GPa)	MOE (GPa)	Density (kg/m³)		
	Mean (MPa)	S.D.		Mean (MPa)	S.D.					
Kapur	103.8	15.10	12.56	119.1	15.48	22.64	13.70	776	12.87	
Merpauh	136.2	14.27	16.71	116.7	15.8	23.13	15.50	875	11.47	Same groupings
Resak	135.4	13.22	16.30	138.0	26.43	28.11	14.60	915	11.51	
Bintangor	80.4	19.30	11.39	116.9	17.09	25.46	14.00	725	12.89	
White Meranti	73.7	7.080	10.17	91.6	16.59	19.50	11.2	594	12.01	
Jelutong	56.2	8.621	7.01	38.7	3.607	10.75	7.90	487	11.56	
Kelampayan	60.7	14.15	6.97	45.6	17.86	12.78	7.60	547	11.71	Same groupings
Sesendok	56.9	8.434	7.33	56.8	7.994	13.09	8.60	483	11.67	
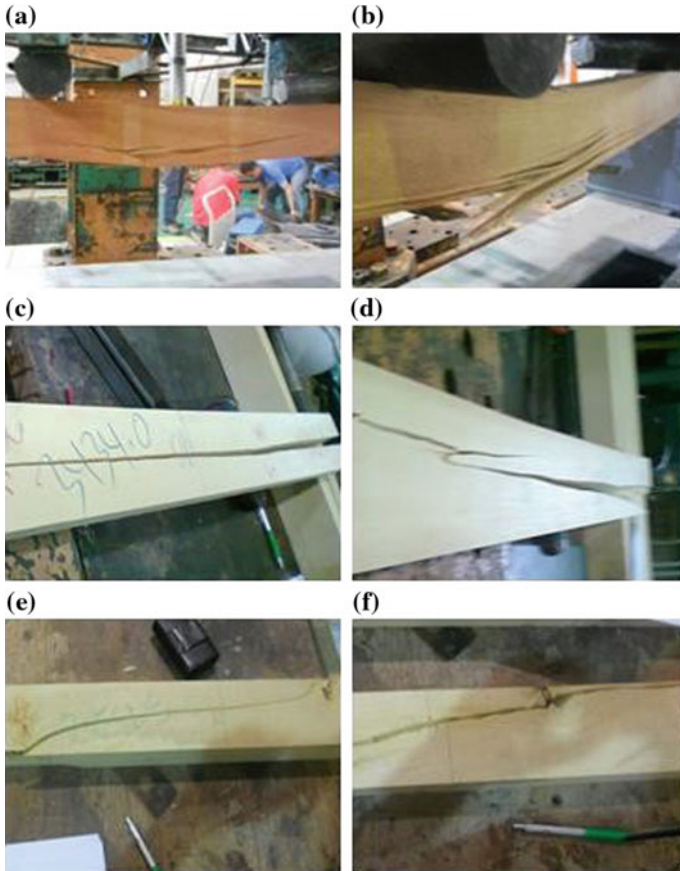
Fig. 4 Failure modes of bending specimens in structural size; **a** tension failure, **b** tension failure, **c** horizontal shear, **d** horizontal shear, **e** tension failure with cracking moving towards knots, **f** failed at the knots

Table 5 Duncan multiple comparison for MOR based on small clear specimens

Adhesive	Subset for alpha = 0.05				
	1	2	3	4	5
Merpauh	136.16[a]				
Resak	135.43[a]				
Kapur		103.81[b]			
Bintangor			80.44[c]		
White Meranti				73.66[d]	
Kelampayan					60.74[e]
Sesendok					56.86[e]
Jelutong					56.21[e]

Note Means in the same column and same superscript are not significantly different at *P* value ≤ 0.05

Table 6 Duncan multiple comparison for MOR based on large size specimens

Adhesive	Subset for alpha = 0.05				
	1	2	3	4	5
Resak	138.01[a]				
Kapur		119.13[b]			
Bintangor		116.89[b]			
Merpauh		116.70[b]			
White Meranti			91.64[c]		
Sesendok				56.54[d]	
Kelampayan					45.66[e]
Jelutong					38.79[e]

Note Means in the same column and same superscript are not significantly different at *P* value ≤ 0.05

Modulus of rupture (MOR) of structural size specimens was much higher than the MOR for small clear specimen except for Merpauh, Jelutong, and Kelampayan. It has the good agreement with the results provided by Branco where the bending strengths of the structural size specimens have greater value compared with the bending strength provided in the DNA–ECS (Portuguese Nationally Determined Parameters of Eurocode 5) based on the small clear specimens. The reduction of MOR in structural size for Merpauh and Kelampayan can be concluded because of the influence of knots.

Resak gives the highest value of 138.0 MPa. Meanwhile, Jelutong has the lowest value of bending strength of 6.54 MPa. As for Sesendok, the characteristic strength of the large size specimen is higher than Jelutong although Sesendok is in lower strength group as given in MS 544: Part 2.

Table 4 shows the mean value of the density of all species. Resak gives the highest density value compared to other species in the same strength group including Kapur and Merpauh. There is not much difference in the mean density of species in SG 5 (Bintangor and White Meranti) and also timbers in SG 6 and SG 7 (Jelutong, Kelampayan and Sesendok). The mean value of moisture content for all species is in the range of 9–13 %. Since all mean value of moisture content is lower than 19 %, the species is can be classified as dry timber which has been stated in MS 544: Part 2.

In Table 6, the values of MOE for all species showed significant differences between small clear specimens and large size specimens. It shows that the MOE for structural size specimens is higher than both MOE produced by the tested small clear specimen and strength values for MS 544: Part 2 except for Kelampayan as the mechanical properties of this species were not published in MS 544: Part 2. Hence, the mechanical properties' values for Kelampayan found in this study will become new set of data for lesser known timber species.

Parker [3] noted that current design practice for structural timber member is based on the elastic theory, which postulates that deformations are directly proportional to stresses. Parker [3] also state that the amount of the force and

deformation produced for bending in structural size will be twice when compared to small clear specimen.

This study shows a significant difference between small clear specimen and structural size in term of strength groupings. As a result, more studies on mechanical and physical properties on structural size should be initiated in future to produce data that will be useful in designing structural size timber in future.

4   Conclusion

From the outcomes, all of the values of mechanical properties (MOR and MOE) determined based on structural size specimens were higher than the values obtained from small clear specimens for timber from strength groups SG 4 and SG 5. As for timber species in SG 6 and SG 7, their bending strength is about the same with the strength stated in MS 544: Part 2. The bending strength properties of Kelampayan are considered new set of data.

The conclusion that can drawn is that the bending strength to the grain in lumber size for medium to higher density specimen are needed to be reexamined since that strength for the tested specimen is much higher than the data given in MS 544: Part 2. This would lead to increment in section and wastage in cost if the designer only referring to the strength properties produced by small clear specimens.

References

1. MS 544: Part 2: 2001. *Code of Practice for Structural Use of Timber*. Department of Standard. Malaysia. Department of Standard. Malaysia.
2. BS 5268-2: 2002, Structural Use of Timber- Part 2: *Code of Practice for Permissible Stress Design, Materials and Workmanship*
3. Parker, H. (1994). *Simplified Design of Wood Structure*, John Wiley & Sons, Inc, Fifth Edition.
4. Aydin, S., Yardimci, M.Y., Ramyar, K. (2007). Mechanical Properties of Four Timber Species Commonly Used In Turkey. *Turkish Journal Engineering Environmental Science*, Turkey, 31, 19–27.
5. Fonselius, M. (1997). Effect of Size on the Bending Strength of Laminated Veneer Lumber. *Wood Science and Technology* 31 (1997) 399–413 © Springer-Verlag 1997
6. Piter, J.C. (2010). Size effect on bending strength in sawn timber of fast-growing Argentinean Eucalyptus grandis. Analysis according to the criterion of European standards. *Euro Journal Wood Product*. (2012) 70:17–24.
7. Branco, J., Varum, H., Cruz, P. (2006). Structural Grades of Timber by Bending and Compression Tests. *Materials Science Forum* Vols. 514–516, Portugal, pp 1663-1667.
8. San, H.P. (2003). *Basic engineering Properties of Laminated Veneer Lumber (LVL) Produced From Tropical Hardwood Species*. Doctor of Philosophy Thesis. Faculty of Forestry Universiti Putra Malaysia. Selangor. Malaysia.

9. Ahmad, Z., Hassan, R. (2012). *Timber Properties using Dielectric Constant in Low Frequency Technique*. VDM Verlag Dr. Muller GmbH & Co. Saarbrucken. Germany.

10. Ahmad, Y. (2010). *Bending Behavior Of Timber Beams Strengthened Using Fiber Reinforced Polymer Bars And Plates*. Doctor of Philosophy Thesis. Faculty of Civil Engineering, Universiti Teknologi Malaysia. Johor. Malaysia.

Part IX
Transportation Systems, Infrastructure and Intelligent Transport

Influence of Warm Porous Asphalt on Permeability Reduction Due to Binder Flow

M.M. Samat, J. Ahmad, M.O. Hamzah and A.K. Arshad

Abstract Warm mix asphalt (WMA) is a new technology in Malaysian context. The technology can help to reduce the global warming issues. In this research, the warm mix asphalt technology was used in porous asphalt pavement which is known as warm porous asphalt (WPA) mix. WPA loses permeability mainly due to clogging. Apart from typical clogging agents such as dust and tyre rubber, the binder flow is also another source of permeability reduction. The objective of this study was to investigate the binder flow phenomenon that affected the permeability reduction in WPA. To obtain the binder flow phenomenon, samples were conditioned at 35 °C for 120 days. The different mixing and compaction temperatures with bitumen 60/70 + 3 % RH-WMA additive were used in preparing the samples. A falling head water permeameter was used to determine the permeability loss which is related to time and temperatures. The result from the permeability loss was significant to high mixing temperatures over time. Due to time, self-weight of the binder and high mixing temperature, the asphalt mastic start to flow down according to gravitational forces and finally the coefficient of permeability reduced, yet the time of flow increased. The outcome of this research indicated that the different temperatures during mixing and compaction were significant to the binder flow. Hence, the low mixing temperature using WMA technologies could reduce the clogging problem due to self-weight of the binder.

M.M. Samat (✉) · J. Ahmad · A.K. Arshad
Faculty of Civil Engineering, Universiti Teknologi MARA,
Shah Alam, Malaysia
e-mail: cemo@pahang.uitm.edu.my

J. Ahmad
e-mail: juraidah@salam.uitm.edu.my

A.K. Arshad
e-mail: drahmadkamil@salam.uitm.edu.my

M.O. Hamzah
Faculty of Civil Engineering, Universiti Sains Malaysia,
Nibong Tebal, Pualau Pinang, Malaysia
e-mail: cemeor@yahoo.com

1 Introduction

Nowadays, global warming issues become one of the main challenges to the world. It occurs due to greenhouse gases mainly produced by manufacturing industries. Besides that, the pavement industry also contributes to the problem. Over the past few years, awareness of environmental impact and reducing emissions has been thriving. The polluted environment with poor air quality and the increasing of energy consumption has led the world to apply WMA technologies in the asphalt industries [1]. Hamzah et al. [2] stated that the WMA is a new technology in asphalt industries where it is able to reduce mixing and compaction temperature as compared to conventional mix such as Hot Mix Asphalt (HMA). Therefore, Wurst and Putman [3] mentioned that the WMA reduces the energy consumption and CO_2 emissions as well as other detrimental produced by asphalt paving.

For the past few years, WMA technologies have been tried on the open graded friction course (OGFC) and it reveals a good future in terms of performance [4, 5]. In 1950, the first trial asphalt pavement performance for OGFC in different parts of the United States has been carried to upgrade the surface friction resistance [6]. The same function of OGFC or porous friction courses (PFC) is a porous asphalt (PA) pavement. These mixtures differ from typical asphalt mixtures in that they have limited amounts of fine aggregate, which results in a permeable mixture having a high void content. According to Hasan et al. [7] PA as an open mixture gives advantages from the aspect of the ability to flow the water due to high degree of air void continuity and minimization of glare effects. The other main benefits of PA including the reduction of noise, skid resistance, splash and spray, and the marking material become visible when it rains. Apart from that, the resistance of permanent deformation improved due to stone-to-stone contact. Nevertheless, these benefits can be adopted if the air void continuity within the PA remains open to accommodate water flow. The study conducted by [8] found that the reduction of effective air voids occurs particularly due to the densification under heavy traffic and voids clogging. The formatter will need to create these components, incorporating the applicable criteria that follow.

2 Literature Review

The main problem of PA is clogging that is caused by storm water, vehicle and wind. As time passes, the sediments are deposited on the pavement surface and cause blockages. According to [9] this makes the pore clogged and do not serve as a

proper function of PA. PA becomes impermeable and works like a conventional mix such as dense graded mix thus the PA advantages are no longer applicable. [10] Also mentioned that besides the particles clogging, the PA may also become clogged due to fraction and deterioration of the mastic inside the mixture. Evidence of this has been observed with research conducted by [11] in Japan the clogging of PA in urban roads normally occurs after 3–4 years after construction. When the clogging occurs, the permeability loss is inevitable. Among the most common clogging agents include small particles such as lorry or truck carrying earth dirt, tyre rubber, dust and local residual soils deposited from dirty wheel [12]. According to [12] the group of research team developed a method to quantify the impact of clogging material on the permeability of four different gradation of PA. Figure 1, shows that the permeability reduction is related rapidly with initial addition of clogging material and finally the reduction of permeability start to level off.

In porous mix, downward migration of asphalt binder is known as binder drain down or binder drainage or binder runoff but gives the same meaning of terminologies. Basically, the binder drainage occurred due to excessive binder content and high mix temperature during mix production, storage and transport.

In recent research, [13] the clogging behaviour of single and two layers of PA systems using laboratory methods in terms of clogging and declogging procedures was evaluated. The results of [13] showed that the continuity of air voids is disturbing due to progressive clogging and cleansing cycles inside PA systems, thus making the mixture easily influenced to clogging with time. Ultimately, the results showed that when the ambient temperature and binder content of the mix increased it also affected the increasing of clogging [14]. The aim of this study is to investigate other causes of permeability loss in PA mix which conducted in the laboratory, postulated due to binder. To determine this phenomenon, permeability measurements were carried out at regular intervals up to 120 days on samples conditioned at 35 °C with different mixing and compaction temperatures to accelerate and mitigate binder flow. Any phenomenon of binder flow, particularly at high mixing temperatures, will be indicated in terms of permeability loss.

Fig. 1 Typical pattern of permeability reduction with increasing of clogging material
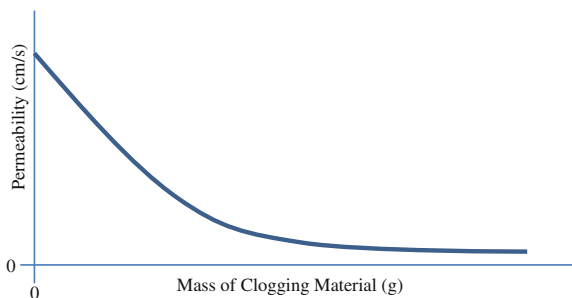
3   Materials and Methods

3.1   Material and Mix Design

The aggregate material used in this study was granite, obtained from Blacktop quarry in Semenyih, Selangor. A conventional bitumen 60/70 penetration grade incorporating RH-WMA additive were used to prepare the porous asphalt specimen. The RH-WMA additive was used to reduce the mixing and compaction temperatures. RH-WMA is a polyethylene wax-based asphalt binder additive produced from cross-linked polyethylene. In this research, the 0 and 3 % RH-WMA additives were used by mass of bitumen. The basic properties of the 60/70 bitumen with and without RH-WMA additives are summarised in Table 1. Aggregate gradation was adopted from Dutch gradation, which was modified by USM to suit Malaysian quarry practice [1]. The modified aggregate gradation was used in specimen preparation as shown in Table 2. The base bitumen 60/70 blended with 3 % RH-WMA additives is known as RH-WMA modified binder. The specimens prepared at 5.7 % RH-WMA modified binder contents and aggregates were blended at their respective mixing and compaction temperatures were compacted via impact mode at 50 blows per face. All compacted specimens were of similar heights. The samples were then left to cool at ambient temperature for 4 h before immediately tested for permeability, after the initial permeability was measured, the specimens were conditioned at the designated conditioning temperature. The duration of testing for permeability evaluation was set to 120 days for the 35 °C conditioned specimen. An incubator was used to maintain the test specimen temperature. The conditioning, mixing and compaction temperatures are shown in Table 3. The mixing and compaction temperatures were obtained

Table 1   Basic properties of 60/70 bitumen with and without RH-WMA additive

Properties	60/70 bitumen	60/70 bitumen + 3 % Additive
Penetration at 25 °C (dmm)	64	81
Softening Point (°C)	49	58
Ductility	>100	>100

Table 2   Modified aggregate gradation [1]

Size of aggregate (mm)	Aggregate percentage (%)	Weight of aggregate (g)
14–10	20	220
10–5	58.5	643.5
5–2.36	11.5	126.5
2.36–0.425	3	33
0.425–0.075	2	22
OPC	3	33
Hydrated lime	2	22
Total	100	1100

Table 3 Mixing and compaction temperatures adopted in this study

RH-WMA additives			
0 %		3 %	
Temperatures (°C)			
Mixing	Compact	Mixing	Compact
165	155	155	140
		145	130
		135	120
		125	110

by using a Brookfield Viscometer and the procedures conducted according to ASTM D4402 [15]. According to [16] the viscosity of 0.17 ± 0.02 Pa.s and 0.28 ± 0.03 Pa.s were used in the semi-logarithmic relationship between viscosity and temperature for binders with and without RH-WMA content.

3.2 Determining of Binder Flow Phenomenon

To determine the permeability loss caused by binder flow, the unextruded sample was used in this study to measure permeability for better result. This is due to binder flow occupied in mixes will be reflected in permeability loss. Apart from that, by conducting permeability measurements without removing the samples from the mould is actually to obtain a strong bond between the samples and the mould walls. It is important to get the accuracy in measuring the time taken for the volume of water that flows through the pores of the sample. Water permeability test was design as shown in Fig. 2, was used throughout the study using the concept of falling head principle [14]. Permeability measured in unit of time (seconds) in which it took into account the number of fixed volume of water flowing through it.

To ascertain binder flow, one conditioning temperature was selected, namely 35 °C. This temperature was chosen to accelerate binder flow. Generally, 35 °C represents the typical high ambient temperature in the Malaysian weather. In this research, the selection of high conditioning temperature was taken to foresee the worst scenario if it happened. An incubator was used to condition the specimens at high temperatures. As cautious and vigilant, in order to maintain a position between the mould and the wall of the specimen in proper condition, the highest temperature was limited to 35 °C.

Permeability data for each specimen was collected and recorded in accordance with the time interval up to 120 days. For the first 10 days, the data was taken regularly as it was a critical time where during that period it can reduce the permeability that occurred rapidly. However, the readings taken after 10 days were not as often as before. When the reading of each sample is taken, it should be done as quickly as possible in order to avoid changes in specimen temperature as it can affect the data of permeability loss. After flow time was taken, the samples were

Fig. 2 Schematic diagram of
permeability test [14]
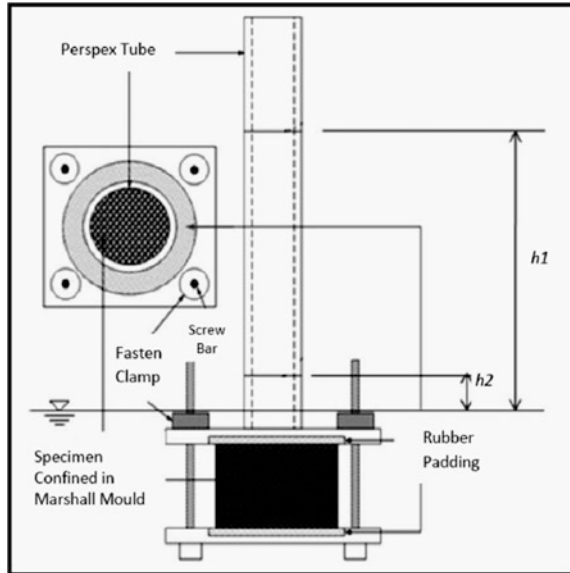
returned into the incubator immediately. The coefficient of permeability of each compacted specimen was calculated from

$$k = 2.3(aL/At) \log_{10}(h_1/h_2) \tag{1}$$

where k is the coefficient of permeability (cm/s), A is a cross section area of specimen (cm^2), a is cross section area of standpipe (cm^2), L is the height of the specimen (cm), t is the time taken for water in the standpipe to fall from h_1 to h_2 (s), h_1 is head at the beginning of time measurement (cm), h_2 is the head at the end of time measurement (cm).

4 Results and Discussion

4.1 Reduction of Permeability due to time

Reduction of permeability also known as permeability loss is caused by two factors namely coefficient of permeability (k) reduced and time of flow (F) increased. The mean values between time of flow and time at different mixing temperatures are shown in Fig. 3. In most cases, the value of F increases with the time for all specimens. Reading at 125 °C of mixing temperature shows the increasing F values until 65 days, afterwards the curve nearly flatten. At 135 °C of mixing temperature, the values of F appear to stabilise on the day 90. However, the mixing temperatures at 145 and 155 °C continually show an increase in the value of F during the study.
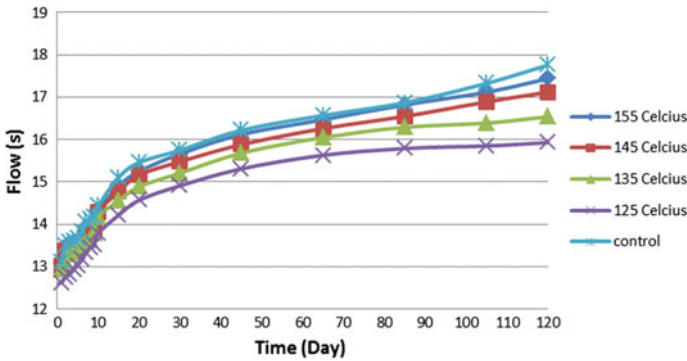
Fig. 3 Relationship between time of flow and time at different mixing temperatures

Table 4 Percentage changes in F and k

Mixing temperature (°C)	F_0 (s)	F_{60} (s)	Percentage increase in F (%)	k_0 (s)	k_{60} (s)	Percentage reduction in k (%)
125	12.62	15.93	26.23	0.359	0.285	20.61
135	12.92	16.54	28.02	0.351	0.274	21.94
145	13.02	17.12	31.49	0.348	0.265	23.85
155	13.08	17.44	33.33	0.346	0.260	24.86
165 (control)	13.12	17.76	35.37	0.335	0.248	25.97

The control sample represented at 165 °C mixing temperature shows the highest value of F. Table 4 indicated that the percentage change in F explicitly proposes the significant effect of mixing temperature on increase in percentage of F and percentage reduction in k. Mixing temperature at 125 °C recorded a 26.2 % increase in F at day 60 (F_{60}) compared to the initial F, while 33.3 % increase in F at 155 °C of mixing temperature.

Table 5 summarised the data obtained between F and time at different mixing temperatures in the form of regression parameters of the linear relationship. The regression parameters present a good result with coefficients of determination, R^2 exceeding 88 % except for sample tested at the lower mixing temperature. For a given test of mixing temperature, the slope of the line reflects the susceptibility of the

Table 5 The regression parameters between F and mixing temperatures

Mixing temperature (°C)	Slope	Intercept	R^2
125	0.0284	13.24	0.81
135	0.0302	13.56	0.85
145	0.0335	13.69	0.88
155	0.0352	13.79	0.89
165 (Control)	0.0364	13.86	0.89
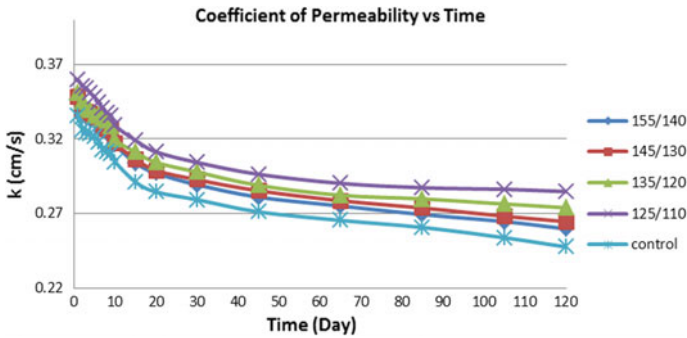
Fig. 4 Relationship between coefficient of permeability and time at different mixing temperatures

mix to change in F, thus the susceptibility of the mix to binder flow. The higher rate of binder flow represents a steeper slope. Basically, the sample mixing at 155 °C with additive 3 % exhibits the higher slope, and is about 2.8 % more susceptible compared to samples mixed at 125 °C with additive. However, the 165 °C without additive which also known as control sample shows the highest slope value.

Figure 4, indicates the relationship between k versus time at different mixing temperatures of the specimen tested. Clearly, during the test the value of k decreases with increasing time and it also depends on temperature change. From the observation, the k value reduces up to 90 days beyond which the value of k tends to level off. From the graph in Fig. 4, the trend of curve can be divided into three phases. Phase 1 (day 0–20) indicates a prompt decrease of k and this occured in the first two weeks, while phase 2 (day 20–90) and phase 3 (day 90–120), respectively, represent the steady state flow and the curves almost tends to flatten. In phase 1, the samples of mixing temperature at 145, 155 and 165 °C indicate that the k value for all mixes is drastically reduced. After the first phase, the value of k began to reduce slowly and it seems to be asymptote at phase 3 except for mixing temperature at 125 °C.

4.2 Permeability Reduction due to Binder Flow

From the laboratory work reported the permeability reduction or permeability loss of PA is basically due to time factor. In this study, the samples were subjected to neither clogging nor traffic loading. Nevertheless, the permeability loss was recorded in the reading of laboratory work. Figure 4 shows that the permeability loss still occurred although exceeded day 120. The simple meaning or easy explanation of permeability loss is binder flow. Binder flow is a time-dependent phenomenon. In relation to this, flow may occur in bitumen or asphalt binder.

The high mixing temperatures are the main factors which expedite the binder flow to occur. This is because the binder easily melts if the high temperature is applied. In addition, the self-weight of the binder or gravitational force also played a main role in terms of binder flow when the long loading time was imposed.

In this study, the bitumen or asphalt binder became less viscous when the high temperatures were imposed and at the same time the binder was easy to flow. Moreover, the permeability test was carried out throughout the study to monitor the results until 120 days. Due to time, self-weight of the binder and high mixing temperature, the asphalt mastic start to flow down according to gravitational forces. Therefore, the binder flow had taken place which disrupted the continuity of air voids and finally the coefficient of permeability reduced yet the time of flow increased. The outcome of this research indicated that the different temperatures during mixing and compaction were significant to the binder flow. Hence, the low mixing temperature using WMA technologies could reduce the clogging problem due to self-weight of the binder.

5   Conclusions

Self-weight of the binder in PA mix for long loading time tend to flow downward by gravitational force. This gravitational force allowed the binder to flow and fill up the voids in the specimen and causing interruption in terms of continuity flow. Therefore, from the results, it is shown that the coefficient of permeability reduced while time of flow increased. Binder flow situation deteriorated further when elevated temperature at 165 °C was used to mix the specimen. In this study, the RH-WMA additive was used to reduce the temperature and at the same time it reduced the flow of binder. Hence, four levels of mixing temperatures were used to compare the effect of high and low temperatures on binder flow. Thus, the simple linear regression equations of permeability versus time were obtained to ascertain the tendency of PA mixture with binder flow phenomenon. Another result also shows that the higher mixing temperatures, the steeper the slope will be. Thus, this finding exhibited the tendency of binder to flow and permeability loss increased. The permeability test must be conducted after 4 h compaction to assure that the influence of binder flow can be eliminated. It is intended that the permeability reduction is caused by the influence of binder flow. Therefore, the binder flow also becomes the cause of the loss of permeability and this requires further study as well as extending the duration of research.

References

1. M. Y. Aman, "Water sensitivity of warm porous asphalt incorporating Sasobit®," PhD Thesis, Universiti Sains Malaysia, 2014.
2. M. O. Hamzah, A. Jamshidi, Z. Shahadan, M. R. M. Hasan, A. S. Yahaya, " Evaluation of engineering properties and economic advantages of WMA using local materials," Journal of Applied Sciences, 10 (20), pp. 2433–2439, 2010
3. J. E. Wurst and B. J. Putman, "Laboratory evaluation of warm-mix open graded friction course mixtures," Journal of Materials in Civil Engineering, Vol. 25, No. 3. March 1, 2013.
4. C. B. Barros and S. Dmytrow, "Weather-mix asphalt," Roads and Bridges, 47(4), pp. 26–28, 2009.
5. D. Jones, B. W. Tsai, and J. Signore, "Warm-mix asphalt study; Laboratory test results for AkzoNobel Rediset WMX," Contract Rep.: UCPRC-CR-2010–01, University of California Pavement Research Center, Richman, CA, 2010.
6. R. B. Mallick, P. S. Kandhal, L. A. Jr. Cooley, D. E. Watson, "Design construction and performance of new generation open graded friction course, NCAT report No. 20000-01. Alabama: National Center for Asphalt Technology, Auburn University, 2000.
7. M. R. M. Hasan, J. Y. Eng, M. O. Hamzah, and J. L. M. Voskuilen, "The effects of break point location and nominal maximum aggregate size on porous asphalt properties," Construction and Building Materials 44 (2013) pp. 360–367.
8. S. N. Suresha, Varghese, George, and R. Shanker, A. Udaya, "Laboratory and theoretical evaluation of clogging behaviour of porous friction course mixes," International Journal of Pavement Engineering, 11: 1, pp 61–70, 2010.
9. W. D. Martin, B. J. Putman, and A. I. Neptune, "Influence of aggregate gradation on clogging characteristics of porous asphalt mixtures," Journal of Materials in Civil Engineering, 10.1061/(ASCE)MT.1943-5533.0000975, pp. 261–267, 2014.
10. C. B. Nielsen, "Ravelling of porous pavement-Assessment of test section," Technical Note 48, Road Directorate, Danish Road Institute, Rosklide, Denmark, 2007.
11. C. B. Nielsen, H. Bendtsen, B. Anderson, H. J. E. Larsen, "Noise reducing pavements in Japan-study tour report," Danish Road Institute (DRI), DRI Technical Note 31, Denmark, 2005.
12. T. F. FWA, S. A. Tan, and Y. K. Guwe, "Laboratory evaluation of clogging potential of porous asphalt mixtures," Transportation Research Record 1681, Transportation Research Board, Washington, DC, 43–49, 1999.
13. M. O. Hamzah, N. H. Abdullah, J. L. M. Voskuilen, and G. von Bochove, "Laboratory simulation of the clogging behaviour of single-layer and two-layer porous asphalt," Road Material Pavement Design 14(1), 107–125, 2013.
14. M. O. Hamzah, M. R. M. Hasan, and M. V. de Ven, "Permeability loss in porous asphalt due binder," Construction and Building Materials, 10.1016/j. conbuildmat. 2011.11.038, 2011.
15. ASTM D4402: Standard Test Method for Viscosity Determination of Asphalt at Elevated Temperatures using a rational Viscometer, American Society for testing and Materials, West Conshohocken, PA 19428–2954, United States, 2005.
16. Asphalt Institute, The asphalt Handbook, MS-4., 7th Edition, Asphalt Institute, Kentucky, USA, ISBN: 978-1-934154-27-4, 2007.

Modelling Operating Speed at Merging Section on the Exclusive Motorcycle Lane

Muhammad Akmal Suhaimi, Muhammad Akram Adnan and Norliana Binti Sulaiman

Abstract The function of Exclusive Motorcycle Lane (EML) is to segregate the motorcycles from the mainstream flow using physical separator or chevron marker. Basically, it is separated along the main stream highway and combines with main road at merging and diverging section. The merging sections of an EML at urban expressway in Malaysia have serious problems about the safety, efficiency and comfortability, because of the increasing traffic demand rate and lack progress of vehicle performance capability at merging section. The improvement of geometric characteristic design is difficult because the spaces are too dense and limited. Therefore, improvements are able only with operational and safety management at merging section. So, this research has been performed to achieve the objective which is to obtain an analysis field data on EML at merging that reflect on the traffic condition on EML at merging section. Then, the data will be analyzed to check the performance on EML. This area of study was done at Federal Highway on EML at merging section for 3 sites and took 3 days data at each site continuously counting using Automatic Traffic Counter (ATC). The 85th and 95th percentile of speed can be determined. Two regressions of model equation had been performed for speed versus flowrate and geometric parameters. For the 85th percentile operating speed, R^2 is 85.8 % and for 95th percentile speed is 78.6 %.

M.A. Suhaimi (✉) · M.A. Adnan · N.B. Sulaiman
Faculty of Civil Engineering, Universiti Teknologi MARA,
Shah Alam, Selangor, Malaysia
e-mail: akmalz_persie@yahoo.com; 2012322929@isiswa.uitm.edu.my

M.A. Adnan
e-mail: akramuitm@yahoo.com

N.B. Sulaiman
e-mail: ns49@yahoo.com

1 Introduction

The goal of the highway design is to maintain the comfortability, speed, convenience, the environmental compability and maintaining or improving the safe system for highway traffic [1]. In recent years, fatalities on Malaysia have become a critical issue especially for the road user. Although there are some reductions [2], when it comes for the future, it continuously becomes a surprising number of fatalities. The cause of rising fuel prices have put more pressure and pressing people to use affordable and fuel saving types of vehicles. So, the best solution is to use motorcycle for daily use. According to the statistic, more than half of the motor vehicles that are registered are motorcycles [3]. Motorcycles are the most affordable, comfortable, economical, fuel saving and facilitate for the road user regarding to the consistency of high percentage registered motorcycles in Malaysia [4, 5]. Motorcycle caused a high degree of congestion in certain cities of Malaysia especially Kuala Lumpur at Federal Highway Route 2. Due to the increasing volume of motorists, motorcycles constitutes more than half of the total registered vehicles and contribute to more than 60 % of casualties to total traffic accidents [6]. Automatically, the safety of this form of transportation has become an important issue that must be emphasized. Because of that, a part of motorcycle safety program has been launched, that is, to build Exclusive Motorcycle Lane (EML), to deduct the number of fatalities. It has been constructed along the expressway such as at the Federal Highway. The EML has its own way in and way out that call as merging and diverging section, respectively. The merge area of EML is formed when motorcycles at mainstream traffic joins the EML to form a single freeway lane [1]. The merging sections or on-ramps of an EML at urban expressway in Malaysia have serious problems about the safety, efficiency and comfortability. It is because lack of geometric characteristic design condition, the high level of traffic flow rate and insufficient progress of vehicle performance capability at merging section. The improvement of geometric characteristic design is difficult because the space of the urban area is too compact or dense to be changed and get very limited spaces around the area. So, the development of driving assistance functions at merging section is a must. It can be the key method to achieve safer, more efficient and more comfortable driving conditions for motorcyclist. With the good performance of traffic, it will certainly sustain the road infrastructure for now or else in the future and help in improving our country's economic activities eventually. The objectives of this study are:

- To obtain and analyze the traffic operational characteristics on EML at merging section.
- To perform several regressions modelling relationship between speed, flowrate and geometric parameters while travelling on the merging section.

Fig. 1 Front view for EML at merging section

2 Problem Statement

EML have particular needs and problem which may not be widely recognized by
those whose responsible, due to lack of bonded design document and no official
guideline to design motorcycle facilities in Malaysia so far. The merging problem is
one of the most complex problems facing the traffic researcher. Motorcyclists at
merging section are exposed to the danger that is probably caused by the sur-
rounded vehicles, geometric design and road structure condition. On merging
section, motorcycles from mainstream traffic are joining with other motorcycles on
EML, and the danger is that no speed limit has been done for EML's user. Figures 1
and 2 shows the merging section of EML at Federal Highway.

Fig. 2 Back view for EML at merging section

3   Literature Review
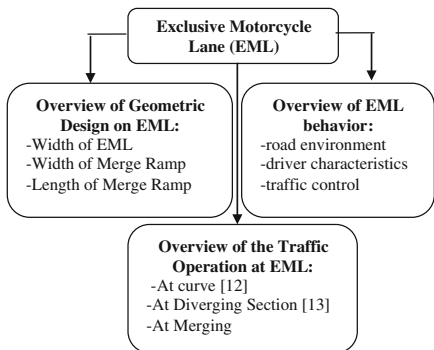
The motorcycle lane program has been launched for the public in order to reduce the accidents among motorcyclists. There are two types of motorcycle lanes, exclusive and non-exclusive. The non-exclusive is separated only by a chevron marker from the traffic mainstream. EML is fully separated from the main traffic and is for use of motorcyclist only. The example is along Federal Highway Route 2 from Shah Alam to Kuala Lumpur, separated using a physical separator and for this example they use guardrails. The other types of transportations are not allowed to use it. The word "Motorcycle" refers to the motor vehicle with two wheels, for example normal motorcycle and scooter [7]. The horsepower of the engine is in the range from 50 to 150 cc. This type of lane is to help in reducing the main traffic congestion besides safer for motorcyclist. EML lanes are used to increase the safety of motorcyclist and reduce fatalities for road users [8]. Basically, with space and financial constraints, the acceptable and practical width for EML is about 2.1–2.9 m. A wider lane may improve comfort but it is also expected that the average of motorcycle speed will increase which may bring speed management problems [9]. Collisions with other motor vehicle were the most accident causes rather than losing control stability [2].

It is important to specify standards for exclusive motorcycle lanes as the optimum control width should be comfortable for all riders. A motorcycle lane, if too wide, will have an impact on the economics of the design. If the motorcycle lane is too narrow it will cause discomfort to the rider and probably leads to a higher risk of collision while overtaking. A study about the determination of a safe control width at 85th percentile operation speed for an EML in Malaysia has been done [11]. This study found that an EML needs a control width of 3.81 m for two riders to travel side by side comfortably at a speed of 70 km/h. Currently, the average width of EML along Federal Highway Route 2 is approximately 3 m, and the change of geometric design is difficult because of the space constraint. There are no official guidelines for EML, it was just developed based on bicycle track.

A study has been done about predicting the operational speed models of horizontal curve on EML [12]. This models estimates 85th percentile operating speed at

points along a roadway by considering its horizontal and vertical alignment. Regression models were developed to predict the 85th percentile speed of motor-cyclists on horizontal curves, based on the geometry of the curves. Speed diminishes before the initiation of a circular curve, constant speed is maintained along it, and then speed increases again. The speed was measured at half length of the horizontal curve (center of the horizontal curve) using laser speed detector. Using the residual analysis, it was determined that there was no statistically significant difference between the observed and the predicted 85th percentile curve speed. Before this, a study about investigating the diverging section has been conducted; the performance of traffic itself looks reasonable and reflects the change of geometric design variables and traffic characteristics [13]. So, this research will be the first attempt, to study about merging section at exclusive motorcycle lane. It is focusing on exclusive motorcycle lane with predicting the 85th and 95th of speed at merging section only.

Background of study	Results/Findings	Identified gaps	Comparison
Faezi et al. (2011) [12]			
This study was focused on developing the speed prediction equation on horizontal curve using geometric characteristics of the curve on EML in Malaysia	1. Using residual analysis, it was concluded that there was no statistically significant difference between observed and predicted 85th percentile curve speed	1. Speeds were collected using portable laser speed detector	1. Speeds were collected using ATC [14]
	2. The operating speeds of motorcycle influence by lane width, deflection angle and length of tangent	2. Speeds were measured at center of the horizontal curve	2. Speeds were measured at EML, before motorcycles merged from main road
	3. V_{85} $_{Curve} = 19.357\ W - 0.394\Delta + 0.654T$	3. 11 sites, at each site at least 100 observations were taken	3. 3 days continuously counting at each site, for all 3 sites
		4. This study was limited to simple horizontal curves on EML	4. This study is focusing on merging section at EML

3.1 Review of Fundamental Traffic Parameter

In order to achieve required data for this study, data collection should be measured correctly. The parameters obtained for an analysis of this study are:

- Volume—traffic volume is defined as the number of vehicles passing a point on a highway, or a given lane or direction of a highway, during a specified time interval [1]. For this research, it represents the differences between motorcycles on merging section and motorcycles on EML.
- Headway—Headway is defined as the time interval between successive vehicles as they pass a point along the lane [1]. From this, we can determine the distance followed by other motorcycle or can be called as gap. The front tire is used as the reference point for this research.
- Time Mean Speed (TMS)—TMS is the average speed of all vehicles passing a point on a highway or lane over some specified time period [1]. TMS is computed by finding each individual vehicle speed and taking a simple average of the result.

4 Methodology of the Research

4.1 Site Selection

- This study is focusing on obtaining data for 72 h continuously counting using Automatic Traffic Counter (ATC) [14] on three of the merging section at EML along the Federal Highway from Shah Alam to Kuala Lumpur. For this research, the merging section at Federal Highway Route 2 was selected. Figure 3 shows the sketching of the merging section on EML. The selected sites were at KM28.4 heading to Kuala Lumpur, and at KM31.2 and KM6.5, heading to Shah Alam on Figs. 4, 5 and 6, respectively.

4.2 Data Collection

- For geometrical characteristic design, it was measured by roller meter such as width of EML, width of merging section and length of merging section, as in Fig. 7.
- For parameters such as speed, volume and headway of motorcycles, it was calculated using Automatic Traffic Counter (ATC). The ATC's tubes called as road tube will be installed on the road at direction 1 and direction 2 as in Fig. 6. The data which were recorded for 72 h continuously include peak and non-peak hours at the selection spot site of EML.

Fig. 3 Sketching of merging section for *Direction 1* and *Direction 2*
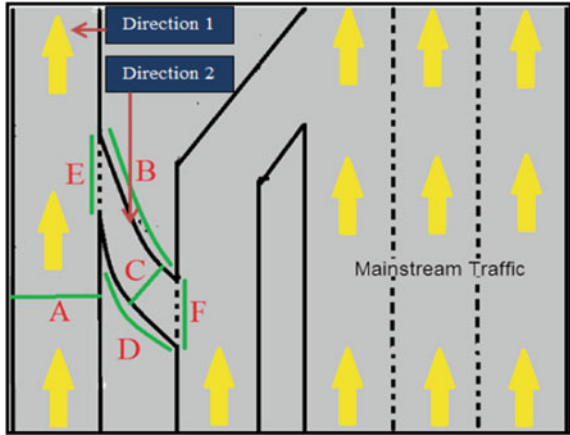
Fig. 4 Place where tubes of ATC are located at Site 1

Fig. 5 Site 2 at KM31.2 heading to Shah Alam

4.3 Data Analysis

- All data on ATC are transferred to the Microsoft Excel to be summarized for simple analysis. For example total of annual daily traffic, time mean speed and headway for every 1 h and average for 72 h counting duration.

4.4 Development of Model

- In the process of development model, all data analysis was computed to develop a model based on TMS and flow rate factor on EML.
- MINITAB software was used to develop the linear regression from the data that have been reduced. This model uses independent variable, flowrate to predict the outcome of dependent variable, TMS.

5 Results and Analysis

Using the data available, the average daily traffic (ADT) defined as the average 24 h volume at a given location over a defined period less than 1 year, can be determined in motorcycle per day unit. Table 1 shows the total volume of motorcycle from day one to day three for each direction at merging section for each site.

Table 2 shows the geometric parameters for each site at merging section. The labelling can be referred in Fig. 3. Average between B and D will be taken as the length of the ramp.

TMS is a point measure. So, the speed of each motorcycle was recorded as it passes a point that had been chosen. From the obtained TMS, the 85th and 95th percentile of speed can be calculated. 85th percentile of speed roughly equates to the speed of the flow, represents the optimal speed to set a maximum speed limit, which gives a general description of the high speed observed by most reasonable drivers [1]. For the 95th percentile of speed, it can be used as the design speed for the EML.

From Tables 3 and 4, using MINITAB software, it shows the predictor, coefficient, standard error, T-Value and P-Value for 85th and 95th percentiles of speed

Table 1 The volume of motorcycles at merging section

Site	Direction 1	Direction 2
1	20,161	27,095
2	51,478	32,232
3	13,193	29,586

Table 2 The geometric parameters at merging section

Site	Geometric parameters (m)				
	A (EML width)	B	C (Ramp width)	D	Ramp length (B + D)/2
1	2.9	38.2	2.7	56.16	47.18
2	2.3	26.7	1.8	38.3	32.5
3	2.2	36.1	3	25.2	30.65

Table 3 Regression analysis for EML model, 85th percentile of speed versus q, width EML, width ramp and length ramp

Predictor	Coefficient	Standard error	T-value	P-value
Constant	12.048	2.098	5.74	0.000
Q (mc/hr/ln)	0.004	0.0005	7.80	0.000
Width EML	49.331	1.659	29.73	0.000
Width ramp	−7.5476	0.496	−15.22	0.000
Length ramp	−1.61737	0.0605	−26.73	0.000

Table 4 Regression analysis for merging section, 95th percentile of speed versus q, width EML, width ramp and length ramp

Predictor	Coefficient	Standard error	T-value	P-value
Constant	14.211	2.867	4.96	0.000
Q (mc/hr/ln)	0.0051075	0.0006695	7.63	0.000
Width EML	57.703	2.213	26.07	0.000
Width ramp	−9.6564	0.6267	−15.41	0.000
Length ramp	−1.97287	0.07793	−25.31	0.000

at merges section, respectively. For this study, four predictors were used, the flow rate, Q, width of EML, width of merge ramp and length of the merge ramp. Equations (1) and (2) show the influence between 85th and 95th as the response and Q, EML width, ramp width, ramp length as the predictor.

$$V85 = 0.004\,Q + 49.3\,\text{width EML} - 7.55\,\text{width Ramp} - 1.62\,\text{Length Ramp} + 12 \tag{1}$$

$$\begin{aligned} V95 = {}& 0.005\,Q + 57.7\,\text{width EML} - 79.66\,\text{width Ramp} \\ & - 1.97\,\text{Length Ramp} + 14.2 \end{aligned} \tag{2}$$

6 Conclusion

In summary, this study is to investigate the traffic operational performance on EML at merging section. From the results that had been collected as in Table 1, it showed that at Site 2, the volume of motorcycles at direction 1 are 51,478, more than the volume of motorcycles at direction 2, which are about 32,232 motorcycles in the 3 days. In the other hand, for Site 1 and 3, more motorcycles used merging ramp than the EML itself. It can be said that a lot of motorcycles often used this merging section rather than other because this merging point was located right after the 4 junctions, so many motorcycles from other directions enter this merging section as their starting point in joining the EML. It can be concluded that motorcycles rarely selects the Site 2 as their joining point with EML, rather than Site 1 and Site 3.

There are two equations can be built from the data collected. For Eqs. (1) and (2), the p-value is less than 0.005, means that the predicting Q can be included in the model for estimating 85th and 95th percentile of speed. R-square is one of the criteria to prove that the linear regression between the response and the predictor fits the data well or not. The R-square is 85.8 and 78.6 % which is having high relationship for both Eqs. (1) and (2) respectively. Referring to the regression analysis for both, the value of R-square, there is high relationship between 85th and 95th percentile of speed with the predictors. The standard error for each equation is small, indicating it is reliable for estimating the 85th and 95th percentile of speed

parameters. So, with this type of equation, the 85th percentile of speed can be used as the speed limit for motorcycle at EML just with flowrate and geometrics parameters at merging section. For the 95th percentile of speed, it can be used for the designer or engineer of transportation as guideline to design the better traffic performance for motorcycles besides reducing the number of accident.

The understanding of the development for motorcycle traffic performance in a major traffic can help the involved authorities to find most suitable and appropriate policies to repair or improve the traffic performance on the road. With a well planned expressway for EML operation, it will ensure the operation of traffic performance go smoothly.

References

1. R. P. Roess, S. P. Elena, and R. M. William, Traffic Engineering, 4th Edition Pearson Education, 2011.
2. R.S. Radin Umar, G.M. Murray, and L.H. Brian, "Preliminary analysis of exclusive motorcycle lanes along the federal highway F02, Shah Alam, Malaysia," IATSS Research, vol. 19, pp. 93–98.
3. RTD. (2013). Official Portal of Road Transportation Department Malaysia, Statistik Pendaftaran Motosikal, http://www.jpj.gov.my/statistik-pendaftaran-motosikal.
4. Harnen, S., Radin Umar, R. S., Wong, S. V., Wan Hashim, "Development of Prediction Models for Motorcycle Crashes at Signalizad Intersections on Urban Roads in Malaysia," Journal of Transportation and Statistics, Vol. 7, 2004.
5. Hsu, T. -P. (2003). A Comparison Study on Motorcycle Traffic Development in some Asian Countries – Case of Taiwan, Malaysia and Vietnam. Final Report, Prepared for The Eastern Asia Society for Transportation Studies (EASTS) International Cooperative Research Activity, 28 October 2003.
6. Road Safety Plan in Malaysia (2006–2010), Status Paper on Road Safety in Malaysia, http://www.unescap.org/ttdw/roadsafety/Reports2007/Malaysia_RSpaper.pdf.
7. Shoji, "The speed, flow and headway analyses of motorcyle traffic," Journal of the Eastern Asia Society for Transportation Studies, vol. 6, pp. 1496–1508.
8. M. Hazmi and M. A. Adnan, "A Comparative Study on the Behaviour of Motorcyclist on Exclusive Motorcycle Lane at Merging Section under Different Configuration of Road Marking." International Civil and Infrastructure Engineering Conference (InCIEC), pp 1209–1219, 2014.
9. C. Cong Minh, S. Kazushi, and M. S. Tetsuo, and Y. Injima, "An analysis of the effect on driver's behaviour of information system at merging section of expressway," pp. 1–10.
10. Hussain et al, "Exclusive motorcycle lane," MRC Draft, pp. 1–8.
11. Teik Hua, L., & Radin Umar, R. S. (2005). Determination of Comfortable Safe Width in an Exclusive Motorcycle Lane. Journal of the Eastern Asia Society for Transportation Studies, Vol. 6, pp. 3372–3385, 2005.

12. S. F. Faezi, H. Hamid, S. R. Davoodi, and D. E. Malaysia, "Predicting Speed Model of Horizontal Curves on Exclusive Motorcycle Lane in malaysia," *Aust. J. Basic Appl. Sci.*, vol. 5, no. 5, pp. 590–598, 2011.
13. M. A. Suhaimi, M. A. Adnan and N. Sulaiman, "Investigation of Diverging Traffic Performance on the Exclusive Motorcycle Lane," *IEEE Symp. Business, Eng. Ind. Appl.*, pp. 437–441, 2013.
14. M.A. Adnan, N.I. Zainuddin, N. Sulaiman and T.B.H. Tuan Besar, "Vehicle Speed Measurement Technique Using Various Speed Detection Instrumentation," IEEE Business Engineering and Industrial Applications Colloquium (BEIAC), 2013, pp. 668–672.

Abrasion Loss and Binder Draindown of Porous Asphalt with Nanosilica-Modified Binder

Khairil Azman Masri, Ahmad Kamil Arshad, Juraidah Ahmad and Mohamad Saifullah Samsudin

Abstract This paper details the performance evaluation of porous asphalt (PA) with nanosilica (NS)-modified binder in terms of binder draindown and abrasion loss. Both tests are widely used to evaluate the lower limit and upper limit of the design binder content for porous asphalt. The existence of nanoparticle with different proportions can affect binder draindown and abrasion resistance behavior of PA. Six different percentages of nanosilica were mixed with PEN 60–70 type of binder in this study. Then, all these blended modified binders were used to prepare PA samples using Marshall mix design method. Nanoparticle used in this study was nanosilica with the average size of 10–15 nm. Binder Draindown test was performed using a metal basket with 3 mm perforation. Then, abrasion loss value was evaluated using Los Angeles Abrasion Machine without steel ball. In accordance to PWD of Malaysia Specification for Road Works, which states that binder draindown for PA should not be more than 0.3 % of total weight of sample, while abrasion loss should not be more than 15 % also by weight of total sample. Based on Cantabro loss Test and Binder draindown test, 2–5 % NS are considered as the effective amounts of NS to be mixed with binder in order to reduce the abrasion loss and binder draindown of PA. In addition, 4 % NS is also considered as the optimum NS proportion. The existence of NS is capable to enhance the physical and rheological properties of asphalt binder, while at the same time it disperses well in asphalt binder. Thus, the performance of PA is also enhanced with the addition of NS in the binder.

Keywords Binder draindown · Cantabro loss · Nanosilica · Porous asphalt · Marshall mix design

K.A. Masri (✉) · M.S. Samsudin
Faculty of Civil Engineering, University Technology MARA,
Shah Alam, Selangor, Malaysia
e-mail: khairilazmanmasri@yahoo.com

A.K. Arshad · J. Ahmad
Institute for Infrastructure Engineering and Sustainable Management,
University Technology MARA, Shah Alam, Selangor, Malaysia
e-mail: drahmadkamil@salam.uitm.edu.my

1 Introduction

Although porous asphalt (PA) is considered as a non-structural layer of flexible pavement, it should possess a sufficient strength in bearing the external loads imposed by traffic. Mechanical properties such as binder draindown, abrasion loss, dynamic modulus, rutting resistance, stripping potential, resilient modulus, indirect tensile strength, and stability should be evaluated for PA. All those performance evaluations are crucial since PA is also having a shorter service life compared to dense graded asphalt due to raveling and clogging [1]. In addition, the design binder content for PA is evaluated by considering lower limit and upper limit using Binder draindown test and Cantabro loss test. The mechanical properties of PA are dependent on several factors such aggregate gradation, types of additive used and the binder used. The main objective of this study is to evaluate whether the existence of nanosilica (NS) is capable of enhancing the abrasion resistance and reducing the binder draindown of PA. This study is limited to PA prepared using PEN 60–70 type of binder modified with different proportions of NS. Figures 1 and 2 show the structure of PA and its application at a parking lot.

Fig. 1 Porous Asphalt (PA)

Fig. 2 PA at parking lot

2　Literature Review

2.1　Cantabro Loss

Cantabro test will decide the lower limit of OBC for PA. This test was developed to evaluate and control the raveling loss of PA under dry condition and soaked condition. Particle loss is one of the disadvantages of porous asphalt. This is also called raveling which is the loss of particles from the road surface. The raveling of PA is influenced by aging, low temperature, moisture and other factors. Therefore, it is necessary to investigate the raveling characteristic of PA in order to ensure the durability of PA. Cantabro test is used to evaluate the particle loss resistance of porous asphalt concrete specimens. The test is done using Los Angeles abrasion machine without steel ball [2].

Allex et al. [3] stated that the Cantabro test is the laboratory test most commonly used to evaluate durability for mix design and evaluation of PA mixtures In the Cantabro test, a compacted specimen is placed in the Los Angeles abrasion machine (without abrasive load) and subjected to 300 revolutions. Yuhong and George [4] also stated that the samples are placed in the Los Angles testing machine without steel ball and the machine is rotated at a speed of 30–33 revolutions per 7 min for 300 revolutions. The Cantabro loss, expressed in percentage, corresponds to the ratio of lost weight to initial weight of the compacted specimen. The test is conducted at a standard temperature (25 °C), since this variable effects the test results. The Cantabro loss is considered as an index of the mixture resistance to disintegration [5]. The disintegration resistance of PA has been evaluated using Cantabro loss test since many years ago [6].

Kimberly and Bradley [7] stated that the abrasion resistance of each mixture was measured using the Cantabro abrasion test after 7 days ageing in an oven at 60 °C. Three compacted specimens were used for this test. The test was conducted by recording the initial mass (M_i) of a specimen then placing it in the Los Angeles abrasion drum for 300 revolutions without the steel charge at 25 °C. After 300 revolutions, the specimen was removed, brushed off, and the final mass (M_f) was recorded. The percent mass loss was then calculated by dividing the mass loss (M_i–M_f) by the initial mass (M_i) of the specimen [7].

2.2　Binder Draindown

Binder draindown test will decide the upper limit of OBC for PA. According to Allex et al. [5], PA mixtures typically exhibited an asphalt binder film thickness of higher than the corresponding thickness for dense-graded HMA. This difference and the small fine aggregate content in PA mixtures (as compared to that of dense-graded HMA) lead to higher susceptibility for the asphalt binder to drain off the aggregate skeleton. The irregular distribution of asphalt binder generated by its

draindown can lead to raveling in zones with low asphalt binder content and reduction of permeability in zones with accumulation of asphalt binder [5].

Binder draindown is also considered as the major problem of PA, since PA is having high air void content, thus the tendency for binder to flow through those air voids is high, resulting in binder drained off from the mix. Binder draindown testing is performed on all the mixes in accordance with AASHTO T305 with the exception that the tests were performed at the mixing temperature for each mix. This testing procedure entailed measuring the binder lost from the loose mix placed in a draindown basket (No. 4 mesh) and conditioned at the mixing temperature for 3 h with the draindown being measured every hour. Two draindown specimens were tested per binder content over a binder content range. The test results will show the amount of binder draindown relative to the total weight of the mix. A maximum draindown of 0.3 % by weight of total mix is typically the maximum value for draindown of a porous asphalt mix [7].

Kimberly and Bradley [7] also studied the potential for binder draindown due to exposure to elevated temperatures over long periods of time. The specimens were conditioned in a 60 °C chamber for 56 days and the porosity and permeability of each specimen was measured at specified intervals (7, 14, 28, 42 and 56 days) to determine the occurrence of binder draindown through the specimen, which would reduce the permeability. During conditioning, each specimen was wrapped using a galvanized steel hardware cloth to prevent deformation or collapse due to the high temperature conditioning. In addition, the top of the specimen remained the top for the entire 56-day conditioning period, so the binder would only be able to flow in one direction [7].

3 Methodology

3.1 Materials

Porous asphalt grading B as per PWD Malaysian Specification for Road Works were used for this study. The weight of aggregate for each sample was approximately 1100 g. PEN 60–70 type of binder was used and the binder was mixed with different proportions of nanosilica (NS) ranging from 1 to 6 % by weight of binder. NS used was in colloidal form with the average size within 10–15 nm (nm). Table 1 below shows the aggregate gradation for Grading B in accordance to PWD Malaysia Standard Specification while Table 2 shows the properties of NS used in this study.

The main objective of this study is to evaluate the effectiveness of NS as an additive of wet mix in order to enhance the performance of PA in terms of its binder draindown characteristics and abrasion resistance. In order to prepare NS-modified binder, NS was mixed in a reactor with continuous stirring. In this study, a control binder (Penetration Grade Pen 60–70) was used to prepare the modified binder. The

Table 1 PA grading B aggregate gradation

Sieve size (mm)	Passing (%)	Retained (%)	Retained (g)
20	100	7.5	82.5
14	85–100	27.5	302.5
10	55–75	47.5	522.5
5	10–25	10	110
2.36	5–10	4.5	49.5
Filler	–	1	22
Hydrated lime	–	2	11

Table 2 Specification of nanosilica

Properties	Value
Appearance	Slight milky transparent
SiO_2 (%)	30 %
Na_2O (%)	0.5 %
pH	8.5–10.5
Density	1.19–1.22 g/cm^3
Particle size	10–15 nm

binder then was heated at 160 °C. The NS blends were then transferred to the hot-melted asphalt and mixed with continuous stirring at 1800 rpm. This process was continued for one hour to obtain nano-modified asphalt binder. The asphalt binder was blended with 0–6 % NS in increments of 1 % by weight of the binders.

3.2 Cantabro Loss

A total of 21 samples were prepared for this test, where 3 samples each for different percentage of NS ranging from 0 to 6 %. Those three samples were tested to obtain the average value of abrasion loss for each different proportion of NS. Those Marshall specimens were kept at a temperature of 25 °C for 6 h before testing. The specimens were weighed after it had been kept for the specified time and placed into the Los Angeles machine without the steel balls. Then, the drum was switched on at a velocity between 188 and 208 rad/s and subjected to 300 revolutions without steel ball. The Cantabro Loss was determined using Formula (1) below and Fig. 3 illustrates the Los Angeles abrasion (LAA) machine that was used to run this test.

$$\text{Cantabro loss} = (M_0 - M_1)/M_0 \times 100 \tag{1}$$

where
M_0 initial mass of specimen before put in LA Machine
M_1 final mass of specimen

Fig. 3 LAA machine

3.3 Binder Draindown

The amount of NS that were blended into binder were in the range of one to six percent (1, 2, 3, 4, 5, and 6 %) by weight of binder. The determination of design bitumen content were performed through Marshall mix design method. For this study, 4.75 % of DBC was used as control sample of PA (0 % NS). To obtain DBC, specimen that were tested had variations in the binder content (4–6 % by weight and differ by 0.5 % increment). In each increment of the binder content, 3 specimens were be prepared, thus, making a total of 30 specimens for Cantabro test and binder draindown test (15 samples each test). For Cantabro test, each specimen was subjected to 300 revolutions in the Los Angeles apparatus (LAAV) together with steel balls at temperature of 25 °C. The analysis on the percentage of mass loss versus binder content reveals the lower limit of bitumen content. For binder draindown test, the wire basket and the aluminum tray were used. The loose samples were tested by putting it into wire basket with 3 mm perforation. Then, the samples were put into oven for 3 hours with the temperature of 180 °C. The binder will flow through wire basket and drop onto the aluminum tray. The analysis on the mass retained versus binder content reveals the upper limit of bitumen content. Drained binder is essential to ensure the accuracy and reliability of upper limit DBC for PA [8]. Formula (2) was used to calculate the binder draindown while Figs. 4 and 5 illustrate the binder basket (100 mm × 100 mm × 100 mm) with 3 mm perforation that was used for this test.

Fig. 4 Top view of binder basket
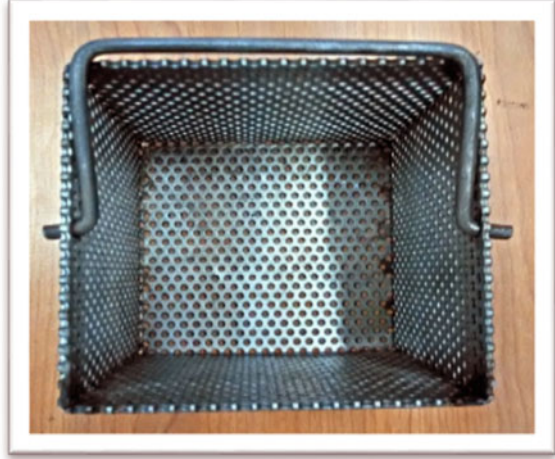
Fig. 5 Side view of binder basket

$$\text{Draindown}(\%) = \frac{D - C}{B - A} \times 100 \qquad (2)$$

where
A   mass of empty wire basket (g)
B   mass of wire basket and sample (g)
C   initial mass of paper plate (g)
D   final mass of paper plate (g)

4 Results and Discussions

4.1 DBC Determination

The DBC is determined by conducting binder draindown test and Cantabro loss test. After both tests were done, two graphs were obtained which were binder draindown (%) versus binder content and Cantabro loss (%) versus binder content (%) as illustrated in Figs. 6 and 7. Both graphs are essential to obtain DBC for PA. Based on PWD of Malaysia the maximum allowable of abrasion loss was 15 % while binder draindown was 0.3 %, both by weight of total sample. After dragging those values, both graphs show that the upper limit of DBC was 4.5 % and lower limit of DBC was 5.0 %. Taking the average of 4.5 and 5.0 %, the DBC obtained for this study was 4.75 % weight of binder. Then, both binder draindown test and Cantabro loss test were performed again but this time, the DBC value (4.75 %) was used as control sample with 0 % NS, while the other samples were prepared using different proportion of NS (1–6 % NS). The value of binder draindown and Cantabro loss versus different proportion of NS were discussed in the following section.
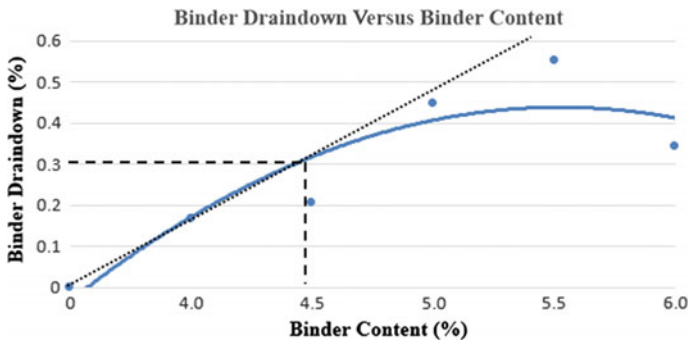
Fig. 6 Binder draindown versus binder content
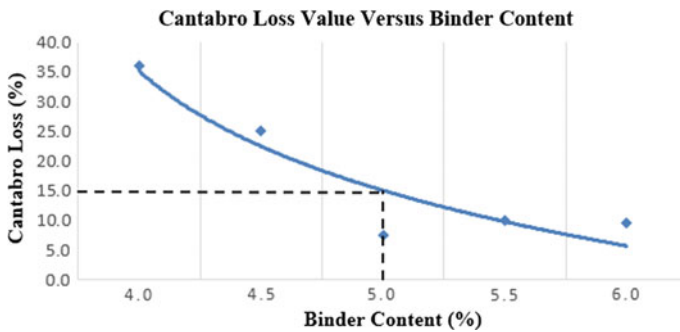
Fig. 7 Cantabro loss versus binder content
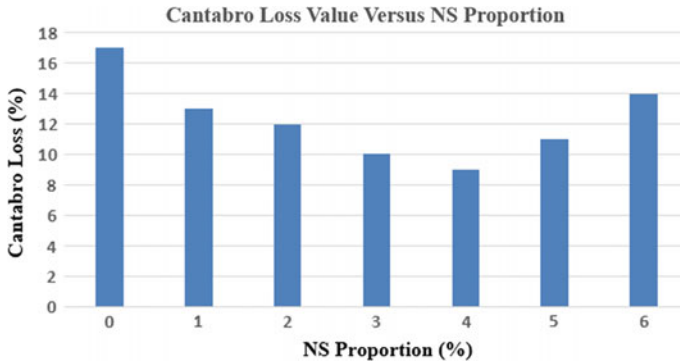
Fig. 8 Cantabro loss (%) versus amount of NS (%)

4.2 Cantabro Loss

From Fig. 8, it could be seen that different percentages of NS produced different values of Cantabro loss. The control sample (0 % NS) obtained the highest value of Cantabro loss which was 17 %, while the lowest Cantabro loss value was 9 % (4 % NS). This happened likely due to the abrasion force between specimens and drum, resulting in disintegrated samples with certain amount of loss [6]. The trend pattern of Cantabro loss value also indicated that 3–5 % NS as the optimum amount to be utilized in order to reduce the abrasion loss of PA. The value of Cantabro loss increased after the addition of 4 % NS thus indicating that too much addition of NS is not suitable in enhancing the abrasion resistance of PA.

4.3 Binder Draindown

Figure 9 presents the percentage of binder draindown with the addition of different percentages of NS. The bar chart shows almost the same pattern as the Cantabro loss bar chart. This indicates that the existence of NS enhances the bonding between binder and aggregates. The value of binder draindown was significantly reduced with the addition of 2–5 % NS. However, the addition of 1 and 6 % NS gave almost similar value of binder draindown as the control sample (0 % NS). This indicates that the optimum proportion of NS to be mixed was around 2–5 % in order to reduce the binder draindown of PA. Figure 10 shows binder draindown value in gram where its ranges from 2 to 3.6 g, while Table 3 illustrates the result summary for both tests.
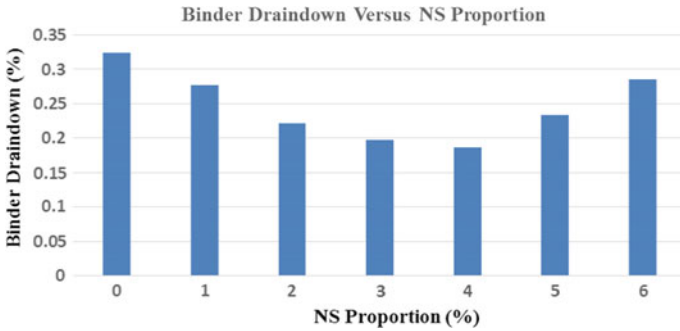
Fig. 9 Binder draindown (%) versus amount of NS (%)
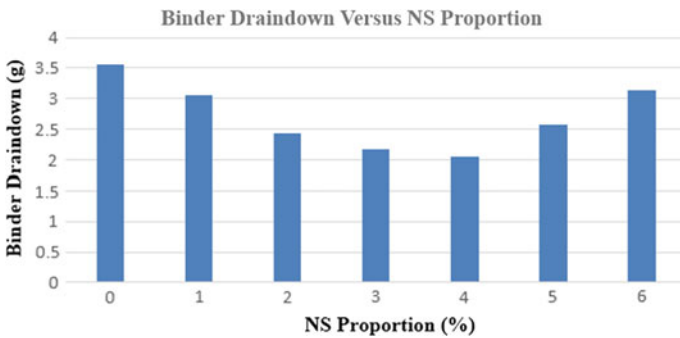
Fig. 10 Binder draindown (g) versus amount of NS (%)

Table 3 Result summary

NS (%)	Cantabro (%)	Draindown (%)	Draindown (g)
0	17	0.324	3.564
1	13	0.277	3.047
2	12	0.222	2.442
3	10	0.197	2.167
4	9	0.186	2.046
5	11	0.234	2.574
6	14	0.285	3.135

4.4 Visual Observation of Binder Draindown Test

From visual observation, there was a significant difference of binder material drained for different proportions of NS. For control sample (0 % NS), binder was drained together with fine particles. A study by Hamzah and Hassan [8] proved that binder was drained together with fine aggregates due to 3 mm perforation used for

Fig. 11 Control sample 0 % NS

Fig. 12 2 % NS
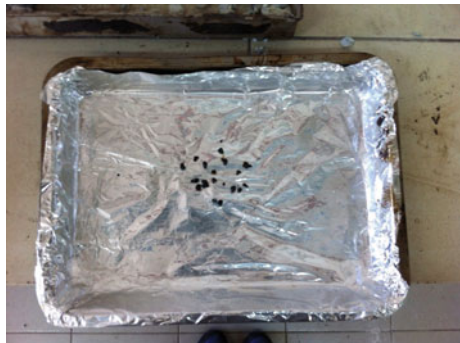
the binder basket. However, binder drained was lower with the increase in the amount of NS. This is shown in Figs. 12, 13 and 14, where less binder was drained compared to Fig. 11 (0 % NS). In addition, based on visual observation, 4 % NS was determined as the optimum amount to reduce the binder draindown of PA since a very little binder was drained compared to other samples. The trend was also consistent with the results discussed in the previous section where the addition of more than 6 % NS increased the amount of binder drained.

Fig. 13 4 % NS

Fig. 14 6 % NS

5 Conclusions and Recommendations

The findings of this study indicate that the existence of nanoparticle is capable for enhancing the performance of PA in terms of its abrasion resistance and binder draindown. Based on Cantabro loss test and binder draindown test, 2–5 % NS are considered as the effective amount of NS to be mixed with binder in order to reduce the abrasion loss and binder drained of PA. In addition, 4 % NS is also considered as the optimum NS proportion. The existence of NS is capable to enhance the physical and rheological properties of asphalt binder. Thus, the performance of PA with the addition of NS in the binder is also enhanced.

For future study, it is recommended that the different types of binder and aggregate gradations are to be considered in order to evaluate the abrasion resistance and binder draindown of PA. The variation of initial temperature, conditioning temperature and test temperature should also be considered in order to obtain extensive and more reliable results regarding both tests.

References

1. M. R. Mohd Hasan, J. Y. Eng, M. O. Hamzah, and J. L. M. Voskuilen, "The effects of break point location and nominal maximum aggregate size on porous asphalt properties," *Constr. Build. Mater.*, vol. 44, pp. 360–367, Jul. 2013.
2. Q. Liu, E. Schlangen, M. van de Ven, G. van Bochove, and J. van Montfort, "Evaluation of the induction healing effect of porous asphalt concrete through four point bending fatigue test," *Constr. Build. Mater.*, vol. 29, pp. 403–409, Apr. 2012.
3. A. E. Alvarez, E. M. Fernandez, A. Epps Martin, O. J. Reyes, G. S. Simate, and L. F. Walubita, "Comparison of permeable friction course mixtures fabricated using asphalt rubber and performance-grade asphalt binders," *Constr. Build. Mater.*, vol. 28, no. 1, pp. 427–436, 2012.

4. Y. Wang and G. Wang, "Improvement of Porous Pavement," 2011.
5. A. E. Alvarez, A. E. Martin, and C. Estakhri, "A review of mix design and evaluation research for permeable friction course mixtures," *Constr. Build. Mater.*, vol. 25, no. 3, pp. 1159–1166, Mar. 2011.
6. M. O. Hamzah, M. R. M. Hasan, M. van de Ven, and A. S. Yahaya, "The effects of initial conditioning and ambient temperatures on abrasion loss and temperature change of porous asphalt," *Constr. Build. Mater.*, vol. 29, pp. 108–113, Apr. 2012.
7. K. R. Lyons and B. J. Putman, "Laboratory evaluation of stabilizing methods for porous asphalt mixtures," *Constr. Build. Mater.*, vol. 49, pp. 772–780, Dec. 2013.
8. M. O. Hamzah and M. R. M. Hasan, "Proportion and Particle Size Distribution of Fine Aggregates Extracted From the Drained Binder in a Binder Drainage Test," pp. 409–412, 2011.

Validation of Operating Speed Prediction Model for Horizontal Curve with Established Models

Nadiah Mohamed, Norliana Sulaiman, Muhammad Akram Adnan and Jezan Md Diah

Abstract Road inconsistency may cause dangerous driving experience that leads to carelessness while handling the vehicle. To determine the road inconsistency, development of models which are based on the 85th percentile of speed is adopted. The models which are taken into consideration are other geometric road characteristics such as superelevation, radius of curve, width of curve, tangent length, and road gradient that can help to minimize the risk of accidents at curve. To further analyze the effectiveness of these developed models, validation of the models using new set of data and comparing it with other established models is crucial. The validation process is conducted by calculating the mean squared error (MSE), mean absolute error (MAE), and mean absolute percentage error (MAPE). MSE value will indicate the differences between the empirical results with the predicted results, while MAE calculates the absolute difference between the empirical results and predicted results. MAPE evaluates the percentage errors between the empirical results with the predicted results. Small values of MSE, MAE, and MAPE is a proof that the models can predict good results.

Keywords 85th percentile speed · Urban road · Modeling · Validation

N. Mohamed (✉) · N. Sulaiman · M.A. Adnan · J.M. Diah
Faculty of Civil Engineering, Universiti Teknologi MARA, Shah Alam, Selangor, Malaysia
e-mail: nadiahmohamed26@gmail.com

M.A. Adnan
e-mail: akram@salam.uitm.edu.my

1 Introduction

About 1000 road accidents with almost 20 fatalities cases are reported daily. In terms of cost, more than RM 9 billion is forfeiture annually in Malaysia [1]. Moreover, according to a research by Transportation Research Institute, University of Michigan; Malaysia is at seventeenth place from 193 countries to be the most dangerous countries for road users. Thirty fatalities were recorded for 100,000 individuals [2]. Further contributing to the increasing number of accidents, are the increasing numbers of vehicles which is believed to lead to changes in geometric design standards which resulted to sections along the same road to have inconsistencies in road geometric features [3]. A mechanism to curb with the high number of accidents and fatalities on the road is vital. One of it is by analysing the relationship between geometric design consistency and road safety. The consistency in road design can be used to improve safety of the road user [4]. The analysis of identifying the relationship between geometric design consistency and road safety is important to identify inconsistent sections of a road alignment so that improvement can be made. According to a study "Geometric design consistency is the conformance of a highway's geometry with driver expectance. When an inconsistency exists which violates driver's expectation, the driver may adopt an inappropriate speed or inappropriate maneuver, leading to collisions" [3]. While [5] had noted that "some spatial relationships of geometric design significantly impact the safety of horizontal curve". A research by [6] further strengthened that geometric design is one of the most important factors affecting accident rates.

Nevertheless, regardless of its importance to road safety, consistencies in road geometric design is not always ensured in current design practice [3, 7] had stated that "The current road design regulations do not explicitly stipulate definition of geometric design consistency as a measure of road section safety. However, they partly deal with some individual elements regarding this issue." Whereas, inconsistencies in road geometric design can lead to speed errors, inappropriate driving maneuvers and undesirable level of accidents. An 85th percentile speed model for reverse horizontal curve is required as it acts as an assessment tool to identify inconsistencies in its geometric features. "A road can always be made safer than it currently is with the increase in safety being measured in terms of a reduction in the number of fatalities and/or injuries or in the severity of the injuries suffered" [8]. The statement by further highlighted that it is possible to implement suitable safety mechanism to the existing road and further support the importance of assessing the consistency of existing geometrical characteristics of road. Counter measures or necessary actions to treat these inconsistencies may later be suggested to improve the reverse horizontal curve, thus hopefully, safety of the road user in Malaysia can be ensured.

2 Data Collection

The goal of this study is to ascertain the relationship of roadway geometrical characteristics that influence operating vehicle speed. To address this, the horizontal simple circular curve for road design standard of U4. The U4 design standard which serves as an intermediate trip length with medium traveling speeds is selected for the purpose of this study. A preliminary site survey will be conducted for site selection. For each site, the width of lane, curve length and radius, road gradient and types of vehicle will be recorded. Road surrounding condition including posted speed limit and signage will be noted as well. The identified sites shall not have any form of traffic calming and no exits or entrance throughout the stretch of road.

For the purpose of identifying the inconsistencies of road, 85th operating speed percentile method was adopted. A number of eight sites around Shah Alam, covering Sections 7–13 were identified to fit the set site criteria. The data collection was conducted during free flow condition and good weather. This is to avoid disruption of traffic, thus, actual operating speed cannot be gauged. Three hours were spent at each site to get the speed data at the start of curve. Once the collection of speed data was completed, road geometrical characteristics, i.e., curves length, CL, width of lane, W, superelevation, e, road gradient GR, and curve radius CR were recorded. The pictorial layouts of these variables are as shown in Fig. 1. 1/3 of these data is isolated for the purpose of model validation. Details of the process flow for data collection process are as shown in Fig. 2. Out of the total 96 data, 32 data were for the purpose of validation, 32 of the total 96 data were secluded from the model development. It is important to use new set of data to eliminate any biasness or misinterpretation of the analysis results.

Fig. 1 Pictorial layouts of variables

Keynote:
CS is the location for beginning of curve
CM is the location for middle of curve
CE is the location for end of curve
CR is the radius of curve (m)
CL is the length of curve (m)
W is the width of roadway measured at middle of curve (m)
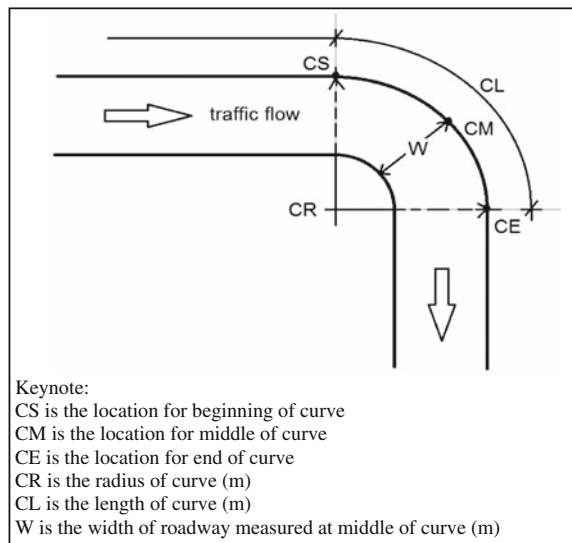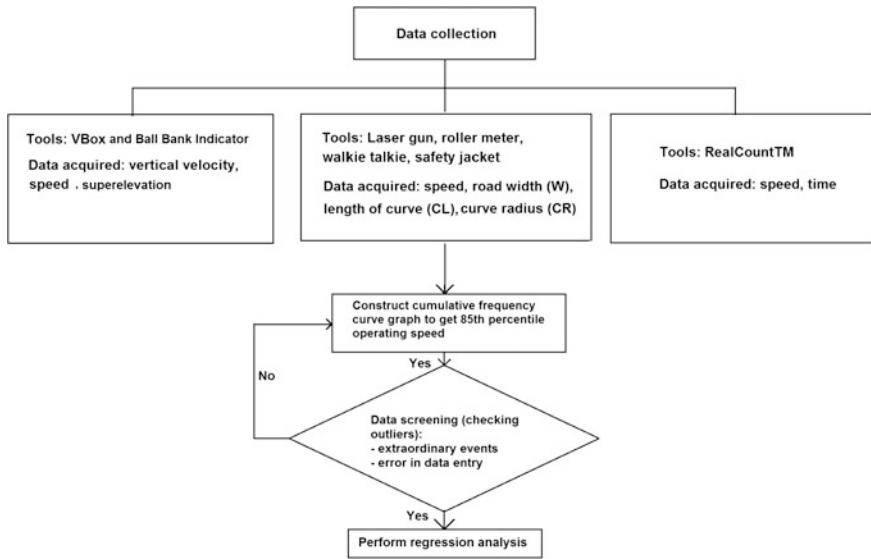
Fig. 2 Framework of data collection

3 Analysis of Data and Results

Try outs to determine variables which are highly significant to the prediction of 85th percentile speeds will be conducted after removal of outliers during filtering process. Then, correlation analysis will be performed to the variables. Once it is done, development of 85th percentile speeds can be initiated. This research is focusing on developing 85th percentile speed models to be utilized as assessment tools for the simple horizontal curve. Verification of 85th percentile speed model will be conducted by comparing it with other models from established research and guidelines.

This step shall be conducted properly to avoid unreliable model being developed. After all the data had been screened, multiple regression analysis on the data was adopted as a tool for model development. Multiple regression analysis is adopted as it let several independent variables been considered in the model development process [9]. By allowing more than one predictor variables, $A, A_1, A_2, A_3...A_n$, the analysis will give better explanation of the dependent variables, B and the model will be highly efficient. The general form of multiple regression analysis is as shown in (1).

$$B = \beta_0 + \beta_1 A_1 + \beta_2 A_2 + \cdots + \beta_k A_k + \varepsilon \tag{1}$$

where

B	is the dependent variables
$A, A_1, A_2, A_3, ...A_n$	is independent predictor variables that should be free from error
$\beta_0, \beta_1, \beta_2, ...\beta_k$	are unknown constants
ε	is the random error

To certify that the data used in this study is free from errors, a detail process of data analysis, as shown in Fig. 3 was established. In the first phase, the data was screened for outliers after the descriptive statistics of the data was developed. After the removal of outliers, correlation analysis was conducted for consideration of variables that were most suitable for the development of model. From the

Fig. 3 Flowchart of data analysis
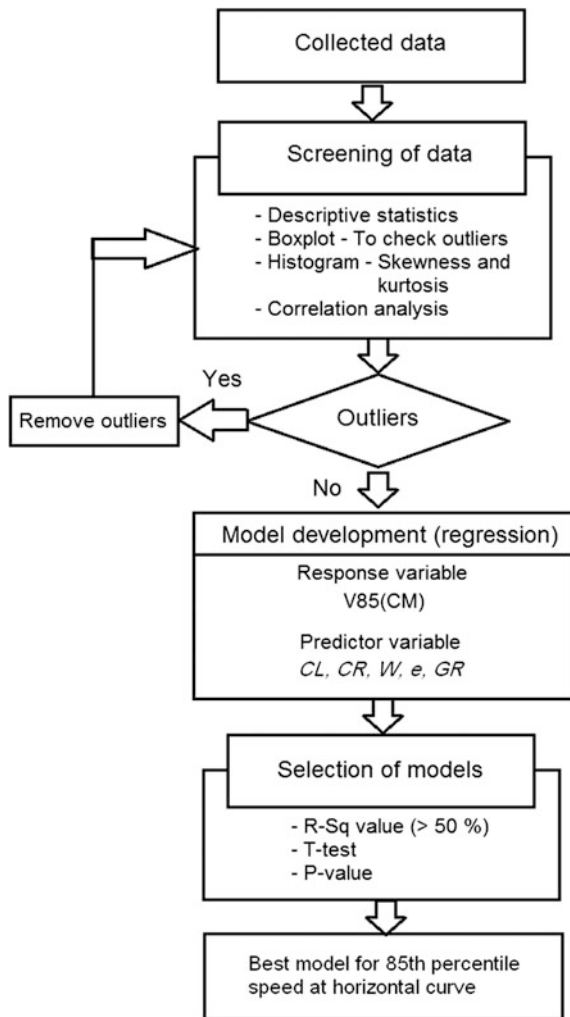
Table 1 Descriptives statistic

Variables	Mean	S.E Mean	ST Dev	Median
V85(CS)	47.75	1.36	11.48	46.0
V85(CM)	49.62	1.16	9.76	49.01
CL	130.83	7.15	60.24	107.3
W	7.175	0.161	1.358	7.40
CR	105.97	8.85	74.59	83.69
e	0.05789	0.00186	0.01567	0.05
GR	0.334	0.207	1.742	0.00

Table 2 Skewness and kurtosis of variables

Variables	Skewness	Kurtosis
V85(CS)	0.28	−0.84
V85(CM)	0.64	−0.53
CL	1.15	−0.34
W	−0.32	−1.03
CR	1.57	1.68
e	0.73	−0.40
GR	0.86	1.30

correlation analysis, it was discovered that length of curve, CL, radius of curve, CR, road width, W, superelevation, e, and road gradient, GR were significant to the 85th percentile operating speed at middle of the curve. Selection of the best model was also conducted in this stage and it was determined from the highest R-Sq value, T-test, and its P-value. In general, all the graphs were normally distributed in mound shape curve and this follows the empirical rule [9] with 95 % confident level. The descriptive statistics for all variables are shown in Table 1 while Table 2 shows the statistics of skewness and kurtosis for all parameters. The small values mean that the data is normally distributed.

Correlation analysis on the variables can assist in identifying the degree of linear relationship of two variables.

The set hypotheses for this analysis is shown in Table 3.

Results of the correlation analysis (Table 4) had revealed that there is no clear correlation between V85(CM) with both W and e. The p-value for both correlation analysis is more than 0.05. Thus, null hypotheses is accepted.

For $V85_{CM}$ model development, the identified variables are CL, CR, W, GR, e, vehicle speed at beginning of curve, V85(CS), and speed at the middle of curve, V85(CM). Multiple regression analysis was adopted to get the best combination of variables to predict the 85th percentile speed at horizontal curve. Hypotheses used for F-test is as shown in Table 5.

ANOVA's hypotheses are in Table 6.

Table 3 Hypothesis for correlation analysis

H$_0$	There is no correlation between these variables
H$_1$	There is correlation between these variables

Table 4 Correlation analysis of variables

	V85(CS)	V85(CM)	CL	W	CR	e	GR
V85(CM)	0.707 0.000						
CL	0.015 0.900	0.502 0.000					
W	−0.393 0.001	0.072 0.553	0.323 0.006				
CR	0.530 0.000	0.741 0.000	0.358 0.002	−0.056 0.641			
e	−0.274 0.021	−0.110 0.360	−0.200 0.095	0.235 0.048	−0.416 0.000		
GR	−0.247 0.038	−0.385 0.001	−0.326 0.006	0.220 0.065	−0.511 0.000	0.155 0.196	

Cell contents: Pearson correlation P-Value

Table 5 Hypothesis for F-test

H$_0$	No significant contribution of predictors to response variables
H$_1$	Minimum one predictors has significant contribution to response variables

Table 6 Hypothesis for anova

H$_0$	The model cannot be used to predict the 85th percentile speed
H$_1$	The model can be used to predict the 85th percentile speed

One model was identified to be the best model as shown in (2) for the prediction of 85th percentile speed at horizontal curve.

$$V85_{HC} = 12.9 + 0.388 \; V85(CS) + 0.0800 \; CR + 168e \tag{2}$$

where

$V85_{HC}$ is the 85th percentile speed at horizontal curve (km/h)

$V85(CS)$ is the 85th percentile speed from speed data at beginning of curve (km/h)

CR   is the radius of curve measured at middle of curve (m)

e is the superelevation

Table 7 Output for *F* test

Predictor	Coef	SE Coef	T	P
Constant	12.914	4.001	3.23	0.002
V85(CS)	0.38802	0.06201	6.26	0.00
CR	0.07995	0.01010	7.92	0.00
e	167.62	42.40	3.96	0.00
S	5.03753			
R-Sq	74.5 %			
R-Sq (adj)	73.4 %			

Regression analysis output is in Table 7.

It was discovered that V85(CS), CR, and *e* in (2) were highly significant to V85$_{HC}$ as indicated in Table 7. This is indicated by *p*-value of 0.000. Analysis on the standard error coefficient, CR, and V85(CS) have minimum variability in the coefficients, but *e* contained about 42.40 of variability in its coefficient (V85 (CS) = 0.06201, CR = 0.01010, *e* = 42.37). Residual error is 5.03753. With *R*-Sq value of 74.5 %, this equation fits very good.

The analysis of variance for V85$_{HC}$ is shown in Table 8. With *p*-value lower than 0.05, the null hypotheses can be rejected. The *p*-value further confirmed that V85$_{HC}$ can be applied for prediction of 85th percentile speed at horizontal curve. In terms of explained total variation, V85(CS) has the highest percentage compared to CR and *e* (V85(CS) = 67 %, CR = 25 % and *e* = 8 %).

The assumption was further confirmed by analyzing the residuals distribution of V85$_{HC}$. This was done by plotting the residuals and its distribution in order to check if the residuals are normally distributed or not. Normal probability plot for V85$_{HC}$ shown in Fig. 4 similar to a 45° straight line that slopes upward signifying ideal distribution. In Fig. 5, residuals versus fit plot of V85$_{HC}$ had showed the distribution of residuals.

Majority of the residuals for V85$_{HC}$ revealed are scattered randomly between 10 and −10. Only small value of residuals was plotted within 15–25. Next, the normality of model was tested by using Anderson–Darling and Kolmogorov Smirnov tests. The hypothesis for these tests is as shown in Table 9.

Table 8 Output for anova

Source	DF	SS	MS	F	P
Regression	3	4973.1	1657.7	65.32	0.00
Residual error	67	1700.2	25.4		
Total	70	6673.3			
	DF	Seq SS			
V85(CS)	1	3332.0			
CR	1	1243.8			
e	1	397.2			

Fig. 4 Normal probability plot
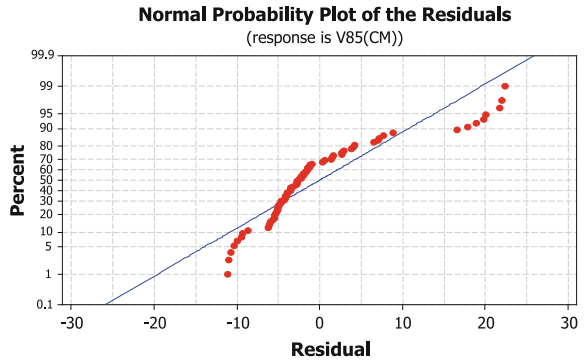
Fig. 5 Residuals versus fitted values plot
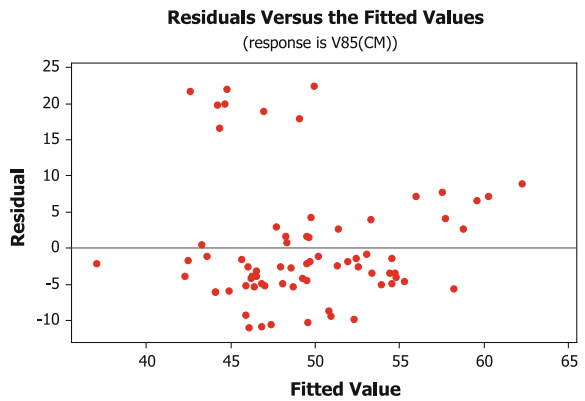
Table 9 Hyopothesis for normality test

H_0	Normal distribution of residuals is observed
H_1	Abnormal distribution of residuals is observed

Table 10 Hyopothesis for normality test

Normality test (P-value)	
Anderson-Darling	Kolmogorov Smirnov
0.102	>0.15

Result of normality test conducted had been discovered to be more than 0.05 for the p-value as shown in Table 10. Therefore, null hypothesis cannot be rejected and residuals for all the models are normally distributed.

4   Validation of Models

V85$_{HC}$ is further validated using the isolated data. This is important to ensure that V85$_{HC}$ is reliable in predicting the value of response variable. Validation was conducted using equation and paired t-test. The equations used are as shown in (3), (4), and (5) below.

$$\text{RMSE} = \sqrt{\frac{\sum_{i=1}^{N}\left(yi - \breve{y}i\right)^2}{N}} \tag{3}$$

$$\text{MAE} = \frac{\sum_{i=1}^{N}\left|(yi - \breve{y}i)\right|}{N} \tag{4}$$

$$\text{MAPE} = \frac{\frac{\sum_{i=1}^{N}\left|\left(yi - \breve{y}i\right)\right|}{yi}}{N} \times 100 \tag{5}$$

where

RMSE   is root mean square error

MAE   is mean absolute error

MAPE   is mean absolute percentage error

$\breve{y}_i$ is the estimate value from model calibrated in this study estimated for the ith dataset

y$_i$ is the empirical value results for the ith dataset

N is the number of dataset considered [10]

Upon calculating the error using the Eqs. (3), (4), and (5), the model is considered good when getting small value as it proved the models can predict good results [9].

For validation purpose, the variables are redefined as in Table 11.

V85$_{emp}$ and V85$_{HC}$ are plotted to determine the relationship between both values. The scattered points were discovered to be randomly scattered along the 45° line as shown in Fig. 6. For V85$_{HC}$, the points are found to be randomly scattered along the 45° line with value ranging from 40 to 80 km/h. Using the equations, it was discovered that the RMSE value for V85$_{HC}$ is 5.33 km/h, MAE is 4.31 km/h, and MAPE is 8.85 % as shown in Table 12.

V85$_{HC}$ is then validated using paired t-test. Hypothesis used for this test is as shown in Table 13.

Table 11 Definitions of variables	V85$_{HC}$ is estimated 85th percentile operating speed at horizontal curve (km/h)
	V85$_{emp}$ is empirical value of 85th percentile operating speed at middle of curve by using independent data set (km/h)

Fig. 6 Relationship of model and empirical data
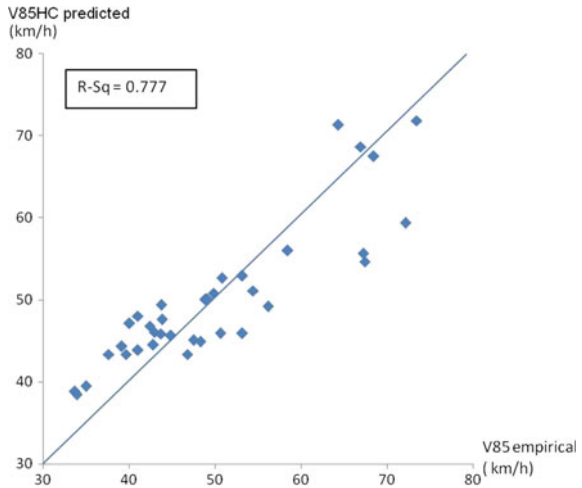
Table 12 Validation by equation

RMSE (km/h)	MAE (km/h)	MAPE (%)
5.33	4.31	8.85

Table 13 Hypothesis for paired *T*-test

H_0	The mean difference for V85emp and $V85_{HC}$ is equals to 0
H_1	The mean difference for V85emp and $V85_{HC}$ is not equals to 0

Table 14 Validation by paired *T*-test

	t-test	*p*-value
$V85_{emp}$ versus $V85_{HC}$	0.27	0.785

Paired *t*-test for $V85_{HC}$ revealed that the *p*-value is more than 0.05 as shown in Table 14. Therefore, the null hypothesis cannot be rejected. This showed that there is no significant difference of mean for V85emp and $V85_{HC}$.

$V85_{HC}$ is then compared with model from other research. The selected model is inserted with predictor variables from validation data and then measured for its 'effectiveness' using formula and scatter plot as its indicator. The models selected for this purpose is as shown in (6).

$$V85_C = 102.45 + 0.0037L - (2741.75 + 1.75L)/R \qquad (6)$$

Fig. 7 Predicted 85th percentile speed model from Canadian Roads (2002) versus empirical 85th percentile speeds measured at middle of *curve*
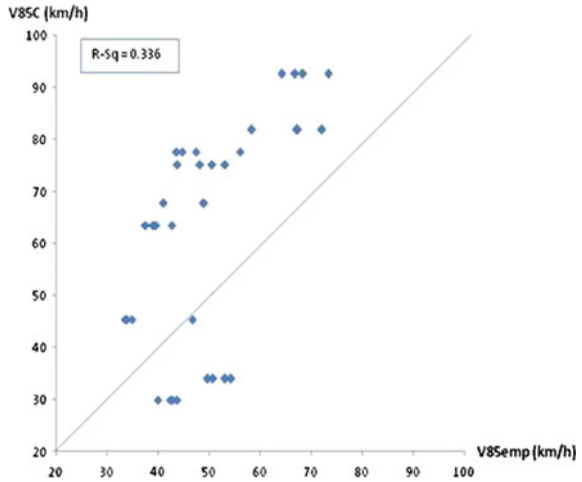
where

V85$_C$ is the 85th percentile speed on curve (km/h)

L is the length of curve (m)

R is the radius of curvature (m) [11]

The scatter plot of V85$_C$ versus V85$_{emp}$ shown in Fig. 7 revealed that only one point falls on the 45° line of the scatter plot. The *R*-Sq is also weak with the value of 0.336. It was discovered in Table 15 that V85$_C$ produced high RMSE value compared to V85$_{HC}$ (V85$_C$ = 21.51 km/h and V85$_{HC}$ = 5.33 km/h). MAE value for V85$_C$ is also high with 20.19 km/h compared to V85$_{HC}$ (V85$_{HC}$ = 4.31 km/h). In addition, V85$_C$ estimates high percentage for mean absolute percentage error with 42.15 % (MAPE for V85$_{HC}$ = 8.85 %).

The difference of V85$_C$ and V85$_{HC}$ in RMSE, MAE, and MAPE values are shown in Table 16 below.

Table 15 Validation by equation

RMSE (km/h)	MAE (km/h)	MAPE (%)
21.51	20.19	42.15

Table 16 Differences between both models

RMSE (km/h)	MAE (km/h)	MAPE (%)
16.18	15.88	33.3

5   Conclusion and Recommendation

Many studies have been conducted to develop the 85th percentile speed model in relation to road geometric characteristics. These studies were conducted both in rural areas as well as in urban areas. Though such study has taken place in Malaysia, this study is different as it attempted to further enhance the potential 85th percentile operating speed model by incorporating many variables. The developed model is also more superior as it is a reflection of Malaysian road condition, that is, the traffic composition, road design, traffic behavior and etc.

Several recommendations are proposed for further research to fully incorporate $V85_{HC}$ in road geometric design in Malaysia. The recommendations are as follows:

   i. For future research, consideration should be given to sites that cover Northern region, Southern region, Sabah, and Sarawak.
  ii. To include various type of curve, for example reverse horizontal curve, compound curve, and vertical curve.
 iii. Utilization of latest technology in data collection is recommended as the high number of data is beneficial as it can closely represent the actual condition.

Therefore, $V85_{HC}$ is proposed to be a starting point of 85th percentile speed model implementation in Malaysia geometric road design guideline.

References

1. Department of Road Safety Malaysia (DRSM) - Jabatan Keselamatan Jalan Raya Malaysia, Road accidents fact for 10 years. Retrieved 13 January 2010, from http://www.jkjr.gov.my/statistics.html.
2. The Star (Star) (2014). *Malaysia has 17th most dangerous roads in the world, according to Michigan university research*. From http://www.thestar.com.my/News/Nation/2014/02/22/Nations-with-deadliest-roads-Malaysia-17th/.
3. Joanne, C.W.N. (2002). *Quantifying the relationship between geometric design consistency and road safety*. Department of Civil Engineering, The University of British Columbia, 2324 Main Mall, Vancouver, Canada.
4. K. Fitzpatrick, I.B. Anderson, K.M. Bauer, J.M. Collins, L. Elefteriadou, P. Green, P., D. Harwood, N. Irizarry, R. Koppa, R.A Krammes, J. McFadden, K.D. Parma, K. Passetti, B. Poggioli, O. Tsimhoni & M.D. Wooldridge, "Evaluation of Design Consistency Methods for Two Lane Rural Highway", Federal Highway Administration, FHWA-RD-99-173, 2000.
5. Findley,D.J., Hummer, J.E., Rasdorf,W., Zegeer, C., Fowler, T.J. (2012). *Modelling the impact of spatial relationship on horizontal curve safety*, Accident Analysis and Prevention 45 (2012) 296–304.
6. Karlaftis, M.G and Golias, I. (2001). *Effects of road geometry and traffic volumes on rural roadway accident rates*. Accident Analysis and Prevention 34 (2002) 357–365, Department of Transportation Planning and Engineering, Faculty of Civil Engineering, National Technical University of Athens, Greece.
7. Senica, G. and Milosevic, D. (2006). *Road design consistency analysis for roads on Serbian road network*. Transport Research Arena Europe 2006, The Highway Institute, Belgrade, Serbia & Montenegro.

8. Lamm, R., Wolhuter, K., Beck, A., Ruscher, T. (2001). *Introduction of a new approach to geometric design and road safety*. 20th South African Transport Conference, 'Meeting the Transport Challenges in Southern Africa'.
9. N.A. Weiss. Introductory statistics.4th Alternate Edition, Addison-Wesley Publishing Company, United States of America, 1997.
10. M.A. Adnan, "Development of entrance ramp merging density model based on an urban expressway traffic condition". School of Civil Engineering, Universiti Sains Malaysia, Malaysia, 2007, unpublished.
11. Transportation Association of Canada, "Geometric design guide for Canadian roads". Part 1. Laurent Blvd Ottawa, Canada, 2002.

Physical Properties of Nanomodified Asphalt Binder

**Mohamad Saifullah Samsudin, Khairil Azman Masri,
Ahmad Kamil Arshad and Juraidah Ahmad**

Abstract Nanomaterials have been widely used around the world for many purposes. This paper details the effect of nanomaterials in improving the physical properties of asphalt binder. Nanosilica (NS) was used to modify base asphalt binder with concentration 1–5 % (increment 1 %) by weight of binder. A series of physical properties test were performed to analyze the performance of nanosilica-modified asphalt binder (NSMB) such as softening point test, penetration test, and viscosity. It observed that the addition of NS increased the softening point and viscosity value while, the penetration value is decreased. These results indicate that NS improved the performance of physical properties of asphalt binder. Penetration index (PI) and penetration viscosity number (PVN) were determined to evaluate temperature susceptibility of binder. It was concluded that the addition of NS to asphalt binder can improve the temperature susceptibility of asphalt binder. Besides that, it was found 4 % of NS have excellent performance and this indicates that 4 % of NS is the optimum concentration for base asphalt binder.

M.S. Samsudin (✉) · K.A. Masri · J. Ahmad
Faculty of Civil Engineering, University of Technology Mara (UiTM),
Shah Alam, Malaysia
e-mail: mohamadsaifullah90@gmail.com

K.A. Masri
e-mail: khairilazmanmasri@yahoo.com

J. Ahmad
e-mail: juraidah@salam.uitm.edu.my

A.K. Arshad
Institute for Infrastructure Engineering and Sustainability Management (IIESM),
Faculty of Civil Engineering, Road Department, Public Work Deparment,
University Teknologi Mara, 40450 Shah Alam, Selangor, Malaysia
e-mail: drahmadkamil@salam.uitm.edu.my

1   Introduction

The use of nanotechnology can produce many new materials and tools with wide-ranging purpose by manipulating matter in the atomic, molecular, and macromolecular scale. Usually, nanomaterial size dimension range from 1 up to 100 nm (nanometer) [1]. The applications of nanomaterial include green chemistry, photocatalytic degradation of organic pollutant, remediation of polluted soils and water, pollutant sensing and detection [2]. Civil engineering is also inseparable from the use of nanotechnology. The uses of nanotechnology in civil engineering are increasing and offer an attractive alternative for asphalt binder modification. There are various nanomaterials that have been used in asphalt modification such as nanoclay, carbon nanotube, nanosilica, and nano fiber [3].

Nanoclay is one of the familiar nanomaterials used in asphalt modification. Nanoclay or layered silicate nanoparticles was first introduce by Kojima [4] as reinforcing agent in production of nylon 6/clay nanocomposites. Shahabadi [5] used bentonite clay (BT) and organically modified bentonite (OBT) to modify asphalt binder. The addition of BT and OBT in asphalt binder showed improvement in softening point, viscosity, rutting resistance, and low temperature cracking resistance. Pamplona [6] investigated the effect of organically modified vermiculite (OVMT) and montmorillonite (OMMT) as second modifier materials in styrene-butadiene-styrene (SBS) modified asphalt binder. The existence of OVMT and OMMT as a third component in SBS modified asphalt binder showed improvement in penetration value, viscosity, stiffening effect, thermal susceptibility, and storage stability. In addition, Cloisite-15A and Nanofill-15 was found to have the potential to increase rutting and aging resistance [7, 8].

Carbon nanofiber (CNF), one of familiar nanomaterial has been used in binder modification. Khattak [9] have studied the effect of CNF as a second modifier in polymer modified PAC30 (PG70-22). To ensure that CNF is fully dispersed in asphalt binder, two different dispersion methods were utilized. First, the CNF was sonicated for a specific time to initially disperse the fibers into a solvent. Second, the mixture was mixed with asphalt binder using mechanical mixer at medium to high temperature. The dynamic shear rheometer (DSR) test was used to determine complex shear modulus (G*) and creep compliance (J[t]). From the analysis of G*-master curve and J[t], it revealed that the addition of CNF improves the visco-elastic response of the asphalt binder. Khattak [10] expanded the research on hot mix asphalt (HMA) mixtures using CNF. Based on the experimental result, the addition of CNF improves fatigue life and resistance to permanent deformation. In addition, stiffness and dynamic modulus also improved.

Silica is an abundant compound around the earth that is naturally occurring, such as quartz sand, rocks, and clays, and is widely used in industries to produce silica gels, colloidal silica, fumed silica, and so on [3]. Nanosilica (NS) also can be produced by agricultural waste materials to produced NS such as, from rice husk ash [11, 12], sorghum vulgare seed heads [13], and bagasse ash [9] by precipitation method, bio-digestion process and sol-gel process. NS has been widely used in

polymer, concrete, and asphalt binder as inorganic filler to improve the properties of polymeric, mechanical, and bituminous materials. NS, which has a maximum dimension of about 30 nm, is an inorganic material that has promise of beneficial properties such as large surface area, good dispersal ability, strong adsorption, high chemical clarity, and excellent stability [8].

Hsieh et al. [14], found that the addition of NS in anhydride-cured epoxy resin to form 'hybrid' nanocomposites improved their Young's modulus and fracture energy, Gc. Also, a good dispersion of the NS was found even at high concentration. Jumahat et al. [5], incorporate NS with polymer to improve tensile properties. The result showed that the addition of 25 wt% NS improved the tensile modulus and strength by about 38 and 24 %, respectively.

NS also have been used as cement replacement or additive in concrete mixture and cement mortar to improve its strength [7, 15–17]. The test results showed that the additional NS improved the compressive strength, tensile strength, and flexural strength of cement mortar and concrete. Besides that, nano coated concrete shows reduction for chloride permeability, which can be used as an external coating for durable construction. Based on the SEM image, cement mortar containing NS have more homogeneity, more adhesion at interfacial zone and less pores.

A study by Yao [18, 19] showed that the addition of NS improved antiaging property, rutting and fatigue resistance of asphalt mixture. In addition dynamic modulus, flow number, and rutting resistance of asphalt mixture also significantly improved.

Therefore, in this study, NS was used as a modifier to modify base asphalt binder. NS was added into base asphalt binder at concentrations of 1–5, at increments of 1 % by weight of the base asphalt binder. Physical characterization of base and NS modified asphalt binder (NSMB) was conducted to evaluate the performance of NSMB as well as to determine the maximum concentration of NS. Figure 1 shows the flow chart that illustrates the methodology of the study.
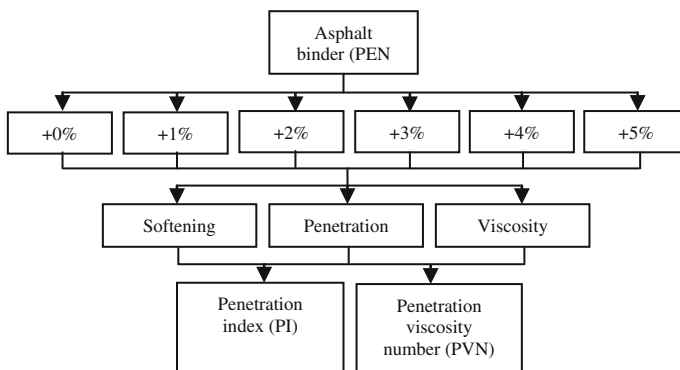
Fig. 1 Test variable used in this study

2 Experimental Works

2.1 Materials

In this study, asphalt binder of 60/70 penetration grade was modified using different concentrations of NS (1–5 % by the weight of the binder). NS used in this study was in colloidal form with the average size within 10–15 nanomater (nm). Table 1 shows the properties of base asphalt binder and NS.

2.2 Binder Preparation

About 400 g of base asphalt binder was heated in a cylindrical container to 160 °C until it achieves the processing viscosity. Cylindrical container was placed on hot plate and mixing temperature was set at 160 °C. Then, NS was gradually added into the heated asphalt binder while stirring the binder with mechanical steel bar stirrer. The speed was increased and fixed to about 2000 rpm. The mixing was continued for about 1 h in order to achieve uniform dispersion of NS in the base asphalt binder. After the modification, binder was put in the oven to remove all the bubbles before pouring the sample into the mold.

2.3 Physical Properties Test

The binder properties were characterized using conventional methods such as softening point, penetration, and viscosity.

Softening point test as to ASTM D36 is used to determine the consistency of binder. Basically, two brass ring filled with asphalt binder, cast in shouldered brass

Table 1 Properties of materials used

Materials	Properties	Value
Asphalt binder	Softening point (°C)	48–56
	Penetration (0.1 mm)	60–70
	Ductility (cm)	>100
	Flash point (°C)	331
Nanosilica	Appearance	Slight milky transparent to translucent liquid
	SiO_2 (wt%)	30 ± 1 %
	Na_2O (wt%)	0.5 %
	pH (20 °C)	8.5–10.5
	Density (20 °C, g/cm^3)	1.19–1.22
	Particle size (nm)	10–15

ring are heated at a controlled rate of temperature (5 °C/min) in a specify liquid while each supports a steel ball approximately 3.5 g. Softening point of asphalt binder are reported based on mean of the temperature at which asphalt binder softens enough to allow steel ball to fall approximately 25 mm in distance.

Penetration test as to ASTM D5 was used to evaluate the consistency of an asphalt binder by measuring the distance in decimillimetre (dmm) of standard needle of penetrometer penetrate vertically into asphalt binder under 100 ± 0.1 g of weight attached at testing temperature of 25, 15, and 5 °C for 5 ± 0.1 s loading time.

Rotational viscometer test ASTM D 4402 was used to measure viscosity of asphalt binder at application temperature to determine handling and pumping properties at the terminal, plant facility, and refinery. Besides that, to determine mixing and compaction temperature that can be used in hot mix asphalt design. Rotational viscosity test were conducted at 135 and 165 °C using a Brookfield viscometer. Temperature was set at a specify temperature, spindle was lowered into the sample chamber containing about 11 g of asphalt binder and rotate at 20 rpm. The torque required to rotate the spindle at a specific shear rate is measured and converted into the viscosity.

2.4 Temperature Susceptibility

Penetration index (PI) and penetration viscosity number (PVN) were calculated to determine the changing of temperature susceptibility of asphalt binder with NS.

The PI was determined from result of penetration test at 25 °C and softening point (ball and ring) test. PI was determined using nomograph or calculated using the following equation:

$$PI = \frac{1952 - 500 \log Pen - 20 S.P}{50 \log Pen - S.P - 120} \tag{1}$$

where Pen is the penetration value at 25 °C and S.P is the softening point value.

The PVN is determined from result of penetration test at 25 °C and viscosity test at 135 °C using the following equation:

$$PVN = -1.5 \frac{4.258 - 0.7967 \log P - \log V}{0.795 - 0.1858 \log P} \tag{2}$$

where P is penetration value at 25 °C and V is viscosity value for 135 °C.

3 Result and Discussion

3.1 Physical Properties

The effects of NS content on physical properties of asphalt binder were evaluated and the results are shown in Tables 2 and 3, Figs. 2, 3, 4, 5, and 6. The results obtained indicate that NS is an effective material in improving the physical properties of asphalt binder. As presented in Table 2 column 2, the addition of 1–5 % of NS into base asphalt binder increased softening point by 13, 15, 19, 21, and 15 %, respectively, compared with base asphalt binder. Higher increasing temperature was obtained at 4 % NS (11.1 °C). The increasing value of softening point indicates that the NS improved the softening temperature of asphalt binder, thus improving its high temperature susceptibility. Figure 2 shows the correlation between NS content and temperature of softening point.

Penetration value of NSMB is shown in Table 2 column 3. Penetration value shows inverse relation compared to softening point value, whereby the addition of NS decreases the penetration value as shown in Fig. 3. Compared to the base asphalt binder, the addition of 1–5 % NS decreased the penetration value by 33, 37,

Table 2 Physical properties for base and nanomodified asphalt binder

Nanosilica concentration (%)	Softening point (°C) Av. 3 reading	Penetration @ 25 °C (dmm) Av. 3 reading	Penetration index (PI) Av. 3 reading	Penetration viscosity number (PVN) Av. 3 reading
1	2	3	4	5
NS0	52.3	65.0	0.02	0.103
NS1	58.9	43.5	0.47	−0.153
NS2	60.3	41.1	0.62	−0.054
NS3	62.4	33.3	0.53	−0.131
NS4	63.4	29.1	0.43	−0.035
NS5	60.0	30.7	−0.08	0.019

Table 3 Rotational viscosity of NSMB

Nanosilica concentration (%)	Viscosity at 135 °C (Pa.s)	Viscosity at 165 °C (Pa.s)
0	0.7	0.3
1	0.8	0.3
2	0.9	0.4
3	1.0	0.4
4	1.2	0.5
5	1.2	0.5

Fig. 2 Softening point of nanomodified binder
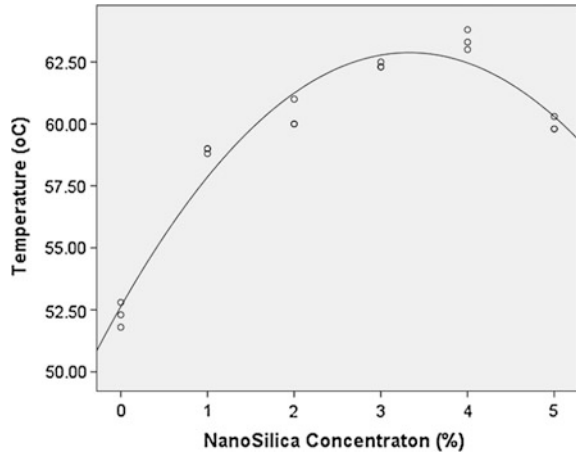
Fig. 3 Penetration value of nanomodified binder
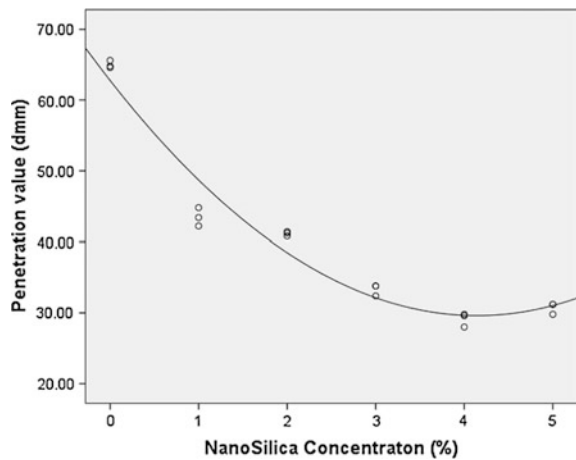
49, 55, and 53 %, respectively. The percentage changes are high compared softening point result. The highest reduction is found at 4 % NS which is 35.9 °C.

Table 3 shows that the viscosity value increased with the addition of NS at both temperatures. The viscosities of base asphalt binder and NSMB decreased as temperature increase as shown in Fig. 4. At temperature of 135 °C, viscosity value increased significantly by addition of 1–4 % NS. Increasing NS content from 4 to 5 % does not have significant effect on viscosity value at 135 °C. Similarly at 165 ° C, increasing NS content from 0 to 1 %, 2 to 3 % and 4 to 5 % did not show any significant effect on the viscosity value. Meanwhile, it is clear that the viscosity value of NSMB at 135 °C were complied with the Superpave standard specification, where NSMB for all percentages had viscosity value lower than the specified maximum limit for Superpave Binder (3 Pa). The maximum increase was found for

Fig. 4 Viscosity of
nanomodified binder
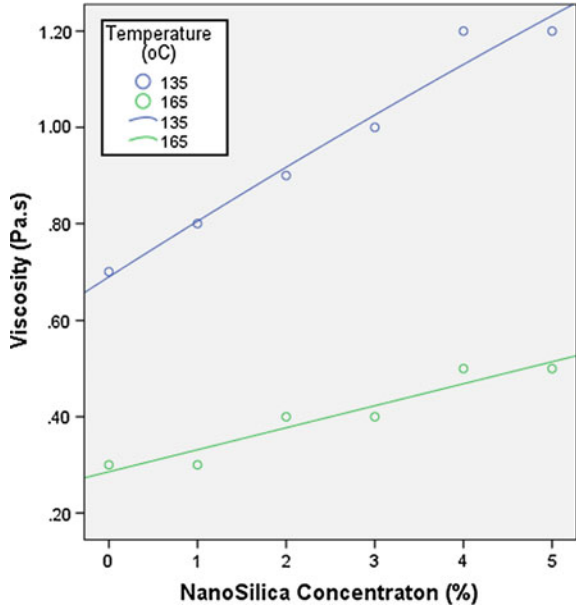
Fig. 5 Penetration index of
nanomodified binder
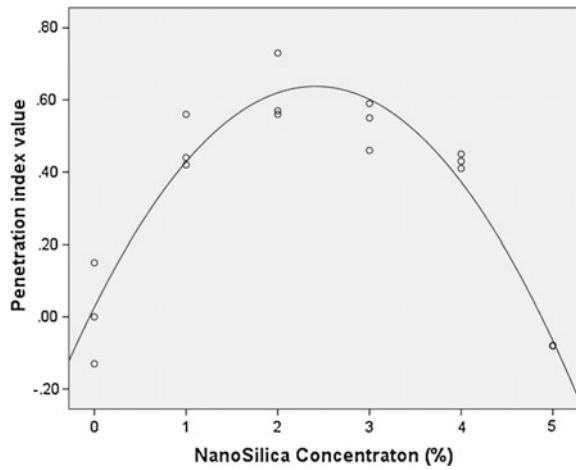
4 % NS for both temperatures which is 71 % for 135 °C and 67 % for 165 °C. The
increase in the viscosity value at high temperature improved rutting resistance. The
difference between 4 and 5 % NS content is not significant, so it is important to
record that for further study 5 % NS can be eliminated.

Fig. 6 Penetration viscosity number of nanomodified binder
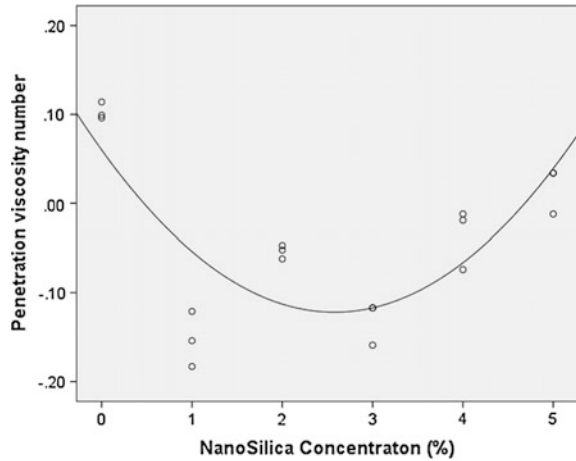
3.2 Temperature Susceptibility

PI and PVN are frequently used to estimate the expected temperature susceptibility for asphalt binder. According to Read and Whiteoak [20] the value of PI ranges from around −3 for high temperature susceptibility bitumen to around +7 for highly blown low-temperature susceptibility (high PI) bitumen. Table 2 column 4 and Fig. 5 show the value of PI. In this study, the maximum and minimum value of PI is 0.62 and −0.08, respectively. PI value of NSMB except 5 % of NS is higher than the PI value of base asphalt binder, this value shows that NSMB of 1–4 % improved resistance to low temperature cracking and permanent deformation (rutting). Since all the values of PI is in between +1 and −1, then NSMB is suitable for road construction for all percentages of NS used in this study.

Table 2 column 5 and Fig. 6 shows the value of PVN. Roberts et al. explained as quoted by Saleh [21] the most paving binder has a PVN between +0.5 and −2.0. Briscoe mentioned in his book that PVN = 0.0 represents a paving asphalt of low temperature susceptibility, while PVN = −1.5 represents a paving asphalt of high temperature susceptibility [22]. The maximum and minimum value in this study is 0.103 and −0.153, respectively, which is in range in the value stated. As compared with PVN value of base asphalt binder, NSMB is less than base asphalt binder. Therefore, these values indicate that all NSMB resist high temperature susceptibility.

Table 4 Ranking based on physical properties

Nanosilica concentration (%)	Softening point (°C)	Penetration value (dmm)	Viscosity value (Pa.s)	PI (low temp.)	PVN (high temp.)
0	6	6	6	5	6
1	5	5	5	3	1
2	3	4	4	1	3
3	2	3	3	2	2
4	1	1	1	4	4
5	4	2	2	6	5

Note 1 = best, 6 = worst

3.3 Ranking of Binder

The general ranking of NSMB based on softening point temperature, penetration value, rotational viscosity, PI (low temperature), and PVN (high temperature) is presented in Table 4.

4 Conclusion

This study investigates the physical properties of NSMB as well as to determine the optimum NS concentration. Based on experimental physical properties result in this study, the following conclusions can be made:

(1) The softening point of asphalt binder increased and penetration decreased by the addition of NS. Therefore, NSMB can improve the hardness and stiffness of asphalt binder.
(2) The viscosity value increased significantly by addition of NS for both temperatures. At very high temperature, viscosity value decreased.
(3) PI and PVN value for NSMB lies between the specified ranges suitable for road construction.
(4) From the overall analyses that have been done, the maximum concentration of NS that should be used in asphalt modification is 4 %. Based on the performance of the physical properties, 4 % NS showed the optimum result for softening point, penetration, and viscosity compared to other percentage of NS.

References

1. Khattak, M.J., Khattab, A., and Rizvi, H.R. (2013). Characterization of Carbon Nano-Fiber Modified Hot Mix Asphalt Mixtures. Construction and Building Materials 40 (2013) 738–745.
2. Khattak. M. J., Baladi. G. Y., and Drzal. L. T. (2004). Binder Rheology, Morphology and Adhesion Effect on Asphalt Mixture.
3. Kojima, Y., Usuki, A., Kawasumi, M., Okada, A., Fukushima, Y., Kurauchi, T. (1993). Mechanical Properties of Nylon 6-clay Hybrid. J mater Res 1993; 8: 1185–1189.
4. Hossain, Z., Zaman, M., Saha, M.C., and Hawa, T. (2014). Evaluation of Viscosity and Rutting Properties Of Nanoclay-Modified Asphalt Binder. Geo-Congress 2014 Technical Papers, GSP 234 © ASCE 2014.
5. Jumahat, A., Soutis, C., Abdullah, S.A., and Kasolang, S. (2012). Tensile Properties of Nanosilica/Epoxy Nanocomposites. Procedia Engineering 41 (2012) 1634–1640.
6. Jahromi, S.G., Andalibizade, B., and Vossough, S. (2009). Engineering Properties of Nanoclay Modified Asphalt Concrete Mixtures. The Arabian Journal for Science and Engineering, Volume 35, Number 1B.
7. El-Baky, S.A., Yehia S., and Khalil, I.S. (2013). Influence of Nano-Silica Addition on Properties of Fresh Hardened Cement Mortar.
8. Hadidy. A. I. A. and Yi-qiu. T. (2010). Comparative Performance of the SMAC made with the SBS and ST Modified Binders. 22: 580–587.
9. Hariharan. V. And Sivakumar. G. (2013). Studies on Synthesized Nanosilica obtained from Bagasse Ash. International Journal of Chemtech Research Vol.5, No.3, pp 1263–1266.
10. Haruehansapong, S., Pulngern, T., and Chucheepsakul, S. (2014). Effect of the Particle Size of Nanosilica on the Compressive Strength and The Optimum of Cement Mortar Containing Nano-SiO2.Construction and Building Materials 50 (2014) 471–477.
11. Thuadaij. N and Nuntiya. A. (2007). Preparation of Nanosilica Powder from Rice Husk Ash by Precipitation Method. Chiang Mai J. Sci. 2008; 35(1): 206–211.
12. Singh. D., Kumar. R., Kumar. A., and Rai. K.N. (2008). Synthesis and characterization of Rice Husk Silica, Silica-Carbon Compoite, and H3PO4 Activated Silica. Ceramica 54 (2008) 203–212.
13. Balamurugan. M. and Saravanan. S. (2012). Producing Nanosilica from Sorghum Vulgare Seed Heads. Powder technology 224 (2012) 345–350.
14. Barik, T.K., Sahu B, Swain V. (2008) Nanosilica-From Medicine to Pest Control Parasitol. Parasitol Res, 103, 253–8.
15. Beigi. M.H., Berenjian, J., Omran, O.L., Nik, A.S., and Nikbin. I.M. (2013). An Experiment Survey on Combined Effect of Fiber and Nanosilica on the Mechanical, Rheoligical, and Durabiity Properties Self-Compacting Concrete. Materials and Design 50 (2013) 1019–1029.
16. Gopinath, S., Mouli, P.CH., Murthy, A.R., Iyer, N.R., and Maheswaran, S. (2012). Effect of Nano Silica on Mechanical Properties and Durability Normal Strength Concrete.
17. Haruehansapong, S., Pulngern, T., and Chucheepsakul, S. (2014). Effect of the Particle Size of Nanosilica on the Compressive Strength and The Optimum of Cement Mortar Containing Nano-SiO2.Construction and Building Materials 50 (2014) 471–477.
18. Yao. H., You. Z., Li. L., Lee. And Goh. S. W. (2012). Evaluation of the Master Curves for Complex Shear Modulus for Nano-modified Asphalt Binder.
19. Yao. H., You. Z., Li. L., Lee. C. H., Wingard. D., Yap. Y. K., Shi. X., and Goh. S. W. (2013). Rheological Properties and Chemical Bonding of Asphalt Modified With Nanosilica. 25: 1619–1630.
20. Read, J and Whiteoak, D. (2003). The shell Bitumen Handbook. Published for Shell Bitumen by Thomas telford Publishing. Thomas Telford Ltd, 1 Heron Quay, London E14 4JD © Shell UK Oil Products Limited, 2003.

21. Saleh, M.F. (2006). Experimental Investigation of Bitumen Physical Properties on Foamability and Mechanical Properties of Foam Bitumen Stabilized Mixes. Third Gulf Conference on Roads (TGCR06), March 6–8, 2006 92-98.
22. Briscoe, O.E. (1985). Asphalt Rheologi: Relationship to Mixture: a symposium Sponsored by ASTM Committee D-4 on Road and Paving Materials, Nashville, TN, 11 Dec. 1985, Issue.

Moisture-Induced Damage Evaluation of Nanopolymer-Modified Binder in Stone Mastic Asphalt (SMA) Mixtures

E. Shaffie, J. Ahmad, A.K. Arshad and D. Kamarun

Abstract This paper presents laboratory investigation on mix design and moisture-induced damage performance of nanopolymer-modified asphalt binder SMA mixture. The effect of nanopolyacrylate (NP) in the mixture was investigated using Marshall mix design and modified Lottman test. Nanopolyacrylate polymer-modified binder was prepared with addition of 0–6 % NP polymer by weight into asphalt binder. Results of SMA14 mixture showed that all the volumetric properties of the mixtures passed the Marshall requirement, which indicates that these mixtures were good with respect to durability and flexibility. The ITS of NC2% and NC4% mixtures increased with an increase in percentage of NP but not as good as the conventional mixture, NC0% which is added with PG76 polymer-modified binder. However, NC6% mixture showed higher tensile strength compared to PG76 modified binder. Results of the moisture-induced damage showed that all the mixes passed the AASHTOT283 criteria with TSR values greater than 80 %. The results also showed that the optimum NP obtained is 6 % by weight of asphalt binder is the most effective and potential proportion to improve moisture-induced damage performance. Thus, addition of nanopolyacrylate polymer to the binder has significantly improved the cohesion as well as adhesion properties of the binder, and hence the performance of stripping.

Keywords Nanopolymer-modified binder · Nanopolyacrylate · Moisture-induced damage · Stone mastic asphalt

E. Shaffie (✉) · J. Ahmad · A.K. Arshad
Institute of Infrastructure Engineering and Sustainable Management (IIESM),
Faculty of Civil Engineering, Universiti Teknologi MARA, 40450 Shah Alam, Malaysia
e-mail: eka@salam.uitm.edu.my

D. Kamarun
Institute of Infrastructure Engineering and Sustainable Management (IIESM),
Faculty of Applied Science, Universiti Teknologi MARA, 40450 Shah Alam, Malaysia

1 Introduction

Malaysia has experienced an incredible period of economic expansion and growth ever since decades ago, especially in population, economy, industrialization and motorization. Due to this rapid advancement, the total length of paved road increased from 60,734 to 71,814 km while registered vehicles increased from 7,210,089 to 13,878,000 vehicles in 2004. Over time, this will cause the traffic volume to increase over the years. Increase in traffic volume will lead to surface distress if the road or pavement is not properly designed and maintained. Moreover, pavement distress will reduce the safety of road users thus leading to road accidents which may result in fatalities. Common defects such as rutting and ravelling caused by hydroplaning contributes to the loss of friction between road surface and tyre.

Moisture-induced damage or stripping is the most common distress on asphalt pavement. Moisture-induced damage is defined as the physical separation of the asphalt cement from the aggregate produced by the loss of adhesion between the asphalt cement and the aggregate which is primarily due to the action of water or water vapour [1]. The main mechanism of moisture-induced damage in asphalt pavement is the loss of cohesion (strength) and stiffness of the asphalt film, and the failure of the adhesive bond between aggregate and asphalt in conjunction with the degradation or fracture of the aggregate [2]. The stresses generated by traffic loads increase significantly and lead to premature rutting, ravelling and fatigue cracking of the HMA layer when the moisture damage reduces the internal strength of the HMA mix [1]. As a result, the performance of asphalt pavement is reduced and the maintenance costs increase.

To minimize the deterioration and increase the long-term durability of pavements, the bituminous layers should be built with enhanced properties, such as resistance to stripping, permanent deformation, fatigue and aging [3]. In recent years, there has been an increased interest to improve pavement service life and eventually reducing the maintenance cost by introducing new approach on stone mastic asphalt (gap graded). Previous studies have shown that the use of Stone Mastic Asphalt (SMA) mix improves resistance to rutting and also increases pavement durability compared to other types of asphalt mixture [4].

There are several methods to reduce pavement distress in asphalt mixtures such as using asphalt additives/modifiers in asphalt binder modification to enhance the engineering properties of the conventional binder and also to extend the asphalt concrete lifespan [4, 5]. Studies have been conducted using few types of polymers such as natural rubber latex (NR), SBS (Styrene Butadiene Styrene Block Copolymer), SBR (Styrene Butadiene Rubber Latex), and EVA (Ethyl Vinyl Acetate) to evaluate the use of polymer modified binder (PMB) which showed improved results on the performance of HMA mix compared to conventional binder [3, 4, 6, 7]. The addition of polymers typically increases the rigidity of the bitumen and improves its temperature susceptibility. Increased stiffness improves the rutting confrontation of the mixture in warm climate and allows the use of relatively softer

base bitumen, which in turn, provides better low temperature presentation [8]. Polymer modified binders also show improved mechanical properties of HMA [9].

Although most studies on developing polymer-modified binder showed improved performance of HMA mix compared to the conventional binder, it will be interesting to explore what nanotechnology offers to improve asphalt binder performance. Asphalt binders modification using nano composite materials has become popular in recent years. Basically, polymer nano composites consist of a blend of one (or more) polymer(s) with various nanomaterials such as nanoclays and carbon nanotubes [10–12]. However, not much has been published on nanocomposites in hot mix asphalt. Currently, studies on the use of nanopolyacrylate (NP) polymer as modifier has not been fully explored. There is a need to use improved materials using nanotechnology technique for the efficiency of the design mix and also to improve binder for better performance, safe riding comfort and also to enable beneficial impact from nanotechnology in pavement engineering. Therefore, the modified asphalt binders with NP polymer need to be studied in detail. The main objective of this study is to evaluate the performance of SMA using the modified asphalt binder. The feasibility of NP polymer modifiers in binder modification is also investigated. It is believed that NP modified asphalt binder would offer better performing asphalt mixes and cost effective for large volume production of asphalt mixes. This study is worthwhile for a sustainable road infrastructure that will provide safe, comfort ridability and economical for the users.

2   Materials and Method

Investigation of this study began with the preparation of SMA mix using nanopolyacrylate (NP) polymer and later evaluation of the moisture-induced damage of the mix, in accordance to JKR, AASHTO and ASTM specifications.

2.1   Material Preparation

All materials used in this study were tested according to physical testing aggregate standard requirement. Granite aggregates, nanopolyacrylate (NP) polymer, asphalt binder of PEN 80/100 and PG 76 asphalt binder are the main materials used in this research. However, only PG76 was used for conventional SMA14. Granite aggregates were supplied by Blacktop Quarry, Rawang located in Klang Valley. The aggregates were processed by washing, oven drying and sieving. All the aggregates were sieved to the appropriate size and stored in individual bins according to the size. This method was used to determine the grading of aggregates including coarse and fine fractions. Washed-sieve (ASTM C 117) was then conducted to determine the

Table 1 Mix designation for conventional and polymer modified binder mixture samples

Mixture grading	Mixture type	Polymer Content (%)	Binder type	Marshall compaction
SMA-14 (Gap graded)	Conventional mix	0	PG76	50 blows/side
	NP-SMA2	2	80/100 PEN	
	NP-SMA4	4		
	NP-SMA6	6		

proportion of mineral filler required for the aggregate gradation. The specific gravity of the coarse (ASTM C127) and fine (ASTM C128) aggregate was conducted to determine the absorption rate and the volume of water in the aggregate expressed as bulk specific gravity, saturated-surface-dry (SSD) specific gravity and apparent specific gravity. The specific gravity of aggregate is important in making weight-volume conversions and to calculate the volumetric properties of compacted HMA specimens. The matrix for the specimen preparation is presented in Table 1.

The NP modified binder was produced by modifying binder of penetration grade 80/100 with addition of 2, 4 and 6 % of nanopolyacrylate polymer by weight of asphalt binder, respectively. For the specimen preparation, 500 g of base asphalt binder was heated up to 110 °C and poured into a 500 ml container. Then, the asphalt binder was heated further in the oven at 150 °C until it was liquified. The NP was then added slowly into the liquid asphalt binder and sheared with a high shear mixer using a mechanical stirrer at selected mixing condition.

2.2 Marshall Mix Design

The optimum binder content of SMA14 mix was determined using Marshall method according to JKR/SPJ/2008-S4 [13] specifications. Table 2 and Fig. 1 illustrate the aggregate gradation semi-log graph and gradation limit for percentage

Table 2 Gradation limit for SMA 14

Sieve size (mm)	Gradation limit	Percentage passing	Percentage retained
19	100–100	100	0
12.5	100–100	100	0
9.5	72–83	77.5	22.5
4.75	25–38	31.5	46
2.36	16–24	20	11.5
0.6	Dec-16	14	6
0.3	Dec-15	13.5	0.5
0.075	8-Oct	9	4.5

aggregate passing versus sieve size to the power of 0.45 for SMA14 mix. The aggregate envelop clearly shows the relative low percentage of fine aggregate and high percentage of filler content.

A total of fifteen specimens were prepared for SMA14 mixture using asphalt binder ranging from 5 to 7 % to produce approximately 1200 g SMA14 specimen. Two percent of hydrated lime was used as anti-stripping agent and incorporated as part of the total combined aggregate. The specimens were mixed and compacted at selected mixing and compaction temperature, then placed in room temperature for 24 h before proceeding with the Marshall, stability and flow test.

All the SMA14 Marshall specimens were compacted at 50 blows/face to ensure that the aggregates do not easily break. SMA mixtures are easily compacted on the roadway to the desired density compared to the effort required for conventional HMA mixtures [14]. After 24 h of setting time, the bulk specific gravity test of the compacted specimen were then determined before the Marshall stability and flow test procedure [15, 16]. Stability and flow test is a measurement of the maximum magnitude of load sustained and resistance to plastic flow of cylindrical samples of bituminous on the lateral surface by means of the Marshall apparatus. An average value of theoretical maximum density was obtained using rice method for each different mixes in loose condition to determine the void in total mix for each sample [17]. The OBC was then obtained from the voids-density analyses which comprise of the results of the Bulk Specific Gravity (SG), Void in Total Mix (VTM), Void Filled with Bitumen (VFB), Void in Mineral Aggregate (VMA) and stability and flow of each compacted specimen. The average values of bulk specific gravity, stability, flow and VTM obtained were plotted separately against the binder content. The mean OBC was determined by averaging four (4) OBC as specified in JKR/SPJ/2008 [13]. The minimum SMA requirement as stipulated in JKR specification is tabulated in Table 3.

Fig. 1 Aggregate structure gradation
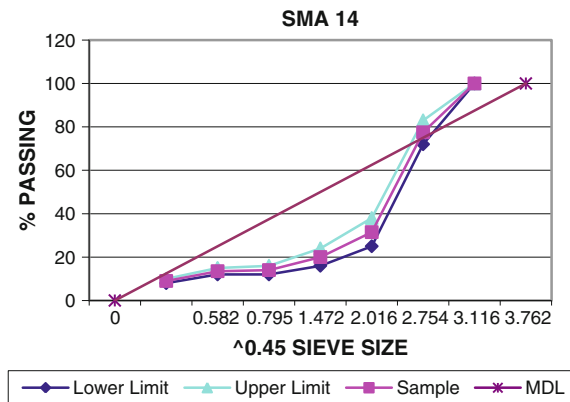
Table 3 SMA and AC mix requirement	Parameter	JKR specification
	VTM	3–5 %
	VMA	Min 17 %
	Stability	Min 6200 N
	Flow	2–4 mm

2.3 Modified Lottman Test

The Modified Lottman test (AASHTO T283) is a widely accepted and commonly used test method to determine moisture susceptibility (also known as stripping) [18]. This test is performed by simulating the field condition by accelerating test conditioning in the laboratory and the specimens were prepared having an average air voids level of 7 % ± 0.5 %. Six specimens were prepared from each mixture and divided into two subsets: three specimens were tested in dry condition and three specimens were saturated at 70–80 % of maximum saturation by immersing in water for 24 h at 60 °C in a water bath. The specimens were then tested for Indirect Tensile Strength (ITS) using UTM-25 machine by placing them between the steel loading strips by loading the samples at constant head rate (50 mm/min vertical deformation at 25 °C) and maximum compressive force required to break the specimens were recorded. The modified Lottman procedure is illustrated in Fig. 2. Tensile Strength Ratio (TSR) results were determined by comparing the Indirect Tensile Strength (ITS) of both dry and wet-saturated conditioned specimens. The maximum compressive load was recorded and the tensile strength of asphalt mixture was calculated as in Eq. 1.

$$S_t = \frac{2P}{\mu Dt} \tag{1}$$

where
S_t Tensile strength, KPa
P   maximum load, N
T   sample thickness, mm
D   sample diameter, mm

The potential for moisture damage is indicated by the Tensile Strength Ratio (TSR) as expressed in Eq. 2.

$$\text{Tensile Strength Ratio} = \left(\frac{S_{tcon}}{S_{tdry}}\right) \times 100 \tag{2}$$

where
S_{tcon} average tensile strength of wet conditioned subset, KPa
S_{tdry} average tensile strength of dry subset, KPa
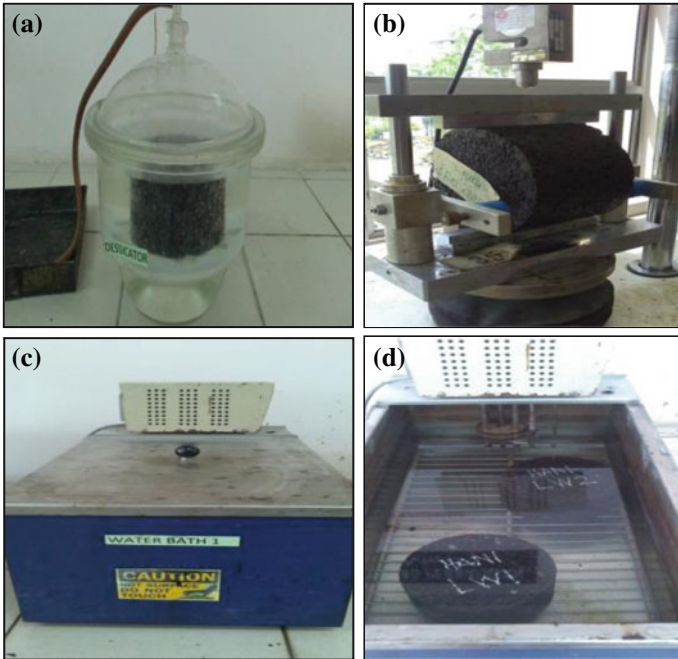
Fig. 2 a Sample under vacuum process. **b** Indirect tensile test. **c** Water bath. **d** Conditioning process

The tensile strength ratio values in the test are an indication of the potential for moisture damage. Retained tensile strength ratio was used with 80 % as the boundary between mixture's resistant and sensitivity to moisture [18].

3 Results and Discussion

3.1 *Effect of NP Modified Binder on Volumetric Properties*

The optimum binder content of the SMA14 mix is obtained based on the relationship between volumetric properties with binder content. The OBC was established at 4 % air voids. The volumetric properties values obtained were compared to the volumetric mixture design of JKR specification requirements as tabulated in Table 4. The obtained volumetric results of SMA mixes generally met the minimum JKR specification and satisfied with the mix design criteria.

Table 4 SMA 14 mix requirements

Properties	Mixtures	
	SMA14	Specification (JKR/SPJ/2008-S4)14
OAC %	5.90	–
Stability (N)	12300	Min 6200
Flow (mm)	3.7	2–4
Air voids (%)	3.8	3–5
Voids filled with asphalt (%VFA)	80	–
Voids in mineral aggregate (%VMA)	20	–

3.2 Effect of NP on Moisture-Induced Damage

In this study, the moisture damage was evaluated by moisture susceptibility test procedures (modified Lottman test-AASHTO T283). This test measures the loss of strength of an asphalt mix due to moisture-induced damage. Moisture damage is also known as stripping. For this test, specimens were prepared at 7 ± 1 % air voids according to AASHTO T283 standard requirements in order to simulate the field condition after compaction before opening to traffic. The indirect tensile strength test was developed to determine the tensile properties of cylindrical samples through the application of a compression load along a diametrical plane of two opposite loading heads. The Indirect Tensile Strength (IDT) results for dry and wet conditioned specimens for four different types of mixture binder is shown in Fig. 3. Results show that the dry specimens for modified binder mixture with 6 % NP gave the highest IDT (511 kPa). Results for 0, 4 and 2 % NP modified binder are 500 kPa, 460 kPa and 379 kPa, respectively. All the mixes are resistant to moisture damage. For wet conditioned specimens, the ITS results showed similar trend to the dry conditioned specimens which showed the NP6% modified binder has the highest indirect tensile strength values. The trend of the bar graph shows that the indirect tensile strength of wet conditioned values is lower than the dry conditioned indirect tensile strength values. This shows that the moisture (wet conditioned sample) will definitely

Fig. 3 Indirect tensile strength of dry conditioned and wet conditioned samples for conventional and modified binder mixes

SMA14	NP0%	NP2%	NP4%	NP6%
ITS Dry (kPa)	500	379	460	511
ITS Wet (kPa)	421	342	420	493
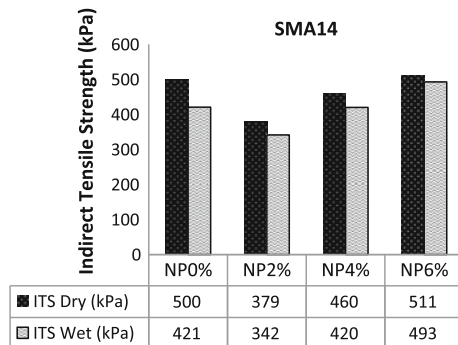
decrease the value of indirect tensile strength. The tensile strength is an indicator of cracking potential. A higher tensile strain at failure indicates that a particular HMA can tolerate higher strains before failing, which are more likely to resist cracking than HMA with a low tensile strain at failure. If the water-conditioned tensile strength is relatively high as compared to the dry tensile strength, the HMA can be considered as reasonably moisture resistant. Results showed a good correlation between ITS dry and ITS wet strength with coefficient of determination, R value of 0.9755. This relationship between these two variables is illustrated in Fig. 4.

The tensile strength ratio results is an indication of the HMA mix susceptibility to moisture damage or stripping. Figure 5 clearly presents that the TSR values for all types of mix are greater than 80 % which passed the AASTHO T283 standard requirement. This indicates that all the mixes are resistant to moisture damage which could sustain the load from vehicles and exposed to severe conditions without a large degradation of the structure. The strength of the asphalt mixes increases with the addition of nanopolycrylate, which absorbs the binder needed to coat the aggregate thus improving the stripping resistance.

Fig. 4 Relationship between ITS dry versus ITS wet
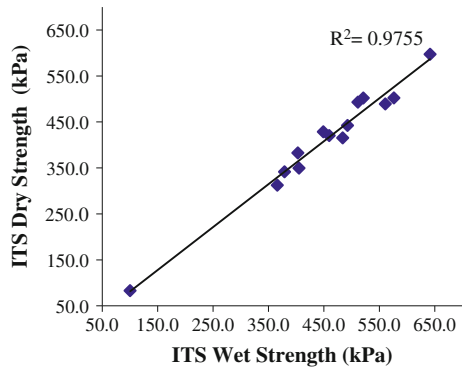
Fig. 5 Tensile strength ratio of SMA mix
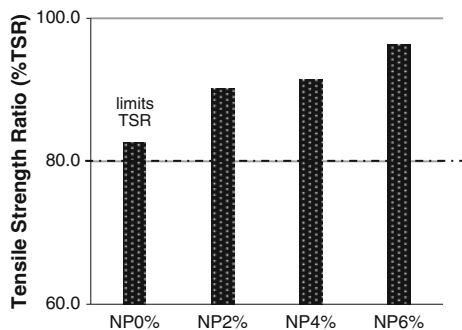
4 Conclusions

Based on the results obtained from this study, the following conclusions have been reached:

1. Nanopolyacrylate polymer can be used as modifier in SMA14.
2. The addition of nanopolyacrylate influences the stripping behaviour of the mixture; hence increasing the tensile strength ratio of the mixes; increase in the NP content increased the stripping resistance. However, all mixes are resistant to moisture damage.
3. Nanopolyacrylate polymer appears to improve the stripping resistance due to insignificant difference between the unconditioned and conditioned results for modified mixes.

Thus, the addition of nanopolyacrylate polymer to the binder has significantly improved the cohesion as well as adhesion properties of the binder, and hence the performance of the mix to stripping.

References

1. B. V. Kok and M. Yilmaz, "The effects of using lime and styrene-butadiene-styrene on moisture sensitivity resistance of hot mix asphalt," *Constr. Build. Mater.*, vol. 23, no. 5, pp. 1999–2006, 2009.
2. R. L. Terrel and S. Al-Swailmi, "Water Sensitivity of Asphalt-Aggregate Mixes : Test Selection. SHRP-A-403," *Strateg. Highw. Res. program. Washingt. Natl. Res. Counc.*, p. 194, 1994.
3. G. D. Airey, "Rheological evaluation of ethylene vinyl acetate polymer modified bitumens," *Constr. Build. Mater.*, vol. 16, no. 8, pp. 473–487, Dec. 2002.
4. Y. Yildirim, "Polymer modified asphalt binders," *Constr. Build. Mater.*, vol. 21, no. 1, pp. 66–72, Jan. 2007.
5. I. M. Nassar, K. I. Kabel, and I. M. Ibrahim, "Evaluation of the Effect of Waste Polystyrene on Performance of Asphalt Binder," vol. 2, no. 10, pp. 927–935, 2012.
6. G. Rusbintardjo, M. R. Hainin, and N. I. M. Yusoff, "Fundamental and rheological properties of oil palm fruit ash modified bitumen," *Constr. Build. Mater.*, vol. 49, pp. 702–711, 2013.
7. G. Airey, "Rheological properties of styrene butadiene styrene polymer modified road bitumens⋆," *Fuel*, vol. 82, no. 14, pp. 1709–1719, Oct. 2003.
8. N. I. M. Yusoff, A. A. S. Breem, H. N. M. Alattug, A. Hamim, and J. Ahmad, "The effects of moisture susceptibility and ageing conditions on nano-silica/polymer-modified asphalt mixtures," *Constr. Build. Mater.*, vol. 72, pp. 139–147, Dec. 2014.
9. B. Sengoz and G. Isikyakar, "Evaluation of the properties and microstructure of SBS and EVA polymer modified bitumen," *Constr. Build. Mater.*, vol. 22, pp. 1897–1905, 2008.
10. S. Morteza, M. Tahmooresi, and R. Jalal, "Modification of Stone Matrix Asphalt with Nano-SiO 2," *J. basic Appl. Sci. Res.*, vol. 2, no. 2, pp. 1338–1344, 2012.
11. A. Zare-Shahabadi, A. Shokuhfar, and S. Ebrahimi-Nejad, "Preparation and rheological characterization of asphalt binders reinforced with layered silicate nanoparticles," *Constr. Build. Mater.*, vol. 24, no. 7, pp. 1239–1244, Jul. 2010.

12. E. Santagata, O. Baglieri, L. Tsantilis, and D. Dalmazzo, "Rheological Characterization of Bituminous Binders Modified with Carbon Nanotubes," *Procedia - Soc. Behav. Sci.*, vol. 53, pp. 546–555, Oct. 2012.

13. Public Work Department of Malaysia, *Standard specificationfor road work,section 4:Flexible pavement. Kuala Lumpur,JKR/SPJ/2008-S4*. 2008.

14. I. M. Asi, "Laboratory comparison study for the use of stone matrix asphalt in hot weather climates," *Constr. Build. Mater.*, vol. 20, no. 10, pp. 982–989, Dec. 2006.

15. American Society for Testing and Materials (ASTM), *Standard Practice for Bulk Specific Gravity and Density of non absorptive compacted bituminous mixtures.Philadelphia U.S, ASTM D2726*. 1992.

16. American Society for Testing and Materials (ASTM), *Standard Practice for Resistance to Plastic Flow of Bituminous Mixtures using Marshall Apparatus.Philadelphia U.S, ASTM D 1559*. 1992.

17. American Society for Testing and Materials (ASTM), *Standard Practice for Theoretical Maximum density.Philadelphia U.S, ASTM D2041*. 1992.

18. American Association of State Highway and Transportation Officials (AASHTO), *Resistance of compacted Hot Mix Asphalt (HMA) to Mixture-Induced Damage. AASHTO T283-07*. 2008.

Engineering Factors of Motorcyclist Red Light Runner in Malaysia

Wan Adilah Ismail, Intan Rohani Endut, Siti Zaharah Ishak and Rizati Hamidun

Abstract Motorcycle became the popular transport vehicle in many developing countries due to its simplicity and is inexpensive compared to other types of vehicles. In spite of this fact, an involvement of this vehicle in road crashes could easily cause fatal to the rider and pillion. In mitigating the road crashes, the factor contribution is needed to recognise and understand. Thus, the objective of this study was to identify the engineering design factors that influenced the RLR among motorcyclists in Shah Alam, Selangor areas. The engineering design factors that have been considered in this study were change interval (amber time, green time and all red) of traffic signal. Then, the number of approach legs also was considered to examine the influenced these factors to motorcyclist RLR. To examine the influenced factors, direct observations were conducted using a video recorder in Shah Alam, state of Selangor. The direct observations were obtained 1 h observations within continuous 3 h. Results from this study showed that the most of motorcycle red light runner occurred at the signalised intersections within shorter amber time, longer cycle and more signal phase and approach legs.

Keywords Factors · Motorcycle red light runner · Signalised intersections

W.A. Ismail (✉) · I.R. Endut
Faculty of Civil Engineering, Universiti Teknologi MARA (UiTM), Shah Alam,
Selangor, Malaysia
e-mail: wadiel@yahoo.com

I.R. Endut
e-mail: intan@salam.uitm.edu.my

S.Z. Ishak
Road Safety Engineering & Environmental Research Center, Malaysian Institute
of Road Safety Research (MIROS), Kajang, Selangor, Malaysia
e-mail: sitizaharah@miros.gov.my

R. Hamidun
Crash Data Analysis & Exposure Unit, Malaysian Institute of Road Safety Research
(MIROS), Kajang, Selangor, Malaysia
e-mail: rizati@miros.gov.my

1 Introduction

The motorcycle is one of the contributors to road crashes and fatalities where M.M. Abdul Manan, 2012 derived that almost 50 % motorcycles were involved in road crashes and fatalities [1]. In Malaysia, greater demand of motorcycle compares than other vehicles encouraged the higher road crashes and fatalities among motorcyclist [2]. T.H. Law et al. (2003) pointed out that red light runner at a signalised intersections is one of caused of these crashes and fatalities.

Red light runner (RLR) was defined as vehicles are disobeying to follow the traffic signals regulations. Strictly, the vehicles completely prohibit to proceed their movement during red light and should be prepared to stop at stop line when displayed in yellow light [3]. Unfortunately, many vehicles, especially among motorcyclist fail to follow traffic signal regulations. Thus, automatically RLR is one of the major causes of road crashes and fatalities at signalised intersections [4].

Signalised intersections reflect the road performance where it solves traffic congestions, especially in urban areas during peak hours. Also, provide right way for the coming traffic alternately and the solution to the problem of intersection congested by increasing a capacity at signalised intersections [5]. However, road users intentionally tend to cross the red light after they had been waiting too long for a green light or speeding up to cross during traffic change interval.

Until now, the RLR study already done investigated by previous researchers in understanding the factors contribution and mitigations [6, 7]. In order to mitigate the motorcycle due to RLR at signalised intersections, it is necessary to understand the factors contribution. The factors contribution may be categorised into human behaviours, engineering and environment elements. Among these factors, the engineering element is most influenced the RLR because it is necessary in designing the traffic signal performances. Thus, the objective of this study is to identify the engineering design factors such as traffic signal timing for each phase either influenced the RLR among motorcyclists in Shah Alam, Selangor areas.

This paper is organised as follows. In Sect. 2, review of the literature on RLR factors. In this section, the factors considered and summaries of finding by previous researchers were summarised. This section also derives the factors considered based on human behaviours, engineering and environment category. Then, the methodology and figure of sites selected were explained in Sect. 3. Details on collected data and result discussion were described in Sect. 4. Finally, in Sect. 5, some conclusions are pointed and indicated about future works.

2 Literature

2.1 *Factors Consideration of RLR*

There are several factors that influenced the frequency of RLR such as signal timing and traffic volume. Table 1 summarises the factors contribution from previous

Table 1 Factors consideration of RLR by previous study

Author	Factor
H.M. Jamil et al. (2014)	Types of vehicles, day, types of traffic light (timer/normal system) and location
W. Hu et al. (2011) [9]	Red light camera enforcement
A.R. Richard et al. (2007) [10]	Change interval and red light camera enforcement
S. Kulanthayan et al. (2007)	Types of vehicles, change interval, day, types of traffic light (timer/normal system), location and red light camera enforcement
T.H. Law et al. (2003)	Change interval and number of approach
B.E. Porter and K.J. England (2000) [11]	Change interval, gender and direction travelled (straight/right)
A.R. Richard et al. (1998) [12]	Traffic volume, gender and speed

studies, where change interval between yellow, green, and amber phase are the command factors that had been considered during the investigation of RLR. Then, red light camera installation also was considered in determining the effective implemented countermeasure of RLR. It is followed by traffic volume and types of vehicles consideration [8]. Other factors that were into consideration were day, types of traffic light, number of approach, gender and speed.

However, the behaviours of riders also caused most of RLR where it is categorised into two types of behaviours; intentions and unintentions. Basically, the intention behaviours occurred when a motorcyclist becomes aggressive and confident to cross during red light signal when they know very well about traffic signal timing. Meanwhile, the shorter of the yellow change interval was influenced by unintention behaviours because they are unable to estimate the change interval between yellow and red light signal [13].

The factors considerations were divided into three categories; human behaviours, engineering and environment as in Table 2.

Table 2 Factors consideration based on each category

Category	Dimension
Human	• Red light runner • Gender • Movement behaviour
Engineering	• Signal setting • Number of approaches • Number of lanes
Environment	• Motorcycle and vehicle speed • Weather condition • Traffic volume

(1) Human behaviours

Data consideration based on the behaviours of riders crossing at signalised intersections using a video recorder. The behavioural issues related to traffic violation have become the most important study in determining the factors and the impact of study behaviours [14]. Based on M.G. Masuri et al. (2011) have been reviewed Traffic African Road Safety Congress 1999, almost 90 % of motorcycle crashes source from human error due to rider's attitude either intentionally or unintentionally to break regulations [15]. Only a small portion of crashes were caused by vehicle defects, poor road design and inadequate maintenance of roads. It was the same situation with driver behaviours, in which younger (aged 16 years) drivers did speeding, traffic violations and single vehicle crashes than older driver (aged 25–49 years) mostly caused by alcohol.

(2) Engineering

Engineering data are relating the information that are controlled by engineering such as a traffic signal cycle, signal phase and timing (red, yellow and green) and number of lanes. It is related with road features provided and operation setting with human like traffic signal operations. The Federal Highway Administration had concluded that factors of road runner intentionally, such as;

a. Signal timing
b. Signal cycle length
c. Amber change intervals
d. All red clearance intervals

(a) Signal Timing

Poor timing of traffic signals may cause rider to frustrate and encouraged the of intention of road runner, especially during non-peak hours. It is because riders will take a time for waiting green light, even though the volume of vehicles is lower. The traffic demand and volume at each intersection must be properly considered and should be always updated at certain periods. In addition, if riders are given the best signal operation, it may reduce red runner, reduce crashes, decrease fatalities and maintain average travel speed [16].

(b) Signal Cycle Length

Signal cycle length is completely cycle of timing for green, yellow and red phase for each approach. It is based on intersection characteristics and the individual approaches. Various characteristics for signal timing depend on specific times of the day like morning or afternoon peak hours and non-peak hours, weekday and weekend. For example, signal cycle length at midnight would shorter than noon hours in reducing the number of opportunities of red light runners.

(c) Amber Change Interval

Proper yellow interval is needed to reduce red runner because rider has their own timing expectation of how the yellow interval would be and make decisions either to proceed or stop based on their previous

experiences. An engineer should ensure the yellow interval is adequate at intersection and deal with traffic demand and riders expectation. A minimum change of the yellow interval should have a duration of three seconds [17].

(d) All Red Clearance Interval

All red clearance is followed after a yellow change interval where all traffic light turning to red light display. The purpose of the all-red interval is the duration to allow the vehicle to clear intersection when entering the yellow interval before opposite approach lanes turn to green. The use of all-red clearance interval at signalised intersections may reduce intersection crashes, particularly those related to signal violations [18]. The maximum duration of all red intervals should not exceed 6 s.

(3) Environment

The data related to surrounding conditions of the site study such as motorcycle volume, motorcycle speed and weather might influence the occurrence and severity of road safety. The influence of the environment may not directly affect the road safety, however, it may cause the behaviourial changes of road users. Due to this behaviourial changes, it might increase the road crashes such as a traffic violation.

2.2 Finding of RLR

Based on finding by Hu et al. (2011), Kulanthayan et al. (2007) and Richard et al. (2007) as shown in Table 3, it is indicated that red light camera installation at a signalised intersection reduced the RLR frequency. Thus, it is the most effective tool in reducing RLR in Malaysia. Besides that, results from Richard et al. (2007) and Law et al. (2003) indicated that shorter yellow timing of signal traffic also reduces RLR.

2.3 Signalised Intersections

The performance of road condition depends on the performance of signalised intersections where it is plays the main role in traffic congestion solving, especially in urban areas during peak hours. Basically, the major problems with traffic congestion are due to the increase in the annual number and the capacity of vehicles in Malaysia. The capacity of a signalised intersection depends on three conditions; there are intersection geometry, duration of the green phase on each intersection and traffic volume on each intersection [19]. It is to determine the passenger car unit (pcu) of traffic volume and optimum signal timing for each intersection.

Table 3 Summaries of finding respect to factors consideration of RLR by previous study

Author	Finding
H.M. Jamil et al. (2014)	The motorcycle is the higher contributions of RLR rate, followed by cars and other types of vehicles. Weekdays showed a higher RLR
W. Hu et al. (2011)	Signalised intersections with red light camera able to decrease the frequency of fatal crashes by 14 % reduced after implemented red light camera
A.R. Richard et al. (2007)	RLR was reduced when yellow timing reduce to 36 % reduced and installation of red light camera, 96 % reduced RLR. But if applied only one of them, it hasn't worked to better enforcement
S. Kulanthayan et al. (2007)	The identified variables: Camera enforcement; without a red light camera, 14.8 % of RLR than when installed, 6.6 % Travel day; 13.6 % violation occurs on weekdays, meanwhile 10.8 % violation on weekends Type of vehicle; 13.5 % of two wheeled higher than four wheeled, 11.1 %. Cycle time; 11.3 % violation happened when a short cycle
T.H. Law et al. (2003)	The frequency of RLR was increased when higher motorcycle volume, shorter yellow time, longer cycle length, shorter change interval time, more signal phases and approach legs
B.E. Porter and K.J. England (2000)	10 red runners per observation hour were recognised at urban area based on these factors; RLR was increased when larger intersection and higher traffic volumes. Time of RLR variations during late afternoon, 3 pm–5 pm and peak hour, 5 pm–6 pm
A.R. Richard et al. (1998)	It is proposed two categories mitigations, there are: –Engineering Measures (removal unwarranted traffic signal) –Enforcement Techniques (enforcement of rider to follow a road regulations trough using red light camera)

The solution to the problem of intersections congest is by increasing the capacity at signalised intersections. Enlarging the intersection is one of method to increase the capacity and reduce delay at signalised intersections. It is also mentioned that basically the signalised intersection is constructed as a function to

- To avoid blockage or conflict point at an intersection by traffic stream, thus capacity can be maintained and smooth traffic flow even during peak traffic conditions;
- To facilitate a vehicle or pedestrian to cross at major road and minor road;
- To reduce the frequency of traffic crashes caused by collisions between vehicles during traffic stream and conflicting directions.

Roadway and environment factors are influenced by the capacity at each signalised intersections, such as physical layout of approaching an intersections, the width of the intersections, the radii along left or right turning, the gradient of approaching the intersections and exits from the intersections.

3 Methodology

The methodology of this study required several observations at signalised intersections to understand the factors of motorcycle RLR. The observations were conducted via direct observations using a video recorder. Direct observations using a video recorder are sensible to record complex instantaneous event based on time and movement. In addition, data recorded can be validated and used by repeatedly watching the played recorder before forming any conclusions [20]. During the observation the signal timing was measured at each site. For each site, the data of RLR was obtained from 1 h observations at five sites during continuous 3 h period between 3:00 pm until 6:00 pm. Based on Law et al. 2013 within this time most weekly crashes occurred in Malaysia.

The sites selection are surrounding Shah Alam areas, Selangor based on the following criteria; visible pavement marking, traffic signal properly functioning, four legs-approach, normal signal and timed signal operation and standard geometry layout. The standard geometry defined as the intersections with an approximately 90° angle with flat approach grades is shown in Fig. 1.

Due to I.A. Fallah and H. Esmaeeli (2011) using manual calculation in terms of determining the traffic signal change interval, the formulae is as follows:

i. Examples of manual calculation to determine all red clearance:

$$\text{All red clearance} = [C - (ag_1 + ag_2 + ag_3 + ag_4) - (a_1 + a_2 + a_3 + a_4)]/4 \tag{1}$$

where

C   cycle time
Ag actual green time
A   amber time

ii.
$$\text{Intergreen time} = \text{Amber time} + \text{all red} \tag{2}$$

Fig. 1 One of the study areas in Shah Alam, Selangor

Fig. 2 Positioning of actual green time (*ag*) and amber time (*a*)
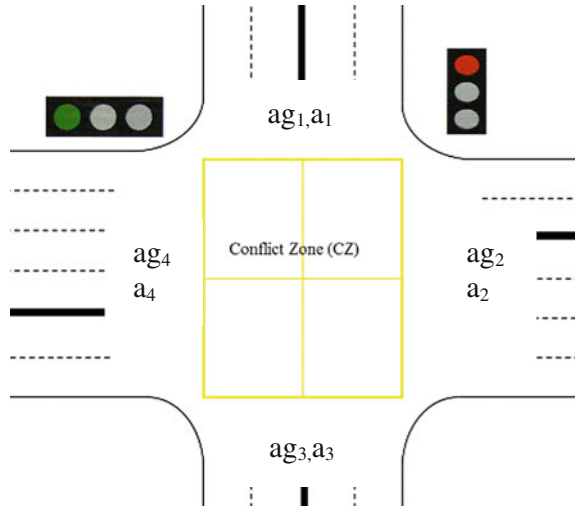
The position of actual green and amber time at signalised intersections as in Fig. 2. These positions were applied in Eqs. 1 and 2 for determining the value of all red clearance and intergreen time.

4 Result and Discussion

Through direct observations, the value of change interval of traffic signal as shown in Fig. 3. This figure describes the timing diagram of traffic light in determining for each phase of change interval. In this study, the time of all red, amber, red, green and cycle time were recorded using a stopwatch as shown in Table 4.

The purpose of the amber time and all-red clearance intervals are to provide a safe transition to avoid the conflicting between two traffic signal phases. The function of amber time as warning traffic due to change of the right-of-way during the green phase to stop traffic during the red phase.

Meanwhile, the function of the all-red clearance interval is to provide additional time after the amber time. It is to clear the intersections before they happen due to any traffic conflict from the opposite approach.

Fig. 3 Timing diagram of traffic signal [21]
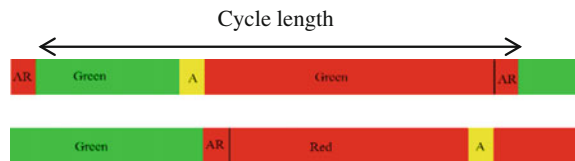
Table 4 Collected data from direct observation at sites selected in Shah Alam area

Sites	Change interval (s)								Number of approach lanes			
	Amber time				Green time							
	a_1	a_2	a_3	a_4	ag_1	ag_2	ag_3	ag_4	1	2	3	4
1	3	3	3	3	49	15	72	83	4	2	4	2
2	3	3	3	3	28	44	22	49	1	2	1	2
3	3	3	3	3	65	35	50	47	3	2	3	3
4	3	3	3	3	30	48	20	43	2	2	2	2
5	2	2	2	2	84	77	109	118	2	2	2	2

Table 5 Result of data collection

Sites	Change interval (s)					Total legs	No. of RLR
	Amber time	Green time	All red	Cycle length	Intergreen time		
1	12	3.32	5	3.48	8	12	5
2	12	2.22	5	2.87	8	6	2
3	12	3.17	5	3.42	8	11	4
4	12	2.21	3	3.27	6	8	6
5	8	4.28	4	3.97	6	8	8

Table 5 shows the data collected during direct observations. Change interval and number of approach lanes at each leg of the signalised intersection were recorded. At each approach legs represent a different phase timing.

Based on summaries result of data collection in Table 5, it was dedicated that the number of approach legs and change interval of traffic signal were influenced the frequency of RLR. Site with shorter amber time and longer cycle length were given the high frequency of RLR among motorcyclist, where 8 s and 4.28 s, respectively. Meanwhile, site with longer amber time and shorter green phase represented the lower of RLR frequency, where 12 s for amber time and 2.22 s for green phase. Then, more of total of approach legs at signalised intersections also shows the increasing number of RLR. It was represented by 6 numbers of approach legs only caused 2 numbers of RLR comparatively than 12 of approach legs were encouraged 5 numbers of RLR.

From these results, it is able to conclude that the frequency of RLR was increased when shorter amber time, longer cycle length and more signal phases and approach legs. Previous by A.R. Richard et al. (2007), T.H. Law et al. (2003), and R.A. Retting and M. Greene (1997) have studied in measuring factors and mitigations, also summarised that, RLR will increase with shorter amber time, longer cycle length and more approach legs [22].

The Manual on Uniform Traffic Control Devices, MUTCD (2003) stated that an amber time should have a minimum duration of 3 s and a maximum duration of 6 s. Then, all red time clearance should have a duration not exceeding 6 s.

5 Conclusion

The results of this study supported the previous study on RLR that decreases change interval and amber time of a traffic signal will increase the frequency of RLR especially among motorcycles. Longer cycle length and amber time are considered as economic measures in reducing RLR. Based on H.S. Stein (1986), inadequate change interval of a traffic signal will cause increase in the vehicle crash rates [23]. Furthermore, more number of approach legs at signalised intersections also increases the frequency of RLR. The riders may get frustrated due to more approach legs and signal timing because they need to wait and patience due to long delay and then violate the red light. Thus, the understanding of the factors contribution of RLR is important to properly mitigation of RLR.

References

1. M. M. Abdul Manan, "Motorcycle fatalities in Malaysia," *IATSS Research*, vol. 36, no. 1, pp. 30–39, Jul. 2012.
2. P. T. Yen, R. Radin Umar, A. A. Aziz, H. Singh, S. A. Wahid, A. H. H. Mansor, Z. Noor, and M. S. Othman, "Fatal injuries in Malaysian motorcyclists," *International Medical Reseacrh Journal*, vol. 3, no. 2, pp. 115–119, 1999.
3. H. M. Jamil, A. Shabadin, and S. A. S. M. Rahim, "The effectiveness of automated enforcement system in reducing red light running violations in Malaysia: Pilot Locations," 2014.
4. R. Ramli, J. Oxley, F. M. Noor, N. K. Abdullah, M. S. Mahmood, A. K. Tajuddin, and R. McClure, "Fatal injuries among motorcyclists in Klang Valley, Malaysia," *Journal of Forensic and Legal Medicine*, vol. 26, pp. 39–45, Aug. 2014.
5. E. Tamin, "The evaluation of traffic performance at several signalized intersections using 1997 Indonesian Highway Capacity Manual," *Proceedings of the Eastern Asia Society for Transportation Studies*, vol. 4, pp. 615–629, 2003.
6. R. A. Retting, R. G. Ulmer, and A. F. Williams, "Prevalence and characteristics of red light running crashes in the United States.," *Accident; analysis and prevention*, vol. 31, no. 6. pp. 687–94, Nov-1999.
7. S. Kulanthayan, Phang. W.K., and Hayati K.S., "Traffic light violation among motorists in Malaysia," *IATSS Research*, vol. 31, no. 2, pp. 67–73, 2007.
8. T. H. Law, L. I. N. Xu, and R. S. Radin Umar, "Factors influencing red light runners among motorcyclists in Malaysia," *Journal of the Eastern Asia Society for Transportation Studies*, vol. 5, pp. 2518–2525, 2003.
9. W. Hu, A. T. Mccartt, and E. R. Teoh, "Effects of red light camera enforcement on fatal crashes in large US cities," 2011.
10. A. R. Richard, S. A. Ferguson, and C. M. Farmer, "Reducing red light running through longer yellow signal timing and red light camera enforcement: results of a field investigation," in *Insurance Institute for Highway Safety*, no. January, 2007, p. 11.
11. B. E. Porter and K. J. England, "Predicting red-light running behavior : A traffic safety study in three urban settings," *Journal of Safety Research*, vol. 31, pp. 1–8, 2000.

12. A. R. Richard, F. W. Allan, and A. G. Michael, "Red light running and sebsible countermeasures," *Transportation Research Record*, vol. 0895, pp. 23–26, 1998.
13. D. J. Tunnicliff, B. C. Watson, K. M. White, M. K. Hyde, C. C. Schonfeld, and D. E. Wishart, "Understanding the factors influencing safe and unsafe motorcycle rider intentions.," *Accident, Analysis and prevention*, vol. 49, pp. 133–41, Nov. 2012.
14. R. Hamidun, S. Z. Ishak, and I. R. Endut, "Assessing pedestrian crossing risk at signalised intersection," *International Journal of Emerging Technology and Advanced Engineering*, vol. 3, no. 1, pp. 31–35, 2013.
15. M. G. Masuri, K. A. Isa, and M. P. M. Tahir, "Children,youth and road environment," *Asian Journal of Environment-Behaviour Studies*, vol. 2, no. 6, pp. 13–20, 2011.
16. P. Koone, L. Rodegerts, K. Lee, S. Quayle, S. Beaird, C. Braud, J. Bonneson, P. Tarnoff, and T. Urbanik, *Signal timing manual*. Federal Highway Administration, 2008, p. 265.
17. Traffic Engineering Manual, "Standardization of yellow and all- red intervals for signalized intersections," in *Standardization of Yellow and All-Red Intervals for Signalised Intersections*, vol. 2010, no. 750, 2010, pp. 4–7.
18. R. R. Souleyrette, M. M. O. Brien, H. Preston, R. Storm, and T. McDonald, "Effectiveness of all-red clearance interval on intersection crashes," 2004.
19. R. Akcelik, *Traffic signals: Capacity and timing analysis*. ARRB Transport Research, 1998, p. 126.
20. E. Taylor-powell and S. Steele, "Collecting evaluation data : Direct observation," *University of Wisconsin-Extension: Cooperation Extension*, 1996.
21. I. A. Fallah and H. Esmaeeli, "Reducing the probability of violating red light," in *In ITS Telecommunications (ITST), 2011 11th International Conference on 2011*, 2011, pp. 521–526.
22. R. A. Retting and M. Greene, "Influence of traffic signal timing on red-light running and potential vehicle conflicts at urban intersections," *Transportation Research Record*, vol. 1595, no. 1, pp. 1–7, 1997.
23. H. S. Stein, "Traffic signal change intervals : Policies,practices and safety," *Transportation Quarterly*, vol. 40, no. 3, pp. 433–445, 1986.

Modeling Operating Speed with Regard to Pavement Roughness Index (IRI) at Two-Lane Highway

Ab Mughni Bin Ab Rahim, Muhammad Akram Bin Adnan, Norliana Binti Sulaiman and Tuan Badrol Hisyam Bin Tuan Besar

Abstract An increase in vehicle production impacts the transportation system due to the maintenance of the pavement. The major factor that influenced the expansion of transportation system is the road structure itself, which played such a vital role, in the development of pavement rapidly in Malaysia. Challenges need to be faced by the authority to ensure the road roughness is smoother and compatible with the expansion of the transportation system. Thus, this study investigates the relation of operating speed and traffic engineering parameters with regard to the pavement roughness index. Meanwhile, this study was conducted to develop a good model that is able to reflect and explain the relationship that exists on traffic engineering parameters to the pavement roughness at two-lane highway.

Keywords Operating speed · Traffic engineering parameters · Pavement roughness · International roughness index

1 Introduction

Increases in transportation systems are parallel with the expansion of vehicles' numbers. Thus, it gives challenges to the development of pavement in Malaysia in terms of pavement maintenance. The acceptance of any new transportation system is taken into account by the condition of pavement roughness. Meanwhile, it represents to which passengers are exposed according to their riding quality or riding comfort. Therefore, to improve the driving conditions of the highway system, pavement roughness should be addressed with priority. Numerous studies have shown that

A.M.B.A. Rahim (✉) · N.B. Sulaiman · T.B.H.B.T. Besar
Faculty of Civil Engineering, UiTM Shah Alam, Shah Alam,
Selangor, Malaysia
e-mail: abmughni8636@yahoo.com

M.A.B. Adnan
Faculty of Civil Engineering, Universiti Teknologi MARA, Shah Alam,
Selangor, Malaysia

initial pavement roughness greatly affects future roughness and roughness pro-gression [1]. The objectives of this study are to conduct survey of road profiling with regard to International Roughness Index (IRI), to classify traffic engineering parameter's relation toward pavement roughness by applying Automatic Traffic Counter (ATC) and to develop model which adheres to the operating speed with the pavement roughness.

The location of this study is at Sepang and Batu Arang, Selangor. Site location criteria's are R5 road design standard, two-lane highways, asphalt pavement surface with characteristic of approximately 2 m width shoulder and 2 m unpaved shoulder. Hence, this study will discover the precedence to acknowledge the operating speed and traffic engineering parameters in collecting the data to incorporate into the pavement profile and defining other significant factors contributing the pavement distress. Therefore, in situ test like Automatic Traffic Counter (ATC) test and International Roughness Index (IRI) test were conducted. The ATC was installed to evaluate the traffic on two-lane highway under study, while International Roughness Index (IRI) was conducted to measure the characteristics of pavement. Data extraction from the ATC test consist of traffic composition data such as actual speed of vehicles, flowrate, density, space mean speed at the site. Data from IRI demonstrate the pavement profile of the two-lane highway as for the pavement roughness evaluation at case study location.

2 Literature Review

2.1 Operating Speed

As an elementary concept in highway transportation, speed has been a much in demand research topic through many years by reason of its enormous impact on highway safety and efficiency. Speed is used both as a design foundation to advocate consistency and as a performance measure to evaluate operation. Regularly, three basic speed terms were established which are design speed, operating speed and speed limit [2].

The absolute meaning of "operating speed," in spite of, is open to debate. Some sources, for an example the AASHTO, currently have exchanged their definitions to meet the common use of the word. Operating speed according to the AASHTO, expressed the highest overall speed at which a driver can travel on a given road under favorable weather conditions and actual traffic conditions without at any time exceeding the design speed on a section by section basis [3]. Nevertheless in 2001, the AASHTO adjusted their definition for the new edition of the Green Book and defined operating speed as "the speed at which drivers are observed operating their vehicles during free-flow conditions" [4].

Space mean speed was difficult to measure in the field, compared to measuring time mean speed. Time mean speed was much easier to measure in the field therefore, the relationship between both speeds was useful as the mathematical equations was

developed. Based on the statistical analysis, the model for two-lane highways in estimating space mean speed from time mean speed for Malaysian conditions can be derived as the equation:

$$Vs = 1.016Vt - 1.704$$

where
Vs   space mean speed
Vt   time mean speed, average spot speed

2.2   Pavement Layer

Flexible pavement is defined as a layered structure consisting of five layers which are subbase course, base course, binder course, and wearing course. Every layer has their own characteristics which are designed according to the traffic volume and traffic capacity of that area [5]. The definition and function of every layer is simply described and shown in the Table 1.

2.3   Pavement Roughness and IRI

Pavement roughness is one of the prime issues regularly faced by the road authorities in this country that is often being embossed by the public due to the

Table 1 Definition and function of layer [5]

Layer	Definition and function
Subgrade	The topmost part of the soil, natural or imported, to support the load transmitted from the overlying layers
Subbase course	The layers of the specified material built up to the required designed thickness immediately overlying the subgrade. It serves as an aid to disperse the load from the base course before transmitting it to the subgrade. (This layer may absent in some designs)
Base course	The layers of specified material built up to the required designed thickness normally overlying the subbase course. This layer plays a prominent role in the support and dispersion of the traffic loads
Surface course	All the bound layers within the pavement wearing course, intermediate course, and binder course are materialized under this general terminology. These layers form an impenetrable and flexible lining of high elastic modulus
Binder course	The bound layers overlying the base course. Apart from supporting and dispersing the traffic load, it also resists shear
Wearing course	The topmost layer of the surface course. It is in direct contact with the traffic and consequently, it must resist decay and prevent skidding

inadequate condition of the road and deliberately deteriorate without addressing the issues effectively [6]. Roughness of a road is a vital parameter which not only indicates the pleasure level of ride over a pavement surface. Roughness of a road is also affiliated to vehicles' vibration, wear and tear of the wheel, operating speed, vehicle operating cost, etc. [7]. Pavement roughness gives absolute impact to the driver comfort. Therefore, to improve the driving conditions of the highway system, pavement roughness should be presiding with priority. Innumerable studies have shown that inceptive pavement roughness greatly affects future roughness and roughness progression [8].

The IRI is essentially a computer-based virtual-response-type system based on the response of a quarter-car vehicle model as it traverses a tested pavement section at a constant speed of 80 km/h. The IRI is defined as the absolute difference in suspension vertical velocity between axle and sprung mass of the quarter-car model with respect to road section length [9].

2.4 Impact of Pavement Roughness on Free Speed

The previous studies investigated the impact of pavement roughness regarding to various types of parameters. Thus, this section will discuss on that parameters and their relationship toward unevenness of the pavement. Some of the studies implicated the pavement roughness as a dependent variable and other parameters as independent variables such as free flow speed, passenger car unit (PCU), traffic capacity, skid resistance, and other variables. The effect of roughness on free speed is when roughness of the road increased, and then the free flow speed at that road tends to decrease according to the following relationship [10]:

$$\text{Free speed of car V ffsc} = 66.9 - 0.034 \text{UI}, R^2 = 0.91$$
$$\text{Speed of HVV ffshv} = 51.6 - 0.0019 \text{UI}, R^2 = 0.84$$

3 Research Methodology

In situ tests that were conducted are divided into two categories, which are traffic data collection strategy and pavement assessment. Automatic Traffic Counter (ATC) equipment (Trax Applyon) was installed to collect the traffic engineering parameters such as flowrate, time mean speed, space mean speed, and density at JKR R5 Road within two locations of Selangor state. Meanwhile, Roughometer III was installed to perform a survey of road profiling using International Roughness Index (IRI). Trax Appolyon was equipped with 14 different programmed layouts

for recording varieties of highways and traffic data. These are designated as L1 through L14 and represent the most common types of layouts used to record traffic data. Each layout is different, but there are some common principles that should be used with any layout that is chosen. Roughometer was used in this research to perform a survey of road profiling using International Roughness Index (IRI). Sensors will be installed at the suspension system of the vehicles to detect any vibration on the pavement within 10 km travel. Then, Roughometer software will calculate the International Roughness Index (IRI) of the pavement that the vehicles experienced when passing to the highways. Figures 2, 3 and 4 shows the test had been performed at the sites (Figs. 1, 5 and 6).

Fig. 1 Flowchart of operating speed model development

To performed visual inspection and in-situ testing suc as Automatic Traffic Counter and IRI test at sites location .

↓

Data Screening, sorting and organizing all data to be analyze

↓

Modeling of operating speed using MINITAB software
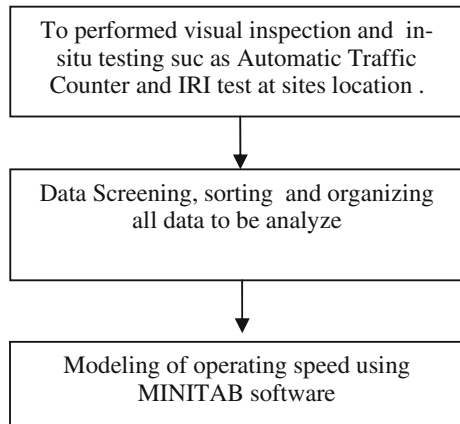
Fig. 2 ATC test-Trax Applyon

Fig. 3 ATC test-Webbing
Tape

Fig. 4 ATC test-road tube
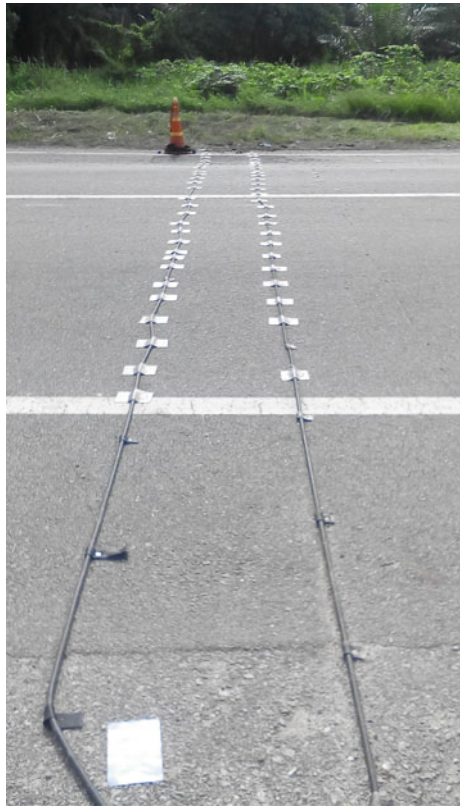
Fig. 5 Roughometer III test
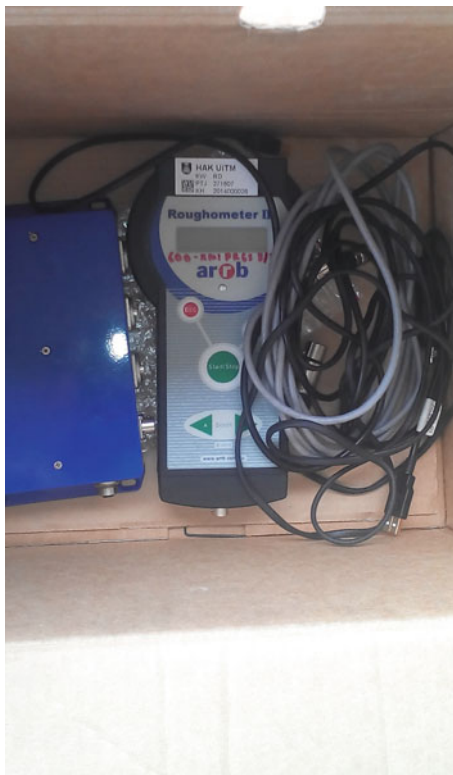
Fig. 6 Roughometer III test

4   Discussion Result for Operating Speed and IRI

An empirical data was collected in 3 days for each of the site location. An inspection was done everyday during those 3 days of the installation. It was to ensure all equipments were in a good condition. Raw data from Trax Applyon need to be screened first to identify errors that exist during the data collection process. Errors were classified as class 14 in the Trax Applyon system and were deleted from the cumulative data. After screening process, the data that involved in this study were 58 183 vehicles for all site locations. The number of vehicles was as shown in the Table 2.

Based on the comprehensive Table 3, space mean speed parameter were identified as dependent variable or response. Parameter flowrate (q), density (k), and International Roughness Index (IRI) were identified as independent variables or predictor for the model development process.

The summary of overall descriptive data as shown in Table 4 was developed before multiple linear regression process has been done. It is done to rescreen the data to ensure the extreme value does not exist in the cumulative data. Table below contained all data and information of all parameters involved, such as space mean speed (SMS), flowrate (q), density (k), and IRI.

Next process of the study was to perform multiple linear regressions to establish the model of space mean speed. The model was regressed using statistical software, which was Minitab software version 16. From Table 5, it was noted that variables

Table 2 Vehicles based on site location

Site location	Total vehicles per day			
	Day 1	Day 2	Day 3	Total
Batu Arang	2/19/2014 11 204 veh	2/20/2014 21 551 veh	2/21/2014 7 610 veh	40 365 veh
Sepang	12/11/2014 6 714 veh	12/12/2014 7 964 veh	12/13/2014 3 140 veh	17 818 veh
			Overall vehicles	58 183 veh

Table 3 Variables for model development

Variables for model development	
Dependent variable (response)	Independent variable (predictor)
Space Mean Speed (SMS)	Flowrate (q)
	Density (k)
	International Roughness Index (IRI)

Table 4 Summary of overall descriptive

Variable	Mean	St Dev	Min	Med	Max	Skew	Kurt
SMS	70.267	6.338	53.759	69.995	89.309	0.05	−0.21
Flowrate	266.32	139.03	4.00	257.08	675.00	0.19	−0.34
Density	3.7738	1.8621	0.0544	3.7375	9.4287	−0.02	−0.26
IRI	3.8262	0.6409	2.8000	3.8000	4.8000	−0.13	−0.55

Table 5 Prediction SMS

Term	Coef	SE Coef	T	P
Constant	72.1601	0.554286	130.186	0.000
Flowrate	0.2286	0.003088	74.040	0.000
IRI	−16.4215	0.231363	−70.978	0.000
Density	−0.2119	0.130383	−1.625	0.105

S 1.50496; *R-Sq* 94.41 %; *R-Sq (adj)* 94.36 %

were significant independent variables for predicting SMS. The p-value of the variables was less than 0.05, meaning that the null hypothesis (H0) was rejected and the alternative hypothesis (H1) was accepted. Hence, these predictors can be accepted in the model for predicting SMS. R-squared (R^2) for space mean speed was produced at 94.41 %.

Based on collected data from various tests, the space mean speed model equation was obtained as Eq. 1 below. Equation 1 was developed from three variables which were flowrate (q), density (k), and IRI. This model was the final and the best result obtained after many trials have been done to get the best fit of regression and to get the uppermost value of R^2.

$$SMS = 72.1601 + 0.228632(q) - 16.4215(k) - 0.211912(IRI)$$
$$With\ R^2 = 94.41\,\%$$
(1)

Based on Eq. 1, space mean speed is directly proportional to flowrate, and inversely proportional to density and IRI. It means when the flowrate increase, space mean speed will also increase. It can be explained due to the uninterrupted traffic stream that happened at both sites, which means the traffic flow at the site remains stable without any traffic jam. So, drivers tend to drive at their desired speed and not interfered by other vehicle or not constrained by control devices. As a result, although flowrate was increased at certain level, space mean speed also increased. Density was a parameter that is inversely proportional to the space mean speed. When density was decreased, space mean speed also increased to the certain level. This can be explained as when the vehicles at the site were low density, drivers feel more comfortable and safe to speed up their vehicles. For the relationship of IRI to the space mean speed, it also represents the inverse proportion. When the IRI decreases, space mean speed tends to increase. This can be explained

as when the pavement roughness was high; drivers did not feel safe and comfortable to speed up their vehicles. Besides, if the drivers experienced high vibration due to the bad pavement roughness index at site, they will slow down their speed to avoid damaged to their vehicles. If the IRI index was lower, drivers tend to increase their speed, because they feel more convenient.

The Eq. 1 that regressed by Minitab software needs to be check via normality test for residuals. Normality test comprises of probability plot and goodness-of-fit test. The use of probability plot and goodness-of-fit tests, such as the Anderson–Darling and Kolmogorov–Smirnov normality test, was to assess whether the residuals were normally distributed. As can be seen in Figs. 7 and 8 the points were scattered closely around the straight line which meant that the residuals were normally distributed [11].
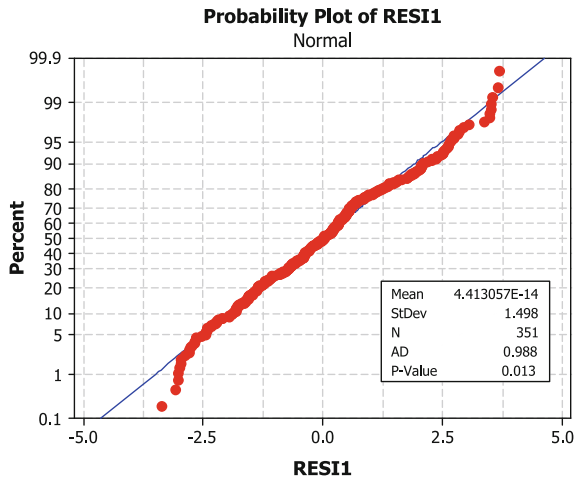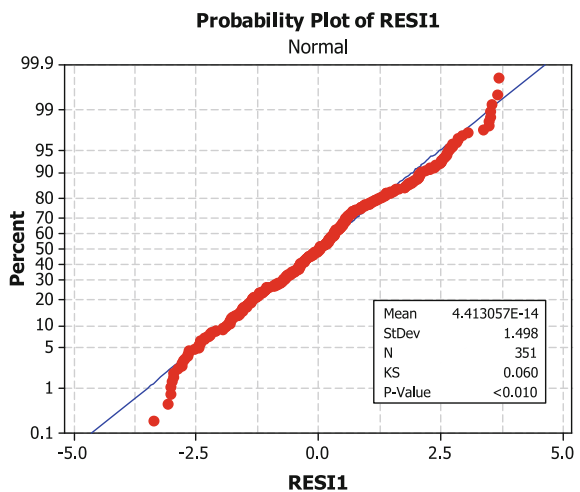
Fig. 7 Anderson–Darling

Fig. 8 Kolmogrov–Smirnov

5 Conclusion

This study has achieved the objectives such as to conduct survey of road profiling with regard to International Roughness Index (IRI), to classify traffic engineering parameter's relation toward pavement roughness by applying Automatic Traffic Counter (ATC) and to develop model which adhere to the operating speed with the pavement roughness. All data and information about the roads at Sepang and Batu Arang in Selangor were tabulated in comprehensive table to develop model of space mean speed which is SMS = 72.1601 + 0.228632 (q) − 16.4215 (k) − 0.211912 (IRI). The value of R^2 for space mean speed equations is 94.41 %, respectively. The study can conclude that the space mean speed is a dependent variable for the model development process. Flowrate, density, and IRI were independent variables to predict space mean speed value. Flowrate was directly proportional to the space mean speed otherwise; density and IRI relationship were inversely proportion to the space mean speed. According to the empirical data on both sites, the traffic flow established a stable movement which does not give an impact of speed decreasing to the vehicles speed, although the flowrate increased.

References

1. C. C. Smith, D. Y. McGehee, and a. J. Healey, "The Prediction of Passenger Riding Comfort From Acceleration Data," *J. Dyn. Syst. Meas. Control*, vol. 100, no. 1, p. 34, 1978.
2. S. Xiaoduan, H. Yulong, W. Shuangjie, and W. Yiyi, "Characteristics of Operating Speed for Proper Speed Limit," *ICCTP 2010 Integr. Transp. Syst. Green•Intelligent•Reliable © 2010 ASCE 3738*, pp. 1678–1689, 2010.
3. A. A. of S. H. and Transportation and Officials, *A Policy on Geometric Design of Highways and StreetsNo Title*. 1994.
4. A. A. of S. H. and Transportation and Officials, *A Policy on Geometric Design of Highways and StreetsNo Title*. 2001.
5. "ATJ 5/85 (Pindaan 2013)," *Manual For The Structural Design of Flexible Pavement*. p. 38, 2013.
6. A. M. A. Rahim and M. A. Adnan, "Investigation of Patching Road Defect with Relation to Soil and Pavement Parameter : A Case Study at Bukit Beruntung.".
7. Z. Hongliang and Y. Wanqiao, "Evaluation Method of Pavement Roughness Based on Human-Vehicle-Road Interaction," *ICCTP 2010 Integr. Transp. Syst. Green•Intelligent•Reliable © 2010 ASCE 3738*, pp. 3738–3746, 2010.
8. H. Wen and C. Chen, "Factors Affecting Initial Roughness of Concrete Pavement," *J. Perform. Constr. Facil.*, vol. 21, no. 6, pp. 459–464, 2007.

9. P. Múčka and J. Granlund, "Is the Road Quality Still Better?," *J. Transp. Eng.*, vol. 138, no. 12, p. 349, 2012.
10. S. Chandra, "Effect of Road Roughness on Capacity of Two-Lane Roads," *J. Transp. Eng.*, vol. 130, no. 3, pp. 360–364, 2004.
11. Minitab, *Minitab Statistical Software, Release 16 for Window, State College, Pennsylvania*. 2010.

Assessing Motorcycle Red Light Runner Crossing Event Sequence at Signalised Intersection

Wan Adilah Ismail, Intan Rohani Endut, Siti Zaharah Ishak and Rizati Hamidun

Abstract Motorcycle collision is one of the major contributors of injury and fatality rates in Malaysia. Between these rates, the motorcycle red light runner (RLR) at the signalised intersections becomes the highest contributor. RLR issues are already investigated by the previous studies, but normally focusing on determining the factors and proposing the countermeasures. However, the view of event sequences when motorcycle crossing red light phase is not studied in detail. Thus, this study proposed to give a view of the event sequences of motorcycle RLR crossing scenario. It has acquired a series of site observations as qualitative data to extract the event sequence of RLR crossing at signalised intersections using a video recorder. This study was conducted in Shah Alam area, state of Selangor during 3:00 pm until 6:00 pm. Through the event sequences, the movement of motorcycle RLR starting from dilemma zone, then crossing the stop line and entering conflict zone was studied. At conflict zone, the conflict might happen when a motorcycle and a vehicle approaches the point of the conflict zone at the same time. Therefore, the assessment of RLR crossing event sequences is needed for understanding the event of RLR and as a guideline for future study in developing the model.

Keywords Crossing event sequences · Motorcycle · Red light runner

W.A. Ismail (✉) · I.R. Endut
Faculty of Civil Engineering, Universiti Teknologi MARA (UiTM),
Shah Alam, Selangor, Malaysia
e-mail: wadiel@yahoo.com

S.Z. Ishak
Road Safety Engineering & Environmental Research Center, Malaysian Institute
of Road Safety Research (MIROS), Kajang, Selangor, Malaysia
e-mail: sitizaharah@miros.gov.my

R. Hamidun
Crash Data Analysis & Exposure Unit, Malaysian Institute of Road Safety
Research (MIROS), Kajang, Selangor, Malaysia
e-mail: rizati@miros.gov.my

1 Introduction

The road transport system is mobilised to move people from one location to others and it consists of three main physical components. Based on the review, Third African road safety congress, 1997, briefly describes road components; there are road users (pedestrian and drivers or riders), the vehicles (cars, motorcycles, lorries and etc.), and the environment (physical condition). In Malaysia, the motorcycle is the most favourable transportation mode [1–5]. The total registered motorcycles in Malaysia were increased year after year, especially during 2010 until 2012 and it was proved that motorcycle is the most favourable transportation [6].

The demands for motorcycles in Malaysia were represented by the increasing trend of registered motorcycles as shown in Fig. 1. Motorcycle demands had increased around one percent in 2005 until 2008. However, during 2008 until 2009 had a reduction of motorcycle demands, where almost three percent of decreasing among those years. It is due to the effect of the national economic crisis during the year. But, after that period, the motorcycle demands increased by 2 % from 2010 to 2012.

Increasing population is one of the factors contributing to increasing of motorcycle demand where the population on January 2005 slightly increased from 25.40 million to 29.95 million, on Jan 2014 in population. Besides that, Department of Statistics (DOS) Malaysia mentioned that the current population till October 2014 is 30,351,019 [7].

The impact of increasing motorcycle demands in Malaysia may contribute to the increase of motorcycle collisions and fatalities. In Klang, Selangor it is found that motorcycle collisions are the highest contributors for road collisions compared the other types of vehicles [8]. Almost 50 % of the motorcycles were involved in road collisions and fatalities [9]. The number of Malaysian road fatality is expected to increase up to 10,716 in the year 2020 [10].

Types of motorcycle collisions consist of ran off road, run traffic control, oncoming or head-on, and others which involve single and multiple vehicle collisions. Ran off road was the higher collision types involving motorcycles followed by running traffic control, oncoming or head-on, left turning oncoming and motorcyclist down [11]. Thus, the RLR issues should be investigated in reducing the collision and to provide the safety for all road usages.

Fig. 1 Registered motorcycles in Malaysia (*Source* JPJ (2014) [6])
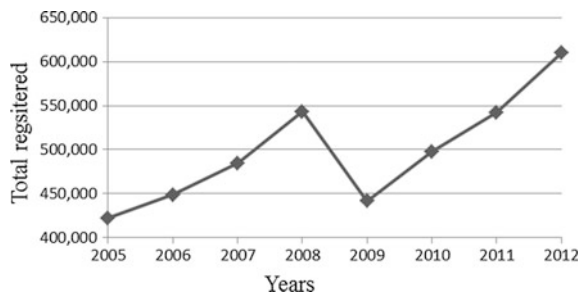
The purpose of this paper is to view the event sequences of motorcycle during RLR and the conflict between vehicles from the opposite approach legs. The event sequence is important in determining and understanding the movement of the motorcycles and vehicles when RLR happens. Due to this event sequence, the factors and solves of RLR are able to be proposed. It is because; from this study the details of movement will be determined. Other than that, it is as an effort for improving the road safety by decreasing RLR at signalised intersections. Other types of examining study are needed to improve the road safety strategies through applying different types of safety model in getting the most suitable road safety strategies [12].

This study is discussed as follows; the variety of RLR definitions from previous researchers will be summarised in Sect. 2. The next sections; will elaborate about the traffic signal timing. Traffic signal timing is the most important part of RLR at signalised intersections. From this section, it also describes the different events of the motorcycles when it violates a red light. The methodology and the result and also discussion of this study are represented in Sects. 4 and 5, respectively. The last section, the conclusion of this study was concluded in Sect. 6. This section also proposes some recommendation as a planning guide in future studies relating the RLR.

2　Definitions of Red Light Runner (RLR)

Red light runner (RLR) is defined as vehicles are disobedient to follow the traffic signals regulations where completely prohibits to proceed their movement during red light and should be prepared to stop at stop line when displayed in yellow light [13]. Unfortunately, many vehicles, especially among motorcyclist fail to follow traffic signal regulations. Thus, automatically the RLR is one of the major causes of road crashes and fatalities at signalised intersections [14].

There has a few of the definitions of RLR by previous studies as follows:

- Disobey a traffic signal when a traffic light turned red, the vehicle still proceeding through [15].
- When a vehicle fails to follow traffic light regulations, a collision will happen [16].
- A vehicle crosses and passing through the stop line of signalised intersections during the onset red light phase [17].
- A vehicle entering intersections at onset of red light with 29 km/h speed or 32 km/h for higher speed limits [18].
- An nonstop vehicle and proceeding movement on signalised intersections after onset of red light phase meanwhile opposing direction was a green light [19].
- Identify the last vehicle crossing the signalised intersections before onset of a traffic light in the opposite direction. Mostly occurred in urban area, which has more signalised intersections compared to the other locations and red runners will increase when a city has more intersections [20].

From the above listed definitions by other previous researchers, mostly mentioned that RLR is a violate action. Violate action when riders or motorcyclists are violating the traffic signal regulations which; to stop at the stop line and entering the yellow box once onset of red light traffic. By road construction law, each entrance of junction or crossing intersections must have a stop line, which is a thick solid white line across junction [21]. Each vehicle must stop behind a stop line and prohibited to enter a yellow box during the red light.

3 Traffic Signal Timing

The traffic signal is commonly used in the intersections in urban areas. It is applied to reduce congestions and delays, making crossing with safety and smooth vehicle flow for all road users including pedestrians. But, if the function of a traffic signal is not properly designed, will cause failure performance of signalised intersections. One of the failure performances of traffic is encouraged of RLR happened. RLR can be categorised into intentional and unintentional violations. The engineering factors like traffic signal performance able to address the intentional and unintentional violators such as yellow phase if too short, it will increase the number of RLR at lanes. Meanwhile, if green phase is too long, it also encourages the intentional RLR at the opposite lanes. Thus, the properly designed of traffic signal performance is really needed in mitigating RLR.

There are two different events of motorcyclist crossing; during the onset of red light phase, which is known as red clearance and during red light phase as shown in Fig. 2.

Onset and during red light phase is selected because many crashes may result from vehicles when entering the intersections during these durations [23]. The onset of red light phase is when the interval of yellow light change to a red light period, which may affect the riders speeding behaviour to cross a junction before the red light appeared. Meanwhile, the RLR during red light periods may cause by the impatience of rider's behaviours.
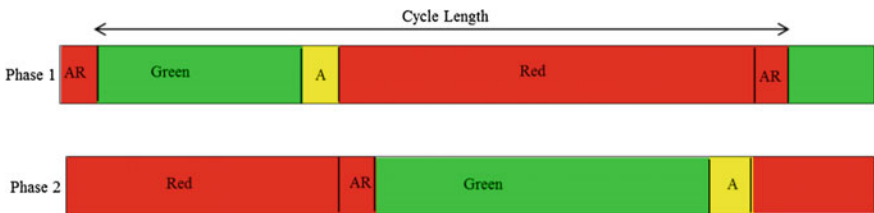

Fig. 2 Periods of RLR happened (*Source* Peter et al. (2008) [22])

The onset red light phase depends on the length of change interval or called as the clearance intervals or intergreen periods. This change interval between the onset of the yellow interval functions as a signal warning for the approaching vehicle to reduce speeding and get ready to stop at the following red interval. However, most of motorcyclists failed to predict the actual time of onset of the yellow interval, which acquire them either to continue through or stop at intersections safely. Review on Manual on Uniform Traffic Control Devices (MUTCD) had indicated that the yellow interval should approximately range 3–6 s based on individual intersection characteristics [23, 24]. If change interval is too short, the motorcyclist may force to emergency brakes or continuous crossing with a green light indicated as red light runner. Thus, the durations of length of change interval must be related to individual intersections characteristics such as traffic speed, traffic deceleration rate, width of intersection and grade [24].

4   Methodology

Event sequences of motorcycle RLR were derived from site locations at Seksyen 7, Shah Alam, Selangor as shown in Fig. 3. Site selections are based on a critical history of accidents that occurred previously in Shah Alam, Selangor area. Based on IPD Shah Alam, 2014, Seksyen 7 is among the highest accident contribution at signalised intersections compare than others area [25]. It may influence the population of surrounding area where located a commercial, residential and institution.

This event sequence was recorded via direct observation using a video recorder as primary data and extracted as qualitative data. Direct observation can be validated and used by repeatedly watching the played recorder before remark any conclusions [26]. Then, the duration of direct observation will be conducted during 3 h continuous periods from 3:00 pm until 6:00 pm where the most weekly crashes happened in Malaysia during that durations [27].

The video tape was captured and film two different events of motorcyclist crossing where during the onset of red light phase and during red light phase. It is as a qualitative data for understanding the event sequences. This study will be an analysed and investigated the motorcyclist crossing from two opposite approach at signalised intersections as in Fig. 6.

Figure 4 describes the flowchart of rider's behaviours at two different approach legs. During these times, motorcycle at red light phase violated a red light and entered the conflict zone at signalised intersections. Meanwhile, vehicle from the opposite also crossed and entered the conflict zone due green light phase. Conflict zone is an interaction point area between more than one vehicles corresponding to different types of directions at specified time. The conflict between motorcycle RLR and vehicle were happened when both motorcycle and vehicle start to increase the speed to enter the conflict zone of intersections.
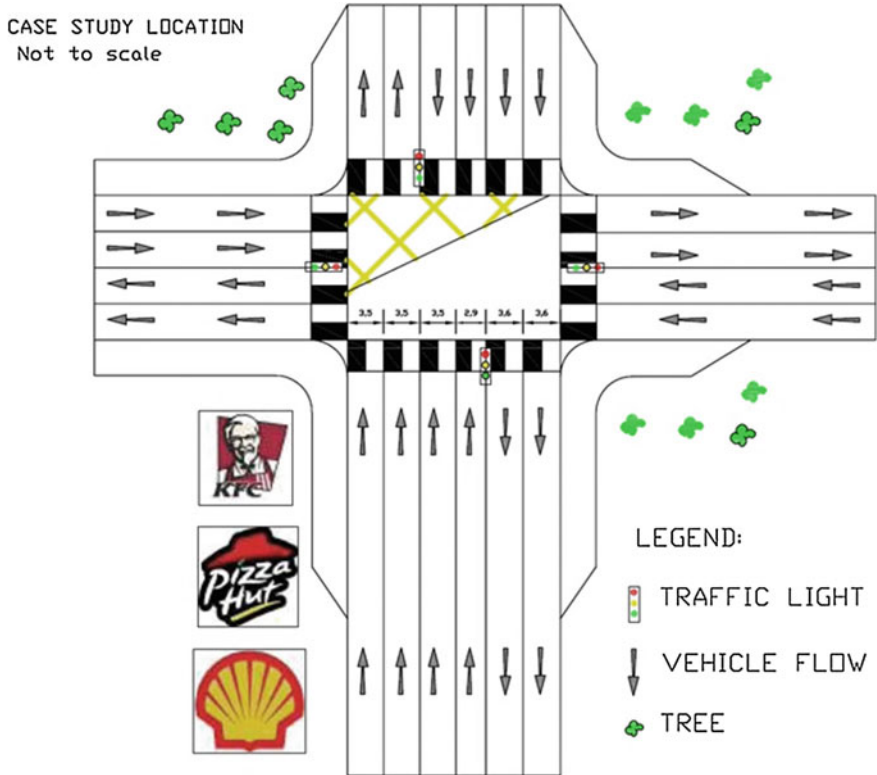
Fig. 3 One of the layout sites selected (*Source* PWD (1886) [28])

Fig. 4 Flowchart of riders' behaviours
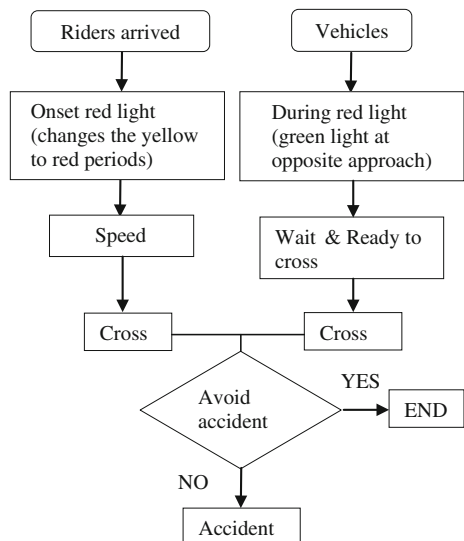
5 Result and Discussion

The crossing event sequences of motorcyclist RLR and vehicle was illustrated in Figs. 5 and 6. Figure 5 shows the examples of traffic conflict during RLR at the conflict zone of signalised intersections. Conflict zone (CZ) is interaction point areas of more than one vehicles interacting together at certain times. The conflict among RLR is expected to happen in conflict zone when motorcycles and vehicles enter the conflict zone at the same time. However, it can be avoided if one of these vehicles enter the conflict area at different times.

Meanwhile, Fig. 6 has shown the observation of interaction between motorcycles and vehicles in determining the conflict risk. The interaction started when the
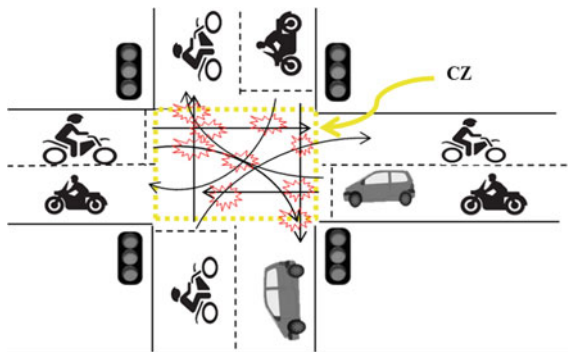
Fig. 5 Conflict patterns between motorcycle and vehicle
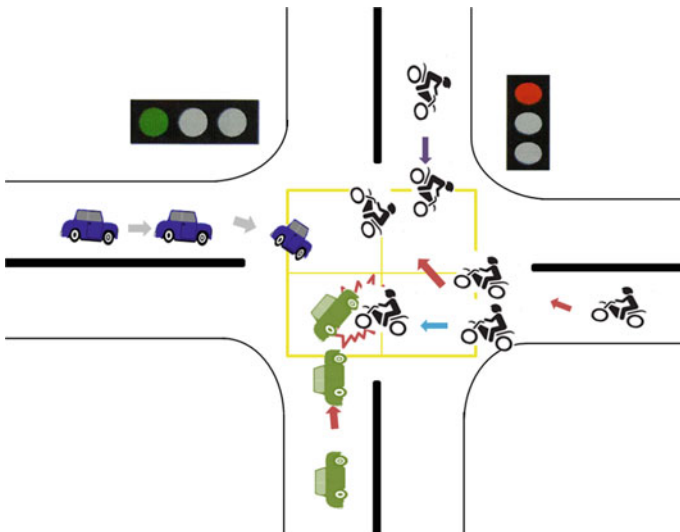
Fig. 6 Crossing event sequence of motorcycle and vehicle

motorcyclist as RLR agent crossed the stop line and entered CZ during the red light phase. Meanwhile, the vehicles continued moving in green light phase. The events were started when the motorcyclist wait and see the surrounding areas like traffic volume and once the traffic volume at the opposite approach was decreased, the motorcyclist crossed and entered the CZ. The conflict between these vehicles happened when approaching the same point at CZ.

The interactions happened when the motorcycle as RLR agent crossed the stop line and entered CZ during the red light phase. At the same times, the vehicle was continued moving in green light phase as shown in Fig. 7. The frame coding method was applied from Frame 1 until Frame 9 to figure the RLR event sequences. Frame 1 shows the motorcyclist wait and sees the surrounding area like traffic volumes. After the traffic volumes at the opposite approach were decreased, the motorcyclist will be crossed and entered the CZ as in Frame 2 and 3. In Frame 4, the motorcyclist slowing down and trying to avoid the conflict between vehicles
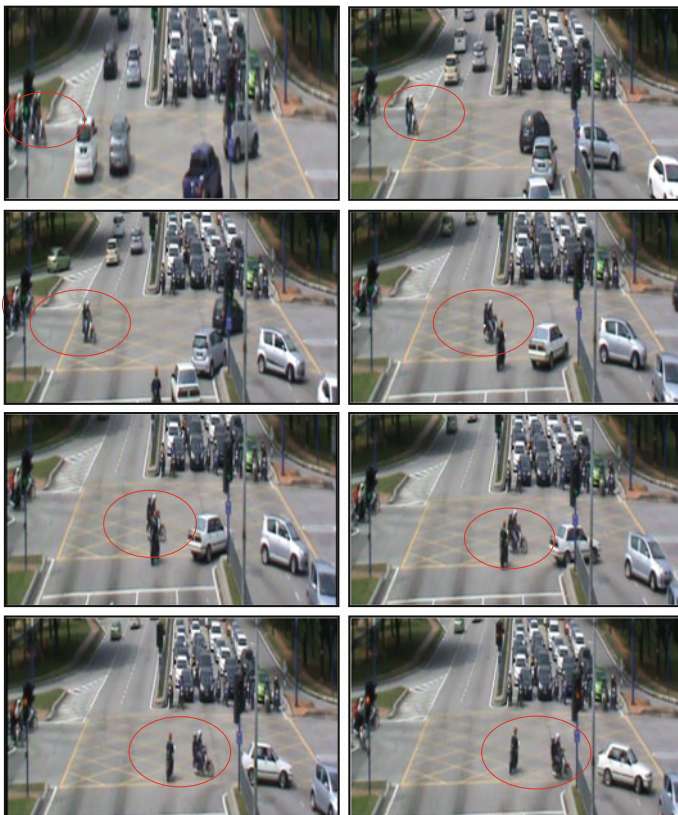
Fig. 7 Event sequence of RLR during crossing the intersection

from the opposite approach where traffic signal appear as a green light phase. Meanwhile, Frame 5 and 6 shows interaction between both vehicles when approaching the same point at CZ. The vehicle was slowing down and motorcyclist speeding to exit the CZ in avoid any conflict happened as in Frame 7. Then, Frame 8 shows the motorcyclist continuous movement to exit CZ. The event sequences of RLR were structured based on these scenario from the stop line, entering CZ, conflict (near or misses interaction), and exit CZ.

Basically, the vehicles positioning in ready condition to give respond due to traffic light when approaching the stop line. Normally, when green onset, vehicles will increase the speed to cross the conflict zone with successful. Behaviours of vehicle at signalised intersection can be viewed when approaching and passing the intersections [29].

6 Conclusion and Recommendation

This paper presents the crossing event sequences of motorcycles during red light runner scenario at signalised intersections. The crossing event sequence was extracted from direct observations using a video recorder at site observations. Crossing event sequences of RLR motorcycle were happened from dilemma zone, then approaching the stop line. After approaching stop line, motorcycle entered the conflict zone. Basically, the conflict between motorcycles and vehicles will happen at conflict zone. This conflict was happened when a motorcycle and vehicle interact at the same points at conflict zone. Furthermore, the RLR among motorcycle also can be happened in difference ways of traffic signal timing, such as onset or during the red light. Commonly, RLR mostly occurs at onset of red light phase. It is because during these times the motorcycle is difficult to stop where signal change interval of amber phase to red light phase traffic.

In further study, the Petri Nets is recommended to estimate the potential conflict risk during RLR. An appropriate measure in improving road safety is expected as an output from this study. Petri Nets is another tool used for the modeling and formal analysis, as previous models for traffic signal study. Petri Net is able to develop models concurrency, shared resources and synchronisation [30]. The developed model using Petri Net is expected to predict the potential risk of conflict between motorcycle and vehicle. Similar approach in predicting the risk of conflict using Petri Nets also proposed by R. Hamidun et al. (2014), but focused on pedestrians crossing scenario [31].

Understanding the crossing event sequence of RLR is important to propose the suitable countermeasure in mitigating the RLR especially among motorcyclist.

References

1. M. M. Abdul Manan, T. Jonsson, and A. Várhelyi, "Development of a safety performance function for motorcycle accident fatalities on Malaysian primary roads," *Safety Science*, vol. 60, pp. 13–20, Dec. 2013.

2. P. T. Yen, R. Radin Umar, A. A. Aziz, H. Singh, S. A. Wahid, A. H. H. Mansor, Z. Noor, and M. S. Othman, "Fatal injuries in Malaysian motorcyclists," *International Medical Reseacrh Journal*, vol. 3, no. 2, pp. 115–119, 1999.

3. H. Hussain, M. Dadang, R. Radin Umar, and M. Ahmad Farhan, "Key components of a motorcycle-traffic system – A study along the motorcycle path in Malaysia," *IATSS Research*, vol. 29, no. 1, pp. 50–56, 2005.

4. T.-P. Hsu, A. F. M. Sadullah, and N. X. Dao, "A comparison study on motorcycle traffic development in some Asian countries – case of Taiwan, Malaysia and Vietnam," 2003.

5. S. Kulanthayan, Phang. W.K., and Hayati K.S., "Traffic light violation among motorists in Malaysia," *IATSS Research*, vol. 31, no. 2, pp. 67–73, 2007.

6. Jabatan Pengangkutan Jalan (JPJ), "Statistic of Registered Motorcyclye," *Official Portal of Road Transport Department Malaysia*, 2014. [Online]. Available: http://www.jpj.gov.my/web/eng/motorcycle-registration-statistics.

7. Department of Statistic Malaysia (DOS), "Populations in Malaysia," *Department of Statistic Malaysia,Official Portal (DOS)*, 2014. [Online]. Available: http://www.statistics.gov.my/portal/index.php?lang=en.

8. M. G. Masuri, K. A. Isa, and M. P. M. Tahir, "Children,youth and road environment," *Asian Journal of Environment-Behaviour Studies*, vol. 2, no. 6, pp. 13–20, 2011.

9. M. M. Abdul Manan, "Motorcycle fatalities in Malaysia," *IATSS Research*, vol. 36, no. 1, pp. 30–39, Jul. 2012.

10. R. Sarani, S. A. S. M. Rahim, J. M. Marjan, and W. S. Voon, "Predicting Malaysian Road Fatalities for Year 2020," 2012.

11. D. F. Preusser, F. W. Allan, and R. G. Ulmer, "Analysis of fatal motorcycle crashes: crash typing," *Accident Analysis and Prevention*, vol. 27, no. 6, pp. 845–851, 1995.

12. B. P. Hughes, S. Newstead, A. Anund, C. C. Shu, and T. Falkmer, "A review of models relevant to road safety.," *Accident, Analysis and Prevention*, p. 21, Jul. 2014.

13. H. M. Jamil, A. Shabadin, and S. A. S. M. Rahim, "The effectiveness of automated enforcement system in reducing red light running violations in Malaysia: pilot locations," 2014.

14. R. Ramli, J. Oxley, F. M. Noor, N. K. Abdullah, M. S. Mahmood, A. K. Tajuddin, and R. McClure, "Fatal injuries among motorcyclists in Klang Valley, Malaysia," *Journal of Forensic and Legal Medicine*, vol. 26, pp. 39–45, Aug. 2014.

15. Federal Highway Administration, "Making intersections safer a toolbox of engineering countermeasures to reduce red light running," *Federal Highway Administration, U.S Department of Transportation*, 2014. [Online]. Available: http://safety.fhwa.dot.gov/intersection/redlight/cameras/rlr_report/chap2.cfm.

16. C. Y. D. Yang and W. G. Najm, "Analysis of red light violation data collected from intersections equipped with red light photo enforcement cameras," *National Highway Traffic Safety Administration*, p. 70, 2006.

17. K. M. Lum and Y. D. Wong, "Impacts of red light camera on violation characteristics," *Journal of Transportation Engineering*, vol. 129, pp. 648–656, 2003.

18. D. E. Ruby and A. G. Hobeika, "Assessment of red light running cameras in Fairfax County, Virginia," 2003.

19. K. L. Schattler, C. Hill, and T. K. Datta, "Clearance interval design and red light violations," in *Today's Transportation Challenge: Meeting Our Customer's Expectations*, 2002, no. 1, p. 13.

20. B. E. Porter and K. J. England, "Predicting red-light running behavior : A traffic safety study in three urban settings," *Journal of Safety Research*, vol. 31, pp. 1–8, 2000.

21. N. H. Yung and A. H. Lai, "An effective video analysis method for detecting red light runners," *IEEE Transactions On Vehicular Tech.*, vol. 50, no. 4, pp. 1074–1084, 2001.
22. P. Koone, L. Rodegerts, K. Lee, S. Quayle, S. Beaird, C. Braud, J. Bonneson, P. Tarnoff, and T. Urbanik, *Signal timing manual*. Federal Highway Administration, 2008.
23. R. A. Retting and M. Greene, "Influence of traffic signal timing on red-light running and potential vehicle conflicts at urban intersections," *Transportation Research Record: Journal of the Transportation Research Board*, vol. 1595, no. 1, pp. 1–7, 1997.
24. H. S. Stein, "Traffic signal change intervals : Policies,practices and safety," *Transportation Quarterly*, vol. 40, no. 3, pp. 433–445, 1986.
25. Polis DiRaja Malaysia (PDRM), "Laporan kemalangan di kawasan Shah Alam, Selangor," 2014.
26. E. Taylor-powell and S. Steele, "Collecting evaluation Data : Direct observation," *University of Wisconsin-Extension: Cooperation Extension*, 1996.
27. T. H. Law, L. I. N. Xu, and R. S. Radin Umar, "Factors influencing red light runners among motorcyclists in Malaysia," *Journal of the Eastern Asia Society for Transportation Studies*, vol. 5, pp. 2518–2525, 2003.
28. Public Work Department Malaysia (JKR), "Manual on traffic control devices: Road marking and dileanation," *Public Work Department Malaysia (JKR)*, 2009.
29. K. I. M. Jumsan, R. Sungmo, and H. Zunhwan, "Vehicle passing behavior through the stop line of signalized intersection," *Journal of the Eastern Asia Society for Transportation Studies*, vol. 6, pp. 1509–1517, 2005.
30. M. dos S. Soares and J. Vrancken, "Road traffic signals modeling and analysis with Petri Nets and Linear Logic," *Proceeding of the 2007 IEEE International Conference on Networking, Sensing and Control, London, UK, 15–17 April 2007*, no. April, pp. 169–174, 2007.
31. R. Hamidun, S. Z. Ishak, and I. R. Endut, "Pedestrian crossing scenario model using Petri Nets," *Procedia - Social and Behavioral Sciences*, vol. 129, pp. 406–413, May 2014.

Evaluation of Operating Speed at Multilane Highway Along Jalan Meru: Case Study of Reliability of Posted Speed Limit

Ab Mughni B. Ab Rahim, Muhammad Akram Bin Adnan, S.Z. Zamalik, F. Jamali, M. Mohammad, Z. Abdul Karim and Norliana Binti Sulaiman

Abstract Operating speed and traffic volume data are collected on different sections of four lanes and six lane roads at three different points along Jalan Meru, Klang. The objective of this study is to identify the vehicular speed at different points which conforms to the geometric design of the road. The speed data compiled is analyzed using the percentile approach, V85, V95, and V15 and describing the condition of traffic compared to posted speed limit along the road. Speed data are analyzed by generating a regression equation using advanced statistical software in order to estimate the precision of the data taken. Hence, graphs illustrate a trend and correlation between speeds at 85th percentile, 95th percentile and 15th percentile with traffic flow rate are plotted. Based on data, the operating speed of V85 at location A and B are lower than the posted speed limit since the speeds taken were interrupted by control device at the upstream and downstream of the traffic stream. While at location C, the operating speed of V85 is higher than the posted speed limit and is not affected by any constraint. The trends on the graph of V85, V95, and V15 versus vehicles flow rate show that the speed is decreasing as the road capacity increases.

Keywords Operating speed · Traffic volume · Speed limit · 85th percentile speed

A.M.B.A. Rahim (✉) · S.Z. Zamalik · F. Jamali · M. Mohammad · Z. Abdul Karim
Faculty of Civil Engineering, UiTM Shah Alam, Shah Alam, Selangor, Malaysia
e-mail: abmughni8636@yahoo.com

M.A.B. Adnan · N.B. Sulaiman
Faculty of Civil Engineering, Universiti Teknologi MARA, Shah Alam, Selangor, Malaysia

1   Introduction

Speed is often regarded as rate of movement of vehicle in distance per unit time [1]. Speed is important in the measurement of traffic performance on a road system. In design, speed is a primary factor in determining the road geometric design.

Appropriate design of speed will fulfill the road function with regard to safety, time, comfort, convenience, and economics.

Higher speeds generally translate to lower time travel, an indication of good mobility. Thus, speed study is a relevant aspect of highway design in establishing the effectiveness of the existing speed limits of road system.

In this study, free flow speeds were taken which is the speed of vehicle when the driver tends to drive at desired speed and not interfered by other vehicle or not constrained by control junction. The use of percentiles in the measurement of speed and regression analysis to establish the correlation between percentile speed and flow rate helps to arrive at an accurate data pertaining to road performance. The amount of time wastage due to traffic slowdown should be measured through the use of regression analysis.

Based on the reliable results it is practically possible to recommend any proposal to improve vehicular speed and flow rate and road conditions. Key parameter toward effective geometric design and control strategies can help to understand the breakdown phenomenon especially at merging sections.

2   Literature Reviews

Based on the Manual of Uniform Traffic Control Devices (MUTCD), "The Speed Limit (R2-1) sign intends to present the limit constituted by law, ordinance, regulation or as embraced by the authorized agency regarding on the engineering study (MUTCD, 2010a)" [2]. Despite, professionals have systematized plenty of models such as USLimit and guidelines to support policy makers in deciding a posted speed limit [3]. Policy makers acknowledge some factors as land use along the adjacent highway, section length, crash rates, design speed, number of intersections, number of driveways, zoning, highway function, and parking presence, as a standard for designing posted speed limits in common. In the manner that, one does not post a six-lane, divided, highway with full control of access at 30 mile/h (50 km/h). One does not post an urban street with on-street parking at 75 mile/h (120 km/h). Further, the MUTCD states, "The speed limits displayed shall be in multiples of 5 mph (MUTCD 2010a)."

At all sites and using a radar gun, the team measured instantaneous speeds within an approximately 50-ft (15 m) midblock or mid-pipe segment length [4]. Hashim [5] found that the absolute difference between speed limit and the 85th percentile speed/design speed plays a significant role in the case of killed or

seriously injured accidents (KSI). His study proved that as this difference increases the KSI accident frequency increases. This would agree with the hypothesis that many drivers prefer to travel constantly near the speed limit. However, the highway alignment may enable drivers to exceed the speed limit substantially. Alternatively the alignment forces the drivers to drive well below the speed limit especially in the case of poor alignment (e.g., sharp curves), interrupting the homogeneity of drivers' speeds. Either of these could lead to severe accidents. This confirms that speed limits should usually be set near the 85th percentile speed.

An operating speed of the vehicles depends on the roadside environment. A study conducted by Horst and Ridder [6] showed that the roadside infrastructure—trees, guardrails, barriers, panels, and emergency lanes—impacts drivers' behaviors on speed and lane positioning. The speed of a car was dependent upon how far the trees or guardrail was. For more than 4.5 m away, there was no impact upon the speed; however, the shorter the distance, the slower the speed of the car. When there was a combination of trees and guardrail, drivers tended to keep their cars away from the right side; nevertheless, if there were only trees, there was no influence on the lateral position. Elvik [7] stated that speed is one of the most important factors causing injury crashes.

The Kentucky Traffic Operation Guidance Manual [8] recommended conducting engineering study in accordance with the Manual on Uniform Traffic Control Devices to setup speed zones. The 85th percentile speed of vehicles, crash history, and location of speed zone are required data for setting up speed zones. The speed limit should be reasonable, adequate, and appropriate and should be reviewed regularly by the district. The manual states that advisory speed warning signs should be provided in road 36 intersections and in turning roads, instead of speed zones. Normal transitions, as mentioned in the manual are 55–45 mph and 35–25 mph. The manual recommended reducing 10 mph speed in school zones from normal posted speed limit. Generally, the speed limits in school zones should not be less than 25 mph nor more than 45 mph. However, lower speed limits can be provided based on factors like sight distance, roadway conditions, and crash history of the road.

Speed data, road geometrics and design, other conditions of roadway, and crash history are the factors considered for setting up speed limits based on the guidelines 39 prepared by Georgia Department of Transportation [9]. The speed determined using those factors is finally confirmed by test driving. The manual does not allow a speed limit below 25 mph in state routes. For state highway segments, the minimum allowed speed limit is 35 mph. The manual does not provide specific details about how the speed limit is calculated and how the factors affecting the speed limits are taken into account.

Methodology

The spot speed study was obtained using Laser gun and the study was conducted around 9 am to 1.30 pm along Jalan Meru, Klang. The case study methodology is summarized and has been shown in Fig. 1.

```
┌─────────────────────────────────────────┐
│  Determination and Selection of the      │
│         Observation Method               │
│      o    Spot Speed Study               │
│      o    Traffic Count                  │
└─────────────────────────────────────────┘
                    ↓
┌─────────────────────────────────────────┐
│  Selection of Location/Area of Observation│
│      o    Jalan Meru Klang               │
└─────────────────────────────────────────┘
                    ↓
┌─────────────────────────────────────────┐
│         Data Collection                  │
│      o    Digital Traffic Classifier     │
│      o    Tru Cam                        │
│      o    Laser Gun                      │
└─────────────────────────────────────────┘
                    ↓
┌─────────────────────────────────────────┐
│         Data Analysis                    │
│      -Using Minitab Software             │
└─────────────────────────────────────────┘
                    ↓
┌─────────────────────────────────────────┐
│         Conclusion                       │
└─────────────────────────────────────────┘
```
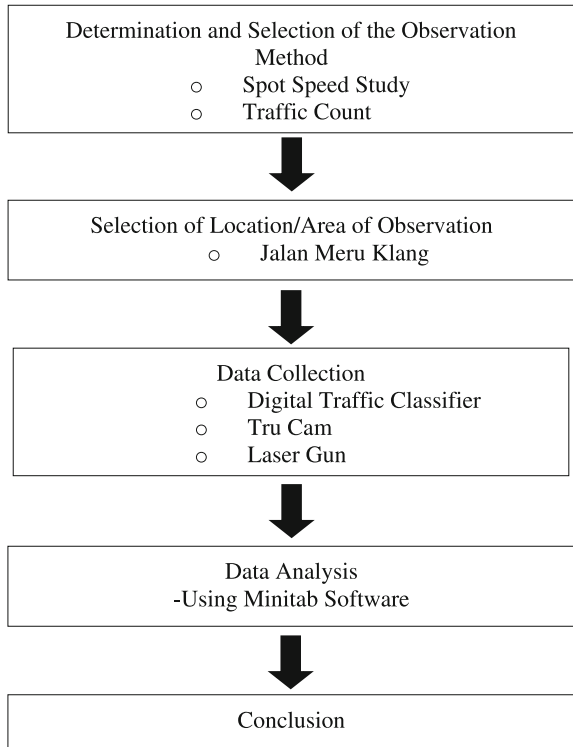
3   Field Data Collection

Spot speed study was used to collect operating speed data at three sites along Jalan
Meru, Klang. The data collection at the site involves observing the operating speed
and recording the speeds of the vehicles. The speeds were collected from four
vehicle types: motorcycles, passenger cars, buses, and trucks. The operating speed
of the different types of vehicles was collected by observing the operating speed
value using a laser gun.

The data was collected during free flow of traffic operation, avoiding peak hours
and night time. For each site, a time period of 1 h 30 min were allocated to collect
spot speed data. Once the collection of speed data was completed, road geometrical
characteristics, i.e., width of lane and total vehicles according to the vehicle type
were recorded. Once the collection of speed data was completed, data analysis was
calculated using statistical software. Details of the process flow for data collection
process are as shown in Fig. 1.

The operating speed data is compiled at three points namely Location A, B, and
C along Jalan Meru, Kelang. The road is an arterial road with some section of four
lane dual carriageway and partially 6 lanes dual carriageway connecting Shah Alam
and Kelang city. From our observation the posted speed limit along Jalan Meru,

Table 1 Sample of analyzed free-flow speed data at location A

Time: 12.50–1.00 pm					
Speed (km/h)	Average speed (km/h)	Frequency	Percentage (%)	Cumulative percent	Speed percentile
40–45	42.5	1	2.8	2.8	–
45–50	47.5	11	30.6	33.4	V15 = 49.9
50–55	52.5	12	33.0	66.4	–
55–60	57.5	5	13.9	80.3	–
60–65	62.5	4	11.1	91.4	V85 = 65.6
65–70	67.5	2	5.6	97.0	V95 = 68.7
70–75	72.5	0	0	97.0	–
75–80	77.5	1	2.8	100.0	–

Kelang, is 70 km/h. The data were taken on weekend April 11, 2015 and analyzed by taking percentile speed for V85, V95, and V15 (Table 1).

4 Data Analysis

4.1 Percentile Speed and Flow Rate Definition

(1) Percentile V85

The speed is regarded as an operating speed at which a driver can travel on a given road under favorable condition and prevailing traffic conditions without at any time exceeding the design speed on a section by section basis [10].

(2) Percentile V95

The V95 normally represents a design speed. Design speed refers to appropriate geometric design elements particularly in horizontal and vertical alignment, super-elevation, sight distance ,etc. In this case the speed data obtained within range of V85 and V95 can be considered as safe.

(3) Percentile V15

At this point of percentile it simply shows that traffic flow is interrupted by obstacles in the form of traffic junctions, small road widths, and substantial slow movement of heavy vehicles.

4) Flow Rate

Flow rate is defined as the equivalent hourly rate at which vehicle pass over a given point or section of highways during a given time interval. The numbers of vehicle were converted into the passenger car equivalent (PCU) which displaced a single heavy vehicle. The PCU factor is obtained from multilane highway, HCM 2011 guideline. The flowrate results were analyzed with percentile speed of V85, V95, and V15. The PCU conversion used is shown in Table 2.

Table 2 Passenger car equivalent (PCU) HCM Mal 2011

Vehicle class	Vehicle type	Passenger car equivalent
Class 1	Cars/small vans/utilities	1
Class 2	Lorries (with 2 axles)/large vans	1.44
Class 3	Large lorry, trailers, heavy vehicles with 3 axles and mores	1.83
Class 4	Buses	1.93
Class 5	Motorcycles	0.96

4.2   Percentile Speed Data Analysis

(1) Percentile speed at location A
     (See Fig. 2, Table 3)
(2) Percentile speed at location B
     (See Fig. 3, Table 4)
(3) Percentile speed at location C
     (See Fig. 4, Table 5)

Fig. 2 Location A

Table 3 Percentile speed at A

Percentile speed	Speed of field data (km/h)	Posted speed limit (km/h)
Operating speed, V85	65.6	70
Design speed, V95	68.7	77
Obstructing speed, V15	49.9	–

Table 4 Percentile speed at B

Percentile speed	Speed of field data (km/h)	Posted speed limit (km/h)
Operating speed, V85	65.3	70
Design speed, V95	70.6	77
Obstructing speed, V15	40.0	–

Fig. 3 Location B

Table 5 Percentile speed at C

Percentile speed	Speed of field data (km/h)	Posted speed limit (km/h)
Operating speed, V85	74.9	70
Design speed, V95	82.6	77
Obstructing speed, V15	53.6	–

Fig. 4 Location C

4.3 Relationship Between Percentile Speed with Flow Rate

Based on the empirical data collected from the urban area, the line graph of speed percentiles show a descending trend in relation with increased in traffic volume per hour. The speeds drop tremendously for the both speed V95 and V15 with increase in flowrate. However, the reduction of speed for V85 is gently decreased with increasing of volume vehicles per hour (Figs. 5, 6 and 7).

4.4 Regression Equation

Based on the output from regression it can be interpreted via the following equation:

$$V85 = -6.6 - 0.00351 \text{ flowrate} - 11.4 \text{ width } L1 \\ + 37.5 \text{ width } L2 - 0.694 \text{ time} \tag{1}$$

Fig. 5 Relationship of V85 versus flow rate
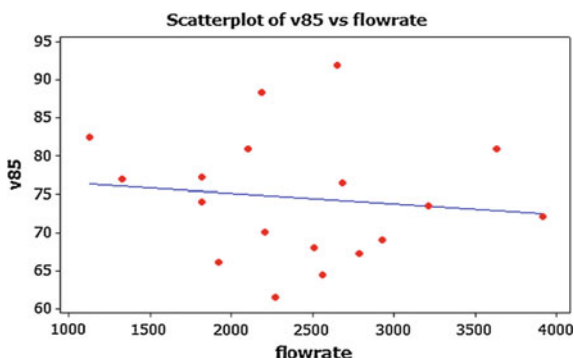

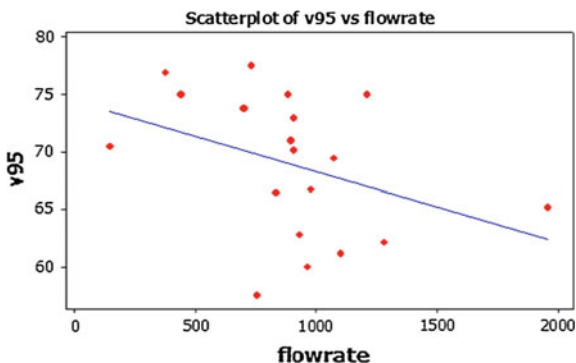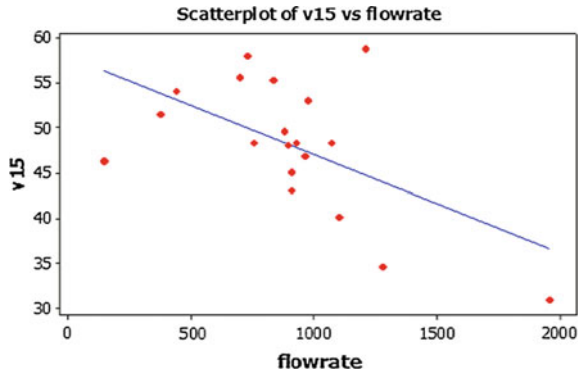**Fig. 6** Relationship of V95 versus flow rate

Fig. 7 Relationship of V15
versus flow rate

5 Discussion

5.1 Percentile Speed

The survey at point A was carried between 12.50 pm and 1.15 pm. Based on the tabulated data, the operating speed at 85th percentile is about 65.6 km/h which is lower than the posted speed limit at 70 km/h. In this case the difference of 4.4 km/h from the posted speed limit is not an issue as many regard their speed as safe and conform to the posted speed.

The speed at 95th percentile is 68.7 km/h which considered low. The design speed is normally 10 % higher than posted speed limit which is approximately 77 km/h. Like wise, the main reason for the low speed is partly due to a signalized junction at the downstream and the need of vehicles to accelerate thereafter after a temporary stop. Therefore, the accuracy of data taken for free flow condition is adversely affected by traffic temporary stoppage and acceleration at the signalized junction.

For better future, we recommend that the case study should be carried out further up from the junction whereby the vehicles are driving at their desire speed without any interference by control junction.

Meanwhile, at location B, the survey was carried during morning time between 9.00 am and 9.34 am where the speed at 85th percentile is 65.3 km/h which is lower than the posted speed limit at 70 km/h. At this location the difference is similar to the location where the speed difference is 4.7 km/h lower than the posted speed limit. However, the speed can be regarded as safe and conform to the posted speed.

However, the speed at 95th percentile is 70.6 km/h which is considered low. The design speed is normally 10 % higher than posted speed limit which is approximately 77 km/h. The reasons for the low speed is due to vehicles tend to stop when approaching a signalized junction at the upstream of the road. Therefore, the accuracy of data taken for free flow condition is affected by the slowdown and temporary stoppage at the signalized junction.

We recommend that the case study should be carried out further down from the junction whereby the vehicles are driving at their desired speed without any interference by control junctions.

At point C, the survey was carried out between 11.35 am and 12.15 pm. The analysis shows that at 85th percentile, the operating speed is 74.9 km/h which is higher than the posted speed limit at 70 km/h; hence, the difference is about 4.9 km/h. This simply indicates that there was an uninterrupted free flow of traffic though the speed taken at the T-junction merges to the road. This is due to provided auxiliary lane where the vehicles can merge to the main stream traffic without any interruption. Hence, the observed data indicate that they are not affected by traffic slowdown.

The speed at 95th percentile is 82.6 km/h which is essentially high compared to the design speed of 77 km/h. At this location we can analyzed that provision of enough lane width and auxiliary lane are the factors for the vehicles to move at comfortable speed and safe. Hence the road served its function as an arterial road.

In view of the aforesaid speed, it is recommended that the existing posted speed limit shall be increased to the speed taken at 85 percentile as the current speed limit is no more appropriate.

5.2 Relationship Between Percentile Speed with Flow Rate

Based on illustration a trend and correlation between speed at 85th percentile, 95th percentile, and 15th percentile with traffic flow rate at Jalan Meru, it can be analyzed that the arterial road is well functioning when vehicles move at V85 speed where the range of speeds are between 76 and 73 km/h. High frequency of vehicles travelling at V95 will immediately stop and cause high road density. This is due to the road capacity in terms of lane width are inappropriate and not suitable for vehicles to travel at high speed. Vehicle moving at low speed also will cause sudden stoppage as well as increase in the road density where the slow moving vehicles tend to back lock the traffic flow.

In view of the trends of the graphs, the existing Meru road can be concluded that it is provided with enough road width or capacity and acceptable interval of the access control with regard to operating speed at V85.

5.3 Regression Equation

Based on the regression equation, the data shows that the P value is more than 0.05 for predictor of flowrate, lane width L1, and time which shows that the values are

insignificant however for predictor of lane width, L2 indicate that it is statistically significant. With at least one of the predictor is significant the regression equation is acceptable. For the graph analysis equation for speed V85 it describes that the line is considered as a best fit with 82.65 % of confidence level. Hence, equation is conclusively reliable or has goodness of fit. On the other hand, the analysis of variance shows that P value is 0.001 which is relatively a low value, indicating precise observation made by our group.

6   Conclusion

The present study demonstrates the effect of geometry design on the speed of the vehicles. In this case study, it can be concluded that the operating speed of V85 at location A and B are lower than the posted speed limit. The speeds taken were interrupted by control device at the upstream and downstream of the traffic stream. While at location C, the operating speed of V85 is higher than the posted speed limit and since the speeds taken is not affected by any constraint. The speed limit at the location can be adjusted to suit the operating speed due to comfortable of the road with provision of sufficient lane width.

In order to obtain the optimum percentile speed of V85 within the design speed limit and to maintain the function of arterial road, it is essential that the access junction should be reduced by providing service road parallel to the Meru road or reduce the interruption of traffic flow by providing tunnel, flyover or interchange.

Based on the graph of V85, V95, and V15 versus vehicles flow rate, the trends show that the speed is decreasing as the road capacity increases. However, the line graph gradients are different for the three different speeds. The line graph of V85 versus vehicles per hour is gently sloping down compared to line graph of V95 and V15 which tremendously drops as the flowrate increase.

The regression analysis equation for V85 has been established and accepted to suit with our road condition. It is pertinent that in this study measurement of speed and traffic flow should be assessed under Malaysian road conditions. In our opinion, it is timely that our government to establish a road design guideline based on local road condition. More research should be carried out on the existing road in obtaining suitable and appropriate operating speed. Based on the operating speed we can establish our own design speed which is useful for further geometric design as well as improvise our road system.

References

1. "Highway Capacity Manual 2011 Malaysia," by Highway Planning Unit Ministry of Works Malaysia, 2–8.
2. Traffic Safety Radar Reference Manuals, Version 2.2. Philadelphi: Kustom Signals, Inc. MUTCD. (2010a, June 21).
3. Washington, D.C.: Highway Research Board, National Research Council. USLimits. (2010, August 7).
4. Berkeley: University of California Berkeley. Kustom Signals, Inc. (2007).
5. SKS Abbas, MA Adnan, IR Endut Exploration of 85th Percentile Operating Speed Model on Horizontal Curve: A Case Study for Two-Lane Rural Highways. Procedia- Social and Behaviral Science 16,352–363,2011 carriageway. In: Proc. of 38th UTSG annual meeting. Dublin, Ireland: Trinity College Dublin; 2006.
6. Elvik, R. (2012). Speed limits, enforcement, and health consequences. Annual Review of Public Health, 33, 225–238. doi: 10.1146/annurev-publhealth-031811-124634.
7. van der Horst, R., & de Ridder, S. (2007). Influence of roadside infrastructure on driving behavior: Driving simulator study.
8. Georgia Department of Transportation. (2012). Traffic control - speed limits: Establishment of speed zones.
9. Transportation Cabinet. (2012). Traffic operations guidance manual. Commonwealth of Kentucky.
10. "A Guide on Geometric Design of Roads," by The Road Engineering Association of Malaysia (REAM – GL 2/2002);

Relevancy of the Installed Posted Speed Limit Based on the Operating Speed Study on Multilane Highway

Megat Nazrin Helmy Shah Nazri, Nur Atikah Ahmad, Nurul Iman Rahim, Afiqah Zakaria, Tuan Badrol Hisham Tuan Besar, Muhammad Akram Bin Adnan and Norliana Binti Sulaiman

Abstract The relationship between the two speeds which are the posted speed limits design speed principle and actual operating speed are among the crucial factors in determining appropriate speed limits in a speed zone. This research paper investigates the speed trend at three different spot locations along Jalan Meru Multilane Highway. The spot speed and traffic volumes data were collected at these spot locations with various roadway width and shoulder width. Then, the 85th percentile speeds were computed at each location and the relationship between flowrate and width of the roadway were established. The regression analysis of the operating speed indicates that the percentage of operating speed exceeded the posted speed limits compared to the existing speed limit value. The relationships established here between operating speed and posted speed limits may be expected to provide some quantifying basis for transportation agencies to set posted speed limits in speed with the similar geometric zones. The end of this study may help the Authority and the Department of Transportation and its districts to quantify and revise the speed limits. This offered more significant, result oriented, technical judgement and insights in setting the appropriate speed limits.

Keywords Posted speed limits · Operating speed · 85th percentile speed · Regression analysis

1 Introduction

As Malaysia is one of the developing countries, road safety is addressed as one of the critical problems. From the number itself, there is 4 % annual increment in 80 s for road traffic fatalities cases, and with the growing number from 5 to 9 % in 90 s.

M.N.H.S. Nazri · N.A. Ahmad · N.I. Rahim · A. Zakaria · T.B.H.T. Besar (✉)
M.A.B. Adnan · N.B. Sulaiman
Faculty of Civil Engineering, Universiti Teknologi MARA, Shah Alam, Selangor, Malaysia
e-mail: tuan.badrol.hisham@gmail.com

As the figure for the first decade of millennium year, there was an incremental of 2 % for the year 2000 until 2009. There were 6,872 fatalities which were recorded by the Royal Malaysian Police [1].

Setting a posted speed limit, which could balance travel efficiency with safety, is an important part of the highway safety management. Thus, the construction of possible reference as guideline in establishing a speed limit can help to maximize travel efficiency and safety for highways in Malaysia. Using design speed as a primary factor in selecting a speed limit has been a common practice since the opening of the first highway in the country. This has been inquired in recent years, mainly due to the definition of design speed for highways. The speed limits dictated by the design speed at a single location with a challenging geometric element for a long stretch of highways have been under intense public scrutiny where it is also known to be similar to a part of the point in the highway that represents the whole part of it, especially at the venue where there is a difference between operating speeds and speed limit regardless of it is higher or lower limits [2]. The difference between these two limits and rules to comply with the speed limit were mostly being omitted and hence, this will diminishes the compliance with the traffic law.

2 Literature Review

Speed is a fundamental factor in transportation engineering; it is often denoted by different terms while applied in different situations such as a design criterion, a measure of the level of service and as an operational control parameter [3]. 'Posted speed limit refers to publishing the posted speed limit value. It is a value that distinguished the speed limit with the design element such as curve radius (with physic equation, running speed and operating speed).

Alternately, traffic flow is an influence by the posted speed limit placed beside the roadside in considering the traffic safety. Posted speed limit can be considered as an early requirement to the road traffic system. Therefore, significant relationship among posted speed limit, in relation to the speed and traffic performance factors would be well meant. As for line of sight, roadways or tangents the actual operations speed of the vehicle is reaching the ceiling of the speed limit. Thus, the 85th percentile speed of the distribution is gathered by observing the most frequently operating speed in relation to a particular location or geometric feature [4].

In addition, there is some highway generalized single value as speed limit for along the whole line, without placing any consideration for difference in highway facilities. It is not only the economical value but also safety reason should be considered. Even though many researcher have started studying the problem of speed limit criterion from the point of operation speed, design speed and line type, it is still lacking a unitary, reasonable method for formulating the value of speed limit,

and the speed limit basis is insufficient and nonstandard [5]. A road can be considered as safe road when it can achieved uniform characteristics, it can avoid sudden changes in operating speed [6].

As indicated by many findings from previous research, it can be considered effective to study posting speed limits based on a statistical analysis by observing the operating speeds. Institute of Transportation Engineers (Technical Committee) [7] had reviewed and noticed, 85th percentile speed as an important factor to be considered in determining the speed limits in reference to the Unites States with 99 agencies. It was also found that other factors such as development by the road side, previous experiences on the accident and geometry of the road itself also should be considered. This has lead to deviation of 5–10 mph of 85th percentile with the reason of politics, accident, roadway area and roadway geometry with the value of 33 %, 13 %, 11 % and 9 % respectively. Speed zone guideline [8] addressed the difficulties of selecting speed limit. It has recommended that a speed limit should be established based on an engineering study. The study includes reevaluation at a highest interval of every 5 years for changes. The speed limit should be applied with an incremental of 5 mph to the 85th percentile speed. A thorough study was completed for a National Highway Cooperative Research Program [9] summing up that strong inter-speed-connection between design speed, operating speed, and posted speed limit are desirable, and that these connections should be adapted on design and build roads that engendered the desired operating speed for a facility.

All in all, the speed limit should be credible, consistently applied and as for the users; it must also be compatible with their expectations.

3   Methodology

To obtain the operating speed under different speed limits, it is essential to identify what exactly is the occurrence in the real situation and this requires the gathering of the individual vehicle speeds on highways in a non-intrusive manner. Focusing on the safety of the researcher's crew together with the data validating process, Laser Gun was used as a tool for data collection instrument to align it to the purpose. The ease of use of the equipment provides higher data accuracy and is also less intrusive. Digital traffic counter was used to collect traffic volume continuously along the hours. It is used to differentiate five classes of vehicles during the observation. Roller meter was used to measure the lane width and lateral clearance. The minimum duration of data collection was four hours during regular weekdays. However, due to unavoidable schedule, the data collection had been conducted on weekend, dated 11 April 2015 (sunday) starting from 9.00 a.m. until 1.30 p.m. with the traffic condition that is at or closed to free-flow speed condition. The free-flow speed is the term used to describe the average speed that a motorist would travel if
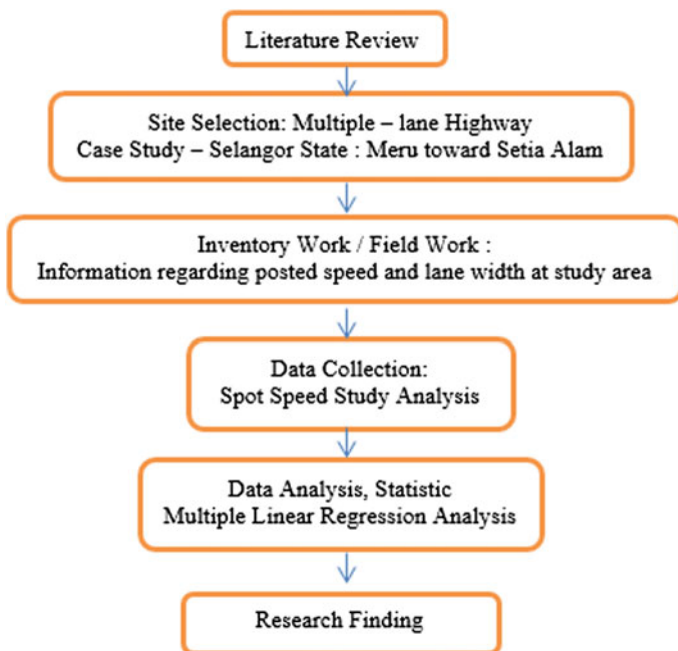
Fig. 1 Flowchart of research process

there were no congestion or other adverse conditions (such as bad weather). The overall research is illustrated by the research flowchart as shown in Fig. 1.

3.1 Selection of Survey Location

With two lanes in every direction, Jalan Meru towards Setia Alam in Klang, Selangor, was selected for the study, and is 1.4 m along from location A until the Location C as in Fig. 2. The road was designed to perform as minor arterial road, and currently it is not functioning as what it was designed to be.

Therefore, the intention of this study is to record the speed characteristics under prevailing conditions at a specific location along that roadway. This road is designed based on the road design standard in Malaysia under Urban group (U4) and it functioned as the minor arterial with speed limit of 70 kph as per REAM guideline [10]. Based on the inventory study, the road was designed with 70 kph posted speed along the roadway at all these three locations. Three locations are selected along the roadway namely location A, location B and location C. The study area was characterized as partially access control with signalized junction and near to commercial and residential area with new developing township.
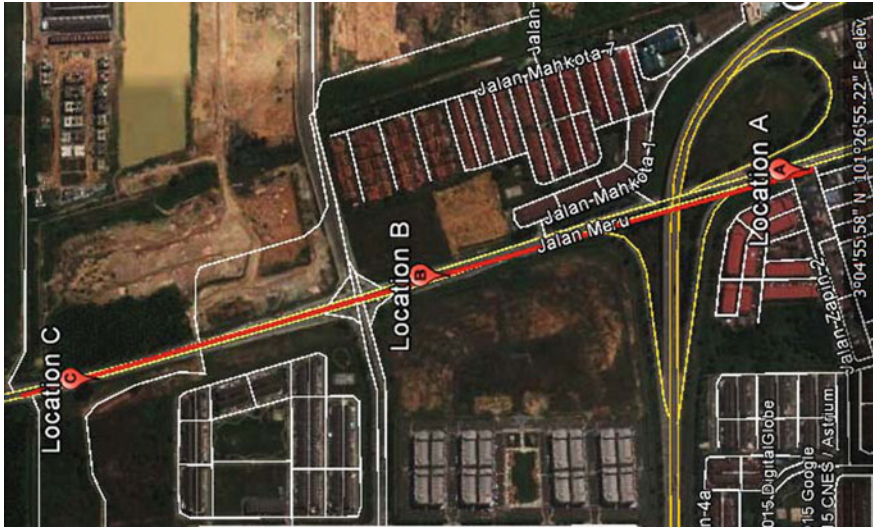
Fig. 2 Location A at Jalan Meru

3.2 Collection of Speed Data

Using Laser Gun, the speed of vehicles can be obtained for the selected location and considered for spot speed study which is the instantaneous speed of vehicle passing a certain location. In this paper, spot speed can be collected by a velocity speed gun. According to the requirements for spot speed surveys, the sample size of the survey is more than 200 in order to achieve 95 % confidence level and accuracy of data. The actual samples collected are 306, 165 and 416, respectively, for location A, B and C. The data were collected only for the free flow lanes and the traffic volumes are counted for both lanes with average time taken at each location is 1 h. For location A, the speed of vehicles collected are just for those passing through signalized junction, for location B the speed of vehicles collected are of those approaching signalized junction and change of manoeuver of vehicles to auxiliary lane for left turning and for location C the speed for the data collection are for those which are near to left turning which might be affected from the entry of vehicles from left.

4 Data Analysis, Statistic and Regression Modelling

4.1 Data Screening and Reduction

The raw data were manually recorded on paper basis and then transferred to Microsoft Excel and were then saved as the event data. The data observed at the

location of study includes speed, traffic volume, lane width and time. The 85th percentile speed was measured under free-flow conditions. It is a primary and renowned consideration in setting the speed limits. [11]. Followed by screening with the aim to remove the outliers residing with the data collected. This data characteristic which had been collected during the weekends might be having significant difference with the data collected on weekdays due to the difference in time or period. The multiple linear regression analysis was used to develop a model that will represent the speed characteristics of the study area. To analyze the 85th percentile speed, 95th percentile speed and 15th percentile the computer software named advanced statistical software, Minitab v16.0 was used.

4.2   Speed Statistical Analysis

According to the data extracted each free-speed sample of the 85th percentile. Table 1 represents a summary of the site statistics, including the mean speed for 85th percentile as the operating speed, 95th percentile for design speed and 15th percentile for obstruction speed. It can be seen that based on Table 1, 2 out of 3 locations with 85th percentile speed exceeded its corresponding posted speed limit which is 70 kph.

4.3   Regression Analysis

Data analysis and model development using advanced statistical software, Minitab is particularly intended to determine the descriptive statistics for the independent and dependent variables after removing outliers. The main objective is to determine the correlation analysis, which is used to measure the degree of linear relationships between two variables. A series of multiple linear regression were also applied to the data to identify the combination and relationship between the flowrate and speed (design speed and speed limit) using Minitab Software. The P-value and R-sq would be used to select the candidate's variable, and also for models with higher R-sq (>40 %) and p-value significant ($p < 0.05$). This multiple regression analysis is an extension of simple linear regression to allow more than one independent variable and it can be applied when several predictor variables exist. ($X1$, $X2$, $X3$…Xn).

Table 1 Mean Speed for 85th percentile, 95th percentile and 15th percentile speed

Location	85th percentile speed (kph)	95th percentile speed (kph)	15th percentile speed (kph)
A	71	76	50
B	65	69	43
C	78	82	51

Table 2 Stratification of speed percentile, flowrate, lane width, time data for each location

Loc.	V85	V95	V15	Flowrate (pcu/h)	Width $L1$ (m)	Width $L2$ (m)	Time (min)
A	74	78	51	1460	3.5	3.5	11:30–11:34
A	68	71	49	3635	3.5	3.5	11:35–11:39
A	74	78	50	1417	3.5	3.5	11:40–11:44
A	72	77	50	2346	3.5	3.5	11:45–11:49
A	75	79	51	1206	3.5	3.5	11:52–11:54
A	68	71	49	3258	3.5	3.5	11:55–11:59
A	70	76	50	2697	3.5	3.5	12:00–12:04
A	70	76	51	2627	3.5	3.5	12:05–12:09
A	68	71	49	3422	3.5	3.5	12:15–12:19
B	65	69	43	1969	3.3	3.3	12:46–12:48
B	67	68	45	2197	3.3	3.3	12:48–12:50
B	64	68	45	2854	3.3	3.3	12:51–12:53
B	66	68	45	2594	3.3	3.3	12:53–12:55
B	68	71	43	1778	3.3	3.3	12:55–12:57
B	56	62	38	3786	3.3	3.3	12:57–12:59
B	65	67	44	2103	3.3	3.3	12:59–1:01
B	54	58	44	3266	3.3	3.3	1:01–1:03
B	60	63	36	3271	3.3	3.3	1:05–1:07
C	76	82	50	3222	3.5	3.5	9:06–9:09
C	80	82	53	2934	3.5	3.5	9:10–9:14
C	74	80	49	3315	3.5	3.5	9:15–9:18
C	74	80	50	3395	3.5	3.5	9:19–9:22
C	80	81	52	2569	3.5	3.5	9:23–9:27
C	80	82	53	2624	3.5	3.5	9:28–9:31
C	80	82	52	2958	3.5	3.5	9:32–9:35
C	78	80	51	2998	3.5	3.5	9:36–9:40
C	80	83	53	2988	3.5	3.5	9:41–9:45

The analysis provides the explanation of dependent variable Y which will be presented by the 85th percentile speed for this case as per Eq. (1).

$$Y = \int (X1, X2, X3) \text{ as V85} = \int (q, w, L) \tag{1}$$

where

Y	is the response variable
$X1, X2, X3$	are the predictors
q	is the flow rate
W	is the lane width; and
L	is the length of mid block.

Table 2 shows the result of the extraction from Microsoft Excel from each table column of the raw data for location (Loc), speed (V85, V95, V15), lane width (Width $L1/L2$), time (Time) and the calculated flowrate (Flowrate) and each percentile of speed used to be analyzed using multiple regression analysis.

Based on the stratification data above, the multiple regression result for 85th percentile speed shows that the predictor P-probability for flowrate is 0.046, which is less than 0.05 and thus, this implied that the predictor is significant in describing the 85th percentile speed. Meanwhile, the value R-sq value is 67.2 % which is more than 40 % and this showed that the multiple linear graph curve fits well. Table 3 explains the result from the multiple regression analysis. The equation itself indicates that; once the speed increases, thus the flowrate will be decreased by which is indicated by the negative sign for flowrate which is −0.00258 flowrate. The summary of the results is as shown in Table 3.

The multiple regression equation for 85th percentile speed

$$V85 = -130 - 0.00258 \, \text{Flowrate} + 60.3 \, \text{Width} \, L1 \tag{2}$$

Same for the analysis of 95th percentile and 15th percentile speed, it is shown that the predictor P-probability for flowrate are 0.048 and 0.045, which are less than 0.05 and thus indicating that the predictor is significant in describing the 95th percentile speed and 15th percentile speed, respectively. Meanwhile, the R-sq value are 73.6 and 81.2 % which are apparently more than 40 % and this denotes that the multiple linear graph curve fits well for 95th percentile speed and 15th percentile speed respectively. The summary of the results is demonstrated in Tables 4 and 5.

Table 3 Result of multiple regression analysis for 85th percentile speed

Predictor	Coef	SE Coef	T	P
Constant	−129.54	30.46	−4.25	0.000
Flow rate	−0.002578	0.0012	−2.10	0.046
Width $L1$	60.306	8.869	6.80	0.000

Table 4 Result of multiple regression analysis for 95th percentile speed

Predictor	Coef	SE Coef	T	P
Constant	−131.31	26.37	−4.98	0.000
Flow rate	−0.002208	0.0010	−2.08	0.048
Width $L1$	61.603	7.678	8.02	0.000

Table 5 Result of multiple regression analysis for 15th percentile speed

Predictor	Coef	SE Coef	T	P
Constant	−90.79	14.10	−6.44	0.000
Flow rate	−0.001199	0.0005	−2.11	0.045
Width $L1$	41.367	4.106	10.07	0.000

Fig. 3 Graph of percentile speed for 85th, 95th and 15th versus flowrate
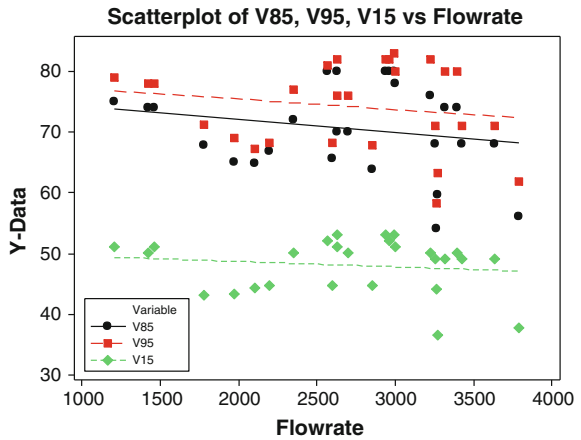
The multiple regression equation for 95th percentile speed

$$V95 = -131 - 0.00221\,\text{Flowrate} + 61.6\,\text{Width}\,L1 \tag{3}$$

The multiple regression equation for 15th percentile speed

$$V15 = -90.8 - 0.00120\,\text{Flowrate} + 41.4\,\text{Width}\,L1 \tag{4}$$

Figure 3 explains the results from the multiple regression analysis equation obtained above and it also demonstrates the 85th, 95th and 15th percentile speed versus flowrate and it indicates that the speed is intended to increase vice versa for the flowrate and it tend to decrease and is in line with speed-flow relationship theory.

5   Discussion

From the result, it can be observed that operating speed at Location C gives the highest speed that is 78 km/h if to be compared to Location A and Location B with 71 km/h and 65 km/h, respectively. It is because at Location C, vehicles start to accelerate from a signalized junction and within 200 m, vehicles tend to speed up to gear 4 or 5 which gives the drivers a desire speed to achieve according to their comfort. Although at Location A vehicles also start to accelerate from a signalized junction, but within 100 m length, the speed of vehicles tends to be a bit slower compared to vehicles speed at location C. As for Location B, the slowest operating speed is obtained as the drivers tend to slow down their vehicles due to fact that they are approaching a signalized junction.

Other than that, lane width also gives an impact to the operating speed of vehicles along Jalan Meru towards Setia Alam. Location B has the smallest lane

width which is 3.3 m thus giving less comfort to the driver to drive in high speed compared to vehicles at Location A and Location C. Even though the lane width at both Location A and Location C are similar which is of 3.5 m, the operating speed at Location A tends to be slower than at Location C. This is due to existing auxiliary lane that is an acceleration (AC) lane at the spot location which then give a 'shy lane to vehicles especially at the fast lane and thus will make them to slow down their vehicles to avoid the vehicle from the auxiliary lane. As for Location C, the speed is effected by the road condition such as bulging, which occured at the spot location.

Lastly, duration of time during this spot speed activity being conducted also contributed to different recorded operating speed. As for example, Location B had the slowest operating speed and it is also due to the time factor as it is done during noon. During that time, the traffic volume is higher due to peak hour, which is lunch hour on weekend compared to the conducting time at Location C which is at 9.00 a.m. and Location A at 11.00 a.m.

6 Conclusion and Recommendation

It can be concluded that from this study, the operating speed at Jalan Meru which represents the 85th percentile speed is inconsistent with the posted speed limit which 70 kph. The roadway selected for the case study is also not relevant to apply the same posted speed limit. The multiple regression analysis also had indicated that the operating speeds for the 3 locations vary with each other and same goes to the road configuration which is the lane width itself that did not appear to be consistent for the 3 locations although it is along the same roadway stretch. Based on the result, it is indicated that the Design speed, 95th percentile speed is higher and thus this should be an indicator that the road was not designed based on the design standard for the road as per stated in the REAM Guidelines. Thus, the posted speed limit should be increased for this road, along from location A to C to be consistent in order for it to be easier for the road users to drive in consistent speed limit and the road configuration also must be improved according to the road design standard.

Several recommendations are proposed for further research to fully incorporate the 85th percentile in design standard of road in Malaysia. The recommendations presented as follows:

- It is suggested to collect more operating speed data for longer road distance in order to identify the actual posted speed limit as for this study, only 3 locations were involved and did not truly represented the operating speed if to be compared with the posted speed limit.
- Data collection should be done on weekdays as it will represent the actual operating speed and it also need to be taken during peak hour (7.00 am to 9.00 am) which in return will give more accurate result.

- Road configuration identified for this study was only the lane width. For future research, additional info should be identified such as the width of additional lane (auxiliary lane) and should be taken into account.
- Reasoning behind the posted speed limit is related not only to the operating speed but also to design speed, geometric element, accident data and other factors.

References

1. Royal Malaysian Police, Annual road accident statistic, Bukit Aman, Kuala Lumpur, 2009.
2. S. Wu, X. Sun, Y. He, and T. Xu, "Research on coordination between operating speed and posted speed limit on clssified highway," CLEM 2010: Logistics fro sustained economic development,ASCE, 2010.
3. Yang, L. *Driver Speed and Acceleration Behaviour on Canadian Roads*. (Unpublished Msc's thesis). Carleton University Ottawa, Ontario, Canada, 2007.
4. D. Zhao, "Brief talks on relationship between running speed and design speed", Shanxi Architecture, 35(30): 285, 2009.
5. X. Li and X. Wang, "Determination method of freeway speed limitation from accident prevention", ICTE, ASCE, 2013.
6. SKS Abbas, MA Adnan, IR Endut Exploration of 85th Percentile Operating Speed Model on Horizontal Curve: A Case Study for Two-Lane Rural Highways. Procedia- Social and Behaviral Science 16,352–363,2011.
7. ITE, " Survey of speed pratice" ITE Infromation Report, Institute Transportaion Engineers, Washignton, DC, Technical Committee (97–12), 2007.
8. K. Fitzpatrick, P. Carlson, A. Marcus, A. Brewer, M.D. Wooldbridge, and S.P. Miaou, "Design speed, post speed and operating speed practices", 2003.
9. NCHRP Report 504, " Design Speed, and posted speed pratices", 2003.
10. Road Engineering Association of Malaysia (REAM), REAM Guideline 2/2002, "A Guide on Geometric Design of Roads", Shah Alam, Malaysia, 2002.
11. NHTSA Traffic Safety facts, National Centre for Statistics and Analysis, Report DOT-HS-810-837.U.S. Department of Transportation, 2006.

Assessing Pedestrian Behavior and Walking Speed on Staircase: A Review

Mohd Khairul Afzan Mohd Lazi, Masria Mustafa, Zanariah Abd Rahman and Nur'Aadila Binti kaman

Abstract Staircases that transport pedestrians from one level to another are important. Pedestrian behavior and walking speeds on staircases must be understood in order to make sure the level of service for the facilities being constructed for the traveler are to their maximum satisfaction. The level of service is based on four criteria that comprise horizontal speed, flow rate space, average, and volume to capacity ratios. In order to achieve good services, a few other aspects that also need to be highlighted during the design and planning stage are direct connection, security, public character, durability, appropriate accessibility, safety, compatibility, and cost-effectiveness. The selection of vertical walking facilities is a result of the relations between pedestrians' rational conclusion making and characteristic behaviors with the mish mash of external and internal factors. All the aspects discussed must be taken note of so that large reconstruction or renovation costs can be avoided in order to achieve the best service for pedestrian facilities. Good planning and design are cheaper than reconstruction or renovation cost. In addition, the effort toward promoting the use of staircases for pedestrians can also be fulfilled with the comfort, safety, and fun of using a staircase compared to escalator. This can give rise to a healthier life, reduce cost of energy, and also support green technology with sustainability aspect; economy, social and environmental.

Keywords Pedestrian · Behavior · Staircase · Ascending · Descending · Walking speeds

M.K.A.M. Lazi (✉) · M. Mustafa · Z.A. Rahman · N.B. kaman
Faculty of Civil Engineering, University of Technology MARA (UiTM),
Shah Alam, Malaysia
e-mail: tmm_afxan@yahoo.com

M. Mustafa
e-mail: masria@salam.uitm.edu.my

Z.A. Rahman
e-mail: zanariah@salam.uitm.edu.my

N.B. kaman
e-mail: dylli586@yahoo.com

1   Introduction

Every social trip begins and finishes with walking, although walking is not usually considered a transportation mode. Even nowadays in the mechanized world, inter-modal transportation and short trips in cities depend on how important movement and walking are, which are impossible to duplicate. In addition, the constantly growing urban population, urbanization, and air pollution, along with the constraints on the percentage increase of vehicles on road, have served to commercialize the natural mode of transportation. In least developing countries, on the other hand, poor traffic management, scarcity of transportation, and less ability to bear transportation fares forces a significant portion of the urban inhabitants to walk long distances. Thus, pedestrianization has turned out to be part of the sustainable modern urban design, where convenient, pollution-free, safe, and comfortable pedestrian facilities are ensured [1]. In structures such as deep underground terminals, deep underground parking area, skyscrapers and huge passenger ships, stair walk speeds can have a significant influence on the assessment times. This is because for most inhabitants for most of the time movement is spent on stairs, either climbing stairs as in deep underground stations, large passenger ships, and underground car park evacuations or down stairs, as in large passenger ships and multi-storey building evacuations [2]. Stair walking is a challenging locomotor mission, and visual information regarding the steps is considered serious to safely walk on the stairs [3].

Most public fitness physical activity courses of action now inspire society to look for a chance to accumulate physical activity all through the day. Climbing stairs in lieu of riding escalators is a key opportunity to take in good health selections that encourage active living [4]. When it comes to getting a great workout, with such numerous workout selections out there, we sometimes overlook the obvious. Climbing stairs is one the most effective and versatile behaviors to workout, no matter what the individual fitness level. Climbing real stairs is good antiquated exercise. Climbing stairs also consists of all fitness components, including anaerobic and aerobic cardiovascular fitness, endurance, strength, balance, coordination, and agility [5].

An appropriate guesstimate of pedestrian speed-flow-density connection is of vital importance, because such relationships are important in developing beneficial tools for improving and analyzing pedestrian facilities in terms of safety and efficiency. To construct walking friendly urbanization, which should correspond to the capacity of pedestrian facilities and the equilibrium of pedestrian demand, proper assessment of local pedestrian flow characteristics and travelling behavior is essential [1]. Along with the increase in pedestrians, the service level in some existing urban pedestrian facilities is greatly decreased by interweaving and crowding pedestrian flow. How to improve the transfer efficiency of pedestrian through optimizing the organization of pedestrian flow has become an interesting topic. In the past years, scholars at home and abroad have achieved great progress in researches on characteristics and evaluation law of weaving behaviors of pedestrian flow [6].

2 State of Art

2.1 Staircase

Stairs can work as pedestrian connections, to reduce walking journeys in places where blocks are huge or where the path system is discontinuous [7]. Staircase is the facility for the vertical transport of pedestrians. However on the stairways, pedestrians are required to use climbing effort. The pedestrian flow on the staircase is bidirectional. In order to increase the staircase capacity, yellow directional floor markings or handrails are commonly employed at some congested stations to separate the pedestrians. The pedestrian movements on staircase are classified into movements in a descending direction and movements in ascending direction. The movement on walkways leading to staircase was also considered because of the sudden change in gradience [8].

2.2 Attributes of a Good Staircase

A few aspects need to be considered and given full attention in order to achieve high good services for pedestrians. Aspects such as security, public character, appropriate accessibility, direct connection, safety, durability, compatibility, and cost-effectiveness need to be highlighted during the design and planning stage. All contributions to security on making walkers feel protected as they pass through the connection, and visibility to and from the connector is sustained to make sure of "eyes on the path." Surface materials are stable and arrange for a rational walking surface over the course of the maintenance recycle and inspection. At compatibility aspect, the design of staircase will respect the environment and the existing condition [7].
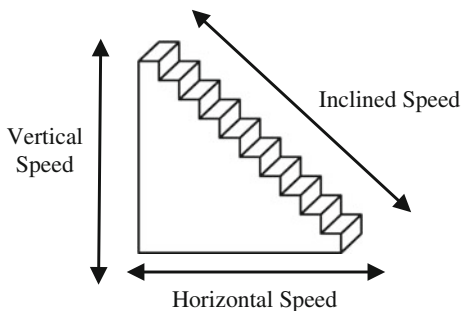
2.3 Pedestrian Level of Services at Staircase

Level of Service (LOS) is the analysis of each pedestrian facility type, because performance measures are different. LOS is measured based on four criteria, space, flow rate, average horizontal speed, and volume to capacity ratios (Fig. 1).

$$\text{Space} = \frac{1}{\text{density}} \tag{1}$$

$$\text{Pedestrian Flow Rate} = \frac{V_{15}}{15 * W_E} \tag{2}$$

where
V_{15} peak 15-min flow rate (p/15-min),
W_E effective width

The volume to capacity (v/c) ratios are based on a staircase capacity of 49 p/min/m. Pedestrian volume may be measured in standings of the maximum number of travellers at staircase per hour. Till now, the physical maximum will unescapably require travellers to endure unpleasant levels of massing. As an alternative of using maximum, the conventional method is to measure capacity that meets a preferred level of service (LOS) [9]. The concept of LOS dates to [10], who established a six-category system for stairways. The system was constructed on crowding density measured in terms of the number of travellers per square metre (PSM). As traveller density increases, movements come to be more restricted and waiting turns out to be less pleasant. [10] categorized the six levels of service A to F with A as the most pleasant and level F the least pleasant. The [10] crowding levels are presented in Table 1. As can be seen, the critical densities differ from A to F.

LOS A describes an adequate region to select rapidity and pass leisurely moving walkers without restrictions. Limited conflicts happen when reverse flows appear. LOS B is an adequate region to freely select rapidity with some struggle in passing leisurelier moving walkers. Minor conflicts happen when reverse flows appears. LOS C is where rapidity is slightly limited due to the inability to pass leisurelier moving walkers. Reverse flows cause some conflicts to happen when reverse flows appear. LOS D is rapidity limited due to the inability to pass leisurelier moving

Table 1 Level of service for staircase

LOS	Unit	
	Flow (p/min/m)	p/m^2
A	≤16	<0.5
B	16–23	0.5–0.7
C	23–33	0.7–1.1
D	33–43	1.1–1.4
E	43–56	1.4–2.5
F	Variable	>2.5

Table 2 LOS criteria for staircase

LOS	Unit			
	Space (m²/p)	Flow rate (p/min/m)	Average horizontal speed (m/s)	v/c Ratio
A	>1.9	≤16	>0.53	≤0.33
B	>1.6–1.9	>16–20	>0.53	>0.30–0.41
C	>1.1–1.6	>20–26	>0.48–0.53	>0.41–0.53
D	>0.7–1.1	>26–36	>0.42–0.48	>0.53–0.73
E	>0.5–0.7	>36–49	>0.40–0.42	>0.73–1.00
F	≤0.5	Variable	≤0.40	Variable

walkers. Significant conflicts happen when reverse flows appear. LOS E is where rapidity of all pedestrians is reduced, intermittent work stoppage to be expected takes place. Serious conflicts happen when reverse flows appear. LOS F is completed interruption in pedestrian flow with a lot of stoppages. Forward progress is reliant on leisureliest moving walkers. For LOS A to E, the flow rate for passageways and access ways increases to a maximum. With further increase in massing, the flow rate turns out to be unstable and complete interruptions can take place. Most of the previous research preferred to refer to this LOS and are unexceptional, whereas new developed LOS thresholds based on the Institute of Transportation Engineers stairways standard have been prepared in Highway Capacity Manual 2000. These modified LOS criteria are to make sure that the basic equation of traffic flow is satisfied [9]. Table 2 refers to LOS criteria for stairways by Highway Capacity Manual 2000.

The description and condition for every categorized of crowding from A to F are still the same as [10], whereby the flow rate for passageways and access ways increases to a maximum. With further increases in massing, the flow rate turns out to be insecure and complete interruptions can take place.

3　Influencing Factor of Pedestrian Behavior

3.1　Pedestrian Mode of Choices

The choice of vertical walking facilities is the outcome of the relations between pedestrians' rational decision making and characteristic behaviors with the mish mash of external and internal factors. External factors mainly consist of facility characteristics and pedestrian route network characteristics. Pedestrian route network characteristics include redundancy among the routes and the number of routes available for pedestrians. Facility characteristics mainly consist of level of congestion, walking time, and walking distance. Internal factors mainly contain decision making mode, personal attribute, behavioral habit, familiarity, and travel purpose. Decision-making mode is separated into dynamic decision making and single-stage

decision making. The latter refers to travellers' decision on routes multiple times during the complete travel process, while the former refers to travellers' decision on travel routes only once at the beginning of the travel. The dynamic decision-making depends on specific traffic situations. Pedestrians usually make decisions based on one decision-making mode. Pedestrian choice is strictly connected to personal attributes and the main personal attributes considered take account of gender, age, and loading capacity of pedestrian carrying heavy things such as large luggage. Behavior habit primarily refers to the fact that pedestrians have the habit of avoiding conflict, selecting the fastest route, avoiding physical exertion, or following the line. Among these factors avoiding physical exertion is the main influence on a passenger's choice in the vertical direction. The degree of pedestrians' familiarity with the station can affect the decision-making mode and different travel purposes will have different impacts on the pedestrian behavior choice [11] (Fig. 2).

3.2   Staircase and Escalator

There is little doubt that the atmosphere in most advanced countries contributes to the overall obesity epidemic. Most open areas are designed to let walkers and
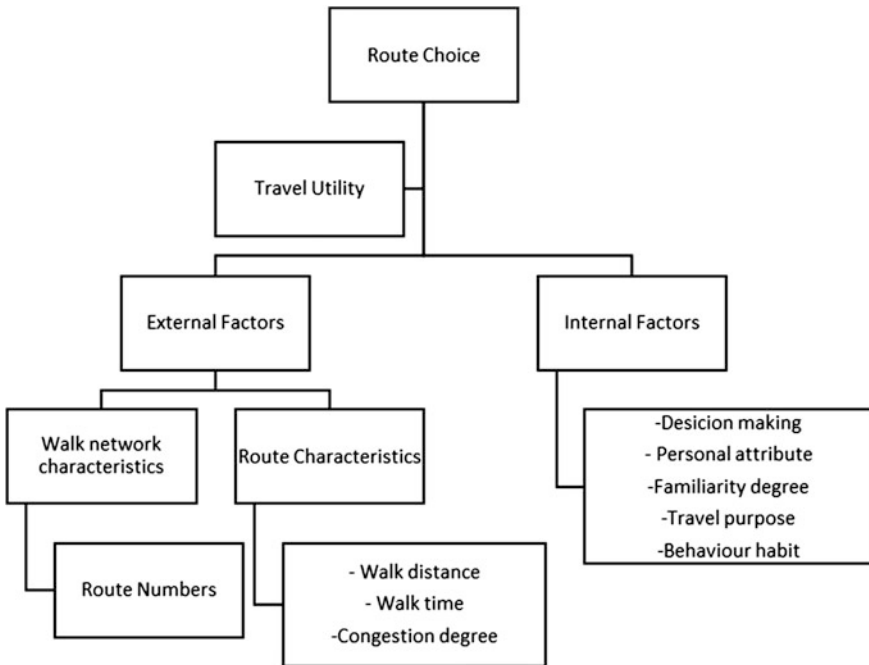

Fig. 2 Impact mechanism for pedestrian choice

travellers to travel efficiently through public places without using much energy. Most adults assume that they are always under time constraints and that they do not have time for exercise. It may be that planning public areas with easy, unbarred access to escalators, moving walkways, and elevator could increase pedestrian congestion and increase the use of more active selections in public [12]. Interestingly, it was reported that those who walked up two flights of stairs arrived at the upper landing faster than those who rode an escalator and were only slightly slower than those who walked up the escalator. Furthermore, several studies have shown that motivational signs encouraging stair use can significantly increase the number of people who choose to walk up the stairs instead of riding an escalator. Figure 3 also shows the patterns of stair and escalator use among pedestrians in times of low, moderate, and high traffic [4].

Pedestrians using escalators are more than pedestrians using staircases at all times during low traffic, moderate traffic, or even high traffic. Pedestrians using escalators comprise more than 60 % for all the time compared to those using stairs. However, the use of stairs increases when the traffic increases, whereas during high traffic, about 20.8 % of pedestrians choose stairs compared to that with during low density, it is only 11.2 %. The situation is the same worldwide, in the West or in Asia. [8] also found that pedestrians using escalator are higher compared to those using stairs. However, pedestrians using the staircase are higher in Asia compared to the West, due to the physical size of Asia which is smaller (Table 3).
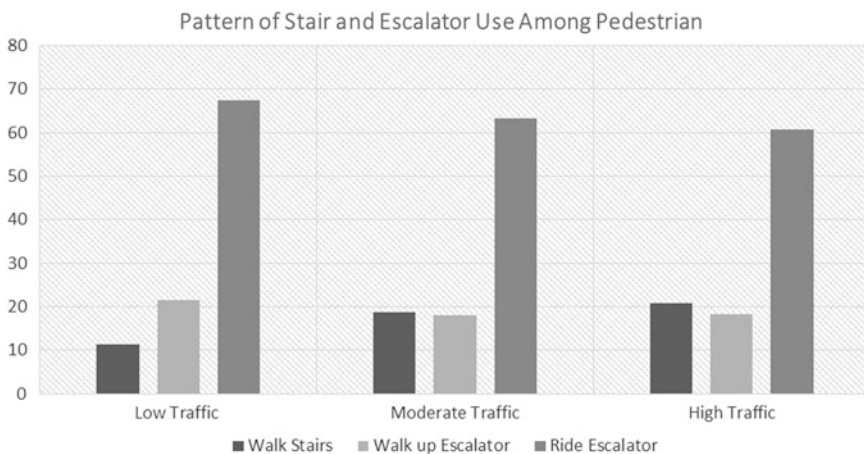

Fig. 3 Pattern of stair and escalator use among pedestrians in times of low, moderate, and high traffic

Table 3 Comparison of the capacities between Asia and the West [8]

Facilities	Capacity (p/m/min)	
	Hong Kong	London
Escalator (Up)	120	120
Escalator (Down)	120	120
Staircase (Up)	70	62
Staircase (Down)	80	68.3

Pedestrians also choose to get off from the train near the escalator more than near the staircase [11]. More interestingly, pedestrians prefer to use the escalator if the escalator stops, whereas [13] found that 32 % of pedestrians use the escalator even if there is breakdown.

3.3 Walking Speeds of Pedestrians

Walking speeds are affected by various factors such as trip purpose, personal (human) characteristic, staircase characteristics, environment, personal safety, and comfort and traffic density. Pauls and Markman [14] proved that the dimension of riser and tread also affect the walking speeds when 7-in. riser with 11.5-in. tread and 6-in. riser with 12-in. tread being used. The comparison is given in Table 4.

Pedestrians walk faster at both ascending and descending when using staircase than lower rise but larger tread compared to higher rise and smaller tread in order of safety and comfort factor. Pedestrians also have a habit of selecting the area for walking on staircase according to the staircase width characteristics. Yi et al. [15] proved that pedestrians choose to walk at the side of the staircase when the staircase use a large width (in the experiment used 3 m width of staircase), while when the staircase is narrow (1.5 m), they prefer to use the middle of the stairs.

Pedestrian speeds also differ according to the environment or according to the region of their stay. In short, Western and Asian people are different in their speeds.

Table 5 gives the ascending and descending speeds on staircase. It is concluded that Asians walk slower compared to the West. It believed that this due to their physical characteristic, wherein Westerners are bigger in size and taller compared to Asians. However, this is only when ascending the staircase because when looking at the descending speeds, the result is almost the same between the regions. Energy consumption during descending is lower than ascending, make the descent easy.

Table 4 Speeds observed, based on horizontal distance

	Feet per second	
	Descending	Ascending
7-in. riser and 11.5-in. tread	2.0	1.6
6-in. riser and 12-in. tread	2.4	1.8

Table 5 Pedestrian walking speeds on staircase in different countries

Author	Result		
	Country	Speeds (m/s)	
		Ascending	Descending
	Asian		
[16]	China	0.48	0.62
[17]	India	0.41	0.48
[18]	Hong Kong	0.43	0.60
	Western		
[19]	German	0.71	0.65
[20]	England	0.59	0.67

Table 6 Pedestrian speeds according to gender

Author	Country	Speeds (m/s)			
		Ascending		Descending	
		Male	Female	Male	Female
[2]	Korea	1.26	0.89	0.85	0.74
[21]	India	0.48	0.41	0.49	0.44
[22]	China	0.63	0.59	0.86	0.67
[23]	London	0.77	0.75	0.82	0.91

Pedestrians also show different speeds as regards gender factors. This is because gender also influences walking speeds on the staircase.

According to Table 6, whether ascending or descending, all male pedestrians are faster compared to female pedestrians except from London, whereas female pedestrians descend faster than males. Overall, Koreans ascend faster compared to other countries but male Chinese are leading when descending followed by London female pedestrians. However, Indians are the slowest while either ascending or descending for both female and male at staircase walking speeds. Pedestrian age also give a huge effect to the speeds of pedestrians as shown in Table 7 whether young, adult, or elderly.

Table 7 Pedestrian speeds according to age

Author	Country	Speeds (m/s)					
		Ascending			Descending		
		Y	A	E	Y	A	E
[20]	Birmingham, England	–	0.59	0.47	–	0.67	0.50
[21]	India	0.40	0.51	0.41	0.55	0.52	0.34
[22]	China	0.65	0.61	0.50	0.88	0.76	0.63
[24]	Pennsylvania, USA	–	–	0.50	–	–	0.52

Y Young, *A* Adult, *E* Elderly

Table 7 shows that adults are faster than the elderly at both ascending and descending. But young pedestrians are faster than adults in India and China except during ascending in India. Hamel and Cavanagh [24] only focus on elderly pedestrians and shows that this category of pedestrians descend faster than ascending.

4 Conclusion

It has been shown that pedestrian choice and speeds are various and are related to a country's culture, topographic, and also environment. This can be to some extent explained by the statement that the smaller Asian figure requires lesser amount of space for movement compared to the Western. However, this does not show whether the Asian or Western is faster because the results are various. Pedestrians who considered the use of energy for walking up the staircase will choose to use the escalator for ascending. Cheung and Lam [18] also suggested a consideration on appropriate design of the locations for staircase to reduce local congestions in order to increase pedestrian movement in the vertical link. One of the ways that can be considered to decrease relative delays is that the staircase should be located based on the pedestrian demand distribution in order to reduce congestion. A handrail should be introduced in the middle of the entry end of the staircase in order to reduce delays due to crossing struggles at the entry of the staircase. It is hoped that this study will further contribute to the field of pedestrian facilities planning for the design and improvement of facilities, especially staircase.

References

1. Rahman, K., Ghani, N., Abdul, Kamil, A., Abdulbasah, & Mustafa, A. (2013). Weighted Regression Method for the Study of Pedestrian Flow Characteristics in Dhaka, Bangladesh. *Canadian Center of Science and Education, 7*(4), 17–30. doi: 10.5539/mas.v7n417.
2. Choi, J.-h., Galea, E. R., & Hong, W.-h. (2014, Mar 2014). Individual Stair Ascent and Descent Walk Speeds Measured in a Korean High-Rise Building. *Fire Technology, 50,* 267–295.
3. Miyasike-daSilva, V., Allard, F., & McIlroy, W. (2011). Where do we look when we walk on stairs? Gaze behaviour on stairs, transitions, and handrails. *Experimental Brain Research, 209* (1), 73–83. doi: 10.1007/s00221-010-2520-z.
4. E. Andersen, & Adrian E. Bauman. (2011). The Effects of Commuter Pedestrian Traffic on the Use of Stairs in an Urban Setting. *American Journal of Health Promotion, 26*(1), 49–51. doi: doi:10.4278/ajhp.100202-ARB-39.
5. Vanderburg, H. (2009). Climbing stairs is good old-fashioned exercise (pp. BODY & HEALTH; Pg. B4).
6. Yao, L., Sun, L., Zhang, Z., Wang, S., & Rong, J. (2012). Research on the Behavior Characteristics of Pedestrian Crowd Weaving Flow in Transport Terminal. Mathematical Problems in Engineering, 2012, 9. doi: 10.1155/2012/264295.

7. Vanderslice, E. (1998). Portland Pedestrian Design Guide. Portland: The Pedestrian Transportation Program.
8. Cheung, C.-y. (1998). Pedestrian flow characteristics in the Hong Kong Mass Transit Railway stations. American Society of Civil Engineers, xvii, 142, [126] leaves: ill. (some col.); 130 cm.
9. Council, T. R. (2000). Highway Capacity Manual 2000 Chapter 18: Pedestrian. Washington, D.C.: Transportaton Research Board 2000 Executive Committee.
10. Fruin J.J (1987), "Designing for Pedestrian", Chapter 8.
11. Zhang, N., Zhang, Y., & Zhang, X. (2015). Pedestrian choices of vertical walking facilities inside urban rail transit stations. KSCE journal of civil engineering, 19(3), 742–748. doi: 10.1007/s12205-012-0331-4.
12. Eves, F. F., Lewis, A. L., & Griffin, C. (2008). Modelling effects of stair width on rates of stair climbing in a train station. Preventive Medicine, 47(3), 270–272. doi: http://dx.doi.org/10.1016/j.ypmed.2007.12.008.
13. Kinsey, M., Galea, E., Lawrence, P., Blackshields, D., Hulse, L., Day, R., & Sharp, G. (2010). Modelling Pedestrian Escalator Behaviour. In W. W. F. Klingsch, C. Rogsch, A. Schadschneider & M. Schreckenberg (Eds.), Pedestrian and Evacuation Dynamics 2008 (pp. 689–695): Springer Berlin Heidelberg.
14. Pauls, J., & Markman, H. (1988). Book Reviews. Fire Technology, 24(3), 279–285. doi: 10.1007/BF01038184.
15. Yi, M.-h., Na, W.-j., Hong, W.-h., & Jeon, G.-y. (2012). Pedestrian walking characteristics at stairs according to width change for application of piezoelectric energy harvesting. Journal of Central South University, 19(3), 764–769. doi: 10.1007/s11771-012-1069-3.
16. Qu, Y., Gao, Z., Xiao, Y., & Li, X. (2014). Modeling the pedestrian's movement and simulating evacuation dynamics on stairs. Safety Science, 70(0), 189–201. doi: http://dx.doi.org/10.1016/j.ssci.2014.05.016.
17. Shah, J., Joshi, G. J., & Parida, P. (2013). Behavioral Characteristics of Pedestrian Flow on Stairway at Railway Station. Procedia - Social and Behavioral Sciences, 104(0), 688–697. doi: http://dx.doi.org/10.1016/j.sbspro.2013.11.163.
18. Cheung, C.-y., & Lam, W., H, K,. (1998). Pedestrian Route Choices between Escalator and Stairway in MTR Stations. Journal of Transportation Engineering, 124(3), 277–285. doi: doi:10.1061/(ASCE)0733-947X(1998)124:3(277).
19. Kretz, T., Grünebohm, A., Kessel, A., Klüpfel, H., Meyer-König, T., & Schreckenberg, M. (2008). Upstairs walking speed distributions on a long stairway. Safety Science, 46(1), 72–78. doi: http://dx.doi.org/10.1016/j.ssci.2006.10.001.
20. Zietz, D., & Hollands, M. (2009). Gaze Behavior of Young and Older Adults During Stair Walking. Journal of Motor Behavior, 41(4), 357–365.
21. Shah, J., Joshi, G. J., & Parida, P. (2013). Walking Speed of Pedestrian on Stairways at Intercity Railway Station in India.
22. Jiang, C. S., Deng, Y. F., Hu, C., Ding, H., & Chow, W. K. (2009). Crowding in platform staircases of a subway station in China during rush hours. Safety Science, 47(7), 931–938. doi: http://dx.doi.org/10.1016/j.ssci.2008.10.003.
23. Fujiyama, T., & Tyler, N. (2004). An Explicit Study on Walking Speeds of Pedestrians on Stairs. Paper presented at the Procs 10th International Conference on Mobility and Transport for Elderly and Disabled People (TRANSED 2004), Hamamatu, Japan.
24. Hamel, K. A., & Cavanagh, P. R. (2004). Stair performance in people aged 75 and older. Journal of the American Geriatrics Society, 52(4), 563–567. doi: 10.1111/j.1532-5415.2004.52162.x.